Proceedings of the 11th Brazilian Congress of Thermal Sciences and Engineering – ENCIT 2006
Braz. Soc. of Mechanical Sciences and Engineering – ABCM, Curitiba, Brazil, Dec. 5-8, 2006

Paper CIT06-1057

NUMERICAL ANALYSIS OF THE AIR-DISPLACEMENT OF VISCOPLASTIC LIQUIDS IN CAPILLARY TUBES

Mônica F. Naccache
Pontifícia Universidade Católica do Rio de Janeiro, Rio de Janeiro - RJ 22453-900, Brazil
naccache@mec.puc-rio.br

Paulo R. de Souza Mendes
Pontifícia Universidade Católica do Rio de Janeiro, Rio de Janeiro - RJ 22453-900, Brazil
pmendes@mec.puc-rio.br

Abstract. *A numerical study of the displacement of viscoplastic fluids in capillary tubes by air is performed. This situation is encountered in many applications such as flow through porous media in enhanced oil recovery and coating flows. In these processes it is important to understand the mechanism of liquid displacement and to determine the amount of liquid left behind adjacent to the wall. The non-Newtonian fluid behavior alters the flow kinematics and changes the amount of mass left at the tube wall as compared to the Newtonian case. The numerical solution is obtained by solving the conservation equations of mass and momentum, via the finite volume method, and using the volume of fluid method to model the multiphase flow. In order to model the viscoplastic behavior of the liquid, the Generalized Newtonian Liquid constitutive equation was employed, in conjunction with a recently proposed viscosity function (de Souza Mendes and Dutra, 2004). Two rheological parameters appear in the dimensionless form of this equation, both of them obtained experimentally via least squares data fit. One parameter is the power-law index and the other one is the jump number, which gives the size of the shear rate jump that occurs as the stress reaches the yield stress while the viscosity undergoes a sharp decrease. The numerical results are obtained for unsteady inertialess flow. Velocity and stress fields, as well as the interface shape and the amount of mass left attached to the wall, are obtained for different combinations of flow and rheological parameters. It was observed that the thickness of the film of liquid left on the wall increases asymptotically with the flow rate and with the power-law index. Also, it is shown that it slightly decreases with the jump number.*

keywords: *Viscoplastic fluid, air-displacement*

1. Introduction

In this work, the displacement of a viscoplastic liquid by air inside a tube is analyzed numerically. This situation is found in several industrial applications, such as coating flows and flow through porous media. In these processes, it is important to determine the amount of liquid that remains adjacent to the wall. Fairbrother and Stubbs, 1935 and Taylor, 1961 determined experimentally the mass fraction deposited on the tube wall for a Newtonian inertialess flow. The mass deposited on the tube wall m is given by:

$$m = \frac{U - \bar{u}}{U} = 1 - \left(\frac{R_b}{R}\right)^2 \tag{1}$$

where U is the velocity of the tip of the interface, $\bar{u}$ is the mean velocity of the viscoplastic liquid far ahead the air-liquid interface, R is the tube radius and R_b is the bubble radius, as it is shown in Fig. 1. The results obtained by Taylor, 1961 were later expanded by Cox, 1962, and show that the mass deposited on the tube wall increases with the Capillary number ($Ca \equiv \mu U/\sigma$, where μ is the viscosity and σ is the surface tension) until an asymptotic value of 0.60, when the capillary number reaches a value of 10.

Lee *et al.*, 2002 and Quintella *et al.*, 2005 analyzed numerically the displacement of viscoelastic fluids by air, using the finite element method. The first ones analyzed the flow between parallel plates, while Quintella *et al.*, 2005 analyzed the flow in capillaries. Giavedoni and Saita, 1997 performed a literature review concerning the theoretical modelling of gas-liquid displacement between parallel plates. Goldsmith and Mason, 1963, Teletzke *et al.*, 1988, Bretherton, 1961 and Soares *et al.*, 2005 studied the liquid-liquid displacement inside tubes. The results obtained by Soares *et al.*, 2005 show the effects of different parameters on the interface shape and on the mass deposited on the wall.

In this work, a numerical analysis of the displacement of a viscoplastic liquid by air inside a tube, is performed. All the results were obtained for low Reynolds numbers and negligible surface tension. The effects of rheological and flow parameters on the mass deposited at wall, and on the flow pattern were obtained and discussed.

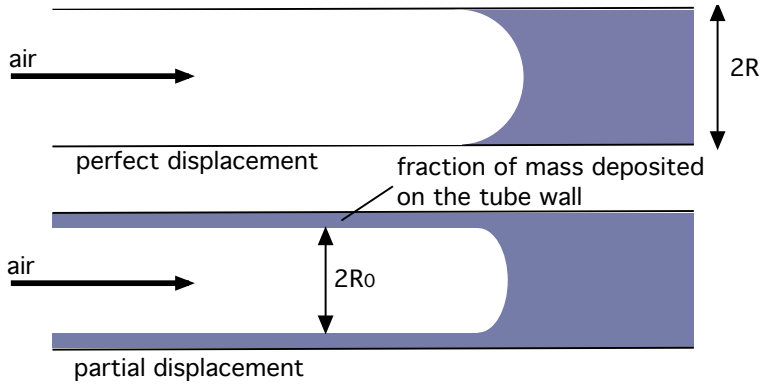

Figure 1: The geometry

2. Mathematical modeling

The flow under study is shown in Fig. (1). The multiphase flow was modeled by the volume of fluid method (VOF), that solves a set of mass conservation equations and obtains the volume fraction of each phase α_i through the domain, which should sum up unity inside each control volume. Therefore, if:

- $\alpha_i = 0$ - the volume does not contain the phase i;
- $\alpha_i = 1$ - the volume contains only the phase i;
- $0 < \alpha_i < 1$ - the volume contains the interface.

In this study, only two phases are present. Both fluids, air and the non-Newtonian liquid, are assumed incompressible. The multiphase flow was solved obtaining the solution of the conservation equations for a transient and laminar flow regime. The properties appearing in the transport equations ϕ, are given by:

$$\phi = \alpha_2 \phi_2 + (1 - \alpha_2)\, \phi_1 \tag{2}$$

The interface between phases is obtained by the solution of continuity equation for the volume fraction α_1:

$$\frac{\partial \alpha_1}{\partial t} + \mathrm{div}\,(\alpha_1 \mathbf{v}) = 0 \tag{3}$$

where $\mathbf{v}$ is the velocity vector. The volume fraction equation for the secondary phase 2 is obtained from the following constraint equation:

$$\alpha_1 + \alpha_2 = 0 \tag{4}$$

The momentum conservation equations for the mixture are:

$$\frac{\partial (\rho \mathbf{v})}{\partial t} + \mathrm{div}\,(\rho \mathbf{v}\mathbf{v}) = -\mathrm{grad\ p} + \mathrm{div}\left[\eta \left(\mathrm{grad}\mathbf{v} + \mathrm{grad}\mathbf{v}^T\right)\right] + \rho \mathbf{g} \tag{5}$$

where ρ is the density, p is the pressure, $\mathbf{g}$ are the components of the gravity acceleration vector and $\eta = (\alpha_1 \eta_1 + \alpha_2 \eta_2)$ is the viscosity of the mixture. In the problem analyzed, η_2 is the air viscosity and η_1 is the viscosity of the viscoplastic fluid, given by the model proposed by Souza Mendes and Dutra (2004), the SMD equation:

$$\eta = \left(1 - \exp\left(-\eta_0 \dot{\gamma}/\tau_0\right)\right) \left(\frac{\tau_0}{\dot{\gamma}} + K \dot{\gamma}^{n-1}\right) \tag{6}$$

In this equation, four rheological parameters appear: the plateau of constant viscosity for lower strain rates η_0, the yield stress τ_0, the behavior index n, and the consistency index K. It is worth mentioning that in this equation, when the stress reaches the yield stress, there is a sharp increase of shear rate with a constant stress. The shear rate jumps from $\dot{\gamma}_0 \equiv \tau_0/\eta_0$ to a much larger value $\dot{\gamma}_1 \equiv (\tau_0/K)^{1/n}$.

2.1. Dimensionless analysis

The governing dimensionless parameters were obtained choosing $\dot{\gamma}_1$ as the characteristic shear rate and τ_0 as the characteristic shear stress. Therefore, $\dot{\gamma}^* = \dot{\gamma}/\dot{\gamma}_1$ and $\tau^* = \tau/\tau_0$. It is also interesting to define a new rheological dimensionless parameter, the Jump number J, which gives a measure of the shear jump that occurs when $\tau = \tau_0$. Then,

$$J \equiv \frac{\dot{\gamma}_1 - \dot{\gamma}_0}{\dot{\gamma}_0} = \frac{\eta_0 \tau_0^{\frac{1-n}{n}}}{K^{1/n}} \tag{7}$$

Therefore, the dimensionless viscosity function, $\eta^* = \tau^*/\gamma^*$, is given by:

$$\eta = \left(1 - \exp\left[-\left(J+1\right)\dot{\gamma}^*\right]\right)\left(\frac{1}{\dot{\gamma}^*} + \dot{\gamma}^{*n-1}\right) \tag{8}$$

It is worth mentioning that when $J \to \infty$ the SMD equation approaches the Herschel-Bulckley model Bird *et al.*, 1987. The dimensionless conservation equations are given by:

$$\frac{\partial \alpha_1}{\partial t^*} + \mathrm{div}\left(\alpha_1 \mathbf{v}^*\right) = 0 \tag{9}$$

$$\frac{\partial \mathbf{v}^*}{\partial t^*} + \mathrm{div}\left(\mathbf{v}^*\mathbf{v}^*\right) = -\mathrm{grad}\ P^* + \frac{1}{Re}\mathrm{div}\left[\eta^*\left(\mathrm{grad}\mathbf{v}^* + \mathrm{grad}\mathbf{v}^{*T}\right)\right] \tag{10}$$

In the above equations, the dimensionless variables are defined as following:

$$t^* = t\dot{\gamma}_1 \qquad x^* = \frac{x}{R} \qquad r^* = \frac{r}{R} \qquad \mathbf{v}^* = \frac{\mathbf{v}}{\dot{\gamma}_1 R} \tag{11}$$

The dimensionless modified pressure is given by:

$$P^* = \frac{p}{\rho(\dot{\gamma}_1 R)^2} - \frac{g r^* \sin\theta}{\dot{\gamma}_1^2 R} \tag{12}$$

The Reynolds number is defined as

$$Re = \frac{\rho \dot{\gamma}_1 R^2}{\eta_c} \tag{13}$$

where η_c is the characteristic viscosity, calculated at the characteristic shear rate, $\dot{\gamma}_1$. Another important dimensionless parameter is the Capillary number, which is here defined as

$$Ca_p = \frac{\tau_0 R}{\sigma} \tag{14}$$

where σ is the surface tension.

3. Numerical solution

The numerical solution of the governing equations was obtained using the Fluent software. The finite volume method (Patankar, 1980) was used to obtain the conservation equations discretization, using a second-order upwind scheme for the momentum equation and a first-order upwind scheme for the volume fraction equation. The unsteady terms were discretized using an implicit fomulation. Staggered velocity components were employed to avoid unrealistic pressure fields and the PISO algorithm (Fluent-User's-Guide, 2006) was used, in order to couple the pressure and velocity. The boundary conditions were the no slip condition at tube wall, symmetry at tube center, constant inlet velocity and fully developed flow condition at outlet boundary. As the initial condition it was assumed that the tube was completely full of the viscoplastic liquid, and at the entrance the volume fraction of air was set equal to unity.

A non-uniform mesh was used in the numerical simulation, with 202 control volumes in the axial direction, and 40 control volumes in the radial direction. Some mesh tests were performed to validate the numerical solution and the mesh used. The Newtonian results were compared to the results obtained by Taylor, 1961. The error obtained for the mass deposited at the tube wall ($e = |m_{num} - m_{Taylor}|/m_{Taylor}$) was equal to 2%. The results for non-Newtonian cases were compared to results obtained with more refined meshes. The difference in the mass deposited at the tube wall, between the mesh used and a 302×60 mesh, was equal to 3%. Another important parameter in the numerical solution is the time step. Some instabilities were observed for higher values of time steps. In the results obtained in this work, the time steps used varied from 10^{-4} to 10^{-5} s. However, it is worth mentioning that the value of mass deposited has shown to be very sensitive to the numerical solution parameters. In some cases, a reliable solution could only be achieved with very low time steps and very strong convergence criterium, leading to extremely large CPU times.

All the numerical results were obtained for negligible surface tension, or $Ca_p \to \infty$. Convergence problems were observed for finite capillary numbers.

4. Results and discussion

All the numerical solutions were obtained for a ratio of tube diameter and tube length equal to 20, since the flow pattern had became invariant before this point. The effects of some governing parameters, on flow pattern and on the amount of mass deposited at wall, were investigated. All the results were obtained for low Reynolds numbers and infinite Capillary numbers. Its worth mentioning that the dimensionless mean entrance velocity (u^*) and the dimensionless developed wall shear stress (τ_w^*) are equivalent parameters. The effects of these parameters and of the rheological parameters J and n were investigated, and are presented below. The values for the rheological parameters used in the simulations were chosen based on real rheological data for a Carbopol aqueous solution.

4.1. Flow pattern results

The flow pattern can be analyzed with the aid of Figs. (2)-(8), which show some results of the dimensionless velocity, strain rate, and shear stress fields. Only the region of the domain that contains the bubble front is shown. The black line appearing in these figures indicates the interface between the fluids, as it is marked in Fig. (2). The interface line was defined as the line where $\alpha_1 = \alpha_2 = 0.5$. Figure (2) shows the velocity magnitude field for $J = 1.5 \times 10^6$ and $n = 0.41$,

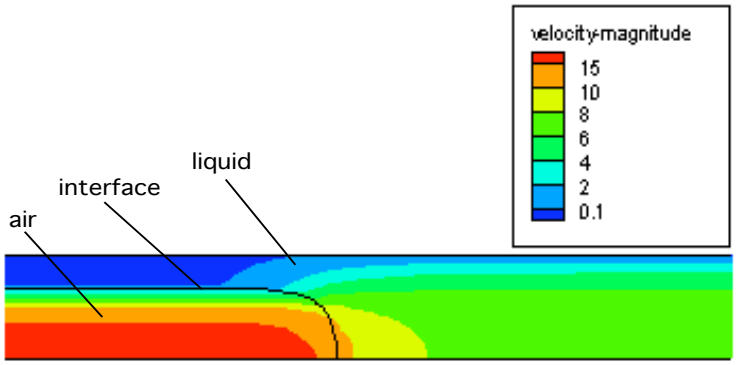

Figure 2: Velocity magnitude for $u^* = 5$, $\tau_w^* = 5.1$, $J = 1.5 \times 10^6$ and $n = 0.41$

and $u^* = 5$. It shows negligible velocity values in a region between the interface and the tube wall, which defines the mass deposited region. Also, it can be observed that the highest velocities occur inside the bubble, as expected. Figures (3)- (8) show the strain rate and shear stress for $J = 1.5 \times 10^6$ and $n = 0.41$, for three different dimensionless inlet velocities, $u^* = 1, 5$ and 10. These cases correspond to a dimensionless shear stress at wall, far away the bubble front, equal to $\tau_w^* = 3.2, 5.1$ and 6.4, respectively.

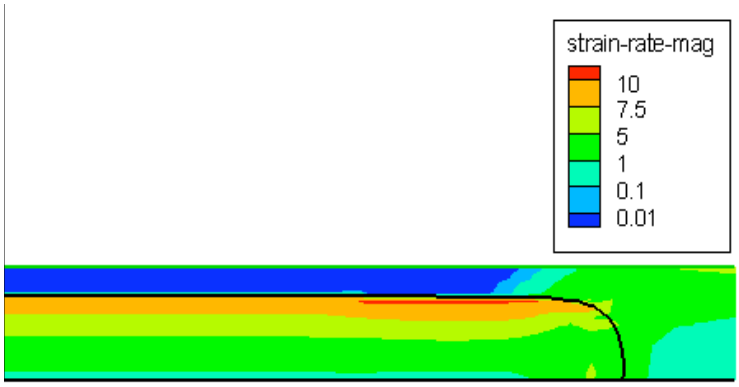

Figure 3: Strain rate field for $u^* = 1$, $\tau_w^* = 3.2$, $J = 1.5 \times 10^6$ and $n = 0.41$

It can be observed that the thickness of the film of liquid left on the wall increases as the flow rate is increased. For each flow rate, it can be noted that the deposited liquid mass, behind the bubble front is shear-stress free, as expected. Ahead of the bubble front, the wall shear stress becomes constant and equal to the the fully-developed flow value. Also, in this region a plug flow zone appears near the centerline, with low strain rates values. For low flow rates the region of

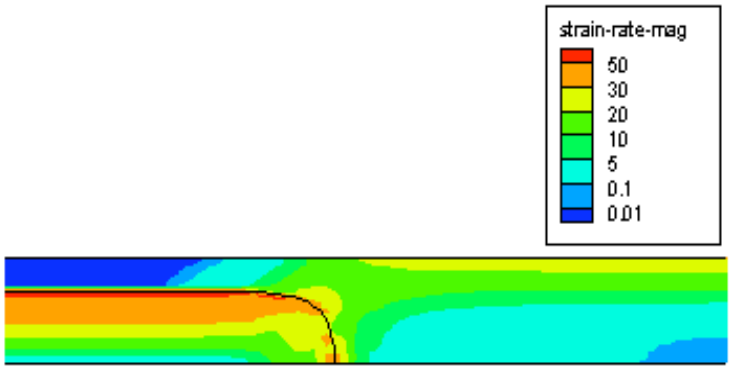

Figure 4: Strain rate field for $u^* = 5$, $\tau_w^* = 5.1$, $J = 1.5 \times 10^6$ and $n = 0.41$

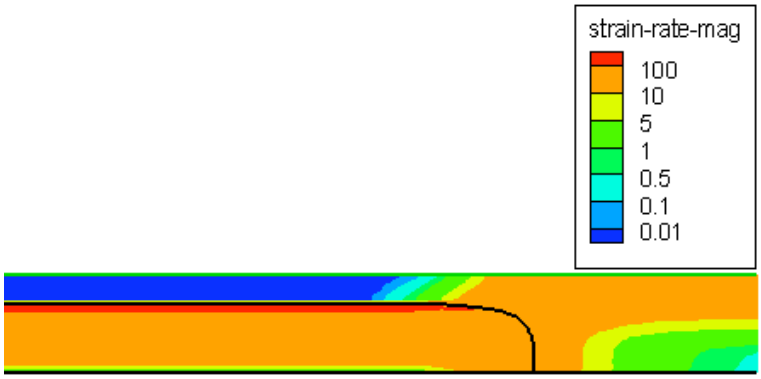

Figure 5: Strain rate field for $u^* = 10$, $\tau_w^* = 6.4$, $J = 1.5 \times 10^6$ and $n = 0.41$

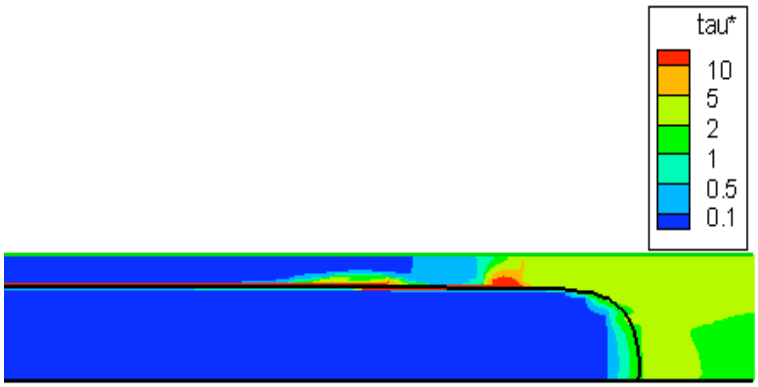

Figure 6: Stress field for $u^* = 1$, $\tau_w^* = 3.2$, $J = 1.5 \times 10^6$ and $n = 0.41$

influence of the bubble front on shear rate and shear stress is rather short. However, this region increases as the flow rate is increased. Therefore, fully developed flow occurs at shorter distances from the bubble front for lower flow rates.

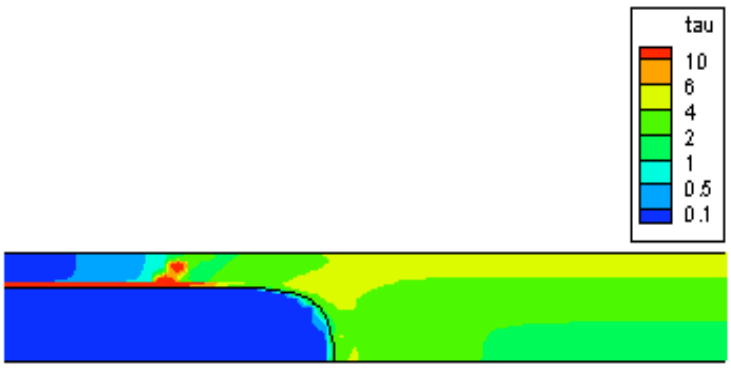

Figure 7: Stress field for $u^* = 5$, $\tau_w^* = 5.1$, $J = 1.5 \times 10^6$ and $n = 0.41$

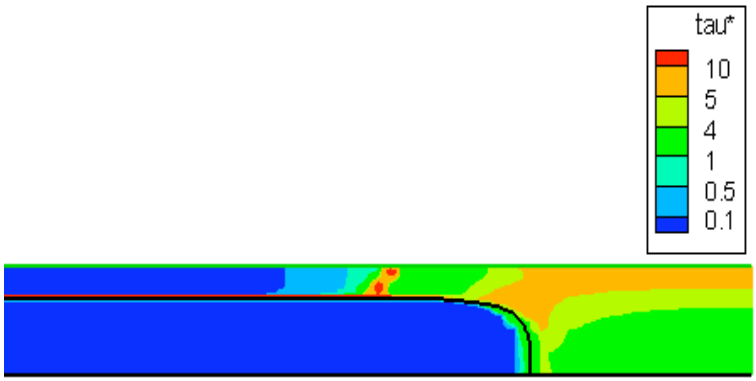

Figure 8: Stress field for $u^* = 10$, $\tau_w^* = 6.4$, $J = 1.5 \times 10^6$ and $n = 0.41$

Figures (9) and (10) show the strain rate and stress field for for $J = 1.5 \times 10^6$ and $n = 1$, $u^* = 5$ and $\tau_w^* = 21.3$. Comparing this result with the ones show in Figs. (4) and (7), it can be observed that an increase in the behavior index n leads to an increase of the curvature of the bubble front, and of the mass deposited. It can be observed that the strain rates are of the same order of magnitude of the case with $n = 0.41$. However, as n is increased, the viscosities are higher, which leads to higher stresses. The region of influence of the bubble front on shear rate and shear stress also seems to increase with n.

The influence of the Jump number on flow pattern can be evaluated comparing the results shown in Figs. (11) and (12), with the ones show in Figs. (4) and (4). Figures (11) and (12) showed the strain rate and stress field for $J = 1.5 \times 10^3$, $n = 0.41$, $u^* = 1$ and $\tau_w^* = 3.2$, while Figs. (4) and (4) show the result for a higher Jump number, $J = 1.5 \times 10^6$. It can be observed that Jump number almost does not affect the stress and strain rate fields. Also, the bubble shape and influence of the bubble front seem to be unaffected by the Jump number. This result was expected, since the viscosity is only affected by the Jump number in regions of lower strain rates, which only occur at the mass deposited region.

4.2. Amount of mass deposited results

The effects of rheological parameters and of the flow rate on the amount of mass deposited in the tube wall can be analyzed with the aid of Figs. (13)-(15). Figure (13) shows the influence of the flow rate on the mass deposited on tube wall. It can be observed that the mass deposited increases as flow rate is increased, until an asymptotic value. This asymptotic value is lower than the Newtonian limit for infinite capillary numbers, which is equal to 0.6. Therefore, viscoplasticity decreases the amount of mass deposited at the tube wall. The effect of Jump number is shown in Fig. (14). Is can be noted that the Jump number slightly decreases the amount of mass deposited at wall. This result also shows that the efficiency of the liquid displacement process is increased by viscoplasticity. Finally, the effect of the behavior index can be analyzed with the aid of Fig. (15). The mass deposited increases with n until an asymptotic value, that is equal to

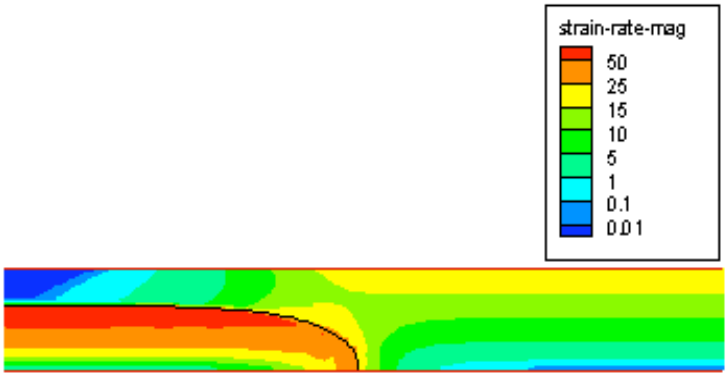

Figure 9: Strain rate field for $u^* = 5$, $\tau_w^* = 21.3$, $J = 1.5 \times 10^6$ and $n = 1$

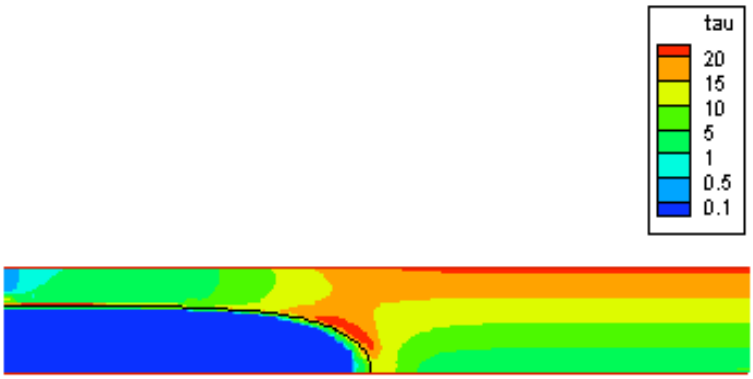

Figure 10: Stress field for $u^* = 5$, $\tau_w^* = 21.3$, $J = 1.5 \times 10^6$ and $n = 1$

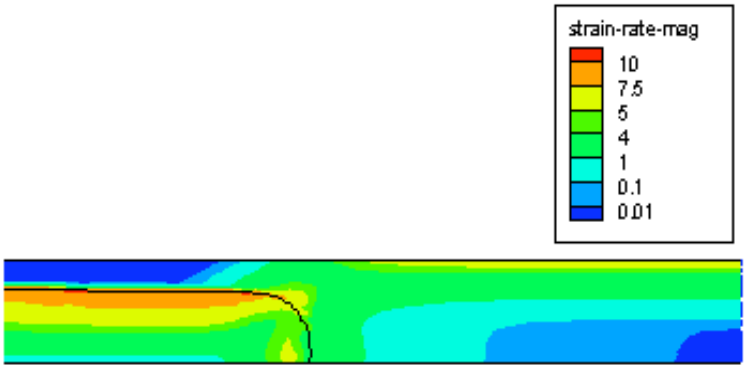

Figure 11: Strain rate field for $u^* = 1$, $\tau_w^* = 3.2$, $J = 1.5 \times 10^3$ and $n = 0.41$

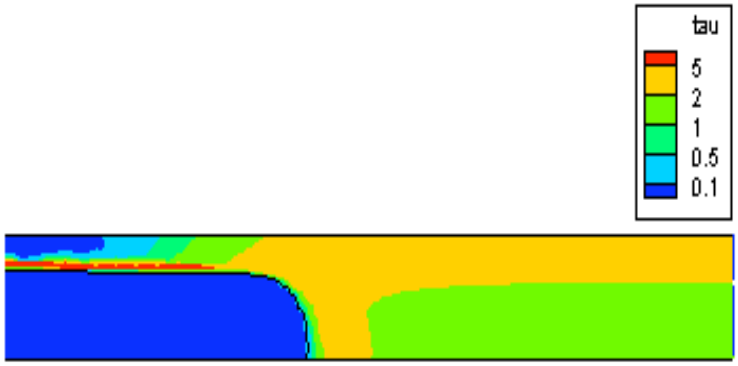

Figure 12: Stress field for $u^* = 1$, $\tau_w^* = 3.2$, $J = 1.5 \times 10^3$ and $n = 0.41$

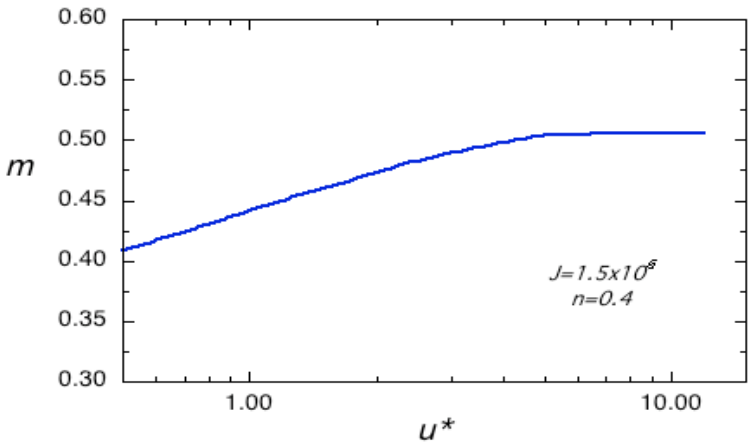

Figure 13: Mass fraction deposited at tube wall *versus* u^* for $J = 1.5 \times 10^6$ and $n = 0.41$

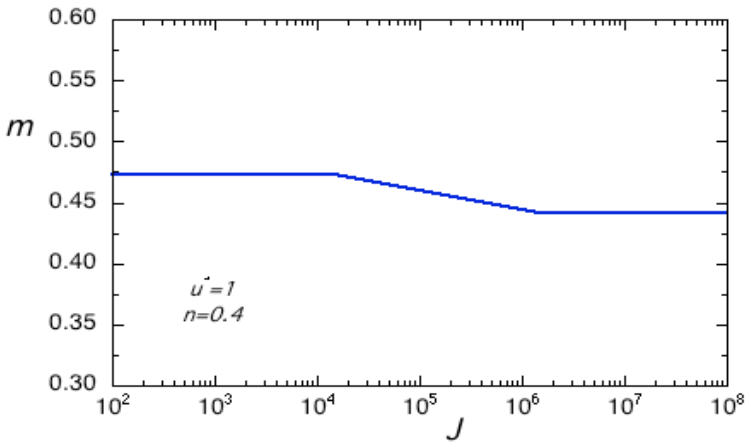

Figure 14: Mass fraction deposited at tube wall *versus* J for $n = 0.41$ and $u^* = 1$

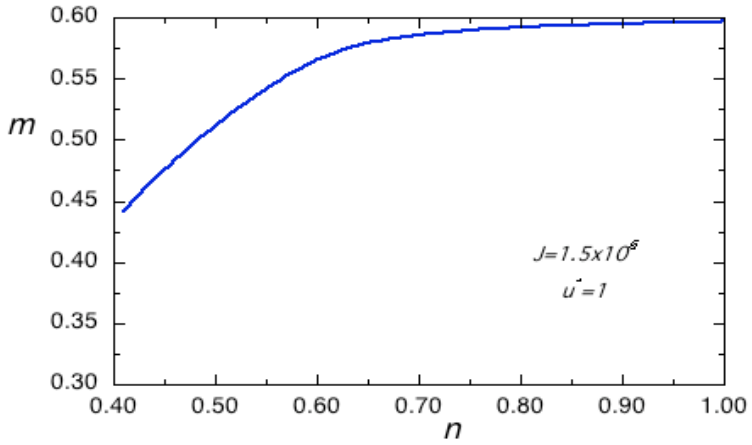

Figure 15: Mass fraction deposited at tube wall *versus* n for $J = 1.5 \times 10^6$ and $u^* = 5$

the Newtonian value. Its worth mentioning that when $n = 1$, the viscosity model is similar to the Bingham model with a constant viscosity plateau when the stress is below yield stress.

5. Final Remarks

In this work, the displacement of viscoplastic fluids by air inside tubes was analyzed numerically. The main goal was to obtain the amount of liquid left behind, adjacent to the wall, for different flow and rheological parameters. Larger amounts of liquid deposited at the tube wall mean lower displacement efficiencies. The results were obtained for unsteady and low Reynolds number flow. The governing conservation equations were discretized via the finite volume technique, using the volume of fluid method to model the multiphase flow. The viscoplastic behavior of the liquid was modeled by the Generalized Newtonian Liquid constitutive equation, using the SMD viscosity function. Velocity, strain rate and stress fields, and the amount of mass left attached to the wall, were obtained for different combinations of flow and rheological parameters. It was observed that the thickness of the film of liquid left on the wall increases with the behavior index, reaching as asymptotic value equal to the Newtonian one, as n goes to one. The amount of mass deposited also increases asymptotically as the flow rate is increased. It was also shown that the amount of mass deposited decreases as the jump number increases, but the Jump number effect is rather small.

6. Acknowledgements

Financial support for the present research was provided by Petrobras, CNPq and MCT - Brazil

7. References

Bird, R. B., Armstrong, R. C., and Hassager, O., 1987, "Dynamics of Polymeric Liquids", Vol. I, John Wiley & Sons.

Bretherton, F. P., 1961, The motion of long bubbles in tubes, "J. Fluid Mech.", Vol. 10, pp. 166–188.

Cox, B. G., 1962, On driving a viscous fluid out of a tube, "J. Fluid Mech.", Vol. 14, pp. 81–96.

de Souza Mendes, P. R. and Dutra, E. S. S., 2004, Viscosity function for yield-stress liquids, "Applied Rheology", Vol. 14, No. 6, pp. 296–302.

Fairbrother, F. and Stubbs, A. E., 1935, Studies in eletroendosmosis. Part IV. The bubble-tube methods of measurement, "J. Chem. Soc.", Vol. 1, pp. 527–529.

Fluent-User's-Guide, 2006, Vol. 6.2, Fluent Inc., New Hampshire.

Giavedoni, M. D. and Saita, F. A., 1997, The axisymmetric and plane cases of a gas phase steadily displacing a newtonian liquid: a simultaneous solution of the governing equations, "Physics of Fluids", Vol. 9, pp. 2420–2428.

Goldsmith, H. L. and Mason, S. G., 1963, The flow of suspensions through tubes, "J. Colloid Sci.", Vol. 18, pp. 237–261.

Lee, A. G., Shaqfeh, E. S., and Khomami, B., 2002, A study of viscoelastic free surface flows by the finite element method: Hele-shaw and slot coating flows, "J. Non-Newtonian Fluid Mech.", Vol. 108, pp. 327–362.

Patankar, S. V., 1980, "Numerical Heat Transfer and Fluid Flow", Hemisphere Publishing Corporation.

Quintella, E. F., de Souza Mendes, P. R., and Carvalho, M. S., 2005, Displacement flows of dilute polymer solutions in capillaries, "J. Non-Newtonian Fluid Mech. (submitted)".

Soares, E. J., Carvalho, M. S., and de Souza Mendes, P. R., 2005, Gas-displacement of non-newtonian liquids in capillary tubes, "Int. J. Heat Fluid Flow (in print)".

Taylor, G. I., 1961, Deposition of a viscous fluid on the wall os a tube, “J. Fluid Mech.”, Vol. 10, pp. 161–165.
Teletzke, G. F., Davis, H. T., and Scriven, L. E., 1988, Wetting hydrodynamics, “Revue de Physique Appliquee”, Vol. 23, pp. 989–1007.

Proceedings of the 11th Brazilian Congress of Thermal Sciences and Engineering – ENCIT 2006
Braz. Soc. of Mechanical Sciences and Engineering – ABCM, Curitiba, Brazil, Dec. 5-8, 2006

Paper CIT06-0100

DISCRETE METHODS IN MICROHYDRODYNAMICS

P. C. Philippi[1], L. O. E. dos Santos[2], C. E. Pico Ortiz[3], F. G. Wolf[4], L. A. Hegele Jr.[5], R. Surmas[6], D. N. Siebert[7]
Mechanical Engineering Department. Federal University of Santa Catarina.
88040-900 Florianópolis. SC. Brazil.
[1]philippi@lmpt.ufsc.br, [2]emerich@lmpt.ufsc.br, [3]capico@lmpt.ufsc.br, [4]fgwolf@lmpt.ufsc.br, [5]hegele@lmpt.ufsc.br, [6]surmas@lmpt.ufsc.br, [7]diogo@lmpt.ufsc.br

Abstract. *In microhydrodynamics we are interested in solving flow problems in micro geometries, e.g., in porous media and micro heat pipes, where the fluid flow is frequently conditioned by surface forces and surface phenomena, such as in capillary flows, coalescence and surface break-off. In micro flows, the interaction forces at the fluid-fluid and fluid-solid interfaces play an important role in the description of the fluid flow. These forces are from a molecular origin and the translation of their effects to our macroscopic scales is a chief problem, considering that by its multiscale nature these phenomena do not, frequently, have a homogeneization scale. In this work, we present a mesoscopic method based on discrete models of the Boltzmann equation, which should provide the establishment of a conceptual bridge between the molecular and the macroscopic domains, in the study of microhydrodynamics.*

keywords: *Continuous Boltzmann equation, Lattice Boltzmann, discretization.*

1. Introduction

The purpose of this work is to discuss fluid mechanics problems when the spatial scale is very small and when the hydrodynamic balance equations cannot be closed by the use of simple rules. This is the case of micro flows, when the interaction forces at the fluid-fluid and fluid-solid interfaces play an important role in their description, Israelachvili, 1992.

Taking into account that these forces are from a molecular nature, the question to be placed here is how to translate the description of their effects from the molecular scale to our macroscopic scales, which are several order of magnitudes larger, considering that by its multiscale nature these phenomena, frequently, do not have a homogeneization scale.

In this work we present a mesoscopic method based on discrete models of the Boltzmann equation, which have been developed in very recent years, after 1990 and which should provide the establishment of a conceptual bridge between the molecular and the macroscopic domains.

Considering the molecular chaos hypothesis, Boltzmann considered a fluid as a mechanical system of particles with the purpose of demonstrating the *irreversibility*, a common attribute of classical thermodynamic systems but a *nonsense* in classical mechanics. Developed, in its origin, for monoatomic rarefied gases the Boltzmann equation has received several contributions in the course of the last 130 years by: i) the inclusion of finite volume effects in the Enskog's kinetic theory of dense gases, Enskog, 1921 ii) the consideration of the rotational, Lifshitz and Pitaevskii, 1999, and vibrational degrees of freedom, Wang Chang and Uhlenbeck, 1970, of the modelled particles, iii) the inclusion of electromagnetic effects in the study of plasmas, Tanenbaum, 1987. Recently, He and Doolen, 2002, proposed a split of the collision term in two parts for taking the long-range intermolecular attraction forces into account, in the kinetic description of liquids.

Lattice-Boltzmann models are discrete forms of the Boltzmann equation, when in addition to the discretization of time and of the physical space, the velocity space is also discretized, with the peculiarity that after each time step and following a local collision process the particles are propagated from each site to its next neighbours. The number of first neighbours to each site is related to the higher order of the kinetic moments that are to be described, Philippi *et al.*, 2006b.

In addition to the lattice-Boltzmann collision-propagation schemes (LBM) a number of alternative discrete velocity methods have been appearing in recent years based on finite differences, finite volumes and, more rarely, on finite elements numerical schemes, but the discussion of these methods is outside the scope of this work.

The lattice-Boltzmann equation (LBE) was introduced by McNamara and Zanetti, 1988, replacing the Boolean variables in the discrete collision-propagation equations by their *ensemble* averages. Higuera and Jimenez, 1989, proposed a linearization of the collision term derived from the Boolean models, recognizing that this full form was unnecessarily complex when the main purpose was to retrieve the hydrodynamic equations,

with a very few relaxation parameters. Following this line of reasoning, Chen *et al.*, 1991, suggested replacing the collision term by a single relaxation-time term, followed by Qian *et al.*, 1992, and Chen *et al.*, 1992, who introduced a model based on the Bhatnagar-Gross and Krook (BGK) collision term (Bhatnagar *et al.*, 1954), retrieving the correct incompressible Navier-Stokes equations, with third-order non-physical terms in the local speed, u. In fact, the BGK collision term describes the relaxation of the distribution function to an equilibrium distribution, but in the above works, this discrete equilibrium distribution was settled by writting it as a *second-order polynomial expansion* in the particle-velocity $\vec{\xi}_i$, with parameters that were adjusted to retrieve the mass density, the local velocity and the momentum flux equilibrium moments, which are necessary conditions for satisfying the Navier-Stokes equations.

In trying to describe non-isothermal full compressible flows, thermal lattice-BGK schemes included higher order terms in the equilibrium distribution function (Alexander *et al.*, 1993, Chen *et al.*, 1994), requiring to increase the lattice dimensionality (Alexander *et al.*, 1993, McNamara and Alder, 1993, Chen *et al.*, 1994), i.e., the number of vectors in the finite and discrete velocity set $\left\{\vec{\xi}_i, i = 0, ..., b\right\}$, but the polynomial expansion form in the particle-velocity $\vec{\xi}_i$, with adustable parameters, was retained, the numerical simulations being peformed on, somewhat, empirically chosen lattices.

In thermal problems, BGK single relaxation time collision term restricts the models to a single Prandtl number. The full description of fluids and fluid flow requires multiple relaxation time models (MRT). A two-parameters model was introduced by He *et al.*, 1998, using two sets of distributions for the particles number density and the thermodynamic internal energy, coupled through a viscous dissipation term and proposed to be runned with a two-dimensional 9-velocities lattice. Full MRT models were firstly introduced in the LBE framework by d'Humières, 1992, d'Humières *et al.*, 2001, by modifying the collision step, considering it to be given by the relaxation to the equilibrium of a set of non-preserved kinetic moments.

Nevertheless, the presently known lattice-Boltzmann equation (LBE) has not been able to handle realistic thermal and fully compressible flow problems with satisfaction, since the simulation of the LBE is, frequently, hampered by numerical instabilities when the local velocity increases, Lallemand and Luo, 2003.

Considering the kinetic nature of the LBE, establishing a formal link between the LBE and the continuous Boltzmann equation, allowing the conceptual analysis of this discrete numerical scheme, could perhaps shed some light on this question. Indeed, there are several features that let the lattice Boltzmann regular-lattice based framework far away from the continuous Boltzmann equation, which would be desirable to be its conceptual support. These features include the particles model, the collision and long-range interaction models and the approach used for the time and the velocity space discretization.

With a few exceptions, in all the above works there is no formal link connecting the LBE to the continuous Boltzmann equation, although the main ideas were based on the kinetic theory fundamentals.

He and Luo, 1997, have directly derived the LBE from the continuous Boltzmann equation for some widely known lattices by the discretization of the velocity space, using the Gauss-Hermite and Gauss-Radau quadrature. Unhappily, excluding the above mentioned lattices, the discrete velocity sets obtained by this kind of quadrature do not generate space-filling lattices.

In a recent paper, Philippi *et al.*, 2006b, the velocity discretization problem was considered as a quadrature problem with prescribed abcissas, starting from the Boltzmann continuous equation, by requiring the discrete equilibrium distribution f_i^{eq} to have the same value of the continuous distribution f^{eq} when evaluated at a quadrature pole $\vec{c}_i$. In this manner, when the order of approximation N of a Hermite polynomial expansion to the MB equilibrium distribution is chosen, a set $\Psi_{\theta,(r_\theta)}$, $\theta = 0, ..., N$, of Hermite polynomials is established, and the infinite and enumerable basis of the Hilbert space $\mathcal{H} : c^D \rightarrow \mathcal{R}$, is replaced by a *finite* set of Hermite polynomial tensors, restricting the solutions to N^{th}-degree polynomials in the velocity $\vec{c}$. The quadrature problem was, then, considered as to select a regular lattice $\{\vec{c}_i\}$, in such a manner that functions $\Psi_{\theta,(r_\theta)}$ preserve the orthogonality with respect to the inner product in the discrete space. This was shown to be posible to be accomplished by assuring that the norm of *each one* of these functions $\Psi_{\theta,(r_\theta)}$ is retrieved, *exactly*, in the discrete space. The number b of the required lattice vectors is proportional to the order N of the polynomial approximation, $b = b(N)$ and, tt was,formally, shown that the lattice dimensionality is directly related to the order of approximation of the discrete equilibrium distribution, with respect to the full Maxwell-Boltzmann distribution and, consequently, to the highest order of the kinetic moments that are to be correctly described. In addition, it was shown that when the quadrature problem is solved, the 2θ-rank velocity tensors are isotropic in the discrete space, for $\theta = 1, ...N$. Similar results were, almost, simultaneously, obtained by Shan *et al.*, 2006, although using a different procedure.

An important practical result from Philippi *et al.*, 2006b, was to show that when the space-filling lattices are built taking lattice-vectors which are integer multiples of the D2Q9 velocity vectors, i.e., the DQ hierarchy, the 4^{th} kinetic moments, important in describing the flow of energy, *cannot be correctly described*.

Although the proposed method in Philippi *et al.*, 2006b leads to MRT collision models, the method has impor-

tant differences with respect to D 'Humières moments method. In D'Humières moments method (d'Humières, 1992, d'Humières *et al.*, 2001), dispersion equations are used as constraints for the adjustable parameters related to the short wave-length, non-hydrodynamic, moments and numerical stability is assured by buffering these higher frequency moments. In Philippi *et al.* method (Philippi *et al.*, 2006b), non-physical lattice effects and numerical instability, in the description of higher-order hydrodynamic phenomena, can be only avoided by increasing the lattice dimensionality, required by the highest order of the kinetic moment to be preserved with the modelled LBE. The highest order of the kinetic moments possible to be correctly described with the LBE equation is limited by the number of lattice velocities, Philippi *et al.*, 2006b, and high-order kinetic moments are not correctly described when all the b-moments in a b-discrete velocities set are considered, as in the moments method. In fact, in currently produced works dealing with applications of the moments method, e.g. Lallemand and Luo, 2003, the main worry is *numerical stability* and *not* the description of non-isothermal, multicomponent or immiscible fluids flows, which, effectively, require additional relaxation parameters with respect to BGK models.

In this work, we present the lattice-Boltzmann framework, as a discrete method with its starting point at the Boltzmann continuous equation. Some important questions are discussed related with the suitability of this framework to solve non-isothermal, multiphase physical problems in microhydrodynamics.

In fact, although the LBM can be used for solving advection-diffusion problems, instead of the full set of macroscopic transport equations, which is the basis of classical CFD methods, some questions have been shown to be important to be answered considering the exciting possibility that is open in building the lattice-Boltzmann framework as a real bridge connecting the molecular to the macroscopic domain:

i) **Collision term**: When the particles are considered as material points without long-range interactions the modelled fluid follows an equation of state for ideal gases, $P = n_d kT$. In this manner the isothermal compressibility χ_T is high and the simulation of incompressible flows are subjected to compressibility effects, Surmas *et al.*, 2006. In LBM, these compressibility effects are usually avoided by working with small local velocities, but this restricts the simulations to low Reynolds numbers or requires to increase the number of lattice sites for high Reynolds number, increasing the computational costs and reducing LBM competitiveness with respect to conventional CFD methods. Enskog's collision term, Enskog, 1921, was derived considering the particles to be rigid spheres with a finite volume and the equation of state was derived as $P = n_d kT\ (1 + \rho b \chi)$ where b is related to the particle volume by unity mass and χ is a correction factor which can be written in terms of the mass density ρ, Chapman and Cowling, 1999. For liquids, the long-range attraction among particles was considered by He and Doolen, 2002, by splitting the collision term in two parts, the first part related to short-range interaction and the second one related to long-range interaction. After some simplifications, this second part was further written in terms of a mean interparticle potential and the equation of state was derived as a van-der-Waals *like* equation $P = n_d kT\ (1 + \rho b \chi) - a\rho^2$.

ii) **Collision model**. The collision term Ω is dependent on the distribution function itself and, indeed, the Boltzmann equation is a non-linear integro-differential equation that has been shown to be too difficult to be solved. Instead of the full collision term, a collision model is required leading to a non-linear partial differential equation, which can be numerically solved, Philippi *et al.*, 2006a.

iii) **Velocity discretization**. The distribution function depends on the particles velocity and this requires the discretization of the velocity space, in addition to the discretization of the physical space. Considering the required accuracy for a given discrete scheme, the problem is how to find the minimal number of discrete velocities for that given accuracy (Philippi *et al.*, 2006b, Philippi *et al.*, 2006c). In the present work, we deal with the lattice Boltzmann method (LBM) in space-filling lattices where, after each time-step, the particles are displaced from a given site to their next neighbors.

iv) **Boundary conditions**. In LBM, the boundary condition are reflection laws for the particle populations, since macroscopic variables such as velocity and temperature are not accessible as primitive variables. In certain cases, these boundary conditions can be related to velocity slips and temperature jumps that are difficult to overcome.

v) **Ideal mixtures**. Particles with different masses, at a given site, but with the same peculiar kinetic energy will be displaced to different points after a given time step, reaching intermediate positions between two contiguous sites and requiring the use of reallocation rules that, localy, preserve mass, momentum and energy. Interpolation schemes may be the source of numerical instability and alternative modelling strategies may show to be necessary, Ortiz *et al.*, 2006.

vi) **Non ideal mixtures and Immiscible fluids**. The electrostatic forces among the molecules produce the non-ideal behavior of fluids and fluid-mixtures and are at the origin of the phase separation process, when two immiscible fluids are put in contact, being responsible for the interfacial tension. These forces must be considered and correctly modelled in LBM.

Topics i), ii), iii), iv) and vi) are treated in some detail in present work.

2. Boltzmann equation as providing an alternative method for solving fluid mechanics problems

The Boltzmann equation can be derived from Liouville's equation, Cercignani, 1969, by supposing statistical independence for the 2-particle distribution function, in the limit when the number of particles N$\rightarrow \infty$, with a finite value of Nσ^2, σ being related to the particles diameter, $\sigma \rightarrow 0$. It reads

$$\partial_t f + \vec{\xi}.\nabla_r f + \vec{g}.\nabla_\xi f = \Omega, \tag{1}$$

where $\vec{r}$ is the position, $\vec{\xi}$ the particles translational velocity and $\vec{g}$ the acceleration due to the external forces.

The particles are considered as *material points without long-range interaction* and the collision term Ω in Eq. (1) must satisfy

$$\int \Omega m d\vec{\xi} = 0, \tag{2}$$

$$\int \Omega m\vec{\xi} d\vec{\xi} = 0, \tag{3}$$

$$\int \Omega \frac{1}{2} m\xi^2 d\vec{\xi} = 0, \tag{4}$$

due to the preservation of mass, momentum and kinetic translational energy in collisions.

In this manner when Eq. (1) is, respectively, multiplied by the mass, m, the momentum $m\vec{\xi}$ and the energy $\frac{1}{2}m\xi^2$, after some straightforward algebra, the following transport equations are obtained,

$$\partial_t \rho + \partial_\alpha (\rho u_\alpha) = 0, \tag{5}$$

$$\partial_t (\rho u_\alpha) + \partial_\alpha (\rho u_\alpha u_\beta + P\delta_{\alpha\beta} + \tau_{\alpha\beta}) = \rho g_\alpha, \tag{6}$$

$$\partial_t (\rho e) + \partial_\alpha (\rho e u_\alpha + q_\alpha) = -\tau_{\alpha\beta}\partial_\beta u_\alpha - P\partial_\alpha u_\alpha, \tag{7}$$

where ρe is the internal energy per unit volume, given, in this case, by

$$\rho e = \int f \frac{1}{2} m \left(\vec{\xi} - \vec{u}\right)^2 d\vec{\xi} \tag{8}$$

The equilibrium solution of the Boltzmann equation, Eq. (1) is the solution of,

$$\Omega = 0, \tag{9}$$

which can be shown to be a Maxwellian distribution, f^{eq}.

When this equilibrium distribution is required to satisfy

$$\int f^{eq} d\vec{\xi} = n_d, \tag{10}$$

$$\int f^{eq} \vec{\xi} d\vec{\xi} = n_d \vec{u}, \tag{11}$$

$$\int \frac{1}{2} m f^{eq} \left(\vec{\xi} - u\right)^2 d\vec{\xi} = \frac{D}{2} n_d kT, \tag{12}$$

where n_d is the local number density of the particles with mass m, $\vec{u}$ is the local velocity T, the local thermodynamic temperature, and D, the Euclidean dimension of the physical space, the Maxwell-Boltzmann distribution is retrieved,

$$f^{eq} = n_d \left(\frac{m}{2\pi kT}\right)^{D/2} e^{-\frac{(\vec{\xi}-\vec{u})^2}{\frac{2kT}{m}}}, \tag{13}$$

and the pressure P is related to the particles number density by the ideal gas law

$$P = n_d kT. \tag{14}$$

Further, a Chapman-Enskog analysis shows that in the continuous limit, $Kn \to 0$, the viscous stress tensor is given by

$$\tau_{\alpha\beta} = -\mu\left(\partial_\beta u_\alpha + \partial_\alpha u_\beta\right) + \kappa\delta_{\alpha\beta}\partial_\alpha u_\alpha, \tag{15}$$

and the heat flow vector by

$$\vec{q} = -\varkappa\nabla e. \tag{16}$$

In this manner, in the continuous limit, the Boltzmann equation, Eq. (1) gives the correct hydrodynamics for Newtonian fluids and can be used for solving advection-diffusion problems, instead of the full set of macroscopic transport equations, Eqs. (5-7), which is the basis of classical CFD methods.

Nevertheless, as a mesoscopic method we must consider the possibility that is open in building this framework not as an alternative numerical method, for solving the advection-diffusion equations, *but as a real bridge connecting the molecular to the macroscopic domain.*

In the next section we show some physical problems that require to downscale to be correctly understood.

3. Some physical problems in microhydrodynamics

Consider a capillary- rising problem, when a liquid raises inside a capillary tube against the gravity force, Figure 1.

Let $x_s(r,t)$ be the position of the liquid surface above the free liquid surface and consider the problem of finding the position x_s for any radius r at a time t. The question that we want to answer is how to find $x_s(r,t)$ from the solely information of the capillary tube diameter and the liquid wettability on the solid surface - given by the equilibrium contact angle, in static conditions, when a small liquid drop is put in contact with the surface of the capillary tube.

This problem has several simplified solutions, but all these solutions are based on an equilibrium contact angle (Lucas, 1918, Stange *et al.*, 2003, Washburn, 1921, Bosanquet, 1923) which is supposed to be constant during the rising process.

Furthermore, the exact solution of this problem via the hydrodynamic Eqs. (5-7) in the Stokes incompressible limit leads to a velocity singularity in the triple line, Dussan *et al.*, 1991. This singularity is easy to explain, since at the same time the triple line is responsible for the interface advancement, it must, also, satisfy an adherence condition of zero velocity at the solid surface.

In fact, the triple-line is not a *line*, but a transition region of some nanometers among the three phases (in this case: solid, liquid and gas) and where a liquid molecule is, simultaneously, subjected to the intermolecular forces from the adjacent liquid molecules - responsible for the liquid surface tension - and to the attractive forces from the solid surface -related to the work of adhesion between the liquid and the solid.

In this manner, the correct understanding of the capillary-rising problem requires, in principle, the knowledge of the fine physical structure of the triple-line and to solve a multi-scale problem, where the scales vary from some nanometers to several micrometers.

For understanding what happens in the triple line, some elementary knowledge of surface physical-chemistry is needed. Surface tension is responsible for keeping a liquid drop at the end of the overhanging branches of a three in rainning days, Figure 2. The intermolecular forces among the liquid molecules produce a tension state at the liquid surface. These forces can be considered as electrostatic forces that depend on the molecular shape, Figure 3. Asymmetric molecules such as the water molecule have a permanent dipole moment and attract themselves with polar (or Keesom) forces. The intermolecular forces among symmetric, non-polar, molecules,

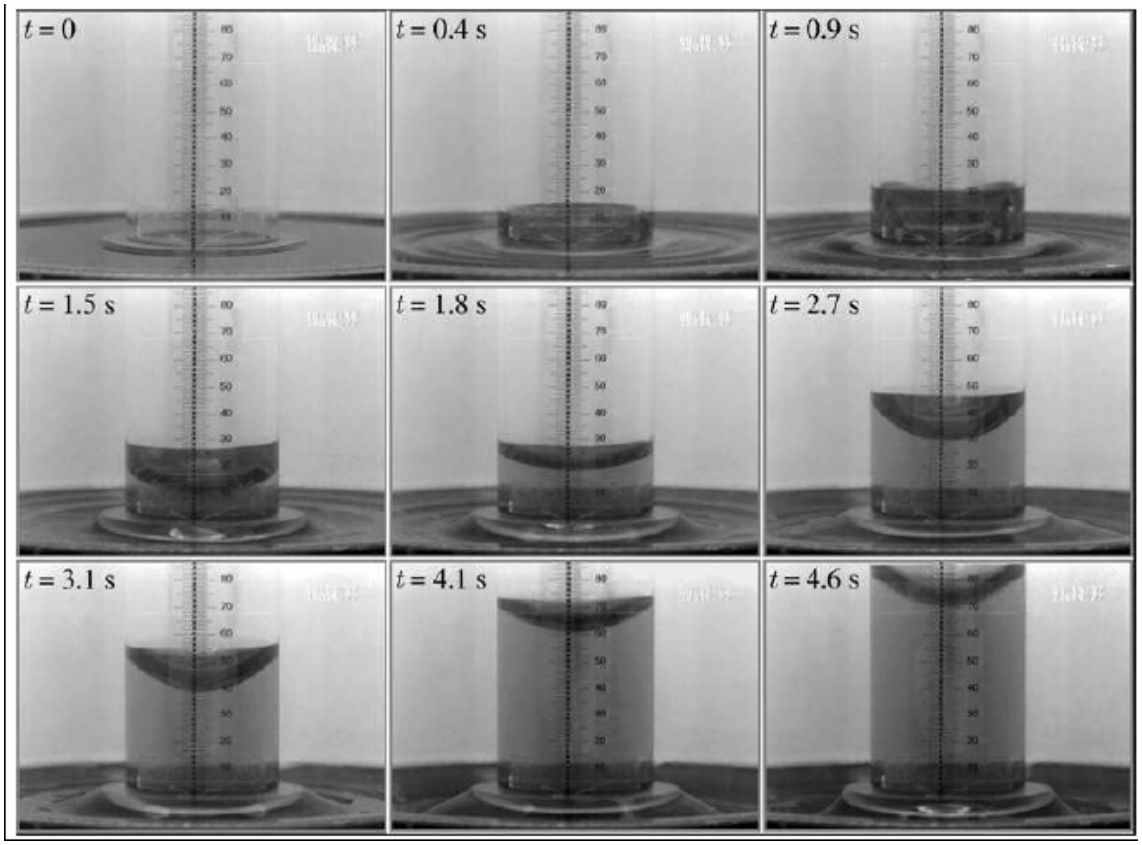

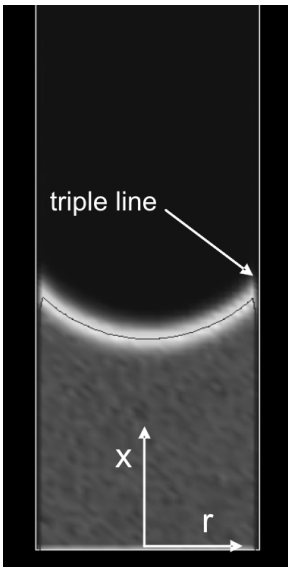

Figure 1: The triple line in capillary rising (from Stange *et al.*, 2003)

Figure 2: The surface tension counteracts the weight of a small liquid drop.

such as the hydrocarbon molecules, are due to the high frequency fluctuations of the geometrical center of theirs electronic clouds. These forces are called Bond or dispersive forces. When a polar molecule is near a non-polar molecule, the dipole moment of the polar molecule is subjected to high-frequency fluctuations due to the electrostatic Debye induction from the non-polar molecule and this interaction produces an attractive force which is of a dispersive nature. This cross force is frequently weaker when compared to the polar forces among the polar molecules and to the dispersive forces among identical non-polar molecules. In this manner, polar and non-polar liquids are, in general, immiscible.

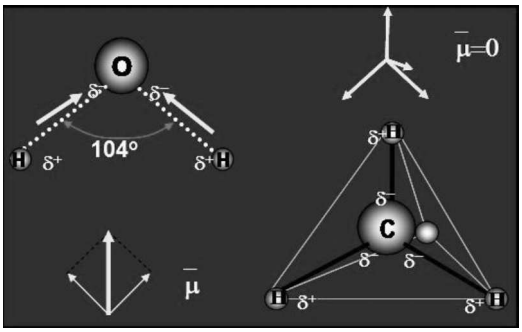

Figure 3: Intermolecular forces are electrostatic forces that are dependent on the molecular shapes.

Fowkes, Fowkes, 1972 has proposed an empirical relationship for the interfacial tension, σ_{ab}, between a polar and a non-polar liquid, where the cross mixing force, responsible for the interfacial tension reduction, is related to the dispersive components of the surface tensions, σ_a, σ_b, of each fluid through a geometrical average,

$$\sigma_{ab} = \sigma_a + \sigma_b - 2\sqrt{\sigma_a^d \sigma_b^d}. \tag{17}$$

The main idea behind Fowkes relation is displayed in Figure 4 where the cross mixing force is, in this case, of a pure dispersive nature.

When two drops of a liquid are close enough they will coalesce. Although the main coalescence driving force is the result of a collective electrostatic effect among the liquid molecules from both drops, the coalescence process is still an open problem, since vapor molecules near the contact point have theirs trajectories constrained by an intensified electrostatic field and, apparently, they preferentially condense on the positions where the liquid surfaces are closest, contributing to the start-up of coalescence. This picture was, indeed, observed in goniometer experiments (Figure 5), when two water drops coalesced in despite of their initial separation distance, of about 0.2 mm, was much larger than their electrostatic interaction length, but further theoretical studies are necessary for a more thorough analysis of this complex process.

When air displaces water inside a capilary channel, a dynamic liquid film forms separating the air phase from the solid surface. This dynamic liquid film has been studied by several authors including some famous ones such as Landau and Levich, 1942 and Bretherton, 1961. It has been shown that the average thickness of this film is dependent on the interface velocity, i.e., on the capillary number. When the air-water interface reachs very small constrictions of a porous medium, a pressure reduction in the invader phase, can give rise to

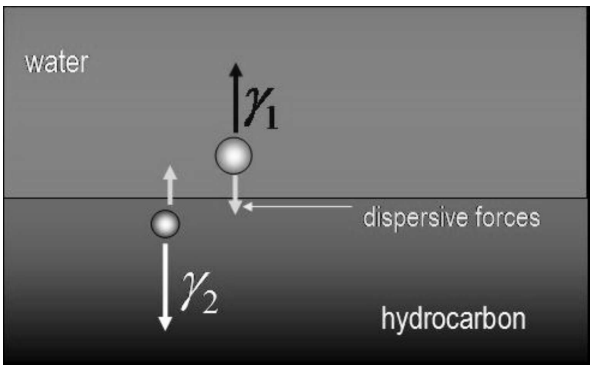

Figure 4: Dispersive forces try to mix water and oil.

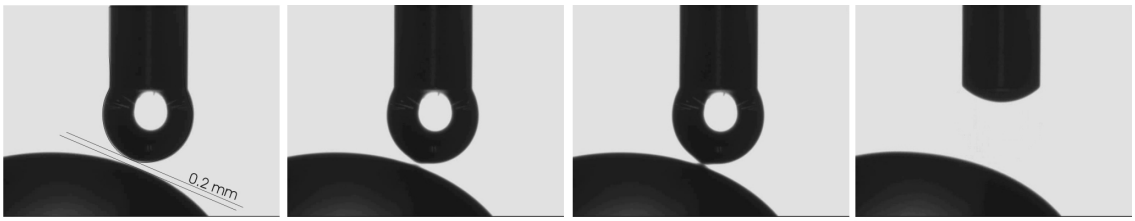

Figure 5: Coalescence process between two water-droplets in a goniometer. The two drops coalesce after a certain time, although they were put at a distance of 0.2 mm, which is much larger than their electrostatic interaction length.

the growing of the film thickness followed by a coalescence process, breaking off the air phase and producing a burst of bubbles from the constriction due to the sucessive pressure decay followed by a pressure restoring after each coalescence process at the constriction. This is pictured in Figure 6.

This dynamical process can be very important in water flooding petroleum extraction, when the extraction is performed with a high capillary number or when the oil mobility is very low. In heavy oils, the presence of surfactants that are soluble in oil can give rise to stable emulsions.

In fact, the addition of surfactants that are soluble in the hydrocarbon phase will produce a polar cross mixing force and a larger decrease in the interfacial tension with respect to Eq. (17), in accordance with

$$\sigma_{ab} = \sigma_a + \sigma_b - 2\sqrt{\sigma_a^d \sigma_b^d} - 2\sqrt{\sigma_a^p \sigma_b^p}. \tag{18}$$

Surfactant molecules such as asphaltens can be pictured as in Figure 7(a), with a long hydrocarbon tail and a polar head. These molecules will move to the water-oil interface forming a monolayer where the molecule tails will be oriented toward the hydrocarbon phase, Figure 7(b).

Even when water wets the porous surface, when it displaces a heavy oil inside a porous medium, it is not able to produce a steady piston displacement, due to the high oil viscosity and water fingers will take form inside the oil-phase. These fingers are not stable and, in flowing through constrictions, they can break-up forming water drops, in the same manner as it was pictured in Figure 3. The presence of surfactants that are soluble in the oil phase, in the water-oil interface, reduces the interfacial tension making the break-up easier and the surfactant molecules will finish by forming a monolayer around each water droplet, difficulting the coalescence of these droplets and producing a stable emulsion in the downflow direction, Figure 7(c).

In concluding this section, in spite of its great technological importance and of the growing scientific interest in microhidrodynamics, the few physical problems that were drawn above give a sample of the great complexity with which we are faced, when trying to correct understand fluid flows, when the spatial scales are very small and when the interfacial physics play an important role.

In the next section the Boltzmann equation is presented, considered as a bridge that should enable to link the microscopic to the macroscopic scales.

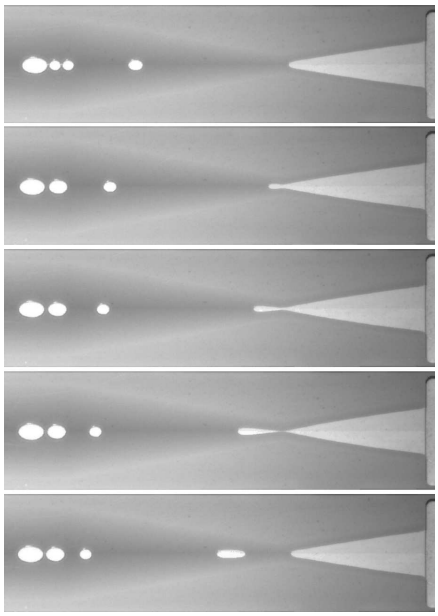

Figure 6: Formation of a burst of drops in a small constriction. Courtesy of O. Amyot, Amyot, 2004.

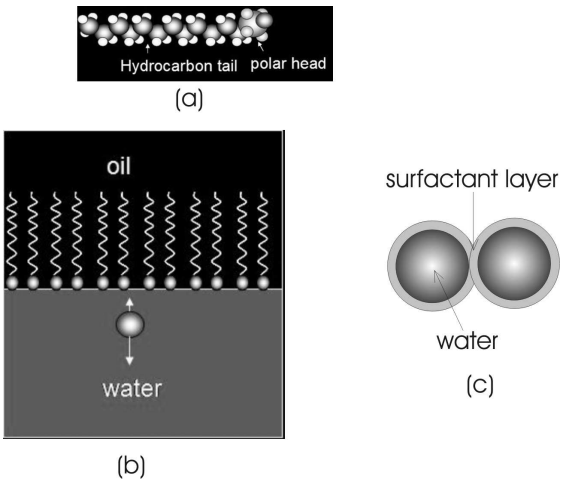

Figure 7: Surfactants and emulsions

4. Boltzmann equation as a bridge linking the molecular to the macroscopic domains

We first investigate the *origins* of the Boltzmann equation.

Figure 8 shows a molecular dynamics simulation of a vapor condensation process based on an N-body simulation of the Newton second law of motion. Each one of the N particles is subjected to a trajectory, in the physical space, given by the solution of the following equations

$$m_i \frac{d^2 \vec{x}_i}{dt^2} = \sum_j F_{ij}, \tag{19}$$

$$\frac{d\vec{x}_i}{dt} = \vec{\mathrm{v}}_i, \tag{20}$$

where $\vec{x}_i$ is the position, $\vec{\xi}_i$ the velocity of particle i and F_{ij} is the force among each $i-$particle and all the remaining particles, evaluated by supposing a Lennard-Jones interaction potential among the particles, Surmas, 2006. Particles are spherical with a diameter that is given by the inversion point of the Lennard-Jones potential, where the attractive forces become repulsive. Each time a particle collide with the container surface, it is reflected back following a *specular* reflection and with only a previously established fraction of the kinetic energy it had before the collision, trying to reproduce a *cooling process* at the walls. Attractive forces between the wall container and the particles where not considered for avoiding condensation at the wall surface.

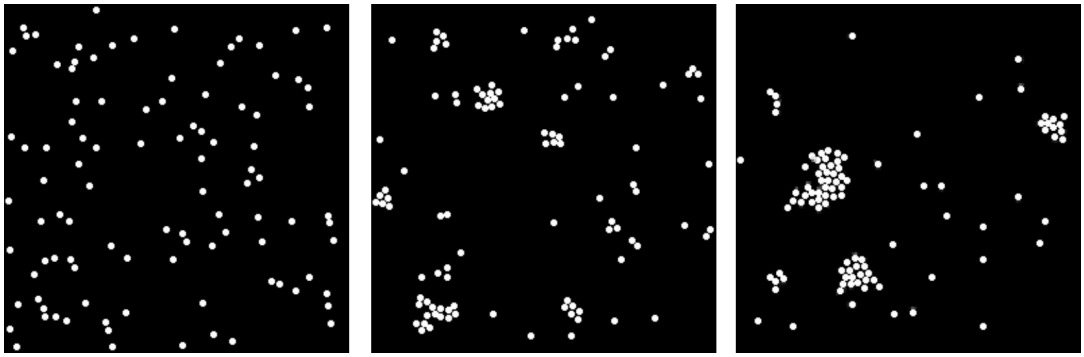

Figure 8: Molecular dynamics simulation of vapor condensation.

The initial state $\vec{x}_1, \vec{\xi}_1, ...\vec{x}_N, \vec{\xi}_N, t = 0$ was randomly set.

We can see that this molecular dynamics simulation gives a good picture of what is to happen in a condensation process at the molecular scale, although the analysis was performed on a *mechanical deterministic system of particles*, subjected to Newton 's second law of motion, without any help of thermodynamic concepts such as thermodynamic energy and entropy.

Nevertheless the results of such analysis is restricted: a) to the very small molecular scales and b) to very small time scales, considering the limitations imposed by the computer rounding-off error.

Consider, now our mechanical system of N particles, when several different initial state $\vec{x}_1, \vec{\xi}_1, ...\vec{x}_N, \vec{\xi}_N, t = 0$ are possible. Suppose that the set of all possible initial states is a dense set in the phase-space $\vec{x}_1, \vec{\xi}_1, ...\vec{x}_N, \vec{\xi}_N$. In this case it is impossible to know where a given particle will be at a given time. Let, however,

$$f^N \left(\vec{x}_1, \vec{\xi}_1, ...\vec{x}_N, \vec{\xi}_N, t \right), \tag{21}$$

to be the *probability* of finding, at time t, dt the particle 1 at the position $\vec{x}_1$, $d\vec{x}_1$ with velocity $\vec{\xi}_1$, $d\vec{\xi}_1$, the particle 2 at the position $\vec{x}_2$, $d\vec{x}_2$ with velocity $\vec{\xi}_2$, $d\vec{\xi}_2$ and so on, until particle N at the position $\vec{x}_N$, $d\vec{x}_N$ with velocity $\vec{\xi}_N$, $d\vec{\xi}_N$. The Liouville equation describing the dynamical evolution of this system is given by, Cercignani, 1969,

$$\partial_t f^N + \sum_i \vec{\xi}_i . \partial_{\vec{x}_i} f^N + \sum_i \vec{\chi}_i . \partial_{\vec{\xi}_i} f^N = 0, \tag{22}$$

where $\vec{\chi}_i$ is the force acting on particle i,

$$\vec{\chi}_i = \vec{\chi}_i^e + \sum_{\substack{j=1 \\ j\neq i}}^{N} \vec{\chi}_{ij}. \tag{23}$$

Force $\vec{\chi}_i^e$ is the force on particle i due to an external field and force $\vec{\chi}_{ij}$ is the force on particle i due to its interaction with particle j,

$$\vec{\chi}_{ij} = -\frac{\partial \Phi\left(x_{ij}\right)}{\partial\left(\vec{x}_i - \vec{x}_j\right)}, \tag{24}$$

where $x_{ij} = |\vec{x}_i - \vec{x}_j|$ and Φ is assumed to be a central potential depending, only, on the distance between particles i and j.

Conjoint probability f^N can be integrated in the phase space $\vec{x}_2, \vec{\xi}_2, ...\vec{x}_N, \vec{\xi}_N$ to give the marginal probability f^1 of finding, at time t, dt the particle 1 at the position $\vec{x}_1$, $d\vec{x}_1$ with velocity $\vec{\xi}_1$, $d\vec{\xi}_1$

$$f^1\left(\vec{x}_1, \vec{\xi}_1, t\right) = \int ... \int f^N d\vec{x}_2 ... d\vec{x}_N d\vec{\xi}_2 ... d\vec{\xi}_N, \tag{25}$$

considering that the probability f^N gives a too detailed description of the system, which is unnecessarily complexe, since the dynamical evolution of an arbitrary, but, single, particle can be a reliable description of the whole mechanical system of particles, when these particles cannot be individually labelled.

After integration, considering $f = Nf^1$ the Liouville equation becomes, for large N,

$$\begin{aligned} \partial_t f + \vec{\xi}.\partial_{\vec{x}} f + \vec{\chi}^e.\partial_{\vec{\xi}} f &= -\partial_{\vec{\xi}} \int\int \vec{\chi}_{12} f^2\left(\vec{x}_1, \vec{\xi}_1, \vec{x}_2, \vec{\xi}_2, t\right) d\vec{x}_2 d\vec{\xi}_2 = \frac{1}{m} \times \\ & \partial_{\vec{\xi}} \int\int \frac{\partial \Phi\left(x_{12}\right)}{\partial\left(\vec{x}_1 - \vec{x}_2\right)} f^2\left(\vec{x}_1, \vec{\xi}_1, \vec{x}_2, \vec{\xi}_2, t\right) d\vec{x}_2 d\vec{\xi}_2 \end{aligned} \tag{26}$$

which is a Boltzmann equation for the distribution function f, with a collision term Ω. This collision term has been split in two collision terms, He and Doolen, 2002, $\Omega = \Omega^{sd} + \Omega^{ld}$, where Ω^{sd} is referred to short distance interactions, $|\vec{r}_1 - \vec{r}| < \sigma$ and Ω^{ld} to long range interactions $|\vec{r}_1 - \vec{r}| > \sigma$.

4.1. Long-range term

Consider, first, the long-range collision term

$$\begin{aligned} \Omega^{ld} &= \frac{\partial}{\partial \vec{\xi}} \int\int_{|\vec{r}_1 - \vec{r}| > \varsigma} \frac{1}{m} \frac{\partial \phi\left(|\vec{r}_1 - \vec{r}|\right)}{\partial\left(\vec{r}\right)} \\ & \times f^2\left(\vec{r}, \vec{\xi}, \vec{r}_1, \vec{\xi}_1, t\right) d\vec{r}_1 d\vec{\xi}_1. \end{aligned} \tag{27}$$

By making the assumption that, for $|\vec{r}_1 - \vec{r}| > \sigma$, the molecular chaos prevails, He and Doolen, 2002,

$$f^2\left(\vec{r}, \vec{\xi}, \vec{r}_1, \vec{\xi}_1\right) = f\left(\vec{r}, \vec{\xi}, t\right) f\left(\vec{r}_1, \vec{\xi}_1, t\right) = f f_1, \tag{28}$$

one obtains,

$$\begin{aligned} \Omega^{ld} &= \frac{1}{m} \frac{\partial f\left(\vec{r}, \vec{\xi}, t\right)}{\partial \vec{\xi}} . \frac{\partial}{\partial \vec{r}} \int_{|\vec{r}_1 - \vec{r}| > \sigma} \phi\left(|\vec{r}_1 - \vec{r}|\right) \\ & \times n\left(\vec{r}_1, t\right) d\vec{r}_1, \end{aligned} \tag{29}$$

The integrand in the above equation is the mean field, i.e., the field exerted by the n molecules placed at $\vec{r}_1 - \vec{r}$, on the molecules at position $\vec{r}$,

$$\phi_m(\vec{r}) = \int_{|\vec{r}_1-\vec{r}|>\sigma} \phi(|\vec{r}_1-\vec{r}|)\, n(\vec{r}_1,t)\, d\vec{r}_1 \tag{30}$$

Cosider $n(\vec{r}_1,t)$ to vary slowly with the spatial coordinate,

$$\begin{aligned} n(\vec{r}_1,t) &= n(\vec{r},t) + \nabla n.(\vec{r}_1-\vec{r}) + \\ \frac{1}{2}\nabla\nabla n &: [(\vec{r}_1-\vec{r})(\vec{r}_1-\vec{r})] + ..., \end{aligned} \tag{31}$$

In this case,

$$\phi_m(\vec{r}) = -an - \varkappa\nabla^2 n, \tag{32}$$

where

$$a \equiv -\int_{\dot{x}>\sigma} \phi(x)\, d\vec{x}, \tag{33}$$

$$\varkappa \equiv -\frac{1}{6}\int_{\dot{x}>\sigma} \phi(x)\, x^2 d\vec{x}, \tag{34}$$

because, $\phi < 0$.

With the above hypotheses, the long-range term can thus be written as

$$\Omega^{ld} = \frac{1}{m}\frac{\partial f\left(\vec{r},\vec{\xi},t\right)}{\partial\vec{\xi}}.\nabla\phi_m(\vec{r}). \tag{35}$$

4.2. Short-Range term

After some lengthy algebra, under the molecular chaos hypothesis and supposing that the collisions involve only a pair of particles, considered as material points, the short-range term collision term can be written as (Kremer, 2005),

$$\begin{aligned} \Omega^{sd} &= \int\left(f\left(\vec{r},\vec{\xi}',t\right) f\left(\vec{r},\vec{\xi}_1{}',t\right) - f\left(\vec{r},\vec{\xi},t\right) f\left(\vec{r},\vec{\xi}_1,t\right)\right) \\ &\quad \times g b db d\epsilon d\vec{\xi}_1. \end{aligned} \tag{36}$$

This is the original Boltzmann collision term, (Boltzmann, 1866), deduced for material points, where $\vec{\xi}'$ and $\vec{\xi}_1'$ mean the velocities of, respectively, the target and the incident particles that rescue $\vec{\xi}$ and $\vec{\xi}_1$ after they collide, $\vec{g} = \vec{\xi}_1 - \vec{\xi}$ is the relative velocity and $g = |\vec{g}|$, b is an impact parameter related to the point where a particle, labeled as 1, reachs a spherical surface of radius σ around a target particle that moves, at the instant t, with the velocity $\vec{\xi}$ and ϵ is an azimuthal angle in the equatorial plane in the σ-sphere that is orthogonal to $\vec{\xi}_1 - \vec{\xi}$.

Enskog, Enskog, 1921, has, further, developed a collision model more appropriate for liquids, considering the particles to have a finite volume, since, in a liquid the mean free path has the same order of magnitude than the molecular diameter and multiple collisions are frequent, writting the collision term as

$$\begin{aligned} \Omega^{sd}_{Ensk} &= \int\int\int \left(\begin{array}{c} \chi\left(r+\frac{1}{2}\sigma\vec{k}\right) f\left(\vec{r},\vec{\xi}',t\right) f\left(\vec{r}+\sigma\vec{k},\vec{\xi}_1',t\right) - \\ \chi\left(r-\frac{1}{2}\sigma\vec{k}\right) f\left(\vec{r},\vec{\xi},t\right) f\left(\vec{r}-\sigma\vec{k},\vec{\xi}_1,t\right) \end{array} \right) \\ &\quad \times\sigma^2\vec{g}.\vec{k}d\vec{k}d\vec{\xi}_1 \end{aligned} \tag{37}$$

where

$$\vec{k} = (\cos\theta, \sin\theta\cos\epsilon, \sin\theta\sin\epsilon) \tag{38}$$

θ is a polar angle in the collision plane,

$$\theta = \arcsin\left(\frac{b}{\sigma}\right) \tag{39}$$

and χ is an *heuristic* correction factor introduced by Enskog to take account of the finite volume effects of the populations $f\left(\vec{r}, \vec{\xi}', t\right)$ and $f\left(\vec{r} + \sigma\vec{k}, \vec{\xi_1}', t\right)$.

5. Kinetic models for the collision term in the continuous velocity space

The collision term Ω is dependent on the distribution function itself and, indeed, the Boltzmann equation is a non-linear integro-differential equation. Instead of the full collision term, a collision model is required leading to a non-linear partial differential equation, which can be numerically solved. We restrict ourselves to the collision terms where the particles were considered without volume. The effect of the particle volume on discrete models, is, presently, still under investigation, He and Doolen, 2002, Surmas *et al.*, 2006.

5.1. BGK collision models

Considering the particles to be material points without volume and admitting the molecular chaos hypothesis, the collision term Ω in the Boltzmann equation, Eq. (1), was derived by Boltzmann in 1868 for binary collisions as Eq. (36).

The above hypothesis are only rigorously true for a rarefied gas without long-range attraction among their molecules. In addition, *molecular chaos* means that the post-collisional states of any two molecules are uncorrelated. If these hypothesis are accepted to be true, the Boltzmann equation is a non-linear integro-differential equation, which solution gives the distribution function $f(\vec{r}, \vec{c}, t)$, when the following molecular parameters are known: a) The molecular mass, m and b) the interaction potential, $\xi\left(|\vec{r}_1 - \vec{r}|\right)$. This means that any thermohydrodynamic problem could, in principle be solved, with solely these molecular informations and with appropriated boundary conditions. In fact, a Chapman-Enskog analysis of the Boltzmann equation with the collision term given by Eq. (36) shows that in the limit $Kn \to 0$, all the thermohydrodynamic equations are retrieved, with transport coefficients that are only dependent on the local physical state and on the above molecular properties.

Nevertheless, numerically solving this integro-differential equation has revealed to be a very complicated task. In addition, the full Boltzmann equation has details which are not, apparently, important, when the main worry is to describe the spatial and time evolution of the first hydrodynamic moments of the distribution function.

In this manner, consider replacing the collision term by a single relaxation term

$$\Omega = \frac{f^{eq} - f}{\tau}, \tag{40}$$

where τ is a relaxation time.

In spite of its apparent simplicity, Eq. (40) satisfy the main properties Eqs. (2-4) and the Boltzmann equation with the collision term given by Eq. (40) satisfy the H-theorem. Further, a Chapman-Enskog analysis shows that the full set of the thermohydrodynamic equations are retrieved with, nevertheless,

$$\frac{\mu}{2} = \frac{3\eta}{2} = \frac{3\varkappa}{10} = \frac{\rho e\tau}{3}, \tag{41}$$

leading to a non-manageable Prandtl number, due to the linear dependence of the viscosity coefficients and the thermal conductivity on the single relaxation parameter τ.

5.2. Deriving collision models with increased accuracy

Writting the distribution $f = f^{eq} + f^{neq}$, with $f^{neq} = f^{eq}\phi$, when f is near f^{eq} the short-range collision term can be written as

$$\Omega = f^{eq}\mathcal{L}(\phi), \tag{42}$$

where $\mathcal{L}$ is a linear operator, $\mathcal{L} : \xi^D \rightarrow \xi^D$.

For each point $\vec{r}$ the perturbation ϕ can be developed in terms of the Hermite polynomial tensors $\Psi_{\theta,(r_\theta)}$, Philippi *et al.*, 2006b, Shan and He, 1998,

$$\phi = \sum_{\theta} a^{\phi}_{\theta,(r_\theta)}\left(\vec{x},t\right)\Psi_{\theta,(r_\theta)}\left(\vec{\mathcal{C}}_f\right), \tag{43}$$

and coefficients a^{ϕ}_{θ} can be related to the macroscopic moments of f. In this way, $a^{\phi}_0 = 0$, $a^{\phi}_{1,\alpha} = 0$. The coefficient $a^{\phi}_{2,\alpha\beta}$ is related to the viscous stress tensor $\tau_{\alpha\beta}$ through

$$a^{\phi}_{2,\alpha\beta} = \frac{\tau_{\alpha\beta}}{2P}, \tag{44}$$

where $P = nkT$ is the thermodynamic pressure.

The peculiar kinetic energy $E(\vec{x},t) = \rho e$ is given by

$$\rho e = \int f\frac{1}{2}m\left(\vec{c}-\vec{u}\right)^2 d\vec{c} = \int f^{eq}\frac{1}{2}m\left(\vec{c}-\vec{u}\right)^2 d\vec{c}. \tag{45}$$

In this way

$$\int f^{neq}\frac{1}{2}mC^2 d\vec{C} = 0, \tag{46}$$

or

$$\int f^{neq}\frac{1}{2}mC_\alpha C_\alpha d\vec{C} = \frac{1}{2}tr\left(\tau\right) = 0. \tag{47}$$

In two-dimensions

$$\tau_{xx} + \tau_{yy} = 0, \tag{48}$$

or

$$a^{\phi}_{2,xx} + a^{\phi}_{2,yy} = 0. \tag{49}$$

For third-order moments

$$\begin{aligned} S_{\alpha\beta\gamma} &= \int fmc_\alpha c_\beta c_\gamma d\vec{c} = \int f^{eq}mc_\alpha c_\beta c_\gamma d\vec{c} + \int f^{neq}mc_\alpha c_\beta c_\gamma d\vec{c} \\ &= S^{eq}_{\alpha\beta\gamma} + S^{neq}_{\alpha\beta\gamma}, \end{aligned} \tag{50}$$

with

$$S^{eq}_{\alpha\beta\gamma} = \rho u_\alpha u_\beta u_\gamma + P\left(\delta_{\beta\gamma}u_\alpha + \delta_{\alpha\gamma}u_\beta + \delta_{\alpha\beta}u_\gamma\right). \tag{51}$$

For the non-equilibrium part,

$$S^{neq}_{\alpha\beta\gamma} = \int f^{neq}mC_\alpha C_\beta C_\gamma d\vec{C} + \left(\tau_{\beta\gamma}u_\alpha + \tau_{\alpha\gamma}u_\beta + \tau_{\alpha\beta}u_\gamma\right), \tag{52}$$

resulting, using $a^{\phi}_{1,\alpha} = 0$, the invariance property with respect to index permutation and Eq. (51):

$$\begin{aligned} P\left(\frac{2kT}{m}\right)^{\frac{1}{2}} a^{\phi}_{3,\alpha\beta\gamma} &= \frac{S_{\alpha\beta\gamma}}{2} - \left[\begin{array}{c} \frac{1}{2}\rho u_\alpha u_\beta u_\gamma + \frac{1}{2}P\left(\delta_{\beta\gamma}u_\alpha + \delta_{\alpha\gamma}u_\beta + \delta_{\alpha\beta}u_\gamma\right) \\ +\frac{1}{2}\left(\tau_{\beta\gamma}u_\alpha + \tau_{\alpha\gamma}u_\beta + \tau_{\alpha\beta}u_\gamma\right) \end{array}\right] \\ &\equiv q_{\alpha\beta\gamma}. \end{aligned} \tag{53}$$

When β and γ are contracted, defining ϵ_α to be the total energy flux along the direction α,

$$P\left(\frac{2kT}{m}\right)^{\frac{1}{2}} a^{\phi}_{3,\alpha\beta\beta} = \epsilon_\alpha - \left[\frac{1}{2}\rho u^2 u_\alpha + P\left(\frac{D}{2}+1\right)u_\alpha + \tau_{\alpha\beta}u_\beta\right] = q_\alpha, \tag{54}$$

where q_α is the *net* heat flux along the direction α, i.e., the total energy flux ϵ_α, excluding the flow of macroscopic kinetic energy $\frac{1}{2}\rho u^2 u_\alpha$, the compression work $P\left(\frac{D}{2}+1\right)u_\alpha$ and the viscous work $\tau_{\alpha\beta}u_\beta$.

Now, using the development, Eq. (43),

$$\mathcal{L}(\phi) = \sum_\theta a^\phi_{\theta,(r_\theta)} \mathcal{L}\left(\Psi_{\theta,(r_\theta)}\right). \tag{55}$$

The θ-order tensor $\mathcal{L}\left(\Psi_{\theta,(r_\theta)}\right)$ is, itself, an element of the $\mathcal{C}^D$ space and can be developed in terms of the θ-order Hermite tensors that belong to the orthogonal basis of this space,

$$\mathcal{L}\left(\Psi_{\theta,(r_\theta)}\right) = \sum_{(s_\theta)} \gamma_{(r_\theta),(s_\theta)} \Psi_{\theta,(s_\theta)}, \tag{56}$$

where $\gamma_{(r_\theta),(s_\theta)}$ designate the $(r_\theta),(s_\theta)$ components of 2θ-order *relaxation tensors*. As $\mathcal{L}$ is a self-adjoint operator, with non-positive eigenvalues, Cercignani, 1969,

$$\gamma_{(r_\theta),(m_\theta)} = \frac{\int e^{-\mathcal{C}_f^2} \mathcal{L}\left(\Psi_{\theta,(r_\theta)}\right) \Psi_{\theta,(m_\theta)} d\vec{\mathcal{C}}_f}{\int e^{-\mathcal{C}_f^2} \left(\Psi_{\theta,(m_\theta)}\right)^2 d\vec{\mathcal{C}}_f} \leq 0. \tag{57}$$

Using Einstein's notation

$$\mathcal{L}(\phi) = \sum_\theta \gamma_{(r_\theta),(s_\theta)} a^\phi_{\theta,(r_\theta)} \Psi_{\theta,(s_\theta)}, \tag{58}$$

where repeated indexes mean summation.

Above equation is an infinite summation on θ. When the terms above a chosen order N are diagonalised, following a Gross-Jackson procedure, Cercignani, 1969,

$$\mathcal{L}^{(N)}(\phi) = \sum_{\theta=0}^{N} \gamma_{(r_\theta),(s_\theta)} a^\phi_{\theta,(r_\theta)} \Psi_{\theta,(s_\theta)} - \gamma_{N+1} \sum_{\theta=N+1}^{\infty} \delta_{(r_\theta),(s_\theta)} a^\phi_{\theta,(r_\theta)} \Psi_{\theta,(s_\theta)}, \tag{59}$$

where

$$\delta_{(r_\theta),(s_\theta)} = \delta_{r_1 s_1} .... \delta_{r_\theta s_\theta}. \tag{60}$$

In this way, using Eq. (43)

$$\mathcal{L}^{(N)}(\phi) = -\left[\sum_{\theta=0}^{N} \lambda_{(r_\theta),(s_\theta)} a^\phi_{\theta,(r_\theta)} \Psi_{\theta,(s_\theta)}\right] - \gamma_{N+1}\phi, \tag{61}$$

where $\lambda_{(r_\theta),(s_\theta)} = -\left(\gamma_{(r_\theta),(s_\theta)} + \gamma_{N+1}\delta_{(r_\theta),(s_\theta)}\right)$ is positive for all r_θ, s_θ, since a) $\lambda_{(r_\theta),(s_\theta)} = -\gamma_{(r_\theta),(s_\theta)}$ for all off-diagonal components and b) the diagonal components $\gamma_{(r_\theta),(r_\theta)}$ are negative with an absolute value that is greater than γ_{N+1} for all θ smaller or equal to N. Eq. (61) can be considered as an N^{th}-order kinetic model to the collision term, with an absorption term $\gamma_{N+1}\phi$ resulting from the diagonalization of the relaxation tensors after the given N. Therefore, all the moments of order higher than N are collapsed into a single non-equilibrium term minimizing the truncation effects on the fine structure of the $\mathcal{L}$-operator spectrum.

Eq. (61) generates increasing accuracy models to Ω when the distribution function f is near the Maxwell-Boltzmann equilibrium distribution, f^{eq}. Each term in the sum, in Eq. (61), gives the relaxation to the equilibrium of second or higher order kinetic moments M_θ that are not preserved in collisions, modulated by a λ_θ relaxation tensor.

5.2.1. A second order collision model in the two-dimensional space

Without any loss in the generality, we restrict ourselves to two-dimensional spaces and second order models, with $N = 2$. In present section, the isotropy of 4^{th} rank tensors will be used to give explicit forms for the second-order collision model.

From Eq. (61)

$$\lambda_{(r_2),(s_2)} a^\phi_{2,(r_2)} \Psi_{2,(s_2)} = \lambda_{\alpha\beta\gamma\delta} a^\phi_{2,\alpha\beta} \Psi_{2,\gamma\delta}. \tag{62}$$

Requiring isotropy of 4^{th} rank tensors and considering the symmetry with respect to index permutation,

$$\lambda_{\alpha\beta\gamma\delta} = \lambda_\mu \left(\delta_{\alpha\beta}\delta_{\gamma\delta} + \delta_{\alpha\gamma}\delta_{\beta\delta} + \delta_{\alpha\delta}\delta_{\beta\gamma}\right). \tag{63}$$

In this way,

$$\begin{aligned} \lambda_{\alpha\beta\gamma\delta} a^\phi_{2,\alpha\beta}\Psi_{2,\gamma\delta} &= \lambda_\mu \left[a^\phi_{2,\alpha\alpha}\Psi_{2,\gamma\gamma} + a^\phi_{2,\alpha\beta}\Psi_{2,\alpha\beta} + a^\phi_{2,\alpha\beta}\Psi_{2,\beta\alpha}\right] \\ &= \lambda_\mu \left[\begin{array}{c} a^\phi_{2,xx}\left(\mathcal{C}^2_{fx} - \frac{1}{2}\right) + a^\phi_{2,yy}\left(\mathcal{C}^2_{fy} - \frac{1}{2}\right) + \\ 2a^\phi_{2,xy}\mathcal{C}_{fx}\mathcal{C}_{fy} \end{array}\right], \end{aligned} \tag{64}$$

since $a^\phi_{2,\alpha\alpha} = 0$. Using Eq.(44)

$$\lambda_{\alpha\beta\gamma\delta} a^\phi_{2,\alpha\beta}\Psi_{2,\gamma\delta} = \frac{\lambda_\mu}{P}\left[\tau_{xx}\left(\mathcal{C}^2_{fx} - \frac{1}{2}\right) + \tau_{yy}\left(\mathcal{C}^2_{fy} - \frac{1}{2}\right) + 2\tau_{xy}\mathcal{C}_{fx}\mathcal{C}_{fy}\right], \tag{65}$$

or, from Eq. (48), the second order model in two dimensions will be, finally, written as

$$\mathcal{L}^{(2)}(\phi) = -\frac{\lambda_\mu}{P}\left[\tau_{xx}\mathcal{C}^2_{fx} + \tau_{yy}\mathcal{C}^2_{fy} + 2\tau_{xy}\mathcal{C}_{fx}\mathcal{C}_{fy}\right] - \gamma_3\phi. \tag{66}$$

Present second-order continuous kinetic model is able for analyzing non-isothermal and fully compressible flows. The thermal conductivity is related to γ_3 diagonalization constant. Consideration of third-order collision models will be, only, necessary in multi-component systems, for correctly describing third-order coupling: the Soret and Dufour effects, Philippi and Brun, 1981a.

6. Velocity discretization

Discretization means to replace the entire continuous velocity space c^D by some discrete velocities $\vec{c}_i$. A Chapman-Enskog analysis shows that the correct macroscopic equations to be retrieved is given by assuring that the discrete distributions f_i^{eq} satisfy:

$$< \varphi_p >^{eq} = \int f^{eq}\left(\vec{\xi}\right)\varphi_p(\vec{\xi})d\vec{\xi} = \sum_i \frac{f_i^{eq}}{h^D}\varphi_p(\vec{\xi}_i), \tag{67}$$

for all $\{\varphi_p = 1, \xi_\alpha, \xi_\alpha\,\xi_\beta\,, \xi_\alpha\,\xi_\beta\,\xi_\gamma\,, ...\}$ of interest, where $f^{eq}\left(\vec{\xi}\right)$ is the MB distribution written in terms of the particles velocity $\vec{\xi}$ in the continuous space, h is the lattice unit, i.e., the smallest physical distance between any two contiguous grid points, D is the Euclidean dimension, $D = 2$ in the plane and $D = 3$ in three-dimnsional grids and $< \varphi_p >^{eq}$ means a macroscopic equilibrium moment of φ_p.

In Philippi *et al.*, 2006b, the discretization is considered as a quadrature problem, i.e., the discrete distributions f_i^{eq} in the right-hand side of Eq. (67) are replaced by $f^{eq}\left(\vec{\xi}_i\right)$, i.e., by the value of the MB distribution evaluated at the pole $\vec{\xi}_i$, multiplied by a parameter ω_i, which means the weight to be attributed to each velocity vector $\vec{\xi}_i$ for satisfying the quadrature condition, considering that, for each coordinate-axis α, the lattice-speeds $\xi_{i\alpha}$ form a discrete and finite set and the continuous velocity space is continuous and extends to infinity.

In this manner, the discretization restrictions, Eq. (67) are replaced by the following quadrature equations,

$$\begin{aligned} < \varphi_p >^{eq} &= \int f^{eq}\left(\vec{\xi}\right)\varphi_p(\vec{\xi})d\vec{\xi} \\ &= \sum_i \omega_i \left(\frac{2kT_0}{m}\right)^{D/2} f^{eq}\left(\vec{\xi}_i\right)\varphi_p(\vec{\xi}_i), \end{aligned} \tag{68}$$

where the factor $\left(\frac{2kT_0}{m}\right)^{D/2}$ was introduced for assuring ω_i to be a dimensionless, real number, since $f^{eq}\left(\vec{\xi}\right)$ is the number of particles per unit volume of the velocity space and per unit volume of the physical space.

When performing the quadrature, an integration variable must be chosen. If the dimensionless fluctuation velocity $\vec{\mathcal{C}}_f = \frac{\vec{\xi}-\vec{u}}{\left(\frac{2kT}{m}\right)^{1/2}}$ is chosen as the integrating variable, the particle velocities result dependent on T and on $\vec{u}$, Philippi *et al.*, 2006b,

$$\vec{\xi}_i = \vec{u} + \left(\frac{2kT}{m}\right)^{1/2} \vec{\mathcal{C}}_{fi} = \vec{\xi}_i\left(T, \vec{u}\right). \tag{69}$$

Another choice is the dimensionless particle velocity $\vec{\mathcal{C}} = \frac{\vec{c}}{\left(\frac{2kT}{m}\right)^{1/2}}$. In this case, the particle velocities are temperature dependent, Philippi *et al.*, 2006b,

$$\vec{\xi}_i = \left(\frac{2kT}{m}\right)^{1/2} \vec{\mathcal{C}}_i = \vec{\xi}_i\left(T\right). \tag{70}$$

Avoiding the $\vec{\xi}_i$ temperature dependence requires to consider the particles velocity $\vec{\xi}$ as the integrating variable when performing the quadrature, i.e., to let c^2 free from T in the exponential part $e^{-\mathcal{C}^2}$ of the equilibrium distribution. This can be accomplished by writing, Philippi *et al.*, 2006b, Shan and He, 1998,

$$e^{-\frac{(c-u)^2}{\frac{2kT}{m}}} = \left(e^{-\mathcal{C}_{fo}^2}\right)^{\frac{T_0}{T}}, \tag{71}$$

where T_0 is a reference (and constant) temperature and $\vec{\mathcal{C}}_{fo} = \frac{\vec{\xi}-\vec{u}}{\left(\frac{2kT_0}{m}\right)^{1/2}}$ is a new dimensionless peculiar velocity referred to the temperature T_o.

When T is near T_0, i.e., when the departures from thermal equilibrium are small, the above expression may be developed in a Taylor series around $\frac{T}{T_o} = 1$. Considering $\Theta = \frac{T}{T_o} - 1$ to be the temperature deviation, this development gives

$$\left(e^{-\mathcal{C}_{fo}^2}\right)^{\frac{T_0}{T}} = e^{-\mathcal{C}_{fo}^2}\left[1 + \mathcal{C}_{fo}^2\Theta + \frac{1}{2}\mathcal{C}_{fo}^2\left(\mathcal{C}_{fo}^2 - 2\right)\Theta^2 + ...\right], \tag{72}$$

which terms are increasing powers of $\mathcal{C}_{fo}^2$.

Consider writing the MB equilibrium distribution as

$$\begin{aligned} f^{eq} &= n_d\left(\frac{m}{2\pi kT}\right)^{D/2} e^{-\mathcal{C}_f^2} \\ &= n_d\left(\frac{m}{2\pi kT}\right)^{D/2} e^{-\mathcal{C}_{fo}^2}\left[1 + \mathcal{C}_{fo}^2\Theta + \frac{1}{2}\mathcal{C}_{fo}^2\left(\mathcal{C}_{fo}^2 - 2\right)\Theta^2 + ...\right] \\ &= n_d\left(\frac{m}{2\pi kT}\right)^{D/2} e^{-\mathcal{C}_o^2} e^{-\mathcal{U}_o^2 + 2\vec{\mathcal{U}}_o.\vec{\mathcal{C}}_o} \\ &\quad \times\left[1 + \mathcal{C}_{fo}^2\Theta + \frac{1}{2}\mathcal{C}_{fo}^2\left(\mathcal{C}_{fo}^2 - 2\right)\Theta^2 + ...\right]. \end{aligned} \tag{73}$$

The exponential term $e^{-\mathcal{U}_o^2 + 2\vec{\mathcal{U}}_o.\vec{\mathcal{C}}_o}$ is the generating function of the Hermite polynomials $\Psi_{\theta,(r_\theta)}\left(\vec{\mathcal{C}}_o\right)$ in the velocity space, where (r_θ) is a sequence of indexes $r_1, r_2, ...r_\theta$,

The Hermite tensors are orthogonal in the Hilbert space $\mathcal{H}$, with respect to the inner product

$$\left(h * g\right)_c = \frac{1}{\pi^{D/2}} \int e^{-\mathcal{C}^2} hg d\vec{\mathcal{C}}, \tag{74}$$

and symmetric wih respect to any index permutation.

After some straightforward algebra, the result for the equilibrium distribution can then be written as an infinite series, Philippi *et al.*, 2006b,

$$f^{eq} = \frac{1}{\pi^{D/2}} \left(\frac{m}{2kT_0} \right)^{D/2} e^{-C_0^2} \sum_{\theta} a^{eq}_{\theta,(r_\theta)} \left(n_d, \vec{\mathcal{U}}_0, \Theta \right) \Psi_{\theta,(r_\theta)} \left(\vec{\mathcal{C}}_o \right). \tag{75}$$

where the coefficients $a^{eq}_{\theta,(r_\theta)}$ are related, respectively, to the f macroscopic properties, at equilibrium: the number density of particles, n_d, the local momentum, $n_d \mathcal{U}_{0,\alpha}$, the momentum flux, $\Pi^{eq}_{\alpha\beta}$, the energy flux, $e^{eq}_{\alpha\beta\gamma}$ and an hyper-flux of momentum, $\Xi^{eq}_{\alpha\beta\gamma\delta}$.

From Eq. (68), it is easy to see that its corresponding discrete form can be written as,

$$f^{eq}_i = W_i \sum_{\theta} a^{eq}_{\theta,(r_\theta)} \left(n, \vec{\mathcal{U}}_0, \Theta \right) \Psi_{\theta,(r_\theta)} \left(\vec{\mathcal{C}}_{o,i} \right). \tag{76}$$

where $n = n_d h^D$ and $W_i = \frac{1}{\pi^{D/2}} \omega_i e^{-C^2_{0,i}}$, Philippi *et al.*, 2006b.

Consider the inner products in the continuous and discrete space, given respectively by,

$$(f * g)_c \equiv \frac{1}{\pi^{D/2}} \int e^{-\mathcal{C}_0^2} f g d\vec{\mathcal{C}}_0, \tag{77}$$

$$(f * g)_d \equiv \sum_i W_i f \left(\vec{\mathcal{C}}_{o,i} \right) g \left(\vec{\mathcal{C}}_{o,i} \right), \tag{78}$$

where $W_i = \frac{1}{\pi^{D/2}} \omega_i e^{-\mathcal{C}^2_{0i}}$ and their induced norms

$$\|f\|^2_c \equiv \frac{1}{\pi^{D/2}} \int e^{-\mathcal{C}_0^2} f^2 d\vec{\mathcal{C}}_0, \tag{79}$$

$$\|f\|^2_d \equiv \sum_i W_i f^2 \left(\vec{\mathcal{C}}_{o,i} \right). \tag{80}$$

Since functions $\Psi_{\theta,(r_\theta)} \left(\vec{\mathcal{C}}_o \right)$ are orthogonal in the continuous space with respect to the inner product Eq. (77), it can be shown, Philippi *et al.*, 2006b, that the quadrature equation, Eq. (68) requires the orthogonality of $\Psi_{\theta,(r_\theta)} \left(\vec{\mathcal{C}}_{o,i} \right)$ and their norm preservation in the discrete space, i.e.,

$$\sum_i W_i \Psi^2_{\theta,(r_\theta)} \left(\vec{\mathcal{C}}_{o,i} \right) = \frac{1}{\pi^{D/2}} \int e^{-C_0^2} \Psi^2_{\theta,(r_\theta)} \left(\vec{\mathcal{C}}_o \right) d\vec{\mathcal{C}}_o \tag{81}$$

In this manner, the still unknown weights W_i and the discrete velocities $\vec{\mathcal{C}}_{o,i}$ must be chosen in such a manner that the orthogonality of the Hermite polynomial tensors $\Psi_{\theta,(r_\theta)}$ is assured in the discrete space and satisfying the norm preservation equation, Eq. (81). In Philippi *et al.*, 2006b, it is shown that the norm preservation equation warrants the orthogonality of $\Psi_{\theta,(r_\theta)} \left(\vec{\mathcal{C}}_{o,i} \right)$, with respect to the inner product, Eq. (78), when the discrete velocity space is a *Bravais* lattice.

The above conclusion is very important because it reduces our discretization problem to find the weights W_i and the poles $\vec{\mathcal{C}}_{oi}$ satisfying, solely, the norm restrictions, Eq. (81).

With the exception of a very few lattices, Gaussian-like quadratures does not give a regular discrete set $\vec{\mathcal{C}}_{oi}$. Nevertheless, if any Bravais velocity set $\{\vec{e}_i\}$, giving a space-filling lattice, is chosen, the quadrature problem can be considered as to find the weights W_i and a scaling factor a such that $\vec{\mathcal{C}}_{o,i} = a\vec{e}_i$, satisfying Eq. (81). Considering that the poles $\vec{e}_i$ are previously known, this quadrature method was named as *quadrature with prescribed abcissae,* Philippi *et al.*, 2006b.

In this way, when the order of approximation N of the Hermite polynomial expansion to the MB equilibrium distribution is chosen, a set $\Psi_{\theta,(r_\theta)}$, $\theta = 0, ..., N$, is established, and the infinite and enumerable basis of the Hilbert space $\mathcal{H} : c^D \rightarrow \mathcal{R}$, which generates the solutions of the continuous Boltzmann equation, is replaced by a *finite* set of Hermite polynomial tensors, restricting the solutions to N^{th}-degree polynomials in the velocity $\vec{c}$. The quadrature problem is, now, to select a regular lattice $\{\vec{e}_i\}$, in such a manner that functions $\Psi_{\theta,(r_\theta)}$

preserve the orthogonality with respect to the inner product in the discrete space and this can be accomplished by assuring that the norm of *each one* of these functions $\Psi_{\theta,(r_\theta)}$ is retrieved, *exactly*, in the discrete space. The number b of the required lattice vectors is proportional to the order N of the polynomial approximation, $b = b(N)$. In addition, we have shown, Philippi *et al.*, 2006b, that when the quadrature problem is solved, the 2θ-rank tensors given by,

$$\Lambda_{(r_\theta),(s_\theta)} = \sum_i W_i \mathcal{C}_{0,i,r_0} ... \mathcal{C}_{0,i,r_\theta} \mathcal{C}_{0,i,s_0} ... \mathcal{C}_{0,i,s_\theta}, \tag{82}$$

are *isotropic* in the discrete space, for $\theta = 1, ...N$.

6.1. Two-dimensional square lattices

We restrict our attention to two-dimensional square lattices, in this work, although the above presented quadrature procedure is general and may be used for deriving two and three-dimensional lattices.

The dimensionless local velocity

$$\vec{\mathcal{U}}_0 = \frac{\vec{u}}{\left(\frac{2kT_0}{m}\right)^{1/2}}, \tag{83}$$

can be scaled for enabling to work with unitary lattice-units. In this manner, the spatial and the time scales, respectively, h and δ, can be chosen so as to satisfy,

$$\frac{h}{\delta} = \left(\frac{2kT_0}{m}\right)^{1/2}, \tag{84}$$

and, since

$$n\vec{\mathcal{U}}_0 = \sum_i f_i \vec{\mathcal{C}}_{oi} = a \sum_i f_i \vec{e}_i, \tag{85}$$

where $\vec{e}_i$ are the usual lattice vectors in 2D lattices, a new local velocity can be defined as

$$n\vec{u}^* = \frac{n\vec{\mathcal{U}}_0}{a} = \sum_i f_i \vec{e}_i. \tag{86}$$

In two dimensions, square lattices like the D2Q9, D2Q13,..., have four discrete velocities at each energy level $\mathcal{C}_o$. Figure 9 summarizes some square lattices that are being used in lattice-Boltzmann simulation: each set of four discrete velocities is superposed to the previous lattice-vectors set when adding a single energy level, following the sequence $\left(0,\ 1,\ \sqrt{2},\ 2,\ 2\sqrt{2},\ 3,\ 3\sqrt{2},...\right)$.

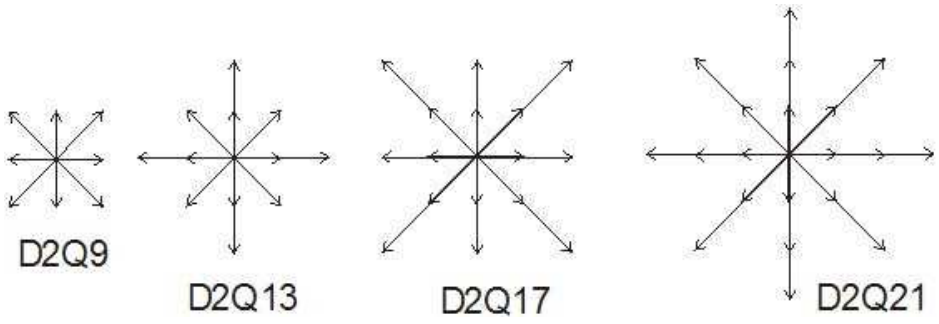

Figure 9: Some two-dimensional square lattices that are usual in LBM.

When $N = 2$ there will be 4 linearly independent equations for 4 unknowns related to the scaling factor a, and the D2Q9 weights W_0, W_1,W_2. This set has a unique solution leading to the widely known values $W_0 = 16/36$, $W_1 = 4/36$,$W_2 = 1/36$ and $a = \sqrt{3/2}$.

The equilibrium distribution for the D2Q9 lattice is, then,

$$f_{i,2}^{eq} = W_i n \left(\begin{array}{c} 1 + 2a^2 u_\alpha^* e_{i,\alpha} + 2a^2 u_\alpha^* u_\beta^* \left(a^2 e_{i,\alpha} e_{i,\beta} - \frac{1}{2}\delta_{\alpha\beta}\right) + \\ \Theta\left(a^2 e_i^2 - 1\right) \end{array} \right), \tag{87}$$

with third-order errors $\mathcal{O}(\Theta u^*, u^{*3})$, with respect to the full MB distribution.

The effect of temperature on the equilibrium distribution can be clearly seen from Eq. (87). In higher temperature sites, the amount of rest particles is reduced and redistributed to higher energy levels, trying to mimic the temperature dependence of the continuous MB distribution. This effect is highly desirable in thermal LBE simulation. An equilibrium distribution similar to Eq.(87) is given as Eq. (18) of Shan and He, 1998.

The D2Q13 and the next lattices are also able to run second-order models. In these cases, the number of unknowns is greater than the number of disposable equations and several solutions will be available, satisfying the quadrature problem.

Nevertheless, contrary to MacNamara and Alder results (McNamara and Alder, 1993) and to the results that would be expected with fitting methods, this lattice is *not able* to run *full* third order models. Indeed, when $N = 3$, it is impossible to find real positive values for a, W_0, W_1,W_2, W_3 satisfying all the norm restrictions, Eq. (81) related to $\Psi_{3,\alpha\beta\gamma}$. This result is the same for the D2Q17 lattice.

Considering the D2Q21 lattice as a next candidate for third order models, there will be, in this case, 7 unknowns a, W_0, W_1,W_2, W_3,W_4, W_5 for 6 norm restrictions, after eliminating identical equations. Letting a to be a free variable, the system gives a solution with real positive roots when a is inside the interval $0.659\,836 \leq a \leq 1.16208$.

The values $a = 0.659\,836$ and $a = 1.16208$ (in fact, $a = \frac{1}{12}\sqrt{5}\sqrt{\sqrt{193} + 25}$) are roots of the polynomials $W_0(a)$ and $W_3(a)$, respectively. In this manner, when the value $a = 1.16208$ is chosen, $W_3 = 0$ and the lattice loss an energy level, giving a modification of the D2Q17 lattice, which has been named D2V17, shown in Figure 10. The weights, with six significant digits, are $W_0 = 0.402005$, $W_1 = 0.116155$, $W_2 = 0.0330064$, $W_3 = 0$, $W_4 = 0.0000790786$, $W_5 = 0.000258415$.

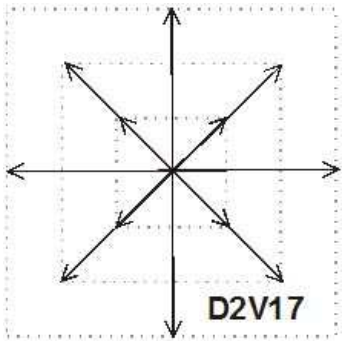

Figure 10: The D2V17 lattice.

This modified square lattice is less expensive considering computer requirements and has the same properties when compared with the D2Q21 lattice, i.e., it retrieves, exactly, all the equilibrium moments up to the 3^{rd} order and ii) gives isotropic tensors up to the 6^{th} rank. Therefore, present method can be, also, considered as a tool for investigating the structure of minimal velocity sets giving regular lattices.The D2V17 equilibrium distribution can be written as

$$\begin{aligned} f_{i,3}^{eq} &= f_{i,2}^{eq} + W_i a_{3,\alpha\beta\gamma}^{eq} \Psi_{3,\alpha\beta\gamma}(i) = \\ & W_i n \left[\begin{array}{c} 1 + 2a^2 u_\alpha^* e_{i,\alpha} + 2\left(a^2 u_\alpha^* u_\beta^*\right)\left(a^2 e_{i,\alpha} e_{i,\beta} - \frac{1}{2}\delta_{\alpha\beta}\right) + \\ \Theta\left(a^2 e_i^2 - 1\right) \\ + \frac{4}{3} a^3 u_\alpha^* u_\beta^* u_\gamma^* \left[\begin{array}{c} a^3 e_{i,\alpha} e_{i,\beta} e_{i,\gamma} - \\ \frac{a}{2}\left(e_{i,\alpha}\delta_{\beta\gamma} + e_{i,\beta}\delta_{\alpha\gamma} + e_{i,\gamma}\delta_{\alpha\beta}\right) \end{array} \right] \\ + 2\Theta a^2 \left(a^2 e_i^2 - 2\right) u_\gamma^* e_{i,\gamma} \end{array} \right], \end{aligned} \tag{88}$$

with fourth-order errors $\mathcal{O}(\Theta u^{*2}, u^{*4})$.

In addition to the equilibrium moments up to order 3, thermohydrodynamics requires the 4^{th}-order equilibrium moments $< \mathcal{C}_0^2 \mathcal{C}_{0,x}^2 >^{eq}$, $< \mathcal{C}_0^2 \mathcal{C}_{0,y}^2 >^{eq}$and $< \mathcal{C}_0^2 \mathcal{C}_{0,x} \mathcal{C}_{0,y} >^{eq}$to be retrieved, McNamara and Alder, 1993. Since these functions are not orthogonal in the continuous velocity space, a Gram-Schmidt orthogonalization procedure was used to find orthogonal polynomials from this set by using the previous Hermite polynomials and the inner product Eq. (77).

The result was

$$\Psi_{4,1} = \mathcal{C}_o^2 \mathcal{C}_{o,x}^2 - \frac{7}{2}\mathcal{C}_{o,x}^2 - \frac{1}{2}\mathcal{C}_{o,y}^2 + 1, \tag{89}$$

$$\Psi_{4,2} = \frac{1}{7}\left(\mathcal{C}_o^2\left(7\mathcal{C}_{o,y}^2 - \mathcal{C}_{o,x}^2\right) - 24\mathcal{C}_{o,y}^2 + 6\right), \tag{90}$$

$$\Psi_{4,3} = \mathcal{C}_{o,x}\mathcal{C}_{o,y}\left(\mathcal{C}_o^2 - 3\right). \tag{91}$$

When we require the norm preservation of the functions $\Psi_{4,1}$, $\Psi_{4,2}$ and $\Psi_{4,3}$ this gives a system of 8 independent equations for 9 unknowns. In this case, a is, again, a free parameter and the solution gave real positive weights for $0.590193 \leq a \leq 0.760569$.

Further, when a is, respectively, taken as 0.590193 or 0.760569 the weights W_1 or W_6 are null, giving two D2V25 lattices that retrieve the correct thermohydrodynamics equations. These lattices are shown in Figure 11. For the first lattice, called D2V25(W1), $a = 0.590193$ and the calculated weights are $W_0 = 0.235184$, $W_1 = 0$, $W_2 = 0.101\,817$, $W_3 = 5.\,921\,34 \times 10^{-2}$, $W_4 = 2.\,004\,09 \times 10^{-2}$, $W_5 = 6.\,795\,23 \times 10^{-3}$, $W_6 = 1.\,143\,76 \times 10^{-3}$, $W_7 = 2.\,197\,88 \times 10^{-3}$. Lattice D2V25(W6) has $a = 0.760569$ and $W_0 = 0.239\,059$, $W_1 = 0.063\,158$, $W_2 = 8.\,759\,57 \times 10^{-2}$, $W_3 = 3.\,118\,00 \times 10^{-2}$, $W_4 = 6.\,198\,96 \times 10^{-3}$, $W_5 = 2.\,020\,13 \times 10^{-3}$, $W_6 = 0$, $W_7 = 8.\,382\,24 \times 10^{-5}$.

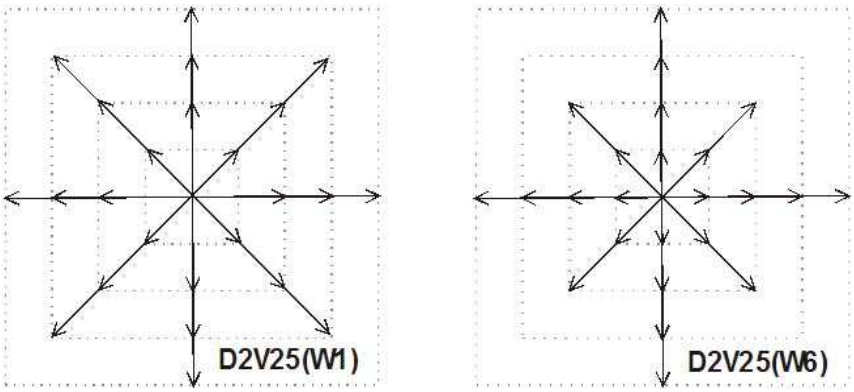

Figure 11: The D2V25 lattices for thermal problems.

Therefore, thermohydrodynamic equations are correctly retrieved with the LBE based on these lattices, but isotropy of 8^{th}-rank tensors cannot be assured. The equilibrium distribution for this lattice can be written as

$$f_{i,th}^{eq} = f_{i,3}^{eq} + W_i\left[a_{4,1}^{eq}\Psi_{4,1}(i) + a_{4,2}^{eq}\Psi_{4,2}(i) + a_{4,3}^{eq}\Psi_{4,3}(i)\right], \tag{92}$$

with, nevertheless, fourth-order errors $\mathcal{O}(\Theta u^{*2}, u^{*4}, \Theta^2)$ with respect to the full MB distribution. Parameters $a_{4,\theta}^{eq}$ can be found by using the orhogonality properties of $\Psi_{4,\theta}\left(\vec{\mathcal{C}}_0\right)$ in the continuous space, giving,

$$a_{4,1}^{eq} = \frac{2}{7}\left(2a^4 u_x^{*2} u^{*2} + \Theta a^2\left(6u_x^{*2} + u^{*2}\right) + 2\Theta^2\right), \tag{93}$$

$$a_{4,2}^{eq} = \frac{1}{12}\left(7a^4 u_y^{*4} + a^4 u_x^{*4} + 6a^4 u_x^{*2} u_y^{*2} + 24a^2 u_y^{*2}\Theta + 6\Theta^2\right), \tag{94}$$

$$a_{4,3}^{eq} = \frac{4}{3} a^2 u_x^* u_x^* \left(3\Theta + a^2 u^2\right).$$

For full fourth-order model, the norm preservation of a full set of Hermite orthogonal polynomials until the 4^{th}-order is required, giving a set of 9 norm restrictions. This system will be, only, closed for a lattice with 8 energy levels. The D2Q29 lattice, with 8 weights $W_0, ...,W_7$, is a natural candidate to be the *minimal* square lattice to run fourth-order models in the square lattices hierarchy. For this lattice, there are 9 linearly independent equations. This closed set of 9 independent equations has, nevertheless, no solution.

This result was the same for the next D2Q33 lattice, when a is let as a free parameter.

Since each function $\Psi_{\theta,(r_\theta)}$ is a linear combination of the monomials $\varphi = \left\{1, \mathcal{C}_{ox}, \mathcal{C}_{oy}, \mathcal{C}_{ox}^2, \mathcal{C}_{oy}^2, \mathcal{C}_{ox}\mathcal{C}_{oy}, ...\right\}$, the norm restrictions, Eq. (81), can be indifferently used on the set Ψ of orthogonal functions or on set φ of monomials. The last choice is, in present case, preferable, for identifying a symmetry overcome in the Q-series hierarchy of square lattices (Figure 9). Indeed, consider the fourth-order functions $\varphi_{4,1} = \mathcal{C}_{oy}^2 \mathcal{C}_{ox}^2$ and $\varphi_{4,2} = \mathcal{C}_{ox}^3 \mathcal{C}_{oy}$. These functions have different norms in the continuous space, respectively, $\frac{3}{4}$ and $\sqrt{\frac{15}{16}}$. Nevertheless, since $\varphi_{4,1} = \left(\mathcal{C}_{oy}\mathcal{C}_{ox}\right)^2$ and $\varphi_{4,2} = \left(\mathcal{C}_{ox}\mathcal{C}_{oy}\right)\mathcal{C}_{ox}^2$ the only contributions for their norms, in the discrete space, came from the diagonal vectors and are the same, because, along these directions, $\mathcal{C}_{o,iy} = \mathcal{C}_{o,ix}$.

This is an important result, since it means that the Q-series of square lattices are unable to run full fourth-order LBE models.

In this way, we have tried another building structure for the lattices, filling completely the available Cartesian space around each site, following the sequence $|e_i| = 0$, 1, $\sqrt{2}$, 2, $\sqrt{5}$, $2\sqrt{2}$, 3, $\sqrt{10}$ with sequentially increasing values for $|e_i|$.

Figure 12 shows a D2V37 lattice, constructed in such a manner, with 37 velocity vectors, but 8 weights W_i. Solution of the 9 norm equations is unique and gives, when 6 significant digits are considered, $a = 0.846393$, $W_0 = 0.233151$, $W_1 = 0.107306$, $W_2 = 0.0576679$, $W_3 = 0.0142082$, $W_4 = 0.00535305$, $W_5 = 0.00101194$, $W_6 = 0.000245301$, $W_7 = 0.000283414$. This lattice came from the solution of a closed system with 9 linearly independent norm restriction for 9 unknowns.

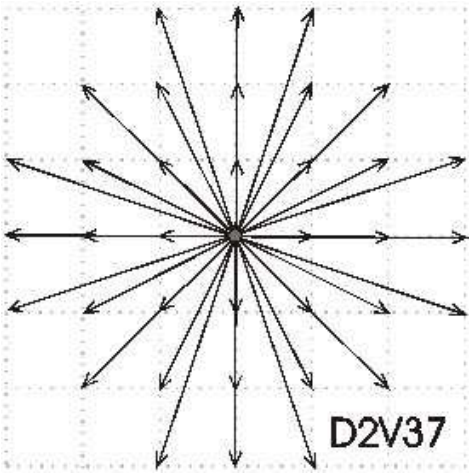

Figure 12: The D2V37 lattice.

Since, in the D2V37 lattice, all the fourth-order Hermite polynomial tensors belong to the orthogonal basis of this lattice, the equilibrium distribution can be written as,

$$
\begin{aligned}
f_{i,4}^{eq} &= f_{i,3}^{eq} + W_i a_{4,\alpha\beta\gamma\delta}^{eq} \Psi_{4,\alpha\beta\gamma\delta}(i) = \\
& W_i n \left\{ \begin{array}{c}
1 + 2a^2 u_\alpha^* e_{i,\alpha} + 2\left(a^2 u_\alpha^* u_\beta^*\right)\left(a^2 e_{i,\alpha} e_{i,\beta} - \frac{1}{2}\delta_{\alpha\beta}\right) \\
+\Theta\left(a^2 e_i^2 - 1\right) \\
+\frac{4}{3} a^3 u_\alpha^* u_\beta^* u_\gamma^* \left[\begin{array}{c} a^3 e_{i,\alpha} e_{i,\beta} e_{i,\gamma} \\ -\frac{a}{2}\left(e_{i,\alpha}\delta_{\beta\gamma} + e_{i,\beta}\delta_{\alpha\gamma} + e_{i,\gamma}\delta_{\alpha\beta}\right) \end{array} \right] \\
+2\Theta a^2\left(a^2 e_i^2 - 2\right) u_\gamma^* e_{i,\gamma} + \\
\frac{2}{3}\left[\begin{array}{c} \left[a^8 \left(u_\alpha^* e_{i\alpha}\right)^4 - 3a^6 u^{*2}\left(u_\alpha^* e_{i\alpha}\right)^2 + \frac{3}{4} a^4 u^{*4}\right] + \\ \Theta\left[\begin{array}{c} 3a^6\left(u_\alpha^* e_{i\alpha}\right)^2 e_i^2 - \\ \frac{3}{2} a^4\left(D\left(u_\alpha^* e_{i\alpha}\right)^2 + 4\left(u_\alpha^* e_{i\alpha}\right)^2 + u^{*2} e_i^2\right) + \\ \frac{3}{4} a^2 u^{*2}\left(D+2\right) \end{array} \right] \\ +\frac{3}{4}\Theta^2\left[a^4 e_i^4 - \frac{1}{2} a^2\left(D+2\right) e_i^2 + \frac{1}{4} D\left(D+2\right)\right] \end{array} \right] \end{array} \right\}. \qquad (95)
\end{aligned}
$$

The D2V37 lattice, with the above equilibrim distribution, can be considered as the *minimal* square lattice giving a fourth-order approximation to the continuous Boltzmann equation, wih errors $\mathcal{O}\left(\Theta^2 u^*, u^{*5}\right)$.

The weights W_i, in general, decrease with i and attain very small values when i is large. The smallness of W_i for large i is expected and is a consequence of: a) the restriction that was imposed on the lattice to be space filling, requiring the norm of each added lattice-vector, $\vec{e}_i$ to be, frequently, an integer multiple of the norm of the lattice-vectors forming the D2Q9 lattice unitary-cell, in square-lattices; b) the required degree of approximation leading to polynomials with terms of $\mathcal{O}\left(e_b^N\right)$.

7. Immiscible fluids

Flow of immiscible fluids is, classically, treated in fluid mechanics by considering that the transition layer has a null thickness and by performing a momentum balance around this layer. At microscopic level, when two immiscible fluids r and b are mixed, the long-range attraction between the molecules of each fluid is the molecular mechanism promoting fluid segregation. Intermolecular forces may be of many different types, including electrostatic forces between permanent dipoles, induction forces between permanent dipoles and induced dipoles, dispersion forces between non-polar molecules and hydrogen bonds. In the transition region between the two fluids, a molecule is, predominantly, subjected to attractive fields from its own phase that acts as a potential barrier and gives rise to fluid-fluid interfacial tension. In addition, molecules that are found in this transition layer are subject to r-b collisions that try to mix the two fluids and are responsible for r-b diffusion. The thickness of the transition layer is, consequently, controlled by the strength and length of long-range potentials and by cross collisions, r-b.

Theoretical difficulty is strongly increased when these two fluids interact with a solid surface. In fact, the interfacial energies ζ^{rs} and ζ^{bs} between fluids r and b and the surface are the main macroscopic mechanisms governing interface advancing or receding on a solid surface. When the interface advances or recedes along a solid surface, dynamic effects will change the contact angle $\theta^{rb/s}$ with respect to its equilibrium value.

Due to the complexity of intermolecular forces and considering their important contribution in defining fluid-fluid and fluid-solid interaction, the lattice Boltzmann method appear to be very suitable as a downscale method that can improve the understanding of complex physical phenomena that are very difficult to describe at the hydrodynamic scale.

In Santos *et al.*, 2003, the field mediators concept, described in dos Santos and Philippi, 2002, was extended for Boltzmann models of immiscible fluids. Mediators are null-mass particles that mimic the action of electrostatic forces. They are emitted from the lattice sites and their only action is to invert the momentum of lattice particles, simulating a long-range field. When a site $\vec{\mathbf{r}}$ can be considered as an attractive center for k particles, $k = r$, b, it will emit mediators of kind k that will be propagated to neighbor sites in the propagation step. Interference of k-mediators pull back to site $\vec{\mathbf{r}}$, k-particles moving away from $\vec{\mathbf{r}}$. In this way, following very simple emission and interference rules, mediators try to simulate the effect of long-range forces in fluid separation. Particles of kind r in the r-b interface that are thrown by collisions toward the b-phase will be pulled back to the r-phase when they found r-mediators in the same site and in the same direction, after propagation step.

Gunstensen *et al.*, 1991, Gunstensen and Rothman, 1992, are attributed to be the first who introduced immiscible fluids color based models in the frame of the lattice Boltzmann method. A more popular two-phase flow model, based on a pseudo-potential function, was derived by Shan and Chen, 1993. This method was later extended to three dimensions, Martys and Chen, 1996. A drawback in the above model is that it become

unstable when used to simulate fluids with very different viscositys (say $\mu_1/\mu_2 > 7$), as reported in J. *et al.*, 2002.

In Santos *et al.*, 2003, immiscible fluids r and b are modelled by splitting BGK collision term, separately considering r-r and r-b collisions. In this way, in contrast with the previous models, viscosity coefficients μ_r and μ_b and binary diffusivity $\mathcal{D}_{rb}$ can be independently managed using three independent relaxation times. Interfacial tension is retrieved by modifying r-b collision term, introducing long-range forces in the transition layer through the use of field mediators. Mediators' action is restricted to the transition layer and ideal gas state equation is retrieved for each fluid, far from the interface. In this way, we limit ourselves to an athermal model and no attempt to describe phase transitions and their related effects will be given here.

7.1. A heuristic BGK model for immiscible fluids

In Santos *et al.*, 2003, considering two immiscible fluids r and b, the long-range attraction between the particles of the same species is simulated by producing field mediators on the lattice-sites, just before the propagation step. Considering $R_i(\vec{\mathbf{r}},t)$ to be the particles distribution of r-particles in site $\vec{\mathbf{r}}$ at time t and, similarly, for $B_i(\vec{\mathbf{r}},t)$, mediators are created just before propagation step, and propagated, following

$$M_i^r(\vec{\mathbf{r}}+\vec{\mathbf{e}}_i\delta,t+\delta) = \alpha M_i^r(\vec{\mathbf{r}},t) + \beta\frac{\sum_j R_j(\vec{\mathbf{r}},t)}{\sum_j R_j(\vec{\mathbf{r}},t)+\sum_j B_j(\vec{\mathbf{r}},t)}, \tag{96}$$

where $\alpha+\beta=1$.

The first term in the right hand side of the above equation is, in fact, a recurrence relation, since $M_i^r(\vec{\mathbf{r}},t)$ depends on $M_i^r(\vec{\mathbf{r}}-\vec{\mathbf{e}}_i\delta,t-\delta)$ and on $K_j(\vec{\mathbf{r}}-\vec{\mathbf{e}}_i\delta,t-\delta)$, $K=R,B$, for all j neighbors sites around site $\vec{\mathbf{r}}-\vec{\mathbf{e}}_i\delta$, through second order terms in α and β. In this way, M_i^r at site $\vec{\mathbf{r}}$, will be dependent on the next neighbors r-particles concentration through first order terms, on the second neighbors r-particles through second order terms and so on. When $\alpha=0$ (or $\beta=1$), mediators are created at site $\vec{\mathbf{r}}$, with the solely information of the concentration of r-particles on next neighbors sites: mediators distribution related to the direction i will be given by the mass fraction of r-particles on site $\vec{\mathbf{r}}-\vec{\mathbf{e}}_i\delta$, at time $t-\delta$. In this case, the interaction length corresponds to 1 lattice-unit. By increasing α with respect to β, interaction length can be, arbitrarily, increased.

Mediators are created at each site $\vec{\mathbf{r}}$ and propagated with the unitary lattice velocity $\vec{\mathbf{e}}_i$. The interference of field mediators with lattice-particles is described in the following.

The lattice-Boltzmann equation for kind K particles, is written as

$$K_i(\vec{\mathbf{r}}+\vec{\mathbf{e}}_i\delta,t+\delta) - K_i(\vec{\mathbf{r}},t) = \Omega(R_0,...,R_{b_m},B_0,...,B_{b_m}) \ , \tag{97}$$

for $K=R,B$. The collision operator Ω_i^k is required to satisfy the mass and momentum preservation equations,

$$\sum_{i=0}^{b_m}\Omega_i^r = 0 \ , \tag{98}$$

$$\sum_{i=0}^{b_m}\Omega_i^b = 0 \ , \tag{99}$$

$$\sum_{i=0}^{b_m}\mathbf{c}_i\left(\Omega_i^r+\Omega_i^r\right) = 0 \ . \tag{100}$$

A three-parameters BGK collision term that satisfies the above restrictions was proposed in Santos *et al.*, 2003, written as

$$\Omega_i^r = \omega^r\frac{R_i^{eq}(n^r,\vec{\mathbf{u}}^r,T)-R_i}{\tau^r} + \omega^b\frac{R_i^{eq}(n^r,\vec{\mathbf{v}}^{rb},T)-R_i}{\tau^m} \ , \tag{101}$$

where

$$n^k = \sum_{i=0}^{b_m}K_i \ , \tag{102}$$

and

$$\vec{\mathbf{u}}^k = \frac{1}{\rho^k}\sum_{i=1}^{b_m} K_i \vec{\mathbf{c}}_i \ , \tag{103}$$

are, respectively, the macroscopic number density of particles and the velocity of component k, $k = r, b$. The ω's in Eq.101 are the molar fractions, $\omega^k = n^k/n$.

The first term in the r.h.s. of Eq. 101 is related to the relaxation of r-particles distribution to an equilibrium state given by the r-component number density and momentum, considering r-r collisions, only. The second term considers r-b collisions and is related to the relaxation of r-particles to an equilibrium state given by the number density n^r and by the momentum $m^b\vec{\mathbf{u}}^b$modified by the action of r-mediators present in the same site,

$$m^r\vec{\mathbf{v}}^{rb} = m^b\vec{\mathbf{u}}^b - A\vec{\widehat{\mathbf{u}}}^m \ , \tag{104}$$

Constant A is to be related to interfacial tension. For ideal miscible fluids, $A = 0$ and this collision term will describe the relaxation of r-particles distribution to an equilibrium state given by n^r and by the momentum $m^b\vec{\mathbf{u}}^b$, as a consequence of r-b cross collisions. In immiscible fluids, Eq. 104 means that particles of kind r will be separated from b-particles by long-range attractive forces from r-phase, represented here by $-\vec{\widehat{\mathbf{u}}}^m$.

In the same way,

$$m^b\vec{\mathbf{v}}^{br} = m^r\vec{\mathbf{u}}^r + A\vec{\widehat{\mathbf{u}}}^m \ . \tag{105}$$

In Eqs. 104 and 105,

$$\vec{\widehat{\mathbf{u}}}^m = \begin{cases} \frac{\vec{\mathbf{u}}^m}{|\vec{\mathbf{u}}^m|} \ when \ \vec{\mathbf{u}}^m \neq 0 \\ 0 \qquad when \ \mathbf{u}^m \ = 0 \end{cases} \ , \tag{106}$$

where mediators velocity at site $\vec{\mathbf{x}}$ is given by

$$\vec{\mathbf{u}}^m = \sum_{i=1}^{b_m}(M_i^r - M_i^b)\vec{\mathbf{e}}_i \ , \tag{107}$$

pointing to the same direction where r-mediators were propagated, i.e., to the b-phase.

In present model, since $\left|\vec{\widehat{\mathbf{u}}}^m\right| = \{0, 1\}$, the long-range effect on the cross-collision part of Ω_i^r is to relax r-particles distribution to an equlibrium distribution with a $\vec{\mathbf{u}}^0$ velocity, modified, in all lattice sites inside lattice-domains where r and b particles are simultaneously found, by a vector which modulus is constant and equal to A, which is to be related to the net value of interfacial tension. This is not the only choice for satisfying the restrictions on *local* mass and momentum preservation, but the simplest one and, although this could appear as a model 's restriction, the *direction* of $\vec{\widehat{\mathbf{u}}}^m$ in a given site $\vec{\mathbf{r}}$ will be dependent on the mediators distribution M_i^r and M_i^b in that site and these distributions are dependent on the r and b particle distributions in the neighbors sites, at the previous time steps.

8. Boundary Conditions

8.1. Monophasic flows inside capillaries

Considering a discrete set of particle velocities $\ell = \{\vec{e_i}, i = 0, ..., b\}$ a boundary condition in the LBM framework can be thought as a reflection law,

$$f_{i^+}(\vec{x}_b^*, t^*) = \sum_j B_{ij} f_{j^-}(\vec{x}_b^*, t^*), \tag{108}$$

where $\vec{e}_{i^+}$ represents a lattice-vector exiting from the solid surface at the site $\vec{x}_b^*$, toward the fluid phase and $\vec{e}_{i^-}$ a lattice vector exiting the fluid phase at the site $\vec{x}_b^*$. The $(b+1)\times(b+1)$ reflection matrix B_{ij} is written in accordance with the macroscopic property it is desired to describe at the boundary.

The simplest and mostly used boundary condition is the bounce-back condition,

$$B_{ij} = \delta_{ij}, \tag{109}$$

giving

$$f_{i^+} = f_{i^-}, \tag{110}$$

which satisfies the adherence condition $\vec{u} = 0$ at the solid boundary.

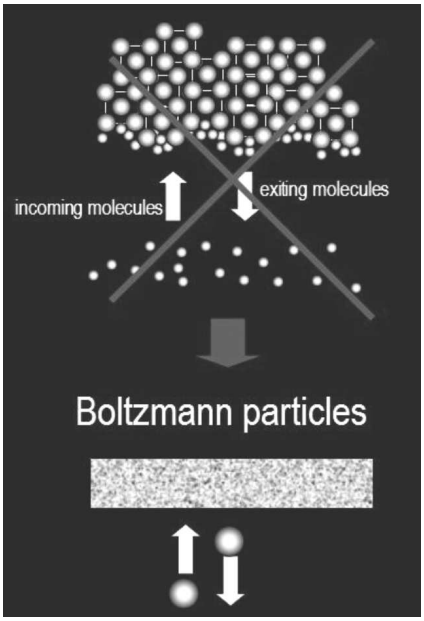

Figure 13: Boundary conditions in LBM.

Bounce-back conditions are pictured in Figure 13. It avoids all the complexity of the description scale related to fluid-solid interaction. At this scale, a certain amount of adsorbed fluid molecules exit the surface, where they, presumably, have reached an equilibrium state with the solid molecules and is replaced by another amount of incoming fluid-molecules from the fluid phase. In steady-state conditions, these incoming and exiting amounts of molecules must be identical. Nevertheless, at this nanometric scale, a slip in the local velocity and a jump in the local temperature are to be expected, since the incoming molecules do not know the equilibrium state that was imposed by the solid surface on the exiting molecules that were adsorbed on it, Philippi and Brun, 1981b. Velocity slips and temperature jumps are dependent on the Knudsen number, i.e., on the ratio between the mean free path and the length of the macroscopic domain of interest. The Knudsen number, itself, is a function of the fluid density and Knudsen discontinuities at the solid surface are only expected to be important, when a low-density gas flows inside a capillary. In this manner, these discontinuities are not expected to be important in liquid-flows. Nevertheless, in the mostly used lattice-BGK collision-propagation schemes, the mean free path is dependent on the dimensionless relaxation parameter τ used for the collision term, since when this parameter grows-up, collisions are less-effective in changing the particles distribution in a given site. In this manner, since the space discretization imposes a numerical lower limit in τ of $1/2$, the Knudsen number is not expected to be small enough, as it is required for a continuum approach, and $\mathcal{O}(Kn^2)$ *numerical* effects are expected to happen in lattice-Boltzmann simulation. These numerical effects are instability sources and these sources are believed to be specially important near the solid walls.

In this way, establishing the correct boundary conditions in LBM is, still, an open problem and a subject of intensive research nowadays.

In athermal problems the bounce-back conditions such as the ones pictured in Figure 13 are in current use and have shown to be suitable for velocity non-slipping problems for several lattices. Adequate boundary conditions for avoiding temperature jumps are still in progress in thermal problems, when a LBE that correctly describes the internal energy balance equation is used.

8.2. Immiscible displacement in capillaries

In immiscible displacement athermal problems, bounce-back conditions are also in use for the particle distributions, but the preferential wettability of one fluid on the solid wall is simulated using different reflection laws for the field mediators (Figure 14). Wettability of a given fluid on a solid surface is related to the relation between the cross adhesion forces among the liquid molecules and the solid and the cohesive forces that happen among the liquid mlecules themselves.

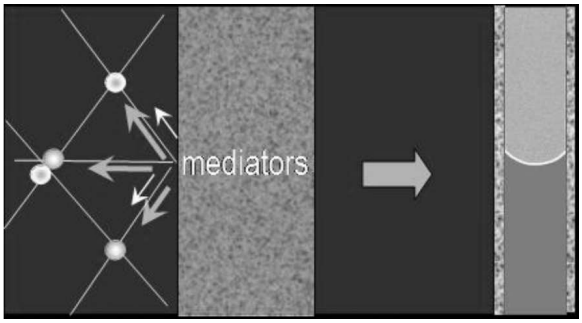

Figure 14: Boundary conditions in immiscible displacement.

The Young's law for liquid drops in contact with a solid surface and with its vapour (or a gas) gives a measurable parameter that quantifies the wettability,

$$\cos\theta_{eq} = \frac{\gamma_{sg} - \gamma_{sl}}{\gamma_l}, \tag{111}$$

where θ_{eq} is the *equilibrium* contact angle, γ_{sg} is the interfacial free energy at the solid-vapour interface reducing to γ_s when the adsorption energy can be neglected, γ_l is the liquid surface tension and, in accordance with Fowkes law,

$$\gamma_{sl} = \gamma_s + \gamma_\ell - \underbrace{\left(2\sqrt{\gamma_s^d\gamma_\ell^d} + 2\sqrt{\gamma_s^p\gamma_\ell^p}\right)}_{\text{adhesion work}}, \tag{112}$$

where the quantity $\left(2\sqrt{\gamma_s^d\gamma_\ell^d} + 2\sqrt{\gamma_s^p\gamma_\ell^p}\right)$ is the adhesion work, W_{ad}.

When $\gamma_{sg} - \gamma_{sl} > \gamma_l$, the adhesive forces are strong and the liquid will spread as a liquid film on the entire solid surface. When $\gamma_{sg} - \gamma_{sl} < \gamma_l$, the cohesive forces among the liquid molecules are dominant.

We have $\gamma_{sg} > \gamma_{sl}$ for a wetting liquid such as water on glass and $\gamma_{sg} < \gamma_{sl}$ for a non-wetting liquid such as mercury. In effect, in accordance with the Fowkes equation above,

$$\gamma_{sg} - \gamma_{sl} = -\gamma_\ell + 2\sqrt{\gamma_s^d\gamma_\ell^d} + 2\sqrt{\gamma_s^p\gamma_\ell^p}, \tag{113}$$

and this quantity can be either positive, when $\gamma_\ell < 2\sqrt{\gamma_s^d\gamma_\ell^d} + 2\sqrt{\gamma_s^p\gamma_\ell^p}$, i.e., when the liquid surface tension is smaller than the mixing cross forces among the liquid molecules and the solid surface, or negative, when the liquid surface tension (related to the intermolecular forces among the liquid molecules themselves) are stronger than the forces among liquid and solid molecules.

Oil and water are both wetting fluids on, e.g., a glass surface. Nevertheless, for water, w, the cross mixing forces with the glass molecules are strong giving a large adhesion work and a small γ_{sw}, when compared with an oil, o, such as isopentano, with a small adhesion work and a large γ_{so}. When water and oil are in contact with a solid surface

$$\cos\theta_{eq} = \frac{\gamma_{so} - \gamma_{sw}}{\gamma_{rb}}. \tag{114}$$

Present lattice-Boltzmann schemes for simulating immiscible displacement in capillaries are based on rather simple rules, by adjusting the reflected amounts of fluids r and b in such a maner as to retrieve the equilibrium contact angle in equilibrium simulations (Figure 15). In this way, in addition to the viscosity ratio, the only experimental information that is needed in these kind of simulations are the equilibrium contact angle, θ_{eq} and the interfacial tension, γ_{rb}. Further studies are necessary for including the polar and dispersive surface energies in the model parameters.

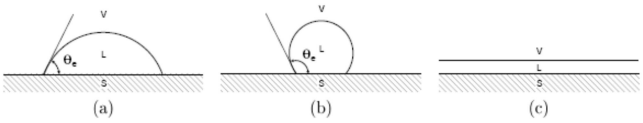

Figure 15: Equilibrium between a liquid drop and a solid surface for (a) a wetting liquid, (b) a non-wetting liquid and (c) a totally spreading liquid.

9. A sample problem: capillary invasion

The simulation results of the capillary invasion of a wetting liquid, r, into a cylindric tube, under zero gravity, is shown in Figure 16. Only capillary forces are considered and, in this way, the pressure in the capillary entrance and exit were kept the same, the non-wetting fluid particles, b, that exit the numerical domain being reintroduced at the capillary entrance, after they change their label as wetting fluid r-particles. A model similar to the one that was developed for immiscible fluids was used. The fluid viscosities and the interfacial tension are the only informations required for the model, when the fluid-solid interaction is not considered.

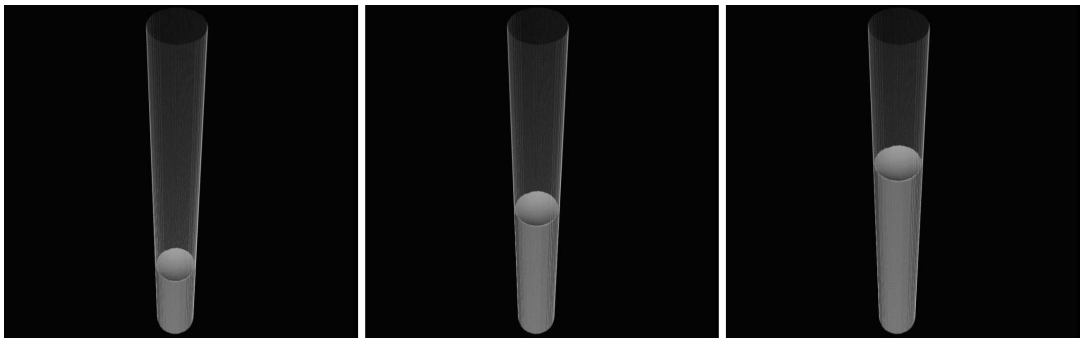

Figure 16: Capillary invasion

The LBM simulation was performed without any velocity singularity in the triple line, since the triple-line is here considered as a *transition region* where the fluid-particles are subjected to electrostatic forces from the wall and from the fluid phases.

In the fluid-fluid interface the electrostatic attractive forces among, e.g., the r-particles and the r-phase are simulated by deviating a certain amount of r-particles to the r-phase in accordance with Eq. (101), in the direction from where the r-mediators were emitted (Figure 16). This amount, which is the same for b-particles, is given by the force parameter A, in Eq. (104), directly related to the γ_{rb} interfacial tension (Santos *et al.*, 2003).

Boundary conditions are reflection laws for the particles and the mediators such as the ones described in the above section. The reflected amounts of r and b mediators are kept constant and adjusted in accordance with a given equilibrium contact angle, θ_{eq} in static conditions.

In this manner, in capillary invasion, the wetting fluid r-particles in the triple line will be simultaneously subjected to the attraction forces from the r-phase and from the solid surface, since the incoming mediators, after reflection on the solid wall, are predominantely r-mediators. From Figure 17, it can be seen that the predominancy of the fluid adhesion to the solid surface with respect to the cohesive forces to the r-phase, will be decided by the larger relative value of the horizontal projection of the attractive force from the wall, with respect to the atractive force from the r-phase.

A Poiseuille parabolic velocity profile was obtained in both phases for points that are far enough from the interface and from the tube entrance. Figure 18 shows the streamlines near the fluid-fluid interface in the

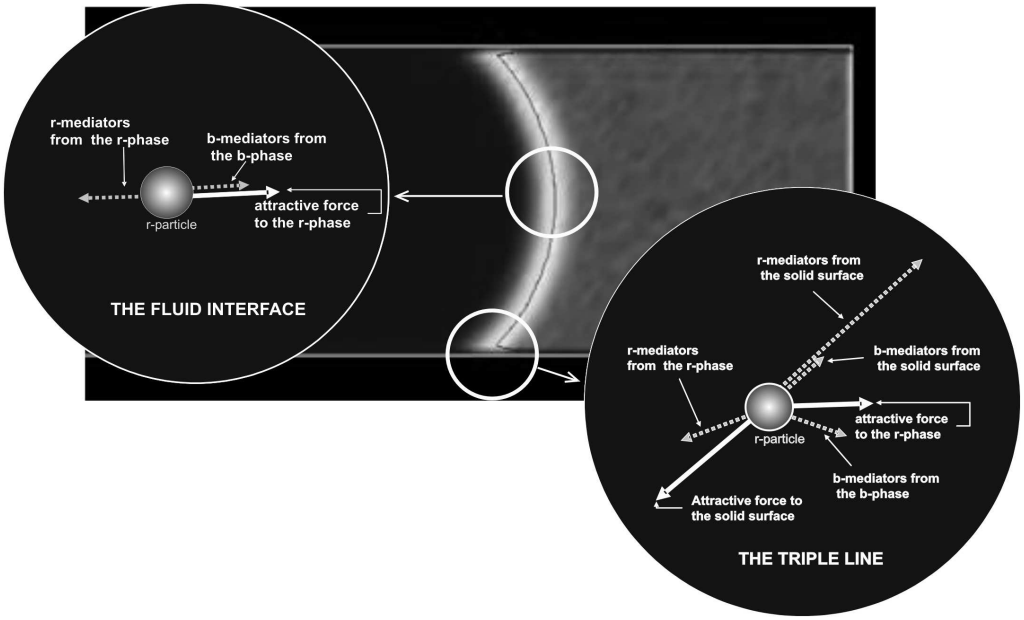

Figure 17: The fluid-fluid interface and the triple line.

course of the capillary invasion, at a symmetry plane. A strong recirculating zone, a vortex, is presented near the triple line. The vortex length is dependent on the strength and on the interaction length of the fluid-fluid and fluid-solid electrostatic forces. It belongs, indeed, to the same nanometric scale that is used for describing the triple-line itself and cannot be accessed by experimental visualizations.

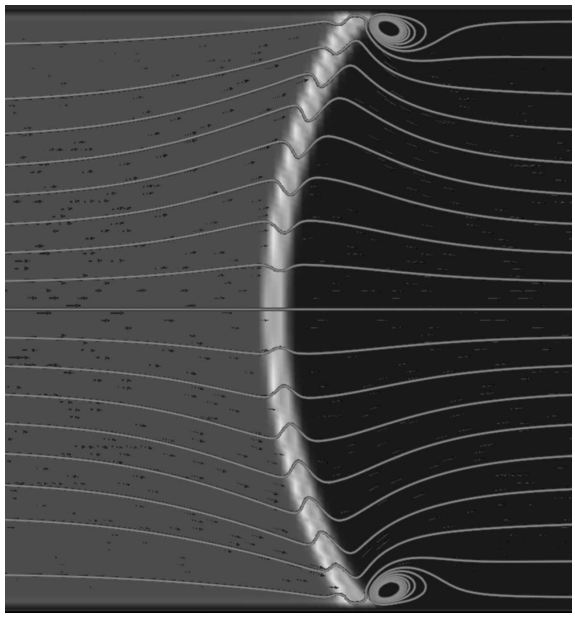

Figure 18: Streamlines near the fluid-fluid interface, showing a recirculating flow close to the triple-line.

In this way, the physical structure of this vortex is dependent on the model that was used for describing the capillary invasion process and this model cannot be validated against experimental results, at this nanometric scale. Nevertheless, Figure 19, a macroscopic result from the present LBM simulations, shows the capillary number dependence of the dynamic contact angle, as

$$\cos\theta_d = \cos\theta_e - \alpha Ca^{\beta} \tag{115}$$

where the capillary number is

$$Ca = \frac{\mu_r}{\gamma_{rb}} u_{int} \tag{116}$$

and u_{int} is the interface velocity. Angle θ_e is the equilibrium contact angle at static conditions. Eq. (115) was verified to be in correct agreement with experimental visualizations.

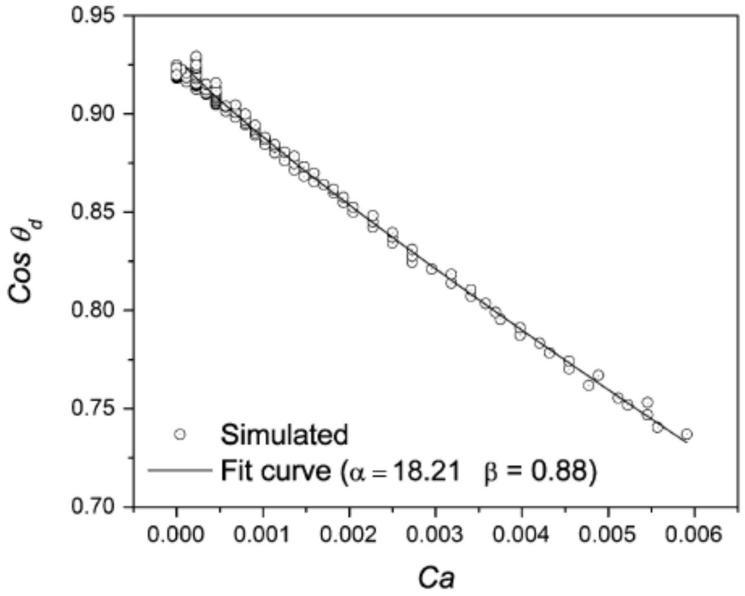

Figure 19: Capillary number dependence of the dynamical contact angle.

10. Conclusion

In spite of its great technological importance and of the growing scientific interest, microhydrodynamics has still a number of open questions to solve since macroscopic methods based on the Navier-Stokes framework have revealed to be insufficient to solve dynamic problems when interfacial forces and surface phenomena play an important role in the description of the problem. Although the great development of up-scaling methods from the molecular to the macroscopic scales based on the Boltzmann mesoscopic equation: a) the Boltzmann equation itself appropriated for liquids, taking the finite volume of particles and long range interaction into account, is still under investigation; b) The discretization of the Boltzmann equation leading to a manageable numerical method has not a unique issue when the computer limitations must be considered.

In this work, these several questions were discussed and some main problems in constructing a numerical method based on the spatial and velocity discretization of the Boltzmann equation were presented.

11. References

Alexander, F. J., Chen, S., and Sterling, J. D., 1993, Lattice Boltzmann Thermohydrodynamics, "Phys. Rev. E", Vol. 47, No. 4, pp. R2249.

Amyot, O., 2004, "Contribution à l' étude des é coulements diphasiques à travers un contact rugueux", PhD thesis, University of Poitiers.

Bhatnagar, P., Gross, E., and Krook, M., 1954, A Model for Collision Processes in Gases. I. Small Amplitude Processes in Charged and Neutral One-Component Systems, "Phys. Rev.", Vol. 94, pp. 511.

Boltzmann, L., 1866, Über die Mechanische Bedeutung des Zweiten Hauptsatzes der Wärmetheorie, "Wiener Berichte", Vol. 53, pp. 195–220.

Bosanquet, C., 1923, "Phils. Mag. ser.", Vol. 6.

Bretherton, F. P., 1961, The Motion Of Long Bubbles In Tubes, "Journal Of Fluid Mechanics", Vol. 10, pp. 166–188.

Cercignani, C., 1969, "Mathematical Methods in Kinetic Theory", Macmillan, London, first edition.

Chapman, S. and Cowling, T., 1999, "The Mathematical Theory of Non-Uniform Gases", Cambridge University Press, Cambridge.

Chen, H., Chen, S., and Matthaeus, W. H., 1992, Recovery of the Navier-Stokes equations using a lattice-gas Boltzmann method, "Phys. Rev. A", Vol. 45, No. 8, pp. R5339.

Chen, S., Chen, H., Martinez, D., and Matthaeus, W. H., 1991, Lattice Boltzmann model for simulation of magnetohydrodynamics, "Phys. Rev. Lett.", Vol. 67, pp. 3776.

Chen, Y., Ohashi, H., and Akiyama, M., 1994, Thermal Lattice Bhatnagar-Gross-Krook Model Without Nonlinear Deviations In Macrodynamic Equations, "Phys. Rev. E", Vol. 50, No. 4, pp. 2776.

d'Humières, D., 1992, Generalized lattice-Boltzmann equation, Shizgal, B. D. and Weaver, D. P., editors, "Progress in Astronautics and Aeronautics", Vol. 159, pp. 450–458.

d'Humières, D., Bouzidi, M., and Lallemand, P., 2001, Thirteen-velocity three-dimensional lattice Boltzmann model, "Phys. Rev. E", Vol. 63, No. 6, pp. 066702.

dos Santos, L. and Philippi, P. C., 2002, Lattice-gas model based on field mediators for immiscible fluids, "Phys. Rev. E", Vol. 65, pp. 046305.

Dussan, E. B., Ramé, V. E., and Garoff, S., 1991, On Identifying The Appropriate Boundary-Conditions At A Moving Contact Line - An Experimental Investigation, "Journal Of Fluid Mechanics", Vol. 230, pp. 97–116.

Enskog, D., 1921, Kinetiske theorie, "Svenska Vet. Akad. Handl.", Vol. 63, No. 4.

Fowkes, F., 1972, Donor-Acceptor Interactions At Interfaces, "Journal Of Adhesion", Vol. 4, No. 2, pp. 155.

Gunstensen, A. and Rothman, D., 1992, Microscopic Modeling Of Immiscible Fluids In 3 Dimensions By A Lattice Boltzmann Method, "Europhysics Letters", Vol. 18, pp. 157–161.

Gunstensen, A., Rothman, D., Zaleski, S., and Zanetti, G., 1991, Lattice Boltzmann Model Of Immiscible Fluids, "Physical Review A", Vol. 43, pp. 4320–4327.

He, X., Chen, S., and Doolen, G. D., 1998, A novel thermal model for the lattice Boltzmann method in incompressible limit, "J. Comput. Phys.", Vol. 146, No. 1, pp. 282–300.

He, X. and Doolen, G. D., 2002, Thermodynamic foundations of kinetic theory and Lattice Boltzmann models for multiphase flows, "J. Stat. Phys.", Vol. 107, No. 1–2, pp. 309–328.

He, X. and Luo, L. S., 1997, Theory of the lattice Boltzmann method: From the Boltzmann equation to the lattice Boltzmann equation, "Phys. Rev. E", Vol. 56, No. 6, pp. 6811–6817.

Higuera, F. J. and Jimenez, J., 1989, Boltzmann Approach To Lattice Gas Simulations, "Europhys. Lett.", Vol. 9, pp. 663.

Israelachvili, J. N., 1992, "Intermolecular and surface forces", Academic Press.

J., C., .S., B. E., and V., C. P., 2002, Lattice Boltzmann simulation of the flow of binary immiscible fluids with different viscosities using the Shan-Chen microscopic interaction model, "Philosophical Transactions Of The Royal Society Of London Series A-Mathematical Physical And Engineering Sciences", Vol. 360, pp. 547–558.

Kremer, G. M., 2005, "Uma Introdução à Equação de Boltzmann", Editora da Universidade de São Paulo.

Lallemand, P. and Luo, L. S., 2003, Theory of the lattice Boltzmann method: Acoustic and thermal properties in two and three dimensions, "Phys. Rev. E", Vol. 68, No. 3, pp. 036706.

Landau, L. D. and Levich, V. G., 1942, Dragging of a liquid by a moving plate, "Acta Phys. Chim. Urss", Vol. 17, pp. 42–54.

Lifshitz, E. and Pitaevskii, L., 1999, "Phyical kinetics", Butterworth-Heinemann, Oxford.

Lucas, R., 1918, Ueber das Zeitgesetz des Kapillaren Aufstiegs von Flussigkeiten, "Kolloid Z.", Vol. 23, No. 15.

Martys, N. S. and Chen, H., 1996, Simulation of multicomponent fluids in complex three-dimensional geometries by the lattice Boltzmann method, "Phys. Rev. E", Vol. 53, pp. 743–750.

McNamara, G. and Alder, B. J., 1993, Analysis Of The Lattice Boltzmann Treatment Of Hydrodynamics, "Physica A", Vol. 194, No. 1–4, pp. 218–228.

McNamara, G. R. and Zanetti, G., 1988, Use of the Boltzmann Equation to Simulate Lattice-Gas Automata, "Phys. Rev. Lett.", Vol. 61, No. 20, pp. 2332.

Ortiz, C. E. P., dos Santos, L., and Philippi, P., 2006, A two-fluid lattice Boltzmann model for ideal mixtures, "15^{th} DSFD - Discrete Simulation of Fluid Dynamics", Geneve.

Philippi, P.C.and Hegele Jr, L. A., Surmas, R., Siebert, D., and dos Santos, L., 2006a, From the continuous to the lattice-Boltzmann equation: beyond BGK collision models, "15^{th} DSFD - Discrete Simulation of Fluid Dynamics", Geneve.

Philippi, P., Hegele Jr., L., and dos Santos, L.O.E. andSurmas, R., 2006b, From the continuous to the lattice Boltzmann equation: The discretization problem and thermal models, "Phys. Rev. E", Vol. 73, No. 5, pp. 056702.

Philippi, P., Hegele Jr, L. A., Surmas, R., Siebert, D., and dos Santos, L. E., 2006c, Thernal lattice-Boltzmann in two dimensions, "15^{th} DSFD - Discrete Simulation of Fluid Dynamics", Geneve.

Philippi, P. C. and Brun, R., 1981a, Kinetic Modeling Of Polyatomic-Gas Mixtures, "Physica A", Vol. 105, No. 1-2, pp. 147–168.

Philippi, P. C. and Brun, R., 1981b, Kinetic Models and Relaxation Effects in the Knudsen Layer of Gas Mixtures, "Progress in Astronautics and Aeronautics", Vol. 74, pp. 428–443.

Qian, Y. H., d'Humières, D., and Lallemand, P., 1992, Lattice Bgk Models For Navier-Stokes Equation, "Europhys. Lett.", Vol. 17, No. 6, pp. 479.

Santos, L. O. E., Facin, P. C., and Philippi, P. C., 2003, Lattice-Boltzmann model based on field mediators for immiscible fluids, "Physical Review E", Vol. 68, No. 5, pp. 056302.

Shan, X. and Chen, H., 1993, Lattice Boltzmann Model For Simulating Flows With Multiple Phases And Components, "Phys. Rev. E", Vol. 47, pp. 1815–1819.

Shan, X. and He, X., 1998, Discretization of the velocity space in the solution of the Boltzmann equation, "Phys. Rev. Lett.", Vol. 80, No. 1, pp. 65–68.

Shan, X., Yuan, X. F., and Chen, H., 2006, Kinetic theory representation of hydrodynamics: a way beyond the Navier-Stokes equation, "Journal Of Fluid Mechanics", Vol. 550, pp. 413–441.

Stange, M., Dreyer, M. E., and Rath, H. J., 2003, Capillary driven flow in circular cylindrical tubes, "Physics of Fluids", Vol. 15, No. 9, pp. 2587–2601.

Surmas, R., 2006, Desenvolvimento de um modelo de Boltzmann para redes adequado a análise de problemas não-isotérmicos envolvendo fluidos não-ideais com transição de fases, Technical report, Mechanical Engineering Graduate Program Federal University of Santa Catarina.

Surmas, R., Ortiz, C. P., and dos Santos, L.O. E.and Philippi, P., 2006, Volume exclusion for reducing compressibility effects in lattice-Boltzmann models, "15^{th} DSFD - Discrete Simulation of Fluid Dynamics", Geneva.

Tanenbaum, B., 1987, "Plasma Physics", McGraw Hill, New York.

Wang Chang, C. and Uhlenbeck, G., 1970, "Sudies of Statistical Mechanics", Vol. 5. North-Holand, Amsterdam.

Washburn, E. W., 1921, The Dynamics of Capillary Flow, "Physical Review", Vol. 17, No. 3, pp. 273.

Proceedings of the 11th Brazilian Congress of Thermal Sciences and Engineering – ENCIT 2006
Braz. Soc. of Mechanical Sciences and Engineering – ABCM, Curitiba, Brazil, Dec. 5-8, 2006

Paper CIT06-0103

Turbulence challenges: flow separation and roughness effects

Atila P. Silva Freire
PEM/COPPE/UFRJ, C.P. 68503, 21945-970 – Rio de Janeiro, Brazil
atila@mecanica.coppe.ufrj.br

Abstract. *The present work strives on showing how two very important and difficult problems in engineering, flow separation and flow over rough surfaces, can be given an elegant treatment. After some detailed consideration on the fundamentals of each problem, the advanced theories are tested against respectively: i) flows over steep hills and ii) flows in micro-channels. Much emphasis is placed here on the description of the near wall turbulence.*

Keywords: *Turbulence, separation, roughness, hill, micro-channel.*

1. Introduction

Fluid dynamics is a profoundly difficult subject with a host of engineering applications. The trouble is that despite the many comprehensive advances that were achieved over the past century, some key and fundamental problems still remain unsolved. Complex engineering projects are then very often obliged to compromise, seeking solutions yielded by *ad hoc* procedures that lack a rigorous treatment.

Turbulence is a most notable problem in fluid dynamics. The presence of a highly irregular variation of the velocity field with time and space makes the flow description extremely complicated. Turbulent flow is an infinite dimension nonlinear system that has to be defined accordingly to some initial conditions. In real flows, the specification of the exact initial conditions from which the equations of motion can be integrated is, however, physically meaningless. Indeed, the exact microscopic description of a given flow would necessarily require the specification of both the position and the velocity of every lump of fluid. This is clearly an impossible undertaking.

If, on the other hand, we recover the notion that in a turbulent flow the fluid particles move in an extremely complex and irregular way, we may consider that over some sufficiently long time interval the effects of the initial conditions on the flow are smoothed out and disappear. Hence, this suggests that turbulent flows may be prone to a statistical representation. Unfortunately, no full theory of turbulence has been developed so far.

The purpose of this work is to show how two very important – but yet very difficult – problems facing turbulence modelers can be tackled: the prediction of separation and of roughness effects on flow properties. These are problems that have been around for a long time now but that still deserve a definitive and rigorous treatment.

In fact, these two problems must be very highly ranked in any list that considers the major unsolved problems of fluid mechanics. Thus, it may appear to the reader that we are faced with an impossible endeavor: the elucidation of problems that have been for years the central concern of researches but that have been left open. Actually, we will show how different thinking schools were developed to provide some useful results on both subjects. This will be made separately. After a section on fundamentals, where a common ground of discussion is established, two other sections will follow where the problem of a separating flow and the problem of flows over a rough surface are discussed.

2. Fundamentals

The equations of motion for a flow of an incompressible fluid are the Navier-Stokes equations:

$$\partial_t u_i + u_j \, \partial_j u_i = -\partial p + \nu \partial^2 u_i, \tag{1}$$

$$\partial_i u_i = 0 \tag{2}$$

where the pressure term incorporates the density and ν denotes the kinematic viscosity.

The above equations must be supplemented by initial and boundary conditions. They describe the motion of many common fluids, including air, water, alcohol, glycerine and most gases. Other more complicated fluids

require different constitutive relationships between the rate of strain and the induced stress. The present work will only deal with flows that are governed by Eqs. 1 to 2.

As it turns out, turbulence is a very irregular phenomenon – in time and space – what makes its detailed description a very difficult affair. However, we have already mentioned in the introduction that a probabilistic approach to turbulence might be a good choice. This would be very in hand since average values of important flow properties such as velocity, pressure, temperature, *et cetera*, would become available. Therefore, we may say that average quantities taken in terms of time, space or ensembles can be defined accordingly to certain characteristic scales of the flow.

Now consider that the Navier-Stokes equations must hold for any instant but also on the average; it results that a decomposition of the flow variables into mean and fluctuating parts yields:

$$\partial_t \overline{u_i} + \overline{u_j}\,\partial_j \overline{u_i} = -\partial \overline{p} + \nu \partial^2 \overline{u_i} - \partial_j \overline{u_i' u_j'}, \tag{3}$$

$$\partial_i \overline{u_i} = 0 \tag{4}$$

where the overbars are used to denote a mean quantity, e.g. in time, and the dashes a fluctuating quantity.

The two equations above are referred to in literature as the Reynolds Averaged Navier-Stokes equations (RANS). They introduce an additional term – the Reynolds stresses ($-\partial_j \overline{u_i' u_j'}$) – which represents the transport of momentum due to turbulent fluctuations.

The above formal procedure naturally isolates the effects of the fluctuations on the mean flow. However, Eq. 3 contains nine unknown quantities that have to be defined through complementary differential or algebraic relationships. This defines what is known as the *closure problem* of turbulence, a very often frustrating prospect.

Before we move forward, we point out to the reader that the simplest possible way of modelling the turbulent terms is to consider that the turbulent stresses act like the viscous stresses so that we may write

$$-\overline{u_i' u_j'} = \nu_t \left(\partial_j \overline{u_i} + \partial_i \overline{u_j}\right) \tag{5}$$

where ν_t denotes the eddy viscosity.

Then by analyzing the random motion of lumps of fluid in a turbulent shear flow (Tennekes and Lumley (1972)), we may consider ν_t to depend on characteristic length and velocity scales. Near to a rigid wall,

$$\nu_t = u_c l_c, \quad u_c = l \left| d\overline{u_1}/dx_2 \right|, \quad l = \varkappa x_2, \, \varkappa = 0.4 \tag{6}$$

In the next sections we will show in full extent how such simple reasonings can result in such powerful results.

3. Flow near a separation point

Boundary layer separation from a rigid body is one of the most challenging problems in fluid dynamics. Classical books including the texts of Goldstein (1938), Landau and Lifshitz (1959) and Batchelor (1967) do not hesitate in saying that "separation is the aspect of laminar flow at high Reynolds number that presents the greatest theoretical difficulty" (Batchelor (1967)). If that is really the case, one may then just wonder the type of difficulties that turbulent separation should hold for us.

Thus, before we consider turbulent separation, let us first establish some results from laminar theory.

3.1. Laminar separation

Goldstein (1948) showed that a crucial result in the theory of separated flow are the compatibility conditions for the boundary layer equations (BLE) at a point of zero wall shear stress. The complicated conditions that arise for the investigation of singularities in separated flows show that, whenever they occur, the boundary layer equations cease to be valid at and near separation, on both its downstream and upstream sides. In fact, a classical result of boundary layer theory is that u_1 $(= u)$ is much large as compared to u_2 $(= w)$. The implication is that fluid particles move predominantly along the wall of the body, and only very slightly away from it. Thus, separation cannot occur but for the presence of singularities in the BLE.

We also know from the boundary layer theory that w/u is of the order of $1/\sqrt{R}$. Hence, if a singularity is reached by the flow in which w and u are to become of the same order this implies an increase of w by a factor of $\sqrt{R}$. In the limit of large Reynolds numbers, we have

$$w(x_s, z) = \infty, \tag{7}$$

where x_s denotes the position of flow separation and z the distance from the wall.

The above reasonings with $\partial w/\partial z = \infty$, together with the continuity equation imply that

$$\text{order}(\partial u/\partial x) = \text{order}(\partial w/\partial z) = \infty, \tag{8}$$

which furnishes immediately $(\partial x/\partial u) = 0$.

Near a point of separation, $x_s - x$ can be expanded in powers of $u - u_s$ provided we take notice that the first-order term in the expansion vanishes identically ($(\partial x/\partial u)_{u=u_s} = 0$). The result is

$$(x_s - x) = A(z)(u - u_s(z))^2, \quad \text{or} \quad u = u_s(z) + B(z)\sqrt{(x_s - x)}, \quad B = 1/\sqrt{A}. \tag{9}$$

Summoning again the equation of continuity,

$$\frac{\partial w}{\partial z} = -\frac{\partial u}{\partial x} = \frac{B(z)}{2\sqrt{x_s - x}} \tag{10}$$

which upon a first integration gives

$$w = \frac{C(z)}{\sqrt{x_s - x}}, \qquad C(y) = (1/2)\int B(z)dz. \tag{11}$$

The above results when applied to the boundary layer equations,

$$\underbrace{u\frac{\partial u}{\partial x} + w\frac{\partial u}{\partial z}}_{infinity} = \underbrace{-\frac{\partial p}{\partial x} + \nu\frac{\partial^2 u}{\partial z^2}}_{limited\ values}, \tag{12}$$

show that both terms on the left-hand side become infinite whereas those on the right-hand side remain limited. Thus, on a first approximation, the flow near to a separation point is a wake-like flow dominated by inertial effects and governed by the equation

$$u\frac{\partial u}{\partial x} + w\frac{\partial u}{\partial z} = 0. \tag{13}$$

The character of the singularity is then such that the transversal wall velocity increases as $(x_s - x)^{-1/2}$ as the separation point is approached.

Substituting $\partial u/\partial x$ = -$\partial w/\partial z$, we may write

$$u\frac{\partial w}{\partial z} - w\frac{\partial u}{\partial z} = u^2\frac{\partial}{\partial z}\left(\frac{w}{u}\right) = 0, \tag{14}$$

that is, we conclude that w/u is independent of z.

The above picture of the problem is given by Landau and Lifschitz (1959). Goldstein (1948) had already constructed a very rigorous theory to show that immediately ahead of separation the boundary layer equations assume a two-layered structure with an inner wall region that decreases according to $z \approx (-x)^{1/4}$. Goldstein also demonstrated that it is impossible to continue the boundary layer solution through the point $x = 0$.

The way out to the troubles considered above is to abandon the hypothesis of regularity of the pressure distribution at the boundary layer separation point. Thus, for flows near to a separation point there is an interaction of the boundary layer flow with the external potential flow such that the pressure gradient leading to separation is always self-induced.

To describe the flow structure in regions of strong interaction, the Prandtl-boundary layer theory has to be specialized and multi-layered structures considered. A typical feature is that the viscous layer is divided into two further layers. One may then speak of triple-deck theory (TD). Stewartson (1969) showed that if massive separation occurs, then TD *cannot* remove Goldstein's singularity. Indeed, the positive pressure gradient imposed on the boundary layer is the important obstacle.

3.2. Turbulent separation

Turbulent separation is a specially difficult problem. In addition to all the conceptual difficulties we saw at the previous section, turbulent flows also require the choice of a representative turbulence model. The possibilities are many. However, in the present work we restrain ourselves to the analysis of simple algebraic models. The type of model that was introduced by Eqs. 5 and 6. The criticism here might be strong since one may argue that mixing-length and eddy viscosity models are physically meaningless in the reverse flow region and have small values in the outer region of the separated flow. In the vicinity of the separation, just ahead of the point of separation itself, however, mixing-length can be taken as a good approximation (Simpson et al. (1981)).

The structure of a turbulent boundary layer far away from a singularity point was studied by Yajnik (1970) through the matched asymptotic method. Working with an underdetermined system of equations, i.e. without any closure consideration, Yajnik showed that the boundary layer can be divided into different layers whose properties can be described through two reference length scales. The resulting expansions present a non-uniformity at the point of zero skin-friction, so that they are not applicable to separating flows. This work was soon followed by contributions by Bush and Fendell (1972) and Mellor (1972) that helped to consolidate a consistent large Reynolds number asymptotic theory for turbulent boundary layers. Of course, as it turns out, all theories present a non-uniform behaviour near a separation point.

To describe the flow in the neighborhood of a point of separation, Sychev and Sychev (1980) employed a multi-structured analysis in which the boundary layer is divided into ten different layers. Without resorting to any closure model, the work uses asymptotic arguments to construct local solutions that can be matched to provide a composite solution. The approaching flow is split into four regions, whereas the interaction region is split into six. The principal findings are that i) the longitudinal mean velocity varies in proportion to $(x_s - x)^{1/4}$, ii) the boundary layer thickness increases as $\ln(x_s - x)$, and iii) the wall shear stress decreases in proportional to $(x_s - x)^{1/2}$. A problem with the theory of Sychev and Sychev is its inability to provide an explanation of how the logarithmic near wall behavior ceases to exist as separation is reached.

The asymptotic structure of a separating turbulent boundary layer was addressed by Melnik (1989) through a complete different route. His new asymptotic theory is based on formal expansions in terms of two parameters: Reynolds number and a constant appearing in the eddy-viscosity model, α. The inner layer solution shows that $\Delta x = \mathrm{O}(\alpha^{1/2})$ is the appropriate length scale near separation. The appearance of a slip velocity with a square root singularity at separation is justified as the main reason for the difference in structure between the laminar and turbulent flow limit solutions.

More recently, other different arguments were used to investigate the asymptotic structure of a separating boundary layer. The single limit concept of Kaplun (1967) was used by Cruz and Silva Freire (1998, 2002) to show how the canonical two-layered structure of the turbulent boundary layer can be described in terms of principal and intermediate equations. The two relevant reference lengths derived by Cruz and Silva Freire (1998) are u_τ^2/U_∞^2 and ν/u_τ. An important point to ponder here is that as a separation point is approached u_τ^2/U_∞^2 decreases whereas ν/u_τ increases. Thus, at a certain distance from the separation point, order(u_τ^2/U_∞^2) = order(ν/u_τ) and the two principal equations merge giving origin to a new structure where the log-solution ceases to exist and the flow solution is given by a combination of a wake-like solution to a viscous solution. In particular, at the very separation point, the flow has a wake solution. Concerning the reference velocity scales, u_R, the authors have shown that scaling analysis can be used to yield

$$u_R^3 - \frac{\tau_w}{\rho} u_R - \frac{\nu}{\rho}\frac{\partial p}{\partial z} = 0. \tag{15}$$

The highest real root from the above algebraic equations gives u_R. Please note that in the limiting cases $\partial p/\partial z \to 0$ and $\tau_w \to 0$, the reference scales reduce respectively to

$$u_R = \sqrt{\frac{\tau_w}{\rho}} = u_\tau, \qquad u_R = \left(\frac{\nu}{\rho}\frac{\partial p}{\partial z}\right)^{1/3}, \tag{16}$$

so that the classical reference scales commonly referred to in literature are recovered. This will be reviewed shortly next.

3.3. Near wall approximations for separating flows

The previous text must have given the reader a clear picture of the difficulties involved in describing the flow near to a wall and to a separation point. Because turbulent flows are rich in scales and the reference near wall scales are very small, typically of the order of ν/u_τ, any numerical simulation of a flow field will have to resort to very fine meshes. This, of course, imposes a heavy penalty on computations that have to be performed over large flow regions. One popular way to overcome this problem is to avoid the near wall region with the specification of an approximate solution at some distance from the wall. The solution procedure then follows the principles enunciated above. Through an asymptotic analysis of the problem, local equations are deducted to yield local solutions. At the near wall region, domains can then be identified where viscous and turbulent effects are the dominant effects. Provided the flow is far from a separation point, local solutions for the turbulence dominated region will result in a logarithmic velocity profile. This can then be used as a wall boundary conditions to the external flow solution. Just for the records, the log-solution in boundary layer theory is normally referred to in literature as the "law of the wall".

In the present section, some different notions of the law of the wall be reviewed. Despite the critics of many researchers, the use of wall functions to by-pass the difficulties involved with the modeling of low Reynolds

number turbulence is still an attractive means to solve problems in a simple way. We must warn the reader that some of the derivations are quite evolving, a recurring feature that has really prevented us from going into too much detail. Still, to assure legibility of the paper, the most relevant equations will be presented here in full. For a complete account of the formulations, the reader is referred to the original references.

3.3.1. The logarithmic law of wall formulation for a smooth wall

For turbulent attached flows over a smooth wall, Prandtl (1925) considered the existence of a region adjacent to the wall in which the total shear stress is nearly constant. Bearing in mind that viscosity must play a role in finding local solutions, a simple scaling analysis furnishes u_τ and ν/u_τ as the two relevant scaling parameters.

The analysis may follow either from dimensional arguments or by mixing-length theory. Here, the second route is taken. Then, for the turbulent part of the wall region we may write

$$\frac{\partial \tau_t^+}{\partial z^+} = \frac{\partial}{\partial z^+}(-\overline{u'^+ w'^+}) = \frac{\partial}{\partial z^+}\left(\varkappa^2 z^{+^2}\left(\frac{\partial u^+}{\partial z^+}\right)^2\right) \tag{17}$$

where the notation is standard. The dash denotes quantity fluctuation, $u^+ = u/u_\tau$, $\tau_t^+ = \tau_t/(\rho u_\tau^2)$, $\tau_t = -\rho\overline{u'w'}$, $\overline{u'^+ w'^+} = \overline{u'w'}/u_\tau^2$ and $z^+ = z/(\nu/u_\tau)$.

Upon two successive integrations, we have

$$u^+ = \varkappa^{-1} \ln z^+ + A, \tag{18}$$

the classical law of the wall for a smooth surface ($\varkappa = 0.4$, $A = 5.0$) and zero-pressure gradient flows.

Equation (18) presents clear difficulties as $u_\tau \to 0$.

3.3.2. Stratford's equation

The action of an arbitrary pressure rise in the inner layer will distort the velocity profile until it is balanced by the gradient of shear stress. At the wall, inertia forces are zero so that this balance is expressed by

$$\frac{\partial p}{\partial x} = \frac{\partial \tau}{\partial z}. \tag{19}$$

A first integration of the above equation yields

$$\tau = z\frac{\partial p}{\partial x}, \quad (\tau_w = 0, z \text{ small}) \tag{20}$$

where we have used the fact that at separation the wall shear stress, τ_w, is zero.

Using the mixing-length theory to model τ, together with the condition u=0 at z =0, Eq. (20) integrates to

$$u = \left(\frac{4}{\rho\varkappa^2}\frac{\partial p}{\partial x}\right)^{1/2} z^{1/2}, \quad (\tau_w = 0, z \text{ small}) \tag{21}$$

that is,

$$u^+ = \frac{2}{\varkappa} z^{+1/2} \tag{22}$$

the so-called Stratford equation, where

$$u^+ = u/u_R,\ z^+ = z/(\nu/u_R), \qquad \text{with} \qquad u_R = \left(\frac{\nu}{\rho}\frac{\partial p}{\partial x}\right)^{1/3}. \tag{23}$$

3.3.3. The law of the wall formulation of Mellor (1966)

The effect of pressure gradients on the behaviour of turbulent boundary layers without restriction to equilibrium was investigated by Mellor (1966) through dimensional arguments. When a large external pressure gradient is applied to a boundary layer, no portion of the defect profile overlaps the logarithmic law. In fact, as previously suggested by Coles (1956) and by Stratford (1959), very near a separation point the logarithmic part of velocity profile ceases to exist. However, if Millikan's (1939) arguments are recast and a new pressure gradient parameter is included in the analysis, an equation can be derived which satisfies the required limiting form as a separation point is approached.

Making the approximation that in the viscous sublayer the stress terms should be balanced only by the pressure term in the motion equations, Mellor (1966) found

$$u^+ = z^+ + \frac{1}{2}p^+ z^{+2} \tag{24}$$

for the inner region of the boundary layer, whereas for the outer layer he wrote

$$u^+ = \xi_{p^+} + \frac{2}{\varkappa}\Big(\sqrt{1+p^+z^+}-1\Big)+\frac{1}{\varkappa}\ln\Big(\frac{4z^+}{2+p^+z^+ +2\sqrt{1+p^+z^+}}\Big) \tag{25}$$

where $z^+ = zu_{p\nu}/\nu$, $u^+ = u/u_{p\nu}$, $u_{p\nu} = [(\nu/\rho)(dp/dx)]^{1/3}$ and $p^+ = [(\nu/\rho)(dp/dx)]/u_\tau^3$. Depending on whether parameter p^+ is small or large, Eq. (25) will follow different asymptotic behaviours in the limiting cases $p^+ \to 0$ or ∞, tending respectively to the classical logarithmic law or to Stratford's equation. Regarding, $u_{p\nu}$, depending on the limiting values of p^+, $u_{p\nu} \to u_\tau$ (small values of p^+) or $u_{p\nu} \to u_{p\nu}$=$[(\nu/\rho)(dp/dx)]^{1/3}$ (large values of p^+). Function ξ_{p^+} is a known parameter having been determined numerically for a range of p^+'s (Table 1).

Eqs. (24) and (25) were specified for the viscous and logarithmic regions respectively. For numerical purposes, these regions were considered to intersect at $z^+ = 11.64$, which was considered to be the point of mathematical intersection of the viscous and logarithmic regions for the classical law of the wall. Regarding the law of the wall formulations which take into account the effects of adverse pressure gradients, the mathematical intersection of the inner and logarithmic functions depends on the value of the dimensionless pressure p^+.

p^+	-0.01	0.00	0.02	0.05	0.1	0.2	0.5	1	2	10
ξ_{p^+}	4.92	4.90	4.94	5.06	5.26	5.63	6.44	7.34	8.49	12.13

Table 1: Integration function (Mellor (1966)), p^+.

3.3.4. The law of the wall formulation of Nakayama and Koyama (1984)

Nakayama and Koyama (1984) obtained a law of the wall for boundary layers subjected to adverse pressure gradients by conducting a one-dimensional analysis on the turbulent kinetic energy equation with assumptions of local similarity. Considering the two possible limiting cases of a constant stress layer and of a zero wall stress layer, the authors propose a turbulent kinetic energy equation that upon integration yields,

$$u^+ = \frac{1}{\varkappa^+}\Big[3(\zeta-\zeta_s)+\ln\Big(\frac{\zeta_s+1}{\zeta_s-1}\frac{\zeta-1}{\zeta+1}\Big)\Big] \tag{26}$$

where

$$\zeta = \Big(\frac{1+2\tau^+}{3}\Big)^{1/2} \tag{27}$$

The above formulation introduces a Von Kármán modified constant, $\varkappa^+$, and the slip value, ζ_s. For a boundary layer subjected to an adverse pressure gradient,

$$\tau^+ = 1+p^+z^+, p^+ = \nu\rho^{1/2}(d\tau/dz)_w/\tau_w^{3/2}, z^+ = (\tau_w/\rho)^{1/2}z/\nu \tag{28}$$

The Von Kármán modified constant was estimated to be

$$\varkappa^+(p^+) = \frac{0.419+0.539p^+}{1+p^+} \tag{29}$$

The slip value ζ_s was determined from the condition that in the limiting case $p^+ \to 0$ the above formulation reduces to the classical law of the wall, Eq. (18). It follows that

$$\zeta_s(p^+) = (1+(2/3)e^{-\varkappa A}p^+)^{1/2} \approx (1+0.074p^+)^{1/2} \tag{30}$$

Nakayama and Koyama (1984) considered their analysis general in the sense that velocity was related to the local shear stress instead of to the distance from the wall. Additionally, the analysis does not have to be restricted to a linear velocity-stress relation but can be applied for any monotonically increasing shear stress layer.

3.3.5. The law of the wall formulation of Cruz and Silva Freire (1998, 2002)

Introducing a new scaling procedure, Cruz and Silva Freire (2002) proposed the law of the wall for a separating flow to be written as

$$u = \frac{\tau_w}{|\tau_w|}\frac{2}{\varkappa}\sqrt{\frac{\tau_w}{\rho} + \frac{1}{\rho}\frac{dP_w}{dx}z} + \frac{\tau_w}{|\tau_w|}\frac{u_\tau}{\varkappa}\ln\left(\frac{z}{L_c}\right), \tag{31}$$

where

$$L_c = \frac{\sqrt{\left(\frac{\tau_w}{\rho}\right)^2 + 2\frac{\nu}{\rho}\frac{dP_w}{dx}u_R} - \frac{\tau_w}{\rho}}{\frac{1}{\rho}\frac{dP_w}{dx}}, \tag{32}$$

$\varkappa = 0.4$, u_τ is the friction velocity, and u_R ($= \sqrt{\tau_p/\rho}$, $\tau_p =$ total shear stress) is a reference velocity.

The total shear stress, τ_p, can be evaluated from

$$\tau_p = C_\mu^{1/2}\rho\kappa_p + \mu\left|\frac{\partial u}{\partial z}\right|_p \tag{33}$$

where the subscript p denotes the first grid point, C_μ (=0.09) is a constant and κ the turbulent kinetic energy.

The reference velocity u_R can then be directly determined from

$$u_R = \sqrt{\frac{\tau_p}{\rho}}. \tag{34}$$

Equation (33) was obtained from a momentum balance in the near wall region; it is similar to a relation usually employed by other authors to relate the wall shear stress to the turbulent kinetic energy in a κ-ϵ formulation (see, e.g., Launder and Spalding (1974), the only difference here is the inclusion of the viscous term to improve calculations when $z/L_c \leq 30$.

To find a first estimate for the wall shear stress, τ_{wo}, Eqs. (18) and (33) can be combined to give

$$\tau_{wo} = \frac{u_p C_\mu^{1/4}{\tau_p}^{1/2}\rho^{1/2}\varkappa}{\ln\left(E\, z\, \frac{(\tau_p/\rho)^{1/2}}{\nu}\right)}. \tag{35}$$

with $E = e^{\varkappa A}$.

The pressure gradient at the wall can be obtained through Eqs. (33) and (35),

$$\frac{dP_w}{dx} = \frac{\tau_p - \tau_{wo}}{z_p}. \tag{36}$$

This equation was obtained directly from the inner layer approximated equations; it represents the balance of forces in that layer.

Next, the characteristic length can be calculated from

$$L_c = \frac{\sqrt{\left(\frac{\tau_{wo}}{\rho}\right)^2 + 2\frac{\nu}{\rho}\frac{dP_w}{dx}u_R} - \frac{\tau_{wo}}{\rho}}{\frac{1}{\rho}\frac{dP_w}{dx}}. \tag{37}$$

Finally, the wall shear stress is calculated from Eq. (31) according to

$$\tau_w = \frac{u_p{\tau_p}^{1/2}\rho^{1/2}\varkappa}{2\sqrt{\left|\frac{\tau_p}{\tau_{wo}}\right|} + \ln\left(\frac{z_p}{L_c}\right)}. \tag{38}$$

Using some production-dissipation equilibrium assumptions and Eq. (31) the kinetic energy dissipation and the production terms can be written respectively as follows:

$$\text{Dissipation} = C_\mu{}^{\frac{1}{2}}\kappa_p\left(\frac{(\tau_p/\rho)^{1/2}}{\varkappa z} + \frac{\frac{1}{\rho}\frac{dP_w}{dx}}{\varkappa(\tau_p/\rho)^{1/2}}\right), \tag{39}$$

$$\text{Production} = \frac{C_\mu{}^{\frac{1}{2}}\kappa_p\rho}{z}\left(\frac{2(\tau_p/\rho)^{\frac{1}{2}}}{\varkappa} + \frac{|\,(\tau_{wo}/\rho)\,|^{\frac{1}{2}}}{\varkappa}\ln\left(\frac{z}{L_c}\right)\right). \tag{40}$$

Table 2: Main characteristics of the laser-Doppler system

Wavelength	514.5 nm
Half-angle between beams	3.415^o
Fringe spacing	4.3183 μm
Frequency shift	0.60 MHz
Dimensions of the measurement volume	
Major axis	1.53 mm
Minor axis	162.0 μm

Equation (31) is a generalization of the classical law of the wall and replaces the three expressions advanced in Cruz and Silva Freire (1998), Eqs. (25, 26, 27). Eq. (32) is an expression for the near wall region characteristic length, which is assumed to be valid in the attached and in the reverse flow regions.

Far away from the separation point, where the wall shear stress is positive and $z(dP_w/dx) << \tau_w$, Eq. (31) reduces to the classical law of the wall, Eq. (18),

$$u = \frac{2}{\varkappa} u_\tau + \frac{u_\tau}{\varkappa} \ln(\frac{z}{L_c}), \quad L_c = \nu/u_\tau. \tag{41}$$

Near to the separation point where $\tau_w = 0$, Eq. (31) leads to

$$u = \frac{2}{\varkappa} \sqrt{\frac{z}{\rho} \frac{dP_w}{dx}}, \tag{42}$$

an equation similar to Stratford's equation, Eq. (21) (see Stratford (1959)).

In the reverse flow region where the wall shear stress is negative and $z(dP_w/dx) << \tau_w$, equation (31) reads

$$u = -\frac{2}{\varkappa} u_\tau - \frac{u_\tau}{\varkappa} \ln(\frac{z}{L_c}), \quad L_c = 2\left|\frac{\tau_w}{dP_w/dx}\right|. \tag{43}$$

The generalization provided by Eq.(31) implies that the friction velocity, u_τ, used in the definition of L_c had to be replaced by the reference velocity u_R. Please, note that the characteristic length in the reverse flow region is different from the classical characteristic length given the classical law of the wall. Equation (43) is in agreement with Simpson et al. (1981), who suggested that a characteristic length for the backflow region should be directly proportional to the absolute value of the wall shear stress.

3.3.6. Theory validation

The theories presented above will now be tested against some experimental data. Of course, two parameters are of major importance for a good assessment of the proposed expressions: mean velocity and wall shear stress profiles. Also an important issue is the geometry to be chosen. Flows over steep hills are a particular difficult test for theories.

Here, we will use the data of Loureiro et al. (2006) of turbulent flow over a steep, smooth hill to compare the theories. Therefore, for further details on the flow conditions the reader is referred to the original paper. In fact, all results presented in this section were taken from Loureiro et al. (2006).

The experiments were performed in the open–channel of the Hydraulics Laboratory of the Civil Engineering Department, University of Oporto, Portugal. The water channel is a 17 m long channel with a cross section of 40 cm width per 60 cm height. The recirculation system consists two underground tanks, a top stabilization tank, and four pumps with a maximum total capacity of 150 l/s. The working section has glass side walls, 3 m in length, and is situated 7.3 m downstream of the channel entrance. The model hill was located 8 m from the channel entrance.

A one component, fiber optic, Dantec laser-Doppler anemometry system was used in the forward scatter mode to measure the mean and the fluctuating velocity fields. The characteristics of the measuring system are given in a Table 2. This system was used to measure both the longitudinal and the vertical velocity components. This was easily made by simply turning the probe 45 deg. around its axis, so that, on both conditions, the fringe distribution was perpendicular to the measured velocity component. Typical uncertainties associated to the mean and fluctuating velocity data, $\overline{U}$, $\overline{W}$, σ_u, σ_w and σ_{uw} were estimated as ± 2.5 %, ± 10 %, ± 6.5 %, ± 6.5% and ± 12 %, respectively.

The model hill used in the present work was two-dimensional and aerodynamically smooth and was defined through equation

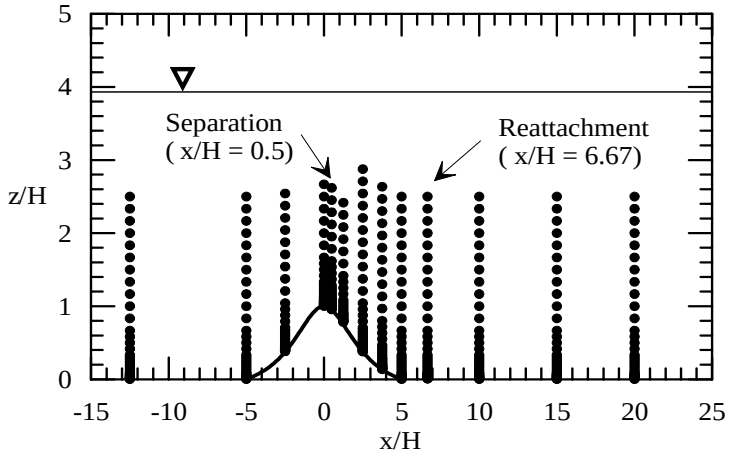

Figure 1: Position of measuring stations and co-ordinate system.

$$z_H(x) = H_1[1 + (x/L_H)^2]^{-1} - H_2 \tag{44}$$

where H (=H_1-H_2)(= 60 mm) is the hill height and L_H (= 150 mm) is the characteristic length of the hill representing the distance from the crest to the half-height point. Co-ordinates, x and z represent the horizontal and vertical axes, respectively.

Measurements were made on the channel centerline at the thirteen stations illustrated in Fig. 1.

The wall shear stress was evaluated from linear fits to the viscous region velocity profiles. In the first 3 mm away from the wall, eight points were considered for the flow characterization and the determination of τ_w.

The numerical simulations were carried out with the code Turbo-2D (Fontoura Rodrigues (1990)), which is a two-dimensional code based on the finite elements method. The application of standard Garlekin discretization to problems that are dominated by convection, frequently leads to non-physical oscillations and convergence difficulties. To alleviate this tendency, code Turbo-2D resorts to the balance dissipation method proposed by Hughes and Brooks (1979) and Kelly et al. (1980) and implemented by Brun (1988). The structure of code Turbo-2D was based on the work of Brison et al. (1985), which uses finite elements of type P1-isoP2 for space discretization and semi-implicit time discretization.

The governing equations for Turbo-2D are the Reynolds averaged equations for an incompressible flow complemented by the eddy viscosity formulation and the standard κ-ϵ model.

Regarding the experimental conditions, the inflow values of the mean velocity, of the turbulence kinetic energy and of the dissipation rate were taken directly from the experimental data. In the region adjacent to the surface, wall functions were used as explained next. At the top, a free surface condition was used. For the outflow, symmetry (zero normal gradient) conditions were applied.

Typical values of computational times for the various law of the wall formulations are shown in Table (3).

Table 3: Correspondent flow time required to achieve numerical convergence for each law of the wall formulation simulated.

Formulation	LogLaw	M (1966)	NK (1984)	CSF (1998)
Time (seconds)	100	2000	2500	2500

The computations were performed with a very fine mesh with 13888 nodes (P1-isoP2). Here we should point out to the reader a mesh with 13888 nodes is considered to be extremely fine for finite elements standards. The computational grid is shown in Fig. 2.

The general flow pattern is shown in Fig. 3. Mean velocity profiles obtained by the different law of the wall formulations are presented in Fig. 4 for the region of separate flow.

The location of flow detachment was best predicted by the model of Nakayama and Koyama (1974). Unfortunately, this same model over predicted the position of flow re-attachment by 34%, as illustrated in Fig. 3d. The formulation of Cruz and Silva Freire (1998) over predicts detachment and under predicts reattachment, resulting in a separated region 13.5% shorter than the experimentally determined length (Fig. 3b). The results obtained through Mellor's formulation over predicted both the detachment and the reattachment points, as shown in Fig. 3c. This yielded a separation region with length $x/H = 6.00$, a value very close to the experimental value, x/H

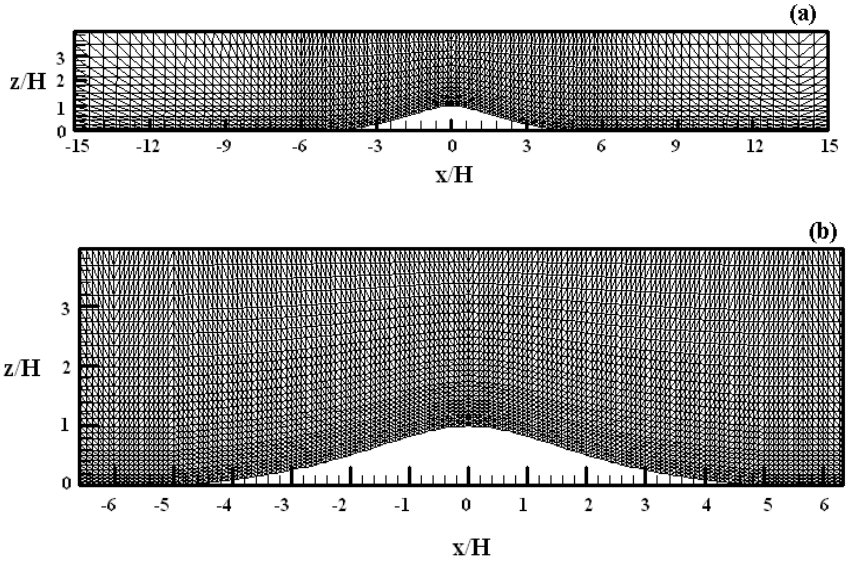

Figure 2: Typical mesh distribution around hill for pressure and velocity fields evaluation. (a) P1 mesh with 1875 nodes and 3472 elements. (b) Iso/P2 mesh with 7221 nodes and 13888 elements.

= 6.17. Under the present mesh conditions, the classical law of the wall was shown to be incapable of promoting flow separation. For the other formulations, however, the differences were marked. Table (4) summarizes the main findings.

Table 4: Length of separation bubbles according to different formulations.

Formulation	Detachment (x/H)	Reattachment (x/H)	Length (x/H)
LogLaw	not predicted	not predicted	not predicted
M (1966)	0.90	7.00	6.00
NK (1984)	0.60	8.90	8.30
CSF (1998)	0.80	6.10	5.30
Experiment	0.50	6.67	6.17

The different mean velocity predictions for the different law of the wall formulations are marked. The results provided by the classical law of the wall fail completely in predicting the separation region. Overall, the predictions obtained through the formulations of Mellor (1966) and of Nakayama and Koyama (1974) give a slower recovery of the mean velocity to the downstream undisturbed levels. Thus for most of the far wall separation region, velocity is under predicted by the models of Mellor (1966) and of Nakayama and Koyama (1974). The near wall formulation of Cruz and Silva Freire (1998) do provide the best results. However, the very strong reverse flow region shown very close to the wall at stations $x/H = 2.5$ and 3.75 was not well predicted in any sense by all three models.

The wall shear stress distribution is shown in Fig. 5. The curves illustrate the findings provided by the four different numerical simulations. Downstream of the hill, all simulations performed well. On the hill top, the inability of the models to resolve the near wall layer resulted in a large overestimation of τ_τ. This is a direct consequence of the largely overestimated near wall velocity gradients. Clearly, the bad predictions in the reversed flow region are due to the simulations that, in fact, could not predict the existence of such region. The models that were capable of resolving the inner flow regions with some accuracy were the ones that furnished the best wall shear stress predictions.

4. Flow over roughness

The description of turbulent flow over a rough surface has been a major concern to researchers over the past eighty years. Because natural surfaces are characterized by a great number of geometrical parameters, their detailed mathematical modeling is a virtually impossible exercise. The following statement by Schlichting is typical in texts: "The desire to explore the laws of friction of rough pipes in a systematic way is frustated by

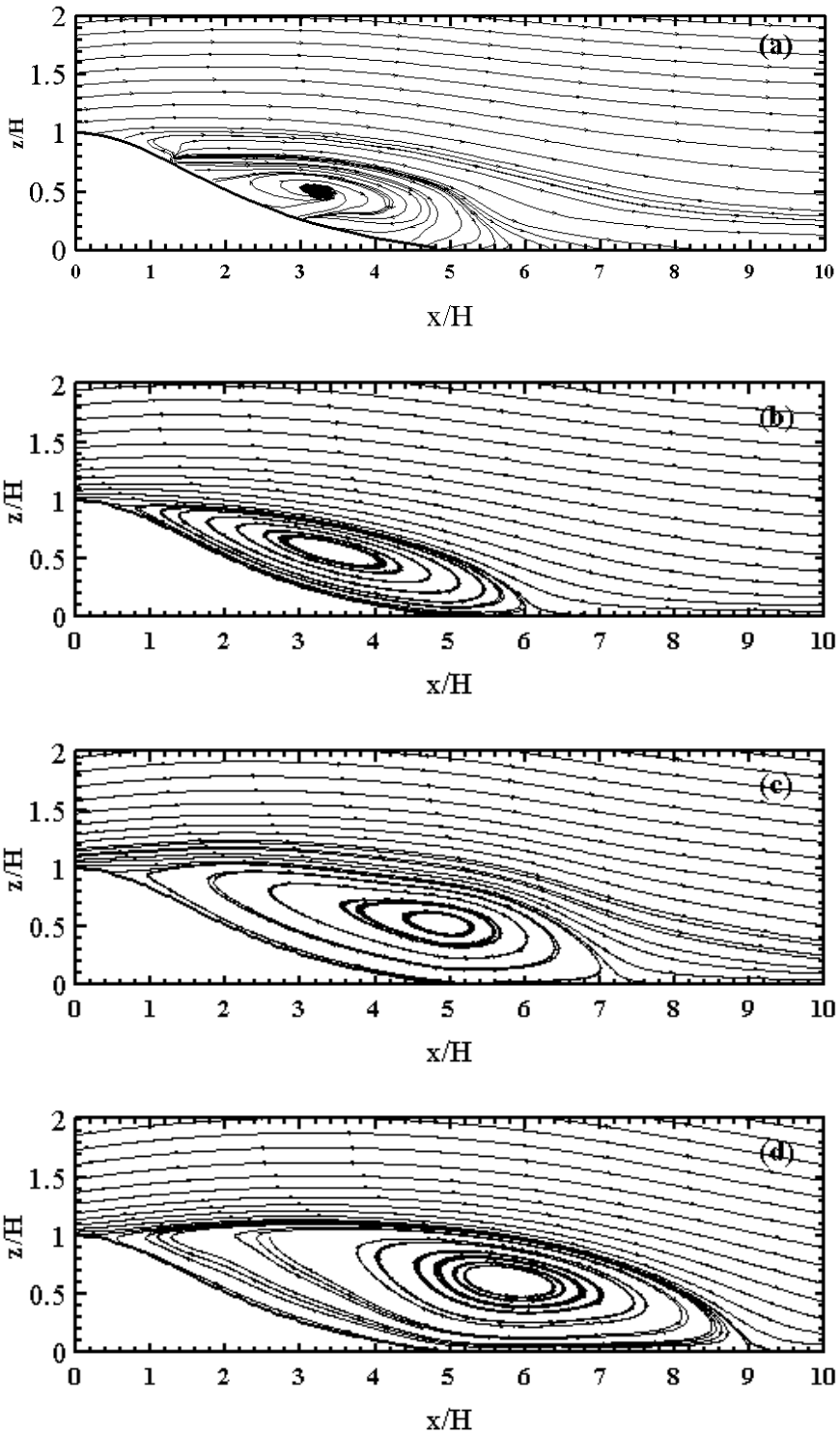

Figure 3: Extension of bubble recirculation region according to (a) Experiments, (b) Cruz and Silva Freire (1998), (c) Mellor (1966) and (d) Nakayama and Koyama (1984).

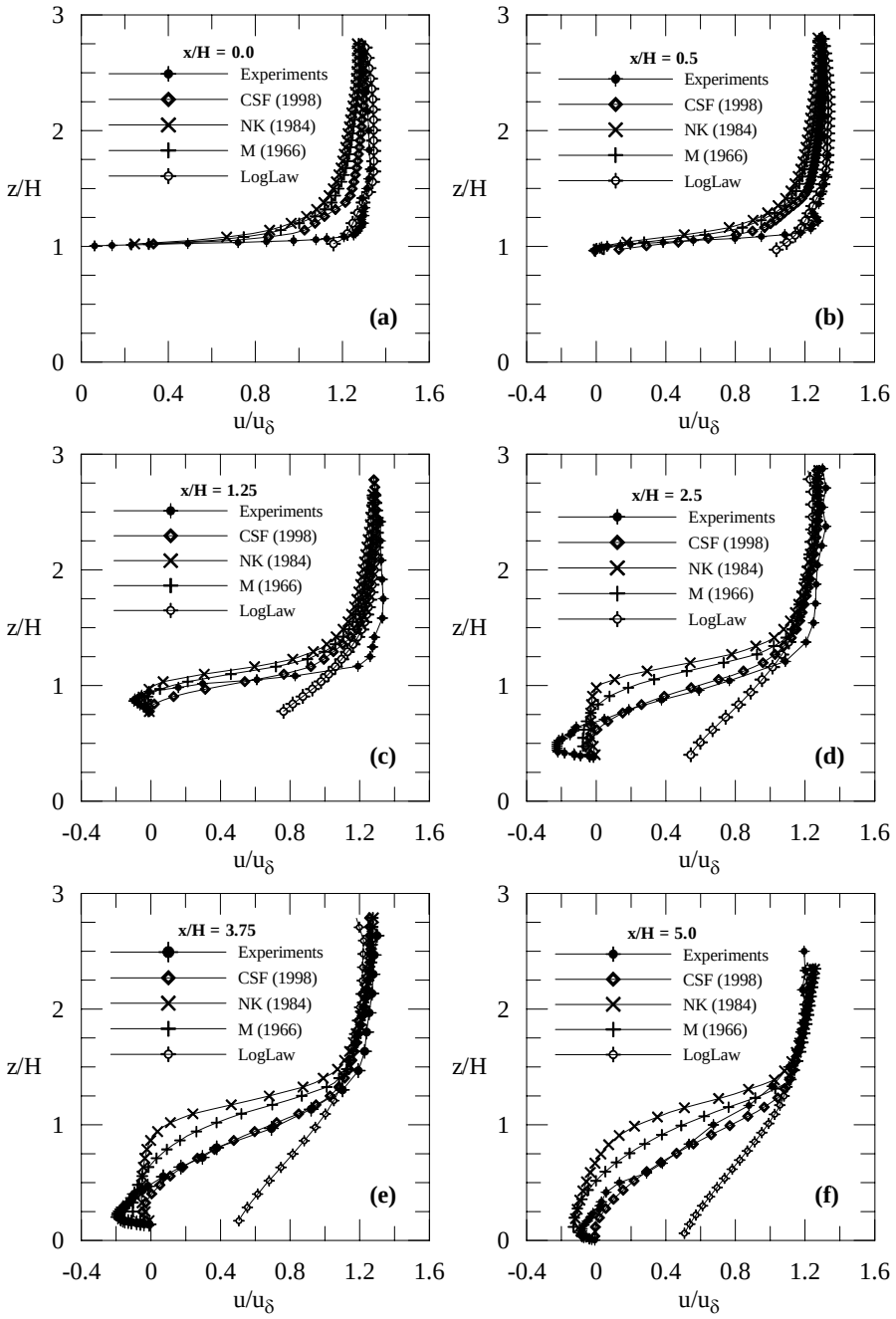

Figure 4: Mean velocity profiles in the region of reverse flow.

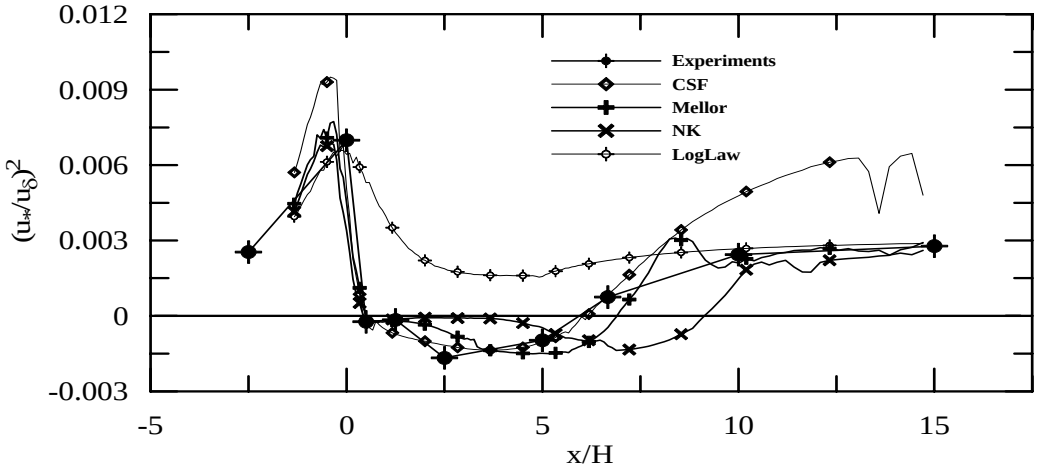

Figure 5: Wall shear stress predictions.

the fundamental difficulty that the number of parameters describing roughness is extraordinarily large owing to the great diversity of geometric forms" (H. Schlichting, Boundary Layer Theory, 7th edition, page 615).

Unfortunately, all surfaces is nature and technology, with a very few exceptions, are rough. That means engineering solutions have to be found to deal with such complex flows. Thus, it is no surprise to find in literature different representations of the same phenomenon – surface roughness – according to the different schools they were developed. Basically two different approaches stand out: the theories advanced by the mechanical engineers and by the meteorologists.

Investigating the flow inside a pipe, and as early as 1923, Hopf identified two types of roughness. If surfaces were formed by relatively coarse and tightly spaced elements (sand grains, cast iron, cement), flow resistance was observed to be proportional to the square of velocity (Reynolds number independence). In this case, the effects of roughness could be expressed with the aid of a single roughness parameter. If, however, surfaces were formed by gentle protrusions distributed over a relatively large area, flow resistance depended both on Reynolds number and on a roughness parameter. A few years later, investigating the flow in a water channel, Einstein and El-Samni (1949) observed that for flow over a rough surface the velocity profiles should be plotted considering that a theoretical wall was set at a distance below the top of the roughness elements. The concept of a displacement in origin was further investigated by Perry and Joubert (1963). These same authors in a sequence paper (Perry et al., 1969) identified two wall geometries that resulted in different log-law behaviors: one type with a reference length based on the size of the roughness (termed a 'k'-type roughness), the other type with a reference length based on the pipe diameter (termed a 'd'-type roughness).

A great difficulty in developing models for flows over rough surfaces is to find reliable measurements for the wall shear stress. For fully developed flows inside a pipe, a simple reading of the pressure drop furnishes the losses. For external flow applications, however, all traditional methods developed for smooth walls including the Preston or Stanton tubes, momentum integral methods and the gradient graphical method are highly inaccurate for application on rough surfaces. As an alternative, more reliable method, Perry et al. (1969) proposed to find the wall shear stress by pressure tapping the roughness elements and assessing their form drag. This can be a good alternative, provided the sizes of roughnesses allow such a practice. Otherwise, the difficulties remain.

The objective of the present work is to assess the current state of turbulent models in regard to the numerical prediction of wall shear stress in turbulent flows over roughness. In particular, we will address a recent and very important controversy. Over the last twenty year, several researchers (see e.g., Wu and Little (1983), Peng and Peterson (1996), Mala and Li (1999), Qu et al. (2000), Guo and Li (2003) and Wu and Cheng (2003)) have claimed that for flows in micro-channels, channels where the internal diameter are less than 250 μm, the classical relations for prediction of pressure losses and of heat transfer do not apply any more. According to these authors, the flows undergo early transition and probable causes of deviation from conventional macroscale results are wall slip effects (gas flow), surface roughness and viscous dissipation. Still, according to Li and Olsen (2006) a common point in early studies is that researchers who found early laminar-turbulent transition concluded that the relative high surface roughness was the major reason for departure from classical results. Our purpose here is to simulate flows in microchannels using the current state of the art for turbulent models so as to obtain a deeper insight onto the applicability or not of the classical expressions. The two test cases will be the flows of Wu and Cheng (2003) and of Li and Olsen (2006). Turbulence models for the numerical simulations will be the eddy-viscosity mixing length (ML), the eddy viscosity shear stress transport (SST) and

the Baseline-ω Reynolds stress model.

4.1. The law of thew wall for flow over roughness

Before considering the experimental data for flows in a microchannel, let us first introduce a short review on the theory of turbulent flow over rough surfaces.

As mentioned before, the description of flows over rough surfaces is greatly complicated by the large number of parameters that are needed to characterize the roughness. This problem was somehow played down in the early experiments by considering homogeneous surfaces, i.e., surfaces where the roughness elements had the same shape and height and were evenly distributed over them. Hopf (1923) showed that if the roughness elements are relatively coarse and tightly spaced, the coefficient of resistance of a pipe is Reynolds number independent. In this case, the characteristics of the rough surface can be expressed in terms of a single length, K_s, the so called relative roughness. If, on the other hand, the protrusions are more sparsely placed and gentle, the resistance coefficient is observed to vary with both the Reynolds number and K_s (Fromm (1923) and Fritsch (1928)).

An extensive experimental program was conducted by Nikuradse (1933) who investigated the flow in sand-roughened pipes. Nikuradse established that, at high Reynolds number, the near wall flow becomes independent of viscosity, being a function of the roughness scale, K_s, the pipe diameter and Reynolds number. He also found that, for the defect layer, the universal laws apply to the bulk of the flow irrespective of the conditions at the wall. The roughness effects are, therefore, restricted to a thin wall layer. For flows in the completely rough regime, that is, flows to which $K_s u_\tau/\nu > 70$ apply, Nikuradse found the following equation to hold

$$\frac{u}{u_\tau} = 2.5 \ln \frac{z}{K_s} + 8.5. \tag{45}$$

Experiments on a hydraulic open channel performed by Einstein and El-Samni (1949) and Moore (1951) showed that a universal expression can be written for the wall region provided the origin for measuring the velocity profile is set some distance below the crest of the roughness elements. This defines a second important characteristic length for the description of roughness. The displacement in origin is normally referred to in literature as the error in origin, ε. A detailed method to determine the displaced origin can be found originally in Perry and Joubert (1963) and more recently in Perry et al. (1986).

Thus, for any kind of rough surface, it is possible to write (Avelino and Silva Freire, 2002):

$$\frac{u}{u_\tau} = \frac{1}{\varkappa} \ln\left[\frac{(z_T + \varepsilon)u_\tau}{\nu}\right] + A - \frac{\Delta u}{u_\tau} \tag{46}$$

where,

$$\frac{\Delta u}{u_\tau} = \frac{1}{\varkappa} \ln\left[\frac{\varepsilon u_\tau}{\nu}\right] + C_i \tag{47}$$

and $\varkappa = 0.4$, $A = 5.0$, and $C_i, i = K, D$; is a parameter characteristic of the roughness (see, for example, Perry and Joubert (1969)).

Equations 46 and 47, although of a universal character, have the inconvenience of needing two unknown parameters for their definition, the skin-friction velocity, u_τ, and the error in origin, ε. A chief concern of many works on the subject is, hence, to characterize these two parameters. These equations are normally summoned for studies on geophysical flows.

If we further consider that Coles's wake hypothesis (Coles (1956)) applies to the outer region of the flow, the law of the wall can be re-written as

$$\frac{u}{u_\tau} = \frac{1}{\varkappa} \ln\left[\frac{(y_T + \varepsilon)u_\tau}{\nu}\right] + A - \frac{\Delta u}{u_\tau} + \frac{\Pi}{\varkappa} W\left(\frac{y}{\delta}\right) \tag{48}$$

where W is a universal function of y/δ and Π is a parameter dependent on the upstream shear stress and pressure distribution.

Equation 48 provides a representation of the velocity field over the whole of the turbulent and defect regions of the boundary layer.

Substitution of (y, u)=(δ, U_∞) into equation 48 furnishes

$$\frac{U_\infty}{u_\tau} = \frac{1}{\varkappa} \ln\left[\frac{\delta + \varepsilon}{\varepsilon}\right] + A - C_i + \frac{2\Pi}{\varkappa} \tag{49}$$

This is a simple algebraic equation that furnishes values of C_f $(= 2u_\tau^2/U_\infty^2)$ for known values of U_∞, δ and ε.

Finally, provided the displacement in origin can be neglected in some applications, the law of the wall can be written as

$$\frac{u}{u_\tau} = \frac{1}{\varkappa} \ln \frac{z}{z_0} \tag{50}$$

where z_0 is the roughness lenght.

Of course, Eqs. 45, 46 and 50 hold between themselves simple algebraic relationships, so that given one characteristic roughness length (say z_0) one can evaluate the others (say, $K_s = e^{8.5\varkappa} z_0 = 29.96 z_0$). However, we must warn the reader to exert some caution here. The relevant characteristic roughness length have been determined in the past based on a large body of works aimed at specific applications. Their straight translation from one type of application to the other may be meaningless. In fact, K_s has been determined for surfaces that are typical in internal flows whereas z_0 has been determined for external flows.

To find a law of resistance for the flow in a pipe, we introduce the coefficient of resistance, λ, through

$$\frac{p_1 - p_2}{L} = -\frac{\partial p}{\partial x} = \frac{\lambda}{D} \frac{\rho}{2} \overline{u}^2, \tag{51}$$

where D denotes the pipe diameter, and $\overline{u}$ is the flow mean velocity.

Then, from Eq. 45 we find

$$\lambda = [2\log(R/K_s) + 1.68]^{-2}. \tag{52}$$

4.2. Turbulence models

Three turbulence models will be used to simulate the flow in a micro-channel: the mixing-length model, the Shear Stress Transport (SST) model and the Reynolds Shear Stress Baseline-ω (RSM-BSL-ω) model. These three models are considered representative enough of the state of the art in turbulence engineering modeling to allow for a good assessment of the numerical computations of the flow over in a channel.

The three chosen models are here considered to be sufficiently well known to dispense a thorough description. Therefore, just a brief description of each model will be offered. For further details the reader is referred to the original sources.

The equations of motion are the Reynolds averaged equations of continuity and momentum for an incompressible flow. Eddy viscosity models consider that the turbulent stresses are related to the mean velocity gradients by a parameter of proportionality, the eddy or turbulent viscosity. Many two-equation turbulence models consider the eddy viscosity to be related to the turbulent kinetic energy, κ, and to the dissipation of turbulent kinetic energy per unit mass, ϵ through $\nu_t = C_\nu \kappa^2/\epsilon$. Transport equations for κ and for ϵ can be derived directly from the Navier-Stokes equations through some algebraic manipulations and some extra subsequent modeling.

Two equation models based on the κ-ϵ formulation are known to suffer limitations in the description of the near wall region since they tend to fail in predicting the correct functional near wall behavior of the logarithmic solution. A perturbation analysis of the κ-ϵ formulation in the near wall region shows that the standard constants yield solutions to the approximate equations that do not follow the classical law of the wall constants, $\varkappa = 0.4$ and $A = 5$. For this reason, a common practice is to use the κ-ϵ model with boundary conditions specified not at the wall, but at some distance above the wall. In this case, the no-slip condition is then replaced by a wall function, the classical law of the wall.

An alternative two equation model that is claimed to circumvent this difficulty is the κ-ω model (Wilcox (1988)). In fact, the great advantage of the κ-ω formulation is supposed to be exactly the near-wall treatment, which can accept higher values of $z^+ = (z u_\tau/\nu)$, the non-dimensional distance from the wall. The κ-ω model has the additional advantage of providing near wall analytical solutions for both the viscous and the fully turbulent regions. In the κ-ω model, the eddy viscosity is taken as $\nu_t = (\kappa/\omega)$.

Despite the superior handling of the wall conditions, the κ-ω formulation struggles with its strong sensitivity to free stream conditions. Thus, given the different zonal strengths and, for that matter, weaknesses of the κ-ϵ and the κ-ω formulations, a good balance can be achieved between both models if a blending is introduced between the κ-ω formulation near the surface and the κ-ϵ model in the outer flow. This solution was proposed by Menter (1994), who introduced the so-called SST-ω model.

A more general way to model a turbulent flow is to compute every component of the Reynolds stress tensor from transport equations derived directly by algebraic manipulations of the Navier-Stokes equations. The resulting loss of information implied by the averaging process must then be recovered by an adequate modeling of each of the terms present in the equations. Most models consider the same basic set of rules to close the equations. All turbulent quantities are considered to be a function of Reynolds stress, κ, ϵ (or alternatively ω), mean flow quantities and related thermodynamics variables. The diffusion of turbulent quantities, in particular,

is taken to be proportional to the local gradient of the quantity. The dissipation of turbulent kinetic energy is supposed to occur at very small scales where turbulence is isotropic. Constants appearing in the models are *ad hoc* so that they must be fixed through experimental calibration. The models also need to be consistent with the common requirements of symmetry, invariance and permutation.

The RSM-BSL-ω model proposes to use a blending function to use the advantages of the two-equation κ-ω model near the wall and a RSM model for the external flow region.

4.3. Flow in micro-channels

We have discussed before that considerations on the laws of resistance for flows in micro-channels have thrown the subject into considerable confusion. Over the last twenty years researchers have found difficult to reach a consensus on whether the classical laws should hold for flows in channels with hydraulic diameters below 200 μm. For example, based on their measurements of pressure losses and of heat transfer, the following authors have suggested the flow to undergo early transition: Wu and Little (1983), Peng and Peterson (1996), Mala and Li (1999), Qu et al. (2000), Guo and Li (2003), Wu and Cheng (2003). Many other researchers, however, have reported that conventional laws can be applied to channel flows: Qu and Mudawar (2002), Judy et al. (2002), Sharp and Adrian (2004), Celata et al. (2004), Li e Olsen (2006).

Here we will use the flow conditions of Wu and Cheng (2003) and of Li and Olsen (2006) to assess the applicability or not of the conventional laws in micro-channels. The simulations were made through the well known code ANSYS CFX, release 5.7. The code solves the Reynolds averaged Navier-Stokes equations (RANS) through a finite-volume approach. The solution strategy consists in solving the momentum equations using a guessed pressure. Next, a pressure correction is obtained which typically needs a large number of iterations to reach a converged solution. The code uses a coupled solver that solves the equations for the flow parameters as a single system. This procedure uses a fully implicit discretization of the equations at any given time. In the present steady state case, the time step behaves like an acceleration parameter to find the approximate solutions in a physically meaningful framework to a time independent solution.

The work of Wu and Cheng (2003) performed an experimental investigation on heat transfer and pressure losses in 13 different trapezoidal silicon micro-channels. Here we analyze the flows in channels number 8 and 10. These channels were chosen for their very different superficial conditions. This is particularly illustrated in Table 5 where the large differences in surfaces roughness are shown. In Table 5, K denotes the rms value of the surface roughness and D_h the hydraulic diameter of the pipe.

Table 5: Geometric parameters of channels (Wu and Cheng, 2003). Dimensions are given in μm.

Channel	W_t (top)	W_b (bottom)	H (height)	K/D_h
8	171.70	0	110.8	$3.62\ 10^{-5}$
10	168.70	0	108.9	$1.09\ 10^{-2}$

The conditions for the experiments of Wu and Cheng (2003) were such that the flow was laminar. Under this condition classical theory says that surface roughness does not affect the laws of resistance. Wu and Cheng (2003), however, have implied in their work that as pipe diameter decreases, surface roughness should becomes important. Thus, present solution strategy consisted in simulating the flow with the RSM-BSL-ω model, incorporating the wall roughness effects through the formulation of Nikuradse.

The major problem then was to evaluate K_s from a given value of K. To do that we followed the main practice of considering $z_0 = 0.1\ K$. Then using the transformation $K_s = z_0 \exp(8.5\varkappa)$, the effective roughness was estimated. The findings are shown in Table 6.

Table 6: Values of K_s for the data of Wu and Cheng (2003). Dimensions are given in μm.

Channel	K	K_s
8	0.003	0.9
10	0.009	2.728

The resistance coefficient, λ, was evaluated from the numerical data through Eq. 51. The pressure values p_2 and p_1 were taken directly from the computations and D was considered to be the hydraulic diameter. The numerical values are compared with the experimental values of Wu and Cheng and the Blasius (1911), Collebrook (1939) and White (1991) resistance formulas in Fig. 6.

The formula of Blasius is empirical and holds for smooth surfaces; it can be written as

$$\lambda = 0.3164 R^{-0.25}. \tag{53}$$

The experimental correlation of Colebrook (1939) is supposed to cover the whole transition region from hydrodynamic smooth to fully rough surface; it can be cast as

$$\frac{1}{\sqrt{\lambda}} = 1.74 - 2\log\left(\frac{K_s}{R} + \frac{18.7}{R\sqrt{\lambda}}\right). \tag{54}$$

For two dimensional, laminar flow between parallel walls, White (1991) proposed to consider

$$\lambda R(L^+) = \frac{3.44}{(L^+)^{0.5}} + \frac{24 + \frac{0.674}{4L^+} - \frac{3.44}{(L^+)^{0.5}}}{1 + \frac{2.9\,10^{-5}}{(L^+)^2}}, \tag{55}$$

where

$$L^+ = \frac{L}{D_h}\frac{1}{R}. \tag{56}$$

accounts for wall entrance effects.

Clearly, the numerical results agree quite well with the predictions given by Blasius' equation. In fact, we must notice that the equation of Blasius was derived for flow in a circular pipe. Our problem geometry consists of a trapezoidal channel, which should yield higher values of λ. Therefore, the present results are consistent and indicate that very much probably the experimental data have some serious problems. There no reason why such a large discrepancy should occur between the predictions of Blasius and the experimental data. For such a low Reynolds number all classical laws should hold. And, indeed, this is exactly what the present analysis points to.

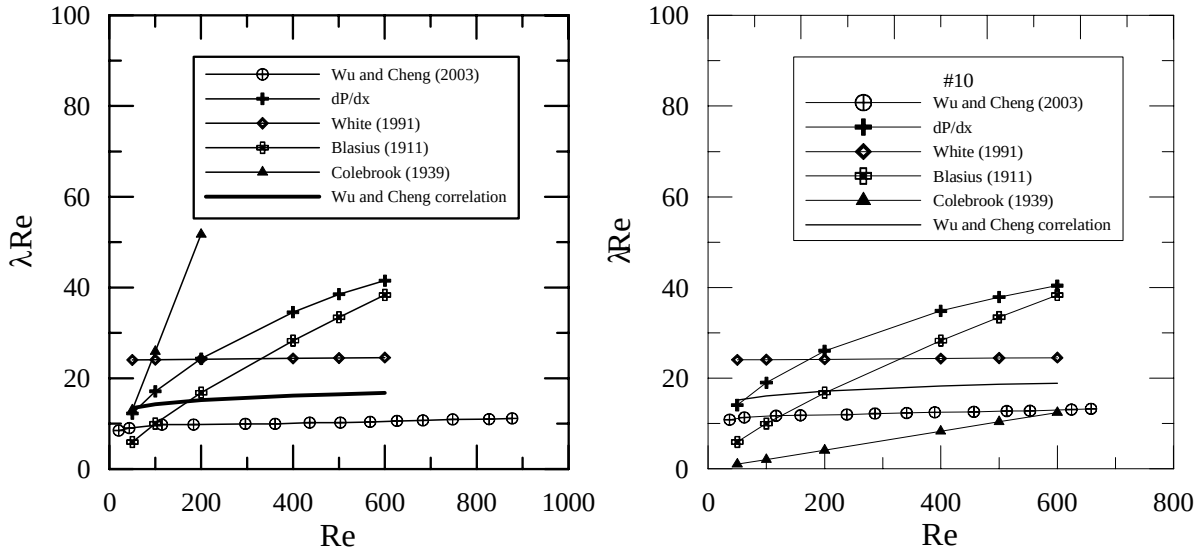

Figure 6: Predictions of coefficient of resistance according to the data of Wu and Cheng (2003).

Li and Olsen (2006) used microscopic particle image velocimetry (microPIV) to investigate rectangular micro-channels with hydraulic diameters ranging from 200 to 640 μm and Reynolds number ranging from 200 to 3971. These authors did not identify early transition and made full measurements of local mean and fluctuating velocity profiles.

To simulate their flow conditions, we use the same procedure as before for the flow of Wu and Cheng (2003). Thus for a value of $K = 0.008$ μm, we find $K_s = 0.02424$ μm. The simulations made use of all three turbulence models suggested previously: ML, SST and RSM-BSL-ω. The typical details are shown in Table 7. The results were obtained with the following computer architecture: Intel D875PBZ Motherboard (With on-board Gigabit Ethernet network interface), Pentium 4, 3.0Gz, 1Mb Cache, 2 Gb DDR400 in dual mode (2 x 512 Mb), 200 GB SATA HD.

The general flow pattern in the rectangular channel is shown in Fig. 7. The eight recirculating cells that are formed can be easily observed. The mean and fluctuating longitudinal velocity profiles are shown in Fig. . The overall agreement of all models is very good. Please note that Li and Olsen's measurements do not span the

Table 7: Simulation Details (Li and Olsen, 2006).

Model	Mesh Elements (Hexahedron)	Inlet speed (m/s)	Total run time
Mixing-length	1,233,400	7.3684	45:40
SST	1,233,400	7.3684	3:09:32
RSM-BSL-ω	1,233,400	7.3684	5:23:02

near wall region so that drawing much conclusion on flow behavior there is difficult. The SST and RSM-BSL models, being based on the ω-equation present the same near wall results. These are quite distinct from the ML results.

The longitudinal velocity fluctuations predictions are not good. The numerical computations much underestimate the values of $\sqrt{\overline{u'^2}}$, in particular, in the near wall region. The roughness effects, however, are well illustrated. Inclusion of K_s in the simulations much improves the results.

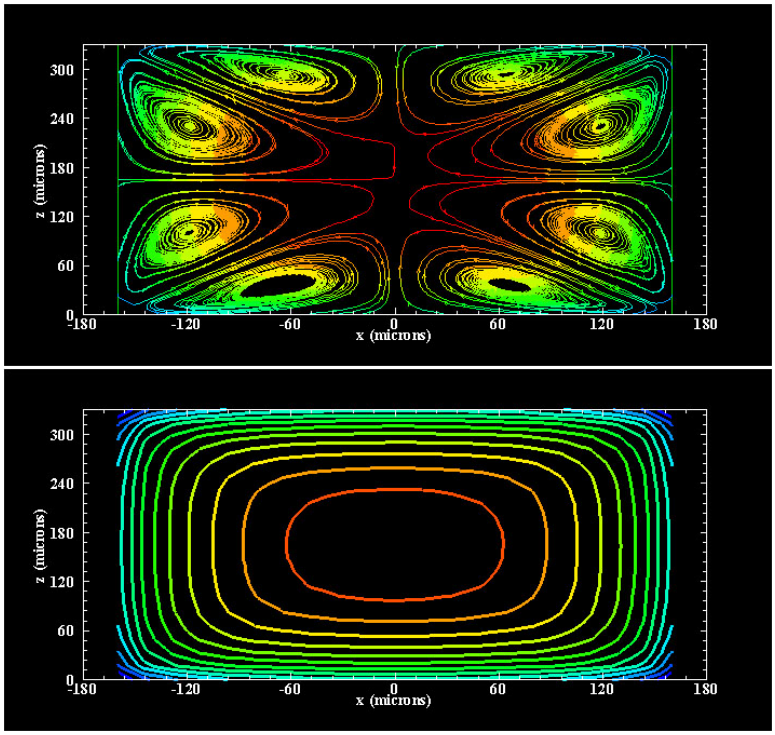

Figure 7: Streamline and isoline profiles according to the data of Li and Olsen (2006).

Finally, Fig. 9 shows a parametric study regarding the velocity prediction dependence on K_s. The three very close values of $K_S = 0.02424$, 0.02121 and 0.01818 give acceptable results. The other two extreme values, $K_s = 0.0$ and 0.07272, provide predictions that are clearly off the mark. We have, therefore, plain evidence that roughness effects are important in micro-channel flow predictions and that the current state of knowledge is capable of providing very good estimates of flow properties in channels.

5. Conclusion

We have shown how some difficult problems in engineering can be given a good representation provided their fundamental knowledge is developed from asymptotic arguments combined with rigorous *ad hoc* experimental evidence. The problem of a separating flow shows how some simple modelling based on algebraic turbulence models can be combined with scaling arguments and local analysis to provide analytical near wall solutions that can be used as boundary conditions for numerical simulations of flows over steep hills. We have, in particular, shown that the region of reverse flow can be well described by those solutions.

The flow over rough surfaces in micro-channels was also numerically simulated to show how the current state of the art in flow modelling is capable of furnishing results that are consistent with the classical laws and the experimental data. Thus, the present results suggest that measurements that report early transition must be seen with much caution. There exists a strong possibility that these experiments be contaminated by uncertain

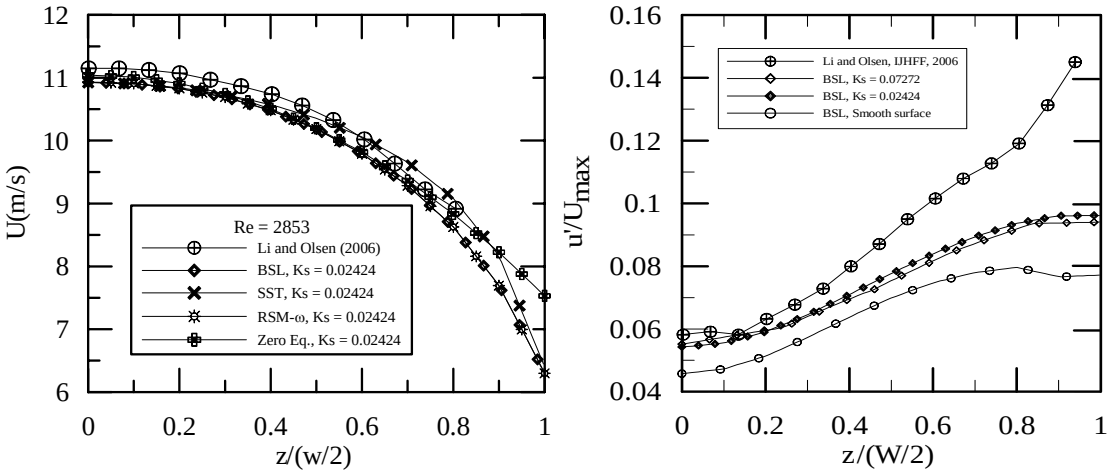

Figure 8: Mean and fluctuating longitudinal velocity profiles according to the data of Li and Olsen (2006).

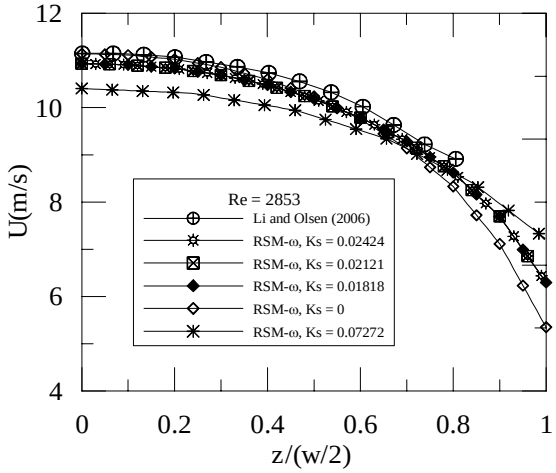

Figure 9: Parametric study on the dependence of velocity predictions on values of K_s (data of Li and Olsen (2006)).

readings and poor planning and execution.

The challenges ahead of any researcher willing to work with flow separation or flow over rough surfaces are many. The mathematical description of the flow near to a separation point is still a very difficult and open problem. Much further studies are necessary before a complete picture of the problem is drawn. The recent advances in computational fluid dynamics have made available to researchers a host of new results that will be of great help in identifying relevant scales to the problem and the local solution behaviour. The expectation then is that much more appropriate turbulence models can be developed.

Finally, we must point out to the reader that a problem where very little progress has been achieved over the last years is separated flow over rough surfaces. The present text has been written with the purpose of providing part of the basic material that should allow such a leap forward. Details on how this can be made will be given in another communication.

Acknowledgments. APSF is grateful to the Brazilian National Research Council (CNPq) for the award of a Research Fellowship (Grant No 304919/2003-9). The work was financially supported by CNPq through Grant No 472215/2003-5 and by the Rio de Janeiro Research Foundation (FAPERJ) through Grants E-26/171.198/2003 (Pronex Research Project) and E-26/152.368/2002.

6. References

Avelino, M.R. and Silva Freire, A.P. 2002 IJHMT **45** 3143-3153

Batchelor, G. 1967 *An Introduction to Fluid Dynamics* CUP

Brison, J.F., Buffat, M., Jeandel, D. and Serres, E. 1985 *Numerical Methods in Laminar and Turbulent Flows* Pineridge Press

Brun, G. 1988 *Thèse de Doctorat* École Centrale de Lyon

Bush, W.B. and Fendell, F.E. 1972 JFM **56** 657-681

Celata, G.P., Cumo, M. and Zummo, G. 2004 ETFS **28** 87-95

Cruz D.O.A. and Silva Freire A.P. 1998 IJHMT **41** 2097–2111

Cruz D.O.A. and Silva Freire A.P. 2002 IJHMT **45** 1459–1465

Coles, D. 1956 JFM **1** 191-226.

Einstein, H.A. and El-Samni, E.-S.A. 1949 Review of Modern Physics **21** 520–524.

Fontoura Rodrigues, J.L.A. 1990 *Thèse de Doctorat* École Centrale de Lyon

Fromm, K. 1923 ZAMM **3** 339-358

Fritsch, W. 1928 ZAMM **8** 199-216

Goldstein, S. 1938 *Modern Developments in Fluid Dynamics I, II* Clarendon Press

Goldstein, S. 1948 QJMAM **1** 43-69

Guo, Z.Y and Li, Z.X. 2003 IJHFF **24** 284-298

Hopf, L. 1923 ZAMM **3** 329-339

Hughes, T.J.R. and Brooks, A. 1979 *Element Methods for Convection Dominated Flows* ASME-AMD **34**

Judy, J., Maynes, D. and Webb, B. W. 2002 IJHMT **45** 3477-3489

Kaplun, S. 1967 *Fluid Mechanics and Singular Perturbation* Academic Press N.Y.

Kelly, D.W., Nakazawa, S. and Zienkiewcz, S. 1980 *Int. J. Num. Meth. Engng.* **3** 269–289.

Landau, L.D. and Lifschitz, E.M. 1959 *Fluid Mechanics* Pergamon Press

Launder, B.E. and Spalding, D.B. 1974 *Computer Methods in Applied Mechanics* **3** 269–289

Li, H. and Olsen, M.G. 2006 IJHFF **27** 123-134

Loureiro, J.B.R., Soares, D.V., Fontoura Rodrigues, J.L.A., Pinho, F.T. and Silva Freire, A.P. 2006 BLM in press

Mala, G.M. and Li, D. 1999 IJHFF **20** 142-148

Mellor, G.L. 1966 JFM **24** 255–274

Mellor, G.L. 1972 IJES **10** 851–873

Melnik, R.E. 1989 Computers and Fluids **17** 165–184

Millikan, C.B. 1939 *Proc. 5th Int. Congress on Applied Mechanics* J. Wiley N.Y.

Moore, W.L. 1951 Ph. D. Thesis State University of Iowa

Nakayama, A. and Koyama, H. 1984 AIAA Journal **22**, 1386–1389

Nikuradse, J. 1933 Stromungsgesetze in Rauhen Rohren, V. D. I. Forshungsheft No 361 1933

Peng, X.F. and Peterson, G.P. 1996 IJHMT **12** 2599-2608

Perry, A.E. and Joubert, P.N. 1963 JFM **17** 193-211.

Perry, A.E., Schofield, W.H. and Joubert, P.N. 1969 JFM **37** 383-413.

Perry, A.E., Lim K.L. and Henbest, S.M. 1987 JFM 1987 **177** 437–466.

Prandtl, L. 1925 ZAMM **5**, 136–139

Qu, W.L., Mala, G.M. and Li, D.Q. 2000 IJHMT **43** 353-364

Qu, W. and Mudawar, I. 2002 IJHMT **45** 2549-2565

Schlichting, H. 1979 *Boundary Layer Theory* McGraw Hill

Sharp, K.V. and Adrian, R.J. 2004 Exp. Fluids **36** 741-747

Stewartson, K. 1969 Mathematika **16** 106-121

Simpson, R.L., Chew, Y.T. and Schivaprasad, B.G. 1981 JFM **113** 23–51

Stratford, B. S. 1959 JFM **5** 1–16

Sychev, V.V. and Sychev, V.V. 1980 USSR Comput Maths Math Phys **20** 133–145

Tennekes, H. and Lumley, J.L. 1972 *A First Course on Turbulence* MIT Press

Yajnik, K.S. 1970 JFM **42** 411–427

White, F. M. 1991 *Viscous Fluid Flow* McGrawHill NY

Wu, H.Y. and Cheng, P. 2003 IJHMT **46** 2547-2556

Wu, P.Y. and Little, W.A. 1983 Cryogenics **23** 273-277

Proceedings of the 11th Brazilian Congress of Thermal Sciences and Engineering -- ENCIT 2006
Braz. Soc. of Mechanical Sciences and Engineering -- ABCM, Curitiba, Brazil, Dec.5-8, 2006

Paper CIT06-0247

THE EFFECTS OF INTERFERENCE BETWEEN TWO CIRCULAR CYLINDERS ARRANGED IN TANDEM BY VORTEX METHOD USING TURBULENCE MODELING

Luiz Antonio Alcântara Pereira
Instituto de Engenharia Mecânica, UNIFEI, CP 50, Itajubá, Minas Gerais, 37500-903, Brasil
e-mail: luizantp@unifei.edu.br

Miguel Hiroo Hirata
FAT/UERJ
Campus Regional de Resende
Estrada Resende - Riachuelo, Resende, RJ
e-mail: hirata@fat.uerj.br

Abstract. *The work presents an investigation of the aerodynamics characteristics of two circular cylinders in a tandem arrangement for various values for the gap between the cylinders at high Reynolds number using the viscous vortex element method. The Vortex Method is also modified to take into account the sub grid-scale phenomena; a second-order velocity structure function model is adapted to the Lagrangian scheme. The dynamics of the wakes is computed using the convection-diffusion splitting algorithm, where the convection process is carried out with a Lagrangian second-order Adams-Bashforth time-marching scheme, and the diffusion process is simulated using the random walk scheme. The aerodynamics forces and pressure distributions acting on two circular cylinders are computed using the integral derived from the pressure Poisson equation; comparisons are made with experimental results available in the literature.*

Keywords: *vortex method, panels methods, tandem arrangement, turbulence model, aerodynamics loads.*

1. Introduction

Flow behavior around circular cylinders have been investigated by numerous researches in the past few decades. In many cases of engineering practices, objects often appear in the form of groups of cylinders of circular shape, e.g. tube banks of compact heat exchangers, cable bundlers, supports of off-shore platform, etc. Due the mutual interference between cylinders at close proximity, the aerodynamics characteristics, such as fluctuating lift and drag forces, vortex-shedding patterns and fluctuating pressure distributions, for each member of a group are completely different from isolated ones. When a cylinder is placed in the wake of another in cross-flow, the so-called tandem arrangement, its unsteady loading becomes dependent not only on the flow activities in its wake, but also on those in the wake of the upstream cylinder.

Numerous investigations have been made of the flow past two circular cylinders, which is the simplest case of a group, in the last three decades. Zdravkovich (1977) and Ohya *et al.* (1989) presented an extensive review of the state of knowledge of flow across two cylinders in various arrangements. Previous investigations of tandem configurations by Biermann and Herrnstein (1933), Kostic and Oka (1972), Novak (1974), Zdravkovich and Pridden (1975, 1977), Okajima (1979), Igarashi (1981, 1984), Hiwada *et al.* (1982), Arie *et al.* (1983), Jendrzejczyk and Chen (1986) have revealed considerable complexity in fluid dynamics as the spacing or gap between the cylinders is changed.

The interference phenomena are highly non-linear and there are many discrepant points in previous works. Arie *et al.* (1983) pointed out that fluctuation in drag force acting both cylinders is weakly dependent on spacing. On the other hand, Igarashi (1981) reported that the fluctuation in pressure associated with fluctuation in aerodynamics forces (lift and drag) acting on a downstream cylinder is strongly dependent on gap between the cylinders.

Recently, the Vortex Method was employed by Teixeira da Silveira *et al.* (2005) to simulate the vortex-shedding flow from two tandem cylinders in cross-flow; the aerodynamic characteristics are investigated at a Reynolds number of 6.5×10^4 and comparisons are made with experimental results presented by Alam *et al.* (2003). As the simulations showed, the numerical results obtained are in overall good agreement with the experimental results used for comparison, especially in the simulations for the upstream cylinder. Some discrepancies observed in the determination of the aerodynamics loads for the downstream cylinder may be attributed to errors in the treatment of vortex element moving away from a solid surface. Because every vortex element has different strength of vorticity, it will diffuse to different location in the flow field. It seems impossible that every vortex element will move to same ε-layer normal to the solid surface. In the present method all nascent vortices were placed into the cloud through a same displacement normal to the panels.

The Vortex Method have been developed and applied for analysis of complex, unsteady and vortical flows in relation to problems in a wide range of industries, because they consist of simple algorithm based on physics of flow (Kamemoto, 2004). Vortex cloud modeling offers great potential for numerical analysis of important problems in fluid

mechanics. A cloud of free vortices is used in order to simulate the vorticity, which is generated on the body surface and develops into the boundary layer and the viscous wake. Each individual free vortex of the cloud is followed during the numerical simulation in a typical Lagrangian scheme. This is in essence the foundations of the Vortex Method (Chorin, 1973; Sarpakaya, 1989; Sethian, 1991; Lewis, 1999, Kamemoto, 2004 and Alcântara Pereira *et al.*, 2004, 2005).

Vortex Method offers a number of advantages over the more traditional Eulerian schemes: (a) the absence of a mesh avoids stability problems of explicit schemes and mesh refinement problems in regions of high rates of strain; (b) the Lagrangian description eliminates the need to explicitly treat convective derivatives; (c) all the calculation is restricted to the rotational flow regions and no explicit choice of the outer boundaries is needed a priori; (d) no boundary condition is required at the downstream end of the flow domain.

For the grid methods, such as finite difference method and finite element method, the governing Navier-Stokes equations are solved directly. However, the flows around cylinder arrays are usually computed at Reynolds number (Re) up to a few hundred (Fornberg, 1985 and Jackson, 1987) while the Re for flows around cylinders in many engineering applications is of much higher order O (10^6). In such circumstance, the traditional Eulerian schemes will not give a satisfactory prediction within a reasonable computational cost. Also, the pre-processing and mesh-generation are time-consuming for the grid method in numerical simulations.

The development of Lagrangian LES models for Vortex Method has been discussed in the literature. Chorin (1993a, 1993b) presented the hairpin-removal schemes, which combine a filament-based method with a local mesh redistribution algorithm that removes the filaments small scales or "hairpin"; these schemes have been used in various applications, including boundary layers (Bernard, 1996), vortex breakdown (Saghbine, 1996) and vortex reconnection (Fernandez *et al.,* 1996). In their simplest form, hairpin-removal schemes rely on the redistribution scheme to filter out the small scales but maintain the same governing equation for the large scales. Thus the effect of the unresolved scales is assumed to be accounted for by the hairpin removal process. The dynamic eddy diffusivity model is not incorporated into a 3D Lagrangian particle scheme. The effect of the sub filter scale (SFS) vorticity stresses on the motion of the resolved scales is not accounted for.

Leonard and Chua (1989) applied the Smagorinsky model in simulations of three-dimensional interaction between interlocked vortex rings and interaction between two colliding vortex rings; a nonlinear core-spreading algorithm was used analogous to the Smagorinsky sub grid scale viscosity used in large eddy simulation. Viscous effects must be included to prevent the physical divergence of the inviscid equations.

A dynamic eddy viscosity model of sub filter scale (SFS) of vorticity stresses was presented by Mansfield *et al.* (1998, 1999); in this model, a Lagrangian particle method was applied in the simulation of collision of coaxial vortex rings. The scheme combines 3D, adaptive, viscous, vortex element method with a dynamic eddy viscosity model of sub filter scale. In addition, it is shown that the Lagrangian LES scheme captures several experimentally observed features of the ring collisions, including turbulent breakdown into small-scale structures and the generation of small-scale radially propagating vortex rings. The computations indicated that the model has some weaknesses, as the simplified nature of the removal process, which is presently based on merging particles lying within a critical cut-off period. Another area where additional work is needed is in clearly quantifying the effect of the SFS model, and distinguishing it from the effect of the removal scheme.

Cotte *et al.* (2002) investigated reliability of numerical analysis of turbulent structures using a vortex-in-cell method presenting a comparison of the performance of the Vortex Method and the spectral method in a homogeneous turbulent flow at low Reynolds number and a vortex reconnection case at a moderate Reynolds number.

Alcântara Pereira *et al.* (2002) proposed a local second-order velocity structure function to take into account the micro scale manifestations of the turbulence and applied it into simulation of vortex shedding flow about a circular cylinder by a Vortex Method.

In the present paper, the Vortex Method is employed to simulate the vortex-shedding flow from two tandem cylinders in cross-flow; the turbulence modeling is taking into account using a second-order velocity structure function model (Alcântara Pereira *et al.*, 2002). The aerodynamic characteristics are investigated at a Reynolds number of 6.5×10^4 and comparisons are made with experimental results presented by Alam *et al.* (2003).

2. Formulation of the Physical Problem

Consider the incompressible fluid flow of a Newtonian fluid around two circular cylinders in a tandem arrangement an unbounded two-dimensional region. Figure 1 shows the incident flow, defined by free stream speed U and the domain Ω with boundary $S = S_1 \cup S_2 \cup S_3$, S_1 being the upstream cylinder surface, S_2 being the downstream cylinder surface and S_3 the far away boundary.

The viscous and incompressible fluid flow is governed by the continuity and the Navier-Stokes equations, which can be written in the form (Alcântara Pereira *et al.*, 2002)

$$\frac{\partial \overline{w_i}}{\partial x_i} = 0 \tag{1}$$

$$\frac{\partial \overline{w_i}}{\partial t} + \overline{w_j}\frac{\partial \overline{w_i}}{\partial x_j} = -\frac{1}{\rho}\frac{\partial \bar{p}}{\partial x_i} + 2\frac{\partial}{\partial x_j}\left[(\upsilon + \upsilon_t)\overline{S_{ij}}\right], \tag{2}$$

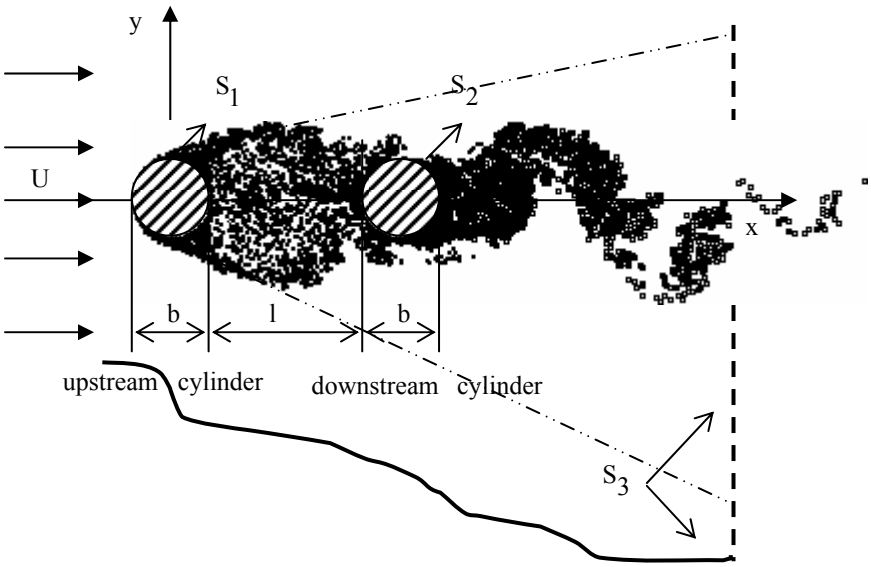

Figure 1. Flow around two circular cylinders in a tandem arrangement.

where the summation convention applies. The above governing equations were filtered ($w_i = \overline{w_i} + w_i'$, w_i' denotes the fluctuation field), υ is the fluid kinematics viscosity coefficient, υ_t is the eddy viscosity coefficient, ρ is the fluid density, $\overline{S_{ij}}$ is the deformation tensor of the filtered field and p is the pressure.

The large structures are governed by Eq. (2) and the eddy-viscosity assumption (Boussinesq's hypothesis) is used to model the sub grid scale tensor $T_{ij} = -2\upsilon_t \overline{S_{ij}}$ (Smagorinsky, 1963).

For a complete definition of the problem the impermeability and no-slip conditions on the two circular cylinders surface are written as

$$w_n = \mathbf{w} \cdot \mathbf{e}_n = 0 \tag{3}$$

$$w_\tau = \mathbf{w} \cdot \mathbf{e}_\tau = 0 \tag{4}$$

where $\mathbf{e}_n$, $\mathbf{e}_\tau$ and $\mathbf{w}$ are unit normal vector, unit tangential vector and velocity vector, respectively. One assumes that, far away, the perturbation caused by the circular cylinders arranged in tandem fades away as

$$|\mathbf{w}| \to 1 \text{ at } S_3 . \tag{5}$$

In order to take into account the local activity of turbulence, Métais and Lesieur (1992) considered that the small scales may not be too far from isotropy and proposed to use the local kinetic-energy spectrum $E_{(k_c)}$ at the cut-off wave number (k_c) to define the eddy viscosity υ_t. Using a relation proposed by Batchelor (1967) the local spectrum at k_c is calculated with a local second-order velocity structure function $\overline{F_2}$ of the filtered field Lesieur and Métais (1996)

$$\overline{F_2}(\mathbf{x},\Delta,t)=\overline{\left\|\overline{\mathbf{w}}(\mathbf{x},t)-\overline{\mathbf{w}}(\mathbf{x}+\mathbf{r},t)\right\|^2}_{\left\|\ \mathbf{r}\ \right\|=\Delta}. \tag{6}$$

From the Kolmogorov spectrum the eddy viscosity can be written as a function of $\overline{F_2}$

$$\upsilon_t(\mathbf{x},\Delta,t)=0.105C_k^{-\frac{3}{2}}\Delta\sqrt{\overline{F_2}(\mathbf{x},\Delta,t)}, \tag{7}$$

where $C_k=1.4$ is the Kolmogorov constant. The great computational advantage of this formulation over the Smagorinsky (1963) model is that in Eq. (6) the notion of velocity fluctuations (differences of velocity) is used instead of the rate of deformation (derivatives). The velocities $\overline{\mathbf{w}}(\mathbf{x}+\mathbf{r})$ are calculated over the surface of a sphere of radius Δ.

Alcântara Pereira *et al* (2002) adapted the definition of the second-order velocity structure function $\overline{F_2}$ to the Lagrangian scheme in 2-D as

$$\overline{F_2}=\frac{1}{NV}\sum_{l=1}^{NV}\left\|\mathbf{w}(\mathbf{x})-\mathbf{w}(\mathbf{x}+\mathbf{r}_l)\right\|_l^2\left(\frac{\sigma_{0\upsilon_t}}{\|\mathbf{r}_l\|}\right)^{\frac{2}{3}}. \tag{8}$$

In Eq. (8), NV is the number of discrete vortices of the cloud found in the region defined by the distances $r_1=0.1\sigma_{0\upsilon_t}$ and $r_2=(1.0+f_2)\sigma_{0\upsilon_t}$ from the centre of the reference vortex, where $\sigma_{0\upsilon_t}$ is the core radius of a Lamb vortex, see Eq. (16), which is used as a model for the discrete vortices of the cloud. A correction $\left(\sigma_{0\upsilon_t}/\|\mathbf{r}_l\|\right)^{2/3}$ is necessary due to the fact that the NV vortices are not located at equal distance from the centre of the reference vortex.

$\overline{F_2}$ represents a local statistical average of square velocity differences between free vortices located in the region defined by the distances $r_1=0.1\sigma_{0\upsilon_t}$ and $r_2=(1.0+f_2)\sigma_{0\upsilon_t}$ from the centre of the reference vortex. Physically, this function represents the flow fluctuation (turbulent activities) in the neighbourhood of the vortex located at **x.**

Defining the Reynolds number as

$$Re=\frac{bU}{\upsilon}, \tag{9}$$

where U and b are representative quantities, the dynamics of the fluid motion, governed by the boundary-value problem (1)-(5), can be alternatively studied by taking the curl of Eq. (2), obtaining the new 2-D vorticity transport equation

$$\frac{\partial\omega}{\partial t}+\mathbf{w}\cdot\nabla\omega=\frac{1+\upsilon_t^*}{Re}\nabla^2\omega, \tag{10}$$

in which ω is the only non-zero component of the vorticity vector and

$$\upsilon_t^*=\frac{\upsilon_t}{\upsilon}. \tag{11}$$

It is also worth to observe that the turbulence is essentially a 3-D phenomenon and yet one is modelling it using a 2-D approach; obviously it is then assumed 2-D turbulence. With this procedure one are still left with important turbulence aspects and the final results are also improved. The use of 2-D turbulence may explain some numerical results that depart from the experimental values.

3. Numerical method

According to the viscous splitting algorithm (Chorin, 1973) convection and the diffusion of vorticity can be handled independently for each time increment. Thus the vorticity convection is governed by

$$\frac{\partial \omega}{\partial t} + \mathbf{w} \cdot \nabla \omega = 0 \tag{12}$$

and diffusion of vorticity by

$$\frac{\partial \omega}{\partial t} = \frac{1 + \upsilon_t^*}{\mathrm{Re}} \nabla^2 \omega \,. \tag{13}$$

3.1 Discrete vortex method (large scale simulation)

In a physical sense vorticity is generated on the circular cylinders surface so as to satisfy the no-slip condition, Eq. (4). The discrete vortex method represents the vorticity by discrete vortices, whose transport at each time increment is carried out in sequence. Convection is governed by Eq. (12) and the velocity field is given by

$$u - iv = 1 + \frac{i}{2\pi} \sum_{n=1}^{2M} \gamma(S_n) \int_{\Delta S_n} \frac{d}{dz} \ln(z - \zeta) d\zeta + \frac{i}{2\pi} \sum_{k=1}^{N} \frac{\Delta \Gamma_k}{z - z_k} \,. \tag{14}$$

Here, u and v are the x and y components of the velocity vector $\mathbf{w}$ and $i = \sqrt{-1}$. The first term in the right hand side is the contribution of the incident flow; the summation of $2M$ integral terms comes from the panels distributed on the two circular cylinders surface. The second summation is associated to the velocity induced by the cloud of N free vortices; it represents the vortex-vortex interaction.

In this paper, an improvement was also introduced in the convective step of the simulation; by using the anti symmetry property of the vortex-vortex velocity induction, the computational effort was reduced; this is an important feature, since the vortex-vortex velocity induction calculation is the most time consuming part of the simulation.

In order to remove the singularity in the second summation of Eq. (14) Lamb vortices are used, whose mathematical expression for the induced velocity of the kth vortex with strength $\Delta \Gamma_k$ in the circumferential direction u_{θ_k}, is (Mustto *et al.*, 1998)

$$u_{\theta_k} = \frac{\Delta \Gamma_k}{2\pi r} \left\{ 1 - \exp\left[-5.02572 \left(-\frac{r}{\sigma_0} \right)^2 \right] \right\} \tag{15}$$

In this particular equation r is the radial distance between the vortex center and the point in the flow field where the induced velocity is calculated. The radius of the Lamb vortex core σ_0, is modified to (Alcântara Pereira *et al.*, 2002)

$$\sigma_{0_{\upsilon_t}} = 4.48364 \sqrt{\frac{\Delta t \left(1 + \upsilon_t^* \right)}{\mathrm{Re}}} \,. \tag{16}$$

Each Lamb discrete vortex distributed in the flow field is followed during numerical simulation according to the Adams-Bashforth second-order formula (Ferziger, 1981)

$$\mathbf{r}(t + \Delta t) = \mathbf{r}(t) + \left[1.5 \mathbf{w}(t) - 0.5 \mathbf{w}(t - \Delta t) \right] \Delta t + \xi \tag{17}$$

in which $\mathbf{r}$ is position of a fluid particle, Δt is the time increment and ξ is the random walk, representing diffusion of vorticity (Lewis, 1991). This displacement is modified to (Alcântara Pereira *et al.*, 2002)

$$\xi = \sqrt{\frac{4 \Delta t \left(1 + \upsilon_t^* \right)}{\mathrm{Re}} \ln\left(\frac{1}{p} \right)} \left[\cos(2\pi Q) + i \sin(2\pi Q) \right] \tag{18}$$

P and Q are random numbers between 0.0 and 1.0.

The pressure calculation starts with the Bernoulli function, defined by Uhlman (1992) as

$$Y = p + \frac{w^2}{2},\ w = |\mathbf{w}| \tag{19}$$

Kamemoto (1993) used the same function and starting from the Navier-Stokes equations was able to write a Poisson equation for the pressure. This equation was solved using a finite difference scheme. Here the same Poisson equation was derived and its solution was obtained through the following integral formulation (Shintani and Akamatsu, 1994)

$$H\overline{Y_i} - \int_{S_1} \overline{Y}\nabla G_i \cdot \mathbf{e}_n \, dS = \iint_{\Omega} \nabla G_i \cdot (\mathbf{w} \times \boldsymbol{\omega}) d\Omega - \frac{1}{Re}\int_{S_1} (\nabla G_i \times \boldsymbol{\omega}) \cdot \mathbf{e}_n \, dS \tag{20}$$

where H is 1.0 inside the flow (at domain Ω) and is 0.5 on the boundaries S_1 and S_2. $G_i = (1/2\pi)\log R^{-1}$ is the fundamental solution of Laplace equation, R being the distance from i^{th} vortex element to the field point.

It is worth to observe that this formulation is specially suited for a Lagrangian scheme because it utilizes the velocity and vorticity field defined at the position of the vortices in the cloud. Therefore it does not require any additional calculation at mesh points. Numerically, Eq. (20) is solved by mean of a set of simultaneous equations for pressure Y_i. The pressure coefficient on a panel control point i is calculated according to $C_{p_i} = 1 + Y_i$.

3.2 Turbulence modeling (micro scale simulation)

The concept of eddy viscosity, υ_t, as defined by Eq. (7), has to be considered in order to take into consideration the micro scale manifestations of the turbulence.

In the numerical simulation, consider a point vortex of the cloud, which is located at point L. The value of the velocity structure function $\overline{F_2}$, which measures the turbulence manifestations, is statistically sound only if the neighbourhood of L is sufficiently populated with other point vortices. After some numerical experiments with the flow around two circular cylinders arranged in tandem, it was assumed that this happens if $(NV/A) \geq 5000$, where NV is the number of point vortices in the region, of area A, defined by two circumferences centred in L and with radius $r_1 = 0.1\sigma_{0_{\upsilon_t}}$ and $r_2 = 1.5\sigma_{0_{\upsilon_t}}$.

It is important to observe that the viscous diffusion of vorticity was taken care of by using the random walk method, a molecular (laminar) diffusion process. In our approach the variation of the core radius is only performed locally where the flow is turbulent, that means an additional (turbulent) diffusion process.

4. Results and discussion

Table 1 presents all cases studied for two circular cylinders in a tandem arrangement at a subcritical Reynolds number of 6.5×10^4 without turbulence modeling (Teixeira da Silveira *et al.*, 2005). In the calculations, each cylinders surface was represented by fifty (M=50) straight-line vortex panels with constant density. All runs were performed with 600 time steps of magnitude $\Delta t=0.05$. The time increment was evaluated according to $\Delta t = 2\pi k/M$, $0 < k \leq 1$ (Mustto *et al.*, 1998). In each time step the nascent vortices were placed into the cloud through a displacement $\varepsilon = \sigma_0 = 0.03b$ normal to the panels. The aerodynamics forces and pressure distributions computations starts at t=15. The aerodynamics force coefficients are calculated through the integration of the pressure coefficient distribution on the each cylinders surface.

Table 1. Comparison of the mean drag coefficient with experimental results without turbulence modeling, for $Re=6.5 \times 10^4$.

Case	l/b	Upstream cylinder		Downstream cylinder	
		C_D^+	$\overline{C_D^*}$	C_D^+	$\overline{C_D^*}$
I	0.1	1.0953	1.1500	-0.5697	-0.5447
II	0.5	---	0.9866	-0.3884	-0.2997
III	1.0	1.0531	1.3664	-0.2366	0.1130
IV	2.0	0.9866	1.3434	-0.1345	0.3652
V	3.5	1.2612	1.3677	0.2766	0.4613
VI	4.0	1.2319	1.4174	0.2661	0.3015
VII	8.0	1.2040	1.4324	0.3604	0.8693

$^+$ Experimental results (Alam *et al.*, 2003) * Present calculation without turbulence modeling

Within the results presented in Table 1, is observed a disagreement of the numerical results to the experimental results (Alam *et al.*, 2003) of cases III, IV and VII on the time-averaged drag coefficient, C_D, of the downstream cylinder. The mean drag coefficients of the downstream cylinder are much higher than the experimental values and, therefore, do not reflect a good simulation of the flow. The differences encountered in the comparison of the numerical results with the experimental results are attributed mainly the inherent three-dimensionality of the real flow for such a value of the Reynolds number, which is not modeled in the present simulation. A purely two-dimensional computation of such flow must produce higher values for the drag coefficient, as obtained for our simulation.

No attempts to simulate the flow for M greater than 50 were made since the operation count of the algorithm is proportional to the square of N. As M increases N also tends to increase, and the computation becomes expensive.

Experiments (Alam *et al.*, 2003) were conducted in a low-speed, closed-circuit wind tunnel with a test section of 0.6 m height, 0.4 m width, and 5.4 m length. The level of turbulence in the working section was 0.19%. The cylinders used as test models were made of brass and were each 49 mm in diameter. The geometric blockage ratio and aspect ratio at the test section were 8.1% and 8.2, respectively. None of the results presented were corrected for the effects of wind-tunnel blockage.

As the simulations show, the numerical results obtained are in overall good agreement with the experimental results used for comparison, especially in the simulations for the upstream cylinder. Some discrepancies observed in the determination of the aerodynamics loads for the downstream cylinder for spacing l/b=1.0, l/b=2.0 and l/b=8.0 may be attributed to errors in the treatment of vortex element moving away from a solid surface. Because every vortex element has different strength of vorticity, it will diffuse to different location in the flow field. It seems impossible that every vortex element will move to same ε-layer normal to the solid surface. In the present method all nascent vortices were placed into the cloud through a displacement $\varepsilon = \sigma_0 = 0.03b$ normal to the panels.

The sub-grid turbulence modeling is of significant importance for the numerical simulation. The results of this analysis, taking into account the sub-grid turbulence modeling are presented in Table 2.

Table 2. Comparison of the mean drag coefficient with experimental results with turbulence modeling, for $Re=6.5 \times 10^4$.

Case	l/b	Upstream cylinder		Downstream cylinder	
		C_D^+	$\overline{C_D^*}$	C_D^+	$\overline{C_D^*}$
I	0.1	1.0953	0.8782	-0.5697	-0.9447
II	0.5	---	0.8751	-0.3884	-0.2225
III	1.0	1.0531	1.0607	-0.2366	0.1142
IV	2.0	0.9866	1.1687	-0.1345	0.5315
V	3.5	1.2612	1.2034	0.2766	0.3202
VI	4.0	1.2319	1.1551	0.2661	0.5609
VII	8.0	1.2040	1.1962	0.3604	0.5224

$^+$ Experimental results (Alam *et al.*, 2003) * Present calculation with turbulence modeling

As it can be seen, qualitatively, the behaviour of the results with sub-grid scale modeling is more regular, showing already the improvements obtained with turbulence modeling. The sub-grid scale modeling improved the results but the drag coefficient is still high especially for downstream cylinder for spacing l/b=1.0 and l/b=2.0.

More investigations are needed and one can imagine that with the use of more panels (and therefore more free vortices in the cloud) the results tend to be in closer agreement with the experiments.

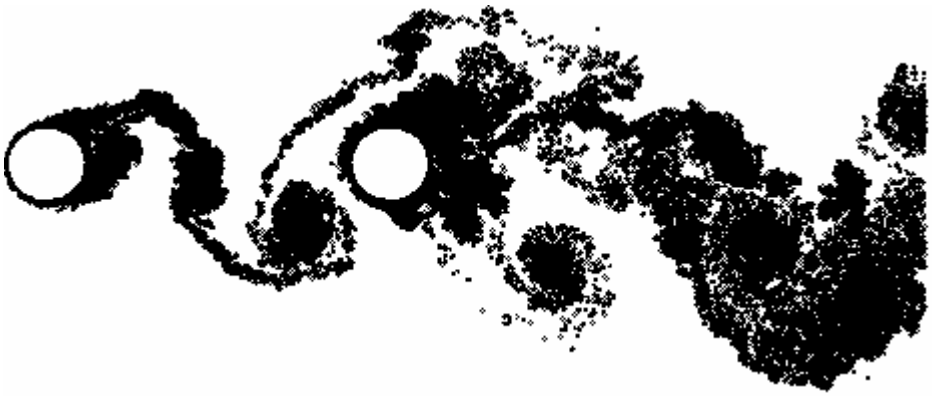

Figure 2. Position of the wakes vortices at t=60 for case VI; $Re=6.5 \times 10^4$, $\varepsilon = \sigma_0 = 0.03b$, $\Delta t=0.05$, M=50, l/b=4.0.

Figure 2 shows the position of the wake vortices for case VI using turbulence modeling at last step of the computation (t=60), where we can clearly observe the formation and shedding of large eddies in the wakes. This process occurs alternately on the upper and lower surfaces of each cylinder arranged in tandem. We can also visualize the vortex pairing process, where the vortices rotate in opposite directions and are connected to each other by a vortex sheet. The separation phenomenon associated with the existence of adverse pressure gradients on the surface of the upstream and downstream cylinders occurs alternately on the top and bottom surfaces.

Computed values for the distribution of the mean pressure coefficient along the cylinders surface is shown in Figure 3 for spacing l/b=3.5. Figure 3a shows the experimental results, which are compared with the ones obtained using the Vortex Method simulation without turbulence modeling, whereas in Fig. 3b the results of the Vortex Method refer to the simulation with turbulence modeling.

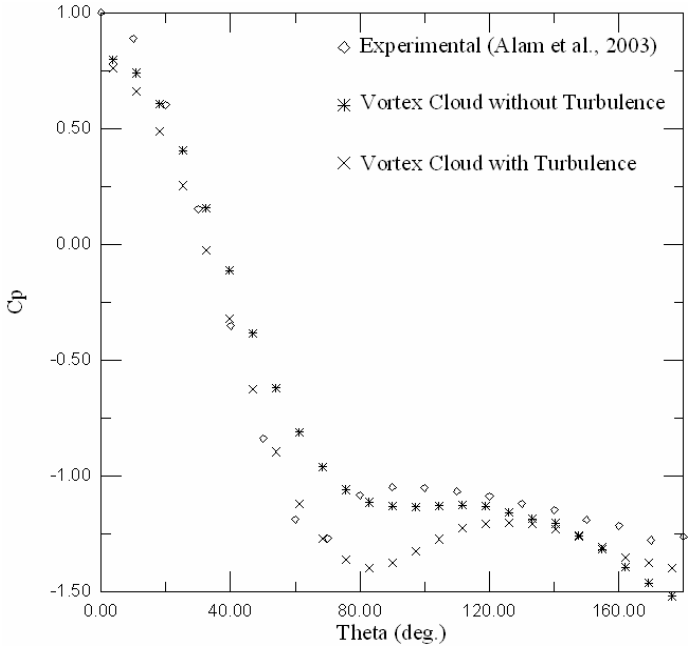

(a) Upstream cylinder (l/b=3.5)

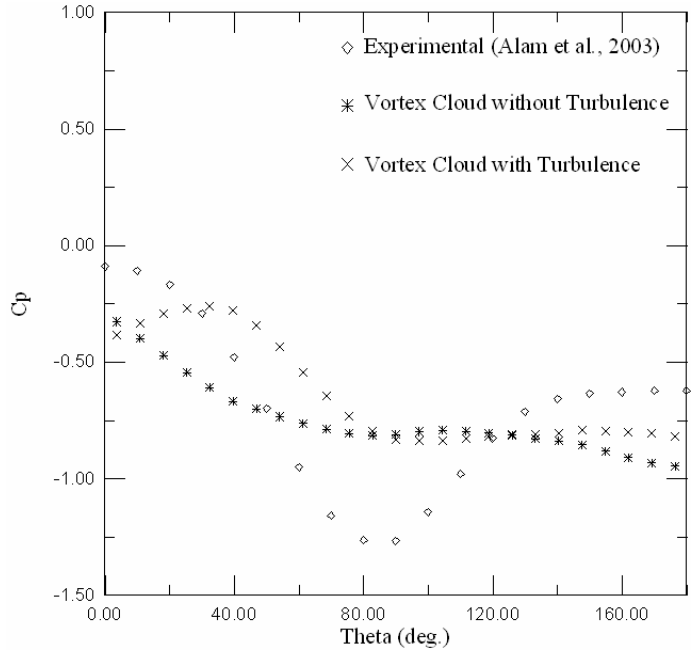

(b) Downstream cylinder (l/b=3.5)

Figure 3. Pressure distribution along the surface of the upstream and downstream cylinders, for $Re=6.5x10^4$.

The graph for the variation with time of the lift and drag coefficients with the sub grid scale modeling can be seen in Fig. 4 for spacing l/b=3.5. Figure 4b shows that the drag coefficient (C_D) for downstream cylinder oscillates around $\overline{C_D^*}$ = 0.3222; the mean value is very good when the sub-grid scale modeling is considered.

Finally the sub-grid turbulence modeling is of significant importance for the numerical simulation, especially for flow around bluff bodies (Alcântara Pereira *et al.,* 2002), and a necessary step for the roughness modeling, which is in preparation to be presented elsewhere.

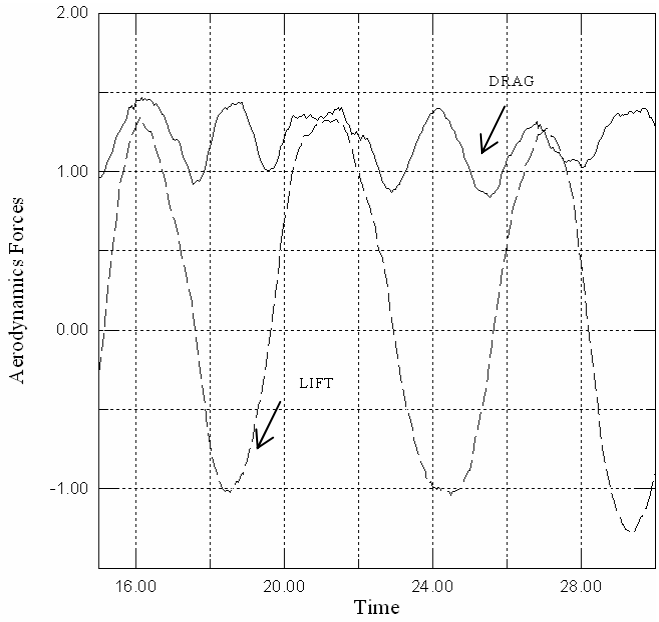

(a) Upstream cylinder (l/b=3.5)

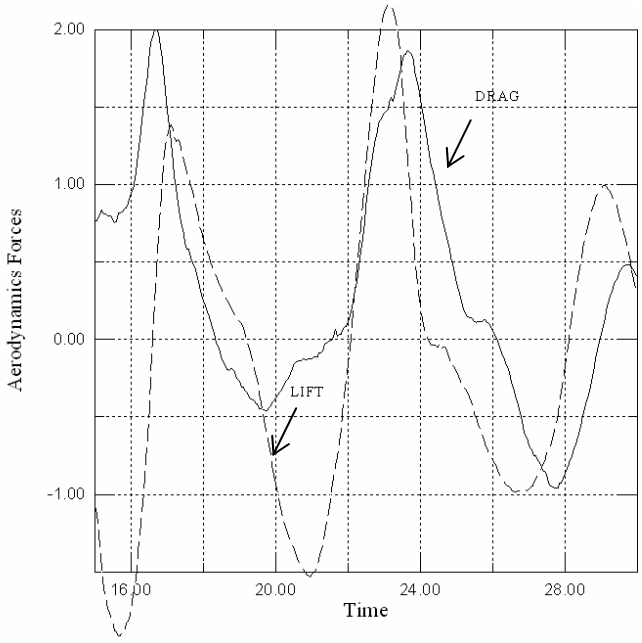

(b) Downstream cylinder (l/b=3.5)

Figure 4. Variation of C_D and C_L with time with turbulence modeling, Re=6.5x10^4, $\varepsilon = \sigma_0$ =0.03b, Δt=0.05, M=50.

5. Conclusions

The main objective of the work with the implementation and initial test of a sub-grid scale model in connection with the Vortex Method has been achieved. The results show that the Vortex Method with turbulence modeling, can improve previously obtained results without modeling, being therefore encouraging. Additional analysis of the

influence of numerical parameters will have to be carried out. The differences encountered in the comparison of the numerical results with the experimental results are attributed mainly to the inherent three-dimensionality of the real flow for such a value of the Reynolds number, which is not modelled in the simulation.

The use of a fast summation scheme to determine the vortex-induced velocity, such as the Multiple Expansion scheme, allows an increase in the number of vortices and a reduction of the time step, which increases the resolution of the simulation, in addition to a reduction of the CPU time, which allows a longer simulation time to be carried out. The present calculation required 18 h of CPU time in an Intel(R) Pentium(R) 4 CPU 1700 MHz.

Future work will investigate the variation in Strouhal number with increase in spacing l/b between two cylinders in a tandem arrangement.

Finally, despite the differences presented in this preliminary investigation, the results are promising, that encourages performing additional tests in order to explore the phenomena in more details.

6. Acknowledgement

The authors would like to acknowledge FAPEMIG (Proc. TEC-748/04) and CNPq for the financial support during the time of this project.

7. References

Alam, M. M., Moriya, M., Takai, K. and Sakamoto, 2003, "Fluctuating Fluid Forces Acting on Two Circular Cylinders in a Tandem Arrangement at a Subcritical Reynolds Number", J. Wind Eng. Ind Aerodyn., 91, pp. 139-154.

Alcantara Pereira, L.A., Ricci, J.E.R. and Hirata, M.H., 2005, "Simulation of Linear Cascade Vortex Cloud Interaction with Turbulence Modeling", Intern'l Society of CFD, Vol. 14, No. 2, July, pp. 1-10.

Alcântara Pereira, L.A., Hirata, M.H. and Manzanares Filho, N. 2004, "Wake and Aerodynamics Loads in Multiple Bodies - Application to Turbomachinery Blade Rows", J. Wind Eng. Ind Aerodyn., 92, pp. 477-491.

Alcântara Pereira, L.A., Ricci, J.E.R., Hirata, M.H. and Silveira-Neto, A., 2002, "Simulation of Vortex-Shedding Flow about a Circular Cylinder with Turbulence Modeling", Intern'l Society of CFD, Vol. 11, No. 3, October, pp. 315-322.

Arie, M., Kiya, M., Moriya, M. and Mori, H., 1983, "Pressure Fluctuations on the Surface of Two Circular Cylinders in Tandem Arrangement", ASME J. Fluids Eng. 105, pp. 161-167.

Batchelor, G.K. , 1967, "An Introduction to Fluid Dynamics", Cambridge University Press, Cambridge, UK.

Bernard, P.S., 1996, "A Vortex Method for Wall Bounded Turbulent Flows", ESAIM Proc., Vol. 1, 15.

Biermann, D. and Herrnstein, Jr., 1933, "The Interference between Struts in Various Combinations", National Advisory Committee for Aeronautics, Thecnical Report 468.

Chorin, A.J., 1993a, "Hairpin Removal in Vortex Interactions, II", J. Comp. Phys., Vol. 107, 1.

Chorin, A.J., 1993b, "Vorticity and Turbulence", Springer-Verlag, New York / Berlin, 1.

Chorin, A.J., 1973, "Numerical Study of Slightly Viscous Flow", Journal of Fluid Mechanics, Vol. 57, pp. 785-796.

Cotte, G.H., Michaux, B., Ossia, S, and VanderLinden, G., 2002, "A Comparison of Spectral and Vortex method in Three-Dimensional Incompressible Flows", J. Comp. Physics, 175, pp. 702-712.

Fernandez, V.M., Zabusky, N.J., Liu, P., Bhatt, S. and Gerasoulis, A., 1996, "Filament Surgey and Temporal Grid Adaptivity Extensions to a Parallel Tree Code for Simulation and Diagnosis in 3D Vortex Dynamics", ESAIM Proc., Vol. 1, 197.

Ferziger, J.H., 1981, "Numerical Methods for Engineering Application", John Wiley & Sons, Inc.

Fornberg, B., 1985, "Steady Viscous Flow Past a Circular Cylinder up to Reynolds number 600", Journal of Fluid Mechanics, Vol. 61, pp. 297-320.

Hiwada, M., Mabuchi, I. and Yanagihara, H., 1982, "Flow and Heat Transfer from Two same Size Circular Cylinders in Tandem Arrangement" (In Japanese), Trans. JSME 48, pp. 499-508.

Igarashi, T., 1984, "Characteristics of the Flow Around Two Circular Cylinders Arranged in Tandem", (Second Report), Bull. JSME 27 (233), pp. 2380-2387.

Igarashi, T., 1981, "Characteristics of the Flow Around Two Circular Cylinders Arranged in Tandem", (First Report), Bull. JSME 24 (188), pp. 323-331.

Jackson, C.P., 1987, "A Finite-Element Study of the Onset of Vortex Shedding in Flow Past Variously Shaped Bodies", Journal of Fluid Mechanics, Vol. 182, pp. 23-45.

Jendrzejczk, J.A. and Chen, S.S., 1986, "Fluid Forces on Two Circular Cylinders in Cross Flow", ASME, PVP 14, pp. 141-143.

Kamemoto, K., 2004, "On Contribution of Advanced Vortex Element Methods Toward Virtual Reality of Unsteady Vortical Flows in the New Generation of CFD", Proceedings of the 10th Brazilian Congress of Thermal Sciences and Engineering-ENCIT 2004, Rio de Janeiro, Brazil, Nov. 29 - Dec. 03, Invited Lecture-CIT04-IL04.

Kamemoto, K., 1993, "Procedure to Estimate Unstead Pressure Distribution for Vortex Method" (In Japanese), Trans. Jpn. Soc. Mech. Eng., Vol. 59, No. 568 B, pp. 3708-3713.

Kostic, Z.G. and Oka, .S.N, 1972, "Fluid Flow and Heat Transfer with Two Circular Cylinders in Cross Flow", Int. J. Heat Mass Transfer, 15, pp. 279-299.

Leonard, A. and Chua, K., 1989, "Three-Dimensional Interaction of Vortex Tubes", Physica D, vol. 37, pp. 490-496.

Lesieur, M. and Métais, O., 1996, "Spectral Large-Eddy Simulations of Isotropic and Stably-Stratified Turbulence", An. Rev. in Fluid Mech., Vol. 28, pp. 45-82.

Lewis, R.I., 1999, "Vortex Element Methods, the Most Natural Approach to Flow Simulation - A Review of Methodology with Applications", Proceedings of 1st Int. Conference on Vortex Methods, Kobe, Nov. 4-5, pp. 1-15.

Lewis, R. I., 1991, "Vortex Element Method for Fluid Dynamic Analysis of Engineering Systems", Cambridge Univ. Press, Cambridge, England, U.K..

Mansfield, J.R., Knio, O.M. and Meneveau, C., 1999, "Dynamic LES of Colliding Vortex Using a 3D Vortex Method", J. Comp. Phys., Vol. 152, pp. 305-345.

Mansfield, J.R., Knio, O.M. and Meneveau, C., 1998, "A Dynamics LES Scheme for the Vorticity Transport Equation: Formulation and a Priori Tests", J. Comp. Phys., vol. 145, pp. 693-730.

Métais, O. and Lesieur, M., 1992, "Spectral Large-Eddy Simulations of Isotropic and Stably-Stratified Turbulence", J. Fluid Mech., Vol. 239, pp. 157-194.

Mustto, A.A., Hirata, M.H. and Bodstein, G.C.R., 1998, "Discrete Vortex Method Simulation of the Flow Around a Circular Cylinder with and without Rotation", A.I.A.A. Paper 98-2409, Proceedings of the 16th A.I.A.A. Applied Aerodynamics Conference, Albuquerque, NM, USA, June.

Novak, J., 1974, "Strouhal Number of a Quadrangular Prism, Angle Iron and Two Circular Cylinders Arranged in Tandem", Acta Tech. CSAV 19 (3), pp. 361-373.

Ohya, Y., Okajima, A. and Hayashi, M., 1989, "Wake Interference and Vortex Shedding", In: Encyclopedia of Fluid Mechanics, Chap. 10 (Gulf Publishing, Houston, 1989).

Okajima, A., 1979, "Flow Around Two Tandem Circular Cylinders at very High Reynolds Numbers", Bull. JSME 22 (166), pp. 504-511.

Saghbine, J.C., 1996, "Simulation of Vorticity Dynamics in Swirling Flows, Mixing and Vortex Breakdown", M.Sc. Thesis, Department of Mechanical Engineering, Massachusetts Institute of Technology.

Sarpkaya, T., 1989, "Computational Methods with Vortices - The 1988 Freeman Scholar Lecture", Journal of Fluids Engineering, Vol. 111, pp. 5-52.

Sethian, J.I., 1991, "A Brief Overview of Vortex Method, Vortex Methods and Vortex Motion", SIAM. Philadelphia, pp. 1-32.

Shintani, M. and Akamatsu, T, 1994, "Investigation of Two Dimensional Discrete Vortex Method with Viscous Diffusion Model", Computational Fluid Dynamics Journal, Vol. 3, No. 2, pp. 237-254.

Smagorinsky, J., 1963, "General Circulation Experiments With the Primitive Equations", Mon. Weather Rev., Vol. 91, pp. 99-164.

Teixeira da Silveira, L., Alcântara Pereira, L.A. and Hirata, M.H., 2005, "The Effects of Interference between Two Circular Cylinders Arranged in Tandem by Vortex Method", 18th International Congress of Mechanical Engineering, Proceedings of COBEM 2005, November 6-11, Ouro Preto, MG.

Uhlman, J.S., 1992, "An Integral Equation Formulation of the Equation of an Incompressible Fluid", Naval Undersea Warfare Center, T.R. 10-086.

Zdravkovich, M.M., 1977, "Review of Flow Interference between Two Circular Cylinders in Various Arrangements", Trans. SAME, J. Fluid. Eng., 99, pp. 618-633.

Zdravkovich, M.M. and Pridden, D.L., 1977, "Interference between Two Circular Cylinders; Series of Unexpected Discontinuites", J. Ind. Aerodyn. 2, pp. 255-270.

Zdravkovich, M.M. and Pridden, D.L., 1975, "Flow Around Two Circular Cylinders", Research Report, Proceedings of the Second US National Conference on Wind Engineering Research, Fort Collins, IV (18).

Proceedings of the 11th Brazilian Congress of Thermal Sciences and Engineering -- ENCIT 2006
Braz. Soc. of Mechanical Sciences and Engineering -- ABCM, Curitiba, Brazil, Dec. 5-8, 2006

Paper CIT06-0248

ANÁLISE DE DESEMPENHO DO MÉTODO DE EXPANSÃO EM MULTIPOLOS ADAPTATIVO APLICADO A SIMULAÇÕES NUMÉRICAS VIA MÉTODO DE VÓRTICES

Victor Santoro Santiago
vsantoro@ig.com.br

Daniel F. C. Silva
danfcs@yahoo.com

Gustavo C. R. Bodstein
Universidade Federal do Rio de Janeiro, Departamento de Engenharia Mecânica – Poli/COPPE
Centro de Tecnologia, Bloco G, sala 204 – Ilha do Fundão, 21945-970 Rio de Janeiro, RJ – Brasil
gustavo@mecanica.coppe.ufrj.br

Resumo. *O transporte de vorticidade simulado na etapa convectiva do Método de Vórtices impõe a necessidade de se calcular a velocidade induzida por cada vórtice sobre todos os outros que compõe uma nuvem de vórtices. Tal procedimento acarreta um tempo de processamento da ordem de N^2, onde N é o número de vórtices presentes na nuvem. Visando reduzir o tempo necessário para realizar simulações de tempo longo, onde o número de vórtices cresce muito ao longo de uma simulação, utiliza-se, neste trabalho, o Método da Expansão em Multipolos Adaptativo (MEMA), que reduz o tempo de processamento para ordem N. As simulações são realizadas aplicando-se o MEMA a cinco nuvens de vórtices diferentes, as quais representam possíveis configurações geométricas instantantâneas de esteiras viscosas. Por último, o MEMA é integrado ao Método de Vórtices Discretos e utilizado para calcular escoamentos com elevados Números de Reynolds ao redor de aerofólios. Os resultados são comparados entre si e mostram o enorme ganho de tempo computacional proporcionado pelo MEMA.*

Palavras-chave*: método de expansão em multipolos, método de vórtices, método dos painéis, aerofólio, aerodinâmica.*

1. Introdução

A avaliação em larga escala da interação entre partículas é parte integrante da simulação numérica de diversos fenômenos físicos. Como exemplo, podem ser citados os cálculos envolvendo o campo gravitacional, os problemas de radiação térmica, a solução da equação de Laplace via Teoria Potencial, a simulação de plasma e o Método de Partículas. O Método de Vórtices, caso particular do Método de Partículas, é utilizado em Mecânica dos Fluidos para o cálculo de escoamentos externos ao redor de corpos rombudos e aerodinâmicos, onde são utilizadas nuvens de vórtices discretos para representar a região rotacional do escoamento.

Neste trabalho, o escoamento ao redor de corpos é resolvido através da combinação do Método dos Painéis com o Método de Vórtices. Para tanto, discretiza-se o corpo em uma série de painéis retos com distribuição de vorticidade linear, e satisfaz-se a condição de contorno de impermeabilidade a cada instante de tempo e em cada ponto de controle dos painéis, transferindo a vorticidade do contorno sólido, onde ela é criada, para o escoamento, através da criação de novos vórtices discretos, um para cada painel.

Outra característica do Método de Vórtices utilizado neste trabalho é que os termos difusivo e convectivo da equação de transporte da vorticidade são calculados seqüencialmente, para cada instante de tempo. Percebe-se, deste modo, que, a cada instante de tempo, cresce o número de vórtices presentes na esteira viscosa, os quais modelam a região rotacional do escoamento.

A etapa convectiva do método inclui, além do cálculo do campo gerado pelos painéis, o cálculo do campo gerado por cada vórtice discreto da nuvem. Assim, no algoritmo do Método de Vórtices, há a necessidade de se calcular a velocidade induzida por cada vórtice sobre todos os outros para que a convecção de cada vórtice seja realizada, o que implica em um custo computacional da ordem de N^2, onde N é o número de vórtices presentes na simulação.

Para lidar com esta limitação, que se torna impeditiva para simulações de tempo longo ou para discretizações mais refinadas do corpo e da região rotacional do escoamento, diversos esquemas de aceleração têm sido propostos. Guedes *et al*. (1999), Mustto e Bodstein (2000) e Ogami (2002), apresentaram aceleradores baseados no Método da Expansão em Multipolos do tipo partícula-caixa, que reduzem o custo computacional para $N\log N$. Greengard e Rokhlin (1987) propuseram um Método da Expansão em Multipolos do tipo caixa-caixa, que reduz o esforço computacional para ordem N, porém o algoritmo apresenta dependência com relação à distribuição espacial das partículas. Esta deficiência foi sanada por Carrier *et al*. (1988), que introduziram o Método da Expansão em Multipolos Adaptativo – MEMA. Este é um esquema adaptativo do tipo caixa-caixa, também de ordem N, que distribui um número maior de caixas nas regiões de escoamento com maior concentração de vórtices e reduz o número de caixas onde a concentração é menor, melhorando o desempenho do método de Greengard e Rokhlin (1987). O emprego do MEMA em simulações com o Método de Vórtices e a avaliação do seu desempenho é o foco do estudo apresentado no presente trabalho.

Especificamente, este trabalho possui dois objetivos. O primeiro consiste em analisar o desempenho do MEMA através de simulações utilizando o código computacional original implementado por Carrier *et al*. (1988) em linguagem FORTRAN e compará-lo ao desempenho do cálculo direto partícula-partícula realizado pela lei de Biot-Savart. O segundo objetivo consiste em incorporar este código computacional ao código numérico do Método de Vórtices desenvolvido por Silva e Bodstein (2005) e testar a aplicabilidade do MEMA em simulações para tempo longo de escoamento incompressível, viscoso e bidimensional ao redor de um aerofólio. Assim, é apresentado na seção 2 um breve resumo do MEMA, que serve de base para seu entendimento geral. Em seqüência, o desempenho do MEMA é testado na seção 3 com relação a sua adaptabilidade espacial quando aplicado a cinco diferentes tipos de distribuição de vórtices, enquanto que a seção 4 testa sua aplicabilidade ao Método de Vórtices Discretos.

2. Método de Expansão em Multipolos Adaptativo - MEMA

Nesta seção o MEMA é apresentado de maneira resumida, o que permite um bom entendimento conceitual do método, mas um entendimento apenas superficial dos seus detalhes de implementação e funcionamento. Para mais detalhes quanto à formulação matemática, as deduções e a descrição completa do algoritmo de MEMA, deve-se consultar o artigo de Carrier *et al*. (1988).

Resumidamente, a estratégia utilizada pelo MEMA é de agrupar os vórtices de uma nuvem em caixas de tamanhos diferentes, de acordo com a densidade local de vórtices, e se avaliar as interações entre as caixas que se encontram suficientemente distantes umas das outras. A avaliação das interações entre as partículas que se encontram na mesma caixa é feita pelo método direto, ou seja, partícula-partícula. Deste modo, suponha que existam m partículas de intensidade q_j localizadas em $z_j = x_j + iy_j$, $j = 1, \ldots, m$, onde $i \equiv \sqrt{-1}$ e $|z_j| < r$, sendo r um número real. Pode-se dizer que, para todo $z \in C$, sendo C o conjunto dos números complexos, e $|z_j| > r$, o potencial $\phi(z)$ pode ser escrito como

$$\phi(z) = Q\log(z) + \sum_{k=1}^{\infty} \frac{a_k}{z^k}, \tag{1}$$

onde

$$Q = \sum_{j=1}^{m} q_j \quad \text{e} \quad a_k = \sum_{j=1}^{m} \frac{q_j z_j^k}{k}. \tag{2a,b}$$

Truncando-se o somatório em p termos, tem-se, para todo $p \geq 1$, que

$$\left| \phi(z) - Q\log(z) - \sum_{k=1}^{p} \frac{a_k}{z^k} \right| \leq \alpha \left| \frac{r}{z} \right|^{p+1} \leq \left(\frac{A}{c-1} \right) \left(\frac{1}{c} \right)^p, \tag{3}$$

onde

$$c = \left| \frac{z}{r} \right|, \quad A = \sum_{j=1}^{m} |q_j| \quad \text{e} \quad \alpha = \frac{A}{1 - \left| r/z \right|}. \tag{4a,b,c}$$

Carrier *et al*. (1988) consideram caixas "bem separadas" aquelas em que $c = 2$. Assim, para este caso, p deve ser da ordem de $-\log_2\varepsilon$, de acordo com a Eq. (3), quando se estabelece uma acurácia ε. O algoritmo tem início, então, com a escolha de ε, que será garantida realizando-se a expansão em multipolos com p termos. Para tanto, o domínio é dividido seqüencialmente em caixas quadradas, até que estas tenham um número de vórtices menor que o número máximo de vórtices por caixa, valor escolhido como dado de entrada. Este parâmetro influencia no desempenho do algoritmo do ponto de vista do tempo de processamento, mas não implica em perda de acurácia.

O código FORTRAN original de Carrier *et al*. (1988) possui a opção de cálculo diferenciado para o campo induzido em pontos muito próximos, o que permite a desingularização do campo de vorticidade de acordo com o modelo que o usuário deseja utilizar. Deste modo, o vórtice de Lamb foi adicionado ao programa, sendo o raio do seu núcleo, σ, o parâmetro utilizado como distância para esta desingularização.

Carrier *et al*. (1988) estabelecem ainda critérios para a formação de listas de caixas de acordo com a proximidade e com o tamanho de cada caixa. Assim, o domínio em questão é dividido inicialmente em quatro caixas iguais, as quais são seqüencialmente divididas em quatro, até que cada caixa contenha um número de partículas inferior ao número máximo de partículas por caixa, parâmetro numérico citado acima. Os autores denominam ainda caixas ascendentes, descendentes e contemporâneas, respectivamente, como aquelas que deram origem, aquelas que foram originadas e aquelas que pertencem ao mesmo estágio do processo de divisão, ou seja, aquelas que têm o mesmo tamanho.

Ao final do processo de divisão sucessiva do domínio, cada caixa terá cinco listas de caixas a ela associadas, como pode ser visto na Fig. 1, onde as cinco listas de caixas numeradas de 1 a 5 estão relacionadas à caixa *b*. Assim, observa-se que: a lista 1 da caixa *b* é formada pelas caixas adjacentes à caixa *b*; a lista 2 da caixa *b* é formada pelas caixas descendentes das contemporâneas da ascendente de *b* que não são adjacentes à *b*; a lista 3 é formada pelas caixas descendentes das contemporâneas adjacentes de *b* que não são adjacentes à *b*; a lista 4 é formada pelas caixas que tem *b* em sua lista 3; e, finalmente, a lista 5 de *b* é formada pelas caixas não adjacentes à ascendente de *b*.

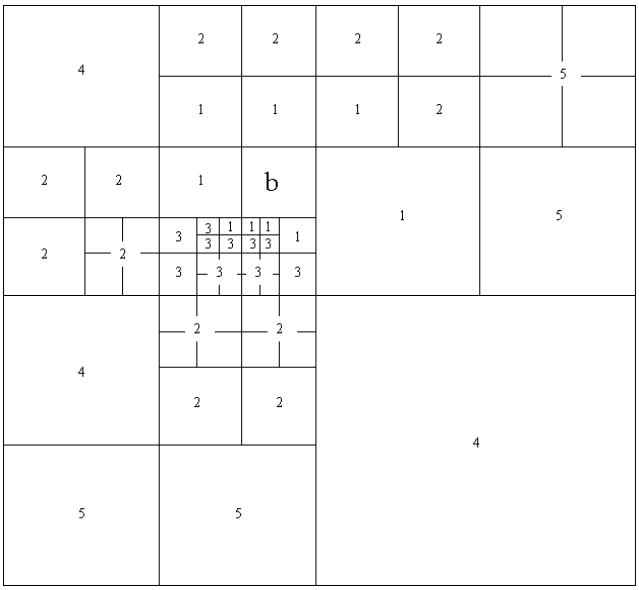

Figura 1. Famílias de caixas (Carrier *et al*., 1988).

A formação das listas citadas acima permite que se perceba a hierarquização das caixas de acordo com a proximidade e com o tamanho de cada caixa. Regiões com caixas menores representam maiores densidades de vórtices, o que justifica o tratamento diferenciado e a conseqüente separação em famílias distintas.

Diversos lemas e teoremas são apresentados em Carrier *et al*. (1988) que fornecem ferramentas para translação do centro da expansão em multipolos e para a conversão de expansões em multipolos para expansões locais. Estas ferramentas se fazem necessárias para avaliar a justaposição de efeitos devido às interações entre as caixas e às interações entre os vórtices que se encontram na mesma caixa.

Na próxima seção são apresentados os resultados dos testes de adaptabilidade espacial do algoritmo em questão, assim como o desempenho correspondente para cada caso estudado. Além da adição do vórtice de Lamb para a desingularização dos vórtices pontuais, o código FORTRAN original desenvolvido por Carrier *et al*. (1988) sofreu pequenas modificações de natureza operacional para ser utilizado neste trabalho.

3. Adaptabilidade espacial do MEMA

A adaptabilidade espacial do algoritmo desenvolvido por Carrier *et al*. (1988) foi avaliada recorrendo-se a quatro tipos de configurações geométricas diferentes, a saber: quadrado com distribuição estatisticamente uniforme (Fig. 2a); distribuição estatisticamente não uniforme em torno quatro pontos com posições aleatórias (Fig. 2b); distribuição estatisticamente não uniforme em linha (Fig. 2c); distribuição estatisticamente não uniforme em senóide (Fig. 2d); e esteira formada por aerofólio estolado (Fig.2e). Para cada caso, as posições exatas dos vórtices são aleatórias, geradas a partir de uma distribuição estatisticamente uniforme.

Estas geometrias representam, qualitativamente, diferentes tipos de configurações instantâneas de esteiras que podem ser obtidas em simulações via método de vórtices, com diferentes níveis de aglomeração e não uniformidade. A Fig. 2a representa uma região com bastante uniformidade na distribuição dos vórtices, enquanto que a Fig. 2b apresenta uma não uniformidade na distribuição limitada a uma região bem definida. A Fig. 2c representa a esteira de um aerofólio com baixo ângulo de ataque, e a Fig. 2d uma esteira com ângulo de ataque elevado. A Fig. 2e foi gerada com a posição dos vórtices obtida ao se simular o escoamento ao redor de um aerofólio com ângulo de ataque 90º.

As Figuras 3a – 3e apresentam as curvas de tempo de processamento obtidas pelo cálculo direto com precisão dupla e pelo MEMA (*Fast Multipole Method* – FMM) para cada geometria citada anteriormente.

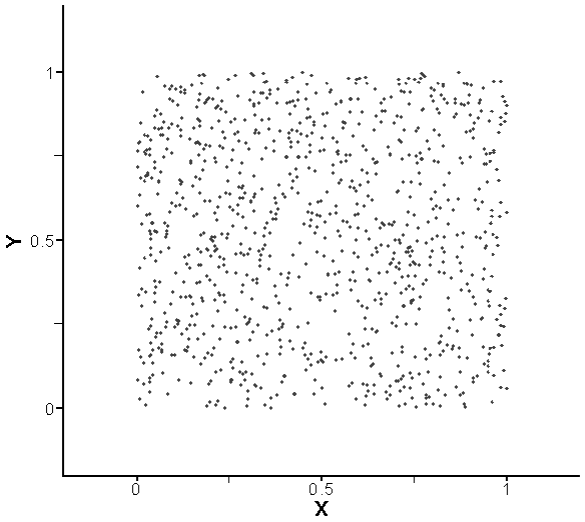

Figura 2a. Quadrado com distribuição uniforme.

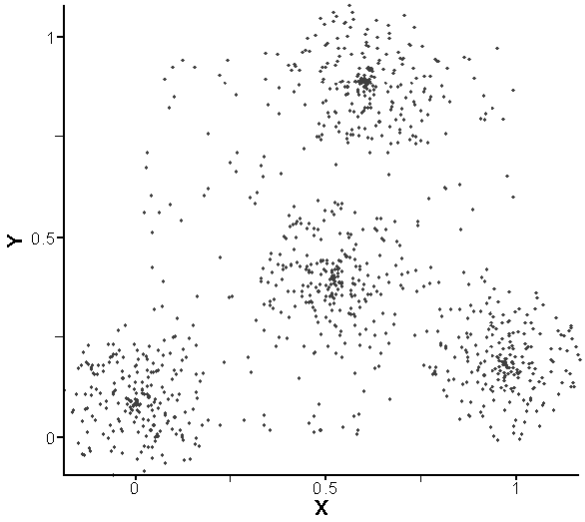

Figura 2b. Distribuição não uniforme.

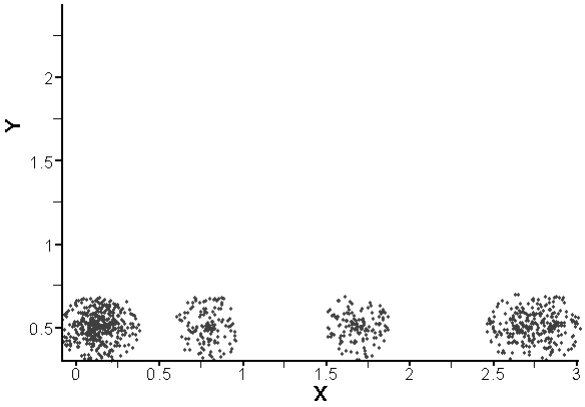

Figura 2c. Distribuição não uniforme em linha.

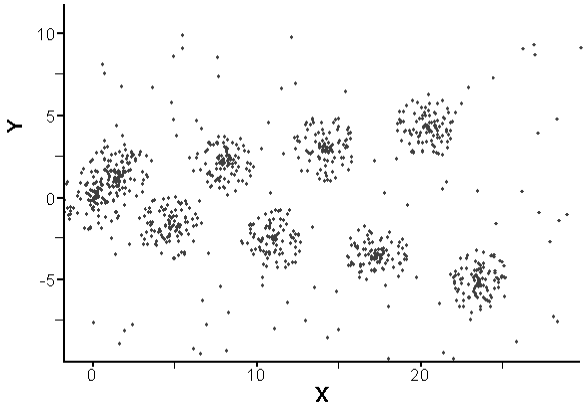

Figura 2d. Distribuição não uniforme em senóide.

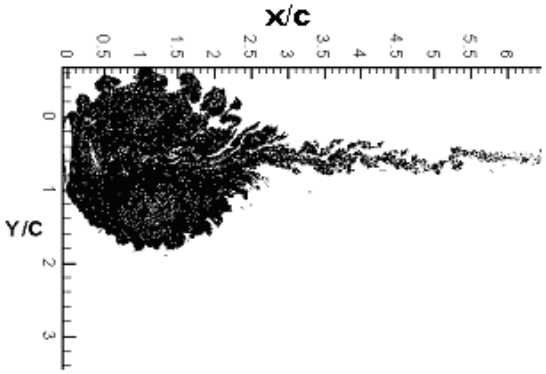

Figura 2e. Esteira formada por aerofólio estolado.

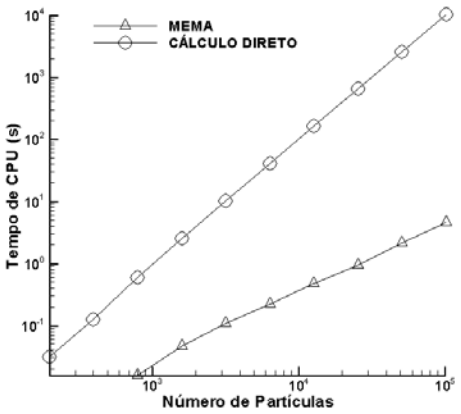

Figura 3a. Quadrado com distribuição uniforme.

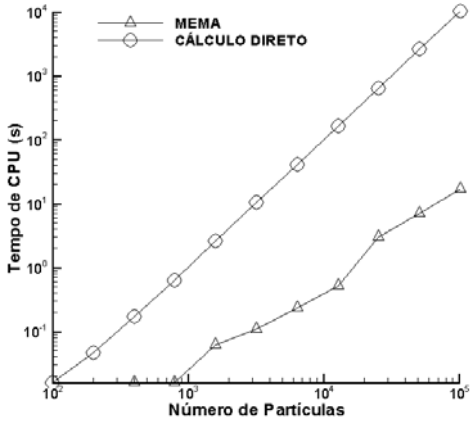

Figura 3b. Quadrado com distribuição não uniforme.

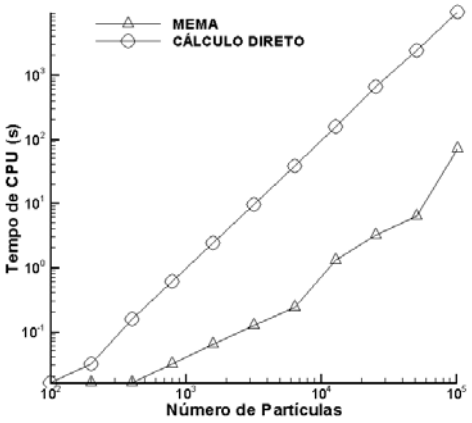

Figura 3c. Linha reta.

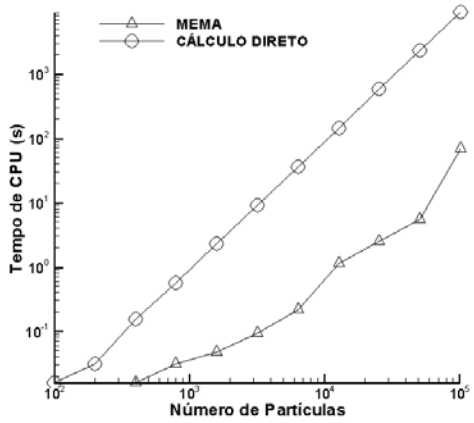

Figura 3d. Senóide.

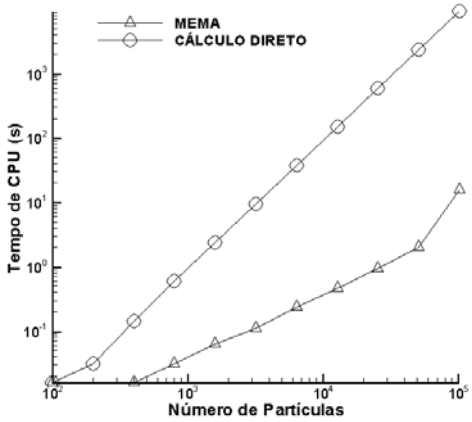

Figura 3e. Esteira formada por aerofólio estolado.

O algoritmo do MEMA requer que o domínio que contém a nuvem de vórtices seja dividido em caixas quadradas seqüencialmente, até que estas possuam um número de vórtices menor que o número máximo de vórtices por caixa. Este parâmetro é importante para o desempenho do algoritmo. Entretanto, este refinamento também é interrompido

quando o tamanho da caixa se torna menor do que a distância para desingularização. Nesta situação, se o refinamento tivesse continuidade, vórtices que devem ser tratados pelo cálculo direto seriam colocados em caixas diferentes, o que faria a interação entre eles ser calculada pela expansão em multipolos. Em outras palavras, a distância para desingularização não pode ser superior ao tamanho da caixa e, por este motivo, regiões com grande densidade de vórtices causam situações em que se deve aumentar o número máximo de vórtices por caixa para se manter o tamanho das caixas superior à distância de desingularização.

Em contrapartida, quando se torna necessário aumentar o número máximo de vórtices por caixa, o tempo de processamento se torna maior, uma vez que o refinamento espacial é interrompido com um número menor de caixas. Como conseqüência, o número de interações diretas partícula-partícula aumenta. Tal prejuízo no desempenho do código pode ser visualizado nas Figs. 3a – 3e, onde as retas de desempenho do MEMA se aproximam das curvas obtidas com o cálculo direto. Este comportamento é conseqüência da multiplicação do número de vórtices por caixa por um fator igual a oito toda vez que a distância de desingularização ultrapassa o tamanho da caixa onde aquele vórtice se encontra. O procedimento adotado tem como objetivo dobrar o tamanho da menor caixa na próxima chamada do MEMA, tendo em vista que, para a confecção dos gráficos das Figs. 3a – 3e, o número de vórtices dobra entre cada chamada. A configuração geométrica da esteira simulada na Fig. 3a não apresenta a necessidade de se utilizar este procedimento, uma vez que a distribuição estatisticamente uniforme de vórtices mostrada na Fig. 2a faz com que não surja localmente nenhuma região com caixas menores que a distância de desingularização. Para o caso da Fig. 3e, verifica-se que ocorre aproximação entre as curvas apenas para o último ponto ($N = 10^5$), o que se deve ao fato de que a distribuição de vórtices gerados pelo aerofólio estolado da Fig. 2e apresenta, estatisticamente, grande uniformidade.

O desempenho do MEMA pode ser medido de duas maneiras. A primeira, a mais facilmente observável nos gráficos das Figs. 3a – 3e, é o fato de que a ordem de grandeza dos tempos de CPU obtidos para as simulações com o MEMA é muito menor do que a ordem de grandeza dos tempos de CPU obtidos com o método direto partícula-partícula. Por exemplo, pelo cálculo direto, são necessários aproximadamente 10^2 s para processar 10^4 vórtices e 10^4 s para processar 10^5 vórtices, em todas as configurações geométricas estudadas. No caso do MEMA, são necessários 0,5 s para processar 10^4 vórtices e 5 s para 10^5 vórtices. Como se pode ver nas figuras, o tempo de CPU requerido pelo MEMA é muito menor. Por outro lado, o exemplo acima serve também para ilustrar a segunda observação que pode ser inferida. O tempo de processamento obtido pelo método direto é multiplicado por 10^2 ao se multiplicar o número de vórtices por 10, enquanto que, no caso do MEMA, multiplicando-se por 10 o número de vórtices, o tempo necessário também é multiplicado por 10. Este comportamento se deve à inclinação que cada reta tem nas Figs. 3a – 3e, o que é mais facilmente notado na Fig. 3a. Deste modo comprova-se que o MEMA é de ordem N, enquanto que o cálculo direto é da ordem de N^2, como esperado.

As Figuras 3a – 3e também mostram que a inclinação da reta se mantém constante nos intervalos em que o número máximo de vórtices por caixa é mantido constante. A inclinação da reta aumenta localmente a sua inclinação nos pontos em que há um aumento do número máximo de vórtices por caixa, como claramente mostrado nas Figs. 3b – 3e, mas o desempenho global do MEMA não é alterado mesmo nesse casos.

O erro quadrático médio, E, pode ser utilizado como uma medida do erro global introduzido ao se calcular as interações entre as partículas pelo MEMA ao invés de se utilizar o método direto. Esta grandeza é definida pela seguinte expressão

$$E = \left(\frac{\sum_{i=1}^{N} \left| f_i - \tilde{f}_i \right|^2}{\sum_{i=1}^{N} \left| f_i \right|^2} \right)^{1/2}, \tag{5}$$

onde f_i é o valor do campo gerado no vórtice i por todos os N–1 vórtices, calculado pelo método direto com precisão dupla, enquanto $\tilde{f}_i$ é o valor do campo no vórtice i calculado pelo MEMA. O máximo valor de E encontrado para todos os casos simulados foi de $1{,}0\times10^{-11}$, nos quais foram utilizados um número máximo de vórtices por caixa inicial igual a 30, e uma distância para desingularização igual $5{,}0\times10^{-03}$.

4. Utilização do MEMA

Como dito anteriormente, o presente trabalho objetiva também avaliar a aplicabilidade do MEMA no Método dos Vórtices Discretos desenvolvido por Silva e Bodstein (2005) para estudar o escoamento viscoso, bidimensional e incompressível de um fluido Newtoniano com propriedades constantes ao redor de um aerofólio. A seguir, o método de vórtices utilizado neste trabalho é descrito de maneira sucinta. A seção 4.1 apresenta o sistema de equações a ser resolvido, montado com base no Método dos Painéis, e que determina a intensidade da vorticidade gerada na superfície do corpo e transferida para o escoamento. A seção 4.2 trata da evolução temporal conduzida pelo Método dos Vórtices Discretos, na qual a vorticidade calculada anteriormente é transportada para o meio fluido por convecção e difusão.

4.1. Método dos Painéis

O Método dos Painéis (Katz e Plotkin, 2001) é uma particularização do Método dos Elementos de Contorno no qual a presença do corpo é modelada por singularidades que induzem no domínio fluido o mesmo efeito que seria obtido pela presença do corpo imerso em um escoamento irrotacional. Os valores destas singularidades são obtidos ao se satisfazer à condição de impermeabilidade em cada um dos painéis que discretizam o contorno do sólido. O Método dos Painéis utilizado permite a discretização do corpo em N painéis retos, com distribuição linear de vorticidade sobre eles. A cada painel corresponde um ponto de controle, onde se impõe a condição de impermeabilidade.

A utilização de uma distribuição linear de vorticidade implica no aparecimento de N+1 incógnitas. No entanto, a imposição da condição de contorno de impermeabilidade gera uma equação para cada ponto de controle, ou seja, N equações. Utiliza-se, adicionalmente, a condição de conservação de circulação para formar um sistema fechado de N+1 equações, que pode ser escrito como

$$U \cdot \vec{n}_i + \sum_{j=1}^{N+1} A_{ij}\gamma_j + \sum_{g=1}^{N_v} G_{ig}k_g = 0\,, \tag{6}$$

$$\sum_{j=1}^{N} \frac{\gamma_j + \gamma_{j+1}}{2}\Delta\ell_j = 0\,. \tag{7}$$

Na Equação (6), o primeiro termo refere-se ao escoamento incidente, o segundo termo refere-se aos painéis retos, e o terceiro termo refere-se aos vórtices liberados na esteira ao final de cada passo no tempo e que compõem a nuvem. Ainda nessa mesma equação, o termo γ_j refere-se à intensidade da vorticidade calculada naquele instante de tempo para cada extremo (nós) dos painéis e que forma um vórtice livre no passo de tempo seguinte, o termo A_{ij} é relativo à geometria dos painéis, também chamado matriz de coeficientes de influência, o termo k_g é a intensidade de cada vórtice presente na esteira, enquanto que o termo G_{ig} representa a função de transferência, que no caso do presente trabalho é a função descrita pelo vórtice de Lamb. Pode-se observar que a Eq. (7), que representa a equação de conservação de circulação, não leva em consideração os vórtices livres, uma vez que no instante de tempo inicial a circulação é nula.

4.2. Método dos Vórtices Discretos

O Método de Vórtices Discretos simula o escoamento externo ao redor de corpos utilizando modelos de vórtices para representar a região rotacional do escoamento, ou seja, considera-se o escoamento irrotacional a não ser nas regiões abrangidas pelos núcleos dos vórtices. O modelo de vórtice utilizado neste trabalho é o vórtice de Lamb.

A utilização do vetor vorticidade $\boldsymbol{\omega} \equiv \nabla\times\boldsymbol{u}$ permite o cálculo do campo de velocidade sem que seja necessário calcular o campo de pressão. Deste modo, considerando escoamento bidimensional incompressível de um fluido Newtoniano, pode-se obter a equação de transporte de vorticidade, como se segue

$$\frac{\partial\omega}{\partial t} + \boldsymbol{u}\cdot\nabla\omega = \frac{1}{Re}\nabla^2\omega\,. \tag{8}$$

Com o objetivo de calcular o avanço temporal do escoamento, Chorin (1973) propõe a decomposição do operador convectivo-difusivo da Eq. (8) em dois, um puramente convectivo e outro puramente difusivo, na forma

$$\frac{\partial\omega}{\partial t} + \boldsymbol{u}\cdot\nabla\omega = 0\,, \tag{9}$$

$$\frac{\partial\omega}{\partial t} = \frac{1}{Re}\nabla^2\omega\,. \tag{10}$$

A Eq. (9) representa o transporte convectivo da vorticidade, realizado neste trabalho pelo esquema de Adams-Bashforth de segunda ordem, enquanto a Eq. (10) representa o transporte difusivo, realizado pelo Método do Avanço Randômico (Lewis, 1990).

Para o cálculo da velocidade de convecção $\boldsymbol{u}$ da Eq. (9) é necessário se levar em consideração o campo de velocidade do escoamento incidente, o campo de velocidade induzido pelos painéis e o campo de velocidade induzido pelos vórtices livres, este último responsável pelo maior custo computacional do método, que é da ordem de N^2, justificando-se neste ponto a aplicação do MEMA para reduzi-lo para N.

De posse da velocidade de convecção $\boldsymbol{u}$, calcula-se o deslocamento convectivo dos vórtices através do esquema de Adams-Bashforth de segunda ordem, o qual, utilizando-se os componentes cartesianos de $\boldsymbol{u}$, pode ser escrito como

$$\begin{pmatrix} \Delta x_C \\ \Delta y_C \end{pmatrix}_i = \begin{pmatrix} 1,5u(t) - 0,5u(t-\Delta t) \\ 1,5v(t) - 0,5v(t-\Delta t) \end{pmatrix}_i \Delta t \,. \tag{11}$$

O Método do Avanço Randômico (Lewis, 1991) utilizado neste trabalho baseia-se na obtenção de números randômicos P e Q de uma distribuição de probabilidade uniforme, o que permite calcular os deslocamentos aleatórios cartesianos dos vórtices pelas equações abaixo

$$\zeta = \sqrt{\frac{8\Delta t}{\mathrm{Re}} \ln\left(\frac{1}{P}\right)} \cos(2\pi Q)\,, \tag{12}$$

$$\eta = \sqrt{\frac{8\Delta t}{\mathrm{Re}} \ln\left(\frac{1}{P}\right)} sen(2\pi Q)\,. \tag{13}$$

A nova posição dos vórtices é calculada levando-se em consideração os deslocamentos convectivo e difusivo, e pode ser expressa como

$$x(t+\Delta t) = x(t) + \Delta x_c + \zeta\,, \tag{14}$$

$$y(t+\Delta t) = y(t) + \Delta y_c + \eta\,. \tag{15}$$

4.3. Resultados

Esta seção apresenta alguns resultados da utilização do MEMA no Método de Vórtices Discretos para simular um escoamento com Re=1,7x10^5 ao redor de um aerofólio NACA 0012, discretizado com 300 painéis, e com Δt = 0,025 e raio do vórtice de Lamb σ = 0,005. O desempenho do método em termos de tempo de processamento é, então, comparado ao obtido pelo método direto.

As Figuras 4 – 7 abaixo apresentam esteiras contendo 240.000 vórtices, geradas com ângulo de ataque α = 0º, 10º, 18º e 45º, respectivamente, no último instante da simulação (t = 20).

Figura 4. Esteira viscosa de 240.000 vórtices; aerofólio NACA 0012, α = 0º.

Figura 5. Esteira viscosa de 240.000 vórtices; aerofólio NACA 0012, α = 10º.

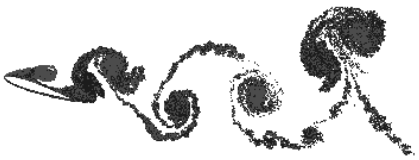

Figura 6. Esteira viscosa de 240.000 vórtices; aerofólio NACA 0012, α = 18º.

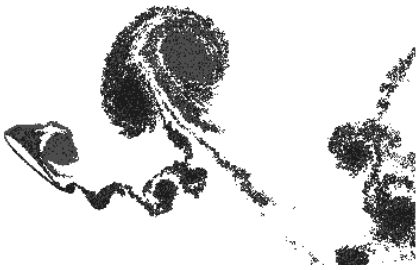

Figura 7. Esteira viscosa de 240.000 vórtices; aerofólio NACA 0012, α = 45º.

Para a obtenção das esteiras apresentadas acima foi necessário gerar 300 vórtices em cada um dos 800 passos no tempo, totalizando os 240.000 vórtices presentes em t = 20. Simulações de tempo longo tornam o tempo de processamento impeditivo no caso do cálculo direto, que chega a 30 horas para apenas 400 passos no tempo. Pode-se estimar em 168 horas, aproximadamente, o tempo necessário para simulações semelhantes às mostradas nas Figs. 4 – 7 utilizando o cálculo direto. A Tabela 1 apresenta os tempos de processamento medidos para as simulações acima utilizando o MEMA. Todas as simulações, com MEMA e com método direto, foram realizadas em uma máquina que possui processador Pentium IV 3.2 GHz, com 2 Gb de memória RAM.

Tabela 1. Tempo de processamento.

Ângulo de Ataque (º)	Tempo de CPU (h): MEMA
0	21
10	19
18	16
45	15

Os tempos de processamento da Tab. 1 mostram que há uma dependência do ângulo de ataque, que é fruto do grau de espalhamento dos vórtices. Como discutido anteriormente, quanto maior for a densidade local de vórtices, maior será o número máximo de vórtices por caixa no cálculo por expansão em multipolos, tendo em vista que o tamanho da menor caixa tem que ser necessariamente maior que a distância de desingularização (raio do vórtice de Lamb). Assim, baixos ângulos de ataque têm a tendência de formar maiores concentrações de vórtices em sua esteira, implicando em maiores tempos de processamento quando se utiliza a expansão em multipolos do que nos casos de alto ângulo de ataque.

5. Conclusões

Este trabalho apresenta de forma geral o Método de Expansão em Multipolos Adaptativo (MEMA) de Carrier *et al*. (1988) e utiliza o código computacional originalmente desenvolvido pelos autores para testar a sua adaptabilidade espacial do MEMA no cálculo da interação entre vórtices de Lamb presentes em esteiras de diversas configurações geométricas. Adicionalmente, o trabalho avalia a aplicabilidade deste código ao Método de Vórtices Discretos (Silva e Bodstein, 2005) e compara os resultados com simulações para um aerofólio obtidas pelo método direto partícula-partícula.

Os resultados de tempo de processamento das simulações que visam testar a adaptabilidade espacial do MEMA para cinco tipos de configurações geométricas da nuvem de vórtices comprovam a grande superioridade em desempenho com relação ao cálculo direto partícula-partícula. Estes resultados atestam que, para todos os casos simulados, o tempo de processamento do MEMA é da ordem de N, sendo N o número de partículas, enquanto que para o cálculo direto é da ordem de N^2. Conclui-se também que a necessidade de se aumentar o número máximo de vórtices por caixa, quando o tamanho da caixa se torna menor do que a distância de desingularização, provoca uma ligeira queda de desempenho do MEMA, e o tempo de processamento das simulações com o método da expansão em multipolos se aproxima do tempo de processamento obtido pelo cálculo direto. Porém, mesmo nesses casos, a inclinação da reta de multipolos volta a ser de ordem N até que um novo aumento do número máximo de vórtices por caixa seja necessário. Este comportamento permite afirmar que o tempo de processamento do MEMA é da ordem de N desde que o número máximo de vórtices por caixa seja mantido constante.

A acurácia do MEMA foi avaliada em todas as situações simuladas. O erro quadrático médio manteve-se sempre abaixo de $1{,}0 \times 10^{-11}$, o que evidencia a grande acurácia do MEMA na avaliação do campo gerado por um conjunto de partículas.

A análise de desempenho do MEMA na etapa convectiva do Método de Vórtices Discretos utilizado para simular o escoamento ao redor de um aerofólio NACA 0012 para ângulos de ataque de 0º a 45º permite concluir que o MEMA pode ser aplicado com segurança tanto em simulações de escoamento perfeitamente colado ao aerofólio, as quais ocorrem com ângulos de ataque baixos, quanto em situações de grande descolamento, as quais acontecem após o estol. As esteiras obtidas permitem a visualização do bom desempenho do MEMA nos diferentes tipos de escoamentos, sejam eles com esteiras viscosas estreitas e grande densidade de vórtices, ou com esteiras oscilatórias e grande espalhamento de vórtices.

Assim, as situações testadas e as simulações conduzidas no presente trabalho permitem que se afirme que o MEMA possui grande adaptabilidade espacial, podendo ser utilizado para avaliar a interação entre os vórtices durante a etapa convectiva do Método de Vórtices Discretos. Da mesma forma, pode-se afirmar que o MEMA reduz o tempo de processamento para ordem N, enquanto que no cálculo direto este é da ordem de N^2, mantendo excelente acurácia e permitindo, deste modo, que simulações mais longas possam ser executadas, uma vez que o aumento do número de vórtices não se torna fator impeditivo como ocorre no cálculo direto.

Agradecimentos

Os autores agradecem ao Prof. Leslie Greengard por ceder o código FORTRAN original do MEMA, o qual sofreu pequenas adaptações implementadas pelos autores para utilização neste trabalho. O autores também agradecem ao Exército Brasileiro, à CAPES e ao CNPq, respectivamente, pelo apoio financeiro a este projeto de pesquisa.

Referências

Carrier, J., Greengard, L. and Rokhlin, V., 1988, "A fast adaptive multipole algorithm for particle simulation", SIAM J. Sci. Stat. Comput., Vol. 9, No. 4, July 1988.

Chorin, A. J., 1973, Numerical Study of Slightly Viscous Flow, Journal of Fluid Mechanics, Vol. 57, part 4, pp. 785-796.

Guedes, V. G., Bodstein, G. C. R. e Hirata, M. H., 1999, "Esquema de Expansão em Multipolos Aplicado ao Cálculo de Interações entre Partículas Baseado na Lei de Biot-Savart", Anais do XV COBEM (em CD-ROM), Águas de Lindóia, SP, 22-26 de novembro, 1999.

Greengard, L. and Rokhlin, V., 1987, "A fast algorithm for particles simulations", Journal of Computational Physics, Vol. 73, No. 2, 1987.

Katz, J. & Plotkin, A., 2001, Low - Speed Aerodynamics, 2nd edition, Cambridge University Press.

Lewis, R. I., 1991, Vortex Element Method for Fluid Dynamic Analysis of Engineering Systems, Cambridge, Cambridge University Press.

Mustto, A. A. e Bodstein, G. C. R., 2000, "Um Novo Esquema do Método de Expansão em Multipolos para a Interação entre Partículas na Presença de um Cilindro Circular", Anais do VIII ENCIT - Congresso Brasileiro de Engenharia e Ciências Térmicas (em CD-ROM), Paper s08p27, Porto Alegre, RS, 03-06 de Outubro, 2000.

Ogami, Y., 2002, "Fast summation algorithms for the particle simulation of far-field potential and rapidly-decaying potential", JSME International Journal, Seriers B., Vol. 45, No. 1., 2002.

Silva, D. F. C. and Bodstein, G. C. R., 2005, "Numerical Simulation of Unsteady Two-Dimensional Incompressible Flows Around Airfoils Using the Vortex Method", Proceedings of the 3rd International Conference on Vortex Flows and Vortex Models (ICVFM2005), Yokohama, JAPAN, November 21 - 23, pp. 173-178.

PERFORMANCE ANALYSIS OF THE FAST ADAPTIVE MULTIPOLE ALGORITHM APPLIED TO VORTEX METHOD SIMULATIONS

Victor S. Santiago
vsantoro@ig.com.br

Daniel F. C. Silva
danfcs@yahoo.com

Gustavo C. R. Bodstein
Federal University of Rio de Janeiro (UFRJ), Department of Mechanical Engineering – Poli/COPPE
Centro de Tecnologia, Bloco G, sala 204 – Ilha do Fundão, 21945-970 Rio de Janeiro, RJ – Brazil
gustavo@mecanica.coppe.ufrj.br

Abstract. *The vorticity transport simulated in the convective step of the Vortex Method imposes the need to compute the velocity induced by each vortex at all the other vortices that make up the cloud. This procedure produces a CPU time of the order N^2, where N is the number of vortices in the cloud. In order to reduce the time to carry out long-time simulations, where the number of vortices increases as time increases, the Fast Adaptive Multipole Algorithm is used in this paper, which decreases the CPU time down to order N. The simulations are carried out applying the Fast Adaptive Multipole Algorithm to five different vortex clouds, each representing one possible instantaneous wake configuration. In addition, the Fast Adaptive Multipole Algorithm is integrated into a Discrete Vortex Method algorithm to calculate high Reynolds number flows around airfoils. The results are compared to those obtained from the direct method and show the enormous advantage of using the Fast Adaptive Multipole Algorithm.*

Keywords: *Fast Multipole Method, Vortex Method, Panel Method, airfoil, aerodynamics.*

Proceedings of the 11th Brazilian Congress of Thermal Sciences and Engineering -- ENCIT 2006
Braz. Soc. of Mechanical Sciences and Engineering -- ABCM, Curitiba, Brazil, Dec. 5-8, 2006

Paper CIT06-0256

A GENERALIZED FORMULATION FOR THE FALKNER SKAN EQUATION

Jerson Rogério Pinheiro Vaz
Universidade Federal do Pará – Departamento de Engenharia de Materiais
Folha 17, Qd 04, Lote Especial, Nova Marabá, Marabá, PA, Brasil – 68505-080
jerson@ufpa.br

Daniel Onofre de Almeida Cruz
Universidade Federal do Pará – Departamento de Engenharia Mecânica
Av. Augusto Correa, s/n - Belém, PA, Brasil – 66075-900
doac@ufpa.br

João Tavares Pinho
Universidade Federal do Pará – Departamento de Engenharia Elétrica
Av. Augusto Correa, s/n - Belém, PA, Brasil – 66075-900
jtpinho@ufpa.br

Abstract. *The Falkne-Skan similar equation represents one of the greatest successes of the boundary layer theory for the laminar flow case. The domain of validity of this equation, however, is restricted to the region far from the leading edge and to very small pressure gradients.*

In the present work a generalized formulation of the boundary layer theory is used to derive an extended version of the Falkner-Skan equation. This generalized Falkner-Skan equation (GFS) is given by a quasi-similar equation, which incorporates the stream wise coordinate non-similar information, but keeping the ordinary differential equation characteristic. It is shown that the GFS can be used to describe the flow for Reynolds numbers as low as one, and for strong adverse pressure gradients.

Keywords: *Falkne-Skan,Kaplun Limits, Separation*

1. Introduction

The Falkner-Skan equation constitutes one of the classical results of the Prandt's boundary layer theory. The variety of applications and the importance of the Falkner-Skan equation for the understanding of the physical features of the laminar flow, submitted to an strong favorable pressure gradient, have motivate many recent works, most related to the numerical nature of it's solution (Schlichting, 1972).

Being a direct consequence of the classical boundary layer theory, the FSE has a restricted domain of validity. That limitation does not permit the description of the separated flow or the flow near the leading edge ($1<Re_x<1000$) using the similarity FSE approach. The above mentioned restriction can be overcome if a more general boundary layer formulation is used to derive an extended version of the FSE.

In the present work the generalized boundary layer theory is used to obtain a expanded formulation of the FSE. The procedure is similar to one used for the deduction of the classical FSE. After the introduction of a set of similar variables into the generalized boundary layer equation, a quasi-similar equation is obtained. That equation contains the classical FSE as a particular case.

The new generalized Falkner-Skan equation is numerically solved and the results show that the domain of validity of the GFSE can be extended not only to the near leading edge region, but also to the separating flow region. This fact represents a great advantage over the FSE, since the last is not valid for large adverse pressure gradients, witch causes the flow separation. The GFSE is used to correlated the laminar separation point of diffusers, to the imposed pressure gradient (or the diverging angle of the diffuser), indicating that the GFSE can be used as a non expensive simple tool for the project of industrial equipment.

2. The Generalized Boundary Layer Equation

The concept of Kaplun limits (1967) is used to determinate the asymptotic behavior of the Navier-Stokes equation as $Re \rightarrow \infty$. The necessary mathematical framework to obtain the high Reynolds number asymptotic behavior of the Navier-Stokes is exhaustively discussed in Cruz (2002) and Silva Freire (1999) here just some of the principal steps are presented. For a laminar incompressible, stationary and two-dimensional flow of a newtonian fluid the continuity and the momentum equations can be written as follows:

$$\frac{\partial u}{\partial x} + \frac{\partial v}{\partial y} = 0 \tag{1}$$

$$u \frac{\partial u}{\partial x} + v \frac{\partial u}{\partial y} = - \frac{\partial P}{\partial x} + \frac{1}{\mathrm{Re}} \left[\frac{\partial^2 u}{\partial x^2} + \frac{\partial^2 u}{\partial y^2} \right] \tag{2}$$

$$u \frac{\partial v}{\partial x} + v \frac{\partial v}{\partial y} = - \frac{\partial P}{\partial y} + \frac{1}{\mathrm{Re}} \left[\frac{\partial^2 v}{\partial x^2} + \frac{\partial^2 v}{\partial y^2} \right] \tag{3}$$

In the above equations the variables are made non-dimensional using a characteristic length and a characteristic velocity of the flow. The parameters u and v represent the non-dimensional velocities on the x and y directions respectively and P is the non-dimensional pressure.

The parameter Re represents the Reynolds number which is assumed to be large i.e. (1/Re<<1)

The intermediate variables ere defined as:

$$\hat{y} = \frac{y}{\eta(\varepsilon)} \tag{4}$$

$$\hat{v} = \frac{v}{\eta(\varepsilon)} \tag{5}$$

where $\varepsilon = \frac{1}{\mathrm{Re}}$.

The insertion of Eq. (4) and (5) into Eq. (1), (2) and (3) results in:

$$\frac{\partial u}{\partial x} + \frac{\partial \hat{v}}{\partial \hat{y}} = 0 \tag{6}$$

$$u \frac{\partial u}{\partial x} + \hat{v} \frac{\partial u}{\partial \hat{y}} = - \frac{\partial P}{\partial x} + \frac{1}{\mathrm{Re}} \left[\frac{\partial^2 u}{\partial x^2} + \frac{1}{\eta(\varepsilon)^2} \frac{\partial^2 u}{\partial \hat{y}^2} \right] \tag{7}$$

$$\eta(\varepsilon) u \frac{\partial \hat{v}}{\partial x} + \eta(\varepsilon) \hat{v} \frac{\partial \hat{v}}{\partial y} = - \frac{1}{\eta(\varepsilon)} \frac{\partial P}{\partial \hat{y}} + \frac{1}{\mathrm{Re}} \left[\eta(\varepsilon) \frac{\partial^2 \hat{v}}{\partial x^2} + \frac{1}{\eta(\varepsilon)} \frac{\partial^2 \hat{v}}{\partial \hat{y}^2} \right] \tag{8}$$

Applying the η-limit onto Eq. (7) and (8) respectively, it is obtained:
For the momentum equation on x-direction:

$$ord(\eta) = ord(1) : \quad u \frac{\partial u}{\partial x} + \hat{v} \frac{\partial u}{\partial \hat{y}} = - \frac{\partial P}{\partial x} \tag{9}$$

$$ord(1) > ord(\eta) > ord\left(\sqrt{\varepsilon}\right) : u \frac{\partial u}{\partial x} + \hat{v} \frac{\partial u}{\partial \hat{y}} = - \frac{\partial P}{\partial x} \tag{10}$$

$$ord(\eta) = ord\left(\sqrt{\varepsilon}\right) : u \frac{\partial u}{\partial x} + \hat{v} \frac{\partial u}{\partial \hat{y}} = - \frac{\partial P}{\partial x} + \frac{\partial^2 u}{\partial \hat{y}^2} \tag{11}$$

$$ord(\eta) < ord\left(\sqrt{\varepsilon}\right) : \frac{\partial^2 u}{\partial \hat{y}^2} = 0 \tag{12}$$

For the momentum equation in the y-direction:

$$ord(\eta) = ord(1) : u \frac{\partial \hat{v}}{\partial x} + \hat{v} \frac{\partial \hat{v}}{\partial y} = - \frac{\partial P}{\partial \hat{y}} \tag{13}$$

$$ord(\eta) < ord(1) : \frac{\partial P}{\partial \hat{y}} = 0 \tag{14}$$

In each of the above two sets of differential Eq. (9) to (12) and (13) to (14) there is only one main equation according to Kaplun's definition. Equation (11) represents the main equation for the *x* momentum equation and Eq. (13) is the main equation for the *y* momentum equation. It should be noted that the terminology "main", is related to the fact that the above mentioned equations exhibit some specific characteristics. In both cases, the Eq. (11) and (13) contains the other equations and are not contained by any other of the remaining expressions (Cruz, 2002). This fact indicates that in the limit as $\mathrm{Re} \to \infty$ the behavior Navier-Stokes equations is adequately described by the following set of equations

$$u \frac{\partial u}{\partial x} + v \frac{\partial u}{\partial y} = - \frac{\partial P}{\partial x} + \frac{1}{\mathrm{Re}} \frac{\partial^2 u}{\partial y^2} \tag{15}$$

$$u \frac{\partial v}{\partial x} + v \frac{\partial v}{\partial y} = - \frac{\partial P}{\partial y} \tag{16}$$

$$\frac{\partial u}{\partial x} + \frac{\partial v}{\partial y} = 0 \tag{17}$$

The Eq. (15) to (16) represent a generalized form of the boundary layer theory which combines the Euler inviscid flow equations and the Prandtl classical boundary layer formulation into a single and more widespread formulation.

3. Flow past a wedge and the quasi-similar Falkner-Skan equation

The classical approach to describe the flow past a wedge problem consists of the use of the Falkner-Skan equation, and its solutions were investigated in detail by Hartree (1937). An important characteristic of that equation, corresponds to the fact that the potential flow is proportional to a power of the length coordinate measured from the stagnation point, i. e. for

$$U(x) = u_1 x^m \tag{18}$$

The transformation of the independents variables *y* and *x*, which leads to an ordinary equations, is:

$$\tilde{\eta} = y \sqrt{\frac{(m+1)}{2} \frac{U}{\nu x}} = y \sqrt{\frac{(m+1)}{2} \frac{u_1}{\nu}} x^{\frac{m-1}{2}} \tag{19}$$

The stream function and the velocity components are:

$$\Psi(x,y) = \sqrt{\frac{2}{m+1}} \sqrt{\nu u_1} x^{\frac{m+1}{2}} f(\eta) \tag{20}$$

$$u = u_1 x^m f'(\eta) = U f'(\eta) \tag{21}$$

$$v = -\sqrt{\frac{m+1}{2} \nu u_1 x^{m-1}} \left\{ f + \frac{m-1}{m+1} \eta f' \right\} \tag{22}$$

Introduction these values into the equation of motion (16) and dividing by $m u_1 x^{2m-1}$, it is obtained:

$$m = \frac{\beta}{2-\beta} \tag{23}$$

$$\beta = \frac{2m}{m+1} \tag{24}$$

Using the stream function and of the Eq. (15) to (17) can be rewritten and the resulting transformed equation is obtained:

$$\begin{aligned}
&\left[-F - \frac{(m-1)\eta F'}{m+1}\right]\left[\frac{1}{2}(m+1)F''' + \frac{(m-1)mF' - \left(m-\frac{3}{4}\right)\eta F'' + \frac{1}{4}\eta^2 F'''}{\xi_0}\right] + \\
&F'\left\{\frac{1}{2}(m+1)\left[\left(1+\frac{2(m-1)}{m+1}\right)F'' + \frac{(m-1)\eta F'''}{m+1}\right] - \frac{1}{\xi_0}\left\{\frac{1}{4}F(m-3)(m-1) + \right.\right. \\
&\left[\frac{(m-3)(m-1)^2\eta}{4(m+1)} - \frac{1}{2}(m-1)\left(1+\frac{m-1}{m+1}\right)\eta + \frac{1}{4}\left(1+\frac{m-1}{m+1}\right)\eta^2\right]F'' + \\
&\left.\left.\left[\frac{1}{2}(m-1)\eta^2 + \frac{1}{4}\left(1+\frac{2(m-1)}{m+1}\right)\eta^2 + \frac{\eta^3}{4}\right]F'' + \frac{(m-1)\eta^3 F'''}{4(m+1)}\right\}\right\} = \frac{1}{2}(m+1)F^{IV}
\end{aligned} \tag{25}$$

Where,

$$F^{(j)} = \frac{\partial^{(j)} F}{\partial\, \tilde{\eta}^{(j)}} \tag{26}$$

$$\xi_0 = \mathrm{Re}_x \tag{27}$$

Where $\tilde{\eta}_\infty$ represents a value of η assumed to be far enough of the solid wall and Re_x is the local Reynolds number. The local Reynolds number represents the non dimensional distance from the leading edge

Equation (25) must be solved according to the following boundary conditions:

$$F'(0,\xi_0) = 0 \tag{28}$$

$$F(0,\xi_0) = 0 \tag{29}$$

$$F'(\tilde{\eta}_\infty,\xi_0) = 1 \tag{30}$$

$$F''(\tilde{\eta}_\infty,\xi_0) = 0 \tag{31}$$

4. Results

Figures 1 to 5 show the velocity profiles obtained from the solution of Eq. (25), for various values of the local Reynolds number. Near the leading edge the results clearly show the overshot of the velocity profiles near the wall, this phenomenon is caused by the abrupt change of the velocity form the undisturbed free stream flow to the flow submitted to the no slip condition. It is important to note that the classical boundary layer theory cannot predict the flow near the leading edge since, the momentum equation perpendicular to the solid surface is not considered in the theory. It is also important to mention that far from the leading edge, the velocity profile assumes the classical FSE shape. It can be show that Eq (25) contains the FSE as a particular case in the limit as $\mathrm{Re}_x \to \infty$ as show below:

$$\lim_{\zeta_0\to\infty}\left\{\begin{array}{l}\left[-F-\dfrac{(m-1)\eta F'}{m+1}\right]\left[\dfrac{1}{2}(m+1)F'''+\dfrac{(m-1)mF'-\left(m-\dfrac{3}{4}\right)\eta F''+\dfrac{1}{4}\eta^2F'''}{\xi_0}\right]+\\ F'\left\{\dfrac{1}{2}(m+1)\left[\left(1+\dfrac{2(m-1)}{m+1}\right)F''+\dfrac{(m-1)\eta F'''}{m+1}\right]-\dfrac{1}{\xi_0}\left\{\dfrac{1}{4}F(m-3)(m-1)+\right.\right.\\ \left[\dfrac{(m-3)(m-1)^2\eta}{4(m+1)}-\dfrac{1}{2}(m-1)\left(1+\dfrac{m-1}{m+1}\right)\eta+\dfrac{1}{4}\left(1+\dfrac{m-1}{m+1}\right)\eta^2\right]F''+\\ \left.\left.\left[\dfrac{1}{2}(m-1)\eta^2+\dfrac{1}{4}\left(1+\dfrac{2(m-1)}{m+1}\right)\eta^2+\dfrac{\eta^3}{4}\right]F''+\dfrac{(m-1)\eta^3F'''}{4(m+1)}\right\}\right\}\end{array}\right\}=\lim_{\zeta_0\to\infty}\left[\frac{1}{2}(m+1)F^{IV}\right]$$

Resulting

$$-FF''+\left(\frac{3m-1}{m+1}\right)F'F''=F^{IV} \tag{32}$$

Integrating the Eq. (32),

$$F'''+FF''-\beta\left(F'\right)^2+C=0 \tag{33}$$

Where C is the integration constant. The boundary conditions (28) to (29), furnishes $C=\beta$. The FSE can now be obtained as follows:

$$F'''+FF''+\beta\left[1-\left(F'\right)^2\right]=0 \tag{34}$$

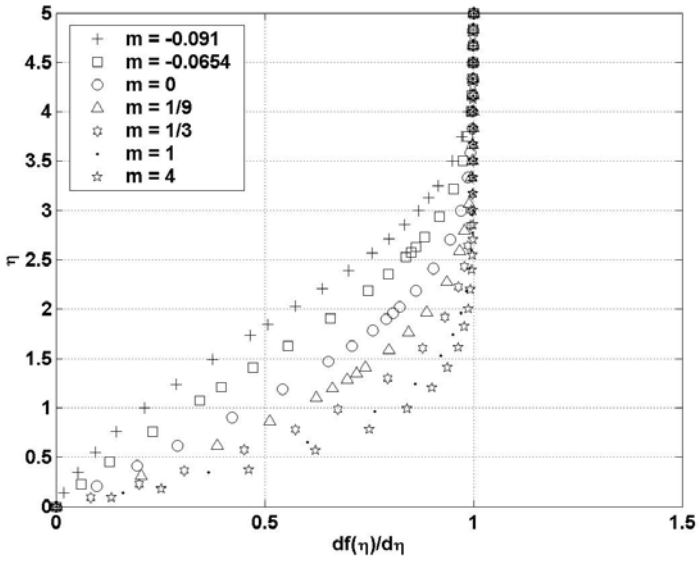

Figure 1 – The nondimensional velocity profiles assumes the classical FSE shape in the limit as $\mathrm{Re}_x\to\infty$. In this case, result for $\mathrm{Re}_x=10^9$.

The boundary layer flow subjected an adverse pressure gradient are presented in Fig. (2) and (3). Figure (3) show the FSE limiting case (m = -0.091) it is clear that the present formulation can predict the whole flow region. An interesting feature of the present formulation can be observed in Fig. (2), it is show that the Eq. (25) can adequately

predict the flow submitted to an adverse pressure gradient that can cause flow separation. This fact is possible due to the quasi-similar character of the proposed Eq. (25) that permits a changeable velocity profile witch can take into account not only the effects of the leading edge but also the influence of the strong pressure gradients and/or separation. Equation (25) can easily be used to determinate the separation point of a diffuser and to calculate its shape for engineering ends.

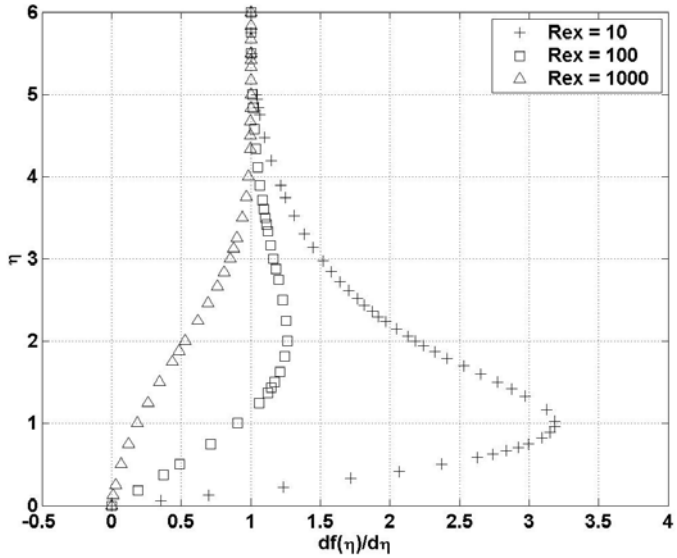

Figure 2 – Nondimensional velocity profiles, result for m = -0.1.

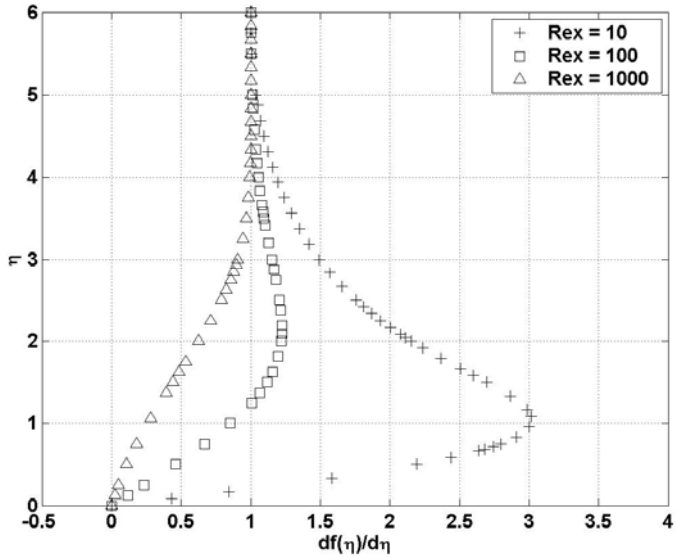

Figure 3 – Nondimensional velocity profiles, Result for m = -0.091.

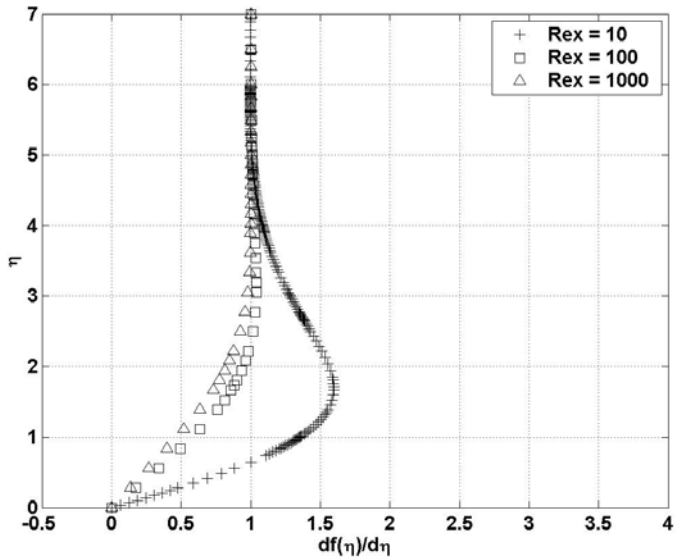

Figure 4 – Nondimensional velocity profiles, Result for m = 0.0.

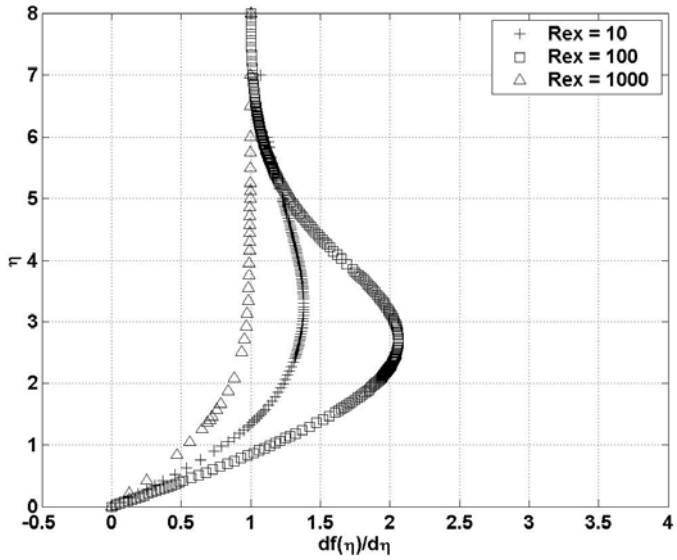

Figure 5 – Nondimensional velocity profiles, Result for m = 0.1.

5. Conclusion

In this work the asymptotic behavior of the Navier-Stokes equation was analyzed using the Kaplun limits-intermediate variable technique. A set of partial differential equations was obtained, which represents a generalization of the classical Boundary Layer Theory. The equations developed here represent a self contained theory, making unnecessary any type of viscid-inviscid interactive process. A quasi-similar equation for the flow over a flat plate was developed witch contains the Falner-Skan formulation as a particular case. A numerical solution of the quasi-similar

equation was presented, showing some characteristics behaviors of the numerical solutions of the Navier-Stokes equation for the flow over a flat plat and other geometries.

The deduction of the equations set (15) to (17) is the central result of the present work. The Kaplun limits approach was used to determine the asymptotic behavior of a set of partial differential equations, resulting in a generalized Boundary Layer formulation.

The main difference between the classical Boundary Layer formulation and the approach used here is that in the later, the central focus of the analysis is to describe the near wall asymptotic behavior of the flow and not exactly, the asymptotic behavior of Navier Stokes equation, at the fluid region as a whole. The use of Kaplun limits permitted to obtain the principal asymptotic equation for each component of the velocity and to compose a "principal set" set of equations witch are in fact, the combination of two well known formulations (the nonlinear inviscid flow and the Boundary Layer) into a single more general theory, witch describes the asymptotic solution of the Navier-Stoke equations for the entire flow region.

6. References

Hartree, D. R., 1949, "A Solution of the Laminar Boundary Layer Equation for Retarded Flow", ARC-RM 2426.

Schlichting, H., 1972, "Teoria de La Capa Limite", Ediciones URMO, BI. 88-1972.

Falkner, V. M., 1939, "A Further Investigation of Solution of Boundary Layer Equations", ARC-RM 1884.

Falkner, V. M., 1941, "A Simplified Calculation of the Laminar Boundary Layer", ARC-RM 1895.

Carrier; G.F. & Lin; C.C. "ON the nature of the leading of the Boundary Layer Nera the Leading edge of a fat Plate" Quart. Appl. Math. 63-68.

Cruz, D. O. A., 2002, "On Kaplun Limits and the Generalized Boundary Layer Theory", Inter. Journal of Eng. Science 40; 1879-1893

Davis, R.T., 1967, "Laminar Incompressible flow Past a Semi-Infinite Flat Plate", J. Fluid Mech. 27 part4; 691-704

Kaplun, S., 1967, "Fluid Mechanics and Singular Perturbation", New York; Academic Press

Goldstein, S., 1956, "Flow of an Incompressible viscous fluid along a semi-infinite flat plate", Inst. Engng. Res. Univ. Calif. Tech. Rep. HE-150-144

Lewis, J. A & Carrier, G.F., 1949, "Some remarks on the flat plate boundary layer", Quart. Appl. Math. 7, 228-234.

Murray; J. D., 1965, "Incompressible viscous Flow past a Semi-Infinite Flat Plate", J. Fluid Mech. 21 part2; 337-344

Silva Freire, A. P., 1999, "On Kaplun Limits and the Multilayered Asymptotic Structure of the Turbulent Boundary Layer", Hybrid Methods in Engineering,Vol.1 pp.185-215.

Van Dyke, M. 1969 Entry Flow in a Channel; J. Fluid Mech. 44; 813-823.

Proceedings of the 11th Brazilian Congress of Thermal Sciences and Engineering – ENCIT 2006
Braz. Soc. of Mechanical Sciences and Engineering – ABCM, Curitiba, Brazil, Dec. 5-8, 2006

Paper CIT06-0262

TRANSIENT SLOT COATING

Oldrich Joel Romero
Department of Mechanical Engineering, Pontifícia Universidade Católica do Rio de Janeiro
Rua Marquês de São Vicente 225, Gávea, CEP 22453-900, Rio de Janeiro, RJ, Brazil
oldrichjoel@yahoo.com.br

Márcio S Carvalho
Department of Mechanical Engineering, Pontifícia Universidade Católica do Rio de Janeiro
Rua Marquês de São Vicente 225, Gávea, CEP 22453-900, Rio de Janeiro, RJ, Brazil
msc@mec.puc-rio.br

Abstract. *In this work, the two-dimensional, transient flow that occurs during the deposition of a Newtonian liquid onto a substrate with a slot die is examined. The effect of an imposed persistent periodic (sinusoidal) perturbation of the liquid flow rate in the coated layer thickness variation is explored at different downstream lip length and coating gap (uniform, overbite and underbite) configurations. Small amplitude disturbances ($\sim 10\%$ and $\sim 1\%$) of the steady-state value are considered. The numerical solutions are obtained solving the governing Navier-Stokes equations, together with elliptic mesh generation technique of (Christodoulou and Scriven, 1992) and (de Santos, 1991) with appropriate boundary and initial conditions, by the Galerkin / finite element method. The temporal discretization is done by a predictor-corrector algorithm. The predictor step consists of a forward Euler method and the corrector step consist of a first-order fully-implicit Euler method. The resulting set of non-linear algebraic equations for the finite element basis functions' coefficients at each time step is solved by Newton's method. The results show how the process configuration may be optimize in order to minimize the effect of flow rate variation in the coated thickness.*

keywords: *slot coating, transient, free surface, galerkin*

1. Introduction

Flows with free surfaces and free boundaries arise in many industrial and biological applications. Examples are coating, polymer processing, ink-jet printing, spraying, deformation of blood cells, blood flow in arteries and capillaries, and flow in the deep pulmonary alveoli.

Many of these flows are time dependent, their dynamics are controlled by the viscosity, elasticity and capillarity of liquid. Modeling such flows requires computational methods which can describe and predict the flow field behaviour, while simultaneously capturing accurately the shape of free surfaces.

An enormous range of manufactured products involves layers deposited as a liquid and then solidified on a solid surface. Frequently, the coating stage of a manufacturing process is significant in cost, time involved and the level of technology required for the production. To be competitive in the marketplace, all aspect of the manufacturing must be efficient and maintain an acceptable level of quality control. Coating a substrate with a liquid is a question of practical interest together with a classical field of interfacial hydrodynamics. Products requiring precise control of coating thickness and avoidance of defects usually are coated with a pre-metering coating technique: the thickness of the coated liquid layer is set by the flow rate fed to the coating die and the speed of the moving substrate, and is independent of other process variables. Slot coating belongs to this class of coating methods. Thus pre-metered methods are ideal for high precision coating. However, the nature of the flow in the coating bead and the uniformity of the liquid layer it delivers can be affected by the substrate speed, liquid properties, configuration of the die lips and cross-web uniformity of the contact lines position.

Slot coating is commonly used in the manufacturing of adhesive and magnetic tapes, specialty papers, imaging films, and many other products. In this process, the coating liquid is pumped to a coating die in which an elongated chamber distributes it across the width of a narrow slot through which the flow rate per unit width at the slot exit is made uniform. Exiting the slot, the liquid fills (wholly or partially) the precise narrow channel (coating gap H_0 in the figure) between the adjacent die lips and the substrate translating rapidly past them. The liquid in the gap, bounded upstream and downstream by gas-liquid interfaces, or menisci, forms the coating bead.

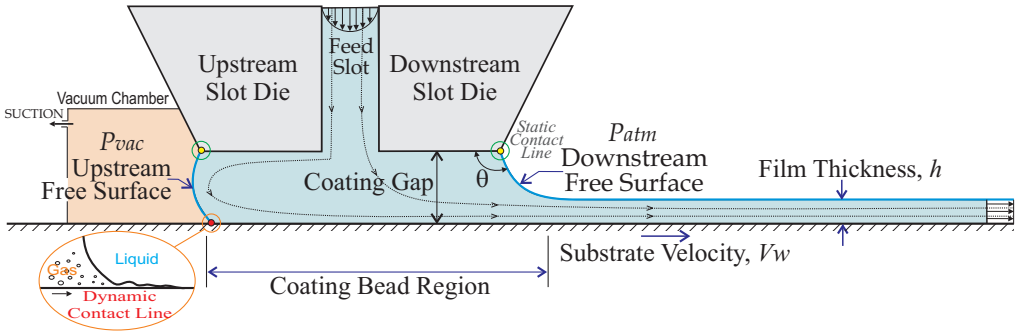

Figure 1: Side profile of the single layer slot coating. It includes many of the features that contribute to the technological complexity of the process.

Figure (1) shows a typical configuration of a die applicator and substrate. (Beguin, 1954) discovered that when layers thinner than about one-half the slot gap are to be coated (or in order to sustain the coating bead at higher substrate speeds), the forces on the coating bead go out of balance and that way to re-balance them is to apply a lower-than-ambient pressure in the upstream meniscus or "vacuum" ($Pvac$ in the figure)), creating a Poiseuille flow that opposes the Couette flow driven by the web. This method has proven ineffective as a means of stabilization when the liquids are very viscous, i.e., thousands of centipoise. If not, instabilities which manifest themselves in a down-web (ribbing) or cross-web (rivulets) variations.

Physical dynamics is required to understand coating flows. The forces important in slot coating are viscous force, capillary force, pressure differences (or pressure gradients) forces, and in some cases inertial and elastic forces. Coating beads themselves are only possible when that forces are balanced.

In a problem with free surface, the physical domain is unknown a priori. Mesh equations must be added to the conservation equations to locate the free boundaries and map the unknown physical domain into a convenient reference one. Elliptic mesh generation method to solve 2-D free surface problem and domain deformation method to solve both 2-D and 3-D free surface problem for both structured and unstructured mesh. By these two methods, the unknown domain is solved simultaneously with the other variables.

In this work, the effect of the flow rate oscillation in the film thickness variation on slot coating process is currently being studied. In early works the effect of gravitational force was found to be usually of secondary importance and therefore not considered here. The mathematical modeling of the transient slot coating flow involves solving a initial boundary value problem in which the location of the free surface is a part of the solution of the problem. The unknown flow domain (physical) is mapped into a fixed domain (computational). The system of equations, with appropriate boundary conditions, for a two-dimensional viscous liquid flow is solved in coupled form by the Galerkin / finite element methods, where the temporal discretization is done by a predictor-corrector algorithm. The set of non-linear algebraic equations for the finite element basis functions is solved by Newton's method.

This paper is organized as follow: First, the physical problem and mathematical formulation is presented. Second, a solution method is described which includes details of the free surface formulation, space and time discretization, and linearization. Finally the results and comments are presented.

2. Mathematical Formulation

The two-dimensional transient free surface flow depicted in Fig. (1) is defined by the governing Navier-Stokes and the continuity equations for a constant-property Newtonian liquid

$$\rho\left(\frac{\partial \mathbf{v}}{\partial t} + \mathbf{v}\cdot\nabla\mathbf{v}\right) - \nabla\cdot\mathbf{T} = 0, \tag{1}$$

$$\nabla\cdot\mathbf{v} = 0, \tag{2}$$

where $\mathbf{v}$ is the liquid velocity, ρ is the liquid density, ∇ is the standard gradient operator, and t is the time. $\mathbf{T} = -p\mathbf{I} + \mu[\nabla\mathbf{v} + (\nabla\mathbf{v})^{\mathrm{T}}]$ is the total stress tensor, the superscript $^{\mathrm{T}}$ denotes transpose, p is the pressure, and μ is the Newtonian liquid viscosity. Body forces (i.e. gravity effects) are neglected.

The geometries where the governing equations are solved is sketched in Fig. (2). Four slot coating configurations with different downstream lip length and upstream coating gap are explored.

Appropriate boundary and initial conditions are necessary to uniquely solve this system of equations.

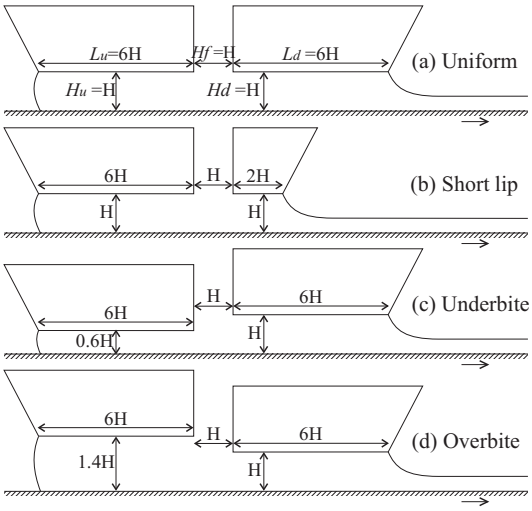

Figure 2: The four geometries used in this work in units of domain dimensions of the fixed downstream slot gap $H_d = 100$ μm. The upstream lip length L_u and feed slot H_f were also kept constant.

2.1. Boundary and initial conditions

The boundaries of the flow domain are labeled in Fig. (3), and the correspondent boundary conditions are:

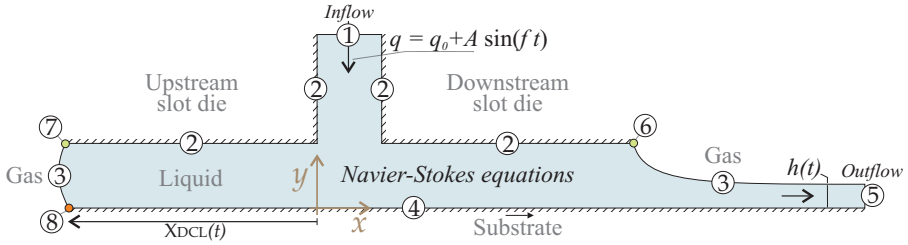

Figure 3: Labels for the boundary conditions in a slot coating process. The location of the two-dimensional cartesian coordinates is also shown.

(1)− At the two inflow planes, that is, at the die feeding slot, fully developed parallel rectilinear flow is assumed, where a Couette-Poiseuille velocity profile is prescribed in function of the base flow rate q_0.

$$u = 0, \quad v = -\frac{6q_0}{H_f}\left[\left(\frac{x}{H_f}\right) - \left(\frac{x}{H_f}\right)^2\right], \tag{3}$$

H_f if the feed slot considerer to be as $H_f = H_d = 100$ μm.

(2)− The no-slip and no-penetration conditions applies at the die walls.

$$u = 0, \quad v = 0. \tag{4}$$

(3)− At the free surfaces, the traction in the liquid balances the capillary pressure and there is no mass flow rate across the gas-liquid interface. The dynamic condition on the free surface are based on the continuity of the tangential stress (no traction) and discontinuity of normal stress caused by the surface tension. Implicitly is assumed that the flow activity outside the free surface is negligible with the atmospheric pressure taken as zero

$$\mathbf{n}_{fs} \cdot \mathbf{T} = \frac{1}{Ca}\frac{d\mathbf{t}_{fs}}{ds} - \mathbf{n}_{fs}\, p_0, \tag{5}$$

$$\mathbf{n}_{fs} \cdot \left(\mathbf{v} - \frac{d\mathbf{x}}{dt}\right) = 0, \tag{6}$$

where $Ca \equiv \mu V_w/\sigma$ is the capillary number, $d\mathbf{t}_{fs}/ds$ represents the curvature of the meniscus, $\mathbf{t}_{fs}$ and $\mathbf{n}_{fs}$ are the local unit tangent and unit normal to the free surface, and p_0 is the pressure on the gas side. At the

downstream free surface, the gas pressure is usually atmospheric, that is $p_0 = P_{atm}$, and at the upstream free surface vacuum is applied in order to stabilize the coating bead, that is $p_0 = P_{vac}$. The evolution of the free surface is dictated by the kinematic condition Eq. (6).

(4)− In the moving substrate, the no-slip and no-penetration conditions are applied

$$u = V_w, \quad v = 0, \tag{7}$$

V_w is the substrate velocity.

(5)− At the outflow plane, fully developed flow is considered

$$\mathbf{n} \cdot \nabla \mathbf{v} = 0, \tag{8}$$

$\mathbf{n} \cdot \nabla$ is here the directional derivative parallel to the substrate.

(6)− The downstream static contact line, $\mathbf{x_d}$, is pinned to the sharp edge of the die

$$\mathbf{x}_d = (x_d, y_d). \tag{9}$$

(7)− The upstream static contact line is free to slide along the upstream die face H_u with a specified upstream static contact angle $\theta_u = 100^0$. The mathematical conditions are

$$y_u = H_u, \qquad \mathbf{n}_w \cdot \mathbf{n}_{fs} = cos(\theta_u), \tag{10}$$

$\mathbf{n}_w$ is the unit vector normal to the wall.

(8)− At the web surface the liquid translates with the web except near the locations where the liquid first appears to contact the web. This sub-microscopic region is called the dynamic contact line, where evidences points a very thin film of air being entrained when the coating speed is high and to that air film breaking down and dissolving within around 100 μm of the dynamic contact line. In this short region the Navier slip condition was used instead of the no-slip condition and a dynamic contact angle $\theta_{dyn} = 110^o$ was specified.

$$\frac{1}{\beta}\mathbf{t}_w \cdot (\mathbf{v} - V_w\mathbf{i}) = \mathbf{t}_w \cdot (\mathbf{n}_w \cdot \mathbf{T}_1), \qquad \mathbf{n}_w \cdot \mathbf{n}_{fs} = cos(\theta_{dyn}), \tag{11}$$

where β is the slip coefficient, $\mathbf{t}_w$ is the unit vector tangent to the wall. Without the slip condition there is a non-integrable singularity in shear stress. For a better description of the flow in this region, a contact angle as a function of a capillary number would be more appropriate or, as is mentioned in the work of (Weinstein and Ruschak, 2004), a new model could be used where the interfaces are considered to be thin fluid phases with equations of state relating in the simplest case, surface pressure to surface mass density.

Finally, an initial condition is needed. In this work, the fluid is assumed to be at rest initially, so the following condition holds

$$\mathbf{v}(x, y, t = 0) = 0. \tag{12}$$

The imposed perturbation liquid flow rate q is a linear combination of the base liquid flow rate q_0 and the disturbance sinusoidal in time mode $\Delta q = A\, sin(f\, t)$

$$q = q_0 + A\, sin(f\, t), \tag{13}$$

where A is the amplitude and f is the frequency of the imposed disturbance, and t is the time respectively. The ongoing disturbance in the liquid flow rate leads to an transient response.

2.2. Dimensionless parameters

The dimensionless parameters that governs the problem are: *(i)* Capillary number $Ca \equiv \mu V_w/\sigma$, which measures the ratio of viscous stress to pressure generated by surface tension in curved meniscus. Increasing the capillary number (which correspond to increase the production speed or the coating viscosity) usually shrinks the ranges of speed — that yield acceptably smooths films, μ is the viscosity of the liquid, V_w is the velocity of the flat wall or substrate, and σ the liquid surface tension. *(ii)* Reynolds number $Re \equiv \rho V_w/\mu$, ρ is the density of the liquid. *(iii)* Dimensionless vacuum pressure $Vac \equiv P_{vac}H_u/\sigma$. *(iv)* Gap-to-thickness ratio $g \equiv H_d/h_0$, h_0 is the base wet coating thickness deposited onto the substrate.

3. Solution method

3.1. Elliptic mesh generation

Because of the free surfaces, the flow domain is unknown *a priori*. The set of differential equations and boundary conditions posed in the unknown physical domain (x, y) has to be transformed to an equivalent set defined in a known reference domain fixed in time (ξ, η) (varying in the range $-1 \leq \xi \leq 1$ and $-1 \leq \eta \leq 1$), wherein a simple mesh tessellation is effected. This can be done with a mapping $\mathbf{x} = \mathbf{x}(\boldsymbol{\xi})$ that connects the two domains, as is shown in (Romero *et al.*, 1994 and Romero *et al.*,).

The mesh generation scheme must efficiently track the interface, maintain accuracy, smoothness, less danger of singularity and automatic local control of mesh properties throughout the entire domain. This is achieved using a elliptic mesh generation technique, described in detail (de Santos, 1991 and Benjamin, 1991). The inverse of the mapping is governed by a pair of elliptic differential equations

$$\nabla \cdot (\mathbf{D} \cdot \nabla \boldsymbol{\xi}) = 0, \tag{14}$$

where $\nabla \equiv \partial/\partial \mathbf{x}$ denotes differentiation in physical space, and $\mathbf{D}$ is the diffusivity-like adjustable tensor that allow for local grid refinement on the interior of the physical domain.

The governing and mesh generation equations written in the physical domain has to be rewritten in the reference domain. This procedure adds complexity.

Boundary conditions are needed before the second-order partial differential equation, Eq. (14), can be solved. The solid walls and synthetic inlet and outlet boundary planes were specified as functions of the coordinates and along them stretching functions were used to distribute the terminii of the coordinate curves selected to serve as element sides. The free boundary − the gas-liquid interface or meniscus − is implicitly located by imposing the kinematic condition, Eq. (6).

In transient problems the frame of reference lies across the space-time domain for which the physical grid points are constantly updated in time, we must transform the time derivative at fixed Eulerian locations in space to time derivatives of any time-dependent quantity $\partial\Phi/\partial t$ at fixed iso-parametric coordinates, denoted by $\overset{\circ}{\Phi}$. The following transformation is employed

$$\frac{\partial \Phi}{\partial t} = \overset{\circ}{\Phi} - \overset{\circ}{\mathbf{x}} \cdot \nabla \Phi, \tag{15}$$

where, $\overset{\circ}{\mathbf{x}}$ is the mesh velocity (Christodoulou and Scriven, 1992). The time t is independent of either the original or he mapped coordinate system.

With relation from Eq. (15), the momentum equation becomes

$$\rho \left(\overset{\circ}{\mathbf{v}} + (\mathbf{v} - \overset{\circ}{\mathbf{x}}) \cdot \nabla \mathbf{v} \right) - \nabla \cdot \mathbf{T} = 0, \tag{16}$$

3.2. Reduction to ordinary algebraic equations by Galerkin finite element method with basis functions

The two-dimensional transient simulation were carried out using our in-house finite element analysis code, with the primitive variable (velocity-pressure) formulation and fully coupled solution methods -the position of the interface and the flow solution are computed simultaneously-.

In the Galerkin's method, the governing partial differential equations, Eqs. (1), (2) and (14), are transformed into a discretized system of time-dependent ordinary differential equations multiplying by appropriate basis functions, integrating over the entire computational domain, and applying the divergence theorem to yield the weighted residual form.

$$R_i^{\mathbf{m}} \equiv \int_{\bar{\Omega}} \left\{ \rho [\overset{\circ}{\mathbf{v}} + (\mathbf{v} - \overset{\circ}{\mathbf{x}}) \cdot \nabla \mathbf{v}] \psi_i^{\mathbf{m}} + \nabla \psi_i^{\mathbf{m}} \cdot \mathbf{T} \right\} \, J \, d\bar{\Omega} - \int_{\bar{\Gamma}} \psi_i^{\mathbf{m}} (\mathbf{n} \cdot \mathbf{T}) \, \frac{d\Gamma}{d\bar{\Gamma}} \, d\bar{\Gamma} = \mathbf{0}; \tag{17}$$

$$R_i^c \equiv \int_{\bar{\Omega}} (\nabla \cdot \mathbf{v}) \, \psi_i^c \, J d\bar{\Omega} = 0; \tag{18}$$

$$R_i^{\mathbf{x}} \equiv - \int_{\bar{\Omega}} \nabla \psi_i^{\mathbf{x}} \cdot \mathbf{D} \cdot \nabla \boldsymbol{\xi} \, J \, d\bar{\Omega} + \int_{\bar{\Gamma}} \psi_i^{\mathbf{x}} (\mathbf{n} \cdot \mathbf{D} \cdot \nabla \boldsymbol{\xi}) \, \frac{d\Gamma}{d\bar{\Gamma}} \, d\bar{\Gamma} = \mathbf{0}; \tag{19}$$

$$R_i^k \equiv \int_{\bar{\Gamma}} \mathbf{n} \cdot (\mathbf{v} - \overset{\circ}{\mathbf{x}}) \, \psi_i^k \, \frac{d\Gamma}{d\bar{\Gamma}} \, d\bar{\Gamma} = 0; \tag{20}$$

Superscripts $\mathbf{m}$, c, $\mathbf{x}$, and k denotes momentum, continuity, mesh, and kinematic residuals; $\mathbf{n}$ is the outward unit normal vector of the boundary Γ; and $J = d\Omega/d\bar{\Omega}$ is the determinant of the mapping deformation gradient. This system is solved simultaneously to calculate the velocities, pressure and grid location of each node. The Galerkin weighted residuals are evaluated by nine-point Gaussian quadrature with three points in each computational direction.

Each independent variable is approximated with a linear combination of a finite number of knows basis functions

$$\mathbf{v} = \sum_{j}^{M} \widetilde{\mathbf{v}}_j(t)\, \varphi_j^{\mathbf{v}}(\xi,\eta), \quad p = \sum_{j}^{N} \widetilde{p}_j(t)\, \varphi_j^{p}(\xi,\eta), \quad \mathbf{x} = \sum_{j}^{M} \widetilde{\mathbf{x}}_j(t)\, \varphi_j^{\mathbf{x}}(\xi,\eta). \tag{21}$$

Here, $\widetilde{\mathbf{v}}_j(t)$, $\widetilde{p}_j(t)$, $\widetilde{\mathbf{x}}_j(t)$, are the basis functions coefficients, and represents the unknowns of the discretized problem. The matrix vector of basis functions of the dependent variables is

$$\mathbf{u} \equiv [\widetilde{\mathbf{v}}_j(t), \widetilde{p}_j(t), \widetilde{\mathbf{x}}_j(t)]^{\mathrm{T}}. \tag{22}$$

An efficient mixed formulation of continuous basis functions are used to expand the independent variables. Lagrangian biquadratic polynomials for velocity $\varphi^{\mathbf{v}}(\xi,\eta)$ and position $\varphi^{\mathbf{x}}(\xi,\eta)$, and linear discontinuous for pressure $\varphi^{p}(\xi,\eta)$ were used. The polynomial basis functions constructed on a standard square domain (ξ,η) (where $-1 \leq \xi \leq 1$ and $-1 \leq \eta \leq 1$) was mapped into each of the deformed quadrilateral elements in the flow domain by the time-dependent isoparametric mapping.

In the weak (Galerkin) form equations, the weighting or test functions are the same of the basis functions, i.e. $\psi^{\mathbf{m}} = \varphi^{\mathbf{v}}$, $\psi^{c} = \varphi^{p}$ and $\psi^{\mathbf{x}} = \varphi^{\mathbf{x}}$.

By means of the Galerkin/FEM combined with the elliptic mesh generation system, equations are reduced into a set of ordinary differential and algebraic equations for the coefficient of the basis functions of the form

$$\mathbf{R}(\mathbf{u}, \dot{\mathbf{u}}, \mathbf{q}) = 0, \tag{23}$$

where $\mathbf{R}$ is the set of weighted residual equations, $\mathbf{u}$ is a matrix vector of basis functions (unknowns) of the dependent variables given by Eq. (22), $\dot{\mathbf{u}}$ is their time derivatives, and $\mathbf{q}$ the vector of input (physical and discretization) parameters. The governing equations are solved in a couple manner, simultaneously everywhere.

3.3. Time integration

The aforementioned Galerkin weighted residuals form a set of nonlinear ordinary differential equations and algebraic equations in time. The temporal discretization of this set of equations is done by a predictor corrector algorithm. The predictor step consists of a forward Euler method and the corrector step consists of a first-order fully implicit Euler method, which is unconditionally stable in the sense that the time step is not restricted by any CFL-condition. The approximate form of the velocity time-derivatives in the momentum conservation equation, Eq. (16), using backward finite difference is

$$\overset{\circ}{\mathbf{v}} \equiv \frac{\mathbf{v}_{n+1} - \mathbf{v}_n}{t_{n+1} - t_n} = f(\mathbf{v}_{n+1}, t_{n+1}), \tag{24}$$

where the index $n+1$ and n indicates current and previous time instant respectively. The difference $t_{n+1} - t_n$ defines the current time step Δt_{n+1}. A similar expression is used for the mesh velocity $\overset{\circ}{\mathbf{x}}$.

3.4. Evaluation of the basis functions coefficients

The resulting set of nonlinear algebraic equations (in $n+1$) is solved simultaneously by the Newton's method with an initial estimate resulting from an explicit Euler step from the solution at the previous time. At each time step solve

$$\left(\frac{1}{\Delta t}\mathbf{M} + \mathbf{J}\right) \delta\mathbf{u}^{(k+1)} = -\mathbf{R}(\mathbf{u}^{(k+1)}, \mathbf{u}^{k}), \tag{25}$$

$$\mathbf{u}^{(k+1)} = \mathbf{u}^{k} + \delta\mathbf{u}^{(k+1)}, \tag{26}$$

Newton's method linearize the equation set and adds the solution of the resulting linear system to the current estimate in order to provide an updated estimate of the flow field. The iteration is repeated until convergence. Here $\mathbf{J} \equiv \partial\mathbf{R}/\partial\mathbf{u}$ is the Jacobian matrix which measure the sensitivity of the residuals to changes in the nodal unknowns and $\mathbf{M} \equiv \partial\mathbf{R}/\partial\dot{\mathbf{u}}$ is the mass matrix and measure the sensitivity of the residuals to changes in the time derivatives of the nodal unknowns (liquid accelerations, velocities and nodal points). The integrals arising

in the residuals and the Jacobian matrices used in Newton's method are evaluated numerically using Gaussian quadrature (Strang and Fix, 1973).

Because the finite element basis functions used are different from zero only over a very small portion of the domain, the Jacobian matrix is sparse and was stored in compressed sparse formats. In each Newton iteration, the linearized equation system was factorized into unit lower L and unit upper U triangular matrix by a Gauss-elimination direct frontal solver (Hood, 1976 and Hood, 1977), as described by (Almeida, 1996).

In order that the Newton process converged within 6 to 8 iterations at each successive new set of operating conditions, the initial estimates were generated by a pseudo-arc-length continuation method as described by (Keller, 1977 and Bolstad and Keller, 1985). The tolerance on the L_2-norm of the residual vector and on the last Newton update of each declared solution was set to 10^{-6}. However, close to turning points where the Jacobian matrix becomes singular, convergence becomes difficult or impossible. Turning points are where a solution branch turns back on itself. Other singular points are the bifurcation points and Hopf points.

3.5. Mesh selection and computer implementation

A mesh convergence analysis was done by comparing the downstream free surface configuration at capillary number $Ca = 0.2$, Reynolds number $Re = 1.33$, dimensionless vacuum pressure $Vac = 12$, and gap-to-thickness ratio $H_d/t = 5$.

The insensitivity of computed solutions to further mesh refinement has been demonstrated by systematically increasing the level of refinement near the interface in the coating bead region for the uniform coating configuration, Fig. 2-a. Three different meshes was tested refined until the results changed by less than 1 %. In this work the mesh selected contains 328 elements with 1,421 nodes.

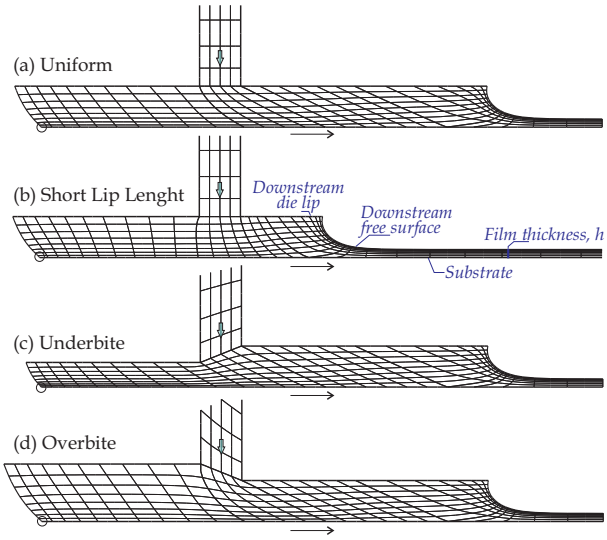

Figure 4: Close-up view of the tessellated domain for each slot coater configuration.

For each geometry explored (uniform, short lip length, underbite and overbite) the typical meshes used are showed in Fig. 4. The total number of basis functions coefficients is 6,668. The resulting algorithm have been programmed in FORTRAN and run on a single 2.4 GHz Intel(R) Pentium(R) IV processor. A typical transient simulation of the slot coater requires roughly 50 minutes for 100 time steps, each Newton's iteration takes around 30 seconds.

4. Results and discussion

Limitations of this computational experiments include the inability to scan the enormous range parameter space encompassed by the single slot coater process. The parameter space is a function of several variables including Reynolds number, Stokes number, capillary number, gap-to-thickness ratio, vacuum level, die shape, and more. Hopefully, the representative studies presented here will raise awareness for the need of more research in the field of one coating analysis.

Solutions were computed at different capillary and Reynolds numbers, and several liquid flow rate, constant gap-to-thickness ratio H_0/t and vacuum level Vac.

Figure (5) displays contours of the transient streamfunction at three time instant $t_1 = 22\Delta t$, $t_2 = 38\Delta t$ and

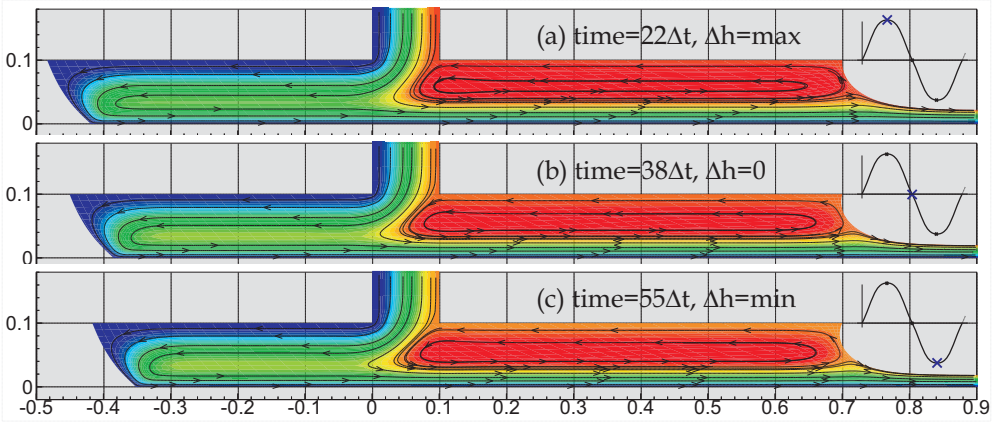

Figure 5: Three time instant showing the flow field variation with time in a parallel coating gap corresponding to the red curve of Fig. (9). The flow rate oscillates with amplitude $A = 10$ % and frequency $f = 500$ Hz.

$t_3 = 55\Delta t$ which correspond to a maximum ($h_1 = h_0 + \Delta h_0$), middle ($h_2 = h_0$) and minimum ($h_3 = h_0 - \Delta h_0$) film thickness respectively. Some fraction of the liquid moves into the upstream bead, whereas a remainder flows into the downstream bead. The net flow into the upstream portion of the bead equals zero, the upstream meniscus bounds the liquid and the flow turns 180^o. The upstream meniscus meets the web at the dynamic contact angle $\theta_{dyn} = 120^o$ and intersects the upstream slot lip at the static contact angle $\theta_{sca} = 70^o$. Under the downstream lip, where viscous and pressure forces balance each other, the flow is largely rectilinear until the liquid squeezes under the downstream meniscus and the streamlines become curved and inertia plays a greater role. The liquid accelerates until it reaches the web speed. Over roughly three gaps downweb from the downstream lip edge, the liquid relaxes to a thin film that is essentially plug flow, viscous and inertial forces diminish. The free surface curvature is highest close to the downstream lip edge, where the contact line is pinned, and drops rapidly away and the free surface levels out. The concavity of the meniscus (from the gas side) requires that the pressure be sub-ambient.

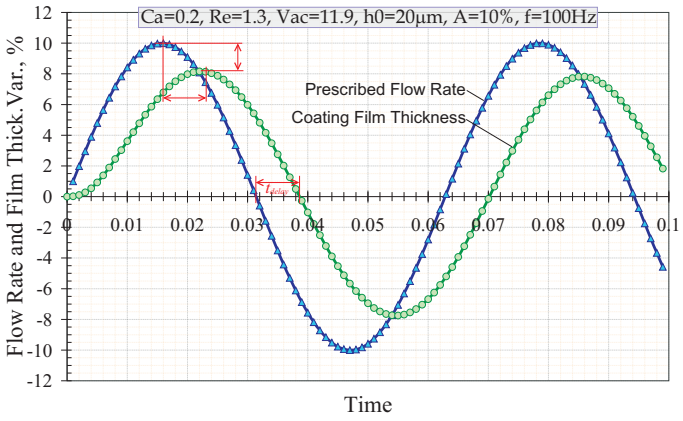

Figure 6: Transient film thickness variation with amplitude A of the sinusoidal perturbation of the input flow rate ($q = q_0 + A\,sin(f\,t)$) in an uniform slot configuration.

The curvature of the downstream meniscus increase and the dynamic contact line moves towards the feed slot diminishing the coating bead length and because the disturbance introduced into the prescribed flow rate is a sinusoidal function, the coating film thickness and the dynamic contact line respond in a similar form. Fig. (6) presents the transient flow rate prescribed at the inflow plane with amplitude $A = 10\%$ and frequency $f = 100$ Hz, and the transient coating film thickness measured at the outflow plane (see Fig. (3)). As observed, the perturbation takes a time until produce a response in the output film thickness, this is the delay time (t_{delay} in the figure) which is function of the operating parameters, liquid properties and perturbation.

The influence of the amplitude of the perturbation in the film thickness is explored in Figs. (7) and (8), shows that the higher the liquid flow rate, the higher the response to ongoing disturbances of the flow rate, and

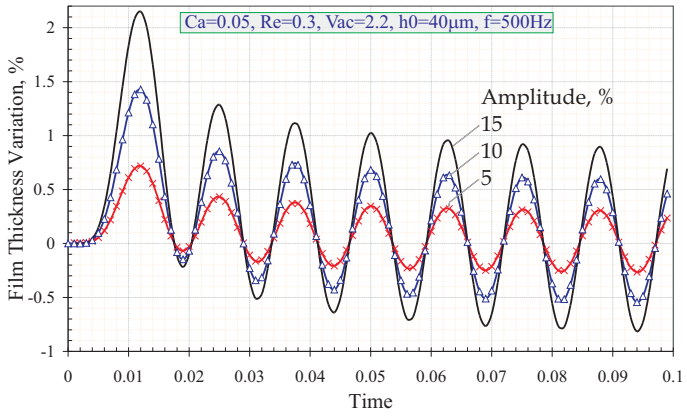

Figure 7: Transient film thickness variation with amplitude A of the sinusoidal perturbation of the input flow rate ($q = q_0 + A\,sin(f\,t)$) in an uniform slot configuration.

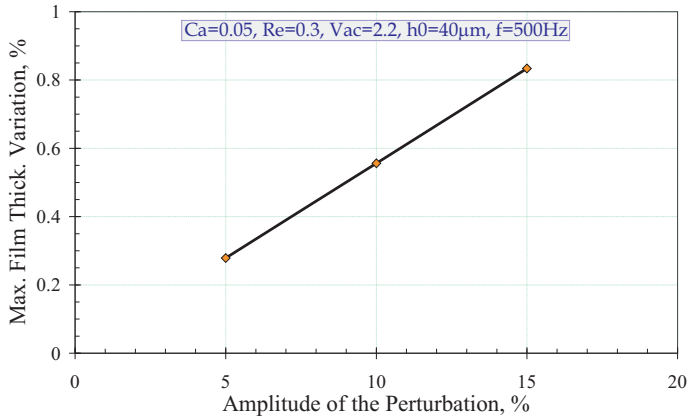

Figure 8: Variation of the final liquid layer thickness with the amplitude of the perturbation of the liquid flow rate in the uniform slot coating.

as is displayed in Fig. (8) this growth is linear. This result agrees very well with the obtained by (Gates, 1999) in his frequency response analysis of slot coating. The perturbations imposed by (Gates, 1999) had amplitude of 1% and frequencies ranging from 1 to 2000 Hz.

Figures (9) and (10) plots the transient coating film thickness variation at frequencies ranging from 100 Hz to 1000 Hz. The results shows that the higher the frequencies of the ongoing disturbances of the flow rate, the lower the film thickness variation. This results are in accordance with the results obtained by (Gates, 1999). Fig. (10) also shows higher the amplitude of the perturbation, the higher the variation of the film thickness.

The influence of the capillary number is plotted in Fig. (11), the coating film thickness varies in inverse proportion to the capillary number. Figure (12) shows how the film thickness change as the coating gap passes from the underbite to overbite configuration at constant capillary and Reynolds number. The underbite configuration is when the upstream gap is narrower than the downstream gap. The overbite is when the upstream gap is wider than the downstream gap.

5. References

Almeida, V. F., 1996, "Gas-Liquid counterflow through constricted passages", PhD thesis, University of Minnesota, USA.

Beguin, 1954, US Patent 2681294.

Benjamin, D. F., 1991, "Roll Coating Flows and Multiple Rolls Systems", PhD thesis, University of Minnesota, USA.

Bolstad, J. H. and Keller, H. B., 1985, A multigrid continuation method for elliptic problems whit folds, "SIAM

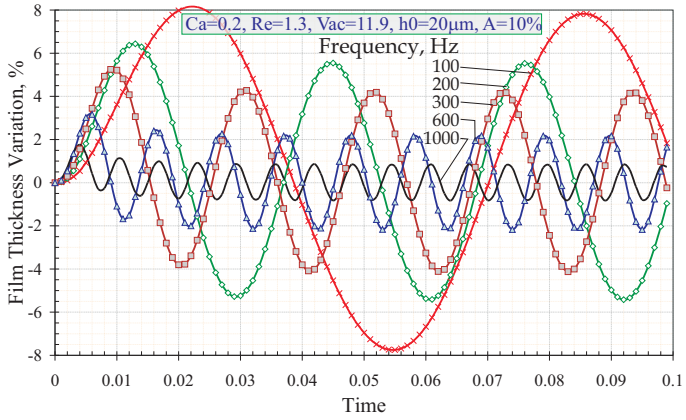

Figure 9: Transient film thickness variation with frequency f of the sinusoidal perturbation of the input flow rate ($q = q_0 + A\,sin(f\,t)$) in an uniform slot configuration.

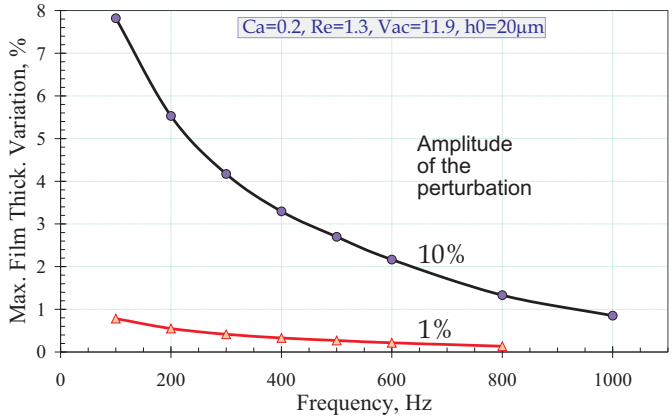

Figure 10: Variation of the final liquid layer thickness caused by 1% and 10% perturbation of the liquid flow rate in the uniform slot coating.

Journal of Science Stat. Comput.", Vol. 7, pp. 1081–1104.

Christodoulou, K. N. and Scriven, L. E., 1992, Discretization of free surface flows and other moving boundary problems, "J. Comput. Phys.", Vol. 99, pp. 39–55.

de Santos, J. M., 1991, "Two-phase Cocurrent Downflow Through Constricted Passages", PhD thesis, University of Minnesota, USA.

Gates, I. D., 1999, "Slot Coating Flows: Feasibility, Quality", PhD thesis, University of Minnesota, USA.

Hood, P., 1976, Frontal Solution Program for Unsymetric Matrices, "Int. J. Numer. Meth. Eng.", Vol. 10, pp. 379–399.

Hood, P., 1977, Correction, "Int. J. Numer. Meth. Eng.", Vol. 11, pp. 1055.

Keller, H. B., 1977, "Numerical solution of bifurcations and nonlinear eigenvalue problems in Applications of Bifurcation Theory", Academic Press, New York, USA.

Romero, O. J., Scriven, L. E., and Carvalho, M. S., Slot coating of mildly viscoelastic liquids, "Journal of Non-Newtonian Fluid Mechanics", , No. doi 10.1016/j.jnnfm.2005.11.010.

Romero, O. J., Suszynsky, W. J., Scriven, L. E., and Carvalho, M. S., 1994, Low-flow Limit in Slot Coating of Dilute Solutions of High Molecular Weight Polymer, "Journal of Non-Newtonian Fluid Mechanics", Vol. 118, pp. 137–156.

Strang, G. and Fix, G. J., 1973, "An Analysis of Finite Element Method", Printice-Hall, USA.

Weinstein, S. J. and Ruschak, K. J., 2004, Coating Flows, "Annu. Rev. Fluid Mech.", Vol. 36, pp. 29–53.

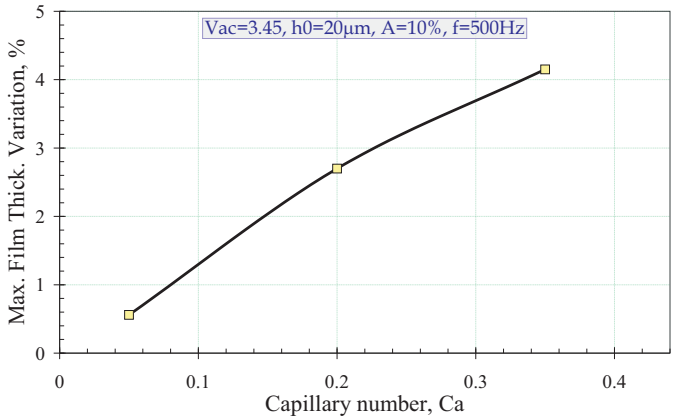

Figure 11: Influence of the capillary number (Ca) in the film thickness.

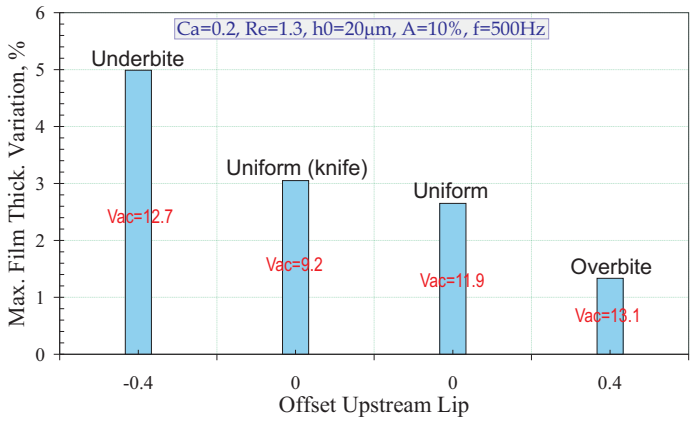

Figure 12: Maximal film thickness variation at different coating gap and lip length configurations.

6. Author rights

The authors are the only responsible for the printed material included in his papers.

Proceedings of the 11th Brazilian Congress of Thermal Sciences and Engineering -- ENCIT 2006
Braz. Soc. of Mechanical Sciences and Engineering -- ABCM, Curitiba, Brazil, Dec. 5-8, 2006

Paper CIT06-0272

ESTUDO EXPERIMENTAL DE ESCOAMENTOS BIFÁSICOS E MEDIÇÃO DE VAZÃO COM PLACA DE ORIFÍCIO

Sonia Magalhães dos Santos
Departamento de Física – Fundação Universidade Federal do Rio Grande (FURG)
Av. Itália, km 8 - Campus Carreiros - Rio Grande/RS – Brasil – CEP: 96201-900
vnsantos@mikrus.com.br

Luiz Alberto Oliveira Rocha
Departamento de Física – Fundação Universidade Federal do Rio Grande (FURG)
Av. Itália, km 8 - Campus Carreiros - Rio Grande/RS – Brasil – CEP: 96201-900
dfsrocha@furg.br

Resumo. *Este trabalho tem por objetivo o estudo experimental do escoamento bifásico água-ar em regime de bolhas dispersas, além da determinação do fluxo mássico deste escoamento. Em um tubo cilíndrico de acrílico transparente, são instalados quatro sensores resistivos e uma placa de orifício. O princípio de medida dos sensores é baseado nas diferentes resistividades do ar e da água. São realizadas aquisições de sinais com os sensores resistivos para diferentes fluxos mássicos, tanto de água como de ar, obtendo-se a fração de vazio local, o diâmetro das bolhas baseado no tempo de contato entre a bolha e o sensor, suas velocidades, flutuações de pressão e a freqüência de passagem das bolhas durante o período de medida. Calcula-se o coeficiente de arraste e os números adimensionais característicos do estudo de bolhas, Morton, Archimedes e Eotvos, que independem da velocidade da bolha e Reynolds, Weber e Froude, que são dependentes da velocidade relativa da bolha, mostrando que a forma da bolha é resultado dos efeitos combinados de forças inerciais, gravitacionais, viscosas e tensão superficial. O fluxo mássico é calculado pela equação de Murdock, conhecendo-se as propriedades termodinâmicas dos fluidos, a fração de vazio e a perda de pressão medida pela placa de orifício, ligada a um sensor diferencial de pressão do tipo capacitivo.*

Palavras-chave: *escoamento bifásico, bolhas dispersas, aquisição de sinais, medição de fluxo, placa de orifício.*

1. Introdução

O estudo experimental do escoamento bifásico realizado neste trabalho é caracterizado pelo escoamento em regime de bolhas dispersas para o caso específico Água – Ar, procurando assim descrever o comportamento de pequenas bolhas de ar ao longo de um escoamento de água, e através de aquisição de sinais determinar sua geometria, velocidade, fração de vazio para uma dada secção de tubo, além da determinação do fluxo mássico do escoamento bifásico através de placa de orifício por equação proposta por Murdock, 1962.

Segundo Lahey, 1974, um escoamento bifásico caracteriza-se por um elevado grau de irregularidade devido as variações aleatórias locais da fração de vazio , as quais podem ser definidas como a probabilidade de que um ponto no espaço seja circundado pela fase gasosa em algum tempo.

Winjgaardem, em 1968, descreveu o escoamento transiente, unidimensional de misturas bifásicas líquido-bolhas e investigou a dispersão linear e não linear de pulsos de pressão em mistura bifásica e concluiu que, embora as aproximações na sua análise não permitissem um resultado quantitativo exato, a teoria desenvolvida tornou claro que as misturas bifásicas água-ar são fortemente dispersivas e que pressões médias elevadas na mistura podem ocorrer durante o colapso não linear de bolhas individuais.

Kuznetsov et al, em 1985, investigaram uma grande faixa de parâmetros adimensionais caracterizando o processo de propagação de perturbações da pressão numa mistura líquido-gás como o número de Reynolds e a relação entre os valores de dispersão.

Theofanous e Sullivan, em 1982, mediram a turbulência em escoamentos bifásicos em tubulações num regime de bolhas dispersas, usando técnicas de velocimetria Laser Doppler e mostraram que as medidas da intensidade de turbulência possuem uma forte dependência com o título do escoamento.

Sheikholeslami e Patel, em 1988, propuseram uma modelagem numérica para calcular o campo de escoamento numa gama de configurações de placas de orifício e parâmetros do escoamento.

Fokin, em 1995, propôs uma descrição matemática aproximada para investigar o escoamento bifásico unidimensional, transiente e estabilizado adiabaticamente. Observou que a ausência de instabilidade das fases podia resultar num decréscimo de perda de energia de atrito quando comparado com o escoamento permanente sem

flutuações. Constatou que as flutuações dos parâmetros do escoamento bifásico real representam a superposição de um processo harmônico com um ruído.

Ponoth(2000a) e Ponoth(2000b) apresenta uma revisão dos diversos experimentos, realizados de 1953 a 1995 e de 1963 a 1996, respectivamente, sobre o movimento de bolhas em água e em outros líquidos.

Moreau(2000b) apresenta um estudo sobre a forma das bolhas e sua dinâmica, mostrando as grandezas físicas envolvidas, como coeficiente de arraste e, também, os números adimensionais característicos no estudo de bolhas, Morton, Archimedes e Eotvos, que independem da velocidade da bolha, e Reynolds, Weber e Froude, que são dependentes da velocidade relativa da bolha, mostrando que a forma da bolha é o resultado dos efeitos combinados de forças inerciais, gravidade, tensão superficial e viscosidade.

Existe uma grande quantidade de problemas em processos industriais que envolvem a medição de fluxo que, intencionalmente ou não apresentam mais de uma fase e que normalmente envolvem altos custos. O estudo do movimento de bolhas de gás em um líquido pode fornecer informações valiosas sobre as propriedades da interface líquido-gás, sendo um problema de engenharia de considerável importância nas indústrias químicas, petroquímicas, nucleares, de alimentação, aeroespaciais, estando presente nos setores de transporte pneumático, transporte hidráulico, bombeamento, pulverização, combustão gás-líquido, combustão com spray de gás, combustão em leito fluidizado, tratamento de água, agitadores, escoamento em reatores, desidratação e processos de granulação para produção de alimentos, tecnologia ambiental além de outros.

2. Bancada de Ensaios

A bancada para o estudo do escoamento bifásico água-ar, é constituída dos elementos apresentados na "Fig. 1":

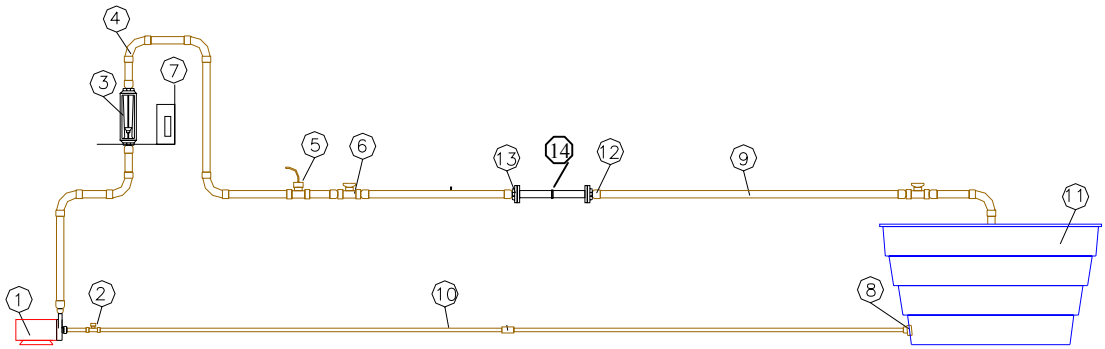

Figura 1. Bancada de Ensaios

Onde: 1) Bomba centrifuga ¾ cv; 2) Válvula de esfera PVC de 1”; 3) Rotâmetro para água; 4) Joelho PVC de 50mm; 5) “T” PVC de 50 mm ; 6) Válvula de esfera PVC de 2 “; 7) Rotâmetro para ar; 8) Flange para caixa d’água PVC de 1’’; 9) Tubulação PVC de 50 mm; 10) Tubulação PVC de 1’’; 11) Reservatório de água de 1000 litros; 12) Adaptador de 2 “ para 50mm; 13) Flange de ferro fundido de 2 “; 14) Placa de orifício em tubo de acrílico de 2".

Um sensor de membrana (Smar, 1996) é usado para transformar uma diferença de pressão, entre as secções a montante e a jusante da placa de orifício, em voltagem, de modo que este sinal possa ser lido por um programa apropriado (Advantech, 2001). Sua incerteza é de 0,2% da leitura do visor do sensor e para a ddp, em volts, é de ± 0,005%. Seu princípio de funcionamento é do tipo capacitivo.

Os sensores resistivos localizam-se no tubo acrílico transparente e consistem em dois fios de níquel-cromo, sendo um deles curvado, ficando alinhado com o outro e tendo entre eles uma distância de 0,5mm, e uma resistência R de 1,5 kΩ ligada a um dos fios, conforme “Fig. 2”. Os sensores são alimentados com uma tensão de 15 volts. No espaço entre os fios estará passando água ou ar, que possuem diferentes resistividades, funcionando como uma resistência em série com a resistência R. É medida a diferença de potencial, ddp, nos terminais do sensor. Como a resistividade do ar é muito maior que a da água, o circuito ficará aberto medindo-se uma ddp alta, equivalente à da fonte de tensão, quando a bolha passa. No caso do escoamento de água, será menor o valor da ddp adquirida pela placa de aquisição de dados numa freqüência estipulada, diferenciando naquele momento se está passando água ou ar no sensor. O esquema de ligação dos quatro sensores resistivos ao computador, é mostrado na “Fig. 3”. Na "Fig. 4" é mostrado o comportamento da ddp medida, durante a passagem de água e de ar.

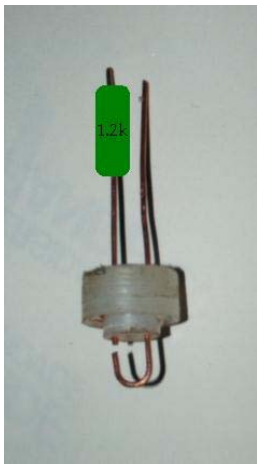

Figura 2. Sensor resistivo.

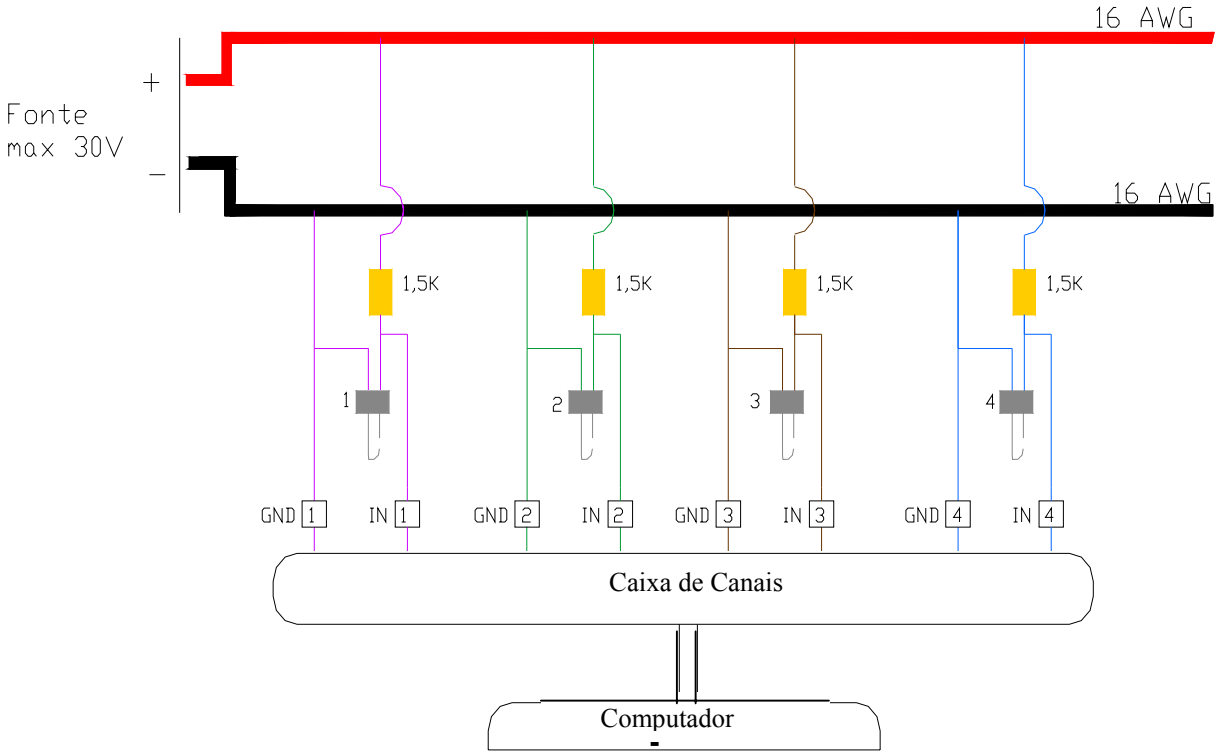

Figura 3. Esquema de ligação dos quatro sensores resistivos ao computador.

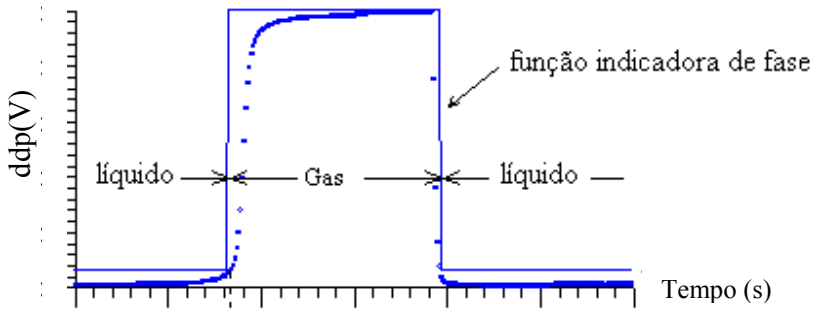

Figura 4. Comportamento da ddp medida, durante a passagem de água e de ar.

Utilizou--se a placa de aquisição de dados PL711B (Advantech, 2001) . Possui 8 canais, resolução de 12 bits, voltagem máxima de entrada de 35 Volts. Tem impedância de entrada de 10MΩ, incerteza de ± 0,01% ± 1 LSB da leitura, faixa de trabalho de ± 10 Volts, freqüência de aquisição de 20 KHz dependente do computador e taxa de conversão de analógico para digital de 40 µs. Os sinais de saída são armazenados em arquivos digitais através do programa de aquisição de dados (Advantech Genie, 2001).

3. Estudo da geometria da bolha por aquisição de sinais

Os sinais captados pelos sensores resistivos possibilitam o cálculo do comprimento de uma das cordas (a) do eixo maior da bolha e a velocidade por esta atingida. A pequena dimensão do sensor garante o mínimo de perturbação ao escoamento. A "Fig. 4, a,b,c" ilustra a passagem da bolha através dos sensores.

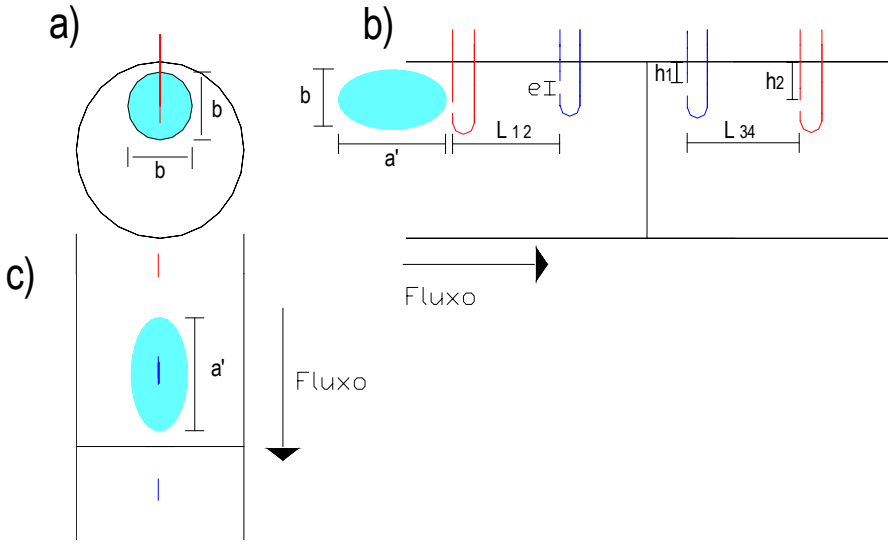

Figura 5. Passagem da bolha através dos sensores.

Sendo:

L_{12} = 58,5mm; L_{34} = 60,7mm; h_1 = 2mm; h_2 = 3mm; e = 1,5mm;

As "Equações 1 a 4" foram utilizadas para cálculo das velocidades *v* e geometria das bolhas através dos sinais adquiridos pelos sensores resistivos, de acordo com a "Fig. 5, a, b, c".

$$v = \frac{L_{12}}{t_{12} - t_{11}} \tag{1}$$

$$v = \frac{a}{t_{21} - t_{11}} \tag{2}$$

$$v = \frac{L_{34}}{t_{14} - t_{13}} \tag{3}$$

$$v = \frac{a}{t_{23} - t_{13}} \tag{4}$$

onde:

t_{11} = tempo inicial da bolha no sensor 1;
t_{12} = tempo inicial da bolha no sensor 2;
t_{21} = tempo final da bolha no sensor 1;
a = corda do eixo maior da bolha;
L_{12} = distância do início do primeiro sensor ao início do segundo sensor.
t_{13} = tempo inicial da bolha no sensor 3;
t_{14} = tempo inicial da bolha no sensor 4;
t_{23} = tempo final da bolha no sensor 3;
L_{34} = distância do início do terceiro sensor ao início do quarto sensor.

4. Classificação das bolhas

Segundo Clift, 1978, as bolhas em movimento sob a influência da gravidade podem ser agrupadas de três maneiras:

Esféricas: O termo "esférico" é utilizado para bolhas em que a razão entre o eixo menor e o eixo maior situa-se próximo de 1.

Elipsoidal: Bolhas oblatas com uma interface convexa (vista de dentro), em torno de toda superfície e achatada nos pólos (como a superfície da Terra).

Capa esférica ou Capa elipsoidal: Grandes bolhas possuem a tendência de adotar a base plana ou dentada, sendo assimétricas em relação aos seus eixos. Se a bolha possui uma depressão na parte traseira, ela é dita freqüentemente que possui uma "cova" (dimpled). Grandes bolhas com formas de capas esféricas ou elipsoidais podem arrastar finas camadas de fluidos dispersos; deformando-se, sua geometria assume a forma de abas.

Para caracterizar as bolhas são determinados os números adimensionais característicos do estudo de bolhas, Morton, Eotvos e Reynolds, a partir das variáveis:

d = diâmetro da bolha;

g = aceleração da gravidade;

ρ_l = massa específica do líquido;

μ_l = viscosidade do líquido;

σ = tensão superficial do líquido;

Q_L = fluxo em volume de líquido (m^3/s);

A = área do tubo de acrílico de 2".

w = velocidade relativa da bolha (velocidade da bolha, *v* - velocidade do líquido, V_L), sendo V_L dado pela "Eq 5".

$$V_L = \frac{Q_L}{A} \tag{5}$$

A "Equação 6" descreve o número de Eotvos (Eo), sendo este a razão entre a força da gravidade e a força devido a tensão superficial. Quando a tensão superficial é dominante sobre a pressão hidrostática, a superfície superior e inferior da bolha mantém-se esférica, caso contrário, ela tende a diminuir de altura, tornando-se um elipsóide ou outra forma de bolha .

$$Eo = \frac{\rho_l g d^2}{\sigma} \tag{6}$$

Em um escoamento em tubulação vertical, o número de Morton representa a tendência relativa das forças viscosas arrastarem lateralmente a bolha na forma de uma capa esférica. O número de Morton (M), é definido pela "Eq. 7", sendo a razão entre as forças viscosas e forças devido a tensão superficial.

$$M = \frac{g\mu_l^4}{\rho_l \sigma^3} \tag{7}$$

O Número de Reynolds(Re), é definido pela "Eq. 8", sendo a razão entre forças de inércia e forças viscosas.

$$\mathrm{Re} = \frac{\rho_l w d}{\mu_l} \tag{8}$$

A "Figura 6" mostra a classificação das bolhas em função dos números de Morton, Eotvos e Reynolds.

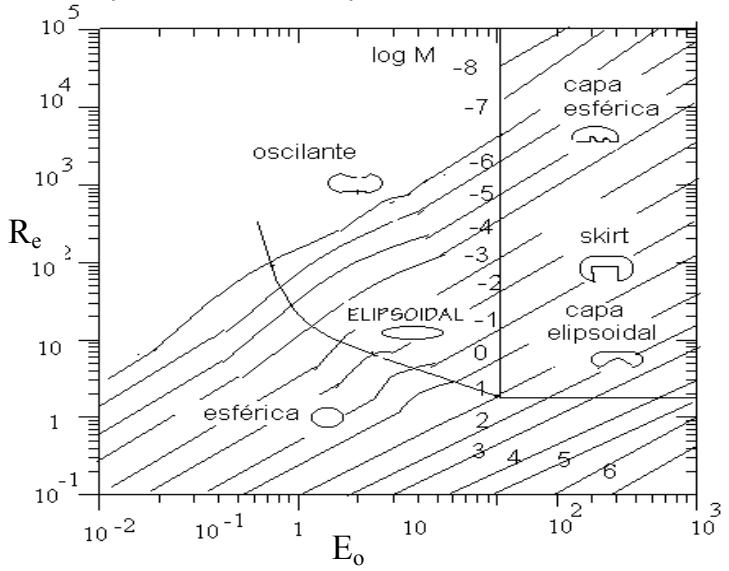

Figura 6. Geometria de Bolhas e Gotas em Movimento através de líquidos (Clift, 1978).

5. Determinação do fluxo de massa

Para obter-se os fluxos de massa dos escoamentos de ar, água e bifásico água-ar, a fração em massa de água, e a fração de vazio, utilizou-se o roteiro de cálculo descrito por Murdock (1962), conforme "Eqs.9 a 15".

$$\omega = \frac{K_G Y_G \; a_o \sqrt{2 \; g \; \Delta P_{TP} \; \gamma_{G1}}}{(1-y) + 1{,}26 \; y \; \frac{K_G Y_G}{K_L} \sqrt{\frac{\gamma_{G1}}{\gamma_{L1}}}} \tag{9}$$

$$\omega_G = a_G \; (K_G \, Y_G)_{TP} \; \sqrt{2g \, \Delta P_{TP} \, \gamma_{G\,1}} \tag{10}$$

$$\omega_G \; = \; \rho_G \times Q_G \tag{11}$$

$$\omega_L = a_o \; K_L \sqrt{2g \; \Delta P_L \; \gamma_{L\,1}} \tag{12}$$

$$\omega_L \; = \; \rho_L \times Q_L \tag{13}$$

$$y = \frac{\omega_L}{\omega_G + \; \omega_L} \tag{14}$$

$$\varepsilon = \frac{\omega_G}{\omega_G \; + \omega_L} \tag{15}$$

onde:
ω = fluxo de massa do escoamento bifásico água-ar (kg/s).
a_o = área do orifício (m^2).
$\Delta P_{t\,p}$ = diferença de pressão no escoamento bifásico (N/m^2)
γ_{G1} = peso especifico do ar antes da placa de orifício (t = 26°C e p = 7bar).
γ_{L1} = peso específico da água antes da placa de orifício (t = 26°C e p = $17x10^4$ N/m^2).
$K_G \; Y_G$ = fator de correção para gás devido a expansão volumétrica e a velocidade.
K_L = fator de correção para água.
ϖ_G = fluxo de massa de gás em (kg/s)
a_G = área ocupada pelo gás durante o escoamento bifásico
ρ_G = massa específica de gás em (kg/m^3)
Q_G = fluxo em volume de gás (m^3/s)
ϖ_L = fluxo de massa da água em (kg/s)
ΔP_L = diferença de pressão na fase líquida (N/m^2), lido só com fluxo de água.
ρ_L = massa específica de líquido em (kg/m^3)
Q_L = fluxo em volume de líquido (m^3/s)
y = fração em massa de água
ε = fração em massa de ar ou fração de vazio

5. Resultados

5.1. Perda de pressão na placa de orifício para escoamento de água

Foram utilizadas quatro vazões de água, para as quais foram lidas, no sensor diferencial de pressão suas correspondentes ddp(volts). Através da curva de calibração do sensor Smar encontra-se os respectivos Δp_L (kPa), conforme "Eq. 16".

$$\Delta p \text{ (kPa)} = 56{,}439.\text{ddp (volts)} - 54{,}684 \tag{16}$$

5.2 Perda de pressão na placa de orifício para escoamento bifásico água-ar

Foram utilizadas 4 vazões de água e 10 de ar, para as quais foram lidas, no sensor diferencial de pressão as ddp (volts), e calculados os respectivos Δp (kPa), conforme mostram as "Figs. 7 e 8".

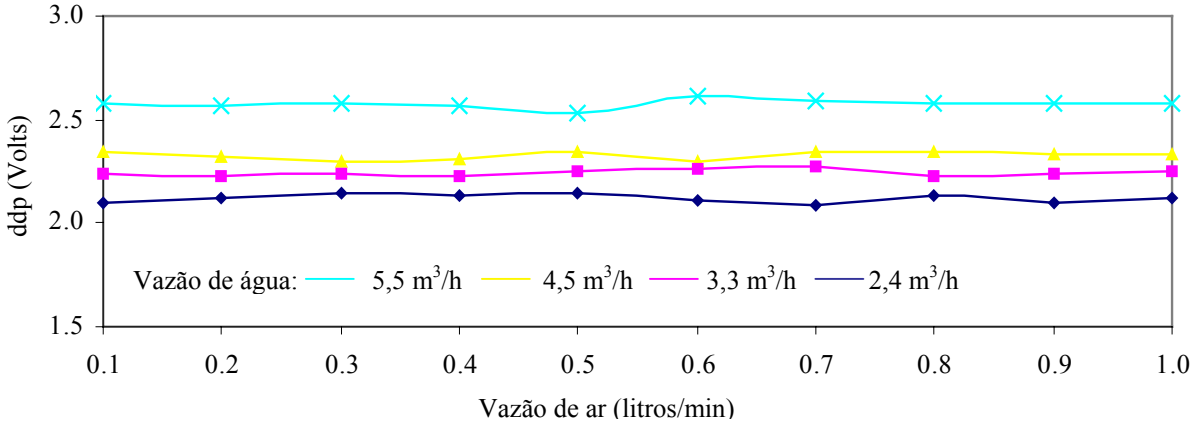

Figura 7. Curva de calibração da placa de orifício para o escoamento bifásico água-ar: ddp(Volts) x Vazão de ar (litros/min).

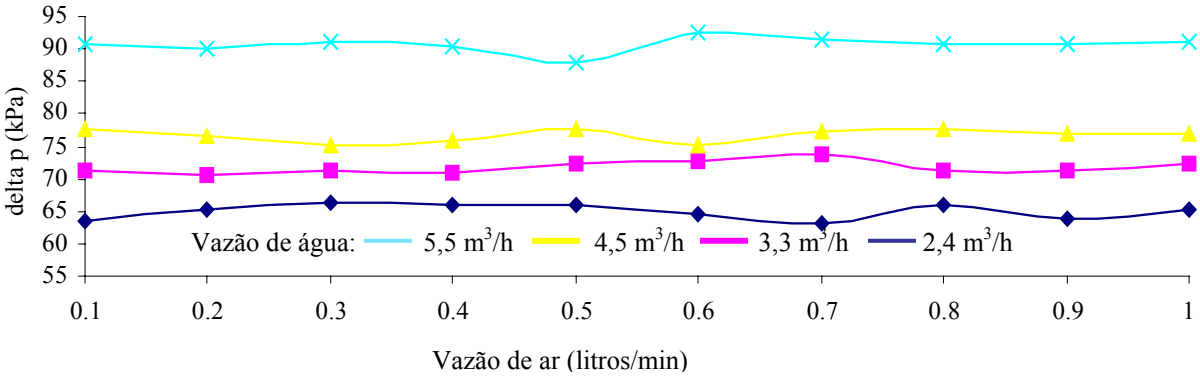

Figura 8. Curva de calibração da placa de orifício para o escoamento bifásico água-ar: deltap (kPa) x Vazão de ar (litros/min).

5.3 Geometria da Bolha por Aquisição de Sinais

Os sinais adquiridos nos sensores resistivos 1-2 no domínio do tempo, são representados na "Fig. 9" , e no domínio da frequência na "Fig. 10" , para as vazões de água e de ar de 4,5 m^3/h e 0,8 l/min, respectivamente.

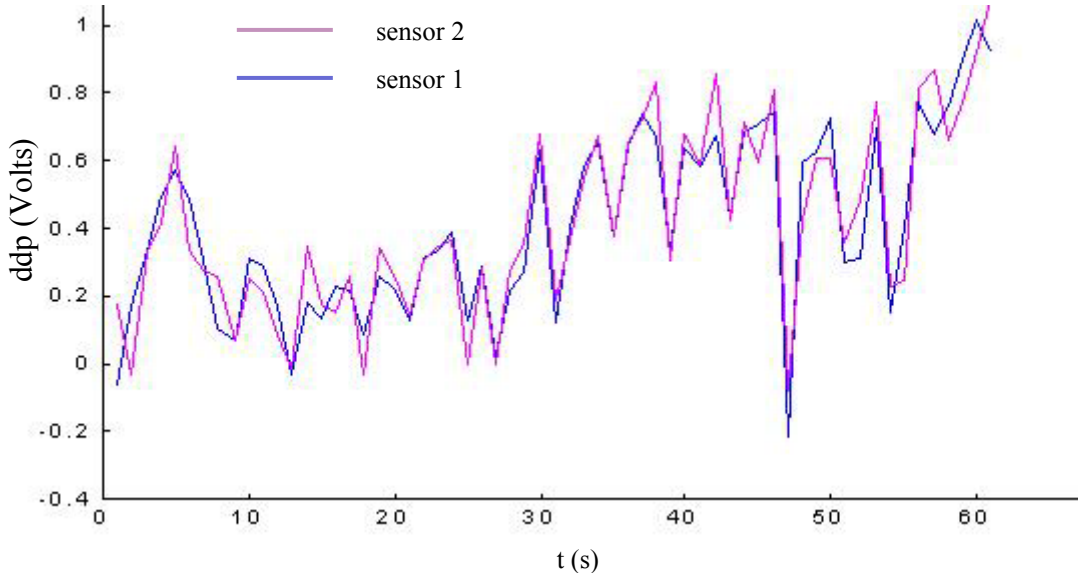

Figura 9. Passagem das bolhas pelos sensores 1 e 2 (água 4,5 m^3/h e ar 0,8 l/min), no domínio do tempo.

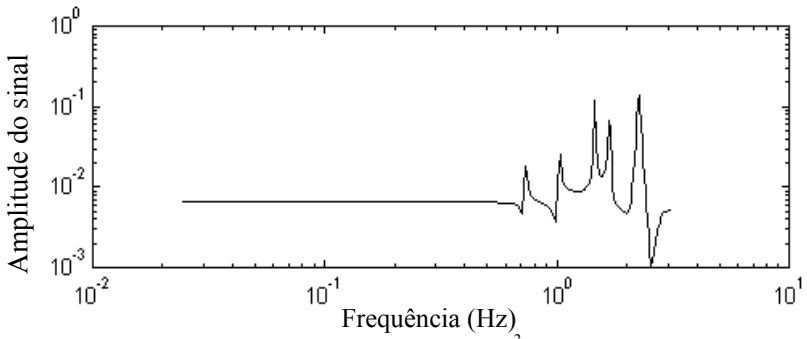

Figura 10. Passagem das bolhas pelos sensores 1 (água 4,5 m^3/h e ar 0,8 l/min), no domínio da frequência.

Foi desenvolvido um programa computacional no Matlab 6.1 versão educacional, que analisa os dados adquiridos caracterizando a passagem da bolha em cada sensor, pela variação da ddp medida, calculando o número de bolhas, o tempo inicial e final da bolha em cada sensor, permitindo o cálculo do comprimento das bolhas, "*a*" (m), e a sua velocidade, "*v*" (m/s), para cada conjunto de vazão de água e de ar. A "Fig. 11" mostra o resultado para 4,5 m^3/h de água e vazões de ar de 0,0 a 1,0 l/min.

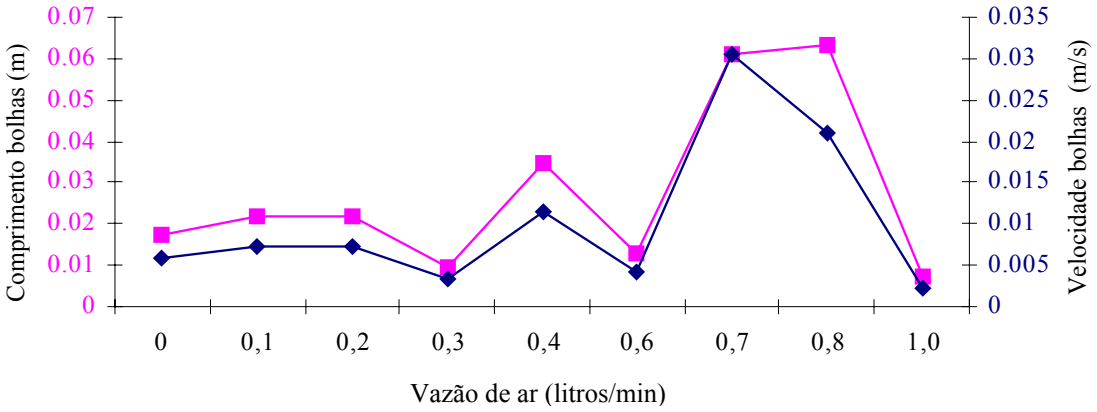

Figura 11. Comprimento médio das bolhas "*a*" (m) e velocidade média das bolhas "*v*" (m/s) para vazão de água de 4,5 m^3/h e vazões de ar de 0,0 a 1,0 l/min.

5.4 Classificação das bolhas

Conforme seção 4 e "Eqs. 5 a 8", para caracterizar as bolhas são determinados os números adimensionais característicos do estudo de bolhas, Morton, Eotvos e Reynolds.

Retirando-se da "Fig. 11" as condições de vazão de ar e de água e as características das bolhas , obtém-se:

Vazão de água = 4,5m^3/h

Vazão de ar = 0.4 l/min

Diâmetro da bolha d = a = 2,07x10^{-2} m

Velocidade média da bolha , v = 1,04x10^{-2}m/s

Velocidade do líquido, V_L = 0,5886 m/s

w = v - V_l (velocidade relativa entre a bolha e o líquido)= 0,5782 m/s

Sendo:

σ = 0,00642 N/m

ρ_{liq}= 1000 Kg/m^3

μ_{liq} = 0,000891 Kg/m/s

Então:

Re = 1,34 x 10^4

M = 2,33 x 10^{-8} ou log M = -7,63

Eo = 6,53 x 10^2

Portanto, classifica-se a bolha, segundo a "Fig. 6", como uma Capa Esférica.

5.5 Fluxo de Massa do Escoamento Bifásico

A "Tabela 1" apresenta o cálculo do fluxo de massa, *w*, para dados obtidos experimentalmente com o escoamento bifásico água-ar, e somente com água na bancada de testes, de acordo com "Figs. 4 a 11" e Eqs. 9 a 15" .

Tabela 1. Determinação do fluxo de massa, ϖ, para escoamento bifásico água-ar.

Q_{ar}	l/min	1	0,8	0,7	0,6	0,4	0,3	0,2	0,1
Q_{ar}	m^3/s	1,67E-05	1,33E-05	1,17E-05	1,00E-05	6,67E-06	5,00E-06	3,33E-06	1,67E-06
$Q_{água}$	m^3/h	4,50E+00	4,50E+00	4,50E+00	4,50E+00	4,50E+00	4,50E+00	4,50E+00	4,50E+00
$Q_{água}$	m^3/s	1,25E-03	1,25E-03	1,25E-03	1,25E-03	1,25E-03	1,25E-03	1,25E-03	1,25E-03
γ_{ar}	N/m^3	1,18E+04	1,18E+04	1,18E+04	1,18E+04	1,18E+04	1,18E+04	1,18E+04	1,18E+04
ρ_{ar}	kg/m^3	1,20E+00	1,20E+00	1,20E+00	1,20E+00	1,20E+00	1,20E+00	1,20E+00	1,20E+00
ω_{ar}	kg/s	2,00E-05	1,60E-05	1,40E-05	1,20E-05	8,00E-06	6,00E-06	4,00E-06	2,00E-06
$\gamma_{água}$	N/m^3	9,80E+03	9,80E+03	9,80E+03	9,80E+03	9,80E+03	9,80E+03	9,80E+03	9,80E+03
$\rho_{água}$	kg/m^3	1,00E+03	1,00E+03	1,00E+03	1,00E+03	1,00E+03	1,00E+03	1,00E+03	1,00E+03
$\omega_{água}$	kg/s	1,25E+00	1,25E+00	1,25E+00	1,25E+00	1,25E+00	1,25E+00	1,25E+00	1,25E+00
$a_{0\ orifício}$	m^2	2,30E-04	2,30E-04	2,30E-04	2,30E-04	2,30E-04	2,30E-04	2,30E-04	2,30E-04
Δp_{TP}	kPa	8,36E+01	8,33E+01	8,49E+01	8,37E+01	8,23E+01	8,24E+01	8,25E+01	8,39E+01
Δp_{TP}	Pa	8,36E+04	8,33E+04	8,49E+04	8,37E+04	8,23E+04	8,24E+04	8,25E+04	8,38E+04
Δp_L	kPa	8,26E+05	8,26E+05	8,26E+05	8,26E+05	8,26E+05	8,26E+05	8,26E+05	8,26E+05
Δp_L	Pa	8,26E+04	8,26E+04	8,26E+04	8,26E+04	8,26E+04	8,26E+04	8,26E+04	8,26E+04
a_G bolha	m^2	2,23E-02	1,98E-01	1,91E-01	1,51E-01	1,08E-01	8,69E-02	6,89E-02	6,89E-02
$K_G Y_G$	kg/N	6,42E-07	5,78E-08	5,19E-08	2,10E-07	5,32E-08	1,41E-07	4,18E-08	2,07E-08
K_L	kg/N	4,29E-02	4,29E-02	4,29E-02	4,29E-02	4,29E-02	4,29E-02	4,29E-02	4,29E-02
y		1,00E+00	1,00E+00	1,00E+00	1,00E+00	1,00E+00	1,00E+00	1,00E+00	1,00E+00
ε		1,60E-05	1,28E-05	1,12E-05	9,60E-06	6,40E-06	4,80E-06	3,20E-06	1,60E-06
ω	Kg/s	1,28E-02	1,46E-03	1,51E-03	1,92E-03	2,66E-03	3,31E-03	4,18E-03	4,18E-03

6. Conclusões

Verificou-se que no escoamento bifásico em regime de bolha dispersas as descontinuidades (bolhas) apresentam suas formas geométricas espaciais aproximadamente elipsoidais e variam sua geometria com o tempo.

Observações mostraram variações na fração de vazio e na dimensão das bolhas que migram para a parte superior da tubulação sobre a influência dominante da força empuxo.

Conforme "Figura 8", a introdução da segunda fase (ar) no fluxo de água, para diferentes fluxos de água, gera flutuações de pressão. Verificou-se visualmente, que com o aumento do fluxo da fase líquida grandes bolhas tendem a se romper devido à turbulência , o que pode ser observado na pouca flutuação de pressão.

A análise dos dados experimentais, gerados pelos sensores resistivos permitiu obter um critério objetivo para discriminar o tipo de fase, de acordo com a "Fig. 9".

O escoamento com bolhas dispersas é um fenômeno de baixa frequência (<10 Hz) e ocorre uma amplificação na faixa de frequência analisada tornando-se mais elevados os picos atingidos, conforme "Fig. 10".

Os dados experimentais coletados através de sensores instalados na bancada de testes, possibilitaram a determinação das características geométricas das bolhas estudadas, além da determinação do fluxo mássico do escoamento bifásico água-ar por equação proposta por Murdock, 1962.

Verificou-se que a fração de vazio é influenciada pelos fluxos de massa da fase líquida e de gás, propriedades do fluido e pela geometria da seção de teste, conforme "Tab. 1".

7. Referências

Advantech Genie Demo, 1993, "Manual da placa de aquisição de Sinais placa PL-711B.

Clift, R., 1978, "Bubles, Drops and Particles", Ed. Academic Press, USA.

Fokin, B.S., 1995, "Calculation of pulsation and Averaged Hydrodynamic Characteristics of Two-Phase Flow", Russ. J. Eng. Thermophys, Vol. 5, N^0 3, pp. 265-292.

Kuznetsov, V.V., Nakorryakov, V.E., Pokusaev, B.G., Shreiber, I.R., 1985, "Propagation of Perturbation in a Gas-Liquid Misture", J.Fluid Mech, Part 1, Vol.85, pp.85-96.

Lahey, R.T.Jr., 1974, "Two-phase flow in boiling water nuclear reactors", NEDO - 13388.

Murdock, J. W. 1962 “Two-Phase Flow Measuriment With Orifices”, Journal of Basic Engineering, December.

Moreau, V., 2000 a, “Two phase flow in industry”, http://www.crs.4.it/~moreau/Twophaseflow/node1.html.

Moreau, V., 2000 b, “Bubbles shape and dynamics”, http://www.crs.4.it/~moreau/Twophaseflow/node8.html.

Ponoth, Shom. S., 2000a. “Experimental Studies of Bubble Motion”, Clarkson University, http://www.clarkson.du/~jmclau/ nersc/node3.html.

Ponoth, Shom. S., 2000b. “Theorical Studies of Bubble Motion”, Clarkson University, http://www.clarkson.du/~jmclau/ nersc/node4.html.

Sheikholeslami, M.Z., Patel, B.R., 1988, "Numerical Modeling of Turbulent Flow Through Orifice Meters - A parametric Study, Second International Conference on Flow Measurement, london, UK, Paper B2, pp. 67-89.

Smar, 1996. “Transmissor inteligente de pressão LD301”, Manual de instruções, operação e manutenção.

Theofanous, T., Sullivan, S.,1982, "Turbulence in Two-Phase Dispersed Flows", J.Fluid Mech, Vol.116, pp. 343-362.

Winjgaardem, L. van, 1968, "On the Equations for motion of Mixtures of Liquid and gas Bubbles", J.Fluid Mech, Vol.33, part. 3, pp. 465-474.

Proceedings of the 11th Brazilian Congress of Thermal Sciences and Engineering -- ENCIT 2006
Braz. Soc. of Mechanical Sciences and Engineering -- ABCM, Curitiba, Brazil,- Dec. 5-8, 2006

Paper CIT06-0278

NUMERICAL SIMULATIONS OF THE LONG RECIRCULATION BUBBLES FORMED IN INCOMPRESSIBLE AERODYNAMIC FLOWS OVER THIN FLAT PLATES AT SHALLOW INCIDENCE

Luiz Eduardo Bittencourt Sampaio
Dept. Mechanical Eng. – PUC/Rio, R. Marques de Sao Vicente 225 – Gávea, 22453-900 Rio de Janeiro, RJ, Brasil
luizebs@mec.puc-rio.br

Angela Ourivio Nieckele
Dept. Mechanical Eng. – PUC/Rio, R. Marques de Sao Vicente 225 – Gávea, 22453-900 Rio de Janeiro, RJ, Brasil
nieckele@mec.puc-rio.br

Margot Gerritsen
Dept. Mechanical Eng. – Stanford University, Stanford, CA, USA
margot.gerritsen@stanford.edu

Steve Collie
Dept. Mechanical Eng. – Stanford University, Stanford, CA, USA
steve.collie@gmail.com

Abstract. *Aerodynamic flows around thin airfoil or membranes has experienced increasing attention from the industry and research institutions lately, and are prone to present complex structures, including geometry-induced separation of the boundary layer, shear layer transition to turbulent behavior, reattachment, relaminarization of the boundary layer, and formation of secondary recirculation bubbles. The particular case of a thin flat plate at 1 degree incidence and high Reynolds number (213000) is a good representative of this class of flows, and is studied in this paper using two different numerical approaches - Reynolds Average Navier-Stokes and Large-Eddy Simulations (LES), for which a mixed numerical scheme is implemented using the freely available open source CFD framework from OpenFOAM. The methodologies are compared to each other and to the available experimental data. LES is shown to better capture the complex structures, in contrast to RANS's intrinsic inability to deal with the strong anisotropy presented by the long and thin recirculation bubbles, observed in this kind of geometry. A physical insight on this complex and important class of flows is also presented, using the extensive amount of data provided by the numerical simulation, which encompass time evolution of most of the energy-containing vortical structures.*

Keywords*. thin flat plate, shallow incidence, turbulence, Large-Eddy Simulations*

1. Introduction

Experimental investigations (Gault, 1955 and Cromptom , 2001) of incompressible aerodynamic flows have shown that recirculation bubbles of different characteristics may be formed close to the leading edge of airfoils, depending on the geometry, incidence angle and Reynolds number. While short bubbles are commonly found in regular airfoils, resulting from an adverse pressure gradient (APG), longer and thinner recirculation structures, also known as "thin airfoil bubbles", are more often seen in thin plates and membranes, being their formation driven by a geometry-induced separation, rather than by a adverse pressure gradient one, as in the former case. Of paramount importance is the understanding of the differences between these two classes of recirculation bubbles, which are certainly not limited to length and thickness, but in fact the differences extend from the genesis mechanism to their influence on the behavior of the whole flow, including pressure distribution and reattachment point, just to cite a few.

Because of their adverse pressure gradient-induced separation, short bubbles formation usually involves a laminar boundary layer separation at some distance from the leading edge, followed by a shear layer transition to turbulence which, in its turn, helps mixing and reattachment. After reattachment, the fluid particles are split into those that follow the (now turbulent) boundary layer toward the trailing edge, and those that are driven back towards the leading edge, closing the recirculation structure. They usually span only 1- 2% of the chord, and don't alter significantly the pressure distribution, unless a burst is observed, which may cause transition to a longer bubble or even a complete stall. Therefore, the main reason for studying these structures is the importance of preventing the bursting and stalling phenomenon, rather than the understanding of their interaction with the rest of the flow.

Long bubbles, on the other hand, are formed after a separation of the boundary layer driven by an abruptness on the geometry, such as a knife-like leading edge on a thin plate, membrane or even thin airfoils (Fig. 1). Since the stagnation point for positive angle of attack is located in the lower surface of the plate, the fluid particles are unable to follow the abrupt curvature of the edge, as the inertial forces are dominant at high Reynolds numbers. The separation thus occurs right at the edge where the boundary layer is still laminar, and the separated layer - now a shear layer - will be developing towards a turbulent regime, after which the improved mixing helps curving the streamlines towards the

reattachment point. The fluid streams that go back towards the leading edge may still experience a relaminarization process, due to the now favorable pressure gradient formed between the reattachment point (higher pressure) and the minimum pressure point close to the center of the bubble. In its path toward the leading edge, the boundary layer, being laminar once again, is more prone to suffer a second separation, originating a secondary recirculation bubble, since from the minimum pressure point (center of the bubble) to the leading edge, another adverse pressure gradient is experienced. In contrast to regular curved airfoils where all the lift comes from the pressure distribution created by the streamlines curvatures, and where the short bubble, when present, causes unnoticeable disturbances, in the case of thin flat plate, most of the lift comes from the pressure developed inside the bubble to provide the centripetal force required to maintain the circular motion. It is also noteworthy that, due to the elongated aspect of these structures, strong anisotropy is expected in the turbulent statistics.

Figure 1. Physics of the Problem.

The alternative terminology "thin airfoil bubbles" to refer to long bubbles was given by Gault in 1957, and only recently, with thinner wing sections requirements imposed by the increasing aircraft speeds and advances in turbomachinery blades, this kind of structure has received more attention from the scientific community. Other important applications which would benefit from long bubble studies are yacht sails, parachute and paragliders. Among the most recent and complete experimental data available is the study performed by Cromptom (2001), which focused on the simple thin flat plate geometry at shallow incidence, shown to be a very good representative and a strong benchmark case candidate for this class of flows.

Following the work of Cromptom, numerical studies based on Reynolds Average Navier-Stokes methodology (RANS) from Collie et al. (2003) have pointed the inability of Reynolds Average models (RANS) to accurately predict the flow around thin flat plates and its complex structures. Since RANS models can not capture the strong anisotropy of this type of flow, Collie et al. (2003) suggested that further investigation was needed. To achieve this, at the present work, the Reynolds Average Navier-Stokes (RANS) and the Large-Eddy Simulation (LES) methodology were applied to the same thin flat plate test case, aiming a better understanding of the physics involved. In this work the opensource code OpenFOAM was used, with some minor modifications.

2. Reynolds Average Modeling

The Reynolds-averaged approach is based on decomposing the velocity as $\mathbf{u} = \bar{\mathbf{u}} + \mathbf{u}'$, where $\bar{\mathbf{u}}$ is the average velocity and $\mathbf{u}'$ the velocity fluctuation. The average continuity and momentum equation (RANS), for a steady state incompressible flow is given by

$$\nabla \bullet \bar{\mathbf{u}} = 0 \quad ; \quad \nabla \bullet (\bar{\mathbf{u}}\,\bar{\mathbf{u}}) = -\nabla(\frac{p}{\rho}) + \frac{\mu}{\rho}\nabla^2 \bar{\mathbf{u}} + \nabla \bullet (-\overline{\mathbf{u}'\,\mathbf{u}'}) \tag{1}$$

where ρ is the density, μ is the molecular viscosity, p is the pressure. Equation (1) has the same form of the Navier-Stokes equation, but now it has an additional term, the turbulent Reynolds stress term, $-\overline{\mathbf{u}'\,\mathbf{u}'}$, representing the influence of the fluctuation on the average flow. In order to close Eq. (1), the turbulent Reynolds stress can be modeled based on the Boussinesq hypothesis as

$$-\overline{\mathrm{u}'\,\mathrm{u}'} = \upsilon_t(\nabla\,\bar{\mathrm{u}} + \nabla\,\bar{\mathrm{u}}^T) - \frac{2}{3}\kappa\,\delta \tag{2}$$

where κ is the turbulent kinetic energy and υ_t is the turbulence viscosity, which is defined in accordance with the κ-ω model of Wilcox (1988) as

$$\mu_t = \frac{\alpha^*\,\kappa}{\omega} \quad ; \quad \alpha^* = \left(\frac{0.008 + \mathbf{Re}_t/6}{1 + \mathbf{Re}_t/6}\right) \quad ; \quad \mathbf{Re}_t = \frac{\rho\,\kappa}{\mu\,\omega} \tag{3}$$

where κ and ω are obtained from their conservation equations

$$\nabla \bullet (\bar{\mathbf{u}}\,\kappa) = \nabla \bullet [(\frac{\mu}{\rho} + \frac{\upsilon_t}{\sigma_\kappa})\nabla\,\kappa] + G_\kappa - \varepsilon \tag{4}$$

$$\nabla \bullet (\,\overline{\mathbf{u}}\;\omega) = \nabla \bullet [(\frac{\mu}{\rho} + \frac{\upsilon_t}{\sigma_\omega})\nabla\;\omega] + \alpha\,\frac{\omega}{\kappa} G_\kappa - \beta\;f_\beta\;\omega^3 \tag{5}$$

$$G_\kappa = \upsilon_t\;S_{ij}\;S_{ij} \quad ; \quad f_\beta = \frac{1+70\;\chi_\omega}{1+80\;\chi_\omega} \quad ; \quad \chi_\omega = \left|\frac{\Omega_{ij}\;\Omega_{jk}\;S_{ki}}{(0.09\;\omega)^3}\right| \quad ; \; \alpha = \frac{0.52}{\alpha^*}\left(\frac{1/9 + \mathbf{Re}_t/2.95}{1+\mathbf{Re}_t/2.95}\right) \tag{6}$$

$$S_{ij} = \frac{1}{2}\left(\frac{\partial \overline{u}_i}{\partial x_j} + \frac{\partial \overline{u}_j}{\partial x_i}\right) \qquad\qquad \Omega_{ij} = \frac{1}{2}\left(\frac{\partial \overline{u}_i}{\partial x_j} - \frac{\partial \overline{u}_j}{\partial x_i}\right) \tag{7}$$

3. Large-Eddy Simulation Modeling

While RANS methodology uses a statistical or temporal filter to reduce the number of degrees of freedom of the original transport equations and all the turbulence is left to be modeled, Large-Eddy Simulation (LES) employs a spatial filtering operator to select the largest and most energetic structures to be computed, leaving only the small eddies to be modeled. Being those small eddies much less sensitive to the geometry and more isotropic, one can expect their modeling to be more universal when compared to RANS methodology.

The application of a filter operator $\langle \quad \rangle$ into the incompressible Navier-Stokes and continuity equations, requires a two-step process to transform $\langle \nabla \bullet (\mathbf{u}\,\mathbf{u}) \rangle$ into $\nabla \bullet (\langle \mathbf{u} \rangle \langle \mathbf{u} \rangle)$. As a result two commutative errors are introduced. The first of one, defined as the commutative error, and hereby denoted by ϵ_{com} is a consequence of commuting the filtering process with a spatial derivative operator

$$\epsilon_{com} = \langle \nabla \bullet (\mathbf{u}\,\mathbf{u}) \rangle - \nabla \bullet (\langle \mathbf{u}\,\mathbf{u} \rangle) \tag{8}$$

while the second which is a commutative product error, arises from commuting the filtering with the product operator. This second commutative error is commonly known as τ_{sgs}, the subgrid error or subgrid model (SGSM).:

$$\tau_{sgs} = \langle \mathbf{u}\,\mathbf{u} \rangle - \langle \mathbf{u} \rangle \langle \mathbf{u} \rangle \tag{9}$$

It is common practice to ignore ϵ_{com} and concentrate more on the subgrid modeling. However, the awareness of its effect on the numerical scheme is extremely important when designing the mesh or when trying to prevent possible "checkered board" spatial instabilities that may arise. As shown by Germano (2000), depending on the filtering process, the effect of the commuting error may be equivalent to a spurious dissipation. In particular, when the mesh spacing increases in the upwind direction, the spurious viscosity coefficient associated with this effect may become too negative, causing numerical instabilities and eventually blowing out the solution. On the other hand, we cannot afford to use the same small mesh spacing required in the neighborhood of the leading edge all the way towards the inlet boundary.

This commutation error is found not only in LES, but also in RANS, since any discretization scheme can be seen as a more general filtering process. The fact that RANS models are not too affected by spatial instability problems is explained by the use of biased, highly dissipative numerical schemes, such as upwind. Large-Eddy Simulations generally cannot use such dissipative schemes, on the penalty of damping some important turbulence structure.

In the particular case of Finite Volume Method (FVM), the filtering operation may be conveniently confused with the volume integral over the control volume. Therefore, no further filtering is needed, and this process is said to be implicit, or embedded in the FVM, in which case it may be defined as:

$$\langle \varphi_i(t) \rangle = \frac{1}{\forall_i} \int_{\forall_i} \varphi(\mathrm{x}, t)\, d\forall \tag{10}$$

where $\langle \varphi_i(t) \rangle$ is the value of the filtered variable located anywhere inside the *i*-th control volume, $\forall_i$, and $\varphi(\mathbf{x},t)$ is the original field variable.

The filtered incompressible transport equations, for the filtered velocity $\langle \mathbf{u} \rangle$ can be written as

$$\nabla \bullet \langle \mathbf{u} \rangle = 0 \tag{11}$$

$$\frac{\partial \langle \mathbf{u} \rangle}{\partial t} + \nabla \bullet (\langle \mathbf{u} \rangle \langle \mathbf{u} \rangle) + \nabla \bullet \tau_{sgs} = - \nabla (\frac{\langle p \rangle}{\rho}) + \frac{\mu}{\rho} \nabla^2 \langle \mathbf{u} \rangle \, . \tag{12}$$

The vast majority of subgrid models (Sagaut, 2002), specially the eddy-viscosity ones, tries to capture only the forward energy cascade, where energy from the large eddies is transferred to small turbulent structures. In the continuous dynamic system, as found in real world, all this energy ends up being dissipated at very small scales, where laminar viscous dissipation becomes important. However, in a simulation environment, there is a limit on the smallest mode a mesh can still represent, and, unless a Direct Numerical Simulation (DNS) is being employed, the mesh is still bigger than the size where dissipation is strong enough to end the energy cascade. In order to prevent the accumulation of energy in the smallest modes, we thus need to add to the Navier-Stokes equations a dissipative term, which is usually done by modeling the subgrid tensor τ_{sgs} as trace free tensor as:

$$\tau_{sgs\,ij} - \frac{1}{3} \tau_{sgs\,kk} \, \delta_{ij} = -2 \, \upsilon_{sgs} \, \langle S_{ij} \rangle \quad ; \quad \langle S_{ij} \rangle = \frac{1}{2} \left(\frac{\partial \langle u_i \rangle}{\partial x_j} + \frac{\partial \langle u_j \rangle}{\partial x_i} \right) \, , \tag{13}$$

where υ_{sgs} is the subgrid viscosity, which is the essence of the SGSM.

Another complicating factor when transforming a continuous dynamic system in a discrete one is that, as we go toward the smallest modes supported by the mesh, the relative resolution becomes very poor, to a point where there can be no structures in-between the smallest one and another twice its size.

3.1. Sub-grid Viscosity

In a general external aerodynamic flow, the important turbulence is commonly confined to regions close to the object of interest (airfoil or thin plate in our case) and, in the worst case, may also include a portion of downstream wake. In such high activity locations, regularity on the mesh spacing is desired anyway to guarantee a low "commutative error-subgrid term" ratio, justifying efforts to improve subgrid models (SGSM). Away from this regions, upwind (or other dissipative schemes) can be safely used, since there is no danger of damping turbulence structures.

Therefore the strategy used here consists in defining, based on previous experience or experimental data, a closed region around the flat plate where turbulence is not insignificant and where a central difference scheme is employed together with a high quality mesh. Outside this region, a dissipative scheme allows increasing mesh spacing towards external boundaries, without penalties for the accuracy of turbulence simulations.

Although this strategy is general enough to be used with many combinations of dissipative schemes and SGSM, this paper is restricted to the use of standard upwind scheme along with the one equation SGSM of Horiuti (1985) to model the subgrid viscosity υ_{sgs}

$$\upsilon_{SGS} = C_\kappa \, \overline{\Delta} \, \sqrt{\kappa_{sgs}} \tag{14}$$

where the sub-grid length scale is proportional to the mesh size $\overline{\Delta}$ and the sub-grid velocity scale is the subgrid kinetic energy κ_{sgs}, which is obtained from its transport equation

$$\frac{\partial \kappa_{sgs}}{\partial t} + \nabla \bullet (\overline{\mathbf{u}} \, \kappa_{sgs}) = \nabla \bullet [(\frac{\mu}{\rho} + \upsilon_{sgs}) \nabla \kappa_{sgs}] + G_{\kappa,sgs} - \frac{C_\varepsilon \, \kappa_{sgs}^{3/2}}{\overline{\Delta}} \; ; \; G_{\kappa,sgs} = \tau_{sgs\,ij} \, \langle S_{ij} \rangle \tag{15}$$

In the derivation of Eq. (15) the turbulent transport and the pressure diffusion have been modeled compactly as a diffusion process.

Although standard first-order upwind scheme is known to be too dissipative, its choice was based on the assumption that its active region will be limited by design to that of laminar flow regime, where no important structure is at risk of being damped. The main motivation for the choice of the one equation SGSM, on the other hand, was its ability to deal with non-equilibrium situations, where turbulent production and dissipation do not necessarily balance each other.

If this SGSM represents a step forward in capturing situations where turbulent production and dissipation are not in equilibrium, one of the key issues regarding LES is still untouched, which is extremely important in the present particular case. Indeed, the length scale $\overline{\Delta}$, usually defined as the cubic root of the elementary volume, $\sqrt[3]{\forall}$ is only reasonable for control volumes whose aspect ratio is close to one. For elongated elements, where aspect ration is important, it proves incapable of representing the complexity of mesh anisotropy, resulting in a viscosity to big for the structures lying in some directions and at the same time too low for structures in other directions.

In the particular case of a external flow over a thin flat plate, the presence of a wall only contributes to further

widen the range of scales, with very small structures in the boundary layer and much bigger ones away from the walls. From the SGSM perspective, this ideally requires a gradual increase in the spanwise mesh spacing away from the wall in its normal direction, which not only increases commutative error, but cannot be obtained with a structured mesh. Therefore it is inevitable that the one equation SGSModel overpredicts the eddy-viscosity in some places and underpredicts it in others. Therefore, mesh validation is a very important part of this work.

It must be reinforced that, without this mixed scheme, or in other words, employing pure central-differences over the entire domain, every tentative of simulation ended with number overflow, due to the mentioned mesh-related instability.

4. Results

The flow field was obtained with the free opensource CFD framework called OpenFOAM (Weller et al. 1998), which easily allows new implementations, as the one presented in this paper. It is based on Finite Volume Method, where all the variables are stored at the control volume's centroid, being face-interpolated when needed. PISO algorithm (Issa, 1985) was employed on all simulations, using second order "backward differencing" time step discretization. Unless otherwise specified, all discretization schemes and other details followed exactly version 1.2 of OpenFOAM.

The geometry of the flat plate follows the work of Cromptom (2001) and Collie et al (2003) and is shown in Fig. (2). However, since LES is an expensive methodology, it was adopted a smaller computational domain, than the one used by Collie et al (2003). Preliminary investigations of the same problem (Sampaio and Nieckele, 2004) showed that the smaller domain did not present any significant influence to the final solution. Numbered auxiliary regions intended to help mesh elements distribution, are shown in the same Fig. (3). Block number 15 is of particular interest, since it was expected to enclose the whole main bubble, according to Cromptom's experiment.

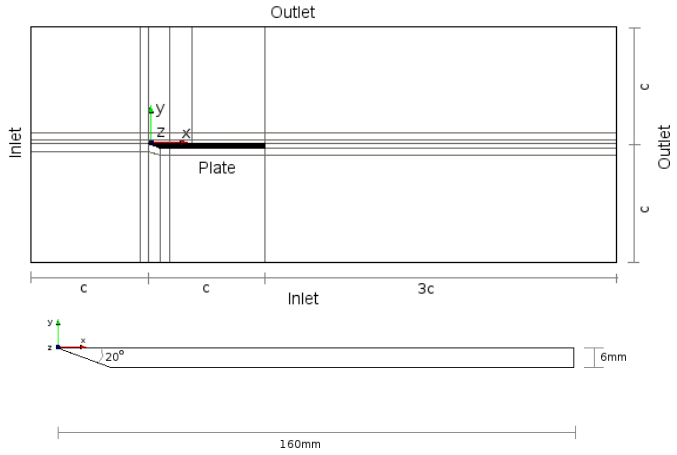

Figure 2. Thin flat plate geometry and domain

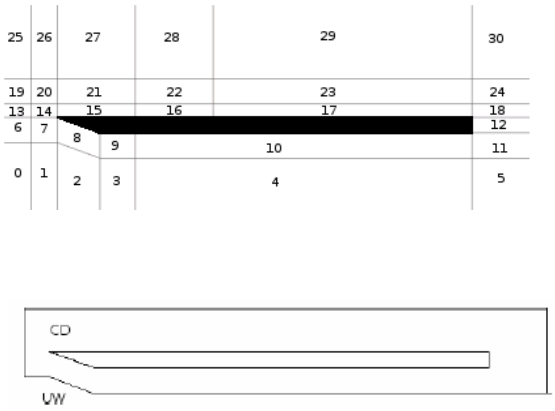

Figure 3. Thin flat plate geometry and auxiliary block

The boundary conditions are also indicated in Fig. (2), and consist of: prescribed velocity, no turbulence kinetic energy and zero pressure gradient in the inlet boundary; zero velocity and turbulence energy gradient and zero pressure in the outlet boundary; zero velocity, zero kinetic energy and zero pressure gradient at the plate walls; and periodic conditions at the z-planes.

Structured meshes were used throughout this work, since they require fewer elements to fill the domain, and potentially present less error due to mesh non-orthogonallity.

Aiming to fully understand the mesh requirements and limitations, several mesh distributions were employed. Initially a coarse mesh was specified, which allowed faster computation time and several subsequent runs were performed, with refinements in different directions, so that conclusions could be drawn as to which direction or which refinement were more crucial to the accuracy of the simulations.

A grid test was performed, with a starting mesh for this set of simulations, hereby referenced as 400k mesh, consisting of 418,992 control volumes, being 16 divisions used in the z direction, which spans $1/4^{th}$ of the chord. For a 16 cm-long plate, the finest control volume, found inside auxiliary block number 15, measures 0.01×0.04×0.25 (Height × Length × Depth) cm, guaranteeing a $y+$ below 10 throughout the top surface of the plate. While this is not enough for LES in wall-sensitive flows, where usually the transition and separation occurs somewhere along the surface, in the present case it should not be a problem, since the separation of the boundary layer is dictated by a abrupt curvature -- actually a knife edge - in the geometry, and happens at a well defined point. Transition of the separated shear layer is also shown experimentally to occur very close to the leading edge for Reynolds numbers above 100,000; which means the rest of the flow is also not very sensitive to this.

For the second mesh, the number of divisions in z direction was doubled for the mesh hereby referenced as 800k, while keeping the same wingspan as the 400k mesh. Finally, a third mesh with 1254096 control volumes, called 1200k,

preserves both wingspan and number of z-direction divisions as the 400k mesh, but it greatly improves regularity downstream of the bubble in the *x-y* plane, particularly along *x* direction in auxiliary blocks number 16 and 17.

Since the main objective of this study was to capture and to understand the mechanisms inside the bubble, usual mesh recommendations were a bit relaxed in the outer region, so that computational costs were kept at reasonable levels. Therefore, the mesh is designed to be as regular as possible inside the auxiliary block number 15, which measures 0.2 $c \times 0.03\ c$, where maximum spreading rate was only 0.5%. Therefore, even if some spurious dissipation and inaccurate results are felt downwind of the bubble, one should not expect this to significantly influence the behavior of the simulation inside the bubble.

To be able to obtain a solution, a closed box containing all the expected turbulent structures was defined as shown in Figure (3). In this particular flow, experimental data helped to define this region, but this is rarely the case, since the ultimate goal of simulations is to predict the behavior of the flow, becoming independent of data availability. Inside this box - which contains auxiliary block numbers 7, 8, 9,10, 14, 15, 16 and 17, as well as a small part of blocks 11, 12, and 18 - the central difference schemes was employed, known to be far less dissipative than upwind, which was used everywhere else. However, central difference schemes require the mesh to be as regular as possible to avoid any numerical instability from spurious mesh effects, and this is why the maximum spreading rate was kept as low as 0.5% inside this box.

The fields were initialized from a solution obtained with a simple Spalart-Almaras (1994) RANS model, so that the time consuming evolution towards steady state is shortened. Only after a long enough period of no significant changes in the average variables, the averaging was initialized and the steady-state results began to be computed. In all simulations, time step was chosen so that maximum Courant number was kept below 0.125.

Results from the three meshes are compared in Fig. (4), where mean velocity profiles at 4 stations along the plate are compared to experimental data from Cromptom (2001) and RANS *k-w* model prediction obtained by Collie et al (2003). Although the results inside the main structure for mean velocity profile (Fig. (4a) and (4b) were encouraging with this first mesh, further downstream, excessive dissipation was found, as seen in Fig. (4c) and (4d), where the mean chordwise velocity component profile presented a smooth curvature instead of piecewise-linear like behavior found experimentally. As subgrid viscosity levels were not enough to explain such behavior, two subsequent mesh refinements in different directions were employed aimed to investigate whether this could be attributed to a spurious viscosity, due to an inappropriately large spreading rate.

Inside the bubble, as shown in Fig. (4a) and (4b), one can see that the *x-y* plane refinement of 1200k mesh did not improve accuracy, while the spanwise refinement (800k) did, specially in the second station, Fig. (4b), located very close to reattachment point. Downstream of the bubble, Fig. (4c) and (4d), all tested meshes failed to provide accurate quantitative results as for-seen, although a slightly better qualitatively result was predicted by 800k mesh, which captured slightly better the piecewise linear trend exhibit by the experiments.

The reattachment lengths for the three meshes tested and for the RANS *k-w* model used by Collie et al (2003) are shown in Tab. 1, where they are compared to the experimental data from Cromptom (2001).

Table 1. Reattachment Lengths

Case	Reattachment Length (% of the chord)	Error relative to Exp. (%)
Exp (Cromptom, 2001)	14	-
k-w (Collie et al. 2000)	18.41	24
400k	14.53	3.8
800k	13.95	0.37
1200k	13.25	5.4

The pressure coefficient, defined as

$$cp = \frac{\langle p \rangle - p_\infty}{\rho U_\infty^2 / 2} \quad , \tag{16}$$

is presented along the top surface at Fig. (5). It reveals that none of the meshes was able to capture the suction on the leading edge of the bubble. Not only is the suction peak lagged in space, as the pressure exhibits an almost linear behavior until it reaches its minimum in the numerical simulations, which is not in agreement with the expected smoothly curved behavior. The fact that the 1200k mesh prediction was closer to experimental data may be an indication that more resolution in the *x-y* plane is required close to the leading edge of the plate, and this refinement is more effective than the wingspan refinement.

To analyze the flow field, it is convenient to determine the second order statistic components, as

$$R_{ij} = \langle u_i' u_j' \rangle \quad ; \quad u_i' = \langle u_i \rangle - \langle \overline{u_i} \rangle \tag{17}$$

where $\langle \overline{u_i} \rangle$ is the time average of the filtered velocity component.

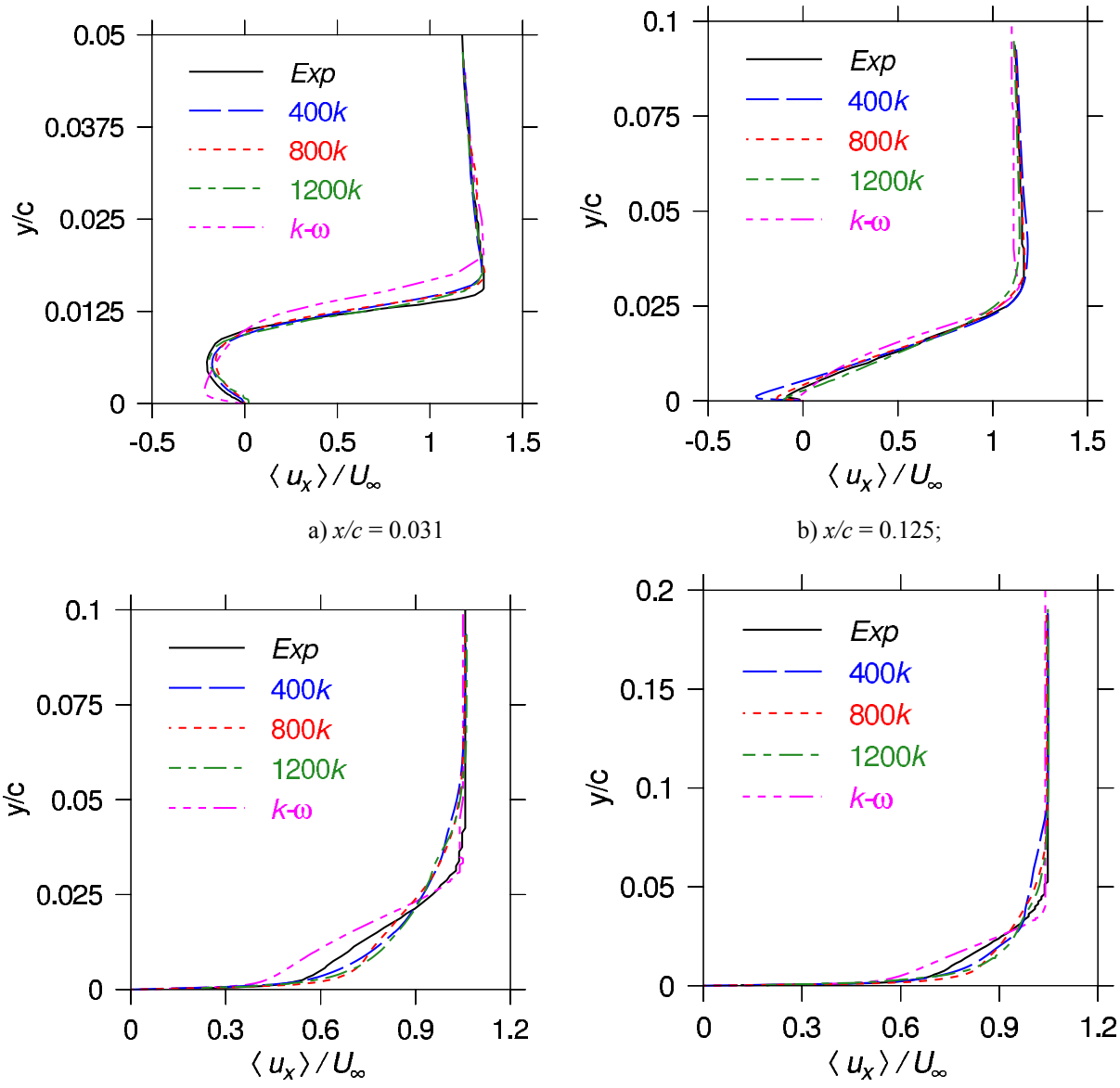

a) $x/c = 0.031$ b) $x/c = 0.125$;

c) $x/c = 0.25$ d) $x/c = 0.375$

Figure 4. Mean velocity profiles at stations located at: a) $x/c = 0.031$; b) $x/c = 0.125$; c) $x/c = 0.25$; d) $x/c = 0.375$.

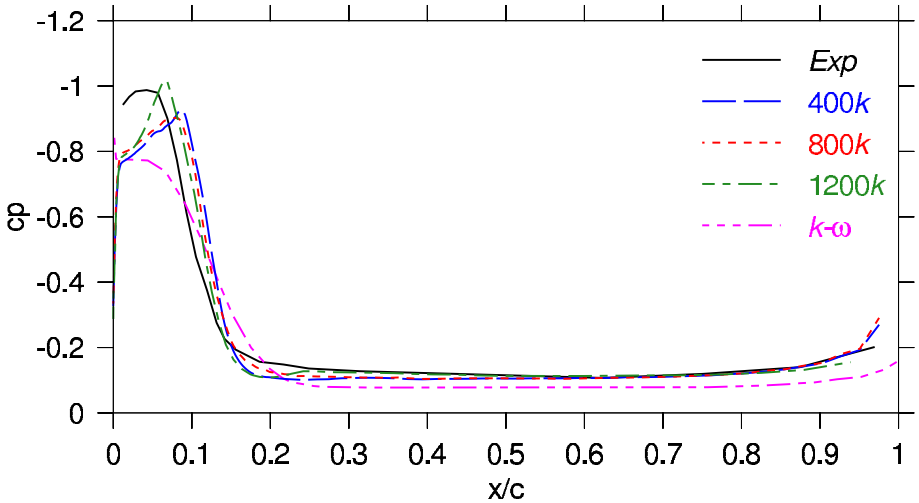

Figure 5. Pressure Coefficient

An analysis of second order turbulent time-statistics, $R_{11}=\langle u' u' \rangle$, at Fig. (6), shows that most of the turbulent kinetic energy is not resolved inside the bubble (station 1). It is also evident that, in the numerical simulations, the maximum of energy happens at station 2, while experiments suggest that the peak should happen earlier, at station 1. A possible explanation for this behavior is that the mesh in this region is too coarse, yielding an excessive dissipation which leaves too much energy to be modeled and delays transition to a complete turbulent regime. It is also worth noticing that the 400k mesh transports too much energy to regions far from the plate in the normal direction, supposed to be turbulent-free, which explains the excessive smoothness of the corresponding velocity profiles there. Although it is reported that experimental set-up suffers from leading-edge fluttering, thus increasing the measured energy, this is not enough to explain the big discrepancies found between numerical and experimental results.

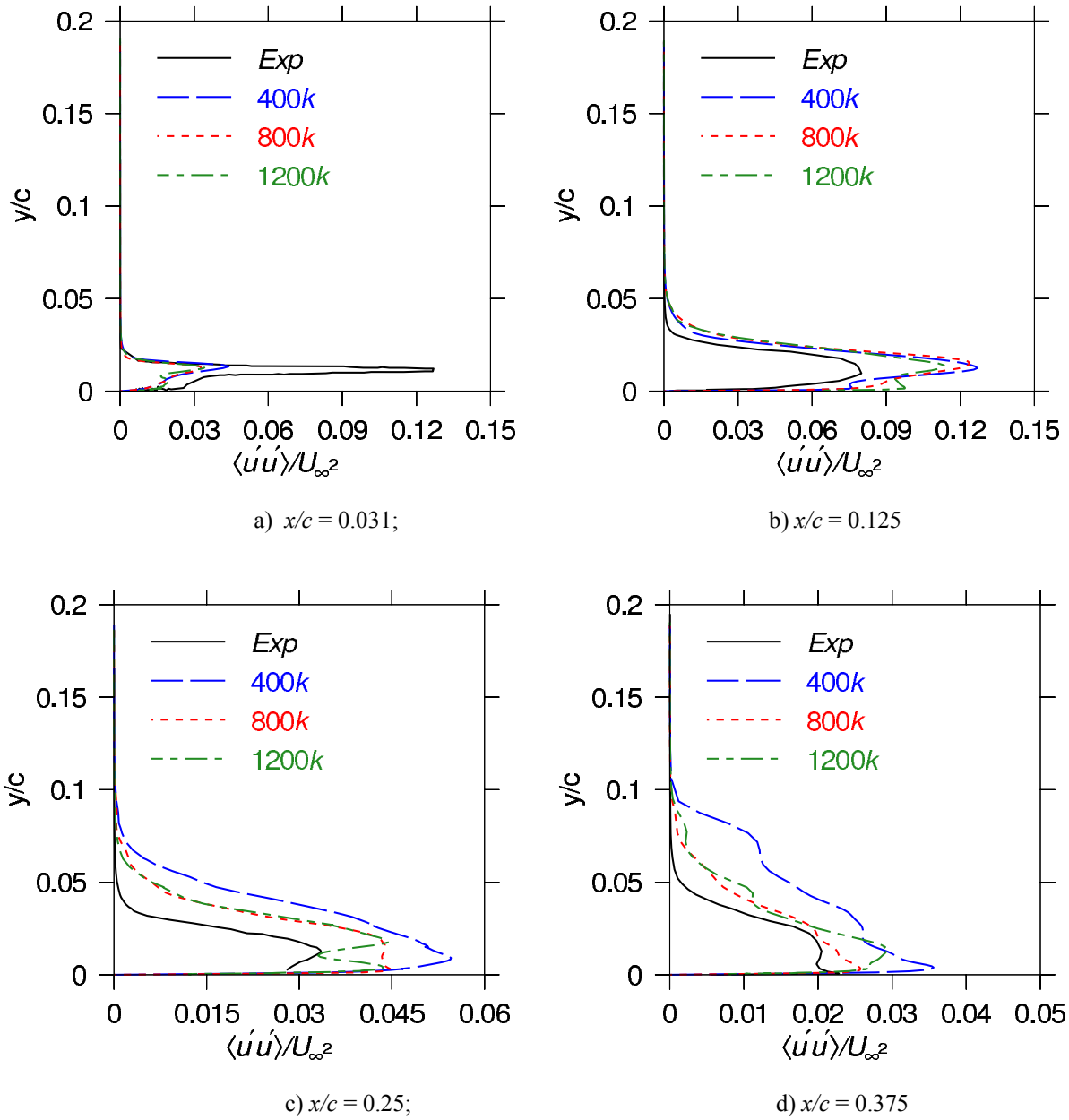

a) $x/c = 0.031$; b) $x/c = 0.125$

c) $x/c = 0.25$; d) $x/c = 0.375$

Figure 6. Profiles of second order statistic R_{11} at: a) $x/c = 0.031$; b) $x/c = 0.125$; c) $x/c = 0.25$; d) $x/c = 0.375$

Figure (7) shows a secondary recirculation bubble inside the main one, which is not captured by any tested RANS models (Collie et al., 2003). This secondary bubble is formed after a relaminarization of the boundary layer in its way back to the leading edge, somewhere in-between the minimum pressure region close to the center of the main recirculation and the higher pressure area close to the forward end of the plate. The adverse pressure gradient there, together with the laminar regime of the boundary layer induces a new separation, thus originating the secondary bubble.

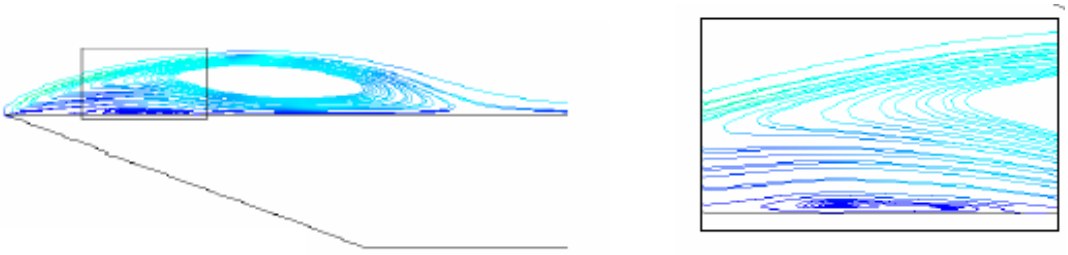

Figure 7. Bubble structure -- Stream traces

One of the reasons why many RANS models fail to capture this structure is their isotropy hypothesis for the turbulent viscosity, which, as we can see from Fig. (8), is not valid at all. It is evident from this same figure that component R_{22} dies much faster than the other two, as wall is approached.

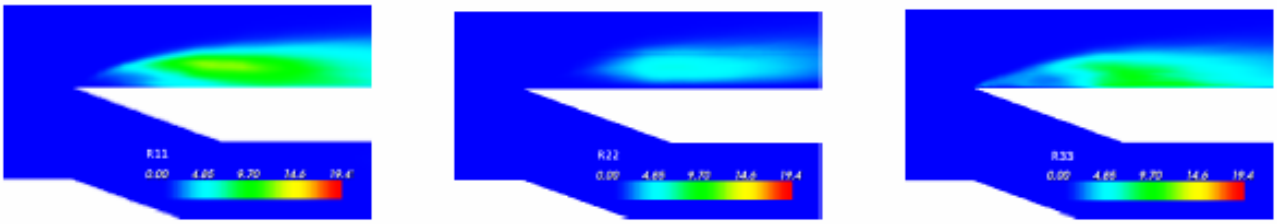

a) R_{11}; b) R_{22}; c) R_{33}

Figure 8. Contours of second order statistics components: a) R_{11}; b) R_{22}; c) R_{33}

The second invariant field can be employed to help identify the coherent vertical structures. It can be defined as

$$Q = \frac{1}{2}(\langle S_{ij} \rangle \langle S_{ij} \rangle - \langle \Omega_{ij} \rangle \langle \Omega_{ij} \rangle) \tag{18}$$

where $\langle S_{ij} \rangle$ and $\langle \Omega_{ij} \rangle$ are defined by Eq. (7) based on the filtered velocity.

Figure (9) is a snapshot of the second invariant field, Q, while Fig. (10) presents contours of vorticity magnitude and vortex tubes. One can see at Fig. (9) the initially spanwise rectilinear structures close to the leading edge evolving towards chaotic ones further downwind, in a mechanism known as coherent vortices breakdown.

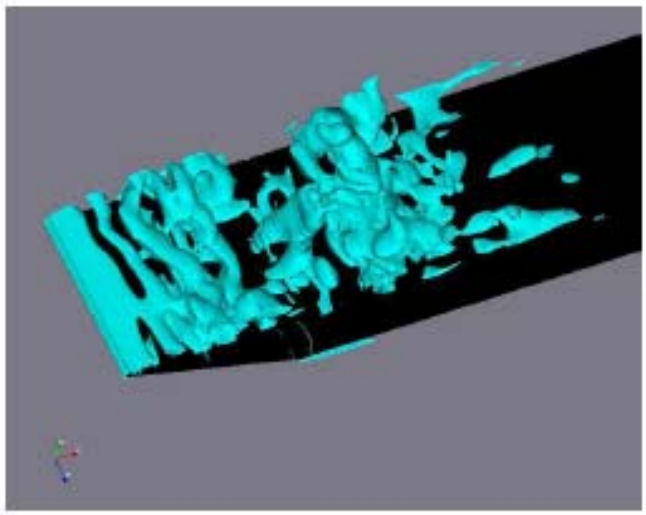

Figure 9. Coherent Vortices according to the Second Invariant criteria.

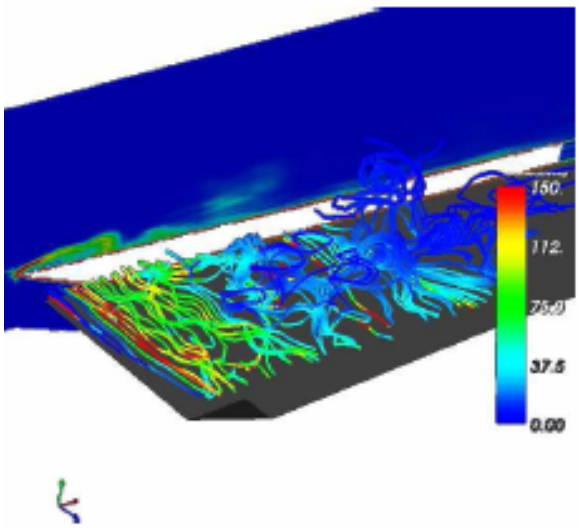

Figure 10. Contours of vorticity magnitude and vortex tubes, colored by vorticity magnitude

It is important to note that, in Fig. (9), what is broken is the coherence of vortical structures according to some criteria - in this case, the *Q* criteria - and not the vortex tubes, which can only terminate in a boundary. As shown in Fig. (10), these tubes in fact never brake, although they also evolve from rectilinear filaments to more disorganized and bended structures as they are transported by the flow.

5. Conclusions

The comparison of the LES and RANS results for a flow over a flat plate at small incidence showed that although a large computational effort is necessary to obtain the solution with LES, several improvements were obtained. The present LES simulations allowed some interesting conclusions on the physical aspects of the flow. It was possible to discriminate between coherence structures that contribute to the averaged field, like the main leading edge bubble, and the non-coherent eddy structures carried by the principal stream, which cancels out in the average process.

The traditional one-equation sub-grid modeling, commonly used in Large-Eddy Simulation has been employed with a mixed "upwind" and central-differences approach. It was shown that it yields good results, even for relatively course meshes. However, the use of a pure central-differences was not possible in the present investigation, since the mesh shrinking towards the inlet boundary would always lead to simulation blow-out. This mixed approach has the inconvenience, however, of requiring prior knowledge of the flow, its turbulent and laminar zones, which no simulation should rely upon.

Therefore a new approach must be developed, where functionalities of both sub-grid modeling and numerical instability treatment are provided.

6. Acknowledgement

The first two authors acknowledge the support awarded to this research by CNPq, and CAPES, as well as UFES and Stanford University for providing computational resources to help develop the present work.

7. References

Collie, S., Jackson, P. S., Gerritsen, M., 2003, “Turbulence Modelling Of The Flat Plate At Shallow Incidence”, Yacht Research Unit, University of Auckland, Private Bag 92019, Auckland, New Zeland.

Cromptom, M. J., e Barret, R. V., 2001, “Investigation Of The Separation Bubble Formed Behind The Sharp Leading Edge Of A Flat Plate At Incidence”, Proc. Instn Mech. Engrs, v. 134 Part G.

Gault, D.E., 1955, “An experimental investigation of regions of separated laminar flow, report NACA TN.

Gault, D.E., 1957, “An investigation at low speed of the flow over a simulated flat plate at small angles of attack using pitot static and hot-wire probes, report NACA TN.

Germano, M, 2000, “On the physical effects of variable filtering lenghts and times in LES”, Advances in LES of Complex Flows, Proceedings of the Euromech Colloquium 412, pp. 3-11, editor Friedrich, R and Rodi, W

Germano, M, 1999, “From RANS to DNS: Towards a Bridging Model”, Direct and Large-Eddy Simulation III, Proceedings of the Isaac Newton Institute Symposium, ERCOFTAC workshop, v. 7, pp. 225-236

Germano, M. and Piomelli, U. and Moin, P. and Cabot, W. H., 1991, “A dynamic subgrid-scale eddy viscosity model”, Phys. Fluids A,, v. 3, pp.1760-1765.

Horiuti, K., 1985, Large eddy simulation of turbulent channel _ow by one-equation modeling, _J. Phys. Soc.Japan_, Vol. 54, No. 8, pp. 2855_2865.

Issa, R., 1985, “Solution of the Implicit Discretized Fluid Flow Equations by Operator-Splitting”, Journal of Computational Physics, v. 62, pp. 40-65.

Sagaut, P., 2002, “Large Eddy Simulation for Incompressible Flows, An Introduction”, Springer, Second Edition.

Sampaio, L. E. B, and Nieckele, A. O., 2004, “Large-Eddy Simulation Of The Turbulent Flow Over A Flat Plate At Small Incidence, ETT3, Proceedings of Escola de Primavera de Transição e Turbulência, Porto Alegre, RS, Brasil

Smagorinsky, J., 1963, General circulation experiments with the primitive equations. I: the basic experiment, Month Wealth, Vol. Rev. 91, No. 3, pp. 99-165.

Spalart, 1994, A one equation turbulence model for aerodynamic flows, La Recherche Aerospatiale, Vol. 1, pp. 5-21.

Weller, H., Tabor, G., Jasak, H., and Fureby, C., 1998, A tensorial approach to computational continuum mechanics using object orientated techniques, Computers in Physics, Vol. 12, No. 6, pp. 620 - 631.

Wilcox, D. C., 1988, “Reassessment of The Scale-Determining Equation For Advanced Turbulence Models”, AIAA Journal, Vol. 26.

8. Copyright Notice

Proceedings of the 11th Brazilian Congress of Thermal Sciences and Engineering -- ENCIT 2006
Braz. Soc. of Mechanical Sciences and Engineering -- ABCM, Curitiba, Brazil,- Dec. 5-8, 2006

Paper CIT06-0281

NUMERICAL INVESTIGATION OF A GALERKIN LEAST-SQUARES MULTI-FIELD FORMULATION FOR VISCOUS FLOWS IN AN AXISYMMETRIC DOMAIN

Flávia Franceschini Zinani[1]
fla@mecanica.ufrgs.br

Sérgio Frey[2]
LAMAC – Laboratory of Applied and Computational Fluid Mechanics
DEMEC – Mechanical Engineering Department
UFRGS – Universidade Federal do Rio Grande do Sul
R. Sarmento Leite, 425, Porto Alegre, RS, Brazil
frey@mecanica.ufrgs.br

Abstract *The investigation of non-Newtonian flows is of paramount relevance in many fields of engineering. Indeed, numerical approximations of non-Newtonian flow models meet some difficulties that may compromise their stability and even prevent physically realistic results. In this article, we exploit the features of a Galerkin least-squares (GLS) finite elements method (FEM) in approximating a multi-field mixed formulation (in extra-stress, velocity and pressure) for isochoric flows of inelastic fluids. We deal about the specific situation when a cylindrical coordinate system is employed to describe non-swirling axisymmetric flows. This treatment adds one degree of freedom to the formulation of 2-D flows, the third normal component of the extra-stress, in the angular direction. We present the mechanical model for such flows, in which the extra-stress tensor is a primal variable, using the equations of mass conservation and momentum balance. We model the stress tensor via a purely viscous constitutive model. We present a GLS approximation which allows the use of equal order finite elements for all variables, overcoming the pressure-velocity and stress-velocity compatibility conditions. The issues of such scheme are expressed by our numerical results. We employ both a Newtonian constant viscosity and a viscosity function given by the Carreau model, which predicts pseudoplastic behavior. We present numerical results for Newtonian and pseudoplastic flows through an axisymmetric contraction. Besides the features of convergence and stability of the GLS approximations, we find good agreement between our results and those from literature. We investigate the role of Carreau's equation parameters and Reynolds number in the flow dynamics near the contraction, interpreting the differences between velocity profiles generated by each fluid with the aid of the extra stress tensor fields, which are directly computed in this formulation.*

.

Keywords: *finite elements, Galerkin least-squares, non-Newtonian fluids, stress-velocity-pressure formulation, axisymmetric flow.*

1. Introduction

The investigation of the flow of non-Newtonian fluids is a subject of a great scope of applications in engineering. Examples of non-Newtonian fluids are products involved in the industries of petroleum, food, polymers, cosmetics, etc. Nevertheless, the difficulties in the study of such flows are many, from the modeling of the fluids non-linear material behavior to the mathematical dealing with the constitutive equations coupled to the flow mechanical models.

The analysis of non-Newtonian flows has always been a challenge for fluid mechanists. Specially since the last decades, an extensive research field, the numerical simulation of non-Newtonian fluid flow, has been found of great interest (Crochet *et al.*, 1984; Owens and Phillips, 2002). Prediction of fluid behavior and detailed flow visualization in complex geometry, mostly not accomplishable in experimental analysis, has stimulated the research in this area.

The mathematical modeling for non-Newtonian flows eventually originates non-explicit constitutive equations for the extra-stress tensor. In the numerical standpoint, this feature is a difficulty, since it becomes unfeasible to deal with only two primal variables (velocity and pressure). It is necessary to compute the extra-stress as an additional variable, which increases the number of functional spaces comprised and also the number of degrees of freedom in the numerical model. In the context of finite element methods, the multi-field discrete model consists of the equations of momentum and mass conservation, plus a general constitutive equation for the extra-stress. In such cases, two compatibility conditions arise between the finite element subspaces for the variables: the classical Babuška-Brezzi condition for velocity and pressure subspaces, and the compatibility condition between the extra-stress and velocity subspaces.

As for the mixed formulations in two variables approach, the classical Galerkin method for incompressible fluids suffers from two major difficulties. First, the need to satisfy Babuška-Brezzi condition (Ciarlet, 1978) in order to achieve a compatible combination of velocity and pressure subspaces in mixed formulations. Further, the inherent instability of central difference schemes in approximating advective dominated equations (Brooks and Hughes, 1982).

---

[1] This author is a graduate student at the Mechanical Engineering Program PROMEC/UFRGS.
[2] Corresponding author.

In the context of the Stokes equations for Newtonian fluids, the Galerkin least-squares method (GLS) (Hughes *et al.*, 1986) was developed to provide stability to the original Galerkin method by adding mesh-dependent terms to Galerkin formulation, which are functions of the residuals of Euler-Lagrange equations evaluated elementwise. Since the residuals of the Euler-Lagrange equations are satisfied by the exact solutions, consistency is preserved in these methods. This idea was also extended to incompressible Navier-Stokes equations in (Franca and Frey, 1992) employing stability parameters designed to optimize stability and convergence.

Multi-field formulations have been analyzed by several researchers, with the aim of constructing formulations that have the properties of stability and convergence, and also establishing the combinations of finite element subspaces which would be effective for each of those formulations. In the context of the Stokes problem, the three-field formulation is already a challenge, being exploited by authors as Marchal and Crochet (1987), Franca and Stenberg (1991), Baranger and Sandri (1992), Baaijens (1998) and references therein, Carneiro de Araújo and Ruas (1998) and references therein, Bonvin *et al*. (2001), among others. A four field formulation known as *Elastic Viscous Split Stress (*EVSS) is an alternative which employs the rate of strain tensor as an additional variable, in order to appease the compatibility conditions between the tensor and velocity subspaces (Guenette and Fortin, 1995; Sun *et al.*, 1996; Gatica *et al.*, 2004). Stabilized formulations based on the Galerkin lest-squares methodology have been employed to multi-field formulations with two main goals. One is the achieving of the necessary stability and convergence for both Newtonian and non-Newtonian models. The other, which may be considered as the main advantage of such methods, is the circumvention of the compatibility conditions between the functional subspaces. Some authors have been successful in achieving these goals via methodologies that may differ in the possible finite elements to employ, in the design of the stability parameter, in the GLS terms which are present in the formulation, in the sign for these terms, and also in the solution algorithms that effectively converge for such formulations. Among the main works one may cite Franca and Stenberg (1991), who give a first GLS formulation for Stokes flows in three fields; Behr *et al.* (1993), who extend the former formulation to inertial flows; and Bonvin *et al.* (2001), who present two GLS formulations for equal-order triangular elements in two dimensional flows.

In this study, we employ a GLS three-field formulation which is based on the stabilized formulations of Behr *et al.* (1993) and Bonvin *et al*. (2001). We have incorporated features of both works to come up with a GLS three-field formulation for isochoric generalized Newtonian flows. It is important to notice that, for flows of pseudoplastic fluids, even if the global Reynolds number of the flow, calculated usually with the fluid's zero-shear-rate viscosity, is low, the asymmetric inertial operator may be locally important in the flows regions where the shear rates are high. Such thing happens because in these regions the viscosity may decrease much, and the advective transport of momentum becomes dominant comparing to the diffusive one. So, for pseudoplastic flows, the stabilization of the advective operator is necessary even for mild Reynolds flows. In addition, the implementation of such formulation for the approximation of non-swirling axisymmetric flows is an innovation. We present some preliminary numerical tests for this formulation which showed good stability features and comprehensive results for lid-driven cavity flows, validating our finite element code for planar flows. For the axisymmetric case, we employ both a Newtonian constant viscosity and a viscosity function given by the Carreau model, which predicts pseudoplastic behavior to approximate flows through an axisymmetric contraction. Besides the features of convergence and stability of the GLS approximations, we find good agreement between our results and those from literature. We investigate the role of Carreau's equation parameters and Reynolds number in the flow dynamics near the contraction, interpreting the differences between velocity profiles generated by each fluid with the aid of the extra stress tensor fields, which are computed directly in this formulation.

2. Mechanical model

The mechanical modeling presented herein concerns a material body $\mathcal{B}$ for which flow is defined by the triple velocity, mass density and stress tensor fields, (**v**, ρ, **T**), and the associated system of contact and body forces, (**t**(**n**), **f**).

Principle of Mass Conservation: The mass of a mechanical body $\mathcal{B}$ does not change with time: Mathematically, this primer principle may be stated as

$$\frac{d}{dt}\int_{\mathcal{P}} \rho dV = 0 \tag{1}$$

where ρ is the mass density, $\mathcal{P}$ is a part of a configuration $\mathcal{B}_t$ of the body $\mathcal{B}$ at the time t. Applying Reynolds transport theorem (Gurtin, 1981) to Eq.(1), and assuming an incompressible fluid model, i.e., constant ρ, a variational principle for isochoric motion may be derived:

$$\int_{\mathcal{P}} q \,\mathrm{div}\,\mathbf{v} dV = 0 \qquad \forall q \in L^2(\mathcal{B}_t) \tag{2}$$

where **v** denotes a virtual velocity field of the flow, and $L^2(\mathcal{B}_t)$, accounts for the functional space of the pressure field.

Principle of Power Expended (Gurtin, 1981): This major dynamic principle is equivalent to the laws of conservation of momentum, formulated in a variational sense. It asserts that, for any part $\mathcal{P}$, with $H^1(\mathcal{B}_t)^{nsd}$ denoting the space of virtual velocities associated to $\mathcal{B}_t$, the power expended on $\mathcal{P}$ by external body forces **f** and surface forces **t**(**n**) is equal to the stress power plus the rate of change of kinetic energy:

$$\int_{\mathcal{P}} \rho \mathbf{f} \cdot \mathbf{v}\, dV + \int_{\partial \mathcal{P}} \mathbf{t}(\mathbf{n}) \cdot \mathbf{v}\, dA = \int_{\mathcal{P}} \mathbf{T} \cdot \mathbf{D}\, dV + \int_{\mathcal{P}} \rho \dot{\mathbf{v}} \cdot \mathbf{v}\, dV \qquad \forall \mathbf{v} \in H^1(\mathcal{B}_t)^{nsd} \tag{3}$$

where **D** is the strain rate tensor, and **T** stands for a second-order symmetric tensor, the stress tensor. The first term on the right side of Eq. (3) accounts for the stress power, i.e., the power expended due to the work of internal contact forces, and the second is the rate of change of kinetic energy.

3. Material Behavior

Although Cauchy theorem (Gurtin, 1981) describes the form of contact forces for any continuous body, the way in which materials deform or flow when submitted to any dynamic condition is not stated by this theorem. Besides, the behavior of continuous bodies submitted to arbitrary conditions differs drastically, due to the material dependent relation between contact forces within the body upon its motion and deformation. This relation is described by the rheological constitutive equations, which are mathematical models for the stress tensor, **T**. These equations are constructed in order to obey certain axiomatic principles (Astarita and Marrucci, 1974): determinism, local action and frame indifference. A functional dependence of **T** with the strain rate tensor, **D**, is acceptable in view that this could represent a frame indifferent model, as **D** is frame indifferent (Gurtin, 1981). The most general linear relation between **T** and **D** tensors may be given as the following isotropic function:

$$\mathbf{T} = (-P + \varpi \operatorname{div} \mathbf{v})\mathbf{I} + 2\mu \mathbf{D} \tag{4}$$

where μ is the fluid viscosity and the parameter ϖ is related to the scalar function κ, called bulk coefficient of viscosity. For an incompressible fluid, the divergence of the velocity field is null, and Eq. (4) may be written as function of a mean pressure, *p*, the mean of the normal components of **T,** as:

$$\mathbf{T} = -p\mathbf{I} + 2\mu \mathbf{D} = -p\mathbf{I} + \boldsymbol{\tau} \tag{5}$$

where $\boldsymbol{\tau}$ is the extra-stress tensor.

The practically observed phenomena of shear-thinning, viscoplasticity and shear-thickening in pure shear flows give rise to the construction of the generalized Newtonian models (Bird *et al.*, 1987). These models apply the empirical viscosity functions which fit the behavior stress versus strain rate in viscometric flows for modeling the stress tensor. They maintain the mathematical structure of a Newtonian fluid, in the form that $\mu = \eta(\dot{\gamma})$, being the non-Newtonian viscosity of the fluid, which is a function of the strain rate, $\dot{\gamma}$. For flows in general, $\dot{\gamma}$ is defined as a Frobenius norm of **D**:

$$\dot{\gamma} = (2II_{\mathbf{D}})^{1/2} = (2 \operatorname{tr} \mathbf{D}^2)^{1/2} \tag{6}$$

An example of an empirical model for the viscosity is the Carreau model (Bird *et al.*, 1987), employed to model the behavior of pseudoplastic fluids. This model is given by the following constitutive equation:

$$\frac{\eta(\dot{\gamma}) - \eta_\infty}{\eta_0 - \eta_\infty} = \left[1 + (\lambda \dot{\gamma})^2\right]^{\frac{n-1}{2}} \tag{7}$$

The Reynolds number for a generalized Newtonian fluid may be defined, for a general characteristic viscosity, η_c, which depends on the model employed, as follows,

$$\mathrm{Re} = \frac{\rho L u_0}{\eta_c} \tag{8}$$

in which *L* and u_0 are the characteristic length and velocity of the flow. Note that for the Newtonian model $\eta_c = \mu$.

For viscoelastic fluids, i.e., fluids with memory, the most common models are the differential constitutive equations (Astarita and Marrucci, 1974; Bird *et al.*, 1987). In general, they are given as functions of the objective derivatives (Astarita and Marrucci) of the extra stress tensor, in order to maintain the necessary feature of frame indifference. Among these viscoelastic models, two are of great importance in numerical simulation of non-Newtonian flows, due to their widespread employment: the Maxwell-B and the Oldroyd-B models, given as:

$$\boldsymbol{\tau} + \lambda \overset{\nabla}{\boldsymbol{\tau}} = 2(\mu_1 \mathbf{D} + \mu_2 \overset{\nabla}{\mathbf{D}}) \tag{9}$$

where λ and μ_i are the material functions for these models, with μ_2=0 for the Maxwell-B model. The symbol ∇ represents the upper convected derivative of the respective variable. In numerical approximations, the Oldroyd-B constitutive equation (Eq. (9)) is sometimes decomposed in the following form (Crochet and Keunings, 1982):

$$\begin{aligned} &\boldsymbol{\tau} = \boldsymbol{\tau}_1 + \boldsymbol{\tau}_2 \\ &\boldsymbol{\tau}_1 + \lambda_1 \overset{\nabla}{\boldsymbol{\tau}}_1 = 2\mu_1 \mathbf{D} \\ &\boldsymbol{\tau}_2 = 2\mu_2 \mathbf{D} \end{aligned} \tag{10}$$

Thus, the model is viewed as the sum of an elastic ($\boldsymbol{\tau}_1$) portion of $\boldsymbol{\tau}$ and a viscous and one ($\boldsymbol{\tau}_2$).

4. Multi-field finite element formulations

The formulation that we are about to present assumes problems defined on a bounded domain $\Omega \subset \Re^{nsd=2,3}$, with a polygonal or polyhedral boundary Γ, formed by the union of Γ_g, where Dirichlet conditions are imposed, and Γ_h, subjected to Neumann boundary conditions. As usual, $L^2(\Omega)$, $L_0^2(\Omega)$, $H^1(\Omega)$, $H_0^1(\Omega)$ stand for Hilbert and Sobolev functional spaces (Ciarlet, 1978). Finally, $\|\ ,\ \|_0$ denotes the $L^2(\Omega)$ norm and $\|\ ,\ \|_{0,K}$ the $L^2(\Omega_K)$ one.

Multi-field formulations are those that employ as primal variables, besides the usual velocity (**u**) and pressure (p), any of the fields of extra stress ($\boldsymbol{\tau}$), strain rate (**D**) or velocity gradient (grad **u**). In this section we make some basic comments on mixed multi-field formulations for isochoric flows and also present the stabilized formulation employed in this study. We use the following notation: C_h is a partition of the closed domain $\bar{\Omega}$ into elements, R_k denote the polynomial spaces of degree k , and $(\cdot\ ,\ \cdot)$ represents the L^2 inner product (Ciarlet, 1978).

The Galerkin formulation for the isochoric flow of a Newtonian fluid may be stated as: given **f**, find the triple ($\boldsymbol{\tau}^h$, p^h, $\mathbf{u}^h$)$\in \mathbf{W}^h \times P^h \times \mathbf{V}^h$ such as:

$$B_1(\boldsymbol{\tau}^h, p^h, \mathbf{u}^h; \mathbf{S}, q, \mathbf{v}) = F_1(\mathbf{S}, q, \mathbf{v}), \quad (\mathbf{S}, q, \mathbf{v}) \in \mathbf{W}^h \times \mathbf{V}^h \times P^h \tag{11}$$

where

$$\begin{aligned} &B_1(\boldsymbol{\tau}, p, \mathbf{u}; \mathbf{S}, q, \mathbf{v}) = \frac{1}{2\mu}(\boldsymbol{\tau}, \mathbf{S}) - (\mathbf{D}(\mathbf{u}), \mathbf{S}) + \rho([\operatorname{grad}\mathbf{u}]\mathbf{u}, \mathbf{v}) + (p, \operatorname{div}\mathbf{v}) - (\boldsymbol{\tau}, \mathbf{D}(\mathbf{v})) + (\operatorname{div}\mathbf{u}, q) \\ &F_1(\mathbf{S}, q, \mathbf{v}) = -(\mathbf{f}, \mathbf{v}) \end{aligned} \tag{12}$$

introducing the finite element subspaces:

$$\begin{aligned} P^h &= \{q \in C^0(\Omega) \cap L_0^2(\Omega) \,\big|\, q_{|K} \in R_l(K), K \in C_h\} \\ \mathbf{V}^h &= \{\mathbf{v} \in H_0^1(\Omega)^{nsd} \,\big|\, \mathbf{v}_{|K} \in R_k(K)^{nsd}, K \in C_h\} \\ \mathbf{W}^h &= \{\mathbf{S} \in C^0(\Omega)^{nsd \times nsd} \cap L^2(\Omega)^{nsd \times nsd} \,\big|\, \mathbf{S}_{ij} = \mathbf{S}_{ji}, i = 1, \ldots, nsd \,\big|\, \mathbf{S}_{|K} \in R_j(K)^{nsd \times nsd}, K \in C_h\} \end{aligned} \tag{13}$$

In the context of the Stokes problem, i.e., when the inertial term is negligible, Franca and Stenberg (1991) proposed a GLS formulation which is stable for any combinations of finite elements. They established the convergence and stability lemmas for such formulation. Behr *et al.* (1993) improved these results presenting a stabilized formulation very similar to this former, but also incorporating the inertia terms which had been neglected by Franca and Stenberg (1991). Behr *et al.* (1993) used a design of the stability parameter which incorporates the local Reynolds number and the mesh size parameter h_K, as in Franca and Frey (1992).

A mixed formulation which is largely employed (Baaijens, 1998) is the one based on a linear version of the Oldroyd-B model, using the split of Eq. (10). The model is linear in view that the parameter λ_1 in Eq. (10) is null. The Galerkin finite element formulation for such model is given as: find the triple ($\boldsymbol{\tau}_1^h$, p^h, $\mathbf{u}^h$)$\in \mathbf{W}^h \times P^h \times \mathbf{V}^h$ such as

$$B_2(\boldsymbol{\tau}_1^h, p^h, \mathbf{u}^h; \mathbf{S}, q, \mathbf{v}) = F_2(\mathbf{S}, q, \mathbf{v}), \quad (\mathbf{S}, q, \mathbf{v}) \in \mathbf{W}^h \times P^h \times \mathbf{V}^h \tag{14}$$

with

$$B_2(\boldsymbol{\tau}_1, p, \mathbf{u}; \mathbf{S}, q, \mathbf{v}) = \frac{1}{2\eta_p}(\boldsymbol{\tau}_1, \mathbf{S}) - (\mathbf{D}(\mathbf{u}), \mathbf{S}) + \rho([\text{grad}\,\mathbf{u}]\mathbf{u}, \mathbf{v}) + 2\eta_s(\mathbf{D}(\mathbf{u}), \mathbf{D}(\mathbf{v})) + (\boldsymbol{\tau}_1, \mathbf{D}(\mathbf{v})) - (p, \text{div}\,\mathbf{v}) + (\text{div}\,\mathbf{u}, q)$$
$$F_2(\mathbf{S}, q, \mathbf{v}) = -(\mathbf{f}, \mathbf{v}) \tag{15}$$

Bonvin *et al.* (2001) prove uniqueness and existence of the problem of Eq. (14), neglecting the inertial term ($\rho = 0$). They also establish the stability lemma for the finite element formulation, which depends on two compatibility conditions, one between the finite element subspaces of stress and velocity, and other between the subspaces of velocity and pressure. The former is the classical Babuška-Brezzi condition for the Stokes problem. Bonvin *et al.* (2001) derive Galerkin least-squares methods that circumvent those compatibility conditions, adding terms to the forms B_2 and F_2, which correspond to the least squares forms of the residual equations. These formulation is valid for equal-order triangular elements.

In this study, we employed a GLS formulation based on the Galerkin scheme of Eq. (14), based on the stabilized formulations of Behr *et al.* (1993) and Bonvin *et al.* (2001): Find the triple $(\boldsymbol{\tau}_1{}^h, p^h, \mathbf{u}^h) \in \mathbf{W}^h \times P^h \times \mathbf{V}^h$ such as:

$$B_{GLS}(\boldsymbol{\tau}_1^h, p^h, \mathbf{u}^h; \mathbf{S}, q, \mathbf{v}) = F_{GLS}(\mathbf{S}, q, \mathbf{v}) \;\; \forall\, (\mathbf{S}, q, \mathbf{v}) \in \mathbf{W}^h \times P^h \times \mathbf{V}^h \tag{16}$$

where

$$B_{GLS}(\boldsymbol{\tau}_1, p, \mathbf{u}; \mathbf{S}, q, \mathbf{v}) = B_2(\boldsymbol{\tau}_1, p, \mathbf{u}; \mathbf{S}, q, \mathbf{v}) + \sum_{K \in C_h} \tau(\text{Re}_K)([\text{grad}\,\mathbf{u}]\mathbf{u} - 2\eta_s\,\text{div}\,\mathbf{D}(\mathbf{u}) + \text{grad}\,p - \text{div}\,\boldsymbol{\tau}_1,$$
$$[\text{grad}\,\mathbf{v}]\mathbf{u} - 2\eta_s\,\text{div}\,\mathbf{D}(\mathbf{v}) + \text{grad}\,q - \text{div}\,\mathbf{S})_K + 2\eta_p\beta\left(\frac{1}{2\eta_p}\boldsymbol{\tau}_1 - \mathbf{D}(\mathbf{u}), \frac{1}{2\eta_p}\mathbf{S} - \mathbf{D}(\mathbf{v})\right) \tag{17}$$
$$F(\mathbf{S}, q, \mathbf{v})_{GLS} = F_2(\mathbf{S}, q, \mathbf{v}) + \sum_{K \in C_h} \tau(\text{Re}_K)(\mathbf{f}, [\text{grad}\,\mathbf{v}]\mathbf{u} - 2\eta_s\,\text{div}\,\mathbf{D}(\mathbf{v}) + \text{grad}\,q - \text{div}\,\mathbf{S})_K$$

where $\tau(\text{Re}_K)$ is the stability parameter, given as suggested by Franca and Frey (1992) and Behr *et al.* (1993):

$$\tau(\text{Re}_K) = \frac{h_K}{2|\mathbf{u}|_\infty}\xi(\text{Re}_K)$$
$$\xi(\text{Re}_K) = \begin{cases} \text{Re}_K, 0 \le \text{Re}_K < 1 \\ 1\ , \text{Re}_K \ge 1 \end{cases}$$
$$\text{Re}_K = \frac{m_k |\mathbf{u}|_\infty h_K}{4\eta_p(\dot{\gamma})/\rho} \tag{18}$$
$$m_k = \min\{1/3, 2C_k\}$$
$$\sum_K h_K^2 \|\text{div}\,\mathbf{T}\|_{0,K} \le C_k \|\mathbf{T}\|_0^2$$

REMARK 1: The differences between our formulation (Eq. (16)) and the formulation of Behr *et al.* (1993) are that ours represents a truly Galerkin least-squares formulation, in the sense that the stabilizing terms are added as the least squares forms of the residual equations; and that the term containing the solvent viscosity η_s is also present. The differences between the formulation of Bonvin et. al. (2001) and ours are the design of the stability parameter and that our formulation also accounts for inertia effects. In addition, this formulation is designed to circumvent the compatibility conditions between all functional subspaces even for quadrilateral elements, allowing the use of structured meshes.

REMARK 2: In this paper we give emphasis to the case of non-swirling axisymmetric flows. The geometric models are made in a two-dimensional manner. The Cartesian components of the frame of reference are x_1, the axial component, and x_2, the radial component. Symmetry in the angular direction of x_3 is assumed, so that all velocity and body force components in this direction are null, and so are all the derivatives of velocity, pressure and forces. Nevertheless, the third normal component of the stress and strain rate tensors may not be assumed as nulls. Being so, in two-dimensional planar problems there are six degrees of freedom per node, namely u_1, u_2, p, τ_{12}, τ_{11} and τ_{22}, and in axisymmetric problems they are seven: u_1, u_2, p, τ_{12}, τ_{11}, τ_{22} and τ_{33}.

5. Numerical results

We implemented the formulation of Eq. (16) in the finite element code named FEM, developed by our laboratory group. We present some results for 2-D isochoric flows which were obtained using meshes of quadrilateral bilinear

elements for all variables ($Q_1/Q_1/Q_1$ - $\boldsymbol{\tau}_1$-p-$\mathbf{u}$). We have also obtained similar results for the combinations of elements $Q_2/Q_1/Q_2$ and $Q_1/Q_1/Q_2$, which are not shown here. To solve the resulting algebraic system of equation, we have implemented a Newton-based method (Dalquist and Bjorck, 1969).

5.1. Newtonian flow in a square lid-driven cavity

In this section, we present the results obtained with formulation of Eq. (16) for Newtonian flow in a lid-driven cavity flow (see Fig. 1 for the problem statement), using a 40x40 mesh, which the problem statement is given as in Fig. 1(a).

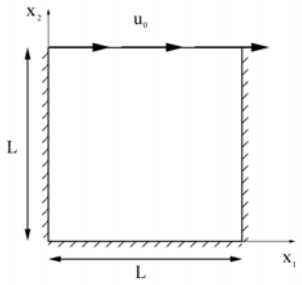

Figure 1. Problem statement for the lid-driven cavity.

We tested three different cases: Stokes flow where the Newtonian viscosity was split in two parts, $\eta_p=\eta_s=0.5$; flows with inertia $\eta_p>\eta_s$; flows with inertia with $\eta_s=0$. For the first two cases, the results were compared to those of Behr *et al.* (1993) and they were found to be in agreement (Zinani and Frey, 2005). The third case was deeply investigate in order to validate our FEM code. The Reynolds number was calculated with the constant viscosity $\eta=\mu$.

Reynolds numbers from 1 to 1000 were approximated. Here we show some results for Re=1, Re=100 and Re=400. These results are compared with some authors: Ghia *et al.* (1982), Screiber and Keller (1983), Ku and Hatziavramidis (1985), Sivaloganathan and Shaw (1988), Jurjevic (1999), for the horizontal velocity and pressure profiles in the line $x_1=0.5L$ and for the eye of vortex position. For all Reynolds number the fields of extra-stress, pressure and velocity were stable and physically comprehensive, as depicted in Figure 2.

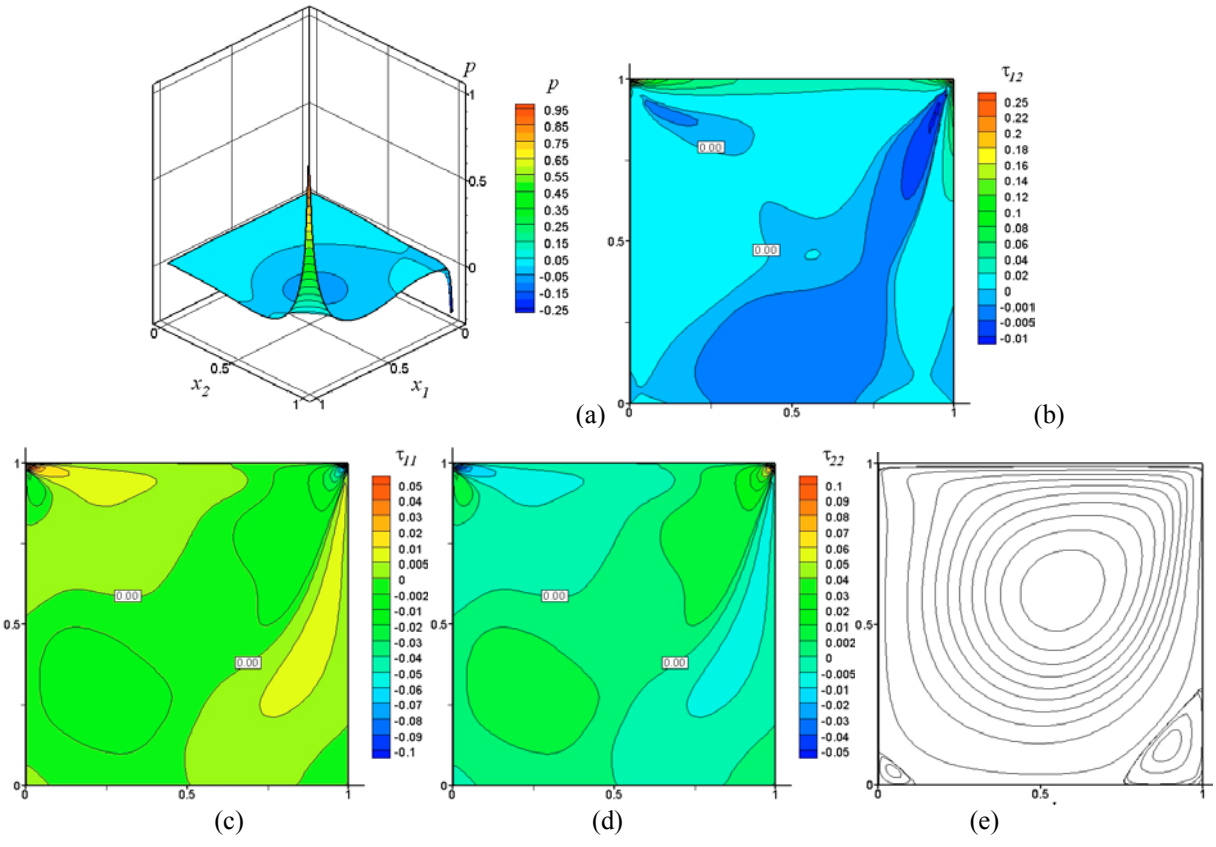

Figure 2. (a) pressure elevation, (b) contours of τ_{12}, (c) contours of τ_{11}, (d) contours of τ_{22}, (e) streamlines

Figure 3 shows our results of the horizontal velocity u_1 versus x_2 in x_1=0.5L, for Re=1 and Re=400, comparing these results with the literature.

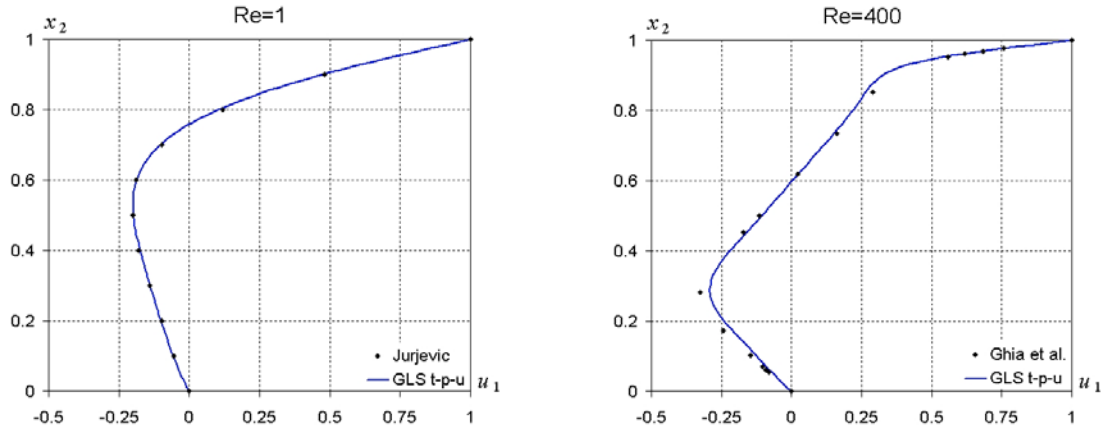

(a) (b)

Figure 3. Horizontal velocity versus position in x_2 (a) Re=1, (b) Re=400.

In Tab. 1 we compare the eye of the vortex position with results found in literature, for Re=100 and Re=400.

Table 1. Eye of the vortex position

Re	Reference	x_1	x_2
100	Screiber and Keller, 1983	0.61667	0.74167
	Ku and Hatziavramidis, 1985	0.62109	0.73752
	Sivaloganathan and Shaw, 1988	0.61	0.73
	FELAB **τ**-*p*-**u** GLS	**0.618**	**0.736**
400	Ku and Hatziavramidis, 1985	0.55463	0.60415
	Sivaloganathan and Shaw, 1988	0.56	0.61
	Jurjevic, 1999	0.564	0.6055
	FELAB **τ**-*p*-**u** GLS	**0.561**	**0.605**

All the numerical results for the lid-driven cavity Newtonian flow agreed with the literature not differing plus than 1% in all cases investigated.

5.2. Pseudoplastic flow through a sudden axisymmetric contraction

In this section we present results for Newtonian and non-Newtonian flows trough an axisymmetric 4:1 sudden contraction. We employed the same Galerkin Least-Squares formulation from Eq. (16), developed in a cylindrical coordinate system with null angular velocity and null gradients in the angular direction. The characteristic length of the problem is the outflow's diameter, L=D_0, the characteristic velocity is the outflow mean velocity, u_0, and the characteristic viscosity is η_0 for non-Newtonian flows and μ for Newtonian flows. The solvent viscosity η_s is set as zero for all cases. The polymeric viscosity function used to predict fluid's shear thinning was the Carreau model (Eq. (7)), for which we varied the parameters λ, n and η_0, setting η_∞=0. The problem statement is given as in Fig. 4, we use only half of problem's actual domain to build the geometric model.

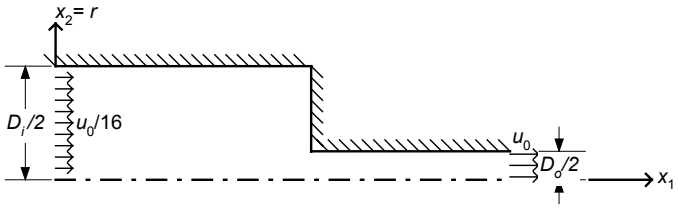

Figure 4. Problem statement: flow through an axisymmetric contraction

We based our investigation in the paper of Kim *et al.* (1983). In this paper, a dimensionless Carreau number, Cu, is defined in order to accomplish for the effects of varying the parameter λ:

$$\mathrm{Cu} = \frac{\lambda u_0}{D_0/2} \tag{19}$$

Kim *et al.* (1983) investigate the flows of Carreau fluid for very low Reynolds numbers, Re=0 to Re=2. In this paper we extend this investigation to a grater range of Re, varying it from Re=0 to Re=10. The Carreau numbers tested were Cu=0.01, Cu=1 and Cu=100, the former predicting the most pseudoplastic behavior because the viscosity shear-thins at lower levels of shear rates. The parameter n tested were n=0 (Newtonian), n=0.4 and n=0.2, where the former is the most pseudoplastic one. A mesh dependency analysis was performed over four meshes, comprised of 1934 to 6266 elements. The results were found to be mesh independent for any mesh from 4368 elements, and the results presented herein correspond to that 4368 finite element mesh, with 4653. In following figures, the components of the frame of reference are dimensionless as: $r^*=x_2/D_0$ and $x_1^*=x_1/D_0$.

Figure 5 deals with the Carreau fluids with 5.(a) Cu=10, n=0.2 and 5.(b) Cu=100, n=0.2, both with Re=2. We show the contours of u_1^*, where $u_1^*=u_1/u_0$, superposed by the flow streamlines. The differences between the axial velocity fields are easily perceived: for lower Cu, this field is similar to that of a Newtonian fluid, in which the axial velocity increases quadratically with the distance from the wall, and experiments a smooth acceleration in the contraction. For the high Cu flow, axial velocity gradients occur close to the walls, and are almost null in the symmetry line, characterizing the flat velocity profile typically pseudoplastic. In the contraction, advective acceleration happens more harshly, because high deformation rates reduce the viscosity in this region and allow the quick acceleration of the fluid. The streamlines show that, for the low Cu, a mild recirculation appears in the contraction corner, as in Newtonian low Reynolds number flows. For the high Cu the recirculation does not occur, the behavior is similar to high Reynolds number Newtonian flows.

Figure 6 and shows the contours for the component τ_{12} (dimensionless as $\tau_{12}^*=(\tau_{12}L)/u_0$) of the extra-stress tensor obtained as a variable of the numerical problem. Figure 7 shows the field of u_2^*, where $u_2^*=u_2/u_0$. One may notice the lower values of τ_{12} and higher values of u_2 in the contraction are obtained for the most pseudoplastic flows, due to the low viscosity that appear in regions of high deformation rates, reducing considerably the resistance to flow. High deformation rates in the contraction promote a great viscosity thinning near to the its corner, and high viscosity gradients in the same place, which may even compromise numerical stability locally, but not compromising the global results. In Fig. 8 we depict the dimensionless viscosity fields, $\eta^*=\eta/\eta_0$, obtained for those cases. These fields showed the expected features of low viscosity in the high strain rate regions, close to the walls of the most narrow duct, with such features being more pronounced in the high Cu flow.

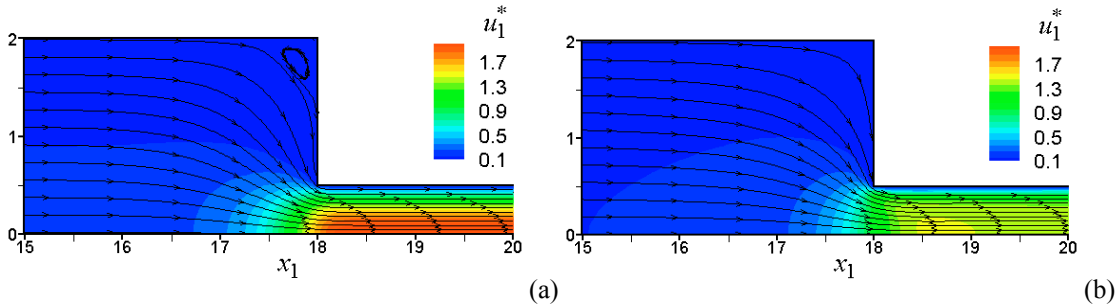

Figure 5: Axial velocity contours and streamlines, Re=2, (a) Cu=10, n=0.2 and (b) Cu=100, n=0.2.

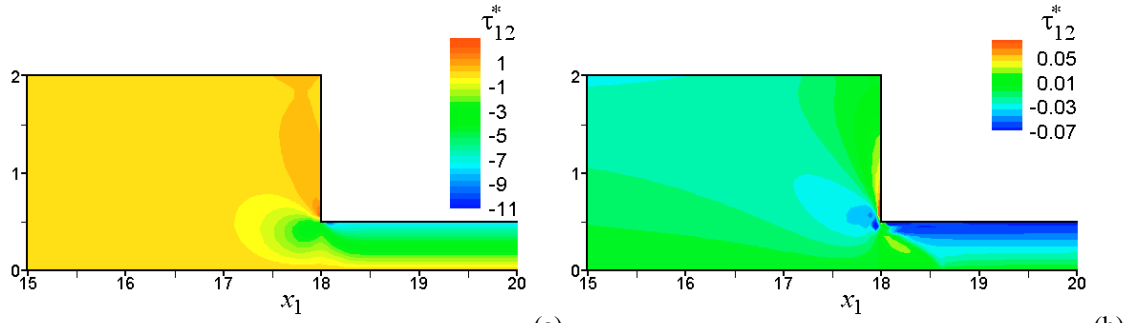

Figure 6: Shear component of the extra stress tensor, Re=2, (a) Cu=10, *n*=0.2 and (b) Cu=100, *n*=0.2.

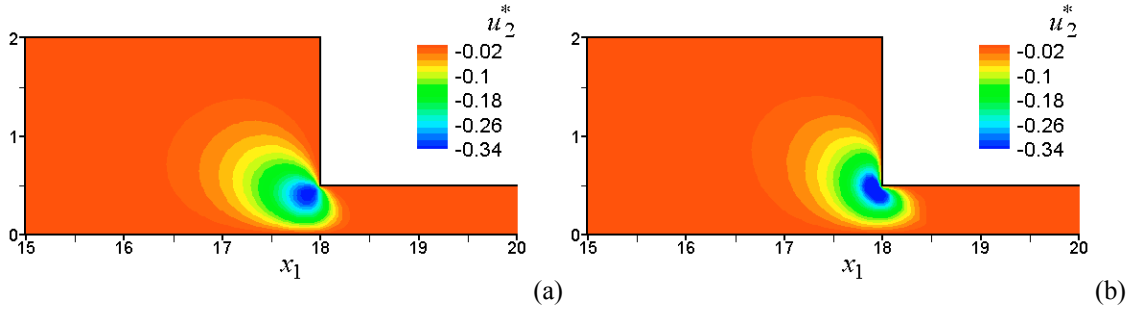

Figure 7: Radial velocity contours and streamlines, Re=2, (a) Cu=10, *n*=0.2 and (b) Cu=100, *n*=0.2.

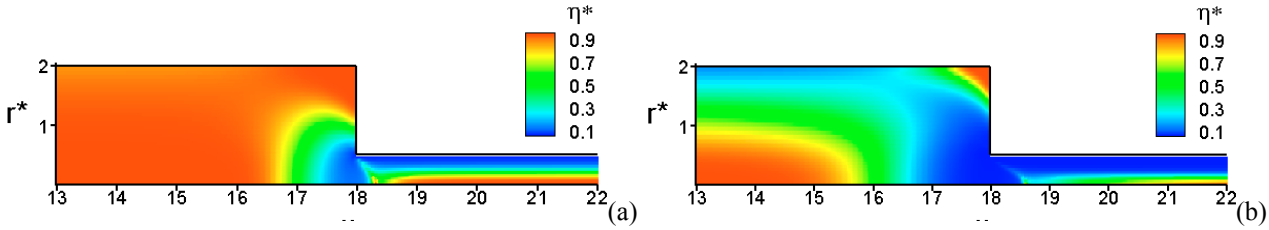

Figure 8: Viscosity contours, Re=2, (a) Cu=10, *n*=0.2 and (b) Cu=100, *n*=0.2.

In the following graphics we investigate the effects of inertia, through the Reynolds number, and the fluid's material behavior, through the Carreau number, in the flow dynamics.

In Fig. 9 we investigate the axial velocity profile in the contraction plane. In Fig. 9.(a) we investigate different Carreau numbers for the same *n*=0.2 and Re=2, plotting this profile for Cu=0 (Newtonian), Cu=10 and Cu=100. In Fig. 9.(b) we investigate different *n* for the same Cu=100 and Re=2, *n*=0 (Newtonian), *n*=0.2 and *n*=0.4. In both cases we observe that the most shear-thinning fluid tend to form a more flattened profile. In Fig. 9.(c) we investigate different Reynolds number for Cu=100 and *n*=0.2, Re=0, Re=2, and Re=10. We observe that, as for Newtonian flows, the increase of the Reynolds number tends to flatten the velocity profile. The tendency of a non-centerline maximum velocity may be seen in the high Reynolds flow (Re=10).

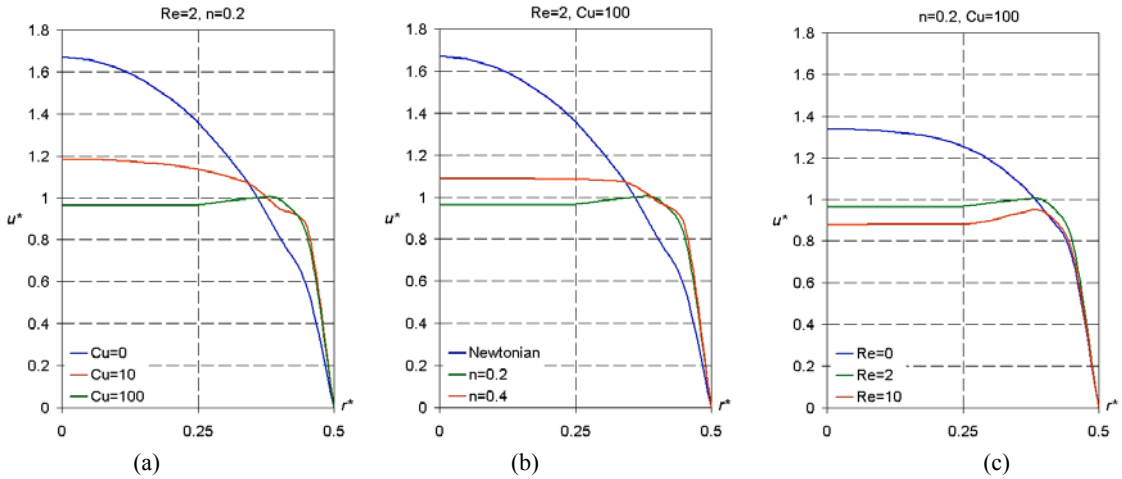

Figure 9. Axial velocity profile in the contraction.

In Fig. 10 we investigate the axial velocity profile in the symmetry line along the domain, for the same cases as above: Fig. 10.(a) n=0.2 and Re=2, Fig. 10.(b) Cu=100 and Re=2, Fig. 10.(c) Cu=100 and n=0.2. We observe that pseudoplasticity decreases the value of the centerline axial velocity. This is understood when we remember the flattened velocity profile that occurs due to shear-thinning, different from the parabolic profile of Newtonian flows. Although, when comparing pseudoplastic fluids with the same Cu and n, in part (c), we notice that the Reynolds number does not have much influence on the value of the centerline velocity, which was expected due to the velocity profile depends only on the fluids parameters.

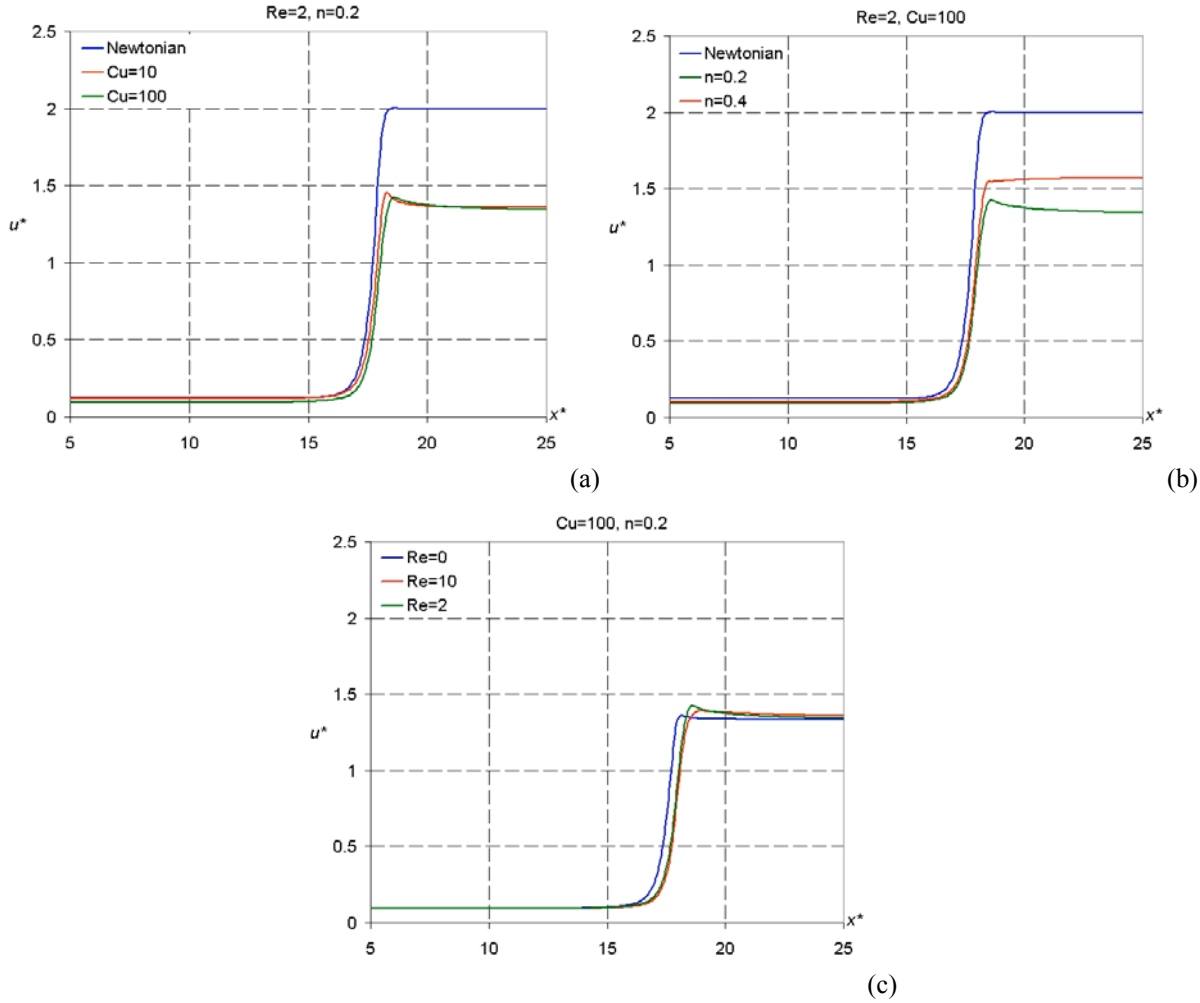

Figure 10. Axial velocity profile in the symmetry line.

In Fig. 11 we investigate the pressure drop in the symmetry line along the domain, for similar cases as above: Fig. 11.(a) n=0.2 and Re=2, Fig. 11.(b) Cu=100 and Re=2, Fig. 11.(c) Cu=100 and n=0.2. In part (a), we may observe the pressure levels of different orders of magnitude when comparing pseudoplastic to Newtonian flows. Pseudoplasticity reduces the total pressure drop. Another interesting feature is that the slope of the pseudoplastic curves differ much from the Newtonian in the region downstream the contraction, i.e., where deformation by shear is more severe and shear-thinning is more pronounced. The pressure drop in the region upstream the contraction is very similar for Newtonian and pseudoplastic fluids, because in this region the Carreau number is locally small (remember that the Carreau number was defined using the velocity and lengths from the most narrow duct). In part (b) the pressure drops for the high Cu fluids are shown, and we observe that the levels of pressure fall much lower than the Newtonian fluid flowing with Re=2, and that they are even lower for the most shear-thinning fluid, with n=0.2. In part (c) the total pressure drop is compared for two equally pseudoplastic fluids flowing with different Reynolds numbers, showing that the increase of Re reduces the pressure drop as expected and similarly to Newtonian flows.

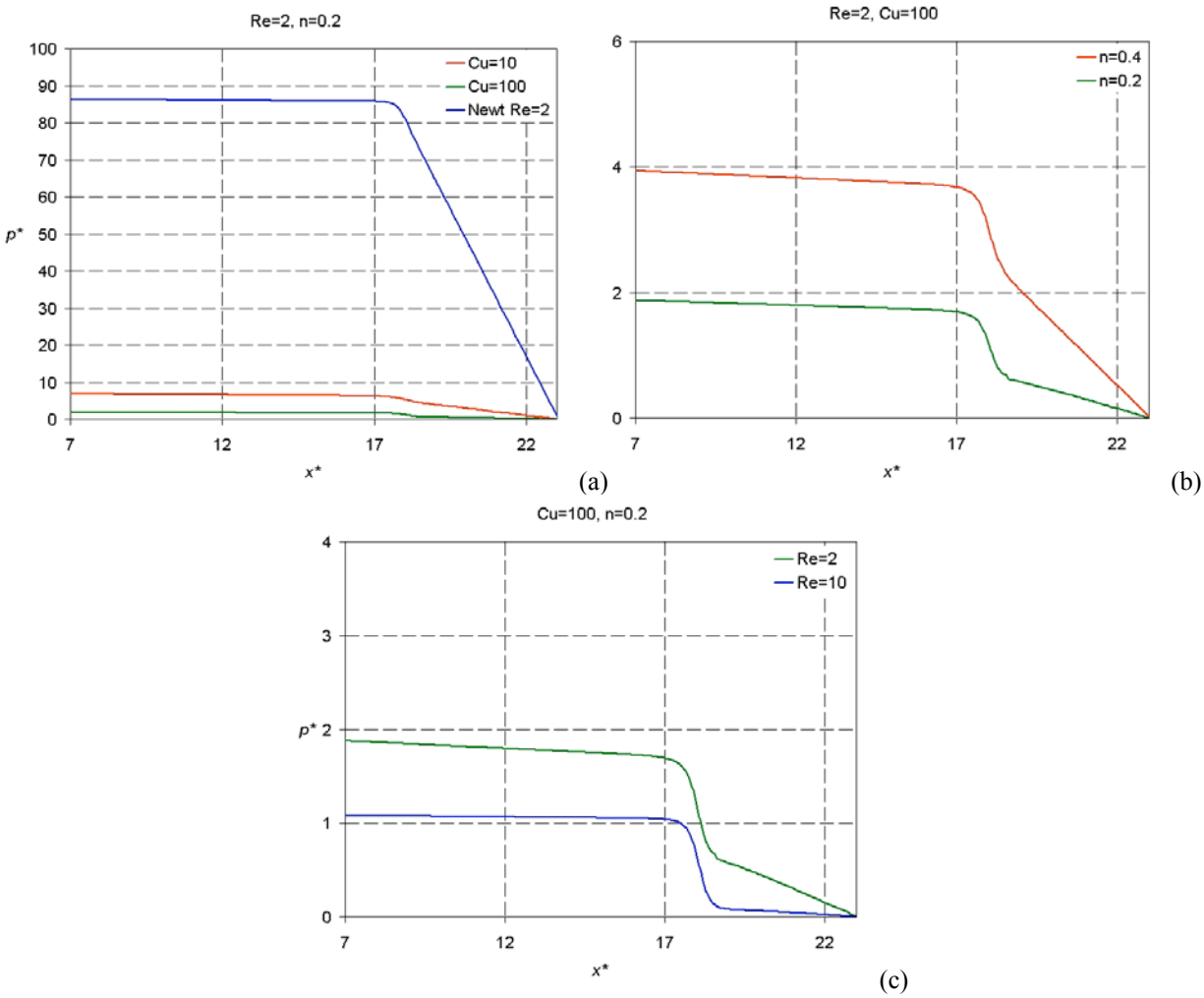

Figure 11. Pressure profile in the symmetry line.

6. Final remarks

We have presented some comprehensive results for Newtonian and generalized Newtonian flows using a three-field finite element formulation stabilized by a GLS scheme. We employed that formulation to approximate non-swirling flows in an axisymmetric domain. We used equal-order finite elements, which were able to circumvent the Babuška-Brezzi conditions required in the classical Galerkin method. We studied the features of pseudoplastic fluids flowing through an axisymmetric contraction, investigating the effects of shear-thinning in the flow dynamics. We found that the main effects that occur due to viscosity reduction are the flattening of the axial velocity profile in the contraction plane and the friction decrease, features that may be accomplished by increasing the Reynolds or Carreau numbers, or by decreasing the *n* parameter in the fluid model. This study is still in progress and we intend to proceed on investigations in the mathematical analysis of the formulation presented, and in the extension of this GLS formulation to non-linear viscoelastic models as Maxwell-B and Oldroyd-B.

7. Acknowledgements

F. S. F. Zinani and S. Frey thank the CAPES doctoral grant and the CNPq researcher grant No. 50747/1993-8, respectively. We also acknowledge MCT/CNPq for the financial support provided by project No. 475432/2003-7.

8. References

Astarita, G., Marrucci, G., 1974, “Principles of non-Newtonian fluid mechanics”, McGraw-Hill, Great Britain.

Baaijens, F. P. T., 1998, “Mixed finite element analysis for viscoelastic flow analysis: a review”, J. Non-Newtonian Fluid Mech., 79, pp. 361-385.

Baranger, J., Sandri, D., 1992, “A formulation of Stokes´s problem and the linear elasticity equations suggested by the Oldroyd model for viscoelastic flow”, M^2AM Anal. Numér., v. 26, pp. 331-345.

Behr, M., Franca, L.P., Tezduyar, T.E., 1993, "Stabilized finite element methods for the velocity-pressure-stress formulation of incompressible flows", Comput. Methods Appl. Mech. Engrg., v. 104, pp. 31-48.

Bird, R. B. Armstrong, R. C. Hassager, O., 1987, "Dynamics of polymeric liquids". v.1, John Wiley and Sons, U.S.A.

Bonvin, J., Picasso, M., Stenberg, R., "GLS and EVSS methods for a three-field Stokes problem arising from viscoelastic flows", Comput. Methods. Appl. Mech. Engrg., v. 190, pp. 3893-3914.

Brooks, A.N., Hughes, T.J.R. , 1982 "Streamline Upwind/Petrov-Galerkin formulations for convective dominated flows with particular emphasis on the incompressible Navier-Stokes equations", Comput. Methods Appl. Mech. Engrg. Vol. 32, pp. 199-259.

Carneiro de Araújo, J. H., Ruas, V., 1998, "A stable finite element method for the axisymmetric three-field Stokes system", Comput. Methods in Applied Mech. Eng. 164, pp. 267-286.

Ciarlet, P. G., 1978, "The finite element method for elliptic problems", North Holland, Amsterdam.

Crochet, M. J., Davies, A. R., Walters, K., 1984, "Numerical simulation of non-Newtonian flow". Rheology Series, v. 1. Elsevier, Netherlands.

Crochet, M.J., Keunings, R., 1982, "Finite element analysis of die swell of a highly elastic fluid". J. Non-Newtonian Fluid Mech., 10, pp. 339-356.

Dahlquist, G., Bjorck, A., "Numerical Methods", Prentice-Hall, Englewood Cliffs, NJ, USA, 1969.

Franca, L. P., Stenberg, R., 1991, "Error analysis of some Galerkin least squares methods for the elasticity equations", SIAM J. Numer. Anal., 28(6), pp. 1680-1697.

Franca, L.P. and Frey, S., 1992, "Stabilized finite element methods: II. The incompressible Navier-Stokes equations", Comput. Methods Appl. Mech. Engrg., Vol. 99, pp. 209-233.

Gatica, G.N., González, M., Meddahi, S., 2004, "A low-order mixed finite element method for a class of quasi-Newtonian Stokes flows. Part I: a priori error analysis", Comput. Methods Appl. Mech. Engrg., v. 193, pp. 881-892

Ghia, U., Ghia, K. N., Shin, C. T., 1982. "Hi-Re solution for incompressible flow using the Navier-Stokes equationsand the multigrid method". J. Comput Physics. vol. 48, pp. 387-411.

Guénette, R., Fortin, M, 1995, "A new mixed finite element method for computing viscoelastic flows", J. Non-Newtonian Fluid Mech., v. 60 pp. 27-52.

Gurtin, M. E., 1981, "An introduction to continuum mechanics", Academic Press, U.S.A.

Hughes , T. J. R. Franca, L.P. Balestra, M., 1986 "A new finite element formulation for computational fluid dynamics: V. Circumventing the Babuška-Brezzi condition: A stable Petrov-Galerkin formulation of the Stokes problem accommodating equal-order interpolations". Comp. Meths. Appl. Mech. Eng. 59.

Jurjevic, R., 1999. "Modelling of two-dimensional laminar flow using finite element method". International Journal for Numerical Methods in Fluids, vol. 31, pp. 601-626.

Kim, M. E., Brown, R. A., Armstrong, R. C., 1983, "The roles of inertia and shear-thinning in flow of an inelastic liquid through an asisymmetric contraction". Journal of Non-Newotonian Fluid Mechanics, vol. 13, pp.341-363.

Ku, H. C., Hatziavramidis, 1985. "Solutions of the two dimensional Navier-Stokes equations by Chebysher expansion methods". Computer & Fluids, vol. 13, pp. 99-113.

Marchal, J. M., Crochet, M. J., 1987, "A new mixed finite element for calculating viscoelastic flow", J. Non-Newtonian Fluid Mech., 26, pp. 77-114.

Owens, R.G. ,Phillips, T.N.; Computational Rheology; Imperial College Press; 2002, 436 pp.

Ruas, V. et *al.*, 2005, "Multi-field finite element methods with discontinuous pressures for axisymmetric incompressible flow", J. Comput. Appl. Math.

Schreiber, R., Keller, H.B., 1983. "Driven cavity flows by efficient numerical techniques". Journal of Computational Physics. vol. 49, pp. 310-333.

Sivaloganathan, S., Shaw, G. J., 1988. "A Multigrid method for recirculating flows", International Journal for Numerical Methods in Fluids. vol 8, pp. 417-440.

Sun, J., Phan-Thien, N., Tanner, R.I., 1996, "An adaptive viscoelastic stress splitting scheme and its applications: AVSS/SI and AVSS/SUPG", J. Non-Newtonian Fluid Mech., v. 65 pp. 79-91.

8. Responsibility notice

The authors are the only responsible for the printed material included in this paper.

Proceedings of the 11th Brazilian Congress of Thermal Sciences and Engineering -- ENCIT 2006
Braz. Soc. of Mechanical Sciences and Engineering -- ABCM, Curitiba, Brazil, Dec. 5=8, 2006

Paper CIT06-294

ANÁLISE DO COMPORTAMENTO DAS ONDAS DE PRESSÃO NO COLETOR DE ADMISSÃO DE UM MOTOR DE COMBUSTÃO INTERNA COM A PRESENÇA DO RESSONADOR.

Alberto José Dutary Rodriguez
Ramón Molina Valle
Universidade Federal de Minas Gerais
Departamento de Engenharia mecânica
Av. Antônio Carlos, 6627
31270-901 – Belo Horizonte – MG – Brasil.
dutary@ig.com.br

Ramon@demec.ufmg.br

Sérgio de Morais Hanriot
Pontifícia Universidade Católica de Minas Gerais / PUC - MG
Rua Dom José Gaspar 500, Coração Eucarístico
CEP: 30535-610 - Belo Horizonte – MG – Brasil.
hanriot@pucminas.br

Resumo. Este trabalho descreve uma metodologia de análise experimental do processo de admissão de ar em motores de combustão interna com o objetivo de determinar as condições em que a massa de ar admitida pode ser influenciada. No presente trabalho é realizado um experimento que simula a condição de um motor mono- cilindro. A metodologia proposta permite fazer um estudo experimental da influência dos fenômenos gerados pelo movimento alternativo das válvulas de admissão e do pistão, com a finalidade de melhorar a eficiência volumétrica do motor. Uma análise dos principais parâmetros que modificam a propagação da onda de pressão no coletor, tais como geometria de coletores, volume instantâneo do cilindro, rotação do motor e utilização de dispositivos ressonadores, são analisados nos resultados. Os resultados mostram que é possível conseguir um aumento de rendimento volumétrico do motor modificando a amplitude e a fase da onda de pressão gerada pelo movimento das válvulas e dos pistões com o uso de um ressonador. Foram realizados testes com as válvulas e os pistões em movimento na presença de um ressonador. O ressonador foi colocado alternadamente em quatro posições distintas, a partir da porta da válvula de admissão. Uma análise espectral da onda de pressão com a inserção de um ressonador na admissão mostra a condição em que ocorre um máximo ou mínimo de vazão, permitindo analisar as condições que levam a um aumento de massa para dentro do cilindro.

Palavras chaves: Motor de combustão interna, Escoamento pulsante, Ressonador

1. Introdução

O crescimento da indústria automotiva e da comercialização de automóveis com motores de combustão interna identificaram a necessidade de um estudo com relação ao melhoramento do desempenho desses motores. Atualmente, estão sendo propostas diversas alternativas de melhoria em seu desempenho, passando por turbo - compressores, sobre - alimentadores, injeção direta de combustível e a compactação do conjunto moto - propulsor, na tentativa de atingir maior flexibilidade em regime de cargas intermediárias.
Dessa forma, após análise do conjunto moto – propulsor destes automóveis e um melhor conhecimento de suas características, nesse trabalho foi priorizado o estudo do aumento do rendimento volumétrico desses motores com o uso de ressonadores. Os motores de quatro válvulas por cilindro tiveram o seu conceito inicial aplicado em carros de corrida de admissão natural, no início dos anos 60, até os motores atuais carros de fórmula 1. Muitas dessas inovações tecnológicas foram transferidas para a produção seriada, que possui configurações e potências específicas bem abaixo. Os métodos e procedimentos de estudo visando ao aumento de potência dos motores mudaram consideravelmente nas últimas décadas, com o emprego principalmente de técnicas de simulação do comportamento termo-fluido-dinâmico, bem como de inovações tecnológicas capazes de estudar aspectos de geometria e visualização experimental do escoamento do fluido. A otimização das condições de trabalho dos motores de combustão interna passa, necessariamente, por uma análise profunda das diversas variáveis envolvidas no processo.

2. APARATO EXPERIMENTAL

2.1 Banco de Fluxo

O aparato experimental denominado banco de fluxo é fonte de pesquisa de estudos. Benson (1982) foi um dos primeiros na utilização de aparato similar. Nishio et al (1991) apresentaram trabalho experimental em um equipamento que denominaram de "Simulados de Pulsos". Hanriot (2001) apresenta uma revisão completa sobre tal aparato experimental e resultados experimentais obtidos no banco de fluxo comparados com uma análise numérica fluidodinâmica. Na Figura 1 podem ser observados o motor ligado ao tanque de equalização de pressão e o ressonador conectado por mangueiras ao tubo de admissão.

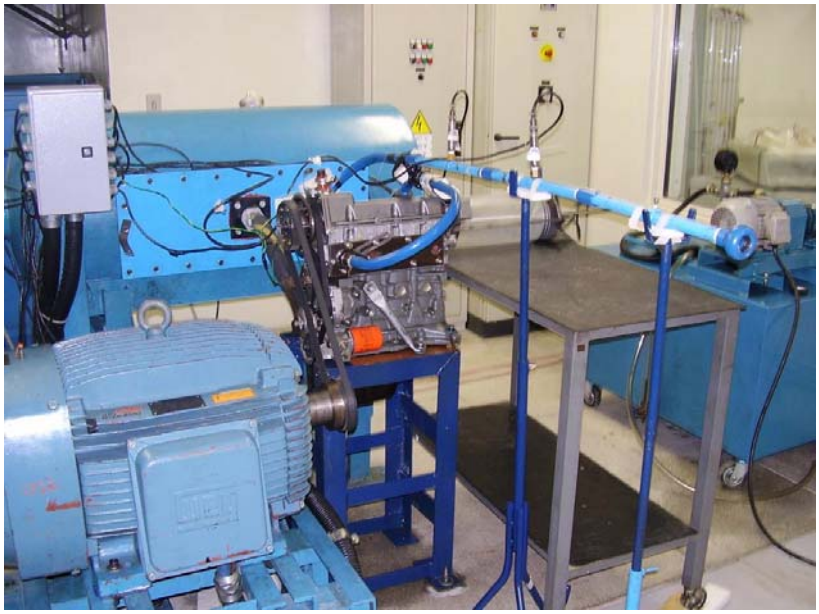

Figura 1 – Vista geral do banco de fluxo

A importância básica para o uso de tal aparato está na sua capacidade de produzir pulsos de pressão através do movimento das válvulas de admissão. Algumas características da simulação de um motor em operação em condição real são diferentes. O banco de fluxo em regime não estacionário possui características que devem ser observadas: É composto basicamente de um soprador (ventilador) de grande porte, um tanque de equalização, medidores de vazão, sistema de aquisição de dados e sistema de controle. O insuflador está ligado ao corpo de prova por meio de um conjunto de tubulações, contendo válvulas de acionamento mecânico ou elétrico, e por dois tanques de equalização e amortecimento de oscilações de pressão. O conjunto de válvulas permite a regulagem da vazão requerida e a escolha do sentido de escoamento do ar (se insuflado ou aspirado).

2.1.1 Transdutores de Pressão

Dois tipos de transdutores de pressão foram utilizados: um de tipo piezo resistivo, capaz de medir sinais dinâmicos; outro de coluna em U de mercúrio, para determinação diferencial da pressão no tanque de equalização. As medições efetuadas pelo manômetro de coluna em U seguiram as normas ASME. Os tradutores de pressão (piezo resistivos) foram inseridos de maneira tal a permitir uma análise dos fenômenos oriundos do movimento das válvulas. A inserção pode ser vista na Figura 7. Como a porta da válvula de aspiração representa o ponto mais importante na determinação do efeito de sintonia ("tunning"), um sensor foi instalado na porta da válvula. O acoplamento do sensor ao tubo foi realizado por meio de um anel cilíndrico externo, que possui como finalidade principal manter o transdutor na posição desejada.

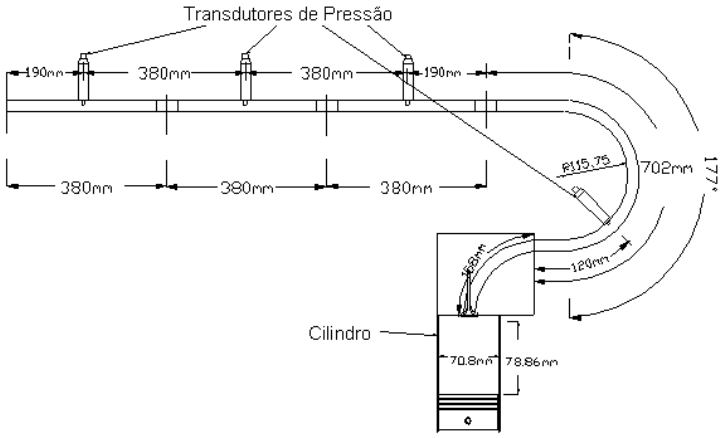

Figura 1 - Posicionamento dos Transdutores no Tubo de Admissão.

2.1.2 Medidores de Vazão

Para aumentar a faixa de medição, o banco de fluxo é composto de dois medidores de fluxo laminar, sendo um com faixa de 0 a 100 L/s e outro de 0 a 200 L/s.

2.1.3 Medidor de Rotação

O posicionamento do sensor de rotação e fase será fixado tangencialmente à polia fônica da árvore de comando das válvulas. O sistema também é capaz de identificar a posição instantânea da árvore pela identificação de uma posição angular específica gerada pela disposição geométrica dos dentes da polia fônica.

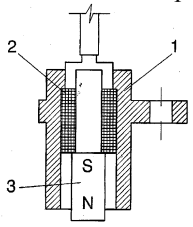

Figura 2- Sensor de Rotação do Motor

(1) Sensor; (2) Bobina; (3) Imã permanente

A Figura 3, mostra a relação do sensor de rotação e fase em conexão com a polia dentada.

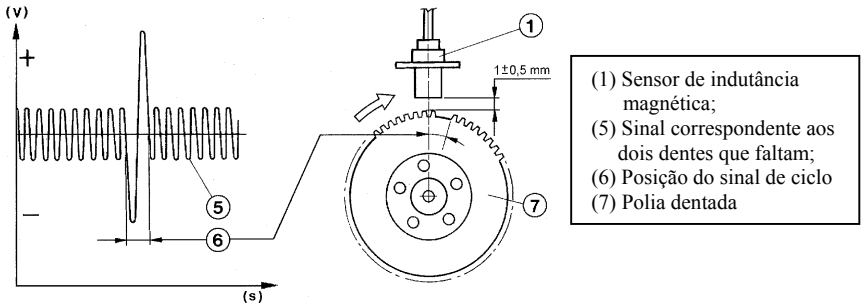

Figura 3 - Posicionamento do Sensor de Rotação e Fase

O espaço dos dentes removidos é utilizado pelo programa do sistema de aquisição para reconhecer a posição inicial da árvore em cada ciclo. Portanto, a área instantânea de escoamento da válvula, como função da posição angular da árvore fica definida em cada instante, permitindo a utilização dos modelos de escoamento para determinação do rendimento volumétrico teórica do sistema simulado. O processo de propagação das ondas de pressão em um conduto reto, em direção ao cilindro, permite a análise do pulso de pressão sem a influência dos outros condutos de admissão dos demais cilindros. Nesta situação, consegue-se determinar a atenuação do pulso de pressão no intervalo de tempo (ciclo) em que a válvula de admissão permanece fechada.

3. METODOLOGIA

3.1 Determinação das Dimensões do Conduto de Admissão

Um tubo de diâmetro interno de 25 mm (DIN 2440 1) foi selecionado devido à área interna ser bem próxima da área de entrada no cabeçote e o que possibilitou fazer uma curva semelhante ao coletor de admissão do motor completo, obtendo assim uma freqüência crítica de 3210,12 Hertz". A freqüência do experimento, para considerar o escoamento unidimensional, não deverá superar a freqüência crítica de 3210,12 Hertz. Esta análise para determinação do conduto de admissão é justificável também pela complexidade da geometria do sistema de admissão nos automóveis, em razão da pouca disponibilidade de espaço para o conjunto moto-propulsor no compartimento dianteiro dos automóveis. Como se desejam adotar coletores de comprimento similar aos usados em automóveis, adotou-se um tubo de comprimento de 2000 mm.

3.2 Levantamento dos Coeficientes de Descarga Estáticos

Para a análise experimental dos coletores de admissão torna-se necessário a determinação experimental dos coeficientes de descarga estáticos. O coeficiente de descarga da válvula de admissão foi obtido através de experimentos em banco de fluxo estacionário. A técnica consiste em aplicar uma diferença de pressão constante entre a entrada e a saída da válvula, sendo a mesma ligada ao reservatório de equalização de pressão. Nessa condição, a válvula de aspiração tem sua posição variada do mínimo ao máximo de abertura. Usualmente, a abertura mínima inicial é igual a 1 mm. O coeficiente de descarga neste experimento foi obtido pela área de referencia fornecida pela Fiat, em função da razão de levante pelo diâmetro da válvula (l/D_v) Para o levantamento dos dados experimentais do coeficiente de descarga, foram realizados dois experimentos. No primeiro obtêm-se a vazão mássica em função do ângulo do eixo comando de válvulas de admissão, mostrado na Fig. (4). No segundo, obtêm-se os dados do curso da válvula de admissão em função do ângulo do eixo comando de válvulas, mostrado na Fig. (5).

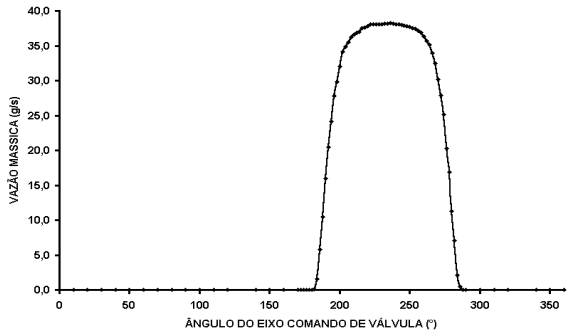

Figura 4. Vazão Mássica em função do Ângulo do Eixo Comando de Válvulas

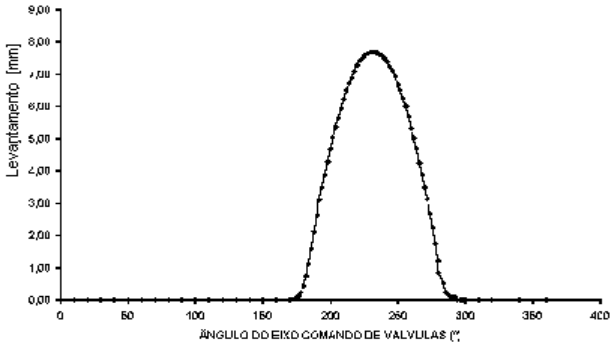

Figura 5. Levantamento da Válvula em função do Ângulo do Eixo Comando de Válvulas

A técnica consiste em aplicar uma diferença de pressão constante entre a entrada e a saída da válvula, sendo a mesma conectada ao reservatório de equalização de pressão. Dessa forma os coeficientes de fluxo são determinados para as várias aberturas da válvula de admissão utilizando os parâmetros experimentais na equação de vazão para escoamento compressível em uma restrição, dada pela expressão:

$$\dot{m} = \frac{C_D A_R P_0}{(RT_0)} \left(\frac{p_T}{p_0}\right)^{1/\gamma} \left\{ \frac{2\gamma}{\gamma - 1} \left[1 - \left(\frac{p_T}{p_0}\right)^{(\gamma-1)/\gamma} \right] \right\}^{1/2} \qquad (1)$$

Esta equação é derivada de uma consideração do escoamento unidimensional, compressível, isentrópico, em que os efeitos do escoamento real são incluídos através do coeficiente de descarga C_D, obtido experimentalmente. O escoamento do ar está relacionado com a pressão e temperaturas de estagnação, p_o e T_o, respectivamente, imediatamente antes da válvula (porta da válvula), com a pressão estática, p_T, imediatamente após a restrição e uma área de referência, A_R, caracterizada por um valor de projeto (Heywood, 1988). Através dos valores da elevação da válvula de admissão obtidos em função da vazão e usando a Eq. (1), determinou-se o coeficiente de descarga, assumindo um diâmetro de referência de 31,0 mm, fornecido pela FIAT Automóveis.

.

3.3 *Estudo do Comportamento das Ondas de Pressão no Coletor de Admissão, com a Presença do Ressonador, Considerando a Influência do Movimento das Válvulas e do Pistão*

Este estudo envolve a inserção de uma cavidade acústica (ressonador) em diferentes pontos do sistema de admissão de um motor de combustão interna. Esta análise tem o objetivo de verificar o efeito da absorção das ondas de pressão pelo ressonador na dinâmica do escoamento de ar no coletor. Na prática, os ressonadores de Helmholtz podem ser utilizados para a redução de níveis de ruído nos coletores de admissão e para melhorar o rendimento volumétrico numa faixa de rotação do motor. No último caso o ressonador ajusta os pulsos de pressão que chegam a porta da válvula no momento em que a mesma está em processo de fechamento, com a finalidade de aumentar a pressão no final da admissão o rendimento volumétrico. Neste trabalho é de interesse particular o estudo da influência dos ressonadores no efeito de sintonia (*Tunning*) dos pulsos de pressão. O ressonador de Helmholtz utilizado é mostrado na Figura 6. Este dispositivo permite variar os parâmetros geométricos, de forma a permitir a modificação da freqüência de ressonância. O dispositivo é construído em acrílico, com formato cilíndrico. O ressonador foi inserido em quatro posições a partir da entrada do conduto de admissão (120, 720, 1100 e 1480 mm) e ajustado para a freqüência de ressonância de 20 Hz, correspondente a 1200 rpm

Figura 6 - Ressonador de Helmholtz Utilizado

As Figura 7 e 8 mostram a montagem completa com as posições em que foi inserido o ressonador. Como mostrado por Nishio (1991), Kostun (1994) e Hanriot (2001), espera-se que a melhor posição seja aquela localizada mais próxima da válvula.

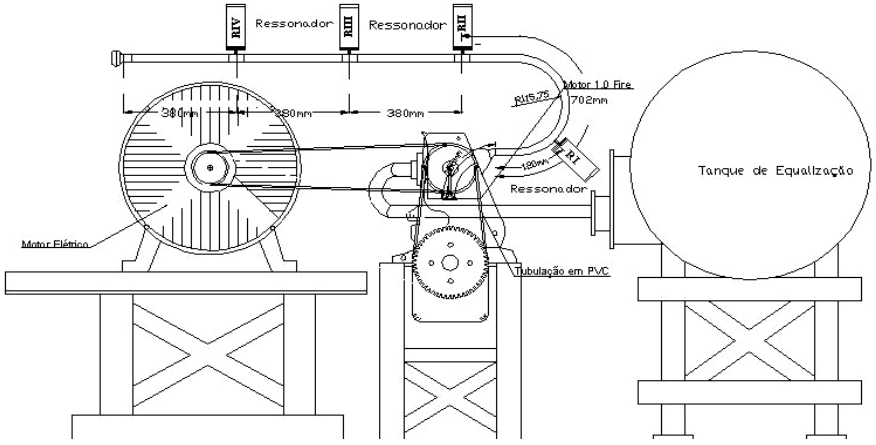

Figura 7. - Ressonador de Helmholtz no Tubo Reto

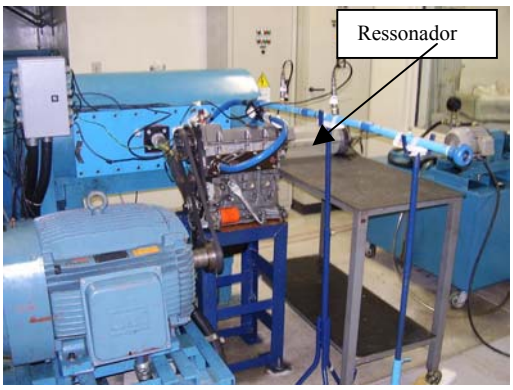

Figura 8 - Posicionamento do Ressonador e detalhes do tubo de admissão

3.4 Analise dos Resultados Experimentais

Para se obter os parâmetros necessários para os cálculos do diferencial de pressão eficaz, responsável pela vazão de ar dentro do cilindro foi utilizada a análise de Fourier como ferramenta. O espectro de linha obtido na análise de Fourier é uma representação gráfica das amplitudes de pressão dos harmônicos da onda de pressão. Dada pela equação

$$P_{RMS} = \sqrt{\left(P_0^2 + \tfrac{1}{2}P_f^2 + \tfrac{1}{2}P_1 + \tfrac{1}{2}P_2^2 + \ldots\ldots \tfrac{1}{2}P_n^2\right)} \qquad (2)$$

Onde P_0 = valor médio das pressões.
P_f = pressão na freqüência fundamental, obtida na análise de Fourier.
P_n = amplitude do harmônico, também obtida do espectrum.
n = harmônico.

Desta forma, o gradiente de pressão eficaz é dada por

$$\Delta P_{RMS} = P_{P1_{RMS}} - P_{PLENUM} \qquad (3)$$

onde

$P_{P1_{RMS}}$ =pressão eficaz na porta da válvula.

P_{PLENUM} =pressão eficaz dentro do cilindro.

ΔP_{RMS} =gradiente de pressão eficaz.

4. RESULTADOS

A Figura 9 mostra as curvas de vazão obtidas com o motor sem e com a presença do ressonador nas quatro posições descritas n metodologia sendo que cada posição representa uma distância diferente da porta da válvula de admissão do motor. A figura 8 mostra as curvas de vazão obtidas com o motor sem ressonador e com a presença do ressonador nas quatro posições descritas anteriormente, sendo que cada posição representa uma distância diferente da porta da válvula de admissão do motor. Nela pode se observar que as maiores vazões de dão quando o ressonador esta mais próximo da válvula posição RI e o efeito vai diminuindo na medida que se afasta desta sendo a menor vazão mostrada na figura, na posição RIV.

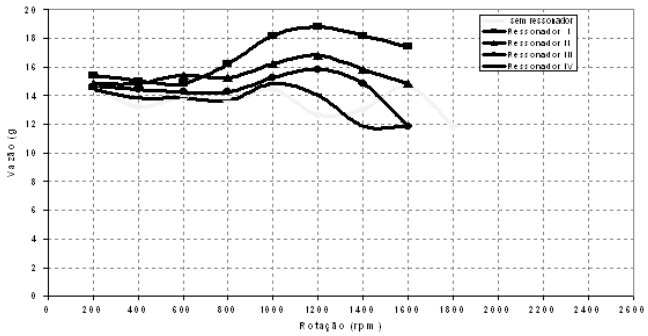

Figura 9 - Comportamento da vazão para as quatro posições do ressonador

Na figura 10 são apresentadas as curvas de vazão geradas para as configurações testadas com e sem ressonador na posição RI do Motor. Observa-se que a vazão para a configuração com ressonador é maior que sem ressonador em toda a faixa de rotação testada. Na prática, esta é uma técnica já usada pelas montadoras para aumentar rendimento

volumétrico e diminuir o ruído do motor em determinadas faixas de rotação. Geralmente esta técnica é utilizada para baixas rotações do motor, onde o rendimento volumétrico torna-se crítico devido ao projeto dos coletores de admissão a favorecer condições de altas rotações.

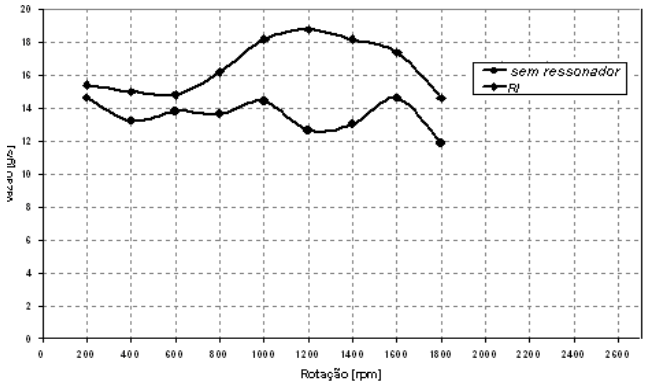

Figura 10 - Comportamento das curvas de vazão, com e sem o ressonador.

A Figura 10 mostra também que a curva de vazão da configuração motor com ressonador torna-se mais estável, diferente da curva obtida sem ressonador, que apresenta flutuações em toda a faixa de rotação. Isto é o resultado de menores flutuações de pressão no coletor de admissão com a presença do ressonador. O comportamento das pressões dentro do ressonador, para as rotações de 400, 600 e 1200 rpm, é apresentado na Figura 10, onde a maior intensidade das flutuações de pressão significa maior atuação do ressonador (maior eficiência). Observa-se, portanto, na figura que para a rotação de 1200 rpm, rotação para a qual o ressonador foi ajustado, as maiores amplitudes de pressão são obtidas. Desta forma, amplitudes pequenas de pressão devem ser observadas dentro do ressonador na medida em que a rotação do motor se distancia da rotação de 1200 rpm, mostrando a menor influência do ressonador (menor eficiência), a medida que se afasta da freqüência de ressonância. Isto ocorre na Figura 11 para as rotações de 600 e 400 rpm.

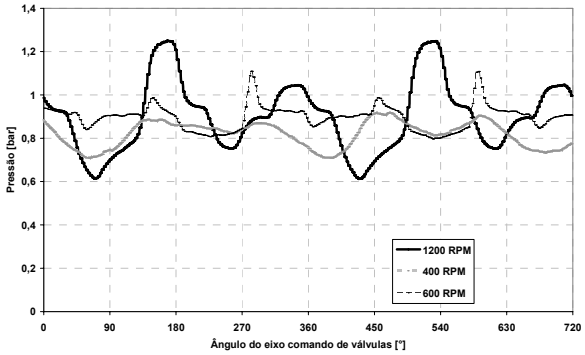

Figura 11 - Pressões dentro do ressonador para as rotações de 400, 600 e 1200 rpm

O aumento do rendimento volumétrico com a presença do ressonador é conseguido através do aumento de pressão no cilindro no instante do fechamento da válvula de admissão. A Figura 12 mostra que durante o período que a válvula de admissão fica realmente aberta, as pressões obtidas para as diferentes posições do ressonador são maiores que aquela obtida para a configuração sem ressonador, indicando maior entrada de massa para dentro do cilindro e conseqüentemente maior rendimento volumétrico. A Figura 12 também mostra que a pressão dentro do cilindro tende a crescer mais rapidamente com a presença do ressonador, atingindo gradientes maiores com o ressonador na posição RI. Pode-se observar também que a presença do ressonador, de um modo geral, gera o mesmo efeito de um turbo compressor em menor escala, aumentando a pressão dentro do cilindro e, conseqüentemente, a densidade do ar, aumentando a massa admitida dentro do cilindro.

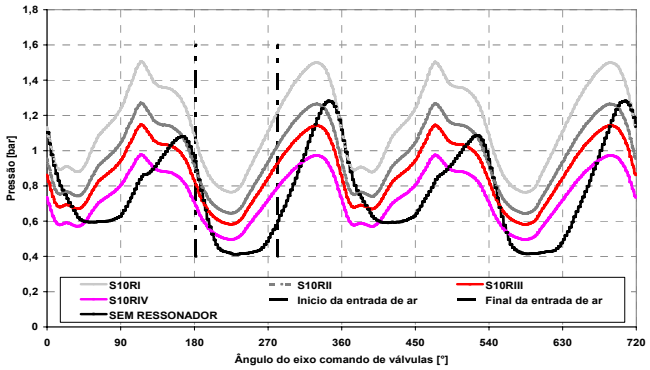

Figura 1211 – Pressão dentro do cilindro com o ressonador
nas posições estudadas e para a configuração sem ressonador a 1200 rpm

Para se determinar a influência da inserção do ressonador no sistema e permitir o cálculo do gradiente de pressão eficaz, foi realizada uma análise espectral das curvas de pressão mostrada na Figura 12. O resultado desta análise é apresentado na Figura 13. Pode ser observado que a colocação do ressonador alterou significativamente o espectro da freqüência. Tanto a freqüência fundamental como os harmônicos tiveram suas amplitudes aumentadas quando comparada com o espectro sem o ressonador para 40 Hz, que é a freqüência de ressonância do tubo de 2000 mm de comprimento. Esta amplitude tende a diminuir a medida que o ressonador é posicionado mais próximo da extremidade do conduto, praticamente se igualando à amplitude obtida para a configuração sem ressonador. Por outro lado, a transformada de Fourier permite o cálculo da pressão eficaz na porta da válvula e dentro do cilindro, a partir das quais pode-se determinar a diferença de pressão eficaz, que representa a verdadeira vazão de ar para o motor, permitindo estabelecer a condição de melhor rendimento volumétrico.

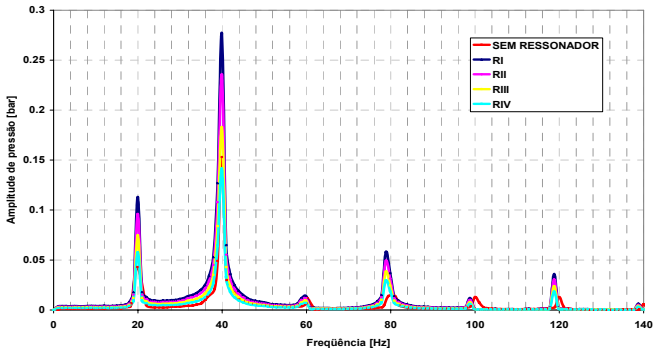

Figura 1312 - Análise espectral da pressão dentro do cilindro
com e sem o ressonador, nas quatro posições estudadas

A Tabela 1 apresenta os valores de ΔP_{RMS} para 1200 e 1600 rpm com o ressonador inserido nas quatro posições. Como era de se esperar, os maiores valores de ΔP_{RMS} ocorrem com o ressonador inserido na posição RI, correspondendo às maiores vazões.

Tabela 1 - Pressões eficazes para o ressonador

ROTAÇÃO [rpm]	ΔP_{RMS} (RI) [bar]	ΔP_{RMS} (RII) [bar]	ΔP_{RMS} (RIII) [bar]	ΔP_{RMS} (RIV) [bar]
200	0.365			
400	0.374			
600	0.395			
800	0.411			
1000	0.529			
1200	0.618	0.522	0.498	0.348
1400	0.554			
1600	0.575	0.471	0.417	0.206
1800	0.475			

Para uma análise mais completa, a Figura 14 mostra o comportamento da vazão com a diferença de pressão eficaz para toda a faixa de rotação estudada. Como esperado, os pontos de máximo e mínimo da diferença de pressão eficaz (ΔP_{RMS}) correspondem aos pontos de máximo e mínimo de vazão, respectivamente.

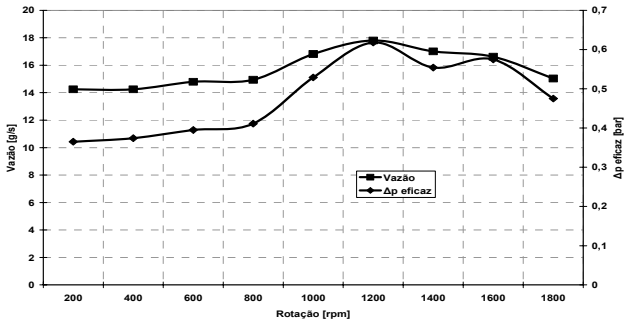

Figura 14 - Vazão e Δp eficaz para a configuração motor com Ressonador (RI)

Desta forma pode-se concluir que o método da pressão eficaz (ΔP_{RMS}), utilizado para determinar o comportamento da vazão de um motor de combustão interna, mostrou-se eficiente para todas as configurações estudadas.

CONCLUSÕES

- Os resultados mostram que é possível dimensionar um ressonador, inserido no local apropriado do conduto de admissão, que possa aumentar o rendimento volumétrico em toda a faixa de rotação do motor.
- A maior eficiência do ressonador se dá quando a freqüência de ressonância se iguala à freqüência natural do conduto e quando colocado o mais próximo possível da válvula de admissão.A curva de vazão pode ser interpretada a partir das curvas de pressão em função da rotação do eixo comando de válvulas.
- Os pontos de máximo e mínimos da curva de vazão mássica em função da rotação não dependem somente de um valor máximo de pressão entre a abertura e o fechamento da válvula de admissão, mas deve ser analisada entre a abertura fluidodinâmica, a partir de um intervalo diferente da abertura geométrica.através da pressão eficaz.
- É passível construir um ressonador eletrônico que permita variar o seu volume em função da freqüência de rotação do motor, obtendo-se desta forma uma melhoria do rendimento volumétrico do motor em toda a sua faixa de rotação.
- A analise de Fourier permite alterar pressões eficazes e calcular os diferenciais de pressão eficaz.
- Os diferenciais de pressão eficaz permitem determinar as flutuações de massa levam a rendimentos volumétricos maiores em motores de combustão interna, constituindo-se em uma ferramenta importante no projeto de motores de combustão interna.

AGRADECIMENTOS

Os autores agradecem a CAPES, a PUC Minas, a UFMG e a FIAT-GM, pelo suporte financeiro a esse projeto.

REFERÊNCIAS

BENSON R.S. "The thermodynamics and gas dynamics of internal combustion engines" Vol. I, Oxford University Press, 1982.

BICEN, F., VAFIDIS, C., and WHITELAW, J.H., 1985, "*Steady and unsteady Air Flow through na Intake Valve of a Reciprocating Engine*" J. Fluids Eng., 107 – 413.

HEYWOOD, J.B., "Internal Combustion Engines Fundamentals" – McGraw Hill, 1988.

HANRIOT, S.M.,2001, "*Estudo dos Fenômenos Pulsantes do Escoamento de Ar nos Condutos de Admissão em Motores de Combustão Interna*" Tese de Doutorado, Departamento de Engenharia Mecânica, UFMG.

KOSTUN, J.D., LIN, J.S., "Effect of resonator location on resonator effectiveness using *NASTRAN* mode shape prediction analysis and *LAMPS,* acoustic model", SAE paper Nº940614, 1994

NISHIO, Y., KOHAMA, T., KURODA, "New approach to low-noise air intake system development", SAE Paper Nº 911042, 1991.

Proceedings of the 11 th Brazilian Congress of Thermal Sciences and Engineering – ENCIT 2006
Braz. Soc. of Mechanical Sciences and Engineering – ABCM, Curitiba, Brazil, Dec. 5-8, 2006

Paper CIT06-0296

INFLUENCE OF ROTATING STALL AND SURGE IN THE DESIGN OF A SMALL GAS TURBINE ENGINE WITH AXIAL FLOW COMPRESSOR

Hugo de Oliveira Dias Filho
Gas Turbine Group - CTA/ITA/IEM
CEP 12.228-900 - FAX: +55-12-3947-5967
hugodias@ita.br

João Roberto Barbosa
Gas turbine Group - CTA/ITA/IEM
CEP 12.228-900 - FAX: +55-12-3947-5967
barbosa@ita.br

Abstract. *Instabilities during operation of axial flow compressors, such as rotating stall and surge, are phenomena that reduce significantly the gas turbine performance. Mathematical and physical models that predict the transient flow in the compression system during these instabilities were developed in the past and have been improved presently. This article utilizes the nonlinear model developed by Moore and Greitzer to determine the mode of instability in compression systems. Mode and intensity of compressor instability are strongly influenced by the compressor rotational speed and the volume of the combustion chamber (plenum) because they are directly linked to the Greitzer non-dimensional B-parameter. For a given compression system, there is a critical value of B that determines the existence of rotating stall or surge. For larger values of B critical there will be surge and, conversely, for smaller values there will be rotating stall. The critical value of B and the volume of the combustion chamber are calculated as a function of the engine speeds for a 5-stage axial flow compressor. The compressor behavior, namely axial flow coefficient, pressure-rise coefficient and surge frequency, is demonstrated for chosen speeds.*

Axial Compressor, Rotating Stall, Surge, Gas Turbines

1. Introduction

At normal operating conditions the flow in axial-flow compressors is stable and nearly axisymmetric. It is subjected to aerodynamic instabilities that significantly reduce the compressor performance and, as a result, the gas turbine performance. These instabilities may give rise to small reduction in efficiency and/or increase of the noise. In more severe cases, these instabilities may cause unacceptable operating conditions. It is investigated, at early design stage of a gas turbine engine, the influence of the combustion chamber volume on some types of instabilities that may lead a 5-stage axial flow compressor, designed for such engine, to unacceptable operating condition, namely rotating stall and surge[1]. It is known that it may be easier to recuperate the stable operation from surge than from rotating stall, the latter requiring almost always engine shut-down.

This paper describes the rotating stall and surge phenomena and applies a model developed by Moore and Greitzer, 1986 for the study of these instabilities at early design stage of a gas turbine, which are influenced by the volume of the combustion chamber and compressor rotational speed.

2. Compressor Performance Maps

Multi-stage axial-flow compressor performance map, or compressor map, usually shows constant corrected speed lines ($N/\sqrt{T_{t1}}$) relating both pressure ratio (P_{t2}/P_{t1}) and isentropic efficiency (η) as functions of corrected mass flow ($\dot{m}\sqrt{T_{t1}}/P_{t1}$), where N, T_{t1}, P_{t1}, $\dot{m}$, P_{t2} and η stand for, respectively, shaft speed, compressor inlet total temperature and pressure, mass flow, compressor outlet total pressure and efficiency. An example of a compressor map is shown in Fig. (1). The instability line indicates the limit up to the compressor operating condition is stable[2]. Above that curve flow distortions may arise circumferentially, causing a non-uniform axial velocity disturbance - the rotating stall - or large oscillations of the axial flow - the surge. Both can be caused by reduction of the mass flow across the compressor due to variation in the shaft speed and by distortions of the flow entering the compressor (inlet distortion).

[1] The term instability is for characterizing either rotating stall or surge

[2] Betchov and Pearson, 1967 apud Greitzer, 1980, define stability as the system ability to overcome small perturbations

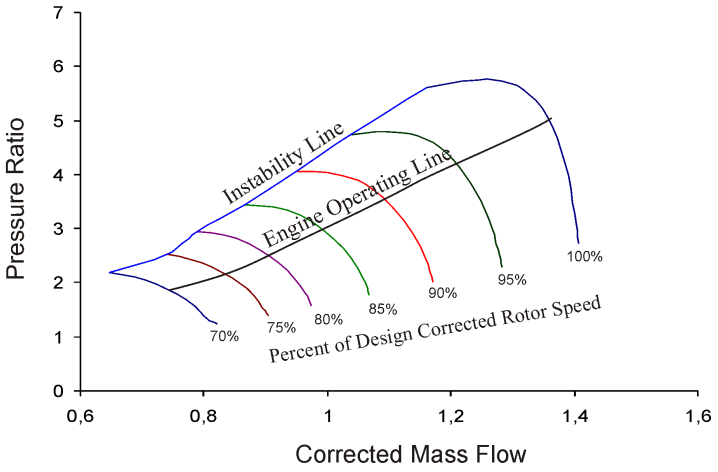

Figure 1: Example of a compressor map

3. Rotating Stall Summary

Stall is the flow separation at a single or at several rotor blades, namely stall cell. A compressor cross-section may have one or several stall cells. These cells move around in the same direction of the shaft rotation, from which the name rotating stall is originated.

Although the rotating stall causes a non-uniform axial velocity disturbance circumferentially, the average main flow remains unaltered. This non-uniform flow disturbance in a compressor of a gas turbine engine may cause excessive vibration of the blades, decrease of pressure and efficiency. A decrease of up to 20% in compressor isentropic efficiency has been observed. Reduction in mass flow may cause increase of turbine entry temperature above the accepted limits (Greitzer, 1980).

Emmons *et al.*, 1955, explain the physics of the stall, which may be expressed as the following: consider a compressor rotor cascade whose flow enters at an incidence angle (Fig. (2)), suppose that a perturbation in the flow, like a reduction of the mass-flow, causes increase of the incidence angle, making blade B entering stall. At this condition, flow separates from the blade suction surface, yielding a flow blockage or delay in the channel between blades B and C. Such a blockage moves the flow tangentially, causing increase in the incidence angle on blade C and reduction in the incidence angle on blade A, as seen in Fig. (2). Therefore, blade C is driven towards stall while stall is inhibited in blade A due to the decrease of the incidence. The stall region, or cell, may extend to several blade passages.

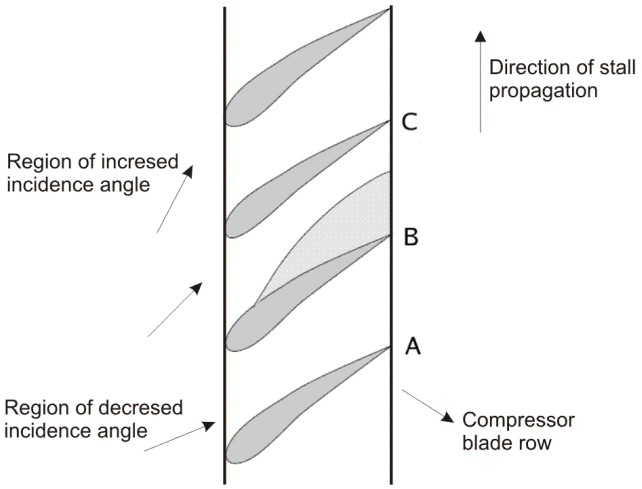

Figure 2: Stall propagation in a compressor blade row

According to Cumpsty, 1989, one may find several stall cells extending all over the blade height (*full-span stall*), or stall cells that cover part of the blade (*part-span stall*), as shown in Fig. (3). The amplitude of the stall cells gives rise to two types of rotating stall: abrupt and progressive. The abrupt stall originates from full-span stall cells. At the beginning abrupt stall causes sudden flow and pressure fall. After it has developed, it stays practically unchanged (Fig. (3a)). While

the progressive stall is characterized by a gradual pressure decrease. It happens, for instance, during engine start and aircraft take-off, i.e., when the mass flow is low and the incidence is high, it requires the on-set of part-span stall cells (Fig. (3b)).

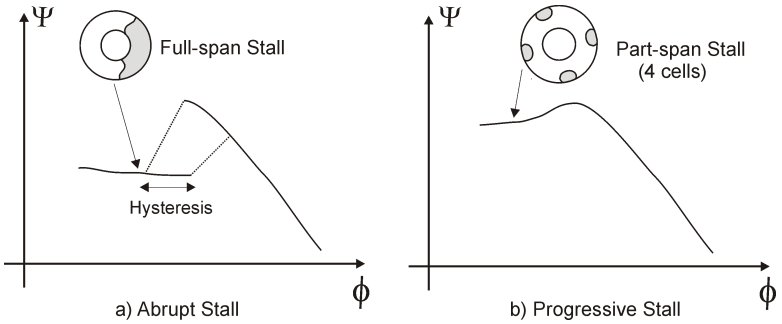

Figure 3: Stall cells types and rotating stall

4. Surge Summary

In this case both compressor average mass flow and pressure vary with time, causing the "operating point" to oscillate due to a process of cause and effect, between the stable and instable region of the compressor map. This phenomenon is known as surge. It may be so violent that the mass flow can be reverted and the hot gases from the combustion chamber emerge from the compressor intake (deep surge), as indicated in Fig. (4a). In the other hand it may be so gentle that the operating point stays close to the maximum operating pressure (classical surge), as indicated in Fig. (4b). This behavior is typical of small gas turbine compressors, prior to the settlement of more severe surge, causing reverse flow (Cumpsty, 1989).

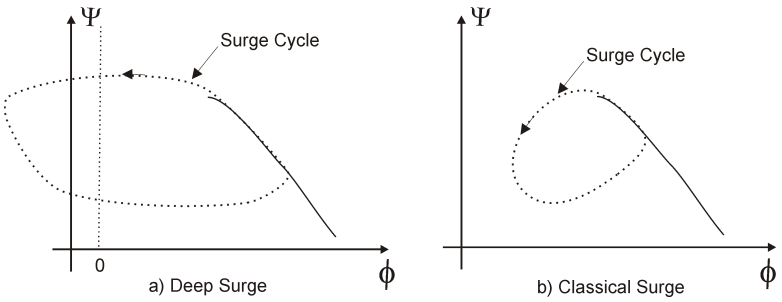

Figure 4: Deep and classical surge

The surge time scale is greater than the one for rotating stall. The frequency of the surge cycle is obtained from the number of times the "reservoir" fills up and empties. Although the surge process may be effectively axisymmetric when fully developed, in the initial transient it is not. Effectively, one of the waste surge effects in high compression ratio axial compressors is the large axial load that the rotor and casing must overcome (Cumpsty, 1989; Walsh and Fletcher, 1998).

5. Fluid Dynamic Model

Greitzer, 1976, proposed a 1-D non-linear model to predict transient responses of a compression system, when forced to operate beyond its stable limit. With this model, Greitzer defines a non-dimensional parameter B, which for a specified compressor characteristic curve, exhibits a critical value that correlates with the onset of rotating stall or surge. For larger values of B_{crit} the system would surge, while for lower values rotating stall would be present. B is defined by Eq. (1), where U is the rotor tangential velocity at blade mid height, a_s is the speed of sound, V_p is the volume of the reservoir following the compressor exit, A_C is the area of the compressor duct and L_C is the compressor length.

$$B = \frac{U}{2a_s}\left(\frac{V_P}{A_C L_C}\right)^{\frac{1}{2}} \tag{1}$$

Moore, 1984a, models the abrupt stall, developing a semi-empirical expression for the calculation of the velocity of propagation of the stall cell for small perturbation amplitudes. It is expressed as a fraction (f) of the rotor speed (U) at

the blade mid height (R), applicable for abrupt stall and depending on, among others, three delay parameters associated with the flow at the inlet, outlet and compressor blades. The first two parameters can be calculated, whilst the last one must be measured. Moore, 1984b, modified his model to accommodate the oscillatory condition of the reverse and stable flows, i.e., he modeled the surge. Mainly based on these publications, the Moore-Greitzer model was developed in Moore and Greitzer, 1986.

5.1. Moore-Greitzer Model

Only the major topics of the Moore-Greitzer model are described in this paper, in order to allow the reader to follow the text. The reader is encouraged to read Moore and Greitzer, 1986 and Greitzer and Moore, 1986. The model is related to a N-stage axial compressor with admission and discharge ducts, a reservoir, a flow control valve and a duct discharging the compressor air from the reservoir to the atmosphere.

This model is a simplified model of a turbojet, where combustion chamber is represented by the reservoir and the turbine by the throttle valve, as indicated in Fig. (5).

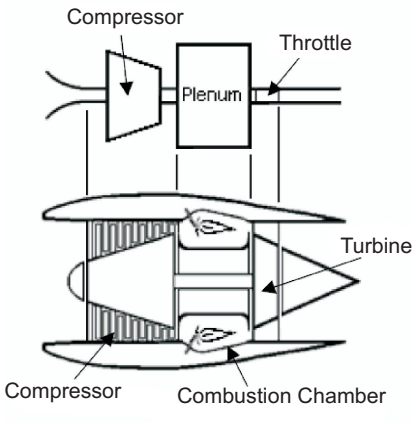

Figure 5: Turbojet and the Moore-Greitzer model schematics (Laderman *et al.*, 2003).

The compressor pumps air from an ambient at total pressure P_t to a reservoir at static pressure P_s. For the sake of simplification, only the reservoir flow is compressible although pressure gradients are taken as negligible. Suck assumptions are not really a problem because stability issues may be relatively independent of the flow Mach number in the regimes of interest (Paduano *et al.*, 2001). The air entering the compressor is considered irrotational and uniform radially. Provided the hub-tip ratio is large, as it happens in the compressor last stages, these assumptions are acceptable. This model is usually referred as low speed model due to the assumptions listed above.

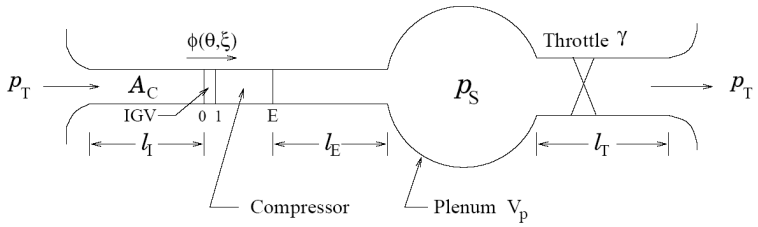

Figure 6: Schematic of the compressor installation for the model.

Figure (6) must be read taking into account that lengths were non-dimensionalised by R. It is calculated the flow at the non-dimensional time ($\xi = Ut/R$), at the tangential (θ) and axial (η) directions through the instantaneous flow (ϕ) and pressure (Ψ) non-dimensional coefficients, where

$$\phi\left(\xi,\theta,\eta\right) = \frac{C_x}{U} \;\; e \;\; \Psi\left(\xi\right) = \frac{P_s - P_t}{\rho U^2}, \tag{2}$$

where C_x is the axial velocity and ρ the air density.

Let $\widetilde{\varphi}(\xi,\theta,\eta)$ represent the flow perturbation field and $(\widetilde{\varphi}_\theta(\xi,\theta,\eta))$ and $(\widetilde{\varphi}_\eta(\xi,\theta,\eta))$ its tangential and axial gradients. The local average flow coefficient at station 0[3] is calculated by

$$\Phi(\xi) = \frac{1}{2\pi}\int_0^{2\pi} \phi(\xi,\theta,\eta=0)\,d\theta \;\Rightarrow\; \phi(\xi,\theta) = \Phi(\xi) + \widetilde{\varphi_\eta}(\xi,\theta,\eta=0)\,. \tag{3}$$

It is possible to show that the pressure coefficient can be calculated as

$$\Psi(\xi) = \psi_c(\Phi + \widetilde{\varphi_\eta})\,|_{\eta=0} - l_c\frac{d\Phi}{d\xi} - m\frac{\partial\widetilde{\varphi}}{\partial\xi}|_{\eta=0} - \frac{1}{2a}\left(2\frac{\partial^2\widetilde{\varphi}}{\partial\xi\partial\eta} + \frac{\partial^2\widetilde{\varphi}}{\partial\theta\partial\eta}\right)|_{\eta=0}, \tag{4}$$

where m is an empirical parameter related to the geometry of discharge duct, l_c is the aerodynamical compressor length and ducts, given by $l_c = l_I + 1/a + l_E$, a is the blade passage flow lag due to inertial effects (Eq.(5)). For one cascade

$$\frac{1}{a} = k\frac{chord}{R\cos\gamma} \tag{5}$$

where γ is the stagger, k is an empirical constant that takes account of the effects of axial spacing of the cascade and ψ_c is the hypothetical compressor characteristic curve calculated for the condition of axisymmetric flow, i.e., absence of rotating stall.

The characteristic curve ψ_c has been approximated by a 3rd degree polynomial (Eq. (6)), based on parameters ψ_{c0}, H and W, as indicated in Fig. (8). Values for H and W were taken such that the inflexion point, which is also a point of symmetry, could be located.

$$\psi_c(\phi) = \psi_{c0} + H\left[1 + \frac{3}{2}\left(\frac{\phi}{W} - 1\right) - \frac{1}{2}\left(\frac{\phi}{W} - 1\right)^3\right] \tag{6}$$

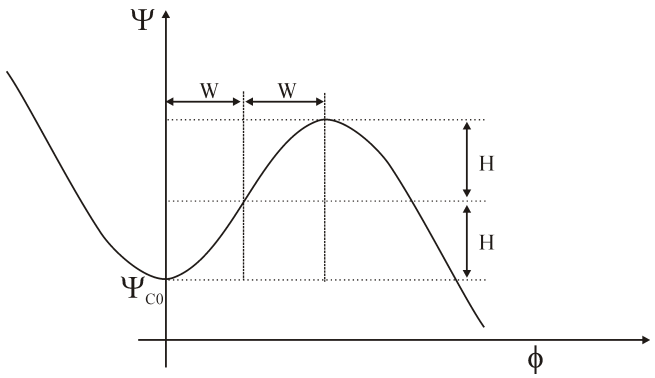

Figure 7: Compressor characteristic curve for axisymmetrical flow.

For isentropic flows, from the continuity equation one can write

$$\frac{\dot{m}_c - \dot{m}_T}{V_p} = \frac{d\rho}{dt} = \frac{1}{a_s^2}\frac{dP_S}{dt}, \tag{7}$$

where $\dot{m}_c$ is the mass flow entering the compressor, $\dot{m}_T$ the mass flow leaving the valve. From Eq. (7) it is possible to write

$$\frac{d\Psi}{d\xi} = \frac{1}{4l_cB^2}(\Phi - \Phi_T)\,, \tag{8}$$

where Φ_T is the valve flow coefficient, given by

[3]Compressor inlet, from the IGV (inlet guide vane) leading edge or 1st rotor

$$\Phi_T(\Psi) = \sqrt{\frac{2\Psi}{K_T}}. \tag{9}$$

Provided that the perturbation is periodic, the first terms of the development of a Fourier series, together with the Galerkin procedure for the solution of Eq. (4), it is possible to write the simplified system of equations:

$$\frac{d\Psi}{d\xi} = \frac{W/H}{4B^2}\left(\frac{\Phi}{W} - \frac{\Phi_T}{W}\right)\frac{H}{l_c} \tag{10}$$

$$\frac{d\Phi}{d\xi} = \left[\frac{\psi_{C0} - \Psi}{H} + 1 + \frac{3}{2}\left(\frac{\Phi}{W} - 1\right)\left(1 - \frac{1}{2}J\right) - \frac{1}{2}\left(\frac{\Phi}{W} - 1\right)^3\right]\frac{H}{l_c} \tag{11}$$

$$\frac{dJ}{d\xi} = J\left[1 - \left(\frac{\Phi}{W} - 1\right)^2 - \frac{1}{4}J\right]\frac{3aH}{(1+ma)\,W} \tag{12}$$

where J is the square of the amplitude of the angular disturbance of the axial-flow coefficient. This model is applicable for abrupt stall and deep surge.

6. Results and Discussion

Equations (10), (11) and (12) were solved numerically using a series of in-house developed softwares and the commercial software $MATLAB$. It has been studied the influence of the volume of the combustion chamber on the type of instable behavior of a 5-stage axial-flow compressor for a 1 MW gas turbine engine, that may show up when the engine is required to work near and above the stable region. Data for this study were obtained using the software developed by Tomita, 2003.

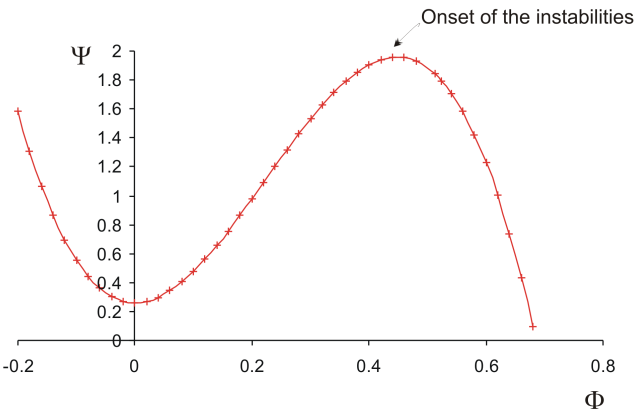

Figure 8: Axisymmetric compressor characteristic.

The nondimensionalization employed transforms the usual family of curves in the compressor map, one for each compressor speed, to one single characteristic (Gravdahl, 1998). Since this study is applicable for a compressor under design, experimental data and the methods of Day, 1994 and Koff, 1983 were used to obtain the complete axisymmetric compressor characteristic (Fig. (8)). Table (1) shows the input data used for this study based in the Moore-Greitzer method.

At the initial count of time ($\xi = 0$) the flow and pressure coefficient values are set as the values at the onset of the instabilities (Tab. 1) and represented by symbols Φ_{inst} and Ψ_{inst}, respectively. The initial value for J_{inst} was set to 0.01, following Greitzer and Moore, 1986.

Figure (9) shows results of the calculations for the 100% design speed. Figure (9a) shows the value of K_t that models the inception of instabilities ($K_{t_{inst}} = 20$). For $K_t \leq K_{t_{inst}}$, that is, the region of compressor stability, the new operating point will always correspond to the values of the intersection point of the characteristic curve with the system curve (throttle characteristic) curve (Fig. (9b)). For $K_t > K_{t_{inst}}$, the region above the stability limit, one may have rotating

Table 1: Compressor model parameters.

Design		**Performance**	
Sym		**Sym**	
Ac	0.0284 m^2	Ψ_{c0}	0.26
Lc	0.228 m	W	0.22
Le	0.1 m	H	0.85
Li	0.1 m	Φ_{inst}	0.44
R	0.112 m	Ψ_{inst}	1.96
N	5	Kt_{inst}	20
m	1.5	J_{inst}	0.01
k	3		
a	0.2		

stall (Fig. (9c)), with the new operating point determined by the intersection of system curve with in-stall characteristic curve, or surge (Fig. 9d)), without a defined operating point. For the calculation of the limiting value of the volume, when rotating stall occurs ($V_{p_{crit}}$), in the region near and above the instability line, K_t was set to $1.05K_{t_{inst}}$ and $V_{p_{crit}}$ was $0.0042\ m^3$, i.e., for a combustion chamber whose volume is greater than $0.0042\ m^3$ the compressor will enter surge.

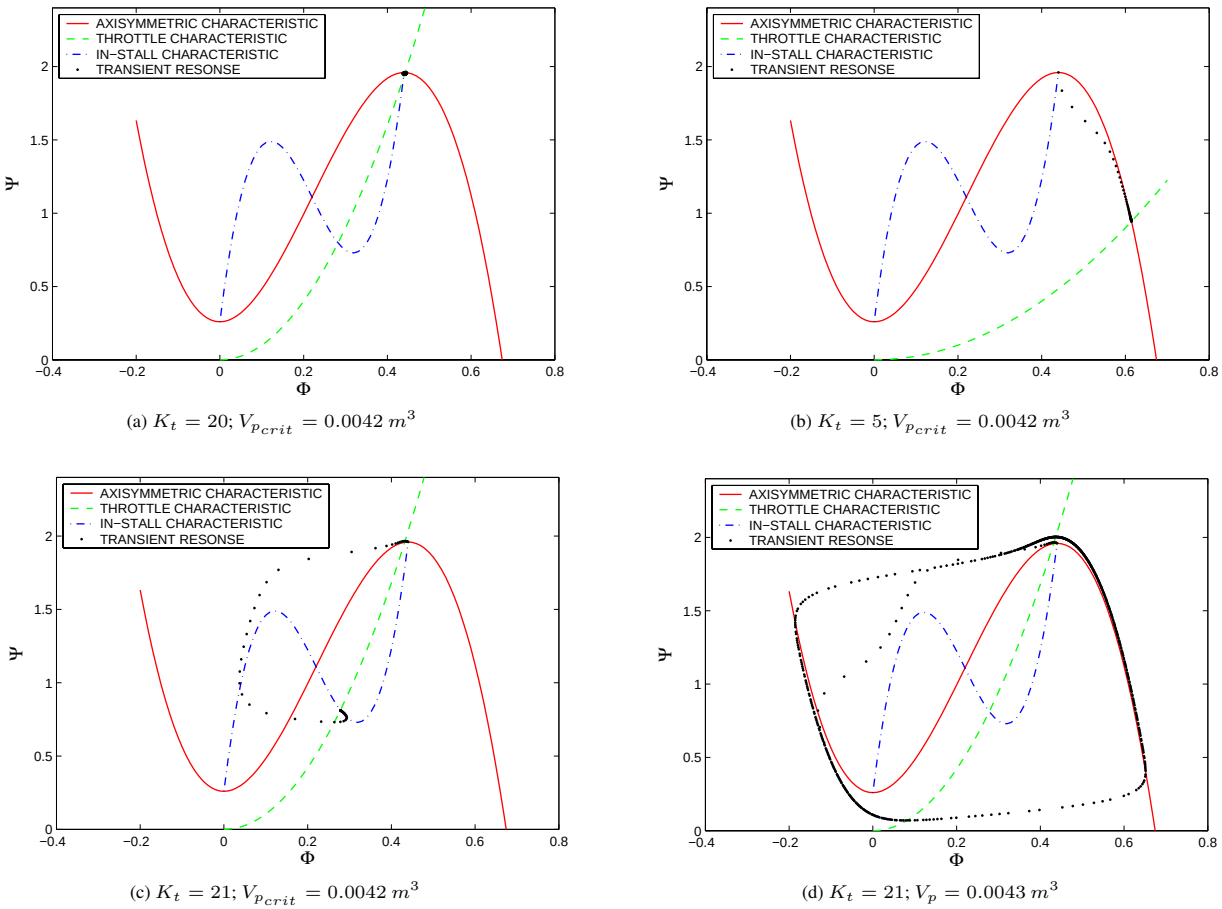

(a) $K_t = 20$; $V_{p_{crit}} = 0.0042\ m^3$

(b) $K_t = 5$; $V_{p_{crit}} = 0.0042\ m^3$

(c) $K_t = 21$; $V_{p_{crit}} = 0.0042\ m^3$

(d) $K_t = 21$; $V_p = 0.0043\ m^3$

Figure 9: Transient responses for 100% design speed.

The critical value for the Greitzer stability parameter for this compressor is $B_{crit} = 0.36$. With this value it is possible from Eq. (1) to obtain $V_{p_{crit}}$ as a function of the rotor speed. Figure (10) shows that if the speed decreases, $V_{p_{crit}}$ increases, in other words, at low speeds it may be possible to enter rotating stall. For example, if the combustion chamber volume is about $0.012\ m^3$ and the rotational speed above 60 $\%N_{design}$, deep surge will be the type of instability that is most likely to occur.

Figure (11) shows the periodic variation of the flow coefficient Φ, pressure coefficient Ψ and squared of amplitude of disturbance J with the non-dimensional time ξ, at the surge inception. From this condition, V_p has been varied and the

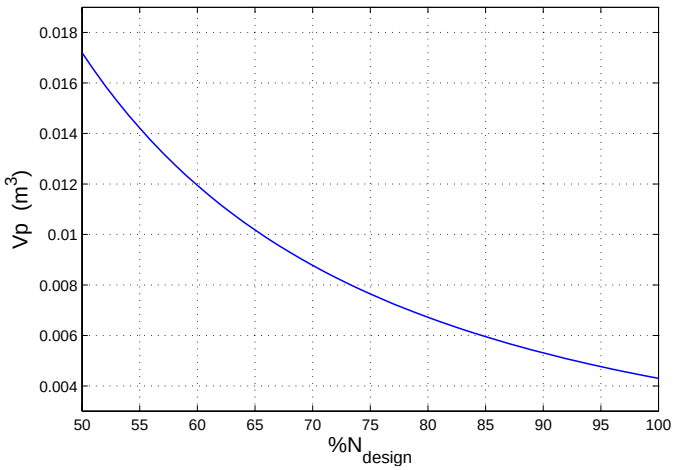

Figure 10: Combustion chamber volumes as function of the rotational speed.

value of the surge frequency, for each curve, was calculated and shown in Fig. (12). From the analysis of these figures it is possible to infer:

- For each constant speed curve the surge frequency is inversely proportional to the combustion chamber volume;
- For fixed values of the combustion chamber volume, the surge frequency decreases with engine speed;
- To avoid the abrupt rotating stall in the speed range of 70% to 100% design speed, it is required that the combustion chamber volume be larger than the critical volume determined for the 70%.

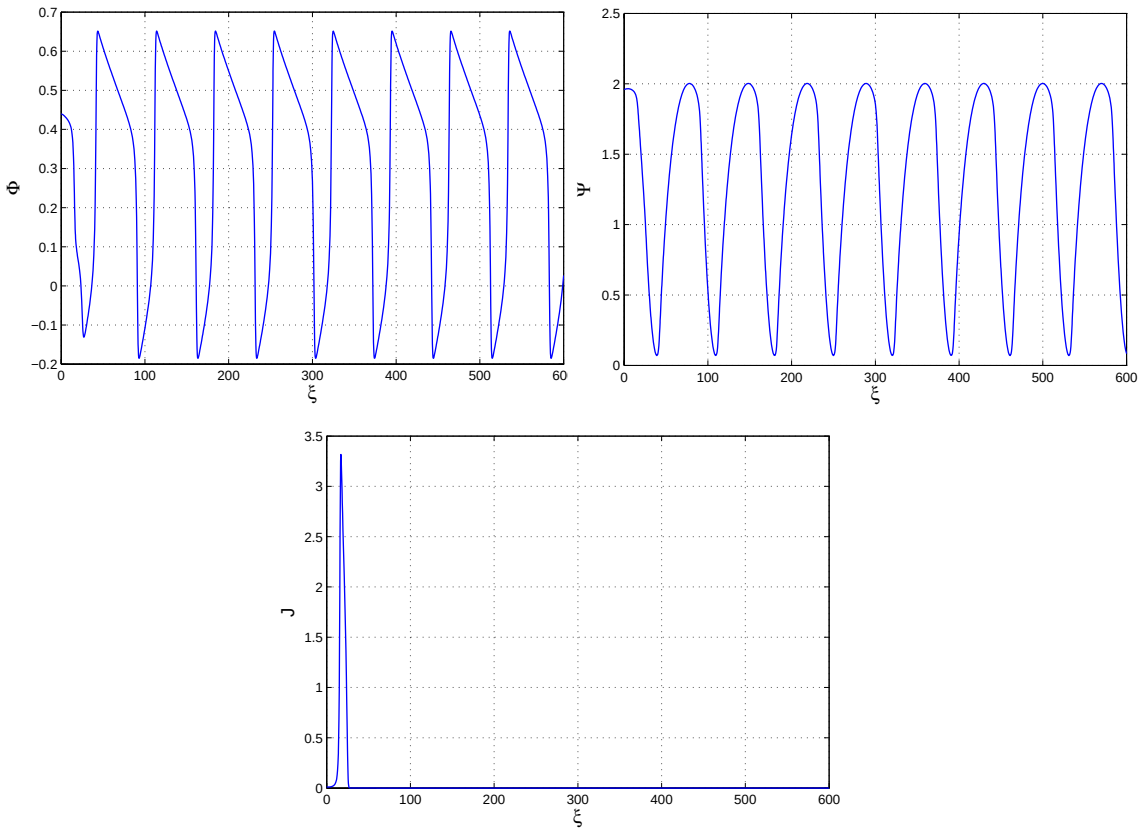

Figure 11: Φ, Ψ and J as function of time at the surge onset.

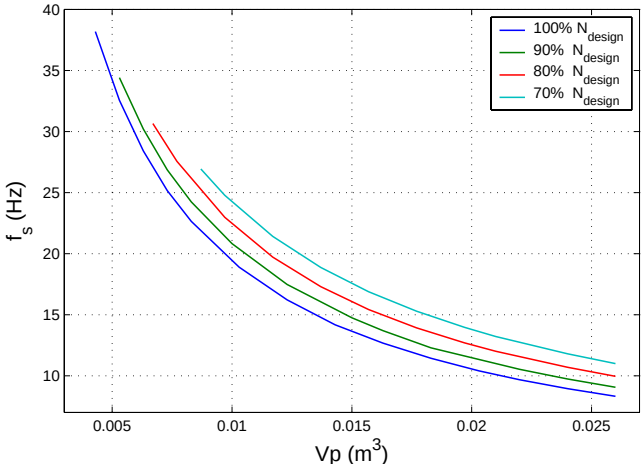

Figure 12: Surge frequencies as function of the combustion chamber volumes and engine speed.

7. Conclusion

The influence of the combustion chamber volume on the onset of surge and rotating stall has been studied giving guidance to the design of the combustor. The Moore-Greitzer model was implemented in a series of in-house computer programs that allowed the investigation of the influence of the combustion chamber volume and engine speeds on the type of the instability that can happen to the compressor under studied. The results presented in this article have shown that at low engine speed it is more likely to enter in rotating stall since the volume of the combustor is less than the critical value for low engine speeds. The surge frequencies for different volumes were also calculated, giving an estimation of the surge cycle for engine tests in the future.

8. Acknowledgements

This paper is part of a research program granted by FAPESP (Fundação de Amparo à Pesquisa do Estado de São Paulo) for a MSc program. The authors acknowledge the support of that foundation not only for this project but for the support for the Gas Turbine Program. Thanks are also extended to J. Takachi Tomita, who supplied the studied compressor data.

9. References

Betchov, R. and Pearson, W., 1967, Stability of Parallel Flows, "Academic Press".

Cumpsty, N. A., 1989, "Compressor Aerodynamics", Longman, 1 edition.

Day, I. J., 1994, Axial Compressor Performance During Surge, "Journal of Propulsion and Power", Vol. 10, No. 3, pp. 329–336.

Emmons, H. W., Person, C. E., and Grant, H. P., 1955, Compressor Surge and Stall Propagation, "ASME Transactions", Vol. 27, pp. 455–469.

Gravdahl, J. T., 1998, "Modeling and Control of Surge and Rotating Stall in Compressores", PhD thesis, Norwegian University of Science and Technology, Trondheim.

Greitzer, E. M., 1976, Surge and Rotating Stall in Axial Flow Compressors. Part I: Theoretical Compression System Model, "ASME Journal of Engineering for Power", Vol. 98, pp. 190–198.

Greitzer, E. M., 1980, REVIEW - Axial Compressor Stall Phenomena, "Journal of Fluids Engineering", Vol. 102, No. 2, pp. 134–151.

Greitzer, E. M. and Moore, F. K., 1986, A Theory of Post-Stall Transients in Axial Compression Systems: Part II - Application, "Journal of Engineering for Gas Turbines and Power", Vol. 108, pp. 231 – 239.

Koff, S. G., 1983, Stalled Flow Characteristics for Axial Compressors, Master's thesis, MIT.

Laderman, M., Greatrix, D., and Liu, G., 2003, Fuzzy Logic Control of Surge in a Jet Engine Model, "13th Propulsion Symposium, 50th CASI Annual Conference", pp. 28 – 30.

Moore, F. K., 1984a, A Theory of Rotating Stall of Multistage Axial Compressors: Part I - Small Disturbances, "ASME J. of Engineering for Gas Turbines and Power", Vol. 106, pp. 313–320.

Moore, F. K., 1984b, A Theory of Rotating Stall of Multistage Axial Compressors: Part II - Finite Disturbances, "ASME J. of Engineering for Gas Turbines and Power", Vol. 106, pp. 321–326.

Moore, F. K. and Greitzer, E. M., 1986, A Theory of Post-Stall Transients in Axial Compression Systems: Part I - Development of Equations, "ASME J. of Engineering for Gas Turbines and Power", Vol. 108, No. 1, pp. 68–76.

Paduano, J. D., Greitzer, E. M., and Epstein, A. H., 2001, Compression System Stability and Active Control, "Annual Review of Fluid Mechanics", Vol. 33, pp. 491–517.

Tomita, J. T., 2003, Numerical Simulation of Axial Flow Compressors, Master's thesis, ITA.

Walsh, P. P. and Fletcher, P., 1998, "Gas Turbine Performance", Blackwell Science, Oxford, Edinburgh, Malden.

Proceedings of the 11th Brazilian Congress of Thermal Sciences and Engineering -- ENCIT 2006
Braz. Soc. of Mechanical Sciences and Engineering -- ABCM, Curitiba, Brazil,- Dec. 5-8, 2006

Paper CIT06-0313

PHYSICAL ASPECTS OF THE FLOW OVER SHALLOW CAVITIES: A NUMERICAL INVESTIGATION

P.S.B. Zdanski
Department of Mechanical Engineering
State University of Santa Catarina
89223-000 – Joinville – SC - Brazil
zdanski@joinville.udesc.br

M.A. Ortega
Department of Aeronautical Engineering
Technological Institute of Aeronautics
12228-900 – São José dos Campos – SP - Brazil
ortega@ita.br

N.G.C.R Fico Júnior
Department of Aeronautical Engineering
Technological Institute of Aeronautics
12228-900 – São José dos Campos – SP – Brazil
nide@ita.br

Abstract. *The flow over shallow cavities is numerically investigated. The analysis is performed for both, laminar and turbulent regimes. Some interesting features, previously detected, are discussed on the physical basis. The results obtained demonstrate that the vorticity shed at the upstream corner and the stagnation region formed at the downstream vertical wall dictate the physical scenario in terms of flow topology inside the cavity for both turbulent and laminar regime. The heat transfer budget for the turbulent cavity revealed an interesting feature of the convection fluxes inside the cavity, e.g., a symmetric behaviour. The mathematical model corresponds to the incompressible, Reynolds-averaged, Navier-Stokes equations plus a two-equation k-e turbulence model. Two numerical schemes are adopted in the analysis. The SIMPLER method, based in finite volume formulation, is used in the laminar study. Otherwise, for turbulent analysis, a finite difference scheme that has recently been developed by the present authors was applied.*

Keywords*. Shallow cavities, incompressible flows; numerical methods*

1. Introduction

The flow over cavities is of great practical interest, being extensively studied with the aim of analyze solar energy collectors, combustion chambers and environmental problems. Previous work, by the present authors, revealed some interesting aspects about this kind of flow, i.e., the opposite behavior on the displacement of the vortices inside the cavity for laminar and turbulent regimes (Zdanski et al., 2003), and the role played by the turbulent diffusion upon heat transfer rate at the cavity floor (Zdanski et al., 2005). These features were not fully explored on its physical aspects. Thus, the main goal here is to discuss these issues in more detail.

The flow inside cavities is characterized by the appearance of large re-circulation regions. The literature data available is mainly devoted to the analysis of deep cavities and there is little information about cavities of large aspect ratios, or shallow cavities. Sinha et al. (1982) have reported experimental results for deep cavities as well as for shallow ones. This particular work reveals some important aspects about flow topology inside shallow cavities, but only for the laminar case. Frigo et al. (2004) presents numerical results for transient flow in free cavities with aspect ratios 1 and 2. This work emphasizes the analysis of time evolution of streamlines and velocity profiles inside the cavity. For a more complete review about this topic the reader may access the works of Zdanski et al. (2003, 2005).

The numerical analysis was performed with two distinct schemes, i.e., the SIMPLER algorithm (Patankar, 1980) and the one developed by the present authors (Zdanski et al., 2004). The SIMPLER method is completely standardized in the literature and the other scheme adopts central difference formulas to discretize both convective and diffusive terms in a collocated mesh. To control odd-even decoupling problem, artificial viscosity terms are added externally. The laminar flow simulations were obtained through the SIMPLER algorithm while all turbulent cases were simulated with our "in-house" code. Although not shown here some laminar cases were re-calculated with the new method and the results were very similar to the ones obtained by the classical Patankar's algorithm. That is, all major flow characteristics were recovered, thus, ruling out the possibility that the numerical scheme is a determinant factor on the flow aspects discussed hereafter. Further, a careful mesh refinement study was performed yielding grid-independent results. The results obtained demonstrate that vorticity shed at the cavity corner has the major influence upon the

bubbles position inside the cavity. Another result, related to heat transfer budget, indicates a symmetric behavior on the convection fluxes inside the cavity.

An important point that should be clear is that ours is essentially an engineering approach. Therefore, the interest lies on the steady mean flow. We are aware that the dynamics inside the cavity is extremely complicated, and that the instantaneous flow plays a very important role. But, the emphasis of this paper is on the engineering aspect of the problem.

2. Theoretical formulation

2.1. Governig equations

The flow is modeled by the two-dimensional, Cartesian, incompressible, Reynolds-averaged, continuity, Navier-Stokes, and energy equations. In the Einstein notation the equations can be written as

$$\frac{\partial U_j}{\partial x_j} = 0 \,, \tag{1}$$

$$\frac{\partial(\rho U_i)}{\partial t} + \frac{\partial(\rho U_j U_i)}{\partial x_j} = -\frac{\partial p}{\partial x_i} + \frac{\partial}{\partial x_j}\left(2\mu S_{ij} - \rho\overline{u_i' u_j'}\right), \tag{2}$$

$$\frac{\partial(\rho c_p T)}{\partial t} + \frac{\partial(\rho c_p U_i)}{\partial x_i} = \frac{\partial}{\partial x_i}\left(\kappa\frac{\partial T}{\partial x_i} - \rho c_p \overline{u_i' T'}\right), \tag{3}$$

where the mean strain rate is given by

$$S_{ij} = \frac{1}{2}\left(\frac{\partial u_i}{\partial x_j} + \frac{\partial u_j}{\partial x_i}\right). \tag{4}$$

For modeling the turbulent flow, we have adopted the Boussinesq approximation, where the turbulent fluctuations are correlated to mean flow properties as

$$-\rho\overline{u_i' u_j'} = \mu_T\left(\frac{\partial U_i}{\partial x_j} + \frac{\partial U_j}{\partial x_i}\right) - \frac{2}{3}\delta_{ij}\rho k \,, \tag{5}$$

$$-\rho c_p \overline{u_i' T'} = \kappa_T \frac{\partial T}{\partial x_i} \,, \tag{6}$$

being μ_T and κ_T the turbulent eddy viscosity and turbulent thermal conductivity, respectively. For computation of turbulent viscosity it was adopted the standard κ-ε turbulence model (Launder and Spalding, 1974). For determination of the turbulent thermal conductivity we have adopted the definition of constant Prandtl turbulent number, i.e., $P_{rT} = 0.9$.

2.2. Numerical method

The numerical scheme adopted for the laminar analysis was the SIMPLER algorithm (Patankar, 1980). Otherwise, for the turbulent studies, the method developed by the present authors (Zdanski et al., 2004) is employed. The SIMPLER scheme is completely standardized in literature, while the other scheme is a recent proposal. The novel method discretizes the equations in a collocated mesh with central difference formulas. Artificial smoothing terms are added to control the odd-even decoupling and non-linear instabilities. The equations, written in conservation law form, are solved implicitly. A Poisson equation for pressure is solved to assure free divergence for velocity field. Distinctly of traditional pressure-correction methods, the convergence of the present scheme is assured without resorting to any kind of relaxation parameters. For more details about the scheme the reader is addressed to reference Zdanski et al. (2004).

3. Results and discussions

3.1 Problem statement and boundary conditions

The shallow cavity with the main dimensions is depicted at fig. (1). Boundary conditions were enforced as follows: at the inlet plane distributions of velocity, temperature, turbulent kinetic energy and turbulent dissipation rate are specified. The parabolic condition was enforced for all variables at the exit section. At the upper boundary coupling with the free stream flow is used. At solid walls the condition of zero velocity was enforced and the shear stress and heat flux are obtained from the law of the wall (Mansour et al., 1983) together with the standard κ-ε model (Launder and Spalding, 1974). The values of pressure and turbulent kinetic energy at the wall are obtained by a zero-order extrapolation from the values at the first cell.

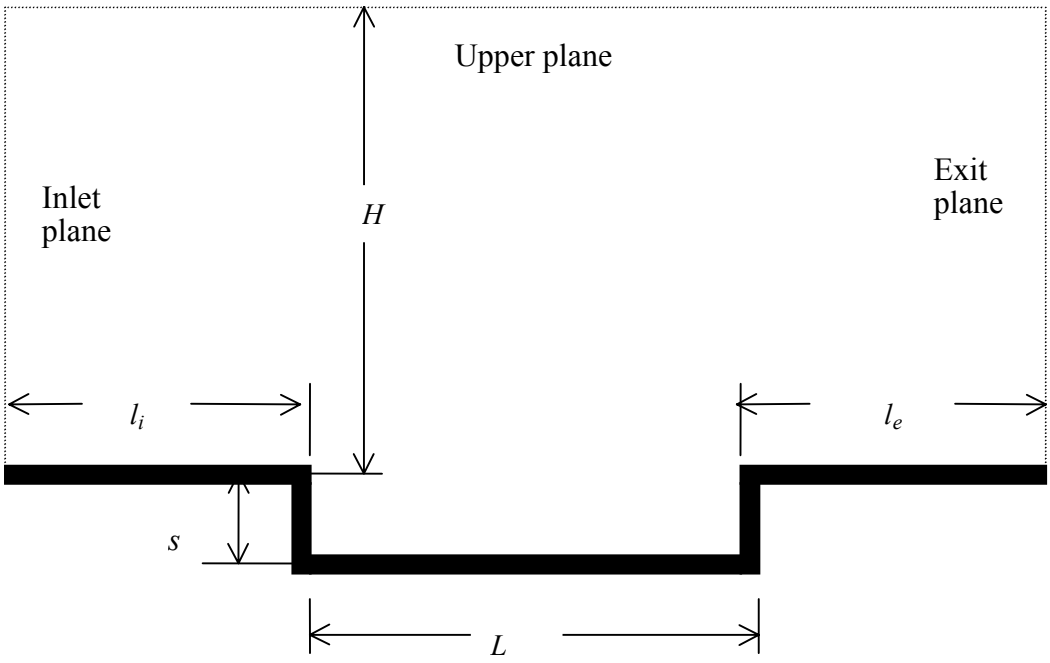

Figure 1. Shallow cavity with the main dimensions.

The codes used in the present analysis were extensively tested in previous works (Zdanski et al., 2003, 2004, 2005). Comparisons with experimental and theoretical literature data have ever been satisfactory. These facts corroborate for the credibility of the results presented herein. A typical computational mesh used in the cavity analysis presents points clustering close to solid walls and to the horizontal plane connecting the two corners. The first grid point is set at $y^+ \approx 30$ (for turbulent flow), and the maximum stretching factor for the mesh was 9%.

3.2 Displacement of the vortices inside the cavity

It was discovered in the authors' previous work (Zdanski et al., 2003) that the Reynolds number affects the bubbles position inside the cavity for the laminar and turbulent regime. In the laminar case, for lower velocities, we have the flow reattached at the cavity floor, and the two bubbles encapsulate for higher velocities (Zdanski et al., 2003). This is so because increasing Reynolds number causes the greater bubble displaces in the downstream direction (Zdanski et al., 2003). Otherwise, for the turbulent regime, the opposite occurs, i.e., the bubbles are encapsulated for lower velocities and the flow reattaches at the cavity floor with higher velocities (Zdanski et al., 2003, 2005). Furthermore, for the turbulent flow the bubble center does not change the position with increasing Reynolds number (Zdanski et al., 2005). What is the reason for this fact? This paper aims at understanding better this physical scenario.

The aspect ratios considered for the present analysis were equals to 8 for the turbulent case and 12 for the laminar flow. These values were chosen to ensure the formation of two vortexes inside the cavity. The variation of the Reynolds number, based upon the cavity depth Re_s, was a consequence of the variation of the entrance velocity. For the turbulent case, values of U_{in} equal to 5m/s, 8m/s, and 12m/s, corresponding to Re_s equal to 13285, 21255, and 31880, are simulated. For the laminar regime we have adopted U_{in} equal to 0.4 m/s, 0.8m/s, 1.2m/s, and 1.8m/s corresponding to Re_s=147, 294, 442 and 662, respectively.

In Table (1), it is represented the vorticity (evaluated as U_{in}/δ) for the velocities tested. This quantity was calculated at the cavity upstream corner, where the boundary layer separates. The first conclusion, 'the obvious one' was that for higher velocities we have more vorticity being shed at the cavity corner. The most important conclusion can be drawn from figs. (2) and (3), where the pressure distribution along the cavity floor is represented. The values of pressure shown in these figures are dimensional, representing the differences between the pressure at a particular station along the cavity floor and the pressure at the inlet section. It can be realized that for the turbulent regime, increasing the Reynolds number will cause the pressure decreases at the greater bubble region ($x/s < 4.0$) and augments in the region near the downstream vertical face ($x/s > 4.0$). The physical scenario that explain this behavior is as follows: increasing Reynolds number will leads to higher vorticity (see Table (1)), thus lowering the pressure at the bubble center and, as a consequence, at the cavity floor ($x/s < 4.0$). Moreover, the pressure increase for $x/s > 4$ is linked to the flow stagnation that occurs at the downstream vertical face. Therefore, in the region $x/s > 4$, the higher vorticity effect is overwhelmed by the pressure rise due to flow stagnation. This pressure distribution can explain why, in the turbulent regime, the greater bubble does not change its position with increasing velocities. In effect, the net pressure force augments in downstream direction forcing the bubble against the upstream vertical cavity wall. Figure (3), representing the laminar case, show a rather distinct picture. Increasing the velocities (and consequently vorticity) will lead to a pressure decrease along the whole cavity floor. Therefore, the effect of vorticity is more important, overwhelming the pressure increasing caused by the stagnation region. Although the net pressure force increases, in the downstream direction, the gradient is much smaller than in turbulent case, permitting the greater bubble to move downstream (Zdanski et al., 2003). The major conclusion is the following: for the turbulent regime the vorticity being shed at the cavity corner is higher but their influence is restricted to the greatest bubble region ($x < 4$), and the pressure gradient does not permit the greater bubble to change the position with increasing Reynolds number. However, for the laminar case, the vorticity increasing, which causes a pressure decrease, is felt along the entire cavity floor. Thus, the pressure driven force is lower and the greater bubble moves downstream with increasing velocities.

Table (1) – Cavity corner vorticity as a function of Reynolds number, Re_s

Re_s	Vorticity (s^{-1})	Re_s	Vorticity (s^{-1})
147	45.13	13285	1178.50
294	93.35	21255	1867.92
442	144.10	31883	2700.00
662	229.12		

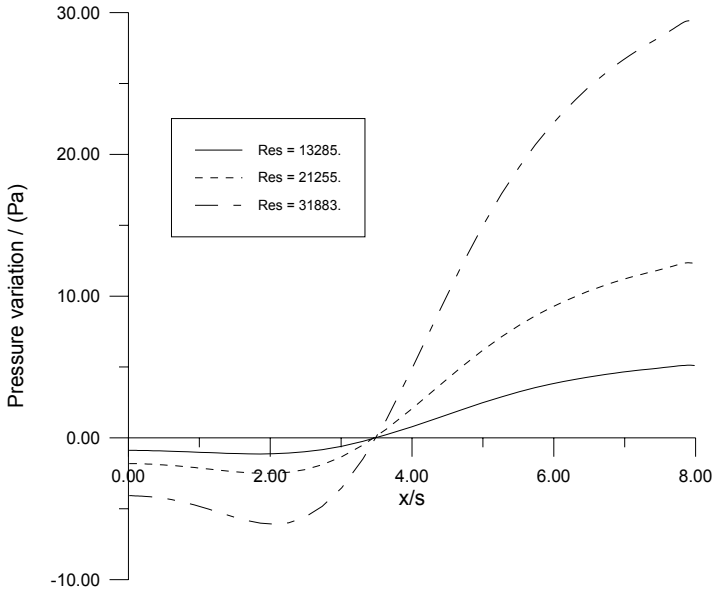

Figure 2. Pressure difference between the floor and the entrance section for cavity with (w/s) = 8

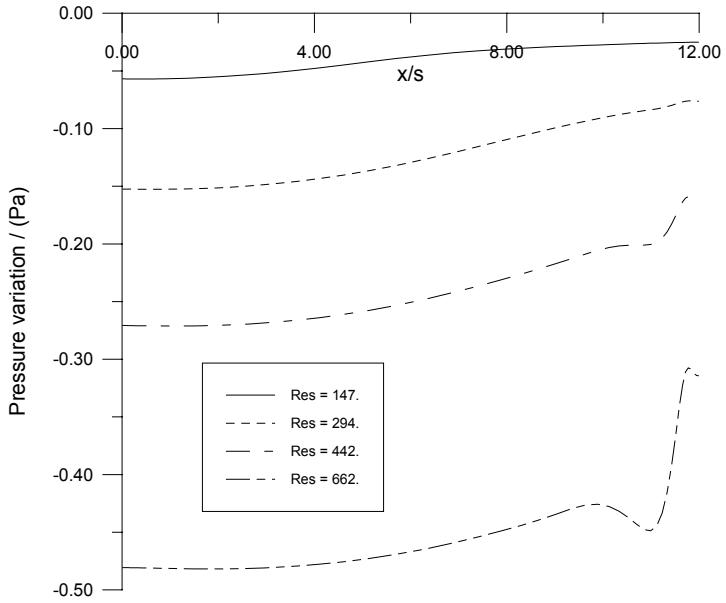

Figure 3. Pressure difference between the floor and the entrance section for cavity with (w/s) = 12

Aiming at better understanding the phenomenon the non-dimensional vorticity is plotted in figs. (4) and (5), i.e.,

$$Vorticity = \left(\frac{s}{U_{in}}\right)\left[\frac{\partial v}{\partial x} - \frac{\partial u}{\partial y}\right]. \tag{7}$$

The attention is focused at the cavity region. The fig. (4) presents results for a laminar simulation where Re_s = 442 whereas fig. (5) represents the turbulent picture for Re_s = 21,255. Clearly, we can realize that for turbulent flow the vorticity diffusion processes is more intense. Otherwise, if one analyzes the region near the cavity floor the immediate conclusion is the following: for turbulent flow we have the maximum positive vorticity near upstream step (x/s < 2) whereas for laminar flow this maximum vorticity region extends basically for the whole cavity floor. This observation is in agreement with the pressure distributions presented in figs. (2) and (3).

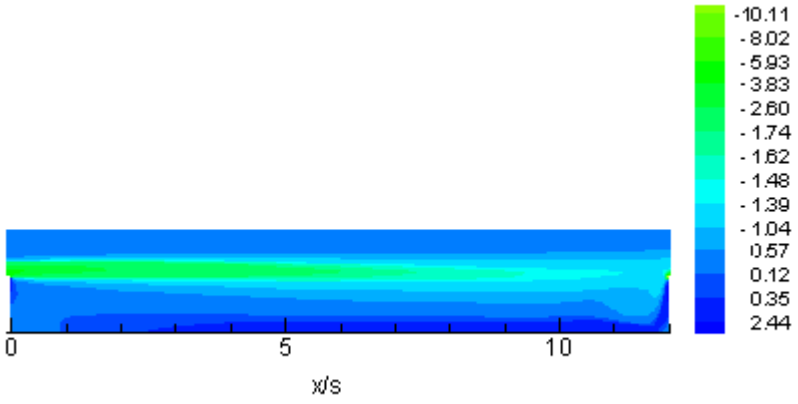

Figure 4. Vorticity distribution for laminar flow regime with (w/s) = 12.

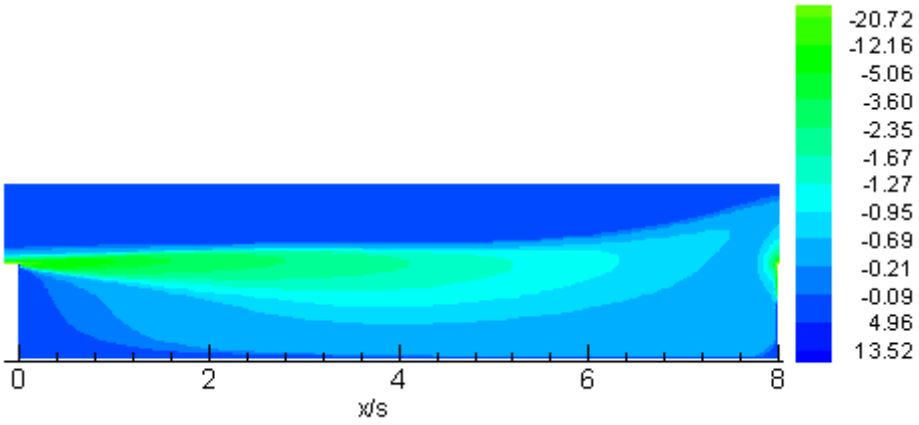

Figure 5. Vorticity distribution for turbulent flow regime with (w/s) = 8.

3.3 Heat transfer budget inside the cavity

It was demonstrated by the authors (Zdanski et al., 2005) that heat flux at the cavity floor is related to turbulent diffusion near cavity floor. Aiming a better understand of the phenomenon, we present the heat transfer budget inside the cavity. The convection and diffusion terms of the energy equation are evaluated at control volumes taken along the cavity length, as shown in fig. (6).

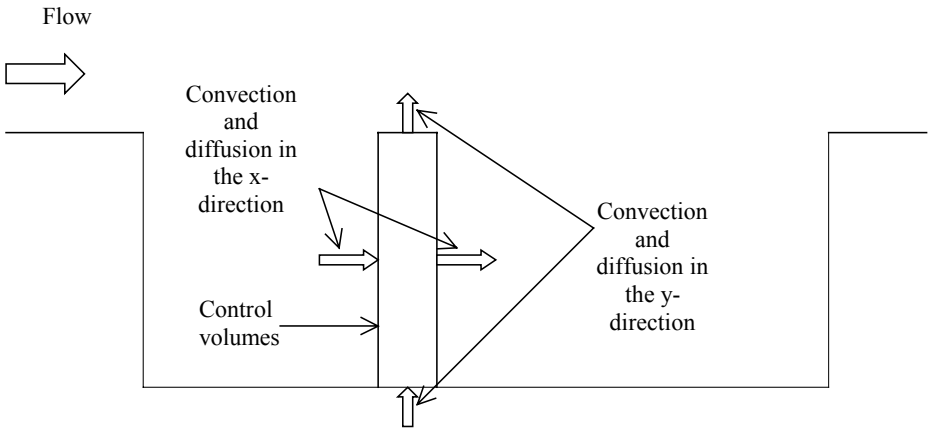

Figure 6. Control volume representation for heat transfer budget.

The integration of energy equation over the control surfaces leads to

$$\textit{Net x-convection} = \left[\left(\rho u c_p T\right)_{i+1/2} - \left(\rho u c_p T\right)_{i-1/2}\right]\Delta y\,,$$

$$\textit{Net y-convection} = \left[\left(\rho v c_p T\right)_{j+1/2} - \left(\rho v c_p T\right)_{j-1/2}\right]\Delta x\,,$$

$$\textit{Net x-diffusion} = \left[\left(\kappa_{eq}\frac{\partial T}{\partial x}\right)_{i+1/2} - \left(\kappa_{eq}\frac{\partial T}{\partial x}\right)_{i-1/2}\right]\Delta y\,, \quad 1 \tag{8}$$

$$\textit{Net y-diffusion} = \left[\left(\kappa_{eq}\frac{\partial T}{\partial y}\right)_{j+1/2} - \left(\kappa_{eq}\frac{\partial T}{\partial y}\right)_{j-1/2}\right]\Delta x\,.$$

The results for the energy budget are presented in Figs. (7) and (8). These results correspond to a cavity of aspect ratio equal to eight. The entrance velocity is set to 8 m/s, corresponding to Res = 21,255. The temperature at the entrance section is uniform, T_{in} = 300 K. The same value was enforced at solid walls, except at the cavity floor, where T_w = 350 K. The control volumes adopted have a length Δx and cover all the cavity height, i.e., from y = 0 until y = s (see fig. (6)). In this way we take into account the mean effect of convection and diffusion along the cavity height and its local variation along cavity length.

Noticeable, the most interesting aspect that may be observed in fig. (7) is the symmetrical behavior for the convection fluxes along x and y directions. Besides, the convection terms have greater magnitude than the diffusion terms (see fig. (8)). In spite of this fact, the net contribution due to convection (summing up x and y fluxes) has the same order of magnitude than y-diffusion term. This is so because for a steady state problem without heat sources, the energy conservation principle states that net energy entering or leaving the control volume by convection must be equal its counterpart by diffusion. It interesting to note that in this case (cavity with aspect ratio 8) we have two bubbles encapsulated inside the cavity, i.e., the flow does not reattach at the cavity floor (Zdanski et al., 2003; 2005). Perhaps, this is the reason for the symmetrical behavior of convection fluxes in the energy budget. Furthermore, from Fig. (8), we realize that the y-diffusion term is more important than its counterpart in the x-direction.

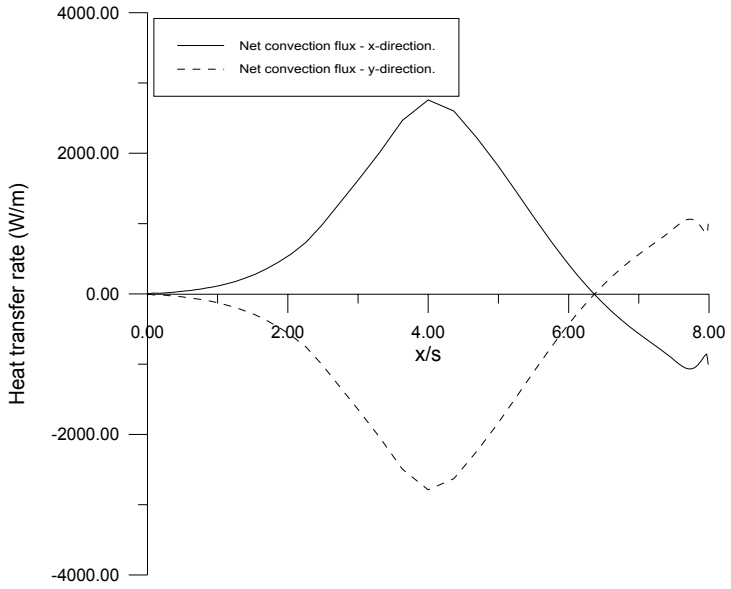

Figure 7. Net convection fluxes inside the turbulent cavity with aspect ratio 8.

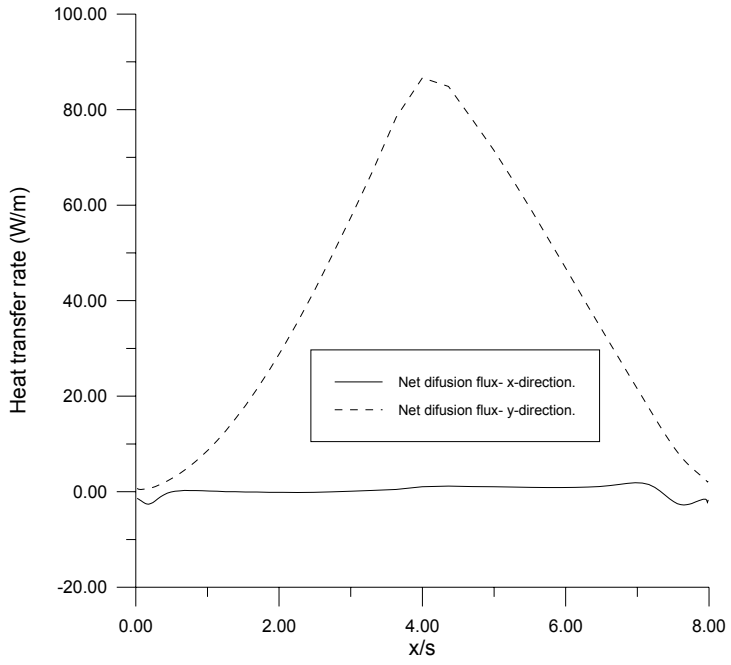

Figure 8. Net diffusion fluxes inside the turbulent cavity with aspect ratio 8.

4. Conclusions

The results presented help to clarify some interesting aspects of the incompressible flow over shallow cavities. The vorticity shed at the upstream corner and the stagnation region formed at the downstream vertical face has a major influence on vortices position inside the cavity. For the turbulent regime, the effect of vorticity is less important than in the laminar case. This basically explains the opposite behavior of the bubbles inside the cavity as function of the Reynolds number. Furthermore, the energy budget inside the cavity shows an interesting aspect related with the net convection fluxes inside the cavity, i.e., the symmetrical behavior.

5. References

Frigo, L. M., Mansur, S. S., Campregher, R., De Arruda, J. M. and Silveira Neto, A., 2004, "Análise Numérica de Escoamentos Sobre Cavidades Abertas Bidimensionais", Proceedings of the 10th Brazilian Congress of Thermal Science and Engineering, Rio de Janeiro, Brazil.

Launder, B. E. and Spalding, D. B., 1974, "The Numerical Computation of Turbulent Flows", Computer Methods in Applied Mechanics and Engineering, Vol.3, pp. 269-289.

Mansour, N. M. and Kim, J. and Moin, P., 1983, "Computation of turbulent flows over a backward-facing step", Nasa Technical Memorandum, 85851.

Patankar, S. V., 1980, "Numerical Heat Transfer and Fluid Flow", McGraw-Hill Book Company, New York, EUA, 196 p.

Sinha, S. N., Gupta, A. K. and Oberai, M. M., 1982, "Laminar Separating Flow over Backsteps and Cavities part II: Cavities", AIAA Journal, Vol.20(3), pp. 370-375.

Zdanski, P. S. B., Ortega, M. A. and Fico JR, N.G.C.R., 2003, "Numerical Study of the Flow over Shallow Cavities", Computers & Fluids, Vol.32(7), pp. 953-974.

Zdanski, P. S. B., Ortega, M. A. and Fico JR, N.G.C.R., 2004, "Numerical Simulation of the Incompressible Navier-Stokes Equations", Numerical Heat Transfer Part B: Fundamentals, Vol.46(6), pp. 459-479.

Zdanski, P. S. B., Ortega, M. A. and Fico JR, N.G.C.R., 2005, "Heat Transfer Studies in the Flow over Shallow Cavities", Journal of Heat Transfer (ASME), Vol.127(7), pp. 699-712.

6. Copyright Notice

Proceedings of the 11th Brazilian Congress of Thermal Sciences and Engineering -- ENCIT 2006
Braz. Soc. of Mechanical Sciences and Engineering -- ABCM, Curitiba, Brazil, Dec. 5-8, 2006

Paper CIT06-0332

LARGE EDDY SIMULATION OF ASH PARTICLE DEPOSITION AROUND TUBES OF A BOILER SUPERHEATER

Lourival Jorge Mendes Neto
Federal University of Santa Catarina, Department of Mechanical Engineering, Campus Trindade, Florianópolis, SC, Brazil 88040-900
mendes.lourival@gmail.com

João Luis Toste de Azevedo
Instituto Superior Técnico, Department of Mechanical Engineering, Av. Rovisco Pais, 1049-001 Lisboa, Portugal.
toste@ist.utl.pt

Edson Bazzo
Federal University of Santa Catarina, Department of Mechanical Engineering, Campus Trindade, Florianópolis, SC, Brazil 88040-900
ebazzo@emc.ufsc.br

Abstract. *Low rank coal is currently used in Brazilian thermal power plants. A number of problems are associated to the ash particle deposition on heat exchange surfaces causing unplanned shutdowns and reducing power output and plant efficiency. Several mechanisms involved in particulate and alkaline vapour deposition have been recently investigated by Knudsen (2001), such as inertial impact and vapour diffusion. The present work concentrates on inertial impact and investigates the deposition of particles around a circular tube based on Large Eddy Simulation. The turbulent flow is calculated based on two different grids and two subgrid models (Smagorinsky and dynamical model). Particle trajectories are traced in the Lagrangian framework based on one-way coupling and a discrete random walk model is used to simulate the subgrid-turbulence. Simulations are presented for one representative tube from the superheater of Jorge Lacerda thermo power plant to evaluate the hitting rate of particles with different diameters. The deposition rate of the particle around the cylinder is the input for particle deposition models.*

Key words: Large eddy simulation, Particle deposition, Ash deposit, Coal, Boiler.

1. Introduction

The use of low rank coal in boilers has many consequences. One of the primary problems associated with the use of coal is the deposition of fly ash on heat transfer surfaces. All coals have a significant content of ash, forming inorganic material, which can not be economically removed before combustion. This material forms deposits on the surface of the heat exchanger tubes and on the walls, causing unplanned shutdowns and reducing power output and efficiency of the boiler.

Nowadays, thermal power plants account for 21% of the Brazilian energy matrix and in future it is expected to have an increase to 60%. Coal as a fuel is expected to represent 10% of the installed capacity in the next years (ANEEL, 2006). The coal used as fuel for thermal power generation is mostly provided from the southern of Brazil and 42% of the annual production comes from Santa Catarina. The possible savings that could be made by better control of ash deposition in coal fired boilers in the US have been estimated at 400 million US$/yr (*apud* Bouris et al, 2001).

In this context, the present paper has the objective of providing a detailed description of the gas-particle flow around one tube from a heat exchanger, based on conditions from the Jorge Lacerda thermo power plant. The approach used here is to analyse the flow and temperature distribution around a single tube based on large eddy simulation. All the calculations were performed using the commercial code FLUENT, (Fluent Inc. 2005).

The flow around bluff bodies is characterized by complex interactions between different phenomena such as boundary layers, separation and reattachment, shear layers, large two and/or three dimensional vertical structures, etc. Although models based on the Reynolds Average Navier Stokes equations (RANS) have been applied successfully in many practical computations, these tend to fail for flows involving large unsteady structures. The Large Eddy Simulation (LES) approach has a better potential to determine these complex structures and interactions between the flow field and the bluff body (Fröhlich *et al*, 1998).

Many studies involve comparison between LES and RANS (*apud* Fröhlich, *et al*, 1998 and Lübcke *et al*, 2001). The superiority of the LES predictions is attributed to the fact that LES is better suited to flows where the size of the eddy (integral length scale of the turbulence) is comparable to that of the obstacles in the flow. In fact the LES approach involves the direct solution of the large vortices and only the vertical structures with size below the filter size are modelled. This is a primary advantage, since the influence of the turbulence model is reduced; in contrast, it significantly increases the computational effort in comparison to RANS (Fröhlich *et al*, 1998 and Lübcke *et al*, 2001).

In LES, the large eddies that depends strongly on the flow configuration and its boundary conditions are resolved numerically whereas only the fine scale turbulence has to be modelled by a subgrid scale model. The Large Eddy Simulation method solves the Navier Stokes equations by a spatial average over a small volume. Due to the non-linearity of the Navier Stokes equations its average forms contains additional terms for which models are needed, these are termed subgrid or subfilter scale models, (Franke and Frank, 2002).

Mostly two subgrid models are commonly used, the Smagorinsky subgrid scale model (SM) and the dynamic Smagorinsky model (DSM) of Germano *et al*, (1991). Both models are based on the Boussinesq hypothesis; they depend on the turbulent viscosity and this viscosity is assumed as proportional to the strain rate tensor.

Understanding the large scale vortex dynamics it is possible to predict the particle dispersion in a bluff body flow. This is of a great significance, once the ash deposition depends on the interaction of the particle with the vortex structure behind the tube.

The particle trajectories were traced in a Lagrangian framework based on one way coupling, it means that they do not affect the gas flow. The particle tracking used here is the Discrete Random Walk (DRW), based on the Eddy Life Time model.

The present work is organized as follows: Following this introduction, the numerical methodology is briefly discussed and the test cases are presented. The impact of the grid on the LES calculation is analysed by comparing the results of two three-dimensional 3D different grids and a two-dimensional (2D) grid. The particle deposition is analysed considering the stochastic model of the DRW and without it. At the end, the paper discusses the impact of the analysis in the first tube of an in-line tube arrangement of the boiler resulting in a deposition rate that can be considered in a deposition model such as those presented by Mendes *et al*, (2006).

2. Modelling Approach

The Large Eddy Simulation (LES) is an intermediate methodology between the Direct Numerical Simulation (DNS) and the Reynolds Averaged Navier Stokes (RANS) equations. In the DNS approach, the Navier Stokes equations are solved by a numerical methodology resolving the smallest scale in turbulent flow, namely the Kolmogorov length and time scale (Breuer, 1998; Lübcke *et al*, 2001; Franke and Frank, 2002; Silveira, 2002). In the framework of RANS all aspects of turbulence are modelled, which enhances the numerical efficiency at the expense of a strong model dependency.

As opposed to the RANS approach, a major portion of the turbulence scales is numerically resolved within LES. Both methods solve averaged Navier Stokes equations, both on time and space. In the LES framework calculations are done along time and therefore the average over time is limited to the calculation time step, while the averaging in space is dictated by the grid resolution. Due to the non linearity of the Navier Stokes equations their average forms contain additional terms for which models are needed. They are termed turbulence models in RANS and subgrid or subfilter scale models in LES. The filtered incompressible equations used in LES approach are:

$$\frac{\partial \overline{u}_i}{\partial x_i} = 0\,, \tag{1}$$

$$\frac{\partial \overline{u}_i}{\partial t} + \frac{\partial \overline{u}_i \overline{u}_j}{\partial x_j} = -\frac{1}{\rho}\frac{\partial \overline{p}}{\partial x_i} - \frac{\partial \tau_{ij}}{\partial x_j} + \nu \frac{\partial^2 \overline{u}_i}{\partial x_j \partial x_j}\,, \tag{2}$$

where $\overline{u}_i, \overline{p}, \rho$ denote the filtered velocity, pressure and density. The viscous stress is given by $\tau_{ij} = \overline{u_i u_j} - \overline{u}_i \overline{u}_j$.

The filtering procedure provides the governing equations for the resolvable scales of the flow field. They include an additional term for the non resolvable subgrid scale stress which describes the influence of the small scale structures in the larger eddies. To model these non resolvable subgrid scales two different models are applied namely the Smagorinsky model and the dynamic model proposed by Germano *et al* (1991). Both use an eddy viscosity concept, the main difference being the choice of the *ad-hoc* constant by the Smagorinsky model or a dynamic function in the Germano model.

The effective conductivity in the energy equation is the sum of the molecular conductivity of the fluid and the turbulent contribution related to the eddy viscosity by the turbulent Prandlt number, here assumed as 0.7.

2.1. Smagorinsky Eddy Viscosity Model

The Smagorinsky model employs the Boussinesq approximation, which means that the Reynolds stresses is considered proportional to an eddy viscosity and the velocity gradient. The Reynolds tensor can be written as a function of the filtered velocity field and turbulent kinetic energy by (Silveira, 2002):

$$\tau_{ij} = -\nu_t\left(\frac{\partial \overline{u}_i}{\partial x_j} + \frac{\partial \overline{u}_j}{\partial x_i}\right) + \frac{2}{3}k\delta_{ij}, \tag{3}$$

where ν_t, k, δ_{ij} are the eddy viscosity, turbulent kinetic energy and the Kronecker delta. The turbulent kinetic energy subgrid can be incorporated with pressure resulting in a modified pressure term. The eddy viscosity can be modelled by:

$$\nu_t = (C_S\Delta)^2\left|\overline{S}\right|, \tag{4}$$

where C_S is the Smagorinsky constant, here used as been 0.1, Δ is the filter width of the box filtering method, obtained from the volume of the computational cells and S the strain rate tensor, $\left|\overline{S}\right| = \sqrt{2\overline{S}_{ij}\overline{S}_{ij}}$.

This model tends to fail if applied to the flow near the walls and transition flows where the separation of the boundary layer occurs determining the generation of large vortices. Therefore the Germano dynamic model is also considered.

2.2. Dynamic Eddy Viscosity Model

Dynamic models are sensitive to the local state of the flow and thus predict more accurately transition and have the correct near wall behaviour as opposed to the constant coefficient Smagorinsky model. The dynamic model overcomes this limitation of the dependence of an *ad hoc* constant imposed by making use of two different filters, the grid filter and the test filter.

The filtering process consists of filtering the Navier Stokes equations by using a filter width similar to the grid size followed by the same filtering process but with a filter width two times larger than the first one, know as test filter. Based on this concept it is possible to note that the dynamic model makes use of the lower resolved scales, situated between the two filters, to model the energy transfer between the resolved and non resolved scales. This is obtained by minimizing the mean square error in the Germano identity, which equals the difference between the subgrid and subtest tensor to the Leonard tensor. This process of filtering is described elsewhere (Saugaut and Grohens, 1999; Silveira, 2002).

2.3. Particle Phase

The mass flux of the ash particles inside the boiler, calculated by Reinaldo (2004), is $\dot{G}_p = 0.07$ [kg/m^2/s]. This flux compared with the gas flux, $\dot{G}_g = 1.5$ [kg/m^2/s] leads to a mass loading of 4.8%. The ash content of the coal used in the boiler is about 41%, in dry basis, so one possible estimative is that the density of the ash particles can be around of 41% of the coal density in dry basis, resulting in 535 kg/m^3. Besides if compared to the gas density $\left(\rho_p/\rho_g \cong 10^3\right)$, the particle concentration in volume can be estimated as 10^{-5}. In these conditions inter-particle effects are negligible and it is close to the limit where the effect of particles in the gas flow can be neglected (10^{-6}).

Based on the high density ratio the Basset force and the added mass term are small and are therefore neglected. The ratio of the lift to drag force is given by the relation between the Saffman and drag force $F_{Saff}/F_{drag} \cong d_p^2(du/dy)^{0.5}/\mu$, where d_p, du/dy, μ are the diameter of the particle, the derivate of the gas velocity and the molecular viscosity of the gas. For particles with small diameter and low inertia this force can be neglected in comparison to the drag force, (Crowe, 1979). Under these assumptions, the Lagrangian equations governing the particle motion become:

$$\frac{dx_p}{dt} = u_p, \tag{5}$$

$$\frac{du_p}{dt} = \frac{f}{St_p}\left(u - u_p\right), \tag{6}$$

where f is a correction factor for large Reynolds number of the drag coefficient, here considered from spherical particle. St_p is the particle Stokes number defined as

$$St_p = \frac{\tau_p}{\tau_f} = \frac{\dfrac{\rho_p d_p^2}{18\mu}}{D/U_\infty}, \tag{7}$$

where τ_p, τ_f, are the particle relaxation time [s] and the mean flow time scale [s].

As the flow is turbulent and only the large eddy are solved through LES approach. The fluctuating gas flow velocity considered using the stochastic method in the Discrete Random Walk model (DRW). In this model, the fluctuating velocity components are discrete piecewise constant functions in time. Their random value is selected from a Gaussian distribution and is kept constant over an interval time given by the characteristic lifetime of eddies. Further details can be found on Fluent, 2005. The DRW is necessary for particle sizes with particle relaxation time comparable or smaller than the subgrid time scales. The particle flow simulation is based on the computed trajectories of .representative particles. The number of particles represented by each trajectory is based on the mass flow rate and the particle size distribution.

3. Numerical Methodology

The computational domain is described in a fixed Cartesian coordinate system (x, y, z). The y-axis is along the streamwise mean flow direction, the z-axis is along the spanwise direction and the x-axis is perpendicular to both y- and z-axis. The origin of the coordinate system and the size of the computational domain are shown in Fig.1.

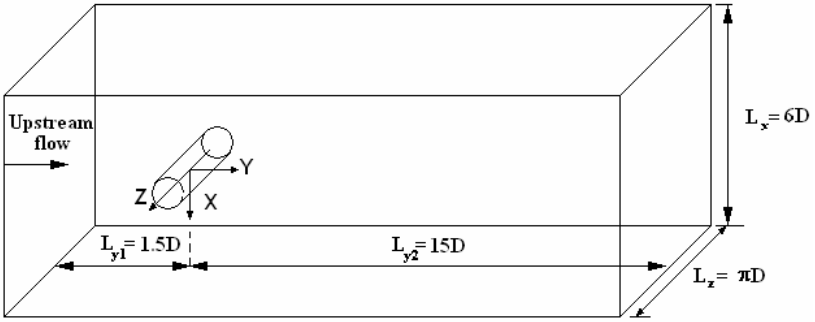

Figure 1. Physical configuration of the cylinder flow.

The diameter of the cylinder is 31.8 mm, the blockage ratio is 16%, close to the value used by the papers referred here. The spanwise direction is usually estimated from the experimental measurements or prior knowledge of the sizes of the streamwise vortex structures. Many authors have reported that the spanwise direction should be at least πD to represent the three dimensional structures (Frölich *et* al, 1998, Breuer, 1998, Lübcke *et* al, 2001, Liang and Papadakis, 2006).

In the present situation two meshes were used to analyse the grid dependence, A0 and A1. Further a 2D simulation (A2) was also carried out to analyse the 3D aspects of turbulence. For the finer grids, 32 layers are used in the spanwise direction with two different quantities of cells in the periphery of the cylinder, 128 and 256 cells for the coarse and finer mesh, respectively. A constant expansion of 1.1 is used for the cell spacing in the radial direction away from the cylinder wall with the smaller spacing in the radial direction being $\Delta r_{min}/D = 1.96 \times 10^{-2}$. The details about the cases considered are shown in Tab. 1. All calculations were performed under isothermal conditions except case B1S which is based in case A1S considering heat transfer.

Table 1. Overview of all simulations for the circular cylinder.

Run	N_{Total} Cells	Grid N_θx N_Z	Domain	Subgrid Model	L_r/D	y+ (maximum)
A0D	206848	128x32	6Dx16.5DxπD	Dynamic	1.45	4.00
A1D	370688	256x32	6Dx16.5DxπD	Dynamic	1.05	4.25
A2D	60928	128x8	6Dx16.5Dxπ/4D	Dynamic	–	6.00
A0S	206848	128x32	6Dx16.5DxπD	Smagorinsky	0.75	4.50
A1S	370688	256x32	6Dx16.5DxπD	Smagorinsky	1.35	4.35
A2S	60928	128x8	6Dx16.5Dxπ/4D	Smagorinsky	–	5.85
B1S	370688	256x32	6Dx16.5DxπD	Smagorinsky	1.00	4.85

The smaller spacing in the radial direction was determined considering the Taylor microscale, λ [m]. The Taylor scale is located between the flow integral scale and the Kolmogorov scale and can be estimated by (Arpaci, 1997):

$$\frac{\lambda}{D} = \frac{1}{\sqrt{Re_D}} \tag{8}$$

Re_D is the Reynolds number based on the diameter of the tube, D [m]. Considering the inlet velocity of 10 m/s with a gas temperature of approximately 1020ºC (Reinaldo, 2004) results in Re_D, of 2600. The maximum y+ found in the calculations is indicated in table 1.

The theoretic Strouhal number, for this Reynolds number, is approximately 0.2 providing an estimative of vortex shedding frequency as 53Hz (0.02 [s]). Based on this, the time step selected was 0.0002 [s] for all cases. Around 20 iterations are required for convergence of the equations, within each time step to within a prescribed tolerance of 10^{-3} for the normalized residuals. Statistics are then collected after 200 time steps, necessary to create the instabilities and some few vortexes shedding, and then all dates presented here were collected with approximately nine shedding cycles.

The boundary conditions used on the exit surface is the convective boundary condition equal to zero. This boundary condition ensures that vortices can approach and pass the flow boundary without significant disturbances or reflections into the inner domain (Breuer, 1998).

Non slip condition is used at solid walls. In the spanwise as in the cross stream direction periodic boundary conditions are assumed. At the inlet flow a plane constant velocity profile is imposed (no perturbations added). We do have in mind that this is not the real conditions of the flow near the heat exchange tubes, but as the LES approach is very suitable to the flow field, the insertion of turbulence intensity can change the conditions from one case to the other making difficult the comparison with calculated or experimental results from other authors.

All the equations are solved using a commercial code FLUENT 6.2.16 that uses a cell centred finite volume method with central differences to solve the incompressible Navier Stokes equations. For the momentum equations the bounded central differencing scheme is used in order to lead to low oscillations in the solution fields, the pressure values at the faces are interpolated using the momentum equation coefficients. The solver is segregated with implicit formulation and the temporal discretization is second order. The pressure velocity coupling is achieved by the use of the SIMPLE algorithm.

4. Results and Discussion

4.1. Gas flow Analysis

In order to show the three dimensionality of the turbulence in bluff body flow for LES simulation the cases A0D, A0S, A1S and A1D are compared with the A2D and A2S. All simulations were done using the same inlet conditions. Fig. 2 shows the time average streamwise velocity along the centreline. Experimental results presented are for a comparable case with Re_D= 3900.

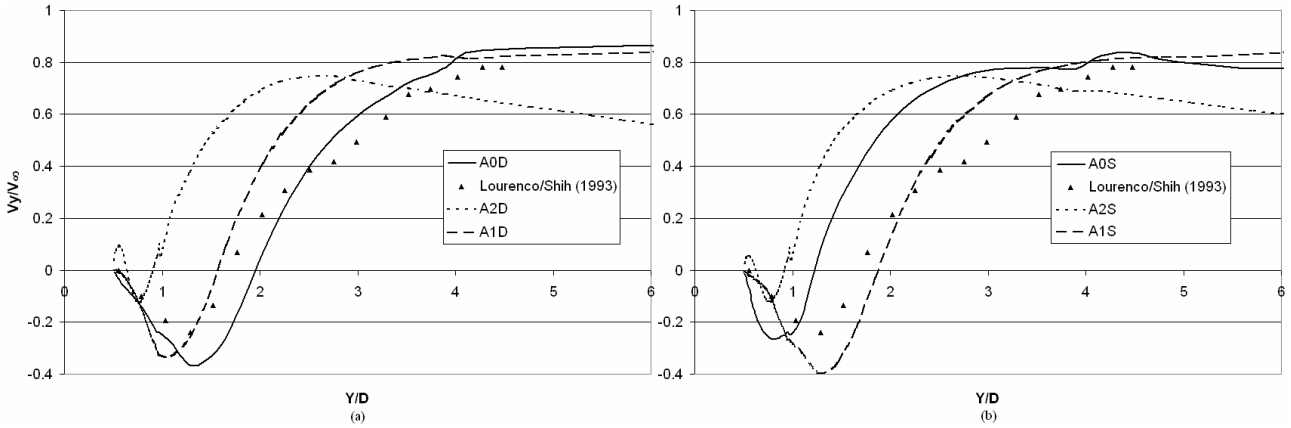

Figure 2. Mean streamwise velocity along the centerline, (a) Dynamic subgrid model; (b) Smagorinsky subgrid model.

As can be seen the run A2D and A2S show a secondary recirculation within the main recirculation in the wake. The extension of the recirculation is under predicted by the grid (A2) with small number of nodes in the spanwise direction as noted by other authors (Breuer, 1998).

The experimental observations were taken from Lourenco and Shih, (1993), *apud* Breuer (1998) and were obtained for a slightly higher Reynolds number (3900) for which the size of the recirculation zone is expected to be smaller. Calculations for a similar Reynolds number, 2580, is presented by Liang and Papadakis (2006) leading to a recirculation zone length, L_r/D of 1.75, close to the A0D and A1S runs.

Once the grid has an insufficient resolution the large eddies became more dependable of the viscosity model and this results in an early transition on the shear layers separating from the cylinder which led to a shorter recirculation zone, the same happened to the run A0S, specially because it used a fixed constant in the model. This grid resolution possibly led to an under prediction of the turbulence in the A1D run resulting in an early separation of the shear layer.

Figure 3 presents a comparison of the streamwise velocity profile across the wake at a distance Y/D = 1. The axes are normalized by the free stream velocity and the results in the border of the computational domain the ratio V_y/V_∞ is 1.10 due to the blockage ratio of 16%.

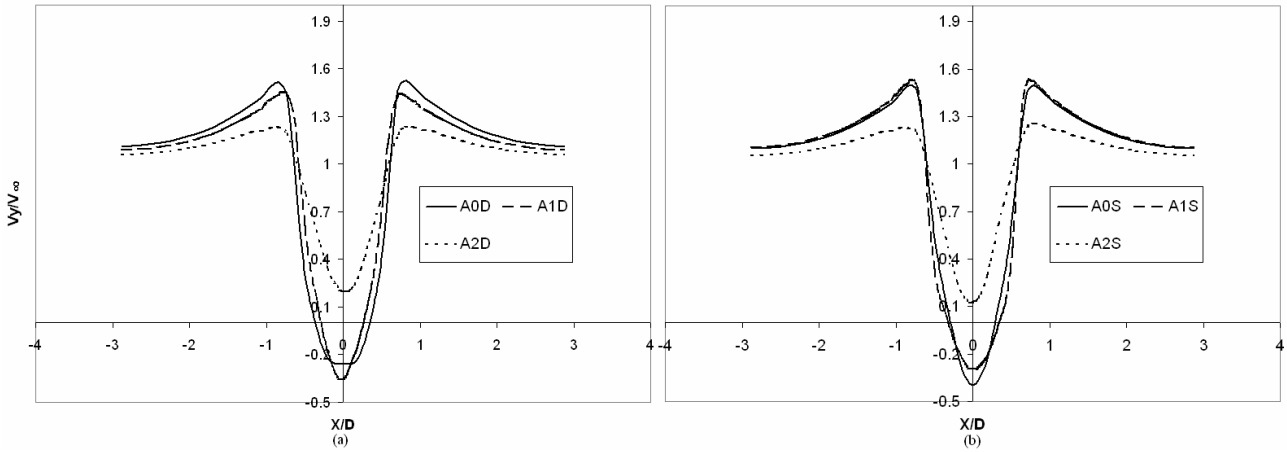

Figure 3. Streamwise velocity in the wake (Re = 2600), (a) Dynamic subgrid model, (b) Smagorinky subgrid model.

Considering the results presented here, the runs used to determine the particle deposition on the tube will be A0D and A1S.

4.2. Particle Flow Analysis

Figure 4 displays the relative rate of 1 μm particle deposition on the tube for the runs A1S and A0D. The Stokes number for this particle size is $St_P = 1.83x10^{-4}$ which is much smaller than the ratio between the time step in the calculations and the characteristic flow time (10^{-2}) so these particles are influenced by the subgrid turbulence as can be observed from the differences between figures 4a and 4b. The particle deposition rate displayed in Fig. 4 is the number of particle deposited on the wall for sectors of 5º arcs around the tube perimeter. Results concerning the particle phase are averaged over the 625 time steps, which correspond to, roughly, eight shedding vortex thus giving the mean values over this time period.

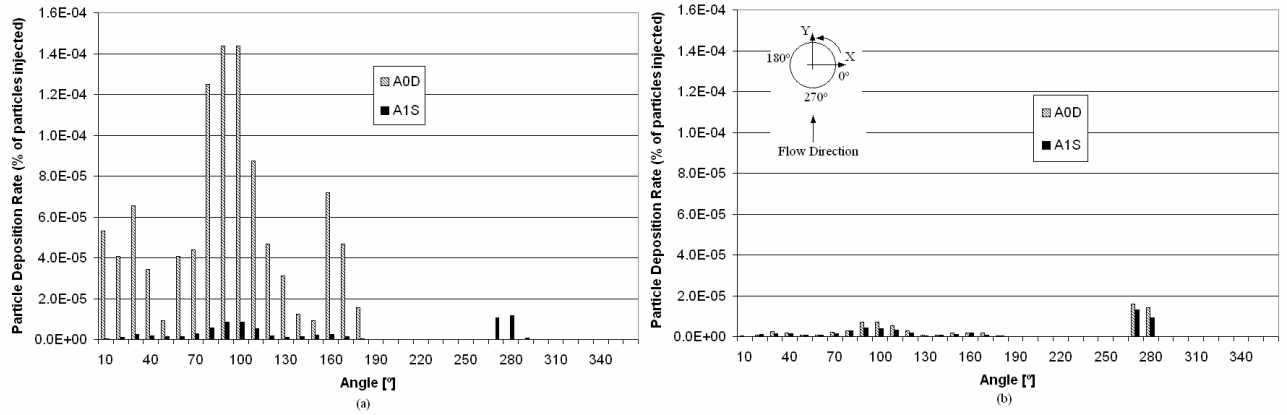

Figure 4. Percentage of particle deposited during the 625 time step for a 1 μm diameter. (a) with the DRW model, (b) without the DRW model.

As the 1 μm particle has a very low Stokes number it follows the fluid without slip and most particles congregate in the core regions of the large scale vortex structures. Despite the two grids considered provide similar size of the wake recirculation, the coarser grid, with more turbulent energy simulated in the small scales, leads to a large influence of the DRW model as can be observed. The main impact of the DRW is on the downstream side of the tube, as expected, providing a more coherent rise on the number of particles deposited on the tube. For the heat exchange tube case we are going to consider the run A1S.

4.2. Heat Exchanger Tube

The heat exchanger tube is considered with a uniform surface temperature of 800 K that is the vapour temperature on the outlet of the superheater for the design conditions. All the other boundary conditions are considered as being the same. Fig. 5 shows the impact of considering the heat transfer of the wall on the particle deposition.

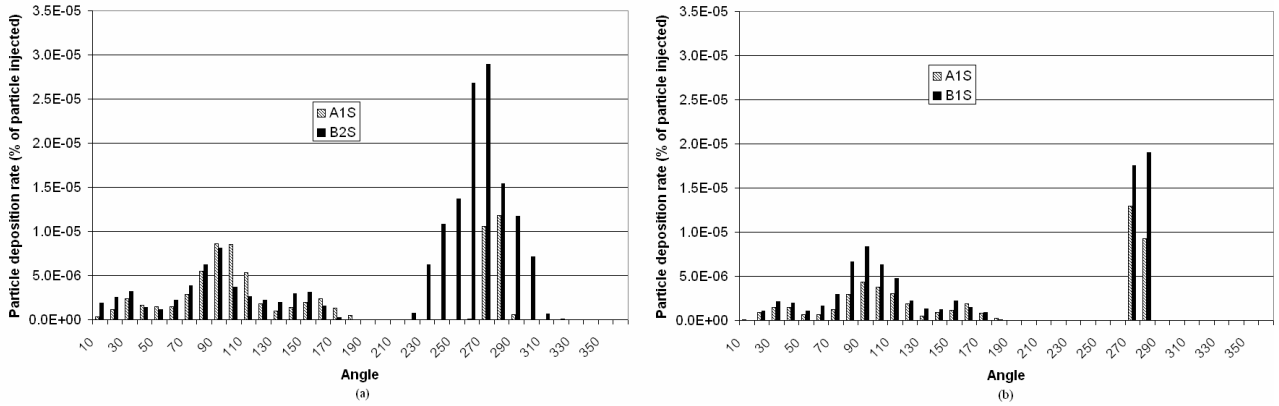

Figure 5. Comparative analysis of the impact on the heated tube on the deposition of the 1μm particle. (a) with DRW, (b) without DRW.

From Fig. 5 it is possible to observe that the heated wall tends to spread the particle deposition in both cases analysed here (with and without the DRW model). Due to the gas cooling the deflection of the flow is lower and hence more particles reach the upstream size of the tube. This leads also to an increase of deposition of this small scale particle, in the upstream side of the tube, while in the wake region the results are not strongly affected.

Fig. 6 presents the distribution of particles hitting the tube for particle sizes 30; 45; 60 and 90 μm. From this figure it is clear that the particle collection efficiency increases with diameter, as expected. The decrease of particle hitting around the tube is consistent with the flow field around it, so the number of particle deposited must be higher on the stagnation point and decreases as the stream lines change around the tube. Nevertheless, on Fig. 6 (a) it is possible to observe that the larger particles have higher impact rates not in the centre of the tube but around ± 10º from this location. These are the limits of the moving of the stagnation point as the vortex shed from the cylinder. The results show that no large size particles hit the downstream side of the tube. This can be explained by the relatively smaller velocities in the vortices and because the particles are deflected around the tube and can not be captured by the vortices. The minimum Stokes number for 30 μm particles is 0.16 and therefore the particle characteristic time is comparable with the time step in the simulations.

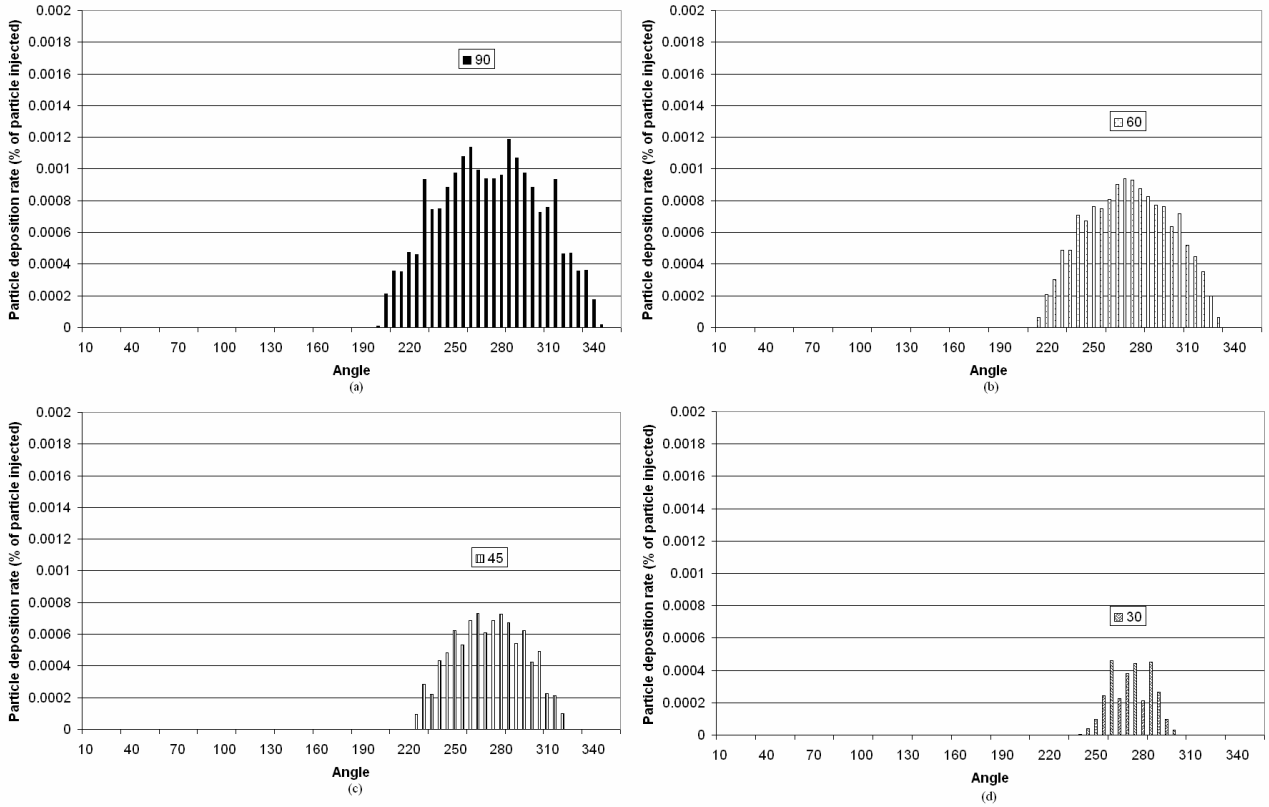

Figure 6. Percentage of particle deposited during the 625 time step. (a) 90 µm diameter, (b) 60 µm diameter, (c) 45 µm diameter, (d) 30 µm diameter.

5. Conclusions

The use of large eddy simulation to solve the flow around a tube is analysed and shown to represent the average flow characteristics. The calculated size of the wake recirculation is sensitive to the spanwise size of the grid. Appropriate selection of the minimum size of the domain and the size of grid close to the walls leads to satisfactory results. The use of 2D domains leads to erroneous results.

The LES calculations provide a basis for the prediction of particle deposition on a heat exchanger tube located inside the boiler. The consideration of gas cooling leads to more disperse distribution of small particles hitting the tube. For the larger particle sizes the expected influence of particle diameter is observed. The results suggest that the particles hitting the upstream side of the tube have more intensity between two positions that correspond to the oscillation of the position of the stagnation point.

The approach presented here can estimate in a good way the particle deposition on the heat exchange tube, supplying the input data to the models that simulate the surface grow.

6. Acknowledgement

Thanks to the Brazilian agencies CNPq (Conselho Nacional de Desenvolvimento Científico e Tecnológico), CAPES (Coordenação de Aperfeiçoamento de Pessoal de Nível Superior) and GRICES (Gabinete de Relações Internacionais da Ciência e do Ensino Superior) for the financial support. Acknowledgement is also given to FCT through project POCTI/EME/47900/2002. Also, special thanks are given to Tractebel Energy and to the Mechanical Engineering Luis Fellipe to permit the easy access to the data of the velocity and temperature as the access to the ash deposit.

7. References

ANEEL, 2006, (Brazilian Electricity Regulatory Agency), available at www.aneel.gov.br, April.

Arpaci V.S., 1997, "Microscales of turbulence, heat and mass transfer correlation", Gordon and breach science Publishers, Amsterdam, Netherlands.

Bouris D., Papadakis G., Bergeles G., 2001, "Numerical evaluation of alternate tube for particle deposition rate reduction in heat exchanger tube bundles", International Journal of Heat and Fluid Flow, Vol 22, pp 525 – 536.

Breuer M., 1998, "Numerical and modeling influences on large eddy simulations for the flow past a circular cylinder", International Journal of Heat and Fluid Flow, Vol 19, pp 512 – 521.

Crowe C.T. 1979, "Gas particle flow", in "pulverized coal combustion and gasfication. Thery and applications for continuous flow process", Smoot L.D., and Pratt D.T., (ed.), Plenum Press, New York.

Fluent (version 6), 2005, User's Guide, Fluent Inc.

Fröhlich J., Rodi W., Kessler Ph., Parpais S., Bertoglio J.P., Laurence D., 1998, "Large eddy simulation of flow around circular cylinders on structured and unstructured grids". In: Hirschek E., (ed) Numerical Flow Simulation I. Notes on numerical fluid mechanics, vol 66, Vieweg, pp319 – 338.

Franke J., Frank W., 2002 "Large eddy simulation of the flow past a circulr cylinder at Re_D=3900", Journal of Wind Engineering and Industrial Aerodynamics, Vol 90, pp 1191 – 1206.

Germano M., Piomelli U., Moin P., Cabot W., 1991 "A dynamic subgrid scale eddy viscosity model", Phys Fluids A, Vol 3, pp 1760 – 1765.

Knudsen, S., K., 2001, "Numerical investigation of ash deposition in straw-fired boilers - Using CFD as the framework for slagging and fouling predictions", PhD Thesis, Institute of Energy Technology, Aalborg University, Denmark.

Liang C., Papadakis G., 2006, "Large eddy simulation of pulsating flow over a circular cylinder at a subcritical Reynolds number", Computers and fluids, vol 35, Article in press.

Lübcke H., Schmidt St., Rung T., Thiele F., 2001, "Comparision of LES and RANS in bluff body flow", Journal of Wind Engineering and Industrial Aerodynamics", Vol 89, pp 1471 – 1485.

Mendes, L.J.N., Forgerini, F. L., Figueiredo, W., Bazzo, E., Azevedo, J.L.T., 2006, "Comparison analysis of boiler ash deposit and porous structure simulated by the ballistic model", ECOS 2006, Crete Greece, July, pp 12-14.

Reinaldo R. F., 2004 "Estudo numérico de transferência de calor e deposição de cinzas em caldeiras de carvão pulverizado", Doctoral thesis, Federal University of Santa Catarina, Florianópolis, Brasil, 2004.

Saugaut P., Grohens R., 1999, "Discrete filters for large eddy simulation", International Journal for Numerical Methods in Fluids, vol 31, pp 1195 – 1220.

Silveira N.A., 2002,"Simulação de grandes escalas de escoamentos turbulento" in Turbulência: Anais da I escola de primavera em transição e turbulência", Silva A.P.F., Menut P.P.P., Su J., (ed.), ABCM publisher, Rio de Janeiro,in Portuguese.

Proceedings of the 11th Brazilian Congress of Thermal Sciences and Engineering -- ENCIT 2006
Braz. Soc. of Mechanical Sciences and Engineering -- ABCM, Curitiba, Brazil, Dec. 5-8, 2006

Paper CIT06-0334

Distribuição de Velocidade em Canais Compostos: Investigação numérica e experimental

J. N. V. Goulart [1]
jhongoulart@yahoo.com.br

S.V. Möller [2]
svmoller@ufrgs.br

A. P. Petry [3]
adrianep@mecanica.ufrgs.br

PROMEC - Universidade Federal do Rio Grande do Sul [1-2-3]
Rua Sarmento Leite, 425
90050-170 - Porto Alegre, RS, BRASIL

Resumo. *O propósito deste trabalho é investigar numérica e experimentalmente a distribuição de velocidade, bem como a estrutura da turbulência em um canal composto formado por um canal principal retangular e duas placas paralelas conectadas a uma das paredes laterais, de forma que o comprimento total, L, pudesse ser variado. Para tanto foi utilizada a anemometria de fio quente, como técnica experimental e o software CFX®, versão 5.6, na simulação do escoamento, utilizando os modelos de turbulência k-ε e Simulação de Grandes Escalas, SGE. Os dados, tanto numéricos como experimentais, mostraram um escoamento altamente cisalhante na fronteira entre os dois canais com estruturas coerentes carregadas pelo escoamento médio.*

Palavras chave:simulação numérica, canais compostos, escoamento cisalhante, estruturas coerentes.

1. Introdução

De maneira geral os canais classificados como compostos são caracterizados pela presença de um canal principal e um ou mais canais secundários, sendo o uso destas estruturas bastante vasto na dentro engenharia, começando em trocadores de calor, passando pelo interior de reatores e até mesmo em canais de água, principalmente canais artificiais. No entanto as investigações sobre o escoamento turbulento neste tipo de canal mostram características peculiares em relação à distribuição das tensões turbulentas e o coeficiente de transferência local de calor na fronteira entre dois canais.

Medições experimentais realizadas por Möller, 1991, em um feixe de barras, com apenas uma linha, mostraram altos valores de intensidade de turbulência, para as componentes axial e azimutal de velocidade, na região das fendas e uma forte dependência entre o aumento destas quantidades e o decrescimento da distancia entre os tubos. As flutuações das diferentes componentes de velocidade mostraram um comportamento quasi-periódico próximo as fendas, tal qual como identificado por Rowe et al., 1974, que sugeria que estas pulsações do escoamento eram responsáveis pelo aumento das intensidades turbulentas junto na fenda.

Meyer e Rheme, 1995, investigaram, experimentalmente, a distribuição de velocidade e a características do escoamento turbulento em canais retangulares com slots na parede lateral, para uma faixa de número de Reynolds de 2300 até 10^5. Para todas as configurações, a seção de teste foi assumida longa o suficiente para o desenvolvimento do escoamento, a relação entre o comprimento das seções e o diâmetro hidráulico, L/D_h, variou entre 45 e 94. Neste trabalho, além das diferentes configurações das seções de teste, também foi analisada a influência da viscosidade e dos parâmetros geométricos do slot, como largura "g" e profundidade "d", na formação dos campos de velocidade e no comportamento dinâmico da turbulência dentro da fenda. De forma geral os campos de velocidade mostram-se qualitativamente muito semelhantes com o aumento da viscosidade, enquanto os auto-espectros de flutuação de velocidade mostraram picos, mesmo para valores de Reynolds tão baixos quanto Re=150, indicando a presença destas estruturas coerentes, que segundo o autor estão presentes em qualquer slot longitudinal onde a profundidade é maior ou igual a duas vezes a largura da fenda, d>= 2g. O comprimento de onda destas pulsações do escoamento mostrou-se ser constante para uma dada geometria e revelou-se uma função exclusivamente da geometria.

Biemüller et al. 1996, investigou numericamente as características do escoamento turbulento em dois canais retangulares conectados por uma fenda, junto a parede superior, usando Simulação de Grandes Escalas, SGE. A altura e largura do canal eram, respectivamente, 180 e 331,6 mm e seu comprimento 504 mm. A fenda que conecta os dois canais principais possui altura, g, e largura, d, de 10,20 e 40,6 mm, respectivamente, portanto uma relação g/d=4. No domínio computacional a seção transversal foi considerada infinita, com condições de contorno periódicas nesta

direção. Também obteve condições de contorno periódicas a direção principal do escoamento. O número de Reynolds da simulação variou entre 3,30x10³ a 5,80x10^5.

Os resultados mostraram picos de tensões de Reynolds junto às fendas e grandes vórtices carregados pelo escoamento médio girando em direções opostas, como modelado por Möller, 1991.

O propósito deste trabalho é estudar numérica e experimentalmente a característica dos campos de velocidade para um escoamento turbulento que se desenvolve entre duas placas paralelas. Para tanto foram utilizadas técnicas de anemometria de fio quente e como ferramenta numérica os modelos de turbulência k-ω e a Simulação de Grandes Escalas.

2. Seção de Testes e Técnica Experimental

As investigações foram feitas em um canal retangular com 146 mm de altura e 193 mm de largura, onde, em uma das paredes laterais, estão conectadas duas placas paralelas, onde o escoamento se desenvolve. As placas possuem um comprimento "L" e estão distante entre si, por uma largura 14 mm, formando uma fenda (slot) lateral de profundidade, p= 70 mm, portanto possuindo uma relação profundidade/largura igual a 5. Neste trabalho foram investigadas seções de teste de dois comprimentos diferentes, 650 e 2020 mm. O fluido de trabalho utilizado é o ar, a temperatura ambiente, sendo este dirigido por um ventilador centrifugo, passando por um difusor, um homogenizador e duas telas, chegando a seção de testes com intensidade de turbulência menor que 1%. Após a passagem pelas telas está localizado um tubo de Pitot, fixo, 150 mm a jusante das telas de proteção, através do qual a velocidade de referência, U_{ref}, pode ser avaliada. Em ambas as configurações foi montada na saída do canal um tubo Venturi que proporcionou uma relação entre a velocidade de referência, lida através do tubo de Pitot, e a vazão, afim de conhecer a velocidade média, grandeza necessária a simulação numérica. O número de Reynolds dos experimentos e da simulação foram calculados utilizando a velocidade média da seção e seu diâmetro-hidraúlico, Dh = 113,85 mm, portanto, Re= 131500.

A fig. 1 mostra uma visão esquemática das seções de testes estudadas, onde a linha tracejada em vermelho mostra a localização do slot, formado pelas placas paralelas.As fig 1 (a) e(b), são visões laterais do canal em suas duas configurações, enquanto na fig. 1 (c), tem-se uma visão frontal do canal, todas as dimensões estão em mm.

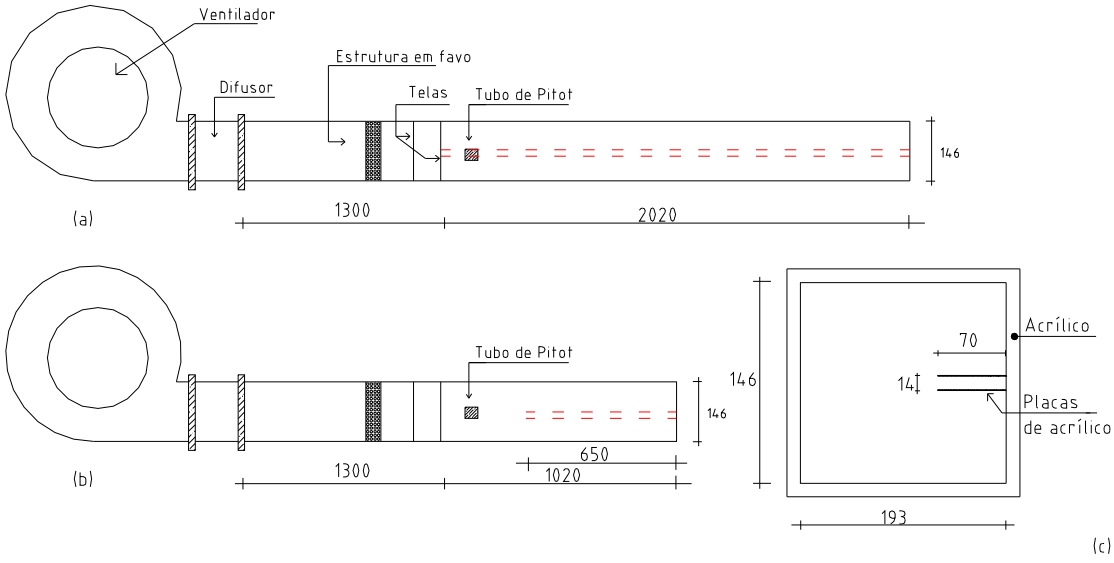

Figura 1. Visão esquemática da seção de testes.

Os valores médios da componente axial de velocidade foram medidos utilizando um tubo de Pitot com diâmetro externo de 1.25 mm. Enquanto as flutuações das componentes, axial, w, e transversal, u, de velocidade foram avaliadas via anemometria de fio quente, utilizando uma sonda de temperatura constante DANTEC StreamLine. Na medição simultânea de duas componentes de velocidade foi utilizada uma sonda dupla, que possui como uma especial característica um fio perpendicular ao escoamento principal e outro inclinado 45°, na calibração da sonda dupla utilizou-se o método proposto por Collins e Williams, 1959, no entanto com modificações importantes feitas por Indrusiak, 2003, que permitiram as diferentes componentes de velocidade, mais detalhes em Goulart, 2004 e Olinto e Möller, 2004.

O tubo de Pitot e a sonda de fio quente foram localizados entre as placas, no plano de simetria do canal e movidos ao longo desta linha por meio de um posicionador tri-axial. Neste trabalho a componente transversal de velocidade, u, é paralela a linha de simetria e a componente axial, w, é paralela a direção principal do escoamento.

A aquisição dos sinais de flutuação de velocidade foi feita utilizando uma placa conversora analógica digital, A/D, com 12 bit marca Keithley DAS58, uma freqüência de amostragem de 3KHz e filtro passa baixa em 1KHz. O comprimento das séries temporais de flutuação de velocidade foi de 21,84 s.

A análise de incerteza dos resultados mostra uma contribuição de 1,4 % proveniente dos equipamentos de medição, anemômetro e placa conversora.

3. Simulação numérica

A simulação numérica, dos campos de velocidade e pressão, foi feita utilizando o software comercial CFX®, versão 5.6. Neste trabalho foram avaliadas duas diferentes modelagens de turbulência, o modelo k-ϖ, para a solução estacionária do problema e uma avaliação transiente utilizando-se Simulação de Grandes escalas, SGE / Smagorinsk, sendo que para este último o passo de tempo utilizado e a constante de Smagorinsk, C_s, foram respectivamente, 5 x 10^{-4} s e 0,10. Os detalhes do equacionamento podem ser vistos em Goulart et al., 2004.

3.1. Discretização geométrica do domínio, condições de entrada e de contorno

Os domínios geométricos, para ambas seções, são mostrados na fig. 2 (a) e (b). Em ambos os casos somente foram simulados o escoamento dentro do canal, a partir das telas de proteção. Foi gerado em todo o domínio uma malha não estruturada, utilizando elementos tetraédricos e adjacente as paredes foram geradas camadas de elementos prismáticos, possibilitando uma análise mais relevante dos efeitos viscosos na região. O número necessário de elementos na discretização de ambos os domínios foi de 529544 na seção de 1020 mm e 80300 para a seção maior. Para a seção maior, 2020 mm, tentou-se uma discretização com 675000, no entanto os resultados preliminares foram bastante ruins, fazendo-se necessário uma maior quantidade de elementos, o que tornaria a solução muito lenta. Portanto a solução encontrada para o problema foi utilizar um plano de simetria, como mostrado na fig. 2 (a), na qual aparece somente parte do domínio na direção z. Em ambos os casos o escoamento se dá na direção z e os planos de saída indicados nas figuras.

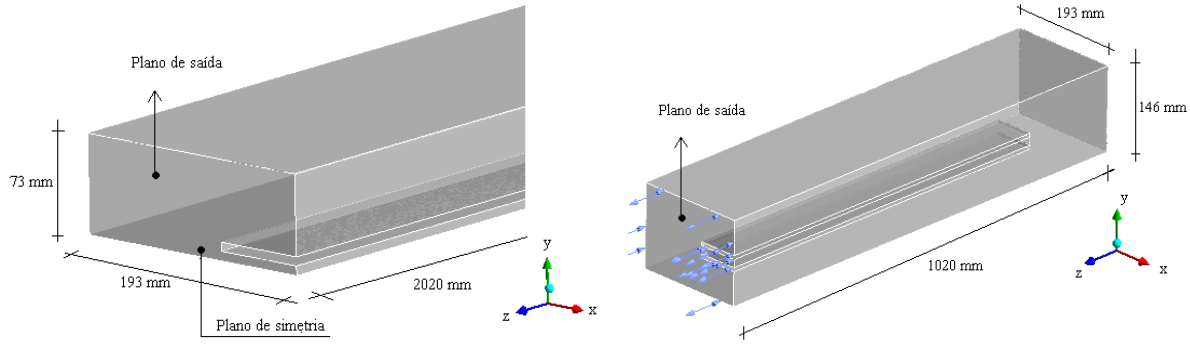

Figura 2. Discretização computacional do problema. a) seção maior, 2020 mm. b) seção menor, 1020 mm

Na região de entrada foi definido um campo de velocidade média com uma intensidade de turbulência de 1%. A velocidade média pode ser avaliada experimentalmente através da utilização de um tubo Venturi, colocado na saída do canal, para qual foi feita uma relação entre a velocidade de referência,U_{ref}, medida através do Pitot fixo, e a velocidade média do canal. A fig. 3 mostra esta relação para a seção de testes da fig. 2 (b).

Na região da saída foi definida uma pressão relativa igual a zero, sem escoamentos secundários assegurando vetores perpendiculares ao plano de saída. A condição de saída imposta permite o retorno do escoamento caso exista zonas de recirculação, neste caso, foi determinado que o fluido que retorna possui uma intensidade de turbulência de 5%.

A condição de não deslizamento foi imposta para todas as paredes.

Nos modelos k-ω e SGE/Smagorinsk, foram adotadas como condição inicial campos nulos de velocidade e pressão.

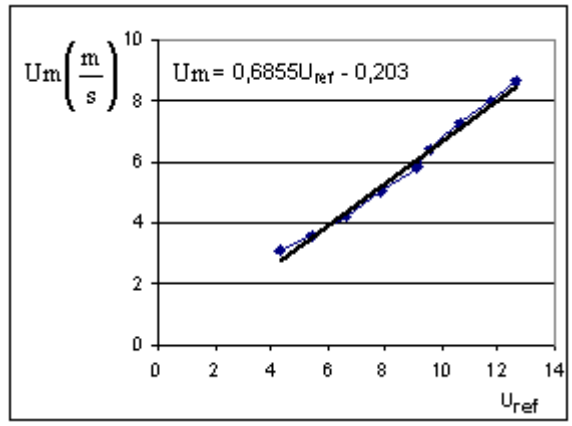

Figura 3. Relação entre velocidade de referência, U_{ref}, e velocidade média da seção, Um.

4. Resultados

A fig. 4 (a) e (b), mostra a distribuição das componentes de velocidade média axial ao longo da linha de simetria, para as seções de teste (a) e (b), respectivamente. Nota-se que o modelo numérico empregado obteve bastante sucesso na predicção do campo de velocidades, balizando as conclusões que possam ser tomadas a partir de então. As maiores diferenças.podem ser encontradas na seção de testes (a), na região do canal principal, com uma diferença máxima entre os dados experimental e numérico de 7,40 %, podendo, esta diferença, ser atribuída ao sistema de medições de vazão, no qual fora utilizado manômetros diferenciais eletrônicos e de coluna de água.

Embora ambas as seções possuam a mesma relação profundidade/largura, a forma do perfil de velocidades se mostra diferente em ambas as seções, enquanto as velocidades máximas dentro do canal principal possuem os mesmos valores, as velocidades dentro da fenda são menores, indicando claramente que o escoamento não se encontra desenvolvido para estes comprimentos de entrada.

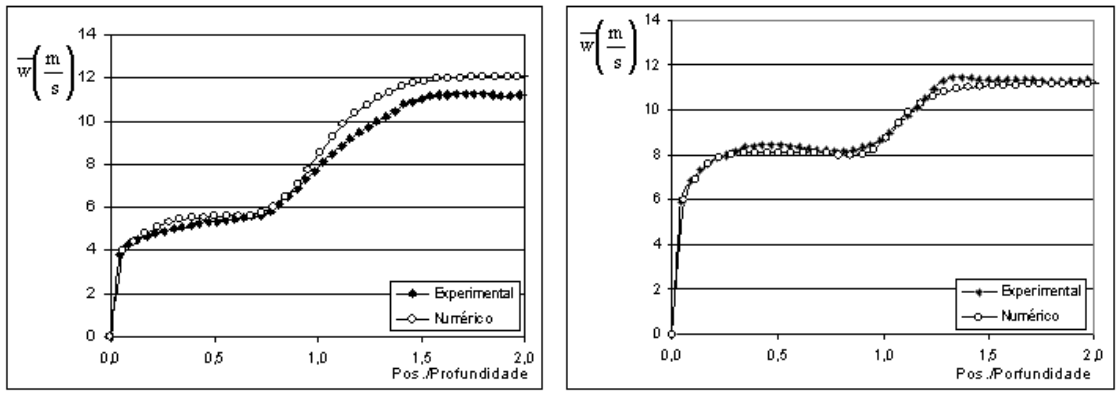

a) b)

Figura 4. Distribuição da velocidade média axial ao longo da linha de simetria. A) seção de teste (a). b) seção de testes (b).

Os campos de velocidade média axial, 20 mm a montante da saída, são mostrados na fig. 5 (a) e (b), nota-se em ambas as figuras, os mapas de velocidade são bastante simétricos, no entanto, na seção maior, fig. 5 (a), há uma região de máxima velocidade ocorrendo no canal principal, diferentemente da fig 5(b) que possui velocidades maiores na região a fenda e uma região de velocidade máxima que se estende por boa parte do canal principal, tal como mostrado no perfil de velocidades na fig. 4 (b) na qual existe um patamar de velocidade praticamente constante a partir da região da fenda.

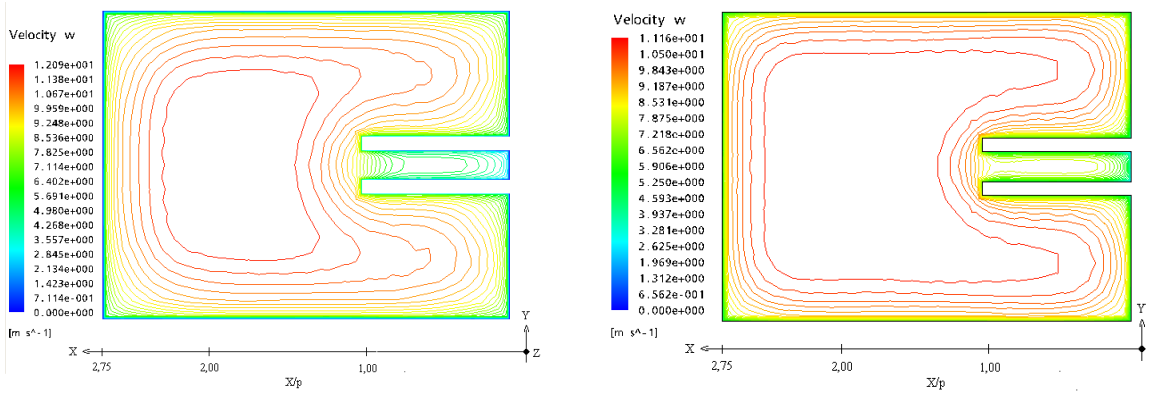

a) b)

Figura 5. Contornos de velocidade média axial. a) seção de testes maior. b) seção de testes menor.

4.1 A estrutura da turbulência

A fig. 6(a) e (b), mostra o mapa de isovorticidade no plano médio da fenda, próximo a região da saída. Em ambos os casos são evidenciadas regiões de maiores vorticidade próximas às paredes e na fronteira entre o subcanal e o canal principal, no entanto a seção menor, fig. 6 (b), se difere por apresentar maior vorticidade em uma região mais estreita, na fronteira entre os dois canais, possuindo o valor máximo dentro do canal principla.

A vorticidade no plano XZ é dada pela equação 1, no entanto assumindo que o gradiente da componente "u" de velocidade na direção principal do escoamento é muito menor em pequeno em relação ao gradiente da componente axial de velocidade na direção transversal, "x", então a vorticidade neste plano, pode ser assumida como e gradiente de da componente "w" em relação a "x", eq 2.

$$\Omega_y = \frac{1}{2}\left[\left(\frac{\partial u}{\partial z}\right) - \left(\frac{\partial w}{\partial x}\right)\right] \tag{1}$$

$$\Omega_y \sim \left(\frac{\partial w}{\partial x}\right) \tag{2}$$

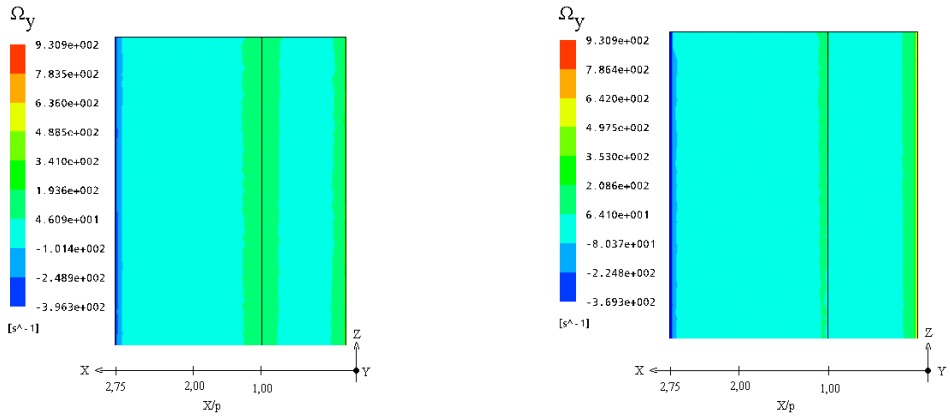

a) b)

Figura 6. Regiões de isovorticidade. a) seção de testes maior. b) seção de testes menor.

A fig. 7 (a) e (b), mostra o gradiente de "w" em relação ao eixo "x", com ambas as quantidades adimensionalizadas pela velocidade máxima e pela profundidade das placas, portanto, tem-se $\varphi = u(x)/U_{max}$ e $\eta = x/p$.

Nota-se que os resultados experimentais e numéricos possuem uma boa concordância, enquanto na seção de testes maior, ambos resultados mostram picos de vorticidade dentro do sub canal e uma banda mais larga desta quantidade, na seção menor acontece o oposto, picos de vorticidade fora do subcanal e uma faixa mais estreita desta quantidade.

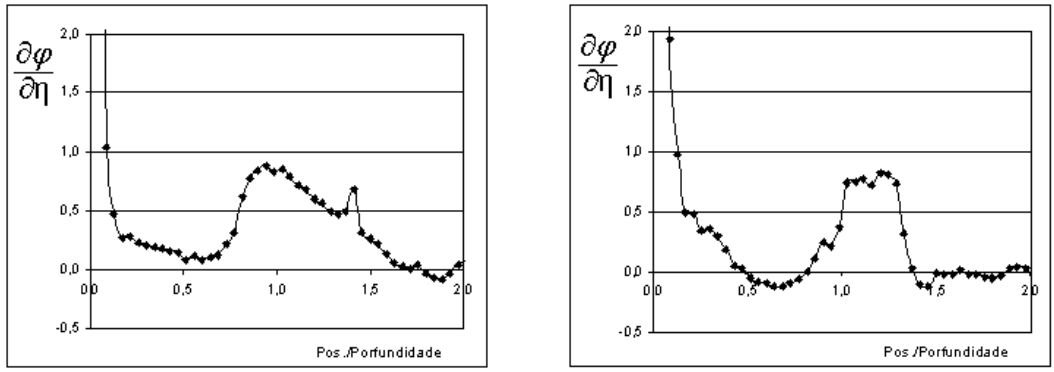

a) b)

Figura 7. Gradientes de velocidade na direção "x". a) seção de testes maior. b) seção de testes menor

A visualização feita por Meyer e Rehme, 1995, em um canal retangular com um slot longitudinal, onde L/D_h= 94, mostrou estruturas coerentes, estáveis e igualmente espaçadas, sendo carregadas pelo escoamento médio dentro do subcanal e segundo os autores com velocidade de convecção, U_c= 0,70 U_e, sendo U_e a velocidade da borda. A fig. 8 (a) e (b) mostra os vetores médios de velocidade no plano de simetria longitudinal da fenda, subtraídos da velocidade de convecção, Uc. Na seção maior são visíveis estruturas coerentes carregadas pelo escoamento médio com diâmetro da ordem da profundidade do slot, no entanto, diferentemente de Meyer e Rehme, 1995 e Biemüller et al., 1996, estes vórtices mostram-se quase que sobrepostos, enquanto nos trabalhos destes autores estas estruturas coerentes guardam uma distância entre si.

Na fig. 9 (a) e (b), são mostrados os autoespectros de flutuação de velocidade para as componentes axial (preta) e transversal (verde), tomados na mesma posição relativa, x/p= 0,68. Ambos os espectros confirmam os resultados numéricos, enquanto na seção maior os picos de freqüência são bastante pronunciado, principalmente na componente transversal, o mesmo não ocorre na seção menor, fig. 9 (b).

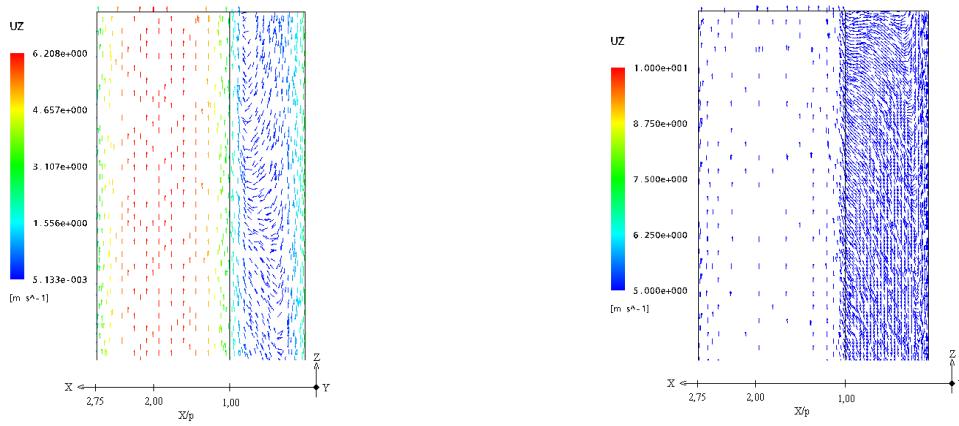

a) b)

Figura 8. Vetores de velocidade no plano médio da fenda. a) seção de testes maior. b) seção de testes menor

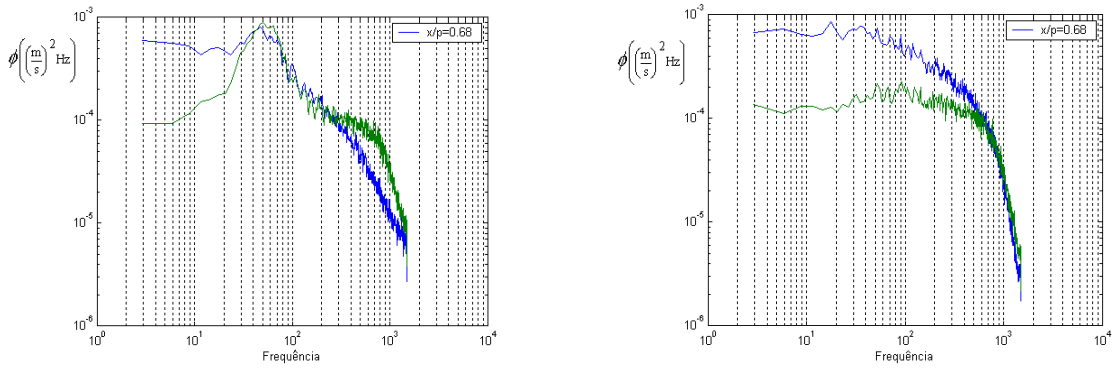

a)

Figura 9. Autoespectros de flutuação de velocidade tomados em x/p = 0,68. a) seção de testes maior. b) seção de testes menor.

Os escoamentos secundários no plano, x- y, 20 mm a montante da região de saída, são mostrados na fig. 10 (a) e (b). Os resultados concordam qualitativamente com os resultados apresentados por Biemüller et al., 1996, e estão presentes em ambas seções de testes.

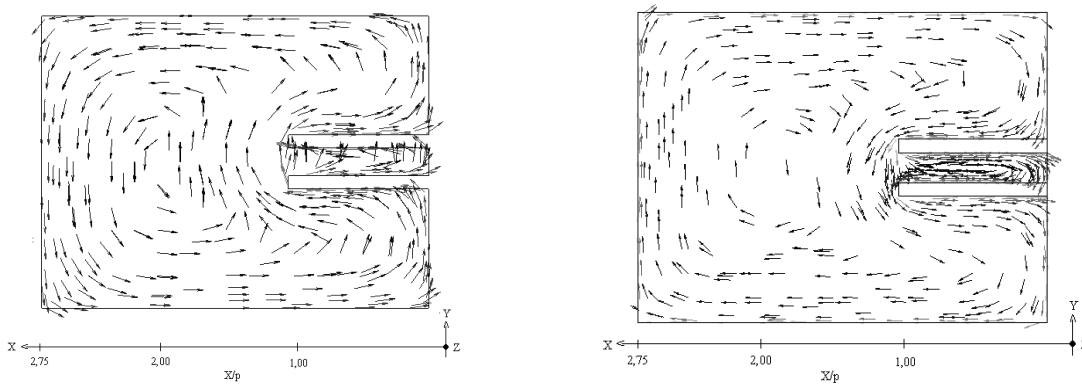

Figura 10. Escoamentos secundários no plano x-y, em ambas seções de teste.

Empregou-se Simulação de Grandes Escalas/Smagorinsk na maior seção de teste, L= 2020 mm. Quanto aos resultados, estes não foram satisfatórios devido ao pequeno tempo de simulação, somente, somente 0,5 s, no entanto o resultado parcial do perfil de velocidade média axial, fig. 11, mostra uma certa concordância com os dados experimentais, indicando que a solução evolui satisfatoriamente. Os resultados da fig. 11 foram avaliados na linha de simetria, 20 mm a montante da saída da seção.

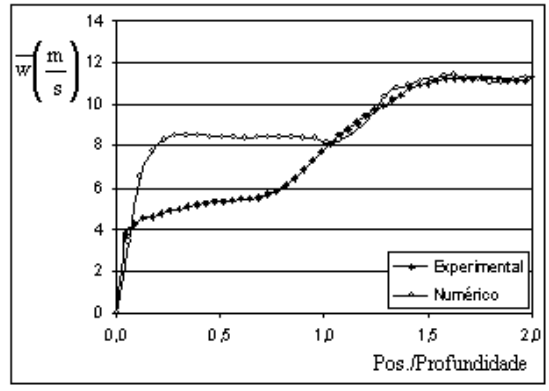

Figura 11. Perfil de velocidade no plano de simetria para a maior seção de testes.

5. Conclusões

O propósito deste trabalho é investigar a distribuição de velocidade, bem como a ocorrência de estruturas coerentes em um canal composto. Para tanto foram utilizadas ferramentas experimentais, sondas dupla de fio quente e ferramentas numéricas, simulação do escoamento via os modelos de turbulência k-ω e SGE/Smagorinsk.

A simulação numérica utilizando k-ω obteve uma boa concordância com os dados experimentais, principalmente porque o escoamento em questão não possui zonas de recirculação. Os resultados de distribuição da componente axial de velocidade mostraram que a variação de velocidade entre o canal principal e a região do "slot", cresce a medida que o comprimento aumenta, bem como a região onde o gradiente de velocidade é maior, possibilitando a ocorrência de instabilidades.

Quanto ao uso de a modelagem via LES, na simulação do escoamento cisalhantes, os autores acreditam que a visualização transiente do campo de velocidades será de suma importância, no entanto o esforço computacional demandado combinado com a quantidade de elementos necessários na discretização do domínio, tornam bastante demorada a solução do problema.

No que diz respeito a formação de estruturas coerentes no plano médio das placas, o modelo permitiu observar e dirimir dúvidas quanto a existência destas estruturas, mostrando que a presença das mesmas e como estas se apresentam no interior do escoamento, não é somente uma função da profundidade e largura do slot, mas também do comprimento da seção de testes.

6. Agradecimentos

Os autores agradecem todo o tipo de suporte dado pelo CNPq – Conselho Nacional de Desenvolvimento Científico e Tecnológico.

Jhon N. V. Goulart agradece também a CNPq, pelo pela bolsa de estudos.

7. Referências

Biemüler, M., Meyer, L. And Rehme, K., Large eddy simulation and measurement of the structure of turbulence in two rectangular channels connected by the gap, Engineering Turbulence Modeling and Experiments 3, Editors: Rodi, W. and Bergeles,G., 249-258, 1996.

Goulart, J. N. V., Estudo experimental dos campos de pressão e velocidade em feixes de tubos utilizando placas defletoras; Dissertação de Mestrado, Universidade Federal do Rio Grande do Sul, 2004.

Goulart, J. N. V., Aguirre Oliveira Jr, J. A., Petry, A. P., Möller, S. V. Escoamento Trubulento e Feixe de tubos: Análise Numérica e Experimental. In: 10º Congresso Brasileiro de Engenharia e Ciências Térmicas - ENCIT, 2004, Rio de Janeiro, 2004.

Guellouz, M.S. and Tavoularis, S., The structure of the turbulent flow in a rectangular channel contening a single rod – Part 1: Reynolds-Average mesurements, Exp. Thermal and Fluid Sci., **23**, 59-73, 2000.

Indrusiak, M. L. V. Caracterização de escoamentos turbulentos transientes usando a transformada de ondaletas; Tese de Doutorado, Universidade Federal do Rio Grande do Sul, 2003.

Lesieur, M., Turbulence in Fluids, Third Edition, Kluwer Academic Publishers, Dordrecht, The Netherlands, 1997.

Meyer, L. and Rehme, K., Large-scale turbulence phenomena in compound rectangular channels, Exp. Thermal Fluid Sci., **8**, 286-304, 1994.

Meyer, L. and Rehme, K., Periodic vortices in flow though channels with longitudinal slots or fins, 10th Symposium on turbulent shear flows, The Pennsylvania State University, University Park, August 14-16, 1995.

Möller, S. V., On Phenomena of Turbulent Flow Through Rod Bundles. Experimental Thermal and Fluid Science, v. 4, n.1, pp. 25-35, 1991.

Olinto, C. R. and Möller, S. X-probe calibration using Collis and William's equation. In: 10º Congresso Brasileiro de Engenharia e Ciências Térmicas - ENCIT, 2004, Rio de Janeiro, 2004.

Rowe, D.S., Johnson, B.M. and Knudsen, J. G., Implications concerning rod bundle crossflow mixing based on mesurements of turbulent flow structure, Int. J. Heat Mass Transfer, **17**, 407-419, 1974.

Schlichting, H. 1968. Boundary Layer Theory. 6th edn. N. York: McGraw-Hill.

Soldini, L., Piattella, A., Brocchini, M., Mancinelli, A. e Bernetti, R. Macrovortices-induced horizontal mixing in compound channels, Ocean Dynamics, **54** , 333 – 339, 2004.

Velocity Distribution in Compound Channels: Numerical and Experimental Investigations

J. N. V. Goulart [1]
jhongoulart@yahoo.com.br

S. V. Möller [2]
svmoller@ufrgs.br

A. P. Petry [3]
adrianep@mecanica.ufrgs.br

PROMEC - Universidade Federal do Rio Grande do Sul [1-2-3]
Rua Sarmento Leite, 425
90050-170 - Porto Alegre, RS, BRASIL

Abstract

The purpose of this paper is to investigate, numerical and experimentally, the velocity distribution, as well the cture turbulence structure, inside a compound channel, formed by the main channel and two parallel plate connected on the lateral wall. In this channel the length "L" could be changed. Hot wire probes were used and, how numerical tool, was used the CFX® software, version 5.6, with k-ε and Large Eddy Simulations/Smagorinsk, models to predict the turbulence. The numerical and experimental results showed a shear flow, on the boundary of two sub channels and the coherent structures transported by the mean flow.

Keywords: numerical simulation, compound channels, shear flow, coherent structures.

Proceedings of the 11th Brazilian Congress of Thermal Sciences and Engineering -- ENCIT 2006
Braz. Soc. of Mechanical Sciences and Engineering -- ABCM, Curitiba, Brazil, Dec.5-8, 2006

Paper CIT06-0344

ON INTERFRENCE BETWEEN CIRCULAR CYLINDERS IN CROSS FLOW AT HIGH REYNOLDS NUMBER USING SURFACE VORTICITY METHOD

Luiz Antonio Alcântara Pereira
Instituto de Engenharia Mecânica, UNIFEI, CP 50, Itajubá, Minas Gerais, 37500-903, Brasil
e-mail: luizantp@unifei.edu.br

Miguel Hiroo Hirata
FAT/UERJ
Campus Regional de Resende
Estrada Resende - Riachuelo, Resende, RJ
e.mail: hirata@fat.uerj.br

Abstract. *A two-dimensional discrete-vortex model is used to investigate vortex interaction inside the near wakes of circular cylinders in cross flow. The numerical simulation is accomplished by using the vortex method, which takes into account the viscous effect in the flow field. The dynamics of the wakes is computed using the convection-diffusion splitting algorithm, where the convection process is carried out with a Lagrangian second-order Adams-Bashforth time-marching scheme, and the diffusion process is simulated using the random walk method. Aerodynamics loads are calculated using an integral equation derived from the pressure Poisson equation. Comparisons of the computed results with the experimental measurements showed that the present discrete vortex method is able to replicate most of the salient features observed in cylinder array experiments.*

Keywords: *vortex method, panels method, interference, flow patterns, aerodynamics loads.*

1. Introduction

In engineering practice, most structures on land and in the ocean often appear in groups and are confronted by a fluid flow. The flow field around pipes in a cluster is very complex and has been studied extensively. The main goals of that research line have been among others, the measure the fluid force and pressure distribution acting on each cylinder, flow velocity profile, vortex shedding, and to understand the resultant flow patterns.

Due the mutual interference between cylinders at close proximity, the aerodynamics characteristics, such as fluctuating lift and drag forces, vortex-shedding patterns and fluctuating pressure distributions, for each member of a group are completely different from isolated ones. When a cylinder is placed in the wake of another in cross-flow its unsteady loading becomes dependent not only on the flow activities in its wake, but also on those in the wake of the upstream cylinder.

A host of studies have addressed the interference effects between two, three, and even four cylinders in a uniform and/or turbulent flow.

Numerous investigations have been made of the flow past two circular cylinders, which is the simplest case of a group, in the last three decades. Zdravkovich (1977) and Ohya *et al.* (1989) presented an extensive review of the state of knowledge of flow across two cylinders in various arrangements. Previous investigations of tandem configurations by Biermann and Herrnstein (1933), Kostic and Oka (1972), Novak (1974), Zdravkovich and Pridden (1975, 1977), Okajima (1979), Igarashi (1981, 1984), Hiwada *et al.* (1982), Arie *et al.* (1983), Jendrzejczyk and Chen (1986) have revealed considerable complexity in fluid dynamics as the spacing or gap between the cylinders is changed.

The interference phenomena are highly non-linear and there are many discrepant points in previous works. Arie *et al.* (1983) pointed out that fluctuation in drag force acting both cylinders is weakly dependent on spacing. On the other hand, Igarashi (1981) reported that the fluctuation in pressure associated with fluctuation in aerodynamics forces (lift and drag) acting on a downstream cylinder is strongly dependent on gap between the cylinders. Alam *et al.* (2003) presented an experimental study in which fluctuating lift and drag forces acting on the cylinders was measured. In their work they elucidated the discrepant points and clarified the flow patterns over the cylinders.

Recently, the Vortex Method was employed by Teixeira da Silveira *et al. (2005)* to simulate the vortex-shedding flow from two tandem cylinders in cross-flow; the aerodynamic characteristics are investigated at a Reynolds number of 6.5×10^4 and comparisons are made with experimental results presented by Alam *et al.* (2003). As the simulations showed, the numerical results obtained are in overall good agreement with the experimental results used for comparison, especially in the simulations for the upstream cylinder. Some discrepancies observed in the determination of the aerodynamics loads for the downstream cylinder may be attributed to errors in the treatment of vortex element moving away from a solid surface. Because every vortex element has different strength of vorticity, it will diffuse to different location in the flow field. It seems impossible that every vortex element will move to same ε-layer normal to

the solid surface. In the present method all nascent vortices were placed into the cloud through a same displacement normal to the panels.

When either one or both cylinders are elastic and vibrate, the flow field becomes significantly more complicated because of the interaction of the fluid flow and the cylinders motion. Efforts have been made to understand the phenomena involved. Motivated by concern over the large oscillations frequently occurring in transmission lines exposed to the high wind, most of the studies of elastic cylinders have focused on characterizing the motion of two cylinders in tandem. The disturbed flow caused by the windward cylinder striking the leeward cylinder can induce dynamic instability, called wake induced flutter. In addition, cylinders are also subjected to other fluctuating forces associated with vortex shedding and turbulence in the incoming flow or generated by the cylinder motion. The phenomena have been studied, experimentally and analytically, by Zdravkovich (1977), Simpson and Flower (1977) and Williamson and Roshko (1988).

Kareem *et al* .(1998) presented an experimental study of the interference effects between two and three cylinders of finite height immersed in a turbulent boundary layer at subcritical Reynolds number utilizing a pneumatic averaging manifold system to measure the fluctuating force at various levels.

Lam *et al.* (2001a) employed the Vortex Method to simulate flows around four equi-spaced cylinders. The surface of the each cylinder was represented by straight-line panels with a point vortex located at the control point; the coalescence of vortices when they are too close to each other was introduced, and the pressure on the airfoil surface was calculated according to the inviscid flow analysis. A comparison of the aerodynamics loads obtained with the experimental results by Lam and Fang (1995) showed a better agreement in the drag direction. A more sophisticated scheme is required to obtain better prediction on pressure and force characteristics. He and Su (1994) showed that the results for the pressure calculation could be improved by considering the nonlinear acceleration terms.

The Vortex Method have been developed and applied for analysis of complex, unsteady and vortical flows in relation to problems in a wide range of industries, because they consist of simple algorithm based on physics of flow (Kamemoto, 2004). In this method, the vorticity in the fluid region is numerically simulated using a cloud of discrete vortices with a viscous core (Lamb vortex). To simulate the vorticity at the solid surfaces, nascent vortices are generated there at each time step of the simulation. In order to take care of the convection and the diffusion of the vorticity one makes use of the convection-diffusion splitting algorithm; accordingly the convection of the vortices in the cloud is carried out independently of the diffusion for each time step of the simulation. This is in essence the foundation of the Vortex Method (e.g. references Chorin, 1973; Sarpkaya, 1989; Sethian, 1991; Kamemoto, 1994; Lewis, 1999; Ogami, 2001 and Alcântara Pereira *et al.*, 2002). Please note that with the Lagrangian formulation a grid for the spatial discretization of the fluid region is not necessary. Thus, special care to handle numerical instabilities associated to high Reynolds numbers is not needed. Also, the attention is only focused on the regions of high activities, which are the regions containing vorticity; on the contrary, Eulerian schemes consider the entire domain independent of the fact that there are sub-regions where less important, if any, flow activity can be found. With the Lagrangian tracking of the vortices, one need not take into account the far away boundary conditions. This is of important in the wake regions (which is not negligible in the flows of present interest) where turbulence activities are intense and unknown, a priori.

In the present paper, the Vortex Method is employed to simulate the interference effects for a group of finite cylinders. The interference phenomena are highly non-linear and at present beyond a reliable theoretical or numerical analysis. The main feature of the present vortex code is to simulate numerically the two-dimensional, incompressible, unsteady flow around of pipe clusters: (a) for two pipes, for three-pipes clusters, (c) for regular square multiple clusters, (d) and for irregular multi-pipe clusters.

The present Vortex Method has been used to simulate the macro scale phenomena, therefore the smaller scale ones are taken into account through the use of a second order velocity function (Alcântara Pereira et *al*., 2002). In this approach, the effect of small scale is not considered.

2. Formulation of the Physical Problem

Consider, e.g., the incompressible fluid flow of a Newtonian fluid around three-pipe clusters an unbounded two-dimensional region. Figure 1 shows the incident flow, defined by free stream speed U and the domain Ω with boundary $S = S_1 \cup S_2 \cup S_3 \cup S_4$, S_1 being the upstream cylinder surface, S_2 being the intermediate cylinder surface, S_3 being the downstream cylinder surface and S_4 the far away boundary.

The viscous and incompressible fluid flow is governed by the continuity and the Navier-Stokes equations, which can be written in the form

$$\nabla \cdot \mathbf{u} = 0 \tag{1}$$

$$\frac{\partial \mathbf{u}}{\partial t} + \mathbf{u} \cdot \nabla \mathbf{u} = -\nabla p + \frac{1}{Re} \nabla^2 \mathbf{u} . \tag{2}$$

In the equations above $\mathbf{u}$ is the velocity vector field and p is the pressure. As can be seen the equations are non-dimensionalized in terms of U and b (a reference length). The Reynolds number is defined by

$$\mathrm{Re} = \frac{bU}{\upsilon} \tag{2a}$$

where υ is the fluid kinematics viscosity coefficient; the dimensionless time is b/U.

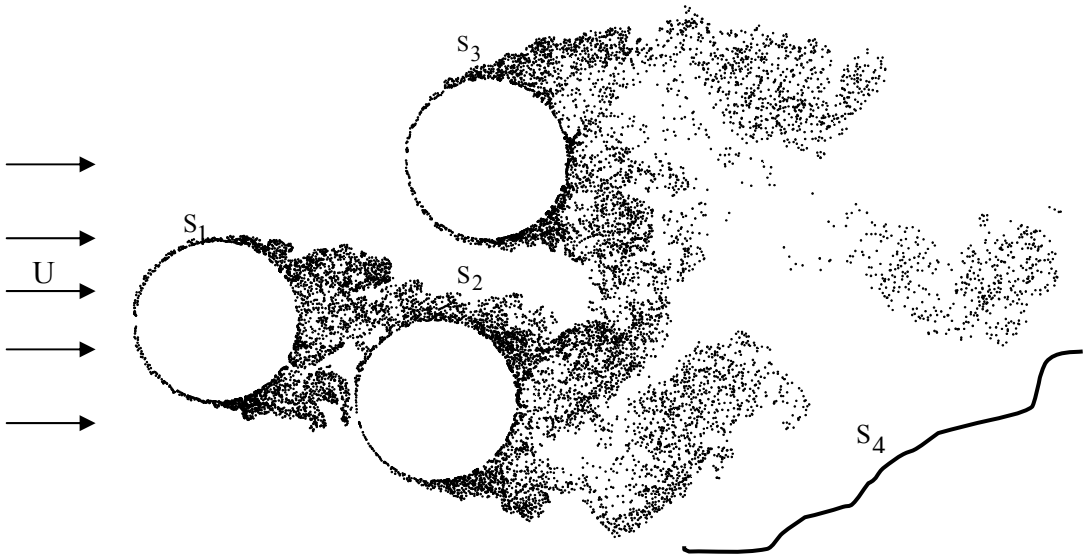

Figure 1. Flow around three circular cylinders.

The impermeability and no-slip conditions on the two circular cylinders surface are written as

$$u_n = \mathbf{u} \cdot \mathbf{e}_n = 0 \tag{3a}$$

$$u_\tau = \mathbf{u} \cdot \mathbf{e}_\tau = 0 \tag{3b}$$

$\mathbf{e}_n$ and $\mathbf{e}_\tau$ being, respectively, the unit normal and tangential vectors. One assumes that, far away, the perturbation caused by the bodies fades as

$$|\mathbf{u}| \to 1 \text{ at } S_4 . \tag{3c}$$

The dynamics of the fluid motion, governed by the boundary-value problem (1), (2) and (3), can be studied in a more convenient way when is taked the curl of the Navier-Stokes equations to obtain the vorticity equation. For a 2-D flow this equation is scalar, and it can be written as

$$\frac{\partial \omega}{\partial t} + \mathbf{u} \cdot \nabla \omega = \frac{1}{\mathrm{Re}} \nabla^2 \omega \tag{4}$$

in which ω is the only non-zero component of the vorticity vector (in a direction normal to the plane of the flow). One of the advantages of working with the Eq. (4) is the elimination of the pressure term, which always requires special treatment in most numerical experiments.

3. The discrete vortex method

According to the convection-diffusion splitting algorithm (Chorin, 1973) it is assumed that in the same time increment the convection and the diffusion of the vorticity can be independently handled and are governed by

$$\frac{\partial \omega}{\partial t} + \mathbf{u} \cdot \nabla \omega = 0 \tag{5}$$

$$\frac{\partial \omega}{\partial t} = \frac{1}{\mathrm{Re}} \nabla^2 \omega . \tag{6}$$

In a physical sense vorticity is generated on the circular cylinders surface so as to satisfy the no-slip condition, Eq. (3b). The discrete vortex method represents the vorticity by discrete vortices, whose transport at each time increment is carried out in sequence. Convection is governed by Eq. (5) and the velocity field is given by

$$u - iv = 1 + \frac{i}{2\pi} \sum_{n=1}^{M} \gamma(S_n) \int_{\Delta S_n} \frac{d}{dz} \ln(z - \zeta) d\zeta + \frac{i}{2\pi} \sum_{k=1}^{N} \frac{\Delta \Gamma_k}{z - z_k} . \tag{7}$$

Here, u and v are the x and y components of the velocity vector $\mathbf{u}$ and $i = \sqrt{-1}$. The first term in the right hand sides is the contribution of the incident flow; the summation of α M integral terms comes from the panels distributed on the circular cylinders surfaces. The second summation is associated to the velocity induced by the cloud of N free vortices; it represents the vortex-vortex interaction.

In this paper, an improvement was also introduced in the convective step of the simulation; by using the anti symmetry property of the vortex-vortex velocity induction, the computational effort was reduced; this is an important feature, since the vortex-vortex velocity induction calculation is the most time consuming part of the simulation.

In order to remove the singularity in the second summation of Eq. (7) Lamb vortices are used, whose mathematical expression for the induced velocity of the kth vortex with strength $\Delta \Gamma_k$ in the circumferential direction u_{θ_k}, is (Mustto *et al.*, 1998)

$$u_{\theta_k} = \frac{\Delta \Gamma_k}{2\pi r} \left\{ 1 - \exp\left[-5.02572 \left(-\frac{r}{\sigma_0} \right)^2 \right] \right\} \tag{8}$$

where σ_0 is core radius of the Lamb vortex.

In this particular equation r is the radial distance between the vortex center and the point in the flow field where the induced velocity is calculated.

Each Lamb discrete vortex distributed in the flow field is followed during numerical simulation according to the Adams-Bashforth second-order formula (Ferziger, 1981)

$$z(t + \Delta t) = z(t) + [1.5u(t) - 0.5u(t - \Delta t)]\Delta t + \xi \tag{9}$$

in which z is the particle position of a vortex particle, Δt is the time increment and ξ is the random walk displacement. According to Lewis (1991), the random walk displacement is given by

$$\xi = \sqrt{4\beta \Delta t \ln\left(\frac{1}{P}\right)} [\cos(2\pi Q) + i \sin(2\pi Q)] \tag{10}$$

where $\beta = \mathrm{Re}^{-1}$ for the vortex particles; P and Q are random numbers between 0.0 and 1.0.

The pressure calculation starts with the Bernoulli function, defined by Uhlman (1992) as

$$Y = p + \frac{u^2}{2}, \quad u = |\mathbf{u}| \tag{11}$$

Kamemoto (1993) used the same function and starting from the Navier-Stokes equations was able to write a Poisson equation for the pressure. This equation was solved using a finite difference scheme. Here the same Poisson equation was derived and its solution was obtained through the following integral formulation (Shintani & Akamatsu, 1994)

$$H\overline{Y_i} - \int_{S_1} \overline{Y} \nabla G_i \cdot \mathbf{e}_n dS = \iint_{\Omega} \nabla G_i \cdot (\mathbf{u} \times \omega) d\Omega - \frac{1}{\mathrm{Re}} \int_{S_1} (\nabla G_i \times \omega) \cdot \mathbf{e}_n dS \tag{12}$$

where H is 1.0 inside the flow (at domain Ω) and is 0.5 on the boundaries S_1 and S_2. $G_i = (1/2\pi)\log R^{-1}$ is the fundamental solution of Laplace equation, R being the distance from ith vortex element to the field point.

It is worth to observe that this formulation is specially suited for a Lagrangian scheme because it utilizes the velocity and vorticity field defined at the position of the vortices in the cloud. Therefore it does not require any additional calculation at mesh points. Numerically, Eq. (12) is solved by mean of a set of simultaneous equations for pressure Y_i. The pressure coefficient on a panel control point i is calculated according to $C_{p_i} = 1 + Y_i$.

4. Results and discussion

The numerical simulations were restricted to the interference effects between two, three, and four cylinders in a uniform flow. Here, L is the spacing between cylinders, and D is the cylinders diameter. In the calculations, each boundary S_i, i = 1, 2, 3 or 4, of Fig. 1 was by fifty (M=50) straight-line vortex panels with constant density. All runs were performed with 600 time steps of magnitude $\Delta t=0.05$. The time increment was evaluated according to $\Delta t=2\pi k/M$, $0<k\leq 1$ (Mustto *et al.*, 1998). In each time step the nascent vortices were placed into the cloud through a displacement $\varepsilon=\sigma_0=0.03b$ normal to the panels.

All the aerodynamics forces and pressure distributions computations starts at t=15. The aerodynamics force coefficients are calculated through the integration of the pressure coefficient distribution on the each cylinders surface.

Computed values for the distribution of the mean pressure coefficient along the single cylinder surface is shown in Fig. 2. As expected the simulation predicts the occurrence of a (mean) stagnation point at the front of the cylinder. The value of C_p then decreases and reaches a plateau, in the separated flow region. The magnitude of pressure becomes zero at $\theta=32^\circ$ and becomes maximum negative at $\theta=72^\circ$, whereas the experimental values is $\theta=34^\circ$ and $\theta=69^\circ$, respectively.

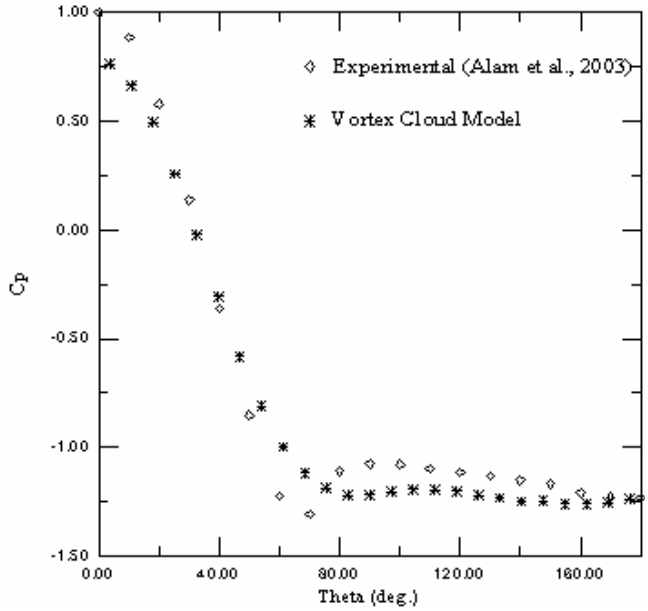

Figure 2. Comparison of the single cylinder case, experimental and numerical results of C_p, for Re=6.5x10^4.

Table 1 presents all cases studied for two circular cylinders in a tandem arrangement at a subcritical Reynolds number of 6.5x10^4 (Teixeira da Silveira *et al.,* 2005).

Within the results presented in Table 1, we observe a disagreement of the numerical results to the experimental results (Alam *et al.*, 2003) of cases III, IV and VII on the time-averaged drag coefficient, C_D, of the downstream cylinder. The mean drag coefficients of the downstream cylinder are much higher than the experimental values and, therefore, do not reflect a good simulation of the flow. The differences encountered in the comparison of the numerical results with the experimental results are attributed mainly the inherent three-dimensionality of the real flow for such a value of the Reynolds number, which is not modeled in the present simulation. A purely two-dimensional computation of such flow must produce higher values for the drag coefficient, as obtained for our simulation.

No attempts to simulate the flow for M greater than 50 were made since the operation count of the algorithm is proportional to the square of N. As M increases N also tends to increase, and the computation becomes expensive.

Table 1. Comparison of the mean drag coefficient with experimental results, for Re=6.5x10^4.

Case	L/D	Upstream cylinder		Downstream cylinder	
		C_D^+	$\overline{C_D^*}$	C_D^+	$\overline{C_D^*}$
I	0.1	1.0953	1.1500	-0.5697	-0.5447
II	0.5	---	0.9866	-0.3884	-0.2997
III	1.0	1.0531	1.3664	-0.2366	0.1130
IV	2.0	0.9866	1.3434	-0.1345	0.3652
V	3.5	1.2612	1.3677	0.2766	0.4613
VI	4.0	1.2319	1.4174	0.2661	0.3015
VII	8.0	1.2040	1.4324	0.3604	0.8693

$^+$Experimental results (Alam *et al.*, 2003) *Present results (Teixeira da Silveira *et al.*, 2005)

Experiments (Alam *et al.*, 2003) were conducted in a low-speed, closed-circuit wind tunnel with a test section of 0.6 m height, 0.4 m width, and 5.4 m length. The level of turbulence in the working section was 0.19%. The cylinders used as test models were made of brass and were each 49 mm in diameter. The geometric blockage ratio and aspect ratio at the test section were 8.1% and 8.2, respectively. None of the results presented were corrected for the effects of wind-tunnel blockage.

Figure 3 presents the distribution of pressure coefficient, C_p along the surface of the upstream and downstream cylinders for spacing L/D=0.1 (case I).

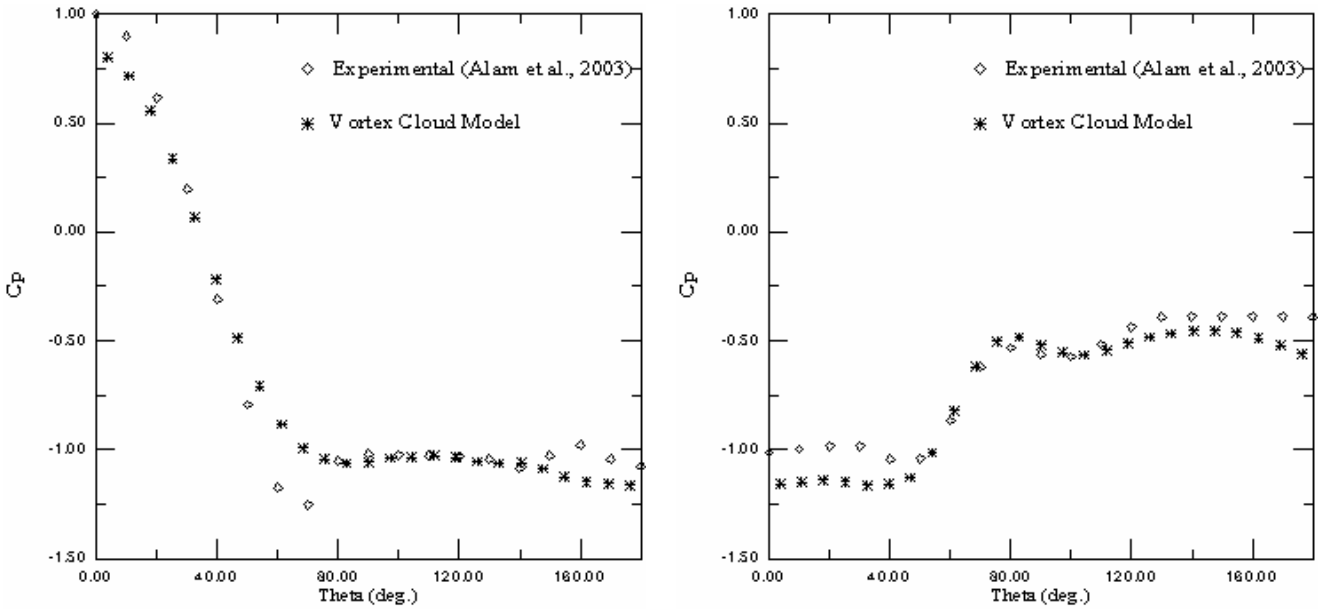

Upstream cylinder (L/D=0.1) Downstream cylinder (L/D=0.1)

Figure 3. Pressure distribution along the surface of the upstream and downstream cylinders, for Re=6.5x10^4.

Figure 4 shows the position of the wake vortices for three cylinders last step of the computation (t=60), where we can clearly observe the formation and shedding of large eddies in the wakes. This process occurs alternately on the upper and lower surfaces of each cylinder arranged in tandem. We can also visualize the vortex pairing process, where the vortices rotate in opposite directions and are connected to each other by a vortex sheet.

Numerical simulations of the flow around four cylinders in a square configurations have been carried out at sub-critical Reynolds number (Re=1.3 x10^4) and several spacing ratios. However, typical results for four equal size cylinders at spacing ratios L/D=1.5 and L/D=4.0, and with flow incident angles that vary from 0° (normal configuration) to 45° (rotate square configuration) have been investigated. The reason for this choice of parameters is due the experimental data obtained at subcritical Reynolds numbers (2.0 x10^2 - 1.3 x10^4) can be found in Lam and Lo (1992) Lam and Fang (1995) and Lam *et al.* (2001b).

The results of the mean drag coefficient and mean lift coefficient for L/D=4 at α=45° obtained in the present simulation are presented in Table 2. In this table one can find also experimental (Lam and Fang, 1995) and numerical

results Lam *et al.* (2001a). The numerical results of Lam *et al.* (2001a) were also obtained using the Vortex Method where surface of the each cylinder was represented by straight-line panels with a point vortex located at the control point and the pressure on the airfoil surface was calculated according to the inviscid flow analysis.

As one can see, the agreement between the two numerical methods is very good for the mean drag coefficient and both results are close to the experimental values. However, as mentioned earlier, the three-dimensional effects present in the experiments are very important for the Reynolds number used in the simulations. Therefore a purely two-dimensional computation of such flow must produce higher values for the drag coefficient, as obtained for our simulation. Lam and Fang (1995) do not furnish results for the Strouhal numbers.

Table 2. Comparison of the mean drag coefficient and lift coefficient for L/D=4 and α=45°, for Re=1.3x10^4.

Results	L/D	Cylinder 1	Cylinder 2	Cylinder 3	Cylinder 4
C_D^+	4.0	1.02	1.3	0.62	1.3
$\overline{C_D^*}$	4.0	1.06	1.1	0.5	1.29
$\overline{C_D^\circ}$	4.0	1.22	1.27	0.83	1.26
C_L^+	4.0	-0.01	-0.02	-0.02	-0.03
$\overline{C_L^*}$	4.0	-0.14	-0.15	-0.13	-0.16
$\overline{C_L^\circ}$	4.0	-0.07	-0.09	-0.12	-0.14

$^+$ Experimental results (Lam and Fang, 1995)
* Numerical results (Lam *et al.*, 2001a)
$^\circ$ Present simulation

No attempts to simulate the flow for M greater than 50 were made since the operation count of the algorithm is proportional to the square of N. As M increases N also tends to increase, and the computational efforts becomes expensive. This is a major source of difficulties, and it can only be handled through the utilization of faster schemes for the induced velocity calculations, such as the multipole technique (Greengard and Rokhlin, 1987) and/or parallel computers to run long simulations (Takeda *et al.*, 1999).

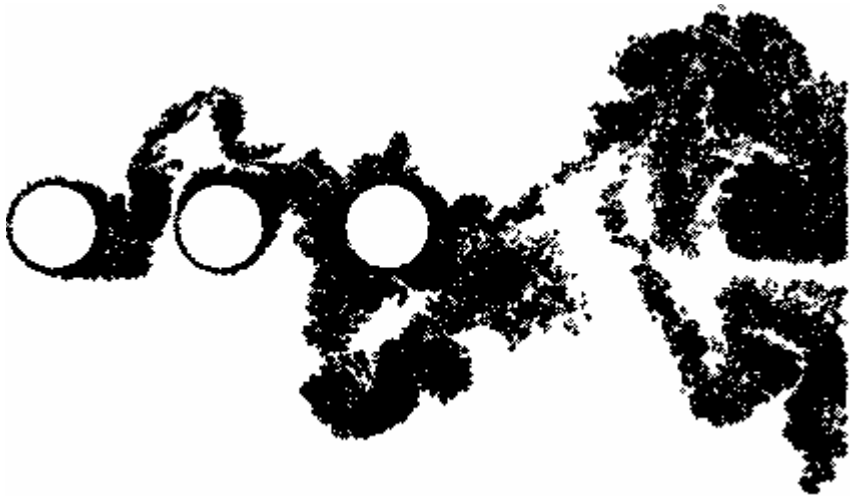

Figure 4. Position of the wakes vortices at t=60; Re=6.5x10^4, $\varepsilon = \sigma_0$ =0.03b, Δt=0.05, M=50, L/D=2.0.

The sub-grid turbulence modeling is of significant importance for the present numerical simulation. The development of Lagrangian LES models for Vortex Method has been discussed in the literature. In the present study, a methodology for the numerical simulation of a viscous turbulent flow will be carried out (Alcântara Pereira *et al.*, 2002), where the large structures of the flow are described using a cloud of discrete Lamb vortices, which is used to

simulate the vorticity present in the fluid region. In order to take into account the smaller scale manifestations of the flow and still keeping the computational effort within a manageable range, a second-order velocity structure function model was adapted to the Lagrangian scheme. This methodology has been used to simulate the flow around a cascade of NACA 65-410 airfoils (Alcântara Pereira *et al.*, 2004, 2005).

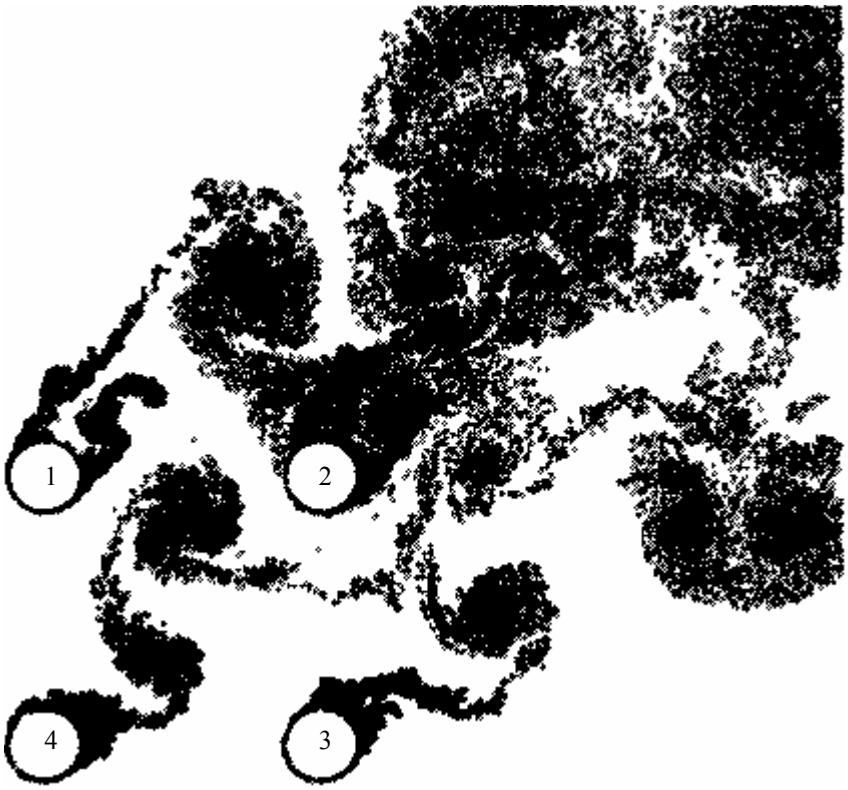

Figure 5. Position of the wakes vortices at t=60 for L/D=4, α=45°, Re=1.3x10^4, $\varepsilon = \sigma_0$ =0.03b, Δt=0.05, M=50.

5. Conclusions

The main objective of the work was to implement the algorithm and to get some insight into the potentialities of the model developed; this was accomplished since the results show that the behavior of the quantities of interest is the expected one.

The three-dimensional effects present in the experiments are very important for the Reynolds number used in the simulations. Therefore a purely two-dimensional computation of the flow must produce differences in the comparison of the numerical results with the experimental results. The differences encountered in the comparison of the computed values with the experimental results for the distribution of the mean pressure coefficient along the cylinder surface as shown in Figure 2 are attributed mainly to the inherent three-dimensionality of the real flow for such a value of the Reynolds number, which is not modeled in the simulation. The results for the pressure distribution indicated that there was a lack of resolution near the stagnation point and the position of the separation point. The position of the separation point is predicted to occur at about 72°, whereas the experimental value (Alam *et al.*, 2003) is about 69°. This seems to indicate that a higher value of M would improve the resolution and probably produce a better simulation with respect to the pressure distribution. More investigations are needed and one can imagine that with the use of more panels (and therefore more free vortices in the cloud) the results tend to be in closer agreement with the experiments.

Some discrepancies observed in the determination of the aerodynamics loads may be also attributed to errors in the treatment of vortex element moving away from a solid surface. Because every vortex element has different strength of vorticity, it will diffuse to different location in the flow field. It seems impossible that every vortex element will move to same ε-layer normal to the solid surface. In the present method all nascent vortices were placed into the cloud through a displacement $\varepsilon = \sigma_0$ =0.03b normal to the panels.

The use of a fast summation scheme to determine the vortex-induced velocity, such as the Multiple Expansion scheme, allows an increase in the number of vortices and a reduction of the time step, which increases the resolution of the simulation, in addition to a reduction of the CPU time, which allows a longer simulation time to be carried out.

The sub-grid turbulence modeling (Alcântara Pereira *et al.,* 2002) is of significant importance for the numerical simulation. The results of this analysis, taking into account the sub-grid turbulence modeling, are also being generated and will be presented in due time, elsewhere.

Finally, despite the differences presented in this preliminary investigation, the results are promising, that encourages performing additional tests in order to explore the phenomena in more details.

6. Acknowledgement

The authors would like to acknowledge FAPEMIG (Process TEC-748/04) and CNPq for the financial support during the time of this project.

7. References

Alam, M. M., Moriya, M., Takai, K. and Sakamoto, 2003, "Fluctuating Fluid Forces Acting on Two Circular Cylinders in a Tandem Arrangement at a Subcritical Reynolds Number", J. Wind Eng. Ind Aerodyn., 91, pp. 139-154.

Alcantara Pereira, L.A., Ricci, J.E.R. and Hirata, M.H., 2005, "Simulation of Linear Cascade Vortex Cloud Interaction with Turbulence Modeling", Intern'l Society of CFD, Vol. 14, No. 2, July, pp. 1-10.

Alcântara Pereira, L.A., Hirata, M.H. and Manzanares Filho, N. 2004, "Wake and Aerodynamics Loads in Multiple Bodies - Application to Turbomachinery Blade Rows", J. Wind Eng. Ind Aerodyn., 92, pp. 477-491.

Alcântara Pereira, L.A., Ricci, J.E.R., Hirata, M.H. and Silveira-Neto, A., 2002, "Simulation of Vortex-Shedding Flow about a Circular Cylinder with Turbulence Modeling", Intern'l Society of CFD, Vol. 11, No. 3, October, pp. 315-322.

Arie, M., Kiya, M., Moriya, M. and Mori, H., 1983, "Pressure Fluctuations on the Surface of Two Circular Cylinders in Tandem Arrangement", ASME J. Fluids Eng. 105, pp. 161-167.

Biermann, D. and Herrnstein, Jr., 1933, "The Interference between Struts in Various Combinations", National Advisory Committee for Aeronautics, Thecnical Report 468.

Chorin, A.J., 1973, "Numerical Study of Slightly Viscous Flow", Journal of Fluid Mechanics, Vol. 57, pp. 785-796.

Ferziger, J.H., 1981, "Numerical Methods for Engineering Application", John Wiley & Sons, Inc.

Greengard, L. and Rokhlin, V., 1987, "A Fast Algorithm for Particle Simulations", Journal of Computational Physics, Vol. 73, pp. 325-348.

He, F. and Su, T.C., 1998, "A Numerical Study of Bluff Body Aerodynamics in High Reynolds Number Flows by Viscous Vortex Element Method", J. Wind Eng. Ind. Aerodyn., 77/88, pp. 393-407.

Hiwada, M., Mabuchi, I. and Yanagihara, H., 1982, "Flow and Heat Transfer from Two same Size Circular Cylinders in Tandem Arrangement" (In Japanese), Trans. JSME 48, pp. 499-508.

Igarashi, T., 1984, "Characteristics of the Flow Around Two Circular Cylinders Arranged in Tandem", (Second Report), Bull. JSME 27 (233), pp. 2380-2387.

Igarashi, T., 1981, "Characteristics of the Flow Around Two Circular Cylinders Arranged in Tandem", (First Report), Bull. JSME 24 (188), pp. 323-331.

Jendrzejczk, J.A. and Chen, S.S., 1986, "Fluid Forces on Two Circular Cylinders in Cross Flow", ASME, PVP 14, pp. 141-143.

Kamemoto, K., 2004, "On Contribution of Advanced Vortex Element Methods Toward Virtual Reality of Unsteady Vortical Flows in the New Generation of CFD", Proceedings of the 10th Brazilian Congress of Thermal Sciences and Engineering-ENCIT 2004, Rio de Janeiro, Brazil, Nov. 29 - Dec. 03, Invited Lecture-CIT04-IL04.

Kamemoto, K., 1993, "Procedure to Estimate Unstead Pressure Distribution for Vortex Method" (In Japanese), Trans. Jpn. Soc. Mech. Eng., Vol. 59, No. 568 B, pp. 3708-3713.

Kareem, A., Kijewski, Po-Chien, L., "Investigation of Interference Effects for a Group of Finite Cylinders", 1998, J. Wind Eng. Ind. Aerodyn. 77&78, pp. 503-520.

Kostic, Z.G. and Oka, .S.N, 1972, "Fluid Flow and Heat Transfer with Two Circular Cylinders in Cross Flow", Int. J. Heat Mass Transfer, 15, pp. 279-299.

Lam, K., So, R.M.C. and Li, J.Y., 2001a, "Flow Around Four Cylinders in a Square Configurations Using Surface Vorticity Method", Proceedings of The Second International Conference on Vortex Methods, September 26-28, Istanbul, Turkey.

Lam, K., Chan, K.T., So, R.M.C. and Li, J.Y., 2001b, "Velocity Map and Flow Pattern of Flow around Four Cylinders in a Square Configuration at Low Reynolds Number and Large Spacing Ratio Using Particle Image Velocimetry", Proceedings of The Second International Conference on Vortex Methods, September 26-28, Istanbul, Turkey.

Lam, K. and Fang, X., 1995, "The Effect of Interference of Four Equal-Distance Cylinders in Cross Flow on Pressure and Forces Coefficientes", Journal of Fluid Structures, Vol. 9, pp. 195-214.

Lam, K. and Lo, S.C., 1992, "A Visualization Study of Cross-Flow around Four Cylinders in a Square Configuration", Journal of Fluids and Structure, Vol. 6, pp. 109-131.

Lewis, R.I., 1999, "Vortex Element Methods, the Most Natural Approach to Flow Simulation - A Review of Methodology with Applications", Proceedings of 1st Int. Conference on Vortex Methods, Kobe, Nov. 4-5, pp. 1-15.

Lewis, R. I., 1991, "Vortex Element Method for Fluid Dynamic Analysis of Engineering Systems", Cambridge Univ. Press, Cambridge, England, U.K..

Mustto, A.A., Hirata, M.H. and Bodstein, G.C.R., 1998, "Discrete Vortex Method Simulation of the Flow Around a Circular Cylinder with and without Rotation", A.I.A.A. Paper 98-2409, Proceedings of the 16th A.I.A.A. Applied Aerodynamics Conference, Albuquerque, NM, USA, June.

Novak, J., 1974, "Strouhal Number of a Quadrangular Prism, Angle Iron and Two Circular Cylinders Arranged in Tandem", Acta Tech. CSAV 19 (3), pp. 361-373.

Ohya, Y., Okajima, A. and Hayashi, M., 1989, "Wake Interference and Vortex Shedding", In: Encyclopedia of Fluid Mechanics, Chap. 10 (Gulf Publishing, Houston, 1989).

Okajima, A., 1979, "Flow Around Two Tandem Circular Cylinders at very High Reynolds Numbers", Bull. JSME 22 (166), pp. 504-511.

Ogami, Y., 2001, "Simulation of Heat-Fluid Motion by the Vortex Method", J.S.M.E. International Journal, Series B, Vol. 44, No. 4, pp. 513-519.

Sarpkaya, T., 1989, "Computational Methods with Vortices - The 1988 Freeman Scholar Lecture", Journal of Fluids Engineering, Vol. 111, pp. 5-52.

Sethian, J.I., 1991, "A Brief Overview of Vortex Method, Vortex Methods and Vortex Motion", SIAM. Philadelphia, pp. 1-32.

Shintani, M. and Akamatsu, T, 1994, "Investigation of Two Dimensional Discrete Vortex Method with Viscous Diffusion Model", Computational Fluid Dynamics Journal, Vol. 3, No. 2, pp. 237-254.

Simpson, A. and Flower, J.W., 1977, "An Improved Mathematical Model for the Aerodynamic Forces on Tandem Cylinders in Motion with Aerolastic Applications", J. Sound Vib., Vol. 51, pp. 183-217.

Takeda, K., Tutty, O.R. and Nicole, D.A., 1999, "Parallel Discrete Vortex Method on Commodity Supercomputers; an Investigation into Bluff Body Far Wake Behaviour", ESAIM: Proceedings, Third International Workshop on Vortex Flows and Related Numerical Methods, Vol. 7, pp. 418-428.

Teixeira da Silveira, L., Alcântara Pereira, L.A. and Hirata, M.H., 2005, "The Effects of Interference between Two Circular Cylinders Arranged in Tandem by Vortex Method", 18th International Congress of Mechanical Engineering, Proceedings of COBEM 2005, November 6-11, Ouro Preto, MG.

Uhlman, J.S., 1992, "An Integral Equation Formulation of the Equation of an Incompressible Fluid", Naval Undersea Warfare Center, T.R. 10-086.

Williamson, C.H.K. and Roshko, A., 1988, "Vortex Formation in the Wake of an Oscillating Cylinder", J. Fluids and Structures, Vol. 2, pp. 239-381.

Zdravkovich, M.M., 1977, "Review of Flow Interference between Two Circular Cylinders in Various Arrangements", Trans. SAME, J. Fluid. Eng., 99, pp. 618-633.

Zdravkovich, M.M. and Pridden, D.L., 1977, "Interference between Two Circular Cylinders; Series of Unexpected Discontinuites", J. Ind. Aerodyn. 2, pp. 255-270.

Zdravkovich, M.M. and Pridden, D.L., 1975, "Flow Around Two Circular Cylinders", Research Report, Proceedings of the Second US National Conference on Wind Engineering Research, Fort Collins, IV (18).

Proceedings of the 11th Brazilian Congress of Thermal Sciences and Engineering -- ENCIT 2006
Braz. Soc. of Mechanical Sciences and Engineering -- ABCM, Curitiba, Brazil, Dec.5-8, 2006

Paper CIT06-0361

ANALYSIS OF THE FLOW AROUND AN OSCILLATING CIRCULAR CYLINDER IN GROUND EFFECT

Washington Humberto de Moura
Instituto de Engenharia Mecânica, UNIFEI, CP 50, Itajubá, Minas Gerais, 37500-903, Brasil
e-mail: whmoura@unifei.edu.br

Hélia Silva
Instituto de Engenharia Mecânica, UNIFEI, CP 50, Itajubá, Minas Gerais, 37500-903, Brasil
e-mail: heva@unifei.edu.br

Luiz Antonio Alcântara Pereira
Instituto de Engenharia Mecânica, UNIFEI, CP 50, Itajubá, Minas Gerais, 37500-903, Brasil
e-mail: luizantp@unifei.edu.br

Miguel Hiroo Hirata
FAT/UERJ
Campus Regional de Resende
Estrada Resende - Riachuelo, Resende, RJ
e-mail: hirata@fat.uerj.br

Abstract. *The aim of this work is to simulate numerically the two-dimensional, incompressible Newtonian fluid flow around a circular cylinder oscillating with small amplitude in the presence of ground plane. The vorticity generated on the body surface interacts with the vorticity generated on the ground plane surface to form the viscous wake; the vorticity is discretized and is numerically simulated using discrete Lamb vortices. The influence of the clearance and of the amplitude oscillation on the aerodynamics loads are analyzed.*

Keywords: *vortex method, panels methods, ground effect, small amplitude, aerodynamics loads, lagrangian description.*

1. Introduction

The analysis of the unsteady vorticity-dominated flow is a long-standing interest of many researches. In this paper we consider one small aspect of the total problem: the numerical simulation of the wake generated by an oscillating circular cylinder, which moves with constant velocity in the presence of a ground plane. The amplitude of the oscillatory motion is considered to be small compared to the body length; therefore, to the first approximation one is allowed to transfer the body boundary condition from the actual position to a mean position of the body surface. The numerical simulation is accomplished by using the Vortex Method, which takes into account the viscous effect in the flow field.

Oscillatory motions of small amplitude are important in the analysis of immerse vibrating bodies and special care should be taken in the lock-in condition.

The problem described can be compared with many engineering situations where is possible verify changes in the velocity field around a body thus a surface localized near the neighborhood. An automobile near the ground and an aircraft landing or taking off are examples of this phenomenon.

In the literature a model of the single airfoil, near a ground plane, immersed in an upstream shear flow is referred to as "the airfoil-vortex interaction in ground effect" – AVIG – and can be viewed as a combination of three interacting flows: airfoil-vortex interaction (AVI), airfoil-ground interaction (AGI), and vortex-ground interaction (VGI). A large number of papers on the unsteady, incompressible, two-dimensional AVI flow have been published. Within the context of the (two-dimensional) parallel AVI that occurs around helicopter rotors, known as blade-vortex interaction (BVI), Panaras (1987), Poling *et al.* (1989) and Lee and Smith (1991), among others, have devised numerical models based on the inviscid discrete vortex method coupled with linearized potential flow theory. More elaborate numerical models have also been employed, such as those based on Euler (Srinivasan and McCroskey, 1993) and Navier-Stokes (Rai, 1987) mesh-based methods. Detailed experimental investigations on the aerodynamics of parallel BVI have been performed by Seath *et al.* (1989), Straus *et al.* (1990), Chen and Chang (1997). See the review articles of McCune and Tavares (1993) and Mook and Dong (1994) for additional references on unsteady, incompressible flows over airfoils and the numerical simulation of wakes and BVI.

Chacaltana *et al.* (1995) analyze the flow around a thin airfoil immersed in a shear flow, in presence of a ground plane. The authors use the potential flow theory and taking into account the fact that the airfoil is thin were able to derive a simple algorithm. In this paper, the shear flow was simulated by a single moving free vortex.

Fonseca *et al.* (1997, 2003) in a series of two papers applied a numerical, inviscid, vortex method to simulate the unsteady, two-dimensional and incompressible flow that occurs during a parallel blade-vortex interaction in ground effect. A panel method was used to discretize the airfoil bound vorticity, where each panel has a linear and piecewise-continuous distribution of vorticity. The impermeability condition was enforced on the airfoil contour, but the no-slip condition is not. The Kutta condition was imposed through the continuity of the pressure field at the airfoil trailing edge, which, combined with the condition that the circulation in the whole flow must be conserved, provides a model for the vorticity generation at the trailing edge. Thus the viscous wake was modeled by potential vortices shed into the flow at the trailing edge and the oncoming shear flow was modeled by a single potential vortex that interacts with the airfoil and its wake.

Ricci *et al.* (2001) presented a new methodology that utilizes the Vortex Method for the analysis of the vorticity generated in the surface of the airfoil with that generated on the ground plane. Lamb vortices are generated along the airfoil surface and ground plane to ensure that the no-slip condition is satisfied. Images clouds are provided in the lower half ground to ensure that the impermeability condition is satisfied. With the images clouds the computation becomes expensive. This is a major source of difficulties, and it can only be handled through the utilization of method of distributed singularities, the Panels Method.

Silva de Oliveira *et al.* (2005) employed the Vortex Method to simulate the airfoil-vortex cloud interaction in ground effect. The no-slip condition is satisfied using Lamb vortices to simulate the vorticity generated in the airfoil surface and that generated in the ground surface. The impermeability condition is imposed through the application of a source panel method. The main feature of the paper is the oncoming shear flow that has two important characteristics. The first is that the shear flow is continuously generated is a plane perpendicular to the main flow, a feature not found in any of the previous paper, and the second characteristic is the possibility of having a time variation of the vorticity carried out by this shearing flow, see Silva de Oliveira *et al.* (2004).

Silva (2004) applied the Vortex Method to analyze the flow around an oscillating airfoil, which moves with constant velocity. The amplitude of the oscillatory motion is considered to be small compared to the airfoil length, therefore, to the first approximation, one is allowed to transfer the body boundary condition from the actual position to a mean position of the body surface. Aerodynamic loads are calculated using an integral equation derived from the pressure Poisson equation (Alcântara Pereira *et al.,* 2004). An analysis of the oscillation effect on the mechanism of lift generation is also presented. The influence of the ground effect is not considered.

As mentioned, the model is analyzed using the Vortex Method which is a meshless numerical method or a particle method. In this method, the vorticity in the fluid region is numerically simulated using a cloud of discrete vortices with a viscous core (Lamb vortex). To simulate the vorticity at the solid surfaces, nascent vortices are generated there at each time step of the simulation. In order to take care of the convection and the diffusion of the vorticity one makes use of the convection-diffusion splitting algorithm; accordingly the convection of the vortices in the cloud is carried out independently of the diffusion for each time step of the simulation. The convection process is carried out with the Adams-Bashforth time-marching scheme and the diffusion process is simulated using the random walk method. This is in essence the foundation of the Vortex Method (e.g. references Chorin, 1973; Sarpkaya, 1989; Sethian, 1991; Lewis, 1999; Alcântara Pereira *et al*., 2002 and Kamemoto, 2004). Please note that with the Lagrangian formulation a grid for the spatial discretization of the fluid region is not necessary. Thus, special care to handle numerical instabilities associated to high Reynolds numbers is not needed. Also, the attention is only focused on the regions of high activities, which are the regions containing vorticity; on the contrary, Eulerian schemes consider the entire domain independent of the fact that there are sub-regions where less important, if any, flow activity can be found. With the Lagrangian tracking of the vortices, one need not take into account the far away boundary conditions. This is of important in the wake regions (which is not negligible in the flows of present interest) where turbulence activities are intense and unknown, a priori.

The present Vortex Method has been used to simulate the macro scale phenomena, therefore the smaller scale ones are taken into account through the use of a second order velocity function (Alcântara Pereira et *al*., 2002). In this present approach, the effect of small scale is not considered.

2. Description of the numerical model of the flowfield

2.1. Basic concepts

Consider the incompressible flow of a Newtonian fluid in a large two-dimensional domain around a circular cylinder which moves with constant velocity U in ground effect. An oscillatory moving with finite amplitude A and constant angular velocity ω is added to body as shown in Fig. 1. In this figure the (x, o, y) is the inertial frame of reference and the (X, O, Y) is the coordinate system fixed to the cylinder; this coordinate system oscillates around the x-axis as $y_o = A\cos(\omega t)$.

The boundary S of the fluid domain Ω is $S = S_1 \cup S_2 \cup S_3$; being S_3 the far away boundary, which can be viewed as $r = \sqrt{x^2 + y^2} \to \infty$, and S_1 the body surface and S_2 the ground plane surface.

In the body fixed coordinate system, the surface $S_1 \equiv S_b$ is defined by the function

$$F_b(X,Y) = Y_b - \eta(X) = 0 \tag{1}$$

Thus, in the inertial frame of reference

$$S_b : F_b(x,y,t) = y_b - [y_0(t) + \eta(x)] = 0\,, \tag{2}$$

and, for a symmetrical body

$$F_b(x,y,t) = y_b - y_0(t) \mp \eta(x) = 0\,. \tag{3}$$

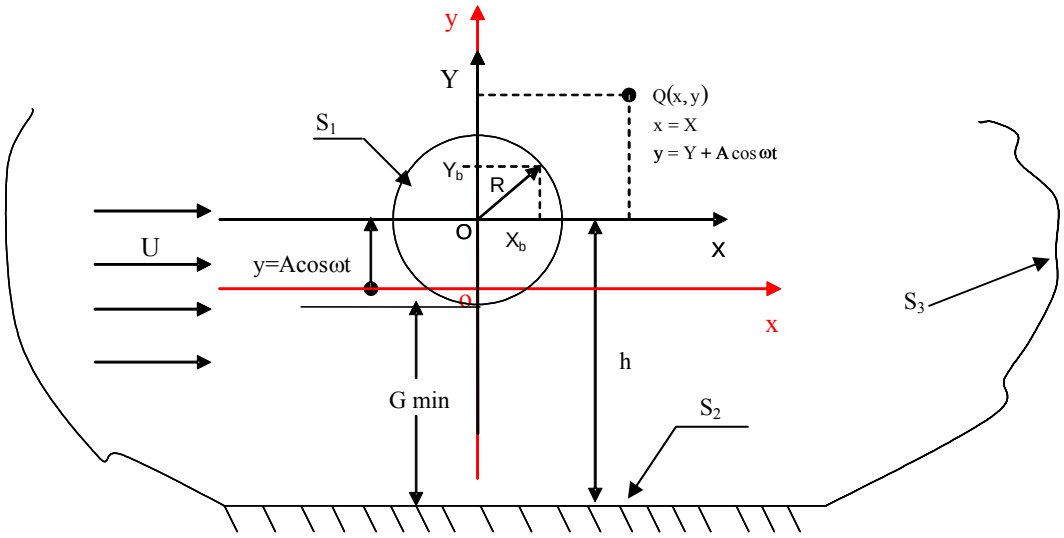

Figure 1. Definitions.

The cylinder surface $S_1 \equiv S_b$ is defined according the following form

$$S_b(X,Y) = \sqrt{X^2 + Y^2} = R \tag{4}$$

and the boundary surface S_2 is defined as

$$y = -h,\ -\infty < x < \infty \tag{5}$$

2.2. Governing equations

The viscous and incompressible flow is governed by the continuity and the Navier-Stokes equations, which can be written in the form

$$\nabla \cdot \mathbf{u} = 0 \tag{6}$$

$$\frac{\partial \mathbf{u}}{\partial t} + \mathbf{u} \cdot \nabla \mathbf{u} = -\nabla p + \frac{1}{Re} \nabla^2 \mathbf{u}\,. \tag{7}$$

where $\mathbf{u} \equiv (u, v)$ is the velocity vector. As can be seen the equations are non-dimensionalized in terms of U and b (cylinder diameter: b = 2R). The Reynolds number is defined by

$$Re = \frac{bU}{\upsilon} \tag{7a}$$

where υ is the fluid kinematics viscosity coefficient; the dimensionless time is b/U.

On the body and ground plane surfaces the adherence condition has to be satisfied. This condition is better specified in terms of the normal and tangential components as

$$(\mathbf{u}\cdot\mathbf{n}) = (\mathbf{v}\cdot\mathbf{n}) \text{ on } S_1 \text{ and } S_2 \text{, the impenetrability condition} \tag{8a}$$

$$(\mathbf{u}\cdot\boldsymbol{\tau}) = (\mathbf{v}\cdot\boldsymbol{\tau}) \text{ on } S_1 \text{ and } S_2 \text{, the impenetrability condition, the no-slip condition.} \tag{8b}$$

Here $\mathbf{n}$ and $\boldsymbol{\tau}$ are unit normal and tangential vectors and v is the surfaces velocity: S_1 and S_2.

Far from the surfaces S_1 and S_2 one assumes that the perturbation due to the oscillating body fades away, that is

$$|\mathbf{u}| \to 1 \text{ at } S_3 . \tag{9}$$

Is considered an small amplitude around the axis x, therefore

$$\frac{A}{2R} = O(\varepsilon) \text{, where } \varepsilon \to 0 \text{ and } \omega = O(1). \tag{10}$$

Thus, the boundary conditions on S_1 are written directly in the inertial frame of reference as

$$u_n(x,y,t) \equiv \left[v_n(x,y,t)\right] \text{ on } S_1 \text{, the impenetrability condition} \tag{11a}$$

$$u_\tau(x,y,t) \equiv \left[v_\tau(x,y,t)\right] \text{ on } S_1 \text{, the impenetrability condition .} \tag{11b}$$

The transference of the boundary conditions on S_1 from actual position to the mean position is defined as

$$y_c = y_0 + \eta(x) \to \bar{y}_c = \eta(x) + O(y_0) \tag{12a}$$

$$u_n(x_c, y_c, t) = u_n\left(x_c, y_0 + \eta, t\right) = u_n\left(x_c, \eta(x_c), t\right) + y_0 \frac{\partial u_n\left(x_c, \eta(x_c), t\right)}{\partial y} + \cdots \tag{12b}$$

$$u_\tau(x_c, y_c, t) = u_\tau\left(x_c, y_0 + \eta, t\right) = u_\tau\left(x_c, \eta(x_c), t\right) + y_0 \frac{\partial u_\tau\left(x_c, \eta(x_c), t\right)}{\partial y} + \cdots \tag{12c}$$

The dynamics of the fluid motion, governed by the above boundary-value problem, can be alternatively studied by taking the curl of Eq. (7), obtaining the well-known 2-D vorticity transport equation

$$\frac{\partial\omega}{\partial t} + \mathbf{u}\cdot\nabla\omega = \frac{1}{Re}\nabla^2\omega \tag{13}$$

where ω is the only non-zero component of the vorticity vector $\boldsymbol{\omega} = \nabla\times\mathbf{u}$.

2.3. Discrete vortex method

According to the convection-diffusion splitting algorithm (Chorin, 1973) it is assumed that in the same time increment the convection and the diffusion of the vorticity can be independently handled and are governed by

$$\frac{\partial\omega}{\partial t} + \mathbf{u}\cdot\nabla\omega = 0 \tag{14}$$

$$\frac{\partial \omega}{\partial t} = \frac{1}{Re}\nabla^2 \omega . \tag{15}$$

Convection is governed by Eq. (14) and the velocity field is given by

$$u - iv = 1 + \frac{1}{2\pi}\sum_{n=1}^{2M} \sigma(S_n) \int_{\Delta S_n} \frac{d}{dz}\ln(z-\zeta)d\zeta + \frac{i}{2\pi}\sum_{k=1}^{N} \frac{\Delta\Gamma_k}{z - z_k} . \tag{16}$$

Here, u and v are the x and y components of the velocity vector $\mathbf{u}$ and $i = \sqrt{-1}$. The first term in the right hand sides is the contribution of the incident flow; the summation of $2M$ integral terms comes from the sources panels with constant density distributed on the circular cylinder and ground surfaces. The second summation is associated to the velocity induced by the cloud of N free vortices; it represents the vortex-vortex interactions.

The incident flow and the vortex-vortex interactions calculations present no problems and they follow the usual Vortex Method procedures; to the first approximation the same happens with the summation of $2M$ integral terms when the body (circular cylinder) oscillation amplitude is small, see Silva (2004). For large amplitude body oscillations, however, the body boundary conditions can not be transferred from the actual position to the mean position.

The fluid velocity on the circular cylinder surface is written as

$$\mathbf{u}(X, Y; t) = U\mathbf{i} - \dot{y}_0(t)\mathbf{j} \text{ ; with } \dot{y}_0(t) = \frac{d}{dt}\left[A\cos(\omega t)\right] \tag{17}$$

As a consequence of the j component of the right hand side of the fluid velocity (in the above expression) one gets an additional singularities distribution on the body surface. Of course, the induced velocity due to this additional singularities distribution fades away from the body.

The velocity induced by the body, according to the Panels Method calculations, is indicated by [uc(X,Y), vc(X,Y)]; this is the velocity induced at the vortex (i), located at the point [x(t), y(t)]; thus

$$uc^{(i)}(x, y; t) = uc(X, Y; t) \tag{18a}$$

$$vc^{(i)}(x, y; t) = vc(X, Y; t) \tag{18b}$$

where the following relations remains

$$x^{(i)}(t) = X \tag{19a}$$

$$y^{(i)}(t) = y_0(t) + Y \tag{19b}$$

The process of vorticity generation is carried out from Eq. (8b), so as to satisfy the no-slip condition. According to the discussion above the Panels Method guaranties that the impermeability condition is satisfied in each straight-line element, or panel, at pivotal point. At each instant of the time 2M new vortices are created a small distance ε of the body and ground plane surfaces, whose strengths are determined from Eq. (8b) applied at 2M point's right below the newly created vortices, along the radial direction. This procedure yields an algebraic system of 2M equations and 2M unknowns (the strengths of the vortices).

In order to remove the singularity in the second summation of Eq. (16) Lamb vortices are used, whose mathematical expression for the induced velocity of the kth vortex with strength $\Delta\Gamma_k$ in the circumferential direction u_{θ_k} , is (Mustto *et al.*, 1998)

$$u_{\theta_k} = \frac{\Delta\Gamma_k}{2\pi r}\left\{1 - \exp\left[-5.02572\left(-\frac{r}{\sigma_0}\right)^2\right]\right\} \tag{20}$$

where σ_0 is core radius of the Lamb vortex.

In this particular equation r is the radial distance between the vortex center and the point in the flow field where the induced velocity is calculated.

Each vortex particle distributed in the flow field is followed during numerical simulation according to the Adams-Bashforth second-order formula (Ferziger, 1981)

$$z(t+\Delta t) = z(t) + [1.5u(t) - 0.5u(t-\Delta t)]\Delta t + \xi \tag{21}$$

in which z is the position of a particle, Δt is the time increment and ξ is the random walk displacement. According to Lewis (1991), the random walk displacement is given by

$$\xi = \sqrt{4\beta\Delta t \ln\left(\frac{1}{P}\right)}\left[\cos(2\pi Q) + i\sin(2\pi Q)\right] \tag{22}$$

where $\beta = Re^{-1}$; P and Q are random numbers between 0.0 and 1.0.

The pressure calculation starts with the Bernoulli function, defined by Uhlman (1992) as

$$Y = p + \frac{u^2}{2},\ u = |\mathbf{u}|. \tag{23}$$

Kamemoto (1993) used the same function and starting from the Navier-Stokes equations was able to write a Poisson equation for the pressure. This equation was solved using a finite difference scheme. Here the same Poisson equation was derived and its solution was obtained through the following integral formulation (Shintani and Akamatsu, 1994)

$$H\overline{Y_i} - \int_{S_1} \overline{Y}\nabla G_i \cdot \mathbf{e}_n \, dS = \iint_{\Omega} \nabla G_i \cdot (\mathbf{u}\times\omega) d\Omega - \frac{1}{Re}\int_{S_1} (\nabla G_i \times \omega)\cdot \mathbf{e}_n \, dS \tag{24}$$

where H is 1.0 inside the flow (at domain Ω) and is 0.5 on the boundaries S_1 and S_2. $G_i = (1/2\pi)\log R^{-1}$ is the fundamental solution of Laplace equation, R being the distance from ith vortex element to the field point.

It is worth to observe that this formulation is specially suited for a Lagrangian scheme because it utilizes the velocity and vorticity field defined at the position of the vortices in the cloud. Therefore it does not require any additional calculation at mesh points. Numerically, Eq. (24) is solved by mean of a set of simultaneous equations for pressure Y_i.

4. Results and conclusions

The numerical simulations were restricted to the flow around a circular cylinder and for the calculations each boundary S_1 and S_2 in Fig. (1) was represented by fifty (M=50) source panels; the time step and Reynolds number were taken as Δt=0.05 and Re=10^5, respectively. In each time step the nascent vortices were placed into the cloud through a displacement $\varepsilon = \sigma_0$ =0.0009b normal to the panels. The aerodynamics forces computations starts at t=10.

Table 1: Strouhal number, lift and drag coefficients for a circular cylinder with h/b $\to\infty$.

Re = 10^5, A = 0 and ω = 0	$\overline{C}_L$	$\overline{C}_D$	$\overline{S}_t$
Blevins (1984)	-	1.20	0.19
Mustto *et al.* (1998)	-	1.22	0.22
Alcântara Pereira *et al.*(2002)	0.04	1.21	0.22
Present simulation	0.06	1.20	0.19

As first case we consider A=0, ω=0 and h/b $\to \infty$. The result of the first case is presented in Table 1. In this table one can find also experimental, Blevins (1984) (with 10% uncertainty) and numerical results Mustto *et al.* (1998). The numerical results of Mustto *et al.* (1998) were also obtained using the Vortex Method with the Circle Theorem (Milne-Thompson, 1955), while the Panels Method, using straight-line vortex panels with constant density, was used in the results of Alcântara Pereira *et al.* (2002). The agreement between the two numerical methods is very good for the Strouhal number, and both results are close to the experimental values. One should observe, however, that three-dimensional effects are non-negligible for the Reynolds number used in the simulations. Therefore one can expect that a

two-dimensional computation of such a flow must produce higher values for the drag coefficient. On the other hand, the Strouhal number is insensitive to these three-dimensional effects.

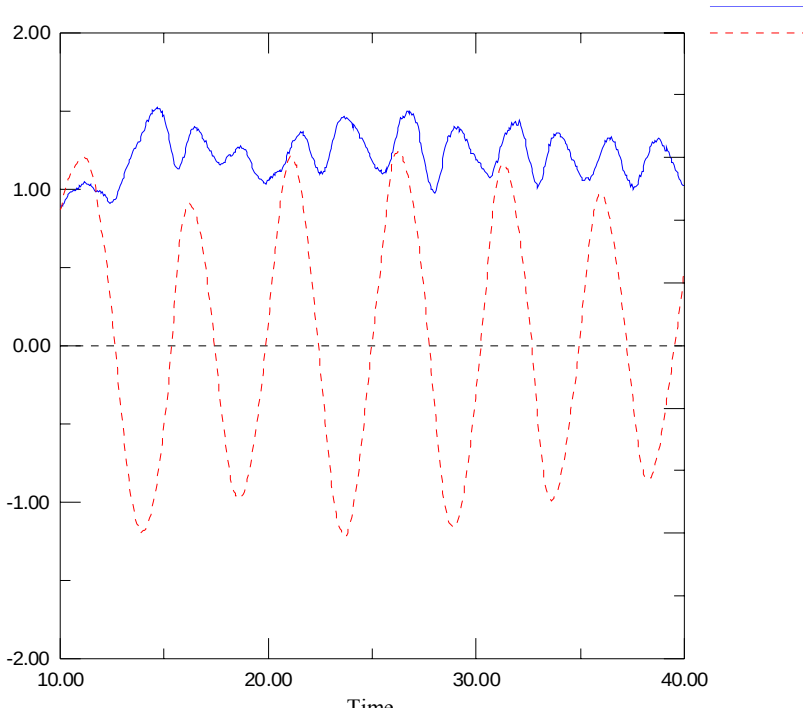

Figure 2: Circular cylinder: drag and lift coefficients during the numerical simulation; A = 0, ω = 0 and Re = 10^5.

Figure 3 shows the mean value of pressure coefficient around the discretized circular cylinder surface. The present result is compared with others results available in the literature and current simulation agree very well with the experimental ones. From the simulation the predict separation points occur around 86°, while the experimental value is around 82°. In other experimental investigation by Son and Hanratty (1969); determined a value of 78° for the separation angle.

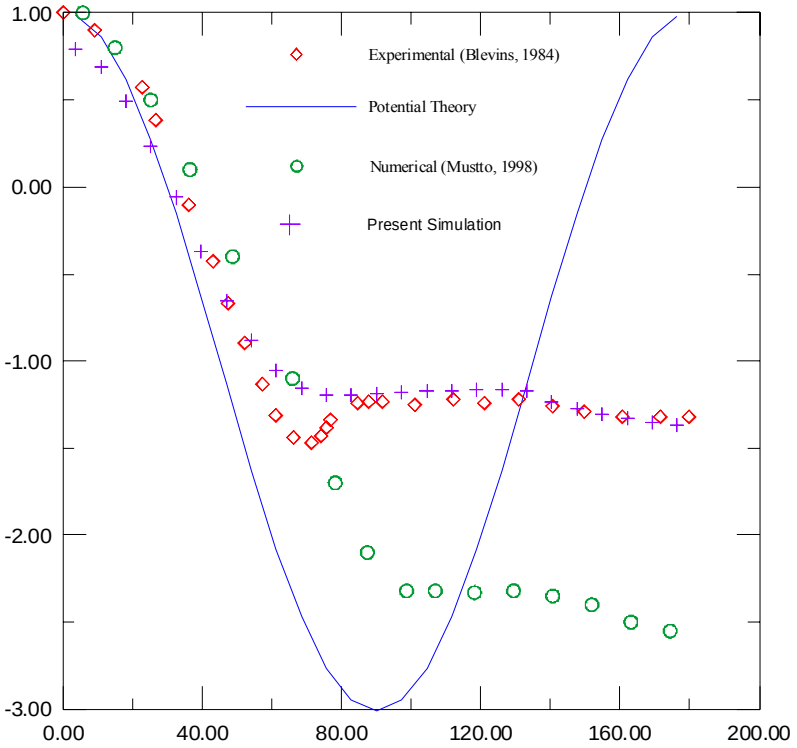

Figure 3. Comparison of the circular cylinder case, experimental and numerical results of C_p, for A = 0, ω = 0, Re=10^5.

We believe that better approximation for the experimental curve and numerical curve is obtained increasing the number of panels to approximate the real surfaces. Also, use of the turbulence modeling (Alcântara Pereira *et al.*, 2002) will produce a better numerical result.

Figure 2 shows that the lift coefficient oscillates around zero, as expected. However the mean value is slightly different from zero.

The influence of the ground effect, with A = 0 and ω = 0, is preliminary investigated and presented in the Fig. 4. News simulations will be carried out to investigate the present phenomena. The numerical results seem to indicate that the higher value of N would improve the resolution and probably produce a better simulation with respect to the ground effect.

Table 2 shows samples of others results obtained. Case I presents the results for a stand still cylinder, while Cases II to XII represent typical values for small amplitude motions with ω = 1.0 and Re = 10^5.

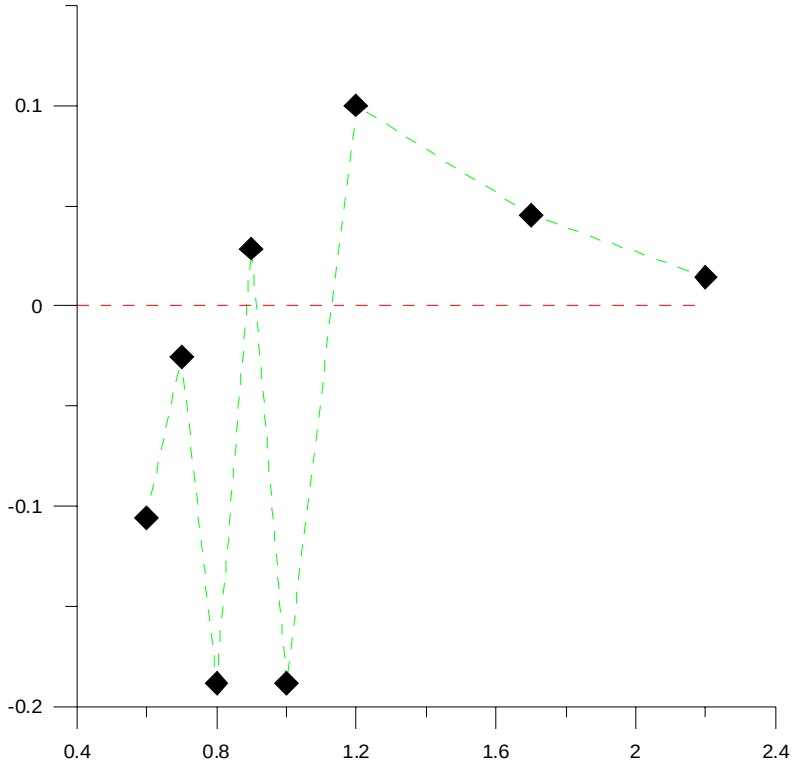

Figure 4. Influence of ground effect in the simulations, for A = 0, ω = 0, Re=10^5.

To better understand what is happening let us start analyzing the flow behind a stand still cylinder. From each side of the symmetry line (x-axis passing through the cylinder center) large structures formed by clusters of point vortices are shed alternately forming the Karmann vortex street. For low frequency of the body oscillation in ground effect (Case IV in Tab. 2), the behavior is almost the same although the positions of the cluster shedding move according to the oscillation amplitude; this is shown in Fig. 5.

Table 2: Results of C_L and C_D with ω=1.0 and Re = 10^5.

Case	A	ω	$\overline{C}_L$	$\overline{C}_D$	h/b	G_{min}
I	0	0	-0.07194976	1.28201151	0.7	0.2
II	0.05	1.0	-0.02525930	1.28331304	0.7	0.15
III	0.10	1.0	0.01069086	1.20050287	0.7	0.10
IV	0.15	1.0	0.12925778	1.09118962	0.7	0.05
V	0.05	1.0	-0.10624658	1.43586683	0.6	0.05
VI	0.05	1.0	-0.0252593	1.28331304	0.7	0.15
VII	0.05	1.0	-0.18872733	1.57669175	0.8	0.10
VII	0.05	1.0	0.02866777	1.23376429	0.9	0.25
IX	0.05	1.0	-0.18839182	1.45015180	1.0	0.45
X	0.05	1.0	0.10019104	1.26521969	1.2	0.65
XI	0.05	1.0	0.04547872	1.26271951	1.7	1.15
XII	0.05	1.0	0.01448197	1.15907335	2.2	1.65

For a heaving cylinder in the transition regime, the wake structure becomes intermittent and the vortex clusters are shed irregularly from the cylinder in ground effect.

Figure 6 is assembled with the data from the same simulation used in the Fig. 5; it is presented to illustrate the variation of lift and drag coefficients during the numerical simulation referred as Case IV in Tab. 2. As can be observed the lift coefficient oscillates with the same frequency of the circular cylinder. In this figure the green line is the cylinder motion and the red one is the lift coefficient. This phenomenon is the lock-in regime. This shows that the numerical method is able to predict the generation of lift force on an oscillating cylinder in lock-in regime.

Our simulation for the oscillating cylinder case, which moves with constant velocity in the presence of a ground plane, provided a very good estimate of lock-in regime. The amplitude of the oscillatory motion is considered to be small compared to the body length; therefore, to the first approximation one is allowed to transfer the body boundary condition from the actual position to a mean position of the body surface.

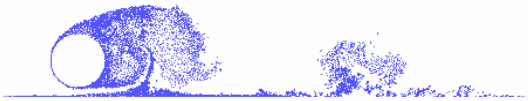

(a) t = 5.1

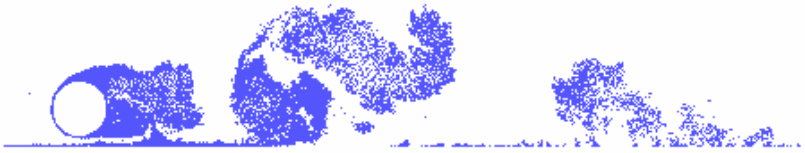

(b) t = 10.2

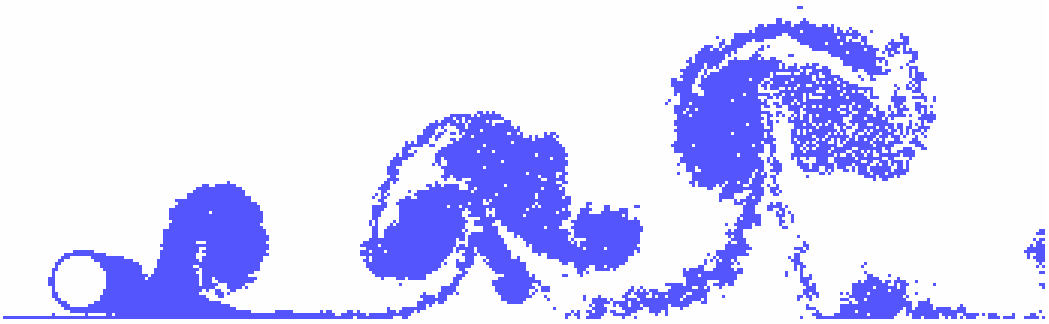

(c) t = 20.4

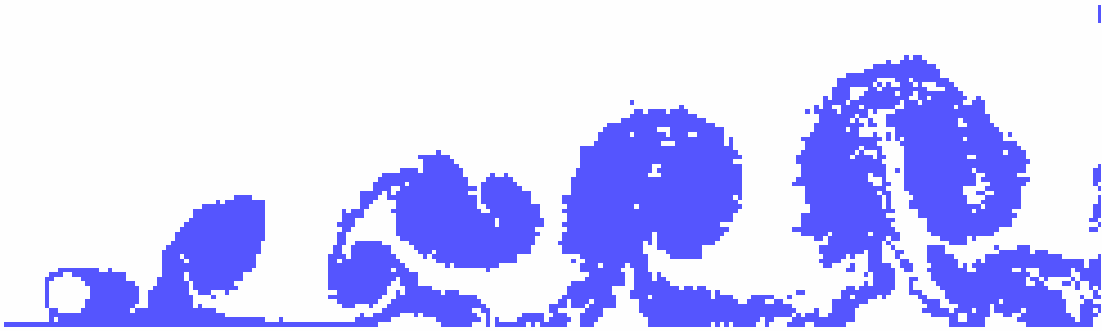

(d) t = 40

Figura 5. Wake evolution for t= 5.1, t= 10.2, t= 20.4, t= 40 with A= 0.15, ω=1.0, h/b = 0.7 and Re = 10^5.

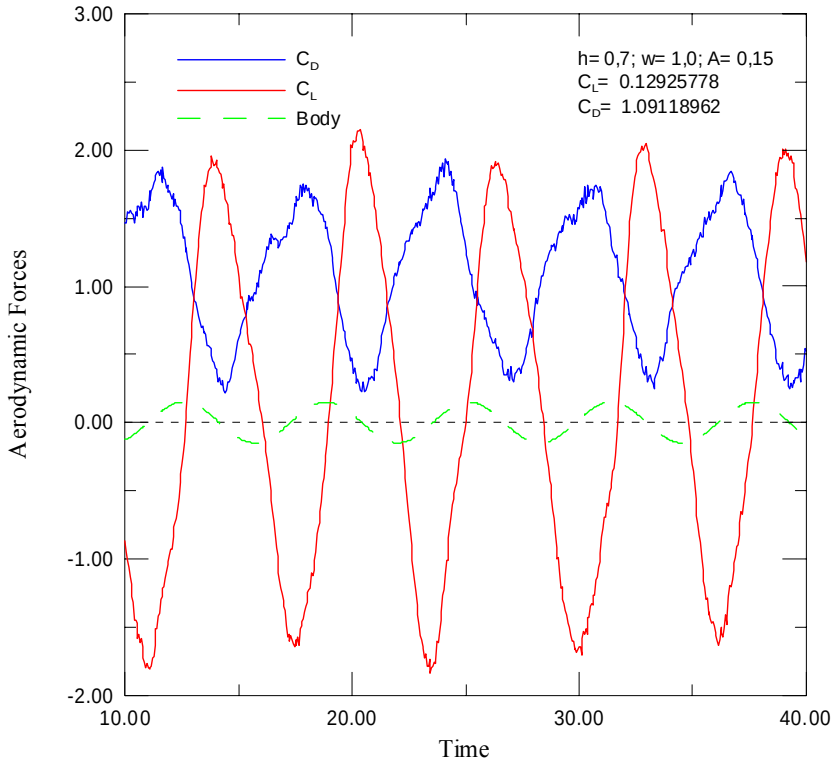

Figure 6: Lift coefficient during the numerical simulation with A= 0.15, ω=1.0, h/b = 0.7 and Re = 10^5.

As the results for a non-oscillating circular cylinder show the method developed here is very encouraging. It is capable of predicting very well the main global quantities inherent to the flow. The analysis of the influence of the numerical parameters on the simulation has pointed out the importance of choosing suitable values for M, A, ω and h/b. The influence of the numerical parameters on the simulation is extremely important and will be carried out.

The differences encountered in the comparison of the computed values with the experimental results for the distribution of the mean pressure coefficient along the cylinder surface as shown in Figure 3 are attributed mainly to the inherent three-dimensionality of the real flow for such a value of the Reynolds number, which is not modeled in the simulation. This seems to indicate that a higher value of M would improve the resolution and probably produce a better simulation with respect to the pressure distribution. More investigations are needed and one can imagine that with the use of more panels (and therefore more free vortices in the cloud) the results tend to be in closer agreement with the experiments.

The sub-grid turbulence modeling is of significant importance for the numerical simulation. The results of this analysis, taking into account the sub-grid turbulence modeling, are being generated and will be presented in due time, elsewhere.

Our simulation for the oscillating circular cylinder case provided a very estimative of the lock-in regime, and it needs further investigation.

5. Acknowledgement

The authors would like to acknowledge FAPEMIG (Proc. TEC-748/04) and CNPq for the financial support during the time of this project.

6. References

Alcântara Pereira, L.A., Hirata, M.H. and Manzanares Filho, N. 2004, "Wake and Aerodynamics Loads in Multiple Bodies - Application to Turbomachinery Blade Rows", J. Wind Eng. Ind Aerodyn., 92, pp. 477-491.

Alcântara Pereira, L.A., Ricci, J.E.R., Hirata, M.H. and Silveira-Neto, A., 2002, "Simulation of Vortex-Shedding Flow about a Circular Cylinder with Turbulence Modeling", Intern'l Society of CFD, Vol. 11, No. 3, October, pp. 315-322.

Blevins, R.D., 1984, "Applied fluid dynamics hanbook", Van Nostrand Reinhold Co.

Chacaltana, J.T.A., Bodstein, G.C. R. and Hirata, M.H., 1995, "Analytical Sutdy of the Time-Dependent 2D Inteaction of a Thin Airfoil and a Vortex in the Presence of a Ground Plane", XIII Brazilian Congress of Mechanical Engineering - XIII COBEM - Belo Horizonte, MG, Brazil.

Chen, J.M. and Chang, D.M., 1997, "Unsteady Pressure Measuriments for Parallel Vortex-Airfoil Interaction at Low Speed", Journal of Aircraft, Vol. 34, No. 3, pp. 330-336.

Chorin, A.J., 1973, "Numerical Study of Slightly Viscous Flow", Journal of Fluid Mechanics, Vol. 57, pp. 785-796.

Ferziger, J.H., 1981, "Numerical Methods for Engineering Application", John Wiley & Sons, Inc.

Fonseca, G.F., Bodstein, G.C.R. and Hirata, M.H., 2003, "Numerical Simulation of Inviscid Incompressible Two-Dimensional Airfoil-Vortex Interaction in Ground Effect", Journal of Aircraft, Vol. 40, No. 4, July-August, pp. 653-661.

Fonseca, G.F., Bodstein, G.C.R. and Hirata, M.H., 1997, "A Numerical Inviscid Vortex Model Applied to Parallel Blade-Vortex Interaction", Journal of the Brazilian Society of Mechanical Sciences, Vol. 19, No. 3, pp. 341-356.

Kamemoto, K., 2004, "On Contribution of Advanced Vortex Element Methods Toward Virtual Reality of Unsteady Vortical Flows in the New Generation of CFD", Proceedings of the 10th Brazilian Congress of Thermal Sciences and Engineering-ENCIT 2004, Rio de Janeiro, Brazil, Nov. 29-Dec. 03, Invited Lecture-CIT04-IL04.

Kamemoto, K., 1993, "Procedure to Estimate Unstead Pressure Distribution for Vortex Method" (In Japanese), Trans. Jpn. Soc. Mech. Eng., Vol. 59, No. 568 B, pp. 3708-3713.

Lee, D.J. and Smith, C.A., 1991, "Effect of Vortex Core Distortion on Blade-Vortex Interaction", A.I.A.A. Journal, Vol. 29, No. 9, pp. 1355-1362.

Lewis, R.I., 1999, "Vortex Element Methods, The Most Natural Approach to Flow Simulation - A Review of Methodology with Applications", Proceedings of 1st Int. Conference on Vortex Methods, Kobe, Nov. 4-5, pp. 1-15.

Lewis, R. I., 1991, "Vortex Element Method for Fluid Dynamic Analysis of Engineering Systems", Cambridge Univ. Press, Cambridge, England, U.K..

McCune, J.E. and Tavares, T.S., 1993, "Perspective: Unsteady Wing Theory - The Karman/Sears Legacy", Journal of Fluids Engineering, Vol. 115, Dec., pp. 548-560.

Milne-Thompson, L.M., 1955, Theorical Hydrodynamics; MacMillan & Co.

Mook, D.T. and Dong, B., 1994, "Perspective: Numerical Simulations of Wakes and Blade-Vortex Interaction", Journal of Fluids Engineering, Vol. 116, March, pp. 5-21.

Mustto, A.A., Hirata, M.H. and Bodstein, G.C.R., 1998, "Discrete Vortex Method Simulation of the Flow Around a Circular Cylinder with and without Rotation", A.I.A.A. Paper 98-2409, Proceedings of the 16th A.I.A.A. Applied Aerodynamics Conference, Albuquerque, NM, USA, June.

Panaras, A.G., 1987, "Numerical Modeling of the Vortex/Airfoil Interaction", A.I.A.A. Journal, Vol. 25, No. 1, pp. 5-11.

Poling, D.R., Dadone, L. and Telionis, D.P., 1989, "Blade-Vortex Interaction", A.I.A.A. Journal, Vol. 27, No. 6, pp. 694-699.

Rai, M.M., 1987, "Navier-Stokes Simulations of Blade-Vortex Interaction Using High-Order Accurate Upwind Schemes", A.I.A.A. Paper 87-0543, November.

Ricci, J.E.R., Alcântara Pereira, L.A., Hirata, M.H. and Manzanares Filho, N., 2001, "Influence of a Ground Plane in the Aerodynamic Loads on an Airfoil" (In Portuguese), Proceedings of COBEM 2001, Fluid Mechanics, Vol. 8, pp. 130-138. Uberlândia, MG.

Sarpkaya, T., 1994, "Vortex Element Method for Flow simulation", Advances in applied Mechanics, Vol 31, pp. 113-247.

Seath, D.D., Kim, J.M. and Wilson, D.R., 1989, "Investigation of Parallel Blade-Vortex Interaction at Low Speed", Journal of Aircraft, Vol. 26, No. 4, pp. 328-333.

Shintani, M. and Akamatsu, T, 1994, "Investigation of Two Dimensional Discrete Vortex Method with Viscous Diffusion Model", Computational Fluid Dynamics Journal, Vol. 3, No. 2, pp. 237-254.

Silva, H., 2004, "Análise do Escoamento ao Redor de um Corpo Oscilante que se Desloca com Velocidade Constante". In Portuguese, UNIFEI, Itajubá, MG, Brasil, M.Sc. Dissertation.

Silva de Oliveira, L., Alcântara Pereira, L.A. and Hirata, M.H., 2005, "Numerical Simulation of the Airfoil – Vortex Cloud Interaction in Ground Effect", 18th International Congress of Mechanical Engineering, Proceedings of COBEM 2005, November 6-11, Ouro Preto, MG.

Silva de Oliveira, L., Alcântara Pereira, L.A., Hirata, M.H. and Manzanares Filho, N., 2004, "Numerical Modelling of the Airfoil-Vortex Cloud Interaction", Proceedings of the 10th Brazilian Congress of Thermal Sciences and Engineering - ENCIT 2004, Rio de Janeiro, Brazil, Nov. 29 - Dec. 03, Paper CIT04-0253.

Son, J.S., Hanratty, 1969, "Velocity Gradients at the Wall for Flow Around a Cylinder at Reynolds Number from $5x10^3$ to 10^5"; Journal of Fluid Mechanics, Vol. 35, no. 2, pp. 353-368.

Srinivasan, G.R. and McCroskey, W.J., 1993, "Euler Calculations of Unsteady Interaction of Advancing Rotor with a Line Vortex", A.I.A.A. Journal, Vol. 31, No. 9, pp. 1659-1666.

Straus, J., Renzoni, P. and Mayle, R.E., 1990, "Airfoil Pressure Measurement During a Blade Vortex Interaction and a Comparison with Theory", A.I.A.A. Journal, Vol. 28, No. 2, pp. 222-228.

Uhlman, J.S., 1992, "An Integral Equation Formulation of the Equation of an Incompressible Fluid", Naval Undersea Warfare Center, T.R. 10-086.

Proceedings of the 11th Brazilian Congress of Thermal Sciences and Engineering -- ENCIT 2006
Braz. Soc. of Mechanical Sciences and Engineering -- ABCM, Curitiba, Brazil, Dec.5-8, 2006

Paper CIT06-0362

HARMONIC OSCILLATIONS OF A CIRCULAR CYLINDER MOVING WITH CONSTANT VELOCITY IN A QUIESCENT FLUID

Jan Novaes Recicar
Instituto de Engenharia Mecânica, UNIFEI, CP 50, Itajubá, Minas Gerais, 37500-903, Brasil
e-mail: recicar@unifei.edu.br

Luiz Antonio Alcântara Pereira
Instituto de Engenharia Mecânica, UNIFEI, CP 50, Itajubá, Minas Gerais, 37500-903, Brasil
e-mail: luizantp@unifei.edu.br

Miguel Hiroo Hirata
FAT/UERJ
Campus Regional de Resende
Estrada Resende - Riachuelo, Resende, RJ
e-mail: hirata@fat.uerj.br

Abstract. *The flow around an oscillating circular cylinder which moves with constant velocity in a quiescent Newtonian fluid with constant properties is analyzed. The influences of the frequency and amplitude oscillation on the aerodynamic loads and on the Strouhal number are presented. For the numerical simulation a cloud of discrete Lamb vortices are utilized. For each time step of the simulation a number of discrete vortices are placed close to the body surface; the intensity of then are determined such as to satisfy the no-slip boundary condition.*

Keywords: *vortex method, panels methods, aerodynamic loads, Strouhal number, oscillating body.*

1. Introduction

Understanding and being able to analyze the flow around an oscillating body which moves with constant velocity in a quiescent fluid with constant properties is of great fundamental and practical importance in aero and hydrodynamics analysis. Oscillatory motions of small amplitude are important in the analysis of immerse vibrating bodies and special care should be taken in the lock-in condition. Large amplitude motions, on the other hand, are of relevance in the analysis of bodies located in waves and currents such as the ones found in the offshore structures (Williamson and Roshko, 1988).

The oscillatory motion of small amplitude mainly modifies the near field changing the boundary layer flow and, as a consequence, having an important effect on the aerodynamic forces and the pressure distribution. If the amplitude of the oscillatory motion is large one observes, additionally, substantial changes in the far field wake which can be of importance in the presence of other bodies or near by surfaces.

This paper deals with the analysis of a body oscillating around a fixed position which is located in an incoming uniform flow with constant velocity; to simplify matters the oscillatory motion is restricted to heave. In previous works Silva (2004) analyzed the same situation with the restriction of small amplitude of oscillation and Mustto *et al.* (1998) presented results for a rotating cylinder.

A simpler approach to the present problem would consider a fixed body located in an oscillating incoming flow; notice, however, that with this approach the whole fluid mass would oscillate with the same frequency and amplitude, which is not quite what, happens in real situations, mainly in the far field region.

For the numerical simulations a Lagrangian approach is used, more specifically the Vortex Method (Chorin, 1973), (Lewis, 1999), (Kamemoto, 1994, 2004), (Sarpkaya, 1994), (Hirata *et al.,* 2003). In the Lagrangian discrete vortex method the vorticity generated on the body surface is discretized and represented by a cloud of particles carrying vorticity. Lamb vortices with a viscous core are used for that matter (Mustto *et al.,* 1998).

Results for a circular cylinder fixed and heaving in a uniform flow are presented and compared with results found in the literature; these are experimental results as well as results obtained using numerical simulations. It is important to mention that although the Reynolds number used in the simulations is high, no attempt to include turbulence modeling (Alcântara Pereira *et al*., 2002) was made.

In the present simulations the integrated aerodynamic loads (such as lift and drag coefficient), the pressure distribution and the Strouhal number agree quite well with the experimental results when the cylinder is kept without oscillation. Due to the alternate vortex shedding the lift coefficient oscillates, around zero, during the numerical simulation; the amplitude of the lift coefficient oscillation is increased with the cylinder oscillation keeping, however, the mean value almost identically to zero.

It is also possible to identify three different types of flow regime as the cylinder oscillation frequency increases. The first type – Type I - is observed for low frequency range of the cylinder oscillation; in this situation the Strouhal

number remains almost constant. Type I is followed by an intermediate range of frequency – Type II, the transition regime - where apparently the shedding frequency does not correlate to the frequency of the cylinder oscillation. Finally in Type III – high frequency of cylinder oscillation – the vortex shedding frequency is locked-in with the cylinder oscillation frequency.

2. Problem definition and mathematical model

2.1. Definitions

Consider the incompressible flow (of a Newtonian fluid) around a moving body in a large two-dimensional domain. The body moves to the left with constant velocity; an oscillatory motion with finite amplitude A and constant angular velocity ω is added to body motion.

This is represented, in Fig. 1, by a heaving cylinder immersed in a uniform incoming flow with velocity U. In this figure the (x, o, y) is the inertial frame of reference and the (X, O, Y) is the coordinate system fixed to the cylinder; this coordinate system oscillates around the x-axis as $y_o = A\cos(\omega t)$.

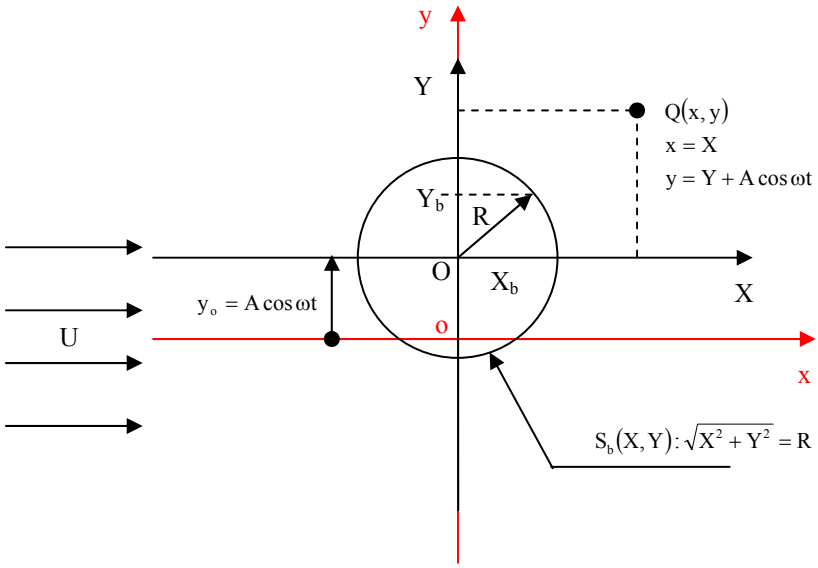

Figure 1. Problem definition.

The boundary S of the fluid domain is $S = S_b \cup S_\infty$; being S_∞ the far away boundary, which can be viewed as $r = \sqrt{x^2 + y^2} \to \infty$, and S_b the body surface.

In the body fixed coordinate system, the surface S_b is defined by the function

$$F_b(X, Y) = Y_b - \eta(X) = 0 \tag{1}$$

Thus, in the inertial frame of reference

$$S_b : F_b(x, y, t) = y_b - [y_0(t) + \eta(x)] = 0\,, \tag{2}$$

and, for a symmetrical body

$$F_b(x, y, t) = y_b - y_0(t) \mp \eta(x) = 0\,. \tag{3}$$

2.2. Governing equations

For an incompressible fluid flow the continuity is written as

$$\nabla \cdot \mathbf{u} = 0 \tag{4}$$

where $\mathbf{u} \equiv (u, v)$ is the velocity vector.

If, in addition, the fluid is Newtonian with constant properties the momentum equation is represented by the Navier-Stokes equation as

$$\frac{\partial \mathbf{u}}{\partial t} + \mathbf{u} \cdot \nabla \mathbf{u} = -\nabla p + \frac{1}{Re} \nabla^2 \mathbf{u} \,. \tag{5}$$

Re stands for the Reynolds number defined as $Re = \frac{bU}{\upsilon}$ where b = d = cylinder diameter.

On the body surface the adherence condition has to be satisfied. This condition is better specified in terms of the normal and tangential components as

$$(\mathbf{u} \cdot \mathbf{n}) = (\mathbf{v} \cdot \mathbf{n}) \ \text{on} \, S_b \,, \text{ the impenetrability condition} \tag{6}$$

$$(\mathbf{u} \cdot \boldsymbol{\tau}) = (\mathbf{v} \cdot \boldsymbol{\tau}) \ \text{on} \, S_b \,, \text{ the no-slip condition} \tag{7}$$

here $\mathbf{n}$ and $\boldsymbol{\tau}$ are unit normal and tangential vectors and v is the body surface velocity.

Far from the body one assumes that the perturbation due to the oscillating body fades away, that is

$$|\mathbf{u}| \to 1 \,. \tag{8}$$

One should mention that the above boundary value problem was made non-dimensional using U and d as characteristic quantities.

3. The vortex method

3.1. Viscous splitting algorithm and aerodynamics loads

Taking the curl of the Navier-Stokes equation and with some algebraic manipulations one gets the vorticity equation which presents no pressure term. In two-dimensions this equation reads

$$\frac{\partial \omega}{\partial t} + \mathbf{u} \cdot \nabla \omega = \frac{1}{Re} \nabla^2 \omega \,, \tag{9}$$

which is an scalar equation since ω is the only component of the vorticity vector $\boldsymbol{\omega} = \nabla \times \mathbf{u}$.

The left hand side of the above equation carries all the information needed for the convection of vorticity while the right hand side governs the diffusion. Following Chorin (1973) we use the viscous splitting algorithm, which, for the same time step of the numerical simulation, says that

Convection of vorticity is governed by

$$\frac{\partial \omega}{\partial t} + \mathbf{u} \cdot \nabla \omega = 0 \,. \tag{10}$$

Diffusion of vorticity is governed by

$$\frac{\partial \omega}{\partial t} = \frac{1}{Re} \nabla^2 \omega \,. \tag{11}$$

Having determined the vorticity field the pressure calculation starts with the Bernoulli function, defined by Uhlman (1992) as

$$Y = p + \frac{u^2}{2}, \ u = |\mathbf{u}| \tag{12}$$

Following Shintani and Akamatsu (1994) this function is then obtained using the following integral formulation

$$H\overline{Y_i} - \int_{S_l} \overline{Y}\nabla G_i \cdot \mathbf{e}_n \, dS = \iint_{\Omega} \nabla G_i \cdot (\mathbf{u} \times \omega) d\Omega - \frac{1}{Re} \int_{S_l} (\nabla G_i \times \omega) \cdot \mathbf{e}_n \, dS \tag{13}$$

where H = 1 in the fluid domain, H= 0.5 on the boundaries and G is a fundamental solution of the Laplace equation, Alcântara Pereira *et al.* (2002).

3.2. Convection and diffusion of vorticity

For the numerical implementation the vorticity in the fluid domain is simulated by a cloud of Lamb vortices.

For each time step of the simulation, a number of discrete vortices are generated on the body surface; the intensity of these newly generated vortices is determined using the no-slip condition, see Eq. (7).

For the convection of the discrete vortices of the cloud, Eq. (10) is written in its Lagrangian form as

$$\frac{dx^{(i)}}{dt} = u^{(i)}(x, y, t), \tag{14a}$$

$$\frac{dy^{(i)}}{dt} = v^{(i)}(x, y, t), \tag{14b}$$

being i = 1, N; N is the number of vortices in the cloud.

A second order solution to this equation is given by the Adams-Bashforth formula (Ferziger, 1981)

$$x^{(i)}(t + \Delta t) = x^{(i)}(t) + \left[1.5u^{(i)}(t) - 0.5u^{(i)}(t - \Delta t)\right]\Delta t \tag{15a}$$

$$y^{(i)}(t + \Delta t) = y^{(i)}(t) + \left[1.5v^{(i)}(t) - 0.5v^{(i)}(t - \Delta t)\right]\Delta t \tag{15b}$$

The diffusion of vorticity is taken care of using the random walk method (Lewis, 1991). The random displacement $Z_d \equiv (x_d, y_d)$ is defined as

$$x_d^{(i)} = \left[\cos(2\pi Q)\right]\sqrt{\frac{4\Delta t}{Re}\ln\left(\frac{1}{P}\right)} \tag{16a}$$

$$y_d^{(i)} = \left[\sin(2\pi Q)\right]\sqrt{\frac{4\Delta t}{Re}\ln\left(\frac{1}{P}\right)} \tag{16b}$$

Therefore the final displacement is written as

$$x^{(i)}(t + \Delta t) = x^{(i)}(t) + \left[1.5u^{(i)}(t) - 0.5u^{(i)}(t - \Delta t)\right]\Delta t + x_d^{(i)} \tag{17a}$$

$$y^{(i)}(t + \Delta t) = y^{(i)}(t) + \left[1.5v^{(i)}(t) - 0.5v^{(i)}(t - \Delta t)\right]\Delta t + y_d^{(i)} \tag{17b}$$

4. Numerical implementation

The $u^{(i)}$ and $v^{(i)}$ components of the velocity induced at the location of the (i) vortex can be written as

$$u^{(i)} = ui^{(i)} + uc^{(i)} + uv^{(i)} \tag{18a}$$

$$v^{(i)} = vi^{(i)} + vc^{(i)} + vv^{(i)} \tag{18b}$$

where: $\mathbf{ui}^{(i)} \equiv [ui^{(i)}, vi^{(i)}]$ is the incident flow velocity,

$\mathbf{uc}^{(i)} \equiv [uc^{(i)}, vc^{(i)}]$ is the velocity induced by the cylinder at the location of vortex (i),

$\mathbf{uv}^{(i)} \equiv [uv^{(i)}, vv^{(i)}]$ is the velocity induced at the vortex (i) by the other vortices of the cloud.

The $\mathbf{ui}^{(i)}$ and $\mathbf{uv}^{(i)}$ calculations present no problems and they follows the usual Vortex Method procedures; to the first approximation the same happens with the $\mathbf{uc}^{(i)}$ when the body oscillation amplitude is small, see Silva (2004).

For large amplitude body oscillations, however, the body boundary conditions can not be transferred from the actual position to the mean position. As the body surface is simulated by M straight line panels on which singularities are distributed (Panels Method) it is convenient to calculate the body induced velocity in the moving coordinate system. For that one has to observe the following

- The fluid velocity on the body surface is written as

$$\mathbf{u}(X, Y; t) = U\mathbf{i} - \dot{y}_0(t)\mathbf{j}\ ; \text{with}\ \dot{y}_0(t) = \frac{d}{dt}\left[A\cos(\omega t)\right] \tag{19}$$

As a consequence of the j component of the right hand side of the fluid velocity (in the above expression) one gets an additional singularities distribution on the body surface. Of course, the induced velocity due to this additional singularities distribution fades away from the body.

- The velocity induced by the body, according to the panel method calculations, is indicated by [uc(X,Y), vc(X,Y)]; this is the velocity induced at the vortex (i), located at the point [x(t), y(t)]; thus

$$uc^{(i)}(x, y; t) = uc(X, Y; t) \tag{20a}$$

$$vc^{(i)}(x, y; t) = vc(X, Y; t) \tag{20b}$$

where the following relations remains

$$x^{(i)}(t) = X \tag{21a}$$

$$y^{(i)}(t) = y_0(t) + Y \tag{21b}$$

5. Results and conclusions

We start presenting the results for a stand still circular cylinder immersed in a uniform flow. Table 1 shows the results for a circular cylinder, $Re = 10^5$. Line 1 (Blevins, 1984) are experimental results while line 2 (Mustto *et al.,* 1998) and line 3 (Alcântara Pereira *et al.*, 2002) are numerical results obtained using different implementation of the Vortex Method. The results presented in line 4, as well as all the other results presented elsewhere in this paper were obtained carrying out the simulations with M=50 sources panels to replace the cylinder surface and lasted for t = 40 dimensionless time. In each time step the nascent vortices were placed into the cloud through a displacement $\varepsilon = \sigma_0 = 0.0009b$ normal to the panels. As mention before, no attempt to include turbulence modeling (Alcântara Pereira *et al.,* 2002) in the algorithm was made.

Table 1: Strouhal number, lift and drag coefficients for a circular cylinder.

$Re = 10^5$, A = 0 and $\omega = 0$	$\overline{C}_L$	$\overline{C}_D$	$\overline{S}_t$
Blevins (1984)	-	1.20	0.19
Mustto *et al.* (1998)	-	1.22	0.22
Alcântara Pereira *et al.*(2002)	0.04	1.21	0.22
Present simulation	0.06	1.20	0.19

The numerical results represent average values calculated from t = 10 to t = 40 of the numerical simulation. As can be observed all the numerical obtained results are consistent with the ones obtained experimentally. The drag coefficient is about 1.2, while the lift coefficient is almost zero, as it should be.

The Strouhal number, which measures the frequency of vortex shedding f, is defined as usual and, for future use a body Strouhal number is also defined

$$S_t = \frac{Uf}{d} \qquad S_{tc} = \frac{Uf_c}{d} \qquad 2\pi f_c = \omega \tag{22}$$

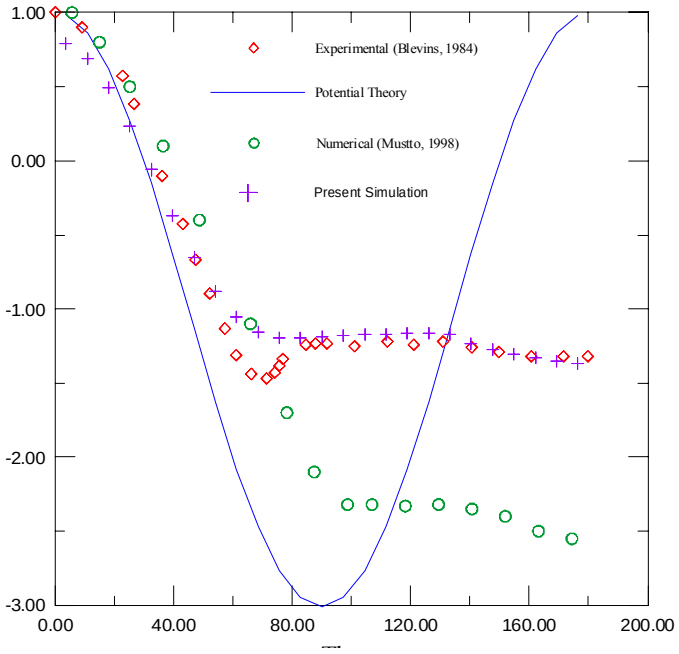

Figure 2. Comparison of the circular cylinder case, experimental and numerical results of C_p, for Re=10^5.

Figure 2 shows the pressure distribution on the cylinder surface. As can be noted the obtained values follows closely the ones obtained experimentally; there are some small discrepancies from 60° to 80° which probably could be reduced with a proper turbulence modeling.

Table 2 shows samples of results obtained. CASE I are the results for a stand still cylinder, CASE II represent typical values for small amplitude (A=15) motions while CASE III refers to a large amplitude (A=1.5) motions.

Table 2: Circular cylinder: results for an oscillatory motion, Re = 10^5.

CASE	Amplitude (A)	Angular Velocity (ω)	$\overline{C}_L$	$\overline{C}_D$	$\overline{S}_{tc}$	$\overline{S}_t$
I	0	0	0.06	1.20	0	0.19
II	0.15	0.02	0.0928	1.2572	0.00318	0.1912
		0.05	0.0846	1.2054	0.00796	0.1901
		0.1	0.0706	1.2270	0.01592	0.2128
		0.2	-0.0430	1.2430	0.03183	0.2016
		0.3	-0.0291	1.2049	0.04775	0.1961
		0.4	0.0049	1.1622	0.06366	0.1947
		0.6	-0.0256	1.0553	0.09549	0.1988
		0.9	-0.0272	1.0080	0.14324	0.1399
		1.2	0.0102	1.2988	0.19099	0.1908
		1.5	0.0062	1.0211	0.23873	0.2395
III	0.5	0.02	0.0286	1.2360	0.00318	0,1968
		0.05	0.1024	1.1635	0.00796	0,1950
		0.1	0.0931	1.1953	0.01592	0,1980
		0.2	0.0040	1.0997	0.03183	0,2051
		0.4	0.0034	0.5936	0.06366	0,0766
		0.6	0.1809	0.4512	0.09549	0,0948
		0.9	0.0785	0.9328	0.14324	0,1435
		1.2	0.0095	0.8443	0.19099	0,1876
		1.5	0.1380	0.5499	0.23873	0,2410

A significant range of the cylinder oscillation frequency is covered in this table. A careful analysis of the Strouhal number (S_t) shows three different flow regimes. For low frequency of the body oscillation (low value of S_{tc}) the S_t value is very close to 0.19, the stand still value for the Strouhal number. On the other extreme, for high value o S_{tc}, lock-in is observed and the vortex shedding frequency is equal to the body oscillation frequency. Between these two extreme there is a transition regime with no definite behavior could be observed; lock-in could be partially observed. This is particularly clear for large amplitude motions as illustrated in Fig. 3.

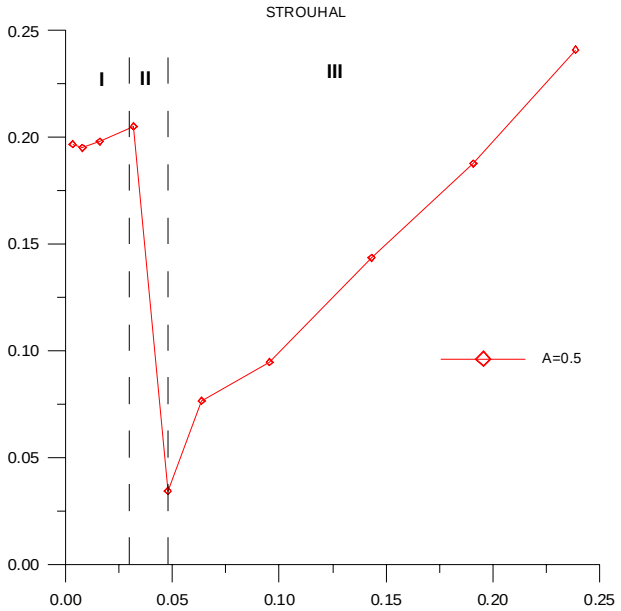

Figure 3. Strouhal number behavior as a function of the body oscillation frequency, Re = 10^5.

To better understand what is happening let us start analyzing the flow behind a stand still cylinder. From each side of the symmetry line (x-axis passing through the cylinder center) large structures formed by clusters of point vortices are shed alternately forming the Karmann vortex street. For low frequency of the body oscillation, the behavior is almost the same although the positions of the cluster shedding move according to the oscillation amplitude; this is shown in Fig. 4.

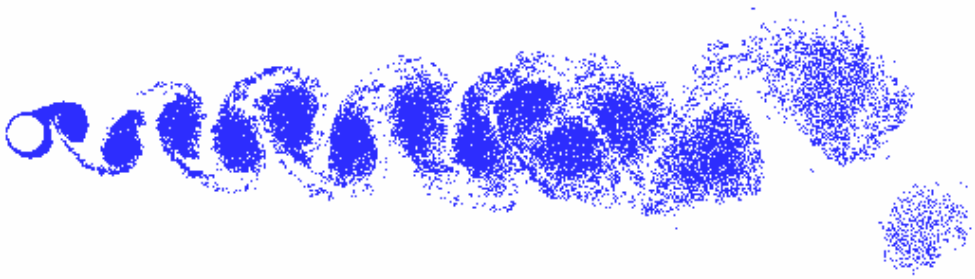

Figure 4. Wake pattern when the body oscillates with small amplitude and low frequency, Re = 10^5.

For a heaving cylinder in the transition regime, the wake structure becomes intermittent and the vortex clusters are shed irregularly from the cylinder.

For the lock-in regime a high strength cluster of vortices just behind the cylinder is observed when it passes through the symmetry line; this situation is illustrated in Fig. 7, when the cylinder is moving from top to bottom. This cluster – referred as the actual cluster – has a slow rotation in the anti-clockwise direction which decelerates the flow in the upper part of the cylinder and accelerates the flow in the lower part; thus vorticity is fed into a new cluster, which has started to develop in the upper part, enhancing its strength. This newly developed cluster pushes the actual cluster and when the cylinder reaches its lower position it separates into the wake, see Fig. 5. This figure shows the near field wake pattern at t = 15, when the cylinder is its lowest position.

Of course, the opposite is observed when the cylinder is moving from its lower position to the upper position; Figure 6 shows the near field wake pattern at t = 23, when the cylinder is in its uppermost position.

Figure 8 is assembled with the data from the same simulation used in the previous figure; it is presented to illustrate the lift coefficient behavior during the numerical simulation. As can be observed the lift coefficient oscillates

with the same frequency of the body oscillation and its amplitude can reach values as high as 1.5 to 2.0. In this figure the black line is the cylinder motion and the blue one is the lift coefficient.

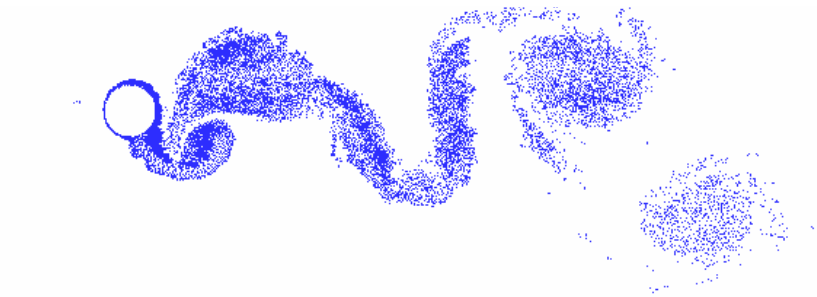

Figure 5: Cylinder in its lowest position (t = 15, when ω = 1.5 and A = 0.5).

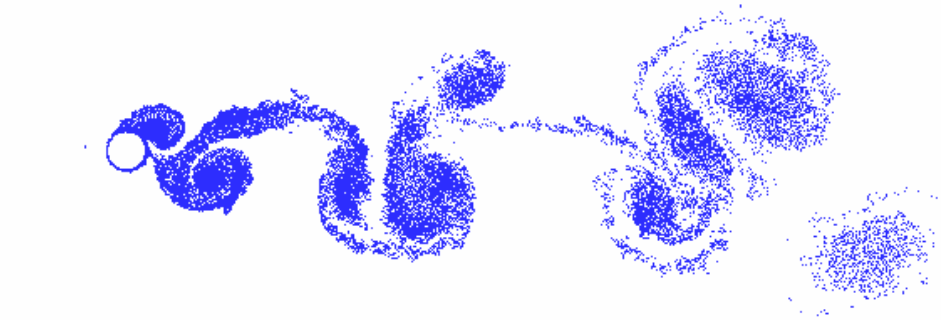

Figure 6: Cylinder in its uppermost position (t = 25, when ω = 1.5 and A = 0.5).

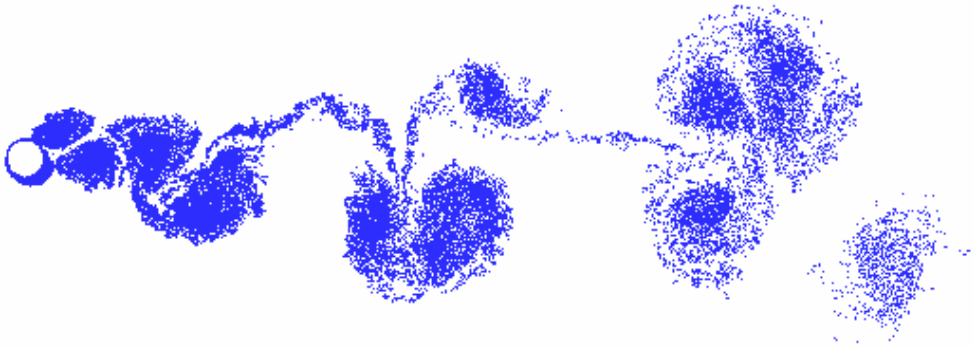

Figure 7: Center of the cylinder passing through the symmetry line in the downward motion (t = 30, when ω = 1.5 and A = 0.5).

The data from Tab. 2 also shows a reducing trend in the drag coefficient as the frequency of the cylinder oscillation increase. No solid explanation can be presented about this subject at this moment.

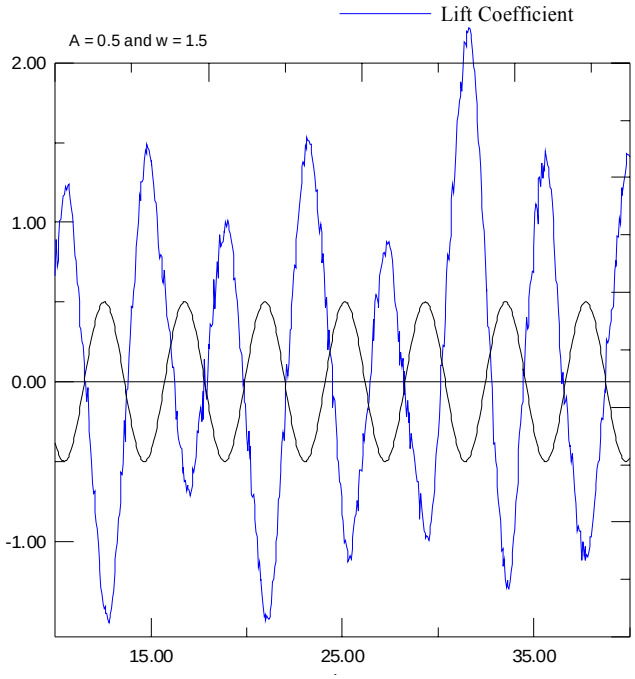

Figure 8: Lift coefficient during the numerical simulation

The three-dimensional effects present in the experiments are very important for the Reynolds number used in the simulations. Therefore a purely two-dimensional computation of the flow must produce differences in the comparison of the numerical results with the experimental results. The differences encountered in the comparison of the computed values with the experimental results for the distribution of the mean pressure coefficient along the cylinder surface as shown in Figure 2 are attributed mainly to the inherent three-dimensionality of the real flow for such a value of the Reynolds number, which is not modeled in the simulation. The results for the pressure distribution indicated that there was a lack of resolution near the stagnation point and the position of the separation point. The position of the separation point is predicted to occur at about 78°, whereas the experimental value (Blevins, 1984) is about 82°. This seems to indicate that a higher value of M would improve the resolution and probably produce a better simulation with respect to the pressure distribution. More investigations are needed and one can imagine that with the use of more panels (and therefore more free vortices in the cloud) the results tend to be in closer agreement with the experiments.

Some discrepancies observed in the determination of the aerodynamics loads may be also attributed to errors in the treatment of vortex element moving away from a solid surface. Because every vortex element has different strength of vorticity, it will diffuse to different location in the flow field. It seems impossible that every vortex element will move to same ε-layer normal to the solid surface. In the present method all nascent vortices were placed into the cloud through a displacement $\varepsilon = \sigma_0 = 0.0009b$ normal to the panels.

The use of a fast summation scheme to determine the vortex-induced velocity, such as the Multiple Expansion scheme, allows an increase in the number of vortices and a reduction of the time step, which increases the resolution of the simulation, in addition to a reduction of the CPU time, which allows a longer simulation time to be carried out. The present calculation required 9 h of CPU time in an Intel(R) Pentium(R) 4 CPU 1700 MHz.

The sub-grid turbulence modeling is of significant importance for the numerical simulation. The results of this analysis, taking into account the sub-grid turbulence modeling, are also being generated and will be presented in due time, elsewhere.

Finally, despite the differences presented in this preliminary investigation, the results are promising, that encourages performing additional tests in order to explore the phenomena in more details.

6. Acknowledgement

The authors would like to acknowledge FAPEMIG (Proc. TEC-748/04) and CNPq for the financial support during the time of this project.

7. References

Alcântara Pereira, L.A., Ricci, J.E.R., Hirata, M.H. and Silveira-Neto, A., 2002, "Simulation of Vortex-Shedding Flow about a Circular Cylinder with Turbulence Modeling", Intern'l Society of CFD, Vol. 11, No. 3, October, pp. 315-322.

Blevins, R.D., 1984, "Applied fluid dynamics hanbook", Van Nostrand Reinhold Co.

Chorin, A.J., 1973, "Numerical Study of Slightly Viscous Flow", Journal of Fluid Mechanics, Vol. 57, pp. 785-796.

Ferziger, J.H., 1981, "Numerical Methods for Engineering Application", John Wiley & Sons, Inc.

Hirata,M.H, Oliveira, W, Ricci, J.E.R. e Alcântara Pereira, L.A., 2003, "Método de Vórtices" – CD do Departamento de Mecânica, IEM, UNIFEI, Itajubá, MG, Brasil.

Kamemoto, K., 2004, "On Contribution of Advanced Vortex Element Methods Toward Virtual Reality of Unsteady Vortical Flows in the New Generation of CFD", Proceedings of the 10th Brazilian Congress of Thermal Sciences and Engineering-ENCIT 2004, Rio de Janeiro, Brazil, Nov. 29 - Dec. 03, Invited Lecture-CIT04-IL04.

Kamemoto, K., 1994 "Development of vortex methods for grid-free lagrangian direct numerical simulation", Proceedings of the 3th. JSME-KSME Fluids Engeneering Conference. July 25-27, Sendai, Japan.

Lewis, R.I., 1999, "Vortex Element Methods, the Most Natural Approach to Flow Simulation - A Review of Methodology with Applications", Proceedings of 1st Int. Conference on Vortex Methods, Kobe, Nov. 4-5, pp. 1-15.

Lewis, R. I., 1991, "Vortex Element Method for Fluid Dynamic Analysis of Engineering Systems", Cambridge Univ. Press, Cambridge, England, U.K..

Mustto, A.A., Hirata, M.H. and Bodstein, G.C.R., 1998, "Discrete Vortex Method Simulation of the Flow Around a Circular Cylinder with and without Rotation", A.I.A.A. Paper 98-2409, Proceedings of the 16th A.I.A.A. Applied Aerodynamics Conference, Albuquerque, NM, USA, June.

Sarpkaya, T., 1994, "Vortex Element Method for Flow simulation", Advances in applied Mechanics, Vol 31, pp. 113-247.

Shintani, M. and Akamatsu, T, 1994, "Investigation of Two Dimensional Discrete Vortex Method with Viscous Diffusion Model", Computational Fluid Dynamics Journal, Vol. 3, No. 2, pp. 237-254.

Silva, H., 2004, "Análise do Escoamento ao Redor de um Corpo Oscilante que se Desloca com Velocidade Constante". In Portuguese, UNIFEI, Itajubá, MG, Brasil, M.Sc. Dissertation.

Uhlman, J.S., 1992, "An Integral Equation Formulation of the Equation of an Incompressible Fluid", Naval Undersea Warfare Center, T.R. 10-086.

Williamson, C.H.K. and Roshko, A., 1988, "Vortex Formation in the Wake of an Oscillating Cylinder", J. Fluids and Structures, Vol. 2, pp. 239-381.

Proceedings of the 11th Brazilian Congress of Thermal Sciences and Engineering -- ENCIT 2006
Braz. Soc. of Mechanical Sciences and Engineering -- ABCM, Curitiba, Brazil, Dec. 5-8, 2006

Paper CIT06-0365

CARACTERIZAÇÃO DE ESCOAMENTOS EM CAVIDADES CÚBICAS COM MOVIMENTAÇÃO DIAGONAL DA TAMPA

Elie Luis M. Padilla
epadilla@mecanica.ufu.br

Tiago de Assis Silva
tasilva@mecanica.ufu.br

Aristeu da Silveira Neto
Universidade Federal de Uberlândia
Faculdade de Engenharia Mecânica
aristeus@mecanica.ufu.br

Resumo. *Escoamentos em cavidades com tampa deslizante são de natureza tridimensional e apresentam diversas estruturas características em função do número de Reynolds e da razão de aspecto. Na atualidade, devido às muitas aplicações em engenharia e ao interesse pela compreensão da física do problema, uma grande quantidade de pesquisas aborda este problema, focados especificamente no caso de a tampa da cavidade se movimentar paralela a um dos eixos coordenados. Uma vez que, na realidade, os escoamentos externos à cavidade (representados pela tampa deslizante) nem sempre são paralelos aos eixos, o presente trabalho apresenta a caracterização e análise numérica de escoamentos no interior de cavidades cúbicas com tampa deslizante paralela (0°, 90º) e diagonal (15º, 30°, 45°), considerando números de Reynolds na faixa de 100-2000. Apresenta-se também uma comparação quantitativa de transferência de momento através da integral volumétrica de momento, paralela e transversal ao movimento da tampa. As equações de Navier-Stokes são discretizadas com o método dos volumes finitos em coordenadas cartesianas, com malhas deslocadas e esquemas temporal e espacial de segunda ordem. Para o acoplamento pressão-velocidade usa-se o método dos passos fracionados.*

Palavras chave: escoamento estável, cavidade, simulação tridimensional .

1. Introdução

O escoamento em cavidades com tampa deslizante tem diversas aplicações tecnológicas importantes em diferentes áreas da engenharia. A simplicidade da geometria que delimita o problema contrasta com a diversidade de estruturas que formam, e de acordo com a literatura, estas características fazem da cavidade, provavelmente, o problema mais estudado no campo da fluidodinâmica computacional para testes de modelos numéricos.

A representação de cavidades de seção quadrada com comprimento axial infinito, cavidades bidimensionais, tem sido largamente estudada e é agora um caso teste padrão para novos esquemas computacionais. Benjamim e Denny (1979), Ghia *et al.* (1982) e Botella e Peyret (1998) são alguns dos muitos trabalhos existentes, dentre estes Ghia *et al.* (1982) é freqüentemente referenciado. Eles empregaram o método das diferenças finitas com a formulação função corrente-vorticidade, usando malha cartesiana uniforme.

Devido à dificuldade de abordar o problema em três dimensões, somente nos anos de 1980 o trabalho experimental pioneiro de Koseff e Street (1984) permitiu mostrar que o escoamento em cavidades é naturalmente tridimensional. Além do mais, características padrão, como vórtices primários e secundários, estruturas como os vórtices de canto e os vórtices do tipo Taylor-Gortler foram observados.

O recente progresso dos métodos numéricos e do poder de cálculo dos computadores tem tornado possível uma análise tridimensional adequada destes problemas. Ku *et al.* (1987) e Babu e Korpela (1994) através da resolução das equações de Navier-Stokes em três dimensões, apresentaram comparações entre resultados bi e tridimensionais para cavidade cúbica. Por outro lado, Iwatsu *et al.* (1989) fizeram uma análise da topologia do escoamento por meio da projeção de linhas de corrente em planos para vários números de Reynolds. Sheu e Tsai (2002) fizeram a análise para Reynolds igual a 400.

O estudo do escoamento em cavidades com tampa deslizante não se restringe somente à movimentação paralela da tampa em relação às paredes. Em muitos escoamentos de interesse prático a movimentação preferencial pode-se dar em várias direções.

Recentemente Povitsky (2005), utilizando-se de um pacote de CFD comercial, estudou o escoamento em cavidades com movimentação diagonal e paralela da tampa. O autor conduziu um estudo comparativo para as duas configurações de movimentação da tampa em diferentes números de Reynolds. Abordando o problema de forma qualitativa e quantitativa, o autor conseguir evidenciar as diferenças no padrão do escoamento para as duas configurações de movimentação da tampa.

Tendo isto em vista, o presente trabalho trata do estudo do escoamento em cavidades com movimentação da tampa em diagonal, usando um código computacional tridimensional em coordenadas cartesianas, Padilla e Silveira-Neto (2005), para resolver as equações de Navier-Stokes.

2. Problema Físico

Trata-se de escoamentos no interior de cavidades cúbicas com tampa deslizante, de comprimento característico L, como mostrado na Fig. 1(a). A tampa se movimenta com velocidade U, considerando quatro configurações em função do ângulo α: movimentação paralela ao eixo x, $\alpha = 0°$; movimentação diagonal da tampa com $\alpha = 15°$; movimentação diagonal da tampa com $\alpha = 30°$; movimentação diagonal da tampa com $\alpha = 45°$. Para efeitos de análise, definem-se alguns planos (Fig. 1b): o plano $(y, \sqrt{x^2 + z^2})$ denominado plano A; o plano (x, y) em z/L =0,5, denominado plano B; plano (y, z) em y/L =0,5, denominado plano C.

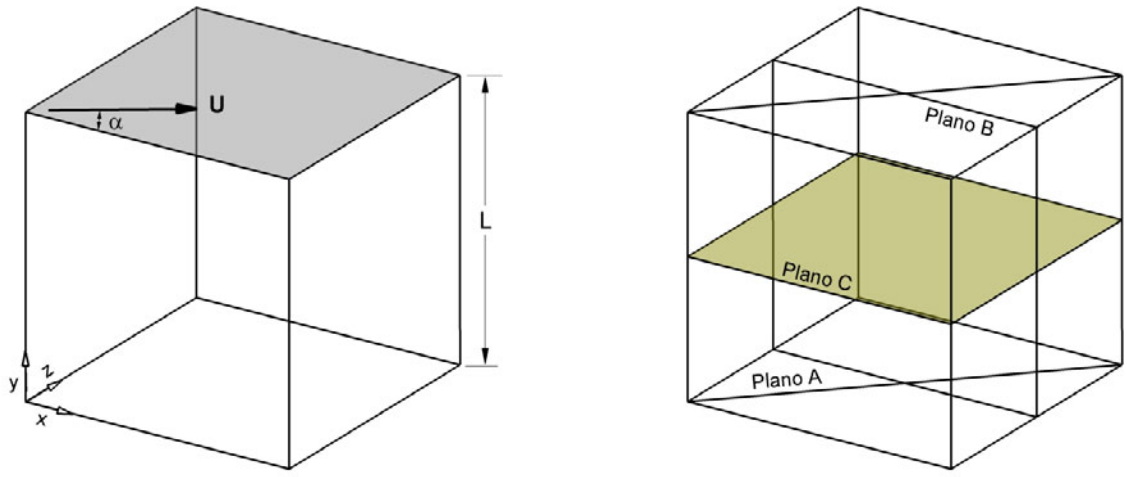

(a) (b)

Figura 1. Cavidade cúbica; (a) com movimentação diagonal da tampa, (b) com movimentação paralela.

3. Modelagem Matemática e Método Numérico

Considera-se um fluido newtoniano e incompressível com densidade ρ e viscosidade dinâmica μ. O escoamento do fluido no interior de cavidades é regido pelas equações de Navier-Stokes, expressas na sua forma conservativa e em coordenadas cartesianas na Eqs. (1-4),

$$\frac{\partial u}{\partial x} + \frac{\partial v}{\partial y} + \frac{\partial w}{\partial z} = 0\,, \tag{1}$$

$$\rho\left[\frac{\partial u}{\partial t} + \frac{\partial uu}{\partial x} + \frac{\partial vu}{\partial y} + \frac{\partial wu}{\partial z}\right] = -\frac{\partial p}{\partial x} + \frac{\partial \tau_{xx}}{\partial x} + \frac{\partial \tau_{yx}}{\partial y} + \frac{\partial \tau_{zx}}{\partial z}\,, \tag{2}$$

$$\rho\left[\frac{\partial v}{\partial t} + \frac{\partial uv}{\partial x} + \frac{\partial vv}{\partial y} + \frac{\partial wv}{\partial z}\right] = -\frac{\partial p}{\partial y} + \frac{\partial \tau_{xy}}{\partial x} + \frac{\partial \tau_{yy}}{\partial y} + \frac{\partial \tau_{zy}}{\partial z}\,, \tag{3}$$

$$\rho\left[\frac{\partial w}{\partial t} + \frac{\partial uw}{\partial x} + \frac{\partial vw}{\partial y} + \frac{\partial ww}{\partial z}\right] = -\frac{\partial p}{\partial z} + \frac{\partial \tau_{xz}}{\partial x} + \frac{\partial \tau_{yz}}{\partial y} + \frac{\partial \tau_{zz}}{\partial z}\,, \tag{4}$$

em que *u*, *v*, e *w* são as componentes da velocidade nas direções coordenadas *x*, *y*, *z*, respectivamente, *p* a pressão e τ_{ij} são as tensões viscosas. O parâmetro adimensional que governa este tipo de escoamentos é o Número de Reynolds baseado na velocidade de tampa e na altura da cavidade, definido como:

$$\mathrm{Re} = \frac{\rho U L}{\mu}, \tag{5}$$

A equações foram discretizadas pelo método dos volumes finitos, como proposto por Patankar (1980), os termos advectivo e difusivo foram aproximados por um esquema de diferenças centradas, Ferziger e Péric (1999). O acoplamento pressão-velocidade foi feito pelo Médodo dos Passos Fracionado, Kim e Moin (1985), e para a evolução temporal foi utilizado o esquema de Adams-Bashforth de segunda ordem. O sistema de equações para o campo de pressão é resolvido usando o método fortemente implícito (Stone, 1968), conhecido como método SIP.

4. Testes Preliminares

Diversos tamanhos de malhas não uniformes foram usadas para o escoamento a Re=400. Os resultados para a componente horizontal da velocidade u, ao longo da direção vertical y na posição $x/L = y/L = 0{,}5$, são mostrados na Fig. 2. Para cavidade com movimentação diagonal da tampa (Fig. 2a), os perfis de velocidade obtidos com malhas 30x30x30 e 40x40x40 são muito próximos e apresentam diferença com a solução para malha 20x20x20, principalmente no pico formado na parte inferior da cavidade. Para cavidade com movimentação paralela da tampa (Fig. 2b), a solução em função do tamanho da malha é similar ao caso apresentado, sendo que a solução com malha 50x50x50 se apresenta idêntica à solução com malha 40x40x40. Quando comparados com os resultados numéricos de Kato *et al.* (1990), Babu e Korpela (1994) e Sheu e Tsai (2002), observa-se boa concordância, no entanto, os resultados para as malhas mais densas mostram melhor aproximação com os dados de Sheu e Tsai (2002).

Considerando a análise dos resultados da Fig. 2, o número de Reynolds máximo a ser estudado e o custo computacional relacionado a cada tamanho de malha, a malha 40x40x40 foi escolhida para gerar os resultados do presente trabalho.

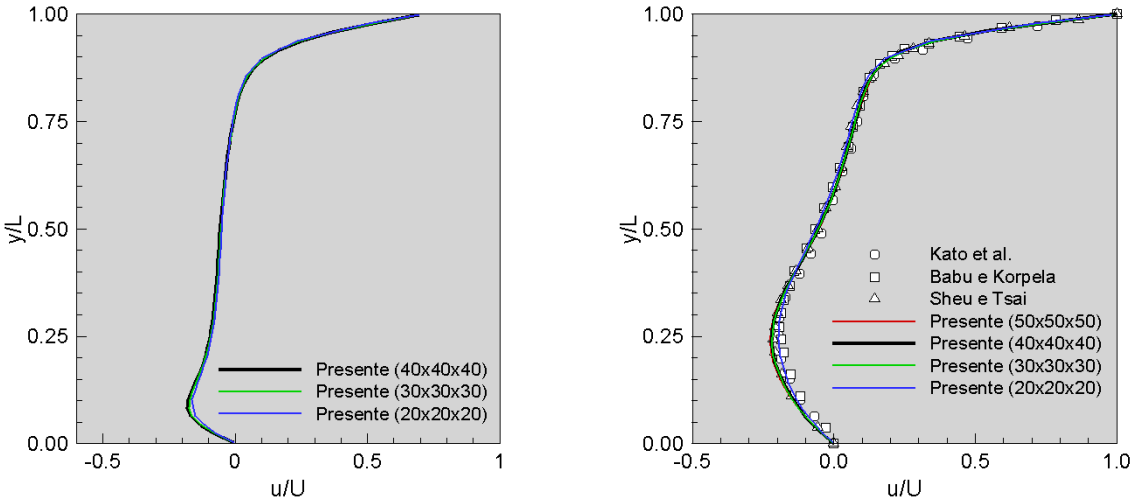

Figura 2. Distribuição da componente horizontal da velocidade, Re=400; (a) movimentação diagonal da tampa, (b) movimentação paralela da tampa.

5. Resultados e Discusão

As simulações de escoamentos no interior de cavidades com movimentação diagonal da tampa foram realizadas para diversos valores do número de Reynolds compreendidos na faixa $100 \le Re \le 2000$, usando malha não uniforme de 64000 volumes. Um computador Pentium IV de 2.8 GHz foi usado para executar os cálculos. O custo computacional aumenta em função do incremento do número de Re, como exemplo, pode-se mencionar que para o caso de $Re = 1000$ são necessários 13,94 e 12,17 minutos para simular um segundo físico do problema considerando as configurações de movimentação diagonal ($\alpha = 45^{o}$) e paralela da tampa, respectivamente. O tempo necessário para atingir regime permanente para o caso de cavidade com movimentação diagonal da tampa é de aproximadamente 70 s, maior que para o outro caso (em torno de 50 s).

5.1. Escoamento com $\alpha = 0^{o}$

Este tipo de configuração se caracteriza pela presença de um vórtice primário, um ou dois vórtices secundários e

vórtices de canto nas proximidades das paredes laterais ($z/L = 0$ e 1), assim como por serem simétricos respeito do plano B, fato que pode ser observado na Fig. 3, bem como em trabalhos como Babu e Korpela (1994), Sheu e Tsai (2002) e Padilla e Silveira Neto (2005). Os vórtices secundários estão localizados na região inferior da cavidade, entre as paredes inferior, anterior ($x/L = 1$) e posterior ($x/L = 0$). Um vórtice secundário aparece para os escoamentos com $500 \leq Re$, próximo das parede anterior e inferior; nos outros casos, dois vórtices secundários aparecem. Por outro lado, os vórtices de canto são visualizados para a maioria dos casos, exceto para os escoamentos com $400 < Re$. A projeção das linhas de corrente para $Re = 1200$ sobre o plano de simetria e sobre paredes laterais são mostradas na Fig. 3(a), e sobre o plano C e sobre os planos inferior e superior são mostrados na Fig. 3(b). O plano de simetria permite observar a dimensão dos vórtices primário e secundário, sendo que o vórtice secundário próximo da parede anterior é maior que o outro. Os planos C e os correspondentes ás paredes laterais permitem visualizar as características dos vórtices de canto, quais ficam mais confinados em relação às paredes inferior e posterior à medida que o Re é incrementado. A topologia apresentada pelos diversos casos é muito similar à apresentada nos trabalhos citados anteriormente.

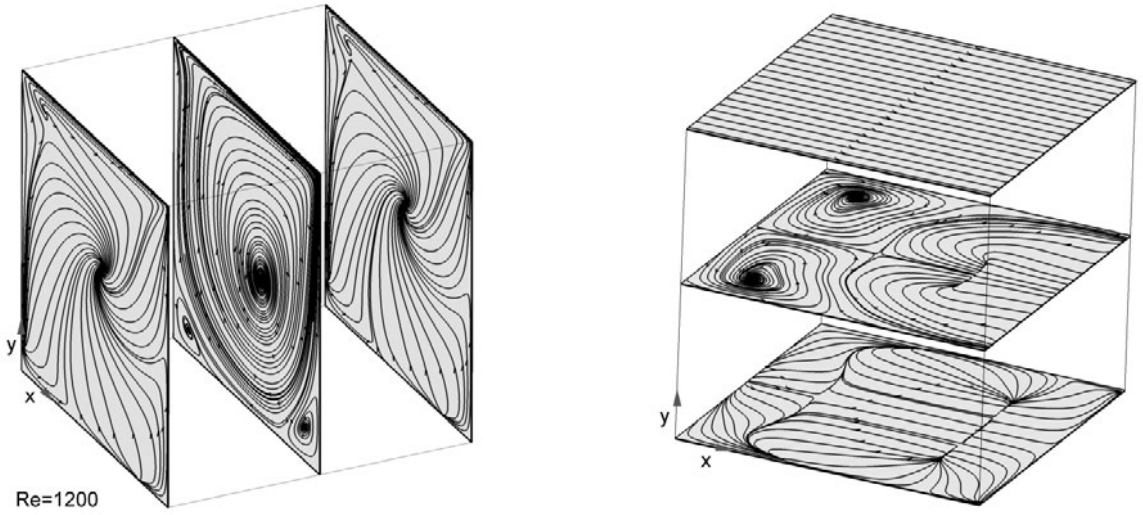

(a) (b)

Figura 3. Projeção das linhas de corrente, $Re = 1200$ e $\alpha = 0^o$; (a) sobre as paredes laterais e o plano B , (b) sobre o plano inferior, o plano C e a tampa.

Sendo que o vórtice primário é a estrutura principal do escoamento, é importante reportar as mudanças desta estrutura em função do número de Reynolds através da posição da linha do centro do vórtice. A Tab. 1 mostra a posição do centro do vórtice primário no plano de simetria, de todos os casos considerados. O centro do vórtice primário se desloca desde $x/L = 0{,}6767$ e $y/L = 0{,}7559$, correspondente a $Re = 100$, até a posição localizada em $x/L = 0{,}6169$ e $y/L = 0{,}463$, correspondente a $Re = 2000$. Quando comparado o escoamento para $Re = 400$, com os resultados numéricos de Sheu e Tsai (2002), encontra-se uma diferença de 1,4 e 3,5 % nas direções coordenadas x e y, respectivamente.

Tabela 1. Posição do centro do vórtice principal no plano de simetria para configuração de cavidade com movimentação paralela da tampa.

Re	100	400	500	600	700	750
x/L	0,6767	0,6248	0,6152	0,6083	0,6036	0,6017
y/L	0,7559	0,5794	0,5415	0,5143	0,4960	0,4886
Re	800	850	1000	1200	1500	2000
x/L	0,6002	0,5989	0,5967	0,5968	0,6016	0,6169
y/L	0,4823	0,4777	0,4686	0,4628	0,4607	0,4630

5.2. Escoamento com $\alpha = 15^o$

Os escoamentos para a configuração de cavidade com movimentação diagonal da tampa, com ângulo $\alpha = 15^o$, apresentam as mesmas estruturas da configuração da cavidade com tampa deslizante paralela à direção coordenada x, porém distorcidas devido à assimetria característica desta configuração, como visualizado claramente nas Figs. 4 e 5.

Estas figuras mostram as projeções das linhas de corrente, sobre os mesmos planos da figura anterior, para $Re = 700$ e $Re = 1500$. O plano correspondente a parede lateral em $z/L = 0$ e o plano B mostram a presença dos vórtices primário, secundários e de canto, onde aparentemente só um vórtice de canto é formado, a projeção sobre o plano C não permite mais confirmar a presença deste tipo de vórtices. As linhas de corrente sobre a tampa da cavidade permitem ver o grau de inclinação com que esta se movimenta. O número de vórtices no plano C aumenta quando o Re passa de 700 a 1500. A linha que descreve o centro do vórtice principal apresenta notória inclinação respeito dos planos anterior e inferior; na região próxima da parede lateral $z/L = 0$ localiza-se abaixo da linha horizontal média, já na região próxima da parede lateral $z/L = 1$ localiza-se na parte superior direita.

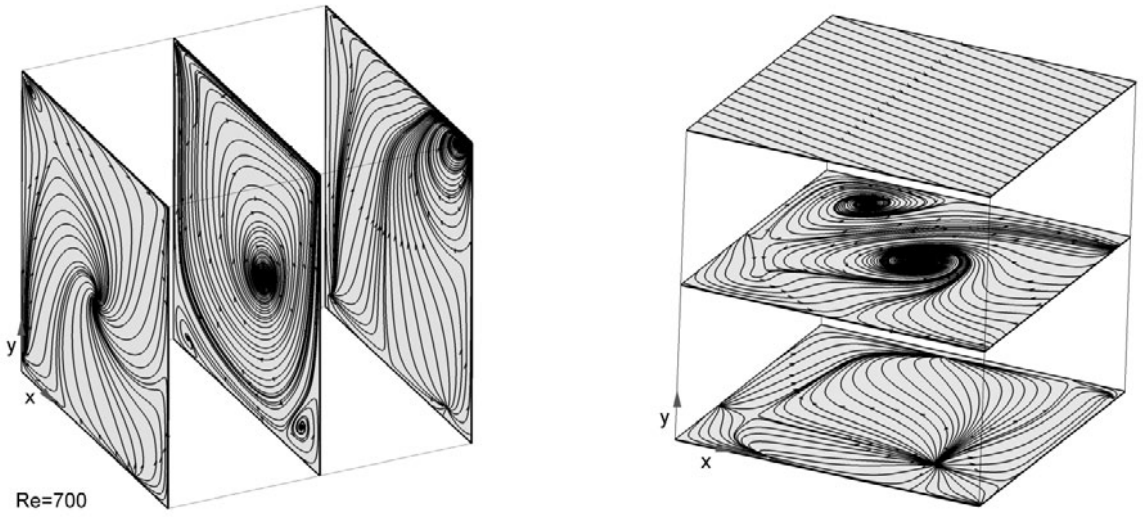

(a) (b)

Figura 4. Projeção das linhas de corrente, $Re = 700$ e $\alpha = 15^{o}$; (a) sobre as paredes laterais e o plano B , (b) sobre o plano inferior, o plano C e a tampa.

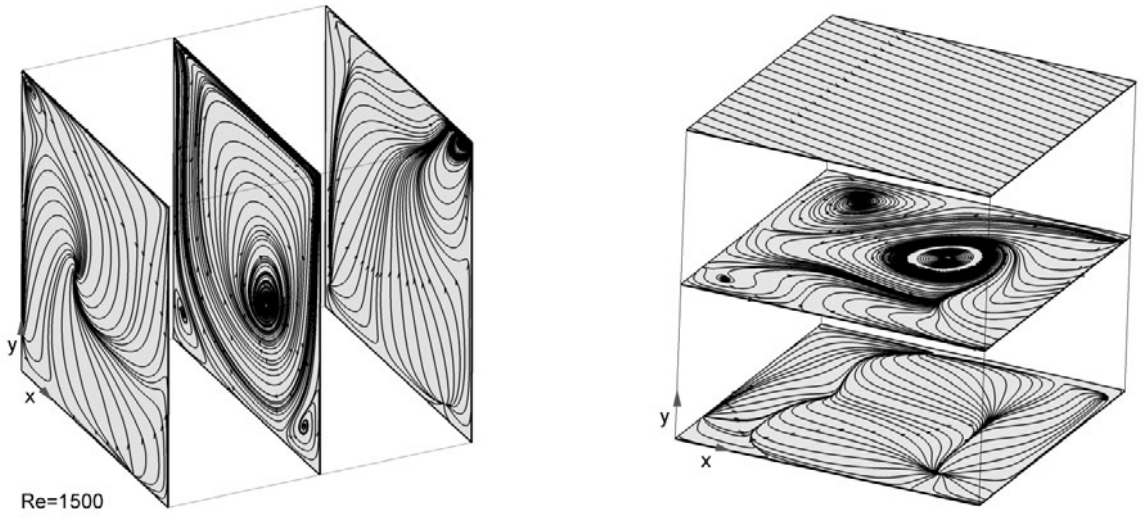

(a) (b)

Figura 5. Projeção das linhas de corrente, $Re = 1500$ e $\alpha = 15^{o}$; (a) sobre as paredes laterais e o plano B , (b) sobre o plano inferior, o plano C e a tampa.

5.3. Escoamento com $\alpha = 30^{o}$

Nesta configuração, em que o ângulo de movimentação diagonal da tampa se incrementa a 30°, observam-se mudanças mais acentuadas, se a análise continua através da projeção das linhas de corrente nos planos eqüidistantes e paralelos nas direções coordenadas y e z. Por exemplo: o centro do vórtice principal para $Re = 700$ (Fig. 6a, plano B) se localiza aproximadamente na parte central, enquanto que para $Re = 1500$ (Fig. 7a) deslocou-se para a parte inferior esquerda; o número de vórtices que aparecem no plano C (Figs. 6b e 7b) aumentam consideravelmente, passando de

dois ($Re = 700$) para cinco ($Re = 1500$). Evidentemente, há a necessidade de uma análise mais cuidadosa que permita identificar claramente as características dos vórtices presentes, principalmente dos novos vórtices secundários que aparecem, pois a análise através das projeções das linhas de corrente resulta insuficiente. Critérios como o Q (Jeong e Hussain, 1995) e o H (Hussain, 1993) são parâmetros a ser considerados para posterior análise.

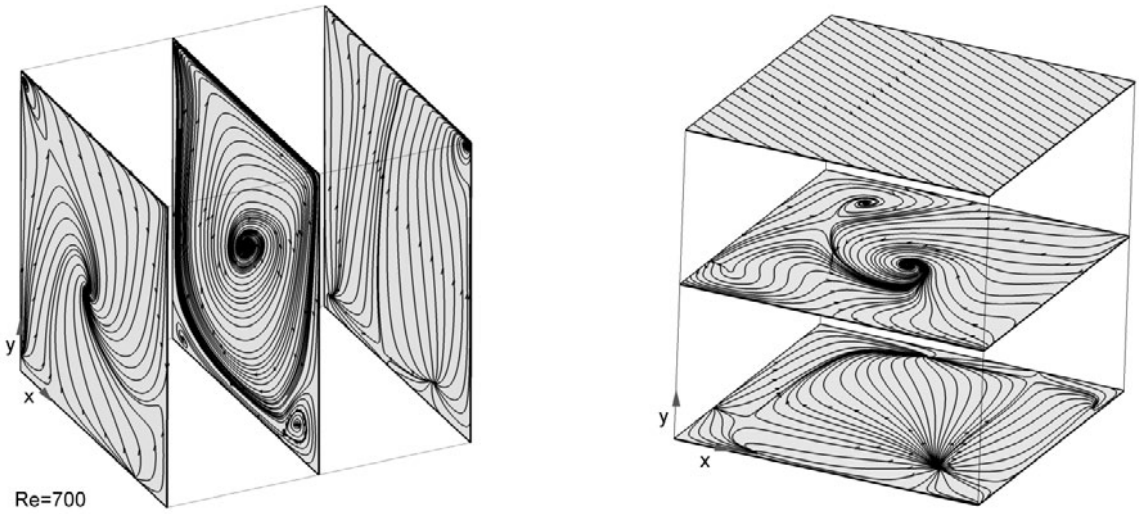

(a) (b)

Figura 6. Projeção das linhas de corrente, $Re = 700$ e $\alpha = 30º$; (a) sobre as paredes laterais e o plano B , (b) sobre o plano inferior, o plano C e a tampa.

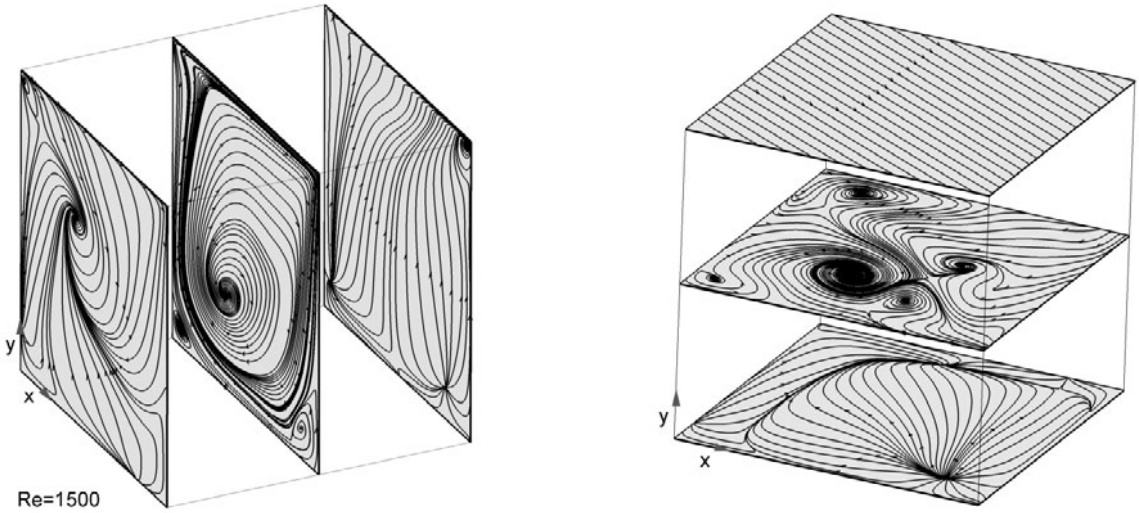

(a) (b)

Figura 7. Projeção das linhas de corrente, $Re = 1500$ e $\alpha = 30º$; (a) sobre as paredes laterais e o plano B , (b) sobre o plano inferior, o plano C e a tampa.

5.4. Escoamento com $\alpha = 45º$

As características do padrão do escoamento no interior de cavidades com movimentação diagonal da tampa, configuração com $\alpha = 45º$, são apresentadas nas Figs. 8-10. Devido à existência de simetria dos escoamentos respeito ao plano A, os resultados são apresentados com projeções das linhas de corrente sobre os planos A, transversal ao plano A e C.

Na Fig. 3 mostra-se a topografia do escoamento no plano A, observando-se um vórtice primário, que passa por grandes mudanças à medida que o Re aumenta, e dois vórtices secundários nos extremos inferiores do plano. Para os menores Re (100), o padrão do escoamento é similar ao padrão do escoamento bidimensional (Padilla *et al.* 2005, Ghia *et al.* 1982) com centro do vórtice primário localizado em x/L =0,5716, y/L = 0,7663 e z/L =0,5716. À medida que

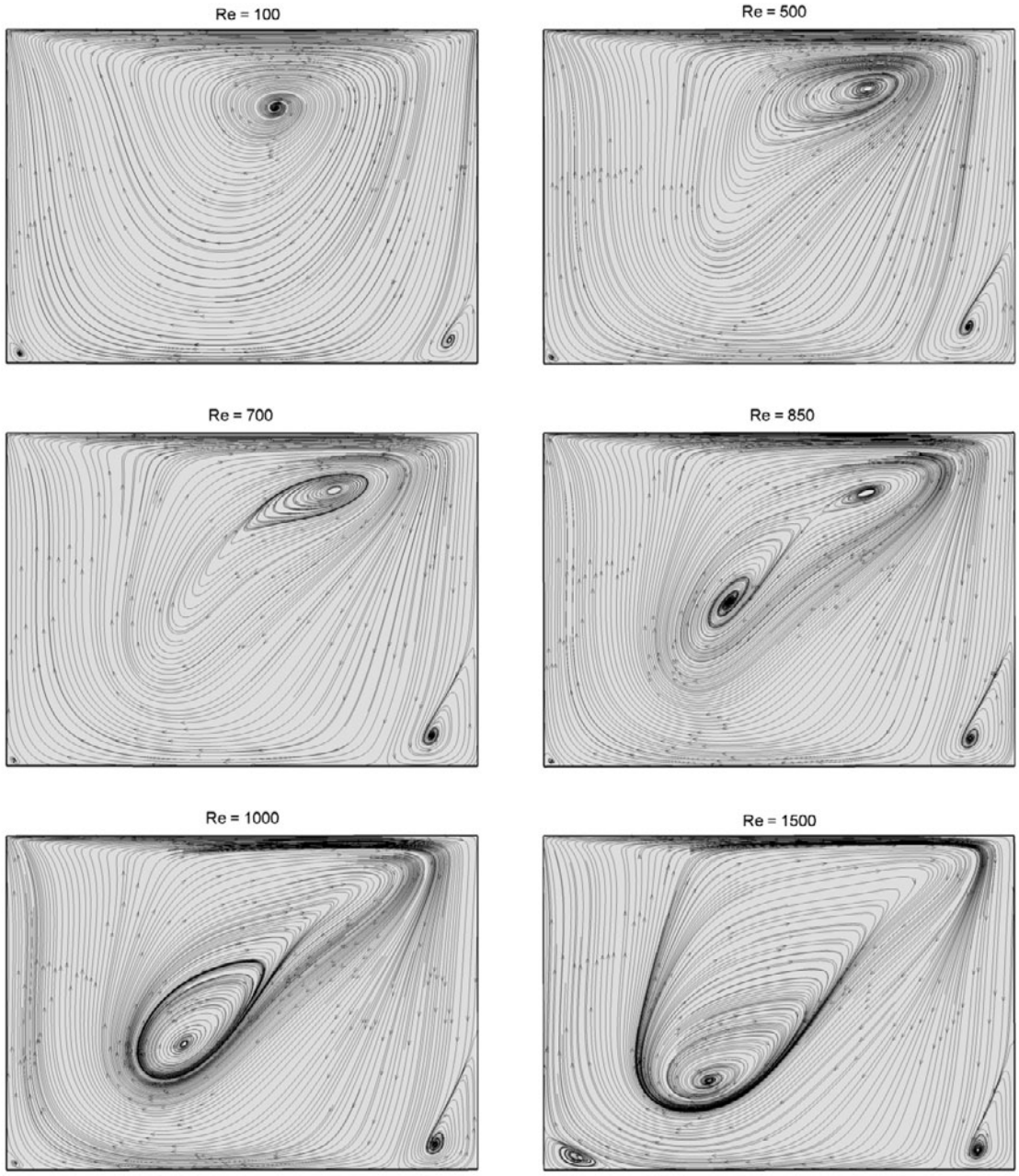

Figura 8. Projeção das linhas de corrente no plano A.

Tabela 1. Posição do centro do vórtice principal para no plano de simetria para configuração de cavidade com movimentação diagonal da tampa, $\alpha = 45^{o}$.

Re	100	400	500	600	700	750
x/L	0,5716	0,6743	0,6900	0,6949	0,6959	0,6944
y/L	0,7663	0,8128	0,8233	0,8278	0,8285	0,8260
z/L	0,5716	0,6743	0,6900	0,6949	0,6959	0,6944
Re	800	850	1000	1200	1500	2000
x/L	0,6914	0,3937	0,3766	0,3673	0,3515	0,3202
y/L	0,8214	0,4935	0,3759	0,3187	0,2674	0,2206
y/L	0,6914	0,3937	0,3766	0,3673	0,3515	0,3202

Re é incrementado, o centro do vórtice primário se desloca para a direita ($Re = 700$) e logo passa para a parte inferior da cavidade ($Re = 1000$). A posição exata do centro do vórtice principal, para os diversos *Re* considerados, são

apresentados na Tab. 2. Um fenômeno interessante é evidenciado para $750 \leq Re \leq 850$, trata-se do surgimento e coexistência de dois vórtices secundários no interior do vórtice primário. Inicialmente, o vórtice secundário formado próximo da região central é menor ($Re = 750$), mais logo passa a ser dominante ($Re = 850$), até anular o outro e se posicionar como centro do vórtice principal.

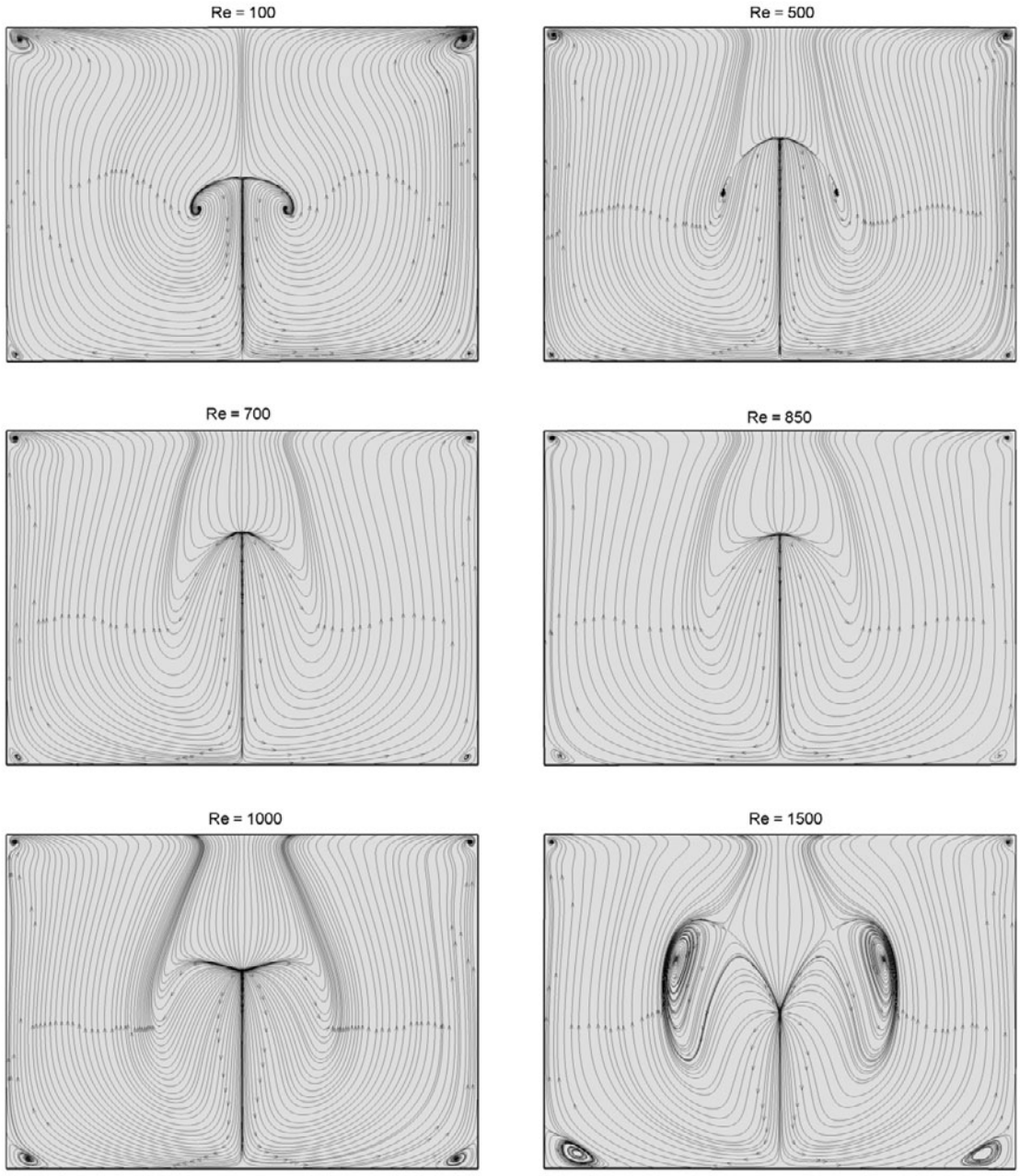

Figura 9. Projeção das linhas de corrente no plano transversal ao plano A.

As características dos escoamentos no plano transversal ao plano A são mostrado na Fig. 9. Observam-se quatro vórtices pequenos dispostos nos extremos do plano, para todos os casos. Por outro lado, na parte central as mudanças são notórias. Para $100 \leq Re \leq 500$, um par de vórtices estão presentes nos extremos da linha de recolamento (Sheu e Tsai, 2002). Para $600 \leq Re \leq 1000$, os vórtices não estão mais presente, observando-se um ponto de repulsão (ponto de onde emergem linhas de corrente); este ponto é chamado por Povitsky (2005) de ponto de estagnação (visualizado através do campo de vetores). A partir de $Re = 1200$, o ponto de repulsão coexiste com o par de vórtices, os quais surgem novamente, porém diferentes em forma e tamanho e dispostos com centro acima da metade superior do plano, como visualizado para $Re = 1500$. As linhas de corrente no plano C são mostradas na Fig. 10. Para $Re > 400$ aparecem pares de vórtices dispostos simetricamente, até três pares para $Re = 2000$. A partir de $Re > 400$ observam-se também linhas de separação (Sheu e Tsai, 2002) e pontos de repulsão e atração.

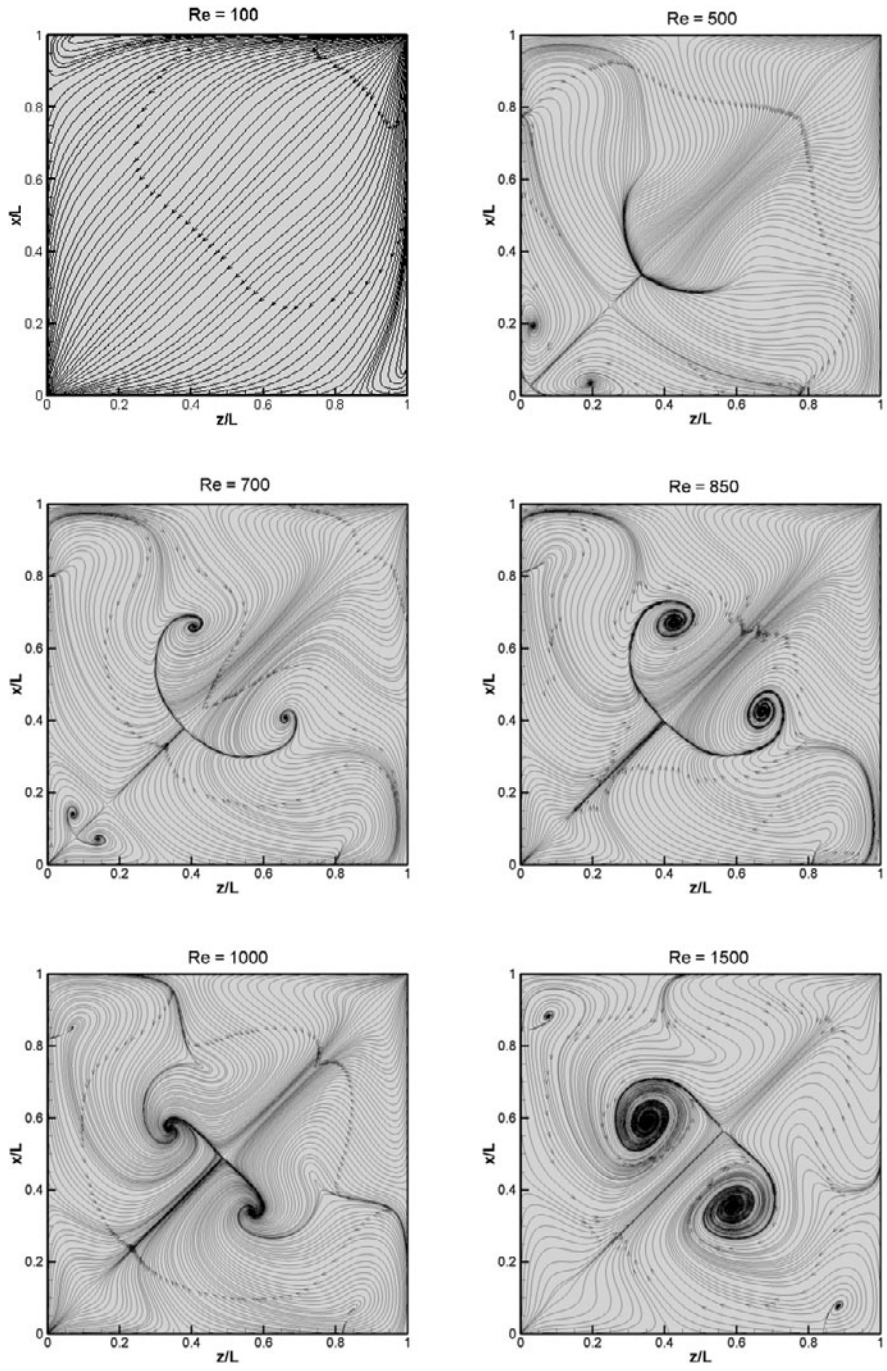

Figura 10. Projeção das linhas de corrente no plano C.

5.5. Comparação

Para comparar quantitativamente as duas configurações de escoamentos em cavidades, foi calculada a transferência de quantidade de movimento volumétrico. Segundo Povitsky (2005), define-se a quantidade de movimento por unidade de massa na direção paralela à movimentação da tampa como $M_p = u\ \cos\alpha + w\ sen\alpha$ e a quantidade de movimento na direção transversal à movimentação da tampa como $M_t = w\ \cos\alpha - u\ sen\alpha$. Assim, a integral de volume é calculada da seguinte forma:

$$L_p = \frac{1}{V}\int_V M_p\ , \tag{5}$$

$$L_t = \frac{1}{V}\int_V M_t \, . \tag{6}$$

Na Fig. 8 tem-se a quantidade de movimento volumétrico paralelo e transversal como função do número de Reynolds. A quantidade de movimento paralela (Fig. 11a) decresce à medida que Re se incrementa, sendo que a magnitude para a configuração de cavidade com movimentação paralela da tampa é maior que a magnitude que para a configuração de cavidade com movimentação diagonal da tampa, por tanto a magnitude de L_p cresce à medida que o ângulo da tampa decresce. Em relação à quantidade de movimento volumétrico transversal (Fig. 11b), a distribuição se apresenta crescente ate aproximadamente $Re = 800$ e 500 para as configurações com ângulo $\alpha = 45º$ e 0°, respectivamente, para logo decrescer suavemente até os maiores valores de Re. L_t cresce em função do incremento do ângulo α. Os parâmetros L_p e L_t transportam a informação de quão tridimensional é o escoamento com incremento no número de Reynolds.

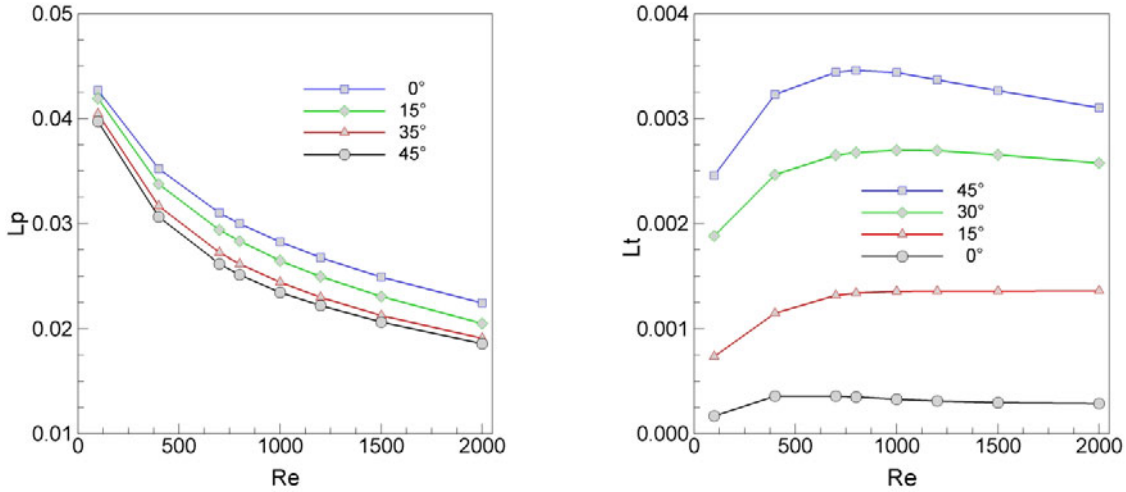

(a) (b)

Figura 11. Integral de quantidade de movimento volumétrico; (a) paralela, (b) transversal.

6. Conclusões

Uma grande quantidade de simulações tridimensionais de escoamentos estáveis no interior de cavidades com tampa deslizante foram realizadas para caracterizar o padrão do escoamento para quatro configurações, dependentes do ângulo de movimentação da tampa (movimento diagonal). Os resultados mostram que tratam-se de escoamentos muito diferentes, sendo que a complexidade aumenta para as configurações que não apresentam simetria, como são as configurações com $\alpha = 15º$ e 30º. Estruturas como os vórtices primário, secundários (localizados na parte inferior da cavidade) e de canto são comuns a todas as configurações, porém com deformações originadas pelo ângulo de incidência do escoamento mais acelerado (próximo da tampa). Quando o ângulo α é diferente de 0, outros vórtices secundários aparecem e geralmente aumentam em número com o incremento do número de Reynolds. A quantidade de movimento na direção paralela à tampa aumenta à medida que o ângulo α decresce e a quantidade de movimento na direção transversal da tampa aumenta à medida que ângulo α cresce. A diferença em magnitude da quantidade de movimento na direção paralela e transversal da tampa é de uma ordem de grandeza. Como comentado, existe a necessidade do uso de novos procedimentos de análise que permitam entender melhor a natureza das estruturas.

7. Agradecimentos

Os autores agradecem à FAPEMIG, CNPq e ao CENPES-PETROBRAS pelo apoio financeiro.

8. Referências

Aidum, C. K., Triantafillopoulos, N. G. and Benson, J. D. 1991, Global Stability of a Lid-Driven Cavity with Through Flow: Flow Visualization Studies", Phys. Fluids A 3, pp. 2081-2091.

Babu, V. and Korpela, S. A., 1994, Numerical Solution of the Incompressible Three-Dimensional Navier-Stokes Equations, Computers Fluids 23(5). Pp. 675-691.

Benjamin, A. S. and Denny V. E., 1979, On the Convergence of Numerical Solutions for 2D Flows in a Cavity Large Re, J. Comput. Phys., 33, pp. 340-358.

Botella, O., and Peyret, R., 1998, "Benchmark Spectral Results on the Lid-Driven", Comput Fluids, vol 27(4), pp. 421-433.

Deshpande, M. D. and Milton, S. G., 1998, Kolmogorov Scales in a Driven Cavity Flow, Fluid Dyn. R*es.*, 22, pp. 359-381.

Ferziger, J. H., Peric, M. 1999, Computational methods for fluid dynamics, 2nd Ed., Springer.

Ghia, U., Ghia, K. N. and Shin, C. T., 1982, High-Re Solutions for Incompressible Flow Using the Navier-Stokes Equations and a Multigrid Method, J. Comput. Phys., 48, pp. 387-411.

Iwatsu, R. Ishi, K., Kawamura, T., Kawahara, K. and Hyun, J. M., 1989, Simulation of Transition to Turbulence in a Cubic Cavity, AIAA Pap. No 98-0040.

Jeong, J. e Hussain, F., 1995, "On the Identification of a Vortex", Journal of Fluid Mechanics 285, 69-94

Koseff, J. R. and Street R. L., 1984, Visualization of a Shear Driven Three-Dimensional Recirculation Flow, J. Fluids Eng., 106, pp. 21-29.

Ku, H. C., Hirsh, R. S. and Taylor, T. D., 1987, A Pseudospectral Method for Solutions of the Three-dimensional Incompressible Navier-Stokes Equations, J. Comput. Phys., 70, pp. 439-462.

Moin, P., Kim, P., 1982, Numerical Investigation of Turbulent Channel Flow, Journal of Fluid Mechanics, vol. 118, pp. 341-377.

Padilla, E. L. M. e Silveira Neto, A., 2005, Desenvolvimento de um Código Computacional Tridimensional para Solução de Escoamentos em Transição e Turbulência, XXVI Iberian Latin-American Congress on Computational Methods in Engineering, Guarapari - ES. Procceding of the CILAMCE 2005, v. 1, p. 1-12.

Padilla, E. L. M., Martins, A. L. E Silveira Neto, A., 2005, Large-Eddy Simulation of the Three-Dimensional Unstable Flow in a Lid-Driven Cavity. In: 18TH International Congress of Mechanical Engineering, Ouro Preto, Proceedings of COBEM 2005, v. 1, p. 1-8.

Padilla, E. L. M., 2004, Simulação de Grandes Escalas da Transição à Turbulência em Sistemas Rotativos com Transferência de Calor, Tese de Doutorado, Universidade Federal de Uberlândia, Uberlândia.

Patankar, S. V., 1980, Numerical heat transfer and fluid flow, Hemisphere.

Povitsky, A., 2005, Three-dimensional flow in cavity at yaw, Nonlinear Analysis 63. Pp. E1573-e1584.

Sheu, T. W. H. and Tsai, S. F., 2002, Flow Topology in a Steady Three-Dimensional Lid-Driven Cavity, Comput. Fluids, 31, pp. 911-934.

Stone, H. L., 1968, Iterative Solutions of Implicit Approximations of Multidimensional Partial Differential Equations, SIAMJ Num. Anal., vol. 5, pp 530-558.

CHARACTERIZATION OF FLOWS INSIDE DIAGONAL LID-DRIVEN CAVITIES

Elie Luis M. Padilla
epadilla@mecanica.ufu.br

Tiago de Assis Silva
tasilva@meanica.ufu.br

Aristeu da Silveira Neto
Federal University of Uberlândia
School of Mechanical Engineering
aristeus@mecanica.ufu.br

Abstract – Lid-driven cavity flows are three-dimensional with many characteristics structures that are function of Reynolds number and aspect ratio of the cavity. In present time, in view of many engineering applications and physical problem understanding, there are many researches about this kind of flow. At the classical benchmark case the lid moves in the direction parallel to the cavity side wall. New studies have been done by considering the lid of cavity moving along the lid diagonal with arbitrary angle. The 3-D lid-driven cavity flow is studied by numerical solution of the 3-D Navier-Stokes equations using a computational code developed in house. Computational results for lid moving with angles 15^o, 30^o e 45^o are compared to the case when the lid moves in the direction parallel to the cavity side walls. A flow is investigated numerically for the range of Reynolds numbers corresponding to existence of a laminar solution (100 – 2000). The volume integrals of momentum in the direction of lid motion and perpendicular to it an introduced to compare cases in a quantitative way. The Navier-Stokes equations were discretized with finite volume method in a staggered grid with second-order time advance schemes and second-order spatial schemes. The fractional step method was used to resolve velocity and pressure coupling.

Keywords: stable flow, cavity, three-dimensional simulation.

Proceedings of the 11th Brazilian Congress of Thermal Sciences and Engineering -- ENCIT 2006
Braz. Soc. of Mechanical Sciences and Engineering -- ABCM, Curitiba, Brazil,- Dec. 5-8, 2006

Paper CIT06-0371

A CBS-FINITE ELEMENT METHOD FOR COMPLEX FLOWS OVER FORESTED RELIEFS

Antonio C. P. Brasil Junior and Rafael Pereira de Melo
Laboratory of Energy and Environment (LEA). Department of Mechanical Engineering.
Universidade de Brasília. 70910-900. Brasília. Brazil; brasiljr@unb.br

Maria Laura Martins-Costa and Alcindo de A. Maranhão Neto
Laboratory of Theoretical and Applied Mechanics (LMTA), Mechanical Engineering Department (TEM-PGMEC)
Universidade Federal Fluminense, Rua Passo da Pátria, 156, 24210-240 Niterói/RJ, Brazil; laura@gar.uff.br

Abstract. *In this work a numerical methodology combining a finite element approach and CBS (Characteristic Based Splitting) method is used to simulate canopy flows non-homogeneous forests. The particular interest is to simulate the atmospheric fluid flow over complex relieves, or in a proximity of discontinuity of vegetative layer distribution (clearings or rivers). A turbulence model is used to describe the flow within the forest canopy. This model uses a first order closure approach, with a computation of the eddy viscosity by an algebraic model. The vegetative drag force effects are taken into account by means of a quadratic term. The computation of velocity statistics is performed using anisotropy estimative of the distribution of kinetic energy of turbulence. The implementation of the CBS algorithm for the turbulence model was performed in a 2D code that use triangular elements with an equal order of velocity and pressure interpolation. Results for homogeneous forest, forest edges and clearings are presented and compared in situ measurements.*

Keywords *canopy flows, CBS finite element, turbulent boundary layer.*

1. Introduction

The description of the atmospheric turbulent air flow within and above vegetative canopies has become an important research interest, which has been associated to comprehension and quantification of physicochemical and ecological processes in forests and plantations. The modeling of this kind of turbulent flow is inserted in a perspective of the advanced closuring of statistical turbulent moments in averaged fluid mechanics governing equations, and the use of the this models to simulate real and complex situation have to be associated to the properly numerical implementations.

On the last decade a great interest for the numerical solutions of inhomogeneous canopy flow problems has arisen (Lee, 2000), involving, for instance, situations like flows through forest cut blocks (Wilson and Flesh, 1999) or over complex forested relieves (*e. g* Kobayashi et al., 1994, Ross et al., 2004 or Ross and Vosper, 2004). For this kind of problem, advanced turbulence models considering the vegetative canopy layers have been proposed, and its numerical implementation, using algorithms that can treat complex geometries, have to be employed. A real complex flow through and over forested relieves occurs in a domain with a bottom surface issued from the topography of geographic regional terrain database. Sometimes, great gradients of elevation are encountered, and over this relief the vegetation is often distributed non-uniformly, due to different structures of the vegetative layer and to the existence of clearings.

The use of a detailed description of vegetative elements individually is impossible to be considered in this scale of analysis, and the modeling of the vegetative layer has to be represented in a sense of a local spatial averaging procedure. The actual approach for simulating canopy flows considers the averaging the flow variables within the forest layer, using a physical control volume of an order of some meters in the vertical direction and hundred of meters in the horizontal direction. On this scale, one can evaluate some features of the flow related to the local variations. It can allow the comprehension and quantification of heat and mass exchanges between the vegetation and the atmosphere.

The turbulence models issued from this averaging approach have some distinct characteristics from the conventional models for free-flows, and the numerical methodologies have to be adapted to this new condition. Considering this averaging process for the fluid flow modeling, the closuring of the governing equations can either use second or first-order models.

The present paper proposes a simple modeling approach based on first-order with algebraic eddy viscosity. An alternative approach to compute the length scale non-homogeneous canopy situations is explored.

In a context of first-order turbulence closuring models (K-l or K-ε), it has already been shown that these simple models can accurately describe both the mean velocity and the kinetic energy profiles in homogeneous forest boundary layers (Katul et al., 2004; Pinnard and Wilson, 2001).

In some non-homogeneous vegetation distribution, like in forest cutblocks for instance (Wilson and Flesh, 1999}, the numerical results show good agreement with the field data, taken into account some corrections of the internal parameters of the model. The low computational cost of the first-order models, in particular for 2D or 3D problems, is the great motivation of the development of this class of models.

The aim of the present paper is to present an alternative zero-equation model for canopy flows. A canopy flow model was implemented in a finite element code using the *Characteristic-Based Splitting* approach, with P1-P1 triangular elements. The present finite element model also uses the same order of interpolation for the pressure and velocity fields, considering the self-stabilization behavior of the CBS algorithm by means of the time step control.

This paper is organized as follows: In the section 2 the modeling approach is described and the specifically closuring assumptions are discussed. In the section 3 the numerical implementation of the turbulence model is presented and the stability consideration is explored. At a last part, some illustrative results are presented concerning the flow over different forest configurations, where experimental data is compared to the present numerical results.

2. Turbulence modeling

2.1 Basic Equations

Let us consider a multidimensional air flow within and above vegetative canopies, defined for generality in a 3D domain. The modeling of canopy turbulent flows considers a *rationale* based in a double averaging process: In a first step all flow quantities are averaged on time using a characteristic time interval, like for free turbulent flows (this averaging operator being denoted by a over line bar symbol $\overline{(.)}$). In the second step a spatial averaging is performed within a reference volume (this operator being denoted by a bracket symbol $\langle(.)\rangle$). Discussions of the use and necessity of this formalism are developed in Raupach and Shaw (1982) or Finningan (2000), for instance.

Applying this double averaging approach to the instantaneous mass and momentum conservation equations for the air flow, the set of governing equations can be obtained. The assumptions of incompressibility of the air flow under neutral buoyancy conditions and no-waving behavior of canopy elements were considered. The continuity and the Navier-Stokes equations for the canopy flows are thus given by:

$$\nabla.\langle\overline{\boldsymbol{u}}\rangle = 0 \tag{1}$$

$$\frac{\partial\langle\overline{\boldsymbol{u}}\rangle}{\partial t} + \left(\nabla\langle\overline{\boldsymbol{u}}\rangle\right)\langle\overline{\boldsymbol{u}}\rangle = -\frac{1}{\rho}\nabla\langle\overline{p}\rangle + \nabla.\left(2\nu\boldsymbol{S}(\langle\overline{\boldsymbol{u}}\rangle) - \langle\overline{\boldsymbol{u}'\otimes\boldsymbol{u}'}\rangle - \langle\boldsymbol{u}''\otimes\boldsymbol{u}''\rangle\right) + \boldsymbol{f} \tag{2}$$

In these equations $\langle\overline{\boldsymbol{u}}\rangle$ and $\langle\overline{p}\rangle$ are the averaged velocity and pressure fields, ρ and ν denote the density and kinematical viscosity of the air and $\boldsymbol{S}(\langle\overline{\boldsymbol{u}}\rangle)$ is the mean rate of strain tensor given by:

$$\boldsymbol{S}(\langle\overline{\boldsymbol{u}}\rangle) = \frac{1}{2}\left(\nabla\langle\overline{\boldsymbol{u}}\rangle + \nabla^T\langle\overline{\boldsymbol{u}}\rangle\right) \tag{3}$$

The extra terms of Eq. (2), present due to the use of double averaging operations on the momentum conservation equation, are the volume averaged Reynolds stress $\langle\overline{\boldsymbol{u}'\otimes\boldsymbol{u}'}\rangle$ and the dispersive flux $\langle\boldsymbol{u}''\otimes\boldsymbol{u}''\rangle$. These terms denote the statistical correlation of fluctuating velocity parts associated to the time average, $\boldsymbol{u}'$ and to the space, $\overline{\boldsymbol{u}}''$, respectively. In the present work the tensor term related to the dispersive flux is neglected, considering the density of the canopy elements for some kinds of forest structures it can be taken into account.

The last term in the Eq. (2), $\boldsymbol{f}$, accounts for the mechanical interaction between the air flow and the vegetation elements by viscous and form drag forces. It can be modeled by:

$$\boldsymbol{f} = -C_D A(x_3)\left|\langle\overline{\boldsymbol{u}}\rangle\right|\langle\overline{\boldsymbol{u}}\rangle \tag{4}$$

Where C_D and $A(x_3)$ denote respectively the drag coefficient and plant area density, with x_3 coordinated aligned to the vertical direction.

2.2. Closuring parameterization

In the framework of first-order turbulence closuring, the Reynolds stress tensor is often modeled by the Boussinesq eddy-viscosity assumption, namely

$$\langle\overline{\boldsymbol{u}'\otimes\boldsymbol{u}'}\rangle = \frac{2}{3}K\boldsymbol{I} - 2\nu_T\boldsymbol{S}(\langle\overline{\boldsymbol{u}}\rangle) \tag{5}$$

where *K* represents the kinetic energy of turbulence (which will be combined to compose the apparent pressure) and ν_T is the eddy viscosity. In the present paper a zero-equation model is employed as:

$$\nu_T = \ell_m^2 \left[\boldsymbol{S}(\langle \overline{\boldsymbol{u}} \rangle) : \boldsymbol{S}(\langle \overline{\boldsymbol{u}} \rangle) \right]^{1/2} \tag{6}$$

in which ℓ_m represents the mixing length of the turbulent process. For homogeneous forest it can modeled simply as:

$$\ell_m = \begin{cases} \ell_h \text{ ; if } z \le h^* \\ \kappa(z - h^*) \text{ , if } z > \mathrm{h}^* \end{cases} \tag{7}$$

In the above equation h^* is the vertical position where the leaf area density is maximum (A_{max}) and z is the vertical distanced of the closest ground surface. The length scale for the canopy region ℓ_h, is given as

$$\ell_h = \frac{\kappa h^*}{1.5 - 2.5 A_{\max}} \tag{8}$$

where $\kappa = 0.44$ represents the Karmann constant.

2.3 Boundary conditions

Four types of boundary condition are considered for the atmospheric boundary layer flow simulations. On the ground non-slip boundary conditions is imposed for the velocity flow. On the free flow surface, located three times the forest height, the free velocity is imposed. For the problems related to a 2D evolution of the boundary layer (forest edge, for instance) the inflow condition is composed by a vertical profile of the velocity field, based in a power-law atmospheric boundary variation. For the outflow boundary condition homogeneous Neumann conditions for the velocity field and a reference value for the pressure are imposed.

3. Numerical methodology

The governing equations presented on the last section are solved by employing a finite element method with an equal order interpolation for pressure and velocity fields (linear triangle elements have been selected). A CBS algorithm is implemented taking into account the regions with and without forest canopies, always for 2D domains. In this methodology the continuity and momentum equations are solved using a splitting strategy, considering an incremental time integration algorithm with multiple steps. This approach can assure the stability for pressure and velocity, as well as for high local Reynolds number, only by controlling the size of the time step.

The aim of the CBS algorithm involves two major ideas (e.g. Zienkiewicz and Taylor, 2000, Codina et al., 1998): First the momentum equation is re-written along a characteristic path, in order to reduce the spurious effects due to Galerkin discretization for high Reynolds number. This gives rise to an additional stabilized term in the formulation on streamline direction, equivalent to the streamline-diffusion term. The second feature of this algorithm is to decouple the pressure and velocity fields by means of a fractional step algorithm, like in classical splitting-projection schemes (Chorin, 1968 and Temann, 1969). It is shown that this last approach allows a stabilization term for the pressure and velocity discretization spaces (Codina, 2001). Those two ingredients of the method permit a stable scheme for convective-advection treatment and for pressure-velocity discretization. The stabilization parameter now is the time step. It can be shown that this scheme has equivalent stabilized properties of other methodologies (Codina and. Zienkiewicz, 2002).

Given the set of variables known in a previous time step *t*, $\{\boldsymbol{u}^n, p^n\}$. The solution $\{\boldsymbol{u}^{n+1}, p^{n+1}\}$ of the conservation equations in a time step $t + \Delta t$, is obtained by the following steps:

Step 1: Solving Momentum Equation

$$\Delta \boldsymbol{u}^* = \boldsymbol{u}^* - \boldsymbol{u}^n = \Delta t \left[-\boldsymbol{u}^n \nabla . \boldsymbol{u}^n + \nabla . \left((\nu + \nu_T) \nabla \boldsymbol{u}^n \right) + \boldsymbol{f}(\boldsymbol{u}^n) \right] + \frac{\Delta t^2}{2} \left(\boldsymbol{u}^n . \nabla \right) \nabla . \left[\left(\boldsymbol{u}^n \otimes \boldsymbol{u}^n \right) - \boldsymbol{f}(\boldsymbol{u}^n) \right]$$

Step 2: Solving Pressure Field

$$\nabla^2 p^{n+1} = -\Delta t \left[\nabla . \boldsymbol{u}^n + \nabla . \Delta \boldsymbol{u}^* \right]$$

Step 3: Velocity Correction – Divergence-Free Projection

$$\boldsymbol{u}^{n+1} = \boldsymbol{u}^{n} - \Delta t \nabla p^{n+1}$$

The term ***f(u)*** is computed by using Eq. (4).

Using the Galerkin method for spatial discretization of the equations on the steps 1-3, coupled to the classical finite element base functions, a matrix form of the algorithm can be written as set of three symmetrical linear systems for each time step.

$$\begin{cases} \boldsymbol{M}.\boldsymbol{\Delta u}^{*} = \boldsymbol{f}_{u}^{*} \\ \boldsymbol{H}.\boldsymbol{p} = \boldsymbol{f}_{p} \\ \boldsymbol{M}.\boldsymbol{\Delta u} = \boldsymbol{f}_{u} \end{cases}$$

In those equations ***M*** and ***H*** are the mass and discrete Laplacian matrices given by:

$$\boldsymbol{M}_{ij} = \int_{\Omega} \boldsymbol{N}_i \boldsymbol{N}_j d\Omega \quad ; \quad \boldsymbol{H}_{ij} = \int_{\Omega} \nabla \boldsymbol{N}_i \nabla \boldsymbol{N}_j d\Omega$$

Remarks:

• The linear systems of the steps 1 and 3 involve the mass matrix. In order to enhance the convergence rate of the computations, this matrix is lumped in a diagonal form. This is performed only once, at the beginning of the iterative computation.

• The linear system for the pressure correction problem (step 2) is solved by employing the Conjugated Gradient Method, preconditioned by partial Cholesky factorization. This matrix is stored by means of a sparse Morse strategy, and the preconditioning is also performed only once, when this matrix is firstly computed.

In the present paper the time step is controlled by the following expression:

$$\Delta t \leq \frac{\Delta t_c \Delta t_d}{\Delta t_c + \Delta t_d} \tag{9}$$

where

$$\Delta t_c = \left(2 \left\| \boldsymbol{u}.\nabla N_i \right\|_{\max}\right)^{-1} \quad ; \quad \Delta t_d = \left(2\nu^{e} \left\| \nabla N_i.\nabla N_j \right\|_{\max}\right)^{-1} \tag{10}$$

For those two expressions ones considers the characteristic time for the diffusion and convection counterpart of the discrete problem, at each element. The viscosity in the element, ν^{e}, must take into account the molecular and turbulent parts.

It can be verified that the critical time step proposed by Eq. (9) is compatible with the following relation:

$$\Delta t \leq \left(c_1 \frac{\nu^{e}}{h^2} + c_2 \frac{\left|\boldsymbol{u}^{n}\right|}{h} \right)^{-1} \tag{11}$$

where c_1 and c_2 are constants and *h* denotes the characteristic length of the element. The above described procedure can assure the stability of the scheme, following the analysis of Codina and Zienkiewicz (2002). The present choice of the time step value stabilize both the convective and pressure-velocity problems.

4. Results and discussions

The first test case concerns the 1-D developed boundary layer over and within a homogeneous canopy. This problem is used to check the quality of the simulations using the simply first order model for different density canopy distributions. It is considered that the forest canopies have the height *H*. The computational domain for the canopy problem is considered *3H* height, where a free velocity is imposed. A non slip boundary condition is used on the ground. All general characteristics of those forests are resumed in Tab. 1, and the leaf area density of forest sites are presented in the Fig. 1.

Table 1: General forests characteristics

Forest type	Drag Coefficient (C_D)	Height (H)	Leaf Area Index (LAI)	Reference
Amazon Rain Forest	0.25	38 m	4.9	Kru et al (2000)
Pine Forest	0.21	14 m	2.9	Katul et al (2004)
Oak Forest	0.1	24 m	2.9	Poggi et al (2004)
Stika Spruce	0.2	7 m	2.15	Irvine et al (1997)

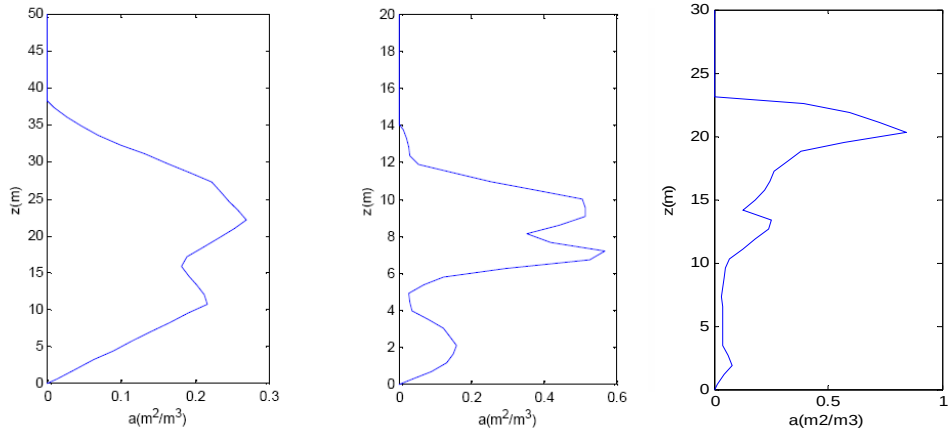

(a) (b) (c)

Figure 1. Leaf Area Density: (a) Amazon Rainforest (b) Pine Forest (c) Oak Forest.

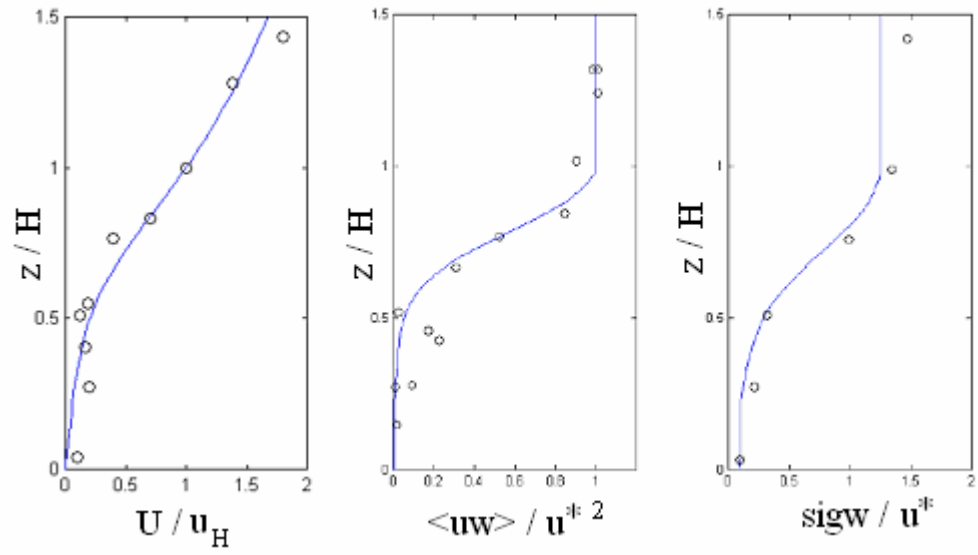

Figure 2. Developed boundary layer for Amazon rainforest : Velocity and turbulence profiles.

The results for developed flow – after the boundary layer development, are presented in Figs. 2 and 3, in which the numerical results are compared to the experimental measurements for Amazon and pine forests. The mean horizontal velocity profiles for both simulations could reproduce well the experimental data. The turbulence statistics given by the

Reynolds Shear stress ($\overline{u'w'}$) and the vertical velocity variance (σ_w) are obtained by using the following simply parameterizations:

$$-\left\langle \overline{u'w'} \right\rangle = \nu_T \left(\frac{\partial \left\langle \overline{u} \right\rangle}{\partial z} + \frac{\partial \left\langle \overline{w} \right\rangle}{\partial x} \right) \tag{12}$$

$$\sigma_w = \sqrt{\frac{2}{3}k} \; ; \quad k = 2.357 \frac{\nu_T^2}{\ell_m^2} \tag{13}$$

All the displayed results are presented by considering dimensionless values, using the velocity scales (u_* or u_H) proposed by the experimental works. The results obtained in the simulations show good agreement with the *in situ* measurements, considering the simplicity of the first order model used in the present paper. In Fig. 4 a complete comparison between the in situ experiments and numerical simulations is presented for the mean velocity field as well as for the turbulent shear stress. These plots have shown the relative quality of the proposed model. The model limitation for the high velocity values is observed in the spread of the data in the upper side of the graphics, mainly for the simulations of the shear stress. The main dispersion is encountered in the simulations of lower density canopies (oak) over the canopy.

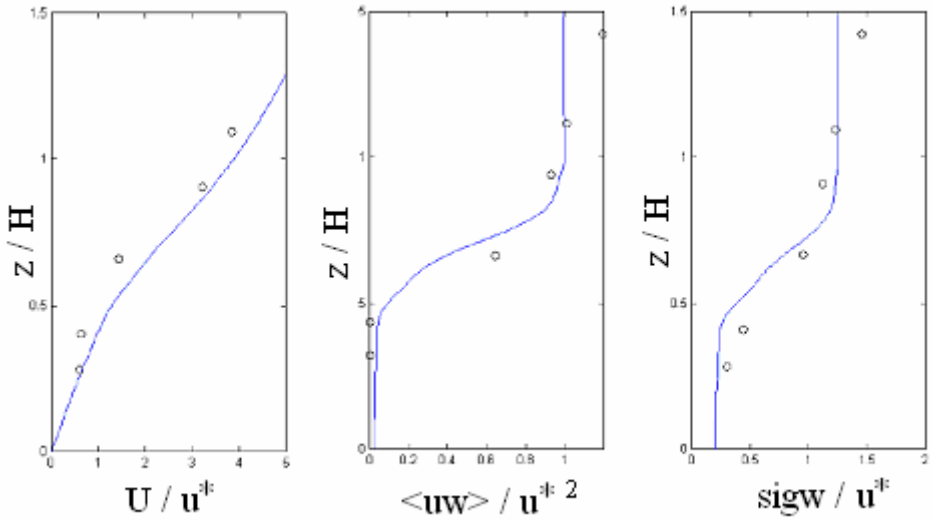

Figure 3. Developed boundary layer for Pine Forest: Velocity and turbulence profiles. (symbols are experimental measurements. Lines are simulations)

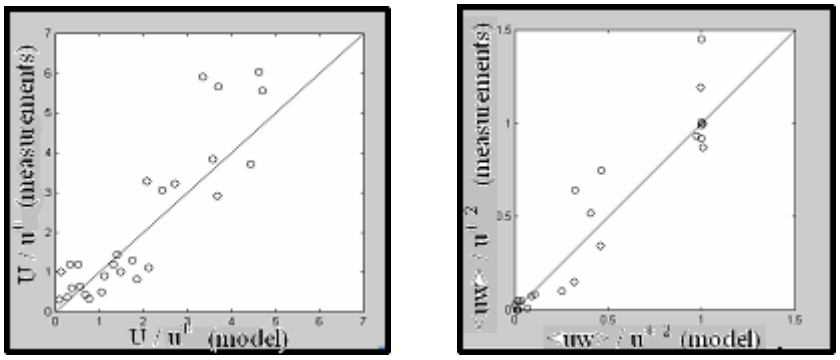

Figure 4. Comparisons for four dense forests (mean velocity and shear stress).

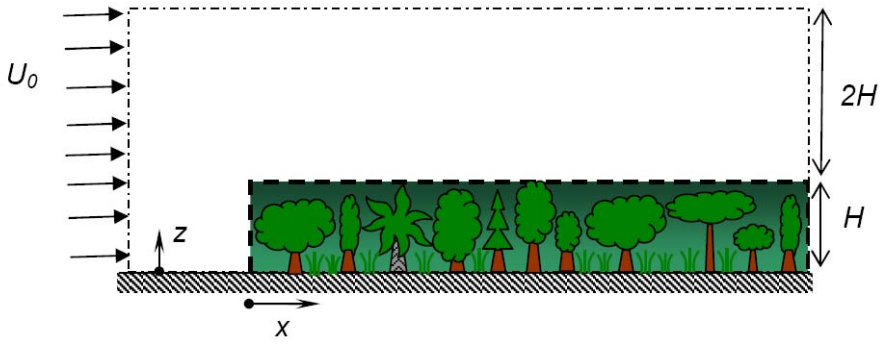

Figure 5. Forest edge test case.

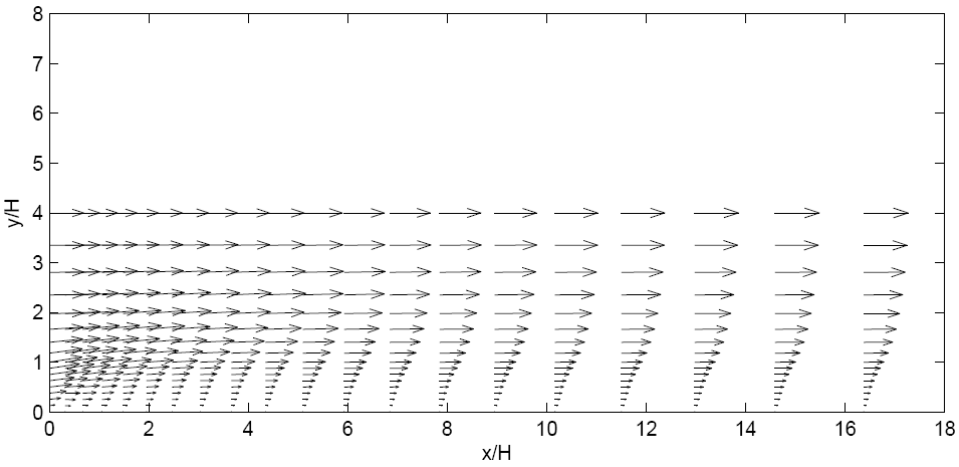

Figure 6. Boundary layer development from the forest edge.

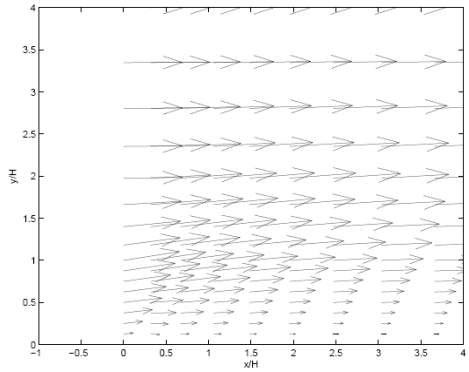

Figure 7. Details of the velocity field on the forest edge.

The second set of results was obtained for a test case concerning the development of boundary layer flow after a forest edge, as shown in Fig. 5. The canopy has a height *H*, and the computation domain is contained in a box with

18*Hx*3*H*. The velocity field is developed from the beginning of the canopy layer ($x = 0$) just at a condition with zero vertical velocity and an established vertical profile of the wind velocity. The domain is discretized with 2200 triangular finite elements and the measured canopy structures is used for the simulations ($a(z)$). The simulation is performed for the uniform plantation of Sitka spruce to verify the development of the air flow within the canopy, near to the forest edge. Experimental results are available for this situation.

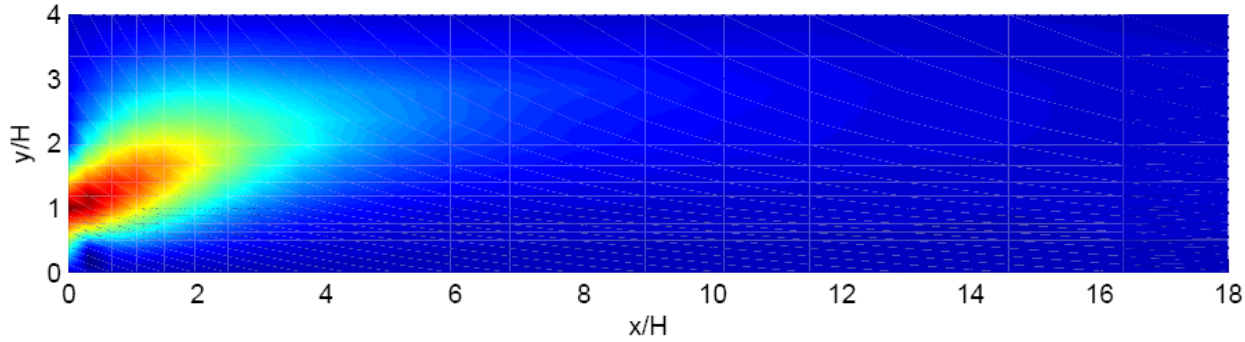

Figure 8. Vertical velocity levels

On Figures 6-8 the numerical results for the developing flow in the forest edge are visualized. The velocity vectors characterized the same qualitative streamlines behavior of the experimental observations of Irvine et al. (1997) and Morse et al. (2002). Near the inlet forest edge, the vertical velocity component of the velocity has a great positive value, as a consequence of the deceleration of the air flow due to the drag in the vegetation elements. At this region the velocity has an angle of some degrees, directing the flow to the top of the canopy, as shown in the pictures. It can be observed that the results are overestimated within the canopy, comparing it to the experimental observations. Two considerations have to be taken into account: First, the exact leaf area density distribution is only estimated in this experimental case. The data for the function $a(x)$ is not available for this experiments - only the integral value (LAI) had been effectively measured. The authors proposed an estimative as a conical distribution, which can be explain the difference between the results. The second consideration is based in the modeling used for this paper. The simply first order model considers a constant length scale within the canopy, and the computation of the turbulence viscosity is performed and calibrated only for the developed boundary layer flows. Advanced models have to be used to enhance the accuracy of the estimates for the air flow, for inhomogeneous distributions of vegetative layer, in particular to describe the flow in near ground regions.

5. Acknowledgement

The authors gratefully acknowledge the financial support provided by the Brazilian agencies CNPq and CAPES, as well as by the ELETRONORTE Company.

6. References

Codina, R., Vazquez, M. and Zienkiewicz, O.C., 1998, A general algorithm for compressible and incompressible flow - part III. The semi-implicit form, Iternational Journal for Num. Methods in Fluids Vol. 27, pp. 13–32.

Codina, R., 2001, Pressure stability in fractional step finite element methods for incompressible flows, J. of Comp. Physics, Vol. 170, pp. 112–140.

Codina, R. and Zienkiewicz, O. C., 2002, CBS versus GLS stabilization of the incompressible Navier-Stokes equations and the role of the time step stabilization parameter, Comm. in Num. Methods in Engneering, Vol. 18, pp. 99–112.

Chorin, A.J., 1968, Numerical solution od the Navier-Stokes equations, Mathematics of Computation, Vol. 22, pp. 745–762.

Finnigan, J.J., 2000, Turbulence in plant canopies, Annual Review of Fluid Mechanics, Vol. 32, pp. 519–571.

Katul, G.G., Mahrt, H., Poggi, D. and Sanz, C. 2004, One- and Two-Equation Models for Canopy Turbulence, Boundary-Layer Meteorology, Vol. 113, pp. 81-109.

Kobayashi, Pereira, J. and Siqueira, M., 1994, Numerical Study of the Turbulent Flow over and in a Model Forest on a 2D Hill, J. Wind Eng. Ind. Aerodyn. Vol. 53, pp. 357-374.

Irvine, M.R., Gardiner, B.A. and Hill, M.K., 1997, The Evolution of Turbulence Across a Forest Edge, Boundary-Layer Meteorology, Vol. 84, pp. 467-496.

Lee, X., 2000, Air motion within and above forest vegetation in non-ideal conditions, Forest Ecology and Management Vol. 135, pp. 2–18.

Morse, A.P., Gardiner, B.A. and Marshall, B.J, 2002, Mechanims Controlling Turbulence Development Across a Forest Edge, Boundary-Layer Meteorology, Vol. 103, pp. 227-251.

Pinard, J.P. and Wilson, J.D., 2001, First- and Second-Order Closure Models for Wind in a Plant Canopy, J. Appl. Meteorology, Vol. 40, pp. 1762–1768.

Poggi, D., Katul, G.G. and Albertson, J.D., 2004, Momentum Transfer and Turbulent Kinetic Energy Budgets within a Dense Canopy, Boundary-Layer Meteorology, Vol. 111, pp. 589–614.

Raupach, M.R and Shaw, R.H., 1982, Averaging Procedures for Flow Within Vegetation Canopies, Boundary-Layer Meteorology Vol.2(1), pp. 79–90.

Ross, A.N., Arnold, S., Vosper, S.B., Mobbs, S.D. Dixon, N. and Robins, A.G., 2004, A Comparison of Wind-Tunnel Experiments and Numerical Simulations of Neutral and Stratified Flow Over A Hill, Boundary-Layer Meteorology Vol. 113, pp. 427-459.

Ross, A.N and Vosper, S.B., 2004, Turbulent flow over a forested hill. Part 1: Numerical modelling and comparison with experimental data, Q. J. R. Meteorol. Soc. Vol. 113, pp. 427-459.

Temam, R., 1969, Sur l'approximation de la solution des ´equations de Navier-Stokes par la Méthode de pas fractionaires, Archives for Rational Mechanics and Analysis, Vol. 32, pp. 135– 153.

Wilson, J.D. and Flesch, T.K., 1999, Wind and remnant tree sway in forest cutblocks. III. a wind flow model to diagnose spatial variations, Agricultural and Forest Meteorology Vol. 93, pp. 259–282.

Zienkiewicz, O.C and Taylor, R.L., 2000, The Finite Element Method - Fluid Mechanics, Butterworth-Heinemann Pub., Vol. 3.

8. Copyright Notice

Proceedings of the 11th Brazilian Congress of Thermal Sciences and Engineering -- ENCIT 2006
Braz. Soc. of Mechanical Sciences and Engineering -- ABCM, Curitiba, Brazil,- Dec. 5-8, 2006

Paper CIT06-0372

RADIAL ADVECTIVE TRANSPORT OF A POLLUTANT IN AN ATMOSPHERE

Maria Laura Martins-Costa and Alexandre Felipe Cobo
Laboratory of Theoretical and Applied Mechanics (LMTA), Mechanical Engineering Department (TEM-PGMEC)
Universidade Federal Fluminense, Rua Passo da Pátria, 156, 24210-240 Niterói/RJ, Brazil; laura@mec.uff.br

Rogério M. Saldanha da Gama
Mechanical Engineering Department, Universidade do Estado do Rio de Janeiro
Rua São Francisco Xavier, 524, 20550-013, Rio de Janeiro, RJ, Brazil; rsgama@domain.com.br

Antonio C. P. Brasil Júnior
Laboratory of Energy and Environment (LEA), Mechanical Engineering Department
Universidade de Brasília, 70910-900, Brasília/DF, Brazil;: brasiljr@unb.br

Abstract. *A preliminary hyperbolic model is used to describe the transport phenomena in an environment representing an atmosphere containing a pollutant, in which the atmosphere is modeled as an ideal polytropic gas, the is pollutant transported radially and the rate of pollutant production or destruction due to chemical reactions is accounted for. The resulting mathematical description consists of a nonlinear hyperbolic system of three partial differential equations representing mass and momentum conservation for the air-pollutant mixture and the pollutant mass balance. This system simulation is performed by combining Glimm's scheme (whose implementation requires the solution of a Riemann problem for each two consecutive steps) and an operator splitting technique to deal with the non-homogeneous part of the hyperbolic operator, accounting not only for terms arising from the problem spherical geometry but also for the rate of production or destruction of the pollutant.*

Keywords*. Pollutant radial transport, pollutant generation, Glimm's scheme, operator splitting technique.*

1. Introduction

This work employs a preliminary hyperbolic model to describe transport phenomena in an environment representing the atmosphere containing a pollutant. The atmosphere is modeled as an ideal polytropic gas and the pollutant is transported radially. The resulting mathematical representation of this phenomenon consists of a nonlinear hyperbolic system of three partial differential equations representing mass and momentum conservation for the air-pollutant mixture and the pollutant mass balance – in which a term representing the rate of pollutant production or destruction due to chemical reactions is considered.

The nature of this mathematical problem does not allow, in general, classical solutions, in which the differential equations are verified at every spatial point, thus requiring an enlargement of the admissible solutions space, in order to allow for the presence of discontinuities satisfying a certain solution criterion – given by the entropy condition, besides satisfying a weak formulation of the conservation equations.

This system hyperbolic feature suggests its approximation by means of a numerical method specially designed to deal with discontinuous problems. Its simulation is performed by following a systematic procedure consisting of three distinct steps – namely the construction of a Glimm's scheme for time evolution with arbitrary initial condition, the complete generalized solution of the associated Riemann problem (since Glimm's scheme implementation requires, for every time step, the solution of a Riemann problem for each two consecutive steps) and an operator splitting into a hyperbolic part and an ordinary one.

Glimm's scheme is a numerical methodology to treat discontinuous problems, preserving the shock waves magnitude and position. Although its applicability is restricted to one-dimensional problems, this methodology exhibits features such as low storage costs and low computational effort, when compared to other numerical procedures to approximate nonlinear problems. The operator splitting technique is a simple and effective tool that consists, essentially, in treating a simultaneous problem as a sequential one. A decomposition in two parts of the operator defined in the hyperbolic system is performed so that the merely hyperbolic part of the operator – namely the homogeneous associated problem – is split away from its purely time evolutionary one.

2. Mechanical model

The transport of a pollutant in the air is described by considering the mass and linear momentum conservation for the air-pollutant mixture and the mass balance for the pollutant along with some simplifying assumptions. First the mass transfer is supposed to be caused by an advection-diffusion process of the pollutant – from now on denoted as *A* constituent, in the air, which is assumed as an ideal gas (all viscosity effects being neglected). The most important

simplifying assumption is to suppose the presence of a sufficiently small quantity of the constituent *A* in the mixture – at any time instant, so that the mass and linear momentum balance equations for the mixture can be approximated by mass and linear momentum balances for the air. This simplifying assumption allows to define ρ as the air mass density, $\mathbf{v}$ as its velocity, and p and $\mathbf{g}$ as the pressure and specific body force acting on the air.

$$\begin{aligned}
&\frac{\partial \rho}{\partial t} + \nabla \cdot (\rho \mathbf{v}) = 0 \\
&\frac{\partial (\rho \mathbf{v})}{\partial t} + \nabla \cdot (\rho \mathbf{v}\mathbf{v}) = -\nabla p + \rho \mathbf{g} \\
&\frac{\partial (\rho \omega_A)}{\partial t} + \nabla \cdot (\rho \omega_A \mathbf{v}) = \nabla \cdot (\rho D \, \nabla \omega_A) + r_A
\end{aligned} \tag{1}$$

The concentration of the constituent *A* in the mixture, ω_A, is defined as the mass fraction of this constituent in the mixture, being expressed by the following equation $\omega_A \equiv \rho_A / \rho$. Besides, D represents the diffusion coefficient of the constituent *A* in the mixture and r_A the rate of production of the constituent *A*. At this point it is important to state additional simplifying assumptions to be considered in the present work. First, the pressure is considered as being a function of the mass density ρ only, $p = \hat{p}(\rho)$ its derivative with respect to ρ being given by p' and satisfying $p'(\rho) > 0$. Also, considering a one-dimensional radial flow, the velocity field may be reduced to a single component on the flow direction $\mathbf{v} = v\mathbf{e}_r$. Besides, gravitational effects will be omitted – a reasonable hypothesis for a radial flow and, finally, diffusion may be neglected, when compared to advection – this latter assumption being expressed by letting the diffusion coefficient $D = 0$ and being an admissible one for an isotropic explosion. So, the mechanical model stated in equation (1) is reduced to:

$$\begin{cases}
\dfrac{\partial \rho}{\partial t} + \dfrac{\partial (\rho v)}{\partial r} = -\dfrac{2\rho v}{r} \\
\dfrac{\partial}{\partial t}(\rho v) + \dfrac{\partial}{\partial r}(\rho v^2 + p) = -\dfrac{2\rho v^2}{r} \\
\dfrac{\partial}{\partial t}(\rho \omega_A) + \dfrac{\partial}{\partial r}(\rho \omega_A v) = -\dfrac{2\rho v \omega_A}{r} - \alpha \omega_A, \\
\qquad\qquad \text{since} \quad r_A = -\alpha \omega_A
\end{cases} \tag{2}$$

It is important to keep in mind that, in the particular problem addressed in this work, a decay in the concentration of the constituent *A* in the mixture (the pollutant) is taken into account in the term r_A. In equation (2) a constitutive relation to describe the rate of pollutant production – accounting for generation or destruction of pollutant, which may be caused by chemical reactions – is assumed as $r_A = -\alpha \omega_A$, where α is a constant. This particular constitutive equation gives rise to a decay in the pollutant concentration along the time.

System (2) may be rewritten by considering $F \equiv \rho$, $G \equiv \rho v$, $H \equiv \rho \omega_A$ as

$$\begin{aligned}
&\frac{\partial F}{\partial t} + \frac{\partial G}{\partial r} = -\frac{2}{r} G \\
&\frac{\partial G}{\partial t} + \frac{\partial}{\partial r}\left(\frac{G^2}{F} + p \right) = -\frac{2}{r}\frac{G^2}{F} \\
&\frac{\partial H}{\partial t} + \frac{\partial}{\partial r}\left(\frac{GH}{F} \right) = -\frac{2}{r}\frac{GH}{F} - \alpha \frac{H}{F}
\end{aligned} \tag{3}$$

It is worth mentioning that in order to solve the above stated problem; initial data for the mass density, the velocity and the pollutant concentration are required. Eventually boundary conditions may also be employed in the solution.

3. Numerical procedure

In this section a scheme, developed to simulate nonlinear hyperbolic problems, is employed to obtain numerical approximations for the nonlinear system of partial differential equations described in equations (3). Two main

ingredients have been used to achieve this goal: an operator splitting technique together with the Glimm's scheme, successfully employed in the simulation of other nonlinear hyperbolic problems. The procedure consists in a decomposition of the operator in such a way that its merely hyperbolic part is split away from its purely time evolutionary one. Glimm's method, specifically developed to deal with hyperbolic non-linear problems, consists in marching from a time n to a time $n+1$ through the solution of the associated Riemann problem for each two consecutive time steps. It is based on a theory whose mathematical formulation has a solid thermodynamic basis, which could be expressed by the entropy condition (Smoller, 1983). A wide range of non-linear hyperbolic problems have already been simulated by combining Glimm's scheme and an operator splitting technique among which are the wave propagation in gas pipelines, shock propagation in gas dynamics problems and wave propagation in a damageable elasto-viscoplastic pipe (see (Freitas Rachid et al, 1994) and references therein). Other relevant examples that could be quoted are the response of non-linear elastic rods (Saldanha da Gama, 1990) and the isothermal and non-isothermal flow of either ideal or Newtonian fluids through unsaturated porous media – covering most one-dimensional cases of interest (see (Martins-Costa et al., 2001) and references therein). It is remarkable that the problems addressed in these works, due to their hyperbolic nature, do not require boundary conditions. They are essentially initial value problems (John, 1982).

Glimm's method, which deals with the homogeneous part of the hyperbolic operator represented in equation (3), employs the solution of the associated Riemann problem to march from a time n to a time $n+1$. Before using Glimm's scheme for solving equations (3) with appropriated initial data, the solution of the associated Riemann problem must be known. In short, Glimm's method allows building a solution for an initial value problem – namely nonlinear hyperbolic systems subjected to arbitrary initial data, through the solution of a certain number of associated Riemann problems. The arbitrary initial condition given by a function of the position r is approximated by piecewise constant functions, known as step functions – with equal width steps. In the sequence a Riemann problem – an initial value problem whose initial condition must be a step function, is to be solved for each two consecutive steps [MAR, 03]. The main idea behind the method is to appropriately gather the solution of as many Riemann problems as desired to successively march from time $t = t_n$ to time $t_{n+1} = t_n + \Delta t$.

The first step consists in obtaining an initial approximation for (F, G, H) by advancing Δt in time through the homogeneous (merely hyperbolic) part of the operator via Glimm's method, using the values of (F, G, H) at time $t = t_n$ as initial data. The numerical approximation for the solution at time $t = t_n$ is then obtained by advancing in time with the same time step Δt through the purely time evolutionary system. This procedure is repeated until reaching a specified simulation time.

The numerical procedure employed to advance from the time $t = t_n$ to $t = t_{n+1}$ may be defined as:

$$\left.\begin{aligned} &\frac{\partial F}{\partial t} + \frac{\partial G}{\partial r} = -\frac{2}{r} G \\ &\frac{\partial G}{\partial t} + \frac{\partial}{\partial r}\left(\frac{G^2}{F} + p\right) = -\frac{2}{r}\frac{G^2}{F} \\ &\frac{\partial H}{\partial t} + \frac{\partial}{\partial r}\left(\frac{GH}{F}\right) = -\frac{2}{r}\frac{GH}{F} - \alpha\frac{H}{F} \end{aligned}\right| \qquad \left.\begin{aligned} F &= \hat{F}_n(r) \\ G &= \hat{G}_n(r) \\ H &= \hat{H}_n(r) \end{aligned}\right\} \text{at } t = t_n \tag{4}$$

in which $F = \hat{F}_n(r,t)$, $G = \hat{G}_n(r,t)$ and $H = \hat{H}_n(r,t)$.

3.1. Operator splitting technique

The fist step to approximate the fields F, G and H at the time $t = t_{n+1}$ in the non-homogeneous problem described in equation (4) is to employ an operator splitting technique, described in details by [MAR, 01]. It consists of a decomposition of the operator defined in equation (4) so that its merely hyperbolic part – namely the homogeneous associated system, is split away from its purely time evolutionary one – an ordinary system. This technique gives rise to an initial approximation, obtained by advancing Δt in time through the equations representing the homogeneous problem, by employing Glimm's method.

Once this approximation has been evaluated, the numerical approximation for the solution (F, G, H) at time t_{n+1} is finally reached by advancing in time to solve the following time evolutionary problem, with the same step $\Delta t = t_{n+1} - t_n$ through equations:

$$\left\{\begin{array}{l}\dfrac{\partial F}{\partial t}=-\dfrac{2}{r}G \\ \dfrac{\partial G}{\partial t}=-\dfrac{2}{r}\dfrac{G^2}{F} \\ \dfrac{\partial H}{\partial t}=-\dfrac{2}{r}\dfrac{GH}{F}-\alpha\dfrac{H}{F}\end{array}\right. \qquad \left.\begin{array}{l}F=\hat{F}_{n+1}(r) \\ G=\hat{G}_{n+1}(r) \\ H=\hat{H}_{n+1}(r)\end{array}\right\} \text{ at } t=t_n \tag{5}$$

as follows:

$$\begin{aligned} F=\hat{F}_{n+1}(r) &\approx \tilde{F}_{n+1}(r)-\left\{\frac{2}{r}\tilde{G}_{n+1}(r)\right\}\Delta t \\ G=\hat{G}_{n+1}(r) &\approx \tilde{G}_{n+1}(r)-\left\{\frac{2}{r}\frac{\left[\tilde{G}_{n+1}(r)\right]^2}{\tilde{F}_{n+1}(r)}\right\}\Delta t \\ H=\hat{H}_{n+1}(r) &\approx \tilde{H}_{n+1}(r)-\left\{\frac{2}{r}\frac{\tilde{G}_{n+1}(r)\tilde{H}_{n+1}(r)}{\tilde{F}_{n+1}(r)}+\alpha\frac{\tilde{H}_{n+1}(r)}{\tilde{F}_{n+1}(r)}\right\}\Delta t \end{aligned} \tag{6}$$

3.2. Glimm's scheme

The fields $\tilde{F}_{n+1}(r)$, $\tilde{G}_{n+1}(r)$ and $\tilde{H}_{n+1}(r)$ used as initial data in (5) are obtained by advancing Δt in time via Glimm's method through the following homogeneous problem:

$$\left\{\begin{array}{l}\dfrac{\partial F}{\partial t}+\dfrac{\partial G}{\partial r}=0 \\ \dfrac{\partial G}{\partial t}+\dfrac{\partial}{\partial r}\left(\dfrac{G^2}{F}+p\right)=0 \\ \dfrac{\partial H}{\partial t}+\dfrac{\partial}{\partial r}\left(\dfrac{GH}{F}\right)=0\end{array}\right. \qquad \left.\begin{array}{l}F=\hat{F}_n(r) \\ G=\hat{G}_n(r) \\ H=\hat{H}_n(r)\end{array}\right\} \qquad \text{at } t=t_n \tag{7}$$

In other words, $\tilde{F}_{n+1}(r)$, $\tilde{G}_{n+1}(r)$ and $\tilde{H}_{n+1}(r)$ are the solutions of (7) evaluated at the time $t=t_{n+1}$. The main idea behind Glimm's scheme (Smoller, 1983) is to appropriately gather the solution of as many Riemann problems as desired to successively march from time $t=t_n$ to $t=t_{n+1}$. Glimm's scheme, specifically developed to deal with discontinuous problems, preserves the shock waves magnitude and position, within an uncertainty of Δr (width of each step). Such features are not found in the usual numerical procedures (e.g. finite elements and finite differences). Besides, Glimm's method presents a clear advantage of saving computer storage memory, when compared to other methodologies such as a finite element method associated with a shock capture procedure, however its limitation to one-dimensional problems is an important shortcoming. In order to employ this scheme a piecewise constant function is used to approximate the initial data, as follows:

$$\left.\begin{array}{l}F=\hat{F}_n(r)\approx F_{n_i}=\hat{F}_n(r_i+\theta_n\Delta r) \\ G=\hat{G}_n(r)\approx G_{n_i}=\hat{G}_n(r_i+\theta_n\Delta r) \\ H=\hat{H}_n(r)\approx H_{n_i}=\hat{H}_n(r_i+\theta_n\Delta r)\end{array}\right\} \qquad \text{for} \quad r_i-\frac{\Delta r}{2}<r<r_i+\frac{\Delta r}{2} \tag{8}$$

in which θ_n is a number randomly chosen in the open interval $(-1/2\,,\ +1/2)$ and Δr is the width of each step ($\Delta r=r_{i+1}-r_i$).

The above approximations for the initial data give rise, for each two consecutive steps, to the following Riemann problem – whose detailed solution is presented in (Martins-Costa and Saldanha da Gama, 2003):

$$\left.\begin{aligned}&\frac{\partial F}{\partial t}+\frac{\partial G}{\partial r}=0\\&\frac{\partial G}{\partial t}+\frac{\partial}{\partial r}\left(\frac{G^2}{F}+p(F)\right)=0\\&\frac{\partial H}{\partial t}+\frac{\partial}{\partial r}\left(\frac{GH}{F}\right)=0\end{aligned}\right\}\quad\begin{cases}(F,G,H)=\left(F_{n_i},G_{n_i},H_{n_i}\right)\ \ t=t_n\ ,-\infty<r<r_i+\dfrac{\Delta r}{2}\\(F,G,H)=\left(F_{n_{i+1}},G_{n_{i+1}},H_{n_{i+1}}\right)\ \ t=t_n\ ,\ \mathrm{r}_{i+1}-\dfrac{\Delta r}{2}<r<\infty\end{cases}\tag{9}$$

Denoting by $F_{n_i}^R$ $G_{n_i}^R$, and $H_{n_i}^R$ the generalized solution of the Riemann problem (9), the approximation for the solution of (7) at the time t_{n+1} is given as follows:

$$\begin{aligned}&F=\hat{F}_{n+1}(r)\approx F_{n_i}^R(r,t_{n+1}) &&\mathrm{r}_i<r<r_{i+1}\\&G=\hat{G}_{n+1}(r)\approx G_{n_i}^R(r,t_{n+1}) &&\mathrm{r}_i<r<r_{i+1}\\&H=\hat{H}_{n+1}(r)\approx H_{n_i}^R(r,t_{n+1}) &&\mathrm{r}_i<r<r_{i+1}\end{aligned}\tag{10}$$

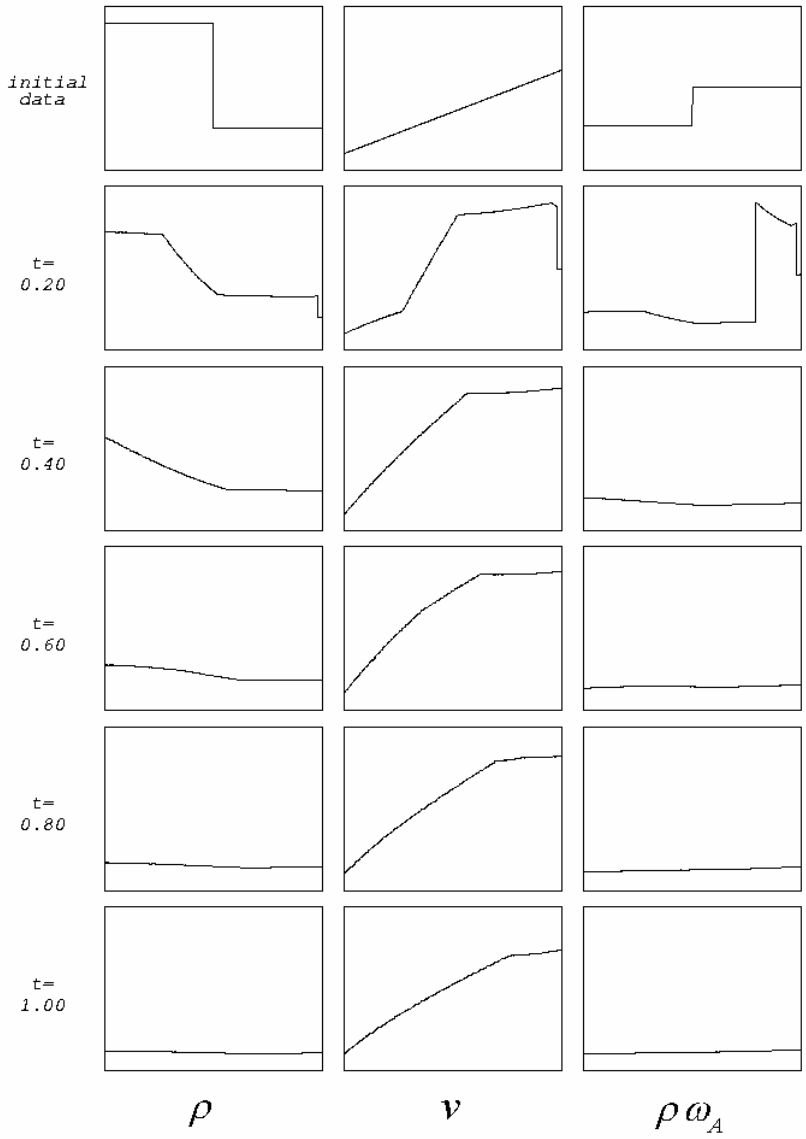

Figure1. Gas density, velocity and pollutant concentration per unit volume variation with position – considering $\alpha=0.01$ and a spherical shell with $r_i=1.00$ and $r_e=2.00$.

In order to prevent interactions among nearby shocks of adjacent Riemann problems, the time step Δt, and consequently, t_{n+1} must be chosen in such a way that the Courant-Friedrich-Lewy (Smoller, 1977) condition is satisfied:

$$t_{n+1} - t_n \leq \frac{\Delta r}{2|\lambda|_{\max}} \tag{11}$$

where $|\lambda|_{\max}$ is the maximum (in absolute value) propagation speed, considering all the Riemann problems.

At this point a further comment is worth mentioning: the Courant-Friedrich-Lewy condition, expressed in equation (11), although sufficient to assure an adequate treatment of the homogeneous associated problem with absence of interactions among shocks of adjacent Riemann problems, is not sufficient to guarantee the physical validity of the employed operator splitting technique. In the particular problem treated in this work, in which spherical waves are considered, the ratio between the time step Δt and the considered value of the radius *r* must be sufficiently small. In other words, a value ten times smaller than the one computed in equation (11) is employed for the time step Δt, in order to avoid convergence problems.

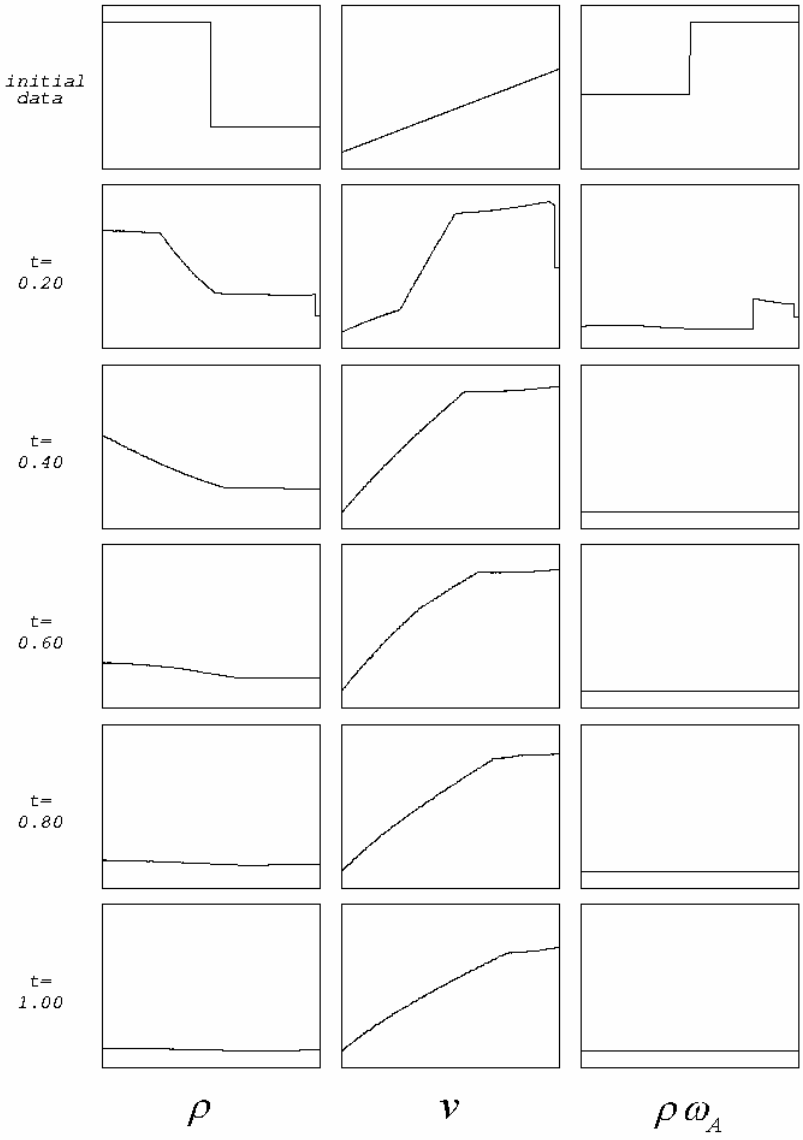

Figure 2. Gas density, velocity and pollutant concentration per unit volume variation with position – considering $\alpha = 10$ and a spherical shell with $r_i = 1.00$ and $r_e = 2.00$.

4. Numerical results and discussion

Figures 1 to 4 show – in all depicted sketches, the evolution of gas density ρ ρ, velocity v and pollutant concentration per unit volume $\rho\omega_A$ along with radial position for five selected time instants. In all the considered cases, the initial data, presented in the three graphs shown in the first line, consists of distinct step functions for gas density ρ (with $\rho_L > \rho_R$) and pollutant concentration in the mixture ω_A (with $\omega_{AL} < \omega_{AR}$), resulting in a pollutant concentration per unit volume given by $\rho\omega_{AL} < \rho\omega_{AR}$.

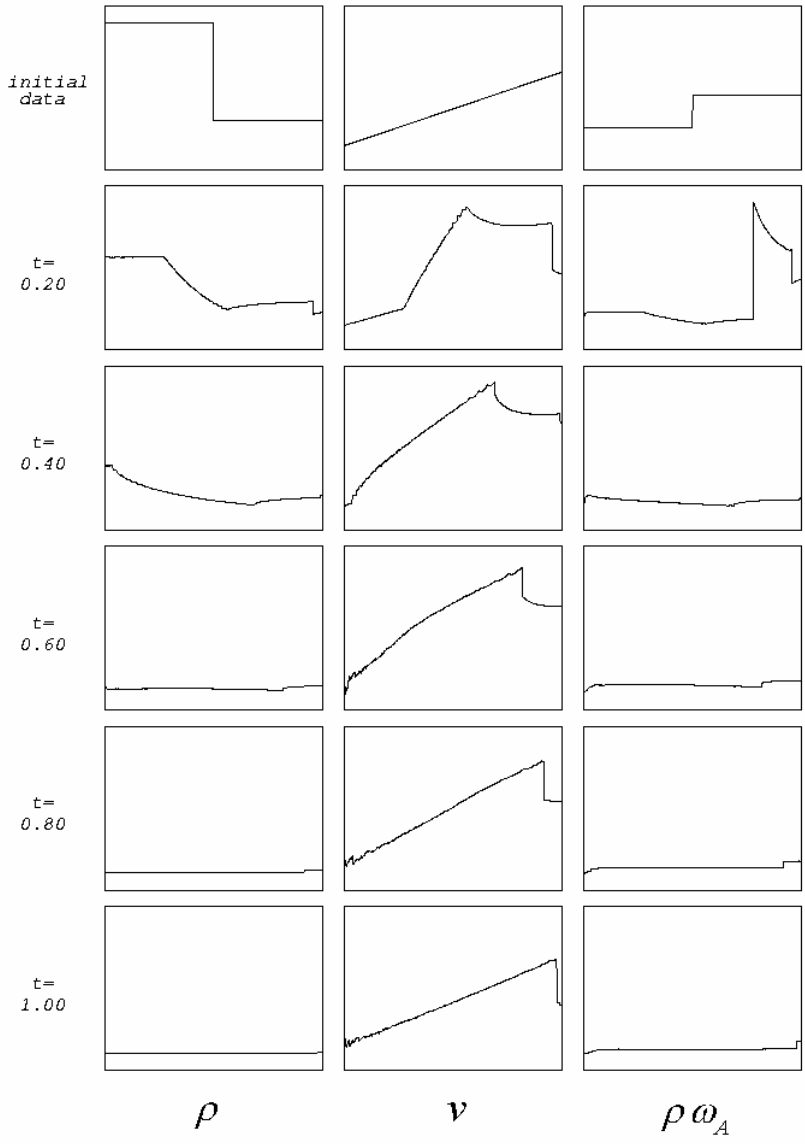

Figure 3. Gas density, velocity and pollutant concentration per unit volume variation with position –considering $\alpha = 0.01$ and a spherical shell with $r_i = 0.01$ and $r_e = 1.01$.

The velocity v initial value is given by a linear increasing function. All these results have been obtained by employing Glimm's difference scheme combined with an operator splitting technique to account for the non-homogeneous portion of the hyperbolic operator and have been achieved with 600 steps.

All results have been obtained by considering a spherical shell unitary thickness. The influence of the behavior of ρ, v $\rho\omega_A$ may be observed by comparing figures 1 (in which the internal and external radii have been made equal to $r_i = 1.00$ and $r_e = 2.00$) and 3 (with $r_i = 0.01$ and $r_e = 1.01$).

In fact, as the spherical shell curvature is increased the effect of the shocks becomes less visible. In other words, a shock dissipation effect could be associated with the curvature increase.

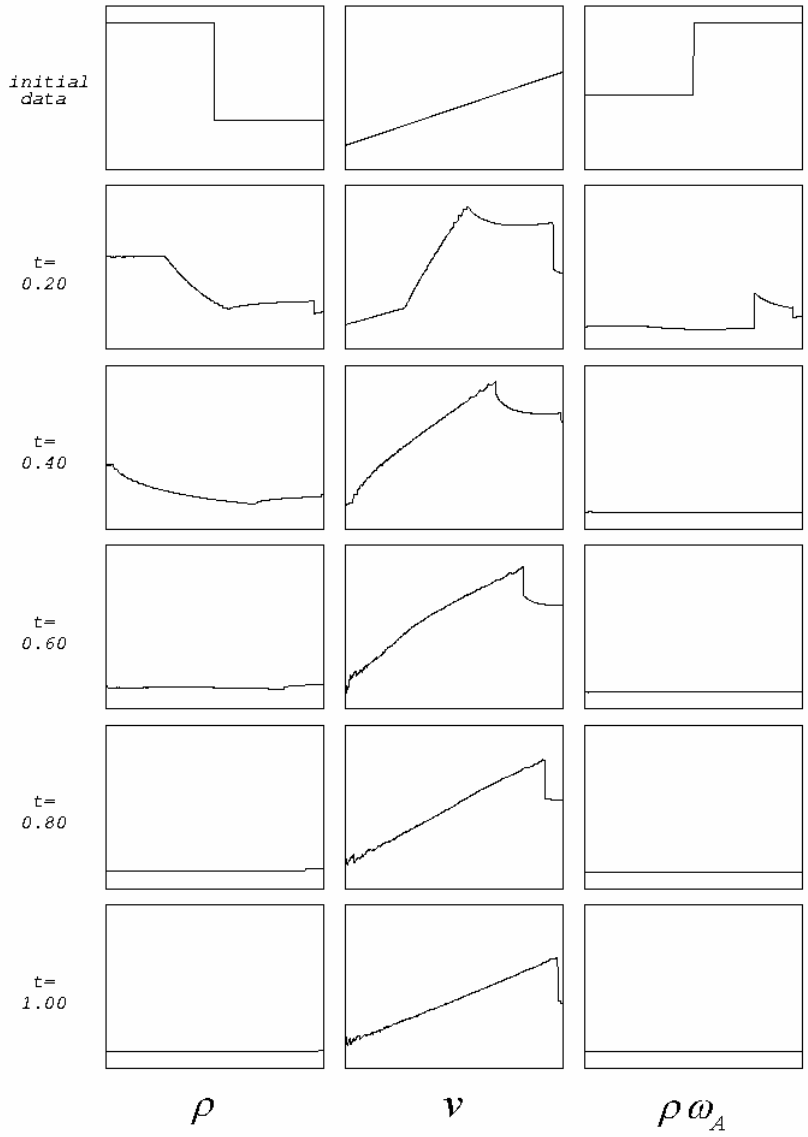

Figure 4. Gas density, velocity and pollutant concentration per unit volume variation with position –considering $\alpha = 10$ and a spherical shell with $r_i = 0.01$ and $r_e = 1.01$.

The influence of the α coefficient may be observed by comparing figure 1 ($\alpha = 0.01$) with figure 2 ($\alpha = 10$) and figures 3 ($\alpha = 0.01$) and 4 ($\alpha = 10$). These results show that the term r_A plays the role of a pollutant sink – giving rise to decay in the pollutant concentration ω_A along the time.

5. Final remarks

Glimm's method, besides preserving shock waves magnitude and position, is a convenient tool for solving one-dimensional nonlinear problems, exhibiting features such as low storage costs and low computational effort, when compared to other numerical procedures to approximate nonlinear problems. Besides, combined with an operator splitting technique this numerical methodology allows the accurate approximation of a nonlinear system of non-homogeneous partial differential equations representing mathematically the transport of a pollutant in the atmosphere in a spherical geometry and accounting for a pollutant generation term (acting in the sense of pollutant destruction) which simulates chemical reactions, causing a damping effect in ω_A variation.

6. Acknowledgement

The authors gratefully acknowledge the financial support provided by the agencies CNPq and CAPES.

7. References

Freitas Rachid, F.B. Saldanha da Gama, R.M. and Costa-Mattos, H., 1994, Modelling the Hydraulic Transients in Damageable Elasto-Viscoplastic Piping Systems, Appl. Math. Modelling, Vol. 182, pp. 207-215.

Jacobson, M.Z., 2000, Jacobson Fundamentals of Atmospheric Modelling, Ed. Cambridge, New York.

John, F., 1982, Partial Differential Equations, Ed. Springer-Verlag, Berlin.

Martins-Costa, M.L. and Saldanha da Gama, R.M., 2003, "Glimm's Method Simulation for the Pollutant Transport in an Isothermal Atmosphere", Comput. Mech., Vol. 32, No. 3, pp. 214-223.

Martins-Costa, M.L. and Saldanha da Gama, R.M., 2001, Numerical Simulation of One-Dimensional Flows with Shock Waves, Int. J. Numer. Meth. Engng., Vol. 52, No. 10, pp. 1047-1067.

Perkins, H.C., 1974, Air Pollution, Ed. McGraw-Hill, Tokyo.

Saldanha da Gama, R.M., 1990, An Alternative Procedure for Simulating the Dynamical Response of Non-Linear Elastic Rods, Int. J. Num. Meth. Engng., Vol. 29, pp. 123-139.

Smoller, J., 1983, Shock Waves and Reaction-Diffusion Equations, Ed. Springer-Verlag, New York.

8. Copyright Notice

Proceedings of the 11th Brazilian Congress of Thermal Sciences and Engineering – ENCIT 2006
Braz. Soc. of Mechanical Sciences and Engineering – ABCM, Curitiba, Brazil, Dec. 5-8, 2006

Paper CIT06-0373

Numerical modeling of the heat transfer in the turbulent boundary layer

Rafael Gabler Gontijo
Universidade de Brasília - Departamento de Engenharia Mecânica - 70910-900 - Brasília - DF
rafaelgabler@yahoo.com.br

Rodrigo Carrijo Lino
Universidade de Brasília - Departamento de Engenharia Mecânica - 70910-900 - Brasília - DF
rccarrijo@unb.br

José Luiz Alves da Fontoura Rodrigues
Universidade de Brasília - Departamento de Engenharia Mecânica - 70910-900 - Brasília - DF
fontouta@unb.br

Abstract. *The main goal of this work is the numerical modeling of the forced convective turbulent heat flux , for the turbulent incompressible flow of air over a flat plate, with unheated starting lengths, for a variety of four step positions at Reynolds number up to 5.6 x* 10^6*. The numerical algorithm applied a consolidate Reynolds and Favre averaging process for the turbulent variables. The turbulence model is the classical* $\kappa - \epsilon$*. The turbulent inner layer is modeled by velocity wall laws and temperature wall laws. The remaining non-linearities, due to laws of wall, are treated by a minimal residual method. The numerical results for heat transfer, velocity, temperature, hydrodynamic and thermal boundary layers are compared with experimental data, in addition the numerical results are also compared with empirical correlation results. The Reynolds number range of the modeled flows, based on the length of flat plate is placed between* $10^5 < Re < 10^7$*. Two different physical cases are analyzed, in the first one the velocity and the temperature field are uncoupled. In the second case the velocity and the temperature field are strongly coupled.*

keywords: *Convection, Flat plate, turbulence, wall laws, turbulence models, finite elements.*

1. Introduction

The objective of this work is to analyze the efficiency of the methodology used by the solver Turbo2D in the modeling of the forced convection heat transfer in turbulent boundary layers, with and without the coupling between the velocity and the temperature fields.

To make these analysis two distinct physical situations, in the point of view of the relation between the velocity and temperature fields, were chosen. In the flows studied experimentally by Reynolds et al. (1958) and by Taylor et al. (1990) the thermal and hydrodynamic boundary layers are clearly uncoupled. In the Ng (1981) test case a strong dependency between both fields is observed.

The extension and the complexity of the coupling existing between the turbulent fields of momentum and energy depends on the intensity of the velocity, pressure and temperature gradients involved, on the geometry of the physical solid boundary of the flow and also, on the thermodynamic behavior of the fluids involved in the process. The degree of difficulty and the computational cost of the numerical modeling of the problem are directly related to existing coupling degree between the turbulent fields of momentum and energy.

The test cases of Reynolds et al. (1958) and of Taylor et al. (1990) represents forced, turbulent and incompressible flows of air over horizontal, smooth, flat plates. The temperature fields are specified so that the beginning of the thermal and the hydrodynamic boundary layers are separated by an unheated starting length ξ.

There is an adiabatic length in the beginning of each plate, created by the equality of the temperatures of the wall and the flow. The thermal boundary layer begins in the point were both temperatures are differentiated, originating a heat flux between the wall and the flow. In all the studied situations the thermal boundary layer is developed over isothermal walls.

The turbulent air flows studied by Reynolds et al. (1958) and by Taylor et al. (199), occurs with such velocities, that so in the faster situation, creates Mach numbers under 0,2. The geometry in the solid boundary of the flow is incapable to provide the detachment of the hydrodynamic boundary layer or changing the curvatures of the fluid movement. Under these conditions, the existing pressure gradients are of low intensity. The higher

differences of temperature imposed are of 18 K, this means that the heated plate can not change in a significant way the specific mass, the thermal conductivity and the dynamic viscosity of the air.

In the absence of significant pressure and temperature gradients, it is possible the adoption of the hypothesis that the thermodynamic proprieties of the fluid are constants, this condition is capable to break the coupling existing between the equations of conservation of momentum and energy and to make linear the conservation equation of energy.

The system of governing equations, simplified by the non variance of the thermodynamic proprieties, admits analytical solution and, in the computational point of view, allows the use of less expensive computational algorithms of numerical resolution.

Even with the restriction represented by the hypothesis of constant values for the fluid thermodynamic proprieties, many problems of technological interest can be modeled with this formulation, being distinguished because of its recent importance, the problem created by the necessity of cooling plates used in electronic circuits used in the computational area.

In the Ng (1981) test case, a turbulent flow of air at 293 K, totally developed in a wind tunnel is conduced to an horizontal smooth flat plate, heated up to 1250 K. The great difference between the temperature of the wall and of the flow, produces important variations in the specific mass, in the dynamic viscosity, in the specific heats and in the thermal conductivity of the fluid. The variation of those proprieties with temperature is responsible by the coupling between the equations of conservation of momentum and energy and by the non linear behavior of the energy conservation equation.

The solver Turbo2D is a program of research, that is been developed in the Group of Complex Fluid Dynamics - Vortex, of the Mechanical Engineering Department of the University of Brasília. This solver is based on the adoption of the finite elements technique, under the formulation of pondered residuals proposed by Galerkin, adopting in the spatial discretization of the calculus dominium the triangular elements of the type P1-isoP2, as proposed by Brison, Buffat, Jeandel and Serres (1985).

Considering the uncertainties normally existing in the initial conditions of the problems that are numerically simulated, it is adopted the temporal integration of the governing equations system. In the temporal integration process the initial state corresponds the beginning of the flow, when velocity and pressure fields are considered nulls. The end of the process occurs when the temporal variations of the velocity, pressure, temperature and other turbulent variables stop. The temporal discretization of the system of the governing equations, implemented by the algorithm of Brun (1988), uses sequential semi-implicit finite differences, with truncation error of order $0(\Delta t)$ and allows to make linear the equation system at each step of time.

The resolution of the coupled equations of continuity and momentum is done by a variant of Uzawa´s algorithm proposed by Buffat (1981). The statistical formulation, responsible for the obtaining of the system of average equations, is done with the simultaneous usage of the Reynolds (1895) and Favre (1965) decomposition. The Reynolds stress of turbulent tensions is calculated by the $\kappa - \varepsilon$ model, proposed by Jones and Launder (1972) with the modifications introduced by Launder and Spalding (1974). The turbulent heat flux is modeled algebraically using the turbulent Prandl number with a constant value of 0,9.

In the program Turbo2D, the boundary conditions of velocity and temperature can be calculated by four velocity and two temperature wall laws. The wall laws used in this work are of velocity are: Mellor wall law (1966), Nakayama and Koyama wall law (1984), the classic logarithm wall law and the velocity wall law of Cruz and Silva Freire (1998). The temperature wall laws available are: the Cheng and Ng (1982) and the Cruz and Silva Freire temperature wall law. In this work, as the pressure gradients are very low, we used only the logarithm wall law for velocity and the Cheng and Ng law for temperature. The numerical instability resulted of the explicit calculus of the boundary conditions of velocity, trough the evolutive temporal process, is controlled by the algorithm proposed by Fontoura Rodrigues (199). The numerical oscillations induced by the Galerkin formulation, resulting of the centered discretization applied to a parabolic phenomenon, that is the modeled flow, are cushioned by the technique of balanced dissipation, proposed by Huges and Brooks (1979) and Kelly, Nakazawa and Zienkiewicz (1976) with the numerical algorithm proposed by Brun (1988).

In order to quantify the wideness of range and the consistence of the numerical modeling done by the solver Turbo2D, the parietal heat fluxes obtained numerically are compared to the experimental data of Reynolds et al. (1958), Taylor et al. (1990) and Ng (1981), and also to empirical correlations.

2. Governing Equations

The system of non-dimensional governing equations, for a dilatable and one phase flow, without internal energy generation, and in a subsonic regime is:

$$\frac{\partial \rho}{\partial t} + \frac{\partial \rho u_i}{\partial x_i} = 0, \tag{1}$$

$$\frac{\partial \rho u_i}{\partial t} + \frac{\partial}{\partial x_j}(\rho u_i u_j) = -\frac{\partial \underline{p}}{\partial x_i} + \frac{1}{Re}\frac{\partial}{\partial x_j}\left[\mu\left(\frac{\partial u_i}{\partial x_j} + \frac{\partial u_j}{\partial x_i}\right)\right] - \frac{2}{3Re}\frac{\partial}{\partial x_j}\left(\mu\frac{\partial u_k}{\partial x_k}\delta_{ij}\right) + \frac{1}{Fr}\rho\frac{g_i}{\|g\|}, \tag{2}$$

$$\frac{\partial(\rho T)}{\partial t} + \frac{\partial(\rho u_i T)}{\partial x_i} = \frac{1}{RePr}\frac{\partial}{\partial x_i}\left(k\frac{\partial T}{\partial x_i}\right) \tag{3}$$

$$\rho(T+1) = 1. \tag{4}$$

In this system of equations ρ is the fluid specific mass, t is the time, x_i are the space cartesian coordinates in tensor notation, μ is the dynamic viscosity coefficient, δ_{ij} is the Kronecker delta operator, g_i is the acceleration due to gravity in tensor notation, T is the temperature, τ_{ij} is the viscous stress tensor in tensor notation, γ is the ratio of specific heats, k is the thermal conductivity, Re is the Reynolds number, Fr is the Froud number, Pr is the Prandtl number, M_o is the Mach number, and the non dimensional components of pressure are:

$$\underline{p} = \frac{p - p_m}{\rho_o U_o^2} \qquad \text{and} \qquad \widehat{p} = \frac{p}{p_o} \tag{5}$$

More details about the dimensionless process are given by Brun (1988). In order to simplify the notation adopted, the variables in their dimensionless form have the same representation as the dimensional variables. The Reynolds, Prandtl, Froude and Mach numbers are defined with the reference values adopted in this process.

2.1. The Turbulence Model

In this work all the dependent variables of the fluid are treated as an average value plus a fluctuation of this variable in a determinate point of space. In order to account variations of specific mass, the model used applies the well known Reynolds (1985) decomposition to pressure and fluid density and the Favre (1965) decomposition to velocity and temperature. In the Favre (1965) decomposition a randomize generic variable φ is defined as:

$$\varphi(\vec{x},t) = \widetilde{\varphi}(\vec{x}) + \varphi''(\vec{x},t) \qquad \text{with} \qquad \widetilde{\varphi} = \frac{\overline{\rho\varphi}}{\bar{\rho}}\ . \tag{6}$$

Applying the Reynolds (1895) and Favre (1965) decompositions, to the governing equations, and taking the average value of those equations, we obtain the mean Reynolds equations:

$$\frac{\partial \overline{\rho}}{\partial t} + \frac{\partial}{\partial x_i}(\overline{\rho}\widetilde{u}_i) = 0, \tag{7}$$

$$\frac{\partial}{\partial t}(\overline{\rho}\widetilde{u}_i) + \frac{\partial}{\partial x_j}(\overline{\rho}\widetilde{u}_j\widetilde{u}_i) = -\frac{\partial \overline{p}}{\partial x_i} + \frac{\partial}{\partial x_j}\left[\overline{\tau_{ij}} - \overline{\rho u_j'' u_i''}\right] + \overline{\rho} g_i, \tag{8}$$

where

$$\overline{\tau_{ij}} = \mu\left[\left(\frac{\partial \widetilde{u}_i}{\partial x_j} + \frac{\partial \widetilde{u}_j}{\partial x_i}\right) - \frac{2}{3}\frac{\partial \widetilde{u}_l}{\partial x_l}\delta_{ij}\right], \tag{9}$$

$$\frac{\partial(\overline{\rho}\widetilde{T})}{\partial t} + \frac{\partial(\widetilde{u}_i\widetilde{T})}{\partial x_i} = \frac{\partial}{\partial x_i}\left(\alpha\frac{\partial \widetilde{T}}{\partial x_i} - \overline{\rho u_i'' T''}\right) \tag{10}$$

$$\overline{p} = \overline{\rho} R\widetilde{T} \tag{11}$$

In these equations α is the molecular thermal diffusivity and two news unknown quantities appear in the momentum (8) and in the energy equation (10), defined by the correlations between the velocity fluctuations, the so-called Reynolds Stress, given by the tensor $-\overline{\rho u_i'' u_j''}$ and by the fluctuations of temperature and velocity, the so-called turbulent heat flux, defined by the vector $-\overline{\rho u_i'' T''}$.

The Reynolds stress of turbulent tensions is calculated by the $\kappa - \varepsilon$ model, proposed by Jones and Launder (1972) with the modifications introduced by Launder and Spalding (1974), where

$$-\overline{\rho u_i'' u_j''} = \mu_t\left(\frac{\partial \widetilde{u}_i}{\partial x_j} + \frac{\partial \widetilde{u}_j}{\partial x_i}\right) - \frac{2}{3}\left(\overline{\rho}\kappa + \mu_t\frac{\partial \widetilde{u}_l}{\partial x_l}\right)\delta_{ij}, \tag{12}$$

with

$$\kappa = \frac{1}{2}\overline{u_i'' u_i''}. \tag{13}$$

and

$$\mu_t = C_\mu \bar{\rho} \frac{\kappa^2}{\varepsilon} = \frac{1}{Re_t} \ . \tag{14}$$

The turbulent heat flux is modeled algebraically using the turbulent Prandl number Pr_t equal to a constant value of 0,9 by the relation

$$-\overline{\rho} \overline{u_i'' T''} = \frac{\mu_t}{Pr_t} \frac{\partial \widetilde{T}}{\partial x_i}. \tag{15}$$

In the equation (14) C_μ is a constant of calibration of the model, that values $0,09$, κ represents the turbulent kinetic energy and ε is the rate of dissipation of the turbulent kinetic energy. Once that κ and ε are additional variables, we need to know there transport equations. The transport equations of κ and ε were deduced by Jones and Launder (1972), and the closed system of equations to the $\kappa - \varepsilon$ model is given by:

$$\frac{\partial \bar{\rho}}{\partial t} + \frac{\partial \bar{\rho} \widetilde{u}_i}{\partial x_i} = 0 \ , \tag{16}$$

$$\frac{\partial \left(\bar{\rho} \widetilde{u}_i\right)}{\partial t} + \widetilde{u}_j \frac{\partial \left(\bar{\rho} \widetilde{u}_i\right)}{\partial x_j} = -\frac{\partial \bar{p^*}}{\partial x_i} + \frac{\partial}{\partial x_j} \left[\left(\frac{1}{Re} + \frac{1}{Re_t} \right) \left(\frac{\partial \widetilde{u}_i}{\partial x_j} + \frac{\partial \widetilde{u}_j}{\partial x_i} \right) \right] + \frac{1}{Fr} \bar{\rho} g_i \ , \tag{17}$$

$$\frac{\partial \left(\bar{\rho} \widetilde{T}\right)}{\partial t} + \widetilde{u}_j \frac{\partial \left(\bar{\rho} \widetilde{T}\right)}{\partial x_j} = \frac{\partial}{\partial x_j} \left[\left(\frac{1}{Re\, Pr} + \frac{1}{Re_t\, Pr_t} \right) \frac{\partial \widetilde{T}}{\partial x_j} \right] \ , \tag{18}$$

$$\frac{\partial \left(\bar{\rho} \kappa\right)}{\partial t} + \widetilde{u}_i \frac{\partial \left(\bar{\rho} \kappa\right)}{\partial x_j} = \frac{\partial}{\partial x_i} \left[\left(\frac{1}{Re} + \frac{1}{Re_t\, \sigma_\kappa} \right) \frac{\partial \kappa}{\partial x_i} \right] + \Pi - \bar{\rho} \varepsilon + \frac{\bar{\rho} \beta g_i}{Re_t\ Pr_t} \frac{\partial \widetilde{T}}{\partial x_i} \ , \tag{19}$$

$$\begin{aligned} \frac{\partial \left(\bar{\rho} \varepsilon\right)}{\partial t} + \widetilde{u}_i \frac{\partial \left(\bar{\rho} \varepsilon\right)}{\partial x_j} &= \frac{\partial}{\partial x_i} \left[\left(\frac{1}{Re} + \frac{1}{Re_t\, \sigma_\varepsilon} \right) \frac{\partial \varepsilon}{\partial x_i} \right] \\ &\quad + \frac{\varepsilon}{\kappa} \left(C_{\varepsilon 1} \Pi - C_{\varepsilon 2} \bar{\rho} \varepsilon + C_{\varepsilon 3} \frac{\bar{\rho} \beta g_i}{Re_t\ Pr_t} \frac{\partial \widetilde{T}}{\partial x_i} \right) \ , \end{aligned} \tag{20}$$

$$\bar{\rho} \left(1 + \widetilde{T}\right) = 1 \ , \tag{21}$$

where:

$$\frac{1}{Re_t} = C_\mu \bar{\rho} \frac{\kappa^2}{\varepsilon} \ , \tag{22}$$

$$\Pi = \left[\left(\frac{1}{Re_t} \right) \left(\frac{\partial \widetilde{u}_i}{\partial x_j} + \frac{\partial \widetilde{u}_j}{\partial x_i} \right) - \frac{2}{3} \left(\bar{\rho} \kappa + \frac{1}{Re_t} \frac{\partial \widetilde{u}_l}{\partial x_l} \right) \delta_{ij} \right] \frac{\partial \widetilde{u}_i}{\partial x_j} \ , \tag{23}$$

$$p^* = \bar{p} + \frac{2}{3} \left[\left(\frac{1}{Re} + \frac{1}{Re_t} \right) \frac{\partial \widetilde{u}_l}{\partial x_l} + \bar{\rho} \kappa \right] \ , \tag{24}$$

with the model constants given by:

$$C_\mu = 0,09 \ , \ C_{\varepsilon 1} = 1,44 \ , \ C_{\varepsilon 2} = 1,92 \ , \ C_{\varepsilon 3} = 0,288 \ , \ \sigma_\kappa = 1 \ , \ \sigma_\varepsilon = 1,3 \ , \ Pr_t = 0,9 \ .$$

2.2. Near Wall Treatment

The $\kappa - \epsilon$ model is incapable of properly representing the fluid behavior in the laminar sub-layer, in the buffer sub-layer and in the beginning of the logarithmic regions of the turbulent boundary layer. To solve this inconvenience, the standard solution is the use of wall laws, capable of properly representing the flow in the inner region of the turbulent boundary layer. There are four velocity and two temperature laws of the wall implemented on Turbo2D code. In this work, considering that no significative pressure gradients are involved, are used the logarithm law for velocity. The logarithm law of the wall for velocity is already well known, and further explanations are unnecessary.

For the near wall temperature, Cheng and Ng (1982) derived an expression similar to loga-rithmic law of the wall for velocity. For the numerical calculation purposes, the intersection point between laminar and logarithmic sub-layers are defined at $y^* = 15,96$, with $y^* = u_f \delta / \nu$, where u_f is the friction velocity calculated by the relation

$$u_f = \left[\left(\frac{1}{Re} + \frac{1}{Re_t} \right) \frac{\partial \widetilde{u}}{\partial x_j} \right]_\delta \ , \tag{25}$$

ν is the kinetic viscosity and δ is the distance until the wall. The temperature wall laws for laminar and logarithmic sub-layers are respectively

$$\frac{(T_0 - T)_y}{T_f} = y^* \; Pr \quad \text{and} \quad \frac{(T_0 - T)_y}{T_f} = \frac{1}{K_{Ng}} ln \; y^* + C_{Ng} \;\; , \tag{26}$$

where T_0 is the environmental temperature and T_f is the friction temperature, defined by the relation

$$T_f u_f = \left[\left(\frac{1}{Re \, Pr} + \frac{1}{Re_t \, Pr_t} \right) \frac{\partial \widetilde{T}}{\partial x_j} \right]_\delta . \tag{27}$$

In the equation (26) the constants K_{Ng} and C_{Ng} are, respectively, 0,8 and 12,5. The turbulent Prandtl number Pr_t is assumed constant and equal to 0,9.

For the turbulent kinetic energy κ and for the rate of dissipation of the turbulent kinetic energy ε, the near wall values are taken by the following relations

$$\kappa = \left[\frac{{u_f}^2}{\sqrt{C_\mu}} \right]_\delta \quad \text{and} \quad \varepsilon = \left[\frac{{u_f}^3}{K\delta} \right]_\delta , \tag{28}$$

with $K = 0,419$.

2.3. The Stanton number

In this work the parietal heat flux is estimated in a non dimension form by using the local Stanton number, calculated numerically by two distinct manners. The first one is based on a classical way to turn the local parietal heat flux q_x in a dimensionless form:

$$St_x = \frac{q_x}{\rho c_p u_\infty (T_w - T_\infty)} \qquad \text{where, for a flat plate} \qquad q_x = -k \left(\frac{\partial T}{\partial y} \right)_{y=0} . \tag{29}$$

In the equation above, the numerical method to compute the temperature gradient was by taking the temperature difference between the first node of our mesh and the temperature in the wall, and dividing it by the distance of the first node and the wall. This procedement was made, because the solver uses wall laws, and by this reason our calculus does not goes until the wall.

Another way to compute the local Stanton number is derived from a diversification of the Reynolds analogy made by Colburn (1933), for fluids with the Prandtl number equal or larger than $0,5$. The Colburn (1933) empirical correlation establish a relationship between the local Stanton number St_x, the local friction coefficient C_{fx} and the Prandtl number Pr:

$$St_x = \frac{C_{fx}}{2Pr^{\frac{2}{3}}}. \tag{30}$$

The second form to calculate the local Stanton number used in this work, proposed by Kays and Crawford (1993), is an improvement of the equation (30) by the use of the $\frac{1}{7}$ power law for temperature and velocity profiles, where δ_u and δ_T are, respectively, the thickness of the velocity and temperature boundary layers,

$$St_x = \frac{C_{fx}}{2Pr^{\frac{2}{5}}} \left(\frac{\delta_u}{\delta_T} \right)^{\frac{1}{7}} . \tag{31}$$

In the equation above, the numerical values for δ_u and δ_T were obtained by taking the heights of 300 points in the direction of the flow, with velocities equal to $0,99u_\infty$ for the hydrodynamic boundary layer, and temperatures equal to $T_w - 0,99(T_w - T_\infty)$ for the thermal boundary layer.

To evaluate the accuracy of the numerical results is possible to determine the local Stanton number by using the empirical correlation for the unheated starting length problem over flat plate:

$$St_x = \frac{1}{2} \frac{C_{fx}}{Pr^{\frac{2}{5}}} \left[1 - \left(\frac{\xi}{x} \right)^{0,9} \right]^{-\frac{1}{9}} . \tag{32}$$

To calculate the local friction coefficient C_{fx} used in equation (31), it was used the numerical value of the local friction velocity calculated by the Turbo2D

$$\frac{C_{fx}}{2} = \frac{\tau_w}{\rho u_\infty^2} \qquad \text{with} \qquad \tau_w = \rho u_f^2 \qquad \text{so} \qquad \frac{C_{fx}}{2} = \frac{u_f^2}{u_\infty^2}. \tag{33}$$

To calculate the local friction coefficient C_{fx} used in the empirical correlation, equation (32), is employed the empirical value for turbulent boundary layer

$$\frac{C_{fx}}{2} = 0.0287 Re_x^{-\frac{1}{5}}. \tag{34}$$

3. Numerical methodology

The numerical solution of a dilatable turbulent flow, has as main difficulties: the coupling between the pressure, velocity and temperature fields; the non-linear behavior of the momentum and energy equations; the explicit calculations of boundary conditions in the solid boundary; the methodology of use the continuity equation as a manner to link the coupling fields of velocity and pressure.

The solution proposed in the present work suggests a temporal discretization of the system of governing equations with a sequential semi-implicit finite difference algorithm proposed by Brun (1988) and a spatial discretization using finite elements of the type P1-isoP2. The temporal and spatial discretization implemented in Turbo 2D is presented in Fontoura Rodrigues (1990).

4. Numerical Results

All the studied experimental test cases consisted in an horizontal heated flat plate, witch receives air in a parallel direction. The difference between the cases studied are in the value of properties such as the free stream velocity of the flow, the size and temperature of the plate, and the size of the unheated starting length. The physical parameter compared from the numerical simulation to experimental data is basically the local Stanton number. The numerical value of the local Stanton number was calculated of two different ways, by using the equations (29) called "numerical 1", and using equation (31) called "numerical 2".

The Reynolds et al. (1958) test case is characterized by free stream velocities of $19,5m/s$ and $21,9m/s$. In this work the variation range of the local Reynolds number is placed between $10^5 < Re_x < 3,5x10^6$. There is a difference of $11K$ between the temperature of the plate and of the free stream flow. The test section has $1,53m$ long.

The test cases of Taylor et al. (1990) are characterized by free stream velocities of $28m/s$ and $67m/s$. In this work the variation range of the local Reynolds number is placed between $10^5 < Re_x < 10^7$. There is a difference of $18K$ between the temperature of the plate and of the free stream flow for the flow of $28m/s$ and a difference of $12K$ for the flow of $67m/s$.The test section has $2,4m$ long.

In the test cases of Reynolds et al. (1958) and Taylor et al. (1990), the values of the unheated starting length ξ, change as the free stream velocity changes. In this work, the following profiles were considered: for $u_\infty = 67m/s$ the values of ξ are $0,56m$, $0,86m$, $1,36m$; for $u_\infty = 28m/s$ the values of ξ are $0,36m$, $0,76m$, $1,36m$; for $u_\infty = 21,9m/s$ the value of ξ is $0,7243m$; for $u_\infty = 19,5m/s$ the value of ξ is $0,415m$. The simulations were made for all available results, in both works.

The Ng (1981) test case is characterized by a free stream velocity of $10,7m/s$. In this work the variation range of the local Reynolds number is placed between $5x10^5 < Re_x < 7,8x10^5$. There is a difference of $957K$ between the temperature of the plate and of the free stream flow. The test section has $0,25m$ long. In this case the plate has the same temperature in all the length of the test section.

The inlet conditions for Reynolds et al. (1958) and Taylor et al. (1990) test cases are uniform profiles for velocity, temperature, kinetic turbulent energy and its dissipation rate. In the Ng (1981) test case, a turbulent developed profile for velocity, temperature, turbulent kinetic energy and its dissipation rate. In the top part of both meshes was imposed conditions of atmospheric pressure, ambient temperature and null derivations for κ, ε, temperature and velocity. In the exit of both meshes was imposed condition of atmospheric pressure and null derivations of all other variables.

In the figure bellow, are presented ampliations of the wall region of the two meshes used to simulate the three test cases.

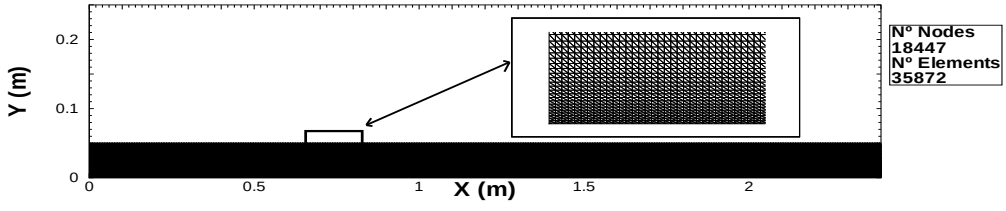

Figure 1: Velocity mesh used in Taylor et al. (1990) and Reynolds et al. (1958) test cases

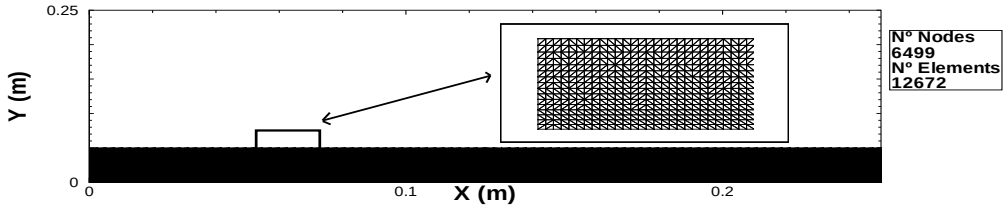

Figure 2: Velocity mesh used in Ng (1981) test case

The adoption of the same mesh in two different test cases was based in the fact that the plate used in the Reynolds et al. (1958) simulations is smaller than the plate used in the Taylor et al. (1990) simulations, besides, by the first analysis done for Taylor et al. (1990) test cases, was observed that the refinement level of the mesh was sufficient to describe the physical phenomenon.

In the following graphics, figures 3, 4 and 5, done for Taylor et al. (1990) and Reynolds et al. (1958) simulations, the empirical correlation was obtained by the use of equation (32) with the local friction coefficient calculated by equation (34), and to the numerical solutions it was used equation (29), called "numerical 1" and equation (31), called "numerical 2". So we could compare, with the experimental data, the numerical and the empirical correlation adjust term of a step wall temperature distribution in the calculus of the local Stanton number.

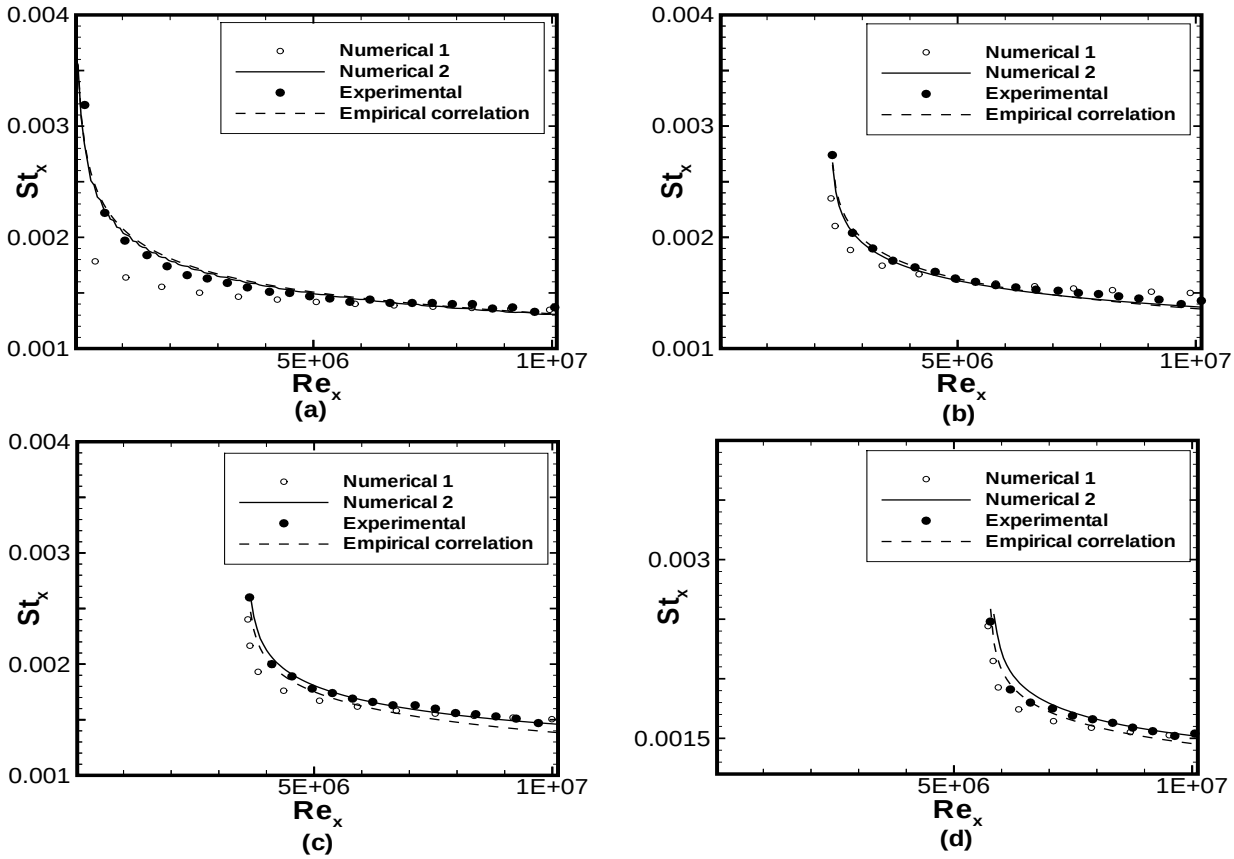

Figure 3: Local Stanton number for Taylor et al. (1990) test case. $U_\infty = 67$ - Isothermal plate (a), ξ=0,56 m (b), ξ=0,86 m (c) and ξ=1,36 m (d)

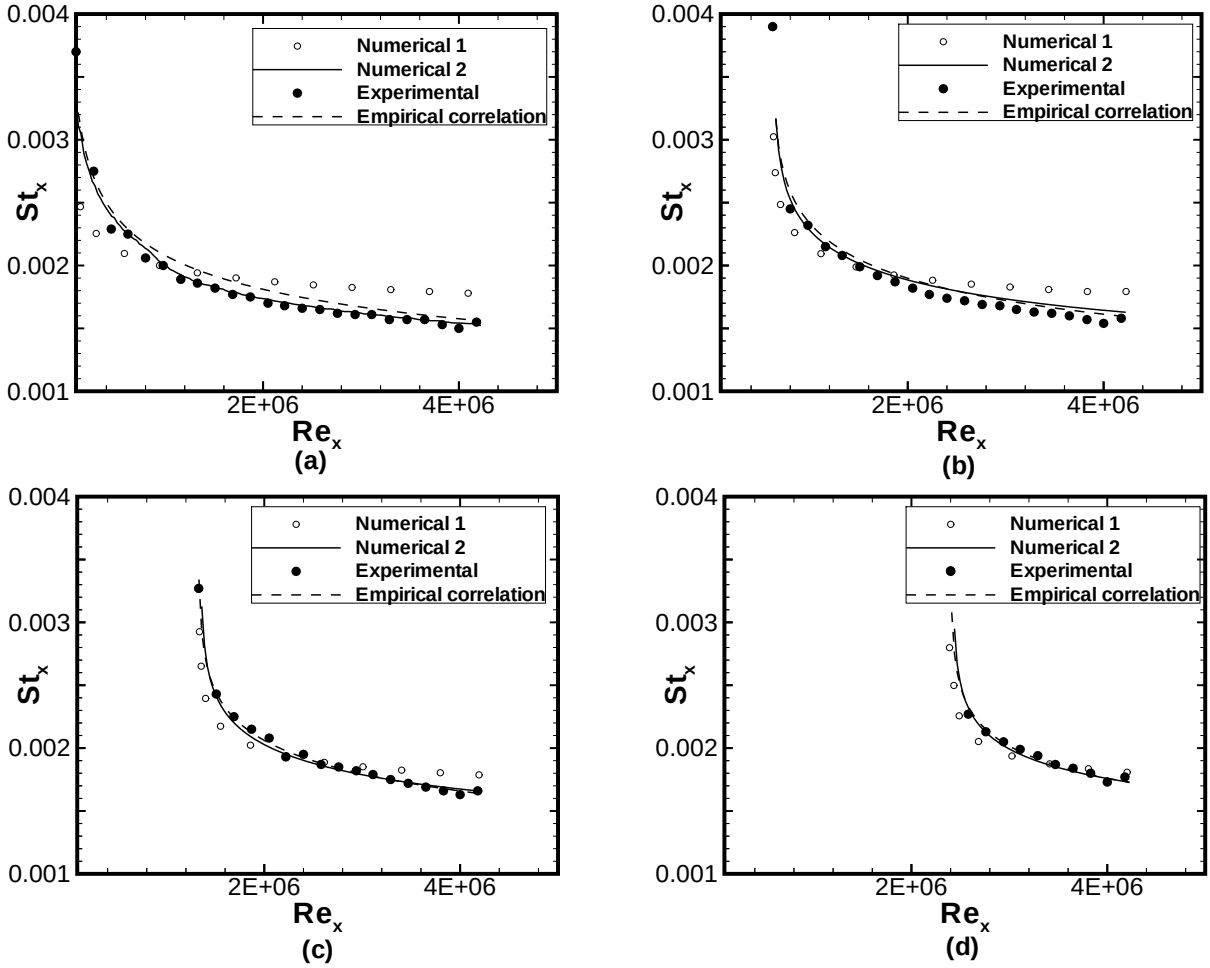

Figure 4: Local Stanton number for Taylor et al. (1990) test case. U_∞ = 28 - Isothermal plate (a), ξ=0,36 m (b), ξ=0,76 m (c) and ξ=1,36 m (d)

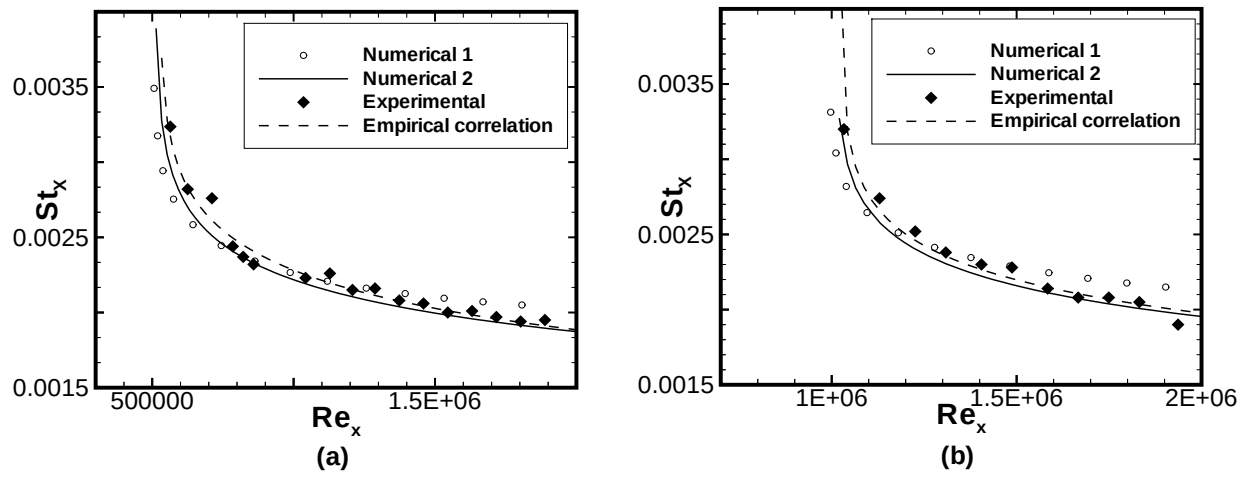

Figure 5: Local Stanton number for Reynolds et al. (1958) test case. U_∞ = 19.5 m/s with ξ= 0,415 m (a) - and 21.9 m/s with ξ=0,7243 m (b)

The following graphics, figures 6 and 7, done for the Ng (1981) test case, tries to show the precision of the code to calculate the thermal and hydrodynamic field, in cases were the velocity and the temperature field are

strongly coupled.

In the graphic of the figure 6 is shown the variation of the hydrodynamic and thermal boundary layer thickness as the air flows over the strongly heated plate of Ng (1981) test case.

In the figure 7 is shown the variation of the local Stanton number calculated of two numerical ways. The first numerical value was calculated though the derivation of the temperature in the first node of our mesh, Eq.(29), and the second one was obtained with the relation between the thermal and the hydrodynamic boundary layer thickness, Eq.(31), using the numerical value of C_{fx}.

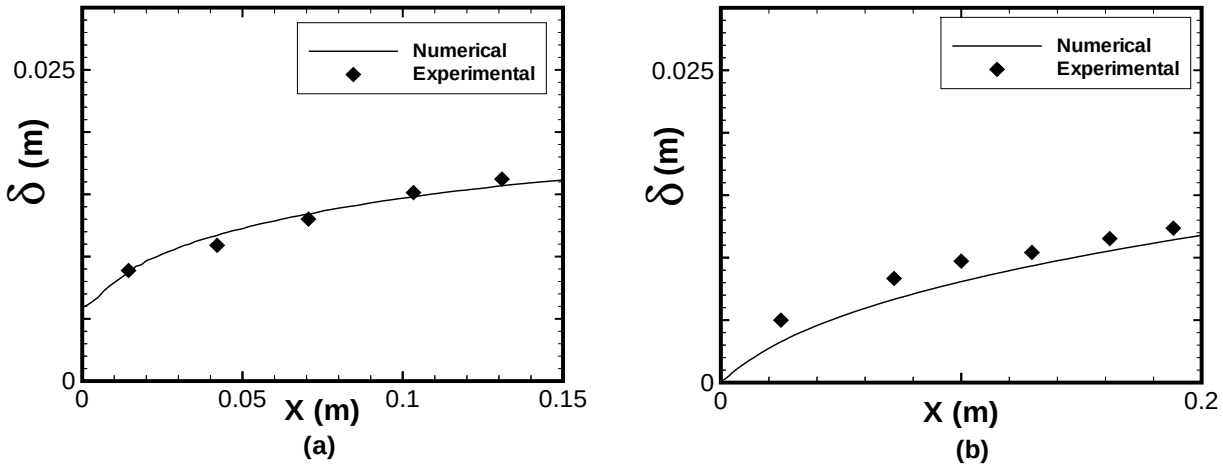

Figure 6: Hydrodynamic (a) and thermal (b) boundary layer thickness for Ng (1981) test case.

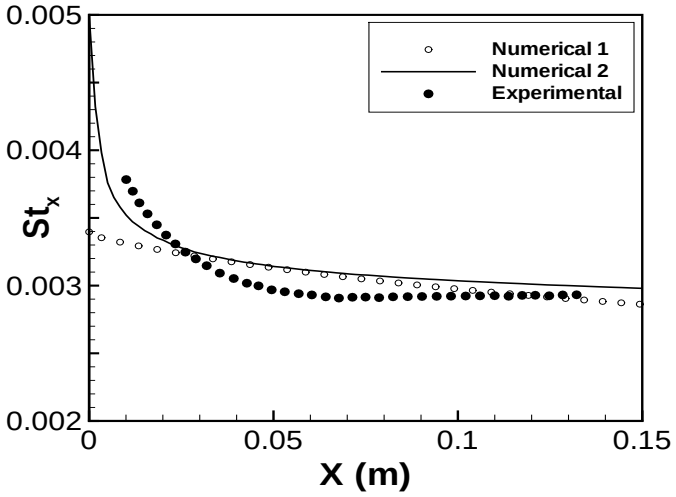

Figure 7: Stanton number - Ng (1981) test case.

5. Conclusions

We can conclude by this work, that the numerical simulation of a complex turbulent flow, done by the numerical methodology employed by the program Turbo2D, produces great results in the modeling of the forced convective turbulent heat flux, in problems were the velocity and temperature fields are coupled or uncoupled.

The results shown in figures 3, 4, 5, 6 and 7, shows that the numerical results calculated by Turbo2D solver produces very good agreement with the experimental and empirical correlation results. So, for a consolidate computational method that provides good values of the thermal and hydrodynamic boundary layer thickness along the wall, the numerical heat flux determined by using equation(31) is very accurate for turbulent flows over flat plate boundary layers.

All the results obtained numerically show that the determination of the turbulent parietal heat flux using equation (31), based on the thermal and hydrodynamical boundary layer thickness, produces better results than the ones obtained with equation (29), based on the temperature gradient in the normal direction to the wall. The results obtained with the equation (29) can be improved if more refined calculation meshes are employed.

6. Acknowledgements

We are grateful to the colleagues, professors and students of the Group of Complex Fluid Dynamics - Vortex, from the Department of Mechanical Engineering of University of Brasília, for the encouragement and technical support during the accomplishment of this work. We also thank the Technology and Scientific Enterprize Foundation - FINATEC, for the material and financial support, which made this work possible.

7. References

Boussinesq, J., 1877, "Théorie de l´Écoulement Tourbillant" , Mem. Présentés par Divers Savants Acad. Sci. Inst. Fr., vol. 23, pp. 46-50.

Reynolds, O., 1895, "On The Dynamical Theory of Incompressible Viscous Fluids and the Determination of the Criterium" , Philosophical Transactions of the Royal Society of London, Series A, Vol 186, p. 123

Brun, G., 1988, "Developpement et application d´une methode d´elements finis pour le calcul des ecoulements turbulents fortement chauffes " , Doctorat thesis, Laboratoire de Mécanique des Fluides, Escola Central de Lyon.

Buffat, M., 1981, "Formulation moindre carrés adaptées au traitement des effets convectifs dans les équation de Navier- Stokes", Doctorat thesis, Université Claude Bernard, Lyon, France.

Brison ,J. F., Buffat, M., Jeandel,D., Serrer,E., 1985, "Finite elements simulation of turbulent flows, using a two equation model", Numerical methods in laminar and turbulent flows, Swansea. Pineridg Press.

Cheng, R.K. and Ng, T.T., 1982, "Some aspects of strongly heated turbulent boundary layer flow". Physics of Fluids, vol. 25(8).

Colburn, A.P., 1933 , "A method for correlating forced convection heat transfer data and a comparison with fluid friction " Transaction of American Institute of Chemical Engineers, vol. 29, pp. 174-210.

Favre, A., 1965, "Equations de gaz turbulents compressibles". Journal de mecanique, vol. 3 e vol. 4.

Fontoura Rodrigues, J. L. A., 1990, "Méthode de minimisation adaptée à la techinique des éléments finis pour la simulation des écoulements turbulents avec conditions aux limites non linéaires de proche paroi", Doctorat thesis, Ecole Centrale de Lyon, France.

Jones, W. and Launder, B.E., 1972, "The prediction of laminarization with a two equations model of turbulence", International Journal of Heat and Mass Transfer, vol. 15, pp. 301-314.

Launder, B.E. and Spalding, D.B., 1974, "The numerical computation of turbulent flows", Computational Methods in Applied Mechanical Engineering, vol. 3, pp. 269-289

Mellor, G.L., 1966, "The effects of pressure gradients on turbulent flow near a smooth wall", Journal of Fluid Mechanics, vol. 24, n^o 2, pp. 255-274

Nakayama, A., Koyama, H., 1984, "A wall law for turbulent boundary layers in adverse pressure gradients", AIAA Journal, vol. 22, n^o 10, pp. 1386-1389

Cruz, D.O.A., Silva Freire, A.P., 1998, "On single limits and the asymptotic behavior of separating turbulent boundary layers", International Journal of Heat and Mass Transfer, vol. 41, n^o 14, pp. 2097-2111

Bejan, A., 1994, "Convective Heat Transfer", John Wily & Sons, USA.

Kays,W.M., Crawford, M.E. 1993, "Convective Heat and Mass Transfer", McGraw Hill, INC., USA

Ng, T.T., 1981., "Experimental study of a chemically reacting turbulent boundary layer", Ph. D. Thesis, Lawrence Berkley Laboratory, University of California.

Taylor, R.P. , Love, P.H. , Coleman, H.W. and Hosni, M.H. 1990. "Heat Transfer Measurements in Incompressible Turbulent Flat Plate Boundary Layers With Step Wall Temperature Boundary Conditions", Journal of Heat Transfer, vol.112, pp 245-247.

Reynolds, W.C., Kays, W.M. and Kline, S.J., 1958, "Heat Transfer in The Turbulent Incompressible Boundary Layer - II - Step Wall-Temperature Distribution", NASA Memorandum.

Proceedings of the 11th Brazilian Congress of Thermal Sciences and Engineering -- ENCIT 2006
Braz. Soc. of Mechanical Sciences and Engineering -- ABCM, Curitiba, Brazil, Dec. 5=8, 2006

Paper CIT06-0378

SOLUÇÃO HIDRODINÂMICA E MODELO CINÉTICO PARA MISTURAS BINÁRIAS

Valdete dos Santos Coqueiro
vcoqueiro@yahoo.com.br

Liliana Madalena Gramani Cumin
Departamento de Matemática – UFPr – Caixa Postal 19044, Cep 81531-990 – Curitiba – Paraná - Brasil
gramani@mat.ufpr.br

Resumo. *O problema do escoamento de Couette estudado, consiste de uma mistura binária de gases nobres confinada entre duas placas paralelas suficientemente longas de forma que os efeitos de borda podem ser desprezados. Inicialmente o sistema encontra-se em equilíbrio, sendo fracamente perturbado através do movimento relativo das placas que caracteriza o escoamento de Couette. A função de distribuição para cada constituinte da mistura obedece a um sistema de equações íntegro-diferenciais acopladas que se baseiam na equação de Boltzmann. As soluções são estudadas com base no modelo cinético de McCormack para a equação de Boltzmann. Os cálculos numéricos são realizados para três misturas de gases nobres: Nêonio e Argônio, Hélio e Argônio, e Hélio e Xenônio. Foram calculados o tensor tensão, a velocidade hidrodinâmica de cada constituinte e da mistura em todo o intervalo do número de Knudsen. As concentrações molares dos gases são consideradas nas proporções de 10%, 50% e 90%. Foram comparados os resultados obtidos quando se utilizam diferentes potenciais de interação entre as partículas, como por exemplo, o potencial de esfera-rígida e o potencial de Lennard-Jones. Também foi comparado a solução cinética e a solução hidrodinâmica para o tensor tensão e a velocidade hidrodinâmica da mistura.*

Palavras chave: Fluxo de Couette, Misturas de gases, Potencial intermolecular, Número de Knudsen.

1. Introdução

O escoamento de Couette plano é um problema clássico da dinâmica de gases rarefeitos, o qual tem sido pesquisado por vários autores quando se refere ao caso de gás único (Cercignani, 2000). Assim, o interesse sosbre este tipo de fluxo em misturas de gases tem freqüentemente aumentado, pois o estudo dos fenômenos de transporte no escoamento de gases rarefeitos é utilizado para o desenvolvimento tecnológico de equipamentos de vácuo, indústria aeronáutica, microengenharia, etc. Porém, existem poucos trabalhos na literatura sobre este fluxo para misturas de gases dentro de um amplo intervalo do número de Knudsen. Então, o fluxo de Couette será estudado para o caso de uma mistura binária confinada entre duas placas paralelas suficientemente longas de forma que os efeitos de borda podem ser desprezados.

Em escoamento de gases rarefeitos costuma-se caracterizar o regime de escoamento pelo chamado número de Knudsen *Kn* o qual é um parâmetro que indica o grau de rarefação de um gás. É definido como a razão entre o livre caminho médio molecular e um comprimento característico do problema em estudo. Assim, o regime de escoamento se divide em três tipos: regime de moléculas livres ($Kn \to \infty$), regime hidrodinâmico ($Kn \to 0$) e regime de transição ($Kn \cong 1$). A Mecânica do Contínuo é aplicada somente ao regime hidrodinâmico. Para abranger todo o intervalo do número de Knudsen é necessário aplicar a Dinâmica dos Gases Rarefeitos, cujos métodos se baseiam: (i) na solução da equação de Boltzmann (Cercignani, 1988 e Cercignani, 2000) (ii) ou na simulação de Monte Carlo (Bird, 1976), o qual não será abordado neste trabalho.

A equação de Boltzmann é uma equação íntegro-diferencial, complexa devido a integral de colisões entre as partículas. Para simplificar a equação de Boltzmann usando todo o intervalo do número de Knudsen surgiu a idéia de simplificar a integral de colisões utilizando um modelo matemático para essa integral. A escolha desse modelo matemático, deve satisfazer as seguintes condições: (i) a conservação da massa, do momento linear e da energia de cada colisão entre as partículas; (ii) a equação modelo, também denominada de equação cinética deve fornecer corretamente todos os coeficientes de transporte (viscosidade, condutividade térmica, etc) e (iii) no estado de equilíbrio a integral de colisões deve ser nula.

Ao se considerar uma mistura de gases monoatômicos, a diferença entre os constituintes ocorrerá entre as suas massas atômicas, diâmetros moleculares e formas de iteração entre as moléculas dos diferentes constituintes. Por exemplo, quando as moléculas são consideradas como esfera-rígida a diferença entre os diâmetros das moléculas torna-se representativa. Ainda, o tratamento matemático é baseado na Teoria Cinética dos Gases que envolverá uma função de distribuição $f_\alpha \ (\alpha = 1, 2, ..., n)$ presente na equação de Boltzmann, para cada um dos *n* constituintes da mistura. Então se tem, de uma forma geral, que o sistema constituí-se de um sistema de *n* equações de Boltzmann acopladas para as *n* funções de distribuição.

Neste trabalho, o objetivo é estudar o problema do fluxo de Couette plano para uma mistura binária de gases monoatômicos com base no modelo cinético de McCormack (McCormack, 1973) para um amplo intervalo do número de Knudsen.

2. Estudo do Problema

Considera-se uma mistura binária de gases monoatômicos confinada entre duas placas paralelas fixadas a uma distância $y' = \pm D/2$. O estado de equilíbrio é fracamente perturbado por um movimento das placas na direção x' com velocidades $\pm U/2$ respectivamente. Assume-se que as velocidades do plano são pequenas comparadas com a velocidade molecular característica da mistura, isto é,

$$U << v_0,\ v_0 = \left(\frac{2kT_0}{m}\right)^{1/2}, \tag{1}$$

onde *k* é a constante de Boltzmann, T_0 é a temperatura de equilíbrio, e *m* é a massa molecular média

$$m = C_0 m_1 + (1 - C_0) m_2, \tag{2}$$

e C_0 a concentração molar da mistura em equilíbrio, m_1 e m_2 são as massas moleculares de cada constituinte.

Será calculado a velocidade hidrodinâmica e o tensor tensão de cada constituinte e da mistura para as três misturas binárias: Neônio e Argônio; Hélio e Argônio; e Hélio e Xenônio, para um amplo intervalo do número de Knudsen $0 < Kn < \infty$. As misturas apresentam razões de massas m_1 / m_2 bem distintas 0,505, 0,100 e 0,030, além das razões entre os seus diâmetros d_2 / d_1 serem de 1,406, 1,665 e 2,226, respectivamente. As concentrações consideradas para estas misturas serão nas proporções de 10%, 50% e 90%, para o primeiro constituinte. Estes cálculos serão feitos para dois tipos de potenciais intermoleculares: esfera-rígida e Lennard-Jones, ambos considerando uma temperatura inicial de 300K.

3. Solução Hidrodinâmica e Resultados

O objetivo é calcular o tensor tensão P'_{xy} entre as placas e a velocidade da mistura u'_x, com base na Mecânica do Contínuo. A velocidade da mistura u'_x está relacionada com as velocidades médias de cada constituinte $u'_{\alpha x}(\alpha = 1, 2)$ através de

$$u'_x = \frac{1}{\rho_1 + \rho_2}(\rho_1 u'_{1x} + \rho_2 u'_{2x}), \qquad \rho_\alpha = n_{0\alpha} m_\alpha \tag{3}$$

onde ρ_α, $(\alpha = 1, 2)$ representa a densidade de massa de cada constituinte da mistura, $n_{0\alpha}$ a distribuição da densidade em equilíbrio do número de partículas do constituinte α e m_α a massa da partícula do constituinte α. O parâmetro de rarefação do gás, δ, que caracteriza a rarefação do gás é definido como:

$$\delta = \frac{DP_0}{\mu v_0} \tag{4}$$

onde P_0 denota a pressão em equilíbrio, μ a viscosidade do gás considerado e D representa a distância entre as placas paralelas suficientemente longas para que os efeitos de borda possam ser desprezados.

No regime hidrodinâmico $(\delta \to \infty \text{ ou } Kn \to 0)$ o livre caminho médio é muito menor que o comprimento característico do escoamento e, consequentemente, o meio gasoso pode ser considerado como um meio contínuo no qual as equações da hidrodinâmica podem ser aplicadas. Neste regime, utiliza-se a equação de Navier-Stokes (Landau, 1976), com as condições de contorno sem deslizamento da velocidade escritas abaixo:

$$u'_x = \frac{U}{D} y', \tag{5}$$

$$P'_{xy} = -\mu \frac{\partial u'_x}{\partial y'}, \tag{6}$$

ou reescrevendo,

$$P'_{xy} = -\mu \frac{U}{D}. \tag{7}$$

É conveniente introduzir quantidades adimensionais para a velocidade da mistura, posição e o tensor tensão

$$u = \frac{u'_x}{U}, \qquad y = \frac{y'}{D}, \text{e} \quad \prod = -\frac{v_0}{2UP_0} P'_{xy}. \tag{8}$$

Em Mecânica do Contínuo é comum considerar as seguintes condições de contorno para a velocidade e o tensor tensão na superfície das placas

$$u'_x = u'_{\text{superfície}}, \qquad P'_{xy} = P'_{xy\,\text{superfície}} \tag{9}$$

isto é, a velocidade e o tensor tensão da mistura são iguais a velocidade e o tensor tensão da superfície.

As expressões (9) são válidas quando o número de Knudsen é pequeno, isto é, se está no regime hidrodinâmico. Entretanto quando o número de Knudsen aumenta, isto é, o gás se torna mais rarefeito, as condições acima não são mais válidas, pois há um deslizamento da velocidade.

Para avaliar a condição de deslizamento da velocidade escreve-se, de acordo com (Sharipov & Seleznez, 1998) que

$$u'_x = \pm\frac{U}{2} \mp \sigma_P \frac{\mu v_0}{P} \frac{\partial u'_x}{\partial y'}, \text{ em} \qquad y' = \pm\frac{D}{2} \tag{10}$$

onde σ_P é o coeficiente de deslizamento viscoso. A velocidade u'_x é escrita como uma função da posição, sendo representada por

$$u'_x = A + By', \tag{11}$$

onde A e B são constantes a serem determinadas. Substituindo-se as condições de contorno (10) em (11) encontra-se as constantes A e B. Assim, será possível expressar a velocidade u'_x por

$$u'_x = \frac{U}{D}\left(1 + \frac{2\sigma_P}{\delta}\right)^{-1} y' \tag{12}$$

Utilizando-se a Eq. (12) na Eq. (6) tem-se,

$$P'_{xy} = -\mu \frac{U}{D}\left(1 + \frac{2\sigma_P}{\delta}\right)^{-1}. \tag{13}$$

Utilizando-se a Eq.(8) nas equações (12) e (13) obtém-se as equações para a velocidade da mistura e o tensor tensão em termos das quantidades adimensionais como sendo

$$u = \left(1 + \frac{2\sigma_P}{\delta}\right)^{-1} y, \tag{14}$$

e,

$$\Pi = \frac{1}{2\delta + 4\sigma_P}. \tag{15}$$

Os valores do coeficiente de deslizamento viscoso σ_P são encontrados em (Sharipov & Seleznez, 1998) para um gás único, e em (Cercignani, Lampis & Lentati, 1994; Ivchenko, Loyalka & Thompson, 1997; Ivchenko, Loyalka & Thompson, 2002; Sharipov & Kalempa, 2003) para misturas de gases.

As equações (14) e (15) são equações que expressam a velocidade adimensional da mistura e o tensor tensão da mistura em função do parâmetro de rarefação e o coeficiente de deslizamento viscoso.

Na Tab.(1) são representados valores da velocidade u da mistura na distância $y = 1/2$ e o tensor tensão Π da mistura em função do parâmetro de rarefação δ. Os valores do coeficiente de deslizamento σ_P foram retirados do artigo (Sharipov & Kalempa, 2003) para todas as misturas consideradas.

Tabela 1. Velocidade u da mistura na distância y = 1/2 e o tensor tensão Π da mistura vs o parâmetro de rarefação δ para as misturas Ne-Ar, He-Ar e He-Xe.

	Ne-Ar $\sigma_P = 1{,}040$		He-Ar $\sigma_P = 1{,}150$		He-Xe $\sigma_P = 1{,}259$	
δ	u	Π	u	Π	u	Π
0,4	0,08065	0,2016	0,07407	0,1852	0,06854	0,1714
0,1	0,02294	0,2294	0,02083	0,2083	0,01910	0,1910
1	0,1623	0,1623	0,1515	0,1515	0,1421	0,1421
2	0,2451	0,1225	0,2326	0,1163	0,2213	0,1107
4	0,3289	0,08224	0,3175	0,07937	0,3068	0,07671
10	0,4139	0,04139	0,4065	0,04065	0,3994	0,03994
20	0,4529	0,02264	0,4484	0,02242	0,4441	0,02220
40	0,4753	0,01188	0,4728	0,01182	0,4704	0,01176

4. Modelo Cinético

A função de distribuição para cada constituinte α da mistura obedece a equação de Boltzmann

$$v'_{\alpha i} \frac{\partial f_\alpha}{\partial x'_i} = \sum_{\beta=1}^{2} Q_{\alpha\beta}(f_\alpha, f_\beta). \tag{16}$$

A Equação (16) representa uma equação íntegro-diferencial, não-linear para o caso de mistura de gases monoatômicos em regime de escoamento estacionário $(\partial f_\alpha / \partial t = 0)$ e sem a presença de forças externas $(F_i = 0)$. A integral de colisões entre as partículas α e β esta sendo representado pelo operador de colisão quadrática $Q_{\alpha\beta}(f_\alpha, f_\beta)$, também denominada de termo de colisão. A principal dificuldade matemática apresentada na equação de Boltzmann está associada com o termo de colisão $Q_{\alpha\beta}(f_\alpha, f_\beta)$. Muitas alternativas são analisadas com o objetivo de simplificar o termo de colisão facilitando assim a solução da equação de Boltzmann. Expressões mais simples para este termo tem sido propostas por diversos autores. Estas são conhecidas como modelo de colisão e a equação de Boltzmann na qual o termo de colisão é substituído por um modelo passa a ser chamada de equação modelo (Bird, 1976; Ohwada, 1998) O objetivo desta substituição é facilitar a resolução da equação de Boltzmann de forma a fornecer resultados satisfatórios, isto é, a equação modelo deve apresentar bons resultados que podem ser comparáveis aos resultados da solução exata da equação de Boltzmann (Sharipov & Seleznez, 1998). Assim o termo de colisão poderá ser substituído por um operador o qual deverá ter a conservação da massa, conservação do momento linear e a conservação da energia de cada colisão de uma partícula α com uma partícula β.

No modelo cinético utilizado neste trabalho, a expressão do operador de colisão que quadrática é dada por

$$Q_{\alpha\beta} = -\upsilon'_{\alpha\beta}(f_\alpha - f^R_{\alpha\beta}). \tag{17}$$

$\upsilon'_{\alpha\beta}$ denota a freqüência de colisão independe das velocidades das partículas, f_α representa a função de distribuição dos constituintes e $f^R_{\alpha\beta}$ a função de distribuição de referência.

Substituindo-se a expressão do operador de colisão quadrática Eq. (17) na Eq. (16) encontra-se a equação modelo

$$v'_{\alpha i}\frac{\partial f_\alpha}{\partial x'_i} = -\sum_{\beta=1}^{2}\upsilon'_{\alpha\beta}\,(f_\alpha - f^R_{\alpha\beta}), \tag{18}$$

Para este problema tem-se para a função de distribuição dos constituintes

$$f_\alpha(\vec{x}',\vec{v}'_\alpha) = f_\alpha^M(\vec{v}'_\alpha)\left[1+h_\alpha(y',\vec{v}'_\alpha)\frac{U}{v_0}\right], \tag{19}$$

onde f_α^M é a função de distribuição Maxwelliana (Kremer, 2003) correspondente ao estado de equilíbrio

$$f_\alpha^M = n_{0\alpha}\left(\frac{m_\alpha}{2\pi kT_0}\right)^{3/2}\exp\left(-\frac{m_\alpha}{2kT_0}v'^2_\alpha\right), \tag{20}$$

$h_\alpha(y',\vec{v}'_\alpha)$ representa a perturbação da função de distribuição do sistema que obedece a equação de Boltzmann e $n_{0\alpha}$ é a distribuição da densidade em equilíbrio do número de partículas do constituinte α entre as placas. É conveniente introduzir quantidades adimensionais para as quantidades da velocidade molecular do constituinte α, $\vec{v}'_\alpha$ e a posição $\vec{x}'$. Desta forma a velocidade dimensional $\vec{v}'_\alpha$ esta relacionada com a velocidade adimensional $\vec{c}_\alpha$ através do parâmetro $\beta_{0\alpha}=(m_\alpha/2kT_0)^{1/2}$, ou seja

$$\vec{v}'_\alpha = \beta_{0\alpha}^{-1}\vec{c}_\alpha \tag{21}$$

e introduz-se a grandeza adimensional

$$\vec{x} = \frac{\vec{x}'}{D}. \tag{22}$$

Substituindo-se Eq. (19) – Eq. (22) na Eq. (18) tem-se a equação adimensional

$$c_{\alpha y}\frac{\partial h_\alpha}{\partial y} = D\left(\frac{m_\alpha}{2kT_0}\right)^{1/2}\sum_{\beta=1}^{2}\hat{L}_{\alpha\beta}h, \qquad \alpha=1,2, \tag{23}$$

O modelo cinético proposto por McCormack representa $\hat{L}_{\alpha\beta}h$ como uma expansão de um polinômio da velocidade adimensional c_α, ou seja,

$$\hat{L}_{\alpha\beta}h = -\gamma_{\alpha\beta}h_\alpha + A + A_k c_{\alpha k} + B_{kl}c_{\alpha k}c_{\alpha l} + D_k c_{\alpha k}c_\alpha^2. \tag{24}$$

O parâmetro $\gamma_{\alpha\beta}$ é proporcional a freqüência de colisão entre os constituintes α e β (Cercignani & Sharipov, 1992).

Para uma mistura binária, confinada entre duas placas paralelas, com velocidades relativas sujeitas a uma mesma temperatura, tem-se

$$\hat{L}_{\alpha\beta}h = -\gamma_{\alpha\beta}h_\alpha + 2\left(\frac{m_\alpha}{m}\right)^{1/2}\left[\gamma_{\alpha\beta}u_\alpha - \upsilon^{(1)}_{\alpha\beta}(u_\alpha - u_\beta) - \frac{\upsilon^{(2)}_{\alpha\beta}}{2}\left(q_\alpha - \frac{m_\alpha}{m_\beta}q_\beta\right)\right]c_{\alpha x}$$
$$+ 4\left[\left(\gamma_{\alpha\beta} - \upsilon^{(3)}_{\alpha\beta}\right)\Pi_\alpha + \upsilon^{(4)}_{\alpha\beta}\Pi_\beta\right]c_{\alpha x}c_{\alpha y} + \frac{4}{5}\left(\frac{m_\alpha}{m}\right)^{1/2}\left[\left(\gamma_{\alpha\beta} - \upsilon^{(5)}_{\alpha\beta}\right)q_\alpha + \upsilon^{(6)}_{\alpha\beta}\left(\frac{m_\beta}{m_\alpha}\right)^{1/2}q_\beta\right.$$
$$\left. - \frac{5}{4}\upsilon^{(2)}_{\alpha\beta}(u_\alpha - u_\beta)\right]c_{\alpha x}\left(c_\alpha^2 - \frac{5}{2}\right), \qquad \alpha,\beta = 1,2, \tag{25}$$

e as quantidades $\upsilon^N_{\alpha\beta}$, representam a freqüência de colisões entre os constituintes α e β. Os momentos adimensionais da função de distribuição são escritos (Ivchenko, Loyalka & Thompson 2002) do seguinte modo:

$$u_\alpha(y) = \frac{1}{\pi^{3/2}}\left(\frac{m}{m_\alpha}\right)^{1/2}\int \exp\left(-c_\alpha^2\right)h_\alpha\left(y,\vec{c_\alpha}\right)c_{\alpha x}\,d\vec{c_\alpha}, \tag{26}$$

$$q_\alpha(y) = \frac{1}{\pi^{3/2}}\left(\frac{m}{m_\alpha}\right)^{1/2}\int \exp\left(-c_\alpha^2\right)h_\alpha\left(y,\vec{c_\alpha}\right)c_{\alpha x}\left(c_\alpha^2 - \frac{5}{2}\right)d\vec{c_\alpha}, \tag{27}$$

$$\Pi_\alpha(y) = \frac{1}{\pi^{3/2}}\int \exp\left(-c_\alpha^2\right)h_\alpha\left(y,\vec{c_\alpha}\right)c_{\alpha x}c_{\alpha y}\,d\vec{c_\alpha}, \tag{28}$$

onde u_β, q_β e Π_β são semelhantes as equações (26), (27) e (28), respectivamente bastando trocar α por β.

As condições de contorno para a perturbação h_α da Eq. (23) são dadas por:

$$h_\alpha\left(y,\vec{c_\alpha}\right) = h_\alpha\left(\pm\frac{D}{2},\vec{c_\alpha}\right) = \pm\left(\frac{m_\alpha}{m}\right)^{1/2}c_{\alpha x}, \quad \text{para } c_{\alpha x} > \text{ou} < 0. \tag{29}$$

4.1. Método de Solução

A Eq. (23) é função das componentes da velocidade adimensional $c_{\alpha i} = (c_{\alpha x}, c_{\alpha y}, c_{\alpha z})$. Como a solução independe das coordenadas *x* e *z*, para eliminar as variáveis $c_{\alpha x}$ e $c_{\alpha z}$ da Eq. (23) duas funções são introduzidas:

$$\Phi_\alpha = \frac{1}{\pi}\int_{-\infty}^{+\infty}\int_{-\infty}^{+\infty}\exp\left[-\left(c_{\alpha x}^2 + c_{\alpha z}^2\right)\right]h_\alpha c_{\alpha x}dc_{\alpha x}dc_{\alpha z}, \tag{30}$$

$$\Psi_\alpha = \frac{1}{\pi}\int_{-\infty}^{+\infty}\int_{-\infty}^{+\infty}\exp\left[-\left(c_{\alpha x}^2 + c_{\alpha z}^2\right)\right]\left[c_{\alpha x}^2 + c_{\alpha z}^2 - 2\right]h_\alpha c_{\alpha x}dc_{\alpha x}dc_{\alpha z}, \tag{31}$$

Para se escrever a Eq. (23) em função de Φ_α e Ψ_α deve-se multiplicá-la pelos respectivos fatores $c_{\alpha x}e^{-(c_{\alpha x}^2 + c_{\alpha z}^2)}/\pi$ e $c_{\alpha x}[c_{\alpha x}^2 + c_{\alpha z}^2 - 2]e^{-(c_{\alpha x}^2 + c_{\alpha z}^2)}/\pi$ e depois integrar este sistema de equações em todo o intervalo da velocidade, em relação a $dc_{\alpha x}$ e $dc_{\alpha z}$ que transformam a Eq. (23) em um sistema de equações para Φ_α e Ψ_α,

$$c_{\alpha y}\frac{\partial\Phi_\alpha}{\partial y} = \delta_\alpha\left\{-\Phi_\alpha + \left(\frac{m_\alpha}{m}\right)^{1/2}\left(u_\alpha - \frac{\upsilon^{(1)}_{\alpha\beta}}{\gamma_{\alpha\beta}}(u_\alpha - u_\beta) - \frac{\upsilon^{(2)}_{\alpha\beta}}{2\gamma_{\alpha\beta}}\left(q_\alpha - \frac{m_\alpha}{m_\beta}q_\beta\right)\right)\right.$$

$$+2\left(\left(1-\frac{\upsilon_{\alpha\alpha}^{(3)}+\upsilon_{\alpha\alpha}^{(4)}-\upsilon_{\alpha\beta}^{(3)}}{\gamma_{\alpha\beta}}\right)\Pi_\alpha+\frac{\upsilon_{\alpha\beta}^{(4)}}{\gamma_{\alpha\beta}}\Pi_\beta\right)c_{\alpha y}$$

$$+\left(\frac{m_\alpha}{m}\right)^{1/2}\left[\frac{4}{5}\left(\left(1+\frac{\upsilon_{\alpha\alpha}^{(6)}-\upsilon_{\alpha\alpha}^{(5)}-\upsilon_{\alpha\beta}^{(5)}}{\gamma_{\alpha\beta}}\right)q_\alpha+\frac{\upsilon_{\alpha\beta}^{(6)}}{\gamma_{\alpha\beta}}\left(\frac{m_\beta}{m_\alpha}\right)^{1/2}q_\beta\right)\right.$$

$$\left.-\frac{\upsilon_{\alpha\beta}^{(2)}}{\gamma_{\alpha\beta}}\left(u_\alpha-u_\beta\right)\right]\frac{1}{2}\left(c_{\alpha y}^2-\frac{1}{2}\right)\Bigg\}, \qquad \text{e} \tag{32}$$

$$c_{\alpha y}\frac{\partial\Psi_\alpha}{\partial y}=\delta_\alpha\left\{-\Psi_\alpha+\left(\frac{m_\alpha}{m}\right)^{1/2}\left[\frac{4}{5}\left[\left[1+\frac{\upsilon_{\alpha\alpha}^{(6)}-\upsilon_{\alpha\alpha}^{(5)}-\upsilon_{\alpha\beta}^{(5)}}{\gamma_{\alpha\beta}}\right]q_\alpha+\frac{\upsilon_{\alpha\beta}^{(6)}}{\gamma_{\alpha\beta}}\left(\frac{m_\beta}{m_\alpha}\right)^{1/2}q_\beta\right]\right.\right.$$

$$\left.\left.-\frac{\upsilon_{\alpha\beta}^{(2)}}{\gamma_{\alpha\beta}}\left(u_\alpha-u_\beta\right)\right]\right\}. \tag{33}$$

É utilizado com maior freqüência o parâmetro de rarefação do constituinte α da mistura δ_α ao invés do número de Knudsen *Kn*, definido por,

$$\delta_\alpha=D\left(\frac{m_\alpha}{2kT_0}\right)^{1/2}\gamma_\alpha, \tag{34}$$

onde $\gamma_\alpha=P_\alpha/\mu_\alpha$ com P_α e μ_α representando a pressão parcial e a viscosidade parcial, respectivamente, (Cercignani & Sharipov, 1992). Nas equações (32) e (33) os momentos adimensionais da função de distribuição $u_\alpha, u_\beta, q_\alpha, q_\beta, \Pi_\alpha$ e Π_β são descritos nas equações (34)-(36) e representam as incógnitas. Estes momentos escritos em função de Φ_α e Ψ_α são:

$$u_\alpha(y)=\frac{1}{\sqrt{\pi}}\left(\frac{m}{m_\alpha}\right)^{1/2}\int\exp\left(-c_{\alpha y}^2\right)\Phi_\alpha dc_{\alpha y}, \tag{35}$$

$$q_\alpha(y)=\frac{1}{\sqrt{\pi}}\left(\frac{m}{m_\alpha}\right)^{1/2}\int\left[\Psi_\alpha+\Phi_\alpha\left(c_{\alpha y}^2-\frac{1}{2}\right)\right]\exp\left(-c_{\alpha y}^2\right)dc_{\alpha y}, \tag{36}$$

$$\Pi_\alpha(y)=\frac{1}{\sqrt{\pi}}\int\exp\left(-c_{\alpha y}^2\right)c_{\alpha y}\Phi_\alpha dc_{\alpha y}, \tag{37}$$

onde u_β, q_β e Π_β são semelhantes as equações (35), (36) e (37), respectivamente bastando trocar α por β.

O objetivo é resolver este sistema de equações íntegro-diferenciais (32) e (33) e nas quais utilizando Eq. (29) em Eqs. (30) e (31), se obtém as respectivas condições de contorno. Este sistema de equações pode ser reduzido à um sistema de equações de integrais para os momentos da função de distribuição. Entretanto, este método requer um grande tempo computacional, especialmente para grandes valores do parâmetro de rarefação δ, que é o inverso do número de Knudsen *Kn***.** Este é um dos motivos pelos quais deve-se usar o método das velocidades discretas (Kogan, 1969; Sharipov & Subbotin, 1993).

4.2. Resultados Numéricos e Discussões

O parâmetro δ_α presente nas equações (40) e (41), corresponde ao parâmetro de rarefação do constituinte α da mistura. No programa numérico utiliza-se o parâmetro de rarefação da mistura, denotado por δ , como um parâmetro de entrada. Conseqüentemente, é necessário estabelecer uma relação entre os parâmetros de rarefação da mistura e dos constituintes. Esta relação (Cercignani & Sharipov, 1992; Sharipov & Kalempa, 2003) é dada por

$$\delta_\alpha = \frac{\mu}{\mu_\alpha}\frac{P_\alpha}{P}\left(\frac{m_\alpha}{m}\right)^{1/2}\delta, \tag{38}$$

onde μ e μ_α denotam, respectivamente, a viscosidade da mistura e a viscosidade parcial, cujas expressões são dadas em (Sharipov & Kalempa, 2002). P e P_α representam a pressão da mistura e a pressão parcial, respectivamente.

O sistema de equações cinéticas (32) e (33) foram resolvidas numericamente para um amplo intervalo do parâmetro de rarefação δ , pelo método das velocidades discretas (Kogan, 1969; Sharipov & Subbotin, 1993) com um erro numérico relativo menor que 0,1%. Os valores considerados para o parâmetro de rarefação δ variam de $0{,}01 \le \delta \le 40$. Deve-se ressaltar que este intervalo abrange o regime das moléculas livres para $\delta \to 0$ (especificando o intervalo $0{,}01 \le \delta < 1$), o regime de transição $\delta \cong 1$ e o regime hidrodinâmico para $\delta \to \infty$ (especificando o intervalo $\delta \ge 40$). Portanto o maior valor considerado para δ é 40, o qual já representa com certeza o regime hidridinâmico. Todos os cálculos foram feitos para um amplo intervalo do parâmetro de rarefação δ , isto é, 0,01 à 40. Foram considerados três valores de concentração C_0 , isto é, 10%, 50% e 90%, em relação ao primeiro constituinte da mistura. variam de $0{,}01 \le \delta \le 40$.

Para investigar a influência da lei de interação intermolecular no tensor tensão e velocidade, dois tipos de potenciais foram usados: o potencial de esfera-rígida e o potencial Lennard-Jones.

Quando trata-se do potencial de esfera-rígida, para calcular os diâmetros moleculares d_α , utiliza-se a seguinte razão entre suas massas e viscosidades

$$\frac{d_2}{d_1} = \left(\frac{\mu_1}{\mu_2}\right)^{1/2}\left(\frac{m_2}{m_1}\right)^{1/4}. \tag{39}$$

Estas viscosidades são obtidas experimentalmente à uma temperatura de T=300K (Kestin, Knierim, Mason, Najafi, Ro & Waldman, 1984). Estes diâmetros d_α aparecem nas integrais de Chapman-Cowling.

Pode-se expressar a razão entre os parâmetros de rarefação dos constituintes em termos das pressões e das massas de cada constituinte utilizando-se a Eq. (38). Usando a expressão $P_\alpha = n_\alpha k T_\alpha$, obtem-se a razão entre os parâmetros de rarefação dos constituintes em função das densidades e dos diâmetros, ou seja,

$$\frac{\delta_1}{\delta_2} = \left(\frac{n_1}{n_2}\right)^{1/2}\left(\frac{d_1}{d_2}\right)^{2}. \tag{40}$$

Os valores dos parâmetros δ_1 e δ_2 são apresentados nas tabelas (2)-(4) para as concentrações 0,1, 0,5 e 0,9, respectivamente. Observa-se que para $0{,}01 \le \delta < 1$ os constituintes encontram-se no regime de moléculas livres. Para $\delta \cong 1$ tem-se duas situações: os constituintes encontram-se no regime das moléculas livres ou um deles encontra-se no regime de transição e o outro no regime de moléculas livres. Para $\delta \to \infty$ ambos se encontram no regime hidrodinâmico. Os resultados numéricos do tensor tensão Π da mistura são fornecidos nas tabelas (5)-(6) para o potencial de Lennard-Jones e esfera-rígida, respectivamente. Da análise numérica destes valores concluí-se que:

i) O tensor tensão Π da mistura sempre decresce com o aumento do parâmetro de rarefação δ .

ii) Os dados do tensor tensão de cada constituinte, Π_1 e Π_2 , para a mistura binária He-Xe são apresentadas nas tabelas (7)-(8) para o potencial Lennard-Jones e o de esfera-rígida, respectivamente. Pode-se observar que o constituinte de maior massa tem um tensor tensão maior e a medida que o parâmetro de rarefação cresce o tensor

tensão de cada constituinte decresce. Então Π_α diminui com o aumento de δ e o gás mais pesado apresenta maior Π_α pois o transporte é maior e é proporcional a massa.

Quanto a velocidade de cada constituinte e da mistura concluí-se que:

i) O perfil da velocidade de cada constituinte, isto é, u_1 e u_2, são praticamente funções lineares de coordenada *y*. Assim, é suficiente analisar somente a velocidade perto do plano superior, isto é em $y = 1/2$. Neste ponto as velocidades variam de 0 para 1/2 quando o parâmetro de rarefação δ varia de 0 para ∞, pois as placas foram movidas com uma velocidade relativa de $U/2$. Os valores da velocidade de cada constituinte, perto do plano superior ($y = 1/2$), para a mistura Ne-Ar, são dadas na Tab. (9) para o potencial Lennard-Jones. Pode ser visto que para $C_0 = 0{,}1$ e 0,5, o constituinte de massa menor tem uma velocidade menor. Em $C_0 = 0{,}9$ as velocidades dos constituintes são praticamente iguais. Tem-se este mesmo comportamento para as outras duas misturas He-Xe e He-Ar .

ii) Na Tab. (10) tem-se os valores da velocidade *V* das misturas Ne-Ar, He-Ar e He-Xe para o potencial Lennard-Jones em função de y. Para o caso de mistura binária, a velocidade dimensional da mistura $V' = \sum_{i=1}^{2} u_\alpha$, que adimensionalmente é dada por $V = (m_1u_1 + m_2u_2)/(m_1 + m_2)$. Esta velocidade V é tomada como a média ponderada entre as velocidades u_1 e u_2 que são grandezas adimensionais dadas pela Eq. (35).

iii) As placas foram movidas com uma velocidade relativa de $U/2$. Em $y = 0$, $u_1 = u_2 = 0$ e a velocidade da mistura é nula.

iv) O perfil da velocidade *V* da mistura é linear e simétrico em relação a origem, conforme a Fig. (1), para o potencial de esfera-rígida. Este mesmo comportamente se obtém para o potencial Lennard-Jones e independente do parâmetro de rarefação e concentração utilizados, ou seja, as três misturas apresentam o mesmo comportamento e velocidades praticamente iguais. Assim basta analisar os dados apenas entre uma das seguintes razões, $-\frac{D}{2} \le y \le 0$ ou $0 \le y \le \frac{D}{2}$.

v) Nota-se também que para o perfil da velocidade positiva, as partículas que se encontram mais próximas das placas apresentam uma velocidade maior enquanto que esta velocidade vai diminuindo chegando a zero no ponto $y = 0$.

Tabela 2. Análise de δ_1 e δ_2 para misturas binárias e concentração $C_0 = 0{,}1$

	$C_0 = 0{,}1$					
	Ne-Ar		He-Ar		He-Xe	
δ	δ_1	δ_2	δ_1	δ_2	δ_1	δ_2
0,01	0,0081	0,01	0,0076	0,0099	0,0059	0,0098
0,1	0,081	0,1	0,076	0,099	0,059	0,098
1	0,81	1	0,76	0,99	0,59	0,98
2	1,62	2	1,52	1,98	1,18	1,96
4	3,24	4	3,04	3,96	2,36	3,92
10	8,1	10	7,6	9,9	5,9	9,8
20	16,2	20	15,2	19,8	11,8	19,6
40	32,4	40	30,4	39,6	23,6	39,2

Tabela 3. Análise de δ_1 e δ_2 para misturas binárias e concentração $C_0 = 0{,}5$

	$C_0 = 0{,}5$					
	Ne-Ar		He-Ar		He-Xe	
δ	δ_1	δ_2	δ_1	δ_2	δ_1	δ_2
0,01	0,0088	0,011	0,0078	0,0093	0,006	0,0087
0,1	0,088	0,11	0,078	0,093	0,06	0,087
1	0,88	1,1	0,78	0,93	0,6	0,87
2	1,76	2,2	1,56	1,86	1,2	1,74
4	3,52	4,4	3,12	3,72	2,4	3,48

10	8,8	11	7,8	9,3	6	8,7
20	17,6	22	15,6	18,6	12	17,4
40	32,2	44	31,2	37,2	24	34,8

Tabela 4. Análise de δ_1 e δ_2 para misturas binárias e concentração $C_0 = 0{,}9$

	$C_0 = 0{,}9$					
	Ne-Ar		He-Ar		He-Xe	
δ	δ_1	δ_2	δ_1	δ_2	δ_1	δ_2
0,01	0,0097	0,012	0,0088	0,0089	0,0073	0,0071
0,1	0,097	0,11	0,088	0,089	0,073	0,071
1	0,97	1,2	0,88	0,89	0,73	0,71
2	1,94	2,4	1,76	1,78	1,46	1,42
4	3,88	4,8	3,52	3,56	2,92	2,84
10	9,7	12	8,8	8,9	7,3	7,1
20	19,4	24	17,6	17,8	14,6	14,2
40	38,8	48	35,2	35,6	29,2	28,4

Tabela 5. Tensor tensão Π da mistura vs o parâmetro de rarefação δ e concentração C_0, Potencial Lennard-Jones

	Π								
	Ne-Ar			He-Ar			He-Xe		
δ	$C_0 = 0{,}1$	0,5	0,9	0,1	0,5	0,9	0,1	0,5	0,9
0,01	0,2866	0,3220	0,3744	0,2931	0,3773	0,6419	0,2943	0,3902	0,7857
0,1	0,2660	0,2983	0,3429	0,2736	0,3541	0,6039	0,2753	0,3683	0,7498
1	0,1663	0,1873	0,2089	0,1766	0,2356	0,4081	0,1796	0,2519	0,5439
4	0,07857	0,09031	0,09988	0,08602	0,1190	0,2092	0,08852	0,1309	0,3012
10	0,03870	0,04527	0,05008	0,04298	0,06080	0,1073	0,04448	0,06781	0,1610
40	0,01096	0,01304	0,01445	0,01230	0,01777	0,03147	0,01278	0,02002	0,04856

Tabela 6. Tensor tensão Π da mistura vs o parâmetro de rarefação δ e concentração C_0, Potencial esfera-rígida

	Π								
	Ne-Ar			He-Ar			He-Xe		
δ	$C_0 = 0{,}1$	0,5	0,9	0,1	0,5	0,9	0,1	0,5	0,9
0,01	0,2783	0,2758	0,2778	0,2731	0,2484	0,2471	0,2701	0,2292	0,2019
0,1	0,2583	0,2577	0,2598	0,2549	0,2336	0,2326	0,2525	0,2164	0,1919
1	0,1614	0,1678	0,1699	0,1643	0,1568	0,1572	0,1648	0,1485	0,1361
4	0,07591	0,08256	0,08406	0,07990	0,07965	0,08055	0,08115	0,07729	0,07394
10	0,03742	0,04143	0,04230	0,03985	0,04067	0,04134	0,04075	0,04004	0,03935
40	0,01051	0,01188	0,01216	0,01138	0,01182	0,01206	0,01169	0,01177	0,01183

Tabela 7. Tensor tensão de cada constituinte para a mistura He-Xe, Potencial Lennard-Jones

	$C_0 = 0{,}1$		$C_0 = 0{,}5$		$C_0 = 0{,}9$	
δ	Π_1	Π_2	Π_1	Π_2	Π_1	Π_2
0,01	0,05146	0,2701	0,06817	0,2292	0,1371	0,2019
0,1	0,04859	0,2526	0,06462	0,2164	0,1300	0,1920
1	0,03312	0,1650	0,04511	0,1485	0,09111	0,1364
4	0,01676	0,08134	0,02374	0,07730	0,04880	0,07404
10	0,008380	0,04087	0,01226	0,04404	0,02582	0,03934
40	0,002282	0,01173	0,003502	0,01176	0,007717	0,01180

Tabela 8. Tensor tensão de cada constituinte para a mistura He-Xe, potencial esfera-rígida

	$C_0 = 0{,}1$		$C_0 = 0{,}5$		$C_0 = 0{,}9$	
δ	Π_1	Π_2	Π_1	Π_2	Π_1	Π_2
0,01	0,05137	0,2944	0,06808	0,3903	0,1370	0,7860
0,1	0,04787	0,2753	0,06391	0,3690	0,1295	0,7528

1	0,03072	0,1797	0,04259	0,2544	0,08941	0,5564
4	0,01476	0,08853	0,02157	0,1330	0,04726	0,3141
10	0,007130	0,04449	0,01092	0,06915	0,02492	0,1692
40	0,001652	0,01281	0,002895	0,02064	0,007407	0,05163

Tabela 9. Velocidade de cada constituinte na distância $y = 1/2$ para a mistura Ne-Ar, potencial Lennard-Jones

	$C_0 = 0{,}1$		$C_0 = 0{,}5$		$C_0 = 0{,}9$	
δ	u_1	u_2	u_1	u_2	u_1	u_2
0,01	0,01080	0,01297	0,01074	0,01385	0,01188	0,01120
0,1	0,06544	0,07627	0,06529	0,07872	0,07033	0,08942
1	0,2385	0,2627	0,2371	0,2624	0,2469	0,2735
4	0,3765	0,3914	0,3732	0,3883	0,3789	0,3934
10	0,4393	0,4467	0,4365	0,4441	0,4393	0,4466
40	0,4830	0,4849	0,4819	0,4839	0,4826	0,4846

Tabela 10. Velocidade *V* da mistura vs o parâmetro de rarefação δ e concentração C_0, potencial Lennard-Jones

	V								
	Ne-Ar			He-Ar			He-Xe		
δ	$C_0 = 0{,}1$	0,5	0,9	0,1	0,5	0,9	0,1	0,5	0,9
0,01	0,01224	0,01281	0,01541	0,01227	0,01148	0,01150	0,01216	0,01055	0,008709
0,1	0,07263	0,07421	0,08301	0,07234	0,06859	0,06802	0,07166	0,06665	0,05592
1	0,2546	0,2539	0,2646	0,2519	0,2420	0,2383	0,2496	0,2330	0,2114
4	0,3864	0,3832	0,3885	0,3829	0,3739	0,3704	0,3807	0,3664	0,3475
10	0,4442	0,4416	0,4441	0,4417	0,4358	0,4338	0,4403	0,4311	0,4191
40	0,4843	0,4833	0,4839	0,4834	0,4813	0,4807	0,4829	0,4797	0,4757

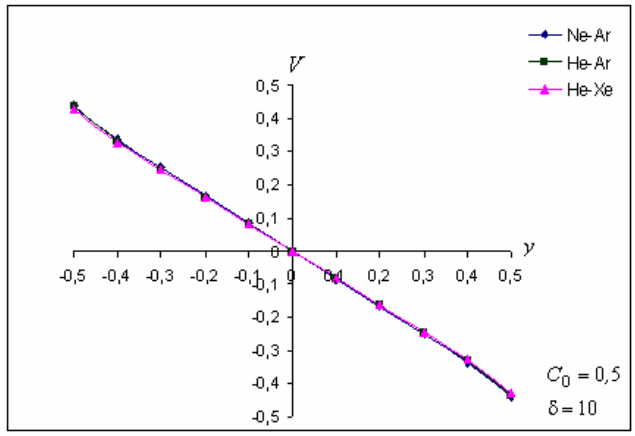

Figura 2. Distância *y* vs a velocidade *V* da mistura e concentração $C_0 = 0{,}5$ para as misturas Ne-Ar, He-Ar e He-Xe, potencial esfera-rígida, $\delta = 10$

5. Conclusões

Foi realizado um estudo do fluxo de Couette plano de misturas binárias de gases monoatômicos. O tensor tensão, a velocidade hidrodinâmica de cada constituinte e da mistura foram calculadas para três misturas de gases nobres, Neônio-Argônio, Hélio-Argônio e Hélio-Xenônio, nos três regimes de escoamento: regime de moléculas livres $(\delta \to 0,\ Kn \to \infty)$, transição $(\delta \cong 1,\ Kn \cong 1)$, e hidrodinâmico $(\delta \to \infty,\ Kn \to 0)$. Foram usados os potenciais intermoleculares: potencial Lennard-Jones e esfera-rígida e concentrações nas proporções de 10%, 50% e 90% em relação ao primeiro constituinte das misturas consideradas.

No regime cinético o parâmetro de rarefação δ pode assumir valores muito pequenos enquanto que no regime hidrodinâmico este mesmo parâmetro poderá assumir valores muito grandes. Portanto o objetivo é poder comparar

através da variação do parâmetro de rarefação δ o comportamento do tensor tensão e a velocidade hidrodinâmica da mistura pois, no limite do regime cinético para o regime hidrodinâmico, o tensor tensão e a velocidade hidrodinâmica da mistura obtidos na solução cinética formada pelo sistema de equações (32) e (33), tem que ser aproximadamente igual aos obtidos através da solução hidrodinâmica de equações (14) e (15).

Uma comparação dos valores numéricos do tensor tensão Π da mistura obtidos na solução cinética com os valores analíticos obtidos na solução hidrodinâmica (15) na condição de deslizamento estão mostrados na Tab. (11). Pode ser visto que para $\delta \geq 10$ a solução analítica (15) coincide com a solução numérica da equação cinética dentro da precisão numérica. No alcance $1 \leq \delta < 10$ a solução (15) fornece uma boa aproximação. Para $0{,}01 \leq \delta < 1$ a solução analítica e a solução cinética não coincidem pois se está no regime de escoamento de moléculas livres. Concluí-se que para grandes valores do parâmetro de rarefação δ , a solução analítica da equação de Navier-Stokes com a condição de deslizamento na velocidade pode ser aplicada com sucesso se o coeficiente de deslizamento viscoso correspondente for correto.

Concluí-se que o tensor tensão decresce com o aumento do parâmetro de rarefação e é fracamente afetado pelo modelo de interação intermolecular.

A Tab. (12) mostra os valores numéricos da velocidade *V*, da mistura obtidos na solução cinética com os valores analíticos obtidos na solução hidrodinâmica (14) na condição de deslizamento. Pode ser visto que para $\delta = 40$ a solução (14) se aproxima da solução numérica da equação cinética. Percebe-se que a diferença entre os valores da velocidade hidrodinâmica da solução (14) com a solução numérica para a mistura Ne-Ar são menores, enquanto que para a mistura He-Xe a diferença entre os valores são maiores. Pode-se observar que a velocidade hidrodinâmica cresce com o aumento do parâmetro de rarefação.

Tabela 11. Comparação da solução numérica do tensor tensão Π da mistura com a solução analítica (15) para $C_0 = 0{,}5$, Lennard-Jones

	Π					
	Ne-Ar $\sigma_P = 1{,}040$		Ne-Ar $\sigma_P = 1{,}150$		Ne-Ar $\sigma_P = 1{,}259$	
δ	resultado numérico	Eq (15)	resultado numérico	Eq (15)	resultado numérico	Eq (15)
0,1	0,2660	0,2294	0,2983	0,2083	0,3429	0,1910
1	0,1663	0,1623	0,1873	0,1515	0,2089	0,1421
4	0,07857	0,08224	0,09031	0,07937	0,09988	0,07671
10	0,03870	0,04139	0,04527	0,04065	0,05008	0,03994
40	0,01096	0,01188	0,01304	0,01182	0,01445	0,01176

Tabela 12. Comparação da solução numérica da velocidade *V* da mistura com a solução analítica (14) para $C_0 = 0{,}5$, Lennard-Jones

	Π					
	Ne-Ar $\sigma_P = 1{,}040$		Ne-Ar $\sigma_P = 1{,}150$		Ne-Ar $\sigma_P = 1{,}259$	
δ	resultado numérico	Eq (14)	resultado numérico	Eq (14)	resultado numérico	Eq (14)
0,1	0,07263	0,02294	0,07421	0,02083	0,08301	0,01910
1	0,2546	0,1623	0,2539	0,1515	0,2646	0,1421
4	0,3864	0,3289	0,3832	0,3175	0,3885	0,3068
10	0,4442	0,4139	0,4416	0,4065	0,4441	0,3994
40	0,4843	0,4753	0,4833	0,4728	0,4839	0,4704

Acknowledgements

Os autores agradecem ao Dr. G. M. Kremer por sua discussões sobre este artigo. Os autores também agradecem a Fundação Araucária pelo suporte a esta pesquisa.

6. Referências

Bird, G. A., 1976, "Molecular gas dynamics", Clarendon Press – Oxford.
Cercignani, C., 1988, "The Boltzmann Equation and its Application",(Springer, New York).

Cercignani, C., & Sharipov, F., 1992, "Gaseous mixture slit flow at intermediate Knudsen numbers", Fhys. Fluids, vol. 16, pp. 2095.
Cercignani, C., Lampis, M., & Lentati, A., 1994, "Calculation of the slip coefficient for a mixture. in: B.D. Shizgal, D.P. Weaver (Eds.), Rarefied Gas Dynamics: Theory and Simulation", 18th. Symp., Vancuver, Canada, Progr. Astron. Aeron., AIP, Washington, vol. 159, pp. 565-573.
Cercignani, C., 2000, "Rarefied Gas Dynamics". (Cambridge University Press).
Chadwick, P., 1976, "Continuum mechanics – concise theory and problems", London George Allen & Unwin Ltd.
Ivchenko, I. N., Loyalka, S. K., & Thompson, R. V., 1997, "Slip coefficients for binary gas mixture", J. Vac. Sci. Technol. A, vol. 15, pp. 2375-2381.
Ivchenko, I. N., Loyalka, S. K., & Thompson, R. V., 2002, "Boundary slip phenomena in a binary gas mixture", Z. Angew. Math. Phys, vol. 53, n. 1, pp. 58-72.
Kestin, J.., Knierim, K., Mason, E. A., Najafi, B., Ro, S. T., & Waldman, M., 1984, "Equilibrium and Transport Properties of the Noble Gases and Their Mixtures at Low Density", J. Phys. Chem. Ref. Data, vol. 13, n. 1.
Kogan, M. N., 1969, "Rarefied Gas Dynamics". (Plenum, New York).
Kremer, G. M., 2003, "Uma introdução à Equação de Boltzmann". Departamento de Física, UFPR.
Landau, L. D., & Lifshitz, E. M., 1976, "Theoretical physics", Statistical Physics, Part 1 (Nauka, Moscow) ch. XII, 5.
McCormack, F. J., 1973, "Construction of linearized kinetic models for gaseous mixtures and molecular gases", Physics of Fluids, vol. 16, pp. 2095.
Ohwada, T., 1998, "Higher order approximation methods for the Boltzmann Equation", J. of Computational Physics, vol. 139, n. 1.
Sharipov, F., & Subbotin, E. A., 1993, "On optimization of the discrete velocity method used in rarefied gas dynamics", ZAMP, vol. 44.
Sharipov, F., & Seleznez, V., 1998, "Data on internal gas flows", J. Phys. Chem. Ref. Data 27, pp. 657-706.
Sharipov, F., & Kalempa, D., 2002, "Gaseous mixture flow through a long tube at arbitrary Knudsen number", J. Vac. Sci Technol, vol. 20, n. 3.
Sharipov, F., & Kalempa, D., 2003, "Velocity slip and temperature jump coefficients for gaseous mixtures. I. Viscous slip coefficient", Fhys. Fluids, vol. 15, n. 6, pp. 1800-1806.

7. Direitos Autorais

HYDRODYNAMICAL SOLUTION AND KINETIC MODEL FOR BINARY MIXTURES

Coqueiro Valdete dos Santos
vcoqueiro@yahoo.com.br

Liliana Madalena Gramani Cumin
Department of Mathematics – UFPr – Postbox 19044, PC 81531-990 – Curitiba – Paraná - Brasil
gramani@mat.ufpr.br

Abstract
The problem studied the Couette flow, consists of a binary mixture of noble gases confined between two parallel plates long enough so that the border effects could be neglected. In the beginning the system is in equilibrium, being slightly disturbed by of the plates relative movement, which characterizes the Couette flow. The distribution function for each constituent of the mixture obeys a coupled integral-differential equation system that is based on Boltzmann equation. The solutions are studied by considering McCormack kinetic model as the basis for Boltzmann equation. Numerical calculations were carried out for three mixtures of noble gases: Neon and Argon, Helium and Argon, and Helium and Xenon. The stress tensor, hydrodynamic velocity of each constituent and of the mixture were calculated, over the whole Knudsen number interval. The molar concentrations of the gases were considered in the proportions of 10%, 50% and 90%. The results obtained were compared when different interaction potentials between the particles are used, as for example, the hard sphere potential and the Lennard-Jones potential. It also compared the kinetic and the hydrodynamic solutions for the stress tensor of the mixture.

Key-words: Couette flow, mixtures of gases, intermolecular potential, Knudsen number.

Paper CIT06-0426

NUMERICAL SIMULATION OF A RADIAL DIFUSOR AIRFLOW CONSIDERING DIFFERENT TURBULENCE MODELS AND COMPUTATIONAL PARAMETERS

Alysson Kennerly Colaciti
Tecumseh do Brasil LTDA, Product Research & Development. Rua Cel. J.A. de Oliveira Salles, 478, Caixa Postal 54 – CEP 13560-971, São Carlos – SP - Brasil
Alyssonkennerly@gmail.com

Luis Miguel Valdés López
Tecumseh do Brasil LTDA, Product Research & Development. Rua Cel. J.A. de Oliveira Salles, 478, Caixa Postal 54 – CEP 13560-971, São Carlos – SP - Brasil
llopez@tecumseh.com.br

Luben Cabezas Gómez
Tecumseh do Brasil LTDA, Product Research & Development. Rua Cel. J.A. de Oliveira Salles, 478, Caixa Postal 54 – CEP 13560-971, São Carlos – SP - Brasil
lcabezas@tecumseh.com.br

Abstract. *In the present work are presented results from numerical simulations performed with the ANSYS-CFX® code. It is studied a radial diffuser flow case, which is the main academic problem used to study the flow behavior on flat plate valves. The radial flow inside the diffuser has important behaviors such as the turbulence decay downstream and recirculation regions inside the valve flow channel due to boundary layer detachment. These flow structures are present in compressor reed valves configurations, influencing in a greater extent the compressor efficiency. The main target of the present paper was finding the simulation set-up (computational domain, boundary conditions and turbulence model) that better fits with experimental data published by Tabatabai and Pollard (1987). The local flow turbulence and velocity profiles were investigated using four different turbulence models, two different boundary conditions set-up, two different computational domains and three different flow conditions (Re_{in} – Reynolds number at the diffuser inlet). Where used the Baseline (BSL) k-ω; the k-ε; the RNG k-ε; and the Shear Stress Transport (SST) k-ω turbulence models. The performed computational results analysis and comparison with experimental data show that the choice of the turbulence model, as well as, the choice of the other computational conditions, play an important rule on results physical quality and accuracy.*

Keywords*. Radial diffuser flow, turbulence models, numerical simulation, ANSYS-CFX® code*

1. Introduction

Radial outward flow between stationary disks has industrial and scientific applications such as in radial diffusers (present in hermetic compressor reed valves), non-rotating air bearings and disk-type heat exchangers. Such flows are rather complex, having a pressure gradient either positive or negative depending on the radial location and radius values. A positive pressure gradient, resulting from a decrease in the velocity with increasing radius, may lead to separation and secondary flows. In some cases, a flow that starts as turbulent flow may revert to laminar flow at some distance downstream (Tabatabai and Pollard, 1987; Ervin *et al*., 1989).

Many investigations have been performed to study the laminar radial flow between parallel disks. For example, Livesey (1960), Moller (1963), Savage (1964), Jackson and Symmons (1965), among others, developed analytical and experimental studies, while Hayashi *et al*. (1975), Raal (1978), and Piechna and Meier (1986) among others, developed numerical studies with the same aim. After that, other investigations where performed to study how behaves a turbulent radial flow between parallel disks. Two important experimental works concerning this kind of study are those developed by Tabatabai and Pollard (1987) and Ervin *et al*. (1989).

Recently, many other works has been developed to study more deeply the flow inside radial diffusers taking advantage of the flow details that Computational Fluid Dynamics (CFD) techniques allows to obtain. Cyklis (1994) investigate the suitability of CFD techniques for analysis of compressor valves. Using a simplified geometry of compressor valve consisting of a radial diffuser with axial feeding was computed the steady planar mass-flow rate as a function of pressure difference, being the results slightly lower than measured data. Deschamps *et al*. (1996) considered a turbulent flow using the Renormalization Group *k-*ε model and fixed walls. The pressure distribution along the frontal disc showed good agreement with experimental data, for different valve openings and Reynolds numbers. With this work the authors obtained some flow details that where not possible to obtain with the previous models used in Deschamps *et al*. (1988 and 1989), where they used the *k-*ε model for high Reynolds numbers and two versions of the k-e models for low Reynolds numbers.

In 1999, Perez-Segarra *et al*. (1999) considering three different versions of the *k-ε* model showed significant differences in computed flow force and effective flow area. This agrees with the comparison of Ottitsch and Scarpinato (2000) developed for different types of valves. In a next step in using CFD techniques for compressor valves Matos *et al*. (1999) simulated the fluid-structure interaction. The authors considered an axis-symmetric laminar flow around a circular plate with prescribed pressure difference. The structure was modeled as a mass-spring system with a single degree of freedom. The gas force was found to be in phase with the harmonically varying pressure difference, except near valve closure when this force experiences a temporary drop. When both pressure difference and flow force become negative, the mass-flow rate at the exit becomes negative too.

Possamai *et al*. (2001) computed laminar flow between concentric inclined disks and conclude that this flow is significantly affected by the inclination for inclinations as small as 0.1°. For some combinations of Reynolds number, valve opening and inclination, the pressure distribution showed regions of negative pressure difference, which produce a restoring moment tending to force the disks to become parallel. In the work of Matos *et al*. (2002) was computed an axi-symmetric turbulent flow around a circular plate, which was modeled as a mass-spring system. CFD techniques, along with other techniques, also where applied by Having (2005), which presents a very detailed study about the flow through compressor valves.

In the present paper four turbulence models are tested, comparing the obtained simulation results for a radial air diffuser flow with the experimental data of Tabatabai and Pollard (1987). The influence of three computational parameters over the simulation results also is addressed in the present paper. These parameters include, the type of boundary condition at the lateral walls of the computational domain, the type of the employed computational geometry, and the inlet follow conditions through the inlet Reynolds number. Among the tested models the shear stress transport (SST) model proposed by Menter (1994) and implemented into the ANSYS-CFX® code, seems to the best compromise for obtaining a good quality results with a reasonable computational cost. In the next section are presented the balance equations of each turbulence model.

2. Mathematical model

In the present paper are used four different turbulence models. Three of then are a two-equations turbulence models, namely the traditional *k-ε* model, the *RNG k-ε* model and the *SST* model, obtained by Menter (1994) from the *k-ω* turbulence model, initially formulated by Wilcox (1993). The other turbulence model is a version of the Reynolds Stress Turbulence kind of model, using a differential equation to compute the Reynolds stresses. The models are presented in the above-mentioned order, considering only the main equations used in the numerical simulations. Models constants are also introduced. It is important to note that are presented the model definitions and formulation used in the ANSYS-CFX® manual (2006), because the numerical simulations were performed with this commercial code. The main interest is to study how different models can lead to very different computational results only considering the defaults definition of each model, including the default boundary conditions.

2.1 *k-ε* model

The standard *k-ε* model (see Launder and Spalding, 1974) introduces two new variables into the equation system. One is for the computation of the turbulent kinetic energy, *k*, m^2/s^2; and the other is for the calculation of the turbulence eddy dissipation, ε, m^2/s^3. The following equations are then obtained:

Continuity equation:

$$\frac{\partial \rho}{\partial t} + \nabla \cdot (\rho U) = 0 \tag{1}$$

Momentum equation:

$$\frac{\partial (\rho U)}{\partial t} + \nabla \cdot (\rho U \otimes U) = -\nabla p' + \nabla \cdot \left(\mu_{eff} \left(\nabla U + (\nabla U)^T \right) \right) + B \tag{2}$$

where *B* is the sum of body forces, μ_{eff} is the effective viscosity accounting for turbulence, and *p'* is the modified pressure. μ_{eff} and *p'* are given respectively by:

$$\mu_{eff} = \mu + \mu_t \tag{3}$$

$$p' = p + \frac{2}{3} \rho k \tag{4}$$

The *k-ε* model uses the eddy viscosity concept, assuming that the turbulence viscosity is computed by:

$$\mu_t = C_\mu \rho \frac{k^2}{\varepsilon} \tag{5}$$

where C_μ is a model constant.

The quantities *k* and ε are computed directly from the resolution of the following differential transport equations:

$$\frac{\partial(\rho k)}{\partial t} + \nabla \cdot (\rho U k) = \nabla \cdot \left[\left(\mu + \frac{\mu_t}{\sigma_k} \right) \nabla k \right] + P_k - \rho\varepsilon \tag{6}$$

$$\frac{\partial(\rho \varepsilon)}{\partial t} + \nabla \cdot (\rho U \varepsilon) = \nabla \cdot \left[\left(\mu + \frac{\mu_t}{\sigma_\varepsilon} \right) \nabla \varepsilon \right] + \frac{\varepsilon}{k} (C_{\varepsilon 1} P_k - C_{\varepsilon 2} \rho\varepsilon) \tag{7}$$

being $C_{\varepsilon 1}$, $C_{\varepsilon 2}$, σ_k and σ_e model constants and P_k is the turbulence production due to viscous forces. The buoyancy forces are not considered in the present work. This last term is modeled as:

$$P_k = \mu_t \nabla U \cdot \left(\nabla U + \nabla U^T \right) - \frac{2}{3} \nabla \cdot U \left(3\mu_t \nabla \cdot U + \rho k \right) \tag{8}$$

If the flow is incompressible, ∇·U is very small. In this case the second term of the Eq. (8) does not contributes to the turbulence production. In the present simulations the flow is considered compressible and all this terms are taking into account. The standard *k-ε* model employs values for the constants that were found by a comprehensive data fitting for a wide range of turbulent flows. The values of these constants are:

$$C_\mu = 0.09;\ C_{\varepsilon 1} = 1.44;\ C_{\varepsilon 2} = 1.92;\ \sigma_k = 1.00;\ and\ \sigma_\varepsilon = 1.30 \tag{9}$$

2.2 *RNG k-ε* model

The *RNG k-ε* model is based on renormalization group analysis of the Navier-Stokes equations (Yakhot et al., 1992). The transport equations for turbulence generation and dissipation are the same as those for the standard *k-ε* model, but the model constants differ. The equations for the momentum and continuity are also the same.

For the *RNG k-ε* model the transport equation for turbulence dissipation becomes:

$$\frac{\partial(\rho \varepsilon)}{\partial t} + \nabla \cdot (\rho U \varepsilon) = \nabla \cdot \left[\left(\mu + \frac{\mu_t}{\sigma_{\varepsilon RNG}} \right) \nabla \varepsilon \right] + \frac{\varepsilon}{k} (C_{\varepsilon 1 RNG} P_k - C_{\varepsilon 2 RNG} \rho\varepsilon) \tag{10}$$

where

$$C_{\varepsilon 1 RNG} = 1.42 - f_\eta \tag{11}$$

and

$$f_\eta = \frac{\eta \left(1 - \frac{\eta}{4.38} \right)}{\left(1 + \beta_{RNG} \eta^3 \right)};\ \eta = \sqrt{\frac{P_k}{\rho C_{\mu RNG} \varepsilon}}\ . \tag{12a,b}$$

The values of the constants are:

$$C_{\mu RNG} = 0.085;\ C_{\varepsilon 2 RNG} = 1.68;\ \sigma_{kRNG} = 0.7179;\ and\ \sigma_{\varepsilon RNG} = 0.7179 \tag{13}$$

2.3 *SST* model

The other two-equations turbulence model refers to the Shear Stress Transport (SST) model of the ANSYS-CFX® manual (2006). This model was proposed by Menter (1994), and grew from the denominated Baseline *k-ω* model (see the ANSYS-CFX® manual, 2006). The Baseline *k-ω* model makes use of the *k-ε* model in regions far away from the walls and the *k-ω* Wilcox model near the surface (Wilcox, 1993). The SST model is an improvement of the Baseline *k-ω* model, taking into account the transport of the turbulent shear stress by a limitation of the eddy viscosity ν_t by the following equation:

$$\nu_t = \frac{a_1 k}{\max(a_1 w, SF_2)} \tag{14}$$

where: $\nu_t = \mu_t / \rho$ and S represents an invariant measure of the strain rate. F_2 is a blending function, which restricts the limiter to the wall layer computed by:

$$F_2 = \tanh(\arg_2^2) \tag{15}$$

with:

$$\arg_2 = \max\left(\frac{2\sqrt{k}}{\beta' wy}, \frac{500\nu}{y^2 w}\right) \tag{16}$$

The turbulent kinetic energy, *k* and turbulent frequency, ω are computed by the following relations:

$$\frac{\partial(\rho k)}{\partial t} + \nabla \cdot (\rho U k) = \nabla \cdot \left[\left(\mu + \frac{\mu_t}{\sigma_{k3}}\right)\nabla k\right] + P_k - \beta' \rho k \omega \tag{17}$$

$$\frac{\partial(\rho \omega)}{\partial t} + \nabla \cdot (\rho U \omega) = \nabla \cdot \left[\left(\mu + \frac{\mu_t}{\sigma_{\omega 3}}\right)\nabla \omega\right] + (1 - F_2) 2\rho \frac{1}{\sigma_{\omega 2}\omega} \nabla k \nabla \omega + \alpha_3 \frac{\omega}{k} P_k - \beta_3 \rho \omega^2 \tag{18}$$

The constants used in the *SST* model equations are:

$$\begin{aligned} &\beta' = 0.09;\ \alpha_1 = 5/9;\ \beta_1 = 0.075;\ \sigma_{k1} = 2;\ \sigma_{\omega 1} = 2; \\ &\alpha_2 = 0.44;\ \beta_2 = 0.0828;\ \sigma_{k2} = 1;\ \textit{and}\ \ \sigma_{w2} = 1/0.856 \end{aligned} \tag{19}$$

The coefficients of the *SST* model are a linear combination of the corresponding coefficients of the underlying models:

$$\Phi_3 = F_2 \Phi_1 + (1 - F_2)\Phi_2 \tag{20}$$

It should be noted that the stress tensor is computed from the eddy-viscosity concept. Is used the Eq. (1) for the conservation of mass.

2.4 Reynolds Stress Turbulence (*BSL*) model

The last model considered in this paper is the Reynolds Stress Turbulence model. This kind of model is based on transport equations for all components of the Reynolds stress tensor and dissipation rate. The eddy viscosity concept is not used, and is solved an equation for the transport of Reynolds stresses in fluid. The transport equations are solved for the individual stress components. In the present model is used a differential equation for the Reynolds stress transport computation, based on the turbulence frequency *ω*. As the turbulence frequency ω is computed using the Baseline *k-ω* model, the present Reynolds Stress model is denominated as the BSL Reynolds Stress model following the ANSYS-

CFX® manual denomination. There are various Reynolds stress turbulence models as those published by Launder *et al*. (1975) and Speziale *et al*. (1991). The present *BSL* model haves some differences in relations to these models. In this case the modeled equation for the Reynolds stresses are written as:

$$\frac{\partial\left(\rho\tau_{ij}\right)}{\partial t}+\frac{\partial\left(U_k\rho\tau_{ij}\right)}{\partial x_k}=-\rho P_{ij}+\frac{2}{3}\beta^{'}\rho\omega k\delta_{ij}-\rho\Pi_{ij}+\frac{\partial}{\partial x_k}\left(\left(\mu+\frac{\mu_t}{\sigma^*}\right)\frac{\partial\tau_{ij}}{\partial x_k}\right) \tag{21}$$

where the constitutive relation for the pressure-strain correlation is given by:

$$\Pi_{ij}=\beta^{'}C_1\omega\left(\tau_{ij}+\frac{2}{3}k\delta_{ij}\right)-\hat{\alpha}\left(P_{ij}-\frac{2}{3}P\delta_{ij}\right)-\hat{\beta}\left(D_{ij}-\frac{2}{3}P\delta_{ij}\right)-\hat{\gamma}k\left(S_{ij}-\frac{1}{3}S_{kk}\delta_{ij}\right) \tag{22}$$

The production tensor of Reynolds stresses is given by:

$$P_{ij}=\tau_{ik}\frac{\partial U_j}{\partial x_k}+\tau_{jk}\frac{\partial U_i}{\partial x_k};\ \ and\ \ \ P=\frac{1}{2}P_{kk} \tag{23a,b}$$

The tensor D term only differs from the above equation in the dot-product indices:

$$D_{ij}=\tau_{ik}\frac{\partial U_k}{\partial x_j}+\tau_{jk}\frac{\partial U_k}{\partial x_i} \tag{24}$$

The turbulent viscosity in the diffusion terms of the balance equations of the Reynolds stresses equation is computed as in the Wilcox (1993) *k*-ω model:

$$\mu_t=\rho\frac{k}{\omega} \tag{25}$$

In the above equations the constant coefficients are equal to:

$$\beta^{'}=0.09;\ \hat{\alpha}=\left(8+C_2\right)/11;\ \hat{\beta}=\left(8C_2-2\right)/11;\ \hat{\gamma}=\left(60C_2-4\right)/55;\ C_1=1.8;C_2=0.52 \tag{26}$$

Finally should be computed the turbulent frequency ω. For this purpose the reader should consult the equations on pages 84 and 85 of the ANSYS-CFX® manual (2006).

For more detailed information about the formulation of the above models should be consulted the ANSYS-CFX® manual (2006) and the literature cited herein. The formulation present in this manual is extensively used in the paper, considering that the CFX code was extensively used for all the reported numerical simulations. The books by Tennekes and Lumley (1972), Wilcox (1993); Versteeg and Malalasekera (1995) and Pope (2000) present the theory of turbulence modeling more deeply and can be consulted.

3. Setup of the numerical simulations

In this section are described all the computational conditions assumed in the numerical simulations. In Figures 1 and 2 are shown the two different computational domains used in simulations. The first one, (see Figure 1) it is composed by the inlet section (blue color), the two valve plates, the lateral walls and the outlet section (yellow color). The second domain (see Figure 2) it is composed by all these sections, including an opening section (green color), right after the plate diameter, D. In this case the outlet section is displayed after the opening section. The simulated geometry is composed from two valve plates with diameter D and a central orifice of the diffuser of diameter, d = 75 mm. The valve configuration is characterized by the diameters relation equals to D/d = 16. Each valve plate haves a thickness of 25 mm. This is the height of the inlet region shown in Figures 1 and 2. The separation between the plates is equal to 10 mm. The computational geometry (Figures 1 and 2) were made rotating one lateral wall for 10°, making a three dimensional domain in the form of wedge. In Figures 1 and 2 are also shown six reed lines, denoting the position where were obtained the experimental profiles of the mean time local gas velocity along the plate radius and where will be compared the numerical results. Next are presented the other tested and assumed simulation conditions.

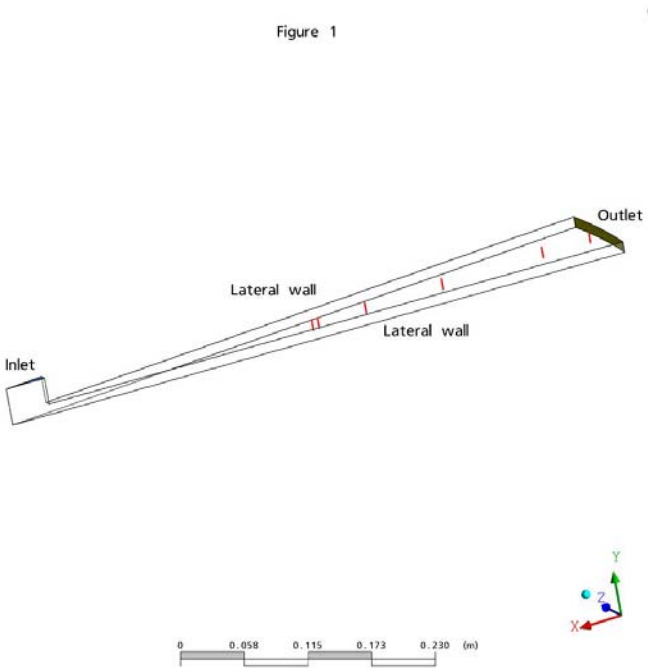

Figure 1. Computational domain considering the outlet section situated at the disc diameter.

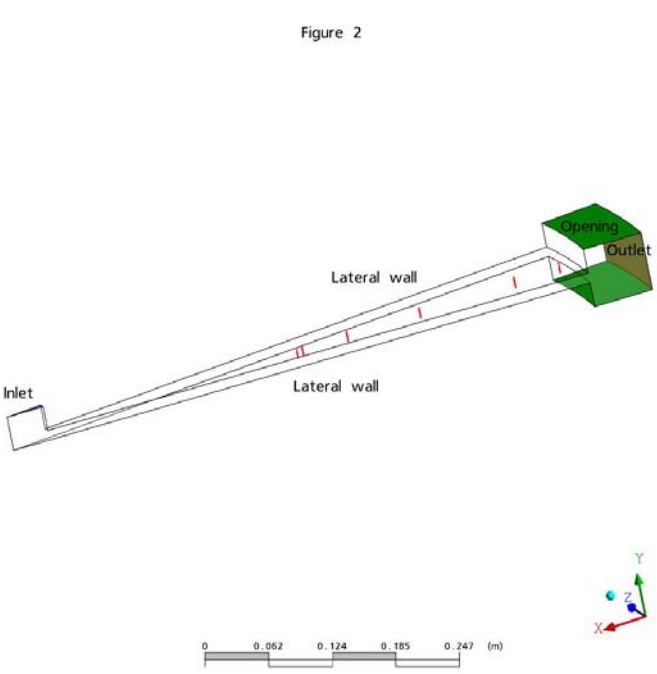

Figure 2. Computational domain considering an extension of the outlet section situated after the disc diameter.

Before the specification of the different boundary conditions assumed it should be specified which type of fluid was used for the simulations. In the case of the first geometry (Figure 1) the air was simulated as an incompressible fluid using the ANSYS-CFX® database (Air at 25°C fluid type from ANSYS-CFX® code). For the second geometry the air was considered as a compressible ideal fluid, but without any heat transfer with the walls and exits, assuming an air temperature equals to 298.15 K in the entire domain. In this case was computed the total energy equation considering the works terms due to the viscous dissipation. The interested reader should consult the ANSYS-CFX® manual (2006) to know what energy balance equation was used for this geometrical configuration.

With the exception of the above difference, regarding the kind of fluid used in the numerical simulations for each geometrical configuration, the other parameters were tested for both the geometrical configurations. Thus, besides the four different turbulence models, also where considered two different boundary conditions for the lateral walls of each

geometry, and three different inlet conditions depending on the inlet Reynolds number. The following boundary conditions (BC) were assumed:

- Inlet: It is specified the inlet velocity normal to the domain in the negative direction regarding the Y-axes (This velocity changes for each assumed inlet Reynolds number). It is assumed medium turbulence intensity, *I*, and, eddy viscosity ratio (see the ANSYS-CFX® manual). For the compressible fluid the inlet temperature is provided equal to 298.15 K.
- Outlet: It is assumed a subsonic flow with an average static pressure, over the entire outlet region, equal to 0.0 Pa. At the outlet the fluid can flows only out of the domain.
- Opening: It is assumed a relative pressure of 0.0 Pa and a static temperature equal to 298.15 K (This kind of BC is used only for the compressible fluid). At the openings the fluid can flow in and out of the computational domain. It is assumed medium turbulence intensity and eddy viscosity ratio.
- Lateral walls: For these walls are assumed two BC. One is a symmetry boundary condition, and the other is the free slip BC. At the symmetry BC the normal velocity at the wall is zero and the scalar variable gradients normal to the boundary are also zero. For the free slip walls, the velocity component parallel to the walls has a finite value, but the velocity normal to the wall, and the wall shear stress, are both set to zero. For the compressible fluid the walls are assumed as adiabatic.
- Other walls: In this case it is assumed the no slip BC, meaning that the fluid velocity at the wall has a zero value. For the compressible fluid the walls are assumed as adiabatic.

For all the turbulence models used in the work were assumed the ANSYS-CFX® software default turbulent wall functions. A detailed explanation about the formulation of these functions is presented in Volfang *et al*. (2002). The formulae are not presented here due to space limitations. The flow is simulated to obtain the steady state solution considering a maximum of 200 false time temporal iterations. These temporal iterations do not represent a truly transient flow behavior, and are used to achieve the steady state solution. In Table 1 is shown the main parameters assumed for the construction of computational meshes. The mesh used for the Fig. 1 geometry is much more refined than that used for Fig. 2 geometry. Nevertheless, even considering these two different meshes the Fig. 2 geometry leaded to better simulation results, indicating how the computational domain greatly influences the results and flow behavior. Due to the great number of performed simulations other computational meshes were not considered for the present work. The computations were run out in parallel using a cluster with eight processors.

Table 1. Computational mesh parameters.

Geometry type	Total number of nodes	Total number of elements	Total number of faces
Figure 1	1,244,489	2,742,344	203,293
Figure 2	343,008	956,403	66,946

4. Numerical results

In Figures 3 to 6 are shown the profiles of the mean time local gas velocity at different radial positions, considering the four turbulence models, the two different BC at the lateral walls and the two computational geometries considered in the paper (see Figures 1 and 2). In all figures are displayed the experimental data taken from Tabatabai and Pollard (1987) to be able to compare the numerical results. The displayed velocity profiles are disposed in the red lines shown in Figures 1 and 2. Now is performed a discussion considering the obtained results. It is very important to note that the results are shown partially, due to the quantity of parameters analyzed and the space limitation.

The first aspect that can be addressed is the performance of the turbulence models in relation to the experimental data. Considering all displayed results it is seen clearly that the k-ε and *RNG* k-ε models lead to simulation results, which are not in agreement with the experimental data and also with the physics of the flow. The more distorted results obtained with these two turbulence models are those shown in Figures 3 and 4, over all for the smaller and mean inlet Reynolds number values. For the high value Reynolds number (Figure 3c and 4c) the velocity profiles are more adequate, but very inaccurate at the discs walls, where the no slip BC it is not represented. This kind of behavior describes well that these two turbulence models are adequate for high Reynolds numbers in regions far away from the domain walls. In fact there are several modifications of the k-ε model for low Reynolds number flow simulation. Hrenya *et al*. (1995) presents a comparative study of ten different models of this type. However, even considering these low Reynolds number k-ε models, it is known that these models uses complex non-linear damping functions for the wall treatments, leading to very erroneous results. This conclusion can be extended even for high Reynolds number flows as can be see from Figures 3c and 4c, where these two models faults to catch the right behavior at the disc's walls. The same comments apply for the results displayed in Figures 5 and 6, obtained for other geometrical configuration and fluid model (compressible fluid). In this case, the velocity profiles are more coherent in relations to Figures 3 and 4 results, mainly at the centerline, but have a very poor behavior at the channel walls. In several works Churchill and coworkers (Churchill, 2000; and other related works) discussed and showed that the k-ε turbulence type of models have determined failures, because they use the concepts of eddy viscosity and mixing length to compute the turbulent viscosity. The failures are associated with the unbounded character of the eddy viscosity and mixing length at some locations of channels, and also with the assumption of negative values over some adjacent to the walls finite

regions, although the turbulent stresses remains well behaved. Considering all these comments and the presented results, it can be concluded that simulation results of the turbulent diffuser flow obtained with the *k-ε* and *RNG k-ε* should be treated with care, to avoid obtaining erroneous conclusions about the flow structures and main characteristics.

Now analyzing the results obtained for the *SST* and *BSL* models, can be said that both models allows obtaining numerical results physically coherent and generally very adequate in relation to the experimental data. However, some differences between these two turbulence models can be pointed out. In Figures 3 and 4 it is seen that there are shown results for the *BSL* model only for the smaller inlet Reynolds number (Re_{in} = 19096). In the case of the *SST* model, are displayed results only for Re_{in} equals to 19096 and 32804. The main reason for not to show the other results is that in these cases the code does not converge inside the number of temporal iterations fixed, equally to 200 iterations. These iterations are related to false time iterations to obtain a steady state solution. In the case of the *BSL* model, the time step was reduced to obtain a converged solution, considering the quantity of equations that should be solved for this model. When it is simulated the Figure 2 geometry and fluid model, the above two models converge, except the *BSL* model for Re_{in} = 164441. The same conditions where considered in this case.

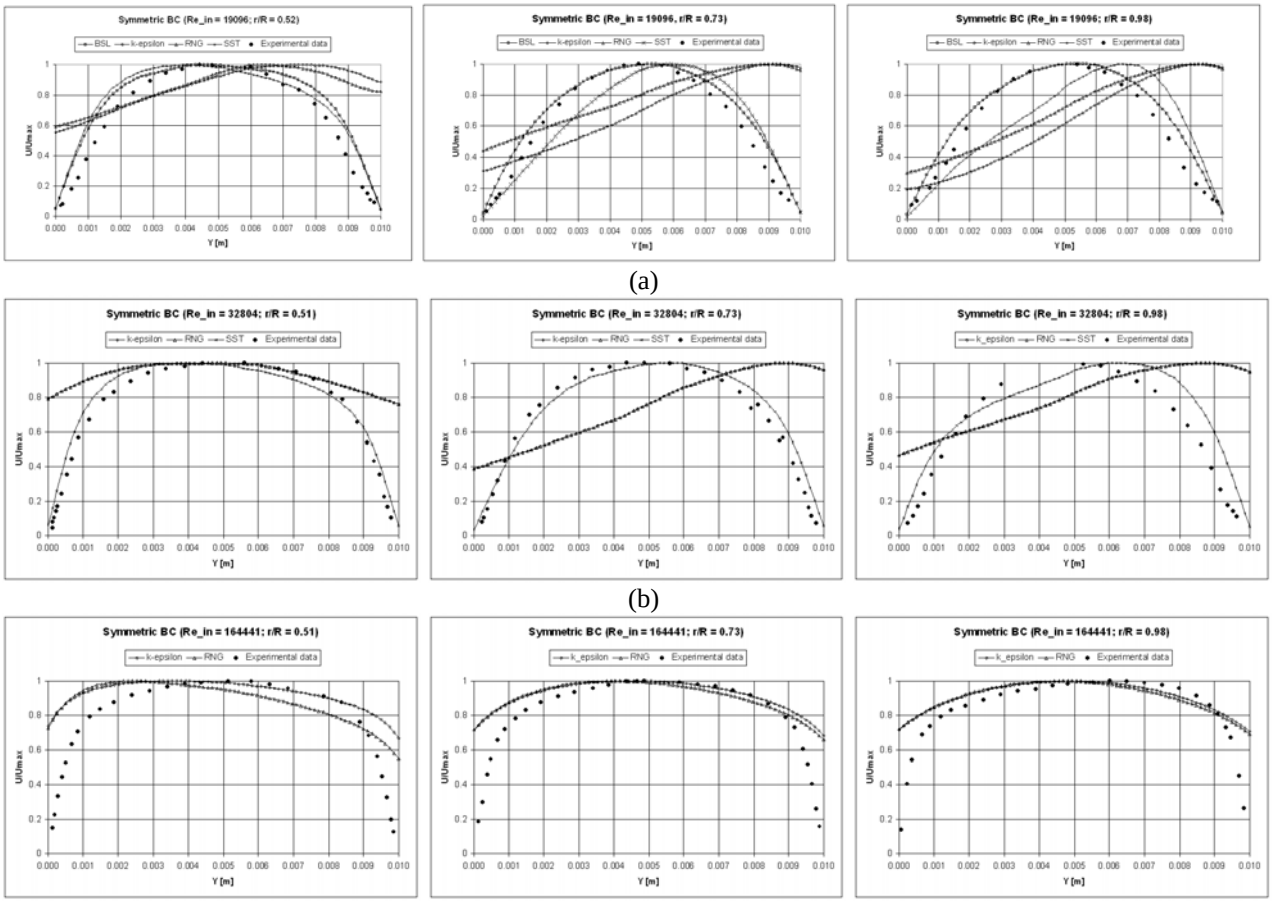

Figure 3. Mean velocity distribution across the discs gap at various radial locations, considering the geometry shown in Figure 1, the symmetric BC at the lateral walls and the four turbulence models. [(a) – Re_{in} = 19096; (b) – Re_{in} = 32804; (c) – Re_{in} = 164441].

Considering only the results displayed in Figures 3 and 4, it can be said that the *BSL* model leads to more correct results, at least for the low inlet Reynolds number (Re_{in} = 19096) for which both models can be compared. The more accentuated differences between the models, are observed at the radial coordinate r/R = 0.98, where the *SST* model presents a very not symmetric profile. This behavior is not correctly, because at this radial distance the flow dissipates the initial asymmetric due to the cross-stream momentum transfer as pointed out by Tabatabai and Pollard (1987). However, this does not means that the SST model leads to erroneous results for the other flow cases, as can be observed in Figures 3b and 4b. For this value of Re_{in} the *SST* model presents a more coherent behavior in relation to the experimental data, showing the asymmetry at r/R = 0.98 but, to a less extend.

For results showed in Figures 5 and 6, it is noted that both the models present a very similar behavior, showing small differences between each other and in comparison with the experimental data. For these simulations, the *SST* model converged for all the tested cases, contrary to the *BSL* model, which, does not converged for the high value of Re_{in}. Thus, even knowing that the *BSL* model is more universal, due to the use of transport equations for the Reynolds stress computations, the present results indicates that the *SST* model can be preferred for simulating different flow

conditions characteristics of a design phase of any engineering project. In fact, the *BSL* model is more time consuming that the *SST* model, leading in the case of Figures 5 and 6, to results that are very similar and of the same quality. In Table 2 are displayed values of the computational time for these two models for some of the performed simulations. As can be seen, the *SST* has a very small computational time regarding the *BSL* model. Considering this advantage of the *SST* model and the good results, which can be obtained with this model, it seems that this turbulence model is a good choice for numerically simulating the diffuser turbulent flow.

Table 2. Comparison of the running computational time for the *BSL* and *SST* models.

Turbulence Model	Re_{in} = 19096 (Symm. BC)	Re_{in} = 32804 (Symm. BC)	Re_{in} = 19096 (Free BC)	Re_{in} = 32804 (Free BC)
SST	42m58s	47m4s	43m41s	46m45s
BSL	1h2m59s	1h4m6s	1h3m5s	1h3m51s

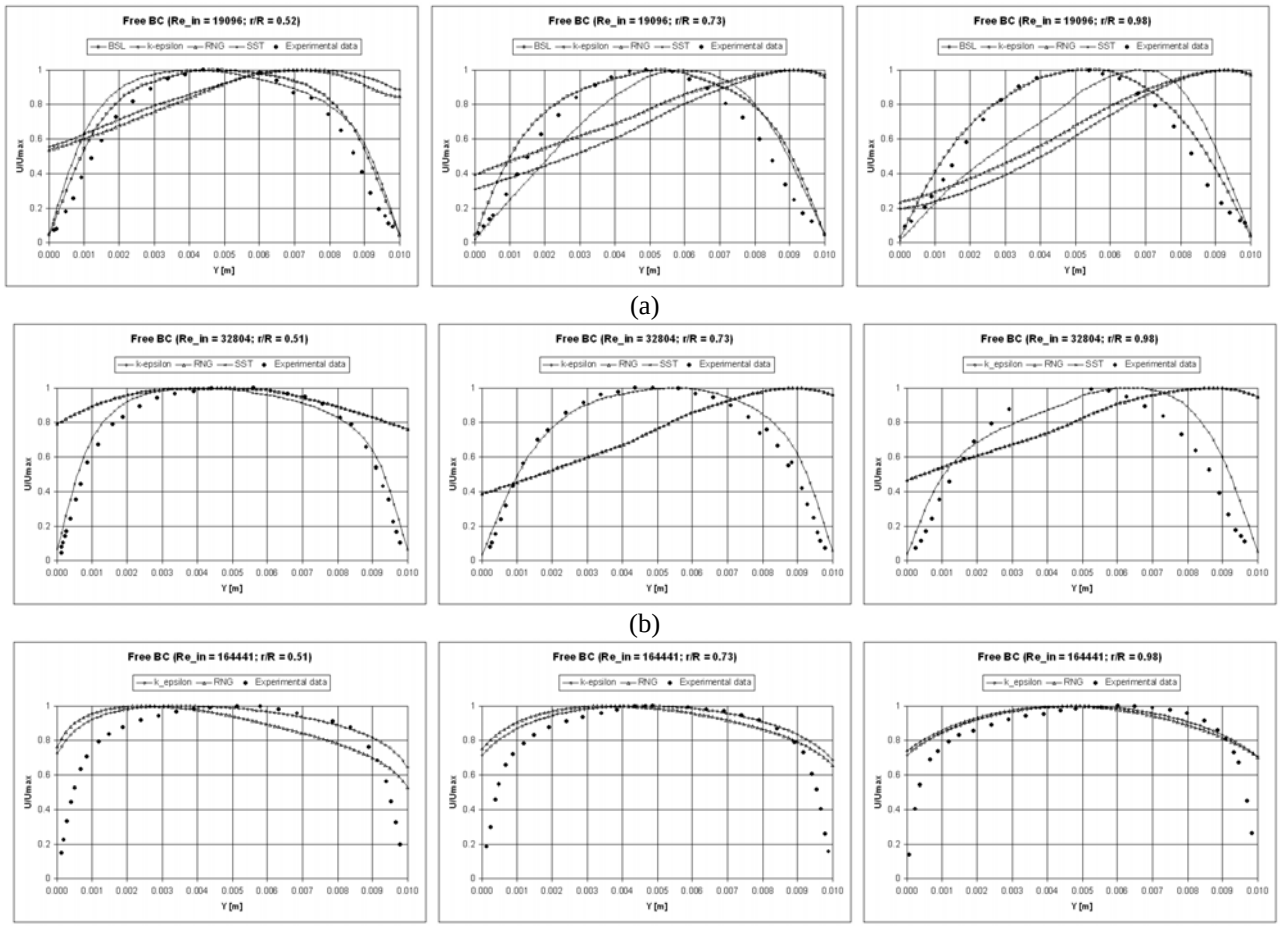

Figure (4). Mean velocity distribution across the discs gap at various radial locations, considering the geometry shown in Figure 1, the free slip BC at the lateral walls and the four turbulence models. [(a) – Re_{in} = 19096; (b) – Re_{in} = 32804; (c) – Re_{in} = 164441].

Focusing now on the influence of the type of BC applied for the lateral walls over the studied gas turbulent flow inside a diffuser, the results show that this influence is very small in all the analyzed cases. The only slightly differences are perceived for the results of Re_{in} = 164441 displayed in Figures 5c and 6c. As seen in these pictures, the *k-ε* and *RNG k-ε* models depend more on the type of this BC, that the *SST* model. Making a careful comparison it is seem that the symmetric type of BC is more adequate to the kind of flow simulated in comparison with the free slip type of BC. It should be commented that the use of these BCs is a necessary steep in order to decrease the required computational time. The risk of this type of assumption is the lost of tri-dimensional flow effects or the formation of artificial flow structures. However, observing the obtained results, it is noted that in the kind of flow studied, these types of BC represent well the flow behavior.

A more pronounced influence over the diffuser turbulent flow is noted when is compared the kind of computational domain and fluid model used in the simulations. Comparing the results from Figures 3 and 4 with those represented in Figures 5 and 6, it is noted that the extended computational domain (see Figure 2) allows obtaining better computational results for all the tested turbulence models, including both the BC at the domain lateral walls. This points to the facts that the use of one or another computational domain is an important aspect to be taking into account when are

performed CFD numerical simulations. Many simulations in the literature, of problems similar to the present one, uses only the geometry shown in Figure 1, when the disc's radius is higher in relation to the diffuser orifice radius. Nevertheless, when turbulent flows are considered, as the present one, the type of computational geometry exerts a considerable influence over the simulation results. In the present case it is perceived that even if the flow have a symmetrical characteristics, properly of laminar flows near the domain exit, i.e., at largely values of the radial coordinate, the free stream turbulence can influence in a very high degree the numerical results. Note that the higher differences between the two types of computational domains are noted at the exits of the domains, namely at the r/R = 0.98 cross-section.

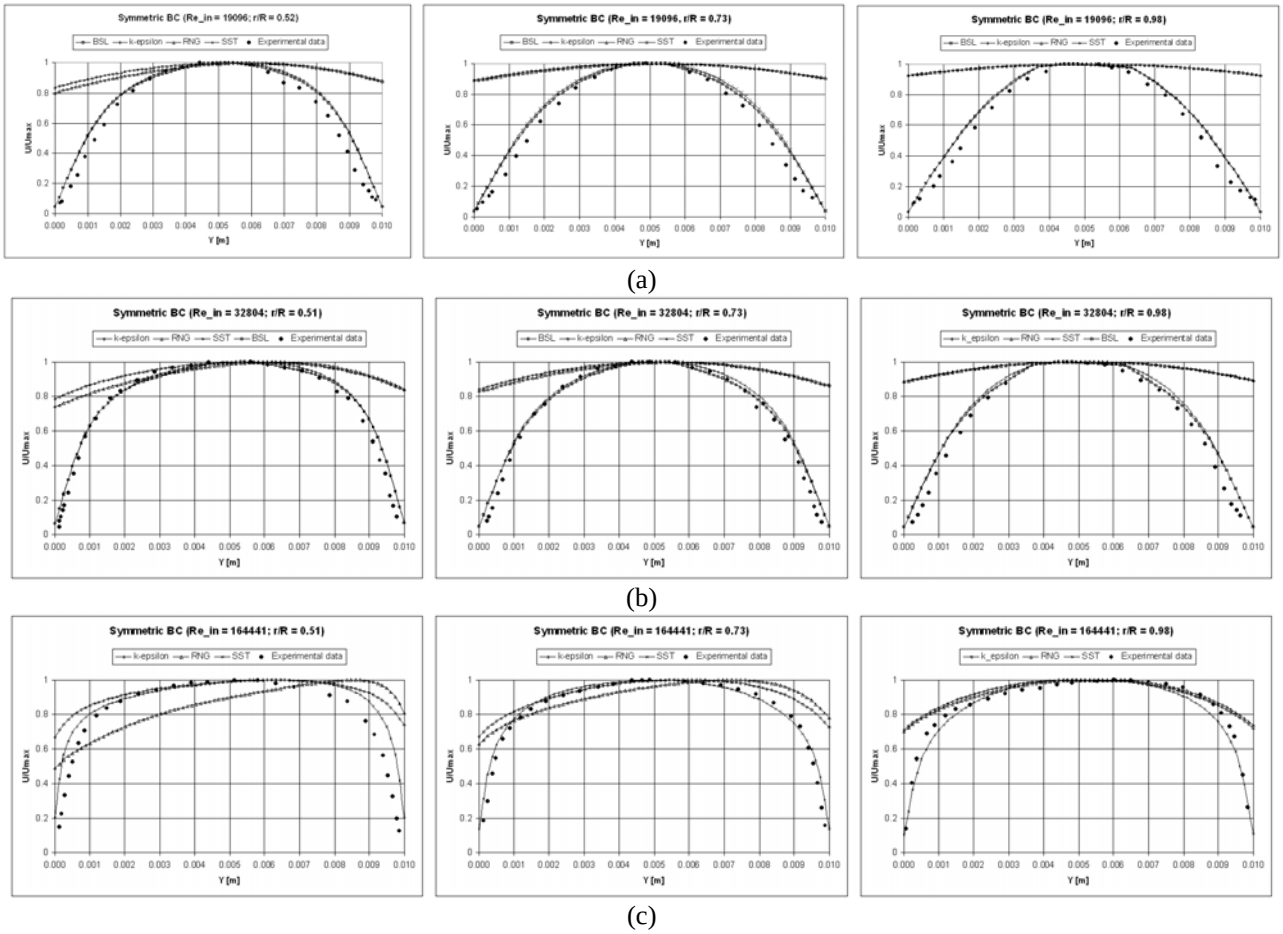

(a)

(b)

(c)

Figure 5. Mean velocity distribution across the discs gap at various radial locations, considering the geometry shown in Figure 2, the symmetric BC at the lateral walls and the four turbulence models. [(a) – Re_{in} = 19096; (b) – Re_{in} = 32804; (c) – Re_{in} = 164441].

Table 3. Values of the y^+ variable for the *RNG k-ε* and *SST* models and two Reynolds number values.

Turbulence Model	Re_{in} = 19096 (Regions near inlet)	Re_{in} = 19096 (Regions near outlet)	Re_{in} = 164441 (Regions near inlet)	Re_{in} = 164441 (Regions near outlet)
RNG k-ε	$1.0 \le y^+ \le 3.8$	$y^+ \le 1.0$	$7.7 \le y^+ \le 30.2$	$y^+ \le 7.7$
SST	$1.5 \le y^+ \le 5.7$	$y^+ \le 1.5$	$7.5 \le y^+ \le 30.3$	$y^+ \le 7.5$

For instance, should be noted, that besides the difference in the computational domain geometry in the present work are used two different fluid models. One is an incompressible and the other considers the compressibility effects on the flow turbulence. Thus, it cannot be associate all the reported results' differences only for the type of computational domain. Nevertheless, the simulations for the compressible fluid were performed assuming an adiabatic flow with the same inlet and outlet flow static temperatures. Considering that the flow velocities are not so high, it is seem, that the computational domain is the parameter, which is contributing more for the presented results' differences.

In Table 3 are presented some data regarding the value of y^+ at the walls for the *RNG k-ε* and *SST* models. There are not presented graphics due to paper space constraints. According to the ANSYS-CFX® manual it is recommended to have the following values of y^+: $20 \le y^+ \le 100$ for wall functions (*RNG k-ε* model) and $y^+ \le 2$ for low Reynolds numbers models (*SST* model). As can be seen from Table 3 the y^+ values should be improved for the *RNG k-ε* model. For the SST model the y^+ values are in better agreement with the recommendations, excepting for Re_{in} = 164441. In this case the mesh should be refined more in the regions near the diffuser inlet (extending up to the middle of the diffuser

radius). Table 3 results indicate that it is necessary to improve the computational mesh, mainly for the *RNG k-ε* and *k-ε* models to have better resolution of these models at the walls. Nevertheless these models lead to not physically coherent simulation results (see Figs. 3-6) even for Re_{in} = 164441 case, where y^+ values are inside the recommended interval. This fact validates the conclusions of the present work.

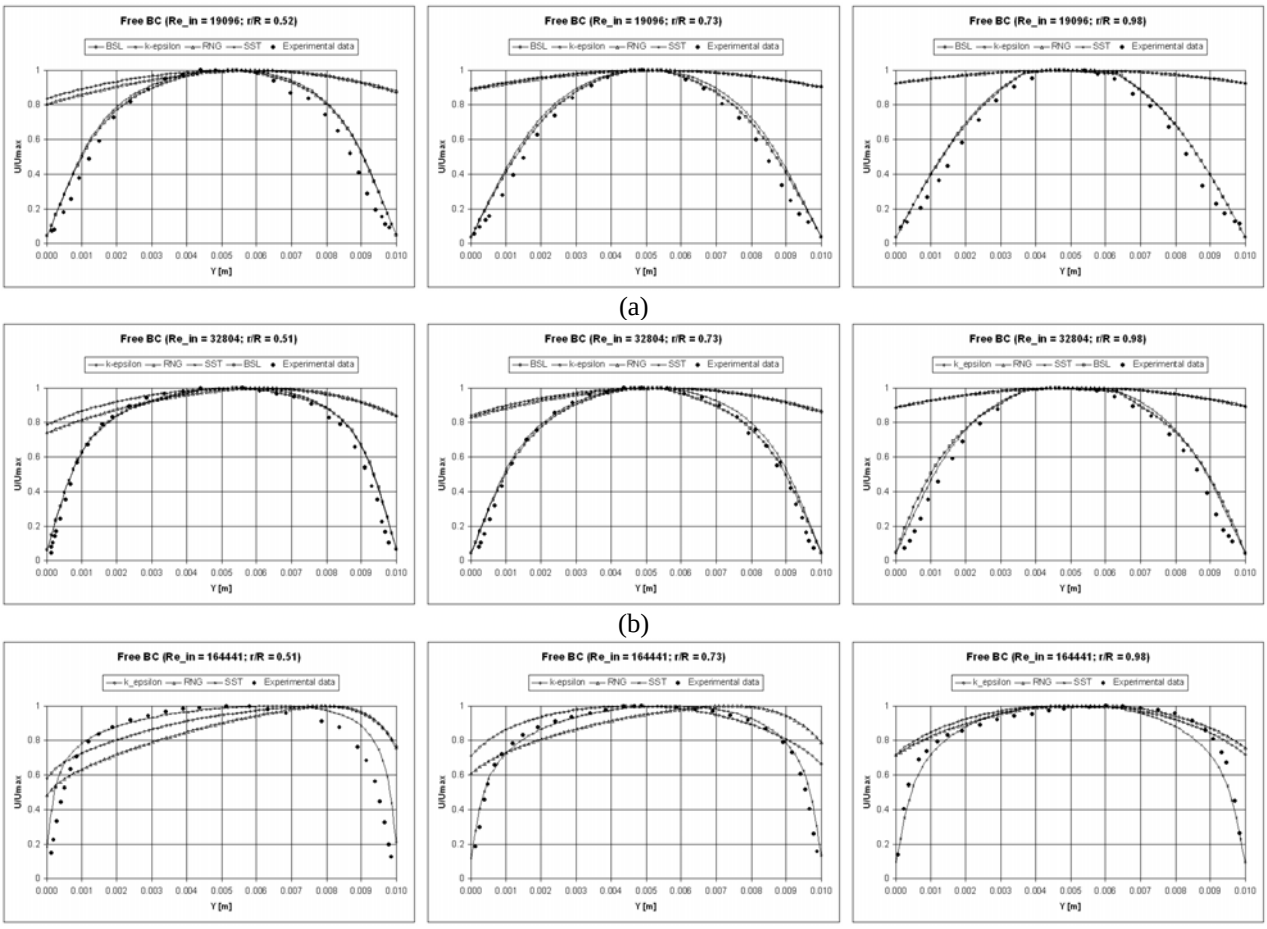

Figure 6. Mean velocity distribution across the discs gap at various radial locations, considering the geometry shown in Figure 2, the free slip BC at the lateral walls and the four turbulence models. [(a) – Re_{in} = 19096; (b) – Re_{in} = 32804; (c) – Re_{in} = 164441].

5. Conclusions

Taking into account the above discussion, it is seem that the use of one or another turbulence model, depend on a compromise between the quality of the results, the number of simulations needed and the geometrical and computational characteristics employed in the simulations. Using as a base the present simulation results can be affirmed that for the turbulent diffuser flow simulation the *SST* model is a good choice, considering the use of the *BSL* model for a comparative purpose for some simulation cases, when the converge is achieved. The use of the *k-ε* and *RNG k-ε* models is strongly not recommended, even is these models are more stable from the numerical point of view and consume less computational time. In any case, the obtained results with these two last models are not correct when compared with the experimental data and physically incorrect at the walls.

The obtained results confirm the poor influence exerted over the flow by the type of BC applied at the lateral walls. Nevertheless, it is recommended the use of the symmetric BC with base on the results showed for the *SST* model at Re_{in} = 164441 and Figure 2 geometry. Finally, it was found that the type of computational domain, can exert a significantly influence over the simulation results, even if the domains only differs in the exit zone configuration. It is very important to note, that for turbulent flows this region is characterized by complex flow structures and should be modeled with caution.

6. Acknowledgement

The authors fully acknowledge the support obtained from the Tecumseh do Brasil LTDA Company for the development of the present research work.

7. References

ANSYS-CFX®-Solver Theory manual, Release 10.0, 1996.

Churchill, S. W., 2000, "Progress in the Thermal Sciences: AIChE Institute Lecture", AIChE Journal, Vol.46, N°9, 1704-1722.

Cyklis, P., 1994, "CFD Simulation of the Flow Through Reciprocating Compressor Self-acting Valves", Proccedings of the International Compressor Engineering Conference, Purdue, pp. 427-432.

Deschamps, C. J., Ferreira, R. T. S. and Prata, A. T., 1988, "Application of the k-ε Model to Turbulent Flow in Compressor Valves", Proceddings of the 2nd Brazilian Thermal Science Meeting, São Paulo, Brasil, pp. 259-262.

Deschamps, C. J., Ferreira, R. T. S. and Prata, A. T., 1989, "Turbulent Flow Modeling in Precense of Stagnation Recirculation, Acceleration and Adverse Pressure Gradient", Proccedings of the X Brazilian Congress of Mechanical Engineering, Vol.1, pp. 57-60, (in Portuguese).

Deschamps, C. J., Ferreira, R. T. S. and Prata, A. T., 1996, "Turbulent Flow Through Valves of Reciprocating Compressors", Proccedings of the International Compressor Engineering Conference, Purdue, pp. 377-382.

Ervin, J. S., Suryanarayana, N. V. and Ng, H. C., 1989, "Radial, Turbulent Flow of a Fluid Between Two Coaxial Disks", ASME J. Fluids Engineering, Vol.111, pp. 378-383.

Hayashi, S., Matsui, T. and Ito, T., 1975, "Study of Flow and Thrust in Nozzle-Flapper Valves", ASME J. of Fluid Engineering, Vol.97, pp. 39-50.

Having, R. A., 2005, "Flow and Plate Motion in Compressor Valves", PhD. Thesis, University of Twente, Enschede, Netherlands, 156 p.

Hrenya. C. M., Bolio, E. J., Chakrabarti, D and Sinclair, J. L., 1995, "Comparison of Low Reynolds Number *k-ε* Turbuelence Models in Predicting Fully Depeloped Pipe Flow", Chemical Engineering Science, Vol.50, N°12, pp. 1923-1941.

Jackson, J. D. and Symmons, G. R., 1965, "An Investigation of Laminar Radial Flow Between Two Parallel Discs", Applied Scientific Research, Section A, Vol.15, pp. 59-75.

Launder, B. E. and Spalding, D. B., 1974, "The Numerical Computation of Turbulent Flows", Comput, Methods Appl. Mech. Eng., Vol.3, pp. 269-289.

Launder, B. E., Reece, G. J. and Rodi, W., 1975, "Progress in the Developments of a Reynolds-Stress Turbulence Closure", J. Fluid Mechanics, Vol.68, pp. 537-566.

Livesey, J. L., 1960, "Inertia Effects in Viscous Flows", International J. Mechanical Science, Vol.1, pp. 84-88.

Matos, F. F. S., Prata, A. T. and Deschamps, 1999, "Numerical Analysis of the Dynamic Behaviour of Plate Valves in Reciprocating Compressors", Proccedings ImechE Conference Transactions, C542/031, pp.453-462.

Matos, F. F. S., Prata, A. T. and Deschamps, 2002, "Numerical Simulation of the Dynamics of Reed Type Valves", Proccedings of the International Compressor Engineering Conference, Purdue, C15-2.

Menter, R. F., 1994, "Two-equation Eddy-viscosity Turbulence Models for Engineering Applicaitons" AIAA Journal, Vol.32, N°8, pp. 269-289.

Moller, P. S., 1963, "Radial Flow Wothout Swirl Between Parallel Discs", The Aeronautical Quaterly, Vol.14, pp. 163-186.

Ottitsch, F. and Scarpinato, P., 2000, "CFD a Viable Engineering Tool for Compressor Valve Desing or Just a Toy?", Procceding International Compreessor Engineering Conference, Purdue, pp. 423-428.

Perez-Segarra, C. D., Cadafalch, J., Rigola, J. and Oliva, A., 1999, "Numerical Study of Turbulent Fluid-flow Through Valves", Proccedings ImechE Conference Transaction, C542/021, pp. 399-408.

Piechna, J. R. and Meier, G. E. A., 1986, "Numerical Investigation of Steady and Unsteady Flow in Valve Gap", International Compressor Engineering Conference, Purdue, pp. 1-14.

Pope, S. B., 2000, "Turbulent Flows", Cambridge University Press, U.K., 771 p.

Possamai, F. C., Ferreira, R. T. S. and Prata, A. T., 2001, "Pressure Distribution in Laminar Radial Flow Through Inclined Disks", International J. of Heat and Fluid Flow, Vol.22, pp. 440-449.

Raal, J. D., 1978, "Radial Source Flow Between Parralel Discs", J. Fluid Mechanics, Vol.85, pp. 401-416.

Savage, S. B., 1964, "Laminar Radial Flow Between Parallel Plates", ASME J. of Applied Mechanics, Vol.31, 594-596.

Speziale, C. G., Sarkar, S. and Gatski, T.B., 1991, "Modelling the Pressure-Strain Correlation of Turbulence: an Invariant Dynamical Systems Approach", J. Fluid Mechanics, Vol.277, pp. 245-272.

Tabatabai, M. and Pollard, A., 1987, "Turbulence in Radial Flow between Parallel Disks at Medium and Low Reynolds Numbers", J. Fluid Mechanics, Vol.185, pp. 483-502.

Tennekes, H. and Lumley, J. L., 1972, "A First Course in Turbulence", MIT Press, Cambridge MA, p.

Versteeg, H. K. and Malalasekera, W., 1995, "An Introduction to Computational Fluid Dynamics. The Finite Volume Method", Prentice Hall, U.K., 257 p.

Volfang, V., Thomas, E. and Florian M., 2002, "Heat transfer predictions using advanced two-equation turbulence models." CFX Technical Memorandum-CFX-VAL10/0602.

Wilcox, D. C., 1993, "Turbulence Modeling for CFD", DCW Industries, La Cañada, CA,

Yakhot, V., Orszag, S. A., Thangam, S., Gatski, T. B. and Speziale, C. G., (1992), "Development of Turbulence Models for Shear Flows by a Double Expansion Technique", Physics of Fluids A, Vol.4, N°7, pp. 1510-1520.

Proceedings of the 11th Brazilian Congress of Thermal Sciences and Engineering -- ENCIT 2006
Braz. Soc. of Mechanical Sciences and Engineering -- ABCM, Curitiba, Brazil, Dec. 5-8, 2006

Paper CIT06-0429

ESTUDO COMPARATIVO DE QUATRO DIFERENTES MÉTODOS DE DIFUSÃO VISCOSA PARA APLICAÇÃO NO MÉTODO DE VÓRTICES

Victor Santoro Santiago
vsantoro@ig.com.br

Gustavo C. R. Bodstein
Universidade Federal do Rio de Janeiro, Departamento de Engenharia Mecânica – Poli/COPPE
Centro de Tecnologia, Bloco G, sala 204 – Ilha do Fundão, 21945-970 Rio de Janeiro, RJ – Brasil
gustavo@mecanica.coppe.ufrj.br

Resumo. *O Método de Vórtices vem ganhando popularidade em diversas áreas da ciência, sobretudo na aplicação em problemas de mecânica dos fluidos. Tal crescimento se deve à utilização de uma metodologia puramente Lagrangiana, sem a necessidade de utilizar uma malha, o que em muito facilita o estudo de escoamentos externos ao redor de corpos com geometrias complexas. No método de vórtices os fenômenos de transporte de vorticidade por difusão e convecção são separados para resolver a equação de transporte da vorticidade. Diversas metodologias vêm sendo desenvolvidas para modelar a etapa difusiva. Neste trabalho são implementados quatro métodos de simulação da difusão: Avanço Randômico (MAR); Redistribuição de Vorticidade (MRV); Crescimento do Núcleo Modificado (MCNM); e Velocidade de Difusão (MVD). Utilizando-se como referência a solução analítica puramente difusiva para o Vórtice de Lamb, os quatro métodos são comparados dos pontos de vista de acurácia e custo computacional visando a aplicação destes ao Método de Vórtices. Por último, o MCNM mostra acurácia superior ao MAR no problema convectivo/difusivo de simulação do desenvolvimento da camada limite de Blasius sobre placa plana.*

Palavras-chave*: método do avanço randômico, método da redistribuição de vorticidade, método do crescimento do núcleo modificado, método da velocidade de difusão, método de vórtices.*

1.Introdução

O estudo de escoamentos externos ao redor de corpos com geometria complexa representa uma área de grande interesse para a ciência e, sobretudo, para a engenharia, uma vez que situações práticas deste tipo ocorrem com freqüência. Pode-se citar como exemplos os escoamentos ao redor de corpos rombudos, como cilindros de seção circular, e ao redor de corpos esbeltos, como aerofólios. A abordagem desses problemas utilizando métodos numéricos Eulerianos, baseados em malhas, nem sempre é conveniente para escoamentos externos, uma vez que o refinamento espacial das malhas pode acarretar erros por difusão numérica e/ou um esforço computacional desnecessário. Assim, o Método de Vórtices Discretos apresenta-se como alternativa viável, pois sua metodologia puramente Lagrangiana permite o completo abandono das malhas e sua modelagem se concentra nas regiões rotacionais do escoamento, que passa a ser representada por uma nuvem de vórtices. Na sua abordagem mais utilizada, o Método de Vórtices Discretos separa algoritmicamente os processos convectivo e difusivo durante a solução da equação de transporte da vorticidade.

A primeira metodologia aplicada ao Método de Vórtices para tratar a difusão viscosa foi desenvolvida por Chorin (1973). Denominado Método do Avanço Randômico (MAR), este foi rapidamente difundido devido a sua facilidade de implementação e rapidez de execução. Porém, a característica estocástica do método fez com que outras alternativas de natureza determinística fossem buscadas. Shankar e Van Dommelen (1996) propuseram o Método da Redistribuição de Vorticidade (MRV), cuja principal característica é a redistribuição da intensidade de um vórtice entre seus vizinhos através da solução de um sistema de equações algébricas que otimiza este processo. Quando não há solução para este sistema, novos vórtices são criados e passam a integrar a nuvem de vórtices. Ogami e Akamatsu (1991) desenvolveram o Método de Velocidade de Difusão (MVD), o qual simula a difusão da vorticidade através da inserção de uma velocidade extra no processo convectivo puramente devido à difusão. Tal velocidade é relacionada à viscosidade cinemática do fluido, ao campo de vorticidade e ao gradiente do campo de vorticidade. Rossi (1996) apresentou uma correção ao Método do Crescimento do Núcleo proposto por Leonard (1980), o qual havia sido abandonado após Greengard (1985) provar que esta metodologia não converge para as equações de Navier-Stokes. No método de Rossi (1996), denominado Método do Crescimento do Núcleo Modificado (MCNM), o campo de vorticidade evolui à medida que o raio do núcleo de desingularização dos vórtices pontuais cresce até um valor máximo. Neste ponto é necessário que o vórtice seja dividido, dando origem a novos vórtices, cujos raios podem novamente se expandir. Este processo garante a convergência do método. Takeda *et al.* (1997) fez um estudo comparativo desses quatro métodos e concluiu que o MRV produz melhores resultados que os demais. No entanto, o estudo não mantém o número de vórtices aproximadamente igual entre os métodos, o que inviabiliza uma comparação mais efetiva.

Utilizando-se como referência a solução analítica puramente difusiva para o Vórtice de Lamb, este artigo analisa novamente, do ponto de vista de acurácia e custo computacional, os mesmos quatro métodos de simulação da difusão viscosa estudados por Takeda *et al.* (1997): MAR, MRV, MCNM e MVD. Os resultados permitem apontar mais claramente algumas vantagens e desvantagens de cada método na aplicação destes ao Método de Vórtices. Em seguida, são apresentados alguns resultados preliminares obtidos ao se comparar o MCNM ao MAR para o estudo do problema convectivo/difusivo de desenvolvimento da camada limite de Blasius sobre placa plana.

2. Formulação Matemática Geral do Método dos Vórtices Discretos

O Método de Vórtices Discretos se constitui em uma ferramenta extremamente eficaz para simular escoamentos onde a vorticidade se concentra em regiões finitas do domínio fluido e a dinâmica de transporte convectivo/difusivo da vorticidade é modelada através do movimento de uma nuvem de vórtices discretos. O desenvolvimento no tempo do campo de vorticidade é calculado a partir da equação de transporte da vorticidade. No caso bidimensional, foco deste trabalho, o termo de esticamento e deformação das linhas de vorticidade é nulo e a vorticidade possui apenas uma componente não nula, a componente ω normal ao plano do escoamento. Logo, a equação de transporte da vorticidade se reduz a

$$\frac{\partial \omega}{\partial t} + \mathbf{q} \cdot \nabla \omega = \frac{1}{Re} \nabla^2 \omega \,. \tag{1}$$

Considerando-se a discretização no tempo da Eq. (1) necessária para se calcular numericamente a evolução temporal do campo de vorticidade, pode-se impor uma separação dos fenômenos de transporte difusivo e convectivo durante um mesmo intervalo de tempo. Partindo desta concepção, Chorin (1973) propôs a decomposição da Eq. (1) em dois operadores, um puramente convectivo e outro puramente difusivo, dando origem às seguintes equações

$$\frac{\partial \omega}{\partial t} + \mathbf{q} \cdot \nabla \omega = 0 \,, \tag{2}$$

$$\frac{\partial \omega}{\partial t} = \frac{1}{Re} \nabla^2 \omega \,. \tag{3}$$

As Equações (2) e (3) representam, deste modo, o transporte da vorticidade devido aos efeitos convectivo e difusivo, respectivamente, presentes no escoamento. A solução da Eq. (3), em particular, é o objeto dos diversos métodos implementados e comparados neste trabalho. A seguir tais métodos são apresentados com mais profundidade, evidenciando suas particularidades e seus detalhes de implementação.

3. Apresentação Geral dos Métodos de Difusão Viscosa Implementados

3.1. Método do Avanço Randômico - MAR

O MAR foi inicialmente desenvolvido por Chorin (1973) para aplicação em escoamentos com alto número de Reynolds e tem sido bastante utilizado desde então. Seu princípio fundamental é substituir o processo difusivo por deslocamentos randômicos de partículas que carregam vorticidade de modo a simular o campo de vorticidade.

A Eq. 3 possui solução analítica para um vórtice inicialmente potencial, a qual pode ser escrita na forma adimensional como

$$\omega(r,t) = Re \frac{\Gamma}{4\pi t} \exp\left(-Re \frac{r^2}{4t} \right). \tag{4}$$

Pode-se mostrar que a solução da Eq. (4) pode ser reproduzida pelo movimento aleatório de uma nuvem vórtices, de maneira similar ao movimento Browniano molecular. Chorin (1973) demonstrou que, quando o número de vórtices tende ao infinito, o movimento aleatório da nuvem aproxima-se da solução exata da Eq. (4). Lewis (1991) propôs uma alteração à metodologia apresentada por Chorin (1973). Se a probabilidade de se encontrar um vórtice em uma determinada posição no instante t for representada por $\omega(t)$, pode-se encontrar os deslocamentos radial e polar deste vórtice, Δr e $\Delta\theta$, respectivamente, invertendo-se a Eq. (4) para obter

$$\Delta r = \sqrt{\frac{4t}{Re} \ln\left(\frac{1}{P} \right)} \qquad \text{e} \qquad \Delta\theta = 2\pi Q \,, \tag{5a e 5b}$$

onde P e Q são números randômicos entre 0 e 1 retirados de uma distribuição estatisticamente uniforme. As Eq. (5a) e (5b) podem ser escritas em coordenadas cartesianas como

$$\begin{pmatrix} \Delta x_D \\ \Delta y_D \end{pmatrix}_i = \begin{pmatrix} \Delta r \cos(\Delta\theta) \\ \Delta r \,\mathrm{sen}(\Delta\theta) \end{pmatrix}. \tag{6}$$

3.2 Método da Redistribuição de Vorticidade – MRV

O MRV, desenvolvido por Shankar e Van Dommelen (1996), se propôs a ser uma alternativa determinística ao MAR, mantendo a grande vantagem de ser completamente livre de malhas, o que não ocorre com o Método da Troca de Intensidade das Partículas – MTIP (Cottet e Koumoutsakos, 1999). Tanto o MRV quanto o MTIP baseiam-se na troca de parcelas de circulação entre vórtices vizinhos, o que simula o transporte difusivo de vorticidade.

O algoritmo do MRV é estruturado para achar a parcela de circulação f_{ij}^n que é transferida do vórtice *i* para o vórtice *j* (vórtices vizinhos) no instante de tempo *n*. Vórtices vizinhos são aqueles que se encontram à uma distância inferior à distância de difusão, a qual é da ordem de $h_v = \sqrt{\nu \Delta t}$ .O sistema para a determinação de f_{ij}^n é obtido comparando-se a transformada de Fourier do campo de vorticidade obtido pela redistribuição com a transformada de Fourier do campo de vorticidade exato, e representa uma aproximação de ordem Δt. Deste modo, o sucesso do método reside em se achar uma solução positiva válida para o seguinte sistema,

$$\sum_j f_{ij}^n = 1 , \tag{7}$$

$$\sum_j f_{ij}^n \xi_{1ij} = 0 , \ \sum_j f_{ij}^n \xi_{2ij} = 0 , \tag{8}$$

$$\sum_j f_{ij}^n \xi_{1ij}^2 = 2 , \ \sum_j f_{ij}^n \xi_{1ij} \xi_{2ij} = 0 , \ \sum_j f_{ij}^n \xi_{2ij}^2 = 2 , \tag{9}$$

onde $\vec{\xi}_{ij} = (\vec{x}_j - \vec{x}_i)/h_v$, ou seja, ξ_{1ij} e ξ_{2ij} são as componentes cartesianas de $\vec{\xi}_{ij}$. Assim, o vórtice *j* está na vizinhança do vórtice *i* se $\left|\vec{x}_j - \vec{x}_i\right| \le R h_v$, onde *R* é uma constante. Shankar e Van Dommelen (1996) definem o valor de *R* como $R = \sqrt{12}$. O sentido físico das Eqs.(7), (8) e (9) pode ser entendido respectivamente como sendo a conservação de circulação, conservação do centro de vorticidade e a correta expansão do diâmetro médio, ou seja, a conservação do momento linear e do momento angular. Outra restrição imposta é de que $f_{ij}^n > 0$, que representa o fato de que a vorticidade não pode ser criada ou destruída no interior do fluido.

O sistema formado pelas Eqs.(7), (8) e (9) é do tipo de "fase I" em programação linear e pode ser resolvido por deslocamento de variáveis. Entretanto, Shankar e Van Dommelen (1996) propuseram uma transformação de variáveis do tipo $w_j = f_{ij}^n - 1/2$. Assim, o universo alvo da solução do sistema passa de [0,1] para [−1/2,1/2], o que permite dizer que a norma máxima do vetor solução é $\left\|\vec{w}\right\|_\infty = \max_j \left\{\left|w_j\right|\right\}$. O sistema, então, pode ser resolvido por um algoritmo de otimização que minimize a norma máxima até um valor limite de ½. A partir deste valor não é possível encontrar solução, ou seja, faz-se necessário adicionar novos vórtices ao sistema. Shankar e Van Dommelen (1996) citam a distância de $\sqrt{6}$ do vórtice *i* para o nascimento de novos vórtices, em intervalos de 30º, até que o sistema apresente solução possível.

O sistema formado pelas Eqs.(7), (8) e (9) pode ser reescrito para cada vórtice *i* como

$$A\vec{w}_j = \vec{b} . \tag{10}$$

Trocando a igualdade acima por ≥ e ≤ e inserindo-se $\left\|\vec{w}\right\|_\infty$ como incógnita, pode-se resolver o problema através de uma rotina de otimização que minimize $\left\|\vec{w}\right\|_\infty$, como se segue

$$\begin{pmatrix} A & \vec{0} \\ I & \vec{1} \\ -A & \vec{0} \\ -I & \vec{1} \end{pmatrix} \begin{pmatrix} \vec{w}_j \\ \left\|\vec{w}\right\|_\infty \end{pmatrix} \ge \begin{Bmatrix} \vec{b} \\ \vec{0} \\ -\vec{b} \\ \vec{0} \end{Bmatrix} . \tag{11}$$

A primeira e a terceira equações do sistema de Eqs. (11) são: $A\vec{w}_j \ge \vec{b}$ e $A\vec{w}_j \le \vec{b}$, ou seja, $A\vec{w}_j = \vec{b}$. A segunda e a quarta equações são: $\left\|\vec{w}\right\|_\infty \ge -\vec{w}_j$ e $\left\|\vec{w}\right\|_\infty \ge \vec{w}_j$, ou seja, $\left\|\vec{w}\right\|_\infty = \max_j \left\{\left|w_j\right|\right\}$. Deste modo, o objetivo se torna resolver o sistema de equações (11), minimizando-se o valor de $\left\|\vec{w}\right\|_\infty$ e, caso $\left\|\vec{w}\right\|_\infty > 1/2$, novos vórtices devem ser acrescentados. Neste trabalho as Eqs. (11) são resolvidas utilizando-se a rotina DDLPRS da IMSL.

3.3 Método da Velocidade de Difusão - MVD

O Método da Velocidade de Difusão desenvolvido por Ogami e Akamatsu (1991) acrescenta uma parcela de velocidade relativa à difusão da vorticidade para o deslocamento de cada vórtice. Tal equacionamento é obtido manipulando-se a equação de Navier-Stokes e comparando o resultado com a equação que descreve o movimento de uma função 2D qualquer. Os detalhes podem ser vistos em Ogami e Akamatsu (1991).

Define-se então a velocidade de difusão $\vec{u}_d$, cujas componentes em coordenadas cartesianas são

$$u_d = -\frac{\nu}{\omega}\frac{\partial \omega}{\partial x} \quad \text{e} \quad v_d = -\frac{\nu}{\omega}\frac{\partial \omega}{\partial y}. \tag{12a, 12b}$$

Para que se obtenha uma distribuição de vorticidade suavizada, desingulariza-se os vórtices pontuais, o que neste trabalho foi realizado através da utilização do vórtice de Lamb. Assim, a vorticidade induzida pela nuvem de vórtices *j* sobre o vórtice *i* pode ser escrita como

$$\omega_i = \frac{1}{\pi\sigma^2}\sum_j \exp\left[-\frac{\left(x_j - x_i\right)^2 + \left(y_j - y_i\right)^2}{\sigma^2}\right]\Gamma_j, \tag{13}$$

sendo σ o raio do núcleo do vórtice. Substituindo-se a Eq. (13) nas Eqs. (12a) e (12b), chega-se às componentes da velocidade de difusão em coordenadas cartesianas

$$u_{di} = \frac{2\nu}{\pi\sigma^4 w_i}\sum_j \left(x_i - x_j\right)\exp\left[-\frac{\left(x_j - x_i\right)^2 + \left(y_j - y_i\right)^2}{\sigma^2}\right]\Gamma_j, \tag{14}$$

$$v_{di} = \frac{2\nu}{\pi\sigma^4 w_i}\sum_j \left(y_i - y_j\right)\exp\left[-\frac{\left(x_j - x_i\right)^2 + \left(y_j - y_i\right)^2}{\sigma^2}\right]\Gamma_j. \tag{15}$$

As Eqs. (14) e (15) representam a parcela a ser somada na velocidade de convecção que permite a determinação da posição futura dos vórtices.

3.4 Método do Crescimento do Núcleo Modificado – MCNM

O método do crescimento do núcleo de Leonard (1980) estabelece uma aproximação para a evolução no tempo do campo de vorticidade devido à difusão através do crescimento do raio do núcleo dos vórtices. Este método deixou de ser estudado quando Greengard (1985) provou que sua solução não converge para a equação de Navier-Stokes para longos tempos de simulação. Rossi (1996) apresentou uma modificação que tornou o método de Leonard convergente.

A modificação implementada por Rossi (1996), denominada "refinamento espacial", torna o método do crescimento do núcleo convergente porque se baseia na escolha de parâmetros numéricos que controlam a evolução temporal do raio do núcleo, realizando uma divisão dos vórtices em intervalos regulares. Assim, o Método do Crescimento do Núcleo Modificado (MCNM) de Rossi tornou-se uma opção como um método de difusão determinístico, de fácil implementação e completamente livre de malhas. Outra particularidade do MCNM é o fato deste não utilizar a decomposição da equação de transporte de vorticidade, Eq. (1), nas Eqs. (2) e (3). Apesar de não pesar negativamente na convergência, esta decomposição introduz um erro numérico que não está presente no MCNM.

No MCNM, a taxa de crescimento do raio do núcleo é determinada por

$$\frac{\partial \sigma}{\partial t} = \sqrt{\nu}. \tag{16}$$

Define-se os parâmetros numéricos α e l que determinam a freqüência do referido refinamento espacial. Deste modo, um vórtice com intesidade inicial γ terá seu raio variando de um valor mínimo inicial αl à um valor máximo l, quando sofrerá uma divisão em quatro novos vórtices, como sugerido por Rossi (1996), com vorticidades de $\gamma/4$. Estes novos vórtices são posicionados a 90° uns dos outros e a uma distância r em torno do vórtice original, o que garante a conservação do momento de segunda ordem. O valor de r é dado por

$$r = 2\sigma\sqrt{1-\alpha^2}. \tag{17}$$

4. Difusão de um Vórtice Pontual

O problema clássico de difusão de um vórtice pontual é simulado pelo MAR, MRV, MVD e MCNM, tendo em vista a existência de uma solução analítica que permite uma comparação geral entre estes quatro métodos de difusão. Entretanto, a escolha dos diversos parâmetros numéricos influencia os resultados encontrados e dificulta um pouco esta comparação, uma vez que tais parâmetros não mantêm correspondência entre os diferentes métodos analisados.

4.1 Formulação do Problema de Difusão para um Vórtice Pontual

A taxa de variação da vorticidade de um vórtice pontual centrado na origem, com intensidade inicial Γ, é descrita pela Eq. (3), a qual em coordenadas polares pode ser escrita como

$$\frac{\partial \omega}{\partial t} = \nu \left\{ \frac{\partial^2 w}{\partial r^2} + \frac{1}{r}\frac{\partial w}{\partial r} \right\}. \tag{18}$$

Batchelor (1970) apresenta a solução para a Eq. (18), relacionando a distribuição espacial com a temporal. O resultado pode ser expresso por

$$\omega(r,t) = \frac{\Gamma}{4\pi\nu t}\exp\left(-\frac{r^2}{4\nu t}\right). \tag{19}$$

Definindo-se as variáveis adimensionais $\tau = \frac{t\nu}{L^2}$, $r^* = \frac{r}{L}$, $\omega^* = \frac{2\pi L^2 \omega}{\Gamma}$, a Eq. (19) se torna

$$\omega^* = \frac{1}{2\tau}\exp\left(-\frac{r^{*2}}{4\tau}\right). \tag{20}$$

4.2. Resultados para o Vórtice Pontual

A seguir são apresentados os resultados para o caso de difusão de um vórtice pontual, localizado na origem, simulada pelo MAR, MRV, MVD e MCNM, de acordo com a adimensionalização mostrada na Eq. (20). Após a simulação, o campo de vorticidade é determinado utilizando-se a metodologia descrita por Lewis (1991), onde são traçados anéis concêntricos, sobre os quais é calculada a vorticidade de acordo com o número de vórtices encontrados em cada anel. Alternativamente, o campo de vorticidade também é calculado desingularizando-se os vórtices e aplicando o princípio da superposição de efeitos, ou seja, utilizando-se a Eq. (13) para cada ponto de interesse.

4.2.1. Método do Avanço Randômico – MAR

Lewis (1991) propõe a simulação da difusão de um vórtice pontual através do deslocamento randômico de um conjunto de N vórtices com intensidade $2\pi/N$, todos partindo da origem e se deslocando como descrito na seção 3.1. Tal procedimento foi executado para N = 1000, utilizando inicialmente um único passo no tempo (NT = 1). Os resultados para $\tau = 1$ e $\tau = 2$, obtidos calculando-se ω^* através de anéis concêntricos, são comparados à Eq. (20) na Fig. 1, onde se observa alguma dispersão dos resultados calculados pelo MAR em relação à curva teórica.

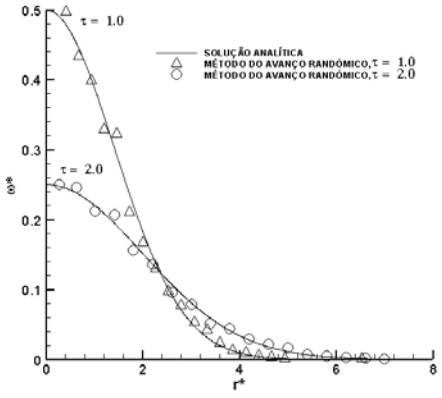

Figura 1. Vórtice pontual – MAR: N = 1000 e NT = 1.

As Fig. 2 e Fig. 3, geradas utilizando-se o princípio da superposição e a Eq. (13), apresentam a análise de convergência ao se variar o número de passos no tempo para atingir $\tau = 1$ e $\tau = 2$, respectivamente. Verifica-se, em primeiro lugar, que o princípio da superposição fornece resultados mais acurados que os anéis concêntricos para comparação com a solução analítica. Em segundo lugar, há uma melhora nos resultados com o aumento de *NT*.

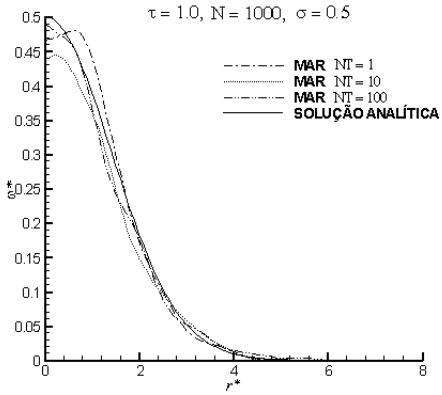

Figura 2. Vórtice pontual – MAR: $\tau = 1$; $N = 1000$; $\sigma = 0.5$.

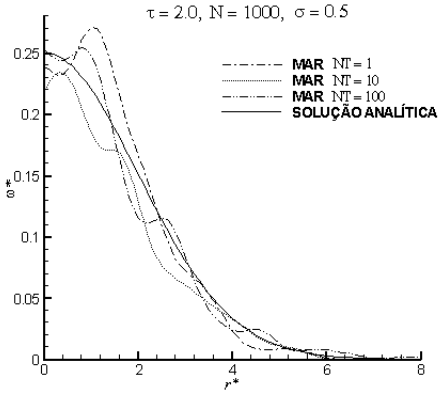

Figura 3. Vórtice pontual – MAR: $\tau = 2$; $N = 1000$; $\sigma = 0.5$.

As Figuras 4 e 5, geradas com o princípio da superposição, apresentam a análise de convergência para o raio do núcleo do vórtice σ, para $\tau = 1$ e $\tau = 2$, respectivamente. Verifica-se um aumento de acurácia com o aumento de σ.

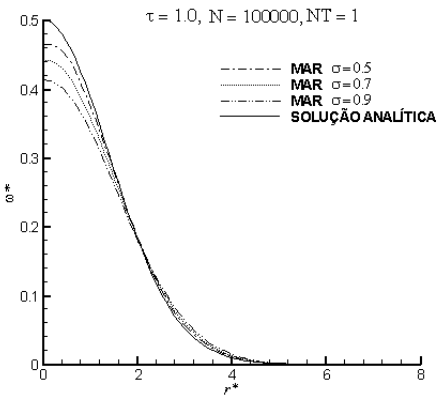

Figura 4. Vórtice pontual – MAR: $\tau = 1$; $N = 100000$; $NT = 1$.

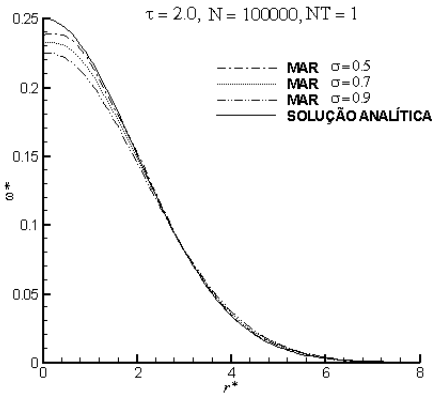

Figura 5. Vórtice pontual – MAR: $\tau = 2$; $N = 100000$; $NT = 1$.

As Figuras 6 e 7, mais uma vez geradas com o princípio da superposição, apresentam a análise de convergência para o número de vórtices *N*, para $\tau = 1$ e $\tau = 2$, respectivamente. Há uma clara melhora de acurácia quando *N* aumenta.

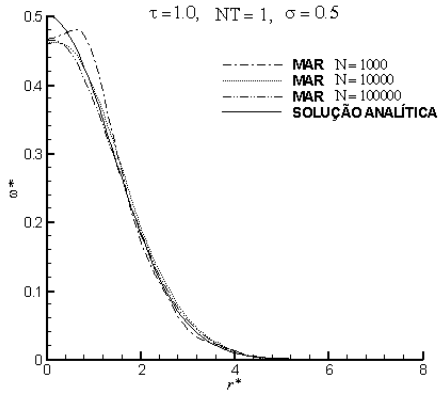

Figura 6. Vórtice pontual – MAR; $\tau = 1$; $NT = 1$; $\sigma = 0.5$.

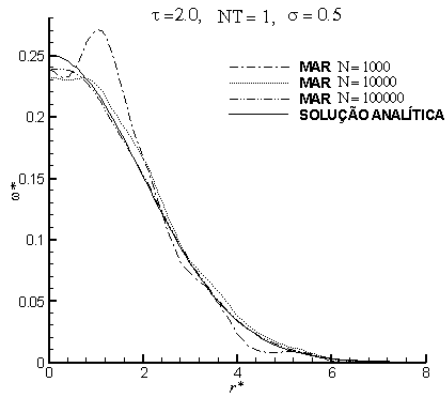

Figura 7. Vórtice pontual – MAR; $\tau = 2$; $NT = 1$; $\sigma = 0.5$.

4.2.2. Método da Redistribuição de Vorticidade - MRV

A simulação da difusão de vorticidade do vórtice pontual utilizando-se o MRV foi realizada seguindo-se a formulação apresentada na seção 3.2 e os resultados são comparados com a solução analítica da Eq. (20). Deste modo, um vórtice com intensidade inicial 2π é posicionado na origem no instante $t = 0$, dando início à simulação. Uma vez que não existem vórtices vizinhos, o sistema de Eqs. (11) não apresenta solução possível, sendo necessária a criação de seis novos vórtices, distando $\sqrt{6}$ do vórtice inicial. Deste modo, novos vórtices são criados a cada passo no tempo, o que aumenta a área abrangida pelos vórtices a partir da origem e possibilita que o sistema de Eqs. (11) seja resolvido, determinando-se, assim, as parcelas de vorticidade que devem ser trocadas entre os vórtices.

As Figuras 8 e 9 apresentam os resultados das simulações para o campo de vorticidade calculados, respectivamente, pelo método da divisão do domínio em anéis concêntricos, seguida da contagem do número de vórtices nos anéis (Lewis, 1991), e pelo procedimento de superposição de efeitos, Eq. (13). Novamente observa-se que o princípio da superposição fornece resultados mais acurados que o método dos anéis concêntricos e com menos dispersão. Além disso, nota-se a grande acurácia dos resultados produzidos pelo MRV em comparação com a solução analítica.

F

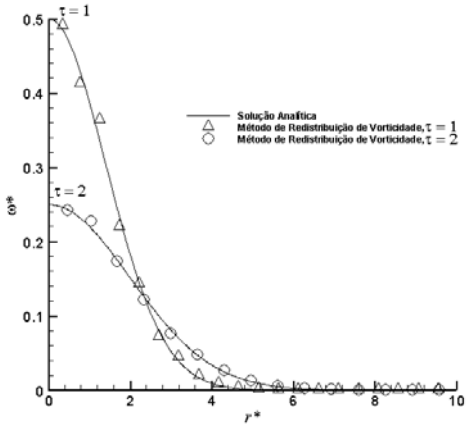

Figura 8. Vórtice pontual – MRV: anéis concêntricos.

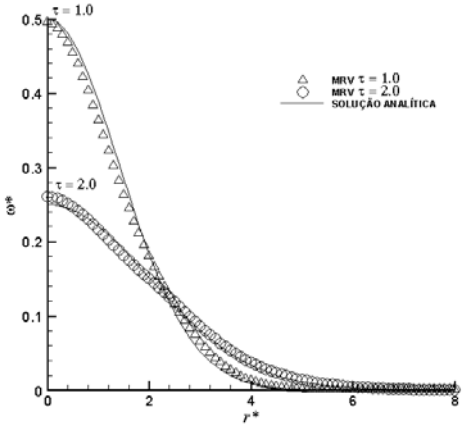

Figura 9. Vórtice pontual – MRV: superposição.

4.2.3. Método da Velocidade de Difusão – MVD

A difusão de um vórtice pontual foi simulada desta vez utilizando-se a metodologia apresentada na seção 3.3. No entanto, esta implementação apresenta a dificuldade adicional de não se contar com o gradiente do campo de vorticidade em $\tau = 0$, uma vez que toda a vorticidade está concentrada na origem. Para contornar este problema, deixou-se a simulação evoluir a partir da condição inicial de um vórtice com intensidade 2π, utilizando-se o MCNM por 30 passos consecutivos, gerando-se, assim, um gradiente de vorticidade que permitiu a utilização do MVD a partir deste ponto.

A Fig. 10 apresenta os resultados desta simulação para $\tau = 1$ e $\tau = 2$ utilizando-se o método de contagem de vórtices em anéis concêntricos proposto por Lewis (1991). Como observado nos resultados anteriores com o método dos anéis concêntricos, os resultados acompanham a curva teórica, mas apresentam alguma dispersão.

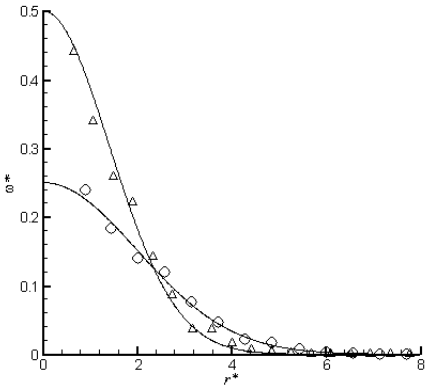

Figura 10. Vórtice pontual – MVD (anéis concêntricos).

As Figuras 11 e 12, geradas para $\tau = 1$ e $\tau = 2$, respectivamente, analisam a convergência do MVD com relação à variação do número de vórtices *N*, utilizando o princípio da superposição descrito pela Eq. (13). Estas figuras permitem observar que os resultados apresentam melhora à medida que o número de vórtices na simulação, *N*, cresce.

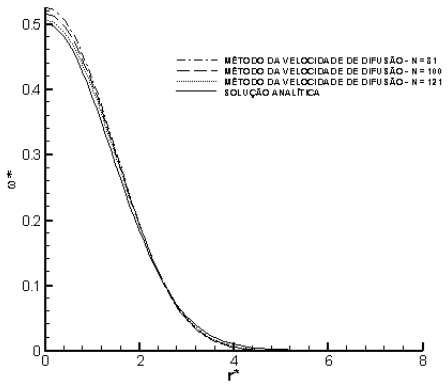

Figura 11. Vórtice pontual – MVD: $\tau = 1$.

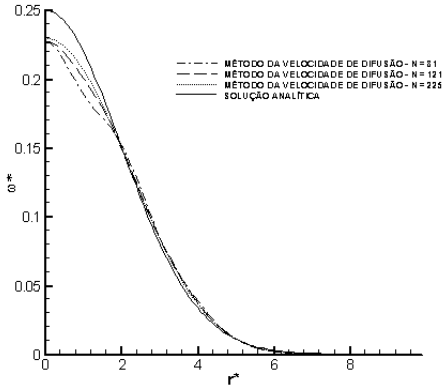

Figura 12. Vórtice pontual – MVD: $\tau = 2$.

4.2.4. Método do Crescimento do Núcleo Modificado – MCNM

Os resultados a seguir foram gerados utilizando-se o MCNM para simular a difusão de um vórtice pontual centrado na origem, com intensidade 2π, de acordo com a formulação apresentada na seção 3.4. A Figura 13 refere-se novamente à aplicação do princípio da contagem de vórtices distribuídos em anéis concêntricos (Lewis, 1991). Mais uma vez observa-se que o cálculo de ω^* utilizando-se o método dos anéis produz alguma dispersão nos resultados.

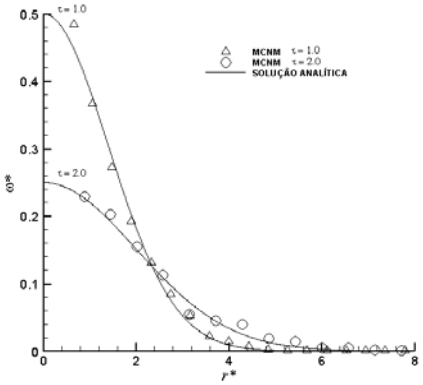

Figura 13. Vórtice pontual – MCNM: anéis.

As Figuras 14 e 15 mostram a convergência de ω^* com relação a α para $\tau = 1$ e $\tau = 2$, respectivamente, calculada pelo MCNM utilizando-se o princípio da superposição. Nota-se claramente resultados mais convergidos quando α aumenta.

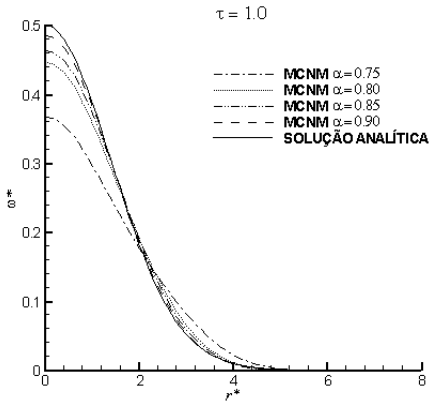

Figura 14. Vórtice pontual – MCNM: $\tau = 1$.

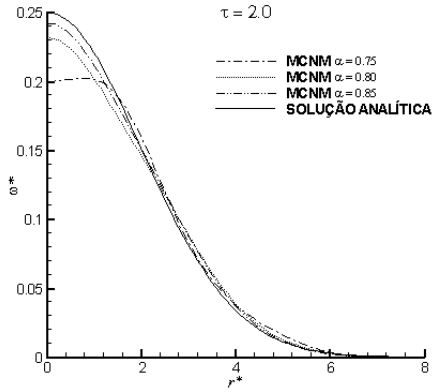

Figura 15. Vórtice pontual – MCNM: $\tau = 2$.

4.3. Análise dos Resultados para a Difusão do Vórtice Pontual

A Tabela 1 apresenta resultados que permitem uma análise comparativa entre os métodos quanto à acurácia de cada um. Manteve-se o Δt fixo para todos os casos, variando-se τ apenas para o MRV e para o MCNM com o objetivo de produzir um número de vórtices semelhante para todos. Os demais parâmetros numéricos são os que geram os melhores resultados para cada método, no que se refere ao erro máximo ($E_{\max}$) e ao erro médio ($\bar{E}$) do valor da vorticidade, calculada com a Eq. (13) e comparados à solução analítica. Define-se o erro médio como a média aritmética do módulo da diferença entre o valor da vorticidade calculada pelo método numérico em questão e o valor exato em cada ponto.

Tabela 1. Erro máximo ($E_{\max}$) e erro médio ($\bar{E}$) da vorticidade.

	$E_{\max}$	$\bar{E}$	N	Δt	τ	σ	α
MAR	5,51205 x 10^{-3}	3,32237 x 10^{-2}	1000	0,05	2	0,005	-
MVD	6,76687 x 10^{-3}	3,46612 x 10^{-2}	1089	0,05	2	0,005	-
MRV	1,97361 x 10^{-3}	8,49746 x 10^{-2}	1024	0,05	1,65	0,005	-
	2,67586 x 10^{-3}	1,11671 x 10^{-2}	1521	0,05	2	0,005	-
MCNM	1,07325 x 10^{-3}	5,35153 x 10^{-3}	4447	0,05	2	0,005	0,97
	2,06599 x 10^{-3}	1,02798 x 10^{-2}	1027	0,05	1	0,005	0,97

Do ponto de vista de acurácia, os resultados da Tabela 1 permitem que se conclua que o MCNM é superior aos demais métodos porque apresenta os menores erros, enquanto que o MVD é o que apresentou pior desempenho, com acurácia ligeiramente inferior ao MAR. Porém, deve-se ressaltar que tanto o MAR quanto o MVD produzem oscilações na distribuição de vorticidade resultantes da baixa ocorrência de interseção entre os núcleos dos vórtices, como mostrado nas Figs. 2, 3, 6 e 7, para o MAR, e Fig. 12 para o MVD. Nota-se, entretanto, que as oscilações dos resultados obtidos com o MAR são bem maiores que as do MVD. Estas oscilações impossibilitam o uso do MAR em simulações de grande acurácia, sem um mecanismo que introduza vórtices na região rotacional, de modo a eliminar tais flutuações e garantir a convergência. Nas simulações realizadas, o MVD possui ainda uma limitação quanto ao estabelecimento da condição inicial, pois o gradiente de vorticidade necessário para o cálculo da velocidade de difusão é inexistente em t = 0. Esta limitação, porém, não existe na sua aplicação no método de vórtices para escoamento externo sobre corpos. Os outros dois métodos, MRV e MCNC, são os que se mostram mais acurados de um modo geral, além de não apresentarem o problema de convergência resultante da baixa ocorrência de interseção entre os núcleos dos vórtices. No entanto, o MCNC possui erros um pouco menores e é muito mais simples de ser implementado.

A Tabela 2 ilustra os tempos de CPU obtidos para $\tau = 1$ e $\tau = 2$, variando-se o passo de tempo, $\Delta\tau$, e o número de vórtices. A comparação entre os quatro métodos simulados, MAR, MRV, MVD e MCNM, quanto ao custo computacional é tarefa bastante complexa e difícil de ser realizada, tendo em vista a inexistência de uma relação entre os diversos parâmetros numéricos de cada método. Como conseqüência, nem sempre é possível manter o número de vórtices constante entre as diversas simulações. Apesar deste fato tornar difícil o estabelecimento de critérios que permitam uma comparação definitiva, pode-se observar que os resultados, organizados do método mais lento para o mais rápido, são: MRV, MVD, MCNC e MAR. As diferenças em tempo de CPU são muito grandes entre o MAR e os demais métodos porque o contador de operações do MAR é proporcional a N. Essa diferença, no entanto, diminui muito se considerarmos que, para reduzir drasticamente as oscilações no campo de ω, seria necessário povoar a região rotacional do escoamento com um número muito maior de vórtices, o que aumentaria muito o tempo computacional. O MVD é intrinsecamente um método lento porque possui contador de operações proporcional a N^2, mas seu desempenho nos resultados obtidos é superior ao MCNC e ao MRV porque N é menor nas simulações realizadas. Os resultados em termos de tempo de CPU para o MCNC e o MRV são bastante piores que para o MAR e o MVD porque os algoritmos do MCNC e do MRV povoam continuamente a região rotacional com novos vórtices para garantir convergência, o que gera um número muito maior de vórtices na região fluida e um grande aumento no tempo de CPU, apesar de produzir resultados mais acurados.

Tabela 2: Tempos de CPU (s) e número de vórtices (N) para os quatro métodos estudados.

MÉTODO	Δt	τ=1	τ=2
MAR	0.025	N=1000; t=3,12 x 10^{-2} s	N=1000; t=6,25 x 10^{-2}s
	0.050	N=1000; t=1,56 x 10^{-2} s	N=1000; t=3,12 x 10^{-2} s
MRV	0.025	N=4921; t=2,30 x 10^{3} s	N=19441; t=1,35 x 10^{5} s
	0.050	N=1261; t=4,75 x 10^{1} s	N=4921; t=2,31 x 10^{3} s
MCNM	0.025	N=1600; t=9,68 x 10^{2} s	N=6400; t=1,33 x 10^{5} s
	0.050	N=400; t=7,25 x 10^{0} s	N=1600; t=9,57 x 10^{2} s
MVD	0.025	N=961; t=3,50 x 10^{1} s	N=961; t=7,23 x 10^{1} s
	0.050	N=961; t=1,79 x 10^{1} s	N=961; t=3,60 x 10^{1} s

Dois fatores adicionais devem ser ressaltados quando se analisa tempo de CPU. Em primeiro lugar, métodos que geram muitos vórtices, como o MCNC e o MRV, podem reduzir a quantidade de vórtices presentes no escoamento utilizando um algoritmo de aglomeração de vórtices, como o desenvolvido por Rossi (1997). Em segundo lugar, outro fator que deve ser levado em consideração na comparação quanto ao custo computacional é a grande particularidade do problema de difusão do vórtice pontual, que tende a encobrir deficiências que seriam aparentes em um problema que envolvesse convecção. Como exemplo, pode-se citar a criação de vórtices coincidentes no MRV e no MCNM, o que só ocorre em um problema puramente difusivo como o do vórtice pontual estudado. Em simulações de escoamento externo utilizando o método de vórtices, a convecção presente no escoamento movimenta vórtices coincidentes e produz a mesma modelagem da região rotacional do escoamento com menos vórtices, o que também reduz o tempo de CPU.

5. Camada Limite sobre Placa Plana Alinhada com o Escoamento Incidente

Nesta seção são apresentados os resultados para o problema convectivo/difusivo do desenvolvimento de camada limite sobre placa plana alinhada com o escoamento incidente. Utiliza-se o algoritmo do método de vórtices proposto por Lewis (1991), simulando-se o processo difusivo pelo MAR e pelo MCNM.

A escolha do problema de desenvolvimento de camada limite em placa plana deve-se à existência de solução teórica para este problema, o que permite uma análise dos resultados em uma situação que envolve convecção e difusão simultaneamente, e que por esta razão se torna uma análise mais representativa.

5.1. Formulação do Problema

O problema da camada limite de Blasius sobre uma placa plana sem espessura pode ser modelado pelo método de vórtices como o resultado de um escoamento uniforme U que incide impulsivamente sobre a placa em $t = 0$ e que resulta na geração de uma folha de vorticidade na placa de intensidade $\gamma(s_i) = U$ em $0 \le x \le l$. Esta vorticidade gerada na placa se difunde para o meio fluido e sofre, em seguida, convecção e difusão, dando origem a uma nuvem de vórtices que representa a região rotacional do escoamento.

A folha de vorticidade gerada na placa plana é dividida em N elementos que satisfazem automaticamente à condição de não escorregamento sobre a placa, a cada passo no tempo. Estes elementos são transformados em vórtices, formando uma nuvem. Utilizando o Método das Imagens para satisfazer automaticamente à condição de contorno de impermeabilidade sobre a placa, o campo de velocidade total sobre cada elemento da folha de vorticidade pode ser calculado subtraindo-se a velocidade induzida pela nuvem de vórtices do escoamento incidente, de acordo com a equação abaixo, a qual, considera a influência dos vórtices j e de suas imagens sobre o elemento i da placa, ou seja,

$$\gamma(s_i) = U - \frac{1}{\pi}\sum_{j=1}^{N}\frac{\Delta\Gamma_j y_j}{\left(x_i - x_j\right)^2 + y_j^2}\,. \tag{21}$$

A vorticidade calculada pela Eq. (21) dá origem a um vórtice de Lamb, o qual é posicionado a uma distância da placa igual ao seu raio, definido por $\sigma = 4.48364\,(\Delta t/Re)^{1/2}$ e cuja intensidade é $\Delta\Gamma_i = \gamma_i \Delta s_i$, onde $\Delta s_i = l/N$. Os vórtices se deslocam por ação da convecção gerada pela nuvem e por suas imagens, que levam em conta a influência do vórtice i e de sua imagem sobre o vórtice j, de acordo com

$$\Delta u_j = \frac{\Delta\Gamma_i}{2\pi}\left(\frac{y_j - y_i}{r_1^2} - \frac{y_j + y_i}{r_2^2}\right) \quad \text{e} \quad \Delta v_j = \frac{\Delta\Gamma_i}{2\pi}\left(x_j - x_i\right)\left(\frac{1}{r_2^2} - \frac{1}{r_1^2}\right), \tag{22a e 22b}$$

onde $r_1^2 = \left(x_j - x_i\right)^2 + \left(y_j - y_i\right)^2$ e $r_2^2 = \left(x_j - x_i\right)^2 + \left(y_j + y_i\right)^2$. Deve-se atentar para a necessidade de cálculo em separado da influência da imagem do vórtice j sobre o mesmo, conforme as equações

$$\Delta u_j = -\frac{\Delta\Gamma_i}{4\pi y_i} \quad \text{e} \quad \Delta v_j = 0\,. \tag{23}$$

Lewis (1991) propõe uma aproximação para a influência dos vórtices cujos raios cortam a placa, a qual é utilizada neste trabalho e descrita pela equação

$$\Delta\gamma(s_i) = \frac{\phi\Delta\Gamma_j}{2\pi\Delta s_i}\,, \tag{24}$$

onde, ϕ é o ângulo formado pelo vórtice j e pelos extremos do elemento i da placa. Assim, a influência do vórtice j sobre o elemento i da placa é calculada com a Eq. (24), caso o raio do vórtice seja maior que sua distância à placa.

5.2. Resultados para Placa Plana

O problema formulado acima é resolvido utilizando-se o MAR e o MCNM, o que dá origem ao conjunto de resultados apresentados a seguir. Para ilustrar as esteiras obtidas, as Figuras 16 e 17 apresentam as nuvens de vórtices geradas utilizando-se respectivamente o MAR, para Re = 500, e o MCNM, para Re = 50000, onde $Re \equiv Ul/\nu$.

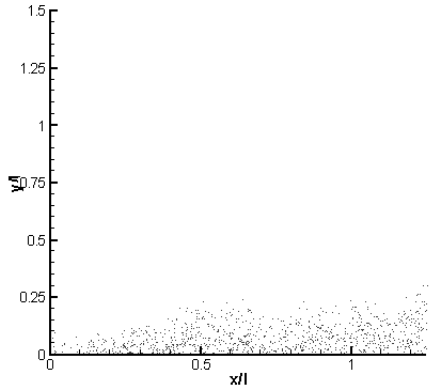

Figura 16. Camada limite – MAR: Re = 500.

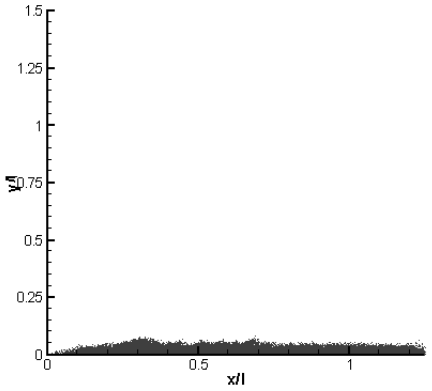

Figura 17. Vórtice pontual – MCNM: Re = 50000.

O perfil de velocidade é calculado e comparado à solução de Blasius para camada limite. Os resultados encontrados permitem uma comparação efetiva entre a acurácia do MAR e do MCNM, conforme visto na Fig. 18.

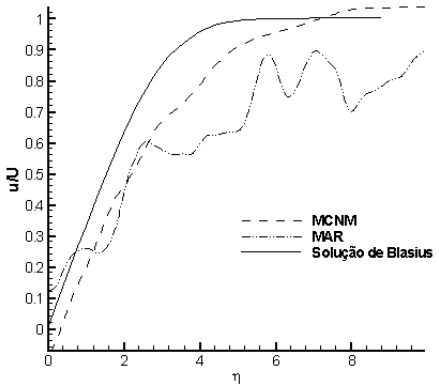

Figura 18. Camada limite: perfil de velocidade.

A Figura 18, gerada para $Re_x \equiv Ux/\nu$ = 50000, onde $\eta \equiv y(U/(\nu x)^{1/2}$, permite que se constate a melhor qualidade dos resultados obtidos pelo MCNM em comparação ao MAR. A grande oscilação observada nos resultados obtidos com o MAR é fruto do caráter estocástico do método e à relativa falta de interseção entre os núcleos dos vórtices. Por outro lado, o MCNC não possui essas deficiências e sua curva de u/U é muito mais suave. Este resultado foi obtido ainda para os instantes iniciais da simulação, mas já mostra a convergência dos métodos em relação ao perfil de Blasius.

6. Conclusões

Neste trabalho foram implementados quatro métodos Lagrangianos para simular a difusão de vorticidade sobre vórtices pontuais: o MAR, o MRV, o MVD e o MCNM. Estas implementações objetivam comparar a acurácia obtida por cada método na simulação de escoamentos externos com vistas a fornecer embasamento para a escolha de um dos três métodos determinísticos, MRV, MVD e MCNM, como alternativa ao tão difundido, porém probabilístico, MAR. Deste modo, a solução analítica para a difusão de um vórtice pontual permite que se conclua que o MCNM possui acurácia superior aos demais, além de ser de fácil implementação numérica. Seu alto custo computacional comparado ao MAR pode ser facilmente contornado utilizando-se um algoritmo de aglomeração de vórtices.

O problema da camada limite de Blasius foi utilizado como teste para a comparação entre o MAR e o MCNM porque é um problema convectivo/difusivo e possui solução exata. Estas simulações são bem mais abrangentes que o caso anterior estudado. Os resultados permitiram concluir que mais uma vez o MCNM apresentou maior acurácia frente ao MAR, desta vez em uma situação que contempla também a convecção e que, por isso, melhor representa uma real aplicação dos métodos testados.

Durante as simulações realizadas, foi percebida a tendência de aumento do custo computacional do MCNM, sobretudo para *Re* pequenos, uma vez que os vórtices são divididos com maior freqüência. Para que esta deficiência não se torne impeditiva é necessário introduzir um esquema de aglomeração que evite um número de vórtices excessivo que surge quando os núcleos dos vórtices se interceptam. Esta é a condição para a convergência do método de vórtices.

A aplicação efetiva do MCNM ao Método de Vórtices requer ainda estudo e pesquisa adicionais, sobretudo no que se refere ao já citado problema do aumento indiscriminado do número de vórtices. Porém, este trabalho permite que se conclua quanto a sua superioridade em acurácia, o que garante a este método a permanência em linhas de pesquisa que buscam aprimorar os resultados de suas simulações com o Método de Vórtices Discretos.

Agradecimentos

Os autores agradecem ao Exército Brasileiro e ao CNPq, respectivamente, pelo apoio financeiro a este projeto de pesquisa.

Referências

Chorin, A. J., 1973, "Numerical Study of Slightly Viscous Flow", Journal of Fluid Mechanics, Vol. 57, part 4, pp. 785-796.

Cottet, G.-H. and Koumoutsakos, P., 1999. "Vortex Methods. Theory and Practice". Cambridge University Press.

Greengard, C., 1985, "The core spreading vortex method aproximates the wrong equation", Journal of Computational Physics, Vol. 61, pp. 345-348.

Leonard, A., 1980, "Vortex methods for flow simulation", Journal of Computational Physics, Vol. 37, pp. 289-335.

Lewis, R. I., 1991, "Vortex Element Method for Fluid Dynamic Analysis of Engineering Systems", Cambridge, Cambridge University Press.

Ogami, Y. and Akamatsu, T., 1991, "Viscous flow simulation using the discrete vortex model – The Diffusion Velocity Method", Computer&Fluids, Vol. 19, No. 3/4, pp. 433-441.

Rossi, L., 1996, "Ressurecting core spreading vortex methods: A new scheme that is both deterministic and convergent", SIAM Journal, Vol. 17, No. 2, pp. 370-397.

Rossi, L., 1997, "Merging Computational Elements in Vortex Simulations", SIAM Journal, Vol. 18, No. 4, pp. 1014-1027.

Shankar, S., and Van Dommelen, L., 1996, "A new diffusion procedure for vortex methods", Journal of Computational Physics, Vol.127, pp. 88-109.

Takeda, K., Tutty, O. R. and Fitt, A. D., 1997, "A Comparison of Four Viscous Models for the Discrete Vortex Method", 13th AIAA Computational Fluid Dynamics Conference, Snowmass Village, CO, June 29 – July 02.

COMPARTIVE STUDY OF FOUR DIFFERENT VORTICITY DIFFUSION METHODS FOR APPLICATIONS TO VORTEX METHODS

Victor S. Santiago
vsantoro@ig.com.br

Gustavo C. R. Bodstein
Federal University of Rio de Janeiro (UFRJ), Department of Mechanical Engineering – Poli/COPPE
Centro de Tecnologia, Bloco G, sala 204 – Ilha do Fundão, 21945-970 Rio de Janeiro, RJ – Brazil
gustavo@mecanica.coppe.ufrj.br

Abstract. *The Vortex Method has become widely used in several areas of science and engineering, mainly in fluid mechanics applications. This is partly due to the fact that vortex methods use a purely Lagrangian methodology, which requires no grid. This characteristic facilitates the study of external flows around bodies with complex geometries. The splitting of the diffusive and convective vorticity transports is the approach most commonly employed to solve the vorticity transport equation. In this paper, we implement four numerical methods to simulate vorticity diffusion: Random Walk, Vorticity Redistribution, Corrected Core Spreading and Velocity Diffusion. Using as a reference the analytical solution for the Lamb vortex, these four models are compared from the point of view of accuracy and computational cost, which allows us to point out the advantages of each one for fluid flow applications. Additionally, we show that the Corrected Core-Spreading method produces superior accuracy over the Random-Walk method in the solution of the Blasius flat plate boundary layer problem.*

Keywords*: random-walk method, vorticity-redistribution method, corrected core-spreading method, velocity-diffusion method, vortex method.*

Proceedings of the 11th Brazilian Congress of Thermal Sciences and Engineering – ENCIT 2006
Braz. Soc. of Mechanical Sciences and Engineering – ABCM, Curitiba, Brazil, Dec. 5-8, 2006

Paper CIT06-0443

Modelagem de um Escoamento Laminar e Turbulento para Filtração Tangencial em Membranas Tubulares

Juliana Maria da Silva
Escola de Engenharia, Departamento de Engenharia Mecânica, Universidade de São Paulo, São Carlos - SP
jmaria02@yahoo.com.br

Sergio Rodrigues Fontes
Escola de Engenharia, Departamento de Engenharia Mecânica, Universidade de São Paulo, São Carlos - SP
srf@sc.usp.br

Resumo. *Nesse trabalho, o escoamento laminar e turbulento em membranas tubulares é estudado numericamente. O modelo matemático inclui as equações de conservação de massa e conservação da quantidade de movimento em coordenadas cilíndricas com associadas condições de fronteiras. A velocidade de sucção é descrita pela equação de Darcy, a qual relaciona o fluxo de permeado com a pressão transmembrana. O modelo de turbulência utilizado é o modelo de comprimento de Prandtl. As equações governantes são discretizadas pelo esquema de diferenças finitas em malha deslocada e resolvidas numericamente pelo método Sola. Valores do fluxo de permeado são comparados com resultados experimentais da literatura e distribuição de velocidades é apresentada.*

Palavras chave: *Laminar, Turbulência, Membrana tubular, Filtração tangencial, Modelagem*

1. Introdução

A filtração tangencial por meio de membranas é uma das mais importantes técnicas usadas em processos industriais, por isso, o estudo de escoamentos de fluidos em tubos porosos tem sido um campo ativo de pesquisas nos últimos 30 anos. Aspectos gerais desse processo são apresentados no trabalho de Ripperger e Altmann (2002). Vários trabalhos são encontrados na literatura tratando-se de estudos analíticos, numéricos e experimentais da filtração tangencial (Damak *et al.*, 2004, Granger *et al.*, 1989, Munson-McGee, 2002). Nassehi e Petera (1994) e Nassehi (1998) apresentaram um modelo numérico do escoamento axissimétrico em paredes permeáveis não-uniforme com a aplicação do esquema de elementos finitos. Damak et al. (2004) estudaram a combinação das equações de Navier-Stokes e Darcy para simular um escoamento de regime laminar em membranas tubulares.

Nesse artigo é investigado o desenvolvimento hidrodinâmico de escoamento incompressível em membranas tubulares, para os regimes laminar e turbulento. Para isso, as equações de conservação de massa e consevação da quantidade de movimento são utilizadas para modelar o escoamento, enquanto que a lei de Darcy representa o escoamento no meio poroso com pequena porosidade (Beavers e Joseph, 1967), essa combinação de equações é também muito encontrada na literatura (Damak *et al.*, 2004; Nassehi e Petera, 1994; Nassehi, 1998) para descrever esse tipo de escoamento. O efeito de turbulência no escoamento é determinado pelo modelo de comprimento de Prandtl ou modelo de zero equação (Cebeci e Bradshaw, 1984). As equações são discretizadas pelo esquema de diferenças finitas em malha desloca, e resolvidas numericamente pelo método SOLA (Hirt *et al.*, 1975).

São apresentados graficamente os perfis de velocidades. Para avaliação da modelagem do presente trabalho, o fluxo médio transmembrana é comparado com resultados experimentais obtidos da literatura (Yeh *et al.*, 2004; Haneda, 2006).

2. DESCRIÇÃO DO MODELO MATEMÁTICO

Considere um escoamento não-desenvolvido, incompressível, isotérmico e axissimétrico em um tubo cilíndrico com paredes porosas. O sistema de coordenadas tem origem na entrada, o eixo z está na linha central, o eixo r é normal à linha central, o raio do tubo é R e o comprimento é L, como ilustrado na Fig. (1).

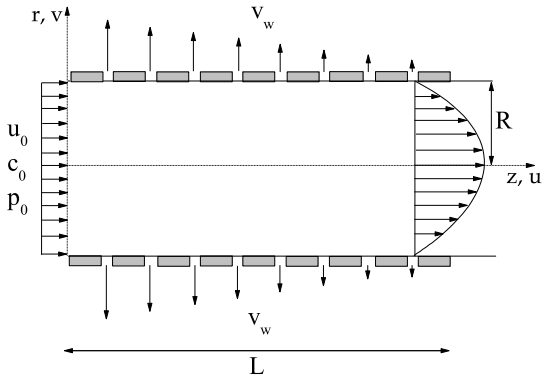

Figura 1: Representação do domínio do problema.

Na filtração tangencial, após um breve período transiente, o fluxo de permeado permanece quase constante, ou seja, em um estado pseudo-estacionário. Nesse estudo é análisado a condição estacionária, porém, uma formulação pseudo-transiente (Fortuna, 2000) é utilizada. Assim, o modelo matemático para os regimes laminar e turbulento é descrito pelas equações definidas nas próximas seções.

2.1. Modelagem laminar

As equações para a modelagem do escoamento laminar na forma conservativa e adimensional são:

$$\frac{\partial u^*}{\partial z^*} + \frac{1}{r^*}\frac{\partial (r^* v^*)}{\partial r^*} = 0, \tag{1}$$

$$\frac{\partial u^*}{\partial t^*} = -\frac{\partial p^*}{\partial \bar{z}} + {N^*}_u, \tag{2}$$

$$\frac{\partial v^*}{\partial t^*} = -\frac{\partial p^*}{\partial r^*} + {N^*}_v, \tag{3}$$

em que

$${N^*}_u = -\frac{\partial (u^* u^*)}{\partial z^*} - \frac{1}{r^*}\frac{\partial (r^* u^* v^*)}{\partial r^*} + \frac{2}{Re}\left(\frac{\partial^2 u^*}{\partial {z^*}^2} + \frac{\partial^2 u^*}{\partial {r^*}^2} + \frac{1}{r^*}\frac{\partial u^*}{\partial r^*}\right)$$

$${N^*}_v = -\frac{1}{r^*}\frac{\partial (r^* v^* v^*)}{\partial r^*} - \frac{\partial (u^* v^*)}{\partial z^*} + \frac{2}{Re}\left(\frac{\partial^2 v^*}{\partial {z^*}^2} + \frac{\partial^2 v^*}{\partial {r^*}^2} + \frac{1}{r^*}\frac{\partial v^*}{\partial r^*} - \frac{v^*}{{r^*}^2}\right)$$

$$Re = \frac{\rho u_0 d}{\mu},$$

em que d é o diâmetro do tubo e μ é viscosidade dinâmica ($kg\ m^{-1}s^{-1}$).

Neste trabalho, as transformações utilizadas para adimensionalização são:

$$z^* = \frac{z}{R}, \qquad r^* = \frac{r}{R}, \qquad u^* = \frac{u}{u_0}, \qquad v^* = \frac{v}{u_0}, \qquad p^* = \frac{p}{\rho {u_0}^2}, \qquad t^* = \frac{t u_0}{R}. \tag{4}$$

2.2. Modelagem turbulenta

Para a modelagem turbulenta utilizou-se o modelo de comprimento de Prandtl ou zero equação.

No regime turbulento, a velocidade em um ponto apresenta-se como a velocidade média acrescida de uma perturbação aleatória, variando continuamente ao longo do tempo. A velocidade real é denominada velocidade instantânea e é representada pela soma da velocidade média e da flutuação:

$$v = \bar{v} + v' \tag{5}$$

em que v' representa a variação aleatória da velocidade ou a flutuação da velocidade.

A velocidade média no tempo T é definida por:

$$\bar{v} = \frac{1}{T}\int_0^T v(t)dt, \tag{6}$$

Sendo assim, substituindo-se nas equações (1), (2) e (3) as variáveis em termos de seus valores médios e flutuantes, calculando-se a média no tempo e utilizando-se as condições de Reynolds (Roma, 2003), obtém-se as equações na forma adimensional para o escoamento turbulento:

$$\frac{\partial u^*}{\partial z^*} + \frac{1}{r^*}\frac{\partial r^* v^*}{\partial r^*} = 0, \tag{7}$$

$$\frac{\partial u^*}{\partial t^*} = -\frac{\partial p^*}{\partial z^*} + {N^*}_u, \tag{8}$$

$$\frac{\partial v^*}{\partial t^*} = -\frac{\partial p^*}{\partial r^*} + {N^*}_u, \tag{9}$$

em que

$$\begin{aligned}
{N^*}_u &= -\frac{\partial (u^* u^*)}{\partial z^*} - \frac{1}{r^*}\frac{\partial (r^* u^* v^*)}{\partial r^*} + \frac{2}{Re}\left(\frac{\partial^2 u^*}{\partial {z^*}^2} + \frac{\partial^2 u^*}{\partial {r^*}^2} + \frac{1}{r^*}\frac{\partial u^*}{\partial r^*}\right) + \frac{2}{Re}\left\{\frac{\partial}{\partial z^*}\left(2{\mu_t}^*\frac{\partial u^*}{\partial z^*}\right) + \right. \\
&\left. + \frac{{\mu_t}^*}{r^*}\left(\frac{\partial u^*}{\partial r^*} + \frac{\partial v^*}{\partial z^*}\right) + \frac{\partial}{\partial r}\left[{\mu_t}^*\left(\frac{\partial u^*}{\partial r^*} + \frac{\partial v^*}{\partial z^*}\right)\right]\right\}, \\
{N^*}_v &= -\frac{\partial (u^* v^*)}{\partial z^*} - \frac{1}{r^*}\frac{\partial (r^* v^* v^*)}{\partial r^*} + \frac{2}{Re}\left(\frac{\partial^2 v^*}{\partial {z^*}^2} + \frac{\partial^2 v^*}{\partial {r^*}^2} + \frac{1}{r^*}\frac{\partial v^*}{\partial r^*} - \frac{v^*}{{r^*}^2}\right) + \frac{2}{Re}\left\{\frac{\partial}{\partial r^*}\left(2{\mu_t}^*\frac{\partial v^*}{\partial r^*}\right) + \right. \\
&\left. + \frac{2{\mu_t}^*}{r^*}\frac{\partial v^*}{\partial r^*} - 2{\mu_t}^*\frac{v^*}{{r^*}^2} + \frac{\partial}{\partial z^*}\left[{\mu_t}^*\left(\frac{\partial u^*}{\partial r^*} + \frac{\partial v^*}{\partial z^*}\right)\right]\right\}, \\
{\mu_t}^* &= \frac{Re}{2}{l^*}^2\left(\frac{\partial u^*}{\partial r^*} + \frac{\partial v^*}{\partial z^*}\right),
\end{aligned}$$

${\mu_t}^* = \frac{\mu_t}{\mu}$ é a viscosidade dinâmica turbulenta ($kg\ m^{-1}s^{-1}$) e l^* é chamado comprimento de mistura e é definido como (Cebeci e Bradshaw, 1984):

$$l^* = 0,14 - 0,08(1-y^*)^2 - 0,06(1-y^*)^4, \tag{10}$$

em que $y^* = 1 - r^*$ denota a distância normal a parede porosa e $\bar{\kappa}$ foi estimado com valor 0,4 (Cebeci e Bradshaw, 1984). Em regiões próximas às paredes, utiliza-se uma equação apropriada para modelar esta região do escoamento, a função de amortecimento de Van Driest (Cebeci e Bradshaw, 1984):

$$l = \bar{\kappa} y^*[1 - exp(-y^*/A)], \tag{11}$$

em que $A = A^+\mu(\tau_w/\rho)^{-1/2}$, $A^+ = 26exp(-5,9v_w)$ e $\tau_w = 0,03325\rho u_0^2\left(\frac{2\mu}{du_0}\right)$ (Fox e MacDonald, 1995).

2.3. Condições de Contorno

Devido a simetria, somente a região entre a parede ($r^* = 1$) e a linha central do tubo ($r^* = 0$) foi numericamente considerada. Assim, as condições de contorno na forma adimensional utilizadas no presente estudo são:

$$z^* = 0, \qquad 0 \le r^* \le 1: \qquad u^* = 1, \qquad v^* = 0; \tag{12}$$

$$z^* = \frac{L^*}{R^*}, \qquad 0 \le r^* \le 1: \qquad \frac{\partial u^*}{\partial z^*} = 0, \qquad \frac{\partial v^*}{\partial z^*} = 0; \tag{13}$$

$$r^* = 0, \qquad 0 \le z^* \le \frac{L}{R}: \qquad \frac{\partial u^*}{\partial r^*} = 0, \qquad v^* = 0; \tag{14}$$

$$r^* = 1, \quad 0 \le z^* \le \frac{L}{R}: \quad u^* = 0, \quad {v^*}_w = K({p^*}_R - {p^*}_e), \tag{15}$$

em que p_e é a pressão externa adimensional do tubo, ${p^*}_R$ é a pressão adimensional na parede porosa, κ é a permeabilidade da parede porosa ($mPa^{-1}s^{-1}$), K é igual a $\kappa\rho u_0$(adimensional) e v_w é definido pela lei de Darcy:

$$v_w = \kappa\Delta p. \tag{16}$$

2.4. Método Numérico

As equações de (1) a (3) e de (7) a (9) associadas com as condições de contorno de (12) a (15) são aproximadas por diferenças finitas em malha deslocada, na qual a célula tem dimensões Δz por Δr, em que a variável pressão p esta definidas no centro da célula, enquanto as velocidades u e v são posicionadas nas faces laterais, que distam do centro $\pm\frac{\Delta z}{2}$ e $\pm\frac{\Delta r}{2}$, respectivamente.

As aproximações para as derivadas temporais são feitas utilizando-se diferenças avançadas (Euler explícito) de primeira ordem, os gradientes de pressão, bem como a equação de conservação de massa e os outros termos das equações da quantidade de movimento, com excessão dos termos convectivos, são aproximados por diferenças centrais de segunda ordem. Os termos convectivos são aproximados pelo esquema de segunda ordem HLPA (Hybrid Linear Parabolic Approximation) (Zhu, 1992).

O campo de velocidades e pressão são calculados pelo método SOLA (Hirt *et al.*, 1975; Fortuna, 2000). Esse método é caracterizado pelo esquema de correção de pressão e velocidades em cada passo no tempo, e pode ser resumido nos seguintes passo:

passo 1: a partir do valores u, v e p no nível de tempo n, calcula-se os valores de $\bar{u}^{*(n+1)}_{i+1/2,j}$ e $\bar{v}^{*(n+1)}_{i,j+1/2}$ definidos pelas equações

$$\bar{u}^{*(n+1)}_{i+1/2,j} = u^{*(n)}_{i+1/2,j} - \Delta t^* \left(\frac{p^{*(n)}_{i+1,j} - p^{*(n)}_{i,j}}{\Delta z^*} + N^{*(n)}_{u_{i+1/2,j}} \right), \tag{17}$$

$$\bar{v}^{*(n+1)}_{i,j+1/2} = v^{*(n)}_{i,j+1/2} - \Delta t^* \left(\frac{p^{*(n)}_{i,j+1} - p^{*(n)}_{i,j}}{\Delta r^*} + N^{*(n)}_{v_{i,j+1/2}} \right), \tag{18}$$

as quais são versões discretas das velocidade. Em que Δt^* é o passo no tempo.

passo2: para cada célula (i, j)
(i) calcula-se a correção para a pressão definida pela expressão:

$$\delta p^{(k)}_{i,j} = \frac{-wD_{i,j}}{2\Delta t^* \left(\frac{1}{(\Delta z^*)^2} + \frac{1}{(\Delta r^*)^2} \right)} \tag{19}$$

em que D é a dilatação $\left(\left.\frac{\partial u}{\partial z}\right|_{i,j} + \left.\frac{\partial v}{\partial r}\right|_{i,j} \right)$, w é um fator de relaxação, com $1 < w < 2$ e k é o número de iterações.
(ii) determina-se $p^*_{i,j}$

$$p^{*(n+1,k+1)}_{i,j} = p^{*(n+1,k)}_{i,j} + \delta p^{*(k)}_{i,j} \tag{20}$$

(iii) corrige-se as velocidades nas faces das células por meio das expressões:

$$u^{*(n+1,k+1)}_{i+1/2,j} = \bar{u}^{*(n+1,k)}_{i+1/2,j} + \Delta t^* \frac{\delta p^{*(k)}_{i,j}}{\Delta z^*}, \qquad u^{*(n+1,k+1)}_{i-1/2,j} = \bar{u}^{*(n+1,k)}_{i-1/2,j} - \Delta t^* \frac{\delta p^{*(k)}_{i,j}}{\Delta z^*}, \tag{21}$$

$$v^{*(n+1,k+1)}_{i,j+1/2} = \bar{v}^{*(n+1,k)}_{i,j+1/2} + \Delta t^* \frac{\delta p^{*(k)}_{i,j}}{\Delta r^*}, \qquad v^{*(n+1,k+1)}_{i,j-1/2} = \bar{v}^{*(n+1,k)}_{i,j-1/2} - \Delta t^* \frac{\delta p^{*(k)}_{i,j}}{\Delta r^*}, \tag{22}$$

passo 3: repete-se o passo (2) até que

$$max|D_{i,j}| \leq \epsilon \tag{23}$$

Com essa condição satisfeita, as velocidades u e v estão no nível de tempo $t = t_0 + \Delta t$.

passo 5: tomando-se adequado valor para Δt, retorna-se ao passo (1) até a convergência.

2.4.1. Controle do passo no tempo

A forma explícita do cálculo de u e v impõe restrições severas aos valores permitidos de Δt. A cada ciclo o tamanho do passo no tempo é obtido segundo as restrições (Fortuna, 2000):

(i) o fluido não pode percorrer uma distância maior que o comprimento de uma célula a cada passo no tempo:

$$\Delta t^* < min\left(\frac{\Delta z^*}{|u^*|_{max}}, \frac{\Delta r^*}{|v^*|_{max}}\right), \tag{24}$$

(ii) a segunda restrição de estabilidade é devido à discretização das equações de conservação da quantidade de movimento e envolve o número de Reynolds e a viscosidade turbulenta, caso o escoamento seja turbulento:

$$\Delta t^* < \frac{Re}{2\mu^*_{t\,max}}\left(\frac{\Delta z^{*2}\Delta r^{*2}}{\Delta z^{*2}+\Delta r^{*2}}\right). \tag{25}$$

em que $\mu^*_{t\,max} = max\{\mu^*_{t\,i,j}\}$

3. Resultados e discussões

O método apresentado acima foi aplicado para simular o escoamento da água em membranas tubulares, com diâmetros de $0,0063\ m$ para o caso laminar e $0,0056\ m$ para o turbulento, comprimento 30 vezes o raio e pressão transmembrana igual 1×10^5 Pa.

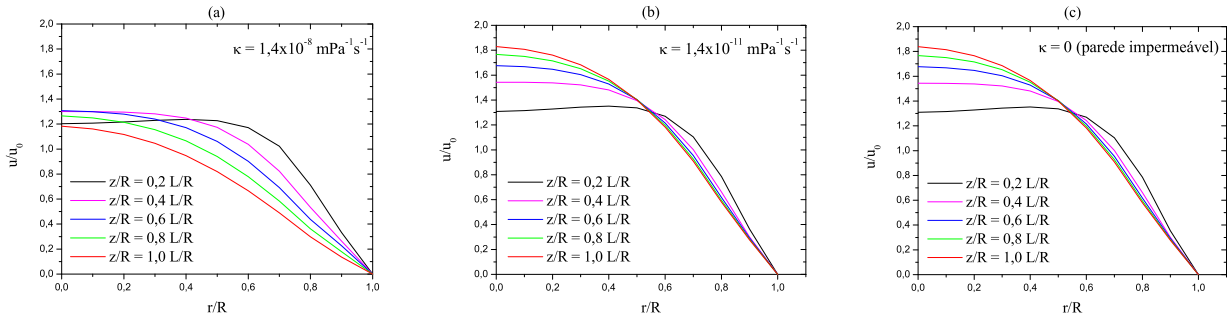

Figura 2: Perfil de velocidade axial como função da coordenada radial para diferentes posições axiais para o regime laminar, $Re = 100$.

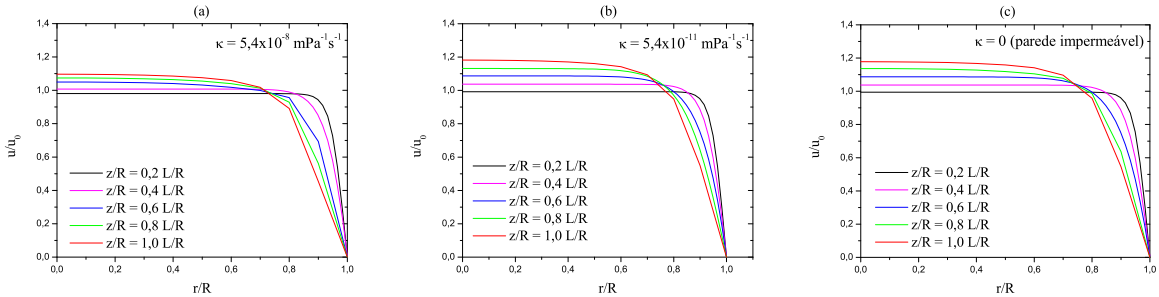

Figura 3: Perfil de velocidade axial como função da coordenada radial para diferentes posições axiais para o regime turbulento, $Re = 4000$.

Nas Fig. (2) e (3) apresentam-se os gráficos dos perfis de velocidade para diferentes posições axiais e para diferentes permeabilidades. Na Fig. (2), observa-se uma razoável diferença entre os perfis do caso (a), (b) e (c), em (a) a permeabilidade da membrana é maior, o que faz com que a sucção de massa junto à superfície permeável seja maior provocando, assim, uma desaceleração do escoamento, fazendo-se com que a velocidade na região central do tubo diminua, já em membranas que possuem baixa permeabilidade, como no caso (b), a sucção de massa quase não interfere no desenvolvimento dos perfis de velocidade, isso pode ser observado quando comparado com o gráfico (c) no qual a parede é considerada impermeável, nesse caso a diferença dos perfis de velocidade de (b) e (c) é praticamente inexistente. Na Fig. (3) devido ao escoamento ser turbulento,

a permeabilidade alta (Fig. (3 a)) não diminui a velocidade axial no centro do tubo a medida que a distância da entrada aumenta, mas ocorre uma pequena diminuição nas velocidades axiais centrais em relação aos perfis dos gráfico (b) e (c).

Essa interferência da permeabilidade no escoamento pode também ser observada na Fig. (4), a qual apresenta gráficos da variação do fluxo de permeado médio como função da permeabilidade da membrana. Observa-se um razoável crescimento do fluxo de permeado médio quando se aumenta o valor da permeabilidade.

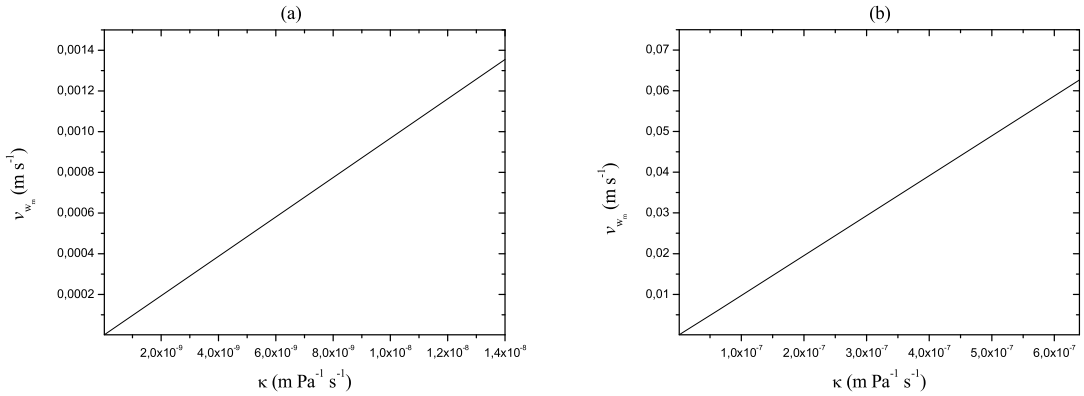

Figura 4: Gráfico do fluxo de permeado médio como função da permeabilidade da membrana para: (a) regime laminar, $Re = 100$; (b) regime turbulento, $Re = 4000$.

A fim de verificar a validação da modelagem, os resultados numéricos do presente trabalho, para o escoamento da água, são comparados com os resultados experimentais da literatura (Yeh *et al.*, 2004; Haneda, 2006), observa-se na Fig. (5), uma boa concordância entre os resultados numéricos e experimentais.

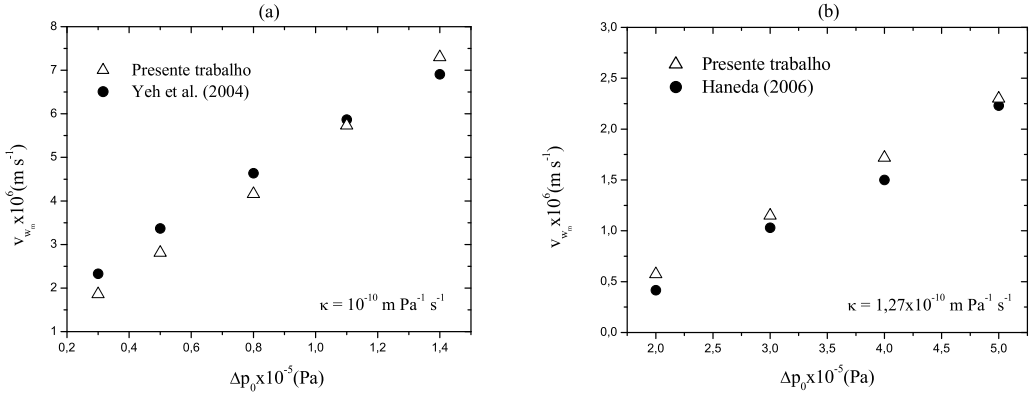

Figura 5: Comparação dos resultados numéricos desse trabalho com resultados experimentais para fluxo de permeado médio do escoamento da água como função da pressão transmembrana inicial para: (a) regime laminar, $Re = 527,5$; (b) regime turbulento, $Re = 22691$.

4. Conclusões

Este artigo descreve um modelo matemático para simular escoamentos em um processo de filtração tangencial em membranas tubulares. O escoamento é descrito pela equação de Navier-Stokes bidimensional em coordenadas cilíndricas e pela equação de Darcy, a qual representa a variação da velocidade de sucção na parede permeável.

Apresentou-se resultados para o desenvolvimento da velocidade axial e variação do fluxo médio em função da permeabilidade da membrana. O modelo foi cuidadosamente analisado por meio de comparações com resultados experimentais. A partir da análise dos resultados produzidos nessa modelagem, pode-se concluir que o modelo numérico se mostrou adequado com o problema físico estudado.

5. Agradecimentos

Os autores agradecem o Conselho Nacional de Desenvolvimento Científico e Tecnológico (CNPq) pelo suporte financeiro dessa pesquisa.

6. Referências

Beavers, G. S. and Joseph, D. D., 1967, Boundary Conditions at a Naturally Permeable Wall, "Journal of Fluid Mechanic", Vol. 30, pp. 197–207.

Cebeci, T. and Bradshaw, P., 1984, "Physical and Computational Aspects of Convective Heat Transfer", Springer-Verlag, New York, Inc.

Damak, K., Zeghmati, B., and Schmitz, P., 2004, A New Navier-Stokes and Darcy's Law Combined Model for Fluid Flow in Crossflow Filtration Tubular Membranes, "Desalination", Vol. 161, pp. 67–77.

Fortuna, A. O., 2000, "Técnica Computacionais para Dinâmica dos Fluidos - Conceitos Básicos e Aplicações", EdUSP, São Paulo, Brasil.

Fox, R. W. and MacDonald, A. T., 1995, "Introdução à Mecânica dos Fluidos", Livros Tecnicos e Cientificos, RJ.

Granger, J., Dodds, J., and Midoux, N., 1989, Laminar Flow in Channels with Porous Walls, "The Chemical Engineering Journal", Vol. 42, pp. 193–204.

Haneda, R. N., 2006, Investigação do Desempenho de Diferentes Estruturas Microporosas Tubulares na Retenção de Bactérias em Suspensão por Microfiltração Tangencial, Master's thesis, Escola de Engenharia de São Carlos, Universidade de São Paulo, São Carlos, Brasil.

Hirt, C. W., Nicolas, B. D., and Romero, N. C., 1975, SOLA - A Numerical Solution Algorithm for Transient Fluid Flows, "Los Alamos Scientific Report LA-5852", Vol. .

Munson-McGee, S. H., 2002, An Approximate Analytical Solution for the Fluid Dynamics of Laminar Flow in a Porous Tube, "Journal of Membrane Science", Vol. 197, pp. 223–230.

Nassehi, V., 1998, Modelling of Combined Navier-Stokes and Darcy Flows in Crossflow Membrane Filtration, "Chemical Engineering Science", Vol. 53, pp. 1253–1265.

Nassehi, V. and Petera, J., 1994, A New Least-Squares Finite Element Model for Combined Navier-Stokes and Darcy Flows in Geometrically Complicated Domains with Solid and Porous Boundaries, "International Journal for Numerical Methods in Engineering", Vol. 37, pp. 1609–1620.

Roma, W. N. L., 2003, "Fenômenos de Transporte para Engenharia", RiMa Editora.

Yeh, H. M., Dong, J. H., and Shi, M. Y., 2004, Momentum Balance Analysis of Flux and Pressure Declines in Membrane Ultrafiltration Along Tubular Modules, "Journal of Membrane Science", Vol. 241, pp. 335–345.

Zhu, J., 1992, On the Higher-Order Bounded Discretization Schemes for Finite Volume Computations of Incompressible Flows, "Computation Methods Aplication Mechanics Engineering", Vol. 98, pp. 345–360.

Modeling of a Laminar and a Turbulent Flow in Cross-Flow Filtration Tubular Membranes

Juliana Maria da Silva
Escola de Engenharia, Departamento de Engenharia Mecânica, Universidade de São Paulo, São Carlos - SP
`jmaria02@yahoo.com.br` if any

Sergio Rodrigues Fontes
Escola de Engenharia, Departamento de Engenharia Mecânica, Universidade de São Paulo, São Carlos - SP
`srf@sc.usp.br` if any

Abstract. *In this work, a laminar and a turbulent flow in a tubular membrane is studied numerically. The mathematical model comprises the conservation of mass and conservation of momentum equations in cylindrical coordinates with the associated boundary conditions. The suction velocity is described by Darcy's law, that relates the permeate flux with the transmembrane pressure. The turbulence model utilized is the Prandtl mixing length model. The governing equations are discretized by a finite-difference scheme on a staggered grid and solved numerically by the method called SOLA. Values to permeate flux are compared with experimental results of literature obtained. Velocity distributions are presented..*

Keywords *Laminar, Turbulence, Tubular membrane, Cross-flow, Modelling*

Proceedings of the 11th Brazilian Congress of Thermal Sciences and Engineering -- ENCIT 2006
Braz. Soc. of Mechanical Sciences and Engineering -- ABCM, Curitiba, Brazil, Dec. 5=8, 2006

Paper CIT06-0446

CONTROLE DE VAZÃO DE METAIS LÍQUIDOS POR BOMBAS ELETROMAGNÉTICAS DE CORRENTE CONTÍNUA

Eduardo Madeira Borges
Instituro de Estudos Avançados (IEAv), São José dos Campos, SP.
e-mail: eduardo@ieav.cta.br

Francisco Antonio Braz Filho
Instituro de Estudos Avançados (IEAv), São José dos Campos, SP.
e-mail: fbraz@ieav.cta.br

Lamartine Nogueira Frutuoso Guimarães
Instituro de Estudos Avançados (IEAv), São José dos Campos, SP.
e-mail: guimarae@ieav.cta.br

Resumo. Sistemas de refrigeração com altas densidades de potência necessitam de fluidos com alta condutividade térmica, como os metais líquidos. Bombas eletromagnéticas podem ser utilizadas no controle de escoamento de metais líquidos em circuitos fechados. O princípio de funcionamento das bombas eletromagnéticas é baseado na força de Lorentz. Esta força pode ser obtida pela interação de campo magnético e corrente elétrica, controladas por fontes externas independentes. Este trabalho apresenta o princípio de operação, o esquema de desenvolvimento de bombas eletromagnéticas de corrente contínua (EM) no Instituto de Estudos Avançados (IEAv) e o programa computacional BEMC-1. Os resultados teóricos, obtidos com o BEMC-1, são comparados a dados experimentais de operação da bomba EM, validando o programa BEMC-1. Este código é utilizado para a avaliação do desempenho da bomba EM aplicada no controle de escoamento de Mercúrio e de outros metais líquidos usados em reatores nucleares rápidos, como Sódio, Chumbo e Bismuto.

Palavras chave: metal líquido, bomba eletromagnética, controle de vazão.

1. Introdução

A pesquisa de bombas eletromagnéticas no Instituto de Estudos Avançados (IEAv) tem por objetivo o desenvolvimento de sistemas de refrigeração que utilizam metais líquidos como refrigerante, pois estes podem retirar altas densidades de potência térmica, como é necessário em reatores nucleares rápidos.

Foram desenvolvidas, com sucesso, as duas primeiras bombas eletromagnéticas (EM) de corrente contínua nacionais. Uma com magneto tipo C e bobinas e a outra com imãs permanentes de Samário-Cobalto, para a geração de campo magnético (Borges, et al., 1995 e Borges, et al., 1996). Ambas funcionaram satisfatoriamente em ensaios de campo magnético, de avaliação de pressão estática e de operação dinâmica. Os dois últimos ensaios citados foram realizados com Mercúrio em circuitos fechados especialmente projetados para este fim.

As bombas eletromagnéticas utilizam o princípio de Faraday, onde a interação da corrente elétrica e campo magnético gera a força magneto-motriz que controla o escoamento do fluido. Sem partes móveis, totalmente selada e com alta confiabilidade, este tipo de equipamento pode controlar o escoamento de um metal líquido de alta condutividade elétrica num circuito fechado e facilitar a circulação natural do líquido, em caso de falhas ou acidentes, em um reator nuclear. Estas características as tornam interessantes para serem utilizadas em reatores nucleares rápidos refrigerados a metal líquido, como no EBR-II (Lentz, et al., 1985), no SAFR (Lancet e Marchaterre, 1985), no PRISM (Kwant, et al., 1988) e no REARA (Prati, et al., 1994), que são reatores experimentais refrigerados a Sódio líquido.

Reatores rápidos refrigerados a Chumbo, a Bismuto e a outros metais líquidos estão sendo projetados usando conceitos avançados de segurança (Myasnikov, et al., 1993, Santos e Nascimento, 2002).

Com relação aos conceitos de segurança inerente e passiva adotada nos reatores nucleares de terceira e quarta geração, como nos projetos SAFR, PRISM e outros. Uma das vantagens do uso de bombas eletromagnéticas, no controle de escoamento do refrigerante do circuito primário, é que apresentam perda de carga muito menor, comparado às bombas centrifugas, além de permitir vazão reversa em caso de acidentes, por não terem partes móveis ou pás que aumentariam a perda de carga.

O programa computacional BEMC-1 foi elaborado com o objetivo de se poder estudar cada etapa do desenvolvimento de uma bomba eletromagnética de corrente contínua e avaliar o seu desempenho. Este programa é bastante versátil, facilita a avaliação e correção de desvios entre dados calculados e experimentais e pode ser utilizado no projeto de bombas eletromagnéticas de corrente contínua e avaliação do seu desempenho no controle do escoamento de metais líquidos em circuitos fechados, que é o principal enfoque deste artigo.

É importante notar que na bomba EM de imãs permanentes de Samário-Cobalto, os imãs estão colocados junto ao canal da bomba para minimizar as perdas de campo magnético, este procedimento é indicado no caso do controle de escoamento de Mercúrio, que é líquido a temperatura ambiente. Para os outros metais, há a necessidade de se aquecer e isolar o canal de escoamento o que poderia inviabilizar a utilização deste tipo de bomba, em especial se a temperatura de trabalho for próxima à temperatura de Curie do imã. Pois, caso os imãs sejam expostos a temperaturas superiores à de Curie estes perdem suas propriedades magnéticas. Já a bomba eletromagnética de magneto tipo C apresenta várias vantagens, com relação ao controle de campo magnético e possibilidade de isolamento do canal e esta será a utilizada para fins de comparação de resultados para os metais líquidos avaliados.

Neste trabalho apresenta-se o princípio de funcionamento de bombas eletromagnéticas, suas equações básicas, resultados experimentais da bomba eletromagnética de corrente contínua com magneto tipo C e bobinas operando em circuitos a Mercúrio, o programa computacional BEMC-1 e avalia a possibilidade da aplicação de bombas eletromagnéticas de corrente contínua no controle de escoamento de reatores rápidos refrigerados a metais líquidos como Sódio, Chumbo e Bismuto.

Os resultados obtidos nas simulações apresentadas neste trabalho reforçam a possibilidade que a nova geração de reatores rápidos avançados refrigerados a Sódio utilize bombas eletromagnéticas nos circuitos primários e secundários de refrigeração e conclui-se que reatores refrigerados a Chumbo e a Bismuto também podem operar com bombas eletromagnéticas.

2. Princípio de funcionamento de bombas eletromagnéticas

Em uma bomba eletromagnética de corrente contínua a força de Lorentz define a intensidade e a direção da força exercida no fluido condutor sob influência da corrente elétrica e do campo magnético impostos. Observa-se, na Figura 1 o princípio de funcionamento de uma bomba eletromagnética de corrente contínua.

Admitindo-se a altura do canal da bomba (a), a largura do canal (b) e o comprimento útil (c), monta-se o equacionamento para a avaliação do seu desempenho (Borges, 1991).

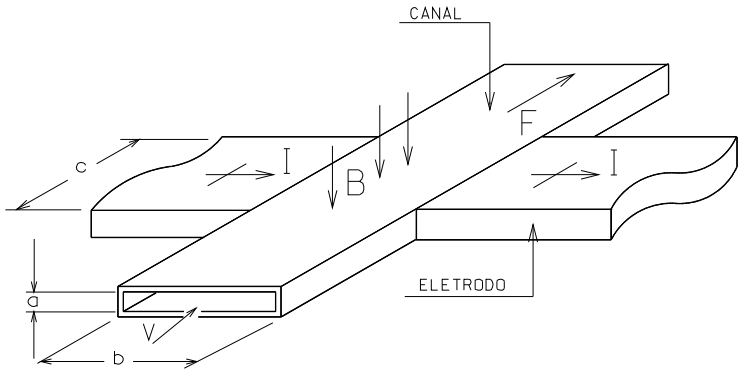

Figura 1. Princípio de funcionamento da bomba eletromagnética de corrente contínua.

2.1. Modelo teórico

Pode-se calcular o campo magnético da bomba EM tipo C, de acordo com a Lei Circuital de Ampere, pela Eq. (1):

$$B = \mu N I_{campo} / d , \quad (1)$$

que relaciona as intensidades de campo magnético (B) em torno de uma trajetória fechada de fluxo magnético e o comprimento da trajetória com a corrente que a circunda, onde N é o número total de espiras e I_{campo} é a corrente de campo fornecida, observando-se ainda, que as perdas no entreferro (d) são muito superiores às do magneto e que para os metais líquidos, a permeabilidade magnética (μ) é igual à do vácuo.

Considerando-se a perfeita perpendicularidade entre o campo magnético, a corrente elétrica principal (I) e a direção do escoamento do fluido, a força (F) resultante da interação entre campo e corrente pode ser calculada, em função da corrente elétrica útil (I_e), pela Eq. (2):

$$F = B I_e b . \quad (2)$$

Pode-se definir a pressão manométrica desenvolvida pela bomba como:

$$P = F/(a b) . \quad (3)$$

Substituindo a Eq. (2) na Eq. (3) tem-se:

$$P = B\, I_e / a \ , \text{em} \ \ [N/m^2] \ ; \text{e} \tag{4}$$

$$P = B\, I_e / (1360\, a) \ , \text{em} \ \ [\text{cm Hg}] \ . \tag{5}$$

A Figura 2 apresenta o circuito elétrico equivalente da bomba eletromagnética de corrente contínua.

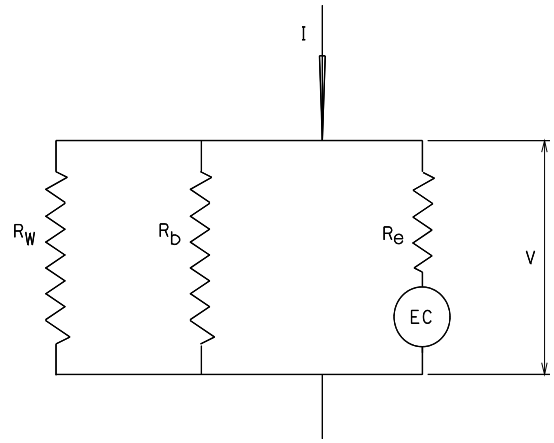

Figura 2. Circuito elétrico equivalente da bomba EM.

A tensão elétrica da bomba é calculada por:

$$V = I_e R_e + E_c = I R_t \ , \tag{6}$$

onde, R_t é a resistência elétrica equivalente do circuito e E_c é a força contra-eletromotriz resultante do deslocamento do fluido no campo magnético. Esta voltagem induzida pode ser obtida pela Eq. (7).

$$E_c = B\, w / a \ . \tag{7}$$

A corrente elétrica útil (I_e) pode ser calculada, pela Eq. (8), em função da corrente principal (I), da força contra eletromotriz (E_c) e das resistências elétricas R_e , R_w e R_b que são respectivamente as resistências elétricas do fluido no canal da bomba, da parede do canal (perpendicular ao campo magnético, na direção da corrente elétrica) e a resistência de "bypass", que é a resistência de fuga de corrente pelo fluido fora da influência do campo magnético. R_b por sua vez é calculada multiplicando-se a resistência elétrica útil (R_e) por um fator de correção empírico, que está relacionado com a geometria da bomba (Watt, 1958). Portanto a corrente elétrica útil é uma função da vazão volumétrica (w).

Observa-se que no estudo de pressão estática (com vazão nula) o último termo da Eq. (8) é nulo e para o estudo de operação dinâmica (com escoamento de fluido) da bomba EM este termo é diferente de zero.

$$I_e = \frac{I}{1 + R_e\left(\dfrac{R_w + R_b}{R_w R_b}\right)} - \frac{E_c}{R_e + \dfrac{R_w R_b}{R_w + R_b}}. \tag{8}$$

3. Método de cálculo

De modo geral as etapas fundamentais do projeto de uma bomba eletromagnética de corrente contínua são: a avaliação do campo magnético, da pressão estática e dos dados de vazão, pressão dinâmica e eficiência.

O programa BEMC-1, escrito em linguagem C++, foi elaborado com o objetivo de se poder avaliar, cada etapa do desenvolvimento de uma bomba EM, possibilitando alteração em todos os parâmetros importantes de projeto. A Figura 3 apresenta o diagrama de blocos com o esquema de cálculo do programa BEMC-1.

Escolhido o metal líquido a ser bombeado e as suas propriedades, assim como, a geometria e materiais do canal da bomba, calcula-se as resistências elétricas envolvidas nas Eq. (6) e (8).

Um parâmetro muito importante é o campo magnético que pode ser calculado pela equação de campo, Eq. (1), em função do entreferro e da corrente de campo e se necessário corrigido pelo fator de correção apropriado.

A pressão estática, valor limite operacional da bomba para vazão nula, é calculada pelas Eq. (4) e (5) e depende do campo magnético e da corrente elétrica útil, que é obtida pela Eq. (8), considerando-se as resistências elétricas, a corrente elétrica principal, sendo nulo o último termo da Eq. (8).

A pressão dinâmica fornecida pela bomba, também pode ser obtida pelas Eq. (4) e (5). Neste caso, a corrente elétrica útil deve ser calculada pela Eq. (8) considerando todos os seus termos, pois é função da vazão, usada na Eq. (7).

Com o BEMC-1 pode-se avaliar a vazão e pressão dinâmica fornecidas pela bomba operando em circuitos fechados, calculando a perda de carga do circuito em função da vazão, do seu diâmetro e do comprimento equivalente.

Com o objetivo de facilitar a otimização do projeto de uma bomba eletromagnética de corrente contínua o programa computacional BEMC-1 permite modificar dados e parâmetros para análise de uma nova condição de operação da bomba, assim como, fluido a ser bombeado, dados geométricos da bomba EM e do circuito, utilizando o ícone de controle apropriado.

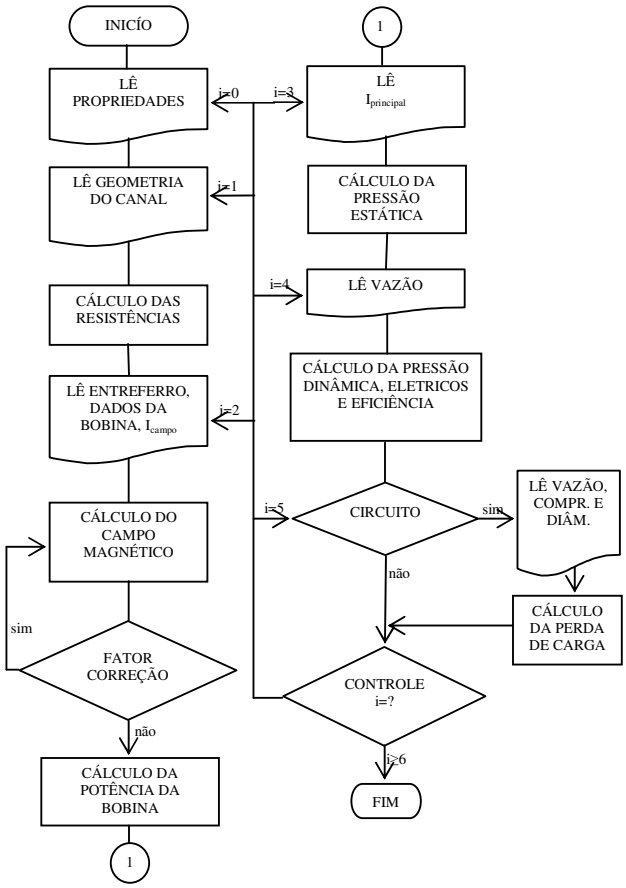

Figura 3. Diagrama de blocos do programa BEMC-1.

4. Avaliações

A bomba eletromagnética de corrente contínua (EM) é formada por um magneto tipo C, com entreferro de 20 mm e 2000 espiras. Com base na geometria do magneto tipo C e do canal da bomba, ou seja, altura do canal (a) de 10 mm, largura do canal (b) de 30 mm e o comprimento útil (c) de 70 mm pode-se, fazer a avaliação experimental de campo magnético, pressão estática e vazão de Mercúrio. Estes dados são comparados aos resultados teóricos, obtidos com o programa BEMC-1, validando-o. Pode-se, ainda, avaliar o desempenho teórico da bomba EM, operando com Mercúrio e com metais líquidos de interesse em reatores nucleares rápidos.

A Figura 4 apresenta o esquema da bomba EM.

A Tabela 1 apresenta as propriedades dos metais líquidos simulados neste trabalho.

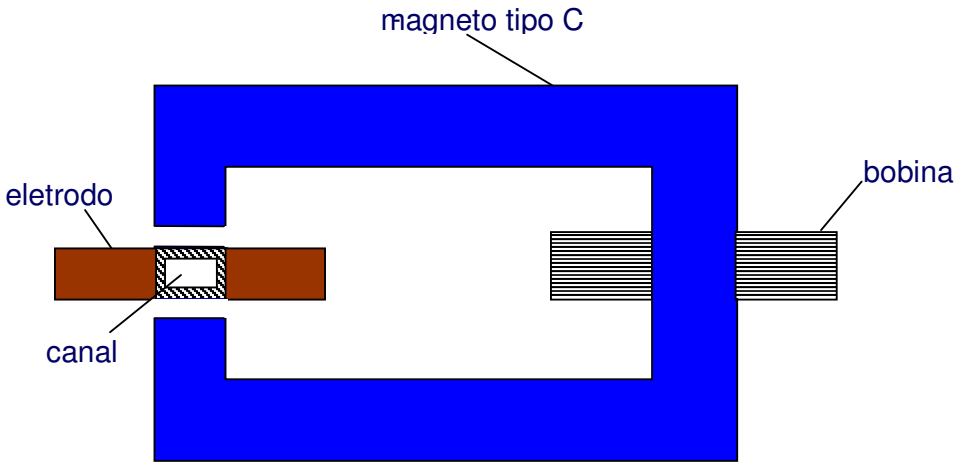

Figura 4. Esquema da bomba EM com magneto tipo C.

Tabela 1. Propriedades dos metais líquidos simulados pelo BEMC-1.

Propriedade \ metal	Mercúrio	Sódio	Chumbo	Bismuto
Temperatura (^oC)	20	500	500	500
Resistividade elétrica (ohm.m)	9.3 e-7	2.0 e-7	2.1 e-7	1.34 e-6
Massa específica (Kg/m^3)	13400	830	10470	9900
Viscosidade dinâmica ($N.s/m^2$)	1.5 e-3	2.4 e-4	1.78 e-3	1.0 e-4

4.1. Campo magnético

A Figura 5 apresenta a curva de campo magnético médio teórico, calculado pelo BEMC-1, com a Eq. (1), e os dados experimentais no centro do entreferro do magneto tipo C, em função da corrente de campo fornecida às bobinas pela fonte HP-6030 A, com fundo de escala de 10 A.

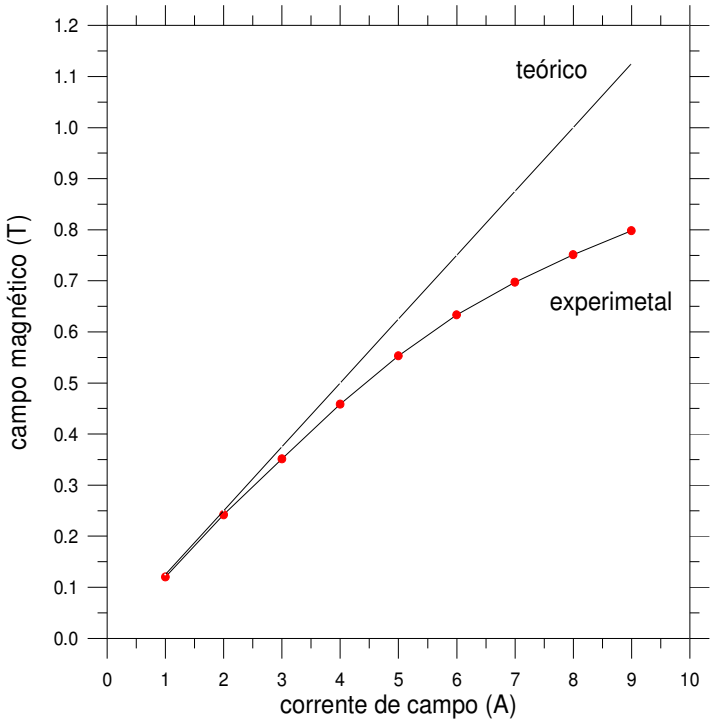

Figura 5. Campo magnético médio no centro do entreferro do magneto tipo C.

Para valores de correntes de campo crescentes a diferença entre os dados teóricos e experimentais se acentua, devido à saturação do magneto tipo C. Portanto há a necessidade do uso de fatores de ajuste no cálculo de campo magnético médio no programa BEMC-1, em função do valor da corrente de campo, pois os dados da simulação devem reproduzir os dados experimentais.

Para não se impor novos erros aos resultados obtidos nos cálculos subseqüentes, com o programa BEMC-1, utiliza-se o campo magnético experimental.

A Tabela 2 apresenta os valores teóricos e corrigidos (experimentais) de campo magnético da bomba EM.

Tabela 2. Campo magnético teórico e experimental.

$B[Wb/m^2]$ - I_{campo} [A]	2	4	6	8	10
B teórico	0,25	0,5	0,75	1	1,25
B experimental	0,24	0,46	0,63	0,75	0,90

4.2. Pressão estática

Para se poder avaliar experimentalmente a pressão manométrica de bombas eletromagnéticas de corrente contínua com vazão nula foi projetado e construído um circuito experimental fechado em aço e vidro, para Mercúrio, cujo esquema é apresentado na Fig. 6. Notam-se as tubulações verticais em vidro, onde se pode verificar o deslocamento do mercúrio e o desnível total ΔL (pressão estática) produzido pela bomba, as demais partes do circuito são feitas em aço.

Os dados experimentais de pressão estática da bomba EM são obtidos variando-se o campo magnético imposto e o valor da corrente principal fornecido por uma fonte de corrente contínua, com fundo de escala de 800 A, e medindo-se o desnível de mercúrio total (ΔL).

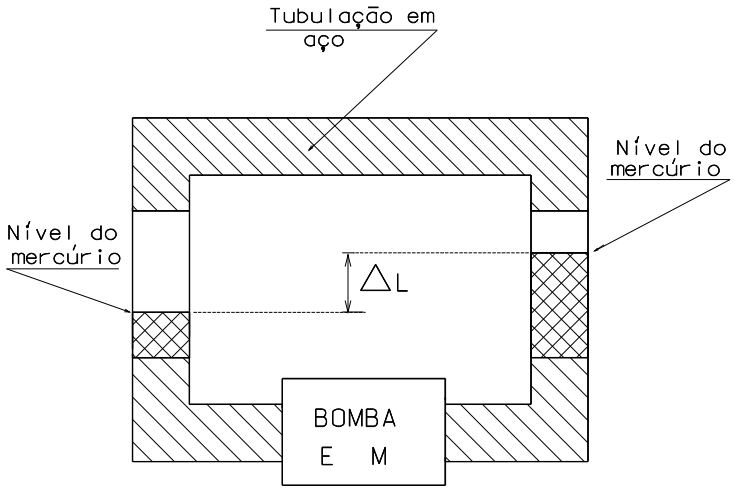

Figura 6. Esquema do circuito experimental para avaliação de pressão estática.

Os valores teóricos de pressão estática são obtidos em função da corrente elétrica média útil, da geometria do canal da bomba e do campo magnético médio teórico corrigido (experimental).

Um parâmetro importante do cálculo da bomba EM é o fator empírico utilizado no cálculo da resistência elétrica de "bypass". Este fator empírico é usado no cálculo da corrente elétrica útil e depende dos parâmetros geométricos da bomba (Watt, 1958). Quanto maior for este fator, menor é a perda de corrente elétrica de fuga. Nota-se ainda que este parâmetro deve ser ajustado para cada projeto de bomba EM.

A pressão estática teórica da bomba EM é obtida pela Eq. (5). O valor da corrente útil (I_e) é calculado, em função da corrente principal (I) pela Eq. (8), considerando o último termo desta equação nulo. Para tanto, utiliza-se as resistividades elétricas dos materiais usados, na temperatura de trabalho e a geometria do canal da bomba para se obter as resistências elétricas. Para Mercúrio tem-se: R_w=15,0 10^{-5} Ohms e R_e= 4,0 10^{-5} Ohms. Admitindo-se que R_b= 5,0 R_e obtêm-se as curvas teóricas de pressão estática da bomba EM de corrente contínua com magneto tipo C obtida pelo BEMC-1, em função da corrente elétrica principal e de campo. A Figura 7 apresenta a comparação entre os dados de pressão estática experimental e teórica (obtidos com o BEMC-1).

Comparando-se os dados de pressão estática experimentais e teóricos da bombas EM, nota-se que, utilizando os valores de campo magnético experimentais, os fatores de "bypass" e de correção apropriados no programa BEMC-1, reproduz-se os dados experimentais, com diferenças quase nulas, validando a metodologia de análise utilizada.

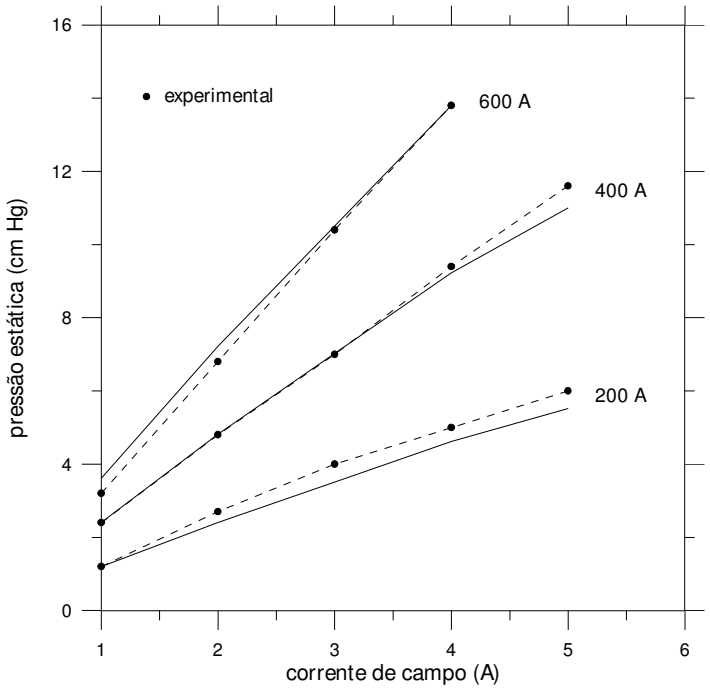

Figura 7. Curvas teóricas e experimentais de pressão estática da bomba EM.

4.3. Vazão

Para os ensaios experimentais de operação de bombas eletromagnéticas de corrente contínua é utilizado o circuito dinâmico de Mercúrio, em aço (com diâmetro interno de 0,0122 metros e comprimento equivalente de 3,8 metros), apresentado na Fig. 8. Onde pode-se notar a bomba EM, o medidor de vazão eletromagnético MV e seu sistema de aquisição de dados SD, assim como os medidores de pressão (manômetros) P1 e P2.

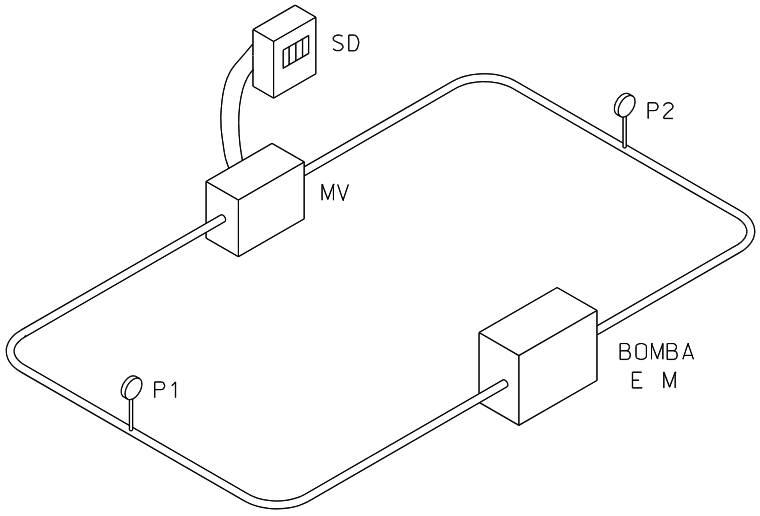

Figura 8. Esquema do circuito dinâmico de Mercúrio para avaliação de bombas EM.

A Figura 9 apresenta as curvas teóricas (obtidas com o BEMC-1) e experimentais de vazão da bomba EM de corrente contínua com magneto tipo C no circuito dinâmico de Mercúrio, apresentando boa concordância. Observa-se que para as avaliações teóricas neste caso utiliza-se a corrente útil calculada pela Eq. (8), com todos os seus termos.

Nota-se que, a vazão fornecida pela bomba EM depende diretamente dos valores das correntes de campo e principal. Experimentalmente obtêm-se vazões inferiores a seis [l/min]. Este valor está associado às limitações das fontes de corrente utilizadas.

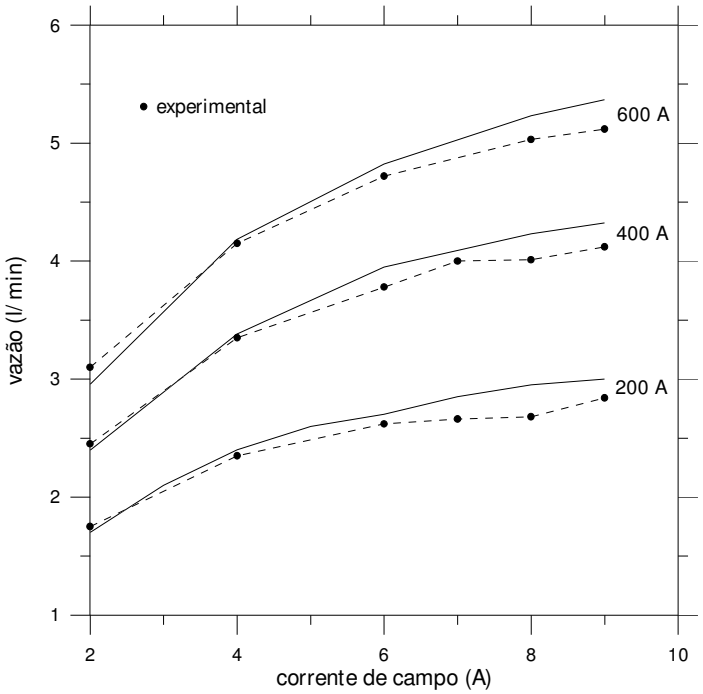

Figura 9. Curvas teóricas e experimentais de vazão da bomba EM com magneto tipo C.

4.4. Desempenho da bomba EM

Observa-se uma boa concordância dos resultados teóricos e experimentais, apresentados nas Figuras 7 e 9, o que valida o programa BEMC-1 e possibilita a avaliação de uso de outros metais líquidos na bomba EM.

Na avaliação teórica de desempenho dinâmico da bomba eletromagnética de corrente contínua deve-se considerar os dados geométricos, as propriedades do fluido a ser bombeado, apresentados na Tabela 1, as correntes elétricas envolvida e as curvas de pressão dinâmica da bomba EM e de perda de carga no circuito (com diâmetro interno de 0,0122 metros e comprimento equivalente de 3,8 metros), em função da vazão, calculadas pelo programa BEMC-1.

A pressão dinâmica teórica da bomba EM pode ser obtida pela Eq. (4). A corrente elétrica útil é calculada pela Eq. (8), considerando todos os seus termos, portanto depende da vazão.

A bomba eletromagnética de corrente contínua (EM) é formada por um magneto tipo C, com entreferro de 20 mm e 2000 espiras. A geometria do canal da bomba é: altura do canal (a) de 10 mm, largura do canal (b) de 30 mm e o comprimento útil (c) de 70 mm. A corrente de campo, fornecida pela fonte HP-6030A (com fundo de escala de 10 A), pode gerar um campo magnético máximo de 0,90 Wb/m^2, como apresentado na Tabela 2. Outra fonte de corrente contínua, com fundo de escala de 800 A, fornece a corrente principal, que interage com o campo magnético e produz no fluido (interno ao canal da bomba) a força magneto motriz que controla o escoamento.

Com o BEMC-1 pode-se obter os pontos de operação do sistema, ou seja, a vazão e pressão dinâmica fornecida pela bomba, operando em circuitos fechados, calculando as perdas de carga do circuito em função da vazão do fluido, do seu diâmetro e do comprimento equivalente.

Na Figura 10 apresentam-se as curvas teóricas de desempenho da bomba eletromagnética de corrente contínua com magneto tipo C, para quatro conjuntos de valores de campo magnético e corrente principal e a curva teórica de perda de carga no circuito dinâmico de Mercúrio, em função da vazão, obtidas com o programa BEMC-1.

As curvas teóricas de pressão dinâmica e de vazão estão correlacionadas, pois a pressão dinâmica é calculada em função da vazão, é sempre inferior ao valor da pressão estática, para a mesma corrente principal e de campo fornecidas, e deve ser compatível com a curva de perda de carga do circuito.

Para bombas mecânicas centrífugas as curvas dinâmicas teóricas e experimentais são curvas, pois as perdas, em especial, devido ao atrito obtido nos mancais, aumentam com a rotação, ou seja, com a vazão.

As curvas de desempenho de bombas eletromagnéticas são retas. No caso da bomba EM com magneto tipo C estas curvas apresentadas não são paralelas, pois, os valores de campo magnético são diferentes para cada uma delas. Quanto maior a corrente fornecida maior a máxima pressão dinâmica da bomba. O valor de pressão dinâmica teórica é menor para vazões maiores.

Na Figura 10, os pontos teóricos de operação da bomba EM com Mercúrio, em função do campo magnético, da corrente principal aplicada e do circuito usado, são os pontos de interseção.

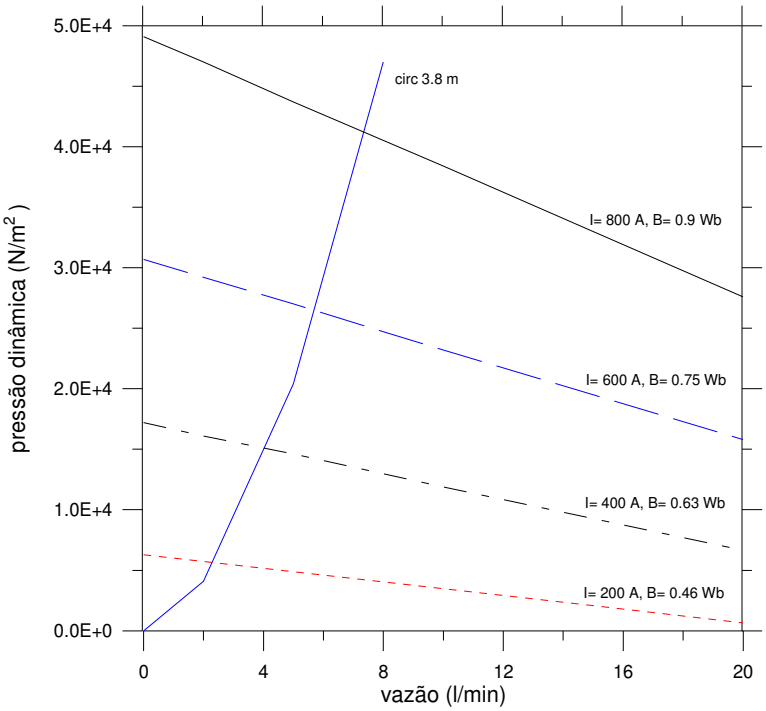

Figura 10. Curvas teóricas de desempenho da bomba EM operando com Mercúrio.

.

A Figura 11 apresenta as curvas teóricas de desempenho da bomba EM operando com Sódio e a curva teórica de perda de carga do circuito dinâmico, obtidas com o BEMC-1.

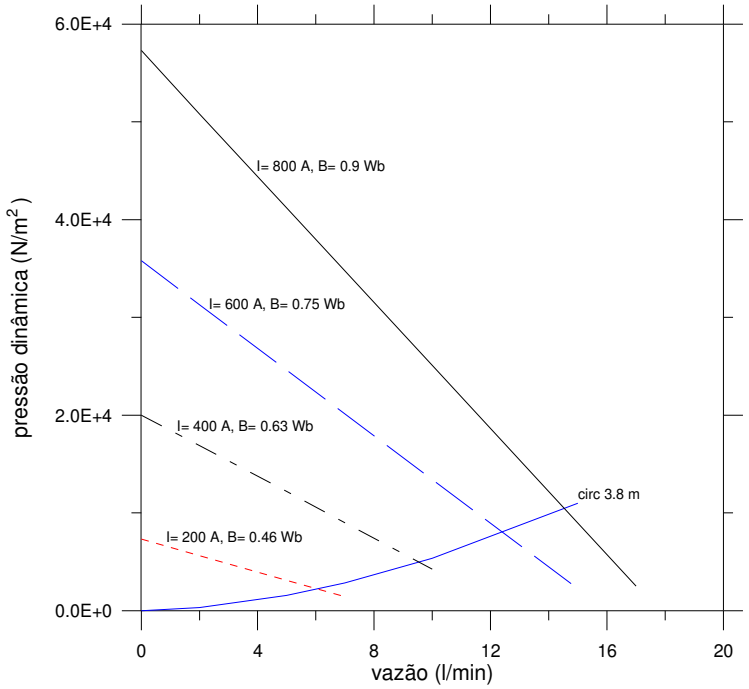

Figura 11. Curvas teóricas de desempenho da bomba EM operando com Sódio.

A Figura 12 apresenta as curvas teóricas de desempenho da bomba EM operando com Chumbo e a curva teórica de perda de carga do circuito dinâmico, obtidas com o BEMC-1.

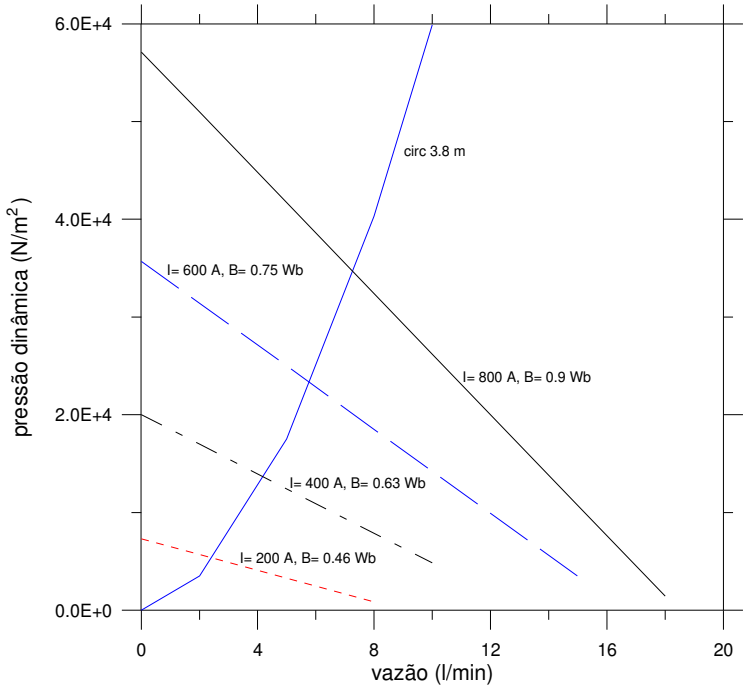

Figura 12. Curvas teóricas de desempenho da bomba EM operando com Chumbo.

A Figura 13 apresenta as curvas teóricas de desempenho da bomba EM operando com Bismuto e a curva teórica de perda de carga do circuito dinâmico, obtidas com o BEMC-1.

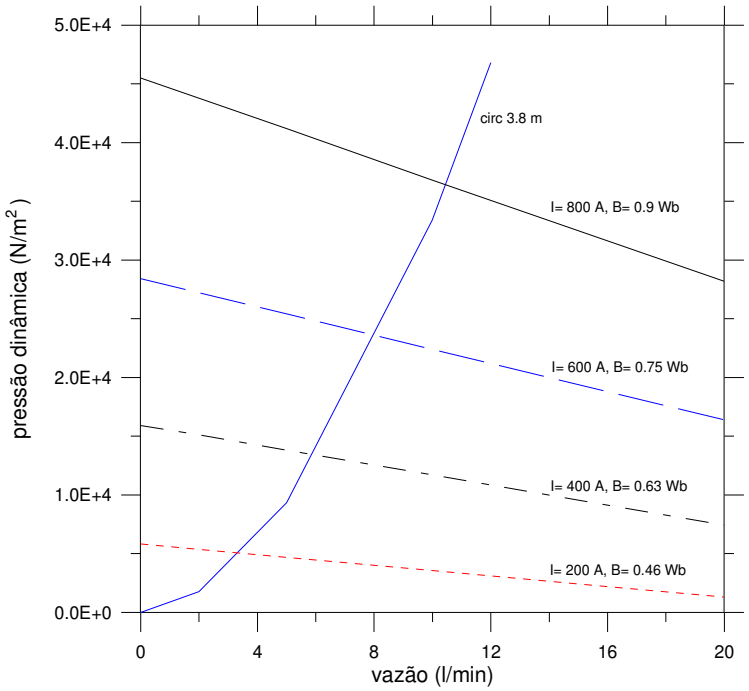

Figura 13. Curvas teóricas de desempenho da bomba EM operando com Bismuto.

A Tabela 3 apresenta os pontos de operação dinâmica da bomba eletromagnética de corrente contínua, operando com a sua máxima capacidade, em função das fontes disponíveis, ou seja, com a corrente principal (I) máxima de 800 A e campo magnético (B) máximo de 0,90 Wb/m^2, para os metais líquidos simulados com o BEMC-1.

Tabela 3. Pontos de operação da bomba EM para os metais líquidos simulados.

Parâmetro\Fluido	Mercúrio	Sódio	Chumbo	Bismuto
Vazão (l/min)	7,3	14,5	7,2	10,4
Pressão (N/m^2)	41200	10400	34600	36500

5. Comentários e conclusão

As bombas eletromagnéticas utilizam o princípio de Faraday, não contem partes móveis, são totalmente selada, tem alta confiabilidade, e podem controlar o escoamento de um metais líquidos de alta condutividade elétrica num circuito fechado e facilitar a circulação natural do refrigerante, em caso de falhas ou acidentes, em um reator nuclear.

O programa BEMC-1 foi elaborado com o objetivo de se poder avaliar, cada etapa do desenvolvimento de uma bomba eletromagnética de corrente contínua, possibilitando alteração em todos os parâmetros importantes de projeto.

Definido o fluido a ser bombeado e suas propriedades, assim como a geometria e materiais do canal da bomba, calcula-se as resistências elétricas envolvidas. Em seguida são calculados o campo magnético, a pressão estática, a vazão e a pressão dinâmica fornecida pela bomba EM, em função das correntes elétricas impostas. Calcula-se ainda as perdas de carga do circuito em função da vazão do fluido, do seu diâmetro e do comprimento equivalente.

Com o BEMC-1 pode-se avaliar o desempenho de bombas EM operando com os metais líquidos de interesse, obtendo os pontos teóricos de operação do sistema bomba-circuito, definidos pela interseção das curvas dinâmicas da bomba e de perda de carga do circuito, com apresentado na Tab. 3.

No caso de Mercúrio tanto a pressão dinâmica como a perda de carga para a mesma vazão são as maiores entre as avaliadas neste artigo. No caso do Bismuto sua curva de operação é próxima à do Mercúrio, mas com menor perda de carga. As curvas dinâmicas da bomba EM operando com Chumbo e com Sódio apresentam inclinações praticamente iguais, pois as suas resistividades elétricas são muito próximas. A perda de carga para o Sódio apresenta valores inferiores, em função de sua massa específica e de sua viscosidade dinâmica serem menores, mostrando maior facilidade de bombeamento do Sódio comparado aos outros metais líquidos simulados. Portanto para a mesma bomba, sob as mesmas condições, o ponto de operação é diferente em função do fluido.

Os resultados teóricos, obtidos com o BEMC-1, mostraram a viabilidade da utilização de bombas eletromagnéticas para o controle de escoamento de metais líquidos, considerados de interesse para remoção de calor, em reatores nucleares rápidos.

6. Referências

Borges, E. M., 1991, "Desenvolvimento e Simulação Computacional de Bombas Eletromagnéticas Termoelétricas para o Controle do Escoamento em Reatores Nucleares Espaciais Refrigerados a Metal Líquido". Tese de Doutorado ITA, São José dos Campos, SP, Brasil.

Borges, E. M., et al., 1995, "Ensaios de Pressão Estática de Bomba Eletromagnética de Corrente Contínua". XIII Congresso Brasileiro de Engenharia Mecânica, Belo Horizonte, MG, Brasil.

Borges, E. M., et al., 1996, "Rare-Earth Magnets Applied to Liquid Metal Flow". XIV International Workshop on Rare-Earth Magnets and Their Applications, Sao Paulo, SP, Brazil.

Kwant, W., et al., 1988, "PRISM Reactor Design and Development". Safety of Next Generation Power Reactors Meeting, Washington, USA.

Lancet, R. T. and Marchaterre, J. F., 1985, "Inherent Safety of the SAFR Plant". In: Proceedings of the International Topical Meeting on FAST REACTOR SAFETY, Tennessee, USA.

Lentz, G. L., et al., 1985, "EBR-II - Twenty Years of Operation Experience". Symposium on Fast Breeder Reactors: Experience and Trends, Lyon, France.

Myasnikov, V. O., et al., 1993, "Conceptual Design of Module Fast Reactor of Ultimate Safety Cooled by Lead-Bismuth Alloy", *Trans. Am. Nucl. Soc.*, **67**, 1, pp. 151, USA.

Prati, A., et al., 1994, "Concepção de um Reator Rápido Experimental para o Brasil". V Congresso Geral de Energia Nuclear, Rio de Janeiro, RJ, Brasil.

Santos, A. and Nascimento, J. A., 2002, "An Integral Lead Reactor Concept for Developing Countries", *Nuclear Technology*, **140**, 3, pp. 233 - 254, USA.

Watt, D. A., 1958, "The Design of Electromagnetic Pumps for Liquid Metals". Atomic Energy Research Establishment, Harvel, Berkshine, AERE R/R 2572, USA.

LIQUID METAL FLOW CONTROL BY DC ELECTROMAGNETIC PUMPS.

Eduardo Madeira Borges
Institute for Advanced Studies (IEAv), Sao Jose dos Campos, SP, Brazil
e-mail: eduardo@ieav.cta.br

Francisco Antonio Braz Filho
Institute for Advanced Studies (IEAv), Sao Jose dos Campos, SP, Brazil
e-mail: fbraz@ieav.cta.br

Lamartine Nogueira Frutuoso Guimarães
Institute for Advanced Studies (IEAv), Sao Jose dos Campos, SP, Brazil
e-mail: guimarae@ieav.cta.br

Abstract

The cooling system of high-density thermal power requires fluids of high thermal conductivity, such as liquid metals. Electromagnetic pumps can be used to liquid metal fluid flow control in cooling circuits. The operation of electromagnetic pumps used to flow control is based on Lorentz force. This force can be achieved by magnetic field and electric current interaction, controlled by external independent power supplies. This work presents the electromagnetic pump operational principles, the IEAv development scheme and the BEMC-1 simulation code. The theoretical results of BEMC-1 simulation are compared to electromagnetic pump operation experimental data, validating the BEMC-1 code. This code is used to evaluate the DC electromagnetic pump performance applied to Mercury flow control and others liquid metal such as Sodium, Lead and Bismuth, used in nuclear fast reactors.

Keywords: liquid metal, electromagnetic pump, fluid flow control.

Proceedings of the 11th Brazilian Congress of Thermal Sciences and Engineering -- ENCIT 2006
Braz. Soc. of Mechanical Sciences and Engineering -- ABCM, Curitiba, Brazil,- Dec. 5-8, 2006

Paper CIT06-0452

LEAST SQUARES FINITE ELEMENT METHOD IN VELOCITY-PRESSURE-VORTICITY FORMULATION THE APPLICATION OF LARGE EDDY SIMULATION METHODOLOGY

Vanessa Davanço Pereira ([1])
vdavanco@fem.unicamp.br
Luis Felipe Mendes de Moura ([1])
felipe@fem.unicamp.br
([1]) UNICAMP, Faculdade de Engenharia Mecânica, Depto de Térmica e Fluido, Rua Mendeleiev, s/n , 13083-970 - Cidade Universitária "Zeferino Vaz" Barão Geraldo - Campinas – SP, Brasil

João Batista Campos Silva ([2])
jbcampos@dem.feis.unesp.br
([2]) UNESP – Ilha Solteira, Faculdade de Engenharia de Ilha Solteira, Depto. de Eng. Mecânica, Av. Brasil 56, 15385-000, Ilha Solteira – SP, Brasil

Abstract. *In this work, simulations of incompressible fluid flows have been done by a Least-Squares Finite Element Method (LSFEM) using velocity-pressure-vorticity formulation, here called u-p-ω formulation. This formulation is used because the resulting equations are partial differential equations of first order, which is convenient for implementation by LSFEM. The main purposes of this work are the numerical computation fluid flows by LSFEM through the application of large eddy simulation (LES) methodology. The Navier-Stokes equations in u-p-ω formulation are filtered and the eddy viscosity of Smagorinsky is used for modeling the sub-grid-scale variables. The backward facing-step flow has been solved to study the influence of the constant of Smagorinsky on the velocity profile for different Reynolds numbers. The results are presented and compared with available results from the literature.*

Keywords: Navier-Stokes equations, large eddy simulation, least-squares finite element, fluid flows.

1 INTRODUCTION

The finite element method (FEM) is one of the most used techniques for numerical solution of partial differential equations in engineering and applied sciences. The mathematical foundation of the finite element method can be based on the weight residual method (WRM), Finlayson, (1972), which originate different formulations according to the weight functions used. The main versions of the FEM are the Bubnov-Galerkin, Petrov-Galerkin, Collocation, Sub-domain and Least-Squares formulations. Another classification underlining the variational principle considers three major groups: the Rayleigh-Ritz method, The Galerkin Method and the Least-squares method. For convection dominated problems the Galerkin-based methods present often spurious oscillation of the solutions (Jiang, 1998). In recent works, Romão et al. (2003) and Romão (2004) applied different versions of the finite element method for convection-diffusion problems. Several authors have investigated the LSFEM for solution of incompressible and compressible fluid flows. Jiang (1998) presented a list of such works. Winterscheidt & Surana (1994) have applied p-versions of least-squares finite element method for fluid flows. The least squares have also been used for stabilization of the Galerkin finite element method. Jansen (1999) presented a LSFEM for computing turbulent flows in unstructured-grids. Some previous works have been presented: Pereira et al. (2004), Pereira and Campos_Silva (2005), Pereira et al. (2006a, b). Pereira (2005) has presented the *u-p-ω* formulation employed in this work. In that work some questions were not satisfactory answered. One of them was the influence of the constant of Smagorinsky in the LES methodology with the present formulation. In Pereira et al. (2006a, b) was tried to continue that investigation, but no high Reynolds number flow was still simulated for the present geometry. This work is a continuation of the previous works. Although, turbulence is a 3D phenomenon, in this work, only 2D simulations have been considered to understand the behavior of the LSFEM in the proposed formulations and due to the computational capacity available.

Jiang (1998) enumerated several features of the LSFEM, among them: universality, efficiency, robustness, optimality, concurrent simulation of multiple physics and general-purpose coding. Jiang also claimed that no upwind technique is necessary for numerical calculation of convection dominated problems, because the resulting matrix systems of equations from the LSFEM application are always symmetrical and positive-definite.

In this work, the backward-facing step flow has been solved with quadratic quadrilateral elements for investigation of different values of the constant of Smagorinsky. The results are compared with results from other authors. Beyond of this introduction, the paper covers some aspects of formulation of the proposed model, presents some results, discussions, conclusions and references.

2- NOMENCLATURE

k = turbulent kinetic energy
L = length of reference
p = pressure
$P = \dfrac{p - p_o}{\rho u_0^2}$ = dimensionless pressure
Re = Reynolds number
t = Time
u = component of dimensional velocity in the x_i - axis direction
u_i = component of velocity in the x_i - axis direction
u_0 = reference velocity
$U = u/u_o$ - dimensionless component of velocity in the *X*-axis direction
U_i = dimensionless component of velocity in the X_i -axis direction
v = component of dimensional velocity in the y -axis direction
$X = x/L$ = dimensionless X coordinate
x_i = ith- axis in Cartesian coordinates
$X_i = x_i/L$ = ith dimensionless coordinate
$Y = y/L$ = dimensionless Y coordinate

Greek Symbols

α = index that indicates local node number inside an element
δ_{ij} = Krönecker delta
θ = time discretization parameter
μ = dynamic viscosity
μ_t = dynamic eddy viscosity
ρ = density
ϕ = any scalar variable
ψ = stream function
ω_j = vorticity around the j-axis
$\varepsilon_{ijk} = 1; if \;\; ijk = 123, 231, 312$
$\varepsilon_{ijk} = -1; if \;\; ijk = 132, 213, 321$
$\varepsilon_{ijk} = 0$ for any two equal indices

Superscripts

n = variable evaluated at time t
n+1 = variable evaluated at time $t + \Delta t$

Subscripts

i = direction of the axis in the system of coordinates or component
j = direction of the axis in the system of coordinates or component
k = direction of the axis in the system of coordinates or component

3 – FORMULATION

3.1 - Governing Equations

The Navier-Stokes equations for incompressible transient fluid flows in vector notation can be written as follow:

$$\rho\left(\frac{\partial \mathbf{u}}{\partial t} + \mathbf{u} \bullet \nabla \mathbf{u}\right) + \nabla p + \mu \nabla^2 \mathbf{u} = \mathbf{f} \tag{1}$$

$$\nabla \bullet \mathbf{u} = 0 \tag{2}$$

where ρ is the fluid density, $\mathbf{u}$ is the velocity vector with components u_i, p is the pressure, μ is the dynamic viscosity and $\mathbf{f}$ is the body forces vector with components f_i.

The Equation (1) is a second order partial differential equation and this is not the most appropriated form for solution by LSFEM. The LSFEM generally is applied for first order differential equations. However, second order partial differential can be transformed in first order system by using auxiliary variables. This is another advantage of the least-squares method: the direct calculation of secondary variables that have physical interpretation such as heat and mass fluxes, stresses and vorticity. According to Brodkey (1967), using vectorial identities: $\mathbf{u} \bullet \nabla \mathbf{u} = \nabla(\mathbf{u} \bullet \mathbf{u})/2 - \mathbf{u} \times \nabla \times \mathbf{u}$ and $\nabla^2 \mathbf{u} = \nabla(\nabla \bullet \mathbf{u}) - \nabla \times (\nabla \times \mathbf{u})$, the Navier-Stokes can be rewritten, now, in tensorial notation as

$$\rho\left(\frac{\partial u_i}{\partial t} - \varepsilon_{ijk} u_j \omega_k\right) + \frac{\partial (p + u_i^2 / 2)}{\partial x_i} + \varepsilon_{ijk} \mu \frac{\partial \omega_k}{\partial x_j} = f_i; \tag{3}$$

$$\frac{\partial u_i}{\partial x_i} = 0 \;; \tag{4}$$

$$\omega_i = \varepsilon_{ijk} \frac{\partial u_k}{\partial x_j} \ . \tag{5}$$

For application of the large-eddy simulation methodology, the equations must be filtered for separation of the large scales from the sub-grid scales. So, the large scales are simulated by solution of the equations for the filtered variables after modeling the sub-grid scales terms that come from the filter process. Large-eddy simulation has been studied by a several researchers. Some few references are Moin & Kim (1982), Germano et al. (1991), Silveira-Neto (2002, 2003), Tejada-Martinez (2002). Chidambaram (1998) presented different filter functions for LES. The filtered Equations (3)–(5) are of the form

$$\rho\left(\frac{\partial \overline{u}_i}{\partial t} - \varepsilon_{ijk}\overline{u}_j\overline{\omega}_k + \frac{1}{2}\frac{\partial \overline{u}_i^2}{\partial x_i}\right) + \frac{\partial[\overline{p} + \rho(\overline{u_i^2} - \overline{u}_i^2)/2]}{\partial x_i} + \\ + \varepsilon_{ijk}\mu\frac{\partial \overline{\omega}_k}{\partial x_j} - \varepsilon_{ijk}\rho\left(\overline{u_j\omega_k} - \overline{u}_j\overline{\omega}_k\right) = \overline{f}_i \tag{6}$$

$$\frac{\partial \overline{u}_i}{\partial x_i} = 0 \ ; \tag{7}$$

$$\overline{\omega}_i = \varepsilon_{ijk}\frac{\partial \overline{u}_k}{\partial x_j} \ . \tag{8}$$

The differences between Eq. (3) and Eq. (6) are the additional term to the pressure and in the fourth term of left hand side of Eq. (6) that originated from the convection term of the Navier-Stokes equations. These terms correspond to the turbulent kinetic energy and the vorticity of the sub-grid scales respectively. The purpose of this work is the modeling of the fourth term, by analogy with the modeling of the sub-grid scale stresses in the conventional formulation of the Navier-Stokes equations. So, it is defined the sub-grid scale effects and the turbulent pressure as

$$\rho(\overline{u_j\omega_k} - \overline{u}_j\overline{\omega}_k) = -\mu_t\frac{\partial \overline{\omega}_k}{\partial x_j} \ ; \ p_t = \overline{p} + \rho(\overline{u_i^2} - \overline{u}_i^2)/2 \, . \tag{9}$$

Now, after modeling of the sub-grid scale effects, the dimensionless form of the Eqs. (6)-(8) is as follow, Pereira (2005):

$$\frac{\partial U_i}{\partial t} + U_j\frac{\partial U_i}{\partial X_j} + \frac{\partial P_t}{\partial X_i} + \varepsilon_{ijk}\left(\frac{1}{\mathrm{Re}} + \nu_t\right)\frac{\partial \Omega_k}{\partial X_j} = S_i \ ; \tag{10}$$

$$\frac{\partial U_i}{\partial X_i} = 0 \ ; \tag{11}$$

$$\Omega_i = \varepsilon_{ijk}\frac{\partial U_k}{\partial X_j} \ . \tag{12}$$

The dimensionless variables in Eqs. (10)-(12) are defined in function of the characteristic parameters of length L and velocity u_0 as

$$X_i = \frac{x_i}{L}; \quad U_i = \frac{\overline{u}_i}{u_0}; \quad P_t = \frac{p_t - p_0}{\rho u_0^2}; \quad t = \frac{t^*}{L/u_0}; \ \nu_t = \frac{\nu_t^*}{u_0 L} = \left(C_s\frac{\Delta}{L}\right)^2\left(2\overline{S}_{kl}\overline{S}_{kl}\right)^{1/2}; \quad \Omega_i = \frac{\overline{\omega}_i L}{u_0}; \quad \mathrm{Re} = \frac{\rho u_0 L}{\mu}.$$

The eddy viscosity is calculated according to the Smagorinsky model in the form

$$\nu_t^* = \left(C_s \Delta\right)^2 \left(2\bar{s}_{kl}\bar{s}_{kl}\right)^{1/2};\ \bar{s}_{ij} = \frac{1}{2}\left(\frac{\partial \bar{u}_i}{\partial x_j} + \frac{\partial \bar{u}_j}{\partial x_i}\right) \tag{13}$$

where C_s is the constant of Smagorinsky and Δ is the filter width defined as: $\Delta = \left(\Delta x \Delta y \Delta z\right)^{1/3}$ for 3D or $\Delta = \left(\Delta x \Delta y\right)^{1/2}$ for 2D geometry.

The first order system (10)-(12) for 2D problems, after discretizing the transient term can be written in a compact form as

$$L\Phi^{n+1} = f^n\ ; \tag{14}$$

where $\Phi = \left[U, V, P, \Omega\right]^T$ is the vector of unknown variables, $f = \left[S_u, S_v, 0, 0\right]^T$ is the vector of independent terms and now *L* is a matrix differential operator defined as

$$L = \begin{pmatrix} \frac{1}{\Delta\tau} + \theta\left(U\frac{\partial(\ )}{\partial X} + V\frac{\partial(\ )}{\partial Y}\right) & 0 & \frac{\partial(\ )}{\partial X} & \nu_e\frac{\partial(\ )}{\partial Y} \\ 0 & \frac{1}{\Delta\tau} + \theta\left(U\frac{\partial(\ )}{\partial x} + V\frac{\partial(\ )}{\partial y}\right) & \frac{\partial(\ )}{\partial Y} & -\nu_e\frac{\partial(\ )}{\partial X} \\ \frac{\partial(\ )}{\partial X} & \frac{\partial(\ )}{\partial Y} & 0 & 0 \\ -\frac{\partial(\ )}{\partial Y} & \frac{\partial(\ )}{\partial X} & 0 & 1 \end{pmatrix} \tag{15}$$

The source terms S_u and S_v are:

$$S_u = f_X + \frac{U^n}{\Delta t} - \left(1-\theta\right)\left(U\frac{\partial U}{\partial X} + V\frac{\partial U}{\partial Y} + \frac{\partial P}{\partial X} + \mu_e\frac{\partial \Omega}{\partial Y}\right)^n; \tag{16}$$

$$S_v = f_Y + \frac{V^n}{\Delta t} - \left(1-\theta\right)\left(U\frac{\partial V}{\partial X} + V\frac{\partial V}{\partial Y} + \frac{\partial P}{\partial Y} - \mu_e\frac{\partial \Omega}{\partial X}\right)^n. \tag{17}$$

and $0 \le \theta \le 1$ is a parameter of time discretization.

The variable Φ in finite element methods, for equal order interpolation of all degrees of freedom, can be interpolated inside an element in the form:

$$\Phi^e(X,Y,t) = \sum_{j=1}^{Ne} N_j(X,Y)\begin{Bmatrix} U \\ V \\ P \\ \Omega \end{Bmatrix}_j(t)\ ; \tag{18}$$

where N_j is the interpolation function associated to the node *j* of the element and Ne is the number of nodes. It has been pointed out that the LSFEM is not restricted by LBB (Ladyzhenskaya-Babuska-Brezzi) condition like the Galerkin-based method, Jiang (1998), Winterscheidt & Surana (1994).

3.2 - Least-Squares Finite Element Method

Substituting Eq. (18) in Eq. (14) a residual vector can be defined inside an element as

$$R = LN\Phi^{n+1} - f^{n}. \tag{19}$$

The application of LSFEM consists in the minimization of a functional defined as the integral of the squared residuals. If inside an element ones define a functional as $J_e\left(\Phi^{n+1}\right) = \int_{A_e} R^T \bullet R dA$, the functional, in the whole domain divided in *Nelem* elements, can be calculated as follow

$$J\left(\Phi^{n+1}\right) = \sum_{e=1}^{Nelem} \int_{A_e} R^T \bullet R dA. \tag{20}$$

The minimization of the functional requires that $\delta J\left(\Phi^{n+1}\right) = 0$, which results in the following matrix system:

$$K\Phi = F \tag{21}$$

Now, in Eq. (21), Φ is the global vector of nodal values. The global matrix *K* is assembled from the element matrices,

$$K_e = \int_{A_e} \left\langle LN_1, LN_2, \cdots, LN_{Ne} \right\rangle^T \left\langle LN_1, LN_2, \cdots, LN_{Ne} \right\rangle dA \tag{22}$$

where A_e is the area of the finite element, *T* denotes the transpose and the global vector *F* is assembled with the contribution of the element vectors

$$F_e = \int_{A_e} \left\langle LN_1, LN_2, \cdots, LN_{Ne} \right\rangle^T f dA \ ; \tag{23}$$

in which

$$LN_j = \begin{pmatrix} \frac{N_j}{\Delta\tau} + \theta\left(U\frac{\partial N_j}{\partial X} + V\frac{\partial N_j}{\partial Y}\right) & 0 & \frac{\partial N_j}{\partial X} & \mu_e \frac{\partial N_j}{\partial Y} \\ 0 & \frac{N_j}{\Delta\tau} + \theta\left(U\frac{\partial N_j}{\partial x} + V\frac{\partial N_j}{\partial y}\right) & \frac{\partial N_j}{\partial Y} & -\mu_e \frac{\partial N_j}{\partial X} \\ \frac{\partial N_j}{\partial X} & \frac{\partial N_j}{\partial Y} & 0 & 0 \\ -\frac{\partial N_j}{\partial Y} & \frac{\partial N_j}{\partial X} & 0 & N_j \end{pmatrix} \tag{24}$$

3.3 - Backward-Facing Step Flow

In this section some results for backward-facing step flow are presented for Reynolds number in the range of 100 to 1000 and values of the constant of Smagorinsky of 0.1, 0.17 and 0.21. The geometry of the problem and dimensions of the channel are shown in Figure 1. The Figure 2 illustrates a mesh utilized composed by 1840 finite elements and 7541 nodes. The ratio of expansion in this case is of 1:2. At the entrance of the channel was imposed a parabolic velocity profile of the form: $u = 3u_0/2\left[2(y-h)/r_w - (y-h)^2/r_w^2\right]$, where *h* is the step height, r_w is the half spacing of the small channel and in this case $r_w = h/2$. At all other walls was imposed zero velocities and at exit of the channel was imposed null pressure. For the vorticity was not necessary to impose any boundary condition, Jiang (1998).

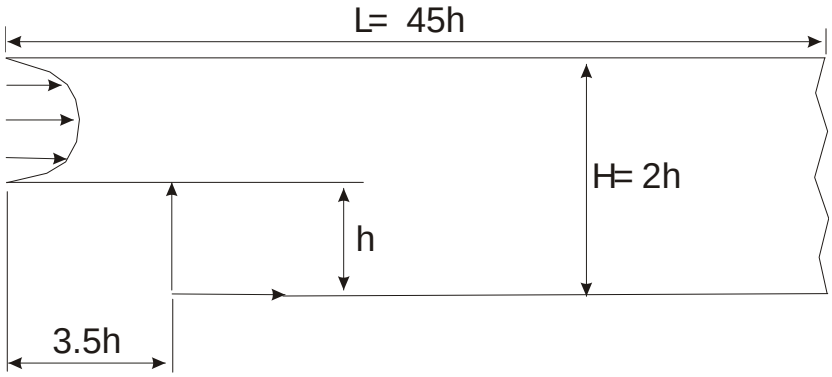

Figura 1. Non symmetric channel with a step.

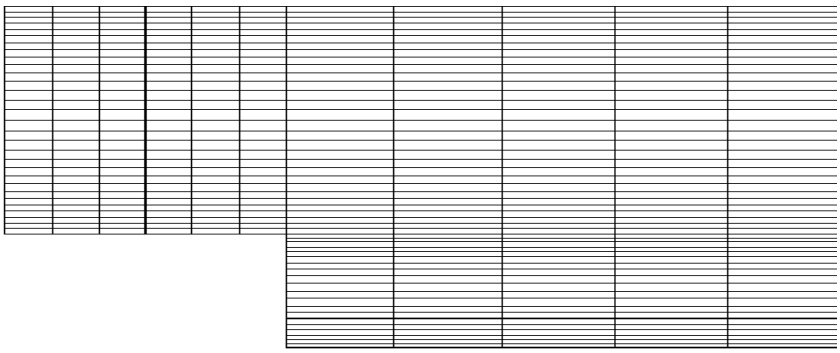

Figura 2. Mesh with 1840 finite elements and 7841 nodes.

The Reynolds numbers has been based on the step height, h. The computational code has been validated by Pereira (2005). Here, the main objective has been to analyze the influence of constant of Smagorinsky, in the simulation of the backward-facing step flow. The results presented below are for Reynolds numbers of 700 and 1000. Others low Reynolds numbers have been considered, in previous works, however, for lacking of spacing was not possible to present all results. The intent of this work is simulating high Reynolds number flows; however, until the present moment due to the computational resource available it was not possible to attain such objective. Figures 3 and 4 show velocity profiles at some positions along the channel, for different values of the constant of Smagorinsky. Differences between the velocities profiles appear only at some intermediate position along the channel. Figures 5 to 7 and 8 to 10 show the streamlines for Re equal to 700 and 1000 respectively for constant of Smagorinsky Cs = 0.1, 0.17 and 0.21. The behavior of the flow has been simulated satisfactorily. The non-dimensional reattachment lengths are approximately, 10 and 15 times step height for Re = 700 and 1000 respectively. The reattachment length result from Barber & Fonty (2003) for a similar flow and a Reynolds number are of 300 is about 7 times step height. Barber & Fonty presented results until Re of 600. For the Reynolds number of 400 and 600 respectively, the reattachment length of 10 and 16 times step height were showed by Barber & Fonty. For this low Reynolds numbers, the use of the Smagorinsky constant seems to create an effect of a more high Reynolds number. Until now, only one case of Re = 2000 has been simulated with Cs = 0.1. The stream functions are presented in Figure 11. This last result, however, presents a strange behavior and shall be investigated in future works. The profiles of velocity of this case, not included by lacking of space, seem to have been qualitatively and correctly simulated.

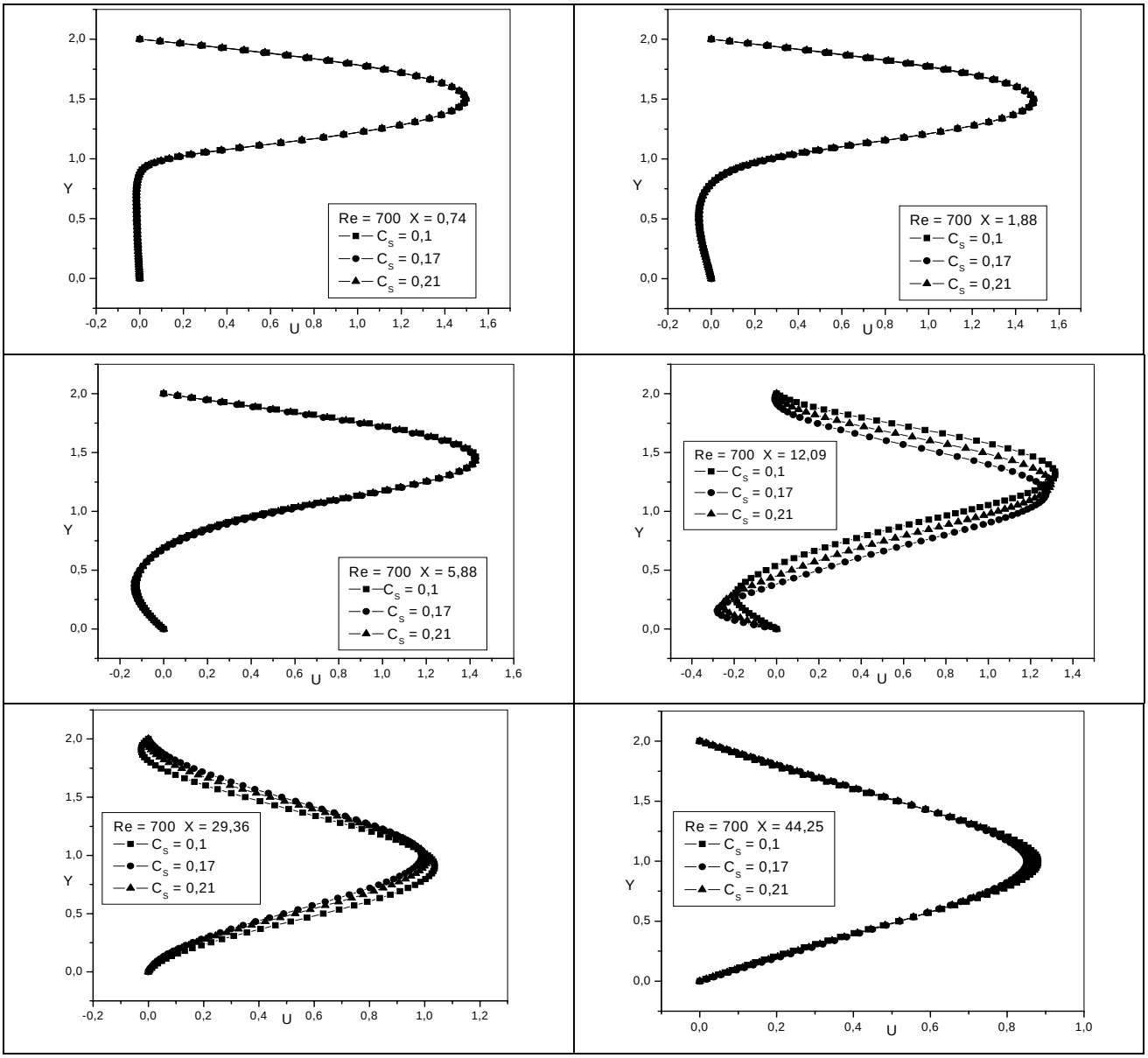

Figure 3. Profiles of velocity at some stations along the channel, for Re =700.

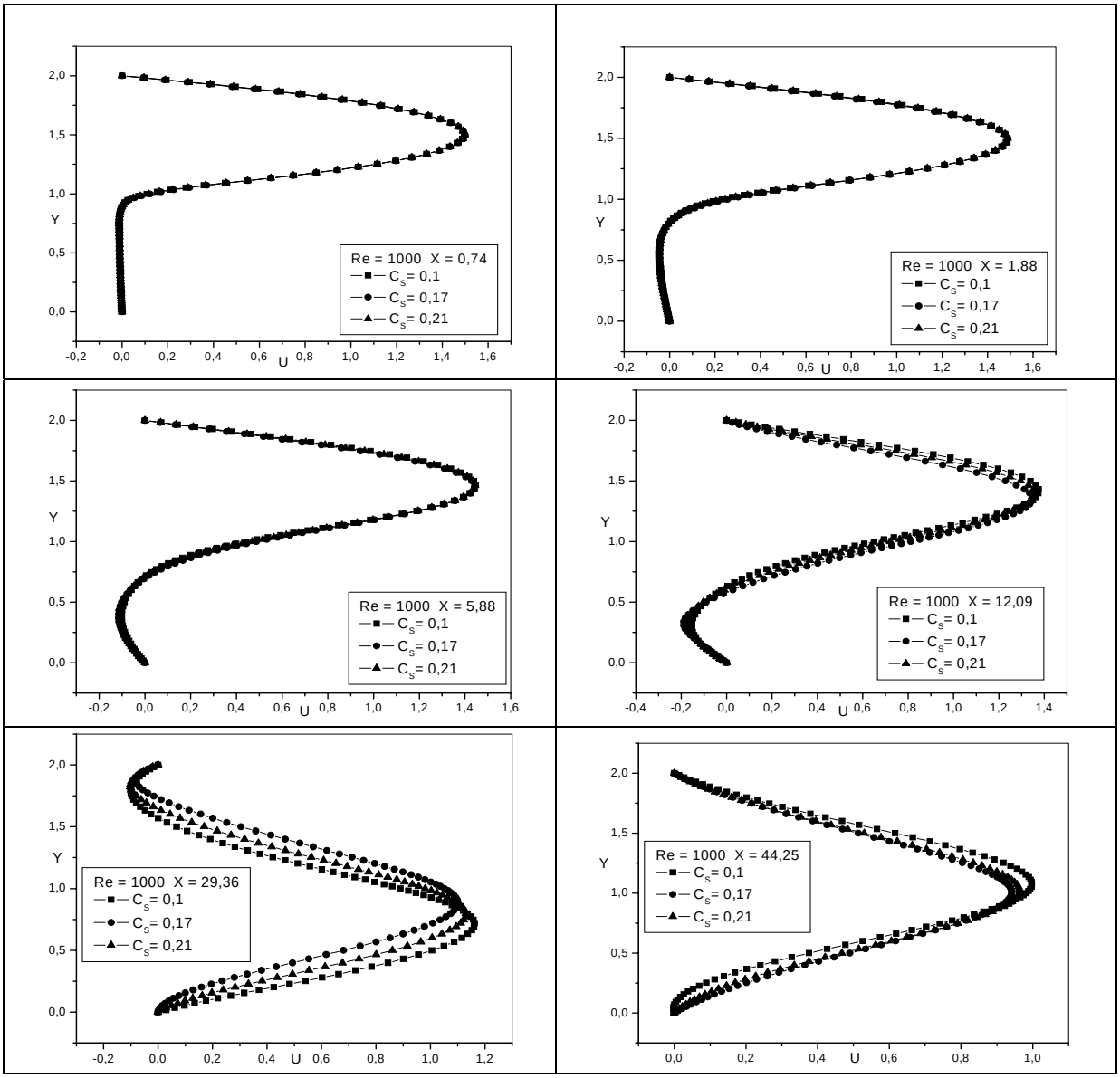

Figure 4. Profiles of velocity at some stations along the channel, for Re = 1000.

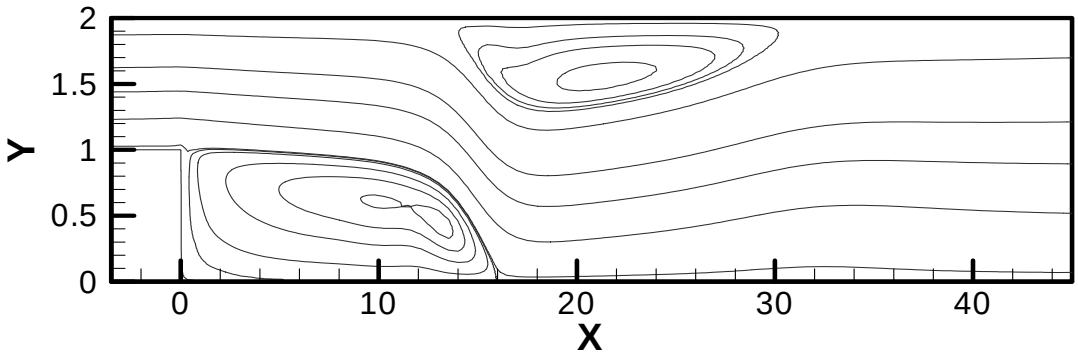

Figure 5. Streamlines for Re = 700 and Cs = 0.1.

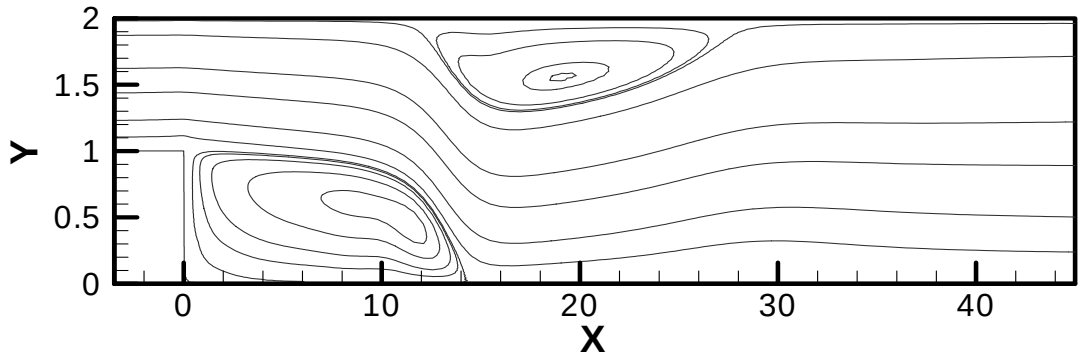

Figure 6. Streamlines for Re = 700 and Cs = 0.17

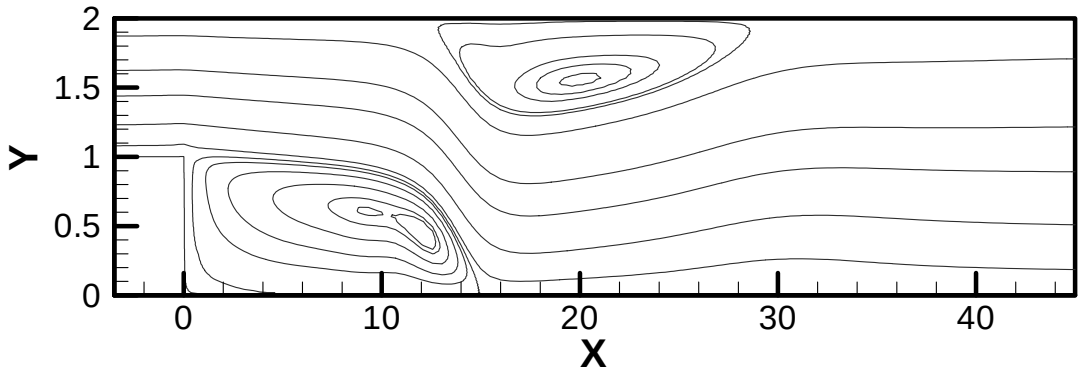

Figure 7. Streamlines for Re = 700 and Cs = 0.21

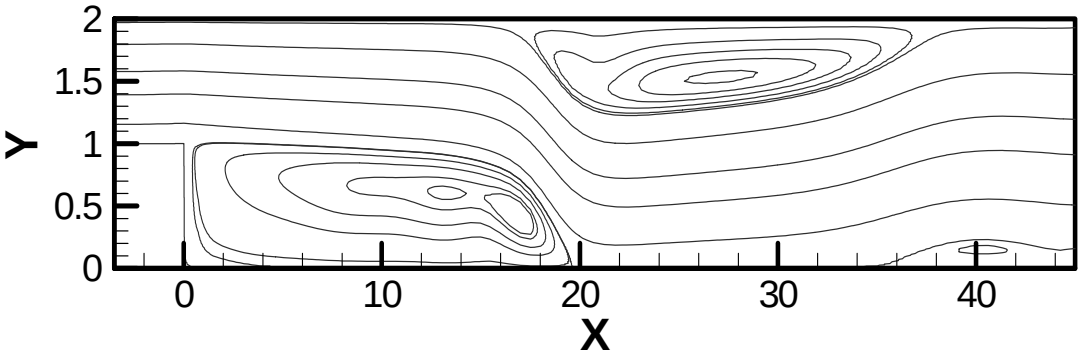

Figure 8. Streamlines for Re = 1000 and Cs = 0.1.

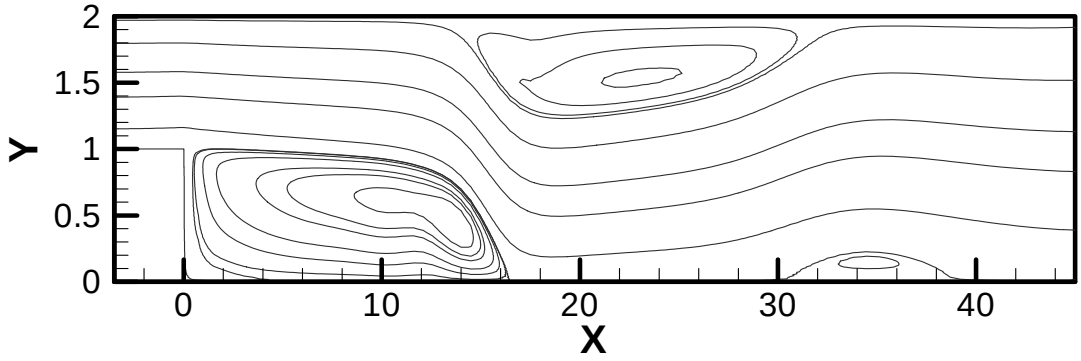

Figure 9. Streamlines for Re = 1000 and Cs = 0.17.

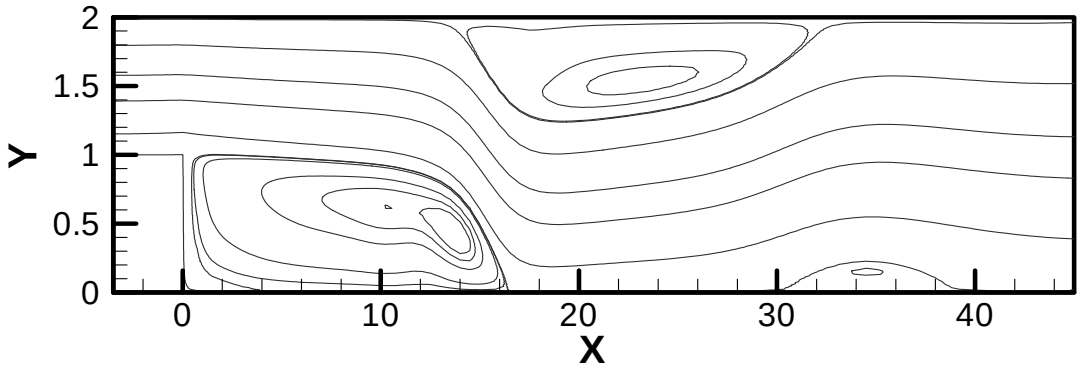

Figure 10. Streamlines for Re = 1000 and Cs = 0.21.

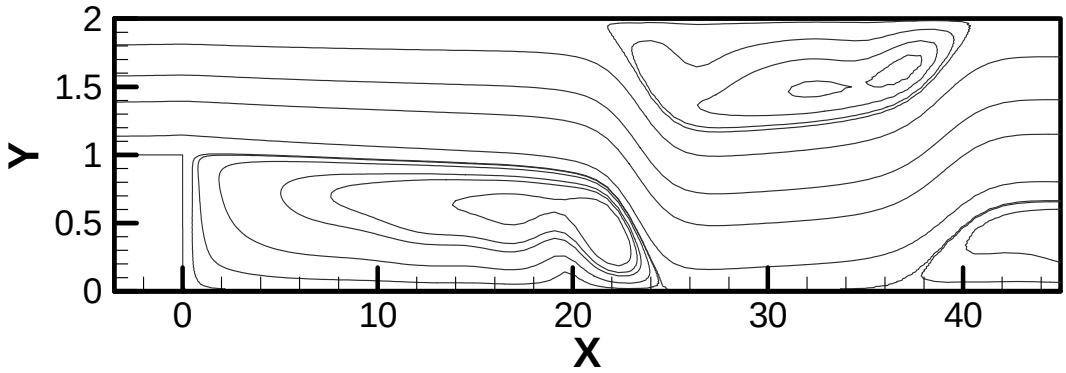

Figure 11. Streamlines for Re = 2000 and Cs = 0.1.

A comparison of Figures 5, 8 and 11 shows a crescent reattachment length with the increase of Reynolds number. However, was not possible to compare the results in this range of Reynolds with another results form the literature. The simulations have to be continued to investigate this behavior. Simulations by other numerical techniques present short reattachment length for high Reynolds number. Even this result is not true, it serves to indicate that the present numerical modeling has to be better investigated and calibrated for this kind of problem. More simulations are need in this case.

4 – CONCLUSIONS

A least-squares finite element method with eddy viscosity model of Smagorinsky has been applied in this work for simulation of Navier-Stokes equations, in u-p-ω formulation. The results were obtained for several low Reynolds numbers and Cs = 0.1; 0.17 and 0.21. Since, the interest is to simulate high Reynolds flows, more investigation is still necessary for improvement of the model. Since turbulence is a three-dimensional phenomenon, cases of 3D geometry shall be treated in future works. In this work, was applied the frontal method, with storage in hard disk and only steady flows have been simulated in personal computers. Unsteady flows need to be also investigated in more details. For 3D and high Reynolds numbers flows the challenge still goes on for the present numerical method in this kind of problem. The solution method has to be changed to a method like conjugate gradient method for symmetrical matrices considering the sparsity of matrices for simulation of very large problems. So the solutions shall be faster than the solution by frontal method.

Acknowledgements

The authors would like to acknowledge the Fundação de Amparo a Pesquisa do Estado de São Paulo = FAPESP for financial the computational resources (Proc. 05/02018-8); the CENAPAD - SP, Centro Nacional de Processamento de Alto Desempenho, and the CNPq for the scholarship to the doctorate student V. D. Pereira.

5 – REFERENCES

Barber, R. W. & Fonty, A., 2003. Comparison of vortex-element and finite-volume simulations of low Reynolds number flow over a confined backward-facing step. *CFD2003 – Vortex Methods*, May, 28-30, Vancouver, Canada.

Brodkey, R. S., 1967. *The Phenomena of Fluid Motions*. Dover Publications, Inc.

Chidambaram, N., 1998. Colocated-grid Finite Volume Formulation for the Large Eddy Simulation of Incompressible and Compressible Turbulent Flows. M.Sc. Thesis. Graduate College, Department of Mechanical Engineering, Iowa State University, Ames, Iowa, USA.

Ding, X. & Tsang, T. H., 2001. Large eddy simulation of turbulent flows by a least-squares finite element method. *International Journal for Numerical Methods in Fluids*, vol. 37, pp. 297–319.

Finlayson, B. A.,1972. *The Method of Weighted Residuals and Variational Principles.* Academic Press.

Germano, M. et al, 1991. A dynamic subgrid-scale eddy viscosity model. *Phys. Fluids A 3*, no. 7, 1760p.

Ghia, U., Ghia, K.N. & Shin, C.T., 1982. High-Re solutions for incompressible flow using the Navier-Stokes equations and a multigrid method. *Journal of Computational Physics*, v. 5, n. 48, p.387-411.

Jansen, K. E., 1999. A stabilized finite element method for computing turbulence. *Comput. Methods Appl. Mech. Engrg*, v. 174, p.299-317.

Jiang, B-N., 1992. A least squares finite element method for incompressible Navier-Stokes problems. *International Journal for Numerical Methods in Fluids*, vol. 14, pp. 843–859.

Jiang, B-N., 1998. *The Least-Squares Finite Element Method: Theory and Applications in Computational Fluid Dynamics and Electromagnetics*. Springer-Verlag.

Moin, P. & Kim, J., 1982. Numerical In vestigation of turbulent channel flow. *Journal Fluid Mechanics*, 118, 341-377p.

Pereira, V.D., 2005. *Numerical Simulation of Fluid Flows by a Least-Squares Finite Elment Method (in Portuguese).* Master Dissertation. UNESP, Faculdade de Engenharia de Ilha Solteira, Depto de Engenharia Mecânica.

Pereira, V. D., Romão, E. C., Mansur, S. S. & Campos Silva, J. B. Large Eddy Simulation of Turbulent Incompressible Fluid Flows by a Least Squares Finite Element Method in Velocity-Pressure-Vorticity Formulation. *XXV Iberian Latin American Congress in Computational Methods in Engineering – CILAMCE2004* (Paper CIL08-049). Nov, 10-12, Recife, PE, Brasil.

Pereira, V. D. and Campos Silva, J. B. Simulations of incompressible fluid flows by a least squares finite element method. *J. Braz. Soc. Mech. Sci. & Eng., July*/Sept. 2005, vol.27, no.3, p.274-282. ISSN 1678-5878.

Pereira, V.D., Moura, L.F.M. & Campos Silva, J. B. Simulation of Fluid Flows by a Least-Squares Finite Element Method in Velocity-Pressure-Vorticity Formulation. In: *VII Simpósio de Mecânica Computacional SIMMEC2006*. Araxá, 31 de maio a 2 de junho de 2006.

Pereira, V.D., Moura, L.F.M. & Campos Silva, J. B. A Least-Squares Finite Element Method in Velocity-Pressure-Vorticity Formulation for Fluid Flows. In*: IV Congresso Nacional de Engenharia Mecânica – CONEM2006*. Recife, 22 a 25 de agosto de 2006.

Romão, E.C., Campos Silva, J. B. & Aparecido, J.B., 2003. Variants of the Finite Element Method for Solutions of Unidimensional Convective-Diffusive Problems. *In Proceedings of 24th Iberain Latin-American Congress on Computational Methods in Engineering – CILAMCE 2003 (paper CIL 198-31)*, October 29-31, 2003, Ouro Preto, Minas Gerais, Brasil.

Romão, E. C., 2004. Variants of the Finite Element Method for Solutions of Two-dimensional Convective-Diffusive Phenomena, (in Portuguese). Master Dissertation. UNESP, Faculdade de Engenharia de Ilha Solteira, Depto. de Engenharia Mecânica.

Silveira-Neto, A. 2002. Fundamentals of turbulence in fluids (in Portuguese) . *III Escola de Primavera de Transição & Turbulencia*. UFSC- Universidade Federal de Santa Catarina. 23-27 de Setembro de 2002, Florianópolis – SC, p. 1-50.

Silveira-Neto, A. 2003. Turbulência nos fluidos aplicada. *Apostila*. UFU- Faculdade de Engenharia Mecânica – Campus Santa Mônica, Uberlândia – MG – Brasil.

Taylor, C. & Hughes, T.G., 1981. *Finite Element Programming of the Navier-Stokes Equations.* Pineridge Press Limited, Swansea, U.K. 244 p.

Tejada-Martínes, A. E., 2002. Dynamic subgrid-scale modeling for large-eddy simulation of turbulent flows with a stabilized finite element method. *PhD Thesis*, Faculty of Rensselaer Polytechnic Institute, Troy, New York, USA, 158p.

Winterscheidt, D. & Surana, K. S., 1994. p-version least squares finite element formulations for two-dimensional, incompressible fluid flow. *International Journal for Numerical Methods in Fluids*, vol. 18, pp. 43–69

Proceedings of the 11th Brazilian Congress of Thermal Sciences and Engineering -- ENCIT 2006
Braz. Soc. of Mechanical Sciences and Engineering -- ABCM, Curitiba, Brazil, Dec. 5-8, 2006

Paper CIT06-0466

EFFECT OF DIE LIP CONFIGURATION ON THE OPERATING WINDOW OF SLOT COATING PROCESS

Danmer Maza Quinones
Department of Mechanical Engineering
Pontifical Catholic University of Rio de Janeiro – PUC-Rio
Rua Marquês de São Vicente 225, Gávea, Rio de Janeiro, Brasil
danmerm@mec.puc-rio.br

Márcio da Silveira Carvalho
Department of Mechanical Engineering
Pontifical Catholic University of Rio de Janeiro – PUC-Rio
Rua Marquês de São Vicente 225, Gávea, Rio de Janeiro, Brasil
msc@mec.puc-rio.br

Abstract. Slot coating is a common method in the manufacture of a wide variety of products. The thickness of the coated liquid layer is set by the flow rate fed to the coating die and the speed of the substrate. The competition among viscous, capillary and pressure forces, and in some cases inertial forces, sets the range of operating parameters in which the viscous free surface flow of the liquid can be two-dimensional and steady. The region in the operating parameters of a coating process where the delivered liquid layer is uniform is referred to as coating window. The geometric configuration of the die has a strong effect on the various forces acting near the free surface. There are several die configurations disclosed in the patent literature claiming to be the optimal one. In this work, the theoretical analysis of the flow in a slot coating bead is developed. The conservation equations are solved with the Galerkin/FEM. The Coating windows are determined theoretically by searching the conditions at which the upstream or the downstream free surface invades the coating bead and the flow becomes unstable. The results show the effect of different geometric parameters on the limits of operability of the process.

Keywords: slot coating, free surface flow, Finite Element Method.

1. Introduction

Slot coating is used in the manufacturing process of adhesive and magnetic tapes, specialty papers, imaging films, and many other products. In this process, the coating liquid is pumped to a coating die in which an elongated chamber distributes it across the width of a narrow slot through which the flow rate per unit width at the slot exit is made uniform as shown in Fig.1. Exiting the slot, the liquid fills (wholly or partially) the gap between the adjacent die lips and the substrate translating rapidly past them. The liquid in the gap bounded upstream and downstream by gas-liquid interfaces, or menisci, forms the coating bead. The competition among viscous, capillary, inertial and pressure forces, sets the range of operating parameters in which the viscous free surface flow of the liquid can be two-dimensional and steady (gravitational effects are neglected because the length scale of a coating bead is so small). It is clear that physics sets the operating parameters at which this two-dimensional free surface flow exists. In order to sustain the coating bead at higher speeds, vacuum is usually applied on the back of the upstream meniscus (Beguin, 1954). This method belongs to a class of coating methods known as *pre-metered coating*: the thickness of the coated liquid layer is set by the prescribed flow rate fed into the coating die and it is independent of the process variables, making this class of method ideal for high precision coating. However, the liquid flow in the application region (coating bead), and therefore the quality of the coated film, is strongly affected by the substrate speed, the viscosity and the configuration of the die lips immediately upstream and downstream of the slot exit.

The region of acceptable coating quality in the space of operating parameters of a coating process is usually referred to as the coating window. Knowledge of coating windows of different coating methods is needed to predict whether a particular method can be used to coat a given substrate at a prescribed production rate. The concept of the Coating windows was first developed for slot coating flow. Coating windows can be constructed either from extensive experimentation or from theoretical model.

Ruschak (1976) analyzed the coating window of a slot coating bead dominated by surface tension force (capillary pressure) in the upstream and downstream menisci; Silliman (1979) and Higgins and Scriven (1980) took the viscous drag of the substrate and die lips into account. More advanced theoretical analyses and experiments on the limits of operability and flow stability within those limits were made subsequently (Sartor (1990), Gates and Scriven (1996), Carvalho and Kheshgi (2000), Romero et al. (2004)). A sketch of the operability limit is presented in Fig. 2. The figure shows that the coating window is bounded by three modes of failure:

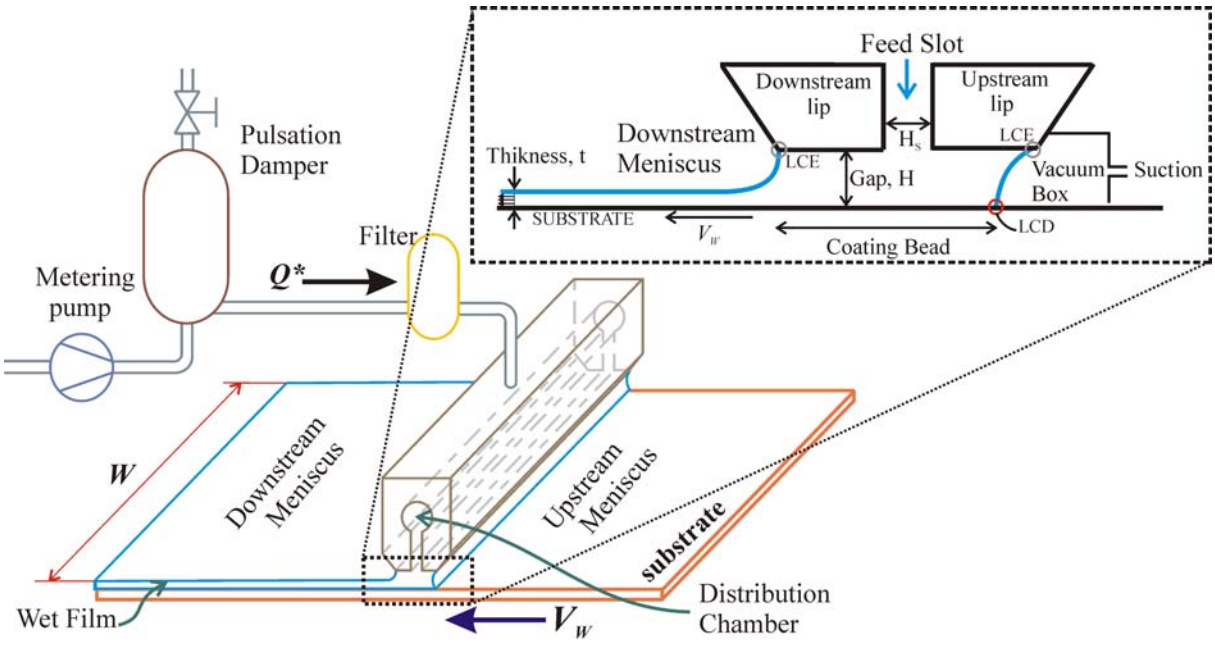

Figure 1. Sketch of the basic elements of Slot Coating and detail of the coating bead with the die lip.

1. When the coated layer is thicker than the thinnest that can be produced at a fixed gap and substrate speed, i.e. $t > t_{\min}$ in Fig. 2, too great a vacuum at the upstream free surface causes liquid to be drawn along the die surface into the vacuum chamber. This diversion of liquid destroys pre-metering.
2. Too little vacuum at the upstream free surface leaves the net viscous drag force on the upstream part of the bead unbalanced by the pressure gradient that is imposed by capillary pressure forces in the menisci upstream and downstream and the difference in external pressure on those menisci (i.e. vacuum). In consequence the upstream meniscus shifts toward the feed slot until the bead drastically rearranges into a three-dimensional form that delivers separate rivulets to the substrate. Between the rivulets are dry lanes that extend upstream through the bead. Along those lanes air is sucked into the vacuum chamber. It is in this regime that, at given vacuum (ambient pressure downstream minus air pressure exerted on upstream meniscus), there is a lower limit to the thickness of continuous liquid layer that can be coated from a downstream gap of specified clearance. As Fig. 2 shows, the limit can be lowered by applying greater vacuum and thereby shifting the upstream meniscus away from the edge of the feed slot.
3. At given substrate speed, too low a flow rate per unit width from the slot causes the downstream meniscus to curve so much that it cannot bridge the gap's clearance H. Consequently the meniscus becomes progressively more three-dimensional, alternate parts of it invading the gap until the bead takes a form that delivers separate rivulets or chains of droplets to the substrate moving past. This transition from a continuous coated liquid layer is what is called here the low-flow limit: the minimum thickness of liquid that can be deposited from a gap of specified clearance at a given substrate speed. And, as Fig. 2 makes plain, it is independent of the vacuum applied, given that the vacuum is great enough to draw the upstream meniscus away from the feed slot. The outcome is the same when at a given flow rate per unit width from the slot; the substrate speed is too high. In this case, the low-flow limit is sometimes referred to as the high-speed limit (see Carvalho and Kheshgi (2000)). The outcome is essentially the same when at a given flow rate per unit width from the slot and a given substrate speed, the clearance of the downstream gap is too great. In this case, the low-flow limit is referred to as the wide-gap limit: the maximum gap from which a given thickness of liquid coating can be deposited on a substrate moving at specified speed.

The center piece in slot coating process is the coating die. Many different die designs are show in the patent literature, publications and brochures form die manufacturers. The external design, in particular the shape and the positioning of the coating die relative to the substrate, is varied to find an ideal design for any application. Fig. 3 show different geometries of the coating die. The lip geometry influences the liquid flow and the pressure distribution in the coating gap (see Kistler and Schweizer (1997)) leading to different flow configurations.

Gates (1999) was able to complete a comprehensive array of flow visualizations of single layer slot coating. In each case the liquid was Newtonian, but a slot die featured interchangeable lips enabled him to make experimental observations about the effects of die lip geometry. The experimental analysis was complemented with a viscocapillary model. Figures 3e), 3f) and 3g) show the die lip shapes that Gates used in his flow visualizations.

The visco-capillary model is only valid at low capillary numbers, i.e., typically low speed and/or low viscosity. However, many coating process do not operate at low capillary numbers, especially those at high web speeds.

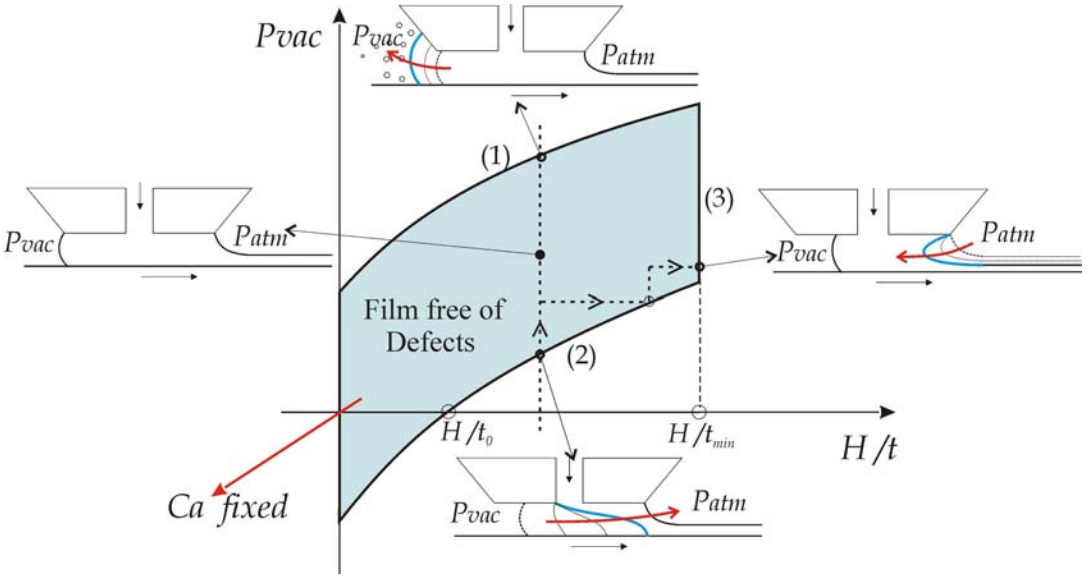

Figure 2. Coating Windows of a slot coating process, in the plane of vacuum *Pvac* vs gap-to-thickness ratio H/t, at a fixed capillary number *Ca*. The boundaries of the window are set by different bead break-up mechanisms. *tmin* represents the minimum film thickness that can be deposited onto the substrate at a given capillary number.

In this work, the coating window at different operating conditions, including high capillary number, was determined by theory, using a theoretical approach that consisted of solving the two dimensional Navier-Stokes equations with free surface that describe liquid flow in the coating bead by the Galerking/finite element method. A Pseudo-arc-length continuation was used to construct a solution path as the flow rate fed into the die was diminished. The minimum film thickness corresponded to the flow rate at which a turning point on the solution path occurred.

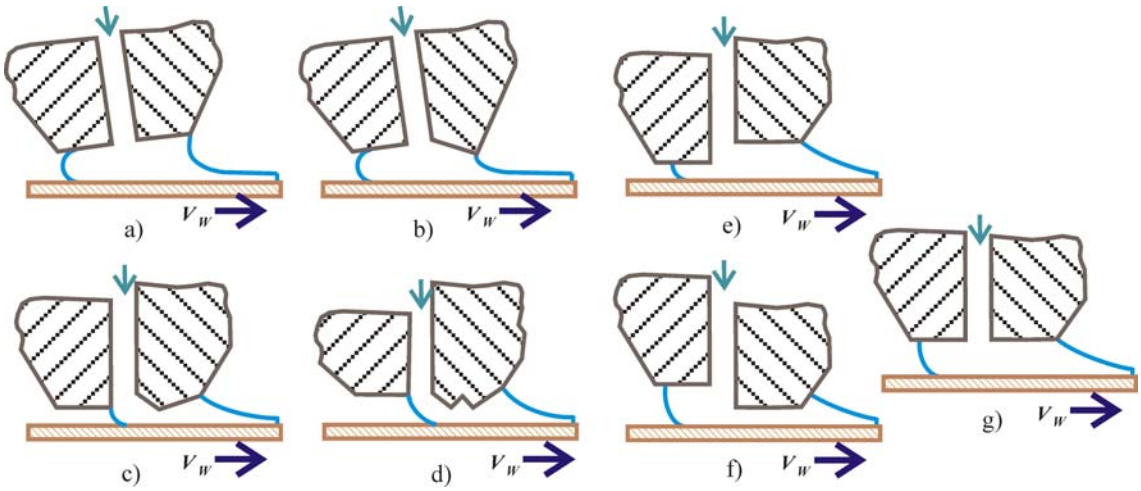

Figure 3. Die design of Slot coater: a) Divergent die lip; b) Convergent die lip; c) Convergent/divergent die lip; d) Two convergent /divergent die lip; e) Underbite lip; f) Overbite lip, g) Uniform or Standard lip.

2. Theoretical model and solution method

The flow in the coating bead is strongly affected by following operating parameters: gap (*H*), flow rate (*Q=Q*/W*), web speed (V_w), die configuration and liquids and roll cover properties.

2.1. Equation of the liquid flow

Figure 4 shows the liquid domain, bounded by two liquid-air interfaces, the coating die surface and the substrate. Coating flows are laminar, and ideally at steady-state and two-dimensional. The motion of the liquid is described by the momentum equation and continuity equation of incompressible flow:

$$\rho \mathbf{v} \cdot \nabla \mathbf{v} = \nabla \cdot \mathbf{T} \tag{1}$$

$$\nabla \cdot \mathbf{v} = 0 \tag{2}$$

For Newtonian liquid, the stress tensor **T** is given by:

$$\mathbf{T} = \left[- p\mathbf{I} + \mu(\nabla \mathbf{v} + \nabla \mathbf{v}^T) \right] \tag{3}$$

ρ and μ are the density and viscosity of the flowing liquid, e **v** the velocity vector.

2.2. Boundary condition

The boundary conditions for theoretical modeling in slot coating are also shown in the Fig. 4.

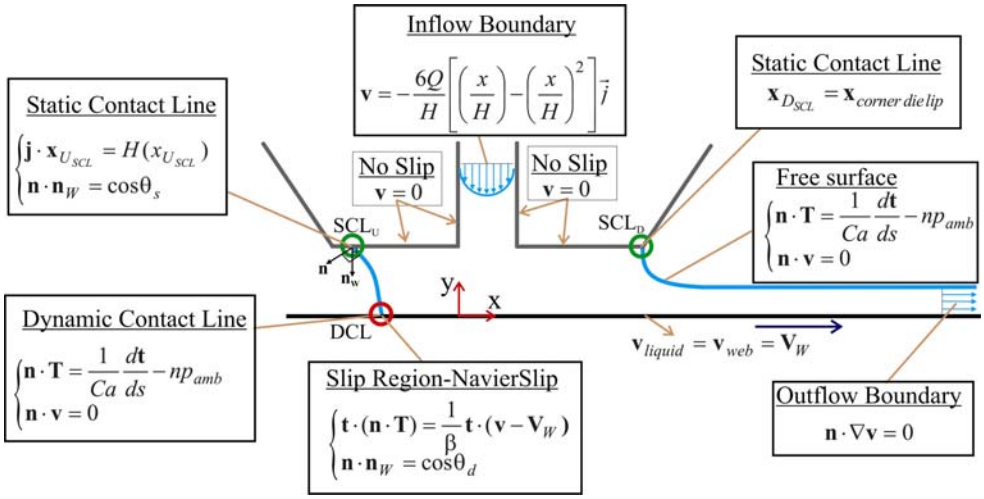

Figure 4. Sketch of the slot coating with boundary conditions for theoretical modeling

The relevant dimensionless parameters are:

- The Capillary number: $Ca = \frac{\mu V_W}{\sigma}$;
- Reynolds number: $\mathrm{Re} = \frac{\rho V_W H}{\mu}$;
- Dimensionless Slot Height: $\frac{H_S}{H}$.
- Vacuum pressure: $Vac = \frac{P_{vac} H}{\sigma}$;
- Gap to thickness ratio: $\frac{H}{t}$;

The governing equations give rise to a free boundary problem, because the positions of the gas-liquid interfaces are unknown a priori. The solution of such problems is recounted briefly here. Fuller accounts were given by Kistler and Scriven (1984), Sackinger, Schunk, and Rao (1996) and Carvalho and Scriven (1997).

2.2. Mapping from the physical to reference domain

In order to solve a free-boundary problem using the standard techniques of boundary value problem, the set of differential equations posed in the unknown physical domain Ω has to be transformed to an equivalent set defined in a suitable known reference domain $\overline{\Omega}$, as sketched in Fig. 5. This is done by the mapping $\mathbf{x} = \mathbf{x}(\xi)$ that connects the two domains. Here, the unknown physical domain is parameterized by the position vector $\mathbf{x}$, and the reference domain by ξ. The reference domain adopted is to some extent arbitrary, with the conditions that the boundaries of the reference domain have to be continuously mapped onto the boundaries of the physical domain and the mapping has to be invertible.

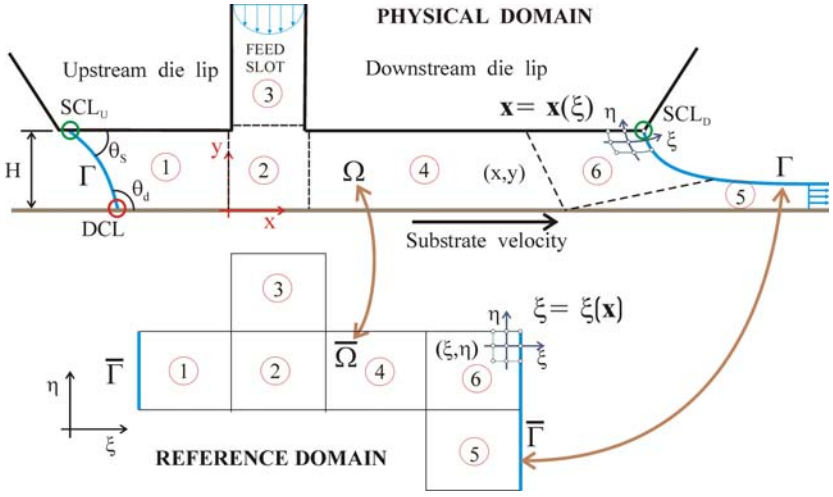

Figure 5. Sketch of mapping from the liquid domain to the reference domain

The mapping used here is presented in detail by de De Santos (1991). He showed that a functional of weighted smoothness can be used successfully to construct the sorts of maps involved here. The inverse of the mapping that minimizes the functional is governed by a pair of elliptic differential equations identical to those encountered in diffusion transport with variable diffusion coefficients. The coordinates ξ and η of the reference domain satisfy:

$$\nabla \cdot D_\xi \nabla \xi = 0 \; ; \quad \nabla \cdot D_\eta \nabla \eta = 0 \tag{4}$$

The coefficients, D_ξ and D_η, are controlled by stretching functions along iso-ξ and iso-η coordinates lines (Benjamin et al 1990)

Boundary conditions are needed to solve the second-order partial differential equations. Along solid walls and synthetic inlet and outlet plates, the boundaries are located by imposing a relation between the coordinates and from the equation that describes the shape of the boundary and stretching functions are used to distribute the points along the boundaries. The free boundary (gas-liquid interface) is located by imposing the kinematic condition. The discrete version of the mapping equations are generally referred to as mesh generation equations. Spatial derivatives with respect to coordinates of the physical domain x and y can be written in terms of derivatives with respect to the coordinates of the reference domain ξ and η by using the inverse of the gradient of the mapping:

$$\nabla_x \phi = \mathbf{J_T}^{-1} \nabla_\xi \phi \tag{5}$$

Where $\mathbf{J_T}$ is the Jacobian of the transformation

2.3. Finite element formulation of the system equations

The system of partial differential equations presented in the previous section is solved by Galerkin's/Finite Element method. The velocity and node position are represented in terms of bi-quadratic basis functions ϕ_j and the pressure with linear discontinuous functions χ_j:

$$\mathbf{v} = \sum_{j=1}^{9} (\mathbf{v}_j \phi_j) \; ; \quad \mathbf{p} = \sum_{j=1}^{3} (P_j \chi_j) \; ; \quad \mathbf{x} = \sum_{j=1}^{9} (\mathbf{x}_j \phi_j) \tag{6}$$

The Galerkin weighted residual of the continuity, momentum and mesh generation (mapping) are given by:

$$\mathbf{R}_c^i = \int_{\overline{\Omega}} (\nabla \cdot \mathbf{v}) \chi_i J_T d\overline{\Omega}, \tag{7}$$

$$\mathbf{R}m_x^i = \int_{\overline{\Omega}} \left[\rho\phi_i \left(u\frac{\partial u}{\partial x} + v\frac{\partial u}{\partial y} \right) + \left(\frac{\partial \phi_i}{\partial x} Txx + \frac{\partial \phi_i}{\partial y} Txy \right) \right] J_T d\overline{\Omega} - \int_{\overline{\Gamma}} \phi_i (\mathbf{n} \cdot \mathbf{T})_x \left(\frac{d\Gamma}{d\overline{\Gamma}}\right) d\overline{\Gamma} \tag{8}$$

$$\mathbf{R}m_y^i = \int_{\overline{\Omega}} \left[\rho\phi_i \left(u\frac{\partial v}{\partial x} + v\frac{\partial v}{\partial y} \right) + \left(\frac{\partial \phi_i}{\partial x} Txy + \frac{\partial \phi_i}{\partial y} Tyy \right) \right] J_T d\overline{\Omega} - \int_{\overline{\Gamma}} \phi_i (\mathbf{n} \cdot \mathbf{T})_y \left(\frac{d\Gamma}{d\overline{\Gamma}}\right) d\overline{\Gamma} \tag{9}$$

$$\mathbf{R}x^i = -\int_{\overline{\Omega}} D_\xi \left(\frac{\partial y}{\partial \eta}\frac{\partial \phi_i}{\partial x} - \frac{\partial x}{\partial \eta}\frac{\partial \phi_i}{\partial y}\right) d\overline{\Omega} + \int_{\overline{\Gamma}} D_\xi \frac{1}{J_T} \left(\frac{\partial y}{\partial \eta}\eta_x - \frac{\partial x}{\partial \eta}\eta_y\right) \phi_i \left(\frac{d\Gamma}{d\overline{\Gamma}}\right) d\overline{\Gamma} \tag{10}$$

$$\mathbf{R}y^i = -\int_{\overline{\Omega}} D_\eta \left(\frac{\partial y}{\partial \xi}\frac{\partial \phi i}{\partial x} - \frac{\partial x}{\partial \xi}\frac{\partial \phi i}{\partial y}\right) d\overline{\Omega} + \int_{\overline{\Gamma}} D_\eta \frac{1}{J_T} \left(-\frac{\partial y}{\partial \xi}\eta_x + \frac{\partial x}{\partial \xi}\eta_y\right) \phi_i \left(\frac{d\Gamma}{d\overline{\Gamma}}\right) d\overline{\Gamma} \tag{11}$$

Where J_T is the determinant of Jacobean of the transformation.

The system of partial differential equations reduces to simultaneous algebraic equations for the coefficients of the basis functions of all the fields. This set of equations is non-linear and sparse. It was solved by Newton's method, which requires evaluation of the full jacobian matrix.

$$\mathbf{c}^{(k+1)} = \mathbf{c}^{(k)} + \delta\mathbf{c}; \quad \mathbf{J}(\delta\mathbf{c}) = -\mathbf{R}; \quad \mathbf{J}_{ij} = \frac{\partial \mathbf{R}_i}{\partial \mathbf{c}_j} \tag{12}$$

Where $\mathbf{c}$ is the vector of the unknowns coefficient of the basis functions for the velocity, pressure and nodal positions, $\mathbf{R}$ is the vector of weighted residuals given by above equations.

The iteration proceeded until $\|\delta\mathbf{c}\|_2 + \|\delta\mathbf{R}\|_2 \le \varepsilon$. For each Newton's iteration, a linear system of equations was solved using **LU** decomposition. A pseudo-arc length continuation method coupled whit Newton's method it was used to automatically construct the entire path of steady state. The minimal film thickness at a given web speed was obtained by decreasing flow rate until a turning-point was found.

3. Results

In all the configurations considered here, i.e., overbite, underbite and standard lip configuration, the domain was divided into 474 elements, with approximately 10,000 unknowns. The representative geometries are shown in Fig. 6. The difference between them is the offset in the upstream die lip. The downstream gap $H_D = H = 100\,\mu\text{m}$ and the feed slot height $Hs/H = 0.75$ were kept constant. The Property number $P_P = \text{Re}/Ca = \rho\sigma H/\mu^2 = 2000$, that is a function of the liquid properties and coating gap and invariant to substrate speed, was also constant in all the cases.

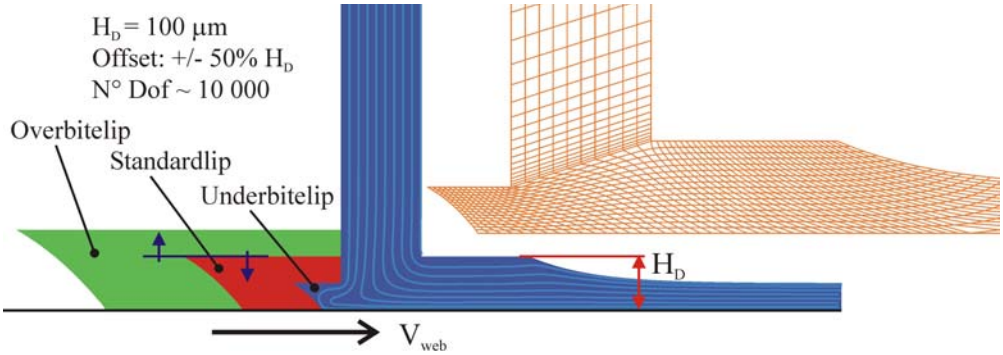

Figure 6. Sketches of the three die configuration used: Overbite, Standard and Underbite and the representative mesh of the Underbite type.

The limits on the operating condition were determined by following the solution path at a fixed web speed. The flow rate, and therefore the film thickness, was decreased until a turning point was encountered on the solution path. The critical gap-to-thickness ratio was calculated from the value of the flow rate at the turning point.

Figure 7 shows a path of solutions computed at different capillary number, Ca = 0.1; 0.5 and 1.0, at a vacuum pressure of Pvac = 14kPa, 80kPa and 160kPa, respectively. Flow states are characterized by the position of the dynamic contact line, X_{DCL}. This plot shows how the position of the dynamic contact line varies with the flow rate fed into the different die. As the coated film becomes thinner, the dynamic contact line is pulled towards the feeding slot. With the underbite configuration, the upstream meniscus was located closer to the feed slot and the position of the upstream meniscus was less sensitive to the film thickness. With the overbite configuration, the position of the upstream meniscus is more sensitive to the coated layer film thickness.

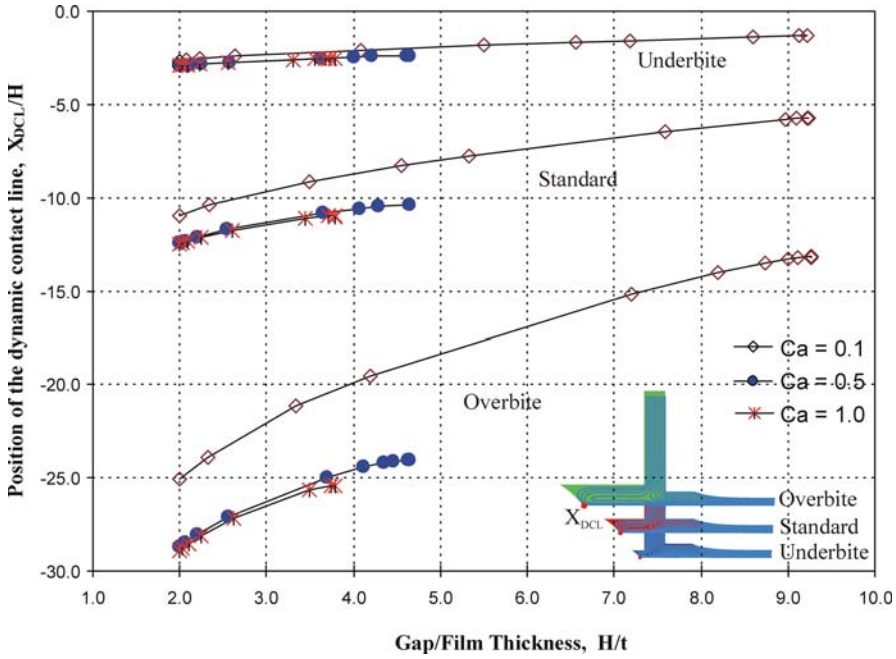

Figure 7. Position of the dynamic contact line as a function of the gap-to-thikcness ratio and capillary number.

Figure 8 shows the vacuum pressure necessary to maintain the process stable for the different upstream die lip configuration at *Ca = 0.1*. The Underbite configuration exhibit a larger range of vacuum operation than the other two configurations tested.

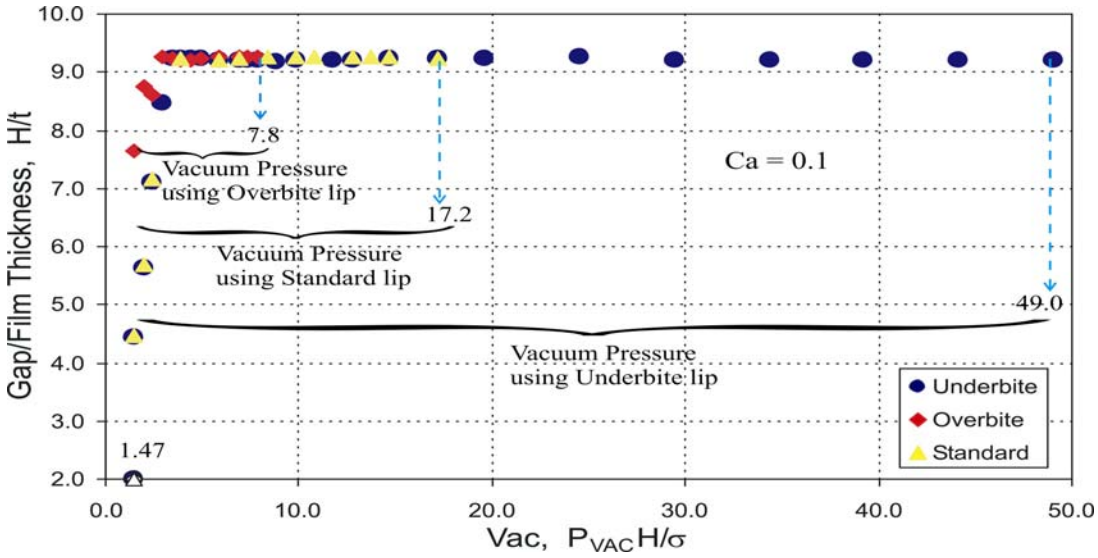

Figure 8. Range of vacuum pressure for different die configuration at *Ca = 0.1.*

The predicted coating window of slot coating process, in the plane of vacuum pressure and gap-to-thickness ratio at different capillary number and die lip configuration is shown in Fig.9. The upper boundary of the coating window is the upper vacuum limited. It was determined by raising the vacuum pressure until the upstream length of the coating bead became larger than the length of the upstream die lip. Beyond this value, the liquid would invade the vacuum box, leading to coating deffects. The lower boundary corresponds to the low vacuum limit. It was determined by decreasing the vacuum pressure until the upstream meniscus invades the region under the feed slot. In practice, the coating bead would break leading to rivulets. The left boundary of the coating window represents the minimum wet thickness that can be coated at a given substrate speed. The onset of this limit corresponds to the operating parameters at which the downstream free surface invades the coating bead. Experimental results indicated that meniscus becomes progressively more three-dimensional, alternate parts of it invading the gap until the bead takes a form that delivers separate rivulets or chains of droplets to the substrate moving past. In the theoretical model, this limit is represented by a turning point in the solution path. The minimum thickness is independent of the vacuum pressure applied, given that the vacuum is large enough to draw the upstream meniscus away from the feed slot.

The predicted coating window for the three geometries tested showed that the minimum thickness rises (gap-to-thickness falls) with capillary number, which means that thinner coating can only be obtained at low speeds. The effect of the die configuration in this process limit is very weak. The main effect of the die configuration is on the low and high vacuum limits. With the overbite coniguration, the pressure is the coating bead is higher because of the contraction in the gap, therefore the amount of vacuum needed to pull the upstream free surface is smaller.

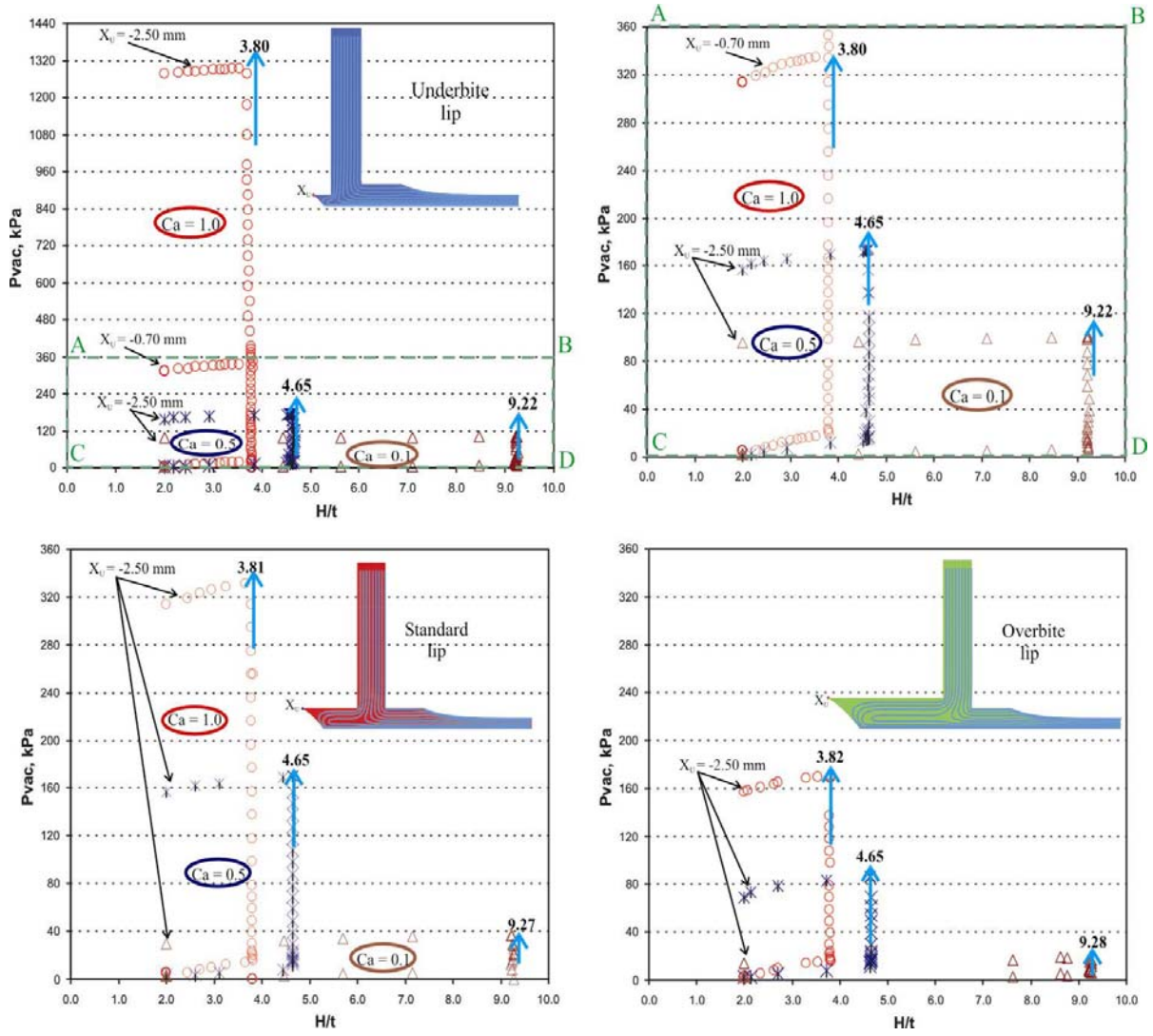

Figure 9. Coating Windows of a slot coating process, in the plane of vacuum *Pvac* vs gap-to-thickness ratio H/t for different configuration of the die slot.

4. Final Remarks

The coating window of slot coating process was obtained theoretically by solving the two-dimensional Navier-Stokes equations with free surfaces. The results show how the die configuration affects the steady-state solutions and the limits of the important manufacturing process.

5. Referências

Beguin, A. L., 1954, "Method of Coating Strip Material", U.S.Pat.2,681,294

Benjamin, D. F., De Santos, J.M. and Scriven, L.E., 1990, "Meshs for viscous free surface flow as solutions to elliptic P.D.E.'s of transport.

Carvalho, M. S., and Scriven, L. E., 1997, "Flows in forward deformable roll coating gaps: Comparison between spring and plane strain models of roll cover". Journal of Computational Physics, 138(2), 449–479.

Carvalho, M. S. and Khesghi, H. S., 2000 "Low-Flow limit in slot coating: Theory and Experiments", AIChE Journal, 46, 1907-1917.

De Santos, J. M., 1991, "Two-phase cocurrent down flow through constricted passages". PhD Thesis, University of Minnesota, MN, USA.

Encit 2004, 2004, "Instruções para a Formatação de Trabalhos Submetidos ao 10º Congresso Brasileiro de Ciências Térmicas e Engenharia", ABCM, Curitiba, Brasil. 3 p.

Gates, I. D. and Scriven, L. E., 1996, "Stability Analysis of Slot Coating Flows", AIChE 1996 Spring National Meeting, New Orleans.

Gates, I.D., 1999, "Slot Coating flows: Feasibility, Quality", Ph. Thesis University of Minnesota. Published by University Microfilms International, Ann Arbor, MI.

Higgins, B. G. and Scriven, L. E., 1980, "Capillary pressure and viscous pressure drop set bounds on coating bead operatibility", Chemical Engineering Science, 35, 673-682.

Kistler, S. F., and Scriven, L. E., 1984. Coating flow theory by 8nite element and asymptotic analysis of the Navier–Stokes system. International Journal for Numerical Methods in Fluids, 4, 207.

Romero, O. J., 2003, Ph.D Thesis, University of PUC-Rio.

Ruschak, K. J., 1976 "Limiting Flow in a pre-metered coating device", Chemical Engineering Science, 31, pp 1057-1060.

Sackinger, P. A., Schunk, P. R., & Rao, R. R., 1996, "A Newton-Raphson pseudo-solid domain mapping technique for free and moving boundary problems, A Finite element implementation". Journal of Computational Physics.

Sartor, L., 1990, "Slot Coating: Fluid Mechanics and Die Design", Ph.D Thesis, University of Minnesota.

Silliman, W. J., 1979, "Viscous Film Flows with Contact Lines: Finite Element Simultions, A Basis for Stability Assessment and Design Optimization". PhD Thesis, University of Minnesota, MN.

6. Responsibility notice

The authors are the only responsible for the printed material included in this paper.

Proceedings of the 11th Brazilian Congress of Thermal Sciences and Engineering -- ENCIT 2006
Braz. Soc. of Mechanical Sciences and Engineering -- ABCM, Curitiba, Brazil, Dec. 5-8, 2006

Paper CIT06-0492

ANÁLISE TEMPO-FREQÜÊNCIA DE UM ESCOAMENTO EM TÊ – COMPARAÇÕES DE DADOS EXPERIMENTAIS COM RESULTADOS NUMÉRICOS OBTIDOS POR SIMULAÇÃO DE GRANDES ESCALAS

Graziela Marchi Tiago
LETeF – SEM - EESC – Universidade de São Paulo
Av. Trabalhador São Carlense, 400, cep:13560-970, São Carlos - SP
graziela@sc.usp.br

Paulo Seleghim Jr.
LETeF – SEM - EESC – Universidade de São Paulo
Av. Trabalhador São Carlense, 400, cep:13560-970, São Carlos - SP
seleghim@sc.usp.br

Resumo. *Escoamentos turbulentos têm sido por muitos anos o objetivo de importantes estudos para descobrir sua dinâmica. Dentre suas características, a mais significativa é a multiplicidade de escalas, desde as maiores estruturas (baixas freqüências) controladas pela geometria que as geram, até as menores estruturas (altas freqüências) limitadas pela viscosidade do fluido. Estes vórtices são importantes em muitas aplicações tecnológicas, sendo necessário entender a dinâmica da organização de seus movimentos para controlar mecanicamente sua produção ou supressão. Neste contexto, a análise de um misturador de ar em um escoamento em tê é o principal objetivo deste trabalho. A geometria em tê é bastante simples, mas propicia o aparecimento de um escoamento com transição de vórtices. Testes experimentais do escoamento, com duas entradas de ar com temperaturas diferentes, foram realizados no laboratório do LETeF. As medidas de temperatura foram obtidas com termopares instalados ao longo da tubulação. Com o software CFX® foram realizados estudos de métodos numéricos de grandes escalas. Estes resultados computacionais foram comparados com os dados experimentais, através da análise tempo-freqüência. Estudos do escoamento mostram regiões de transição de turbulência, e a habilidade da técnica de análise tempo-freqüência em caracterizar a existência e a forma da estruturas turbulentas com grandes vórtices.*

Palavras chave: simulação de grandes escalas, análise tempo-freqüência, turbulência.

1. Introdução

A maioria dos escoamentos encontrados na natureza e em aplicações práticas são turbulentos, com um comportamento caótico de grande complexidade, instáveis e que contém flutuações dependentes do tempo e da posição no espaço. Por ocorrer com muita freqüência na natureza, a turbulência é estudada por físicos, químicos, engenheiros, matemáticos, biólogos, médicos, economistas, meteorologistas, cada um com suas motivações, tentando compreender o problema.

Dentre os exemplos de escoamentos turbulentos, podemos citar o processo de mistura de combustível e oxigênio no interior de uma câmara de combustão, aonde as pequenas escalas de turbulência tornam essa mistura eficiente, aumentando o rendimento do motor e reduzindo os efeitos de poluição dos gases tóxicos liberados pelos automóveis e aviões. Também os fenômenos atmosféricos, como furacões e tornados que causam verdadeiras catástrofes por onde eles passam.

O escoamento turbulento possui várias características. Dentre elas, aumenta o poder de propagação de um escoamento, tornando-se mais eficiente a mistura de massa, contaminantes, energia, quantidade de movimento. Além disto, só ocorre em escoamentos rotacionais e tridimensionais. Suas soluções também são imprevisíveis, e os fatores que influenciam são as imperfeições nos modelos matemáticos e nos métodos de solução das equações, e as imprecisões nos sistemas de medidas do escoamento que fornecem as condições iniciais para a realização das simulações. Outra característica é seu espectro de energia, o qual deverá ser portador de uma larga banda de freqüências ou comprimentos de onda e os altos números de Reynolds. E por fim, a característica mais importante é a multiplicidade de escalas, aonde as maiores estruturas (baixas freqüências) são controladas pela geometria que as geram, e as menores estruturas (altas freqüências) são limitadas pela viscosidade do fluido.

É grande o investimento em pesquisas relacionadas à compreensão e ao controle dos escoamentos turbulentos, e para entender os mecanismos físicos que governam este tipo de movimento. Para a maioria das aplicações da engenharia e mesmo para a compreensão fenomenológica dos escoamentos, a determinação exata da posição e da fase de um turbilhão não é tão indispensável. Desta forma, o importante é colocar em evidência a existência e a forma das estruturas turbilhonares e suas interações. Conhecer as informações estatísticas do escoamento são suficientes para a maioria das aplicações de engenharia, sendo impossível repetir com precisão os resultados obtidos experimentalmente através de simulações numéricas, ou seja, os vórtices produzidos numa simulação numérica não representam

exatamente os turbilhões observados numa experiência de laboratório, em relação à posição no espaço e no tempo, mesmo sendo as condições iniciais e limites bem próximas.

Dentre as técnicas utilizadas para se fazer o estudo da turbulência destacam-se análise tempo-freqüência e análise tempo-escala, aplicadas com muito sucesso a um grande número de problemas tecnológicos e científicos. Seleghim (1993) propôs um critério mais objetivo para a caracterização em escoamento vertical baseado na quantificação do grau de não-estacionaridade, através do desvio padrão da freqüência instantânea de Ville. Este critério foi validado em testes feitos em diferentes circuitos experimentais, discutidos em Seleghim e Hervieu (1994).

Posteriormente, Seleghim (1996), e Seleghim e Hervieu (1998) aperfeiçoaram o critério proposto anteriormente no sentido de torná-lo universal, independente da transição ou grandeza física estudada. O critério proposto para indicar a transição de regime foi a covariância tempo-freqüência associada à transformada de Gabor. A validação do método foi a detecção de todas as transições de configuração de escoamento horizontal indicadas.

Vários são os autores que se valem de simulação numérica para o estudo da turbulência. Podemos destacar, Matos, Pinho e Silveira-Neto (1999) estudaram a simulação de grandes escalas de escoamentos turbulentos sobre uma camada plana livre e uma cavidade plana simétrica, usando o modelo sub-malha de Smagorinsky. Também Goulart, et al. (2004) estudaram experimentalmente e numericamente o desenvolvimento e as características do escoamento ao longo de um feixe de tubos com placas defletoras. Utilizaram o software CFX® com os modelos LES e $k-\varepsilon$.

O escoamento em questão é um misturador de ar em tê, sendo sua geometria bastante simples, mas propicia o aparecimento de um escoamento com transições de vórtices. Vários autores já estudaram o escoamento em tê, considerado um misturador mais rápido e eficiente, dentre eles podemos citar: Maruyama, Suzuki e Mizushina (1981) investigaram experimentalmente um tubo de mistura de dois fluidos com fluxo de encontro numa junção em tê; Tosun (1987) estudou o processo de micro-mistura e misturadores em tê, e fez testes com os diâmetros da tubulação e recentemente, Chapuliot, et al. (2005) estudaram os principais mecanismos de rachadura na canalização como resultado de excesso térmico em um escoamento com zonas de mistura.

Neste contexto, o objetivo deste trabalho é estudar um escoamento de referência ("benchmark"), sendo este um misturador de ar em tê, capaz de produzir resultados que possam validar os modelos de turbulência LES e DES implementados no software comercial CFX®, sobretudo no que se refere à descrição do fenômeno de turbulência de grandes escalas. Isto tudo para garantir a confiabilidade dos resultados numéricos obtidos do escoamento. Faz parte igualmente dos objetivos, o desenvolvimento de técnicas de Análise de Sinais capazes de melhor descrever o fenômeno estudado no escoamento, comparando flutuações de temperatura dos dados experimentais com os resultados numéricos para caracterizar a existência e a forma das estruturas turbulentas com grandes vórtices.

2. Análise de Sinais

Os sinais de temperatura provenientes dos termopares instalados ao longo da tubulação do experimento e da simulação numérica foram analisados de acordo com os fundamentos de Análise de Sinais. Esta consiste em estudar e caracterizar as propriedades básicas dos sinais medidos. O método usado para fazer as comparações foi a análise dos Sinai no plano tempo-freqüência.

2.1. Análise Tempo-Freqüência

A idéia fundamental da análise tempo-freqüência é entender e analisar situações onde a composição frequencial de um sinal está mudando no tempo. O objetivo básico da análise tempo-freqüência é descobrir uma função que descreva a densidade de energia de um sinal simultaneamente no tempo e na freqüência, e que possa ser usada e manipulada da mesma maneira como qualquer densidade. De posse de tal função, pode-se saber qual a fração de energia existente em uma determinada faixa temporal e frequencial, e calcular a densidade de freqüências em um tempo particular, e momentos global e local entre outros.

Para se avaliar as propriedades do sinal para um tempo t desejado, dá-se ênfase ao sinal naquele momento e oculta-o em outros tempos, aonde denota-se o sinal como s(t) e o tempo corrente como t. Segundo Cohen (1995), isso é feito multiplicando o sinal por uma função janela h(t) a fim de se produzir um sinal modificado do tipo:

$$s_t(\tau) = s(\tau)h(\tau - t) \tag{1}$$

Desde que o sinal modificado enfatize o sinal em torno do tempo t, a transformada de Fourier refletirá a distribuição de freqüências em torno daquele tempo, com freqüência w:

$$s_t(\omega) = \frac{1}{\sqrt{2\pi}} \int_{-\infty}^{+\infty} e^{-j\omega\tau} s_t(\tau) d\tau \tag{2}$$

$$s_t(\omega) = \frac{1}{\sqrt{2\pi}} \int_{-\infty}^{+\infty} e^{-j\omega\tau} s(\tau) h(\tau - t) d\tau \tag{3}$$

A densidade de energia espectral no tempo t é:

$$P_{sp}(t,\omega) = \left|s_t(\omega)\right|^2 = \left| \frac{1}{\sqrt{2\pi}} \int_{-\infty}^{+\infty} e^{-j\omega\tau} s(\tau) h(\tau - t) d\tau \right|^2 \tag{4}$$

Assim, para cada tempo t diferente, consegue-se uma densidade de energia espectral e a totalidade dessas densidades é a distribuição tempo-freqüência $P_{sp}(t,\omega)$. Transformada a curto tempo de Fourier e transformada de Gabor são formas de se construir a função $P_{sp}(t,\omega)$. O que distingue cada forma é a função h analisante utilizada. A função junção tempo-freqüência foi obtida através da transformada de Gabor, o qual usa a função gaussiana como função analisante $h(\tau - t) = e^{-\alpha(\tau - t)^2}$. As funções estatísticas usadas para as comparações neste artigo foram a energia e a covariância tempo-freqüência da distribuição tempo-freqüência, calculadas para testes de vazão de ar mantidas constantes.

Sendo F_{min} e F_{max} os limites na freqüência, T_{min} e T_{max} os limites no tempo, a energia E do sinal o qual caracteriza a instabilidade de um sistema, é dada por:

$$E = \int_{F_{min}}^{F_{max}} \int_{T_{min}}^{T_{max}} P_{sp}(t,\omega) dt d\omega \tag{5}$$

A análise tempo-freqüência constitui uma poderosa ferramenta para avaliar a não estacionaridade de um sinal ou de um processo. Quando um sinal não varia em algum sentido, diz-se que ele é estacionário. No contexto dos processos determinísticos, a estacionaridade é geralmente assumida como um estado espectral em que a composição frequencial é constante em relação ao tempo (Seleghim e Hervieu, 1998). Sinais reais, no entanto, nunca são puramente estacionários, logo uma definição mais realista é avaliar o seu grau de não estacionaridade.

A covariância aqui estudada, é uma indicação do quanto a freqüência instantânea e o tempo estão correlacionados. Logo, a covariância será nula quando a freqüência não variar com o tempo. Quanto maior a covariância, maior o grau de não estacionaridade de um sinal, e mais a freqüência varia com o tempo (Cohen, 1995; Lathi, 1968). Portanto, se tempo e freqüência são variáveis independentes, assumi-se que $P_{sp}(t,\omega)$ seja uma função separável, isto é:

$$P(t,\omega) = F(t)G(\omega) \tag{6}$$

Considerando t um instante particular da distribuição tempo-freqüência e definindo um apropriado horizonte T de análise, um tempo central $\Delta_t(\tau)$, uma freqüência central $\Delta_\omega(\tau)$ e um momento misto $\Delta_{t\omega}(\tau)$, temos:

$$\Delta_t(\tau) = \frac{1}{E(\tau)} \int_{-\infty}^{+\infty} \int_{\tau - \frac{T}{2}}^{\tau + \frac{T}{2}} t P(t,\omega) dt d\omega \tag{7}$$

$$\Delta_\omega(\tau) = \frac{1}{E(\tau)} \int_{-\infty}^{+\infty} \int_{\tau - \frac{T}{2}}^{\tau + \frac{T}{2}} \omega P(t,\omega) dt d\omega \tag{8}$$

$$\Delta_{t\omega}(\tau) = \frac{1}{E(\tau)} \int_{-\infty}^{+\infty} \int_{\tau - \frac{T}{2}}^{\tau + \frac{T}{2}} t\omega P(t,\omega) dt d\omega \tag{9}$$

Sendo $\sum(\tau)$ um intervalo de deslizamento centralizado em t com T de duração, e E(t) a energia total de $\sum(\tau)$, eles são definidos como:

$$\sum(\tau) = \left[\tau - \frac{T}{2}, \tau + \frac{T}{2}\right] \tag{10}$$

$$E(\tau) = \int\int_{\sum(\tau)} P(t,\omega)dtd\omega \tag{11}$$

Se o sinal for independente do tempo e da freqüência, é razoável assumir que a média temporal e a média frequencial não estão relacionadas. Sob essa suposição podemos esperar que:

$$\Delta_{t\omega}(\tau) = \Delta_{\omega}(\tau)\Delta_{t}(\tau) \tag{12}$$

Portanto, o excesso de $\Delta_{t\omega}(\tau)$ sobre $\Delta_{\omega}(\tau)\Delta_{t}(\tau)$ é uma boa indicação de quanto o tempo está correlacionado com a freqüência. Logo, a covariância tempo-freqüência é definida como (Seleghim e Hervieu, 1998):

$$\text{cov}_{t\omega} = \left|\Delta_{t\omega}(\tau) - \Delta_{\omega}(\tau)\Delta_{t}(\tau)\right| \tag{13}$$

Assim, quando os sinais são independentes do tempo e da freqüência, $\text{cov}_{t\omega} = 0$.

3. Descrição do circuito experimental

Os testes experimentais foram realizados no Laboratório de Engenharia Térmica e Fluidos da Escola de Engenharia de São Carlos da Universidade de São Paulo. Foi montada uma tubulação em cano PVC do escoamento de ar em tê, com duas entradas e uma saída, como especificadas na Fig. 1 com todas as instalações e respectivas posições no experimento. Os termopares do tipo K, devidamente blindados, foram instalados em direção à saída do tê, sendo que o primeiro está bem no centro do escoamento, o segundo 0,20m após o primeiro, o terceiro 0,20m após o segundo e assim por diante até completar 8 termopares.

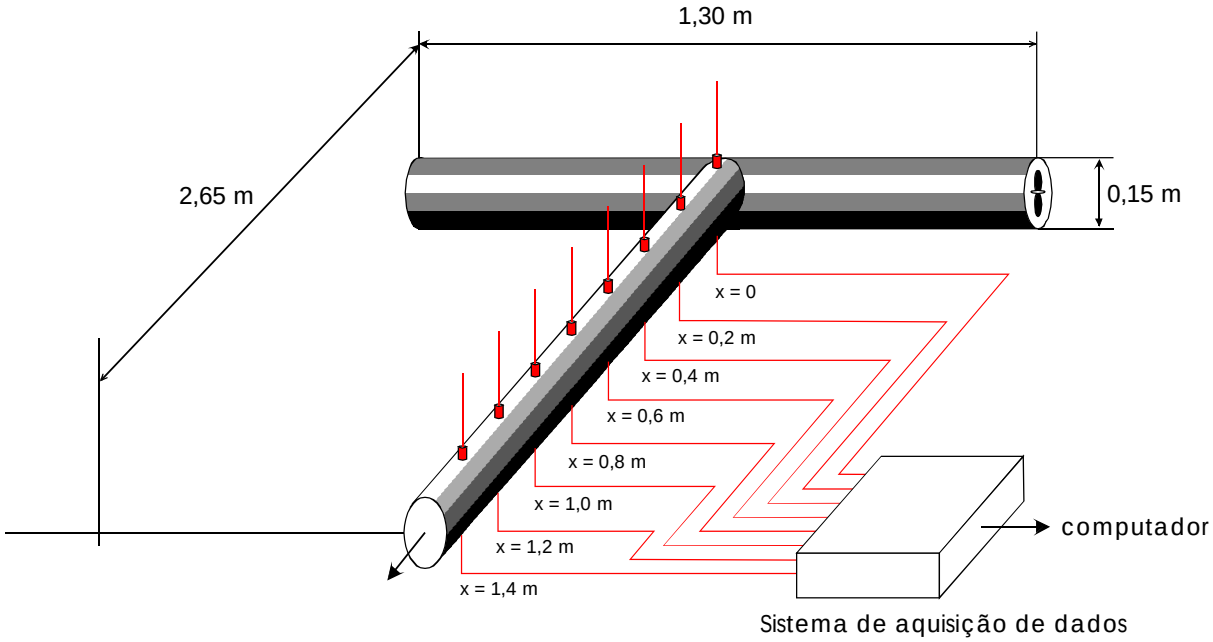

Figura 1. Representação esquemática da instalação experimental.

Para controlar a vazão de ar no experimento foram instalados ventiladores nas duas entradas da tubulação, sendo que de um lado após o ventilador foi colocada uma resistência de chuveiro blindada para elevar a temperatura desta entrada. Estes ventiladores conseguiam imprimir uma velocidade de 2,2m/s em cada entrada, e a resistência era aquecida a uma potência de 90W. Fez-se uma medida no experimento com um termômetro nas duas entradas. De um lado era a temperatura ambiente, e do outro como tínhamos a resistência aquecida, a temperatura era maior, mas oscilava um pouco, por isso resolvemos colocar uma média do que realmente estava marcando no termômetro.

Além dos termopares instalados, o circuito é provido de um sistema de aquisição para obter os sinais de temperatura da National Instruments, composto por um chassi PXI-1000B equipado com um controlador embutido NI

8176 PXI (Pentium III 1.26Ghz) e uma placa I/O multi-função PXI-6025E por 200 KS/s 12-bit de amostragem, que garante a comunicação com o computador.

Para aquisição e armazenamento dos dados foi implementado um programa no software LabVIEW®. Parava-se a aquisição de temperatura quando completasse a quantidade de pontos desejada para fazer comparações com as simulações numéricas, através do programa de análise tempo-freqüência, 2^{15}=32768. O programa permitia escolher quantidade de pontos amostrados por segundo, e a colocação de um filtro Butterworth passa-baixa em 30Hz para eliminar uma fonte de ruído em 60Hz. O efeito aliasing, causado por ruídos em altas freqüências, foi eliminado fazendo a aquisição alta com 1000 pontos de temperatura por segundo.

4. Simulação Numérica

Para as simulações numéricas foi utilizado o software comercial CFX®, versão 5.7, com dois métodos de simulação de grandes escalas, LES e DES. O programa resolve as equações de Navier–Stokes na forma conservativa aproximando-as pelo método de volumes finitos baseado em elementos (Patankar, Taylor e Francis, 1980; Versteeg e Malalasekera, 1995). Considere S_M uma fonte de momento, S_E uma fonte de energia e λ a condutividade térmica, então:

Equação da Continuidade: $$\frac{\partial \rho}{\partial t} + \frac{\partial (\rho U_i)}{\partial x_i} = 0 \tag{14}$$

Equação do Movimento: $$\frac{\partial \rho U_i}{\partial t} + \frac{\partial (\rho U_j U_i)}{\partial x_j} = -\frac{\partial p}{\partial x_i} + \mu \frac{\partial^2 U_i}{\partial x_j \partial x_j} + S_M \tag{15}$$

Equação de Energia Térmica: $$\frac{\partial \rho h}{\partial t} + \frac{\partial (\rho U_j h)}{\partial x_j} = \frac{\partial^2 (\lambda T)}{\partial x_j \partial x_j} + S_E \tag{16}$$

Foi utilizado um computador Pentium4 de 3.0Ghz, com a plataforma Linux RedHat, sendo que cada simulação numérica demorava em média 15 dias.

4.1. Modelo LES

A Simulação de Grandes Escalas (LES/Smagorinsky) (Smagorinsky, 1963) é um processo de filtragem das equações do movimento e decomposição das variáveis do escoamento em grandes escalas (resolvidas) e pequenas escalas (não resolvidas), sendo que o tamanho característico do filtro determina a freqüência de corte. Qualquer variável do escoamento f pode ser escrita como:

$$f = \overline{f} + f' \tag{17}$$

onde $\overline{f}$, a parte de grandes escalas, é definida através do volume médio como:

$$\overline{f}(x_i, t) = \int_{vol} G(x_i - x_i') f(x_i', t) dx_i' \tag{18}$$

onde $G(x_i - x_i')$ é a função filtro (chamada filtro chapéu ou filtro gaussiano). A utilizada é a função filtro por volume, dada por:

$$G(x_i) = \begin{cases} \frac{1}{\Delta^3}, \text{ se } |x_i| \le \frac{\Delta}{2} \\ 0, \quad \text{se } |x_i| > \frac{\Delta}{2} \end{cases} \tag{19}$$

onde Δ é tamanho característico do filtro.

As equações de quantidade de movimento filtradas (filtro gaussiano ou função filtro por volume) tornam-se:

$$\frac{\partial (\rho \overline{U}_i)}{\partial t} + \frac{\partial (\rho \overline{U}_i \overline{U}_j)}{\partial x_j} = -\frac{\partial \overline{p}}{\partial x_i} + \mu \frac{\partial^2 \overline{U}_i}{\partial x_j x_j} - \frac{\partial \rho \tau_{ij}}{\partial x_j} \tag{20}$$

sendo $\bar{U}_i$ a componente de velocidade na direção i com filtro espacial, $\bar{p}$ a pressão filtro no espaço e τ_{ij} o tensor de Reynolds sub-malha, definido como:

$$\tau_{ij} = \overline{U_i U_j} - \bar{U}_i \bar{U}_j \tag{21}$$

Através do modelo de Smagorinsky, o tensor de Reynolds sub-malha é aproximado por:

$$\tau_{ij} = -\frac{1}{3}\tau_{kk} = -2 \cdot \nu_{SGS} \cdot \bar{S}_{ij} = \nu_{SGS} \cdot \left(\frac{\partial \bar{U}_i}{\partial x_j} + \frac{\partial \bar{U}_j}{\partial x_i} \right) \tag{22}$$

sendo ν_{SGS} a viscosidade de escala sub-malha, calculada como:

$$\begin{cases} \nu_{SGS} = (C_S \Delta)^2 \left| \bar{S} \right| \\ \left| \bar{S} \right| = \sqrt{2 \bar{S}_{ij} \bar{S}_{ij}} \end{cases} \tag{23}$$

Para cálculos práticos, a constante de Smagorinsky C_S, é mudada dependendo do tipo de escoamento e da resolução da malha, sendo que se usou o valor padrão 0,1. Um estudo da influência dessa constante sobre os resultados será considerado como uma proposta de trabalhos futuros.

4.2. Modelo DES

O método de Simulação dos Vórtices Separadamente (DES) (Spalart, *et al*., 1997; Strelets, 2001) é uma tentativa de combinar os modelos RANS e LES para gerar uma formulação híbrida, onde RANS (Equações médias de Reynolds) são usadas no interior das camadas limites e o LES é aplicado nas regiões de separação, aonde o comprimento característico da turbulência é maior do que o comprimento da malha. Assim, as estruturas turbulentas podem ser resolvidas maciçamente, e as grandes escalas turbulentas têm a mesma dimensão da estrutura geométrica que as produziu.

O modelo DES implementado no software CFX® é baseado na formulação RANS-SST (Menter e Kuntz, 2002, 2003), o qual suporta a formulação por zonas do modelo DES. O modelo RANS-SST combina o modelo $k-\omega$ nas regiões próximas à parede e o modelo $k-\varepsilon$ em regiões afastadas, aonde o comprimento característico da turbulência for menor do que o comprimento da malha. Esta formulação é uma modificação das equações do modelo $k-\omega$ propostas por Wilcox (1986).

$$\frac{\partial(\rho k)}{\partial t} + \frac{\partial(\rho U_i k)}{\partial x_i} = \frac{\partial}{\partial x_i}\left[\left(\mu + \frac{\mu_t}{\sigma_k} \right) \frac{\partial k}{\partial x_i} \right] + P_k - \beta' \rho k \omega \tag{24}$$

$$\frac{\partial(\rho \omega)}{\partial t} + \frac{\partial(\rho U_i \omega)}{\partial x_i} = \alpha \rho S^2 - \beta \rho \omega^2 + \frac{\partial}{\partial x_i}\left[\left(\mu + \frac{\mu_t}{\sigma_\omega} \right) \frac{\partial \omega}{\partial x_i} \right] + 2(1-F_1)\rho \frac{1}{\sigma_{\omega 2}} \frac{1}{\omega} \frac{\partial k}{\partial x_i} \frac{\partial \omega}{\partial x_i} \tag{25}$$

Além das variáveis independentes, a densidade, ρ, e o vetor velocidade, U, são tratados como quantidades conhecidas das equações de Navier-Stokes. P_k é o índice de produção de turbulência, que é calculado como:

$$P_k = \mu_t \frac{\partial U_i}{\partial x_j}\left(\frac{\partial U_i}{\partial x_j} + \frac{\partial U_j}{\partial x_i} \right) - \frac{2}{3}\frac{\partial}{\partial x_i}\left[U_i \left(3\mu_t \frac{\partial U_i}{\partial x_i} + \rho k \right) \right] + P_{kb} \tag{26}$$

Para escoamentos incompressíveis, $\frac{\partial U_i}{\partial x_i}$ é pequeno e não contribui significativamente para a equação. O termo P_{kb} é modelado no caso de escoamento com força de empuxo.

Além disto, F_1 é uma função mistura definida como:

$$F_1 = \tanh(\arg_1^4) \tag{27}$$

$$\arg_1 = \min\left(\max\left(\frac{\sqrt{k}}{\beta' \omega y}, \frac{500\nu}{y^2 \omega} \right), \frac{4\rho k}{CD_{k\omega} \sigma_{\omega 2} y^2} \right) \tag{28}$$

onde y é a distância para a parede mais próxima, e ν é a viscosidade cinemática e:

$$CD_{k\omega} = \max\left(2\rho \frac{1}{\sigma_{\omega 2} \omega} \frac{\partial k}{\partial x} \frac{\partial \omega}{\partial x_i}, 10^{-10} \right) \tag{29}$$

$F_1 = 0$, quando se está distante da superfície (modelo $k-\varepsilon$ é ativado) e $F_1 = 1$ quando se está na camada limite (modelo $k-\omega$ é ativado).

A viscosidade cinemática turbulenta é definida como:

$$\nu_t = \frac{a_1 k}{\max(a_1 \omega, SF_2)} \tag{30}$$

$$\nu_t = \frac{\mu_t}{\rho} = \frac{k}{\omega} \tag{31}$$

onde S é uma medida invariante da taxa de tensão e F_2 é a segunda função de mistura definida como:

$$F_2 = \tanh(\arg_2^2) \tag{32}$$

$$\arg_2 = \max\left(\frac{2\sqrt{k}}{\beta' \omega y}, \frac{500\nu}{y^2 \omega} \right) \tag{33}$$

Para evitar a construção da energia cinética turbulenta, k, em regiões de estagnação, Menter introduziu um limitante para a produção do termo dentro das equações:

$$\tilde{P}_k = \min(P_k, c_{lim} \rho \varepsilon) \tag{34}$$

com $c_{lim} = 10$ para modelos baseados em ω, freqüência da turbulência. Este limitante não afeta o desempenho da camada de separação no modelo.

Todas as constantes são calculadas pelas mistura das correspondentes constantes dos modelos $k-\omega$ e $k-\varepsilon$ através de:

$$\alpha = \alpha_1 F_1 + \alpha_2 (1 - F_1) \tag{35}$$

As constantes para estes modelos são dadas por: $\beta' = 0,09$, α_1 = 5/9, β_1 = 3/40, σ_{k1} = 2, $\sigma_{\omega 1}$ = 2, α_2 = 0,44, β_2 = 0,0828, σ_{k2} = 1 e $\sigma_{\omega 2}$ = 1/0,856. O tensor de Reynolds, t, é calculado pela fórmula:

$$\tau = \mu_t 2S - \rho(2/3)\delta k \tag{36}$$

A formulação por zonas implementada no CFX®, baseada na distância para a parede mais próxima e na função de mistura do modelo RANS-SST, introduz um multiplicador para o termo na equação-k:

$$\varepsilon = \beta' k\omega \rightarrow \beta' k\omega F_{DES-CFX} \tag{37}$$

$$F_{DES-CFX} = \max\left(\frac{L_t}{C_{DES} \Delta} (1 - F_{SST}), 1 \right) \tag{38}$$

com $F_{SST} = 0, F_1, F_2$ e C_{DES} = 0,61 usado como um limitante que deverá ser ativado na região do modelo $k-\varepsilon$ e ε a dissipação de turbulência. Para o valor de $F_{SST} = 0$, o modelo DES padrão é reestabelecido e pode ocasionar uma

transição indesejada do modelo SST para o modelo LES no interior da camada limite estável e uma separação da malha. Caso se selecione $F_{SST} = F_1$ ou F_2 evita-se esta transição na camada limite estável, por isso foi selecionado o valor padrão de $F_{SST} = F_2$.

Para se calcular o comprimento característico da turbulência, L_t, utiliza-se:

$$k = \frac{3}{2} I^2 U^2 \tag{39}$$

$$\varepsilon = \rho C_\mu \frac{k^2}{\mu_t} \tag{40}$$

$$L_t = \frac{\sqrt{k^3}}{\varepsilon} \tag{41}$$

sendo I a intensidade de turbulência que pode variar de 0,1% à 10%, que corresponde a níveis muito baixos e muito altos de turbulência no escoamento e C_μ uma constante do modelo $k-\varepsilon$, cujo valor é 0,09.

4.3. Geometria e Discretização do domínio

Nas simulações numéricas foi montando uma geometria com as mesmas dimensões e características do experimento, Fig. 1. Como na simulação numérica o escoamento já inicia estabilizado, na montagem da geometria desprezou-se a parte dos ventiladores e da resistência aquecida, mudando a distância entre as duas entradas do escoamento de 1,30m para 1,0m.

O programa permite monitorar pontos dentro do escoamento. Isto foi feito representando as posições exatas dos termopares do experimento, e foi monitorada a temperatura em cada ponto. A malha usada em todas as simulações numéricas é tetraédrica, não-estruturada e possui 34169 nós, 9432 faces e 99307 elementos sendo 54591 tetraedros, 200 pirâmides, 44516 prismas.

O fluido usado no escoamento foi Ar a 25°C, com propriedades específicas do ar (viscosidade e densidade) mantidas constantes a 25°C e 1atm.

Nas duas entradas do escoamento, foi especificada a velocidade 2,2m/s como normal à superfície e selecionada temperatura constante para o fluido, sendo de um lado escoamento frio, e do outro escoamento quente. Além disto, as intensidades de turbulência selecionadas foram 1% e 0,5%.

A pressão de referência foi definida como constante a 101325Pa. Para a saída do escoamento foi colocada a pressão constante relativa de 0Pa.

O passo de tempo foi mantido constante e igual a 0,001s para se ter a mesma freqüência de aquisição de pontos como ocorria no experimento. O tempo de duração das simulações sempre foi para totalizar $32768 = 2^{15}$ pontos de temperatura, ou seja, em torno de 33s, para fazer a análise no plano tempo-freqüência.

O modelo de transferência de calor usado para prever a temperatura por toda parte do escoamento foi o modelo de Energia Térmica. Na parede foi considerado um modelo adiabático. Não foi selecionada a força de empuxo. As paredes são impermeáveis, limitadas, lisas e não-deslizantes.

5. Resultados

Na Tab. 1 temos listagem dos experimentos escolhidos, com as respectivas temperaturas ambiente e aquecida (°C), a freqüência de pontos de temperatura adquiridos por segundo. Nos testes numéricos mostrados na Tab. 2, simulamos os modelos LES e DES, com as principais condições para as simulações especificadas nas seções anteriores, e a partir delas variamos as temperaturas das entradas, levando em consideração as temperaturas (°C) médias nos experimentos, o passo de tempo (em segundos) da simulação, e a intensidade de turbulência.

Os resultados numéricos dos sinais analisados no plano tempo-freqüência possuem freqüências maiores do que os experimentos. Essas oscilações ficaram em até 20Hz dependendo da simulação numérica e do termopar analisado. Para os experimentos foram observadas oscilações de freqüência até 0,5Hz. O experimento não captura todas as faixas frequenciais devido à deficiência no sistema de aquisição, já que o tempo de resposta dos termopares é de aproximadamente 2,0s. Assim, os termopares acabam filtrando as altas freqüências. Nas comparações, analisamos as temperaturas dos termopares até 0,5Hz no plano tempo-freqüência, para ficar coerente com o experimento.

Inicialmente fizemos comparações entre as simulações LES1, LES2, LES3 e LES4 com os experimentos, variando as temperaturas das entradas dos modelos LES, mantendo a intensidade de turbulência em 1% e o mesmo passo de tempo. Depois de analisar os resultados, descartamos o teste numérico com temperatura muito distante dos experimentos, LES2.

Tabela 1. Experimentos.

Ensaios	Temp. ambiente(°C)	Temp. aquecida(°C)	Aquisição(Hz)
ensaio01	19	32	1000
ensaio02	20	34	1000

Tabela 2. Testes numéricos.

Ensaios	Temp. ambiente(°C)	Temp. aquecida(°C)	Passo de tempo(s)	Turbulência
LES1	19	30	0,001	1%
LES2	19	38	0,001	1%
LES3	20	35	0,001	1%
LES4	20	32	0,001	1%
LES5	20	32	0,001	0,5%
DES1	20	32	0,001	1%
DES2	20	32	0,001	0,5%

Para as comparações com o ensaio02, aproveitamos as simulações numéricas LES1 e LES3, e com o ensaio01 o melhor resultado foi o LES4. Este diferença é principalmente pela posição dos termopares em que os vórtices ocorrem, sendo que entre os próprios experimentos eles aparecem em termopares distintos. Por isso o objetivo do trabalho é comprovar a existência e a forma das estruturas turbulentas no escoamento.

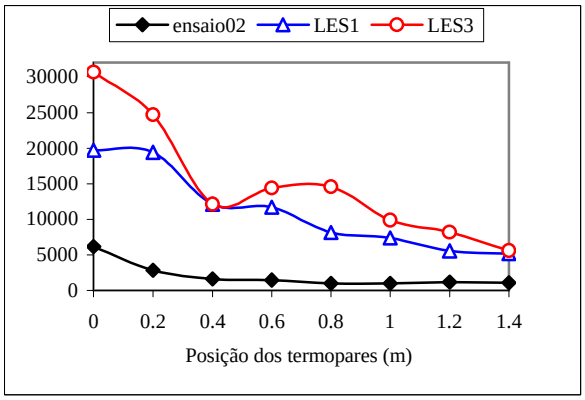

Figura 2: Energia (°C s)^2 (eq. 5)

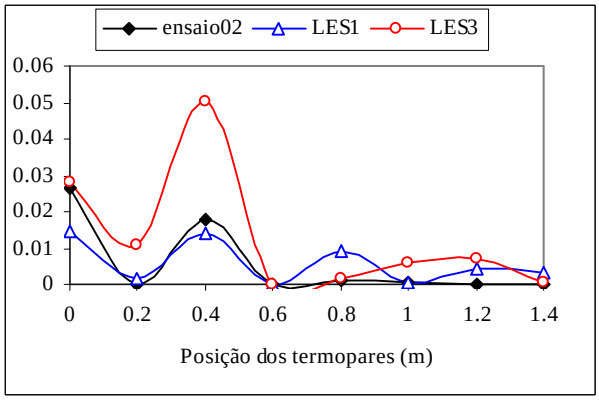

Figura 3: Covariância tempo-freqüência (eq. 13)

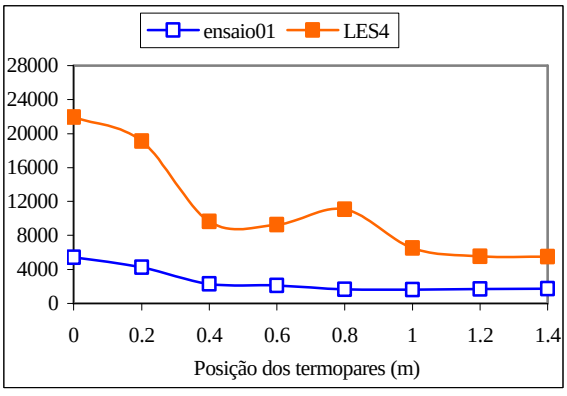

Figura 4: Energia (°C s)^2 (eq. 5)

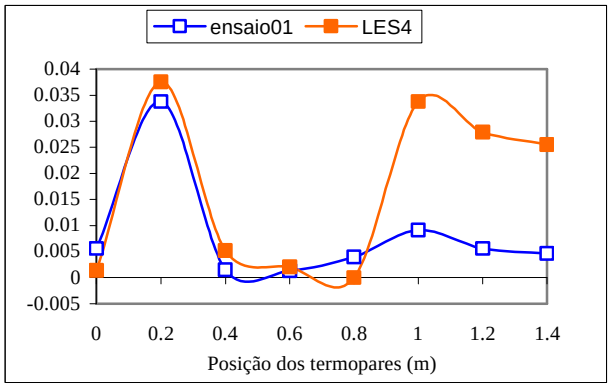

Figura 5: Covariância tempo-freqüência (eq. 13)

Analisando as Fig. 2 e 4, a energia alta no início do escoamento indica um sistema mais instável, e se sabe que a turbulência necessita de energia para se desenvolver. Além disto, os grandes vórtices precisam de energias maiores para se manter, o que se observa nos primeiros termopares. As simulações numéricas LES1, LES3 e LES4 representam os experimentos, apesar de possuírem energias mais altas, provavelmente estejam associadas às várias freqüências que as

simulações numéricas indicam em relação ao experimento. Pelos gráficos de energia fica comprovada a forma destas estruturas turbulentas com grandes vórtices no escoamento.

Pela Fig. 3 de covariância tempo-freqüência, percebemos que a melhor comparação é feita entre o ensaio02 e LES1, e a covariância está alta no início quando os grandes vórtices passam e atingem o máximo nos termopares 1 e 3, ou seja, nestas posições temos as recirculações e a formação de vórtices menores a partir do termopar 3, com um regime mais estável. Ou seja, as transições de escoamento são caracterizadas pelos altos valores da covariância tempo-freqüência quando comparados com os correspondentes valores obtidos enquanto o escoamento está estabilizado. Isto comprova a existência destes vórtices, podendo ter uma variação só na posição, como indicado na Fig. 5, quando se compara a covariância entre o ensaio01 e LES4.

Agora, faremos comparações com a mudança no método numérico, entre o ensaio02, LES1 e DES1, que juntos produziram os melhores resultados, descartando neste caso o ensaio01 e LES4, apenas pela diferença na posição aonde os vórtices ocorrem. Novamente pela Fig. 6, as duas simulações apresentam o mesmo comportamento do ensaio02, apesar de possuírem energias mais altas pelas várias escalas de freqüências que apresentam quando comparadas ao experimento, destacando-se a simulação DES1. Também fica comprovada a forma das estruturas turbulentas com grandes vórtices.

Pela Fig. 7 de covariância tempo-freqüência, a simulação LES1 mostrou uma representação melhor do experimento, sendo que o DES1 apresenta uma discordância no termopar 4, e depois deste as covariâncias são maiores do que no LES1. Novamente, os altos valores da covariância tempo-freqüência quando comparados com os correspondentes valores obtidos enquanto o escoamento está estabilizado, comprova a existência da transição dos regimes com a passagem dos grandes vórtices.

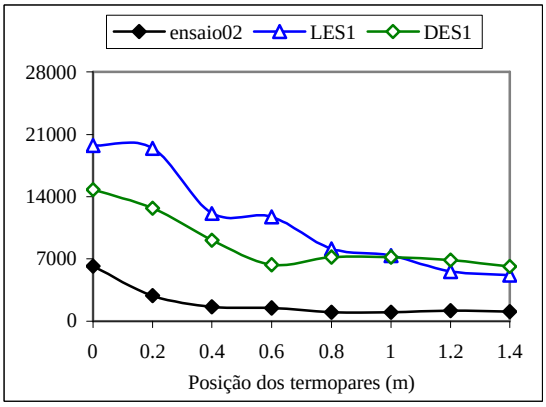

Figura 6: Energia (°C s)^2 (eq. 5)

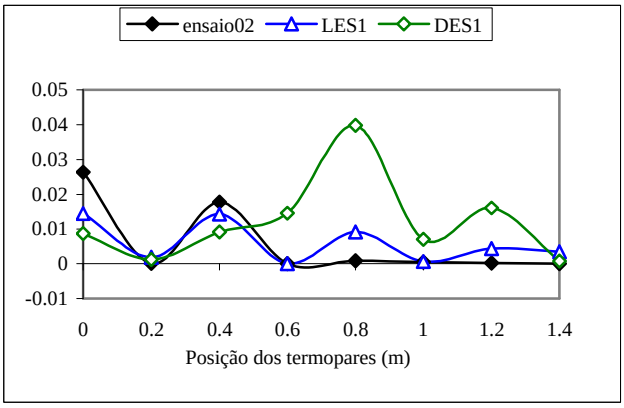

Figura 7: Covariância tempo-freqüência (eq. 13)

Para as comparações com a mudança na intensidade de turbulência, a simulação DES2 não produziu bom resultados na covariância tempo-freqüência quando comparado ao ensaio02, como mostrado na Fig. 8. Já a simulação LES5 se diferenciou na posição do termopar de transição, e ficou melhor quando comparado ao ensaio01. Além disto, vamos descartar o DES2 quando comparado ao ensaio01 no gráfico de covariância tempo-freqüência, Fig. 9, pois não oscilou como o experimento na posição do termopar 2.

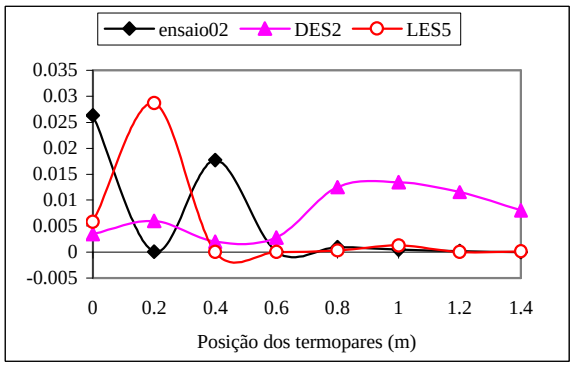

Figura 8: Covariância tempo-freqüência (eq. 13)

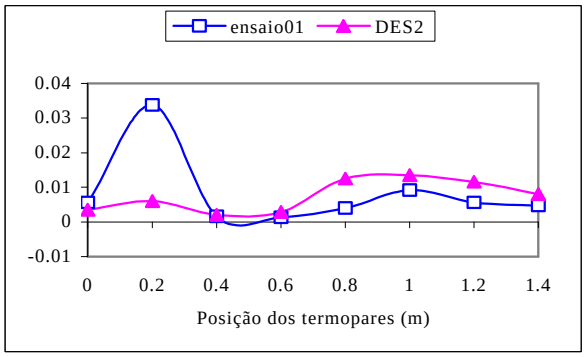

Figura 9: Covariância tempo-freqüência (eq. 13)

Assim mudando a intensidade de turbulência, o ensaio01 será comparado ao LES4 e ao LES5, apenas pela posição aonde os vórtices ocorrem. Pelo Fig. 10, apesar da pouca diferença entre as simulações numéricas, o LES5 representa

melhor o ensaio01, mesmo com energias mais altas. Representam o experimento, já que os valores altos de energia no início do escoamento estão ligados aos maiores vórtices e a região de mais instabilidade do escoamento.

Analisando a Fig. 11 de covariância tempo-freqüência, a simulação LES5 mostrou uma representação muito melhor principalmente nos últimos termopares quando comparado ao LES4. Comprova novamente que existe a transição dos regimes. Apesar da simulação LES5 ter representado melhor, não se pode afirmar com certeza que a intensidade de turbulência do experimentos seja de aproximadamente 0,5%.

Na Fig. 12, temos a distribuição no plano tempo-freqüência do termopar 2 da simulação LES5, indicando a não-estacionaridade do sinal. Também pela Fig. 13, temos uma seção de planos com a distribuição de temperatura da simulação LES5, dispostos nas mesmas posições dos termopares, indicando também as estruturas complexas das recirculações.

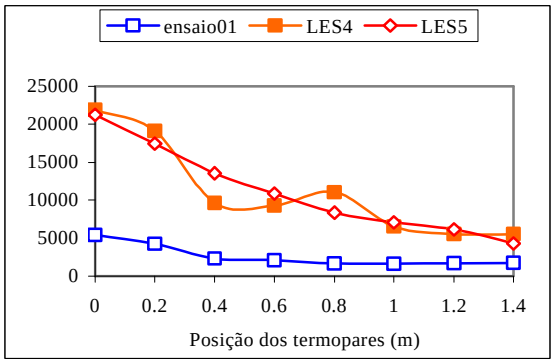

Figura 10: Energia (°C s)^2 (eq. 5)

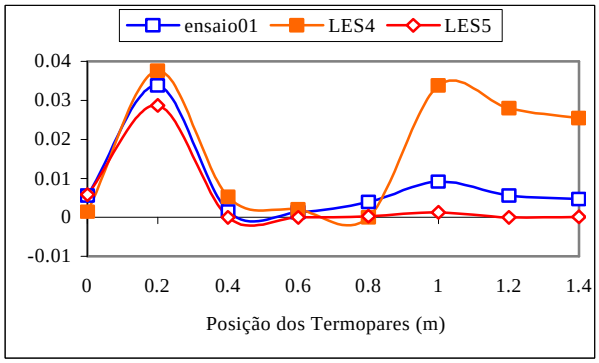

Figura 11: Covariância tempo-freqüência (eq. 13)

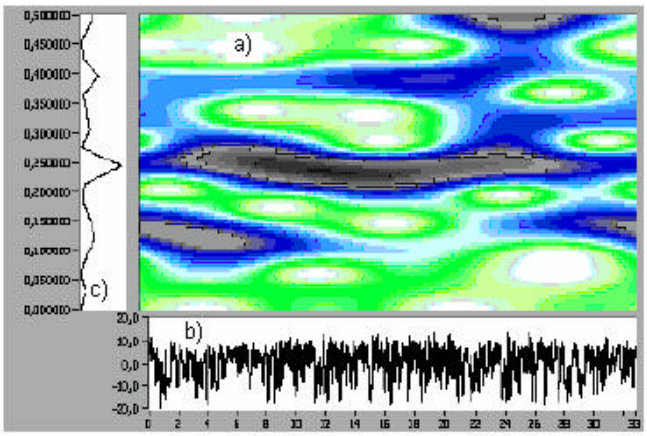

Figura 12: a) distribuição no plano tempo-freqüência;
b) sinal de temperatura em função do tempo em segundos;
c) sinal frequencial em Hz.

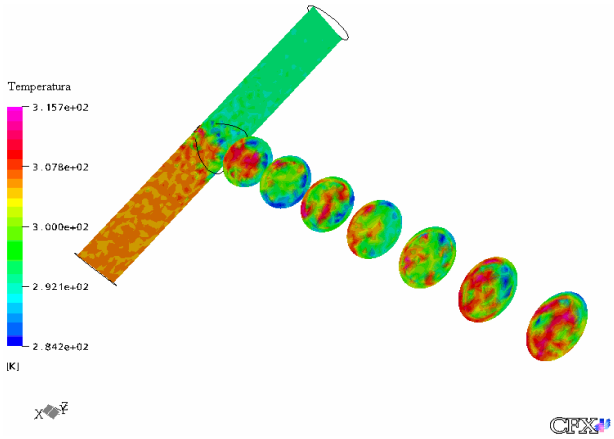

Figura 13: Seção de planos com a distribuição de temperatura (K) da simulação LES5.

6. Conclusões

A comparação de dados experimentais obtidos do escoamento em um misturador de ar em tê com as simulações numéricas de grandes escalas resolvidas pelo software comercial CFX® foi proposta neste trabalho. As comparações são feitas pelas análises da distribuição no plano tempo-freqüência. Elas testaram o desempenho e a eficiência dos métodos numéricos LES e DES em representar a realidade do escoamento, sobretudo no que se refere à descrição do fenômeno de turbulência de grandes escalas, caracterizando a existência e a forma destas estruturas.

Testes numéricos mostraram que os modelos quando comparados ao experimento do misturador de ar em tê, com as especificações da Fig. 1, mostraram freqüências mais altas do que as medidas no experimento. As análises foram feitas até às freqüências de 0,5Hz, para ficar coerente com as faixas frequenciais dos experimentos. Estudos atuais investigam formas de se obter oscilações frequenciais mais baixas e melhores resultados físicos do escoamento. Estes estudos analisarão a influência da mudança de valores da constante de Smagorinsky, mudanças no passo de tempo das simulações, aumento do tempo total de processamento, refinamento da malha numérica e mais testes com a mudança na intensidade de turbulência.

A análise plano tempo-freqüência do experimento conseguiu identificar a existência dos vórtices no escoamento e sua forma, não sendo possível prever com certeza a posição exata aonde estes vórtices ocorrem. Os grandes vórtices

foram comprovados principalmente pela observação do gráfico de energia, se mostrando altas no início e caindo à medida que o escoamento se deslocava para a saída, já que os grandes vórtices necessitam de energia para se manter. A existência foi observada nos gráficos de covariância tempo-freqüência, que indicaram oscilações nos seus valores, e conseqüentemente a não-estacionaridade e a transição do escoamento com a passagem dos vórtices.

Foram feitos alguns testes nas simulações numéricas com condições próximas ao experimento, mudando as temperaturas de entrada, os métodos de solução (LES e DES), e a intensidade de turbulência, mas mantendo sempre o mesmo passo de tempo do experimento e a mesma malha. Estas simulações conseguiram também comprovar a existência e a forma das estruturas turbulentas de grandes vórtices e seus resultados se aproximam dos experimentos. Para as condições testadas, o método LES produziu melhores resultados se comparado ao modelo DES. Para se tentar melhorar os resultados do modelo DES, trabalhos futuros analisarão a influência das funções de mistura aplicadas ao modelo, o refinamento da malha numérica e mais testes com a intensidade de turbulência.

7. Agradecimentos

Este trabalho contou com o apoio financeiro do CNPq (Processo n° 141503/2004-1) e da Fapesp (Processo nº 03/138119-6).

8. Referências

CFX®, Manual. Ansys Inc., 2004.

Chapuliot, S., Gourdin, C., Payen, T., Magnaud, J. P., Monavon, A., 2005, "Hydro-thermal-mechanical analysis of thermal fatigue in a mixing tee", Nuclear Engineering and Design, Vol. 235, pp. 575-596.

Cohen, L., 1995, "Time-frequency analysis", New Jersey, Prentice Hall.

Goulart, J.N.V.; Oliveira Jr., J.A.A.; Petry, A.P.; Möller, S.V., 2004, "Escoamento turbulento em feixe de tubos: análise numérica e experimental", Proceedings of the 10th Brazilian congress of Thermal Sciences and Engineering – ENCIT 2004, Braz. Soc. Of Mechanical Sciences and Engineering – ABCM, Rio de Janeiro, Paper CIT04-0175, 29 Nov. – 03 Dec.

Lathi, B. P., 1968, "An introduction to random signals and communication theory", Scranton, International textbook Co.

Maruyama, T., Suzuki, S., Mizushina, T., 1981, "Pipeline mixing between two fluid streams meeting at a T-junction", International Chemical Engineering, Vol. 21, No. 2, pp. 205-212.

Matos, A. de; Pinho, F.A.A.; Neto, A.S., 1999, "Large-eddy simulation of turbulent flow over a two-dimensional cavity with temperature fluctuation", International Journal of Heat and Mass Transfer, Vol. 42, pp. 49-59.

Menter, F.R.; Kuntz, M., 2002, "Adaptation of eddy-viscosity turbulence models to unsteady separated flow behind vehicles", Proc. Conf. The Aerodynamics of Heavy Vehicles: Trucks, Busses and Trains, Asilomar, Ca.

Menter, F.R.; Kuntz, M., 2003, "Development and Application of a Zonal DES turbulence model for CFX-5", CFX-Validation Report, CFX-VAL17/0503.

Patankar, S.V.; Taylor; Francis, 1980, "Numerical Heat Transfer and Fluid Flow".

Seleghim, P. Jr., 1993, "Analyse temps-fréquence appliqué aux écoulements diphaisques", Mémoire de DEA, Grenoble, Institut National Polytechnique de Grenoble.

Seleghim, P. Jr., Hervieu, E., 1994, "Caractérisation des changements de configuration des écoulements diphasiques gaz-liquide par analyse de la fréquence instantanée", C. R. Acad. Sci. Paris, t. 319, série II, pp. 611-616.

Seleghim, P. Jr., 1996, "Caracterisation des changements de configurations d'un ecoulement diphasique horizontal par l'application de methodes d'analyse temps-frequence. Grenoble. 301p. Tese (Doutorado) - De L'Institut National Polytechnique de Grenoble.

Seleghim, P. Jr., Hervieu, E., 1998, "An objective indicator for two-phase flow pattern transition", Nuclear Engineering and Design, Vol. 184, pp. 421-435.

Smagorinsky, J., 1963, "General circulation experiments with the primitive equations", Month. Weath. Rev., Vol. 93, pp. 99-165.

Sparlat, R.R.; Jou, W.H.; Strelets, M.; Allmaras, S.R., 1997, "Comments on the feasibility of LES for wings, and on a hybrid RANS/LES approach", 1st AFOSR Int. Conf. On DNS/LES, Aug. 4-8, Ruston, LA. In Advances in DNS/LES, C. Liu & Z. Liu Eds., Greyden Press, Colombus, OH.

Strelets, M., 2001, "Detached eddy simulation of massively separated flows", AIAA Paper 0879.

Tosun, G., 1987, "A study of micromixing in tee mixers", Industrial and Engineering Chemistry Research, Vol.. 26, pp. 1184-1193.

Versteeg, H.K.; Malalasekera, W., 1995, "An introduction to computational fluid dynamics, the finite volume method", Longman.

Wilcox, D.C., 1986, "Multiscale model for turbulent flows", In AIAA 24th Aerospace Sciences Meeting. American Institute of Aeronautics and Astronautics.

TIME-FREQUENCY ANALYSIS OF THE FLOW IN A TEE JUNCTION – COMPARING EXPERIMENTAL DATA WITH NUMERICAL RESULTS OBTAINED FOR LARGE EDDY SIMULATION

Graziela Marchi Tiago
LETeF – SEM - EESC – Universidade de São Paulo
Av. Trabalhador São Carlense, 400, cep:13560-970, São Carlos - SP
graziela@sc.usp.br

Paulo Seleghim Jr.
LETeF – SEM - EESC – Universidade de São Paulo
Av. Trabalhador São Carlense, 400, cep:13560-970, São Carlos - SP
seleghim@sc.usp.br

Abstract. *Turbulent flows have been the objective of important studies to discover its dynamic. One important characteristic of these flows is the multiplicity of scales, since the large structures (low frequencies) controlled by the geometry that generates them, until the small structures (high frequencies) limited by the fluid viscosity. These vortices have an important function in many technological applications, it is necessary to understand the dynamics of its movements to control the mechanisms for production or suppression these vortices. In this context, the analysis of air mixer in a tee junction is the main objective of this work. The tee geometry is sufficiently simple, but contributes for the appearance of a flow with vortices transition. Experimental tests of the flow with two different air temperatures inlets were done at the LETeF laboratory. The measures of temperature were acquired with thermocouples installed along the pipe. Numerical studies with Large Eddy Simulation method using CFX® software were applied to the flow. These computational results were compared with the experimental data through the time-frequency analysis. Studing the flow show turbulence transition regions, and the ability of the time-frequency analysis technique in characterizing the existence and the form with large vortices of the turbulent structures.*

Keywords: large eddy simulation, time-frequency analysis, turbulence.

Proceedings of the 11th Brazilian Congress of Thermal Sciences and Engineering -- ENCIT 2006
Braz. Soc. of Mechanical Sciences and Engineering -- ABCM, Curitiba, Brazil, Dec. 5-8, 2006

Paper CIT06-496

Pulsações do Escoamento em Canais Compostos Curtos

J. N. V. Goulart
PROMEC – Universidade Federal do Rio Grande do Sul (1)
jhongoulart@yahoo.com.br

S. V. Möller
PROMEC – Universidade Federal do Rio Grande do Sul(2)
svmoller@.ufrgs.br

Rua Sarmento Leite, 425 – Porto Alegre – Rio Grande do Sul – Brasil
Porto Alegre – Rio Grande do Sul, Brasil
cep: 90050 – 170

Resumo:*Utilizando-se a técnica de anemometria de fio quente investigou-se pulsações no escoamento em canais compostos com pequeno comprimento de entrada. A geometria estudada consiste em duas placas paralelas com profundidade "p" e largura "d", conectados por uma fenda, no qual o escoamento se desenvolve. Foram estudadas três diferentes seções de testes com a mesma relação p/d, embora o comprimento "L" da seção possa ser alterado. O propósito deste trabalho é investigar a presença de estruturas de grande escala neste tipo de escoamento e bem como determinar a influência dos parâmetros geométricos na formação ou detecção destas estruturas. Os resultados mostraram diferentes formas de perfis de velocidade e distribuição das tensões de Reynolds quando os parâmetros geométricos são mudados, sugerindo que a presença ou pelo menos a detecção destas estruturas esteja relacionada a mecanismos de instabilidade do perfil de velocidade.*

Palavras chave:estruturas coerentes, escoamento em canais compostos, anemometria de fio quente

1. Introdução

Escoamentos em canais compostos são caracterizados pela presença de uma estreita região conectando dois canais principais, os quais mostram importantes características na região da fenda. Talvez a principal característica do escoamento neste tipo de canal seja a presença de estruturas de grande escala com comportamento quasi-periódico, sendo transportadas pelo escoamento principal. Tais estruturas são responsáveis pelo aumento das tensões turbulentas na região da fenda. Sendo este fato sempre presente em toda literatura aberta sobre escoamento turbulentos em canais compostos, tais como canais retangulares, conectados por um ou vários sub canais, escoamento em feixes de tubos (presente no interior de reatores nucleares e trocadores de calor), e até mesmo em alguns canais de abastecimento de água, Soldini et al., 2004.

As pulsações do escoamento turbulento em canais compostos foram encontradas por Rowe et al, 1974, em um feixe de barras, este observou uma forte periodicidade na componente axial de flutuação de velocidade, onde a freqüência característica do sinal diminuía quando a relação entre o passo e o diâmetro dos tubos, P/D, aumentava. Möller, 1991, estudou as características do escoamento turbulento em um feixe de tubos na qual o comprimento da seção de testes foi considerado suficiente para o desenvolvimento do escoamento, sendo a relação entre o comprimento do canal, L, e seu diâmetro-hidraúlico, D_h, de L/D_h= 43,75. Foram realizadas medições das quantidades flutuantes na região da fenda entre o feixe e a parede superior do canal, os resultados mostraram um escoamento com padrões periódicos na região da fenda, levando a proposição de um número de Strouhal formado com o diâmetro do tubo, D, a freqüência característica dos sinais de flutuação de velocidade, f, e a velocidade de fricção, u*. Embora um significante número de trabalhos experimentais, envolvendo feixes de tubos, tenham sido realizadas, as conclusões a respeito da formação do número de Strouhal não são unânimes, indo desde equações puramente empíricas até equações formadas unicamente por grandezas do escoamento. Wu e Trupp, 1994, utilizando anemometria de fio quente, realizaram medições de flutuação de velocidade em um canal trapezoidal contendo um único feixe. Os resultados mostraram autoespectros com picos bastante pronunciados, confirmando a forte dependência existente entre a freqüência característica e os parâmetros geométricos da seção, entretanto o número de Strouhal encontrado diverge daquele proposto por Möller, 1991, levando o autor a sugerir uma nova correlação para o número de Strouhal.

A presença destas estruturas de grande escala, também foram observadas em outros tipos de canais compostos. As características do escoamento entre placas ou em uma fenda, os quais se ligam a um canal principal, foram exaustivamente estudadas por Meyer e Rehme, 1995, utilizando anemometria de fio quente e técnicas de visualização. Neste estudo três diferentes seções foram analisadas, na primeira o escoamento se desenvolve em um canal principal com uma fenda na parede lateral, neste estudo a relação L/D_h= 48,15. As segunda e terceira seções de teste possuem duas placas e várias placas paralelas, respectivamente, ligadas a parede lateral do canal, sendo que relação entre o comprimento da seção e seu diâmetro-hidraúlico, L/D_h, variou entre 48,50 e 94,0. Para o estudo em questão a profundidade do sub-canal, d, e sua largura, g, foram adimensionalizadas pela relação d/g e cobriu-se uma faixa de d/g= 1,66 até d/g=10,0. O autor afirma que a presença de grandes vórtices na região da fenda é um fato para este tipo de

canal, desde que d/g≥ 2, sendo tais resultados também confirmados através visualizações e correlações espaciais. Quanto a dependência com o número de Reynolds, o autor afirma que estas estruturas estão presentes para Reynolds tão baixos quanto 150. Na tentativa de formação de um número de Strouhal, o autor sugere uma correlação entre a freqüência destas estruturas, f, a velocidade na borda da fenda, Ue, e a raiz quadrada do produto "d" e "g", entretanto tais resultados mostraram erros consideráveis à medida que a relação profundidade/largura se torna menor que 2 e maior que 7.

Guellouz e Tavoularis, utilizaram técnicas de visualização e anemometria de fio quente, afim de investigar as pulsações do escoamento em um canal retangular contendo um único tubo. As medições foram feitas no plano entre o feixe e a parede inferior do canal. Os resultados mostraram um domínio destas estruturas na região da fenda, mesmo para fendas bastante largas, W/D = 1,35. Estes resultados confirmam os obtidos por Meyer e Rehme, 1995, os quais mostram que características como velocidade de transporte dos vórtices e o espaçamento entre eles é função do tamanho da fenda.

O propósito deste trabalho é investigar a presença de pulsações no escoamento em canais compostos, com pequeno comprimento de entrada, que contém uma única fenda, bem como determinar como os parâmetros geométricos influenciam na formação destas estruturas e na distribuição das tensões turbulentas na região da fenda.

2. Seção de Testes e Técnica Experimental

As investigações foram feitas em um canal retangular com 3320 mm de comprimento e 146 mm de altura. A largura do canal, w, poderia ser variada, sendo assim foram estudadas três diferentes configurações para este canal, apenas variando a dimensão "w" para 60, 120 e 150 mm. O fluido de trabalho utilizado é o ar, a temperatura ambiente, sendo este dirigido por um ventilador centrifugo, passando por um difusor, um homogienizador e duas telas, chegando a seção de testes com intensidade de turbulência menor que 1%. Após a passagem pelas telas está localizado um tubo de Pitot, fixo, através do qual a velocidade de referência, U_{ref}, pode ser avaliada. Em todos casos a velocidade de referência é assumida a mesma, U_{ref}= 13,5 m/s, no entanto pequenas variações no decorrer das trocas de seções foram detectadas e situaram-se na faixa entre 13,40 e 13,60 m/s. O número de Reynolds dos experimentos foram calculados utilizando a velocidade de referência e o diâmetro-hidraúlico da seção, negligenciando o sub-canal formado pelas placas.

Dentro do canal, na parede lateral, foram montadas duas placas finas paralelas, com profundidade "p", largura (distância entre elas), "d" e espessura, e= 1,2 mm, de comprimento "L". Embora as dimensões das placas, p, d e L, mudem de uma seção para outra, a relação existente entre a profundidade e a largura, p/d, permanece constante. A tabela 1, mostra as diferentes configurações das seções de teste em estudo e o número de Reynolds em seção.

Tabela.1: Configurações das seções de testes – (Dimensões em mm)

Número	w	p	d	L	p/d	w/p	$L/(pd)^{0.5}$	D_h	Re_{dh}
01	150	50	10	1250	5	3	55.90	148	$1,26x10^5$
02	120	40	8	1000	5	3	55.90	148	$1,26x10^5$
03	60	20	4	500	5	3	55.90	132	$1,12x10^5$
04	150	50	10	500	5	3	22.36	132	$1,12x10^5$
05	120	40	8	500	5	3	27.95	85	$7,26x10^4$
06	60	20	4	250	5	3	27.95	85	$7,26x10^4$

Os valores médios da componente axial de velocidade e a tensão de cisalhamento na parede foram medidos utilizando um tubo de Pitot e tubo de Preston (O.D.D = 1,25 mm), respectivamente. Enquanto as flutuações das componentes, axial, u, e transversal, w, de velocidade foram avaliadas via anemometria de fio quente, utilizando uma sonda de temperatura constante DANTEC *StreamLine*. Na medição simultânea de duas componentes de velocidade utilizou-se uma sonda dupla, que possui como característica especial um fio perpendicular ao escoamento principal e outro inclinado 45°. Na calibração da sonda, utilizou-se o método proposto por Collins and Williams, 1959, porém com importantes modificações feitas por Indrusiak, 2003, que permitiram a avaliação das diferentes componentes de velocidade, mais detalhes em Goulart, 2004 e Olinto e Möller, 2004.

O tubo de Pitot e a sonda de fio quente foram localizados entre as placas, no plano central, e movidos ao longo da linha de simetria, por meio de um posicionador tri-axial. A fig.1 mostra uma visão esquemática do canal utilizado no estudo, bem como as variáveis geométricas do problema, p, d e w e o sistema de eixo indica a definição das componentes de velocidade axial (u) e transversal (w). Neste trabalho a componente transversal de velocidade, w, é paralela a linha de simetria. As componentes médias de velocidade, suas flutuações e tensão de cisalhamento na parede, foram obtidas 20 mm a montante da saída do canal. As medições de tensão de cisalhamento foram obtidas colando o tubo de Preston na parede lateral do canal no plano central entre as duas placas.

A aquisição dos sinais de flutuação de velocidade foi feita utilizando uma placa conversora analógica digital, A/D, com 12 bit marca Keithley DAS58, uma freqüência de amostragem de 3KHz e filtro passa baixa em 1KHz. O comprimento das séries temporais de flutuação de velocidade foi de 43,69 s.

A análise de incerteza dos resultados mostra uma contribuição de 1,4 % proveniente dos equipamentos de medição, anemômetro e placa conversora.

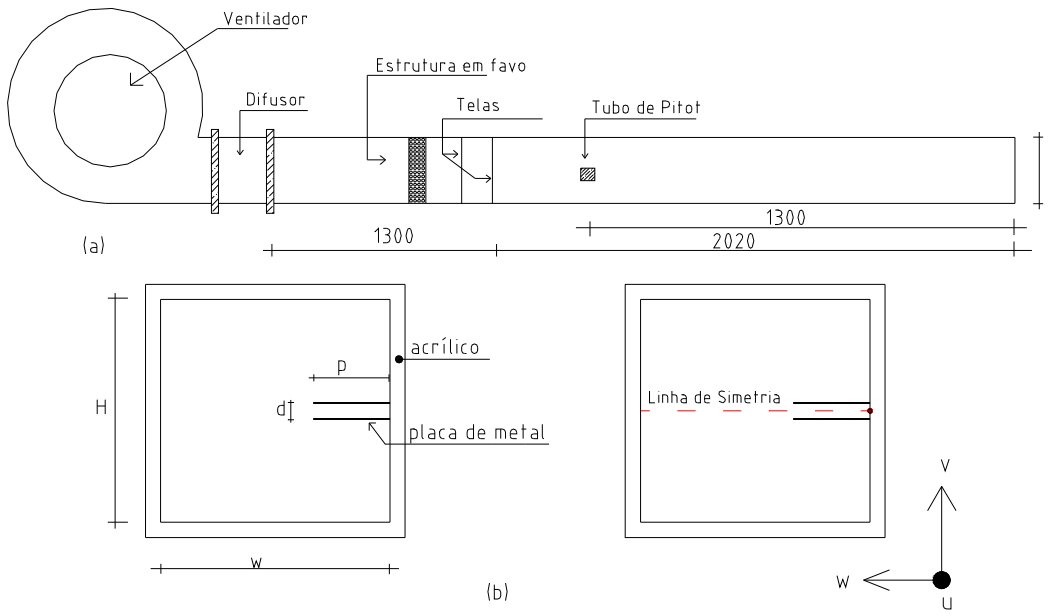

Figura 1. Visão esquemática da seção de testes: (a) configuração do túnel de vento e (b) visão frontal da seção de testes e localização da linha de medições.

3. Resultados

3.1. O Perfil de Velocidades e suas Caracteristicas

A figura 2 (a) e (b), mostra a distribuição da velocidade axial media, ao longo da linha de simetria para todas as seções de teste. Os dados de velocidade foram adimensionalizados pela velocidade máxima, enquanto as posições de leitura foram adimensioanlizadas pela profundidade da seção, dimensão "p". As figuras mostram a grande importância dos parâmetros geométricos na forma do perfil de velocidade, para seções de teste onde a dimensão "d" é menor, os efeitos viscosos são maiores, por conseguinte as velocidades dentro da fenda são menores. Já a profundidade da seção, dimensão "p", tem bastante influência na distribuição de velocidade dentro da fenda, pode-se notar, principalmente na fig. 2(a) uma região de distribuição linear de velocidade que diminui com a redução de "p". Nota-se que ao diminuir-se o comprimento das seções, fig. 2(b), os perfis de velocidade mudam significativamente, obtendo maiores velocidades dentro da fenda.

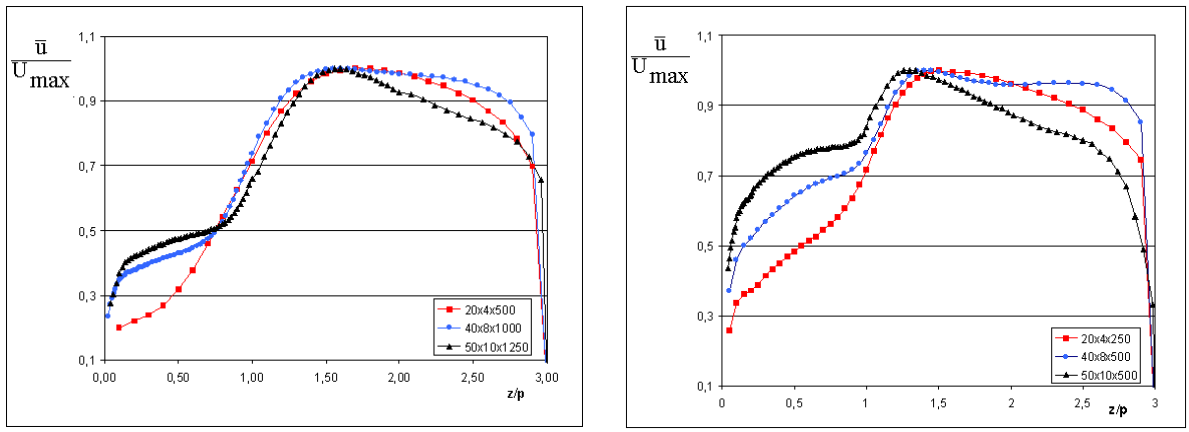

a) b)

Figura 2 – Perfis de velocidade axial. a) seção de testes 1, 2 e 3. b) seção de testes 4, 5 e 6.

Nas figuras 3 (a) e (b), o gradiente da componente axial de velocidade é mostrados, os dados foram adimensionalizados pela velocidade máxima, $\varphi = u(z)/U_{max}$, e a posição (z), adimensionalizada pela profundidade "p", $\eta = z/p$. Em todas a seções, está presente um ponto de inflexão perto da borda, no entanto existe uma sutil diferença,

enquanto nas seções 1 e 2, fig. 3(a), o ponto de inflexão esta dentro da fenda, nas seções 3, 4, 5 e 6, este ponto se move em direção ao canal principal, encontrando-se localizado em torno de z/p = 1,15. A região de distribuição linear de velocidade pode ser bem observada na fig. 3 (a) principalmente nas seções 2 e 3, onde o gradiente de velocidade é quase constante até, aproximadamente, z/p = 0,60.

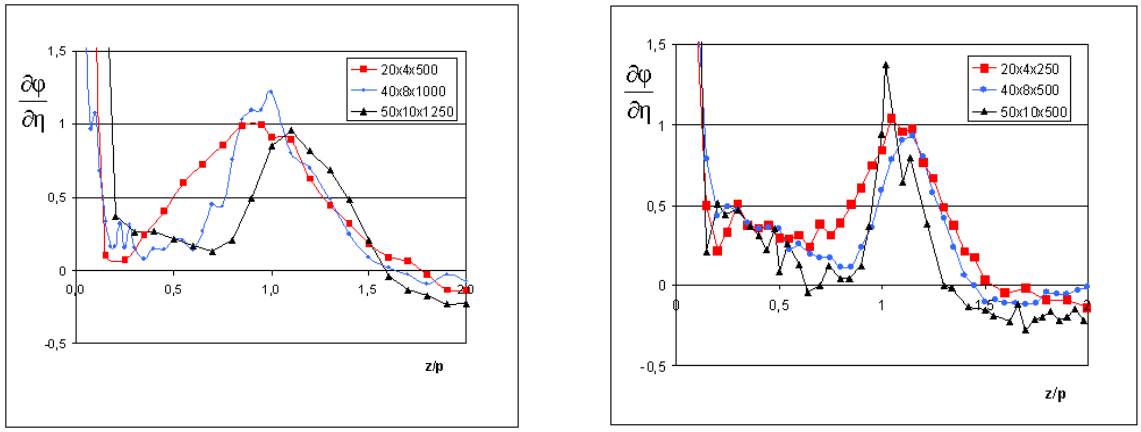

a) b)

Figura 3 – Gradiente dos perfis de velocidade. a) seção de testes, n°:1, 2 e 3. b) seção de testes, n°: 4, 5 e 6.

As figuras 4, 5 e 6, mostram a distribuição das quantidades flutuantes, u', w' e o termo cruzado $\overline{u'w'}$. Os dados foram adimensionalizados pela tensão se cisalhamento na parede lateral, em forma de velocidade de fricção, u*. Todas as medições se deram a partir de 2 mm da parede lateral e estenderam-se até o dobro do valor da profundidade.

De forma geral, nas seções mais curtas, 4, 5 e 6, a distribuição de tensões é bastante localizada junto a borda, possuindo valores menores comparados com seções mais longas, 1, 2 e 3. Nestas seções o máximo valor das tensões turbulentas esta localizado no canal principal e não dentro da fenda.

No entanto, independentemente do comprimento das seções, a magnitude das tensões turbulentas parece ser uma função da largura da fenda, "d", principalmente o valor rms das flutuações de velocidade na componente "w", que cresce com a redução da largura da fenda e alcança um valor maior que a componente "u" somente na seção mais estreita, onde d= 4 mm. Os picos de tensões turbulentas junto a borda das placas, bem como sua distribuição ao longo da linha de simetria, condizem qualitativamente com os resultados obtidos por Meyer e Rehme, 1994 e Biemüller et al. 1996, ou seja, picos de tensões turbulentas junto a borda das placas e o progressivo decrescimento destas quantidades em direção ao canal principal.

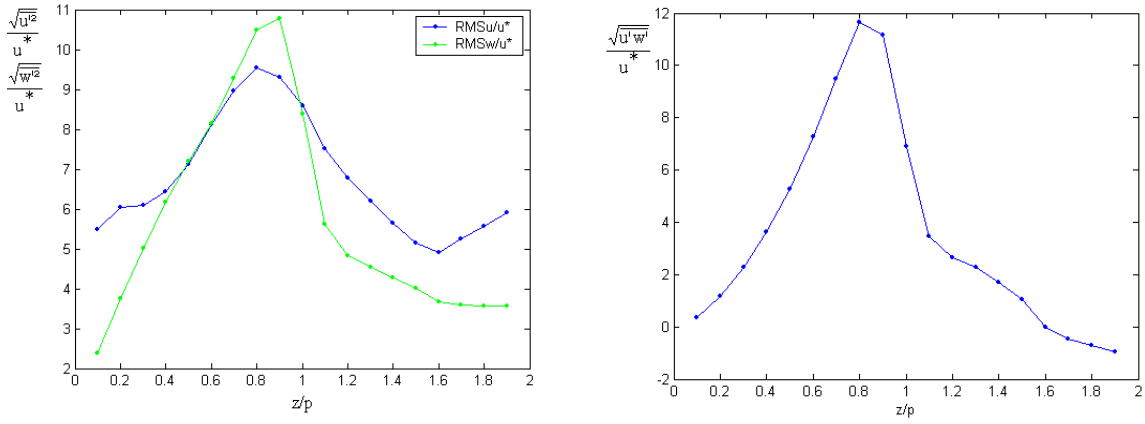

a) b)

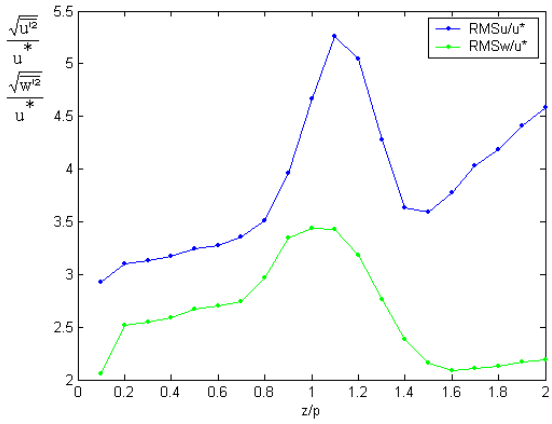

c)

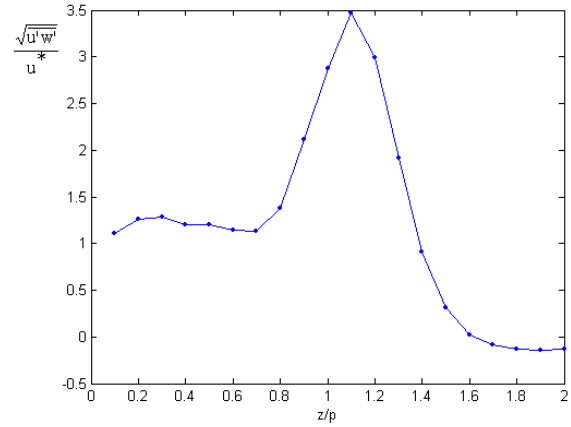

d)

Figura 4 – Valores RMS das flutuações de velocidade e tensões turbulentas como uma função da posição ao longo da linha de medição. Seção de testes 20 x 4 x 500, “a” e “b”. Seção de testes 20 x 4 x 250, “c” e “d”.

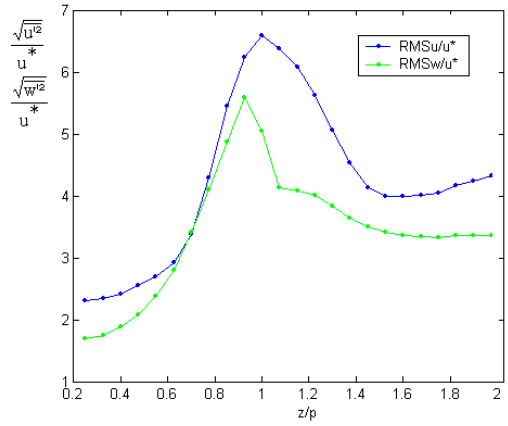

a)

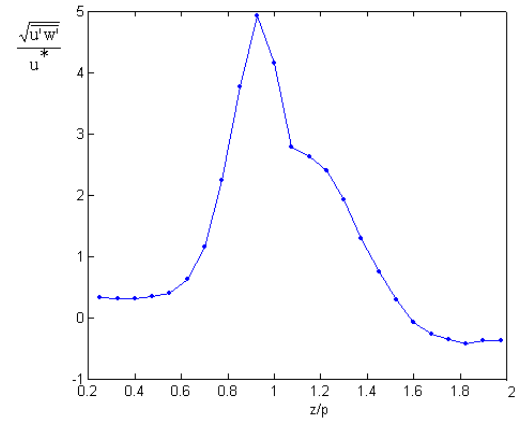

b)

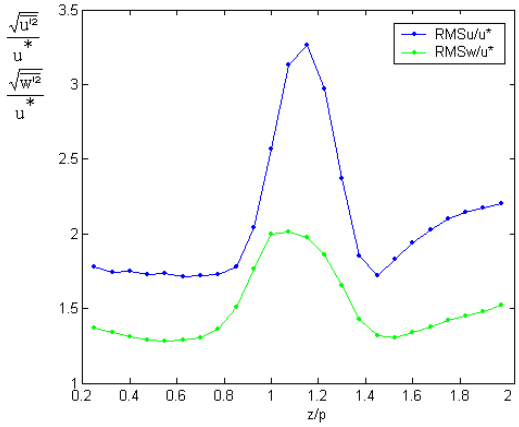

c)

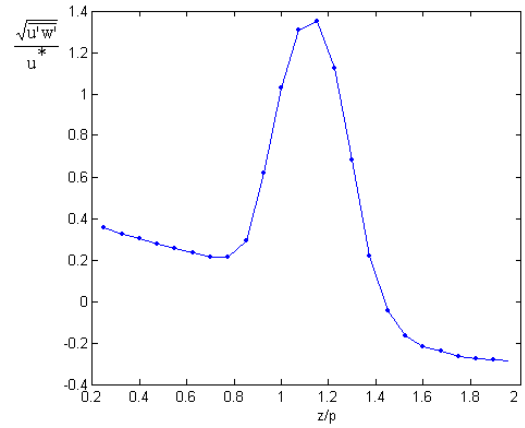

d)

Figura 5 – Valores RMS das flutuações de velocidade e tensões turbulentas como uma função da posição ao longo da linha de medição. Seção de testes 40 x 8 x 1000, “a” e “b”. Seção de testes 40 x 8 x 500, “c” e “d”.

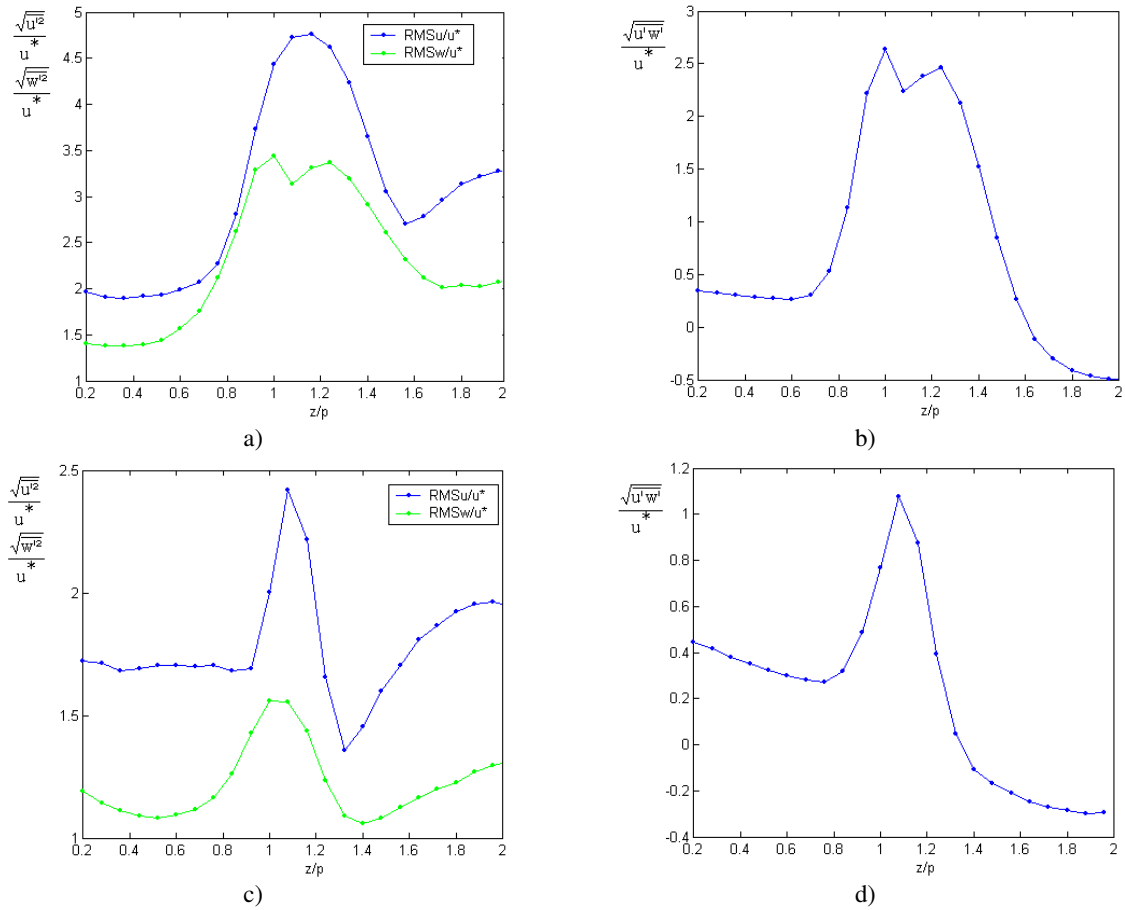

Figura 6 – Valores RMS das flutuações de velocidade e tensões turbulentas como uma função da posição ao longo da linha de medição. Seção de testes 50 x 10 x 1250, “a” e “b”. Seção de testes 50 x 10 x 1250, “c” e “d”.

3.2. Pulsações do Escoamento

Em todos os perfis de velocidade mostrados na fig. 2, os efeitos viscosos dentro da fenda são importantes na redistribuição do escoamento ao longo da linha de simetria. Na fig. 3(b), pode-se observar o inicio da formação de duas camadas com velocidades distintas, uma camada de baixa velocidade (dentro da fenda) e outra com alta velocidade (dentro do canal principal) culminando na fig.3(a). Entre elas existe uma camada onde o escoamento é cisalhante e como tal pode estar sujeita a instabilidades, tais como as instabilidades de Kelvin-Helmholtz , por exemplo, ou outro tipo de instabilidade, estas características também são reportadas por Soldini et al., 2004, simulando numericamente o escoamento de água em um canal trapezoidal.

A equação de Orr-Sommerfeld, eq. (1), permite determinar se um certo escoamento é susceptível ou não a instabilidade, no entanto a formulação diz respeito a instabilidades em escoamentos laminares, que podem ser amortecidas, amplificadas ou neutras, e dependendo do caso podendo levar o escoamento ao estado turbulento. O apóstrofo, na eq. (1), indica o grau da derivada e “v” é a função amplitude.

$$\alpha(U - c)(v''-\alpha^2 v) - U''\alpha v = \frac{i}{Re}\left(v^{iv} - 2\alpha^2 v''+\alpha^4 v\right) \qquad (1)$$

onde:

U= é a velocidade média na direção axial, U=f(z);

c= é a velocidade de onda;

i= $\sqrt{-1}$;

Re= número de Reynolds.

α= amplitude das instabilidades, pode ser maior que zero, menor que zero ou igual a zero.

Em problemas de instabilidade onde o número de Reynolds é muito alto, os termos viscosos podem ser descartados, transformando a equação de Orr-Sommerfeld na equação de Rayleigh, eq. (2). O teorema de Rayleigh diz que a

condição necessária para a instabilidade de um perfil de velocidade é que dentro do domínio exista um ponto de inflexão.

$$\alpha(U - c)(v'' - \alpha^2 v) - U''\alpha v = 0 \tag{2}$$

A partir de então, Fjørtoft derivou um segundo teorema, no qual a condição necessária para que um perfil de velocidade se desestabilize é a existência de um ponto de inflexão no seu domínio e que o perfil satisfaça a eq. (3)

$$(U - U_S)U'' < 0 \tag{3}$$

onde, U_s é a velocidade do ponto te inflexão e U'' é a derivada de segunda ordem da função u(z). No entanto isto é somente uma condição necessária e não suficiente para que o perfil de velocidades se desestabilize e é utilizada na teoria de transição de escoamentos no estado laminar para turbulento. Portanto, segundo Mendonça, 2003 se U é uma função crescente de z, então:

$$z > z_s \rightarrow U > U_s \Rightarrow U'' < 0 \tag{4}$$

$$z < z_s \rightarrow U < U_s \Rightarrow U'' < 0 \tag{5}$$

as eq. (4) e (5) são verificadas para diferentes regiões do perfil de velocidade, z_s indica o ponto onde o perfil de velocidade inflexiona.

As figuras 7(a) e (b) mostram o perfil de velocidade axial e a aplicação do teorema de Fjørtof para a seção 20 x 4 x 500. Os pontos em vermelho na fig. 7 (a) mostram seus pontos de inflexão. O primeiro ponto de inflexão diz respeito a distribuição de velocidade governada pela tensão de cisalhamento na parede, até z/p=0.25, e esta bem representada na fig. 3(a). Na fig. 7(b) pode-se observar que a eq.(3) é negativa para quase todo o domínio, exceto nas proximidades da borda e na região onde a tensão de cisalhamento na parede governa a distribuição de velocidade. No entanto para todos os outros perfis de velocidade a eq. (3), quando plotada contra z/p possui uma distribuição distinta, alternado valores positivos e negativos, sem predominância de um modo ou outro.

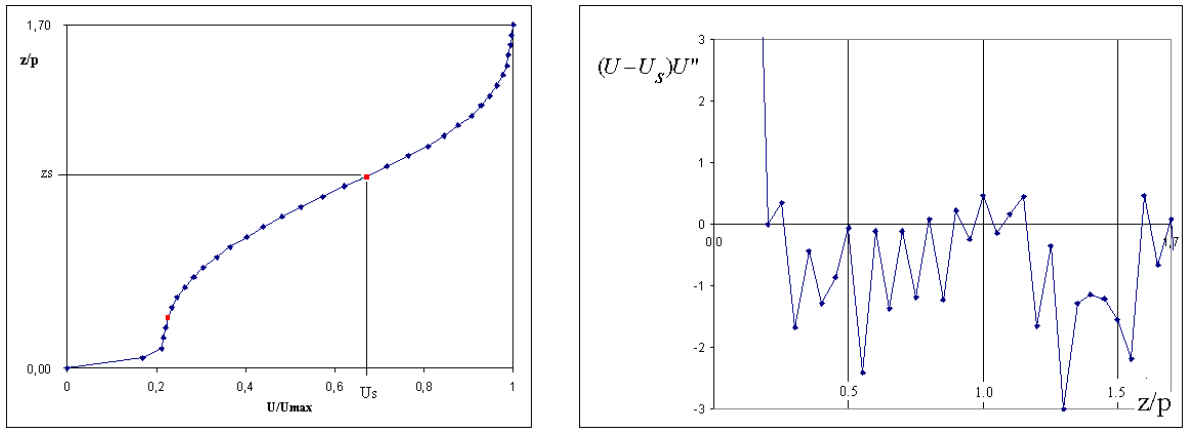

a) b)

Figura 7 – Perfil de velocidade ao longo da linha de medição e a aplicação do Teorema de Fjørtof.

A analise das flutuações de velocidade no espaço de Fourier é mostrada nas figuras 8 a 11 a posição onde foram tomadas as séries de velocidade foram adimensioanlizadas pela profundidade das placas, dimensão "p", as funções autoespectrais das componentes axial e transversal de velocidade são mostradas nas cores azul e verde, respectivamente. A freqüência é mostrada de forma adimensional em função do número de Strouhal, conforme eq. (6).

De maneira geral nas seções menores, 4, 5 e 6, não foram encontrados indícios de estruturas coerentes, os auto espectros de flutuação de velocidade são bastante semelhantes para as mesmas posições, com valores de energia mais altos para as componentes axiais do que nas componentes transversais de flutuação de velocidade e sem qualquer pico característicos. Sendo este resultado bastante surpreendente quando confrontado com os estudos apresentados por Meyer e Rehme, 1996 e Guellouz e Tavoularis, 2000, que afirmam em seus trabalhos que a região da fenda é governada por estruturas coerentes.

Nas seções 1, 2 e 3, onde a relação entre o comprimento da seção "L" e sua outras grandezas "p" e "d" são maiores os auto-espectros de flutuação de velocidade apresentam picos característicos , todos marcados com uma seta, no entanto estes tendem a desaparecer com o aumento das dimensões "p" e "d", tornado-se bastante fraco como mostra a fig. 10 (a).

A analise espectral da componente axial de flutuação de velocidade mostra somente um indício de pico na seção 3, fig. 8 (a),com características distintas daquelas encontradas na componente transversal, como uma largura de banda

maior e uma freqüência característica situada em uma outra posição, desaparecendo por completo nas outras seções estudadas.

É importante notar que os autoespectros de flutuação de velocidade mostrados nas fig. 8(a), 9(a) e 10 (a), são tomados para posições relativas diferentes dentro da fenda, pois as medições mostraram que a periodicidade nas séries de velocidade, tomadas na borda da fenda, é fracamente detectada a medida que as dimensões "p" e "d" crescem. Enquanto nas seções 1 e 2 os indícios de estruturas coerentes nos autoespectros apresentam-se bastante localizados próximos a borda, na seção 3 é diferente, a característica periódica das flutuações de velocidade pode ser vista ao longo da fenda, desde z/p= 0,30 até z/p= 1,10, e o numero de Strouhal se mostra invariável com a posição, conforme visto na fig. 11.

Meyer e Rehme, 1996, realizaram medições de flutuações de velocidade neste mesmo tipo de canal, sendo proposto a construção de um número de Strouhal, utilizando a raiz quadrada do produto das dimensões "p" e "d", a velocidade da borda, Ue, e uma freqüência característica, f, eq. (6). Os resultados mostraram para este tipo de canal uma freqüência adimensional em forma do número de Strouhal, situada em 0,08, com um desvio padrão de 0,01.

Pode-se notar que principalmente na seção n° 03, fig. 8(a), o número de Strouhal proposto pelos autores prediz relativamente bem a freqüência esperada, para o presente trabalho, Str= 0,06.

Quanto às seções n° 01 e 02, seus espectros apresentam diferentes características. Na seção n° 01, fig. 10(a), o pico no autoespectro praticamente não aparece, no entanto, o espectro da flutuação de velocidade da componente transversal é bastante diferente daquele mostrado na componente axial.

Outra forte discrepância, ocorreu na seção de testes n° 02, na qual as escalas utilizadas na adimensionalização da freqüência forneceram um valor de Strouhal, Str= 0,02, sendo mais que no dobro do que aquele esperado pela correlação entre as escalas de velocidade e comprimento.

$$\mathrm{Str} = \frac{\mathrm{f}\sqrt{\mathrm{pd}}}{\mathrm{U_e}} \tag{6}$$

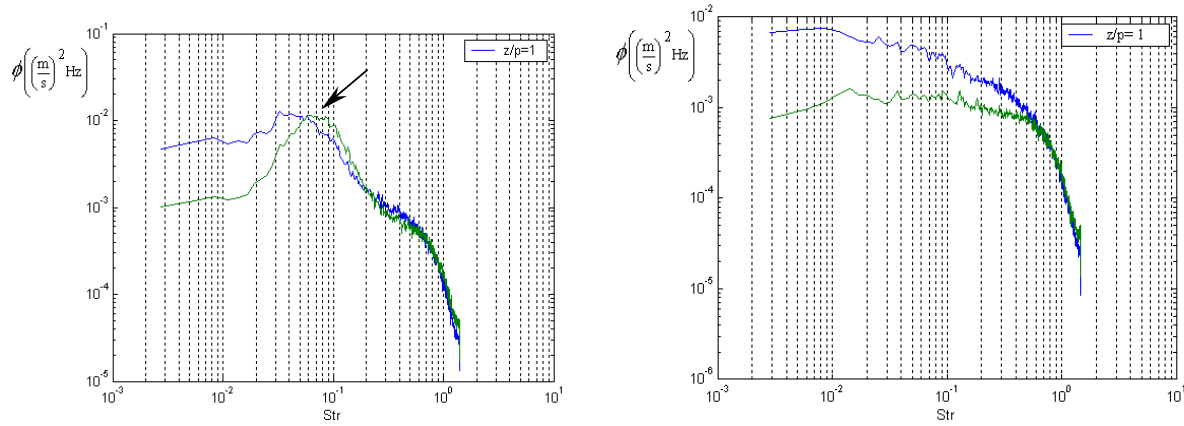

a) b)

Figura 8 – Densidades autoespectrais das componentes axial e transversal de flutuação de velocidade para a seção de testes 20 x 4. a) L= 500 mm. b) L= 250 mm.

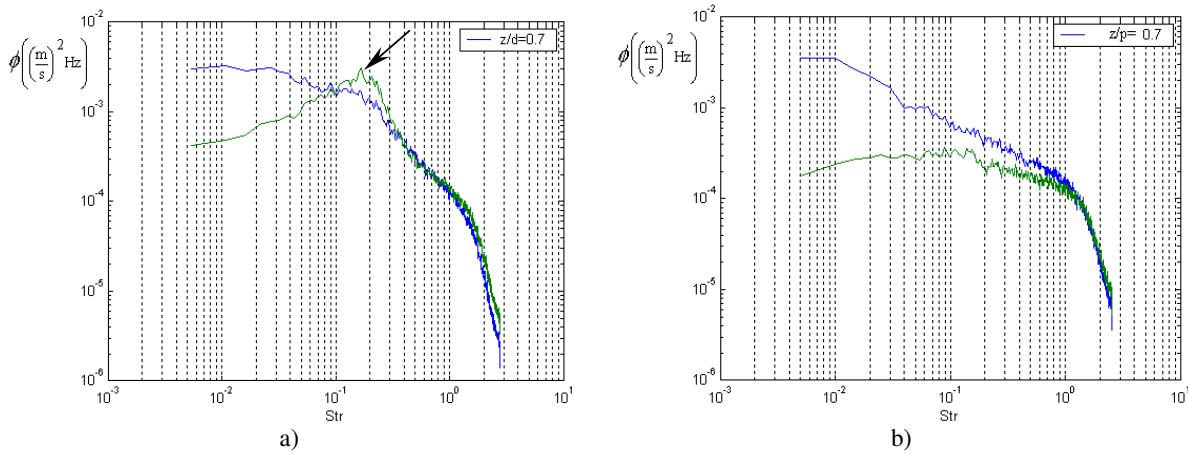

a) b)

Figura 9– Densidades autoespectrais das componentes axial e transversal de flutuação de velocidade para a seção de testes 40 x 8. a) L= 1000 mm. b) L= 500 mm.

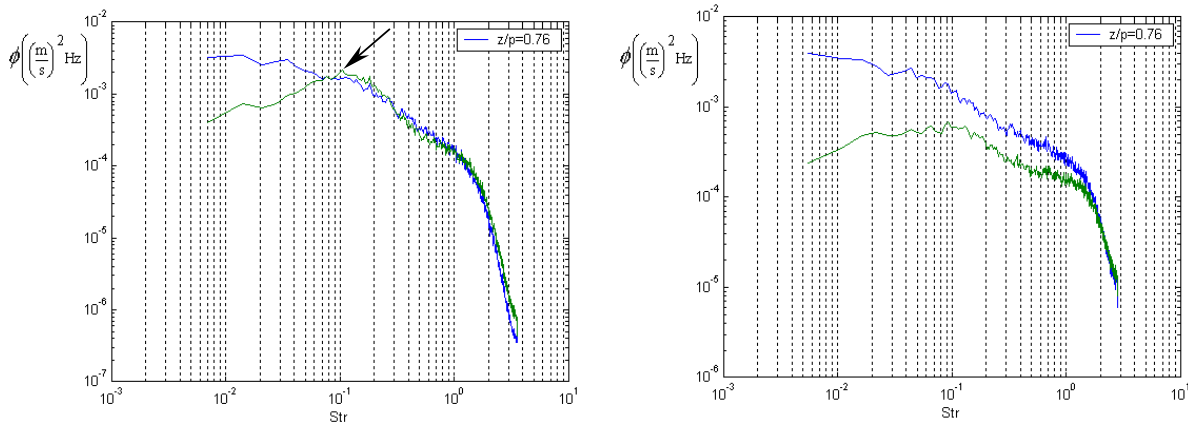

Figura 10– Densidades autoespectrais das componentes axial e transversal de flutuação de velocidade para a seção de testes 50 x10. a) L= 1250 mm. b) L= 500 mm.

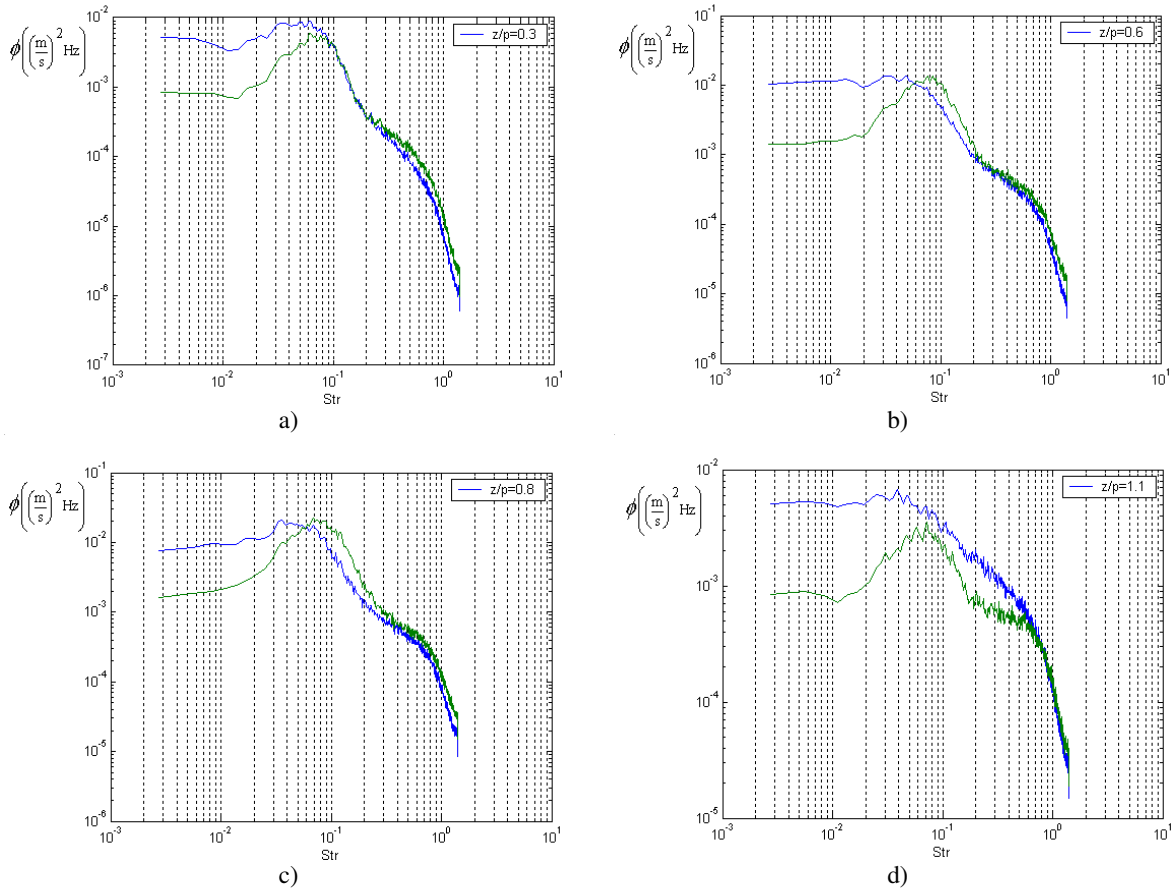

Figura 11– Densidades autoespectrais das componentes axial e transversal de flutuação de velocidade para a seção de testes 20 x 4 x 500. a) z/p= 0,30. b) z/p= 0.60. c).z/p= 0,80. d) z/p= 1.10.

4. Conclusões

Este trabalho apresenta um estudo experimental da distribuição de velocidade e três das seis tensões de Reynolds ao longo da linha de simetria de uma fenda, conectada a parede lateral de um canal. O objetivo deste trabalho é investigar a presença de pulsações do escoamento neste tipo de canal, com um pequeno comprimento de entrada, bem como determinar a influencia dos parâmetros geométricos de seção de testes na detecção destas estruturas, ou até, em sua existência.

De maneira geral os resultados aqui contidos estão de acordo com outros trabalhos, mostrando que em canais compostos, onde há uma região estreita conectada a um canal principal, existe uma distribuição e um aumento anormal das tensões de Reynolds na fronteira dos sub-canais. A investigação dos perfis de velocidade revelou uma forte influencia das características geométricas da seção em sua formação, gerando um escoamento altamente cisalhante entre uma camada de menor velocidade (dentro da fenda) e maior velocidade (canal principal) sujeita a instabilidades.

Embora todos o perfis possuíssem a condição necessária para instabilidade somente em alguns foram detectados picos de freqüência em seus autoespectros, porém o presente estudo não é abrangente o suficiente para concluir se estas instabilidades não existem ou apenas não puderam ser detectadas nas demais geometrias, tornado prematura a afirmação de que estas estruturas "existem para qualquer fenda longitudinal, ranhura em uma parede ou uma fenda conectando dois subcanais." Segundo Guellouz e Tavoularis, 2000, a ausência de picos nos auto-espectros não necessariamente contradiz a presença de pulsações do escoamento, para fendas mais largas as características periódicas dos sinais de flutuação de velocidade podem se obscurecidas pelos processos médios.

O parâmetro adimensional, p/d, se mostra bastante impreciso na predicção do comportamento dinâmico do escoamento, bem como na distribuição de velocidades medias, já que tais características parecem depender mais da geometria como um todo do que de uma relação entre a profundidade e a largura da seção.

Quanto a formulação de um número de Strouhal, relacionando as grandezas de velocidade e comprimento dadas na eq. (6), as conclusões são as mesmas encontradas por Meyer e Rehme, 1996, ou seja, mostram que a escolha das escalas de velocidade e comprimento representativas do escoamento ainda não e´uma questão resolvida.

5. Agradecimentos

Os autores agradecem todo o tipo de suporte dado pelo CNPq – Conselho Nacional de Desenvolvimento Científico e Tecnológico.

Jhon N. V. Goulart agradece também a CNPq, pelo pela bolsa de estudos.

6. Referências

Biemüler, M., Meyer, L. And Rehme, K., Large eddy simulation and measurement of the structure of turbulence in two rectangular channels connected by the gap, Engineering Turbulence Modeling and Experiments 3, Editors: Rodi, W. and Bergeles,G., 249-258, 1996.

Goulart, J. N. V., Estudo experimental dos campos de pressão e velocidade em feixes de tubos utilizando placas defletoras; Dissertação de Mestrado, Universidade Federal do Rio Grande do Sul, 2004.

Guellouz, M.S. and Tavoularis, S., The structure of the turbulent flow in a rectangular channel contening a single rod – Part 1: Reynolds-Average mesurements, Exp. Thermal and Fluid Sci., **23**, 59-73, 2000.

Indrusiak, M. L. V. Caracterização de escoamentos turbulentos transientes usando a transformada de ondaletas; Tese de Doutorado, Universidade Federal do Rio Grande do Sul, 2003.

Lesieur, M., Turbulence in Fluids, Third Edition, Kluwer Academic Publishers, Dordrecht, The Netherlands, 1997.

Mendonça, M. T., 2003. Estabilidade de escoamentos lineares: Teoria Liner, vol. **2**. Editores: A .Silveira Neto e S. S. Mansur, pp.247-300, ABCM, Rio de Janeiro, RJ.

Meyer, L. and Rehme, K., Large-scale turbulence phenomena in compound rectangular channels, Exp. Thermal Fluid Sci., **8**, 286-304, 1994.

Meyer, L. and Rehme, K., Periodic vortices in flow though channels with longitudinal slots or fins, 10th Symposium on turbulent shear flows, The Pennsylvania State University, University Park, August 14-16, 1995.

Möller, S. V., On Phenomena of Turbulent Flow Through Rod Bundles. Experimental Thermal and Fluid Science, v. 4, n.1, pp. 25-35, 1991.

Olinto, C. R. and Möller, S. X-probe calibration using Collis and William's equation. In: 10º Congresso Brasileiro de Engenharia e Ciências Térmicas - ENCIT, 2004, Rio de Janeiro, 2004.

Rowe, D.S., Johnson, B.M. and Knudsen, J. G., Implications concerning rod bundle crossflow mixing based on mesurements of turbulent flow structure, Int. J. Heat Mass Transfer, **17**, 407-419, 1974.

Schlichting, H. 1968. Boundary Layer Theory. 6th edn. N. York: McGraw-Hill.

Soldini, L., Piattella, A., Brocchini, M., Mancinelli, A. e Bernetti, R. Macrovortices-induced horizontal mixing in compound channels, Ocean Dynamics, **54** , 333 – 339, 2004.

Wu, X. and Trupp, A. C., Spectral mesurements and mixing correlations in a sumulated rod bundle subchannels, Int. J. Heat Transfer, **37**, 1277-1281, 1994.

FLOW PULSATIONS IN SHORT COMPOUND CHANNELS

J. N. V. Goulart
PROMEC – Universidade Federal do Rio Grande do Sul
jhongoulart@yahoo.com.br

S. V. Möller
PROMEC – Universidade Federal do Rio Grande do Sul
svmoller@.ufrgs.br

Abstract
Hot-wire anemometry technique was used to investigate the flow pulsations in short compounds channels. The geometry studied consists in two parallel plates with deep " p" and width "d", connected to a wider channel. Three different test sections with the same p/d ratio were studied. The length "L" could be changed. The purpose of this paper is to investigate the presence of large-scale structures in this kind of channel flow and how the geometric parameters influence their formation. The results show different velocity profiles and Reynolds stress distribution when the geometrical parameters were changed, as well the strong dependence between axial velocity profile shape and the flow pulsation detection, suggesting a relationship between flow pulsations and axial velocity profiles instabilities.

Keywords: coherent structures, compound channels, hot wire probes

Proceedings of the 11th Brazilian Congress of Thermal Sciences and Engineering -- ENCIT 2006
Braz. Soc. of Mechanical Sciences and Engineering -- ABCM, Curitiba, Brazil, Dec. 5-8, 2006

Paper CIT06-0522

SIMULAÇÃO NUMÉRICA DE ESCOAMENTOS INTERNOS TRIDIMENSIONAIS USANDO O MÉTODO DA FRONTEIRA IMERSA

Elie Luis M. Padilla
Universidade Federal de Uberlândia
epadilla@mecanica.ufu.br

André Leibsohn Martins
CENPES - PETROBRAS
aleibsohn@petrobras.com.br

Aristeu da Silveira Neto
Universidade Federal de Uberlândia
aristeus@mecanica.ufu.br

Resumo. *O presente trabalho apresenta os avanços relacionados ao desenvolvimento de uma ferramenta numérica para análise de problemas de interação fluido-estrutura, utilizando a metodologia de fronteira imersa com modelo físico virtual. Estes tipos de problemas estão comumente ligados a um grande número de aplicações de engenharia, como exemplo na exploração de gás e petróleo: tecnologia de perfuração em águas profundas e produção através de risers. As equações de Navier-Stokes são resolvidas considerando um fluido newtoniano, isotérmico e incompressível. Neste estágio do desenvolvimento, apresentam-se resultados de simulações tridimensionais dos escoamentos Hagen-Poiseuille e dos escoamentos no interior de cavidades-canais cilíndricos. Os detalhes das estruturas dos diversos escoamentos (estáveis) e a concordância com as soluções analíticas mostram a aplicabilidade desta nova metodologia a problemas de escoamentos internos.*

Palavras chave: método de fronteira imersa, escoamentos tridimensionais.

1. Introdução

Entre as grandes dificuldades presentes nas metodologias clássicas (elementos finitos, diferenças finitas e volumes finitos), estão as relacionadas à solução de escoamentos de fluidos em domínios geometricamente complexos e com a presença de estruturas móveis e deformáveis. Problemas desta natureza são normalmente tratados com métodos de transformação de coordenadas ou com malhas não estruturadas. Dificuldades aparecem, no entanto, devido à necessidade de se remalhar o domínio de cálculo a cada passo de tempo. O processo de remalhagem em domínios tridimensionais é caro e o processo de reprojeção dos campos insere erros numéricos que geram problemas, em especial, no que se refere à evidenciação de instabilidades dinâmicas que caracterizam os processos de transição. Uma alternativa para contornar este problema tem sido os métodos de identificação da interface, que possibilitam avaliar a interface através de propriedades geométricas e físicas.

Nesse contexto, Peskin (1977) apresentou o denominado método da fronteira imersa (MFI), método na qual a interface é representada por uma malha lagrangiana e interage com o domínio do fluido, representado por uma malha euleriana. A interação entre os domínios se dá através de uma força, força que o fluido exerce sobre a interface, a qual é adicionada à equação de balanço de quantidade de movimento. A força interfacial foi modelada baseada na lei de Hooke. A partir do trabalho de Peskin (1977), novas propostas foram apresentadas, onde a diferença se encontra basicamente na forma como é modelada a força interfacial. A seguir, algumas das propostas existentes: Fogelson e Peskin (1988) aplicaram o MFI a escoamentos com a presença de partículas em suspensão, onde modelam a força interfacial em função da resistência da partícula ao movimento do fluido; Unverdi e Tryggvason (1992) estudaram escoamentos com bolhas, usando um modelo da força em função dos parâmetros geométricos (curvatura e normal) e físicos (tensão interfacial) da interface; Golstein et al. (1993) simularam escoamentos sobre um cilindro, com modelo de força baseado na soma das forças interfaciais sobre um corpo de massa desprezível; Mohd-Yusof (1997) propõe modelar a força interfacial usando uma formulação baseada nas equações de movimento e avaliada na região próxima da interface; Lima e Silva at al. (2003) propuseram o modelo físico virtual (MFV), baseado também nas equações de movimento, porém avaliada sobre a interface. Evidentemente, ,os modelos baseados nas equações de balanço de quantidade de movimento são genéricos e livres de constantes ad-hoc.

A aplicação do MFI com MFV a diversos problemas demonstra que se trata de uma técnica promissora. Entre as aplicações têm-se: escoamentos sobre cilindros dispostos em tandem e paralelo e sobre aeorofólios a baixos números de Reynolds, em Lima e Silva et al. (2003); escoamentos em canais (Poiseuille, Couette e Couette-Poiseuille) e cavidade aberta rasa com fundo móvel, em Arruda (2004); escoamentos sobre cilindros de diâmetro variável e sobre aerofólios a

altos números de Reynolds, em Oliveira (2005); escoamentos ao redor de uma esfera estacionária e em movimento, em Campregher (2005). Sendo que só o último trabalho usa configuração tridimensional.

No presente trabalho, apresenta-se a aplicação do MFI com MFV a escoamentos internos tridimensionais, trabalho motivado pelo interesse em desenvolver uma ferramenta numérica para análise problemas ligados à tecnologia de perfuração em águas profundas. Os problemas ligados à tecnologia de perfuração em águas profundas têm como característica um alto grau de complexidade, que está ligada à superposição de escoamentos nas direções axial e azimutal, à interação entre os escoamentos no interior do canal e da cavidade anular (como resultado de movimentação excêntrica da estrutura interna), à presença de partículas sólidas, e às características do fluido (não newtoniano).

2. Modelo Matemático

2.1 Modelo para o Fluido

O modelo para o fluido, aplicado no domínio euleriano (Fig. 1a), que representa a dinâmica dos escoamentos incompressíveis, newtonianos e isotérmicos são modelados pelas equações de Navier-Stokes, equações apresentadas a seguir:

$$\frac{\partial u_i}{\partial x_i} = 0\,, \tag{1}$$

$$\frac{\partial u_i}{\partial t} + \frac{\partial (u_i u_j)}{\partial x_j} = -\frac{1}{\rho}\frac{\partial p}{\partial x_i} + \frac{\partial}{\partial x_j}\left[\nu\left(\frac{\partial u_i}{\partial x_j} + \frac{\partial u_j}{\partial x_i}\right)\right] + \frac{f_i}{\rho}, \tag{2}$$

onde u e p são os campos da velocidade e pressão, respectivamente. O fluido tem densidade ρ e viscosidade cinemática ν. O campo de força f é a força através da qual o fluido sente a presença da interface e é avaliada de acordo a expressão da Eq. (3), esta equação representa a forma como a força lagrangiana F_k é distribuída sobre o domínio euleriano (Fig. 1b).

$$f_i = \sum D_i F_k \Delta A_k \Delta S_k\,, \tag{3}$$

onde ΔA_k é a área do elemento da malha que delimita a interface e ΔS_k é a distância característica entre os centróides dos elementos da malha lagrangiana. A função distribuição D_i (Juric, 1996) é convenientemente definida na forma de uma gaussiana. Ressalta-se que as coordenadas cartesianas são consideradas no domínio euleriano.

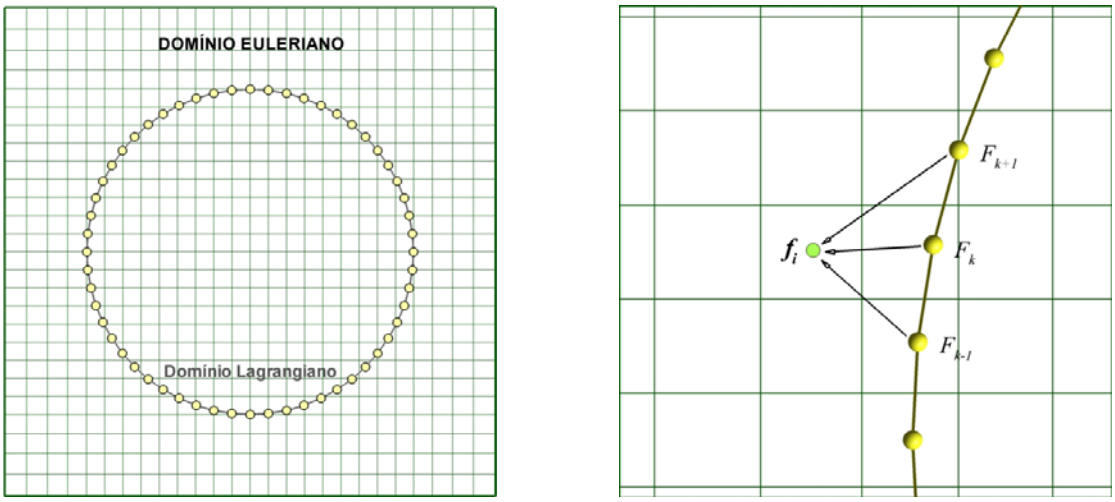

Figura 1. Método de fronteira imersa; (a) representação bidimensional dos domínios, (b) distribuição da força lagrangiana no domínio euleriano.

2.2 Modelo de Turbulência

A metodologia de simulação de grandes escalas SGE (Smagorinsky, 1963) é usada na modelagem da turbulência, esta metodologia baseia-se no conceito de separação de escalas usando um processo de filtragem das equações

governantes, como detalhado em Padilla (2005). O conhecimento do campo filtrado não permite calcular os termos de transporte advectivo $\partial(\overline{u_i u_j})/\partial x_j$, cuja decomposição dá origem a tensores adicionais, que sob certas considerações (Silveira-Neto et. al., 2002) toma a forma:

$$(\overline{u_i u_j}) = \overline{u}_i \overline{u}_j + \tau_{ij}, \tag{4}$$

sendo que τ_{ij} é o tensor de Reynolds sub-malha. Para modelar τ_{ij} usa-se a hipótese de Boussinesq:

$$\tau_{ij} = -\nu_t 2\overline{S}_{ij} + \frac{2}{3}k\delta_{ij}, \tag{5}$$

onde ν_t é a viscosidade turbulenta, $\overline{S}_{ij} = 0.5(\partial\overline{u}_i/\partial x_j + \partial\overline{u}_j/\partial x_i)$ é o tensor deformação do campo filtrado e k é a energia cinética turbulenta. Finalmente, as equações filtradas são expressas como:

$$\frac{\partial \overline{u}_i}{\partial x_i} = 0, \tag{6}$$

$$\frac{\partial \overline{u}_i}{\partial t} + \frac{\partial(\overline{u}_i\overline{u}_j)}{\partial x_j} = -\frac{1}{\rho}\frac{\partial \overline{p}}{\partial x_i} + \frac{\partial}{\partial x_j}\left[(\nu+\nu_t)\left(\frac{\partial \overline{u}_i}{\partial x_j} + \frac{\partial \overline{u}_j}{\partial x_i}\right)\right] + \frac{\overline{f}_i}{\rho}. \tag{7}$$

As pequenas escalas, representadas na Eq. (7) por ν_t, são modeladas usando os modelos sub-malha. No presente trabalho consideram-se os modelos de Smagorinsky (Smagorinky, 1967) e dinâmico (Germano et al., 1991).

2.3 Modelo para a Interface

O modelo físico virtual consiste em calcular a força que o fluido exerce sobre a interface através de um balanço de quantidade de movimento sobre o domínio lagrangiano, que equivale a realizar o balanço sobre cada partícula de fluido que permanece coesa à interface. Assim, a força lagrangiana é definida como segue:

$$F_k = F_a + F_i + F_v + F_p, \tag{8}$$

onde os termos do lado direito são a força de aceleração, força inercial, força viscosa e força de pressão, respectivamente, na forma da Eq. (7).

Cada termo da Eq. (8) é calculado utilizando-se esquemas de interpolação sobre os campos de velocidade eulerianos, segundo Lima e Silva et al., 2003, e de pressão, segundo Oliveira (2006). Uma vez calculada a força sobre o domínio lagrangiano, esta é distribuída sobre o domínio euleriano segundo a Eq. (3). Distribuída a força e gerado o campo de força euleriano equivalente, as equações do movimento são resolvidas sob sua influência. Desta forma, a solução destas equações leva em conta a presença da interface, através de um termo fonte e não por meio de condições de contorno como é feito convencionalmente.

3. Método Numérico e Validação do Código Base

As Equações governantes tridimensionais e em coordenadas cartesianas, são discretizadas usando o método dos volumes finitos, segundo Patankar (1980), considerando esquemas de interpolação espacial e temporal de diferenças centradas e Adams-Bashforth, respectivamente. A equação de Poisson para o campo de pressão é resolvida usando o procedimento fortemente implícito, conhecido como SIP (Stone, 1968). O acoplamento pressão-velocidade é realizado através do método dos passos fracionados (Kim e Moin, 1985).

Foi realizado um rigoroso processo de validação do código computacional base (sem considerar o MFI) entorno de um problema de geometria simples, porém, onde complexas estruturas estão presentes; trata-se de escoamentos no interior de cavidades retangulares com tampa deslizante. A cavidade de seção quadrada (lado L) tem comprimento C e a tampa se movimenta na direção paralela ao eixo x, com velocidade U. As simulações compreendem valores de número de Reynolds na faixa $100 \le Re \le 10000$ e de razão de aspecto C/L=1 e 2. A seguir apresentam-se alguns dos resultados.

Na Fig. 2 tem-se resultados para escoamento estável, Re=400 e C/L=1. Na primeira figura (Fig. 2a) mostram-se linhas de corrente sobre o plano de simetria (z/L=0,5) e no domínio tridimensional, evidenciando estruturas como os vórtices primário e secundário, no plano, e correntes internas ao longo da envergadura dentro do vórtice principal. Na

Fig. 2(b) compara-se o perfil da componente horizontal da velocidade no plano de simetria em x/L=0,5, com dados numéricos de Kato et al. (1990), Babu e Korpela (1994) e Sheu e Tsai (2002). A distribuição de velocidade obtida com ambas as malhas (uniformes) se aproxima muito melhor aos dados de Sheu e Tsai (2002). À medida que o Re se incrementa o escoamento torna-se instável, assim, para Re=3200 o escoamento é notoriamente instável (Padilla et al., 2005). Em regime de turbulência, Re=10000, o escoamento apresenta oscilações com uma ampla gama de freqüências e múltiplas estruturas vorticais, entre as quais encontram-se os vórtices do tipo Taylor-Gortler. Distribuições de velocidade média horizontal (u_m/U) e intensidade de turbulência associada a esta componente ($u_{rms}=\sqrt{(u'^2)_m}/U$) para Re=3200 e Re=10000, respectivamente, são apresentadas na Fig. 3. As distribuições de velocidade média (Fig. 3a) obtidas com modelos sub-malha de Smagorinsky e dinâmico são comparadas com o resultados experimental de Prasad e Koseff (1989) e numérico de Deshpande e Milton (1998). Por outro lado, as distribuições de u_{rms} são comparadas com os dados experimentais mencionados anteriormente. Em relação ao comportamento médio, observa-se uma boa concordância, porém quando se trata de momentos de segunda ordem, o modelo dinâmico é superior ao modelo de Smagorinsky. Maiores detalhes sobre os resultados para escoamentos estáveis, bem como instáveis, podem ser encontrados em Padilla e Silveira Neto (2005) e Padilla et al. (2005).

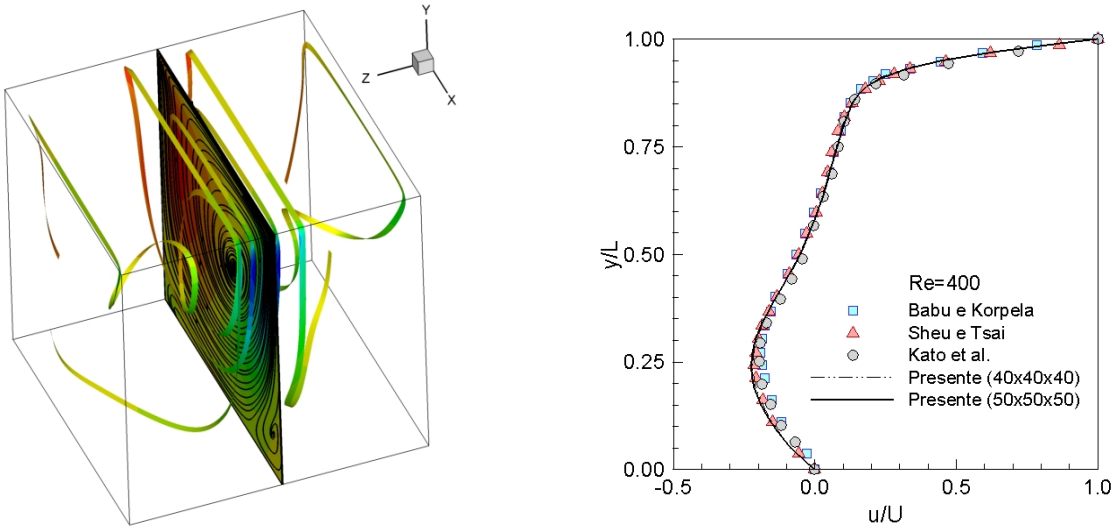

(a) (b)

Figura 2. Escoamento estável, Re=400 e C/L=1; (a) linhas de corrente , (b) comparação da componente horizontal da velocidade.

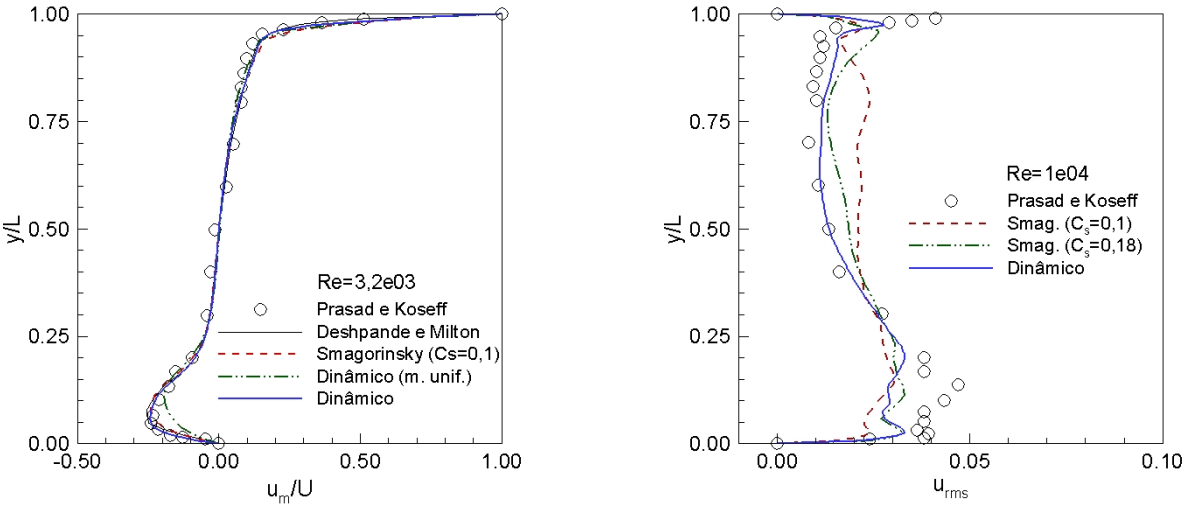

(a) (b)

Figura 3. Comparação dos perfis de intensidade de turbulência para Re=10000, C/L=1; (a) componente horizontal, (b) componente vertical.

4. Resultados

O escoamento Hagen-Poiseuille foi considerado para verificar quantitativamente a validade da metodologia de fronteira imersa, trata-se do escoamento no interior de um canal cilíndrico a Re=103, gerado por uma diferença de pressão imposta na entrada e saída do canal. Como se pode observar na Fig. 4(a), o domínio euleriano está definido por uma razão de aspecto C/L=0,52 (usando a mesma definição para cavidade) e o domínio lagrangiano por uma razão de aspecto C_c/D=0,5, onde D é o diâmetro do canal e C_c é o comprimento. As condições de contorno usadas para o domínio euleriano são do tipo Dirichlet nas direções x e y, e do tipo Neumann na direção do escoamento (z). A malha euleriana tem 44x44x24 volumes nas direções x, y e z, respectivamente.

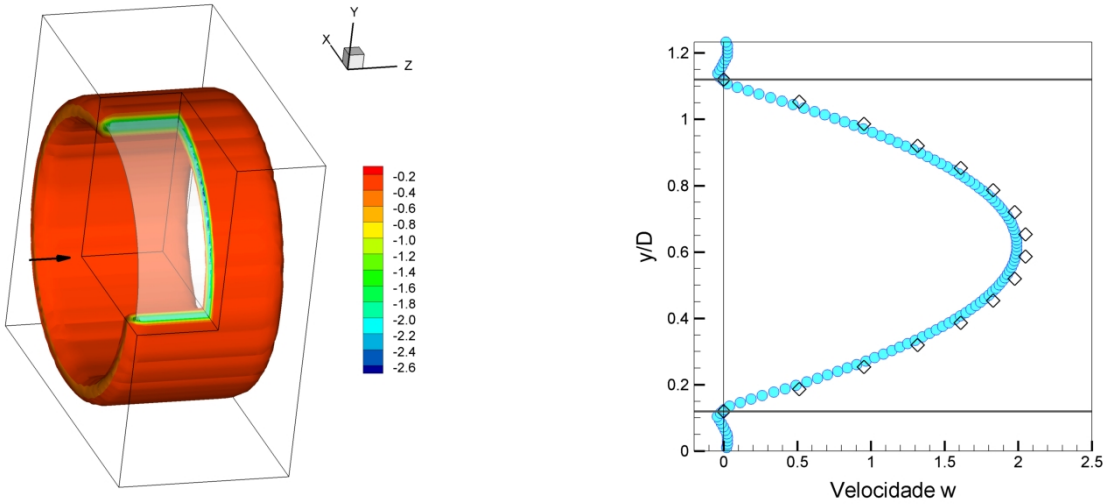

(a) (b)

Figura 4. Escoamento Hagen-Poiseuille, Re=103; (a) campo de força euleriano na direção axial, (b) comparação do perfil de velocidade com a solução analítica (◇) .

Na Fig. 4(a) tem-se iso-superfícies da força euleriana na direção do escoamento (f_z), as quais se concentram entorno da interface que descreve o canal. O campo de força euleriano só existe nas proximidades da interface, sendo que o escoamento reconhece a presença do canal por meio deste campo. O perfil de velocidade na direção z do escoamento desenvolvido é observado na Fig. 4(b), junto a solução analítica, avaliada segundo White (1991). Os resultados estão bastante próximos, sendo que a leve diferença observada na parte central do canal atinge um valor máximo de aproximadamente 3%. Certamente, a velocidade na superfície do cilindro não é nula, porém é muito baixa. Para medir o desvio existente no cálculo da velocidade na superfície do canal, usa-se a norma L_2 (Eq. 9), que para o caso é da ordem de 10^{-4}.

$$L_2 = \sqrt{\sum (u_k - u_{fk})} \Big/ n \,, \tag{9}$$

onde u_k é a velocidade da interface, u_{fk} é a velocidade do fluido na interface e n é o número de volumes lagrangianos.

A seguir apresentam-se os resultados de escoamentos tridimensionais a baixos números de Reynolds, que correspondem ao problema de cavidade com tampa deslizante (usado para validação) com presença de corpos virtuais no seu interior. São considerados os seguintes casos:

- Caso A: cavidade com canal cilíndrico, definido por uma cavidade com C/L=1,5 e um canal cilíndrico com C_c/D=2.
- Caso B: cavidade com dois canais cilíndricos concêntricos, definido por uma cavidade com C/L=1 e canal externo com C_c/D=1.
- Caso C: cavidade com dois canais cilíndricos concêntricos com canal interno rotativo, definido por uma cavidade com C/L=1 e canal externo com C_c/D=1.

Nas Figs. 5 e 6 mostram-se os resultados para o caso A, simulado usando Re=100 com malha euleriana de 36x36x54 volumes e malha lagrangiana de 61x39 (tangencial, axial). A Fig. 5 mostra o padrão do escoamento através da projeção das linhas de corrente sobre dois planos perpendiculares à direção z (plano z). O escoamento percebe a

presença do cilindro através do campo de força euleriana, formando vórtices no interior do canal, bem como na parte exterior (Fig. 5a), como observado no plano z/L=0,5. No outro plano z/L=1,3 (Fig. 5b), que não intercepta a superfície do canal, observa-se um vórtice primário (típico de escoamentos no interior de cavidades) com leves modificações à altura do canal. Esta influência é mais bem observada na Fig. 6(a), onde também se observa que o fluido contorna a superfície do canal, gerando vórtices em torno das extremidades do canal devido aos efeitos de borda, sendo tais vórtices maiores na parte superior do plano. Perfis que descrevem a distribuição das componentes horizontal e vertical da velocidade ao longo das coordenadas x e y, respectivamente, no plano z/L=0,5, são mostrados na Fig. 6(b). Claro está que as velocidades na interface são muito próximas de zero e que os vórtices formados no interior do canal têm baixas velocidades.

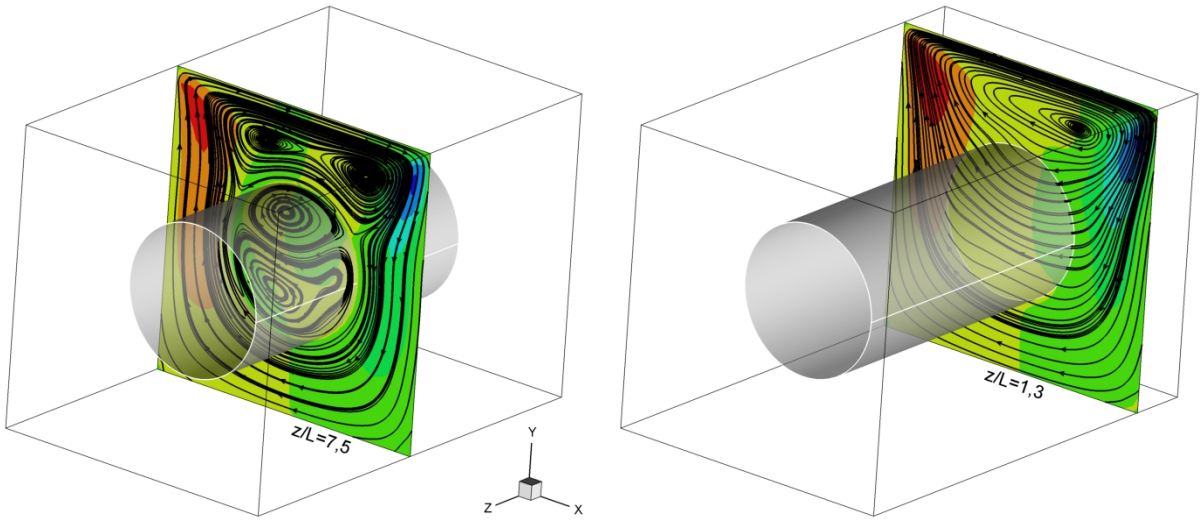

(a) (b)

Figura 5. Cavidade com canal cilíndrico para Re=100; (a) plano médio z, (b) plano z fora do domínio lagrangiano.

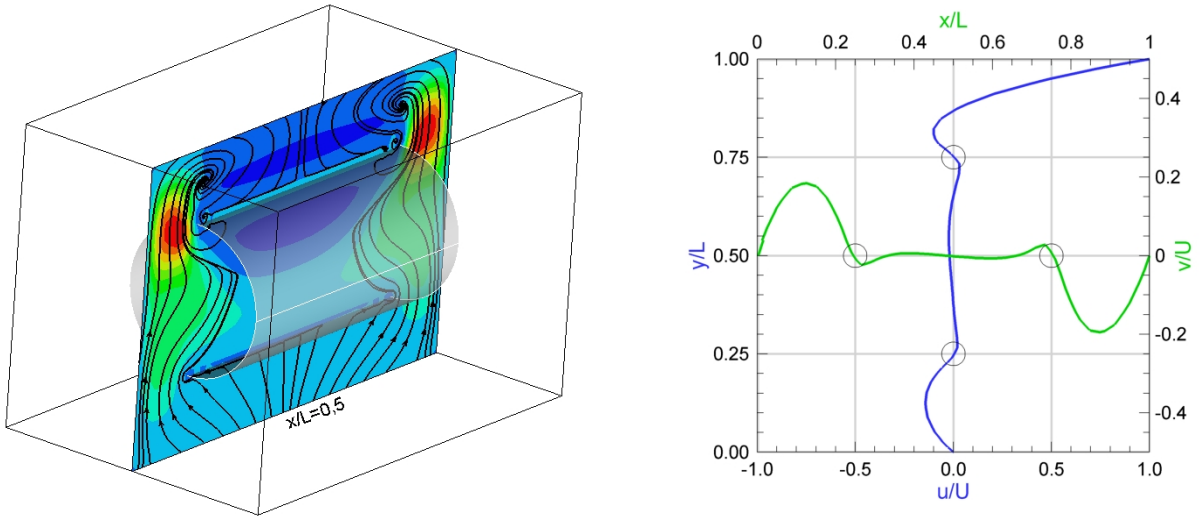

(a) (b)

Figura 6. Cavidade com canal cilíndrico para Re=100; (a) plano médio x, (b) distribuição de velocidade no plano médio z.

Resultados qualitativos para o caso B são apresentados na Fig. 7. O número de Reynolds corresponde a 100, a malha euleriana tem 36x36x38 volumes e as malhas lagrangianas têm 32x21 (canal interno) e 62x211 (canal externo) volumes. O escoamento formado fora dos canais é idêntico ao do problema anterior (Fig. 7a), porém no interior do canal interno observa-se leve diferença. No espaço anular os vórtices são alongados. As linhas de corrente sobre o plano x/L=0,5, Fig. 7b, mostram também alguns detalhes da complexidade do escoamento gerado ante a presença virtual dos canais.

Para o caso C, em que o canal interno rota em sentido anti-horário com velocidade de 436,5 revoluções por minuto, mostram-se linhas de corrente no domínio tridimensional (Fig. 8a) e sobre o plano z/L =0,8 (Fig. 8b). A influência da velocidade de rotação do canal interno atinge praticamente o domínio completo, de maneira que nas regiões localizadas entre os extremos dos canais e as paredes laterais da cavidade, a interação das forças devido à rotação e a velocidade de tampa são mais intensas.

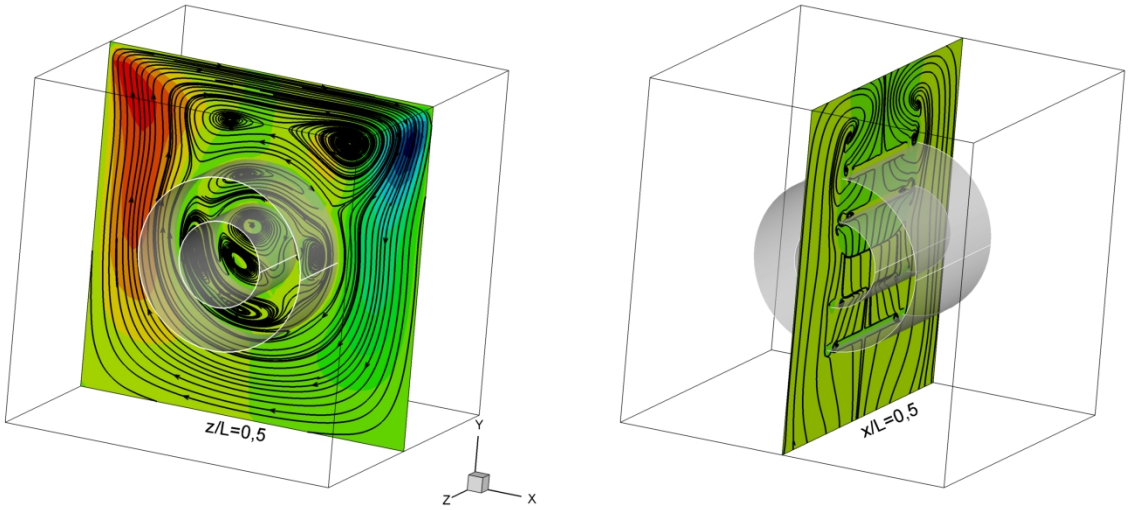

(a) (b)

Figura 7. Cavidade com dois canais cilíndricos concêntricos, Re =100; (a) planos médio z , (b) plano médio x .

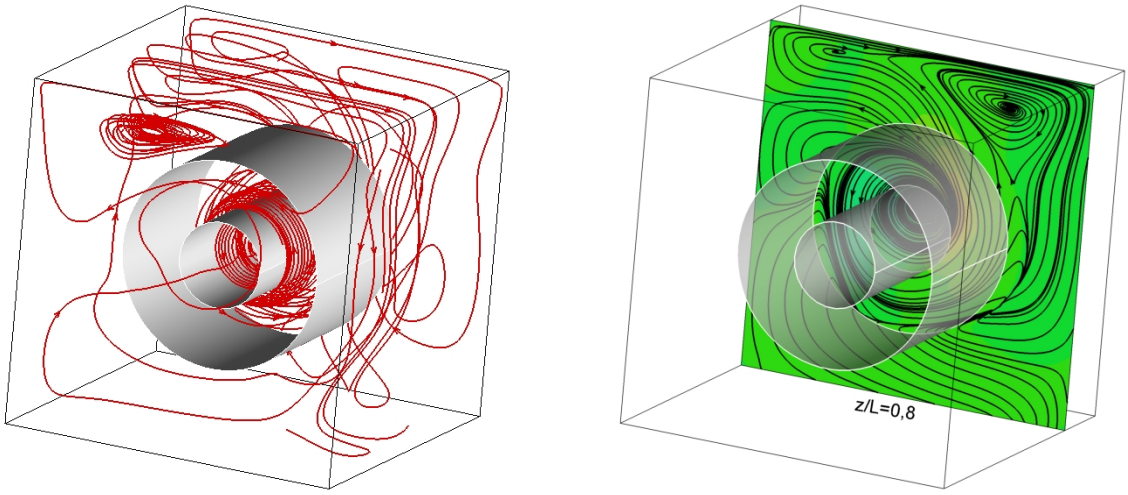

(a) (b)

Figura 8. Cavidade com dois canais cilíndricos concêntricos (canal interno rotativo), Re =100; (a) linhas de corrente no volume, (b) plano z fora do domínio lagrangiano.

5. Conclusões

Escoamentos internos tridimensionais foram simulados, usando o método de fronteira imersa com modelo físico virtual. O processo de validação do código computacional base em coordenadas cartesianas, apresentou uma boa concordância em relação a dados numéricos e experimentais de outros autores, tanto para regime estável quanto para regime instável. Os resultados apresentados demonstram a capacidade da metodologia para resolver escoamentos complexos com presença de corpos sólidos e em movimento. Os resultados qualitativos apresentam coerência com a física dos diversos problemas considerados e os resultados quantitativos mostram que a interface está adequadamente representada pelo modelo físico virtual. A boa aproximação da solução do escoamento Hagen-Poiseulle com a solução analítica deve melhorar para malhas mais densas. É pertinente ressaltar que se tratam de resultados preliminares, os

quais permitem dar continuidade ao presente trabalho considerando dois aspectos importantes: primeiro, de aplicação a escoamentos com maiores números de Reynolds; segundo, de desenvolvimentos que aprimorem a metodologia.

6. Agradecimentos

Os autores agradecem à FAPEMIG e ao CENPES-PETROBRAS pelo apoio financeiro.

5. Referências

Arruda, J.M., 2004, "Modelagem Matemática de Escoamentos Internos Forçados Utilizando o Método de Fronteira Imersa e o Modelo Físico Virtual", Tese de Doutorado, Universidade Federal de Uberlândia.

Campregher, R., 2005, "Modelagem Matemática Tridimensional para Problemas de Interação Fluido-Estrutura", Tese de Doutorado, Universidade Federal de Uberlândia.

Deshpande, M. D. and Milton, S. G., 1998, "Kolmogorov Scales in a Driven Cavity Flow", Fluid Dyn. Res., 22, pp. 359-381.

Fogelson, A. L. and Peskin, C. S, 1988, "A Fast Numerical Method for Solving the Three-dimensional Stokes Equations in the Presence of Suspended Particles", J. of Comp. Physics v. 79(1), pp. 50-69.

Germano, M. Piomelli, U. Moin, P. Cabot, W. H., 1991, "A Dynamic Sub-Grid-Scale Eddy Viscosity Model", Phys. Fluids A 3 (7), pp. 1760-1765.

Goldstein, D., Hadler, R. and Sirovich, L., 1993, "Modeling a No-Slip Flow Boundary with an External Force Field", J. Comput. Physics, 105, pp. 354.

Juric, D., 1996, Computation of Phase Change, Ph.D. Thesis, University of Michigan,.

Kato, Y., Kawai, H., and Tanahashi, T., "Numerical Flow Analysis in a Cubic Cavity by the GSMAC finite-element method", JSME Int. J. Series II 33, pp.649-658.

Kim, J. and Moin, P., 1985, "Application of a Fractional Step Method to Incompressible Navier-Stokes Equations", J. Comp. Phys., 59, pp. 308-323.

Lima e Silva A., Silveira-Neto A. and Damasceno, J. J. R., 2003, "Numerical Simulation of Two-Dimensional Flows Over a Circular Cylinder Using the Immersed Boundary Method", Journal of Computational Physics, 189, pp. 351-370.

Mohd-Yusof, J., 1997, "Combined Immersed Boundaries/B-Splines Methods for Simulations of Flows in Complex Geometries", CTR Annual Research Briefs, NASA Ames/Stanford University.

Oliveira, J. E. S., 2006, "Método da Fronteira Imersa aplicado a Modelagem Matemática e Simulação Numérica de Escoamentos Turbulentos sobre Geometrias Móveis Deformáveis", Tese de Doutorado, Universidade Federal de Uberlândia.

Padilla, E. L. M. e Silveira Neto, A., 2005, "Desenvolvimento de um Código Computacional Tridimensional para Solução de Escoamentos em Transição e Turbulência", XXVI Iberian Latin-American Congress on Computational Methods in Engineering, Guarapari, Procceding of the CILAMCE, v. 1, p. 1-12.

Padilla, E. L. M., Martins, A. L. E. and Silveira Neto, A., 2005, "Large-Eddy Simulation of the Three-Dimensional U|nstable Flow in a Lid-Driven Cavity", 18TH International Congress of Mechanical Engineering, Ouro Preto, Proceedings of COBEM, v. 1, p. 1-8.

Patankar, S. V., 1980, "Numerical Heat Transfer and Fluid Flow", Hemisphere Publishing Corporation, New York.

Peskin, C. S., 1977, "Numerical analysis of blood flow in the heart", Journal of Computational Physics, vol. 25, pp. 220-252.

Prasad, A. K. and Koseff, J. R., "Reynolds Number and End-Wall Effects on a Lid-Driven Cavity Flow", Phys. Fluids A, 1, pp. 208-218, 1989.

Silveira-Neto, A., Mansur, S. S. e Silvestrini, J. H., 2002 , "Equações da Turbulência: Média Versus Filtragem", III Escola de Primavera de Transição e Turbulência", Anais, Florianópolis, pp. 1-7.

Sheu, T. W. H. and Tsai, S. F., 2002, "Flow Topology in a Steady Three-Dimensional Lid-Driven Cavity", Comput Fluids, 31, pp. 911-934.

Smagorinsky, J., 1963, "Genenral Circulation Experiments with Primitive Equations", Montly Weather Rev., 91, pp. 216-241.

Stone, H. L., 1968, "Iterative Solution of Implicit Approximations of Multidimensional Partial Differential Equations", SIAMJ Numer. Anal., vol. 5, pp. 530-558.

Unverdi, S. O. and Tryggvason, G., 1992, "A Front-Tracking Method for Viscous Incompressible Multi-Fluid Flows", J. Comput. Physics, 100, pp. 25-60.

White, F. M., 1991, "Viscous Fluid Flow", McGraw-Hill.

NUMERICAL SIMULATION OF THREE-DIMENSIONAL INTERNAL FLOW USING IMMERSED BOUNDARY METHOD

Elie L. M. Padilla
Federal University of Uberlândia
epadilla@mecanica.ufu.br

André Leibsohn Martins
CENPES-PETROBRAS
aleibsohn@petrobras.com.br

Aristeu da Silveira Neto
Federal University of Uberlândia
aristeus@mecanica.ufu.br

Abstract
This work presents the advances related to the development of a numerical tool for analysis of fluid-structure interaction problems by using of the immersed boundary method with virtual physical model. These kinds of problems are commonly encountered in many engineering applications, for instance in gas and oil exploration: technology of perforation in deepwater and offshore production using risers. The Navier-stokes equations were used, considering a Newtonian, isothermal and incompressible fluid. In this phase of the development, are presented results of three-dimensional simulations of Hagen-Poiseuille flow and flows inside lid-driven cavity-cylindrical channels. The details of the structures of several flows (steady) and the good agreement with the analytical solutions show the applicability of this new methodology to internal flow problems.

Keywords: immersed boundary method, three-dimensional flow.

Proceedings of the 11th Brazilian Congress of Thermal Sciences and Engineering -- ENCIT 2006
Braz. Soc. of Mechanical Sciences and Engineering -- ABCM, Curitiba, Brazil,- Dec. 5-8, 2006

Paper CIT06-0535

PREDICTION OF FLOW FIELD IN A CURVED CHANNEL

Yuu Itai
Grupo de Energia Bioamassa e Meio Ambiente-Departamento de Engenharia Mecânica- Universidade Federal do Pará, Belém-PA-Brasil, CEP:66075-110.
Yuu_itai@yahoo.com.br

Ricardo W. M. Ferreira
Departamento de Engenharia Mecânica- Universidade Federal do Pará, Belém-PA-Brasil, CEP:66075-110.
caco_bassa@yahoo.com.br

Danielle R.S. Guerra
Grupo de Energia Bioamassa e Meio Ambiente-Departamento de Engenharia Mecânica- Universidade Federal do Pará, Belém-PA-Brasil, CEP:66075-110
daguerra@ufpa.br

André L. A. Mesquita
Departamento de Engenharia Mecânica- Universidade Federal do Pará, Belém-PA-Brasil, CEP:66075-110
andream@ufpa.br

Abstract. *Flows with three dimensional effects are encountered in turbo machines and around complex bodies. These effects can be produced by channel with curved walls that provides curvature or change direction of the streamlines. The experimental study of the three-dimensionality and the structure of the turbulent flows, usually require optical techniques like the laser-Doppler anemometry or the particle image velocimetry systems, PIV. However, high costs of the experimental apparatus associated with these methods make these techniques inaccessible to many. Turbulent flows with streamline curvature are of considerable engineering interest. The aim of this work is to present the three dimensional effects of the turbulent air flow in a curved channel through the commercial code FLUENT 6.0. Three turbulence models were applied to obtain the mean velocity field and pressure gradients. In this study the grid of the geometry was development from dimensions of the wind tunnel located at the Fluid Mechanics Laboratory – DEM/UFPA. The wind tunnel has a curved rectangular test section of 150x300mm, with a fully developed channel flow.*

Keywords*.curved channel, streamline, velocity profile.*

1. Introduction

Computational fluids dynamics codes used to simulate cases have had an important place among the methods analysis and structures construction. Although it is necessary the knowledge of what appropriate model had been used in our case. Is completely necessary the use of commercial codes because the expensive costs of optical equipment adopted to measure the three-dimensional effects and draining structure turbulent. These variables usually require the use of optic techniques as anemometry for Laser-Doppler or systems of attainment of the field of speed for particle image, PIV, and it is represent a problem when doesn't have a lot of investments becoming practically inaccessible to some laboratories.

Shao et al. (2002) developed a simulation model which uses Reynolds averages, 3D Navier Stokes equations based on a boundary-fitted orthogonal curvilinear coordinate system. Two approaches for equation system closure are used, i.e, algebric stress models and nonlinear k - ε model for eddy viscosity. The different closure approaches have been discussed and the model was validated using measurements in curved rectangular channels. Predicted turbulence and secondary flow patterns in curved compound channel were compared with straight channels measurements.

Kim et al. (1994) investigated the developing turbulent flow in a 90 deg curved duct of rectangular cross section, and an aspect radio of 6 was investigated. The mean-velocity was measured with a five-hole pressure probe and Reynolds-stress components was measured with two sensors hot-wire probes, in the boundary layers on the duct walls to document the pressure driven secondary motion and the formation of a longitudinal vortex near the corner in the convex wall.

Shima et al. (2000), tested a low-Reynolds-number second-moment closure without wall-reflection redistribution terms in wall-bounded turbulent flows with streamline curvature. The turbulence model was previously shown to give good predictions for a fully developed channel flow, adverse and favorable pressure gradients, plane and round jets, and flows with wall blowing and suction and other good predictions. The model is used to calculate two fully developed curved channel flows and four boundary layers on curved walls. The turbulence model captures main features of the stabilizing and destabilizing effects of streamline curvature, though some notable discrepancies between the predictions and measurements are present in boundary layers on convex walls.

Silva et al. (1998) has an objective and good explanation to turbulence phenomenon and their variants. Treaster et al. (1979) developed programs to calibrate and employ five-hole probes of both angle tube and prismatic geometries and discuss about the applications.

Iacovides et al. (1990) reported a computational and experimental study of turbulent flow around a square-sectioned U-bend. All velocities measurements were obtained with DISA and TSI constant-temperature, hot-wire anemometers using standard DANTEC single and cross-wire probes. The flow prediction was studied by a software including the turbulence model.

Humphrey et al (1981) investigated steady, incompressible, isothermal developing flow in a square-section curved (comprises a 90° perpex bend) duct with smooth walls. The measurements (the longitudinal and radial components of mean velocity and corresponding components of the Reynolds stress tensor) were obtained with a Laser Doppler anemometer. Calculated mean velocity results obtained from solution of elliptic differential equations in finite difference form and incorporating a two-equation turbulence model are not strongly dependent on the model.

Schlichting (1968) presents the explanation of sprouting, development and separation of boundary layer. With a different way these studies insert values to this work.

The documentation of commercial code FLUENT 6.0 (2005) explains very well the equations of transport and turbulent models. What the appropriated cases to apply the turbulence model and the restrictions and vantages of all the models.

The present paper compare three turbulence models inserted on the commercial code FLUENT 6.0 analyzing their performance during the air draining in a wind tunnel, located at the Fluid Mechanics Laboratory – DEM/UFPA. The wind tunnel has a curved rectangular test section of 150x300mm, with a fully developed channel flow.

2. Case Description

The mesh was created in the commercial code GAMBIT 2.0, that was developed to create geometry and meshes, where a boundary layer its developed to facilitate the calculations refining the places closer of the wall. The mesh was constructed with a growth factor of 0.005 and B/A tax of 1.055 to the part that contain the curvature and the rectangular part. The structure has been shared in three parts becoming easier to create the boundary layer and the mesh. Two rectangular parts were meshed with 0.025 of size on the HEX MAP mode and the curvature with 0.008 on the same mode of the rectangular parts.

Two zones were been defined, the entrance with velocity inlet and the exit with pressure outlet. We have to point out the way that the structure will be meshed. It is completely important when the calculation run to converge. The order of mesh command to elements also has been discussed since for each structure has a different way to apply and create the perfect mesh. The first volume presents 15400 elements and 17388 nodes, the second part, that represents the curve, had 179200 elements and 194292 nodes and the third part contains 18200 elements and 20412 nodes, totalizing 212800 elements and 230580 nodes. Figure 1 shows the structure of curvature presents at the wind tunnel located at the Fluid Mechanics Laboratory – DEM/ UFPA. At Fig. 2 it showed a structure of curvature detail and it seemed that the structure presents a uniform and good mesh.

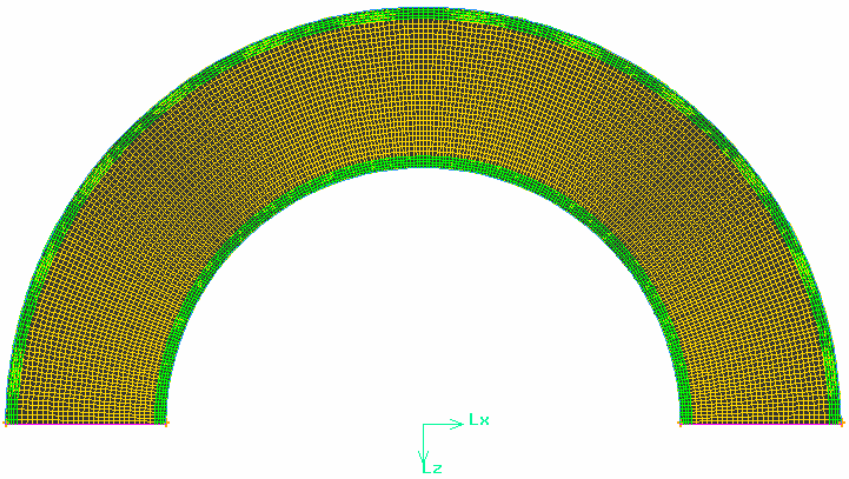

Figure 1 – The grid mesh of curvature of wind tunnel.

At Figure 3 it showed the two rectangular structures that united at the curvature showed at Figure 1 form the complete structure of wind tunnel. Figure 4 shows the grid detail of the mesh of rectangular parts that forms the wind tunnel.

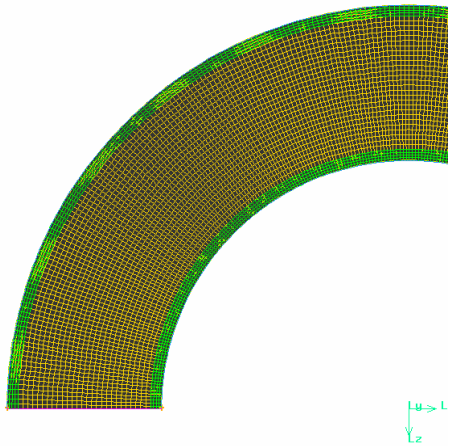

Figure 2 – A specific detail of mesh structure of curvature at wind tunnel.

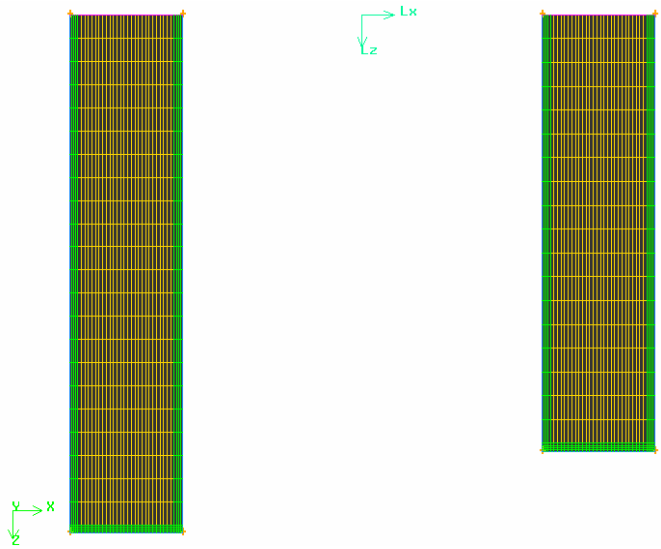

Figure 3 – Rectangular structures presents at the wind tunnel.

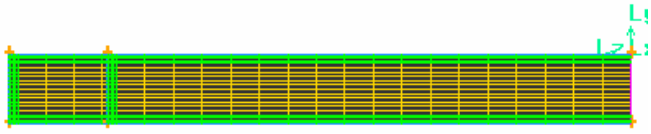

Figure 4 – Grid detail of rectangular structures of wind tunnel.

Figure 5 – The wind tunnel.

3. Turbulence Models

Three turbulence models have been chosen for the accomplishment of this work. The Standard *k* - ε the RNG *k* - ε and the Reynolds Stress Model (RSM). This explanation is based on FLUENT 6.0 Documentation (2005).

3.1. The Standard *k* - ε Model.

The Standard *k* - ε Model are very simple of "complete models" of turbulence are two-equation models in which the solution of two separate transport equations allows the turbulent velocity and length scales to be independently determined. Since it was proposed the standard *k* - ε model becomes the workhorse of practical engineering flow calculation. Robustness, economy, and reasonable accuracy for a wide range of turbulent flows explain the popularity in industrial flow and heat transfer simulations.

The standard *k* - ε model is a semi-empirical model based on model transport equations for the turbulence kinetic energy (*k*) and its dissipation rate (ε). The model transport equation for *k* is derived from the exact equation, while the model transport equation for ε was obtained using physical reasoning and bears little resemblance to its mathematically exact counterpart. In the derivation of the *k* - ε model, it was assumed that the flow is fully turbulent, and the effects of molecular viscosity are negligible. The standard *k* - ε model is therefore valid only for fully turbulent flows. The turbulence kinetic energy, *k*, and rate of dissipation, ε, are obtained from the following transport equations:

$$\frac{\partial}{\partial t}(\rho k)+\frac{\partial}{\partial x_i}(\rho k u_i)=\frac{\partial}{\partial x_j}\left[\left(\mu+\frac{\mu_t}{\sigma_k}\right)\frac{\partial k}{\partial x_j}\right]+G_k+G_b-\rho\varepsilon-Y_M+S_k \qquad (3.1.1)$$

and

$$\frac{\partial}{\partial t}(\rho \varepsilon)+\frac{\partial}{\partial x_i}(\rho \varepsilon u_i)=\frac{\partial}{\partial x_j}\left[\left(\mu+\frac{\mu_t}{\sigma_\varepsilon}\right)\frac{\partial \varepsilon}{\partial x_j}\right]+C_{1\varepsilon}\frac{\varepsilon}{k}(G_k+C_{3\varepsilon}G_b)-C_{2\varepsilon}\rho\frac{\varepsilon^2}{k}+S_\varepsilon \qquad (3.1.2)$$

In these equations, G_k represents the generation of turbulence kinetic energy due to the mean velocity gradients, G_b is the generation of turbulence kinetic energy due to buoyancy, Y_M represents the contribution of the fluctuating dilatation in compressible turbulence to the overall dissipation rate. $C_{1\varepsilon}$, $C_{2\varepsilon}$, and $C_{3\varepsilon}$ are constants. σ_k and σ_ε are the turbulent Prandtl numbers for *k* and ε, respectively. S_k and S_ε are user-defined source terms. The turbulent (or eddy) viscosity, μ_t, is computed by combining *k* and ε as follows:

$$\mu_t=\rho C_\mu\frac{k^2}{\varepsilon} \qquad (3.1.3)$$

Where C_μ is a constant.

The model constants $C_{1\varepsilon}$, $C_{2\varepsilon}$, C_μ, σ_k and σ_ε have the following default values :

$$C_{1\varepsilon}=1.44,\ C_{2\varepsilon}=1.92,\ C_\mu=0.09,\ \sigma_k=1.0,\ \sigma_\varepsilon=1.3 \qquad (3.1.4)$$

These default values have been determined from experiments with air and water for fundamental turbulent shear flows including homogeneous shear flows and decaying isotropic grid turbulence. They have been found to work fairly well for a wide range of wall-bounded and free shear flows.

3.2. The RNG *k* - ε Model.

The RNG *k* - ε model was derived using a rigorous statistical technique (called renormalization group theory). It is similar in form to the standard *k* - ε model, but includes the following refinements: The RNG model has an additional term in its equation that significantly improves the accuracy for rapidly strained flows, the effect of swirl on turbulence is included in the RNG model, enhancing accuracy for swirling flows. On RNG theory provides an analytical formula for turbulent Prandtl numbers, while the standard *k* - ε model uses user-specified, constant values. While the standard *k* – ε model is a high-Reynolds-number model, the RNG theory provides an analytically-derived differential formula for

effective viscosity that accounts for low-Reynolds-number effects. Effective use of this feature does, however, depend on an appropriate treatment of the near-wall region.

These features make this model more accurate and reliable for a wider class of flows than the standard k - ε model. This model is derived from the instantaneous Navier-Stokes equations. The analytical derivation results in a model with constants different from those in the standard k - ε model, and additional terms and functions in the transport equations for k and ε.

3.2. The Reynolds Stress Model.

The Reynolds stress model (RSM) is the most elaborate turbulence model that the commercial code FLUENT 6.0 provides. Abandoning the hypothesis of isotropic eddy-viscosity, the RSM closes the Reynolds-averaged Navier-Stokes equations by solving transport equations for the Reynolds stresses, together with an equation for the dissipation rate. This means that five additional transport equations are required in 2D flows and seven additional transport equations must be solved in 3D.

Since the RSM accounts for the effects of streamline curvature, swirl, rotation, and rapid changes in strain rate in a more rigorous manner than one-equation and two-equation models, it has greater potential to give accurate predictions for complex flows. However, the fidelity of RSM predictions is still limited by the closure assumptions employed to model various terms in the exact transport equations for the Reynolds stresses. The modeling of the pressure-strain and dissipation-rate terms is particularly challenging, and often considered to be responsible for compromising the accuracy of RSM predictions.

The RSM might not always yield results that are clearly superior to the simpler models in all classes of flows to warrant the additional computational expense. However, use the RSM is a must when the flow features of interest are the result of anisotropy in the Reynolds stresses. Among the examples are cyclone flows, highly swirling flows in combustors, rotating flow passages, and the stress-induced secondary flows in ducts.

4. Results

The simulation was conducted considered that the initial velocity was 10 m/s and the outlet pressure was 101325 Pa. Using the turbulence models we compared results of velocity and pressure gradients. All the models have a good convergence. Although some models results are greater than others and lately we discuss the results. We have to create six planes to show better the velocity behavior along the wind tunnel. The Fig. 6 shows where the planes are located.

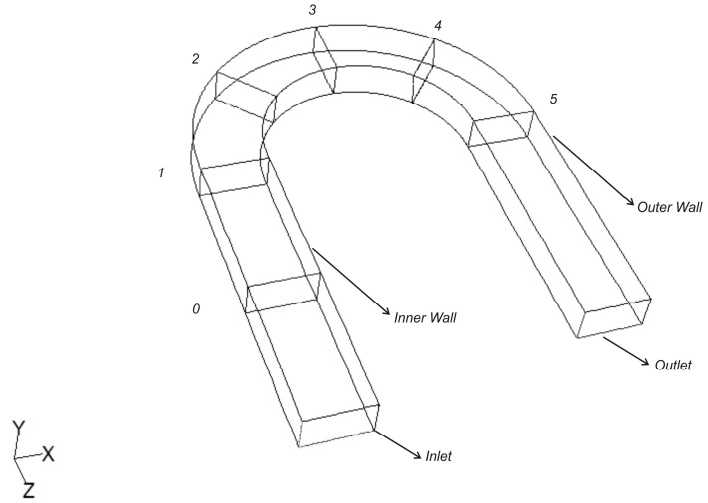

Figure 6 – The six planes created in wind tunnel with a strong curvature.

Figure 7 shows the profiles of the longitudinal velocity component, U, across de duct, from the outer to the inner wall at the six planes. The corresponding distributions of the V and W components are not shown. At plane 0, the velocity profile shows a flat plate type boundary layer. Plane 1 is the position where the curved section begins, at this plane the longitudinal velocity increase near the inner wall.

At plane 2 the longitudinal velocity increases more close to the inner wall and decrease until the outer wall. These effects are repeated in the middle of the curvature at plane 3. However, at the plane 3 the longitudinal velocity near the inner wall begins to decrease.

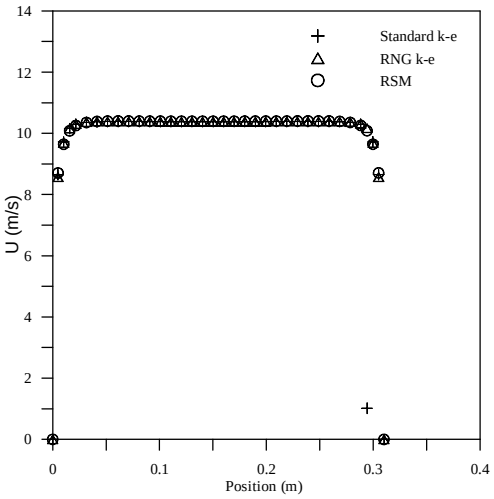

(a) Plane 0, at the middle of the first straight section.

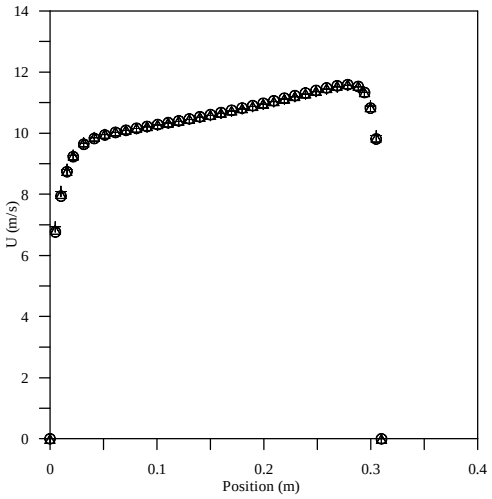

(b) Plane 1, upstream of the bend.

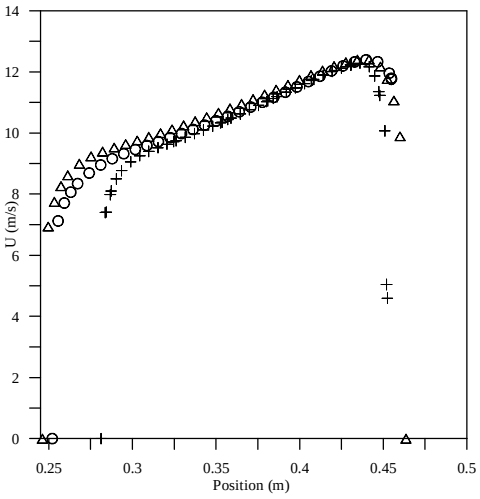

(c) Plane 2, at the first curvature.

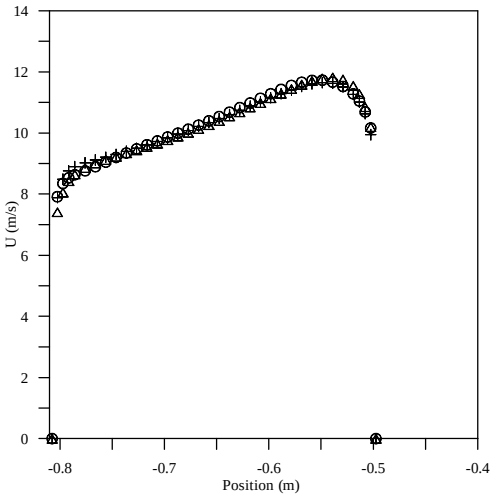

(d) Plane 3, at the middle of the curvature.

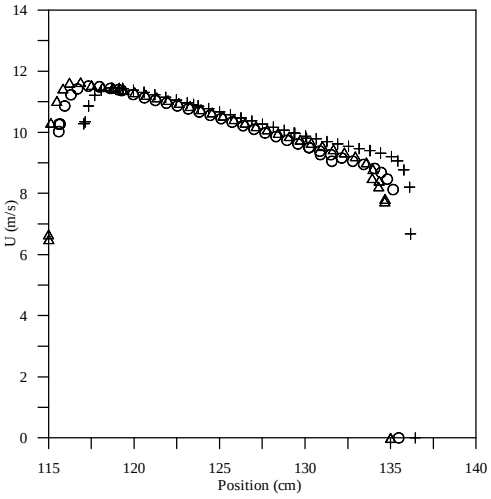

(e) Plane 4, at the second curvature.

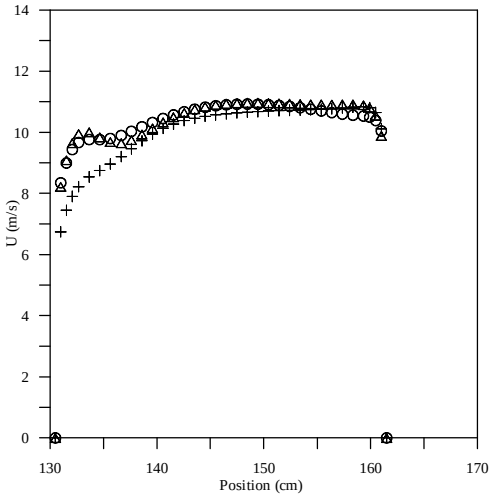

(f) Plane 5, at the exit of bend.

Figure 7 – Longitudinal velocity predicted by the three turbulent models, from outer to inner wall: (a) at plane 0, (b) at plane 1, (c) at plane 2, (d) at plane 3, (e) at plane 4 and (f) at plane 5.

At plane 4, the effect is changed, the longitudinal velocity is increased near the outer wall and presents diminish close to the inner wall. Finally, at plane 5 we can note the presence of a longitudinal vortex through the profiles of U, which depict the two peaks commonly observed in flows with vortex. These observations are consistent with the effect of concave curvature which acts to increase turbulent mixing and leads to increase velocity close to the wall.

It was observed that the pressure distribution along the channel walls is strong determined by the curvature. The pressure gradients induced by the curvature are clearly seen. The results of simulation indicated that on the inner wall, the boundary layer is subjected to a favorable pressure gradient starting upstream of the bend, close to the plane 1, where is found the higher velocities.

According Kim et al (1994) the transition of the flow of the curve for the straight line causes a reduction of the pressure in the concavous wall and increase in the convex wall, generating in this last adverse gradient of pressure, propitious condition to the separation of the boundary layer.

The results for longitudinal velocity profiles predicted by the three turbulent models have shown the same behavior for all planes. At the inlet, plane 0, and upstream the bend, plane 1, all three turbulence models predicted very well the longitudinal velocity. The Standard k - ε model provided poor results for the velocity near the wall when the flow presents a strong curvature, it can be observed in the Figures 7(c) and 7(e), planes 2 and 4. At the exit of the bend, this turbulence model was not able to predict the effect of the longitudinal vortex as shown in the Figure 7(f).

The other two turbulence models, RNG $k - \varepsilon$ and Reynolds stress model, have predicted longitudinal velocity data more close to the wall than the Standard k - ε model. These two models were able to capture the presence effect of a longitudinal vortex. This effect can be seen by the peak on the longitudinal profile in Figure 7(f).

The results below are the bidimensional planes, (x, y), at the planes 0, 1, 2, 3, 4 and 5. Figure 8 (a, b, c, d, e and f), Figure 9 (a, b, c and d) and Figure 10 (a, b, c and d) shown the predicted secondary flow using the three turbulence models described above. The Figures are shown in velocity vectors colored by velocity magnitude (m/s).

In a curved duct of rectangular section it was noticed the secondary flows of first and second type, determined respectively for the bending and the rectangular form of the section.

The results in Figure 8(a) and (b) have shown that in the straight section there was not secondary flow. The same behaviour was seen in the vectors provided by the simulation using the RNG $k - \varepsilon$ and the RSM models, at planes 0, 1 and 3.

At plane 2 in the first curvature, the Standard $k - \varepsilon$ indicated strong inclined currents; this region presents two vortex, one at the right side close to the inner wall, one at the top of the outer wall. At this plane is clearly seen the region of higher velocities. Again, at plane 4, in the second curvature, it can be seen inclined secondary currents; no vortex was predicted by the Standard $k - \varepsilon$ in this region.

Humphrey et al. (1981) considered that the secondary flows of first type is created from the disequilibrium between the centrifugal force and the gradient of radial pressure acting on the fluid of the boundary layer of the sidewalls of the curve, changing it, throughout these walls, for the internal region of the curve. The continuity demands a corresponding movement dislocating fluid, throughout the plan of symmetry, of the convex wall (internal region) for concaves wall (external) of the curve, generating itself thus the two great vortices in against rotation characteristic of the draining in curved duct. And this type of secondary flow can be seen in the Plane 2 and 4.

At plane 5, the model predicted an asymmetric secondary flow. In this region the higher velocities are concentrated close to the outer wall. Schlichting (1968) explain that the secondary flows of second type occur throughout the bisector in direction to the corner, where it bifurcate and it returns in opposing directions. This second type of secondary flows is weak than the first type and it's seemed for the elongation of isolines of velocity in direction to the corner. And this type can be seen at the Planes 3 and 5.

Iacovides et al (1990) explain the secondary motion in modifying the streamwise flow. This flow is deflected down the inside wall toward the duct mid-plane and a return flow occurs from the inside to the outside over the core region of the duct.

This is the classical single-cell vortex flow that pertains at the 45-degree station. By 90 deg, the readjustments to the streamwise velocity field lead, through its coupling with the pressure fields, to the eye of the secondary vortex being pushed far to the inside to the bend. This is what causes the development of “mushroom” shaped velocity contours near the inner wall as the return fluid is deflected away from the center plane; indded, it is displacement of low-momentum fluid near the center plane that is directly responsible for the “troughs”. And it can be seen at the Fig. 7 (f), 8 (f), 9 (c) and 10(c).

Figure 9 shows the results provided by the RNG $k - \varepsilon$. These predictions were different from the predictions provided by the Standard $k - \varepsilon$. Plane 2 presents strong inclined secondary currents that forms two vortex at the opposite position of that predicted by the Standard $k - \varepsilon$.

At Plane 4 appears a vortex close to the outer wall. The same behaviour predicted by the Standard $k - \varepsilon$ for the pane 5 can be seen again. However, the RNG $k - \varepsilon$ can capture the strong curvature of the streamlines and predicted the growth of two vortex close to the inner wall.

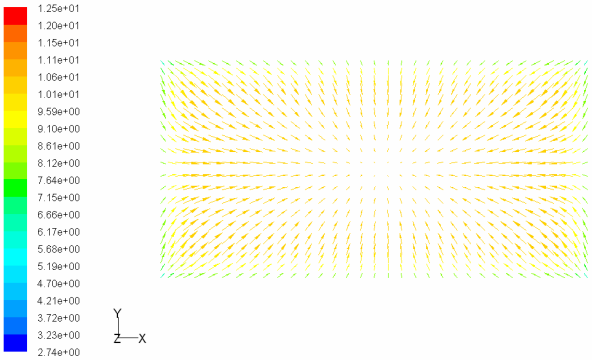

(a) Plane 0, at the middle of the first straight section.

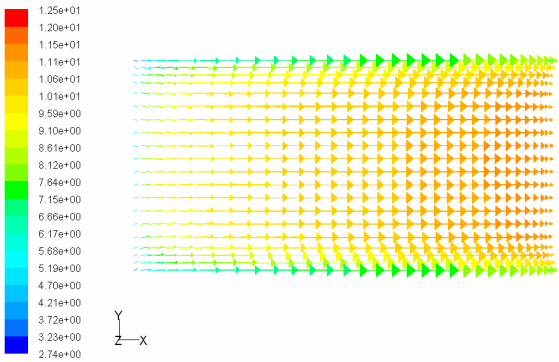

(b) Plane 1, upstream of the bend.

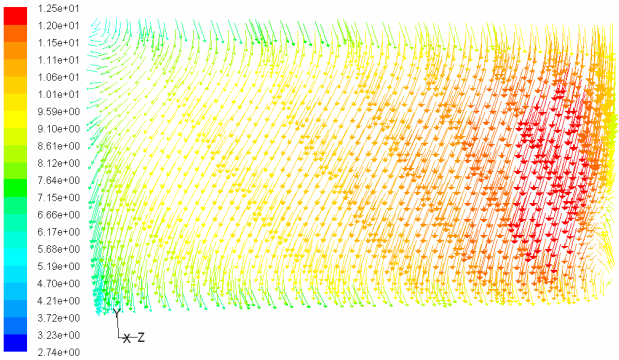

(c) Plane 2, at the first curvature.

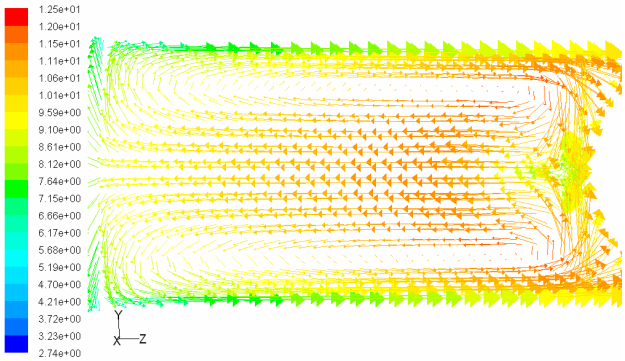

(d) Plane 3, at the middle of the curvature.

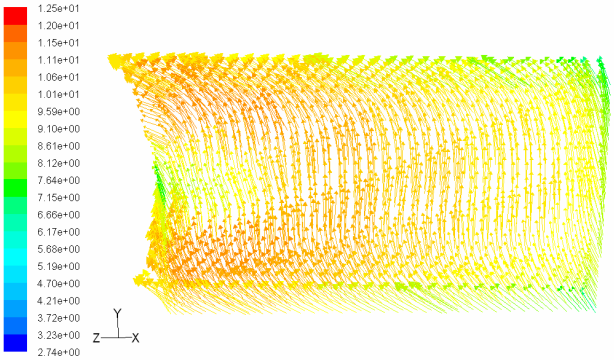

(e) Plane 4, at the second curvature.

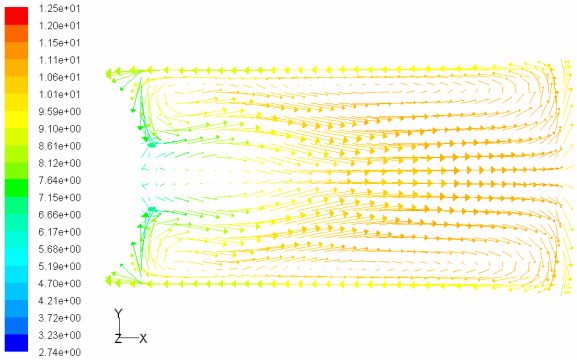

(f) Plane 5, at the exit of bend.

Figure 8 – Secondary flow predicted by the Standard k - ε model, from outer to inner wall: (a) at plane 0, (b) at plane 1, (c) at plane 2, (d) at plane 3, (e) at plane 4 and (f) at plane 5.

Results of the RSM are shown in Figure 10. It can be seen a similar behavior to that have founded by the others turbulence models. However, there was not an agreement on the prediction of the vortex that appears at plane 2. This model can not able to predicted a vortex near the outer wall at plane 4 as seen by the results of RNG k – ε.

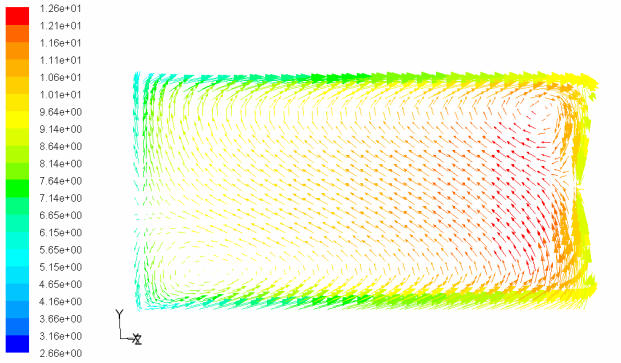

(a) Plane 2, at the first curvature.

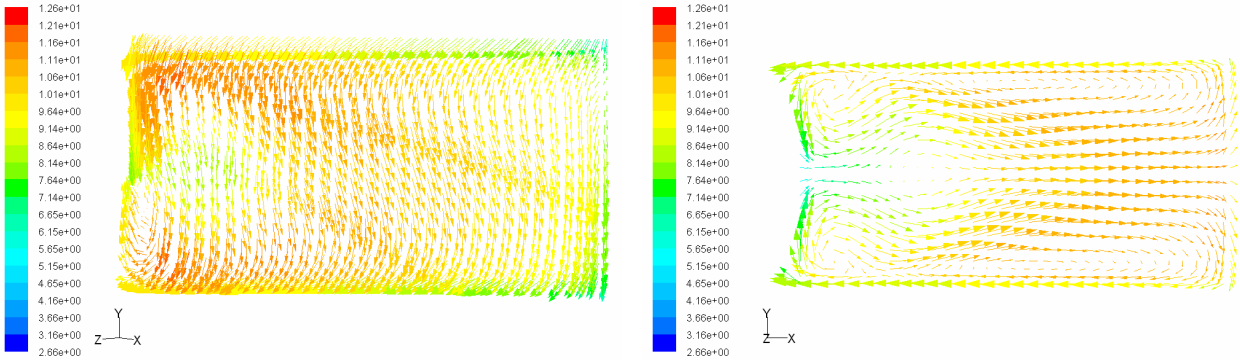

(b) Plane 4, at the second curvature.

(c) Plane 5, at the exit of bend.

Figure 9 – Secondary flow predicted by the RNG k – ε model: (a) at plane 2, (b) at plane 4 and (c) at plane 5.

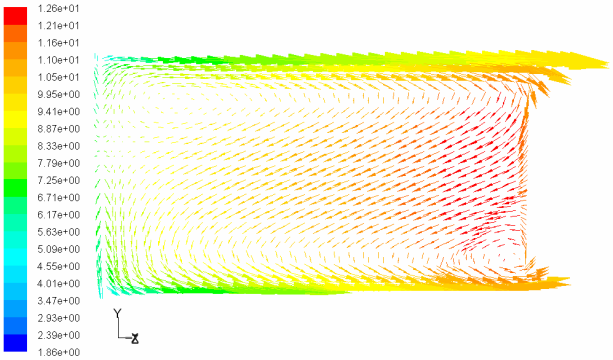

(a) Plane 2, at the first curvature.

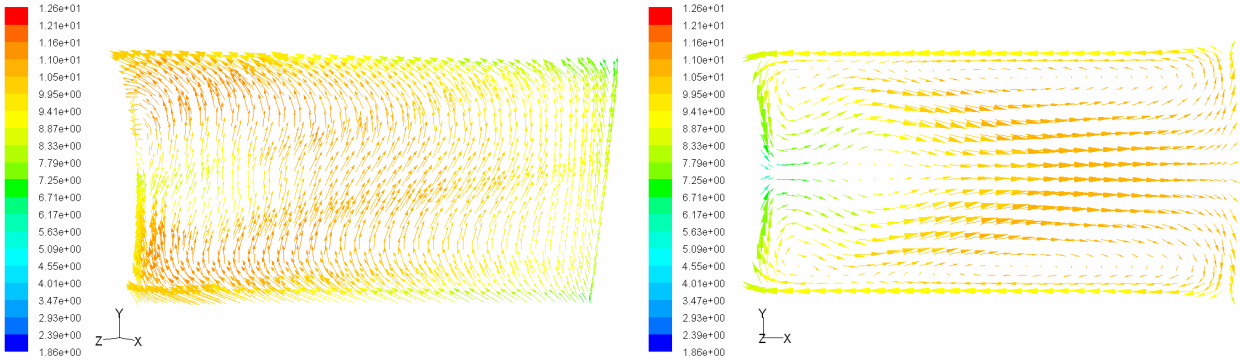

(b) Plane 4, at the second curvature.

(c) Plane 5, at the exit of bend.

Figure 10 – Secondary flow predicted by the RSM: (a) at plane 2, (b) at plane 4, (c) at plane 5.

3. Conclusion

Three turbulence models were tested successfully to the prediction of the longitudinal velocity and secondary flow in a curved test section of a wind tunnel. The RNG $k - \varepsilon$ model has provided better results. This model has indicated the best profile of velocity magnitude at the exit of wind tunnel and has shown the best contour of velocity magnitude. But the profiles of the Standard $k - \varepsilon$ and the RSM model were not bad.

The RNG $k - \varepsilon$ model improves the accuracy for rapidly strained and swirling flows. This characteristic of the model appears on the results of the prediction of the secondary flow. The good results provided by the RSM model is due it is more complete than the others two models because have more equations and has the greater potential to give accurate predictions for complex flows.

The wind tunnel flow is little complex because the constant values of velocity develop a profile that changes a lot during the simulation. At first is constant, in a second time is concentrated at the internal part of curvature and finally changes to opposite side and finish with developed flow.

To the static pressure the profile obtained are similar to three turbulence models. At first time it constant in the curvature, developed a higher value at external part of curvature and at the finish is constant, but with a lesser value than the beginning. It is clearly that this behavior is a consequence of the curved channel.

The aim of this work was to provide the behavior of the flow that occurs in a wind tunnel located at the Fluid Mechanics Laboratory – DEM/ UFPA. Further effects, especially experimental validation are needed to improve the capability of the models for predicting flow with complex boundary conditions.

4. Acknowledgement

To the Energy Biomass and Environment Group – DEM/ UFPA that made possible the execution of this work.

5. References

Cheng, K.C., Yuen, F.P., 1987, “Flow visualization studies on secondary flow patterns in straight tubes downstream of a 180º bend and in isothermally heated horizontal tubes”, Trans. ASME, J. Heat Transfer, Vol.109, pp.49-61.

Humphrey, J. A. C., Whitelaw, J. H. and Yee, G., 1981, "Turbulent flow in a square duct with strong curvature", Journal of Fluid Mechanics, vol. 103 , pp. 443-463.

Iacovides, H., Lauber, B.E., Loizou P.A., Zhao, H.H., 1990, “Turbulent boundary-layer development around a square-sectioned U-bend: Measurements and computation.” ASME, Journal of Fluids Engineering, Vol.112, pp. 409-415.

Kim W.J., Patel V.C., 1994, “Origin and decay of longitudinal vortices in developing flow in a cuved rectangular duct”, Journal of Fluids Engineering, Vol.116, pp.45-52.

Shao X., Wang H., Chen Z., 2003, “Numerical modeling of turbulent flow in curved channels of compound cross section”, Advances in Water Resourses, Vol.26, pp.525-539.

Schlichting, H., 1968, "Boundary-Layer Theory", McGraw-Hill, New York.

Shima N., Kawai T., Okamoto M., Tsuchikura R., 2000, “Prediction of streamline curvature effects on wall-bounded turbulent flows”, International Journal of Heat and Fluid Flow, Vol.21, pp.614-619.

Silva, A.P.S., Menut P. P. P., Su J., 1998, “Turbulência”, Anais da I Escola de Primavera de Transição e Turbulência.

Treaster, A.L., Yocum, A.M., 1979, “The calibration and application of five-hole probes”, ISA Transactions, Vol.18, pp.23-34.

Yamamoto, K., Wu, Xiaoyun, Nozaki, K., Hayamizu, Y., 2006, “Visualization of Taylor-Dean flow in a curved duct of square cross-section”, Fluid Dynamics Research, Vol.38, pp.1-18.

Winters, K.H., 1987, “A bifurcation study of laminar flow in a curved tube of rectangular cross-section”, Journal Fluid Mechanics, Vol.180, pp. 343-369.

6. Copyright Notice

Proceedings of the 11th Brazilian Congress of Thermal Sciences and Engineering -- ENCIT 2006
Braz. Soc. of Mechanical Sciences and Engineering -- ABCM, Curitiba, Brazil, Dec. 5-8, 2006

Paper CIT06-0585

ANÁLISE DO COMPORTAMENTO DO ESCOAMENTO DE AR EM UMA CÂMARA DE COMBUSTÃO TUBULAR USANDO CFD

Giuliano Gardolinski Venson
Universidade Federal de Minas Gerais. Depto. de Engenharia Mecânica. Avenida Antônio Carlos 6627, Campus Universitário
Belo Horizonte, Minas Gerais, Brasil. CEP 31270-901
venson@ufmg.br

Gilberto Augusto Amado Moreira
Universidade Federal de Minas Gerais. Depto. de Engenharia Mecânica. Avenida Antônio Carlos 6627, Campus Universitário
Belo Horizonte, Minas Gerais, Brasil. CEP 31270-901
gilbertomoreira@yahoo.com.br

José Eduardo Mautone Barros
Centro Federal de Educação Tecnológica de Minas Gerais. Depto. de Ensino Superior. Avenida Amazonas 7675, Nova Gameleira
Belo Horizonte, Minas Gerais, Brasil. CEP 30510-000
mautone@des.cefetmg.br

Ramón Molina Valle
Universidade Federal de Minas Gerais. Depto. de Engenharia Mecânica. Avenida Antônio Carlos 6627, Campus Universitário
Belo Horizonte, Minas Gerais, Brasil. CEP 31270-901
ramon@demec.ufmg.br

Resumo. *Neste trabalho é apresentada a modelagem e simulação do escoamento de ar em uma câmara de combustão tubular utilizando um programa computacional comercial baseado no método de volumes finitos. O escoamento turbulento é modelado utilizando os modelos de turbulência k-ε RNG e SST. O objetivo da modelagem é a obtenção e comparação dos perfis de pressão ao longo da câmara. Através da Equação de Bernoulli modificada determinam-se os coeficientes de descarga em cada seção característica, obtendo-se assim a porcentagem de ar que atravessa cada seção. Os coeficientes calculados através dos valores de pressão obtidos nas simulações são comparados com resultados experimentais para validação das modelagens. Os resultados obtidos para a queda de pressão na câmara utilizando o modelo de turbulência SST apresentam desvio médio de -16% em relação aos valores experimentais. Para o modelo k-ε RNG, o desvio médio é -44%.*

Palavras chave: *perfil de pressão, câmara de combustão, método de volumes finitos, CFD.*

1. INTRODUÇÃO

Para se avaliar a qualidade de um processo de combustão é necessário conhecer a quantidade de ar que diretamente participa da combustão. Essa quantidade de ar está diretamente relacionada com a razão de "by-pass" do queimador, que corresponde a parcela de ar que é desviada da sua zona primária em relação à parcela não desviada. Na zona primária é onde ocorre o processo de combustão propriamente dito.

Neste trabalho é apresentada uma metodologia para determinação da razão de "by-pass" de uma câmara de combustão tubular utilizando o conceito de coeficientes de descarga. Os coeficientes são calculados através dos valores de queda de pressão na câmara, considerando diferentes áreas totais de passagem para o escoamento. Os valores de queda de pressão são obtidos através dos perfis de pressão obtidos em simulações do escoamento de ar na câmara, utilizando um programa comercial baseado no método de volumes finitos. O escoamento de ar ao longo da câmara é modelado através dos modelos de turbulência k-ε RNG e SST, ambos baseados nas equações de Navier-Stokes.

1.1. Câmara de Combustão

Uma câmara de combustão consiste de um equipamento térmico no qual a mistura ar-combustível é queimada. A energia química proveniente do combustível é transformada em energia térmica no escoamento de ar através do processo de combustão. As dimensões da câmara de combustão em estudo podem ser vistas na Fig. 1 e as principais partes constituintes na Fig. 2. Na câmara em estudo, o desvio do ar primário é realizado através de um difusor posicionado a montante do orifício primário, o qual pode ser vistos na Fig. 2. O orifício primário é a seção característica de passagem da parcela principal do ar de combustão. A parcela de ar que é desviada da zona primária é novamente introduzida no tubo de chama através dos orifícios secundários e terciários, também mostrados na Fig. 2.

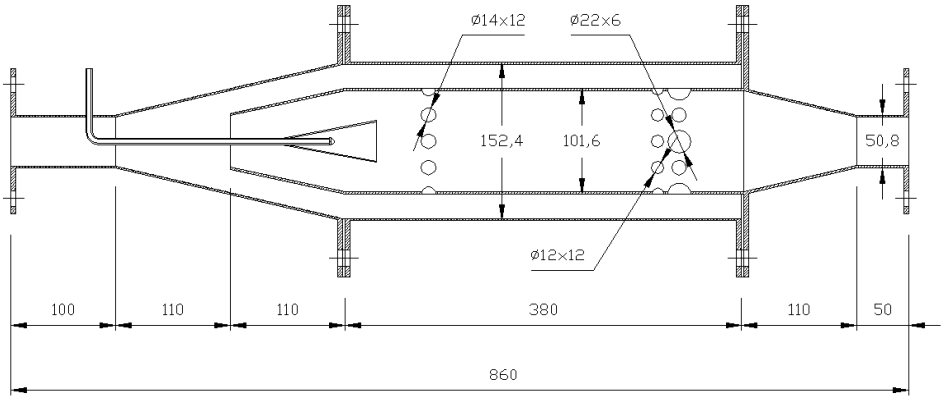

Figura 1. Dimensões da Câmara de Combustão (dimensões em mm)

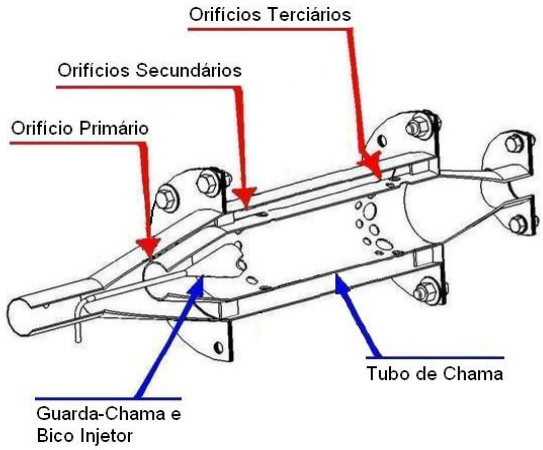

Figura 2. Corte Transversal da Câmara de Combustão

1.2. Modelagem de Escoamentos Turbulentos

Escoamentos turbulentos são definidos como escoamentos viscosos nos quais as partículas fluidas movem-se aleatoriamente, de forma tridimensional, transiente, rotacional e irregular.

Modelos matemáticos específicos são utilizados para prever os diferentes efeitos gerados pelo escoamento, onde a turbulência é um fator sempre presente. Alguns modelos de turbulência têm aplicações limitadas, enquanto outros podem ser utilizados em uma grande classe de escoamentos com certo grau de aproximação. Os modelos são baseados nas equações de Navier-Stokes, sendo classificados como de tensões de Reynolds (*Reynolds stress models*) ou de viscosidade turbulenta (*eddy-viscosity models*) (Maliska, 1995).

Os modelos de tensões de Reynolds surgiram por volta de 1895 quando Osborne Reynolds introduziu as equações médias de Navier-Stokes. Estes modelos eram muito limitados e podiam ser aplicados somente em problemas particulares ou com configurações geométricas semelhantes às anteriormente já estudadas, sendo inapropriados para escoamentos sobre geometrias complexas (Chatot, 2002). Com o avanço da computação no período pós Segunda Guerra Mundial, década de 50 do século XX, surgiram os modelos de turbulência de turbulência de 2ª ordem ou modelos de viscosidade turbulenta. Nestes modelos, as quantidades de transporte turbulento são modeladas por equações diferenciais. Os modelos de 2ª ordem mais empregados são os modelos k-ε, k-ω e o SST.

1.3. Modelo de Turbulência k-ε

O modelo k-ε RNG, aperfeiçoado em relação ao modelo k-ε standart, é o modelo de turbulência mais utilizado em análises de escoamento devido a sua estabilidade e robustez. O modelo k-ε utiliza funções de parede escalonáveis em conjunto com funções de parede convencionais, acarretando boa robustez e precisão quando a malha próxima a parede é muito fina. Conforme Maliska (1995), as duas variáveis principais no sistema de equações de conservação são às da continuidade, Eq. (1), e de momento, Eq. (2):

$$\frac{\partial \rho}{\partial t} + \nabla(\rho U) = 0 \tag{1}$$

$$\frac{\partial \rho U}{\partial t} + \nabla(\rho U \otimes U) - \nabla(\mu_{EFF} \nabla U) = \nabla p' + \nabla(\mu_{EFF} \nabla U)^T + B \tag{2}$$

Onde p é a massa especifica do fluido em kg/m^3, U é o vetor velocidade em m/s, u_{EFF} é a viscosidade efetiva considerando efeitos turbulentos em kg/m.s, dada pela Eq. (3), p' é a pressão modificada em Pa, dada pela Eq. (4), e B é soma de todas as forças atuando sobre o corpo em N.

$$p' = p + \frac{2}{3}\rho k \tag{3}$$

$$\mu_{EFF} = \mu + \mu_T \tag{4}$$

Onde p é a pressão estática em Pa, k é a energia cinética turbulenta por unidade de massa em J/kg, μ é viscosidade dinâmica em kg/m.s e μ_T é a viscosidade dinâmica turbulenta em kg/m.s

O modelo k-ε assume que a viscosidade dinâmica turbulenta está associada à energia cinética turbulenta:

$$\mu_T = \frac{C_\mu \rho k^2}{\varepsilon} \tag{5}$$

Onde C_μ é uma constante adimensional do modelo de turbulência com valor de 0,09 e ε é taxa de dissipação turbulenta em m^2/s^3.

Os valores de k e ε são calculados diretamente segundo as equações diferenciais de transporte de energia cinética turbulenta e taxa de dissipação turbulenta, respectivamente:

$$\frac{\partial(\rho k)}{\partial t} + \nabla(\rho U k) = \nabla\left[\left(\mu + \frac{\mu_T}{\sigma_k}\right)\nabla k\right] + P_k - \rho\varepsilon \tag{6}$$

$$\frac{\partial(\rho \varepsilon)}{\partial t} + \nabla(\rho U \varepsilon) = \nabla\left[\left(\mu + \frac{\mu_T}{\sigma_\varepsilon}\right)\nabla \varepsilon\right] + \frac{\varepsilon}{k}\left(C_{\varepsilon 1} P_k - C_{\varepsilon 2}\rho\varepsilon\right) \tag{7}$$

Onde σ_k e σ_ε são constantes adimensionais das equações com valores iguais a 1 e 1,3 respectivamente, P_k é a produção de turbulência devido a forças viscosas em kg/m.s^3, modelada através da Eq. (8), e $C_{\varepsilon 1}$ e $C_{\varepsilon 2}$ são constantes adimensionais com valores de 1,44 e 1,92 respectivamente.

$$P_k = \mu_T \nabla U\left(\nabla U + \nabla U^T\right) - \frac{2}{3}(\nabla U)(3\mu_T \nabla U + \rho k) + P_{kb} \tag{8}$$

1.3. Modelo de Turbulência SST

Os modelos de turbulência baseados nas equações ε falham na previsão de separação do escoamento sobre geometrias complexas, pois prevêm esta separação com muito atraso (Sklavounos e Rigas, 2004). O modelo SST, ou Shear Stress Transport, foi desenvolvido para superar as deficiências do modelo k-ε tradicional. Este modelo é mais completo se comparado aos modelos k-ε e k-ω pois introduz uma nova equação, a do transporte de tensões de cisalhamento turbulentas. Sendo assim, este modelo é mais recomendado em simulações onde se requer uma grande precisão das condições nas diferentes camadas do escoamento. O modelo k-ω assume que a viscosidade turbulenta está associada à energia cinética turbulenta e a freqüência turbulenta segundo:

$$\mu_T = \frac{\rho k}{\omega} \tag{9}$$

Onde ρ é a massa especifica do fluido em kg/m^3, k é a energia cinética turbulenta por unidade de massa em m^2/s^2 e w é freqüência turbulenta em Hz.

O modelo emprega duas equações de transporte, uma para a energia cinética turbulenta e outra para a freqüência turbulenta, respectivamente:

$$\frac{\partial(\rho k)}{\partial t} + \nabla(\rho U k) = \nabla\left[\left(\mu + \frac{\mu_T}{\sigma_k}\right)\nabla k\right] + P_k - \beta' \rho k \omega \tag{10}$$

$$\frac{\partial(\rho\omega)}{\partial t}+\nabla(\rho U\omega)=\nabla\left[\left(\mu+\frac{\mu_T}{\sigma_\omega}\right)\nabla\omega\right]+\frac{\alpha\omega P_k}{k}-\beta\rho\omega^2 \tag{11}$$

Onde U é o vetor velocidade em m/s, μ é viscosidade dinâmica em kg/m.s, σk e σ_ω são constantes adimensionais das equações com valores iguais a 2, P_k é a produção de turbulência devido a forças viscosas em kg/m.s^3, modelada através da Eq. (8) e α, β, β^* são constantes adimensionais com valores igual a 0,56, 0,075 e 0,09 respectivamente.

Os modelos de turbulência k-ε e k-ω não levam em consideração o transporte das tensões de cisalhamento turbulentas, resultando em uma subestimação nos parâmetros de viscosidade turbulenta. O comportamento correto do transporte turbulento pode ser obtido através do limite da formulação de viscosidade turbulenta, conforme:

$$\nu_T=\frac{\alpha_1 k}{\max(\alpha_1\omega SF)} \tag{12}$$

Onde ν_T é a viscosidade cinemática turbulenta em m^2/s, α_1 é uma constante adimensional do modelo, F é uma função que associa a distância da parede mais próxima com as variáveis do escoamento k e ω.

1.4. Equação de Bernoulli Modificada

A equação de Bernoulli é utilizada para modulação da vazão em elementos geradores de depressão, podendo ser aplicada em escoamentos incompressíveis, onde por definição o número de Mach não supera o valor de 0,3. No dimensionamento destes elementos o coeficiente de descarga é tabelado em função da razão de áreas de passagem do escoamento. A mesma equação pode ser aplicada para determinação do coeficiente de descarga de uma seção característica se conhecida a vazão mássica nessa seção. O coeficiente de descarga é utilizado matematicamente para corrigir as equações de vazão em função dos efeitos reais do escoamento. A equação de Bernoulli modificada, utilizada em sistemas deprimogênitos, é apresentada em Delmée (1983):

$$\dot{m}=C_d E A_2\sqrt{2\Delta p\rho} \tag{13}$$

Onde $\dot{m}$ é a vazão mássica em kg/s, Cd o coeficiente de descarga adimensional, E o coeficiente adimensional de velocidades, definido através da razão de áreas do escoamento, A2 é área da seção transversal da garganta do elemento em m^2, Δp é a perda de carga gerada no elemento em Pa.

Considerando que as áreas de entrada e saída da câmara de combustão em estudo são iguais, que a vazão mássica é conhecida e utilizando a área total de passagem do escoamento de ar como referência, o coeficiente de descarga é expresso na forma:

$$C_d=\frac{\dot{m}}{A_{REF}\sqrt{2\Delta p\rho}} \tag{14}$$

2. Método para Determinação dos Coeficientes de Descarga

A determinação dos coeficientes de descarga dos orifícios primário, secundários e terciários são obtidos de forma diferencial. Utiliza-se o mesmo método empregado em sistemas elétricos para determinação da resistência elétrica equivalente, quando as resistências são ligadas em paralelo, de acordo com a seguinte equação:

$$\frac{1}{R_{eq}}=\frac{1}{R_1}+\frac{1}{R_2}+\frac{1}{R_3}+.....+\frac{1}{R_n} \tag{16}$$

Em função dos coeficientes de descarga de cada seção característica da câmara de combustão, a Eq. (16) reescreve-se na seguinte forma:

$$\frac{1}{C_{d\,eq}}=\frac{1}{C_{d1}}+\frac{1}{C_{d2}}+\frac{1}{C_{d3}} \tag{17}$$

Onde C_{d1}, C_{d2} e C_{d3} são os coeficientes de descarga dos orifícios primários, secundários e terciários, respectivamente.

O método prático para obtenção destes coeficientes consiste na obstrução alternada dos orifícios de passagem de ar. Ao fechar-se um ou mais conjuntos de orifícios, os respectivos coeficientes de descarga tornam-se zero, gerando diferentes coeficientes de descarga equivalentes para cada combinação testada. Monta-se assim um sistema de equações para determinação do coeficiente de descarga de cada conjunto de orifícios. A partir da relação entre estes valores é possível calcular a porcentagem mássica de ar que atravessa cada seção e consequentemente, o "by-pass" da câmara.

3. MODELAGEM DO PERFIL DE PRESSÃO NA CÂMARA DE COMBUSTÃO

3.1. Condições de Simulação do Escoamento de Ar

As simulações do escoamento ao longo da câmara de combustão são realizadas utilizando o programa comercial CFX 9.0. Como condições de entrada da modelagem são definidas a vazão mássica de ar, temperatura e pressão absoluta. A condição de saída é a conservação da vazão mássica de ar. Os valores de entrada são: vazão mássica de 0,085 kg/s, temperatura de 25 ^{o}C e pressão absoluta de 101,3 kPa (1 atm). Foram realizadas simulações utilizando os modelos de turbulência k-ε RNG e SST. Em ambos as modelagens não foram alteradas as constantes de turbulência padrões dos modelos. O volume da câmara de combustão utilizado para a análise foi a sua geometria real.

Para se avaliar o comportamento do coeficiente de descarga da câmara, em função das diferentes áreas de passagem do escoamento de ar, foram realizadas quatro simulações para cada modelo de turbulência utilizado, as quais são descritas na Tab. 1. Nos diferentes casos apresentados, os fechamentos dos orifícios citados foram obtidos alterando-se o desenho base da câmara de combustão.

Tabela 1. Descrição das Condições de Simulação

número da simulação	**descrição**	**equação do coeficiente de descarga equivalente**
1	todos os orifícios abertos	$\frac{1}{C_{d1}}+\frac{1}{C_{d2}}+\frac{1}{C_{d3}}$
2	somente o orifício primário aberto (orifícios secundários e terciários fechados)	$\frac{1}{C_{d1}}$
3	orifícios primário e secundários abertos (orifícios terciários fechados)	$\frac{1}{C_{d1}}+\frac{1}{C_{d2}}$
4	orifícios primário e terciários abertos (orifícios secundários fechados)	$\frac{1}{C_{d1}}+\frac{1}{C_{d3}}$

3.2. Características das Malhas Geradas no CFX

Nas diferentes simulações foram utilizadas as mesmas configurações de malha. A Figura 3 mostra o aspecto externo da malha e a Tab. 2 apresenta os detalhes das malhas, geradas automaticamente pelo software.

Figura 3. Malha Gerada no CFX.

Tabela 2. Detalhes das Malhas Geradas no CFX

parâmetro	número da simulação			
	1	2	3	4
número total de nós	78.575	44.250	55.606	66.569
número total de elementos	408.630	225.484	285.535	345.426
número total de tetraedros	408.630	225.484	285.535	345.426
número total de faces	35.580	22.342	26.764	30.262

3.3. Perfil de Pressão na Câmara nas Condições Simuladas

A partir das simulações do escoamento de ar ao longo da câmara são obtidas as respectivas curvas de pressão relativa ao longo do eixo axial, as quais são mostradas nas Figs. 4 e 5. Os perfis de pressão e velocidade dentro da câmara obtidos através da simulação com o modelo SST, considerando todos os orifícios abertos, são mostrados nas Figs. 6 e 7 respectivamente.

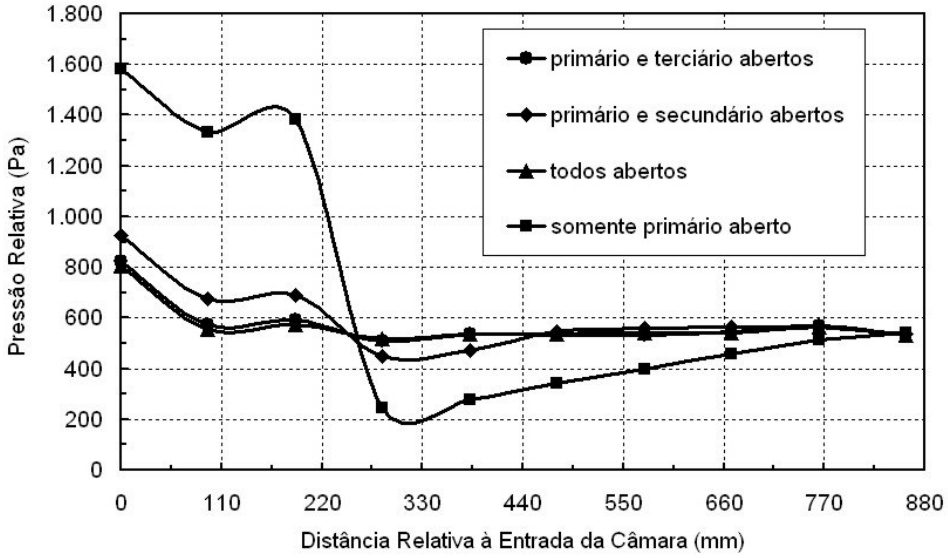

Figura 4. Perfil de Pressão ao Longo da Câmara de obtido com o Modelo k-ε RNG

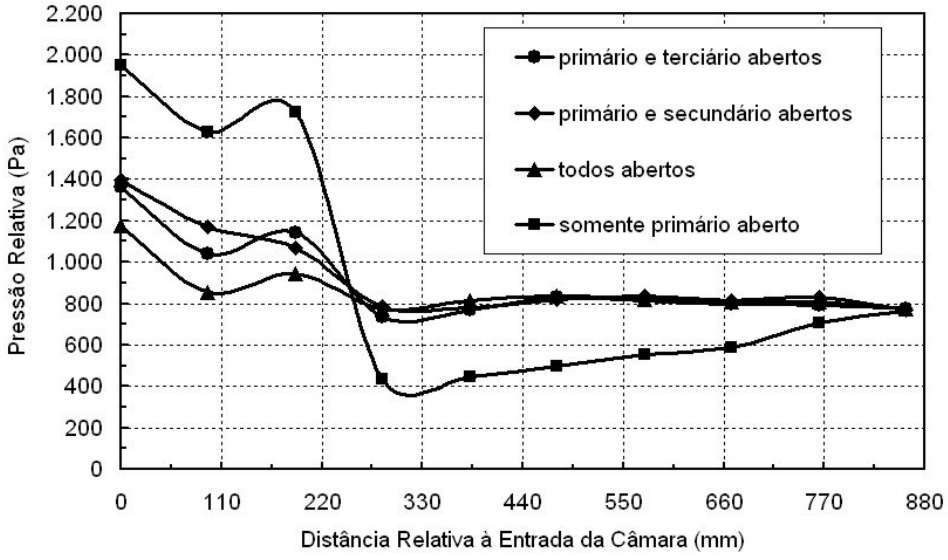

Figura 5. Perfil de Pressão ao Longo da Câmara de obtido com o Modelo SST

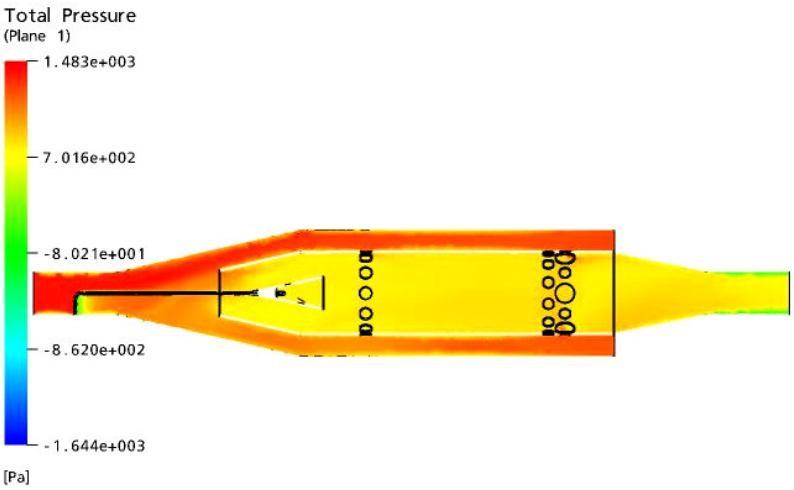

Figura 6. Perfil de Pressão ao Longo da Câmara Utilizando o Modelo SST, para todos os Orifícios Abertos

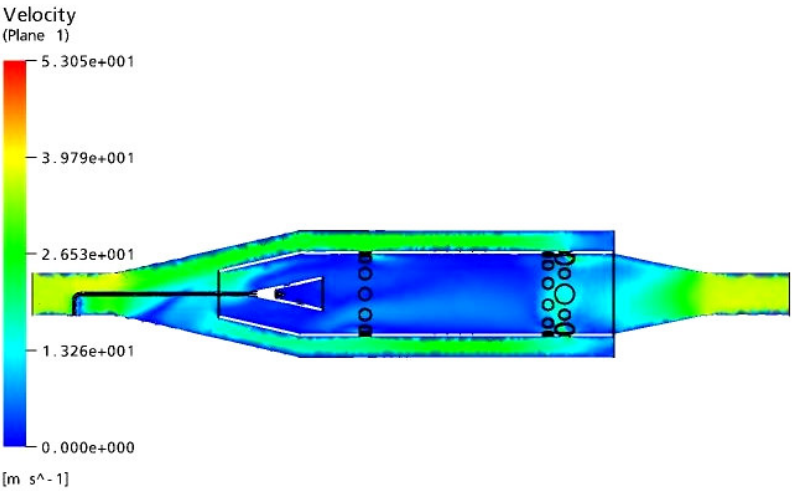

Figura 7. Perfil de Velocidades ao Longo da Câmara Utilizando o Modelo SST, para todos os Orifícios Abertos

A partir dos valores de velocidades obtidos na Fig. 7 verifica-se que a velocidade máxima do escoamento ao longo da câmara é da ordem dos 40 m/s, o que corresponde a um número de Mach de 0,12. Sendo assim, considera-se o escoamento incompressível, podendo ser aplicada a Eq. (14) para cálculo dos coeficientes de descarga.

3.4. Obtenção dos Coeficientes de Descarga

A partir dos valores de queda de pressão mostrados nas Figs. 4 e 5 e das áreas de referência de passagem do ar, calculadas através das dimensões mostradas na Fig. 1, são obtidos os coeficientes de descarga equivalentes em cada condição de simulação, para os dois modelos de turbulência empregados.

Tabela 3. Coeficientes de Descarga Equivalentes obtidos nas Simulações

número da simulação	**vazão mássica de ar (kg/s)**	**área de referência (m^2)**	**modelo de turbulência**			
			k-ε RNG		**SST**	
			queda de pressão (Pa)	**coeficiente de descarga equivalente**	**queda de pressão (Pa)**	**coeficiente de descarga equivalente**
1	0,085	0,00844	272	0,41429	402	0,34078
2	0,085	0,00203	1.040	0,88181	1.190	0,89850
3	0,085	0,00387	389	0,75433	627	0,67437
4	0,085	0,00659	288	0,51550	585	0,38993

Os coeficientes de descarga de cada seção característica são obtidos através dos valores equivalentes, mostrados na Tab. 3, e das respectivas equações, mostradas na Tab. 1. Os valores dos coeficientes são mostrados nas Tabs. 4 e 5. A Tabela 6 apresenta os valores aproximados para a razão de "by-pass" da câmara de combustão, obtidas para cada modelo de turbulência utilizado. O valor do "by-pass" é calculado através da razão da soma dos coeficientes secundários e terciários com o coeficiente de descarga do orifício primário.

Tabela 4. Coeficientes de Descarga das Seções Características com base nas Simulações

número da simulação	**k-ε RNG**				**SST**			
	$1/C_{deq}$	**$1/C_{d1}$**	**$1/C_{d2}$**	**$1/C_{d3}$**	**$1/C_{deq}$**	**$1/C_{d1}$**	**$1/C_{d2}$**	**$1/C_{d3}$**
1	**2,41380**	1,22812	0,28574	-	**2,93447**	1,11297	0,36990	1,45160
2	1,22812	**1,22812**	-	-	1,11297	**1,11297**	-	-
3	1,51386	1,22812	**0,28574**	-	1,48287	1,11297	**0,36990**	-
4	2,12806	1,22812	-	**0,89993**	2,56457	1,11297	-	**1,45160**

Tabela 5. Razão de By-Pass com base nos Coeficientes de Descarga

região da câmara de combustão	**k-ε RNG**		**SST**	
	$1/C_d$	**valor percentual**	**$1/C_d$**	**valor percentual**
todos os orifícios	2,41380	100,00%	2,93447	100,00%
orifício primário	1,22812	50,88%	1,11297	37,93%
orifícios secundários	0,28574	11,84%	0,36990	12,61%
orifícios terciários	0,89993	37,26%	1,45160	49,47%
razão de by-pass	**1:1**		**5:3**	

O número de Reynolds do escoamento, calculado através da vazão mássica de ar e da área transversal na entrada da câmara de combustão, é de 124.000, comprovando que o escoamento está no regime turbulento.

4. Validação da Modelagem

Os resultados obtidos nas simulações foram comparados com resultados experimentais obtidos através da câmara de combustão instrumentada, mostrada na Fig. 8. Na montagem experimental foi empregado um sensor de pressão diferencial, com as respectivas tomadas de pressão fixadas na entrada e saída da câmara, conforme mostrado na Fig 8. O sensor utilizado foi o MPX-5010 DP, com faixa de medição de 0 a 10 kPa e incerteza de 100 Pa. A vazão mássica do escoamento foi obtida a partir da queda de pressão em uma placa de orifício colocada a montante da câmara de combustão. Os resultados experimentais, para as quatro condições estudadas são mostrados nas Tabs. 6 a 8.

Figura 7. Câmara de Combustão Instrumentada

Tabela 6. Coeficientes de Descarga Equivalentes obtidos Experimentalmente

número do ensaio	**vazão mássica de ar (kg/s)**	**área de referência (m^2)**	**queda de pressão na câmara de combustão (Pa)**	**coeficiente de descarga equivalente**
1	0,085	0,00844	499	0,31508
2	0,083	0,00203	1.392	0,76370
3	0,084	0,00387	767	0,58572
4	0,084	0,00659	673	0,36024

Tabela 7. Coeficientes de Descarga de Cada Seção Característica com base nos Valores Experimentais

número do ensaio	**$1/C_{deq}$**	**$1/C_{d1}$**	**$1/C_{d2}$**	**$1/C_{d3}$**
1	**3,17382**	1,30942	0,39787	1,46654
2	1,30942	**1,30942**	-	-
3	1,70729	1,30942	**0,39787**	-
4	2,77596	1,30942	-	**1,46654**

Tabela 8. Razão de By-Pass com base nos Coeficientes de Descarga

região da câmara de combustão	**experimental**	
	$1/C_d$	**valor percentual**
todos os orifícios	3,17382	100,00%
orifício primário	1,30942	41,26%
orifícios secundários	0,39787	12,54%
orifícios terciários	1,46654	46,21%
razão de by-pass	**3:2**	

Os critérios utilizados para validação das modelagens são as comparações entre os valores de queda de pressão e os percentuais de fluxo mássico, de cada seção característica, obtidos nas simulações em relação aos resultados experimentais. Os resultados finais são apresentados nas Tabs. 9 a 11.

Tabela 9. Desvios entre os Resultados Simulados e Experimentais para a Queda de Pressão

número da simulação/ensaio	**queda de pressão na câmara**			**desvio dos valores simulados em relação aos experimentais**	
	experimental	**k-ε RNG**	**SST**	**k-ε RNG**	**SST**
1	499	272	402	- 45,45%	+ 19,38%
2	1.392	1.040	1.190	- 25,29%	- 14,51%
3	767	389	627	- 49,28%	- 18,25%
4	673	288	585	- 57,23%	- 13,12%

Tabela 10. Desvios entre os Resultados Simulados e Experimentais para os Coeficientes de Descarga

região da câmara de combustão	**1 / Cd**			**desvio dos valores simulados em relação aos experimentais**	
	experimental	**k-ε RNG**	**SST**	**k-ε RNG**	**SST**
todos os orifícios	3,17382	2,41380	2,93447	- 23,95%	- 7,54%
orifício primário	1,30942	1,22812	1,11297	- 6,21%	- 15,00%
orifícios secundários	0,39787	0,28574	0,36990	- 28,18%	- 7,03%
orifícios terciários	1,46654	0,89993	1,45160	- 38,64%	- 1,02%

Tabela 11. Desvios entre os Resultados Simulados e Experimentais para os Percentuais de Fluxo Mássico

região da câmara de combustão	**percentuais de fluxo mássico**			**desvio dos valores simulados em relação aos experimentais**	
	experimental	**k-ε RNG**	**SST**	**k-ε RNG**	**SST**
todos os orifícios	100,00%	100,00%	100,00%	-	-
orifício primário	41,26%	50,88%	37,93%	+ 23,32%	- 8,07%
orifícios secundários	12,54%	11,84%	12,61%	- 5,57%	+ 0,55%
orifícios terciários	46,21%	37,28%	49,47%	- 19,31%	+ 7,05%
razão de by-pass	**3:2**	**1:1**	**5:3**	**- 33,33%**	**+ 11,11%**

5. CONCLUSÕES

As simulações do escoamento de ar ao longo da câmara de combustão, utilizando os modelos de turbulência k-ε RNG e SST, retratam o comportamento físico das quedas de pressão nesta, nas diferentes situações analisadas. Utilizando os dois modelos de turbulência, assim como nos ensaios experimentais, a queda de pressão na câmara é menor quanto todos os orifícios estão abertos e maior quanto os orifícios secundários e terciários estão fechados. Este fato está associado diretamente com a área de passagem livre para o escoamento, visto que áreas de passagem maiores acarretam em uma menor perda de pressão.

Utilizando o modelo de turbulência k-ε RNG, os valores de queda de pressão na câmara apresentam desvio médio de -44% em relação aos valores experimentais, com valor máximo de -57% para a condição de orifícios secundários e terciários fechados. Em relação aos coeficientes de descarga, o desvio médio é -24%, com valor máximo de -38%. A razão de by-pass calculada a partir dos coeficientes de descarga apresenta desvio de -33% em relação à calculada experimentalmente. Para o modelo de turbulência SST, os valores de queda de pressão apresentam desvio médio de -16%, com desvio máximo de -19% para a condição de todos os orifícios abertos. Em relação aos coeficientes de descarga, o desvio médio é de -8%, com valor máximo de -15%. A razão de by-pass calculada apresenta desvio de +11% em relação à calculada experimentalmente.

A partir dos resultados mostrados nas Tabs. 9 a 11 verifica-se que o modelo SST se mostra mais adequado para as análises ao longo da câmara de combustão. A comparação e validação dos resultados obtidos permitem estender a metodologia para analisar também os fenômenos de estagnação e recirculação de ar dentro da câmara de combustão.

6. AGRADECIMENTOS

À Fundação de Amparo à Pesquisa do Estado de Minas Gerais, através do apoio financeiro através do projeto FAPEMIG/FINEP EDT 1647/04.

7. REFERÊNCIAS

ANSYS Company, 2003. "CFX Solver Theory Manual". Oxfordshire: CFX.

Chatot, J. J., 2002. "Computational Aerodynamics and Fluid Dynamics: An Introduction". New York: Springer. 186 p.

Delmée, G. J., 1983. "Manual de Medição de Vazão". São Paulo: Editora Edgard Blucher. 474p.

Maliska, C. R., 1995. "Transferência de Calor e Mecânica dos Fluidos Computacional". Rio de Janeiro: Editora Livros Técnicos e Científicos S/A.

Souza, R. A. "Análise de Desempenho de uma Câmara de Combustão para Aplicação em uma Microturbina à Gás". Belo Horizonte: Escola de Engenharia da UFMG, 2005. 60p. (Trabalho de Graduação em Engenharia Mecânica).

Sklavounos S., Rigas F., 2004. "Validation of Turbulence Models in Heavy Gás Dispersion Over Obstacules". Journal of Hazardous Materials, A108 9-20. Elsevier. pp. 12-13.

ANALYSIS OF THE AIR FLOW BEHAVIOR IN A TUBULAR COMBUSTION CHAMBER USING CFD

Giuliano Gardolinski Venson
Federal University of Minas Gerais. Mechanical Engineering Department. Antônio Carlos Avenue 6627
Belo Horizonte, Minas Gerais, Brasil. Zip-Code: 31270-901
venson@ufmg.br

Gilberto Augusto Amado Moreira
Federal University of Minas Gerais. Mechanical Engineering Department. Antônio Carlos Avenue 6627
Belo Horizonte, Minas Gerais, Brasil. Zip-Code: 31270-901
gilbertomoreira@yahoo.com.br

José Eduardo Mautone Barros
Federal Center of Technological Education of Minas Gerais. Amazonas Avenue 7675, Nova Gameleira
Belo Horizonte, Minas Gerais, Brasil. Zip-Code: 30510-000
mautone@des.cefetmg.br

Ramón Molina Valle
Federal University of Minas Gerais. Mechanical Engineering Department. Antônio Carlos Avenue 6627
Belo Horizonte, Minas Gerais, Brasil. Zip-Code: 31270-901
ramon@demec.ufmg.br

Abstract
This work presents the modeling and simulation of the air flow in a tubular combustion chamber using a commercial computational program based at the finite volume method. The turbulent flow is shaped using the Navier-Stokes equation, through the k-ε RNG and SST turbulence models. The objective of the simulation is the achievement and comparison of the pressure profiles along the combustion chamber. Through the modified Bernoulli equation the discharge flow coefficients in each characteristic section are calculated, obtaining the percentage of air that crosses each section. The coefficients calculated through the simulated pressure values are compared with experimental data to validate the modeling process. The pressures drop values obtained using the SST turbulence model presents average deviation of -16% than experimental data. For the k-ε RNG turbulence model, the average deviation is -44%.

Keywords: pressure profile, combustion chamber, finite volume method, CFD.

Paper CIT06-593

OPTIMAL DESIGN OF A MICRO-SCALE VISCOUS PUMPS FOR MAXIMUM MASS FLOW RATE AND MINIMUM POWER CONSUMPTION – PRELIMINARY RESULTS

Alexandre K. da Silva
Department of Mechanical Engineering, University of Hawaii – Manoa, 2540 Dole St., Holmes Hall 302, Honolulu, HI 96822, USA
e-mail: akds@hawaii.edu

Marcelo H. Kobayashi
Department of Mechanical Engineering, University of Hawaii – Manoa, 2540 Dole St., Holmes Hall 302, Honolulu, HI 96822, USA
e-mail: marcelok@hawaii.edu

Carlos F. M. Coimbra
Department of Mechanical Engineering, University of Hawaii – Manoa, 2540 Dole St., Holmes Hall 302, Honolulu, HI 96822, USA
School of Engineering, University of California, P.O. Box 2039, Merced, CA 95344, USA
e-mail: coimbra@hawaii.edu

Abstract. *The present paper addresses the effect of geometric parameters such as channel height and rotor eccentricity on the mass flow rate and power consumption of a two dimensional micro-scale viscous pumps. The objective is to maximize the mass flow rate and at the same time minimize shaft power consumption when an external pressure load is applied along the channel that houses the rotor. Three different viscous micropump configurations were considered, a straight housed pump (I-shaped housing) and two curved housed pumps (L- and U-shaped housings). Because the performance of a micro viscous pumps are based on the asymmetric placement of the rotor within the surrounding housing, the numerical results show that the rotor eccentricity and the channel height have a major effect on the mass flow rate generated by the rotor and on the shaft power demanded by the rotor. Preliminary simulations showed that mass flow rate is maximized when the eccentricity is small. The results also show that micropumps with curved housing (i.e., L and U-shaped configurations) not only provide higher larger mass flow rates when compared with straight housed pumps, but also demand less shaft power to operate. Optimized geometric dimensions of all three configurations are presented for several values of the Reynolds number and pressure load.*

Keywords*. Viscous Pump, Optimal Design, Maximum Mass Flow Rate.*

1. Introduction

Advances in the miniaturization of electro mechanical systems have enabled the fabrication of microsystems or microelectromechanical systems (MEMS) that offer several advantages over conventional devices. These advantages include superior resolution, precision and sensitivity, lower costs, and reliability due to redundancy. In biological applications there is also the possibility of incorporating sensing, processing, and actuation nearby or on the same substrate – see the recent reviews on MEMS Judy (2001) and Ziaie *et al.* (2004). Because of their physical and engineering significance as well as the relevance of their applications, micropumps have figured prominently among the development of MEMS.

Micropumps, broadly defined as having dimensions smaller that 100 μm, have a myriad of applications ranging from single- or two-phase micro cooling devices for the thermal management of transient hot spots in microchips Qu and Mudawar (2002, 2003), to mass spectrometer systems and micropropulsion in space exploration Micci and Ketsdever (2000), to micro total analysis systems (μTAS) Reyes et al. (2002) and Auroux et al. (2002). Common to all these devices is the need to pump fluid at flow rates of up to 1000 milliliter per minute through dimensions of the micro or nano scales. Contrary to microelectronics that succeeded in scaling down its transistors and systems to provide faster and cheaper devices, pumping do not benefit from miniaturization in general. Indeed, ordinary inertia based devices, such as centrifugal pumps, do not work at the very low Reynolds number commonly associated with the micropumping requirements. This is due to the fact that, by its definition, at low Reynolds numbers inertia is small compared to the viscous force. Instead, effective micropumps belong to one of the following two main categories: the positive-displacement or reciprocating pumps and the dynamic or continuous flow pumps – see the recent reviews Nguyen (2002), Laser and Santiago (2004) and Woias (2004).

Typically, reciprocating micropumps use pulsating surface motion to displace the fluid by pressure work. By contrast, the physical-chemical and design principles involved in the continuous flow micropumps vary profusely. They include ultrasonic, electrohydrodynamic, electroosmotic, magnetohydrodynamic or electrochemical actuation. These micropumps do function but require sophisticated fabrication processes and involves complex sealing problems – see

the referred reviews for details. Sen et al. (1996) proposed a rotating micropump, where the relatively large viscous forces at these small scales are used to drive the fluid.

The viscous micropump combines the simplicity in design with effectiveness in pumping. Roughly speaking, the viscous micropump consists of a cylinder asymmetrically placed inside a micro-channel. When the cylinder rotates the difference in shear stresses on the lower and upper half of the cylinder creates a force imbalance that displaces the fluid. After its introduction in 1996, the viscous micropump has been the subject of a stream of publications including Sharatchandra et al. (1997), Sharatchandra et al. (1998), DeCourtye et al. (1998), Abdelgawad et al. (2004), Gad-el-Hak (1999) and Abdelgawad et al. (2005). These authors examined various design features and fundamentals issues associated with such micropumps, including the effects of channel height, rotor eccentricity and angular velocity on the pump performance Sen et al. (1996), slip velocity Sharatchandra et al. (1997), thermal effects Sharatchandra et al. (1998), transient effects Abdelgawad et al. (2004), and multistage configurations Abdelgawad et al. (2005). Yet none of these previous reports have considered the optimization of the mass flow constrained to shaft power consumption, which is a key factor in the design of efficient micropumps. Also, although extensive and detailed, all previous reports have worked with the original I-shaped house micropump.

In the present work we introduce a novel class of curved viscous micropumps with L- and U-shaped house pumps. For each of these house shapes we analyze the effect of the relevant parameters and study the optimum design for maximum mass flow rate at minimum power consumption. We start with a description of the micropump configuration and the numerical modeling in §2. In §3 we validate our numerical results by comparing our present results with the results reported by Sharatchandra et al. (1997) and Abdelgawad et al. (2004). With the validated model we proceed with the definition of the figure of merit and optimization procedure: §4 for unconstrained optimization and §6 constrained by shaft power. In §5 we report the unconstrained optimization of the various micropump shapes and in §7 we report the constrained optimum designs. In the last section §8 we sum up the main findings of this work.

2. Numerical Modeling

Consider the three micropump configurations shown in Fig. 1, where D represents the diameter of the rotor, L_u and L_d are the lengths of the upstream and downstream conduit channels, and H is the height of the conduit channel. Due to viscous diffusion, the clockwise-turning rotor impels the fluid from left to right against an imposed pressure difference $\Delta P = P_H - P_L$.

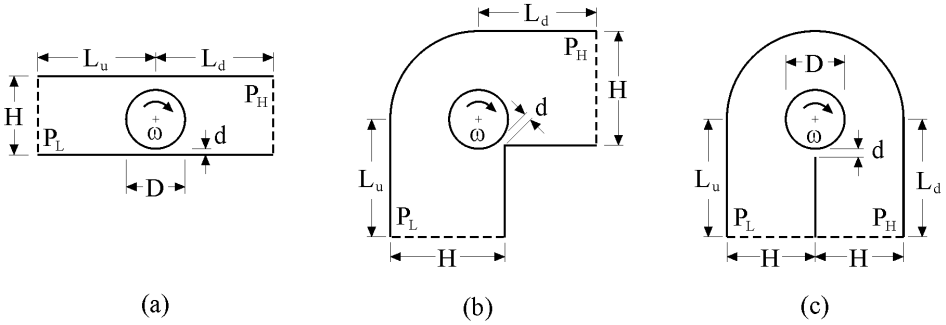

Figure 1. Numerical domain of a viscous micropump: (a) I-shaped channel, L-shaped channel and U-shaped channel.

The effectiveness of a viscous micropump is associated with the eccentricity of the rotor with respect to the surrounding walls. So we introduce a linear dimension d that indicates the distance between the lower wall and the rotor (see Fig. 1). For all three configurations, d = 0 means that the rotor touches the lower wall, not allowing any fluid flow between the lower wall and the rotor. If d > 0, the rotor does not touch the lower wall and fluid is allowed to flow between the rotor and the adjacent surfaces. Finally, d < 0 means that the rotor is partially embedded in the lower wall.Taking D as our length scale, the dimensionless geometrical parameters can be written as

$$(x, y, H, L_u, L_d, d)^* = (x, y, H, L_u, L_d, d)/D \tag{1}$$

The fluid is considered Newtonian with constant properties. Because of the slow character for the flow, no instabilities are expected and the flow is assumed steady, laminar and incompressible. We define the following dimensionless variables

$$(u, v)^* = (u, v)/(\omega D/2), \text{ and } P^* = (P_H - P_L)/(\rho v^2/D^2), \tag{2}$$

and write the governing equations as

$$\nabla \cdot \vec{V}^* = 0\,, \tag{3}$$

$$\mathrm{Re}_D^2 \, (\vec{V}^* \cdot \nabla) \vec{V}^* = - \nabla P^* + \mathrm{Re}_D \, \nabla^2 \vec{V}^* \ , \tag{4}$$

where $\mathrm{Re}_D = (\omega \, D^2/2 \, \nu)$ is the Reynolds number based on the rotor angular velocity and diameter. Due to the definition of the dimensionless pressure drop, Eq. (2), one should note that the pressure head the pump has to overcome is independent of the Reynolds number.

Three different viscous micropump configurations were considered: the standard straight or I-shaped pump, and two novel curved pumps: an L-shaped and a U-shaped. The numerical domain and the nomenclature are also shown in Fig. 1. The flow boundary conditions are: $P^* = P_L^* = 0$ at the inlet and $P^* = P_H^*$ at the exit plane, where $P_H^* = \Delta P^* - P_L^*$. The pressure boundary condition at the inlet and outlet is implemented as $\mathbf{n} \cdot \mathbf{T} = - P_L$ at the inlet and $\mathbf{n} \cdot \mathbf{T} = - P_H$ at the outlet, where $\mathbf{T} = \sigma \mathbf{n}$ is the stress vector and σ is the Stokes stress tensor $\sigma = - P\mathbf{I} + \nu \, (\nabla \mathbf{u} + \nabla \mathbf{u}^T)$. In addition, the tangential components of the velocities are set to zero (i.e., $\mathbf{t} \cdot \mathbf{u} = 0$) at the inlet and outlet of the micropump. Non-slip velocity conditions were used in all internal surfaces of the channel. The velocity of the rotor surface is maintained constant at $U = \omega \, D/2$ for each run. We adopted zero tangential velocities at the inlet and outlet after many numerical tests indicated that fully developed flow conditions at the inlet and outlet were obtained for values of L_u and L_d greater than 4D. In all numerical simulations we take L_u and L_d to be 8D each. It is important to mention that in the case of a U-shaped micro viscous pump (i.e., Fig. 1c), a small gap with a dimensionless length equal to 0.025, was imposed between the inner vertical walls of the inlet and outlet channel located below the rotor. This adaptation was necessary due to the fact the micropump housing was not include in the numerical domain.

Our numerical simulations were performed using the Finite Elements Method toolbox COMSOL Multiphysics®, v. 3.2 from COMSOL, Inc. Second and first order Lagrange p2-p1 mixed finite-elements were used to stabilize the pressure (i.e., 2nd order Lagrange elements to model velocity and linear Lagrange elements for the pressure). The mesh density was exhaustively tested in order to guarantee that the results were mesh-independent. Table 1 exemplifies the mesh convergence of two figures of merit: dimensionless average flow velocity ($\overline{u}^*$) and dimensionless shaft power (W'^*/Re_D^2), which are defined later in the text (§ 3 and 7), for an I-shaped viscous micropump. According to Table 1, the ideal mesh density for the average flow velocity is obtained relatively fast when compared with the mesh density needed for the evaluation of the shaft power, which, through the shear stresses, involves the derivatives of the velocity at the surface of the rotor. For all three configurations, the optimal number of elements is between 10,000 and 15,000, which are distributed unevenly through the numerical domain, with a denser mesh being used in the neighborhood of the rotor. When the computation of the group W'^*/Re_D^2 is required (i.e., Figs. 10-13), an even higher concentration of elements was used around the rotor, which increases the total number of elements to over 20,000 on average, depending on the channel height.

Table 1. Fig. 1a, $\mathrm{Re}_D = \Delta P^* = 1$, $H^*=1.5$ and $d^* = 0.6$.

Number of elements	$\overline{u}^*$	$\left\|(\overline{u}_i^* - \overline{u}_{i+1}^*)/\overline{u}_i^*\right\| \times 10^2$	W'^*/Re_D^2	$\left\|(W'^*_i - W'^*_{i+1})/W'^*_i\right\| \times 10^2$
109	0.073923	< 0.1 %	33.96356	-
436	0.073908	< 0.1 %	31.12104	-
1744	0.073882	< 0.1 %	26.69661	14 %
3486	0.073878	< 0.1 %	25.67958	3.8 %
11216	0.073877	< 0.1 %	25.25148	1.6 %
28662	0.073878	< 0.1 %	25.05145	0.8 %

The solution was obtained with a stationary, non-linear solver based on a damped Newton's Method. The relative error convergence criterion is the weighted Euclidian norm defined as

$$\mathrm{err} = \left[\frac{1}{N} \sum_i \left(\frac{|E_i|}{W_i} \right)^2 \right]^{1/2} \tag{5}$$

where N is the number of degrees of freedom, $\mathbf{E}_i = \mathbf{U}_i - \mathbf{U}_{i-1}$ is the estimated error of the current solution vector $\mathbf{U}_i$ and $W_i = \max(|\mathbf{U}_i|, \mathbf{S}_i)$ are the weighted factors. The $\mathbf{S}_i$ factor is defined as the product of a constant, in this case 0.1, times the average of all $|\mathbf{U}_j|$ for all the degrees of freedom. The damping factor was set initially equal to 10^{-4} and the convergence criterion was set equal to 10^{-6}.

3. Validation of the Method

First, we validate our numerical code for this application against previous results obtained by Sharatchandra et al. (1997) and Abdelgawad et al. (2004). Table 2 compares the effect of the imposed pressure load on the average fluid

velocity ($\bar{u}^*$) at the exit plane between the present results and the results obtained by Sharatchandra et al. (1997), considering $Re_D = 1$, $H^*=1.5$ and $d^* = d^*_{max} = 0.025$, where the average fluid velocity is defined as

$$\bar{u}=H^{-1}\int_0^H u(y)dy\,, \tag{6}$$

and d^*_{max} stands for the minimal distance between the rotor and the lower wall considered by Sharatchandra et al. (1997) in their numerical calculations. In the present work d^*_{max} is set equal to 0.025.
According to Table 2, an acceptable overall agreement with previous results is achieved with an average difference of the order of 1% throughout the relevant range of ΔP^*. Table 3 validates our code for a configuration in which the parameters Re_D, ΔP^* and ε_{mod} are held fixed at 1, 1 and 0.25 respectively, and H^* varies as indicated. ε_{mod} is the modified eccentricity of the rotor defined by Sharatchandra et al. (1997) as

$$\varepsilon_{mod} = 0.5(H - D - d)/D = 0.5(H^* - 1) - d^*\,, \tag{7}$$

where d^* is the dimensionless distance between the rotor and the lower wall shown in Fig. (1). One should notice that, Table. 3 not only shows a good agreement between our results and the data obtained by Sharatchandra et al. (1997), but also, shows the detrimental effect of the channel height (H^*) on the overall performance of the pump for a fixed value of $\varepsilon_{mod} = 0.25$. According to Eq. 7, the larger the channel height (H^*), the closer the rotor is to the centerline of the channel if ε_{mod} is held fixed. In other words, the gap d^* increases with H^*, which in turn reduces the average fluid velocity.

Table 2. Validation of the numerical results for: Fig. 1a, $Re_D= 1$, $H^*=1.5$ and $d^* = d^*_{max} = 0.025$.

ΔP^*	$\bar{u}^*$ Present Work	$\bar{u}^*$ Sharatchandra et al. (1997)	Difference %
0	0.105789	0.106	0.2
7.5	0.074099	0.075	1.2
1.5	0.042410	0.043	1.4
22.5	0.010702	0.011	2.8
30	–0.020967	–0.021	0.16

Table 3. Validation of the numerical results for: Fig. 1a, $Re_D= 1$, $\Delta P^* =1$, and $\varepsilon_{mod} = 0.25$.

H^*	$\bar{u}^*$ Present Work	$\bar{u}^*$ Sharatchandra et al. (1997)	Difference %
1.5	0.101568	0.102	0.42
2	0.055956	0.057	1.8
2.5	0.026987	0.027	0.05

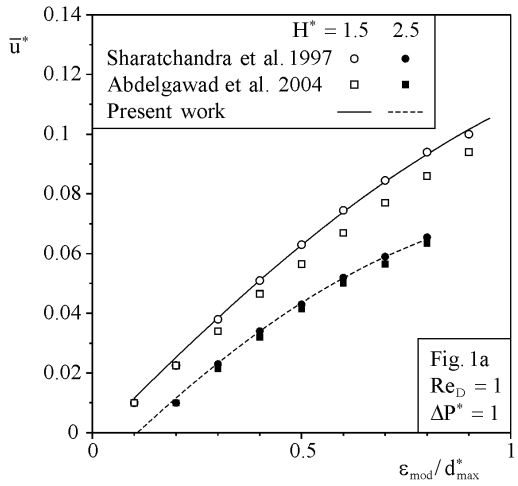

Figure 2. Code validation.

To conclude the code validation, the effect of a third parameter ($\varepsilon_{mod}/d^*_{max}$) on the average fluid velocity is considered. Figure 2 shows the direct comparison between the data obtained in present study and the results from Sharatchandra et al. (1997) and Abdelgawad et al. (2004) for an I-shaped viscous micropump operating with Re_D =

$\Delta P^* = 1$, and two values of the channel thickness: $H^* = 1.5$ and 2.5. According to Fig. 2 a nearly prefect agreement between our results and the results of Sharatchandra et al. (1997) is obtained.

4. Optimization Goal

As previously stated, the present study has two main objectives: to determine the optimal geometrical parameters (i.e., channels thickness H^* and rotor/wall gap d^*) that result in maximum mass flow rate ($\dot{m}^*$), and to study the performance of our newly proposed L- and U-shaped micropumps when compared with the traditional I-shaped design pioneered by Sen et al. (1996). The mass flow rate per unit of length is defined as

$$\dot{m}^* = \bar{u}^* H^* . \tag{8}$$

In the first round of optimization (Figs. 2-9), no constraints were considered and the optimal geometric dimensions (i.e., channels thickness H^* and rotor gap d^*) were determined based on parameters such as Re_D and ΔP^*. In this scenario, the optimization opportunity emerges from the fact that a viscous micropump operates based on two main conditions: the need of a certain level of confinement (i.e., a finite value for H^*), and the asymmetric placement of the rotor inside the channel. The need for the first condition can be understood by noticing that, in the limit where $H^* >> (1 + d^*)$, the fluid average velocity tends to zero ($\bar{u}^* \rightarrow 0$). Consequently, the mass flow rate also tends to zero since $\dot{m}^* \sim \bar{u}^*$. In the other limit of 'small' values of the dimensionless channel thickness (i.e., $H^* \rightarrow (1 + d^*)$), it is clear that the flow is constricted between the rotor and the upper wall of the pump's channel, which also reduces the mass flow rate. Based on the above, an optimal value for H^* such that $\dot{m}$ is maximized must exist.

The need for the rotor asymmetry to displace the fluid in a viscous micropump can be understood by analyzing limiting cases of asymmetry. Consider, for instance, an I-shaped micropump with no pressure load across the channel. Assuming that the rotor is located in the center of the channel, zero net flow is obtained, regardless the direction in which the rotor spins. However, if the symmetry is broken as a clockwise spinning rotor approaches the upper wall, a net flow from the right to the left is generated. In this case, the symmetry break provides a preferential direction for the net flow due to the increase in the shear between the fluid and the surrounding walls. On the other hand, the rotor asymmetry increases the shaft power requirement due to proximity of the rotor to the closest wall. The effect of parameters such as Re_D, ΔP^*, H^* and d^* on the shaft power demand will be addressed later in the text in §6 and §7.

5. Unconstrained Optimization

The search for the optimal geometrical configuration started with the simplest design possible, Fig. 1a. In this case, we have two degrees of freedom, the channel thickness H^* and the gap d^*. Assuming fixed values for d^*, Re_D and ΔP^*, we were able to find an optimal value for the channel height H^* that maximizes the average flow velocity ($\bar{u}^*$) and the mass flow rate ($\dot{m}^*$) just by varying H^*. Figure 3 shows that the channel thickness has a strong effect on $\bar{u}^*$ and $\dot{m}^*$, which strengthens the need for optimizing geometric parameters in a viscous micropump. Figure 3 also shows that different values of the optimal channel height (H^*_{opt}) are needed to maximize $\bar{u}^*$ and $\dot{m}^*$.

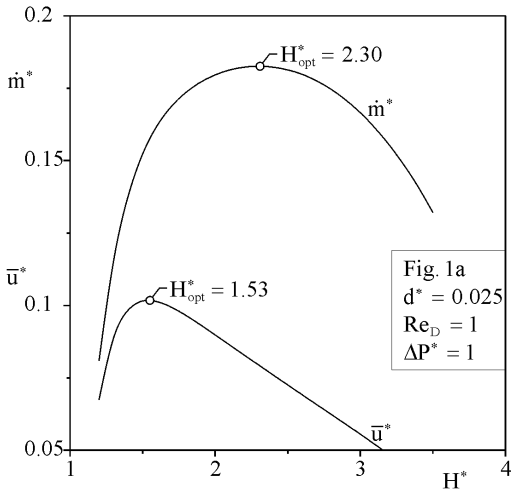

Figure 3. Effect of the channel spacing (H^*) on the mean flow velocity and mass flow rate for an I-shaped channel.

Figure 4 shows the effect of the rotor gap on the mass flow rate and average fluid velocity for an I-shaped pump with the following operating conditions: $Re_D = \Delta P^* = 1$. Each one of the open symbols shown in Fig. 4 represents the

maximum value of $\dot{m}^*$ (squares) and $\overline{u}$ (circles) that can be obtained for a given value of d^*. That is, implicit in each symbol, is the optimization of $\dot{m}^*$ and $\overline{u}^*$ with respect to the channel thickness H^*, which is shown later in Fig. 5. According to Fig. 4, the maximum values of $\dot{m}^*$ and $\overline{u}^*$ are found around $d^*_{opt} \sim 0$, which represent the maximum mass flow rate and average flow velocity optimized with respect to two degrees of freedom, d^* and H^*. Figure 4 also reveals that the gap d^* plays a major role on $\dot{m}^*$ if $d^* \neq d^*_{opt}$ (i.e., $d^* > d^*_{opt}$), similarly to Fig. 3, where values of H^* larger or smaller than H^*_{opt} were equally detrimental to our two figures of merit (i.e., $\dot{m}^*$ and $\overline{u}^*$). On the other hand, Fig. 4 shows that it maybe desirable to have $d^* < d^*_{opt}$ (i.e., the rotor partially embedded in the lower wall) due to the weak effect of the negative eccentricities on the average flow velocity.

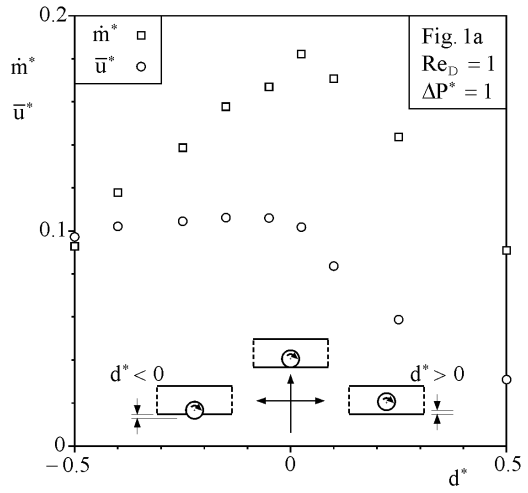

Figure 4. Effect of the rotor gap (d^*) on the maximal mass flow rate and mean velocity.

Figure 5 shows the effect of the gap d^* on the optimal channel height H^*_{opt}. According to Fig. 5, H^*_{opt} increases monotonically with d^*. This behavior can be explained by the fact that, because viscous micropumps need the rotor to be asymmetrically placed inside the channel (§ 5), any increment in d^* is associated with an increment in H^*_{opt} to ensure asymmetry.

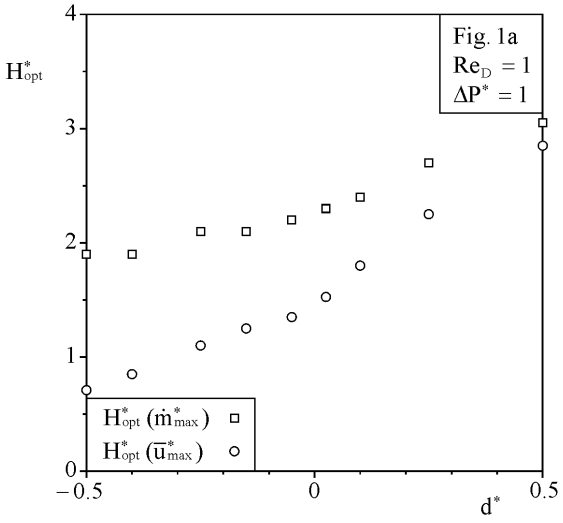

Figure 5. Optimal channel thickness for a fixed value of d^*.

Figure 6 shows the optimal channel thickness versus the Reynolds number for the three configurations given in Fig.1. In order to reduce the number of computational runs, we factored in the results presented in Fig. 4, which showed that $d^*_{opt} \sim 0$. In all simulation shown in Fig. 6, d^* was held constant and equal to 0.025. Figure 6 shows that the optimal channel thickness increases with Re_D for all the configurations. Additionally, a transition between the relative magnitude of H^*_{opt} for the I-, L- and U-shaped pumps can be identified at $Re_D \sim 0.2$. For values of the Reynolds number between $0.01 < Re_D < 0.1$, $H^*_{opt,\,Fig.\,1a} > H^*_{opt,\,Fig.\,1b} > H^*_{opt,\,Fig.\,1c}$. For values the Reynolds number between $0.3 < Re_D < 1$, $H^*_{opt,\,Fig.\,1c} < H^*_{opt,\,Fig.\,1b} > H^*_{opt,\,Fig.\,1a}$. The importance of such results lies in the need for compact micropumps, due to the limited space available to house the micropump itself. In this case, the space occupied by the micropump has to respect

area constraints, which make L-shaped and U-shaped micropumps more attractive when $Re_D < 0.2$ and I-shaped pumps more compact in the limit where $Re_D > 0.2$.

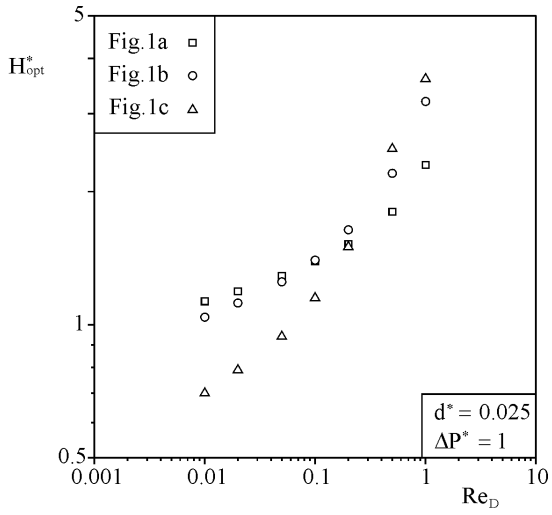

Figure 6. Effect of the Reynolds number on the H^*_{opt} for the three viscous micropumps given in Fig. 1.

Figure 7 depicts the effect of the micropump configuration (Fig. 1a-c) on the figure of merit ($\dot{m}^*_{max}$) for several values of the Reynolds number. According to Fig. 7, pumps with curved housing (i.e., L and U-shaped micropump) perform better (i.e., present higher values of $\dot{m}^*_{max}$) than the I-shaped pump, especially for higher values of the Reynolds number. One reasonable explanation for the latter is that, in the pumps with curve housing the fluid is more aligned to the rotor. This is an important result that extends the applicability of viscous micropump to higher mass flow rates, making it even more attractive when compared with other micropumping methods (see §1).

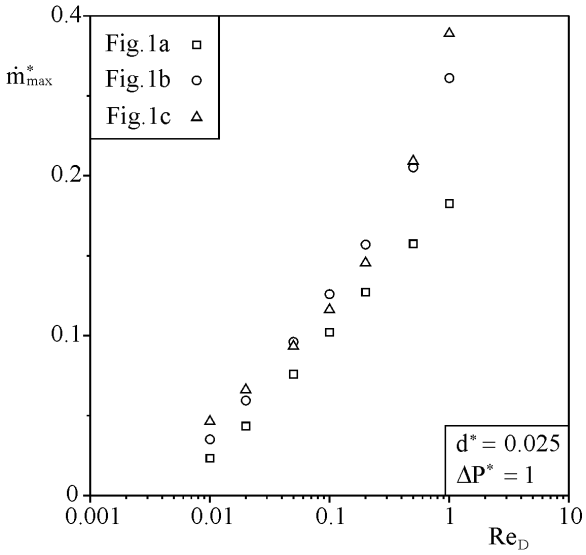

Figure 7. Direct comparison between the maximum mass flow rate ($\dot{m}^*_{max}$) of the three micropumps given in Fig. 1.

Figure 8a shows the effect of the pressure load (ΔP^*) on the optimal channel spacing H^*_{opt} assuming that $Re_D = 1$ and $d^* = 0.025$. According to Fig. 8a, the optimal channel thickness decreases as ΔP^* increases for the three configurations of Fig. 1. Also, a transition between the thickness of the channel housing of the pump can be observed for pressure loads between $5 < \Delta P^* < 10$. In the limit where $\Delta P^* < 5$, pumps with curved housing require larger values of H^*_{opt} when compared with an I-shaped pumps. Figure 8a also suggest that, in the limit where $\Delta P^* > 10$, I-shaped pumps demands a larger channel thickness than curved housed pumps (Fig. 1b and c).

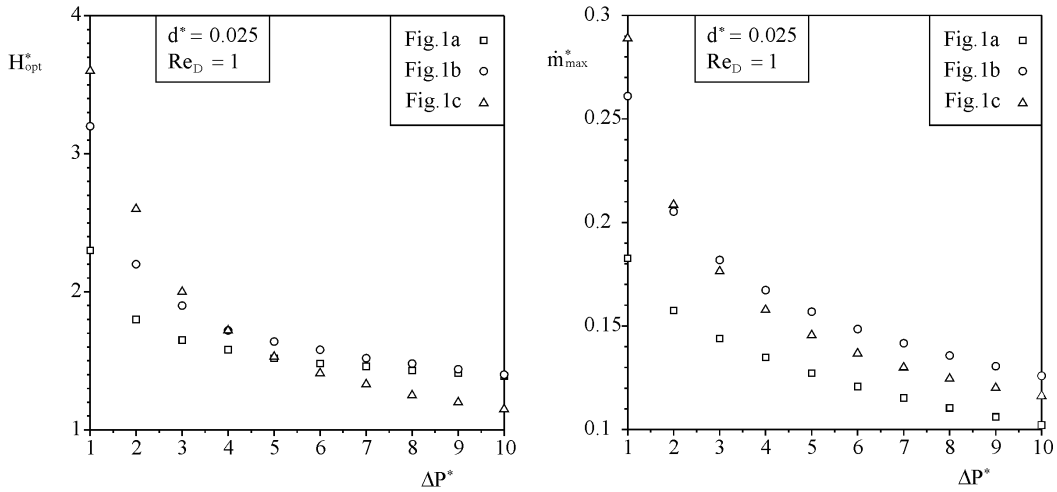

Figure 8. a) Effect of the counter pressure (ΔP^*) on the optimal channel thickness H^*_{max} (left frame). b) Effect of the counter pressure (ΔP^*) on the maximum mass flow rate $\dot{m}^*_{max}$ (right frame).

Figure 8b depicts the importance of the use of pumps with curved housing (Figs. 1b and 1c) when the objective is to maximize the mass flow rate at larger pressure loads. Figure 8b shows that the L and U-shaped pumps present superior performance when compared with an I-shaped throughout the range of load pressure $1 < \Delta P^* < 10$. Also, as expected, the maximized mass flow rate decrease significantly as ΔP^* increases.

6. Minimization of the Shaft Power

Thus far, we have studied the performance and optimization of viscous micropumps with curved or otherwise houses without constraints on the shaft power (See Figs. 7 and 8b). Yet subjacent to these results lays an important question on how does the pump housing, Reynolds number, load pressure and geometric parameters (e.g., d^*, H^*_{opt}) affect the shaft power requirements? To answer this question, we start by defining the rotor's moment coefficient as

$$M = -\int_0^{2\pi} \tau \, d\theta \, . \tag{9}$$

Knowing that the torque per unit of length applied to rotor is $T' = M\, 2\pi\, R^2$ and that shaft power per unit of length is $W' = T\, \omega$, one can define the dimensionless shaft power per unit of length applied at the rotor as

$$W'^* = M^*\, Re_D^2 \, . \tag{10}$$

Intuitively, the shaft power (W'^*) required by the rotor increases with Re_D and also as $d^* \to 0$. That's because higher values of Re_D and small gaps between the walls of the channel surrounding the pump and the rotor increase friction. Such observation is in agreement with Eq. 10, where one can learn that the dimensionless shaft power per unit of length applied to the rotor varies linearly with M^*, and with the square power of the Reynolds number. It is clear that, embedded in the value of M^*, are the geometrical parameters of the pump, such as the rotor gap and channel height.

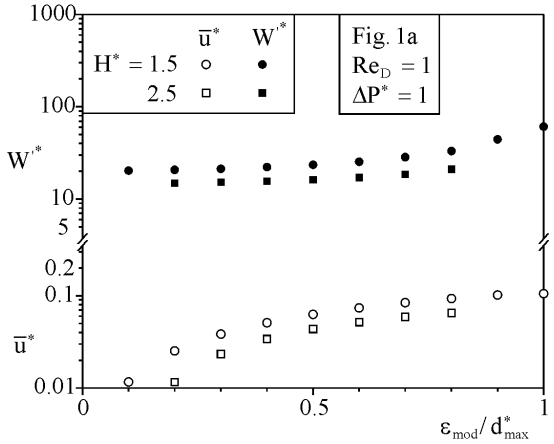

Figure 9. Effect of the modified gap (d^*) on the rotor's shaft power (W'^*).

Our numerical results for the dimensionless shaft power were validated with the numerical data obtained by Abdelgawada et al. (1997) in the steady state limit, since they performed a transient analysis. One should note that the eccentricity in Tables 4 and 5 follows the definition used in Abdelgawada et al. (1997), where

$$\varepsilon_{mod,1} = 1 - 2d^* / (H^* - 1) . \tag{11}$$

Tables 4 and 5 show a good agreement between both set of results.

Table 4. Validation of the numerical results for: Fig. 1a, Re_D= 1, ΔP^* =0, and $\varepsilon_{mod,\,1}$ = 0.95.

H^*	W'^* Present Work	W'^* Abdelgawada et al. (1997)	Difference %
1.5	59.68	~ 60.0	0.5
2.5	35.82	~ 35.9	0.2
3.5	28.49	~ 29.1	1.7

Table 5. Validation of the numerical results for: Fig. 1a, Re_D= 1, ΔP^* = 0, and H^* = 1.5.

$\varepsilon_{mod,\,1}$	W'^* Present Work	W'^* Abdelgawada et al. (1997)	Difference %
0.2	20.69	~ 20.6	0.4
0.8	33.05	~ 34.2	3.5
0.95	59.69	~ 60.1	0.7

Figure 9 shows the effect of the group $\varepsilon_{mod}/d^*_{max}$ on the rotor shaft power demanded (solid symbols) by an I-shaped pump with two different values of channel height, H^* = 1.5 and 2.5, and operating with the following conditions: Re_D = ΔP^* = 1. According to Fig. 9, W'^* increases with the rotor confinement (i.e., W'^* (H^* =1.5) > W'^* (H^* =2.5)). This is an interesting result that allows us to question the superior performance of the pump with small channel height, since it demands more power.

Also, one should notice that, the apparently missing symbols (squares) in Fig. 9 for the curves in which H^* = 2.5, is due to the fact that when the group $\varepsilon_{mod}/d^*_{max}$ < 0.2, the average fluid velocity becomes too small since the rotor is moving towards the channel center line. In the other limit where $\varepsilon_{mod}/d^*_{max}$ > 0.8, the gap between the rotor and the lower wall becomes d^* < 0.05, which also .

Figure 10 compares the effect of the load pressure (ΔP^*) and micropump configurations (Fig. 1a-c) on the shaft power demand W'^*. The three sequences of symbols represent the shaft power needed such that the micropump returns the maximum value of mass flow as indicated in Fig. 9, considering Re_D = 1 and when d^* = 0.025. At first, one should note that the pressure load has a minor effect on W'^*, regardless the housing configuration, since all three curves are nearly flat. However, more important is to realize that curved housed pumps (Fig. 1b and c) not only provide higher mass flow rate (see Fig. 8b) when compared with the I-shaped configuration of Fig. 1a, but also, they require much less shaft power as shown in Fig. 10. The combination of the results provided by Figs. 8b and 10, clearly shows the superiority of the micropump with curved housing, as compared with I-shaped micropumps.

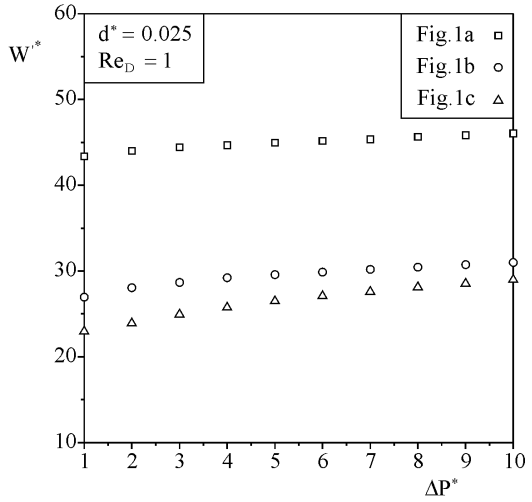

Figure 10. Effect of the counter pressure (ΔP^*) on the rotor's shaft power (W'^*).

Figure 11 further supports the choice of curved housed micropumps in a wider range of the Reynolds number, $0.01 < Re_D < 1$. To better understand why, we have to analyze Fig. 11 in conjunction with Fig.7, which shows that higher mass flow rates are provided by curved housed micropump throughout the whole range $0.01 < Re_D < 1$ in comparison with an I-shaped micropump. In this context, Fig. 11 corroborates our conclusions that configurations with curved housing also require less power to operate.

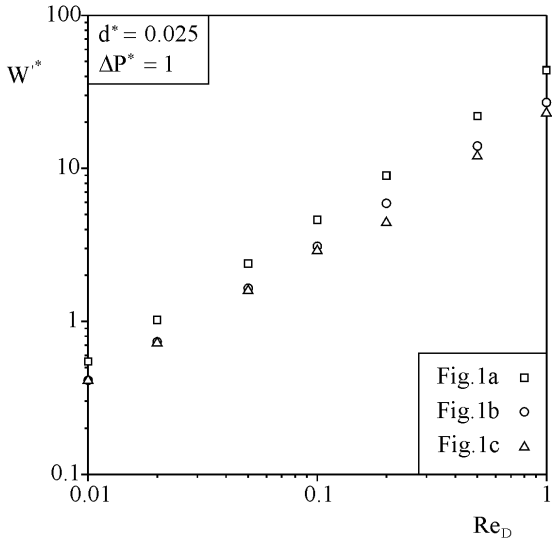

Figure 11. Effect of the Reynolds number on the rotor's shaft power (W'^*).

7. Constrained Rotor's Shaft Power

Our numerical experiments showed that the rotor of a viscous micropump needs to be placed asymmetrically inside the conduit channel in order to generate a net flow, and, as shown in Figs. 4 and 7, the mass flow rate increases with Re_D and when $d^* \rightarrow 0$. Therefore, the micropump designer, who has a limited amount of shaft power available, is entitled to ask the following question: assuming that the rotor's shaft power is constrained, is it better in terms of maximizing the mass flow rate to have the rotor turning faster (i.e., higher values of Re_D) or to place the rotor closer the channel's wall in order to increase the asymmetry level such that $d^* \sim 0$? The optimization opportunity emerges from the need of maximum mass flow and least shaft power.

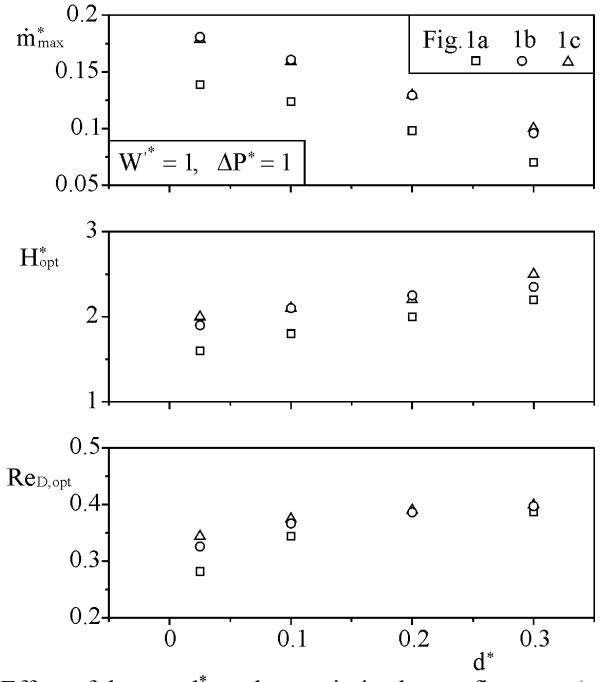

Figure 12. Effect of the gap d^* on the maximized mass flow rate (upper frame), optimal channel height (middle frame) and, optimal Reynolds number (lower frame) assuming that the shaft power is fixed and equal to 10.

In order to answer the previous question, numerical simulations were conducted for the three configurations given in Fig. 1 aiming at the determination of the optimal values of the channel height (H^*_{opt}) and the optimal rotor speed, here represented by the Reynolds number ($Re_{D,opt}$), such that a given (fixed) shaft power availability is respected through Eq. 10. In this case, the available shaft power and the pressure load were set equal to 1. One should notice that $\dot{m}^*_{max}$ represents the maximum mass flow rate obtained for a given value of d^*. However, because the dimensionless shaft power was set equal to $W'^* = 1$, each symbol shown in the Fig. 12 originates from the maximization of $\dot{m}^*_{max}$ with respect to two degrees of freedom, the channel height (H^*) and the rotor speed (i.e., $Re_{D,opt}$). According to the upper frame of Fig. 12, the superior performance of curved housed pumps is evident when compared with an I-shaped configuration since $\dot{m}^*_{max,Figs.1b}$ and $\dot{m}^*_{max,Figs.1c}$ are larger than $\dot{m}^*_{max,Figs.1a}$. Also interesting is that the maximized mass flow rate decreases as gap d^* increases. This result answers the question posed at the first paragraph of the current section, by showing that it is desirable to have the rotor closer to the bottom wall with lower angular speed, rather than have the rotor away from the bottom wall with a larger angular velocity ω. The middle frame of Fig. 12 shows that H^*_{opt} increases with d^* and that micro-scale viscous pumps with curved housing require slightly larger H^*'s when compared I-shaped pump. The increase of H^*_{opt} with d^* is explained based on the two main factors, the need for an asymmetric placement of the rotor within the surrounding walls, and the increase of $Re_{D,opt}$ with d^* (lower frame of Fig. 12), which is an indication that the friction is reduced as the rotor is moved away from the lower wall.

8. Conclusions

In this paper we use a FEM code to simulate and optimize the performance of a micro-scale viscous pump. The objective is to show the importance of geometric optimization on the mass flow rate and power consumption of a micro-scale viscous pump. In the first part of the paper, §5, we illustrated the effect of four parameters (i.e., rotor eccentricity and speed, height of the housing channel height and pressure load) on the performance of an I-housed micro-scale viscous pump proposed by Sen et al. (1996). The numerical results showed that the channel height (H^*) and the rotor eccentricity have a major effect on $\dot{m}^*$ and that geometric optimization of the pump's housing should be considered. At the end, optimized configurations (i.e., H^*_{opt} and ε^*_{opt}) based on maximization of the mass flow rate were generated.

Next, two new configurations of pumps with curved housing (Figs. 1b and 1c) were proposed and numerically optimized for maximal mass flow rate. The numerical results showed that pump with curved housing provide larger mass flow rates when compared with straight housed pumps (Fig. 1a) throughout a whole range of Reynolds number ($0.01 < Re_D < 1$) and pressure load ($1 < \Delta P^* < 10$). Furthermore, the results showed that curved housed pumps also require less shaft power to operate, which is an interesting feature for devices with limited power supply (i.e., laptops etc).

In §7, we reported the performance of all three configurations of Fig. 1 under global constraints. In this case, we fixed the amount of shaft power (W'^*) available to the rotor and varied the geometric parameters (H^* and d^*) and the rotor angular speed (Re_D). The most important finding is that curved housed pumps provided larger mass flow rates than an I-shaped pump. Also interesting is that, because the friction on the rotor surface decreases as the gap increases, the optimal Reynolds number increases with the gap. However, this combination of effects (larger Re_D and large gap) is not enough to guarantee the steadiness of the maximized mass flow rate, and because of that any increase in the rotor gap (d^*) has a detrimental effect on the maximized mass flow rate. In summary, if W'^* is fixed, it is desirable to have a configuration where the rotor is closer to the bottom wall (i.e., small gap) with a lower angular velocity, than a configuration with large d^* and a larger angular velocity.

Nomenclature

d	rotor distance from lower wall, m
D	rotor diameter, m
H	channel height, m
L	channel length, m
$\dot{m}$	mass flow rate, $kg\,s^{-1}$
M	moment coefficient, $N\,m^{-2}$
P	pressure, $N\,m^{-2}$
Re_D	Reynolds number, ($Re_D = \omega D^2/2\nu$)
T	torque, N m
U	rotor surface velocity, $m\,s^{-1}$
$\bar{u}$	mean velocity, $m\,s^{-1}$
$\bar{V}$	velocity vector, $m\,s^{-1}$
W'	rotor shaft power per unit of length, $N\,s^{-1}$

Greek Symbols

ε_{mod}	modified eccentricity, Eq. 7

$\varepsilon_{mod,\,1}$ modified eccentricity, Eq. 11
ν kinematic viscosity, $m^2\,s^{-1}$
ρ density, $kg\,m^{-3}$
ω rotor angular velocity, ($\omega = 2U/D$)

Subscripts

d downstream
H high
L low
max maximum
opt optimum
u upstream

Superscript

* dimensionless variables

Acknowledgement

A. K. da Silva thanks the College of Engineering of the University of Hawaii - Manoa for the support through a 2006 CoE Seed-Grant Award.

References

Abdelgawad, M., Hassan, I., Esmail, N., 2004. Transient behavior of the viscous micropump. Microscale Thermophysical Engineering **8**, 361-381.

Abdelgawad, M., Hassan, I., Esmail, N., Phutthavong, P., 2005. Numerical investigation of multistage viscous micropump configurations. Journal of Fluids Engineering **127**, 734-742.

Auroux, P.-A., Iossifidis, D., Reyes, D. R., Manz, A., 2002. Micro Total Analysis Systems. 2. Analytical standard operations and applications. Analytical Chemistry **74,** 2637 – 2652.

Blanchard, D. B., Ligrani, P. M., Gale, B. K., 2004. Single-disk and double-disk viscous micropump. International Mechanical Engineering Congress, paper # 61705.

COMSOL MultiPhysics Inc., (2005). User's Manual, Los Angeles, CA 90024.

DeCourtye, D., Sen, M., Gad-el-Hak, M. 1998. Analysis of Viscous Micropumps and Microturbines. International Journal of Computational Fluid Dynamics **10, 1**3 – 25.

Gad-el-Hak, M., 1999. The fluids mechanics of microdevices – The Freeman Scholar Lecture. Journal of Fluids Engineering **121**, 5-33.

Judy, J. W., 2001 Microelectromechanical systems (MEMS): fabrication, design and applications. Journal of Smart Materials and Structures **10,** 1115 – 1134.

Laser, D. J., Santiago, J. G., 2004. A review of micropumps. Journal of Micromechanics and Microengineering **14,** R35 – R64.

Micci, M. M., Ketsdever, A. D., 2000. Micropropulsion for Small Spacecraft. American Institute of Aeronautics and Astronautics Inc., Reston, Va., 399 – 422.

Nguyen, N.-T., Huang, X., Chuan, T. K., 2002. MEMS-Micropumps: a review. Journal of Fluids Engineering **124,** 384 – 392.

Qu, W., Mudawar, I., 2002. Experimental and Numerical Study of Pressure Drop and Heat Transfer in a Single-Phase Micro-Channel Heat Sink. International Journal of Heat and Mass Transfer **45,** 2549 – 2565.

Qu, W., Mudawar, I., 2003. Thermal Design Methodology for High-Heat-Flux Single-Phase and Two-Phase Micro-Channel Heat Sinks. IEEE Transactions on Components and Packaging Technologies **26,** 598 – 609.

Reyes, D. R., Iossifidis, D., Auroux, P.-A., Manz, A., 2002. Micro Total Analysis Systems. 1. Introduction, theory, and technology. Analytical Chemistry **74,** 2623 – 2636.

Sen, M., Wajerski, D., Gad-el-Hak, M. 1996. A novel pump for MEMS applications. Journal of Fluids Engineering **118**, 624-627.

Sharatchandra, M. C., Sen, M., Gad-el-Hak, M., 1997. Navier-Stokes simulations of a novel viscous pump. Journal of Fluids Engineering **119**, 372-382.

Sharatchandra, M. C., Sen, M., Gad-el-Hak, M., 1998. Thermal aspects of a novel viscous pump. Journal of Heat Transfer **120,** 99 – 107.

Ziaie, B., Baldi, A., Lei, M., Gu, Y, Siegel, R. A., 2004. Hard and soft micromachining for BioMEMS: review of techniques and examples of applications in microfluidics and drug delivery. Advanced Drug Delivery Reviews **56,** 145 – 172.

Woias, P., 2004. Micropumps – past, progress and future prospects. Sensors and Actuators B **105,** 28 – 38.

Proceedings of the 11th Brazilian Congress of Thermal Sciences and Engineering – ENCIT 2006
Braz. Soc. of Mechanical Sciences and Engineering – ABCM, Curitiba, Brazil, Dec. 5-8, 2006

Paper CIT06-0611

DESENVOLVIMENTO DE REDES NEURAIS PARA O PROCESSAMENTO DE SINAIS ACÚSTICOS VISANDO A MEDIÇÃO DE PROPRIEDADES TOPOLÓGICAS EM ESCOAMENTOS BIFÁSICOS A BOLHAS

Érica Regina Filletti
Escola de Engenharia de São Carlos
Universidade de São Paulo
Av. Trabalhador Sãocarlense, 400
13560-970 São Carlos - SP
filletti@sc.usp.br

Paulo Seleghim Júnior
Escola de Engenharia de São Carlos
Universidade de São Paulo
Av. Trabalhador Sãocarlense, 400
13560-970 São Carlos - SP
seleghim@sc.usp.br

Resumo. *Um novo método para medir a fração volumétrica e a área interfacial em escoamentos bifásicos é proposto neste trabalho, baseado em redes neurais para processar respostas obtidas de sinais acústicos. A distribuição geométrica das fases no escoamento é mapeada pela velocidade local de propagação acústica, considerada na equação diferencial que governa o problema. Esta equação é resolvida numericamente pelo método de diferenças finitas com condições de contorno reproduzindo a estratégia de excitação/medida. Um número significativo de distribuições das velocidades de propagação foi considerado na solução da equação diferencial para construir uma base de dados, da qual os parâmetros da rede são ajustados. O modelo neural é construído para mapear características extraídas dos sinais obtidos de quatro sensores acústicos, localizados no contorno do domínio de sensoriamento, estimando a fração volumétrica e a área interfacial. Os resultados numéricos mostram que o modelo neural pode ser treinado em um tempo computacional razoável e é capaz de reproduzir precisamente a relação entrada/saída do conjunto de treinamento. O erro em avaliar a fração volumétrica e a área interfacial de novas distribuições de velocidade de propagação é menor que 40% no pior caso. Entretanto, este erro pode ser significativamente reduzido com a otimização da arquitetura da rede neural.*

Palavras chave: *escoamentos bifásicos, monitoração acústica, fração volumétrica, área interfacial, redes neurais artificiais*

1. Introdução

A monitoração acústica de processos industriais surge como uma técnica extremamente interessante, sobretudo em aplicações envolvendo o transporte e a manipulação de escoamentos multifásicos. Em específico, tanto podem ser mensurados parâmetros físicos (vazões, densidade, viscosidade, fração volumétrica, temperatura e outros), quanto é possível obter informações mais completas sobre a fenomenologia do processo, normalmente expressas através de imagens montadas diretamente ou reconstruídas numericamente a partir dos sinais de resposta acústica (Lynch, 1991). Dentre as principais vantagens da monitoração acústica (robusteza, imunidade a ruídos elétricos, baixo custo e outras), a possibilidade de se fazer o sensoriamento de forma não intrusiva e não invasiva é fundamental para algumas aplicações em que não são possíveis intervenções mais diretas, seja para a instalação dos equipamentos de medida ou mesmo das próprias sondas. No caso do sensoriamento acústico, a propriedade que o ultra-som tem de atravessar diferentes materiais permite que o sensoriamento seja feito por simples contato com as paredes da tubulação.

Um dos parâmetros mais importantes para descrever regimes de escoamento bifásico é, sem dúvida, a fração de vazio. A medição desse parâmetro apresenta um crescimento importante em muitos processos industriais, tais como físicos, químicos e petrolíferos. Por esta razão, diversas técnicas de medida da fração volumétrica têm sido desenvolvidas por pesquisadores nos últimos anos. Dong *et al.* (2003) empregam um sistema de tomografia de resistência elétrica para calcular a fração volumétrica de escoamentos bifásicos. Huang, Wang e Li (2003) utilizam a técnica de tomografia por capacitância elétrica para o desenvolvimento de um novo método

de medição de fração volumétrica para escoamentos bifásicos. Prasser, Misawa e Tiseanu (2005) medem a fração volumétrica utilizando um sensor de fio elétrico e também através de tomografia de raio-x.

Neste sentido, um dos objetivos deste trabalho é o desenvolvimento de uma ferramenta numérica para o monitoramento acústico de escoamentos bifásicos. Particularmente, deseja-se determinar e quantificar como os campos de sensoriamento acústico se estabelecem, tendo em vista sua interação com a topologia do escoamento, assim como com a geometria da tubulação. De fato, um problema bastante importante relacionado aos métodos ultra-sônicos é a complexidade dos sinais de resposta. Mais especificamente, a resposta a um pulso acústico é composta de múltiplos sinais gerados nas interfaces do escoamento multifásico (reflexões e dispersão), e também nas paredes da tubulação (ecos múltiplos). Conseqüentemente, os sensores acústicos localizados na superfície externa de um tubo metálico que contém um fluido multifásico capturaram formas de ondas complexas, mesmo em resposta a um único pulso de excitação tipo Dirac (onda acústica com todas as freqüências). Recuperar informações sobre a estrutura geométrica do escoamento a partir destes sinais de resposta implica em resolver um problema inverso mal-posto.

Em específico pretende-se investigar a possibilidade de usar uma rede neural para avaliar diretamente a estrutura geométrica do escoamento a partir dos sinais de resposta medidos no contorno do domínio de sensoriamento. Assim, a necessidade de se resolver um problema inverso é evitada e um método de medida muito mais robusto pode ser desenvolvido. Para isto, o problema de monitoração acústica é resolvido no sentido direto para calcular os correspondentes sinais de resposta. A base de dados assim constituída é usada para treinar uma rede neural para produzir as estimativas da área interfacial e da fração volumétrica, tendo como dados de entrada algumas características extraídas dos sinais de resposta. Estas características correspondem ao tempo de chegada da onda acústica e às amplitudes e aos tempos dos três maiores picos.

2. Descrição do Problema

A propagação de ondas acústicas no interior de um volume de sensoriamento Ω pode ser modelada com auxílio da equação (Kinsler *et al.*, 1999)

$$\frac{\partial^2 P(t,\overrightarrow{x})}{\partial t^2} - c^2(\overrightarrow{x})\nabla^2 P(t,\overrightarrow{x}) = 0, \quad \text{para } (t,\overrightarrow{x}) \in \mathbb{R}_+ \times \Omega \tag{1}$$

onde P é a pressão acústica, $c(\overrightarrow{x})$ é a velocidade local do som. É importante enfatizar que a velocidade local do som mapeia a distribuição da fase dentro do volume de medida Ω. As condições inicial e de contorno que modelam a excitação/estratégia da medida são dadas por

$$P(0,\overrightarrow{x}) = \begin{cases} 1, & \text{se } \overrightarrow{x} \in L_{exc} \\ 0, & \text{se } \overrightarrow{x} \in \Omega - L_{exc} \end{cases} \tag{2}$$

$$\overrightarrow{n}.\overrightarrow{\nabla} P(t,\overrightarrow{x}) = 0, \quad \text{para } (t,\overrightarrow{x}) \in \mathbb{R}_+^* \times \partial\Omega \tag{3}$$

$$R_k(t) = \oint_{s \in L_k} P(t,\overrightarrow{x}) ds, \quad \text{para } L_k \in \partial\Omega \tag{4}$$

L_{exc} na Eq. (2) denota o elemento responsável pela excitação, $R_k(t)$ e L_k na Eq. (4) representam, respectivamente, o sinal de resposta e o k-ésimo elemento de medição (que pode corresponder a L_{exc}).

De um ponto de vista físico, a estrutura geométrica de um escoamento disperso pode ser caracterizada pela área interfacial volumétrica, definida como

$$\Gamma(t) = \frac{A_i(t)}{V} \tag{5}$$

onde $A_i(t)$ é a área interfacial instantânea de todas as gotas circunscritas em um volume de controle V. Aceita-se geralmente que $\Gamma(t)$ governa trocas interfaciais com o seguinte princípio (Ishii, 1987, 1990):

$$\text{Transferência interfacial} = \Gamma(t) \times \text{força motriz} \tag{6}$$

Conseqüentemente, $\Gamma(t)$ é relacionado fortemente à massa, momento e transferências de energia e, um conhecimento exato desta variável é crucial para uma operação eficiente de um processo industrial de escoamentos multifásicos.

Um outro parâmetro importante na caracterização de escoamento disperso é a fração volumétrica, definida por

$$\alpha(t) = \frac{V_b(t)}{V} \tag{7}$$

onde $V_b(t)$ representa o volume ocupado pelas gotas no volume V. A fração volumétrica é fortemente relacionada à distribuição da fase e é um parâmetro requerido para projetos hidrodinâmico e térmico de várias aplicações. Por exemplo, a aglutinação das bolhas tende a aumentar significativamente em um reator de coluna para $\alpha > 0,3$, com conseqüente redução na taxa da reação.

Um esboço do sensor proposto é mostrado na Fig. (1). A idéia básica é aplicar um pulso de excitação através de um elemento piezoelétrico e capturar as respostas correspondentes medidas diretamente nos elementos piezoelétricos. Como mencionado antes, apesar do pulso da excitação que é simples na forma, um delta de Dirac por exemplo, as respostas medidas têm geralmente uma forma complexa devido aos ecos múltiplos e às difrações associados com as paredes da tubulação e com a mistura multifásica.

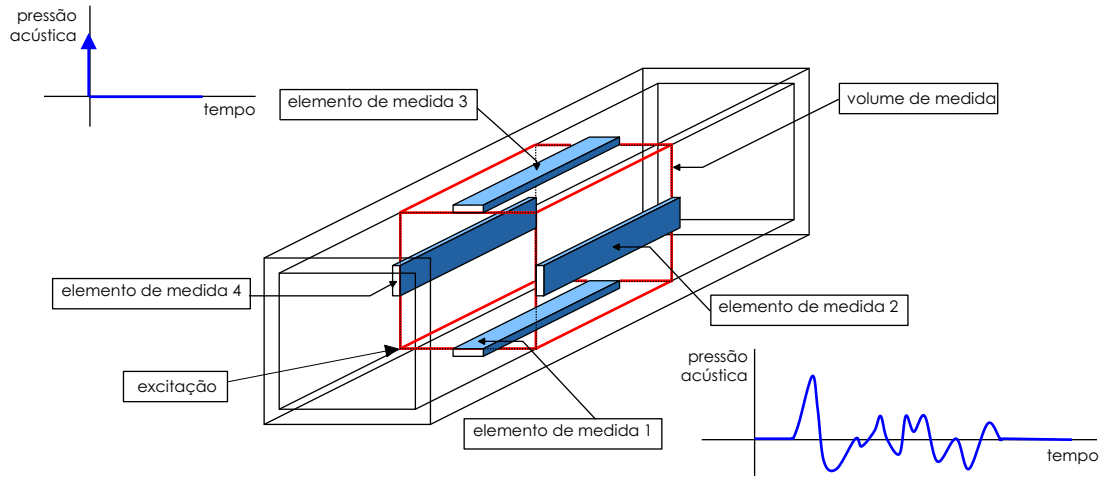

Figura 1: Esboço do sensor proposto - a resposta a um sinal de excitação tipo Dirac tem uma forma complexa devido às reflexões múltiplas e às difrações que ocorrem dentro da mistura multifásica e com as paredes da tubulação.

3. Construção do Modelo Numérico

O problema físico-matemático é transformado em um problema numérico e são formuladas rotinas de solução com base no Método de Diferenças Finitas (MDF), que apresenta algumas vantagens como, por exemplo, ser de fácil e rápida implementação.

Considerando a geometria do problema, sobretudo a disposição dos elementos de medida, justifica-se desprezar as variações axiais de forma a obter uma equação bidimensional. A Eq. (1) é adimensionalizada e discretizada utilizando-se a formulação à esquerda no tempo e a formulação central no espaço. A derivada parcial de segunda ordem com relação ao tempo é aproximada por diferenças à esquerda de segunda ordem e as derivadas parciais com relação ao espaço são aproximadas por diferenças centradas, também de segunda ordem, obtendo-se

$$\frac{1}{\Delta t^2}\left(P_{i,j}^k - 2P_{i,j}^{k-1} + P_{i,,j}^{k-2}\right) - \frac{c_{i,j}^2}{\Delta x^2}\left(P_{i+1,j}^k - 2P_{i,j}^k + P_{i-1,j}^k\right) - \frac{\lambda c_{i,j}^2}{\Delta y^2}\left(P_{i,j+1}^k - 2P_{i,j}^k + P_{i,j-1}^k\right) = 0. \tag{8}$$

onde i e j indicam as coordenadas na malha, nas direções x e y, respectivamente, $\Delta t = 10^{-6}$ e

$$\Delta x = \frac{L_x}{N-1}, \tag{9}$$

$$\Delta y = \frac{L_y}{M-1}, \tag{10}$$

sendo que N e M são os números de pontos nos intervalos $[0, L_x]$ e $[0, L_y]$, L_x e L_y são as dimensões da tubulação nas direções x e y, respectivamente. A tubulação considerada tem geometria quadrada, de lados $L_x = L_y = 1$, e $N = M = 30$.

Reorganizando a Eq. (8) de modo a agrupar os termos em P, obtém-se

$$\begin{aligned}
&\left(\frac{1}{\Delta t^2} + \frac{2c_{i,j}^2}{\Delta x^2} + \frac{2\lambda c_{i,j}^2}{\Delta y^2}\right) P_{i,j}^k + \left(-\frac{c_{i,j}^2}{\Delta x^2}\right) P_{i+1,j}^k + \\
&\left(-\frac{c_{i,j}^2}{\Delta x^2}\right) P_{i-1,j}^k + \left(-\frac{\lambda c_{i,j}^2}{\Delta y^2}\right) P_{i,j+1}^k + \left(-\frac{\lambda c_{i,j}^2}{\Delta y^2}\right) P_{i,j-1}^k + \\
&\left(-\frac{2}{\Delta t^2}\right) P_{i,j}^{k-1} + \left(\frac{1}{\Delta t^2}\right) P_{i,j}^{k-2} = 0,
\end{aligned} \tag{11}$$

Como a velocidade local do som mapeia a distribuição de fase no escoamento, utiliza-se a velocidade de propagação acústica na água, ou seja, $c_{\text{água}} = 1,48 \frac{Km}{s}$ e no óleo, $c_{\text{óleo}} = 1,7 \frac{Km}{s}$ (óleo de motor SAE 30), uma vez que o escoamento simulado neste trabalho é um escoamento óleo-água em que a fase contínua é água e a fase dispersa (gotas) é óleo.

As gotas são geradas aleatoriamente em cada teste numérico de modo que não haja intersecção entre elas. Outra imposição é que a fração volumétrica esteja no intervalo $[0, 0.3]$, já que o escoamento de interesse é um escoamento disperso. Alguns casos são ilustrados na Fig. (2).

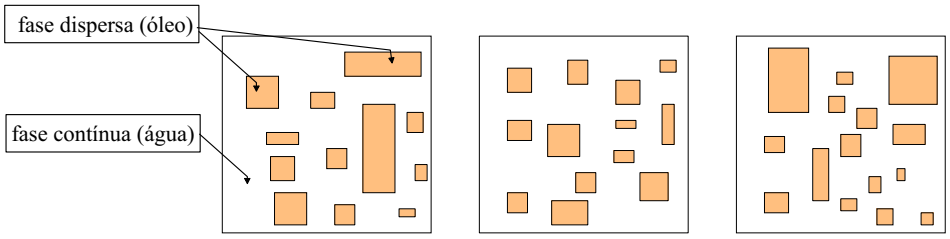

Figura 2: Geração aleatória de gotas.

Na formulação bidimensional, a área interfacial e a fração volumétrica são calculadas, respectivamente, por

$$\Gamma(t) = \frac{\sum P_i(t)}{A} \tag{12}$$

$$\alpha(t) = \frac{\sum A_i(t)}{A} \tag{13}$$

onde P_i e A_i são o perímetro e a área instantâneos de todas as gotas circunscritas na seção transversal da tubulação, respectivamente, e A é a área total da seção transversal.

4. Sinais Acústicos

Os sinais de pressão acústica adquiridos neste trabalho através das simulações numéricas têm uma estrutura muito complexa, mesmo em resposta a um único pulso de excitação tipo Dirac, aplicado em um dos vértices da seção transversal do quadrado, como mostra a Fig. (1). Essa complexidade deve-se aos ecos múltiplos nas paredes da tubulação e também às reflexões e dispersão da onda acústica. Outro fator que influencia na forma dos sinais de resposta é a configuração do escoamento, neste caso, um escoamento disperso, uma vez que a velocidade de propagação acústica é diferente na fase contínua (água) e na fase dispersa (óleo).

Como pode ser observado na Fig. (1), neste trabalho são obtidos 4 sinais de resposta $R_k(t)$, $k = 1, ..., 4$, dados pela Eq. (4), para cada teste numérico realizado. São extraídas algumas características destes sinais, tais

como a tempo de chegada, T, da onda acústica em cada um dos elementos de medida, as amplitudes dos três maiores picos dos sinais, A_1, A_2 e A_3, bem como o tempo de chegada desses picos, indicados por T_1, T_2 e T_3 na Fig. (3), a fim de particularizar a complexidade do sinal em um nível suficiente para a inferência da área interfacial e da fração volumétrica.

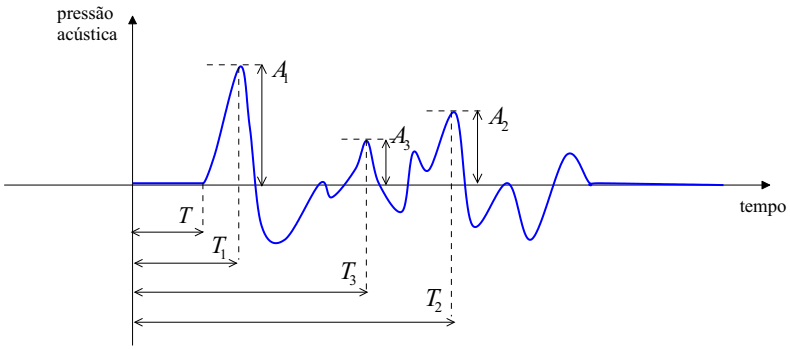

Figura 3: Sinal acústico e as respectivas características extraídas.

5. Redes Neurais Artificiais

Uma rede neural pode ser definida como um mapeamento não-linear dos dados de entrada e saída. Isto é realizado através das camadas de neurônios com suas respectivas funções de ativação, em que as coordenadas de entrada são somadas de acordo com pesos e *bias* específicos para produzir uma única saída. Neste trabalho, a rede utilizada é a rede *feed-forward*, onde o fluxo de informação dos neurônios da camada de entrada até os neurônios da camada de saída segue estritamente adiante, isto é, as conexões de um neurônio são sempre para outros neurônios da camada posterior, como é mostrado na Fig. (4).

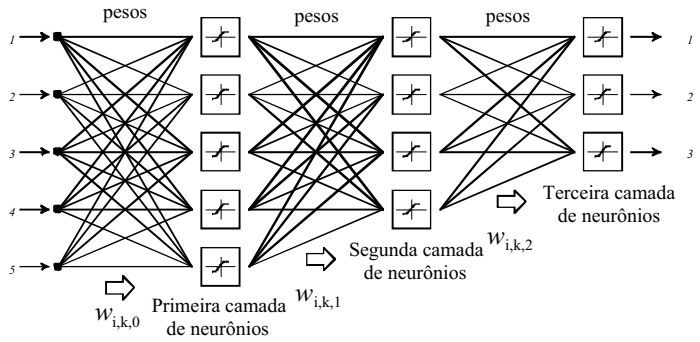

Figura 4: Representação esquemática de uma rede neural feed-forward mapeando um vetor com 5 elementos de entrada em um vetor com 3 elementos de saída.

Formalmente, se a função da ativação do i-ésimo neurônio da j-ésima camada é indicada por $F_{i,j}(.)$, sua saída $s_{i,j}$ pode ser calculada a partir da saída da camada anterior $s_{i,j-1}$ e dos correspondentes *bias* $b_{i,j}$ e pesos $w_{i,k,j-1}$ (o segundo índice k indica o neurônio da $j-1$-ésima camada, na qual a conexão está sendo estabelecida) de acordo com a expressão

$$s_{i,j} = F_{i,j}\left(b_{i,j} + \sum_k w_{i,k,j-1} s_{k,j-1}\right) \tag{14}$$

Os valores da entrada e da saída da rede são denotados, respectivamente, por η_i e ξ_i, a relação que mapeia entrada e saída pode ser obtida aplicando sucessivamente a Eq. (14), que para o exemplo da Fig. (4) resulta

$$\xi_i = F_{i,3}\left(b_{i,3} + \sum_{k=1}^{4} w_{i,k,2} F_{k,2}\left(b_{i,2} + \sum_{m=1}^{5} w_{k,m,1} F_{m,1}\left(b_{m,3} + \sum_{n=1}^{5} w_{m,n,0}\eta_n\right)\right)\right) \tag{15}$$

A Eq. (15) mostra claramente que a relação entre η_i e ξ_i é definida escolhendo-se as funções de ativação e ajustando-se os pesos e *bias*. Entre muitas, uma característica muito importante das redes neurais é a capacidade de aprendizagem, isto é, a possibilidade de ajustar os pesos e *bias* através de uma regra conveniente de treinamento para reproduzir os pares de entrada e saída. O algoritmo de *back-propagation* é a heurística de treinamento mais utilizada e melhor adaptada para as redes *feed-forward*. É baseada na aplicação iterativa do método da redução do gradiente instantâneo, a partir do cálculo das derivadas primeiras de uma função de erro convenientemente definida, cujos argumentos são os parâmetros da rede (pesos e *bias*). Uma descrição detalhada do algoritmo de *back-propagation* é encontrada em Haykin (1999). Em linhas gerais, as etapas básicas da implementação do algoritmo de *back-propagation* utilizado neste trabalho são as seguintes:

(i) Inicializar os parâmetros da rede $b_{i,j}$ e $w_{i,k,j}$ com valores aleatórios.

(ii) A partir de um conjunto de treinamento com pares de entrada/saída, tomar o p-ésimo par (η_i^p, δ_i^p), calcular a saída da rede com a mesma entrada e formar o par (η_i^p, ξ_i^p).

(iii) Calcular o erro entre a saída desejada (δ_i^p) e a saída obtida (ξ_i^p) de acordo com a norma euclidiana

$$e = \sqrt{\sum_i (\delta_i^p - \xi_i^p)^2} \tag{16}$$

(iv) Calcular as derivadas do erro e em relação a $w_{i,k,j}$ e $b_{i,j}$.

(v) Modificar os pesos e *bias* da rede de acordo com o método da redução do gradiente instantâneo, e de uma determinada taxa de aprendizado γ

$$b_{i,j} \leftarrow b_{i,j} - \gamma \frac{\partial e}{\partial b_{i,j}} \tag{17}$$

$$w_{i,k,j} \leftarrow w_{i,k,j} - \gamma \frac{\partial e}{\partial w_{i,k,j}} \tag{18}$$

(vi) Iterar entre os passos 2 e 5, modificando sucessivamente $b_{i,j}$ e $w_{i,k,j}$ até que seja atingido um determinado número de épocas de aprendizado ou que o erro seja inferior a um determinado valor limite.

O desempenho da rede neural é profundamente afetado por sua arquitetura interna (número de camadas ocultas e número de neurônios em cada uma delas) e pelo tipo de interconexões (*feed-forward*, recorrentes). A forma exata da função da ativação limita os efeitos no desempenho geral da rede e é ajustada de acordo com as necessidades da heurística de treinamento (função sigmoidal no exemplo do algoritmo de *back-propagation*).

A rede utilizada neste trabalho foi implementada no *Neural Networks Toolbox* do MATLAB 6.0 em um computador AMD Athlon (TM) XP 2600+ com 2,08 GHz e 1,5 GB de RAM. Sua arquitetura consiste de uma camada de entrada com 24 neurônios, duas camadas intermediárias e uma camada de saída com 2 neurônios. 16 neurônios foram utilizados na primeira camada intermediária e 12 na segunda. As funções de ativação utilizadas são a tangente sigmoidal nas camadas intermediárias e a função linear na camada de saída. Cada neurônio da camada de saída é responsável por estimar um dos seguintes parâmetros do escoamento bifásico disperso: área interfacial e fração volumétrica.

O procedimento de treinamento constitui em adquirir sinais de pressão acústica do escoamento de interesse para cada simulação numérica realizada e extrair algumas particularidades que caracterizam a complexidade do sinal em um nível suficiente para a inferência da área interfacial e da fração volumétrica para compor o conjunto de treinamento.

6. Resultados e Discussão

São realizados 300 testes numéricos simulando escoamento bifásico disperso. Para tanto, impõe-se que a fração volumétrica varie aleatoriamente de maneira uniforme entre 0 e 0,3 conforme mencionado anteriormente. A área interfacial resultante limita-se entre 0 e 2,5 devido à malha utilizada nas simulações. A Tab. (1) ilustra alguns destes casos, mostrando também as respectivas características dos sinais de medida mapeados pela rede neural.

Tabela 1: Características extraídas dos sinais de resposta para diferentes testes numéricos.

Distribuição de gotas	**Elemento de medida 1**	**Elemento de medida 2**	**Elemento de medida 3**	**Elemento de medida 4**
$\alpha = 0,000$ $\Gamma = 0,000$ 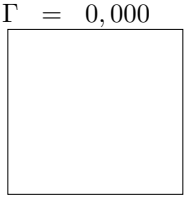	$T = 0,155$ $T_1 = 0,368$ $T_2 = 1,748$ $T_3 = 2,802$ $A_1 = 0,594$ $A_2 = 0,376$ $A_3 = 0,249$	$T = 0,525$ $T_1 = 0,794$ $T_2 = 1,283$ $T_3 = 3,181$ $A_1 = 0,585$ $A_2 = 0,351$ $A_3 = 0,247$	$T = 0,536$ $T_1 = 0,803$ $T_2 = 1,261$ $T_3 = 3,179$ $A_1 = 0,563$ $A_2 = 0,340$ $A_3 = 0,238$	$T = 0,173$ $T_1 = 0,392$ $T_2 = 1,745$ $T_3 = 2,792$ $A_1 = 0,585$ $A_2 = 0,368$ $A_3 = 0,257$
$\alpha = 0,027$ $\Gamma = 0,167$ 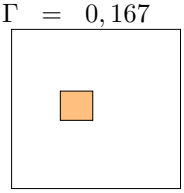	$T = 0,144$ $T_1 = 0,343$ $T_2 = 0,455$ $T_3 = 1,743$ $A_1 = 0,576$ $A_2 = 0,376$ $A_3 = 0,332$	$T = 0,512$ $T_1 = 0,776$ $T_2 = 1,274$ $T_3 = 3,163$ $A_1 = 0,544$ $A_2 = 0,387$ $A_3 = 0,269$	$T = 0,533$ $T_1 = 0,800$ $T_2 = 1,248$ $T_3 = 3,155$ $A_1 = 0,628$ $A_2 = 0,319$ $A_3 = 0,209$	$T = 0,173$ $T_1 = 0,394$ $T_2 = 1,730$ $T_3 = 2,778$ $A_1 = 0,703$ $A_2 = 0,391$ $A_3 = 0,284$
$\alpha = 0,093$ $\Gamma = 0,530$ 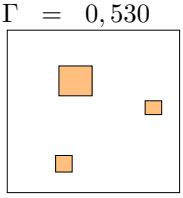	$T = 0,155$ $T_1 = 0,370$ $T_2 = 1,720$ $T_3 = 0,489$ $A_1 = 0,625$ $A_2 = 0,370$ $A_3 = 0,326$	$T = 0,524$ $T_1 = 0,791$ $T_2 = 1,255$ $T_3 = 3,794$ $A_1 = 0,654$ $A_2 = 0,279$ $A_3 = 0,209$	$T = 0,530$ $T_1 = 0,791$ $T_2 = 1,254$ $T_3 = 3,140$ $A_1 = 0,627$ $A_2 = 0,406$ $A_3 = 0,266$	$T = 0,162$ $T_1 = 0,372$ $T_2 = 1,274$ $T_3 = 1,434$ $A_1 = 0,477$ $A_2 = 0,383$ $A_3 = 0,305$
$\alpha = 0,187$ $\Gamma = 1,167$ 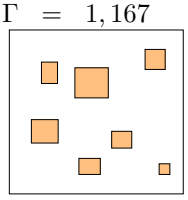	$T = 0,154$ $T_1 = 0,359$ $T_2 = 0,474$ $T_3 = 0,561$ $A_1 = 0,885$ $A_2 = 0,606$ $A_3 = 0,440$	$T = 0,501$ $T_1 = 0,766$ $T_2 = 0,479$ $T_3 = 1,227$ $A_1 = 0,654$ $A_2 = 0,313$ $A_3 = 0,288$	$T = 0,519$ $T_1 = 0,777$ $T_2 = 0,478$ $T_3 = 0,366$ $A_1 = 0,779$ $A_2 = 0,322$ $A_3 = 0,292$	$T = 0,168$ $T_1 = 0,378$ $T_2 = 0,489$ $T_3 = 1,667$ $A_1 = 0,742$ $A_2 = 0,517$ $A_3 = 0,382$
$\alpha = 0,271$ $\Gamma = 1,667$ 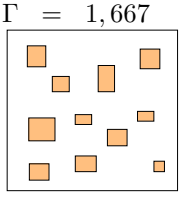	$T = 0,150$ $T_1 = 0,352$ $T_2 = 1,648$ $T_3 = 0,470$ $A_1 = 0,627$ $A_2 = 0,312$ $A_3 = 0,275$	$T = 0,492$ $T_1 = 0,746$ $T_2 = 1,213$ $T_3 = 3,630$ $A_1 = 0,454$ $A_2 = 0,220$ $A_3 = 0,213$	$T = 0,506$ $T_1 = 0,759$ $T_2 = 1,803$ $T_3 = 0,478$ $A_1 = 0,423$ $A_2 = 0,184$ $A_3 = 0,175$	$T = 0,150$ $T_1 = 0,433$ $T_2 = 0,343$ $T_3 = 0,497$ $A_1 = 0,333$ $A_2 = 0,296$ $A_3 = 0,294$
$\alpha = 0,227$ $\Gamma = 1,867$ 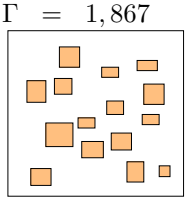	$T = 0,144$ $T_1 = 0,361$ $T_2 = 0,462$ $T_3 = 2,700$ $A_1 = 0,574$ $A_2 = 0,355$ $A_3 = 0,317$	$T = 0,505$ $T_1 = 0,763$ $T_2 = 1,250$ $T_3 = 0,475$ $A_1 = 0,628$ $A_2 = 0,324$ $A_3 = 0,254$	$T = 0,515$ $T_1 = 0,775$ $T_2 = 1,215$ $T_3 = 0,472$ $A_1 = 0,548$ $A_2 = 0,273$ $A_3 = 0,266$	$T = 0,162$ $T_1 = 0,389$ $T_2 = 1,691$ $T_3 = 0,505$ $A_1 = 0,588$ $A_2 = 0,414$ $A_3 = 0,360$

A análise dos histogramas destas características mostra que algumas delas são mais ricas em informação do que outras, sendo conveniente para o treinamento da rede excluir aquelas menos relevantes. Em outras palavras, uma característica que sofre pouca ou nenhuma influência da distribuição interna de velocidade de propagação acústica funciona como um *bias* na entrada da rede. Esta informação, não sendo relevante para o cálculo da fração volumétrica e da área interfacial, tem os respectivos pesos diminuídos durante o processo de treinamento. Porém, estes pesos são inicializados aleatoriamente durante o início do treinamento e, conseqüentemente, o número total de épocas deverá aumentar. Portanto, as características a serem consideradas doravante são as seguintes: T_1, T_2, T_3, A_1, A_2 e A_3. A característica T foi descartada. Abaixo são mostrados alguns destes histogramas a título de ilustração, sendo que na Fig. (5) estão os histogramas da amplitude do maior pico dos sinais de resposta obtidos nos elementos de medida 1 e 2. Já na Fig. (6), encontram-se os histogramas do tempo de chegada da onda acústica nos elementos de medida 1 e 2, característica descartada por não ser muito influenciada pela distribuição local de velocidade de propagação acústica.

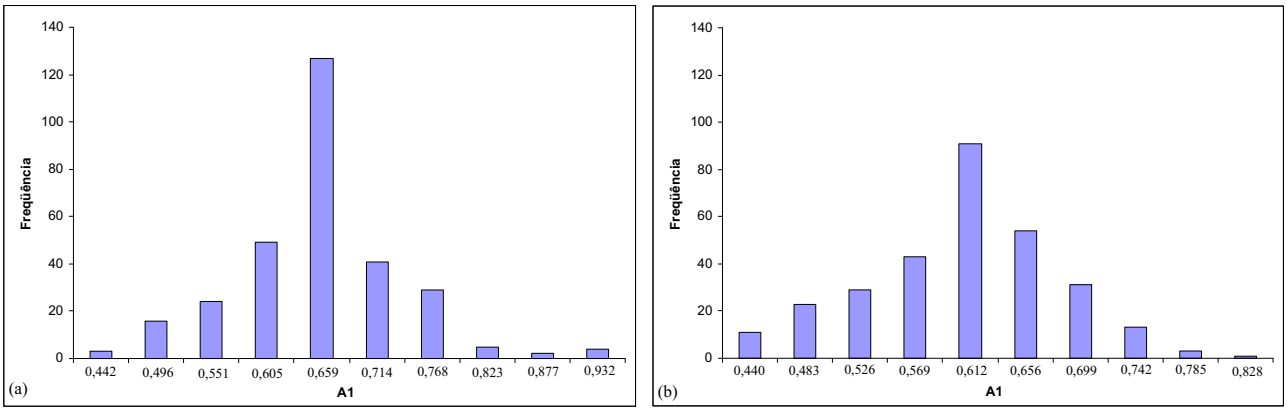

Figura 5: Histogramas da maior amplitude dos sinais de pressão acústica obtidos (a) no elemento 1 e (b) no elemento 2.

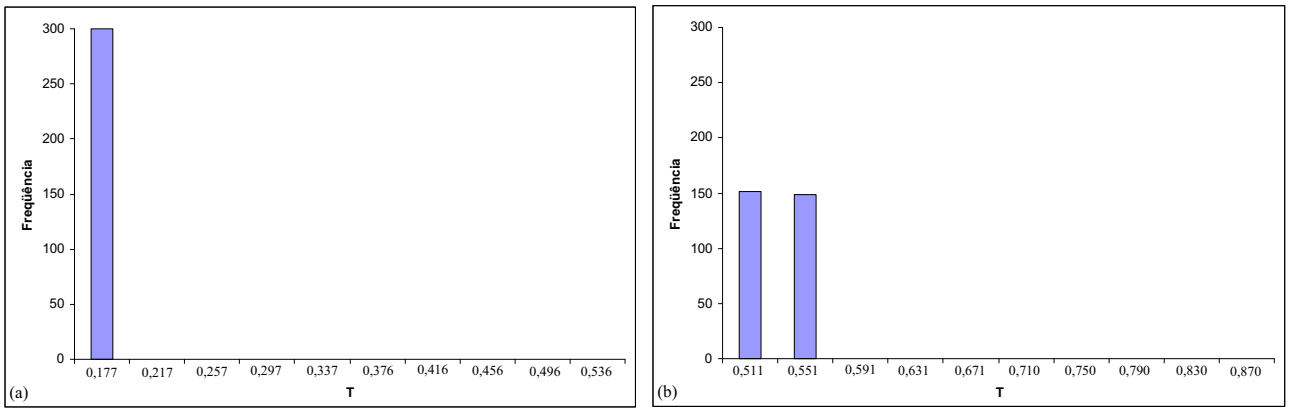

Figura 6: Histogramas do tempo de chegada da onda acústica dos sinais de pressão obtidos (a) no elemento 1 e (b) no elemento 2.

Os resultados do treinamento da rede mostram que ela é capaz de reproduzir precisamente a relação entrada/saída dos dados do conjunto de treinamento, tanto para a fração volumétrica quanto para a área interfacial. Para a generalização, os dados característicos de testes numéricos com novas distribuições de velocidade local de propagação acústica são apresentados à rede neural, e o erro em estimar a fração volumétrica e a área interfacial é menor que 40% no pior caso. A Fig. (7) mostra a comparação entre os valores estimados pela rede neural e os valores reais para a fração de vazio e área interfacial, respectivamente, onde os pontos azuis são referentes ao treinamento da rede e os pontos vermelhos referem-se à generalização.

7. Conclusões

Uma nova metodologia para a medida não intrusiva da fração volumétrica e da área interfacial é proposta neste trabalho, utilizando sensoriamento acústico e resolvendo o problema inverso associado através do desen-

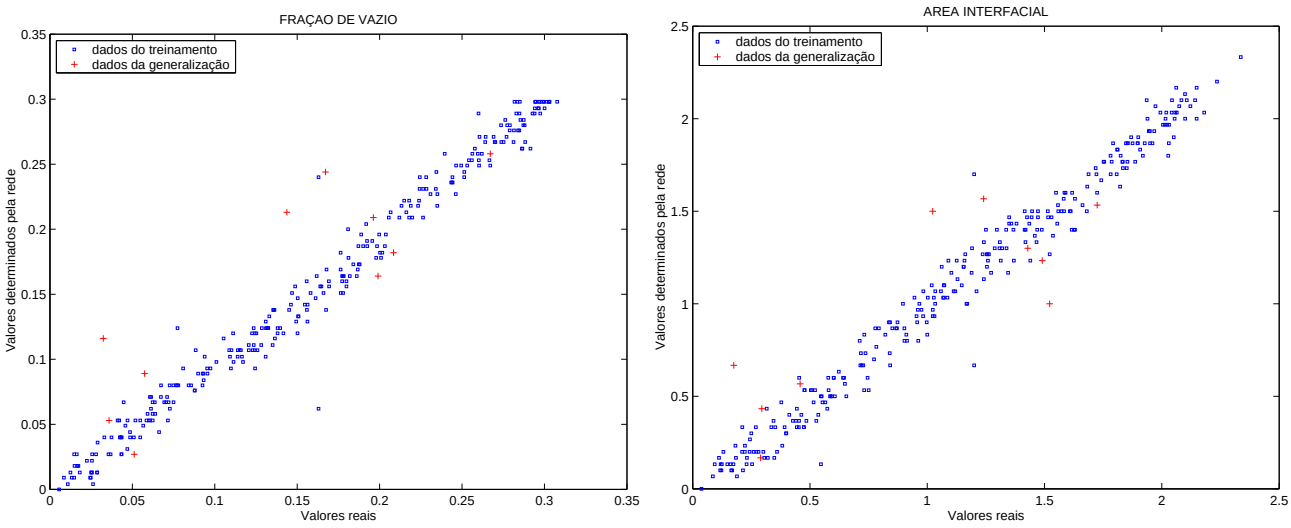

Figura 7: Comparação entre os valores estimados pela rede neural e os valores reais para a fração volumétrica e área interfacial, respectivamente.

volvimento e treinamento de uma rede neural. O modelo matemático é construído a partir das equações de propagação acústica.

A rede neural é treinada com dados oriundos de simulações numéricas. Para a realização de tais simulações, desenvolve-se uma ferramenta numérica capaz de calcular a propagação acústica em meios heterogêneos. Este simulador é utilizado para construir uma base de dados constituída de distribuições de velocidade de propagação acústica geradas aleatoriamente, das quais são extraídas os tempos de chegada das ondas acústicas, a amplitude dos três maiores picos de cada sinal obtido, bem como os tempos de chegada destes picos. Após concluída esta etapa, realiza-se a implementação de uma família de modelos conexionistas. Em seguida, faz-se o treinamento dos melhores modelos com exemplos extraídos da base de dados, buscando determinação de parâmetros como a fração volumétrica e a área interfacial.

Os resultados numéricos mostram que o modelo neural pode ser treinado em um tempo computacional razoável e é capaz de reproduzir precisamente a relação entrada/saída do conjunto de dados do treinamento. O erro em avaliar a fração volumétrica e a área interfacial de novas distribuições de velocidade de propagação acústica é menor que 40% no pior caso. Entretanto, este erro pode ser significativamente reduzido com a otimização da arquitetura da rede neural.

Trabalhos futuros incluem estudos em um domínio tridimensional, além de outras geometrias de tubulação. Também podem ser analisados outros escoamentos, como o escoamento ar-água. Uma outra proposta de trabalho futuro é a implementação de outros tipos de redes neurais. Outra possibilidade, é refinar a malha nas simulações numéricas, afim de obter maiores valores para a área interfacial.

8. Agradecimentos

Este trabalho foi realizado com suporte financeiro do PROSET CT-Petro CNPq 01/2002 (processo no 500101/2002-7) e da FAPESP (processo no 03/13819-6).

9. Referências

Dong, F.; Jiang, Z. X.; Qiao, X. T.; Xu, L. A., 2003, "Application of electrical resistance tomography to two-phase pipe flow parameters measurement". Flow measurement and instrumentation, Vol. 14, pp. 183-192.

Haykin, S., 1999, "Neural Networks: a comprehensive foudation". 2nd ed. New Jersey: Prentice Hall, 900p.

Huang, Z.; Wang, Li, H., 2003. "Application of electrical capacitance tomography to the void fraction measurement of two-phase flow". IEEE Transactions on Instrumentation and Measurement, Vol. 52, No. 1, pp. 7-12.

Ishii M., 1987, "Interfacial area modeling", in G.F. Hewitt, J.M. Delhaye and N. Zuber (eds.), Multiphase Science and Technology, Vol. 3, Hemisphere Publishing/Springer-Verlag, pp. 31-61.

Ishii M., 1990, "Two-fluid model for two-phase flow", in G.F. Hewitt.

Kinsler L.E., Frey A.R., Coppens A.B. E Sanders J.V., 1999, "Fundamentals of Acoustics", John Wiley & Sons,

245p.

Lynch J., 1991, "Non intrusive multiphase flow measurement techniques (bibliographic review)", Revue de l'Institut Francais du Petrole, Vol. 46, No. 1, pp. 59-88.

Prasser, H. M.; Misawa, M.; Tiseanu, I., 2005. "Comparison between wire-mesh sensor and ultra-fast X-ray tomograph for an air-water flow in a vertical pipe". Flow Measurement and Instrumentation, Vol. 16, pp. 73-83.

DEVELOPMENT OF NEURAL NETWORKS FOR THE PROCESSING OF ACOUSTIC SIGNALS AIMING AT THE MEASUREMENT OF TOPOLOGICAL PROPERTIES IN BUBBLY TWO-PHASE FLOWS

Érica Regina Filletti
Escola de Engenharia de São Carlos
Universidade de São Paulo
Av. Trabalhador Sãocarlense, 400
13560-970 São Carlos - SP
filletti@sc.usp.br

Paulo Seleghim Júnior
Escola de Engenharia de São Carlos
Universidade de São Paulo
Av. Trabalhador Sãocarlense, 400
13560-970 São Carlos - SP
seleghim@sc.usp.br

Abstract. *A new method for measuring the void fraction and interfacial area in two-phase flows is proposed in this work, based on neural network processing the responses obtained from an acoustic interrogation signal. The geometrical distribution of the phases within the flow is mapped by the local acoustic propagation velocity, considered in the governing differential equation. This equation is solved numerically by the finite difference method with boundary conditions reproducing the excitation/measurement strategy. A significant number of propagation velocities distributions were considered in the solution of the differential equation in order to construct a database from which the neural model parameters could be adjusted. The neural model is constructed to map features extracted from the signals delivered by four acoustic sensors, placed on the external boundary of the sensing domain, into the corresponding void fraction and interfacial area. Numerical results shown that the neural model can be trained in a reasonable computational time and is capable of reproducing quite accurately the input/output relation of the training data set. The error in assessing the void fraction and interfacial area from new propagation velocity distributions is less then 40% in the worst case. However, this error can be significantly reduced through optimization of the neural network architecture.*

Keywords: *two-phase flow, acoustic monitoring, void fraction, interfacial area, artificial neural network.*

Proceedings of the 11th Brazilian Congress of Thermal Sciences and Engineering – ENCIT 2006
Braz. Soc. of Mechanical Sciences and Engineering – ABCM, Curitiba, Brazil, Dec. 5-8, 2006

Paper CIT06-0646

SCALING LAWS FOR TURBULENT BOUNDARY LAYERS SUBJECT TO ADVERSE PRESSURE GRADIENT AND SEPARATION

J. B. R. Loureiro
jbrloureiro@mecanica.coppe.ufrj.br

Atila P. Silva Freire.
atila@mecanica.coppe.ufrj.br

Federal University of Rio de Janeiro
Mechanical Engineering Program
PEM/COPPE/UFRJ
C. P. 68503, Cep. 21.945-970, RJ, Brazil.

Abstract. *The behaviour of a turbulent flow near a separation point is a very complex phenomenon. Despite the numerous works aimed at understanding this task, it remains still as an unsolved problem. Indeed, the reduction to zero of the main scaling parameters of the turbulent boundary layer flow, e. g. the skin friction velocity, completely breaks down the classical two-deck structure.The purpose of this work is to perform an analyses of the scaling parameters used in different law of the wall formulations which account for the adverse pressure gradient field. The predictions of seven different scaling laws will be compared with three sets of independent experimental results. The characteristic scales of the turbulent boundary layer will be evaluated for the upstream, recirculation and downstream regions. The outcome of this analysis may shed some light on the development of more accurate scaling laws for turbulent boundary layers subjected to large adverse pressure gradients and separation.*

keywords: *Turbulence, Separation, Adverse pressure gradient, Law of the wall, Experiments.*

1. Introduction

Turbulent flow near a separation point is a very complex problem. Despite the many works that have been published particularly in the last forty years, flow separation still remains a great challenge to researchers. The reason for this is very simple, near to a separation point the reduction to zero of the main velocity scaling parameter for the turbulent boundary layer, the skin friction velocity, completely breaks down the classical two-layered asymptotic structure. As a result, analyses where alternative characteristic scaling parameters are advanced must be proposed. These analyses must then explain how the classical former asymptotic structure for zero pressure gradient boundary layers can be modified such that an equation analogous to Stratford's law can replace the log-law at a separation point.

Despite the large number of references that can be found in literature, the present work will focus on a small selected group of works. These are considered representative enough of the state of the art by the present authors. In fact, seven different law of the wall formulations will be analysed here. Five laws that were developed mainly through asymptotic reasoning, namely, the log-laws of Mellor (1966), of Afzal (1983), of Nakayama and Koyama (1984), of Durbin and Belcher (1992) and of Cruz and Silva Freire (1998). Additionally, two laws that were derived mainly on empirical bases, the laws of Simpson (1983) and of Nickels (2004) will be considered.

Specifically, the purpose of this work is to perform a detailed analysis on the applicability of the scaling parameters used in different law of the wall formulations for flow description under an adverse pressure gradient field. Predictions given by the seven above mentioned different scaling laws will be compared with three sets of independent experiments, the data of Simpson et al. (1981), of Dengel and Fernholz (1990) and of Loureiro et al. (2006). The characteristic scales of the turbulent boundary layer will be tested for both the regions of attached and of detached flows. Special attention will be given to an evaluation and comparison of the velocity characteristic scales. The outcome of this analysis might shed some light onto the development of more accurate scaling laws for turbulent boundary layers subjected to large adverse pressure gradients and resulting flow separation.

This manuscript is organized as follows: the next section will present the main derivations required to introduce each scaling law. The section of results will present the selected four sets of experimental data compared with the analytical predictions. Results for the characteristic scales will also be shown.

2. Scaling Laws

This section introduces the different law of the wall formulations that will be evaluated in the present work. Since our main concern is to carry out an analysis of the ability of the chosen laws in predicting flow separation, just the main parts of the original derivations will be presented here. We must warn the reader that some of the derivations are quite complex, a recurring feature that has really prevented us from going into too much detail. For a complete account of the formulations, the reader is referred to the original references.

2.1. Asymptotic correlations

2.1.1. The law of the wall formulation of Mellor (1966)

The effect of pressure gradients on the behaviour of turbulent boundary layers without restriction to equilibrium was investigated by Mellor (1966) through dimensional arguments. When a large external pressure gradient is applied to a boundary layer, no portion of the defect profile overlaps the logarithmic law. In fact, as previously suggested by Coles (1956) and by Stratford (1959), very near a separation point the logarithmic part of velocity profile ceases to exist.

However, if Millikan's (1939) arguments are recast and a new pressure gradient parameter is included in the analysis, an equation can be derived which satisfies the required limiting form as a separation point is approached. Assuming that in the viscous sublayer the stress terms should be balanced only by the pressure term in the motion equations, and by considering some overlap arguments, Mellor (1966) found that for outer layer the velocity profile can be written as

$$u^+ = \xi_{p^+} + \frac{2}{\varkappa}\Big(\sqrt{1+p^+z^+} - 1\Big) + \frac{1}{\varkappa}\ln\Big(\frac{4z^+}{2+p^+z^+ + 2\sqrt{1+p^+z^+}}\Big), \tag{1}$$

where $z^+ = zu_{p\nu}/\nu$, $u^+ = u/u_{p\nu}$, $u_{p\nu} = [(\nu/\rho)(dp/dx)]^{1/3}$ and $p^+ = [(\nu/\rho)(dp/dx)]/u_*^3$. Eq. (1) follows different asymptotic behaviours in the limiting cases $p^+ \to 0$ or ∞, tending respectively to the classical logarithmic law or to Stratford's equation. Function ξ_{p^+} is a known parameter having been determined numerically for a range of p^+'s (see a specific table in Mellor (1966)).

2.1.2. The law of the wall formulation of Afzal (1983)

Afzal (1983) studied the asymptotic behaviour of a boundary layer near a separation point supposing a two-deck asymptotic structure to hold. As main non-dimensional parameters, Afzal took $R_p = \delta U_p/\nu$; $\Lambda = \tau_w/\delta p_x$, $p_x = \partial_x p =$ - UU_x; where, $U_p = (\nu p_x/\rho)^{1/3}$, δ = boundary layer thickness, and τ_w = wall shear stress.

For a boundary layer subject to an adverse pressure gradient, the adequate limiting forms can be written as:

$$\Lambda \to 0; \qquad R_p \to \infty; \qquad \Lambda R_p \to O(1). \tag{2}$$

Appropriate scales for the outer region of the flow in the streamwise direction, x, were taken to be $L =$ $-U/U_x$, and U. For the transversal direction, y, Afzal proposed to consider δ and $U_\delta = (\delta p_x/\rho)^{1/2}$. For the inner layer, Afzal proposed to consider $l = \nu/U_p$ and U_p as the important scales (x-direction). In y-direction, ν/U_p and U_p^2 were considered. Then, through matching arguments, limiting forms for the inner and outer solutions were proposed.

For the inner layer, the resulting solution was

$$\frac{u}{u_p} = A(\Lambda)\sqrt{\zeta} + C(\Lambda R_p), \qquad \zeta = \frac{zU_p}{\nu}, \ \zeta \to \infty. \tag{3}$$

For the outer layer, Afzal found

$$\frac{u}{U} = F_0'(x,0) + (U_\delta/U)[A(\Lambda)\sqrt{Z} + D], \qquad Z = \frac{z}{\delta}, \ Z \to 0. \tag{4}$$

Finally, after comparing his results with the experiments of nine different authors, Afzal proposed:

$$
\begin{aligned}
&A = 3.5 + 19\,\Lambda, \qquad 0 \le \lambda \le 0.2 \\
&C = 2.5\,\Lambda R_p, \qquad 0 \le \lambda R_p \le 2.5 \\
&C = 2.5\,\Lambda R_p - 0.012(\Lambda R_p)^2, \qquad 0 \le \lambda R_p \le 100
\end{aligned} \tag{5}
$$

2.1.3. The law of the wall formulation of Nakayama and Koyama (1984)

Nakayama and Koyama (1984) obtained a law of the wall for boundary layers subjected to adverse pressure gradients by conducting an one-dimensional analysis on the turbulent kinetic energy equation with assumptions of local similarity. Considering the two possible limiting cases of a constant stress layer and of a zero wall stress layer, the authors propose a turbulent kinetic energy equation that upon integration yields,

$$
u^+ = \frac{1}{\varkappa^+}\Big[3(\zeta - \zeta_s) + \ln\Big(\frac{\zeta_s + 1}{\zeta_s - 1}\frac{\zeta - 1}{\zeta + 1}\Big)\Big], \tag{6}
$$

where

$$
\zeta = \Big(\frac{1 + 2\tau^+}{3}\Big)^{1/2}. \tag{7}
$$

The above formulation introduces a von Kármán modified constant, $\varkappa^+$, and the slip value, ζ_s. For a boundary layer subjected to an adverse pressure gradient,

$$
\tau^+ = 1 + p^+ z^+, p^+ = \nu\rho^{1/2}(d\tau/dz)_w/\tau_w^{3/2}, z^+ = (\tau_w/\rho)^{1/2} z/\nu \tag{8}
$$

The von Kármán modified constant was estimated to be

$$
\varkappa^+(p^+) = \frac{0.419 + 0.539 p^+}{1 + p^+}. \tag{9}
$$

The slip value ζ_s was determined from the condition that in the limiting case $p^+ \to 0$ the above formulation reduces to the classical law of the wall. It follows that

$$
\zeta_s(p^+) = (1 + (2/3)e^{-\varkappa A} p^+)^{1/2} \approx (1 + 0.074 p^+)^{1/2}. \tag{10}
$$

Nakayama and Koyama (1984) considered their analysis general in the sense that velocity was related to the local shear stress instead of to the distance from the wall. Additionally, the analysis does not have to be restricted to a linear velocity-stress relation but can be applied for any monotonically increasing shear stress layer.

2.1.4. The formulation of Durbin and Belcher (1992)

Durbin and Belcher (1992) performed a scale analysis for turbulent boundary layers in strong adverse pressure gradients. The authors considered a three-layered asymptotic structured for the boundary layer so that an extra blending layer was inserted between the wall viscous region and the outer region. In the blending layer the mean mean velocity profile was found to follow a $z^{1/2}$ behaviour.

The relevant scales to the problem, were considered by Durbin and Belcher to depend on, α = -$U_\infty U_\infty$; L = U_∞^2/α; $u_p = (\nu\alpha)^{1/3}$.

Based on these definitions, a small parameter can be defined,

$$
\epsilon = \frac{u_p}{U_\infty} = (\nu\alpha/U_\infty^3)^{1/3} = R_L^{-1/3}. \tag{11}
$$

Please note that α denotes the external pressure gradient.

For the inner and blending layers, Durbin and Belcher found the adequate scaling to be

$$\hat{z} = \frac{z u_p}{\nu}, \qquad \hat{u} = \frac{u}{u_p}, \qquad \hat{\nu_t} = \frac{\nu_t}{\nu}, \qquad \hat{\kappa} = \frac{\kappa}{u_p^2}, \qquad \hat{\varepsilon} = \frac{\varepsilon \nu}{u_p^4}. \tag{12}$$

Then, using the κ-ϵ model to close the approximate equations of motion, a solution was proposed for the blending region:

$$\hat{U}_{\hat{z}} = \frac{\hat{z}}{\hat{\nu}_t}, \qquad \hat{U} = A_u \, \hat{z}^n, \tag{13}$$

where $A_u = 7.65$ and $n = 1/2$. The value of A_u is obtained directly from the standard constants of the κ-ϵ model.

The authors thus concluded that a graph of U versus $y^{1/2}$ in inner or in transition coordinates should present a linear region, with all curves collapsing onto each other.

2.1.5. The law of the wall formulation of Cruz and Silva Freire (1998, 2002)

Cruz and Silva Freire (2002) proposed the law of the wall for a separating flow to be written as

$$u = \frac{\tau_w}{|\tau_w|} \frac{2}{\varkappa} \sqrt{\frac{\tau_w}{\rho} + \frac{1}{\rho} \frac{dP_w}{dx} z} + \frac{\tau_w}{|\tau_w|} \frac{u_*}{\varkappa} \ln\left(\frac{z}{L_c}\right), \tag{14}$$

where

$$L_c = \frac{\sqrt{\left(\frac{\tau_w}{\rho}\right)^2 + 2\frac{\nu}{\rho}\frac{dP_w}{dx} u_R} - \frac{\tau_w}{\rho}}{\frac{1}{\rho}\frac{dP_w}{dx}}, \tag{15}$$

$\varkappa = 0.4$, u_* is the friction velocity, and u_R ($= \sqrt{\tau_p/\rho}$, τ_p = total shear stress) is a reference velocity.

Equation (14) is a generalization of the classical law of the wall and replaces the three expressions advanced in Cruz and Silva Freire (1998), Eqs. (25, 26, 27). Eq. (15) is an expression for the near wall region characteristic length, which is assumed to be valid in the attached and in the reverse flow regions.

The generalization provided by Eq.(14) implies that the friction velocity, u_*, used in the definition of L_c had to be replaced by the reference velocity u_R. Please, note that the characteristic length in the reverse flow region is different from the classical characteristic length given by the classical law of the wall. This in agreement with Simpson et al. (1981), who suggested that a characteristic length for the backflow region should be directly proportional to the absolute value of the wall shear stress.

2.2. Empirical correlations

2.2.1. The contribution of Simpson (1983)

From an analysis of available experimental data Simpson proposed velocity expressions for a description of reverse flow. As basic scaling parameters, he proposed to take the maximum negative velocity, U_N, and its distance from the wall, δ_N.

The resulting expressions were:
1) Viscous sublayer.

$$u^+ = z^+ + 0.5(u_p/u_\tau)^3 (z^+)^2, \qquad 0 \le z < z_1. \tag{16}$$

2) Fully turbulent region.

$$\frac{\overline{U}}{U_N} = A\left[\left(\frac{z}{\delta_N}\right) - \log\left(\frac{z}{\delta_N}\right) - 1\right] - 1, \qquad z \ge z_1. \tag{17}$$

The following definitions apply to the above equations:

$$u_p = \left(\frac{\nu}{\rho}\frac{\partial p}{\partial x}\right)^3, \quad A = 0.3, \quad z_1 = 0.02\delta_N. \tag{18}$$

2.2.2. The contribution of Nickels (2004)

Nickels (2004) developed an appropriate functional form for the mean velocity profile to parameterize the DNS data of Spalart (1988) e Osterlund (1999) on flows subject to adverse pressure gradients. The model was based on the concept of a universal critical Reynolds number for the viscous sublayer. In theory, this procedure can explain the shift in the apparent log-law due to pressure-gradient effects and gives an appropriate scaling for the Reynolds stresses. The results are supposed to hold for values of p_x^+ in the range -0.02 < p_x^+ < 0.06 and are presented considering the flow to be divided into three distinct regions: a viscous layer, a blending layer and an external layer.

The model of Nickles for the inner flow in adverse-pressure-gradient flow uses the idea advanced by Clauser (1956) that the viscous sublayer grows until it reaches a critical Reynolds number. Thus, at a certain distance from the wall the sublayer should reach a state in which it becomes unstable and perturbations grow. This critical height is denoted in non-dimensional form by z_c^+ ($=zu_\tau/\nu$) and is normally quoted in literature to be equal to 12 for a zero-pressure-gradient flow.

For flows under an adverse-pressure-gradient u_τ approaches zero so that an alternative scaling velocity has to be chosen. Nickels proposes to consider this scale to be U_T, with $U_T = \sqrt{\tau_T/\rho}$, τ_T = maximum shear stress in the viscous layer.

We may then define a critical Reynolds number,

$$R_c = \frac{U_T z_c}{\nu} \equiv 12. \tag{19}$$

As the wall shear stress becomes zero, the velocity scales reduce to

$$U_T = R_c^{1/3} U_p, \qquad \text{with} \qquad U_p = \left(\frac{\nu}{\rho}\frac{\partial p}{\partial x}\right)^{1/3}. \tag{20}$$

The critical height is then given by

$$z_c = \frac{\nu R_c^{2/3}}{U_p}, \qquad R_c = 12. \tag{21}$$

Nickels defines $z_p = zU_p/\nu$, where ν/U_p represents the thickness of the viscous sublayer.
The resulting law of the wall for adverse-pressure-gradient driven flows is given by ($\varkappa_0 = 0.4$)

$$\frac{u}{u_p} = \frac{R_c^{1/3}}{\varkappa_0} \ln\left(\frac{0.6 z_p}{R_c^{2/3}}\right). \tag{22}$$

3. Results

The above theories will be tested against the data of Simpson et al. (1981), of Dengel and Fernholz (1990) and of Loureiro et al. (2006).

The data of Simpson et al. (1981) were concerned with a two-dimensional, separating turbulent boundary layer for an air-foil type flow. In a wind tunnel with an adjustable wall the flow was accelerated and then decelerated until separation. Measurements were made with the help of hot-wire anemometry, surface hot-wire skin-friction gauges and laser-Doppler anemometry. Profiles of U, W, $\overline{u^2}$, $\overline{w^2}$ and of -$\overline{uw}$ were given at six different stations.

Dengel and Fernholz (1990) studied the effects of small changes in the static pressure distribution on the development of an axisymmetric, incompressible, turbulent boundary layer in the vicinity of separation. The boundary layer was made to develop in a wind tunnel over an inner circular cylinder with an elliptical nose cone. Three types of flows were studied to produce finite regions of approximately zero, slightly positive and slightly negative skin-friction. Measuring techniques consisted of hot-wire anemometry, pulsed-wire anemometry and laser-Doppler anemometry. Mean and fluctuating profiles were presented for five stations.

The experiments of Loureiro et al. (2006) were performed in a water channel. The flow over a smooth, two-dimensional steep hill was characterized at thirteen stations. The large region of reverse flow on the lee of the hill was particularly scrutinized through five stations. Measurements were conducted by laser-Doppler anemometry. Profiles of U, W, $\overline{u^2}$, $\overline{w^2}$ and of -$\overline{uw}$ were presented for all stations.

An assessment of the theories presented in Section 2 will be made by comparing selected profiles of Simpson et al. (1981), of Dengel and Fernholz (1990) and of Loureiro et al. (2006) with the several proposed expressions.

Graphs will be presented so as evaluate the performance of the formulations in four distinct regions: (a) upstream of separation, (b) near to the separation point, (c) in the reverse flow region and (d) downstream of the separation bubble.

The formulation of Mellor, given by Eq. 1, is shown in Fig. 1 in coordinates

$$U_M = u^+ \qquad \text{and} \qquad Z_M = \frac{4z^+}{2 + p^+z^+ + 2\sqrt{1 + p^+z^+}}. \tag{23}$$

Agreement with experimental data was found to be fair just in the vicinity of a separation point (Fig. 1b). In particular, both the near wall data of Simpson et al. (1981) and of Loureiro et al. (2006) agree well with predictions.

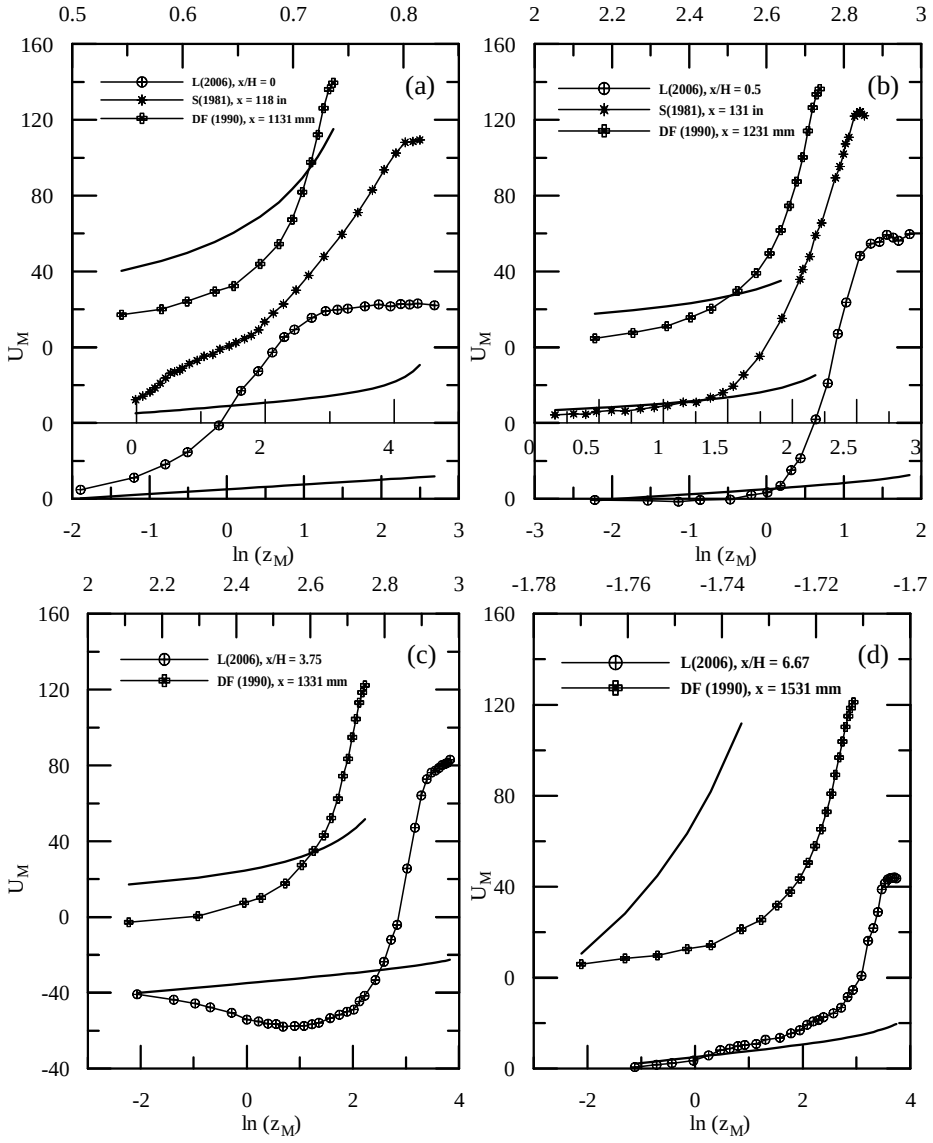

Figure 1: Comparison of Mellor's (1966) theory with the data of Simpson et al. (1981), of Dengel and Fernholz (1990) and of Loureiro et al. (2006).

To test Afzal's (1982) equation, Eq. 3, the following co-ordinate system was used

$$U_{Afzal} = \frac{u}{u_p} \qquad Z_{Afzal} = \zeta = \frac{zU_p}{\nu}. \tag{24}$$

Because Afzal's formulation is supposed to hold for mild adverse pressure gradients, just the data of Loureiro

et al. (2006) could be used here to test its applicability. The results shown in Fig. 2. The overall agreement of the theory is very good but for the description of the reverse flow region.

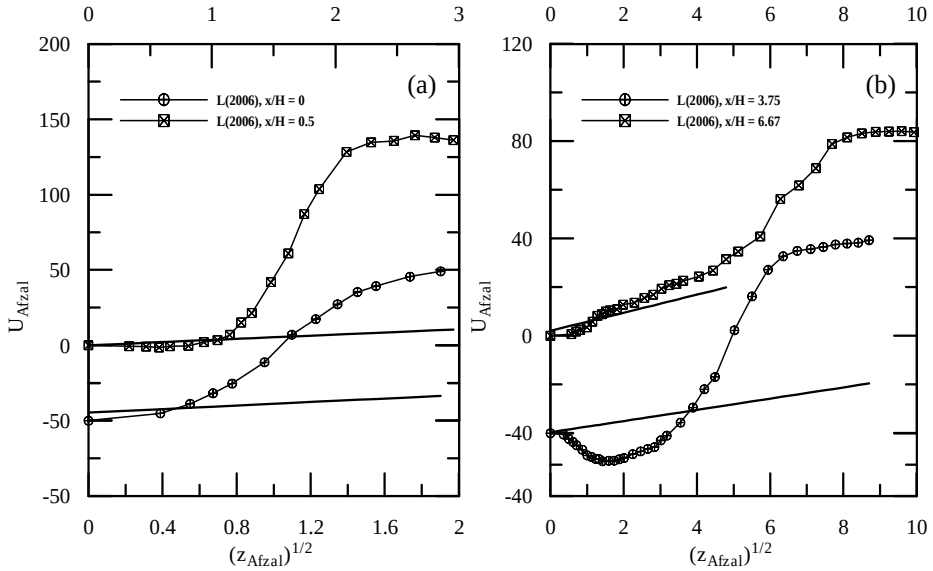

Figure 2: Comparison of Afzal's (1983) theory with the data of Loureiro et al. (2006).

To compare the theory of Nakayama and Koyama (1984) we use the co-ordinate system:

$$U_{NK} = u^+ \qquad Z_{NK} = \frac{\zeta_s + 1}{\zeta_s - 1}\frac{\zeta - 1}{\zeta + 1} \tag{25}$$

Predictions for the data of Simpson et al. (1981) both upstream and in the vicinity of the separation point are reasonable. In the region of reverse flow, the data of Dengel and Fernholz (1990) is fairly adjusted. Comparison to other data is not good.

The arguments of Durbin and Belcher (1992) imply for the existence of a power-law in a region near to separation. This layer would exist to provide matching between the inner and outer solutions. Graphs in 1/2-coordinates are shown in Fig. 4, where the following definitions were used $U_{DB} = u/u_p$, $Z_{DB} = zu_p/\nu$. In the region near to a separation point, Fig. 4b, the data of Simpson suggest to the existence of a possible power-law region very close to the law. The data of Loureiro et al. also provide a good fit in the region of reverse flow. However, that was not the intention of the authors. Their formulation is supposed to hold in regions of attached flow. Overall the agreement with the other data is very poor.

The theory of Cruz and Silva Freire is considered next. This theory was specially advanced to describe reverse flow. Consider $U_{CSF} = u/u_\tau$ and $Z_{CSF} = z/L_c$ so that Eq. 14 can be represented in Fig. 5. The agreement between the theory of Cruz and Silva Freire (2002) and the data of Simpson et al. (1981) and of Loureiro et al. (2006) is remarkable. Note specifically the good agreement near to the separation point and in the reverse flow region. The general trend of the reverse flow is indeed well captured by the theory.

The reverse flow data of Loureiro et al. (2006) is compared in Fig. 6 with the theory of Simpson (1983) for the outer flow description. The agreement is good.

The empirical theory of Nickels (2004) is compared with the data of other authors in Fig. 7. The co-ordinates are defined according to

$$U_{Ni} = u/u_p, \qquad Z_{Ni} = \frac{0.6 z_p}{R_c^{2/3}}. \tag{26}$$

The comparison is not favorable to Nickel's formulation. But for a good agreement regarding the data of Dengel and Fernholz (1990), the other comparisons are very disappointing.

4. Final Remarks

The present work has conducted a detailed analysis on the description of turbulent flow near a separation point, including its region of reverse flow. Predictions given by the seven different scaling laws were compared

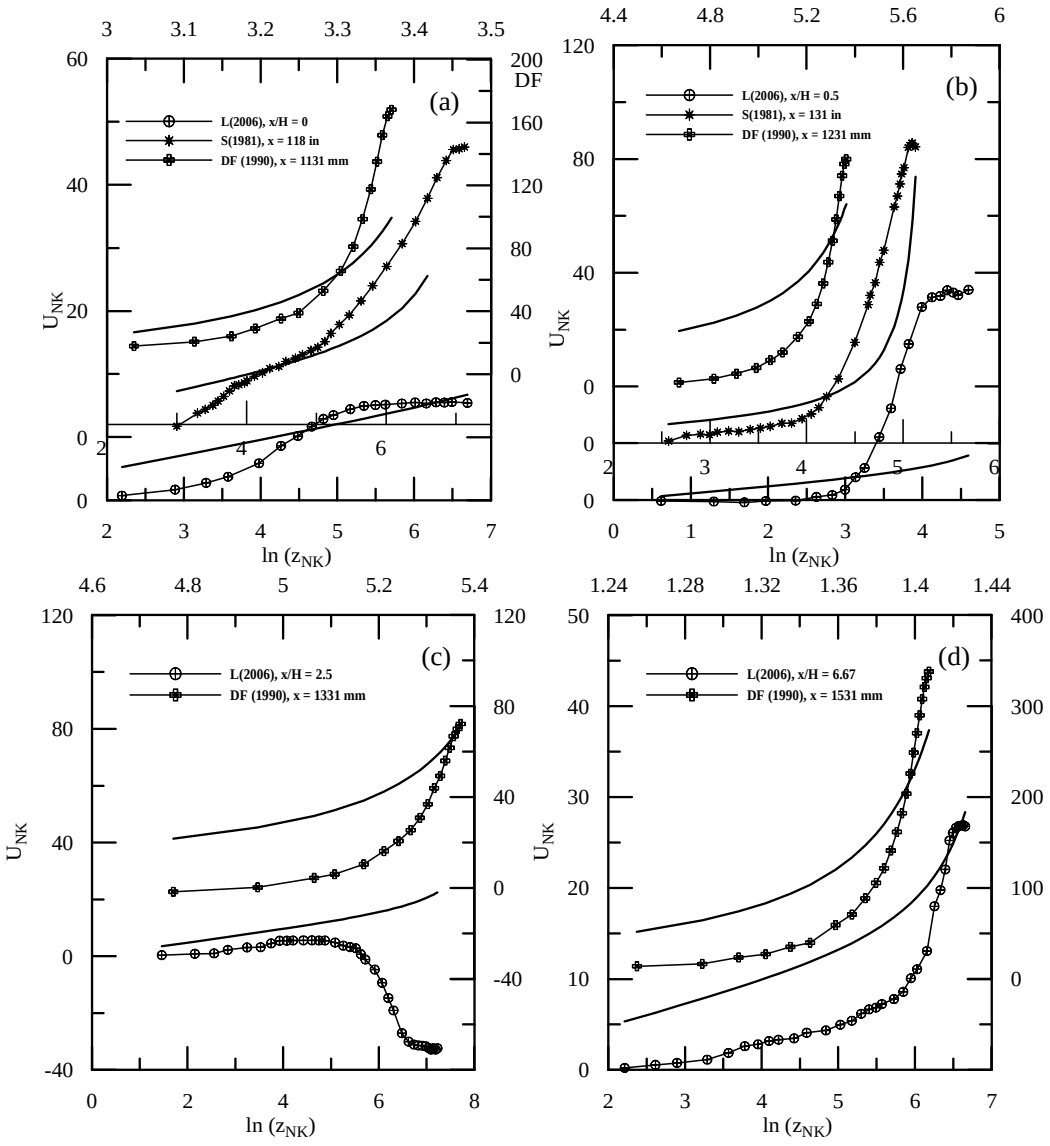

Figure 3: Comparison of Kakayama and Koyama's (1984) theory with the data of Simpson et al. (1981), of Dengel and Fernholz (1990) and of Loureiro et al. (2006).

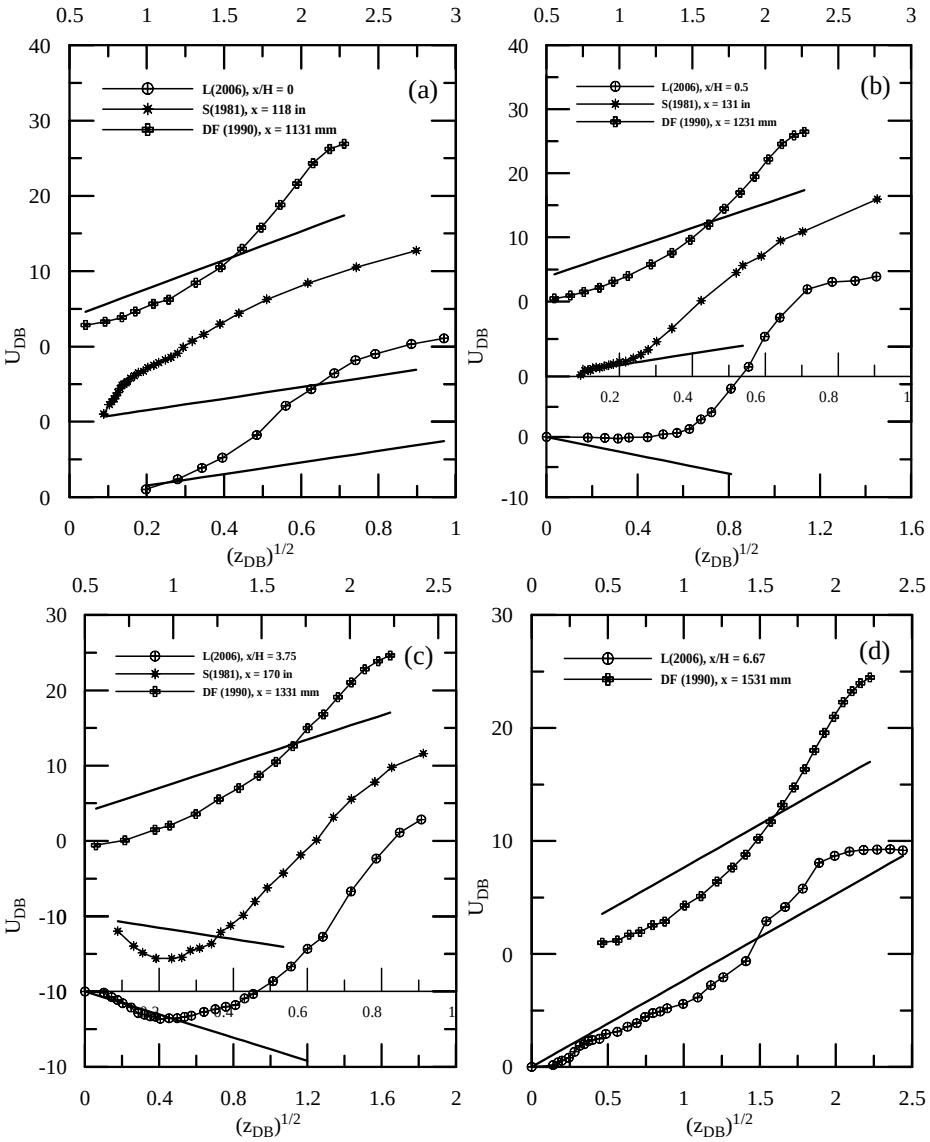

Figure 4: Comparison of Durbin and Belcher's (1992) theory with the data of Simpson et al. (1981), of Dengel and Fernholz (1990) and of Loureiro et al. (2006).

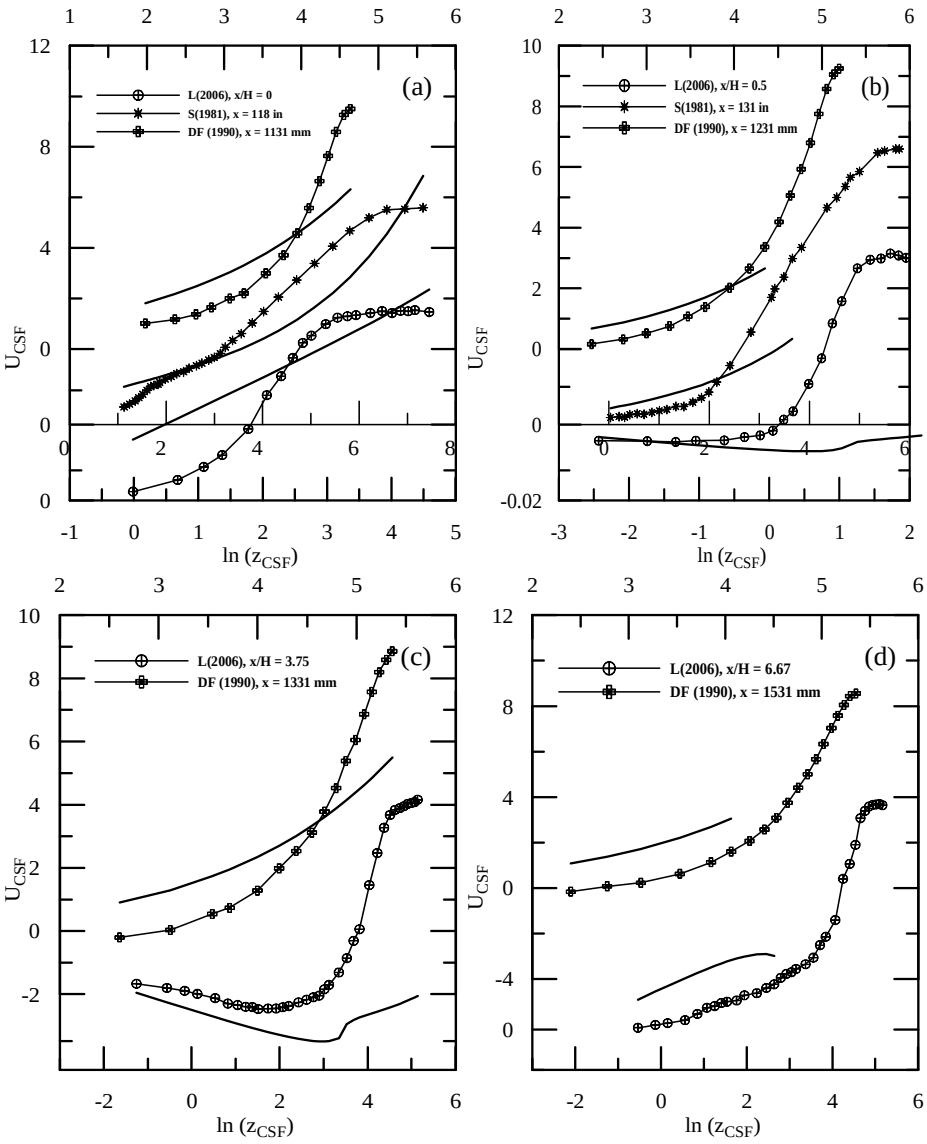

Figure 5: Comparison of Cruz and Silva Freire's (2002) theory with the data of Simpson et al. (1981), of Dengel and Fernholz (1990) and of Loureiro et al. (2006).

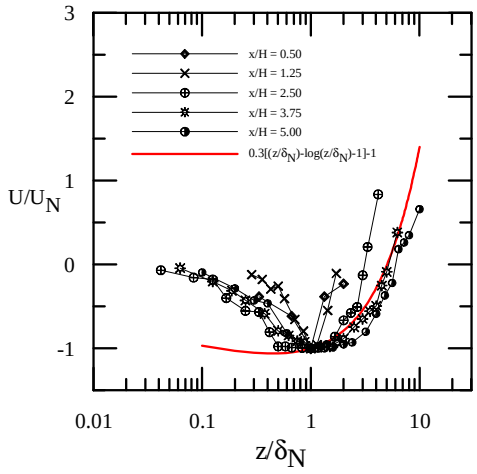

Figure 6: Comparison of Simpson's (1983) theory with the data of Loureiro et al. (2006).

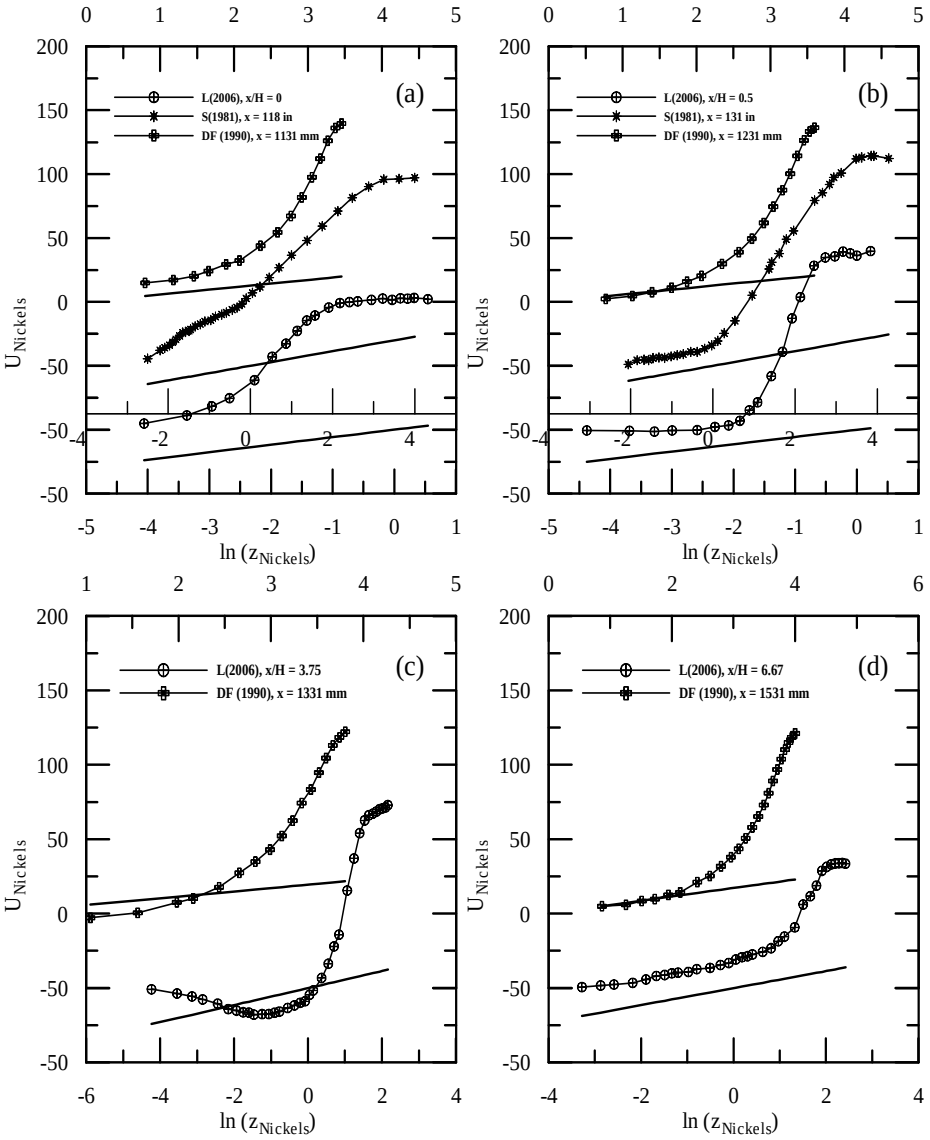

Figure 7: Comparison of Nickels´s (2004) theory with the data of Simpson et al. (1981), of Dengel and Fernholz (1990) and of Loureiro et al. (2006).

with three sets of independent experiments, the data of Simpson et al. (1981), of Dengel and Fernholz (1990) and of Loureiro et al. (2006). The performance of the formulations were evaluated in four distinct regions: (i) upstream of separation, (ii) near to the separation point, (iv) in the reverse flow region and (v) downstream of the separation bubble. Consequently, this study provides a broad and independent analysis of the problem, and investigates the ability of the scaling laws to predict the flow behaviour from upstream of the separation region, along to the recirculation bubble and downstream of the reattachment point.

The results have clearly demonstrated that the more sophisticated laws, where adjustable scaling parameters are used, do perform much better than the others. In this sense, the formulation of Cruz and Silva Freire (2002) appears to be much superior than the others. In fact, this formulation has shown to be adequate for use in regions of attached and of detached flows. This a very unique feature, that makes it a very useful tool.

The formulations which are based solely on the pressure gradient and on the velocity scale derived from this parameter show poor results. These laws are observed to be incapable of providing good results for all the four distinct regions studied. The different performances of the formulations are naturally due to the different characteristic scales used and on the arguments which the derivations are based on.

A further refinement of the present analysis is currently under construction. The seven proposed near wall formulations will be tested against a larger set of experimental data.

Acknowledgements. JBRL benefited from a Research Scholarship from the Brazilian Ministry of Education through CNPq. APSF is grateful to the Brazilian National Research Council (CNPq) for the award of a Research Fellowship (Grant No 304919/2003-9). The work was financially supported by CNPq through Grant No 472215/2003-5 and by the Rio de Janeiro Research Foundation (FAPERJ) through Grants E-26/171.198/2003 and E-26/152.368/2002.

5. References

Afzal, N.: 1983, Analysis of a turbulent boundary-layer subjjected to a strong adverse pressure-gradient, "Int. J. Engng. Sci.", 21, 6, 563–576.

Coles, D.: 1956, The law of the wake in the turbulent boundary layer, "J. Fluid Mech.", 1, 191–226.

Clauser, F. H.: 1956, The turbulent boundary layer, "Adv. Appl. Mech.", 4, 1-51.

Cruz D. O. A. and Silva Freire A. P.: 1998, On single limits and the asymptotic behaviour of separating turbulent boundary layers. "Int. J. Heat Mass Transfer", 41, 2097–2111.

Cruz D. O. A. and Silva Freire A. P.: 2002, Note on a thermal law of the wall for separating and recirculating flows. "Int. J. Heat Mass Transfer", 45, 1459–1465.

Dengel, P. and Fernholz, H. H.: 1990, An experimental investigation of an incompressible turbulent boundary layer in the vicinity of separation. "J. Fluid Mech.", 212, 615–636.

Durbin, P. A. and Belcher, S. E.: 1992, Scaling of Adverse-Pressure-Gradient Turbulent Boundary Layers. "J. Fluid Mech.", 238, 699–722.

Loureiro, J. B. R., Soares, D. V., Fontoura Rodrigues, J. L. A., Pinho, F. T. and Silva Freire, A. P.: 2006, Water tank and numerical model studies of flow around steep smooth two-dimensional hills. "Boundary-layer Meteorol.", (in press).

Mellor, G. L.: 1966, The effects of pressure gradients on turbulent flow near a smooth wall. "J. Fluid Mech.", 24, 255–274.

Millikan, C. B.: 1939, A critical discussion of turbulent flow in channels and tubes. "Proc. 5th Int. Cong. App. Mech.", J. Wiley, N. Y., 386–392.

Nakayama, A. and Koyama, H.: 1984, A wall law for turbulent boundary layers in adverse pressure gradients. "AIAA J.", 22, 1386–1389.

Nickels, T. B.: 2004, Inner scaling law for wall-bounded flows subject to large pressure gradients. "J. Fluid Mech.", 521, 217–239.

Österlund, J. M.: 1999, Experimental studies of zero pressure-gradient turbulent boundary layer flow. "PhD thesis", Royal Institute of Stockolm.

Simpson, R. L., Chew, Y. T. and Schivaprasad, B. G.: 1981, The structure of a separating boundary layer. Part 1: Mean flow and Reynolds stresses. "J. Fluid Mech.", 113, 23–51.

Simpson, R. L.: 1983, "AIAA J.", 41, 142–144.

Spalart, P. R.: 1988, Direct numerical study of a turbulent boundary layer up to $Re_\theta = 1410$. "J. Fluid Mech.", 249, 337–371.

Stratford, B. S.: 1959, The prediction of separation of the turbulent boundary layer. "J. Fluid Mech.", 5, 1–16.

Proceedings of the 11th Brazilian Congress of Thermal Sciences and Engineering – ENCIT 2006
Braz. Soc. of Mechanical Sciences and Engineering – ABCM, Curitiba, Brazil, Dec. 5-8, 2006

Paper CIT06-0660

Simulação numérica de escoamento bi-dimensional sobre aerofólios utilizando a técnica de fronteiras imersas

Vinícius Piovesan de Toledo
SMM – EESC – USP Av. Trabalhador Sancarlense, 400, CEP:13566-590 São Carlos - SP
vinipio@gmail.com

José Alberto Cuminato
SME – ICMC – USP Av. Trabalhador Sancarlense, 400, CEP:13560-970 São Carlos - SP
jacumina@icmc.usp.br

Leandro Franco de Souza
SME – ICMC – USP Av. Trabalhador Sancarlense, 400, CEP:13560-970 São Carlos - SP
lefraso@icmc.usp.br

Resumo. *No presente trabalho é realizado um estudo numérico de escoamentos incompressíveis sobre um perfil bi-dimensional. O aerofólio foi modelado por meio da técnica de Fronteiras Imersas. Essa técnica consiste na adição de um termo forçante nas equações de Navier-Stokes, que modelam o efeito da presença do corpo na evolução do escoamento. Isso faz suas soluções serem mais simples, tornando possível a utilização de malhas Cartesianas. Foi implementado um estiramento da malha na direção normal ao escoamento, para aumentar a acurácia dos resultados próximos ao aerofólio e reduzir o número de pontos nesta direção. O código numérico é baseado na formulação Vorticidade-Velocidade. Métodos de diferenças finitas de alta ordem foram adotados para o cálculo das derivadas espaciais. A integração no tempo foi realizada por um esquema de Runge-Kutta de 4ª ordem. Os resultados numéricos foram obtidos para baixos números de Reynolds (5000). Os resultados mostram que o código implementado fornece bons resultados se comparados a outros resultados obtidos da literatura.*

Palavras chave: *Método das fronteiras imersas, estiramento de malha, métodos de alta ordem, formulação vorticidade-velocidade*

1. Introdução

O estol de asa é um fenômeno típico nas condições críticas de vôo de uma aeronave, no caso, a decolagem e o pouso. Nestes casos, deve-se ganhar o máximo de força de sustentação possível através de um aumento no ângulo de ataque. Em outras palavras, o fenômeno de estol é associado à formação de vórtices no bordo de ataque de uma asa, precedida da separação da camada-limite laminar próxima ao nariz do aerofólio. Com o tempo, estes vórtices chegam ao bordo de fuga e finalmente se separam. Esta situação é responsável pela queda de sustentação. Nas aeronaves modernas, o fenômeno é atenuado com a implementação de dispositivos de hiper-sustentação, no entanto estes são complexos e pesados, além de possuírem altos custos de produção e manutenção. Por isto, o mercado vem exigindo novas soluções baseadas na diminuição da complexidade destes dispositivos, buscando o aumento do desempenho dos aerofólios.

No presente trabalho, o estudo de um escoamento ao redor de um aerofólio foi realizado, utilizando-se o método das fronteiras imersas. O método foi idealizado por Peskin, 1972; Peskin, 1977, para simular o escoamento de sangue em torno das válvulas de um coração. O método de Peskin consiste na utilização de duas malhas, uma Euleriana, utilizada para o cálculo das equações, e outra Lagrangeana, representando o corpo imerso. A interação entre as duas malhas seria representada pela adição de um termo fonte de força às equações de Navier-Stokes. Isto evita a utilização de complexas malhas em torno do corpo. Além disto, as duas malhas de Peskin são geometricamente independentes, indicando que não há necessidade de gerar uma nova malha a cada instante de tempo. Uma boa revisão de métodos de fronteiras imersas pode ser visto em Mittal e Iaccarino, 2005. Ye *et al.*, 1999 apresenta um método de 2a ordem para estudo de escoamentos em torno de corpos com geometrias complexas.

A utilização de métodos de fronteiras imersas para escoamentos em torno de perfis aerodinâmicos, incompressíveis, com baixos números de Reynolds, já vem sido explorada pela comunidade científica (Ortega e Silvestrini, 2004; Oliveira *et al.*, 2005).

Ortega e Silvestrini, 2004 realizaram um estudo de escoamento em torno de um perfil NACA 0012, variando-se o ângulo de ataque para prever o aparecimento do *stall*. Os resultados mostram que o código utilizado, com

fronteiras imersas, apresentam bons resultados. O fenômeno *stall* ocorre quando o ângulo crítico de ataque é excedido, ocasionando perda de sustentação e aumento de arrasto.

Oliveira *et al.*, 2005 realizaram um estudo de escoamento em torno de um perfil NACA 0012, utilizando o método das fronteiras imersas. O número de Reynolds adotado por ele foi de $Re = 10000$ e foi utilizada uma modelagem sub-malha com o modelo de Smagorinsky. Os resultados mostram que o fenômeno de *stall* dinâmico foi capturado, mas que os resultados poderiam ser melhores se fosse utilizado outro modelo sub-malha, ou mesmo um modelo de turbulência.

O presente trabalho consiste na utilização das equações de Navier-Stokes aplicadas ao escoamento ao redor de um aerofólio. Juntamente com o método das fronteiras imersas, foi possível analisar diferentes condições de ângulo de ataque. A utilização de esquemas de alta-ordem de precisão permitiram a adoção de malhas com uma quantidade menor de pontos se comparada a outros estudos.

O presente artigo é dividido como se segue: na seção Formulação é mostrada a formulação adotada no atual trabalho; na seção Método Numérico são mostrados os detalhes do método numérico utilizado; na seção Resultados os resultados numéricos das simulações são dados; as conclusões e comentários finais são dados na última seção.

2. Formulação

As equações de Navier-Stokes modelam o escoamento de fluidos tanto compressíveis como incompressíveis, sejam eles turbulentos ou laminares. Dependendo das propriedades assumidas ao escoamento, as equações de Navier-Stokes podem ser simplificadas consideravelmente, visando reduzir as dificuldades inerentes à sua solução numérica. Neste estudo, apenas a Conservação da Massa (Equação da Continuidade) e a Quantidade de Movimento (2ª Lei de Newton) serão utilizadas para os cálculos. A formulação adimensionalizada e adequada ao método das fronteiras imersas é mostrada abaixo:

$$\frac{\partial u}{\partial x} + \frac{\partial v}{\partial y} = 0 \tag{1}$$

$$\frac{\partial u}{\partial t} + u\frac{\partial u}{\partial x} + v\frac{\partial u}{\partial y} = -\frac{\partial p}{\partial x} + \frac{1}{Re}\left(\frac{\partial^2 u}{\partial x^2} + \frac{\partial^2 u}{\partial y^2}\right) + f_x \tag{2}$$

$$\frac{\partial v}{\partial t} + v\frac{\partial v}{\partial x} + u\frac{\partial v}{\partial y} = -\frac{\partial p}{\partial y} + \frac{1}{Re}\left(\frac{\partial^2 v}{\partial x^2} + \frac{\partial^2 v}{\partial y^2}\right) + f_y, \tag{3}$$

em que u e v representam as componentes da velocidade nas direções horizontal e vertical, respectivamente; x,e y correspondem à direção do escoamento e à direção normal ao escoamento, respectivamente; t é a variável que representa o tempo; Re representa o número de Reynolds; p é a pressão local; e f_x e f_y indicam os termos forçantes nas direções x e y, respectivamente.

No presente estudo foi adotada a formulação Vorticidade-Velocidade, dependente somente das velocidades dadas no domínio bi-dimensional e da vorticidade dada na direção transversal ao domínio. Desta forma pode-se obter a equação de transporte de vorticidade:

$$\frac{\partial \omega}{\partial t} + u\frac{\partial \omega}{\partial x} + v\frac{\partial \omega}{\partial y} = \frac{1}{Re}\left(\frac{\partial^2 \omega}{\partial x^2} + \frac{\partial^2 \omega}{\partial y^2}\right) + \left(\frac{\partial f_x}{\partial y} - \frac{\partial f_y}{\partial x}\right). \tag{4}$$

A equação de Poisson pode ser obtida para a velocidade v:

$$\frac{\partial^2 v}{\partial x^2} + \frac{\partial^2 v}{\partial y^2} = -\frac{\partial \omega}{\partial x}. \tag{5}$$

Juntamente com a equação (1), é formado um sistema de três equações capaz de obter os valores de u, v e ω para a análise do escoamento previamente descrito.

No entanto, as equações de Navier-Stokes são representadas no domínio físico bi-dimensional, dado pelas coordenadas x e y. No presente estudo não se deseja utilizar uma distribuição regular de malha. Desta forma foi adotada uma malha que tivesse um refinamento na região próxima ao perfil, permitindo a obtenção de resultados mais precisos.

Desta forma, optou-se por um domínio computacional com a distribuição de pontos com uma maior concentração em torno do aerofólio imerso. A técnica é conhecida como estiramento, e foi aplicada apenas na direção vertical da malha, gerando uma nova malha de coordenadas (ξ, η). Assim, a coordenada computacional ξ será idêntica à coordenada física x.

Devido a esta característica, as malhas devem respeitar a seguinte condição:

$$\frac{\partial y}{\partial \eta} = \frac{1}{\frac{\partial \eta}{\partial y}} \quad \text{ou} \quad y_\eta = \frac{1}{\eta_y}. \tag{6}$$

Os termos y_η e η_y representarão, a partir de agora, as derivadas relacionadas acima.
Para a coordenada y, há uma formulação que a descreve em relação ao meio computacional, dada por:

$$y = D\left\{1 + \frac{sinh[\beta(\eta - A)]}{sinh(\beta A)}\right\}, \tag{7}$$

onde

$$A = \frac{1}{2\beta} ln\left[\frac{1 + (e^{\beta} - 1)(D/H)}{1 + (e^{-\beta} - 1)(D/H)}\right]$$

e β, D e H são parâmetros ajustáveis. H é a altura da malha, com D correspondendo a metade de seu valor. O parâmetro β indica o nível de refinamento da malha. A malha criada com estes parâmetros é apresentada na Fig. 2.

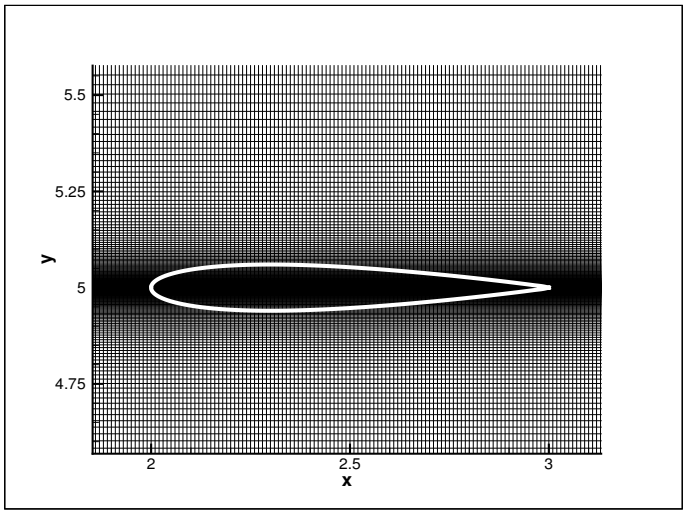

Figura 1: Malha com estiramento

A solução numérica do escoamento exige o conhecimento das primeira e segunda derivadas de η em relação a y, como será visto posteriormente. A literatura fornece esta equações, no entanto, em função de valores de y. Derivando a equação (7) em relação a η, tem-se:

$$y_\eta = \frac{e^{-\eta\beta}(e^{2\eta\beta} + e^{A\beta})\beta D}{e^{2A\beta} - 1}$$

e utilizando-se da equação (6), chega-se à

$$\eta_y = \frac{sinh(\beta A)}{\beta cosh(\beta(\eta - A))D}. \tag{8}$$

A derivada segunda é dada por

$$\eta_{yy} = \frac{\partial^2 \eta}{\partial y^2} = -\frac{\left(\sinh\left(\beta A\right)\right)^3 \left(\frac{y}{D} - 1\right)}{D^2 \left(1 + \left(\frac{y}{D} - 1\right)^2 \left(\sinh\left(\beta A\right)\right)^2\right)^{1,5} \beta}. \tag{9}$$

Desta forma, pode-se utilizar as equações acima para solucionar as equações que governam o movimento dos fluidos, incluindo de forma adequada o estiramento.

3. Método Numérico

Os métodos utilizados até então são tradicionais nos estudos de escoamentos. No entanto, todos devem ser adaptados à condição de estiramento, o que modifica de certa forma as equações utilizadas. No código gerado para a análise, os seguintes esquemas foram abordados:

- Solução das equações de Navier-Stokes bi-dimensional na formulação Vorticidade-Velocidade;
- Esquemas de diferenças finitas de 5ª e 6ª ordem para as derivadas espaciais;
- Integração no tempo pelo método de Runge-Kutta de 4ª ordem;
- Solução da equação de Poisson pelo esquema de Aproximação Total (FAS) e múltiplas malhas;
- Utilização da técnica de Fronteiras Imersas.

3.1. Transformação de coordenadas do domínio físico para o computacional

A nova malha computacional gerada não difere apenas pela resolução de suas linhas em relação ao domínio físico. As derivadas calculadas no novo domínio devem ser transformadas para que mantenham sua coerência, sendo dadas pelas seguintes relações:

$$\frac{\partial f}{\partial y} = \frac{\partial f}{\partial \eta}\frac{\partial \eta}{\partial y} = \frac{\partial f}{\partial \eta}\eta_y \tag{10}$$

$$\frac{\partial^2 f}{\partial y^2} = \frac{\partial^2 \eta}{\partial y^2}\frac{\partial f}{\partial \eta} + \left(\frac{\partial \eta}{\partial y}\right)^2 \frac{\partial^2 f}{\partial \eta^2} = \frac{\partial f}{\partial \eta}\eta_{yy} + \frac{\partial^2 f}{\partial \eta^2}\eta_y^2 \tag{11}$$

Desta forma, a derivada de qualquer variável pode ser calculada no domínio computacional, dado pela coordenada η, e depois ser convertido para o domínio físico, representado por y, através das derivadas η_y e η_{yy}, conhecidas através da relação algébrica entre os domínios. A vantagem em executar este tipo de operação está no fato da malha computacional ser regular, o que implica em resoluções com maior simplicidade e rapidez.

3.2. Equações de Navier-Stokes

As equações de Navier-Stokes foram modificadas após a aplicação de estiramento. O sistema é dado abaixo:

$$\frac{\partial u}{\partial x} + \eta_y \frac{\partial v}{\partial \eta} = 0 \tag{12}$$

$$\frac{\partial^2 v}{\partial x^2} + \eta_y^2 \frac{\partial^2 v}{\partial \eta^2} + \eta_{yy}\frac{\partial v}{\partial \eta} = -\frac{\partial \omega}{\partial x} \tag{13}$$

$$\frac{\partial \omega}{\partial t} + u\frac{\partial \omega}{\partial x} + \eta_y v \frac{\partial \omega}{\partial \eta} = \frac{1}{Re}\left(\frac{\partial^2 \omega}{\partial x^2} + \eta_y^2 \frac{\partial^2 \omega}{\partial \eta^2} + \eta_{yy}\frac{\partial \omega}{\partial \eta}\right) + \left(\eta_y \frac{\partial f_x}{\partial \eta} - \frac{\partial f_y}{\partial x}\right). \tag{14}$$

O método das Fronteiras Imersas, utilizado para inclusão do perfil no escoamento, é realizado através da inclusão dos termos forçantes adicionais às equações. O cálculo desses termos é feito de acordo com as fórmulas:

$$\begin{aligned} f_x(x,y) &= rf\delta(x,y)\,u(x,y) \\ f_y(x,y) &= rf\delta(x,y)\,v(x,y). \end{aligned}$$

Ou seja, os termos forçantes são dependentes das velocidades nas respectivas direções, modificados por um termo de relaxamento (rf) que varia de acordo com o que se deseja na simulação, em termos de velocidade da iteração. A função $\delta(x,y)$ apenas indica que para os pontos internos do perfil o valor de $\delta(x,y)$ é 1. Para pontos fora do perfil, o valor de $\delta(x,y)$ é zero. A transição destes valores, passando pela fronteira imersa, é dada através de uma função exponencial. Sendo assim, os termos forçantes não atuam na região externa ao perfil. No presente método não há existência de uma malha Lagrangeana, os valores da função delta – $\delta(x,y)$, no domínio computacional se encarregam de distribuir os termos forçantes onde se deseja anular as componentes da velocidade.

A solução da equação de Navier-Stokes é realizada através de discretizações por diferenças finitas de quinta e sexta ordem. Os valores da componente da velocidade v são obtidas através do processo iterativo da solução de (13) (explicado abaixo), enquanto que a componente da velocidade u é resultado da equação (12). O avanço no tempo é realizado pelo método de Runge-Kutta de 4ª ordem. A seqüência de operações adotada aqui é a mesma proposta por Souza, 2005.

3.3. Solução da Equação de Poisson

A equação de Poisson, com a utilização de estiramento, é representada por:

$$\frac{\partial^2 v}{\partial x^2} + \eta_y^2 \frac{\partial^2 v}{\partial \eta^2} + \eta_{yy} \frac{\partial v}{\partial \eta} = -\frac{\partial \omega}{\partial x} \tag{15}$$

Para a resolução da equação acima, escolheu-se um método multigrid com quatro malhas, do tipo FAS (do inglês *Full Approximation Scheme*). Este método é ilustrado na figura 3.3.

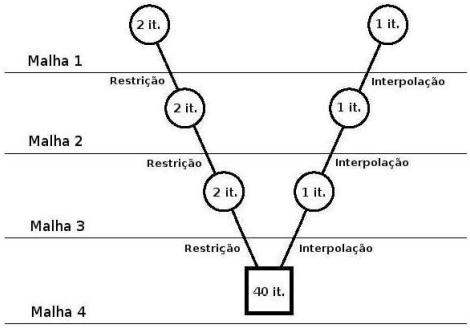

Figura 2: Ilustração do ciclo V utilizado

Utilizou-se para solução numérica da equação de Poisson em cada malha um método iterativo de Sobre-Relaxação Sucessiva por Linha, conhecido como LSOR (do inglês, *Line Successive Over-Relaxation*). Desta forma para cada linha resolveu-se um sistema linear exemplificado abaixo:

$$\left[A\right] \begin{bmatrix} v_{i,1} \\ v_{i,2} \\ \vdots \\ v_{i,jmax-1} \\ v_{i,jmax} \end{bmatrix} = \begin{bmatrix} RHS_1 \\ RHS_2 \\ \vdots \\ RHS_{jmax-1} \\ RHS_{jmax} \end{bmatrix} \tag{16}$$

Nesta representação matricial, $[A]$ indica uma matriz de constantes que variam com as propriedades da malha estirada, como as derivadas em relação ao meio físico (η_y, η_{yy}) e espaçamento da malha computacional $(\Delta\eta)$. A matriz que representa os valores de velocidade v para cada linha, dada uma coluna i da malha, é a matriz incógnita a ser determinada pela solução do sistema. A matriz RHS (do inglês *Right Hand Size*) representa o lado direito da equação. Os termos RHS, em função de cada linha, são dados pela combinação de valores da discretização w_z e também de valores de v, todos na mesma linha, vizinhos à coluna i em que a iteração está sendo realizada. O processo iterativo segue até que a seguinte condição seja estabelecida:

$$res_{i,j} = \frac{\partial^2 v}{\partial x^2} + \eta_y^2 \frac{\partial^2 v}{\partial \eta^2} + \eta_{yy} \frac{\partial v}{\partial \eta} + \frac{\partial \omega}{\partial x} \leq 10^{-7} \tag{17}$$

Nos resultados apresentados aqui, a solução numérica foi considerada como satisfatória a partir do momento o resíduo fosse igual ou menor que 10^{-7}.

4. Resultados

Foram realizadas simulações com 6 ângulos de ataque diferentes do perfil NACA 0012. Nestas simulações foi adotado o número de Reynolds igual a $Re = 5000$. O domínio utilizado se estendeu na direção longitudinal de $x_0 = 0$ a $x_{max} = 5,12$. Foram utilizados 513 pontos nesta direção, igualmente espaçados ($\Delta x = 0,01$). Na direção y o domínio utilizado se estendeu de 0 a 10. Nesta direção foram utilizados 321 pontos, espaçados conforme a Eq. 7. O perfil teve o seu baricentro localizado em $y = 5,0$. O baricentro serviu também como ponto de rotação do perfil. O fator de relaxamento (rf) adotado em todas as simulações foi de $rf = -2000$. Na região entre $x_3 = 4,60$ e $x_4 = 4,90$ foi adotada uma região de relaminarização do escoamento (Souza *et al.*, 2005; Kloker *et al.*, 1993; Meitz e Fasel, 2000), para evitar reflexões de perturbações no contorno de saída.

As Figs. 3 a 8 mostram os contornos de vorticidade obtidos nas simulações até um tempo adimensional de $t = 3,5$. Estes resultados foram obtidos utilizando-se microcomputadores Athlon AMD 64 3200+, e levaram em média 30 horas para serem obtidos. Pode-se observar que, com ângulos de ataque até 10 graus, os resultados mostram que o perfil ainda apresenta sustentação. Com o aumento do ângulo de ataque, ocorre o avanço da região de separação em direção ao bordo de ataque. Pode-se observar, com ângulos de ataque maiores ou iguais a 15 graus, a ocorrência do fenômeno conhecido como *stall*. De acordo com Chandrasekhara *et al.*, 1998 o ângulo de stall deste perfil é de 14 graus. Desta forma entende-se que o código implementado conseguiu obter, qualitativamente, bons resultados.

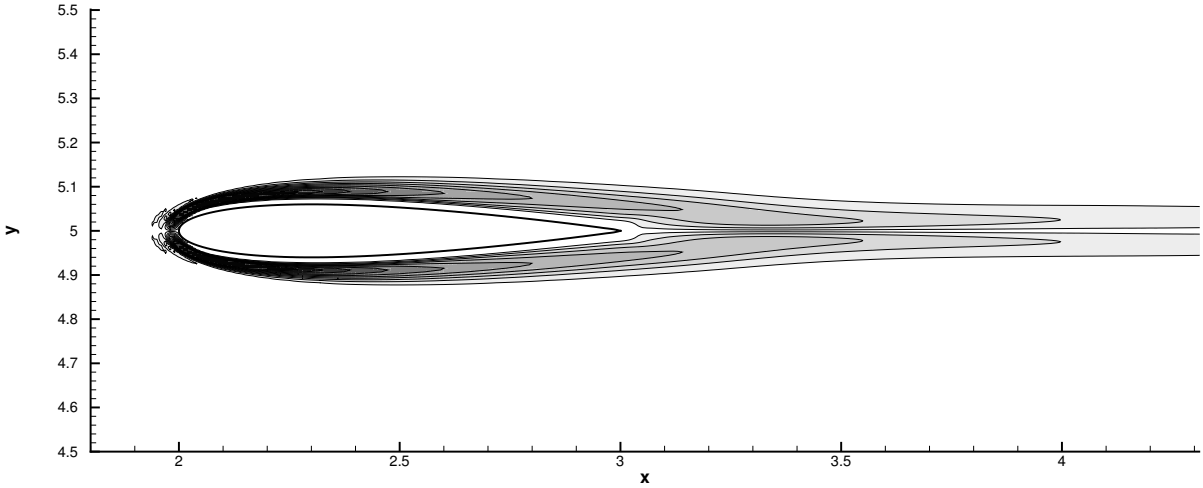

Figura 3: Contornos de vorticidade, ângulo de ataque $\alpha = 0^o$.

Figura 4 mostra que mesmo com um pequeno ângulo de ataque, acontece o desprendimento de sucessivos vórtices no bordo de fuga do perfil. Esta seqüência de vórtices forma a conhecida esteira de Von Karmán.

Pode-se observar na Fig. 5 que, com o ângulo de ataque de 10^o, o escoamento encontra-se sem separação numa região de até no máximo 30% da corda do perfil. Se compararmos este resultado com os resultados apresentados nas Figs. 6 até 8 pode-se observar que a separação ocorre logo após o bordo de ataque, indicando a ocorrência do fenômeno conhecido como *stall*.

5. Conclusões

No presente trabalho foi realizado um estudo numérico de escoamentos incompressíveis em torno de um perfil bi-dimensional. O aerofólio foi modelado por meio da técnica de Fronteiras Imersas. Foi implementado um estiramento da malha na direção normal ao escoamento, para aumentar a precisão dos resultados próximos ao aerofólio e reduzir o número de pontos nesta direção. Métodos de diferenças finitas de alta ordem foram adotados para o cálculo das derivadas espaciais. A integração no tempo foi realizada por um esquema de Runge-Kutta de 4ª ordem.

Os resultados numéricos foram obtidos para baixos números de Reynolds (5000) e seis ângulos de ataque do perfil. Os resultados mostram que o código implementado fornece bons resultados, se comparado qualitativamente, a outros resultados obtidos da literatura. A utilização do estiramento da malha na direção y viabiliza este tipo de estudo, com a utilização de poucos pontos nas regiões que não sofrem altos gradientes de velocidade/vorticidade. Esforços estão sendo realizados na sentido de se obter os valores dos coeficientes de sustentação e de arrasto para que seja realizada uma comparação quantitativa do código.

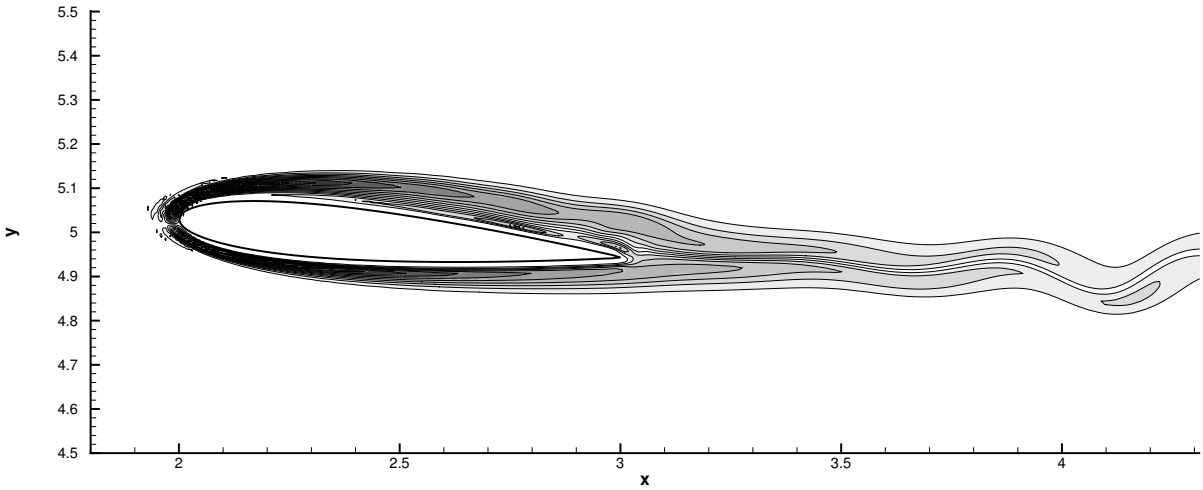

Figura 4: Contornos de vorticidade, ângulo de ataque $\alpha = 5^o$.

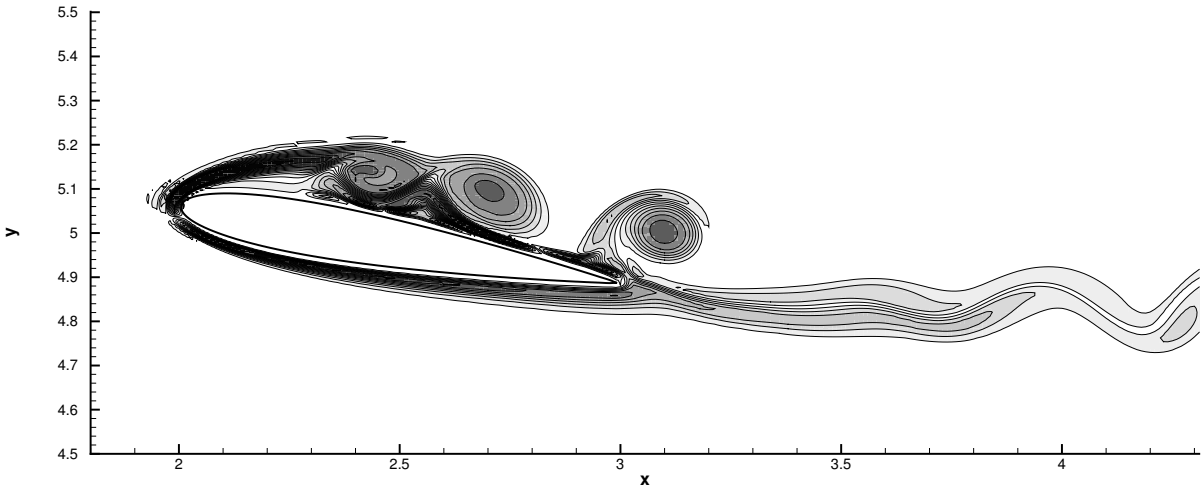

Figura 5: Contornos de vorticidade, ângulo de ataque $\alpha = 10^o$.

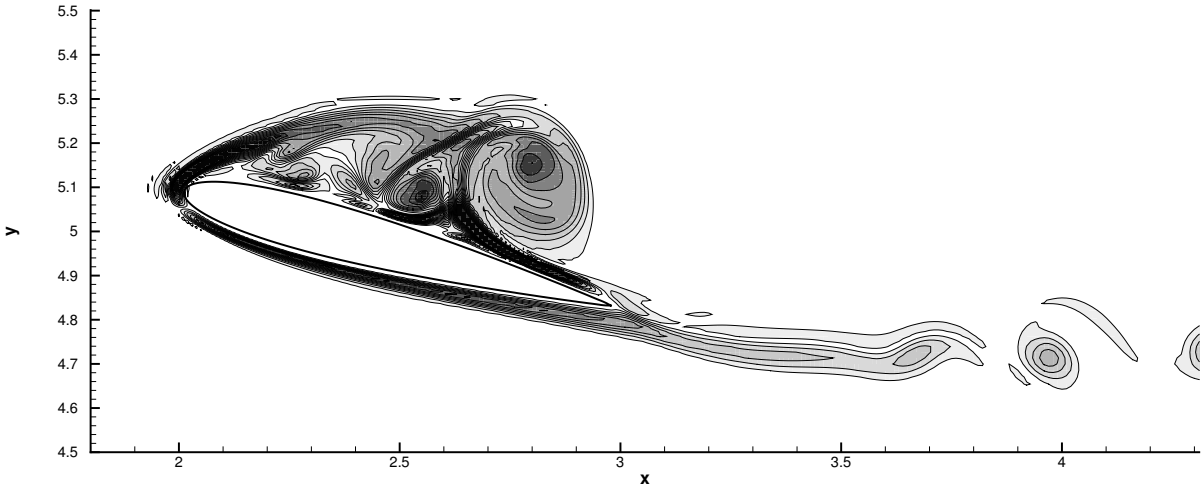

Figura 6: Contornos de vorticidade, ângulo de ataque $\alpha = 15^o$.

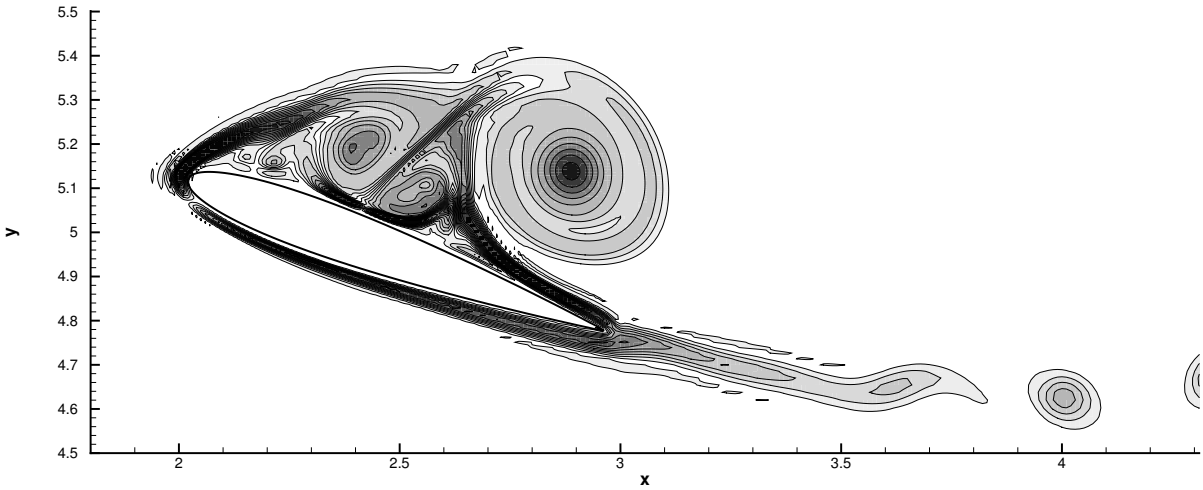

Figura 7: Contornos de vorticidade, ângulo de ataque $\alpha = 20^o$.

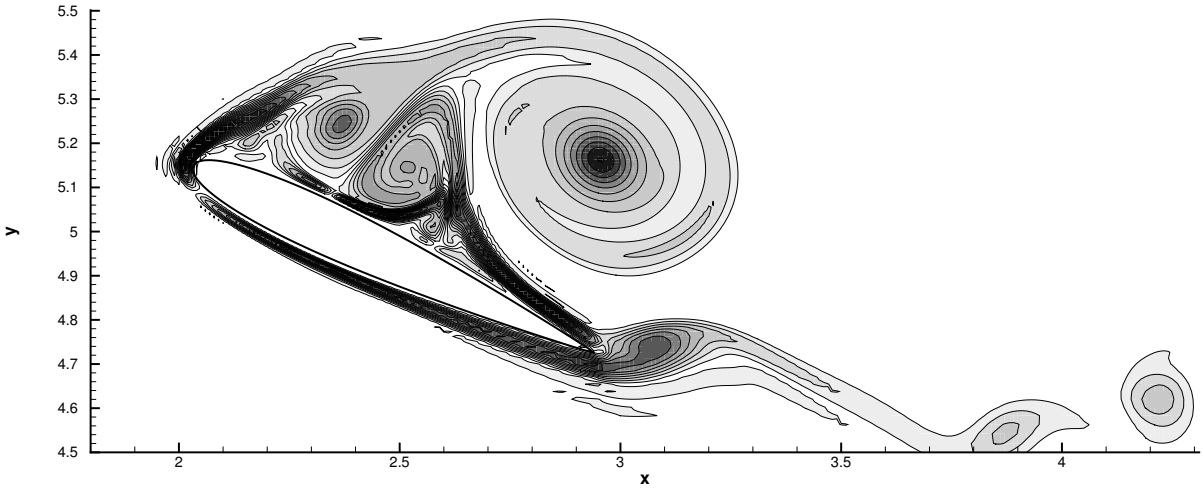

Figura 8: Contornos de vorticidade, ângulo de ataque $\alpha = 25^o$.

6. Agradecimentos

Os autores agradecem o apoio dado pelo CNPq e FAPESP processo No 04/07507-4.

7. Referências

Chandrasekhara, M. S., Wilder, M. C., and Carr, L. W., 1998, Unsteady Stall Control Using Dynamically Deforming Airfoils, "AIAA Journal", Vol. 36, pp. 1792–1800.

Kloker, M., Konzelmann, U., and Fasel, H. F., 1993, Outflow Boundary Conditions for Spatial Navier-Stokes Simulations of Transition Boundary Layers, "AIAA Journal", Vol. **31**, pp. 620–628.

Meitz, H. L. and Fasel, H. F., 2000, A compact-difference scheme for the Navier-Stokes equations in vorticity-velocity formulation., "J. Comp. Phys.", Vol. **157**, pp. 371–403.

Mittal, R. and Iaccarino, G., 2005, Immersed Boundary Methods, "Annu. Rev. Fluid Mech.", Vol. 37, pp. 239–261.

Oliveira, J. E. S., e Silva, A. L. F. L., and Neto, A. S., 2005, Numerical Simulation of Flows around a NACA 0012 airfoil in transient pitching motion using immersed boundary method with virtual physical model, "18th International Congress of Mechanical Engineering", Ouro Preto - MG.

Ortega, M. A. and Silvestrini, J. H., 2004, A DNS prediction of the flow around an airfoil at high angles of attack, "AIAA Paper 2004-5079", Providence, Rhode Island, USA.

Peskin, C. S., 1972, Flow Patterns Around Heart Valves: A Numerical Method, "J. Computational Physics",

Vol. **10**, pp. 252–271.

Peskin, C. S., 1977, Numerical Analisys of Blood Flow in the Heart, "J. Computational Physics", Vol. **25**, pp. 220–252.

Souza, L. F., 2005, Numerical Simulation of a FLow Over a Circular Cylinder Using Immersed Boundary Method in Vorticity-Velocity Formulation, "Proceedings of COBEM 2005", Ouro Preto - MG.

Souza, L. F., Mendonça, M. T., and Medeiros, M. A. F., 2005, The advantages of using high-order finite differences schemes in laminar-turbulent transition studies, "International Journal for Numerical Methods in Fluids", Vol. **48**, pp. 565–592.

Ye, T., Mittal, R., Udaykumar, H. S., and Shyy, W., 1999, An accurate cartesian grid method for viscous incompressible flows with complex Immersed Boundaries, "Jounal of Computational Physics", Vol. 156, pp. 209–240.

Numerical Simulation of a 2D flow over airfoils using immersed boundary method

Vinícius Piovesan de Toledo
SMM – EESC – USP Av. Trabalhador Sancarlense, 400, CEP:13566-590 São Carlos - SP `vinipio@gmail.com`

José Alberto Cuminato
SME – ICMC – USP Av. Trabalhador Sancarlense, 400, CEP:13560-970 São Carlos - SP `jacumina@icmc.usp.br`

Leandro Franco de Souza
SME – ICMC – USP Av. Trabalhador Sancarlense, 400, CEP:13560-970 São Carlos - SP `lefraso@icmc.usp.br`

Abstract. *In the present work a numerical study of incompressible flows over a 2D profile is performed. The airfoil was modeled my means of Immersed Boundary Technique. This technique consists in an addition of a forcing term on the Navier-Stokes equations that model the effect of the presence of the body on the flow evolution. This makes their solutions simpler, turning possible the use of basic Cartesian Meshes. A Stretching grid was used, improving accuracy of results near the airfoil and decreasing computational time. The numerical code is based on Vorticity-Velocity formulation. High order finite difference methods were adopted for spatial derivatives calculation. The time integration was carried out by a 4th order Runge-Kutta scheme. The numerical results were obtained for low Reynolds numbers (5000). The results show that the implemented code gives good results if compared with other results from the literature.*

Keywords *Immersed Boundary Method, streching, High Order Methods, Vorticity-velocity formulation*

Proceedings of the 11th Brazilian Congress of Thermal Sciences and Engineering -- ENCIT 2006
Braz. Soc. of Mechanical Sciences and Engineering -- ABCM, Curitiba, Brazil,- Dec. 5-8, 2006

Paper CIT06-0670

NONLINEAR WAVE-CURRENT INTERACTIONS: THE GENERATION OF REFLECTED WAVES

Gabriel Nunes Coutinho & Roger Matsumoto Moreira
Computational Fluid Dynamics Laboratory (LabCFD)
School of Engineering, Fluminense Federal University
R. Passos da Pátria 156, bl.D, sl.563A, Niterói, R.J., Brazil. CEP: 24210-240.
E-mail: gncoutinho@gmail.com & roger@vm.uff.br

Abstract. *The interaction between wave groups on water surfaces and submerged currents is studied. This work was motivated by the constant change of the breaker line in the nearshore region caused by the irregular nature of the wave motion. For smooth monochromatic wavetrains, the nonlinear numerical results show that surface waves can be focused by adverse surface currents, leading to very rough water surfaces, with sometimes a partial reflection being observed; upstream of these regions the surface of the water is smooth as all short waves are eliminated. For bichromatic waves, the fully nonlinear results show that partial wave blocking occurs at the individual wave components in the wave groups and that waves become almost monochromatic upstream the blocking region. These results agree qualitatively with experiments conducted by Chawla (1999).*

Keywords*: Wave-current interactions, nonlinear effects, boundary integral method.*

1. Introduction

The interaction between wave groups and currents is of special importance when studying the effects of a moving blocking point. For instance, the excess momentum released by waves breaking on a beach acts as a forcing mechanism for fluid motion in the nearshore region. The breaker line is always moving due to the irregular nature of the wave motion and thus it is identified as one of the mechanisms for generating long waves in the coast. The temporally varying amplitude envelope of a narrow banded spectrum can create a moving blocking point.

The sharp steepening of waves prior to the blocking point makes the linear approach valid only for very small waves, which is not the case at river inlet entrances where waves are steep and tend to break at or before the blocking point. Several papers have been published based on data collected directly from the wave field. Wave height measurements in a tidal inlet were presented by Battjes (1982), while Gonzales *et al.* (1985) used SLAR imagery to estimate the wave height for slack and ebb currents at the Columbia river entrance. Other examples where measurements of water waves show correlation with the tides in areas of appreciable tidal currents are given by Vincent & Smith (1976) and Vincent (1979).

Due to the complexity of the wave field, experimental studies on this subject have also been performed. Sakai & Saeki (1984) conducted wave breaking tests for monochromatic waves in the presence of an opposing current but their experimental set up also included a sloping sea bed. The focus of their study was the combined effect of opposing currents and sloping sea bed on wave transformation and breaking, thus adding difficulties to isolate current limited wave breaking from depth limited wave breaking. Lai *et al.* (1989) conducted experimental studies with monochromatic and random waves on strong opposing currents. They limited their study to the kinematics of the wave-current interaction under blocking conditions and confirmed the dispersion relation and the implied reflection, but no measurements on amplitude variations were reported. Ris & Holthuijsen (1996) simulated current induced breaking and blocking with the help of a third generation wind wave spectral model and compared their results with the data of Lai *et al.* (1989). In all these experiments a very limited understanding of the wave energy dissipation due to current limited wave breaking was achieved.

Recent laboratory experiments using recirculating flumes have given a better understanding of the evolution of the wave field through the blocking region and the dynamics of the wave-current interaction. Chawla (1999) used a flume equipped with a perforated wavemaker to study the propagation of a series of monochromatic waves on an opposing blocking current. For very gentle waves, wave reflection from the blocking point was observed with the amplitude envelope confirming linear predictions. As the initial wave amplitude on a blocking current was increased, the wave envelope deviated from the Airy function theory and a transition region was identified between the case where waves are reflected from the blocking point with no breaking to the case where waves break at the blocking point with no reflection. Partial wave reflection was also observed in cases where the required blocking current is slightly greater than the maximum current. Chawla (1999) also carried on tests involving blocking of wave groups, obtained by modulating a carrier wave. His experimental results showed that blocking occurs separately for the individual wave components of the spectrum. However, his numerical simulations using a weakly nonlinear model showed that blocking occurs at the blocking point of the carrier wave instead. In addition, predictions of the blocking point were based on the linear

dispersion relation and thus could not account for nonlinear effects. The varied physical aspects in which wave-current interactions occur and the different mathematical approaches that are applicable to them can be found in the review papers of Peregrine (1976), Jonsson (1990) and Thomas & Klopman (1997).

Using a flume equipped with a wave generator and a perforated false bottom, Suastika *et al.* (2000) performed experiments on partial and complete wave blocking of periodic and random waves. For periodic wave tests, the incident wave steepness is seen to increase monotonically in the direction towards the blocking point. Reflection was also observed but with no systematic variation with the incident waves. The reflected wave steepnesses showed considerable scatter, which was interpreted as saturation due to wave breaking of the incident waves. Care should be taken in this case since the momentum lost from the waves in breaking is transferred to the current. Although this does not make a significant contribution to the mean current in deep water it certainly affects the current distribution in the surface layer that directly influences the waves. It is also important to notice that both Chawla (1999) and Suastika *et al.* (2000) generate turbulent currents with a constant mean velocity in relatively deep water. Reflection was also observed in the random wave tests. The reflected waves became more pronounced towards the blocking region, though the wave field was still dominated by the incident waves.

An amplitude evolution model based on the conservation of wave action, including dissipation and wave breaking, was also presented by Suastika *et al.* (2000). The spectral wave action balance was given by,

$$\frac{\partial}{\partial x}\left[\frac{E_n}{\Omega_n}\left(c_{g_n}+U\right)+\frac{D_n}{\Omega_n}\right]=0,$$

where Ω is the wave frequency in a reference frame moving with the current U, E is a spectral wave energy density in frequency space, D is a spectral wave energy dissipation and the subscript n refers to the n^{th} spectral component. A modified Battjes-Janssen model (Battjes & Janssen 1978) was used to model dissipation due to wave breaking while viscous dissipation along the sidewalls was introduced using the formulation of Hunt (1952). The model does not take into account the reflected waves and overestimated transmission through the blocking point. In the blocking region, model results showed significant discrepancies with observations. There is doubt in the literature about the value of using D_n. However, in the absence of better models, this is still employed.

To shed further light on the subject, we investigate through numerical simulations the behaviour of monochromatic and bichromatic gentle waves interacting with "rapidly" and "slowly" varying surface currents in deep water. In our simplified model the fully nonlinear, unsteady, boundary-integral method developed by Dold & Peregrine (1986) is modified in order to include the underlying current. The current is assumed to be two-dimensional and stationary, being induced by a distribution of singularities located beneath the free surface (Moreira & Peregrine 2001, Moreira 2001). The initial conditions for the boundary value problem are described in the following section.

2. Governing equation and boundary conditions

The free surface flow is assumed to be inviscid and incompressible. The singularities are distributed below the free surface in order to model the required underlying flow. The flow is supposed to be irrotational outside the singular cores and away from the free surface. The velocity field $\vec{u}(x,y,t)$ is given by the gradient of a full velocity potential $\Phi(x,y,t)$ which satisfies Laplace's equation in the fluid domain, excluding the singular points $\vec{x}_{S_i}$,

$$\nabla^2\Phi = 0, \qquad \text{in } D-\bigcup_{i=1}^{n}\vec{x}_{S_i}. \tag{1}$$

The fluid domain with its coordinates and parameters is illustrated in figure (1), with U representing a constant stream velocity.

The full velocity potential Φ is decomposed into a regular part ϕ_w (due to surface waves) and a singular part ϕ_s (due to the singularities),

$$\Phi=\phi_w+\phi_s, \tag{2}$$

which satisfies (1). The free surface´s kinematic and dynamic boundary conditions are given by,

$$\frac{D\vec{r}}{Dt}=\nabla\Phi, \tag{3}$$

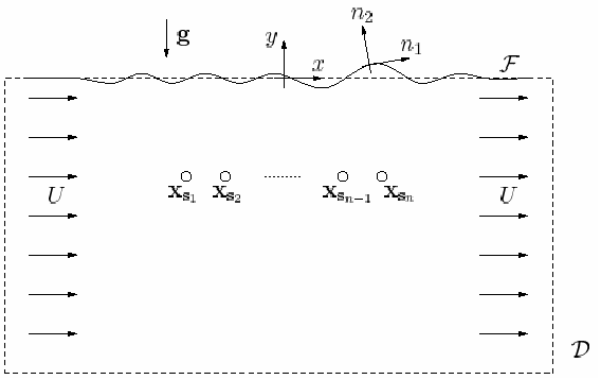

Figure 1. A sketch of the fluid domain *D* with its coordinates and parameters.

$$\frac{D\Phi}{Dt} = \frac{1}{2}|\nabla\Phi|^2 - \frac{p}{\rho} - gy \ . \tag{4}$$

$\vec{r}(x,y,t)$ is the position vector, y is the elevation of the free surface above the undisturbed water level, g is the acceleration due to gravity, ρ is the fluid density and p is the pressure on the exterior side of the surface. We assume deep water conditions i.e. $|\nabla\Phi| \to 0$ as $y \to -\infty$. To complete the boundary value problem an initial condition for the free surface is chosen,

$$\eta(x) = \eta_0(x), \qquad \Phi(x,\eta) = \Phi_0(x,\eta_0), \tag{5}$$

for $t = 0$. Attention is directed to two initial conditions: monochromatic wavetrains with initially uniform wavenumber K_0 and gentle steepness A_0K_0 (see figures 2a and 2b), and bichromatic waves produced by the addition of two wavetrains with same amplitude and slightly different wavenumbers and frequencies (figure 2c).

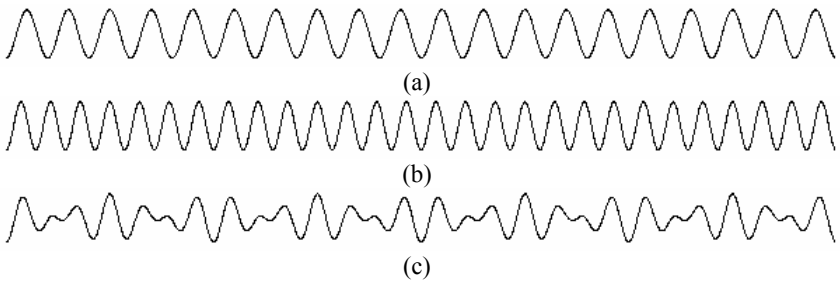

Figure 2. Monochromatic wavetrains with gentle steepness ($A_0K_0=0.04$) and initially uniform wavenumbers: (a) $K_0=10$; (b) $K_0=14$. When added together, they give the bichromatic wave (c).

3. Fully nonlinear boundary-integral solver

The boundary value problem is solved using an adapted version of the fully nonlinear potential flow program developed by Dold & Peregrine (1986), in which a boundary-integral method is applied to a free surface flow problem, reducing significantly the computational demand for the calculation of the fluid motion. The solution method is based on solving an integral equation that arises from Cauchy's integral theorem for functions of a complex variable. The original numerical scheme is modified for the inclusion of singularities. For details see Moreira & Peregrine (2001), Moreira (2001) and Moreira (2003).

The calculation of the free surface velocity $\nabla\phi_w$ becomes relatively simple when applying Cauchy's integral theorem. If we take $z = x + iy$ as the complex equivalent of the position vector $\vec{r} = (x,y)$ for a certain time t, ϕ_w is an analytic function of z. The wave complex potential gradient is defined as,

$$q_w = \frac{\partial \phi_w}{\partial x} - i\frac{\partial \phi_w}{\partial y}, \tag{6}$$

which is also an analytic function of z. On the boundary, z is treated as a function of the parameter ξ and time t. Similarly, taking $Z(\xi,t)$ as the complex equivalent of the surface profile vector $\vec{R}=(x(\xi,t),y(\xi,t))$, q_w can be defined in terms of the tangential and normal gradients of ϕ_w at the surface,

$$\overline{q}_w = \frac{\partial Z}{\partial n_1}\left(\frac{\partial \phi_w}{\partial n_1} + i\frac{\partial \phi_w}{\partial n_2}\right). \tag{7}$$

We assume that the surface contour C that surrounds the fluid domain is smooth; then applying Cauchy's integral theorem leads to,

$$\frac{\partial \phi_w}{\partial n_2} = \frac{1}{\pi}\oint_C \Im\left(\frac{\partial Z / \partial n_1}{Z' - Z}\right)\frac{\partial \phi_w'}{\partial n_2}\,dn_1' + \frac{1}{\pi}\oint_C \Re\left(\frac{\partial Z / \partial n_1}{Z' - Z}\right)\frac{\partial \phi_w'}{\partial n_1}\,dn_1', \tag{8}$$

in which $\partial\phi_w / \partial n_2$ can be determined since $\partial\phi_w / \partial n_1$ can be calculated directly. The arclength n_1' is a scalar variable which increases in an anticlockwise sense around the closed contour C. The primed variables Z', $\partial\phi_w' / \partial n_1$ and $\partial\phi_w' / \partial n_2$ are evaluated at points on the surface corresponding to n_1'.

The singularities distributed beneath the free surface can induce varied surface current profiles, each of them with a certain minimum and maximum velocity and with a gentle or sharp current gradient. Figures (3a) and (3b) show, respectively, surface current profiles obtained from a distribution of sinks/sources and an eddy couple. Here the peak velocities are related to c_0, the phase velocity of surface waves supposing no underlying current. Under the light of linear theory, a train of uniform linear water waves propagating with speed c_0 is expected to break when an adverse surface current reach velocities bigger than $0.25c_0$. For these situations, linear theory breaks down and no wave solution can be determined. A group of three different maximum and minimum velocities are presented: $0.25c_0$, $0.5c_0$ and c_0. In this case the singularity distributions were conveniently chosen aiming to define "slowly" and "rapidly" varying surface currents. For convenience the singularities are assumed to be at fixed positions in time such that steady surface currents are imposed on the waves. Hence waves do not affect the singularities in our nonlinear model. The effects of waves on vortices can be found in the works of Tyvand (1991), Tong (1991) and Barnes *et al.* (1996). The singularity distribution has to be weak enough for little or no effect on the waves such that their existence can be considered unimportant. The velocity potential ϕ_s then satisfies a linear equation beneath the surface. This condition is particularly relevant when "sharp" current gradients are considered.

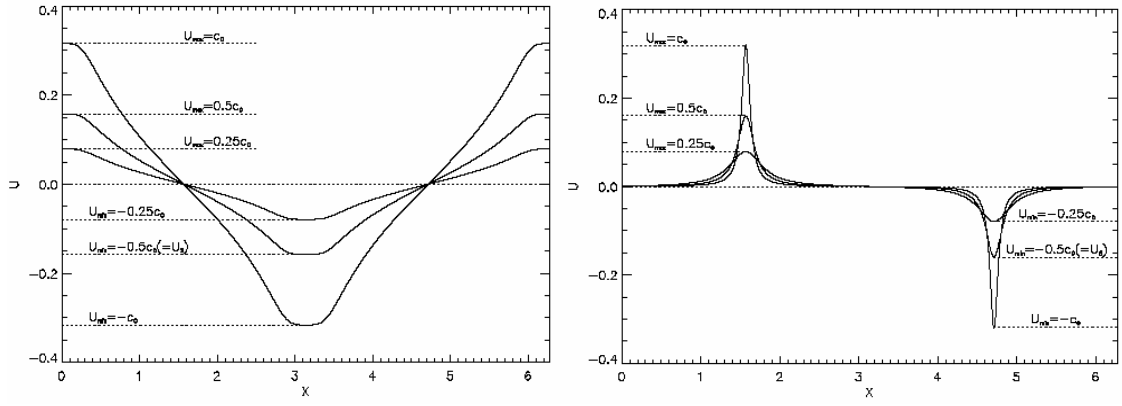

(a) (b)

Figure 3. Surface current profiles induced by: (a) 16 sinks and 16 sources (*Fr=0.015, 0.03, 0.06*); (b) an eddy couple (*Fr=0.08, 0.23, 0.64*).

The method of solution consists of the following stages. Initially the full potential Φ is known on the surface for each time step. The potential ϕ_s due to the singularities is also defined and subtracted from the surface value of Φ such that the remaining surface wave potential ϕ_w, which has no singularities in the fluid domain, can be used with Cauchy's integral theorem to calculate the velocity $\nabla\phi_w$ on the free surface. Then the potential ϕ_s is added back in and corresponding "total" velocities are evaluated. The inclusion of the singularities necessitates the computation of the partial derivatives with respect to *x* and *y* of the velocity potential ϕ_s up to the third derivative, since the time-step criterion uses a Taylor series expansion truncated at the sixth power. Since in our model the singularities are assumed at fixed positions, the partial time derivatives vanish. Once an accurate converged solution is obtained for the full velocity potential Φ on the free surface, the cycle can begin again. Such stages are repeated until either the final time is reached, or the algorithm breaks down. Full details can be found in Dold (1992).

In the calculation of surface waves by the numerical scheme, it is important that a sufficient number of surface points is used in order to guarantee the accuracy of the numerical method. Waves described by only a few surface points have their frequency and phase velocity underpredicted, with the percentage error decreasing rapidly the more points that describe each wavelength. However, an increase in the number of points used in the surface discretisation also leads to a significant increase in computing time and storage requirement. The surface discretisation points tend to drift due to the surface current induced by the singularities, soon developing poor resolution of the surface waves. To ensure a smooth variation of surface variables with point number, a redistribution of points along the surface at regular intervals in time is done by using a tenth-order interpolation algorithm. The computed cases presented here have an initial distribution of 120 points per wavelength for monochromatic waves and 350 points per wavelength of the carrier wave for bichromatic waves. To sum up no smoothing was introduced in the present computations in order to avoid any loss of information. The use of smoothing formulae based on the fitting of high order polynomials to the surface data was not required here since sawtooth numerical instabilities were well controlled by simply choosing an appropriate time step. Thus small waves with just two or three grid points and waves with sharp crests are not numerically dissipated by the scheme. All the computations presented in this work were done on a Intel Pentium 4 processor.

4. Fully nonlinear results

The fully nonlinear results presented in this section refer to monochromatic and bichromatic waves with initial gentle steepnesses interacting with surface currents induced by a distribution of singularities. "Slowly" and "rapidly" varying current gradients are obtained via a suitable distribution of sinks/sources and vortices beneath the free surface. A near-linear surface current is imposed with 16 sinks and 16 sources distributed symmetrically in the period domain at the same depth $d=0.25$. The effect of the singularity distribution on the waves then depends on the strength *k* of the sinks and sources. For convenience we define *k* as the volume flux per length unit of each of the sinks and sources. The desired maximum and minimum velocities are then obtained choosing suitable values for *k*. For "sharper" current gradients, a vortex couple is positioned underneath the free surface. In this case the peak velocities are defined by choosing suitable values for the depth of submergence *d*. The corresponding surface current profiles induced by these singularities are shown in figure (3). The stationary singularities are "turned on" at time $t=0$ and impose a volume flux perpendicular to the plane of motion. In the case of no surface current, surface waves propagate steadily without any distortion since the wave train is too gentle for the Benjamin-Feir instability to develop in the time available.

4.1. Monochromatic waves

Figure (4) shows the evolution of short surface waves ($A_0 K_0=0.04$) propagating over still water conditions and over near-linear and sharp surface current gradients ($U_{min}=-0.25\ c_0$). The nonlinear results are vertically exaggerated 40 times. It is clear from figures (4b) and (4c) the wave transformation that occurs due to the underlying current. A steep and a smooth region can be identified, respectively, downstream and upstream of the U_{min} region after a certain period of time. A strong increase in wave steepness is observed close to the U_{min} region, leading to wave breaking, while wave amplitudes decrease beyond this region. Some of the waves are steep enough to be noticeably affected by nonlinearity. Partial wave blocking is predicted by linear ray theory and thus confirmed by the nonlinear computations. The incident waves are clearly deformed near the maximum and minimum velocity regions U_{max} and U_{min}, while their group velocity remains unchanged near the regions where $U=0$. The positive current accelerates the surface waves nearby the U_{max} region, increasing locally their kinetic energy and group velocity, while in the U_{min} neighbourhood waves start to be partially blocked. When stronger currents are imposed, nonlinear effects take over with wave breaking occurring sooner nearby the U_{min} region.

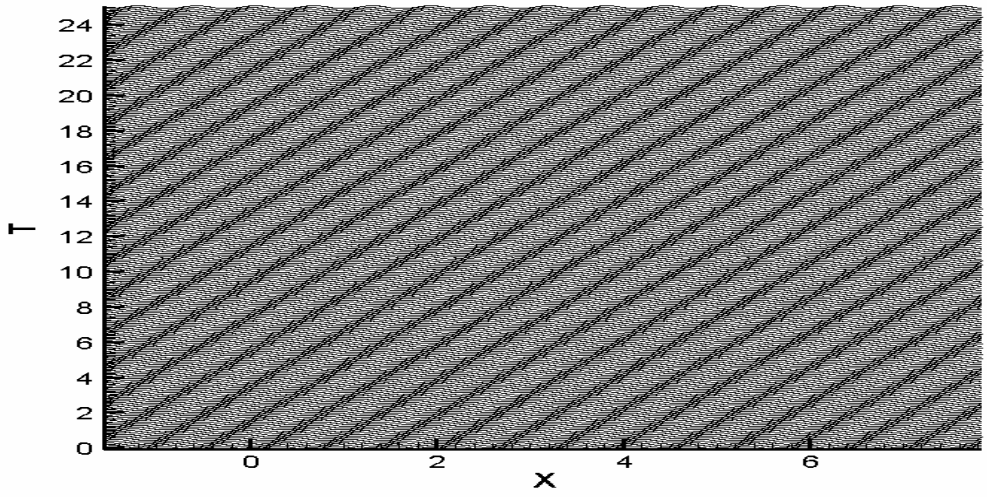

(a)

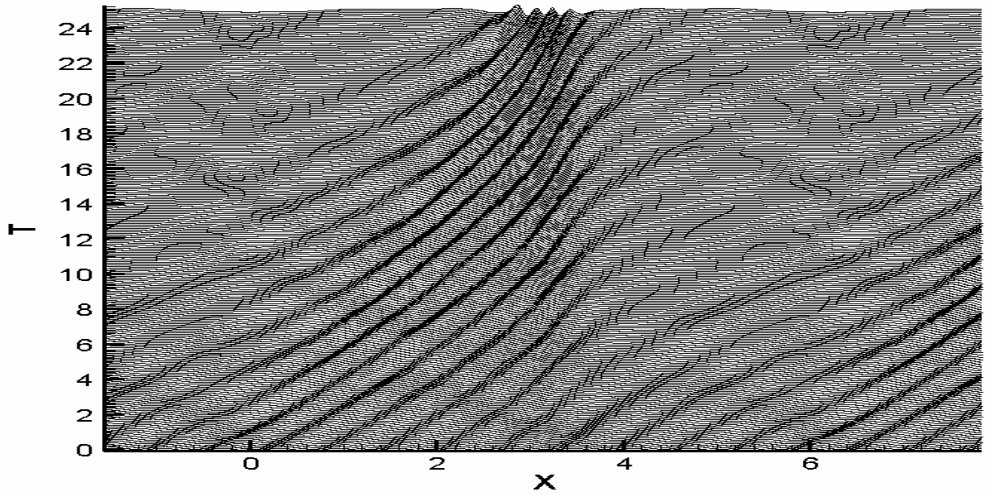

(b)

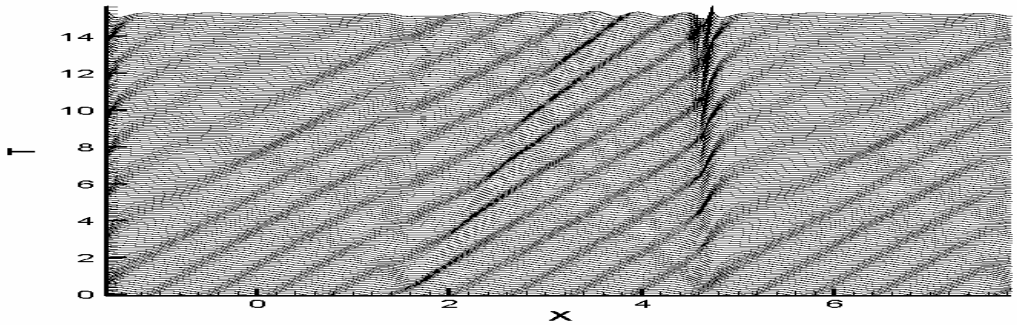

(c)

Figure 4. Free surface evolution of monochromatic waves over: (a) no underlying current; (b) a near-linear current ($t_{breaking}=25.4$); (c) a vortex current ($t_{breaking}=14.8$). $U_{min}=-0.250\ c_0$, $K_0=10$, $A_0\ K_0=0.04$. Vertical exaggeration 40:1.

4.2. Bichromatic waves

Chawla (1999) conducted a series of experiments on narrow banded spectral waves to study if it was possible to similarly generate long waves downstream of a moving blocking point. As already explained in section 1, his experimental results showed that this was not the case, with blocking occurring separately for the individual wave components of the spectrum, while his numerical simulations showed that blocking occurs at the blocking point of the carrier wave instead. Predictions of the blocking point were based on the linear dispersion relation and thus could not account for nonlinear effects. A Boussinesq model for wave blocking also shows a similar effect but is limited due to inaccuracies in its dispersive properties in deep water (Chen *et al.* 1998).

To shed further light in the matter, the numerical scheme proposed in section 3 was used to simulate the interactions between wave groups and currents. The wave groups were constructed by superposing two monochromatic waves having the same amplitude but slightly different frequencies, with the difference between the frequencies determining the number of waves in a group. This spectral approach was also employed by Chawla (1999). Based on his cleanest wave groups i.e. bichromatic waves with no energy transferred to the side bands, we set up our initial condition by superposing two uniform wave train components with $A_0\, K_0=0.06$, 0.084 and $K_0=10$, 14, respectively.

The evolution of these wave groups over "slowly" and "rapidly" varying currents is shown respectively in figures (5b) and (5c). For comparison purposes wave groups propagating over still water are presented in figure (5a). These nonlinear results show that partial wave blocking can occur at the individual wave components in the wave groups and that waves become almost monochromatic beyond the U_{min} region, which is clear from figure (5b). Unfortunately the numerical computations stop due to wave breaking. Wave reflection was not observed. Comparisons with solutions of the nonlinear Schrödinger equation are under development.

5. Summary

We have attempted to simulate the interaction between water waves and currents with special attention to the effects of nonlinearity on the free surface. This was motivated by several theoretical and recent experimental works on the matter. A fully nonlinear model was developed in order to understand the interaction of stationary submerged currents induced by singularities with gentle wavetrains and wave groups. The nonlinear numerical results show that adverse currents induce wave steepening and breaking. Furthermore the wave transformation induced by the underlying currents can be identified by a steep and a smooth region formed, respectively, downstream and upstream the blocking point after a certain period of time. A strong increase in wave steepness is observed within the blocking region, leading to wave breaking, while wave amplitudes decrease significantly beyond this region. In the case of interactions between wave groups and currents, the fully nonlinear results show that wave blocking can occur for the individual wave components in the wave groups and that waves evolve from being groupy to being almost monochromatic, confirming qualitatively the experimental observations of Chawla (1999).

6. Acknowledgement

Gabriel Nunes Coutinho acknowledges the financial support through FAPERJ. This research is supported by CNPq under contract no. 62.0018/2003-8-PADCT III / FAPERJ.

7. References

Barnes, T.C.D., Brocchini, M., Peregrine, D.H. & Stansby, P.K., 1996, "Modelling post-wave breaking turbulence and vorticity." *Proc. 25th Internat. Conf. on Coastal Engng.*, Orlando, ASCE, v.1, pp.186-199.

Battjes, J.A., 1982, "A case study of wave height variations due to currents in a tidal entrance." *Coastal Engineering*, v.6, pp.47-57.

Battjes, J.A. & Janssen, J.P.F.M., 1978, "Energy loss and set-up due to breaking of random waves." *Proc. 16th Internat. Conf. on Coastal Engng.*, Hamburg, ASCE, pp.569-587.

Chawla, A., 1999, "An Experimental Study on the Dynamics of Wave Blocking and Breaking on Opposing Currents." PhD thesis, University of Delaware, U.S.A.

Chen, Q., Madsen, P.A., Schäffer, H.A. & Basco, D.R., 1998, "Wave-current interaction based on an enhanced Boussinesq approach." *Coastal Engineering*, v.33, pp.11-39.

Dold, J.W., 1992, "An Efficient Surface-Integral Algorithm Applied to Unsteady Gravity Waves." *J. Comp. Phys.*, v.103, pp.90-115.

Dold, J.W. & Peregrine, D.H., 1986, "An Efficient Boundary-Integral Method for Steep Unsteady Water Waves." In *Numer. Meth. for Fluid Dynamics II*, Eds. K.W. Morton & M.J. Baines, pp.671-679.

Gonzales, F.I., Cokelet, E.D., Gower, J.F.R. & Mulhern, M.R., 1985, "SLAR and in-situ observations of wave-current interaction on the Columbia River Bar." In *The Ocean Surface*, Eds. Y. Toba & H. Mitsuyasu, pp.303-310.

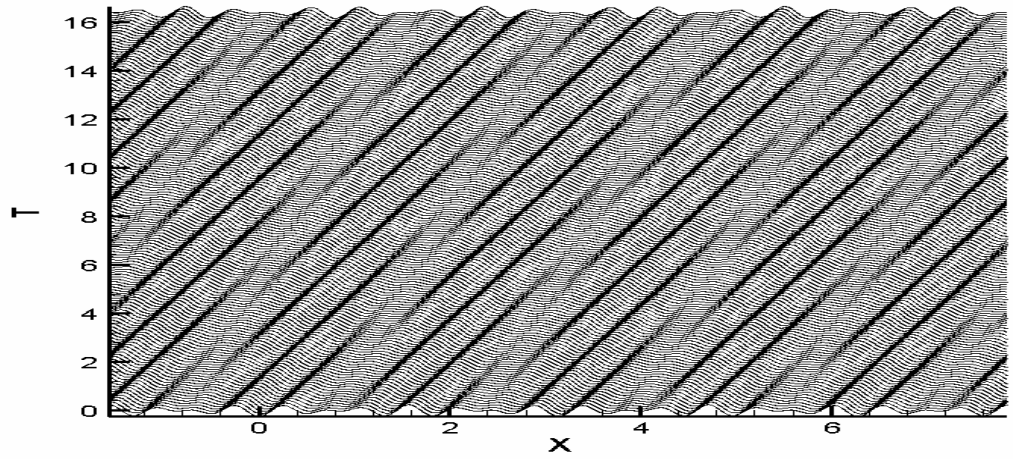

(a)

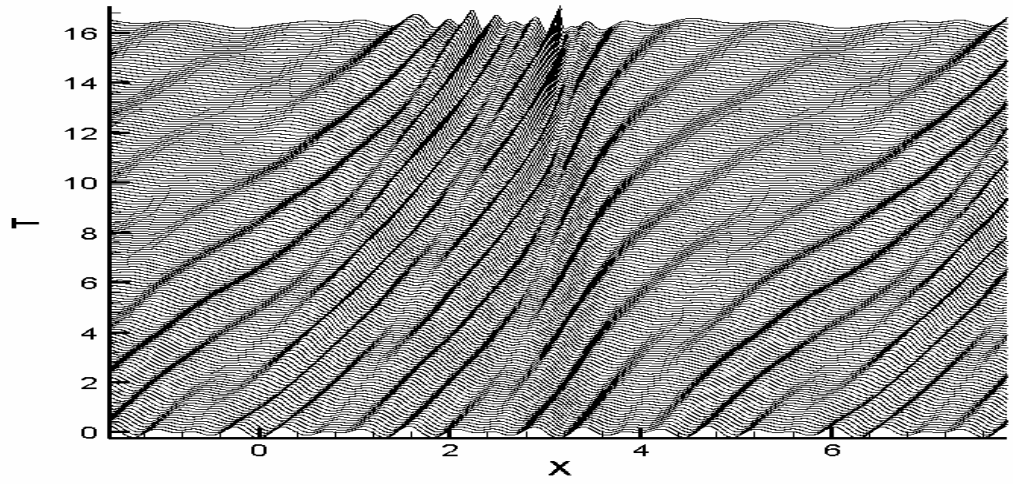

(b)

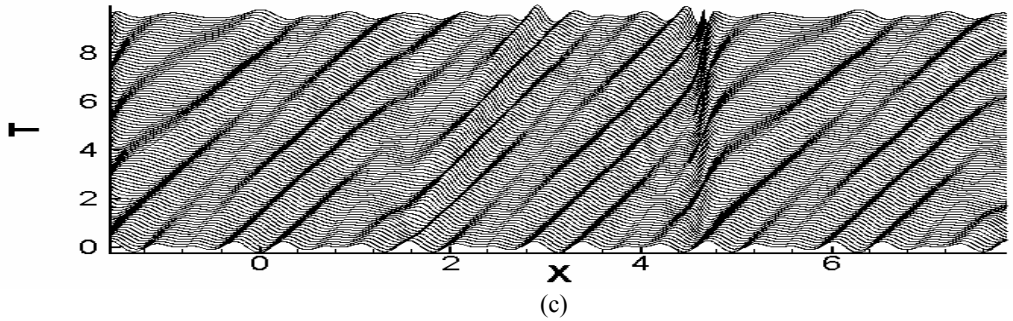

(c)

Figure 5. Free surface evolution of bichromatic waves over: (a) no underlying current; (b) a near-linear current ($t_{breaking}$=*16.4*); (c) a vortex current ($t_{breaking}$=*9.5*). U_{min}=*-0.250* c_0; K_0=*10, 14;* A_0 K_0=*0.06, 0.084*. Vertical exaggeration 40:1.

Hunt, J.N., 1952, "Viscous damping of waves over an inclined bed in a channel of finite width." *La Houille Blanche*, pp. 837-842.

Jonsson, I.G., 1990, "Wave-current interactions." In *The Sea*, Ocean Engng. Science 9A, Eds. B. Le Mehaute & D.M. Hanes, pp.65-120.

Lai, R.J., Long, S.R. & Huang, N.E., 1989, "Laboratory studies of wave-current interaction: Kinematics of the strong interaction." *J. Geophys. Res.*, v.94, pp.16201-16214.

Moreira, R.M., 2001, "Nonlinear interactions between water waves, free surface flows and singularities." PhD thesis, University of Bristol, U.K.

Moreira, R.M. & Peregrine, D.H., 2001, "Interactions between water waves and singularities." In *IUTAM Symp. on Free Surface Flows*, Eds. A.C. King & Y.D. Shikhmurzaev, pp.205-212.

Moreira, R.M., 2003, "Nonlinear interactions between water waves and currents." *Proc. 6th Internat. Conf. on Coastal & Port Engng. in Developing Countries*, Colombo, pp.1-10.

Peregrine, D.H., 1976, "Interaction of water waves and currents." *Adv. Appl. Mech.* 16, pp.9-117.

Ris, R.C. & Holthuijsen, L.H., 1996, "Spectral modelling of current induced wave-blocking." Proc. *25th Internat. Conf. on Coastal Engng.*, Orlando, ASCE, pp.1246-1254.

Sakai, S. & Saeki, H., 1984, "Effects of opposing current on wave transformation." *Proc. 19th Internat. Conf. on Coastal Engng.*, Houston, ASCE, pp.1132-1148.

Suastika, I.K., de Jong, M.P.C. & Battjes, J.A., 2000, "Experimental study of wave blocking." *Proc. 27th Internat. Conf. on Coastal Engng.*, Sydney, ASCE, pp.223-240.

Thomas, G.P. & Klopman, G., 1997, "Wave-current interactions in the nearshore region." In *Gravity Waves in Water of Finite Depth*, Ed. J.N. Hunt, pp.215-319.

Tong, R.P., 1991, "Unsteady Flow with a Free Surface: A Study of Numerical Approximations in the Boundary Integral Method." PhD thesis, University of Bristol, U.K.

Tyvand, P.A., 1991, "Motion of a vortex near a free surface." *Journal of Fluid Mechanics*, v.225, pp.673-686.

Vincent, C.E., 1979, "The interaction of wind-generated sea waves with tidal currents." *Journal of Physical Oceanography*, v.9, pp.748-755.

Vincent, C.E. & Smith, D.J., 1976, "Measurements of waves in Southampton water and their variation with the velocity of the tidal current." *Estuarine Coastal Mar. Sci.*, v.4, pp.641-652.

8. Responsibility notice

The authors are the only responsible for the printed material included in this paper.

Proceedings of the 11th Brazilian Congress of Thermal Sciences and Engineering -- ENCIT 2006
Braz. Soc. of Mechanical Sciences and Engineering -- ABCM, Curitiba, Brazil, Dec. 5-8, 2006

Paper CIT06-0679

ESTUDO EXPERIMENTAL DO ESCOAMENTO TURBULENTO NAS PRIMEIRAS FILEIRAS DE BANCOS DE TUBOS

Cláudio Rodrigues Olinto
Fundação Universidade Federal do Rio Grande
Av. Itália, km 8, Rio Grande, RS
dfscro@furg.br

Luiz Augusto Magalhães Endres
Universidade Federal do Rio Grande do Sul
endres@iph.ufgrs.br

Sérgio Viçosa Möller
Universidade Federal do Rio Grande do Sul
Rua Sarmento Leite, 425, Porto Alegre, RS
svmoller@ufgrs.br

Resumo. *Este trabalho apresenta um estudo experimental das características do escoamento turbulento ao atravessar as primeiras fileiras de bancos de tubos. O objetivo é entender o comportamento das instabilidades e fenômenos aleatórios e transientes que são gerados nas primeiras fileiras e o modo como se propagam através das fileiras mais interiores. As medições experimentais são obtidas em túnel de vento usando a técnica de anemometria de fio quente e as visualizações, usadas para ampliar o entendimento dos fenômenos, são realizadas em canal de água com injeção de tinta. Os dados experimentais são analisados por ferramenteas estatísticas, espectrais e de ondaletas. Os resultados demonstram a presença de instabilidades geradas a partir da segunda fileira do banco de tubos, que se propagam para o interior, gerando um comportamento onde as três componentes ortogonais do escoamento são igualmente importantes.*

Palavras chave: escoamentos turbulentos, bancos de tubos, ondaletas.

1. Introdução

O escoamento de fluidos sobre conjuntos de cilindros está presente em muitas aplicações de engenharia. Dentre os casos mais comuns podem ser citados: tubos de trocadores de calor, plataformas *offshore*, torres e linhas de transmissão de potência, grupos de chaminés, estacas de píeres e pontes, equipamentos de usinas nucleares, etc.

O escoamento de um fluido sobre estruturas sólidas está associado ao aparecimento de cargas dinâmicas causadoras de vibrações, que, em geral, são amplificadas com o aumento da velocidade do fluido. Os escoamentos sobre arranjos de cilindros distinguem-se fenomenologicamente em função da disposição dos tubos. Arranjos com grandes distâncias entre os tubos desenvolvem cargas dinâmicas associadas com o processo de geração e desprendimento de vórtices em freqüências definidas. Nos arranjos com pequenas distâncias, o escoamento é caracterizado por um amplo espectro de energia sem uma freqüência definida, que está relacionado com as flutuações de pressão e periodicidades geradas principalmente nas primeiras fileiras de cilindros sujeitas ao escoamento (Endres, 1997).

Indrusiak (2004) estudou a aplicação das transformadas de ondaletas para a interpretação de escoamentos turbulentos. Durante a aquisição de séries de velocidades na esteira do tubo central da terceira fileira de um banco de tubos alinhados, com razão de espaçamento de 1,26, foi identificado um regime de escoamento não estacionário, diferente do esperado, que só foi revelado através da decomposição dos sinais em bandas de freqüências. Esse escoamento não estacionário apresentou características semelhantes ao que ocorre na esteira do escoamento sobre certas geometrias de dois cilindros posicionados lado a lado, denominado biestável, onde dois regimes metaestáveis são estabelecidos, trocando aleatoriamente entre si. Assim, o presente trabalho foi desenvolvido a fim de estudar geometrias de bancos de tubos empregadas em trocadores de calor, onde tal fenômeno poderia estar presente.

2. Tecnica Experimental

2.1. Canal aerodinâmico

A seção de teste, mostrada na Fig. 1, é um canal retangular com 146 mm de altura por 195mm de largura. Ar é o fluido de trabalho, que movido por um ventilador centrífugo, chega até a seção de teste após passar por uma câmara de homogeneização formada por grades e telas, com um perfil uniforme de velocidade e uma intensidade de turbulência menor do que 1% (Endres, 1997). O espectro de velocidades foi calculado no interior do canal aerodinâmico, não

apresentando nenhum fenômeno com energia relevante na faixa de freqüências estudas. Um tubo de Pitot é colocado antes dos tubos em uma posição fixa para medir a velocidade de referência dos experimentos.

As velocidades instantâneas foram medidas usando a técnica de anemometria de fio quente a temperatura constante através de um equipamento DANTEC *StreamLine*.

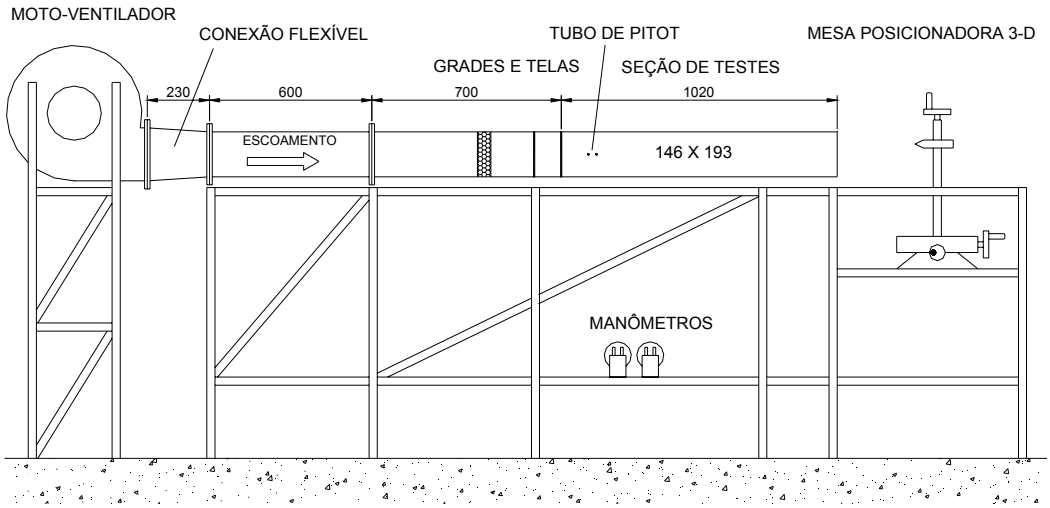

Figura 1. Esquema do canal aerodinâmico

Os dados de velocidade foram adquiridos simultaneamente utilizando uma placa conversora A/D modelo Keithley DAS-58 controlada por um computador pessoal, o qual também foi usado para avaliação dos resultados finais.

Os banco de tubos foram montados com tubos de PVC de 32,1 mm de diâmetro, posicionados verticalmente e distribuídos em 5 fileiras. Foram estudadas três diferentes geometrias de bancos de tubos com arranjos alinhados, onde, para as relações passo/diâmetro (T/D) de 1,4 e 1,6 as fileiras são compostas por 4 tubos e para T/D = 1,26, por 5 tubos. Os tubos têm comprimento de 146 mm e estão em contato com as paredes superior e inferior do canal.

2.2. Canal de água

Os experimentos de visualização de escoamento foram realizados em um canal de água de circuito fechado, pertencente ao Instituto de Pesquisas Hidráulicas da Universidade Federal do Rio Grande do Sul. O banco de tubos usado na visualização foi construído dentro de uma seção de acrílico transparente, com os tubos fixados verticalmente pela sua extremidade superior. Como o canal é de superfície livre, a seção de testes de acrílico também possui a função de evitar os efeitos de oscilações e formação de ondas de superfície. O perfil de velocidades no interior da seção de testes foi levantado (Olinto, 2005) e mostra uma boa uniformidade. O espectro de velocidades não foi possível calcular, devido à falta da instrumentação necessária. Para visualizar as estruturas formadas no escoamento foi usada a injeção de tinta, utilizando agulhas, convenientemente posicionadas. As imagens do campo de escoamento foram gravadas digitalmente na forma de vídeo. As fotografias apresentadas no presente trabalho foram obtidas diretamente dos vídeos.

A seção de testes é mostrada na Fig. 2. Os tubos foram construídos em tubos de PVC com diâmetro de 75 mm. O tubo central foi construído em acrílico transparente e possui um espelho elíptico posicionado a 45º na metade da altura dos tubos do banco (Fig. 3). Esse arranjo permite a visualização do plano vertical do escoamento, na fenda estreita formada entre o tubo de acrílico e seu vizinho lateral. No tubo visto através do espelho, é injetada tinta no interior da fenda por intermédio de uma agulha.

3. Ferramentas Matemáticas

A decomposição dos sinais de velocidade em bandas de freqüências é feita usando transformadas de ondaletas. Essa técnica permite o estudo de fenômenos turbulentos sem a hipótese de estacionariedade, o que é necessário, para o estudo de escoamentos transientes ou quando estruturas não estacionárias estão presentes. A descrição das transformadas de ondaletas discreta e contínua é feita conforme Indrusiak and Möller, 2004. Todas as rotinas de análise matemática foram realizadas na plataforma Matlab 5.3.

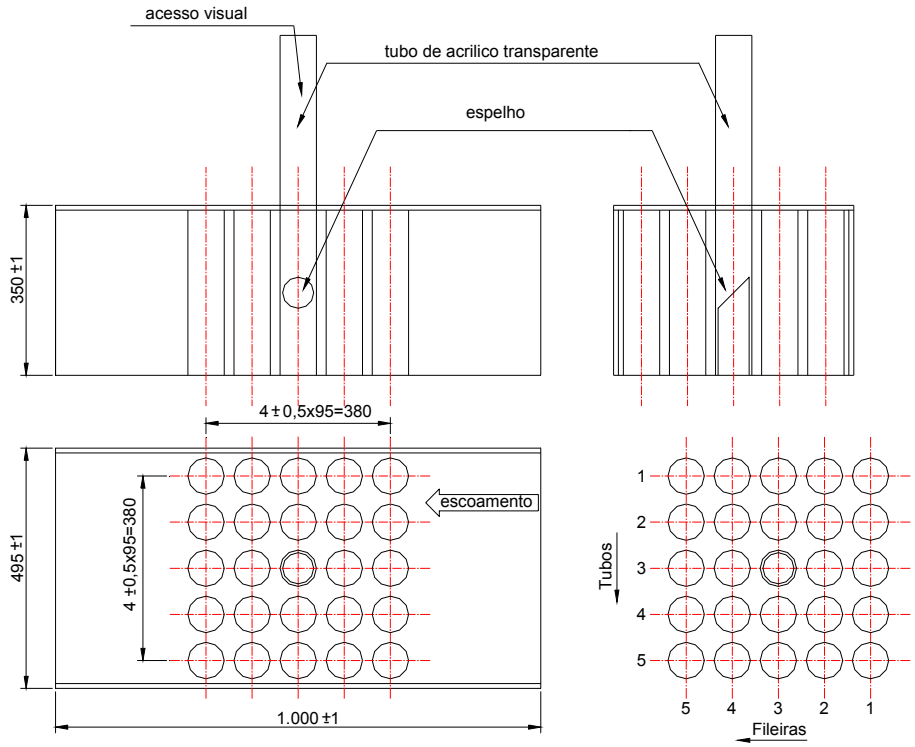

Figura 2. Esquema dimensional da seção de testes para visualização no canal de água (dimensões em mm).

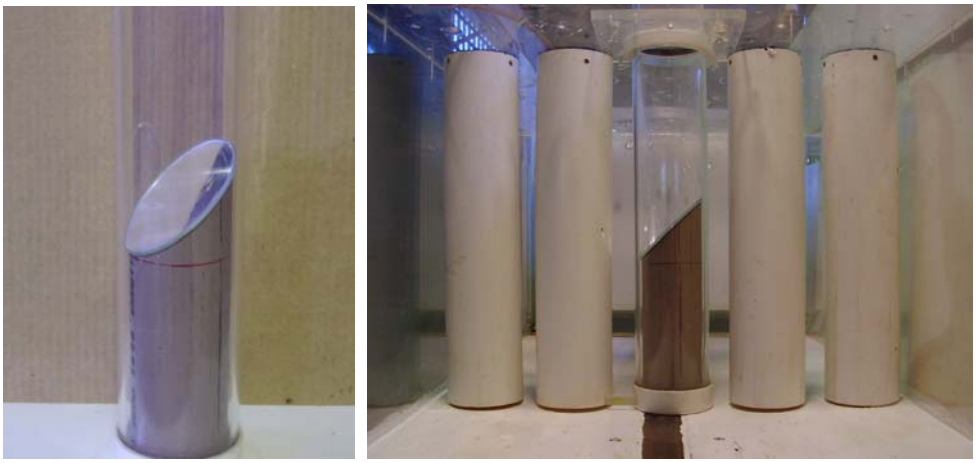

Figura 3. Detalhe do tubo central, mostrando o posicionamento do espelho.

4. Resultados

4.1. Medições de velocidade

Para detectar a presença de componentes transversais ao escoamento, foram realizadas medições de velocidade utilizando-se uma sonda de fio quente dupla do tipo fio reto e inclinado, que permite, além de medir o valor da velocidade na direção do escoamento, identificar o ângulo que essa velocidade faz com uma direção de referência (que neste caso é o eixo da sonda). As medições foram realizadas em diversos pontos no interior dos bancos de tubos, a fim de identificar a presença de trocas no modo de escoamento. Para a identificação das melhores posições a serem medidas, também foram levadas em conta as visualizações realizadas.

Para o banco de tubos com P/D = 1,26, é apresentado na Fig. 4, o resultado da medição de velocidade e o ângulo que a mesma faz com o eixo da sonda, em um escoamento em regime permanente, onde a sonda foi posicionada na esteira do tubo central da terceira fileira. O número de Reynolds, calculado com a velocidade do escoamento na fenda estreita formada entre dois tubos adjacentes e o diâmetro dos tubos, foi de 8,4 x 10^4. A amostragem foi realizada com uma freqüência de 3 kHz. O ângulo é medido em um plano vertical, sendo considerados valores positivos quando a velocidade incidente na sonda é de baixo para cima.

A Figura 5 mostra o detalhe do intervalo entre 3 e 5 s, onde pode-se identificar que determinados padrões no escoamento ocorrem e persistem durante algum tempo, alternando após para um novo padrão. No caso citado, entre os tempos ao redor de 4,2 s e 4,5 s, há uma redução na flutuação de velocidade, ficando os valores de velocidade mais próximos de 30 m/s. Nesse mesmo intervalo, há uma considerável redução na flutuação do ângulo que se direciona mais para 20º. A aplicação da transformada discreta de ondaletas para separar os sinais entre 3 e 5 s em bandas de freqüências permite observar melhor essas características.

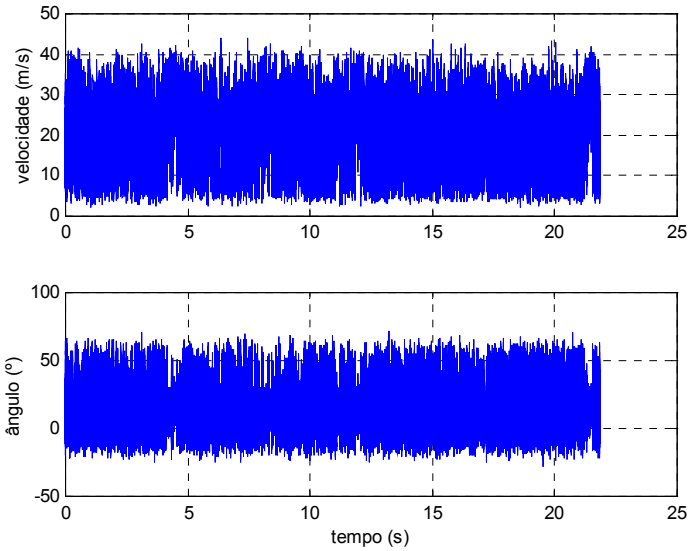

Figura 4. Velocidade e ângulo de incidência medidos atrás do tubo central da terceira fileira (P/D=1,26).

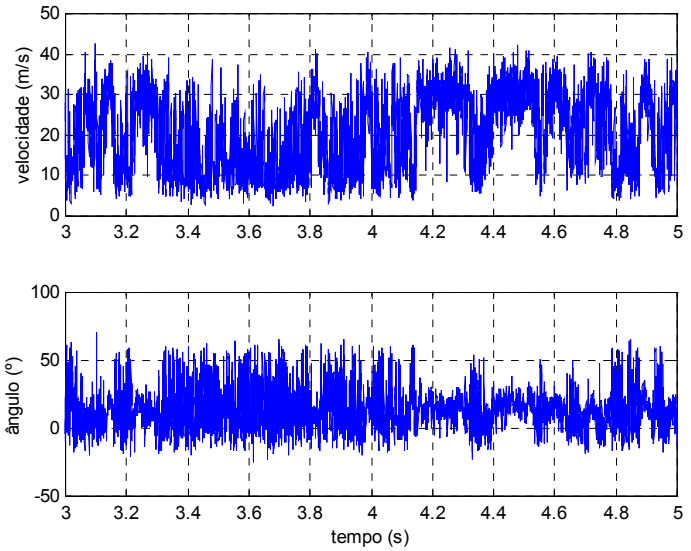

Figura 5. Detalhe entre 3 e 5s do sinal mostrado na Fig. 4.

A decomposição apresentada na Fig. 6(a) mostra, através da aproximação até 2,9 Hz, que o valor da velocidade média no intervalo entre 4,2 e 4,6 s se mantém em um patamar de 25 m/s, sendo modulado por uma freqüência entre 2,9 e 5,8 Hz, o que faz com que haja a queda no valor da velocidade instantânea no tempo de 4,55 s. Também se pode observar que, no intervalo entre 3,5 e 3,8 s, a velocidade média permanece ao redor de 15 m/s. Além disso, nas bandas de freqüência mais altas, no intervalo onde a velocidade média é alta, a amplitude dessas freqüências é menor.

A Figura 6(b) mostra as decomposições feitas para o ângulo de incidência da velocidade. A aproximação de 0-2,9 Hz mostra o comportamento do ângulo médio. Pode-se identificar que associado ao intervalo onde a velocidade média permanece nos valores mais altos estão os menores ângulos médios. Também se observa que para esse intervalo (4,2 a 4,6 s) as amplitudes das oscilações das maiores bandas de freqüência são as menores.

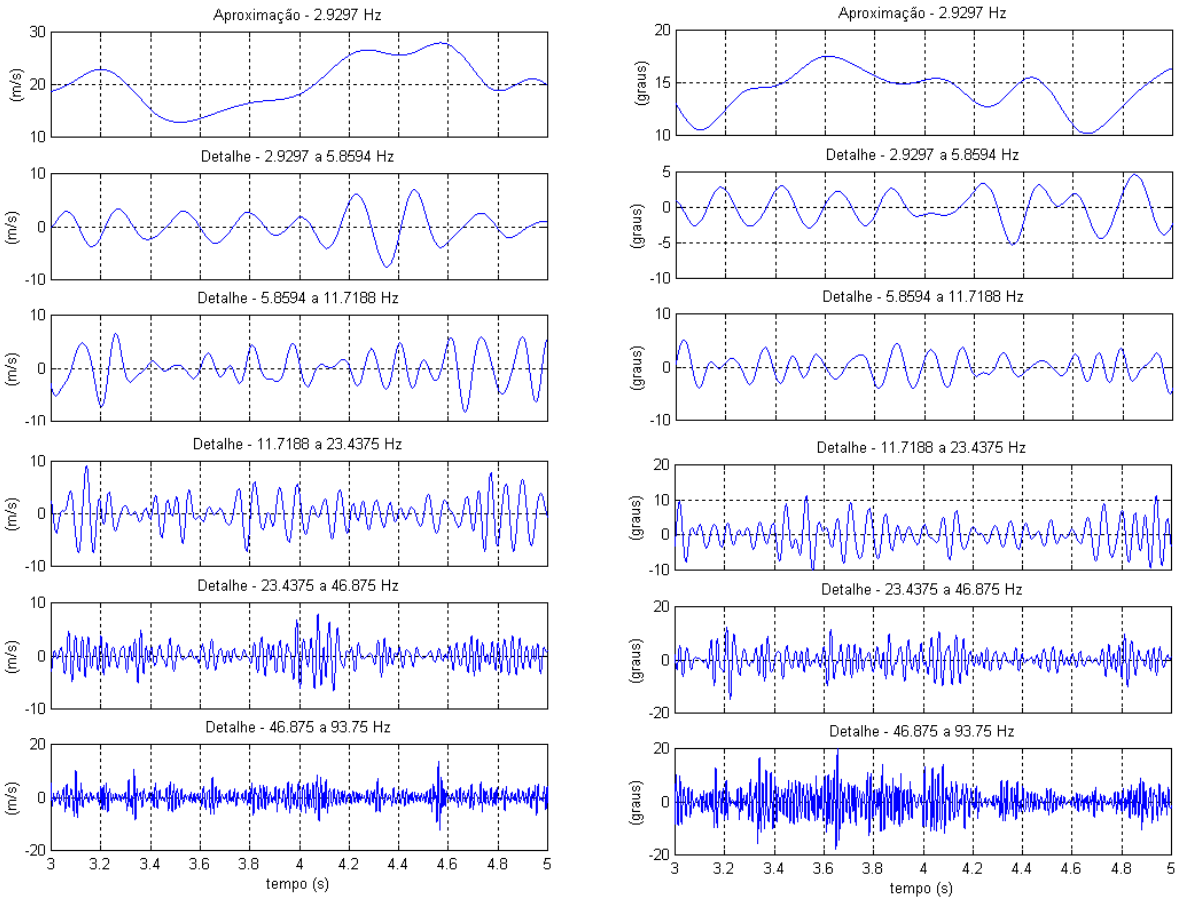

(a) (b)

Figura 6. (a) Decomposição do sinal de velocidade e (b) ângulo de incidência do sinal da Fig. 5 em bandas de freqüência utilizando a transformada discreta de ondaletas.

Para observar de forma mais detalhada as energia envolvidas ao longo do tempo, em termos de freqüências, foram gerados espectrogramas, calculados através de transformadas contínuas de ondaletas. Na Figura 7, é mostrado o espectrograma da velocidade para o mesmo intervalo de tempo apresentado na Fig. 4.45, onde se pode identificar que, nos instantes onde a velocidade flutua ao redor de valores mais altos, há uma maior concentração de energia nas baixas freqüências (intervalos 3-3,3 s e 4,2-4,6 s). Ao contrário, no intervalo onde a velocidade flutua ao redor dos menores valores de velocidade, há um maior espalhamento da energia em diversas freqüências (intervalo entre 3,4-4,2 s).

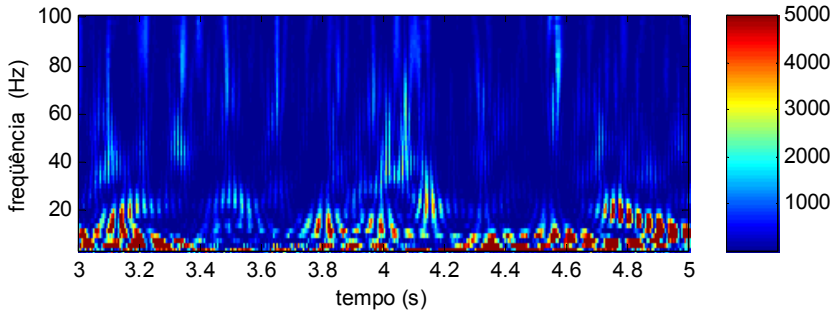

Figura 7. Espectrograma da velocidade no intervalo entre 3 e 5 s para o sinal da Fig. 5 (escala de energia arbitrária).

O espectrograma das flutuações dos ângulos da velocidade apresenta um comportamento exatamente ao contrário. Para os maiores valores de velocidade, o ângulo possui menor energia de flutuação em todas as bandas de freqüência, concentrando alguma energia apenas nas freqüências mais baixas (Fig. 8).

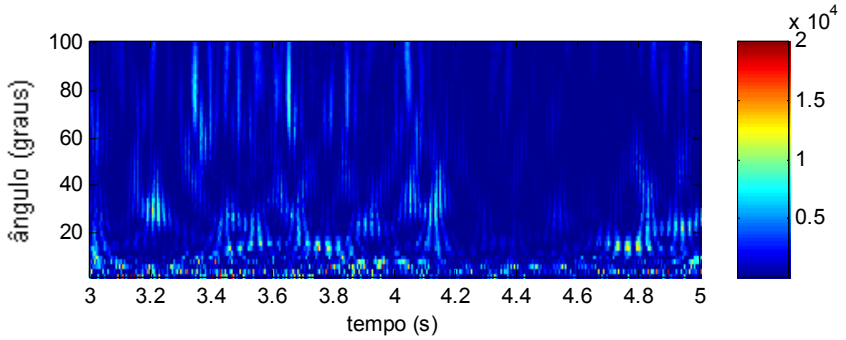

Figura 8. Espectrograma do ângulo de incidência da velocidade no intervalo entre 3 e 5 s para o sinal da Fig. 5 (escala de energia arbitrária).

Para o banco de tubos com razão de espaçamento de 1,4, é apresentada, a seguir, uma série de velocidade e ângulo de incidência obtida na esteira da terceira fileira. A série é obtida com uma freqüência de amostragem de 3 kHz, em regime permanente, com um número de Reynolds de 7,4 x 10^4. Os sinais instantâneos são mostrados na Fig. 9, e as decomposições de velocidade e ângulo de incidência, respectivamente, nas Figuras 4.54 e 4.55. As características apresentadas nessa série são muito semelhantes às apresentadas para o banco de tubos com P/D = 1,26. Quando a velocidade se mantém em valores mais altos, há flutuações com menores amplitudes em todas as bandas de freqüência e o ângulo de incidência se mantém em valores mais baixos e com menores flutuações. Nesse caso, uma troca no modo de escoamento não é visualizada de maneira muito clara, pois ocorrem em intervalos de tempo muito breves. Os tempos de permanência em velocidade elevada são em torno de 1 s e as quedas na velocidade ocorrem quase como pulsos. Dessa forma, pode-se concluir que para a medição realizada com o banco com P/D = 1,4, não ocorreu uma estabilidade entre os dois modos de escoamento, contudo, a flutuação na componente vertical do escoamento pôde ser identificada com muita clareza.

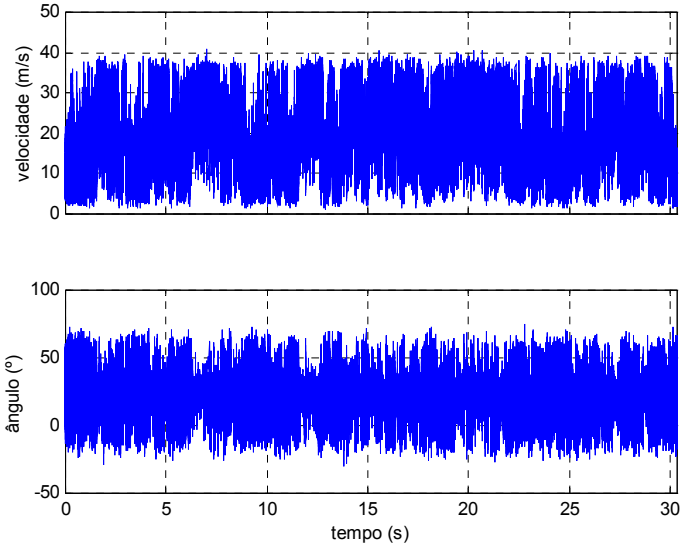

Figura 9. Velocidade e ângulo de incidência na esteira da terceira fileira do banco de tubos com P/D = 1,4.

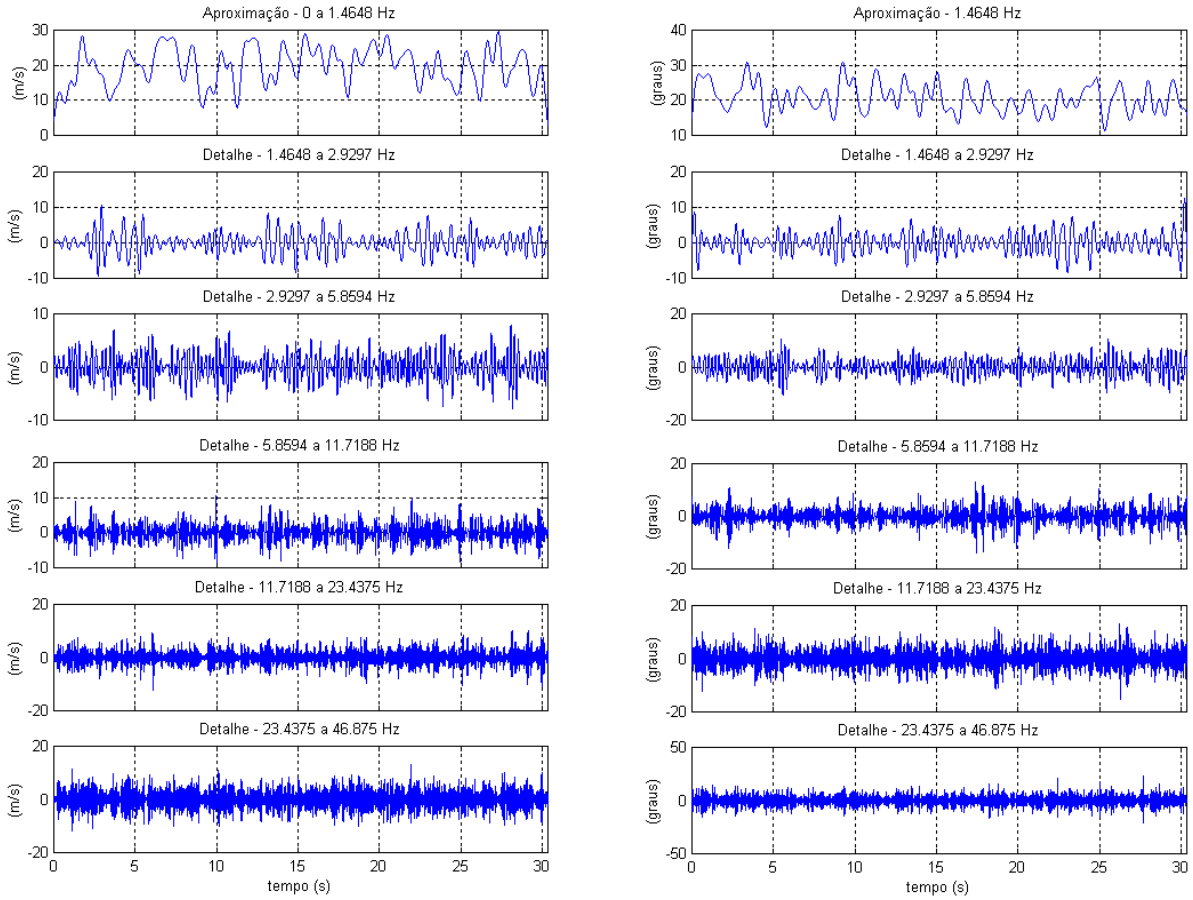

(a) (b)

Figura 10. (a) Decomposição do sinal de velocidade e (b) ângulo de incidência correspondente ao sinal da Fig. 9 em bandas de freqüências.

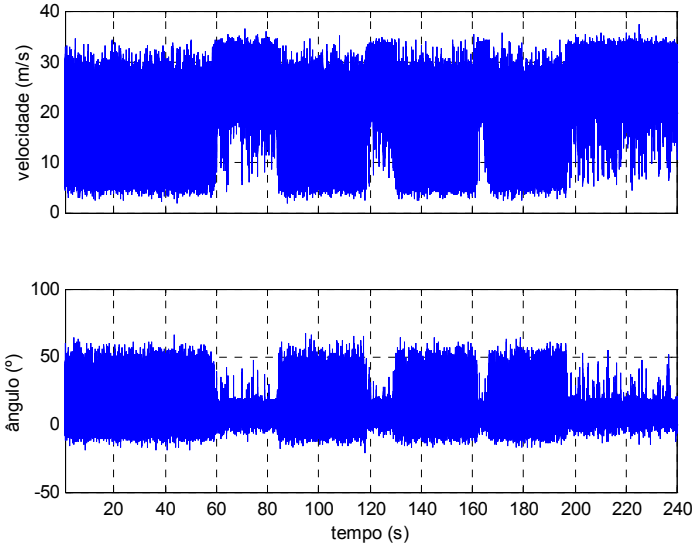

Figura 11. Velocidade e ângulo de incidência medidos atrás da segunda fileira do banco de tubos com P/D=1,6.

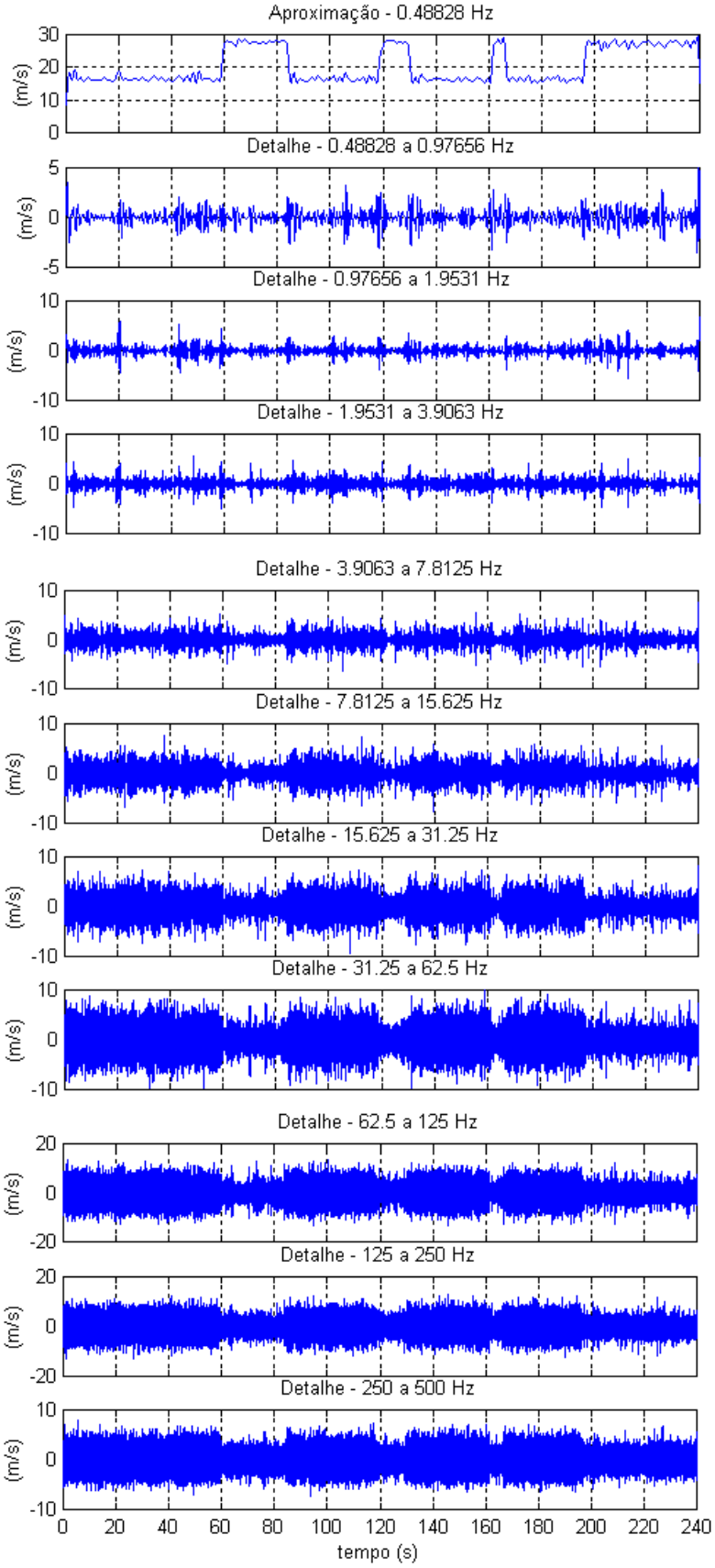

Figura 12. Decomposição do sinal de velocidade da Fig. 11.

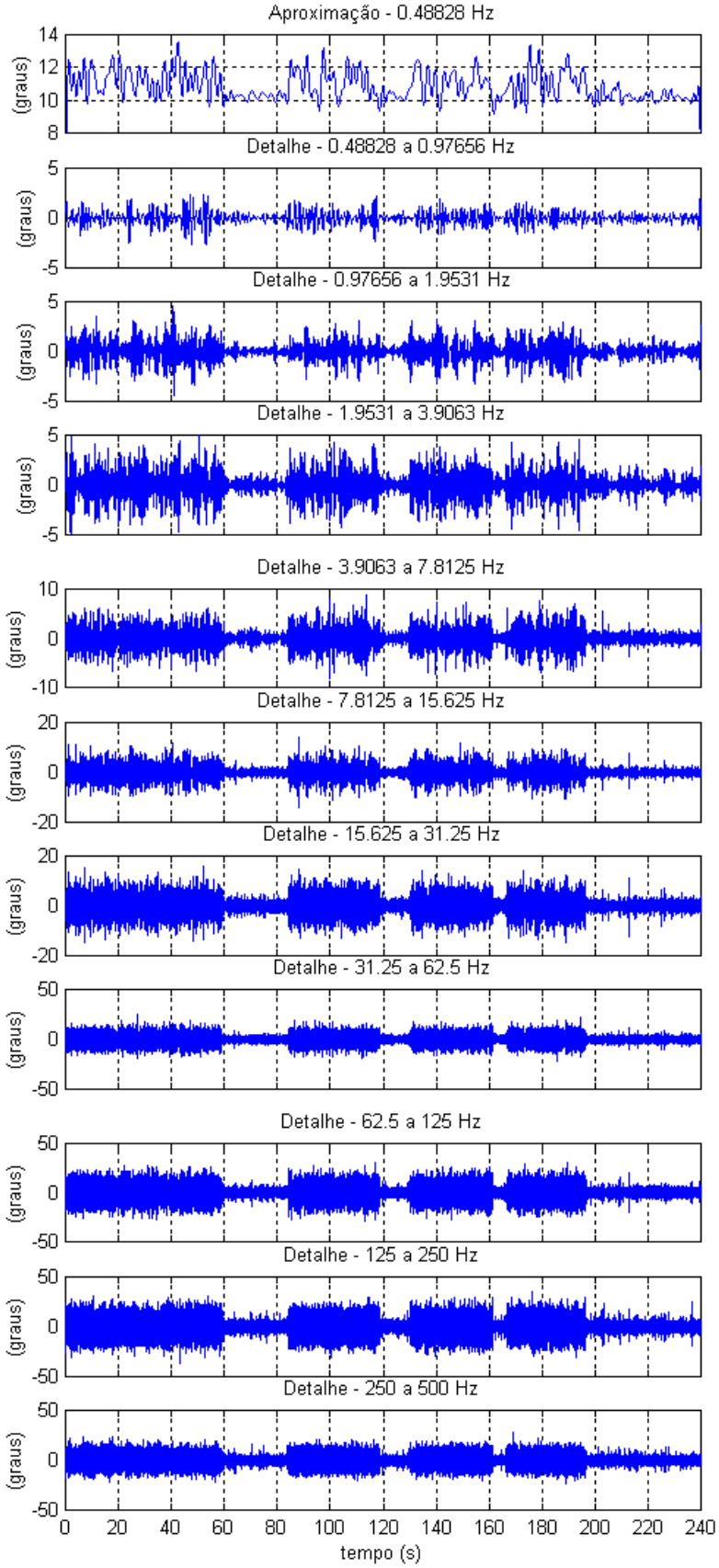

Figura 13. Decomposição do ângulo de incidência da Fig. 11.

Para o banco com razão de espaçamento de 1,6, é apresentada, na Fig. 11, uma série de velocidade e ângulo de incidência obtida atrás da segunda fileira, para um número de Reynolds de 7,4 x 10^4. As Figuras 12 e 13 mostram as decomposições da velocidade e ângulo de incidência em bandas de freqüências. Nessa série, pode-se identificar a troca no modo de escoamento de forma muito clara. Observando-se diretamente os sinais instantâneos de velocidade e ângulo de incidência, é possível identificar a presença de dois modos diferentes no escoamento. As características de cada modo, em termos de freqüências, ocorrem para todas as bandas. Na Figura 12, correspondente à decomposição do sinal de velocidade, pode-se observar que, associado aos intervalos em que a velocidade permanece com valores elevados (~28 m/s), há uma menor amplitude das flutuações em todas as bandas de freqüência. Por outro lado, quando a velocidade flutua ao redor de valores mais baixos (~17 m/s), há uma maior amplitude nas flutuações de velocidade em todas as bandas decompostas. Comportamento semelhante é observado na de decomposição dos ângulos (Fig. 13), onde, nos intervalos em que o ângulo médio tende a um alinhamento na direção de 11º, há uma redução nas amplitudes de flutuação de todas as bandas de freqüência.

Na Figura 14 é mostrado o espectrograma calculado através de transformada de ondaletas contínua do intervalo entre 44 e 76 s. Pode-se verificar que antes de 60 s há um grande espalhamento de energia em todas as freqüências apresentadas. Após 60 s, onde ocorre uma troca no modo de escoamento, o espectrograma apresenta-se com muito menor energia em todas as faixas de freqüência.

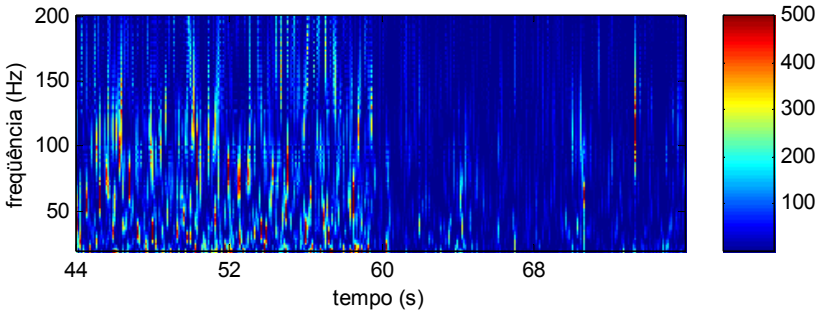

Figura 14. Espectrograma de parte do sinal de velocidade da Fig. 11.

4.3.6. Visualizações

As visualizações do escoamento, efetuadas no canal de água, foram realizadas usando o banco de tubos com razão de espaçamento de 1,26. O objetivo foi auxiliar na compreensão do comportamento do escoamento ao atravessar as primeiras fileiras do banco de tubos. Os escoamentos foram realizados para diversos números de Reynolds, calculados com a velocidade média nas fendas e o diâmetro dos tubos. A velocidade da fenda foi calculada a partir da velocidade de aproximação. A injeção de tinta ocorreu de três formas: através do conjunto de agulhas mostrado que injetam tinta a 60 mm abaixo da parede superior da seção de testes, na direção das fendas estreitas entre os tubos de cada fileira, através da agulha posicionada no interior do tubo vizinho ao tubo de acrílico e através de uma agulha móvel, que permite a injeção de tinta a 60 mm do fundo do canal, em qualquer posição desejada.

O primeiro ensaio, visto na Fig. 15, mostra que o escoamento próximo à parede superior sofre um desvio para a esquerda (visto de montante para jusante) e o filete de tinta, visto através do espelho, no tubo central, tem uma tendência para baixo (Fig. 15(a)). O escoamento próximo ao fundo é desviado para a direita (Fig. 15(b)).

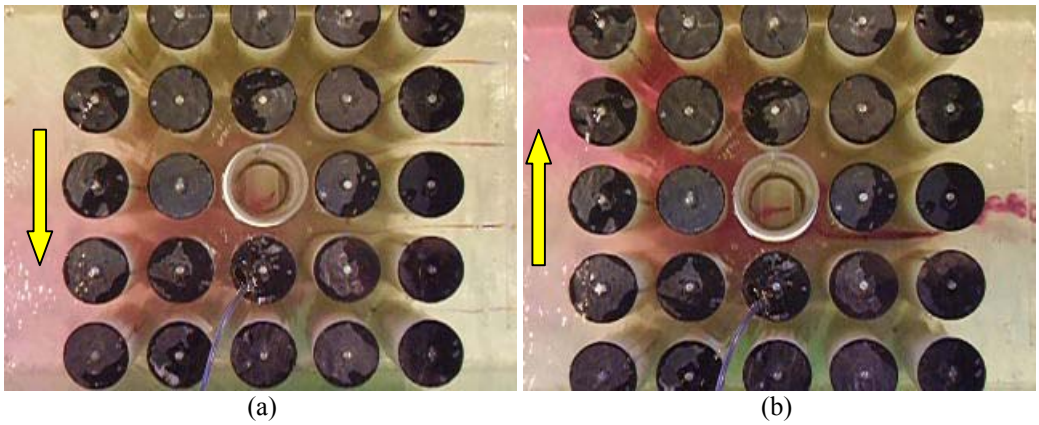

(a) (b)

Figura 15. Visualização do escoamento sobre o banco de tubos. Re = 3,07 x 10^4. (a) injeção a 60 mm da parede superior, (b) injeção a 60 mm do fundo. (as setas indicam a componente transversal gerada)

O segundo ensaio mostrado para o banco de tubos segue um padrão de escoamento oposto ao primeiro ensaio, ou seja, o escoamento próximo à parede superior ocorre com desvio à direita (Fig. 16(a)) e o escoamento de fundo com desvio à esquerda (Fig. 16(b)). No espelho do tubo central é visto um desvio, no plano vertical, para cima na altura média dos tubos.

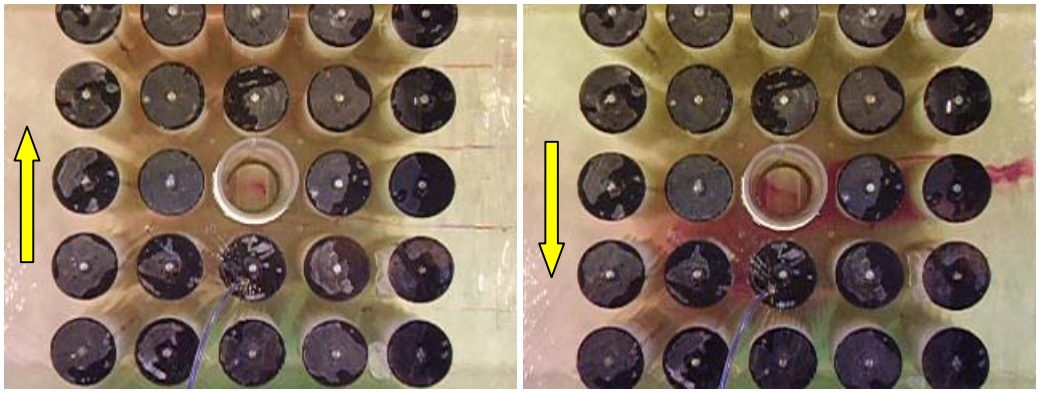

(a) (b)

Figura 16. Visualização do escoamento sobre o banco de tubos. Re = 3,18 x 10^4. (a) injeção próxima a parede superior, (b) injeção próxima do fundo. (as setas indicam a componente transversal gerada)

5. Conclusões

Neste trabalho, é apresentado um estudo experimental do escoamento cruzado sobre as primeiras fileiras de bancos de tubos com arranjo quadrangular. Foram realizadas medições de velocidade, a fim de detectar as instabilidades geradas nessas primeiras fileiras que atuam sobre o escoamento, alterando as suas características. As medições foram realizadas em um canal aerodinâmico com bancos de tubos alinhados e razões de espaçamento de 1,26, 1,4 e 1,6. Para auxiliar na interpretação dos resultados, foram feitas visualizações em um canal de água, com um banco de tubos alinhados com razão de espaçamento de 1,26.

Um fenômeno de alteração aleatória no modo de escoamento, caracterizado pela presença de componentes transversais ao escoamento principal e que leva ao aparecimento de tridimensionalidades com escala da ordem da dimensão do canal, foi identificado. A ocorrência de tal fenômeno pode tornar-se uma importante origem de instabilidades dinâmicas, visto que pode alternar os coeficientes de sustentação e arrasto dos tubos, alterando a resposta dinâmica das estruturas envolvidas. Esse fenômeno foi detectado através de medições de velocidade em bancos de tubos com três razões de espaçamento no canal aerodinâmico. As medições de velocidade foram realizadas na faixa de números de Reynolds denominada regime subcrítico, onde se espera que os fenômenos gerados apresentem um comportamento semelhante e independente da velocidade do escoamento.

O fenômeno identificado é semelhante ao escoamento biestável que ocorre na geometria de dois tubos posicionados lado a lado transversalmente ao escoamento. Fenômeno semelhante, também ocorre no escoamento sobre uma fileira de tubos, onde as esteiras que emergem das fendas estreitas entre os tubos, desviam-se para formar conjuntos instáveis, que podem mudar de configuração aleatoriamente. O jato que emerge entre dois cilindros interage com as esteiras formadas por cada cilindro, como resultado, o jato central é defletido para a direção de um cilindro, podendo permanecer nesta posição durante um tempo, para depois retomar seu comportamento aleatório. A origem desse fenômeno, contudo, não é completamente entendida. Ele tem sua origem na velocidade e assim, na vorticidade, e em flutuações das esteiras da vizinhança. É esperado que, no início do processo, as esteiras sejam geradas independentemente uma da outra. Se os vórtices vizinhos têm a mesma fase, a flutuação irá fazer a esteira crescer. Se a razão de espaçamento P/D é maior do que um, mas pequena o suficiente para garantir a interação entre as esteiras dos cilindros adjacentes, a esteira resultante não se comporta como um único corpo rombudo, devido ao escoamento através da fenda entre os tubos. Preferencialmente, ela permanecerá desviada para detrás de um tubo, até que uma nova perturbação desestabilize a esteira e o processo se inicie novamente.

Em bancos de tubos, o fenômeno de troca é influenciado por um escoamento altamente desordenado após a segunda e a terceira fileira, o qual, em algumas geometrias, não permite a observação de uma freqüência característica. Contudo, o processo de desprendimento de vórtices ainda ocorre. Se a interação das esteiras, descrita para os dois cilindros posicionados lado-a-lado ou para uma fileira de tubos, ocorre, a troca no modo será fortemente influenciada pela presença dos tubos da próxima fileira. Como não há espaço físico para a formação da esteira, devido à presença dos tubos da fileira seguinte, o escoamento será direcionado para cima ou para baixo, ou seja, na direção paralela ao eixo dos tubos, resultando em uma forte característica tridimensional para o escoamento através do banco. Essa componente, no plano formado pelo eixo dos tubos e a direção do escoamento principal, acarreta uma redistribuição do escoamento, gerando componentes transversais ao eixo dos tubos e ao escoamento.

Em função do processo de aceleração/desaceleração que ocorre nos jatos que escoam no interior das fendas na direção do escoamento, as velocidades dentro das fendas do banco de tubos não se distribuem de forma completamente

homogênea. A diferença entre as velocidades pode provocar a geração e desprendimento de vórtices em freqüências diferentes e estar relacionada com as instabilidades que causam o efeito tridimensional.

As medições de velocidade, realizadas no interior das três geometrias de banco de tubos resultaram em diferentes tempos de permanência entre cada modo, em função da razão de espaçamento dos tubos. Para o banco com P/D = 1,26, o tempo de permanência em cada modo foi da ordem de 0,5 s. Para o banco com P/D = 1,4 a troca de modo ocorreu na faixa de 1 a 2 s e, para o banco com P/D = 1,6, foi da ordem 10 s. Isso leva a concluir que o tempo em que ocorrem as trocas no modo de escoamento está associado à geometria do banco de tubos, quanto maior a razão de espaçamento, maior será o tempo de permanência em cada modo.

Os experimentos de visualização permitiram reconhecer que o início desse escoamento transversal ocorre a partir da região de jusante da segunda fileira do banco de tubos

Nos experimentos onde o ar foi o fluido de trabalho, a troca nos modos de escoamento ocorreu de forma natural, seguindo uma característica de aleatoriedade. Nos experimentos de visualização em canal de água, tal fato não pôde ser identificado. As trocas no modo de escoamento só ocorreram a cada novo experimento, ou seja, a cada reinicialização do sistema de circulação de água. Tal fato também é citado por Summer et al. (1999), que relata, que em seus experimentos, a natureza biestável do escoamento desviado não foi detectada nos ensaios em canal de água. Isso, conforme eles, poderia ser atribuído a uma combinação de um pequeno grau de desalinhamento dos cilindros e a efeitos experimentais, como as razões de aspecto e bloqueio. Summer et al. (1999) chamam a atenção, também, para o fato que experimentos prévios, nos quais o padrão de escoamento biestável foi reportado, foram realizados somente em túneis de vento. Este processo, portanto, parece associado às características do fluido e às relações geométricas dos canais empregados nos estudos. Assim, novos trabalhos devem ser realizados a fim de verificar, através do estudo de similaridade, se os grupos adimensionais clássicos são capazes de capturar todas as características da classe de escoamentos estudados.

O estudo realizado, que permitiu a identificação dos efeitos tridimensionais gerados nas primeiras fileiras de bancos de tubos na forma de componentes transversais à direção principal do escoamento, reforça a idéia de que, em sendo a turbulência um fenômeno tridimensional, as hipóteses de bidimensionalidade, por vezes adotada como simplificação na análise, podem não levar em conta importantes características do escoamento.

5. Referências

Endres, L. A.M., 1997, "Análise experimental do campo de pressões flutuante em bancos de tubos submetidos a escaomento transversal turbulento", Tese de Doutorado, PROMEC-UFRGS, Porto Alegre.

Indrusiak, M. L. S., 2004, "Caracterização de escoamentos transientes usando transformada de ondaletas", Tese de Doutorado, PROMEC, UFRGS, Porto Alegre.

Indrusiak, M. L. S. e Möller, S. V., 2004, "Wavelet analysis of experimental turbulence time series", IV Escola de Primavera de Transição e Turbulência, ABCM, Porto Alegre.

Olinto, C. R., 2005, "Estudo experimental das características do escoamento turbulento nas primeiras fileiras de bancos de tubos", Tese de Doutorado, PROMEC, UFRGS, Porto Alegre.

Summer, D., Wong, S. S. T., Price, S. J. and Païdoussis, M. P., 1999, "Fuid Behaviour of side-by-side circular cylinders in steady cross-flow", Journal of Fuids and Structures 13, pp. 309-338.

EXPERIMENTAL STUDY OF THE TURBULENT FLOW IN THE FIRST ROWS OF TUBE BANKS

Cláudio Rodrigues Olinto
dfscro@furg.br

Luiz Augusto Magalhães Endres
endres@iph.ufgrs.br

Sérgio Viçosa Möller
svmoller@ufgrs.br

Abstract: *This work presents an experimental study of the characteristics of the turbulent flow after the first rows of tube banks. The objective is to understand the random and transient behavior of the instabilities and phenomena that occur in the first rows of tube banks and propagates to its interior. The experimental results are obtained through measurements in a wind tunnel and the visualizations in a water canal. For the attainment of the velocity fields the hot wire anemometry technique is used. The experimental data are analyzed by statistical, spectral and wavelets tools. The visualizations are made through the technique of injection of dye directly in the flow. The results show the presence of instabilities generated from the second row of the tube bank, that propagates to the interior of the bank, generating a behavior where the three orthogonal components of the flow are equally important. The three-dimensional behavior of the flow is responsible for a redistribution of mass inside of the bank of tubes that leads to velocity values and Strouhal numbers not expected for the studied geometry.*

Keywords: turbulent flow, tube bank, wavelet.

Proceedings of the 11th Brazilian Congress of Thermal Sciences and Engineering -- ENCIT 2006
Braz. Soc. of Mechanical Sciences and Engineering -- ABCM, Curitiba, Brazil, Dec. 5=8, 2006

Paper CIT06-0680

MÉTODOS PSEUDO-ESPECTRAL E DFERENÇAS FINITAS DE 2ª ORDEM PARA ANÁLISE DA TRANSIÇÃO À TURBULÊNCIA EM JATOS CIRCULARES LIVRES

Ana Marta de Souza
Universidade Federal de Uberlândia- Av. João Naves de Ávila, 2160- Camus Santa Mônica- Uberlândia-MG – Brasil.
amsouza@mecanica.ufu.br

Francisco José de Souza
EMBRAER- Empresa Brasileira de Aeronáutica S.A. – Av. Brigadeiro Faria Lima, 2170. São José dos Campos – SP - Brasil
francisco.souza@embraer.com.br

Aristeu da Silveira Neto
Universidade Federal de Uberlândia- Av. João Naves de Ávila, 2160- Camus Santa Mônica- Uberlândia-MG – Brasil.
aristeus@mecanica.ufu.br

Resumo. A turbulência em jatos tem sido bastante estudada numérica e experimentalmente por pesquisadores, almejando adquirir maiores conhecimentos sobre os fenômenos físicos envolvidos. O presente trabalho tem como foco a análise física do escoamento do tipo jato livre através de simulações tridimensionais. As simulações foram analizadas utilizando um código computacional, previamente desenvolvido por Souza (2003), o qual utiliza diferenças finitas segunda ordem no espaço e no tempo e o modelo de turbulência de Smagorinsky para simular as grandes escalas. No entanto, os resultados das simulações utilizando este código não permitiram realizar as análises fisicas desejadas com sucesso, uma vez que estruturas típicas do escoamento não puderam ser identificadas. Os resultados obtidos através desses códigos demonstraram que alta precisão é necessária para capturar as estruturas do escoamento. Um novo código computacional, o qual emprega um método pseudo-espectral, foi desenvolvido pelos autores para atingir os objetivos propostos. Devido a necessidade de periodicidade imposta pelo método, o jato circular livre foi analisado em evolução temporal. Interessantes resultados foram observados, tais como similaridade entre as estruturas de um jato temporal e experimental, idendificação das fases de evolução do jato especial em diferentes instanes de tempo do jato temporal. Os resultados permitiram ainda identificar as estruturas origindas de diferentes perturbações importas no campo de velocidade inicial, mostrando a relevância do controle do jato.

Palavras chave: jatos circulares livres, métodos das diferenças finitas, método pseudo-espectral, transição à turbulência.

1. Introdução

O interesse dos estudiosos pelos escoamentos do tipo jato justifica-se pela sua considerável importância tecnológica. As aplicações industriais envolvem processos de mistura de componentes, transferência de calor, lubrificação e degelo, injeção de combustível em câmaras de combustão, sistemas de propulsão de aviões e aeronaves. A otimização destes processos pode ser obtida através do controle do jato. Este controle pode ser atingido através da manipulação das já mencionadas "estruturas coerentes", as quais são responsáveis por influenciar fortemente a dinâmica do jato, especialmente na região de transição próxima ao bocal. Além disso, o jato turbulento é um escoamento canônico simples bastante importante do ponto de vista físico. O estudo deste tipo de escoamento serve como modelo simplificado, fornecendo análises importantes para utilização em escoamentos complexos, comumente encontrados na prática.

A importância da compreensão das estruturas coerentes para refinamento de teorias e modelos já existentes, melhoria dos sistemas de engenharia e desenvolvimento de novos métodos e dispositivos para controle da dinâmica do escoamento motivaram a realização do presente estudo. Embora muitos estudos sobre este tema sejam encontrados na literatura, muitos se restringem à comparação de comportamentos médios. Alguns apresentam as estruturas coerentes típicas sob determinadas condições. No entanto, notou-se, dentre os trabalhos encontrados, certa carência no que diz respeito à compreensão das estruturas turbilhonares, da influência das condições iniciais e de diferentes tipos de perturbação sobre a formação e evolução de jatos. A realização de um estudo mais minucioso neste sentido contribuiria de forma relevante para a otimização do controle de jatos.

Diante do contexto apresentado, o objetivo do presente trabalho foi focado na análise física de jatos, através da realização de simulações numéricas tridimensionais. Incluem neste objetivo, análises da influência de diferentes tipos de perturbação sobre a formação e evolução das estruturas turbilhonares, bem como avaliação da importância da resolução espacial e precisão do esquema numérico utilizado na simulação. Objetivou-se ainda a prática e o uso de procedimentos de experimentação numérica. Nestes procedimentos incluem-se a escolha da metodologia numérica

apropriada, a definição dos objetivos almejados, a amostragem das informações e o tratamento estatístico dos dados amostrados.

2. Modelo Matemático e Metodologia Numérica

No presente trabalho foram empregados dois códigos computacionais diferentes para estudos de escoamentos do tipo jatos. O primeiro código utilizado, denominado *CIL3D*, é uma versão atualizada do código desenvolvido por Souza (2003). O segundo código, desenvolvido pelos autores, utiliza o método pseudo-espectral para resolução das equações que compõem o modelo matemático, sendo aqui denominado S*PECTRAL*. Os dois códigos aplicados à resolução das equações que compõem o modelo matemático para escoamentos de jatos livres são apresentados a seguir.

2.1. Código *CIL3D*

O código *CIL3D* (Souza, 2003) resolve as equações de Navier-Stokes na forma incompressível e isotérmica, utilizando um algoritmo do tipo passo fracionário (Kim e Moin, 1985). Há muitas variantes deste método, mas a característica principal da metodologia é um algoritmo não-iterativo para o acoplamento pressão-velocidade, sendo o problema da incompressibilidade desvinculado do avanço no tempo. Este código emprega o esquema de Adams-Bashforth de 2ª ordem para ambos os termos advectivo e difusivo das equações de momento por ser um método explícito e de baixo custo computacional.

As equações governantes na forma tensorial, para um escoamento incompressível, isotérmico são dadas pelas Equações (6):

$$\begin{cases} \dfrac{\partial u_i}{\partial t} + H_i = -\dfrac{1}{\rho}\dfrac{\partial p}{\partial x_i} + \dfrac{\partial}{\partial x_j}\left[\nu\left(\dfrac{\partial u_i}{\partial x_j} + \dfrac{\partial u_j}{\partial x_i}\right)\right] \\ \dfrac{\partial u_i}{\partial x_i} = 0 \end{cases} \tag{6}$$

onde H_i representa o termo advectivo.

Neste trabalho, inovou-se em relação ao trabalho de Souza (2003), que utilizou o método MSI (Modified Strongly Implicit Procedure), através da aplicação da transformada rápida de Fourier (FFT) na direção azimutal de um jato redondo, que é periódica em coordenadas cilíndricas. Este procedimento transforma reduz significativamente o custo da solução da Equaçao de Poisson por passo de tempo.

O emprego de um sistema ortogonal para a resolução das equações de conservação oferece vantagens interessantes, tais como não exigir a adaptação do código computacional a um sistema de coordenadas generalizadas e nem o cálculo de termos adicionais nas equações governantes. Optou-se neste trabalho pelo sistema de coordenadas cilíndricas, no qual é possível representar genericamente a geometria de um jato circular.

O código *CIL3D* emprega coordenadas cilíndricas e o modelo de turbulência submalha de Smagorinsky (1963). As taxas de deformação foram calculadas através de diferenças finitas de 2ª ordem As velocidades utilizadas no cálculo destas taxas de deformação são as do campo filtrado.

2.2. Código *SPECTRAL*

Considerem-se as equações que modelam os escoamentos incompressíveis no espaço físico, com propriedades físicas unitárias:

$$\begin{cases} \dfrac{\partial u_i}{\partial t} + \dfrac{\partial}{\partial x_j}\left(u_i u_j\right) = -\dfrac{\partial p}{\partial x_i} + \dfrac{\partial^2 u_i}{\partial x_j \partial x_j} \\ \dfrac{\partial u_i}{\partial x_i} = 0 \end{cases} \tag{7}$$

A transformada destas equações no espaço de Fourier é dada por:

$$\begin{cases} \dfrac{\partial \hat{u}_\ell}{\partial t} + \nu k^2 \hat{u}_\ell = -ik_m P_{jm}\left(\vec{k}\right) \displaystyle\int_{\vec{p}+\vec{q}=\vec{k}} \hat{u}_\ell(\vec{p})\hat{u}_j(\vec{q})d\vec{p} \\ i\vec{k}\cdot\hat{\vec{u}} = 0 \end{cases} \tag{8}$$

A resolução da integral de convolução não-linear, a qual faz parte da Equação (8) é inviável devido seu elevado custo computacional. Por isso os métodos denominados pseudo-espectrais têm sido muito utilizados. Estes métodos consistem em resolver o produto das velocidades no espaço físico, transformando-os em seguida para o espaço de Fourier, onde se efetua o cálculo das derivadas. Assim, o campo de velocidade transformado é calculado, com o qual efetua-se a transformada inversa e determina-se o campo de velocidade no espaço físico.

Assim, a equação de Navier-Stokes no espaço espectral pode ser escrita da seguinte forma para as componentes de velocidade:

$$\begin{cases} \dfrac{\partial \hat{u}}{\partial t} = -\hat{H}_{u_\pi} + \nu\left(-k_x{}^2 - k_y{}^2 - k_z{}^2\right)\hat{u} \\ \dfrac{\partial \hat{v}}{\partial t} = -\hat{H}_{v_\pi} + \nu\left(-k_x{}^2 - k_y{}^2 - k_z{}^2\right)\hat{v} \\ \dfrac{\partial \hat{w}}{\partial t} = -\hat{H}_{u_\pi} + \nu\left(-k_x{}^2 - k_y{}^2 - k_z{}^2\right)\hat{w} \end{cases}, \tag{9}$$

onde $\hat{u}$, $\hat{v}$ e $\hat{w}$ são os coeficientes de Fourier para *u*, *v* e *w*, respectivamente e $\hat{H}_{u_\pi}$, $\hat{H}_{v_\pi}$ e $\hat{H}_{w_\pi}$ representam os termos advectivos de cada equação projetados no plano π.

Para o avanço temporal das equações no código SPECTRAL foram utilizados os esquemas de Adams-Bashforth e Runge Kutta, ambos de 3ª ordem. O esquema de Runge Kutta envolve três sub-passos para cada passo de tempo. Após os dois passos de tempo iniciais utilizando o esquema de Runge Kutta de 3ª ordem (RK3), o avanço temporal segue o esquema de Adams Bashforth de 3ª ordem (AB3). A cada passo ou subpasso de tempo a equação de Navier Stokes transformada é resolvida.

3. Resultados e Discussões

3.1. Resultados obtidos com o Código *CIL3D*

Foram realizadas duas simulações utilizando o código *CIL3D.* Ambas utilizando malha de discretização de 340.000 pontos (100x34x100) e passo de tempo 0,001s. Lembrando que código é em coordenadas cilíndricas, as dimensões axiais (*L*) e radiais (*R*) do domínio foram definidas em função do diâmetro do jato. A primeira simulação, denominada *1CIL3D*, tem como dimensões *L=16D e R=5,5D* e foi realizada a número de Reynolds 1.600. A segunda simulação, denominada *2CIL3D*, apresenta um domínio de 24D na direção axial e 5,5 diâmetros na direção radial e foi realizada a Reynolds 11.000. As condições de contorno utilizadas e os detalhes referentes a cada uma das simulações são apresentados a seguir.

Foi imposto um perfil de entrada utilizado em simulações numéricas por Urbin e Metais (1997):

$$w(r,\theta,z=0) = \frac{1}{2}\cdot\left[1-\tanh\left(\frac{1}{4}\frac{R}{\theta}\left(\frac{r}{R}-\frac{R}{r}\right)\right)\right] \tag{10}$$

onde R/θ é um parâmetro que depende das condições experimentais (alongamento do bocal, número de Reynolds, rugosidade, ...) e pode variar de 10 a 300 (Zaman e Hussein, 1980). Foram testados diferentes valores deste parâmetro e ele foi fixado em R/θ=28.

Na entrada, as demais componentes de velocidade foram considerads nulas. Na saída do domínio foram aplicadas condições de derivadas nulas para as velocidades. Como é natural em coodenadas cilíndricas, condições de contorno periódicas foram aplicadas na direção azimutal do escoamento.

Para visualização das estruturas do escoamento são apresentados os campos de velocidade e dos módulos de vorticidade no plano xz em diferentes instante de tempo. As Figuras 1e 2 mostram respectivamente o campo de componente axial de velocidade e o módulo da vorticidade para a simulação *1CIL3D* em dois diferentes instantes de tempo.

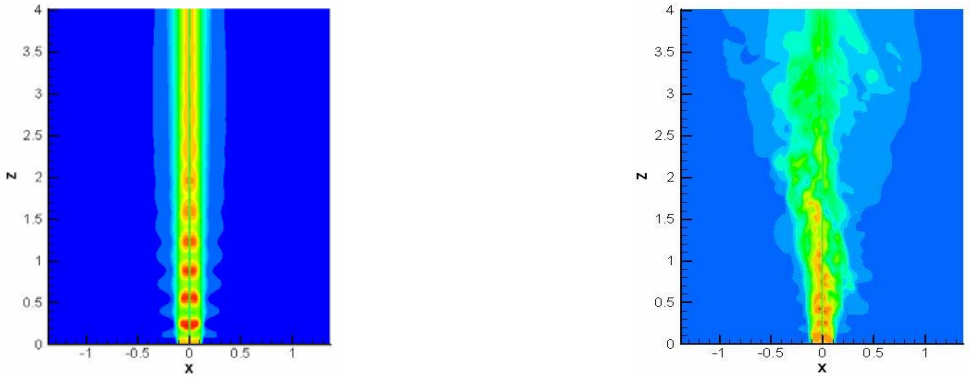

(a) (b)

Figura 1. Campo de Velocidade axial no plano xz (x=0): (a) t=40,0 s e (b) t= 100,0 s físicos – Re=1600.

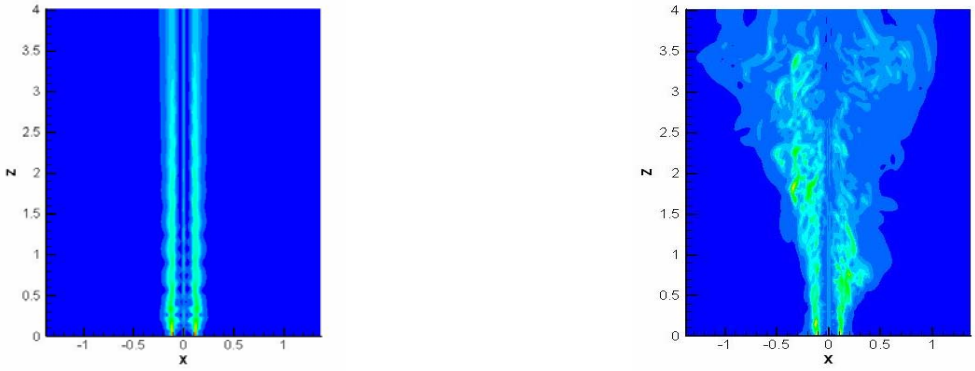

(a) (b)

Figura 2. Módulo de Vorticidade no plano xz (x=0): (a) t=40,0 s e (b) t= 100,0 s físicos –Re=1600.

Observando-se as Figs. 1 (a) e 2 (a) pode-se notar que o escoamento é ainda bem comportado no instante igual a 40,0 segundos. No entanto, algumas instabilidades já podem ser notadas, especialmente nas proximidades do bocal do jato, indicando o início da transição. Na saída do domínio o escoamento ainda apresenta-se laminar. Em 100 segundos de simulação, conforme apresenta as Figs. 1 (b) e 2 (b) nota-se espalhamento do jato na direção transversal ao escoamento, com presença de maior quantidade de estruturas turbulentas geradas pelo desenvolvimento das instabilidades iniciais. No entanto, não se pode evidenciar através da visualização destas figuras as estruturas típicas de um jato.

Vale lembrar que estas simulações foram realizadas a número de Reynolds relativamente baixo (Re=1600). Embora os resultados tenham permitido verificar que a este número de Reynolds já ocorre transição à turbulência, as estruturas primárias do tipo Kelvin-Helmholtz não puderam ser evidenciadas.

As Figuras 3 e 4 mostram respectivamente o campo de componente axial de velocidade e o módulo da vorticidade para a simulação 2*CIL3D* em dois diferentes instantes de tempo. É possível verificar através do campo de velocidade (Fig 3 a) e do módulo de vorticidade (Fig 4 a) que o escoamento já apresenta turbulência tridimensional desenvolvida no instante igual a 11 segundos. Comparando os resultados da simulação *2CIL3D* nos dois diferentes instantes de tempo (11,0 e 40,0 segundos) não é possível notar diferenças significativas.

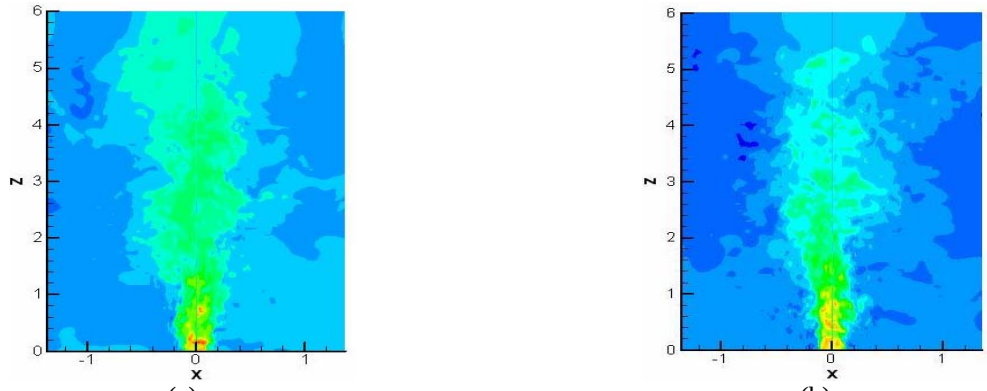

(a) (b)

Figura 3 - Campo de Velocidade no plano xz (x=0): (a) t=11,0 s; (b) t= 40,0 s físicos –Re=11000.

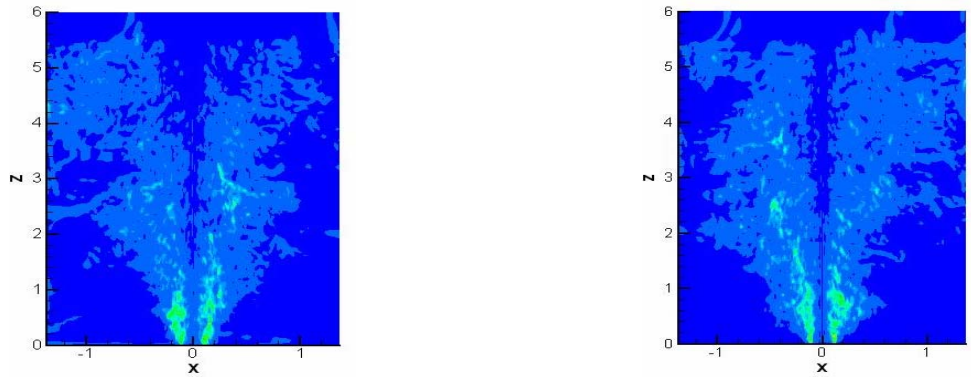

(a) (b)

Figura 4 - Visualização da Vorticidade no plano xz (x=0): t=11,0 s e (b) t= 40,0 s físicos - Re=11000.

Os resultados obtidos através do código *CIL3D* não permitiram identificar as estruturas turbulentas típicas do escoamento em estudo. Diante de resultados insatisfatórios ao estudo, iniciou-se uma investigação sobre as possíveis justificativas para tal fato. O trabalho de Glaze e Frankel (2003) apresenta resultados que permitem constatar diferenças na simulação ao se utilizar um esquema numérico de 2ª ou 6ª ordem. A Figura 5 apresenta as estruturas de vórtices instantâneas obtidas através da simulação utilizando um esquema compacto de alta ordem (GR LES) e utilizando um esquema de 2ª ordem (Fluent LES). Outro resultado interessante que pode ser observado no trabalho de Glaze e Frankel (2003) é com relação à comparação dos resultados simulados a dados experimentais. Verifica-se uma superpredição da Intensidade turbulenta pelo resultado Fluent LES, enquanto boa concordância é obtida através da solução GR LES, conforme pode ser visualizado na Fig. 6a. Já para a velocidade média axial não são notadas discrepâncias com relação aos resultados obtidos pelas resoluções utilizando esquemas de diferentes ordem numéricas, conforme apresenta a Fig. 6b.

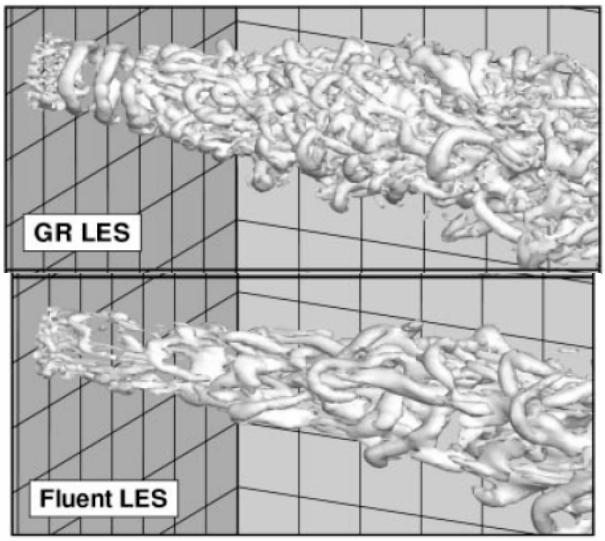

Figura 5. Estruturas de Vórtice instantâneas visualizadas por isosuperfícies negativas de λ_2. (Glaze e Frankel, 2003).

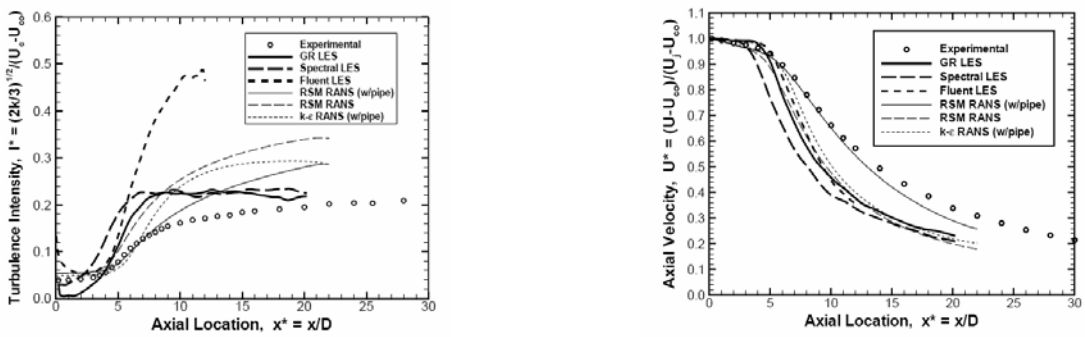

(a) (b)

Figura 6. Intensidade turbulenta (a) e Velocidade axial média (b) ao longo da linha central. (Glaze e Frankel, 2003).

Os resultados apresentados levantaram um questionamento a respeito da relevância da ordem do esquema numérico utilizado para realização das simulações do escoamento do jato livre. Além do trabalho de Glaze e Frankel (2003), vale lembrar que Uzun (2003), cujo trabalho apresenta boa concordância com resultados experimentais a elevado número de Reynolds, também utilizou esquemas compactos de 6ª ordem. O mesmo pôde ser observado no trabalho de Freund (2001) que utiliza diferenças finitas de 6ª ordem nas direções axial e radial e método espectral na direção azimutal.

Assim, a ordem do esquema numérico utilizado para simular o escoamento de jatos parece ser crucial para melhor compreender a formação e evolução das estruturas presentes no escoamento do tipo jato, principal objetivo do presente trabalho. É importante ressaltar ainda que a utilização do modelo de Smagorisky certamente afeta os resultados na região de transição, dissipando a energia das perturbações iniciais originadas da instabilidade do escoamento laminar.

Diante deste contexto, optou-se por utilizar um método de alta precisão numérica (método pseudo-espectral) para realização das simulações. Alguns dos resultados obtidos com o método pseudo-espectral são apresentados a seguir.

3.2. Resultados obtidos com o Código *SPECTRAL*

A validação do código *SPECTRAL* foi realizada através da solução da Equação de Burgers (Canuto et al., 1988) e da simulação dos vórtices de Green-Taylor (Layzet e Lamballais, 2004). Os resultados das simulações coincidiram muito bem com a solução teórica da equação de Burgers a partir de 32 modos de Fourier.O erro máximo diminuiu à medida em que se aumentou a resolução no espaço de Fourier, sendo estes inferiores aos inferiores aos erros máximos apresentados pela solução obtida por Canuto et al. (1988). Os vórtices de Green-Taylor também foram simulados de forma consistente. O erro calculado foi de $2{,}36\text{x}10^{-15}$ ao utilizar 128^2 modos de Fourier. É importante ressaltar que resultados com a mesma precisão já haviam sido obtidos com 8^2 pontos de colocação, com o erro também da ordem de 10^{-15}, confirmando a alta precisão do código *SPECTRAL*.

Realizada a validação do código SPECTRAL, objetivou-se o estudo da evolução temporal do jato circular livre. O código emprega condições de contorno periódicas nas três direções do escoamento, sendo esta uma exigência do método pseudo-espectral utilizado neste trabalho. Devido à condição de contorno periódica na direção do escoamento, esta é uma simulação temporal do jato, e, portanto diferente das realizadas anteriormene. As simulações foram conduzidas com o número de Reynolds 1600, 120^3 modos de Fourier passo de tempo de 0,0025 s, em um domínio cúbico de dimensões *8R x 8R x 8R*, onde *R* é o raio inicial do jato, conforme mostra a Figura 7.

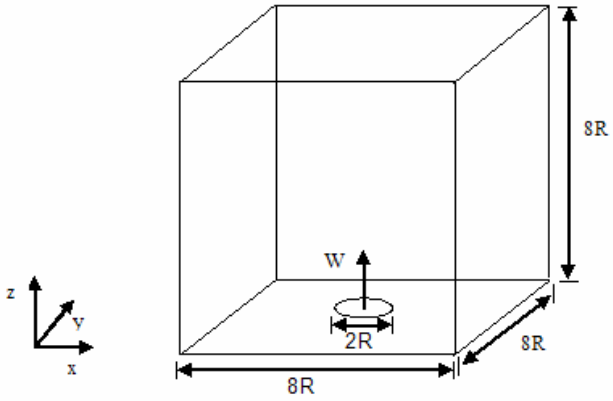

Figura7 - Esquema do domínio de cálculo.

O perfil inicial da componente axial de velocidade é o mesmo em todas as simulações realizadas:

$$w_0(r,\theta,z,0)=\begin{cases}1 & (r\le R-\delta)\\ \dfrac{1}{2}\cdot\left[1-\tanh\left(\dfrac{r-R}{2\delta}\right)\right] & (R-\delta<r<R+\delta)\\ 0 & (r\ge R+\delta)\end{cases}, \tag{12}$$

sendo r dado por $r=\sqrt{x^2+y^2}$, tendo como referência o sistema de coordenadas cartesianas e δ a metade da espessura da camada cisalhante, considerada igual a 2,5/16 m.

Foram simulados os jatos denominados “natural” e “bifurcado”, os quais se diferenciam pelo tipo de perturbaçoa imposta nas componentes de velocidade. O jato natural caracteriza-se pela imposição de uma perturbação randômica tipo “ruído branco” à componente axial de velocidade *w* nas três direções do escoamento:

$$w(x,y,z,t) = w_0(x,y,z,0) + \left(\frac{0,5-a}{100,0}\right), \tag{13}$$

sendo *a* um número aleatoriamente gerado entre 0 e 1.

O jato bifurcado origina-se da imposição de uma perturbação aleatória na componente axial de velocidade *w* (Eq. 14) aliada a uma perturbação imposta às componentes radial de velocidade (Eq. 15).

$$w(x,y,z) = w_0(x,y,z) + \left(\frac{0,5-a}{100,0}\right)\cdot e^{\left[-2\cdot\left(\frac{r-R}{2\delta}\right)^2\right]} \tag{14}$$

$$U_r = \left[0,01\cdot sen\left(2\pi\frac{z}{4,0}\right) + 0,02\cdot sen\left(2\pi\frac{z}{2,0}\right) + 0,03\cdot sen\left(2\pi\frac{z}{1,0}\right)\right]\cdot sinal(\cos\theta) \tag{15}$$

As componentes radiais de velocidade são dadas por:

$$u = U_r\cos\theta\cdot e^{\left[-2,0\cdot\left(\frac{r-R}{2\delta}\right)^2\right]} \quad \text{e} \quad v = U_r\sin\theta\cdot e^{\left[-2,0\cdot\left(\frac{r-R}{2\delta}\right)^2\right]} \tag{16}$$

As Figuras 8, 9 e 10 permitem comparar a evolução dos jatos natural e bifurcado estudados no presente trabalho. É possível notar que a transição à turbulência é mais rápida no jato bifurcado, como já comentado. No jato bifurcado, os anéis formam-se mais rapidamente e se expandem mais na direção transversal *x*. A expansão do jato bifurcado na direção x é considerável no instante t=20,0 s, enquanto o jato natural apresenta uma expansão bem menos expressiva em um instante de tempo maior. Esta comparação sugere a possibilidade de controle do jato em desenvolvimento espacial através da imposição de diferentes tipos de perturbação nas condições iniciais.

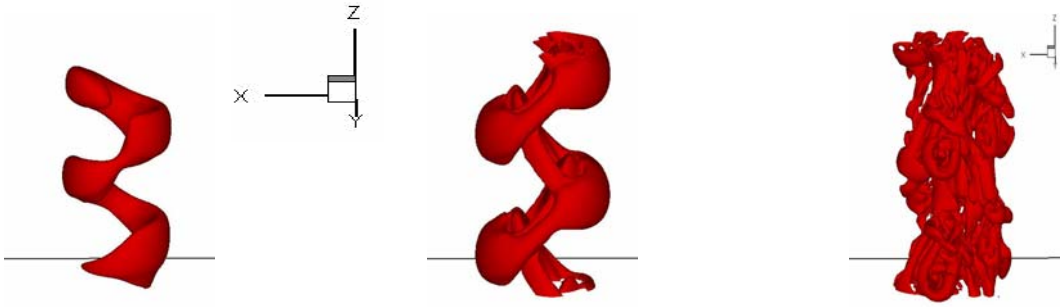

t= 5,0s t=20,0 s t= 30,0s

a) Isosuperfícies do critério Q ao nível 0,01 s^{-2} para Jato Natural

t= 5,0s t=10,0 s t= 20,0s

b) Isosuperfícies do critério Q ao nível 0,1 s^{-2}, para Jato Bifurcado

Figura 8.Comparação da evolução temporal através de isosuperfícies pelo critério Q : Jatos Natural e Bifurcado.

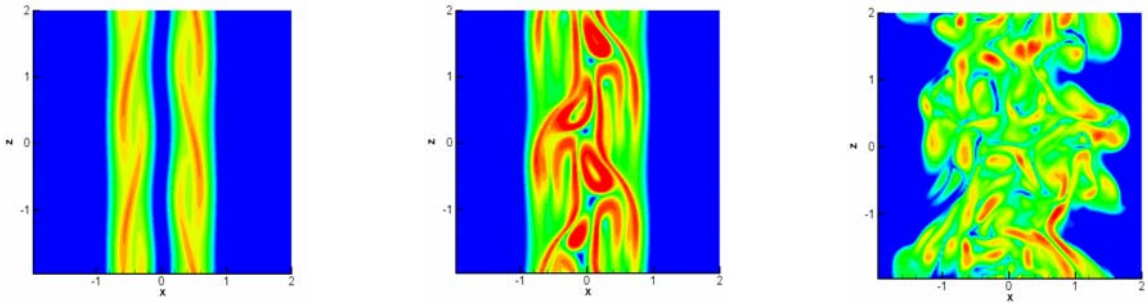

t= 17,0s t=26,0 s t= 40,0s

a) Módulo de Vorticidade $\|\vec{\omega}\|$ no plano xz- Jato Natural

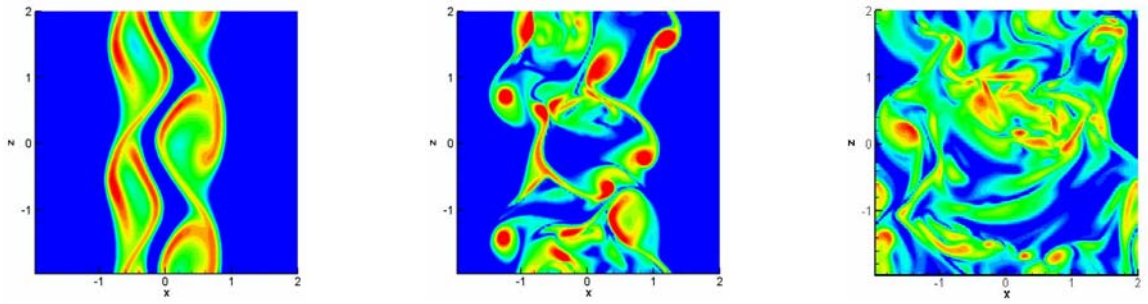

t= 7,5s t=12,5 s t= 20,0s

b) Módulo de Vorticidade $\|\vec{\omega}\|$ no plano xz- Jato Bifurcado

Figura 9. Evolução temporal do Módulo de Vorticidade $\|\vec{\omega}\|$ no plano xz (y=0) para jato natural.

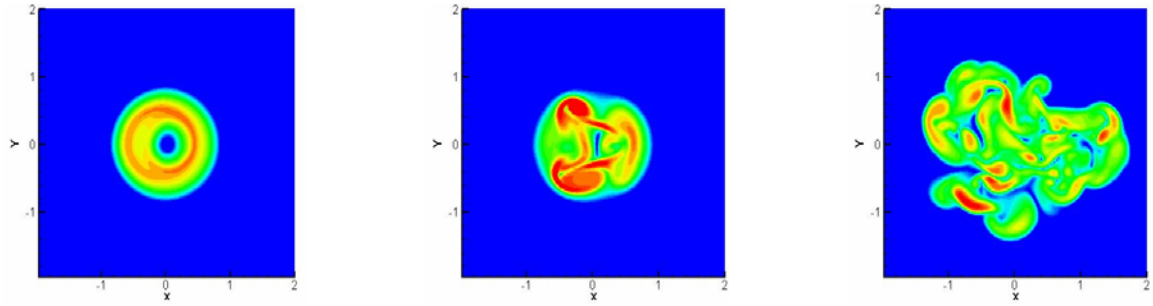

t= 17,0s t=26,0 s t= 40,0s

a) Módulo de Vorticidade $\|\vec{\omega}\|$ no plano xy- Jato Natural

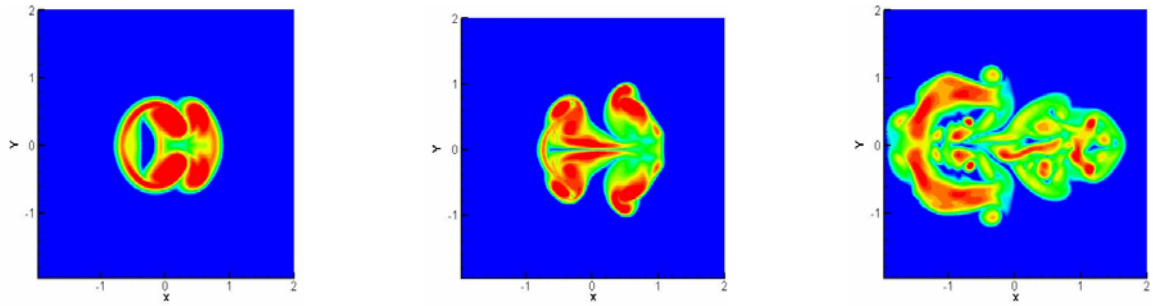

t= 7,5s t=12,5 s t= 20,0s

b) Módulo de Vorticidade $\|\vec{\omega}\|$ no plano xy- Jato Bifurcado

Figura 10. Evolução temporal do Módulo de Vorticidade $\|\vec{\omega}\|$ no plano xy (z=0) para jato natural.

Os resultados obtidos através da simulação do jato natural foram comparados a dados experimentais obtidos via PIV. Estas medidas foram feitas para o escoamento de um jato a Reynolds 1000 (Sakakibara, 2004). Estreita semelhança entre os resultados pode ser observada pela Figura 11, que apresenta a comparação das visualizações da isosuperfície de vorticidade resultante da simulação realizada no presente trabalho e a visualização experimental de Sakakibara (2004). Embora não se disponha das condições exatas sob as quais o experimento foi realizado ou mesmo o valor da isosuperfície experimental apresentada, a presença de filamentos e outras estruturas típicas no experimento aumenta a confiabilidade dos resultados numéricos.

(a) (b)

Figura 11. Visualizações da vorticidade no jato natural: (a) Isosuperfície de vorticidade=1,3s^{-1} (presente trabalho), (b) visualização experimental via PIV (Sakakibara, 2004).

As simulações do jato em evolução temporal não possibilitam uma comparação precisa com dados experimentais. Entretanto, analogias entre as análises temporais e espaciais do escoamento do jato permitem inferências sobre a evolução espacial do jato circular livre com base em sua evolução temporal. A Figura 12 apresenta a visualização do jato espacial simulado a número de Reynolds 1500 (Silva e Métais, 2002) e a evolução temporal do jato natural simulado também a Reynolds 1600 no presente estudo. Boa similaridade entre as estruturas apresentadas para os jatos em desenvolvimento espacial e temporal. As mesmas fases de evolução identificadas no desenvolvimento espacial do jato podem ser identificadas nos diferentes instantes do desenvolvimento temporal. Este comportamento também pode ser verificado na Figura 13. Mesmo diante da resolução insuficiente das escalas do escoamento a Reynolds 5000, semelhanças podem ser identificadas em relação ao jato em desenvolvimento espacial simulado por Glaze e Frankel (2003).

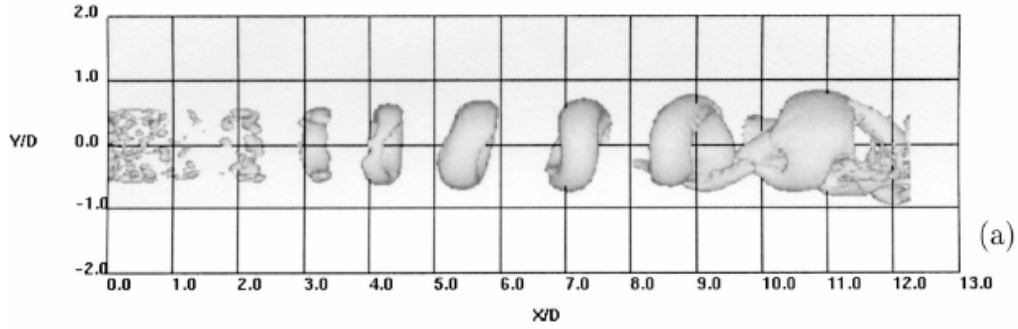

(a) Evolução Espacial do jato simulado por Silva e Métais (2002)

t= 2,5 s t = 11,0 s t =17,5 s

(b) Evolução temporal do jato simulado no presente trabalho

Figura 12. Isosuperfícies pelo critério *Q* para escoamento do jato em desenvolvimentos espacial (a) e temporal (b).

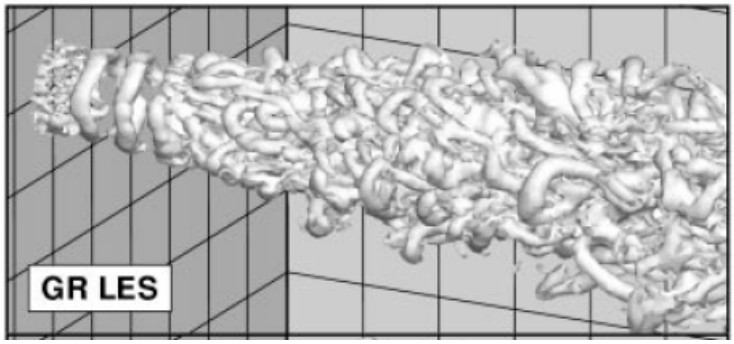

(a) Evolução Espacial do jato simulado por Glaze e Frankel (2003)

t= 6,0 s t = 11,0 s t =40,0 s

(b) Evolução temporal do jato simulado no presente trabalho

Figura 13. Isosuperfícies pelo critério *Q* para escoamento do jato em desenvolvimentos espacial (a) e temporal (b).

4. Conclusões

Foi constatado que esquemas de 2ª ordem não são suficientes para SGE e SND de jatos livres, comprovando o que pôde ser verificado em outros trabalhos (Glaze e Frankel, 2003; Uzun, 2003; Freund, 2001). Vale ressaltar também que o modelo de Smarogisky certamente promove a dissipação das instabilidades no regime de transição, prejudicando a visualização das estruturas.

Embora tal método permita apenas a análise temporal do jato, foi possível verificar que esta análise é similar aos estágios apresentados pelos jatos espaciais, conforme verificado também por outros autores (Basu e Narasimha, 1999; Mathew e Basu, 2000). Embora não haja possibilidade de uma comparação quantitativa com dados experimentais, foi possível verificar a semelhança entre as estruturas presentes em jatos temporais e experimentais e identificar as fases de evolução do jato espacial em diferentes instantes da evolução do jato temporal.

Estruturas típicas do escoamento do jato puderam ser evidenciadas: instabilidades primárias do tipo Kelvin-Helmholtz, vórtices toroidais, vórtices helicoidais, filamentos longitudinais, e ainda fenômenos tais como emparelhamento, transição, espalhamento em direções transversais, e degeneração em turbulência desenvolvida. Os espectros de energia permitiram verificar a proximidade da região inercial do jato à inclinação de -5/3, conforme apresentado pela literatura. A região de decaimento do jato também pôde ser identificada, apresentando acúmulo de energia nos casos em que a resolução espacial não foi suficiente para resolver todas as escalas do escoamento.

A possibilidade de controle do jato, de grande interesse prático, foi comprovada através da formação de diferentes estruturas e espalhamento mais amplo com direção em função do tipo de perturbação imposta. O estudo realizado possibilitou ainda associar o surgimento de modos lineares, sub-harmônicos e azimutais assimétricos ao tipo de perturbação imposta. Este conhecimento é extremamente importante para que tais resultados possam ser obtidos na prática de controle de jatos, ao utilizar-se alto-falantes e atuadores para gerar aqueles mesmos modos fisicamente.

5. Referências

Canuto, C., Hussaini, M.Y., Quarteroni, A. e Zang, T.A., 1988, “Spectral Methods in Fluid Dynamics”, Springer, New York.

Freund, J.B., 2001. “Noise sources in a low-Reynolds-number turbulent jet at Mach 0.9”, Journal of Fluid Mechanics”, vol. 438, pp 277-305.

Glaze, D.J. e Frankel, S.H., 2003, “Stochastic inlet conditions for large-eddy simulation of a fully turbulent jet”, AIAA Journal, 41 (6), pp.164-1073.

Kim, J., Moin, O., 1985, “Application of a Fractional-Step Method to Incompressible Navier-Stokes Equations”, Journal of Computational Physics, Vol. 59, pp 308.

Layzet, S. e Lamballais, E., 2004, "Compact Schemes for the DNS of Incompressible Flows: In what context is the Quasi-Spectral accuracy really useful?", Escola de Primavera de Transição and Turbulência-ETT 2004, Porto Alegre –Rio Grande do Sul, Brasil.

Sakakibara, J., 2004, "Scanning Stereoscopic PIV", http://www.kz.tsukuba.ac.jp/~sakakiba/sspiv/sspiv-e.html.

Silva, C.B. e Métais, O., 2002. "Vortex control of bifurcating jets: A numerical study." Physics of Fluids, 2002, Vol. 14. , n. 11, pp. 3798-3818.

Souza, F.J., 2003, "Simulação de Grandes-Escalas de Escoamentos em um Hidrociclone", Tese de Doutorado, Universidade Federal de Uberlândia.

Urbin, G. e Métais, O., 1997, "Large-eddy simulations of three-dimensional spatially-developing round jets", in Direct and Large-Eddy Simulations 11, edited by Chollet, J.P.; Voke, P.R.; and Kleiser, L. (Kluwer Academic, New York).

Uzun, A. 2003, "3-D Large-Eddy Simulation for Jet Aeroacoustics", Doctor Thesis Purdue University.

PSEUDO-SPECTRAL AND SECOND ORDER-FINITE DIFFERENCE METHODS TO ANALYZE THE TRANSITION TO TURBULENCE IN FREE ROUND JET

Ana Marta de Souza
Federal University of Uberlândia. Av. João Naves de Ávila, 2160. Uberlândia-MG- Brasil
amsouza@mecânica.ufu.br

Francisco José de Souza
EMBRAER-Empresa Brasileira de Aeronáutica. Av. Brigadeiro Faria de Lima, 2170. São José dos Canpos- Brasil
francisco.souza@embraer.com.br

Aristeu da Silveira Neto
Federal University of Uberlândia. Av. João Naves de Ávila, 2160. Uberlândia-MG- Brasil
aristeus@mecanica.ufu.br

Abstract

The turbulence in jets has been widely studied numerically and experimentally in order to acquire knowledge on the physical phenomena involved. The better understanding of the formation and evolution of flow structures allows a more effective control over jets, as well as contributes to refinement of theories and models to the description of turbulent flow.

This work is focused on the physical analysis of free jet flow by means of the three-dimensional numerical simulations. The simulations were carried out using a computational code previously developed (Souza, 2003), which utilize second order scheme in space and time and the Large-Eddy Smagorinsky Turbulence Model. The results obtained through this code did not allow performing the analyses with success, since the typical structures of flow could not be identified. It was concluded, in this way, that second order schemes are not sufficient to perform LES or DNS of free jets. This effect had already been proven in other works (Glaze e Frankel, 2003; Uzun, 2003; Freund, 2001).

The results obtained through the finite difference scheme proved that higher precision was necessary to capture the structures of flow. A new computational code with pseudo-spectral method was used to achieve the goals. Due to necessity of periodicity imposed by the method, the free round jet was analyzed in temporal evolution. Interesting results could be observed, such as the similarity between the structures of temporal and experimental jet and the identification of evolution phases of the spatial jet at different times of the temporal jet. The results allowed to identify the structures resulting from different disturbances imposed on the initial flow field, displaying their relevance for the jet control.

Keywords: free round jets, finite difference method, pseudo-spectral method, turbulence transition.

Proceedings of the 11th Brazilian Congress of Thermal Sciences and Engineering -- ENCIT 2006
Braz. Soc. of Mechanical Sciences and Engineering -- ABCM, Curitiba, Brazil, Dec. 5-8, 2006

Paper CIT06-0713

ESTUDO TEÓRICO E EXPERIMENTAL SOBRE O COMPORTAMENTO DOS ANÉIS DE DESGASTE DE UMA TURBINA FRANCIS OPERANDO EM COMPENSADOR SÍNCRONO

Newton Kimura
Companhia Paranaense de Energia - COPEL
kimura@copel.com

Fernando Tadeu Bóçon
Universidade Federal do Paraná - UFPR
bocon@ufpr.br

Resumo. *Este artigo apresenta o comportamento hidrodinâmico e térmico das turbinas Francis operando em compensador síncrono, com respeito ao escoamento e ao calor que é gerado pelo movimento do rotor da turbina girando em um ambiente confinado. Em função da existência de água de vazamento pelo distribuidor, mostra que termicamente o sistema é auto equilibrado, provando que ocorre redundância na instalação do sistema auxiliar de resfriamento. Entre os anéis de desgaste fixo e móvel, que são partes integrantes da turbina, calor é gerado como resultado de dissipação viscosa sem possibilidade natural de ser resfriado pelo fluido de vazamento. O motivo reside na particularidade construtiva dos anéis de desgaste que funcionam como um labirinto de vedação aberta, o que mantém estagnada a massa de ar quente do seu interstício. Isto exigiu um estudo pormenorizado, sendo que ao final a questão foi elucidada pelo efeito centrífugo provocado pelo cubo do rotor em movimento. Em função do regime de fluxo turbulento através dos anéis de desgaste, um modelo experimental do rotor foi construído, com validação feita através de um modelo numérico utilizando o CFX 5.0, para depois desenvolver estudo de caso de 2 turbinas da usina Gov. Ney Braga (UHE GNB) – COPEL. A partir dos testes realizados em dois protótipos da Usina Gov. Ney Braga, os resultados mostraram que a eficiência do escoamento axial de ar através do labirinto não foi a mesma observada no modelo. Mesmo assim, os resultados dos testes forneceram dados suficientes para possibilitar a desativação do sistema auxiliar de resfriamento dos anéis.*

Palavras chave:anéis de desgaste, compensador síncrono, dissipação viscosa, turbina Francis

1 - Introdução

Numa operação normal de uma usina hidrelétrica, é a turbina que aciona o gerador para gerar energia elétrica. Já na operação em Compensador Síncrono, é o gerador que gira a turbina, ou seja, a turbina fica inativa sendo arrastada pelo gerador. Nesta situação, o gerador funciona como motor (se auto-opera) consumindo energia elétrica de fonte externa para manter em giro todo o conjunto. E para que este consumo seja o menor possível, o rotor da turbina tipo Francis, que normalmente funciona afogado, é movimentado confinado numa câmara de ar formada pelo rebaixamento do nível de água do seu recinto (Fig. 1). Operando desta forma, o rotor da turbina gera calor por atrito (dissipação viscosa), cujo limite de aquecimento é controlado por um sistema auxiliar de resfriamento (sistema de resfriamento dos anéis de desgaste - Fig. 2). Ocorre, porém, que existe um vazamento contínuo de água (massa de fluido refrigerante a temperatura ambiente) para o interior do recinto do rotor, proveniente das folgas construtiva superior e inferior das palhetas do distribuidor da turbina (Fig. 3). Se isto for suficiente para apor o sistema de resfriamento, então este pode ser desativado.

Partes do rotor, como o cubo, as pás e a coroa externa (Fig. 4), ficam expostos diretamente à água de vazamento, não havendo problema de troca térmica. Contudo, os anéis de desgaste, que também são partes integrantes da turbina, não são atingidos diretamente pelo fluido de vazamento, necessitando estudos pormenorizados. Além disso, por causa do regime de fluxo turbulento nos anéis, a solução foi buscar o resultado através de modelo experimental, para depois, desenvolver ensaio em protótipos da usina Gov. Ney Braga (UHE GNB) – COPEL.

Para elaboração deste trabalho foram aplicados vários conceitos relacionados com a mecânica dos fluidos e termodinâmica como:

- Linhas de trajetória, linhas de emissão e linhas de corrente;
- Sistema de escoamento circular de Taylor-Couette;
- Geração de calor por dissipação viscosa;
- Similaridade;
- Programa computacional de Dinâmica dos Fluidos Computacional (Computational Fluid Dynamics - CFD) da ANSYS, Inc – CFX 5.0.;

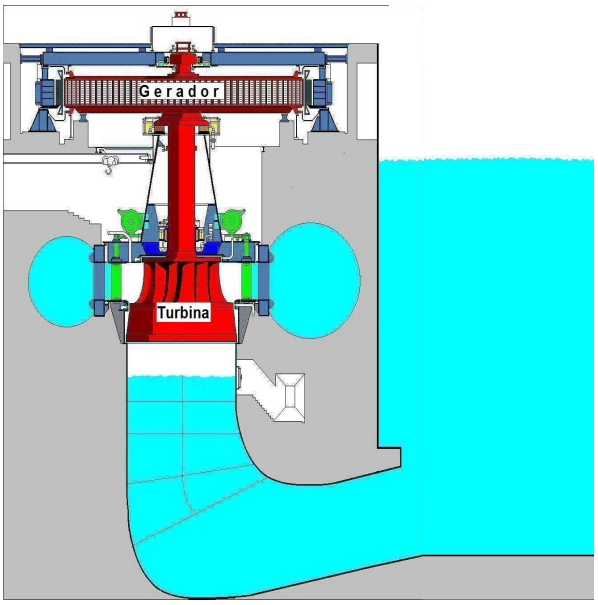

Figura 1 – Turbina operando em compensador síncrono

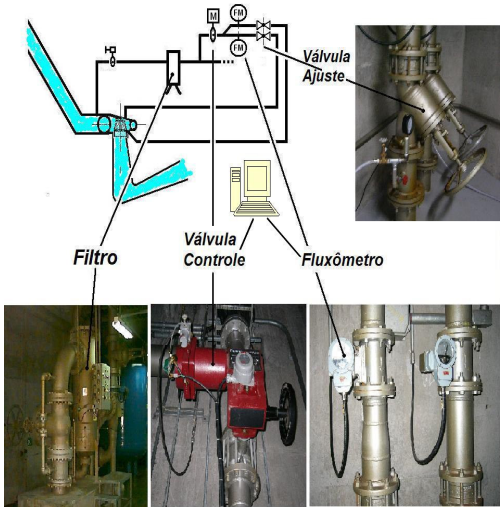

Figura 2 – Sistema de resfriamento do rotor da turbina

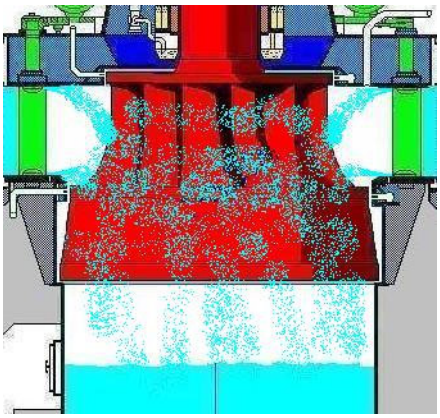

Figura 3 – Vazamento de água pelo distribuidor

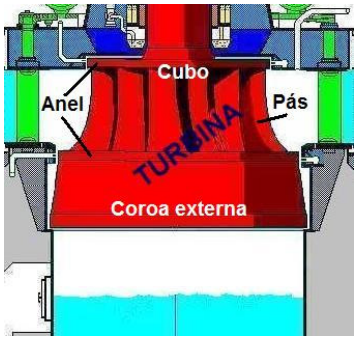

Figura 4 – Principais partes do rotor da turbina

Bibliografias específicas ou trabalhos semelhantes não foram encontrados. Somente alguns assuntos que tem certo relacionamento como a seguir.

- Fernandes Filho (1979) apresenta em seu trabalho, em um dos itens, o *dimensionamento do sistema de resfriamento do rotor e anéis de labirinto*, cujo conteúdo é uma parte deste trabalho, apesar de calculado de outra forma;
- Mendonça (1989) desenvolveu um modelo para análise de transferência de calor em palhetas de turbina a gás, o qual pode ser relacionado com a transferência de calor do ar intersticial para os anéis de desgaste se considerado como uma palheta de largura infinita;
- Loureiro (2004) fez um estudo sobre o escoamento entre dois cilindros concêntricos com uma obstrução parcial, sendo o externo fixo e o interno móvel, onde analisa o escoamento axial em um espaço anular de comprimento longo, diferente dos anéis de desgaste, que comparado ao seu diâmetro, o seu comprimento é ínfimo;
- Braun et al (2002) apresenta resultados entre modelo numérico e experimental sobre instabilidade de escoamento de Taylor. Nesta dissertação, também é objetivo fazer as comparações entre modelo numérico e experimental, porém fazendo análise diretamente numa velocidade de regime de escoamento permanentemente turbulento.

Para alcançar o objetivo, o trabalho foi estruturado em etapas como segue:

- Cálculo do calor gerado pelo movimento do rotor da turbina
- Balanço térmico entre calor gerado e o vazamento
- Análise experimental em modelo
- Análise em modelo numérico para validação do modelo experimental
- Análise experimental em protótipo - Estudo de caso COPEL.

2 - Desenvolvimento

2. 1 – Cálculo do calor gerado pelo movimento do rotor da turbina

A geração de calor é devido ao atrito do ar (dissipação viscosa) ocasionado pela movimentação das partes que compõem o rotor da turbina, que são: pás, cubo, coroa externa e anéis de desgaste superior e inferior, em um ambiente confinado. Existem vários métodos para o cálculo do calor médio gerado pelo rotor da turbina girando no ar:

- Cálculo empírico através de fórmulas teóricas tais como do IEC 41 (1963), ABNT 228 (1990), ASME PTC 18;
- Cálculo real pela potência absorvida pelo gerador para manter em regime o conjunto como compensador síncrono, isolando a parte que cabe à turbina;
- Cálculo pelas fórmulas desenvolvidas pelos próprios fabricantes de turbina.

Neste trabalho foi considerado cálculo empírico segundo ASME PTC 18, cuja fórmula é:

$$P_w = 4{,}6\, n^3\, B_0\, D^4\, 10^{-7} \tag{1}$$

Dados da turbina da UHE GNB:

Rotação da turbina n = 128,56 rpm

Altura de entrada da turbina B_o = 1,427 m

Diâmetro da turbina D = 5,572 m

Substituindo os dados em (1), vem: $\mathbf{P_w}$ = 1.345,3 [kW] ou $\mathbf{P_w}$ = 321,39 [kcal/s]

Portanto, a taxa de transferência de calor gerado pelo rotor da turbina é de: $\mathbf{P_w}$ = 322 [kcal/s]

2. 2 – Balanço térmico entre calor gerado e o vazamento

2.2.1 - Água de resfriamento necessária

Para o cálculo da quantidade de água de resfriamento ou fluido refrigerante necessário é preciso conhecer qual o limite de temperatura suportável sem que ela provoque dilatações que comprometam a movimentação livre entre as partes fixas e girantes da turbina. Neste caso, as partes de menor folga são os anéis de desgaste superior e inferior do rotor da turbina, que considerando as oscilações normais, podem dilatar radialmente até cerca de 1/3 da folga nominal (obs.: esta situação é otimista, podendo ainda dilatar cerca de 50 % além deste valor).

Para a turbina da UHE GNB, o valor da folga nominal radial dos anéis de desgaste é de 2,5 mm. Logo, a dilatação permissível δ= 1/3 de 2,5 mm

δ= 0,75 mm radial ou δ= 1,5 mm diametral

Considerando o material dos anéis de desgaste e dilatações permissíveis, pode-se definir as variações de temperatura ΔT aplicando a expressão da dilatação térmica linear: $\delta = \alpha . \Delta T . D$ (Gere & Timoshenko, 1990)

α - coeficiente de expansão térmica

ΔT - variação de temperatura

D - diâmetro do anel de desgaste

$$\Delta T = \delta / (\alpha . D) \tag{2}$$

2.2.1.1 - Cálculo do ΔT para o rotor da turbina de Caxias:

Sendo: δ= 1,5 mm

α= 17 E–06/°C para aço inoxidável (Gere & Timoshenko, 1990)

D = 5.185 mm

Aplicando em (2), temos:

ΔT = 17 °C

Considerando que a dilatação permissível δ ainda pode ser acrescida de 50 %, a variação de temperatura máxima permissível nos anéis de desgaste pode aumentar até (17 x 1,5 = 25,5 °C).

Isto é, a temperatura permissível sem que haja problema de roçamento entre as partes fixa e girante, com temperatura ambiente considerada de 20 °C, e na condição normal, é de:

T = 20 + 17 = 37 °C

2.2.1.2 - Cálculo do fluido refrigerante necessário (Q_{nec})

Neste ponto, para controle do equilíbrio térmico, não foram consideradas as massas metálicas, mas somente a água de vazamento pela folga superior e inferior do distribuidor.

Para o cálculo da vazão de água necessária $\mathbf{Q_{nec}}$ para evitar uma dilatação linear da parte rotativa maior que 30% da folga do labirinto foi utilizada a expressão da quantidade de calor $\mathbf{\underline{Q} = m . c_p . \Delta T}$ (Máximo e Alvarenga, 1997) e utilizando a expressão do fluxo de calor $\mathbf{q = \underline{Q} / t}$, vem:

$\mathbf{q = \underline{Q} / t = m . c_p . \Delta T / t}$ $\mathbf{m = V . \rho}$

$\mathbf{q = (V / t) . \rho . c_p . \Delta T}$ ou

$\mathbf{V / t = q / (\rho . c_p . \Delta T)}$

Onde:

V volume
t tempo
V/t vazão = $\mathbf{Q_{nec}}$
q fluxo de calor = $\mathbf{P_w}$
ρ massa específica da água
$\mathbf{c_p}$ calor específico da água
ΔT variação de temperatura

Fazendo as substituições, temos: $\mathbf{Q_{nec} = P_w / (\rho . c_p . \Delta T)}$

Dados:

$\mathbf{P_w}$ = 322 [kcal/s] (fluxo de calor ou Calor Gerado Considerado)
ρ = 998 kg/m3 (massa específica da água)
$\mathbf{c_p}$ = 1 kcal/kg°C (calor específico da água)
ΔT = 17 °C (variação de temperatura)

$\mathbf{Q_{nec}}$ = 322 / (998 . 1 . 17)
$\mathbf{Q_{nec}}$ = 0,019 m3/s ou

Q_{nec} **= 1.140 l/min**

2.2.2 - Água de resfriamento disponível (vazamento pelo distribuidor - Q_{disp})

Este vazamento (Fig. 4) é normalmente medido para verificar se não está excessivo, pois caracteriza perdas e principalmente porque faz parte de normas limitantes construtivas.

No caso da UHE GNB, este valor é de $\mathbf{Q_{dispo}}$ = 0,77 m^3/s.

$\mathbf{Q_{dispo}}$ = 46.200 l/min

2.2.3 - BALANÇO TÉRMICO

Fluído refrigerante disponível	46.200 l/min
Fluido refrigerante necessário	1.140 l/min

Ou seja, o vazamento de água disponível é bem superior à quantidade de água necessária para controlar a temperatura de dilatação sem que haja problema de interferência entre as partes fixas e móveis.

2.3 – Análise experimental em modelo

Apesar de ter verificado em 2.2 que o vazamento de água existente é bem superior à quantidade de água necessária para manter em equilíbrio o conjunto girante, há necessidade de detalhar o comportamento térmico na região dos anéis de desgaste em função de sua peculiaridade construtiva. Os anéis de desgaste, sendo um fixo e outro móvel, formam o

labirinto, e tem o papel de funcionar como vedação sem contato. O seu aspecto construtivo assemelha-se ao chamado círculo de Couette, o qual consiste em dois círculos concêntricos sendo um fixo e outro móvel, existindo um fluido entre eles. Nesta configuração, o anel móvel provoca o arraste do fluido, iniciando o escoamento do fluido em forma de camadas em razão do outro anel permanecer fixo, ocasionando um aquecimento deste fluido por dissipação viscosa, dada pela equação $\phi = (\mu U^2 A)/f$, resultando num aumento progressivo de energia da região.

Em função da existência de dutos de equilíbrio de pressão no cubo do rotor da turbina, que interliga a área onde tem fluido refrigerante com o labirinto, foram explorados estes dutos quanto à propiciação de entrada de ar, por efeito centrífugo gerado pelo movimento do cubo do rotor, para ocasionar transferência de massa do labirinto. Desta forma, o calor gerado pelos anéis de desgaste no interior do labirinto seria transferido para a massa de fluido refrigerante de vazamento pelo distribuidor e o aquecimento do labirinto evitado (balanceado).

Como a física do transporte de massa por efeito centrífugo é teoricamente complexo, foi optada a busca direta da solução do caso pela realização de ensaios experimentais em modelo. O modelo foi construído adaptando-se ao volante de um pequeno grupo gerador da Usina Hidrelétrica Pitangui - COPEL (Fig. 5). O volante fez o papel de anel de desgaste móvel, e foi confeccionada uma capa por sobre o volante (carenagem) para simular o anel de desgaste fixo (Fig. 6). Os furos existentes no disco do volante simularam os dutos de equilíbrio de pressão (Fig. 7). Foram realizados ensaios com e sem os dutos, para a verificação da ocorrência de transporte de massa de fluido refrigerante entrando por eles e passando pelo labirinto.

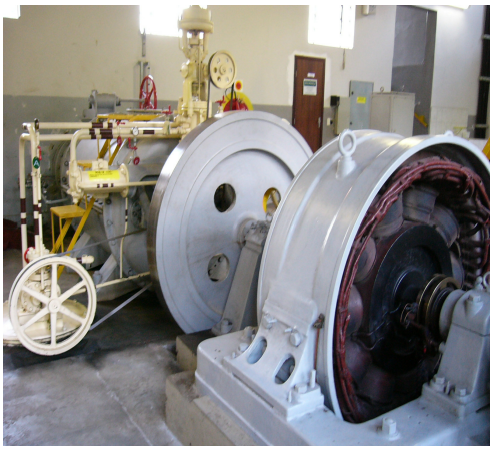

Figura 5 - Grupo gerador da
Usina Hidrelétrica Pitangui – UHE PGI

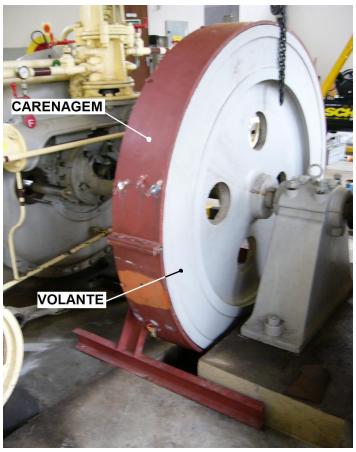

Figura 6 – Modelo experimental adaptado
sobre o grupo gerador da UHE PGI

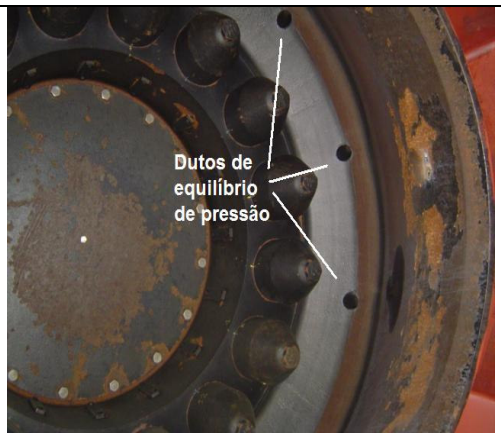

Protótipo

Modelo

Figura 7 – Dutos de equilíbrio de pressão

Para a comprovação do resultado, foram medidos os seguintes parâmetros: vazão de ar pelo labirinto e temperaturas no labirinto e anel de desgaste (Fig. 8). As temperaturas foram medidas através de sensores RTD platina 100 e a vazão por meio de linhas de corrente. Sendo:

TA – temperatura do ar
TM – temperatura do metal
Tamb – temperatura do ambiente
U – vetor velocidade

Linha de corrente - linha de poliester 0,12 mm, de comprimento 450 mm, amarrada na extremidade de uma haste de arame de aço 0,6 mm.

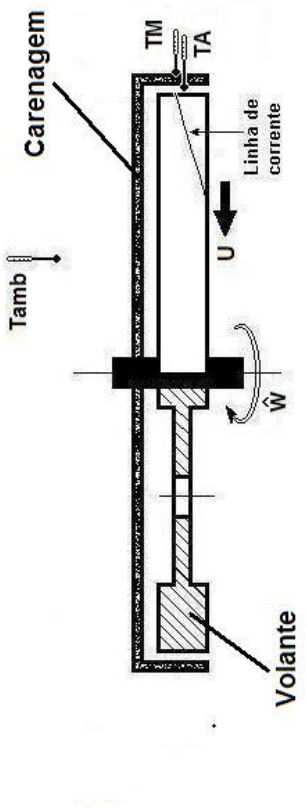

Figura 8 – Posicionamento dos sensores no modelo

2.3.1 - Resultado dos ensaios experimentais em modelo

Nos ensaios com os dutos de equilíbrio de pressão, verificou-se o escoamento de ar axialmente pelo labirinto, medido através de linha de corrente, e consequentemente não houve variações de temperatura. Ou seja, o efeito centrífugo gerado pelo cubo impulsiona a massa de ar (que entra continuamente pelos dutos) do centro para a periferia onde se situa o labirinto. Desta forma, a pressão aumenta na periferia até vencer a barreira de selagem, ocasionando transferência de massa para fora do labirinto e impedindo o aquecimento dos anéis. Para melhor avaliação dos resultados, uma vez que se sabe que o efeito centrífugo é proporcional à velocidade angular, foram realizados ensaios com várias rotações do modelo, validando-se os resultados (Fig. 10). A Figura 9 mostra o resultado do ensaio em vários patamares de rotação (de 200 a 600 rpm) com a temperatura permanecendo sempre constante. Já o ensaio sem os dutos mostrou-se o contrário, não se notando o escoamento de ar axialmente pelo labirinto. A Fig. 11 mostra a elevação progressiva da temperatura em função da inexistência de transferência de massa do labirinto para o meio externo, por não existirem os dutos que permitem a entrada de massa de ar.

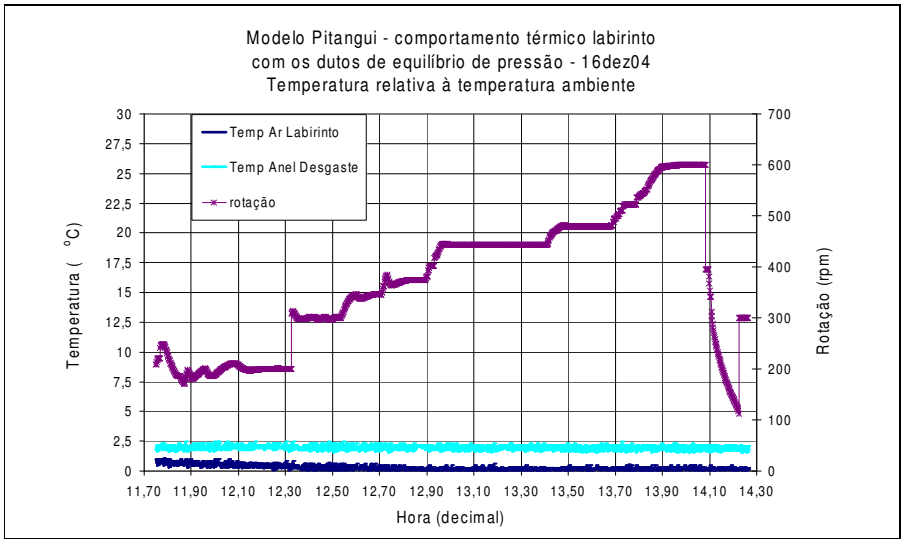

Figura 9 – Ensaio com os dutos de equilíbrio de pressão – rotação variável

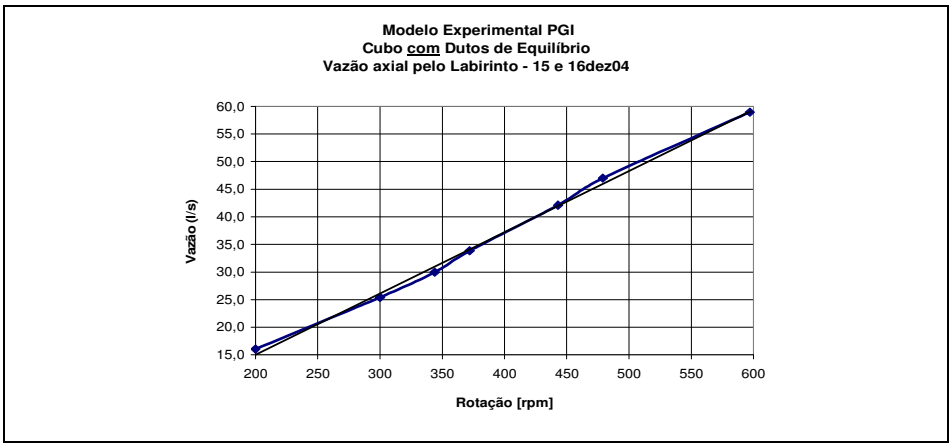

Figura 10 – Modelo Pitangui - Vazão axial no labirinto proporcional à rotação

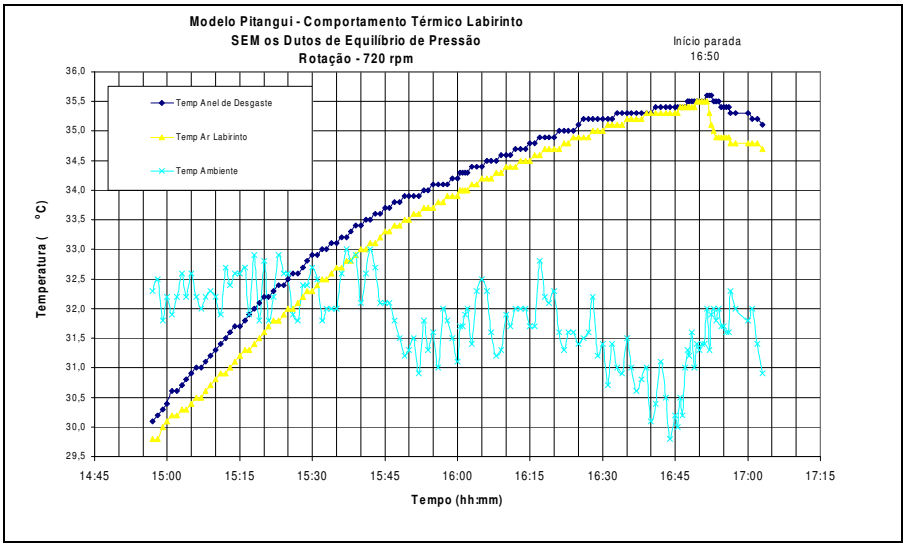

Figura 11 – Ensaio sem os dutos de equilíbrio de pressão – rotação fixa de 720 rpm

2.4 – Análise em modelo numérico para validação do modelo experimental

A fim de validar qualitativamente o modelo experimental, foi aproveitado um modelo numérico (Hidalgo, 2005) utilizando o programa CFX 5.0 repetindo-se as mesmas condições operativas do modelo, ou seja, com os dutos de equilíbrio de pressão e sem eles. As soluções foram voltadas, para o enfoque qualitativo, na reprodução dos vetores de velocidades, focando na existência de escoamento axial tanto pelo labirinto como pelos dutos.

2.4.1 - Características do modelo numérico

a) Parâmetros de malha: malha não-uniforme com elementos tetraédricos e controle de malha do tipo *inflation* apenas na parede da carenagem, onde o fluido escoa. Foram usados 5 elementos no *inflation* (Fig. 13).

b) Números característicos:
- Simulação sem dutos de equilíbrio no cubo: número de nós no domínio: 90995 e número de elementos: 430890
- Simulação com dutos de equilíbrio no cubo: número de nós no domínio: 90618 e número de elementos: 425377

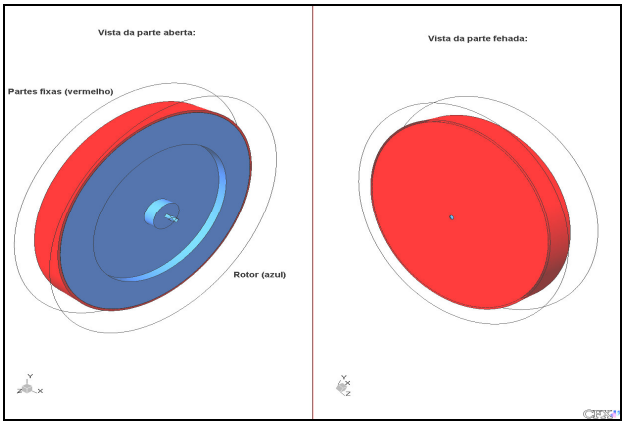

Figura 12 - Vista do domínio

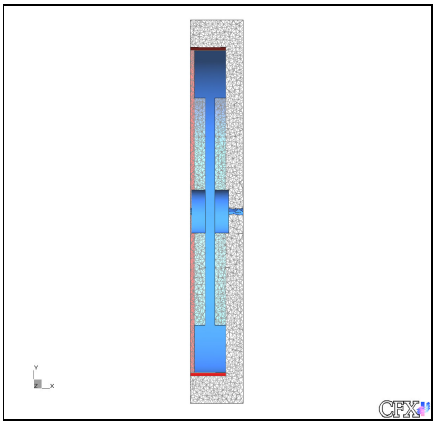

Figura 13 – Vista em corte da malha no domínio

c) Parâmetros de simulação:
- Elementos tetraédricos – tamanho médio de 20 mm
- Equações do modelo matemático:
  - Equação da continuidade (conservação da massa);

$$\frac{\partial \rho}{\partial t} + \vec{\nabla} \bullet (\rho \vec{U}) = 0$$

Equação para a energia cinética turbulenta;

$$\frac{\partial (\rho k)}{\partial t} + \vec{\nabla} \bullet (\rho \vec{U} k) = \vec{\nabla} \bullet [(\mu + \frac{\mu_t}{\sigma_k}) \vec{\nabla} k] + P_k - \rho \varepsilon$$

  - Equação para a taxa de dissipação da energia cinética turbulenta;

$$\frac{\partial (\rho \varepsilon)}{\partial t} + \vec{\nabla} \bullet (\rho \vec{U} \varepsilon) = \vec{\nabla} \bullet [(\mu + \frac{\mu_t}{\sigma_\varepsilon}) \vec{\nabla} \varepsilon] + \frac{\varepsilon}{k} (C_{\varepsilon 1} P_k - C_{\varepsilon 2} \rho \varepsilon)$$

  - Equação da conservação da quantidade de movimento linear (momentum);

$$\frac{\partial (\rho \vec{U})}{\partial t} + \vec{\nabla} \bullet (\rho \vec{U} \otimes \vec{U}) - \vec{\nabla} \bullet (\mu_{eff} \vec{\nabla} \vec{U}) = \vec{\nabla} p' + \vec{\nabla} \bullet (\mu_{eff} \vec{\nabla} \vec{U})^T + B$$

Obs: as equações 2.5.2 e 2.5.3 compõem o modelo de turbulência utilizado modelo K-ε (K-epsilon). Estas equações foram aplicadas também no trabalho de Hjertager, 2003
- Fluido: ar com propriedades a 32.7 °C (temperatura média no dia do ensaio do modelo experimental)
- Condições de contorno:
  - Abertas (entradas e saídas) – pressão relativa ao ambiente igual a zero.
  - Partes do rotor: paredes com velocidade angular prescrita.
  - Partes fixas: condição de parede com velocidade nula.

- Método de resolução: High Resolution
- Critérios de convergência: RMS (root mean square) com resíduo de 0.0001

2.4.2 - Resultados - escoamento axial pelo labirinto, com os dutos de equilíbrio

Assim como no modelo experimental, para melhor avaliação dos resultados, foram realizados ensaios com várias rotações do modelo: 200, 479 e 600 rpm. A Figura 14 mostra a inclinação do vetor velocidade em relação à direção de movimentação do anel móvel, formando o ângulo α menor que 90 °, traduzindo em existência de escoamento de ar axialmente pelo labirinto.

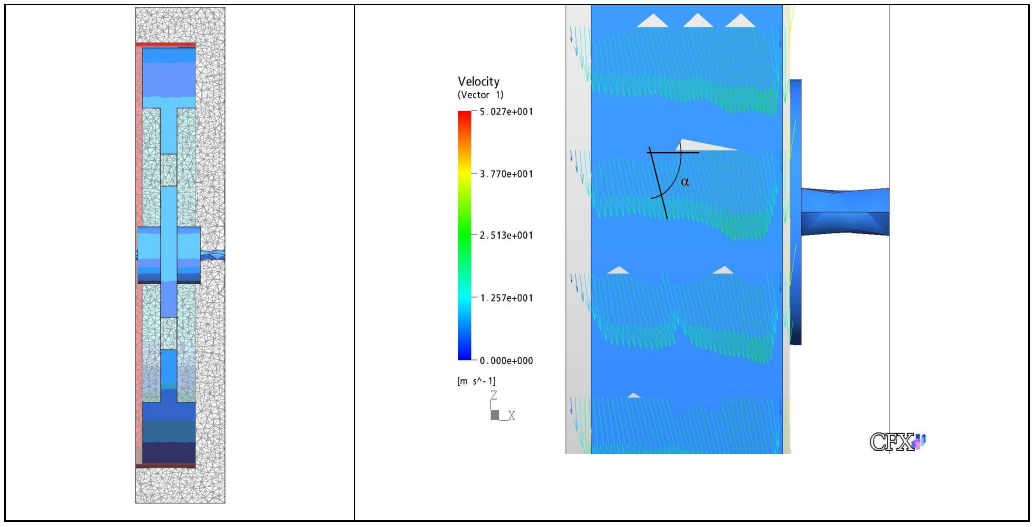

Figura 14 - Vetor velocidade no labirinto - rotação 600 rpm

2.4.3 - Resultado - escoamento pelo labirinto, sem os dutos de equilíbrio

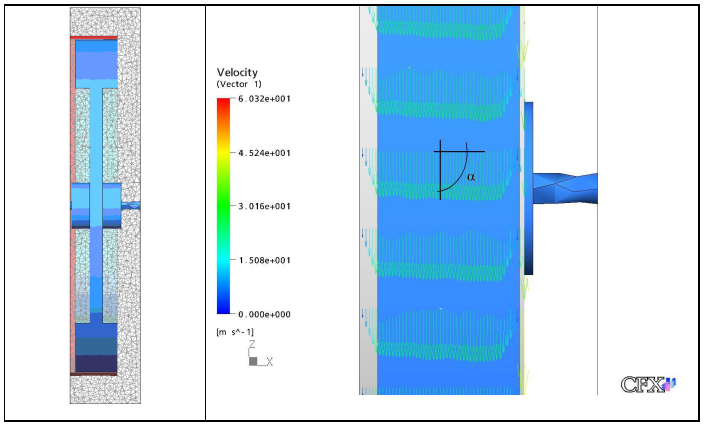

Rotação n_m (rpm)
720

Ângulo α (°)
89,96

Figura 15 - Vetor velocidade no labirinto

Neste modo de simulação, diferentemente da simulação do modelo numérico com os dutos, o ângulo α é praticamente 90° (Fig. 15). Isto que dizer que o escoamento é puramente circular, não havendo uma componente axial da velocidade. Assim a vazão axial através do labirinto é nula.

2.4.4 - Validação

O objetivo principal desta simulação numérica, que foi verificar o comportamento do escoamento de ar pelo labirinto, repetiu-se exatamente como no modelo experimental, ou seja, com a presença dos dutos de equilíbrio aconteceu o fluxo de ar axial pelo labirinto, e sem os dutos, este fenômeno não ocorreu, confirmando o comportamento

do modelo experimental. Portanto, o modelo experimental tem resultados validados pelo modelo numérico, podendo os comportamentos verificados neste ser qualitativamente transpostos para o protótipo, sempre observando as peculiaridades.

2.5 – Análise experimental em protótipo - Estudo de caso COPEL

Considerando os resultados do modelo experimental com os dutos de equilíbrio abertos, foram executados ensaios nos protótipos da Usina Hidrelétrica Gov. Ney Braga - UHE GNB, unidades 2 e 4. Para segurança do teste, as vazões da água de resfriamento dos anéis foram diminuídos gradativamente até fechar completamente o fluxo, acompanhando atentamente todas as medições de temperatura.

2.5.1 - Resultados dos protótipos experimentais

Os resultados de ensaios realizados nos protótipos da UHE GNB, com os dutos de equilíbrio de pressão e sem a água do sistema de resfriamento, não repetiram exatamente os verificados nos ensaios do modelo experimental. Apesar de terem aplicadas condições operativas e técnicas de medições semelhantes as do modelo experimental, observou-se nos protótipos, uma elevação nas temperaturas do labirinto, ainda que quantitativamente pequena em relação ao valor limite de **37** °C. Na Figura 16 observa-se a elevação da temperatura do ar do labirinto inferior de 25 para 27,5 °C e do superior de 25 para 31,5 °C. No metal a temperatura ficou cerca de 1°C menor que do ar. Como os resultados dos ensaios foram semelhantes nas duas unidades realizadas, serão mostrados aqui somente os resultados da unidade 4.

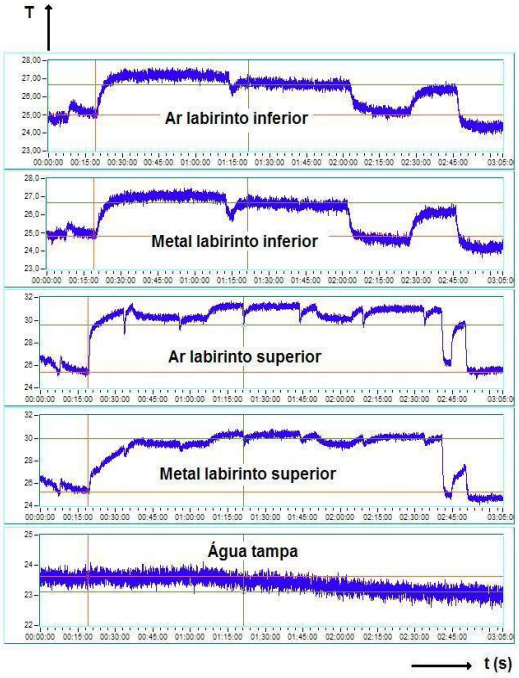

Figura 16: Temperatura nos labirintos

unidade 4 da UHE GNB

Fazendo comparações modelo/protótipo, existem duas razões diferenciadas que foram desconsideradas ou simplificadas no modelo experimental, as quais explicam a variação observada no protótipo. São eles: o desenho do labirinto e o escoamento caótico provocado pelas pás do rotor.

a) No desenho do labirinto do protótipo, além do efeito de turbulência de Taylor, existem dois canais internos (chicanas) longitudinais (Fig. 17), o que no modelo experimental não foi previsto por razão econômica construtiva (Fig. 18). Estes canais são preparados para aumentos de perda de carga, que, se por um lado melhora a questão da vedação na operação convencional, por outro lado dificulta a mudança de direção almejada do escoamento axial em operação como compensador síncrono;

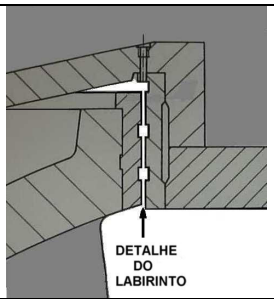

Figura 17: Detalhe de formato do labirinto do protótipo – com chicanas.

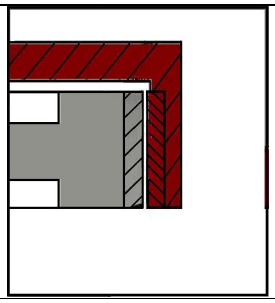

Figura 18: Detalhe de formato do labirinto do modelo - liso.

b) Quanto ao escoamento turbulento complexo que existe no protótipo, provocado pelas pás do rotor operando em ambiente confinado, este influi nas condições de contorno do labirinto dificultando o escoamento de ar axialmente pelo labirinto.

Ou seja, o formato do labirinto mais a característica de escoamento turbulento complexo produzido pelas pás do rotor, juntos impõem uma forte barreira à mudança de direção do escoamento do fluido intersticial aos anéis de desgaste para o sentido axial, dificultando a troca de calor com o meio externo por transferência de massa. De qualquer forma, é fato que existe certo escoamento axial, pois caso contrário, a estabilização da temperatura não ocorreria, o que não foi o caso constatado nos ensaios dos protótipos. Neste caso, ao considerar-se que a eficiência do escoamento de ar axialmente pelo labirinto é baixa, significa que o restante do calor gerado é em parte absorvido pela massa dos anéis fixo e móvel, e que por si só consegue manter a temperatura estabilizada num patamar aquém do limite garantido de operação sem o sistema de resfriamento adicional.

Apesar da ocorrência de aquecimento no labirinto superior dos protótipos, o traçado de estabilização de temperatura, tanto do ar intersticial como do metal, é bem definido, garantindo um comportamento bastante seguro.

3 - Conclusão

O resultado teórico do balanço térmico mostrou que o calor gerado pelo movimento da turbina é bem menor que a capacidade de resfriamento do fluido refrigerante proveniente de vazamento, provando que a instalação do sistema auxiliar de resfriamento está redundante. O sombreamento, porém, estava no comportamento dos anéis de desgaste, que no final, foi esclarecido pela física do efeito centrífugo provocado pelo cubo do rotor, em afinamento com os dutos de equilíbrio de pressão, que provocam transferência de massa de ar do labirinto, resolvendo o problema de aquecimento particularizado dos anéis de desgaste. Este fato foi bem demonstrado pelo modelo experimental.

Os estudos de casos práticos realizados em dois grupos geradores da UHE GNB sem injeção de água de resfriamento nos anéis de desgaste mostraram resultados um pouco diferente dos previstos pelo modelo experimental. Os anéis se aqueceram, conforme conclusões sustentadas atribuídas ao seu formato e ao escoamento turbulento que ocorre entre a parte fixa e móvel, porém, em patamar bastante aquém do limite de segurança operacional. Logo, pode-se concluir, com boa margem de segurança, que os sistemas de resfriamento dos anéis de desgaste dos protótipos testados GNB grupos 2 e 4 estão redundantes, podendo ser desativados.

Cabe salientar que a constatação deste trabalho não deve ser tomada, em hipótese alguma, como um padrão para aplicações em outras turbinas sem análises e ensaios minuciosos, uma vez particularidades existem entre uma instalação e outra.

4. Referências

ABNT NB 228 (Associação Brasileira de Normas Técnicas), Turbinas Hidraulicas - Ensaio de Campo: Método de Ensaio. 1990. 90 p.

ANSYS, INC. CFX-5.0 Solver Theory. Documentação eletrônica que acompanha o *software* CFX-5.0, 2004. **ASME PTC 18** 1949,1992.

BRAUN, M. J. **Flow visualization of the evolution of Taylor instabilities and comparison with numerical simulations**. Computational Technologies for Fluid/Thermal/Structural/Chemical Systems with Industrial Applications. Volume 1 ASME 2002 PVP-vol. 448-1.

FERNANDES FILHO, ALEXANDRE MACHADO **Diretrizes básicas para a elaboração do projeto de motorização das unidades da Usina Hidrelétrica de Passo Fundo – UHPF**. In: V Seminário Nacional de Produção e Transmissão de Energia Elétrica, Grupo I, Produção Hidráulica, 1979. Recife-PE

GERE, J. M.; TIMOSHENKO, S. P. **Mechanics of Materials**. 3 ed. Boston: PWS-Kent Publishing Company, 1990.

Hidalgo, Eduardo Campos Neto - **Modelagem matemática e simulação computacional do escoamento no interstício rotor/carcaça de turbina hidráulica**. UFPR 2005, orientador prof. Fernando Tadeu Bóçon Dr. Eng.

HJERTAGER, L. K; HJERTAGER, B. H.; Solberg, T. **CFD Modelling of Turbulent Mixing in a Confined Wake Flow**. Annual Meeting/Nov. 16-21/Mixing and Chemical Reaction, 2003.

IEC 41 (International Electrotecnical Commission) – 1963.

Kimura, N. **Modelagem do Comportamento Térmico dos Anéis de Desgaste de uma Turbina Francis Operando em Compensador Síncrono** - Dissertação de mestrado do Programa de Pós-graduação em Engenharia Mecânica da UFPR, Curitiba, 2005.

LOUREIRO, BRUNO VENTURINI **Escoamento secundário em um anular parcialmente obstruído com rotação do cilindro interno**. Rio de Janeiro: PUCRJ

MÁXIMO, A.; ALVARENGA, B. **Física.** São Paulo: Ed. Scipione, 1997.

MENDONÇA, M. T. **Modelo para Análise de Transferência de Calor entre Gases de Combustão e Palhetas de Turbina a Gás.** ITA, São José dos Campos – SP, 1989.

Título:

THEORETICAL AND EXPERIMENTAL STUDIES ABOUT THE THERMAL BEHAVIOR OF THE WEARING RINGS OF A FRANCIS TYPE TURBINE OPERATING AS A SYNCHRONOUS CONDENSER

Newton Kimura
Companhia Paranaense de Energia - COPEL
kimura@copel.com

Fernando Tadeu Bócon
Universidade Federal do Paraná - UFPR
bocon@ufpr.br

Abstract

This paper outlines the hydrodynamic and thermal studies carried out on Francis type turbines when operating as synchronous condensers regarding the flow and heat generated by the turbine runner motion within its environment, and the availability of a cooling effect due to water leaks from the distributor. Results have shown that a redundancy occurs in the cooling system when leaks actually exist. However, the wearing rings, being integrating parts of the turbine, generate an amount of heat through their gaps as a result of viscous dissipation. It turns out that heat will build up throughout the wearing rings area hindering the decision to whether or not decommissioning the external cooling system. To that extent, the study has detected a phenomenon related to the centrifugal effect provoked by the external part of runner crown whose energy overcomes partially the barrier formed by the labyrinth sealing function, providing enough forced mass transfer outside the gaps, thus rendering an adequate thermal balance to the rings. In view of the turbulent flow regimen, a simplified analytical calculation was carried out so as to obtain an approximate design, and an experimental model was constructed with validation through a CFX numerical model, and, afterwards, case studies were developed on two turbines of Gov. Ney Braga Hydropower Plant (GNB HPP) – Copel. As to the experimental model, several alternatives were studied, culminating in a design adaptable to a hydraulic turbine at Pitangui Plant, also owned by Copel. While testing the models, special concern was given to the existing pressure balance vent holes in the Francis turbine runner crown as these would be the entrance ports to convey the cooling element, impelled by the centrifugal force, to the wearing rings gaps (labyrinth). From tests performed on the two GNB HPP prototypes, the obtained results, based on repeated tests, denoted that the efficiency of the axial air flow through the labyrinth was not the same as the one observed on the model, nevertheless, they provided sufficient data to determine the decommissioning of the cooling system.

Keywords: wearing rings, synchronous condensers, viscous dissipation, Francis turbine

Proceedings of the 11th Brazilian Congress of Thermal Sciences and Engineering – ENCIT 2006
Braz. Soc. of Mechanical Sciences and Engineering – ABCM, Curitiba, Brazil, Dec. 5-8, 2006

Paper CIT06-0721

Numerical computation of the flow around rough elements

Daniel A. Rodrigues
Programa de Engenharia Mecânica,
Universidade Federal do Rio de Janeiro, C.P. 68503, 21945-970, Rio de Janeiro
darodrigues@mecanica.coppe.ufrj.br

Alexandre T. P. Alho
Programa de Engenharia Naval e Oceânica,
Universidade Federal do Rio de Janeiro, C.P. 68503, 21945-970, Rio de Janeiro
alho@peno.coppe.ufrj.br

Atila P. Silva Freire
Programa de Engenharia Mecânica,
Universidade Federal do Rio de Janeiro, C.P. 68503, 21945-970, Rio de Janeiro
atila@mecanica.coppe.ufrj.br

Abstract. *The present work shows how numerical computations on the flow around a rough element can be used to find reliable results for the wall shear stress and the displacement in origin for the flow over a fully rough surface. The numerical computations are combined with the integral methods of Perry and Joubert (1963, JFM, 17, 193:211) and of Perry et al. (1969, JFM, 37, 383:413) to find reliable data for the error in origin that can be used to explain how the shear stress develops. All procedures are tested against hot-wire data obtained in a low turbulence wind-tunnel. In fact, four different methods are used to find the shear stress at the wall: the classical momentum integral equation, the velocity gradient method of Perry and Joubert (1963), the Reynolds shear stress in the surface layer and a momentum balance around a single rough element.*

keywords: *Roughness, CFD, BSL-RSM, wall shear stress, error in origin.*

1. Introduction

The description of turbulent flow over a rough surface is a central problem in fluid mechanics. Since most surfaces in nature and in technology are rough, the interest arose by this subject is indeed very high. Unfortunately, the physical and mathematical modeling of such flow is inherently difficult. The following statement by Schlichting makes this clear: "The desire to explore the laws of friction of rough pipes in a systematic way is frustated by the fundamental difficulty that the number of parameters describing roughness is extraordinarily large owing to the great diversity of geometric forms" (H. Schlichting, Boundary Layer Theory, 7th edition, page 615).

Despite the aforementioned difficulty, the advances were many. As early as 1923, Hopf identified two types of roughness. If surfaces were formed by relatively coarse and tightly spaced elements (sand grains, cast iron, cement), flow resistance was observed to be proportional to the square of velocity (Reynolds number independence). In this case, the effects of roughness could be expressed with the aid of a single roughness parameter. If, however, surfaces were formed by gentle protusions distributed over a relatively large area, flow resistance depended both on Reynolds number and on a roughness parameter. A few years later, Einstein and El-Samni (1949) observed that for flow over a rough surface the velocity profiles should be plotted considering that a theoretical wall was set at distance below the top of the rough elements. The concept of a displacement in origin was further studied by Perry and Joubert (1963). These same authors in a sequence paper (Perry et al., 1969) identified two wall geometries that resulted in different log-law behaviors: one type with a reference length based on the size of the roughness (termed a 'k'-type roughness), the other type with a reference length based on the pipe diameter (termed a 'd'-type roughness).

A major difficulty in developing models for flows over rough surfaces is to measure the wall shear stress. All traditional methods developed for smooth walls including the Preston or Stanton tubes, momentum integral methods and the gradient graphical method are highly inaccurate. As an alternative, more reliable method, Perry et al. (1969) proposed to find the wall shear stress by pressure tapping the roughness elements and assessing their form drag.

The objective of the present work is to assess the current state of turbulence models in regard to the numerical simulation of flows over a rough surface. In particular, one turbulence model will be considered: the Baseline Reynolds Stress Model (BSL-RSM). This model does not use the eddy viscosity hypothesis but solves a system of transport equations for all components of the Reynolds stress tensor. The possibility of inherently accounting for stress anisotropies makes the BSL-RSM a good choice for the description of complex flows.

A common practice in the numerical simulation of turbulent flows is to consider the existence of a near wall region where local solutions can actually be used to provide wall boundary conditions. For rough walls, a local logarithmic profile can be specified in terms of a roughness reference length, the so-called 'equivalent sand grain roughness' (Nikuradse (1932)). This length, unfortunately, is not exactly equal to the real roughness height; it also depends on other properties of the wall including shape, distribution, etc. This single feature makes the use of log-laws very uncertain for flow over rough surfaces.

Here, the solution strategy will be different. Instead of using log-laws to specify the wall boundary conditions we will follow the following procedure. First, the flow domain is discretized and solved considering every roughness element individually. Having obtained local solutions for the mean and fluctuating quantities, four different methods are then used to post-process the numerical data and find the wall shear stress. These four methods are based on i) the momentum integral equation, ii) the form drag of the individual roughness elements, iii) the spatial average of the Reynolds shear stress and iv) the velocity gradient method of Clauser (1954). With the resulting reliable data that is obtained for the wall shear stress, the logarithmic profile can then be re-constructed to find the reference roughness length of the surface and the displacement in origin. These are the two parameters of engineering relevance.

The present calculation procedure is then compared with some new experimental data. With tunnel experiments over a rib-type surface are carried out to provide data of local mean and turbulent quantities.

2. Determination of wall shear stress

One of the simplest ways to find the wall shear stress is to consider the momentum integral equation, which can be cast as

$$\frac{c_f}{2} = \frac{\theta}{U_1}(2+H)\frac{dU_1}{dx} + \frac{d\theta}{dx} \tag{1}$$

where, U_1 denotes the external flow velocity, δ^* is the displacement thickness, θ is the momentum thickness and $H{=}\delta^*/\theta$ is the shape factor.

Although very useful, Eq. 1 has the disadvantage of relying on a differentiation to find c_f. The consequence is that a large sampling of θ must be considered and any necessary curve fitting must be carefully considered.

The evaluation of c_f by pressure tapping individual roughness elements was described in Perry et al. (1969). By drawing a control volume with a unit lateral length around a single element, a simple balance of the x-momentum results in

$$c_f = \frac{\tau_0}{(1/2)\rho U_0^2} = \frac{k}{\lambda}(C_{D0} - \frac{\Delta P_L}{(1/2)\rho U_0^2}) \tag{2}$$

where, τ_0 is the effective shear stress acting over the wall, k is the roughness height, λ is the roughness pitch, ΔP_L is the external pressure gradient, U_0 is the external flow velocity and

$$C_{D0} = \frac{1}{k(1/2)\rho U_0^2}\int_0^k (P_2(y) - P_3(y))dy \tag{3}$$

with $P_2(y)$ and $P_3(y)$ the pressures measured on the surface of the individual roughness elements as a function of the distance from the wall.

The term C_{D0} can can also be evaluated from an integral momentum balance of the outer flow on the control volume defined in Perry et al. (1969), according to

$$C_{D0} = -\frac{2\Delta\theta}{\Delta x} = \frac{1}{(1/2)U_0^2}(\frac{1}{\lambda}\int_x^{x+\lambda}\overline{(u'v')}dx + \frac{1}{\lambda}\int_x^{x+\lambda}(u_0 v_0)dx) \tag{4}$$

where $\overline{(u'v')}$ denotes the turbulent shear stress and $(u_0 v_0)$ the product of the temporal mean horizontal and vertical velocity components along the top of the control volume.

The local wall shear stress can also be determined by plotting the mean velocity profile on coordinates $\overline{U}$ against y. This procedure is known as the Clauser chart method. For a rough surface, Einstein and El-Samni (1949) showed that the origin of the y-axis must be taken some distance below the top of the roughness elements. This distance, hereafter denoted by ε, defines a coordinate system that will give a logarithmic distribution of velocity near the wall.

Hence, the mean velocity profile is to be written as

$$\frac{u}{u_\tau} = \frac{1}{\varkappa} \ln\left(\frac{(y_T + \varepsilon)u_\tau}{\nu}\right) + A + -\frac{\Delta u}{u_\tau} + W(y/\delta) \tag{5}$$

where u_τ is the friction velocity, $\varkappa$ is von Karman's constant (=0.4), y_T is the distance taken from the top of the roughness elements, A is the classical constant in the law of the wall (=5), Δu is Nikuradse's roughness function, and W Coles' wake function.

On a log-graph, the above equation appears as a straight line so that its slope and position can be used to determine u_τ. Unfortunately, a large number of possible combinations of parameters u_τ, Δu, and ε will give straight lines with a good coefficient of correlation. In this sense, Eq. 5 is of limited use for the determination of u_τ. However, provided u_τ is known, Eq. 5 can be used to find ε and Δu.

The error in origin was shown by Jackson (1981) to correspond to the average displacement height of the total shear stress (defined by Eq. 6 below). In fact, if we make $d = k$ - ε, that is, if we take as the reference surface the bottom of the rough elements, then it is possible to write

$$d - \overline{h} = \frac{1}{\lambda \tau_0} \int_{fluido} (\tau_0 - (T_{12} - \rho uv))\, dxdy \tag{6}$$

with $\overline{h} = (kl/\lambda)$, l = width of rough elements,

$$T_{12} = -\rho\overline{u'v'} + \mu\frac{\partial u}{\partial y}, \tag{7}$$

$$\tau_0 = [T_{12} - \rho\overline{uv}]_{y=\delta_i}, \qquad \delta_i = \text{height of control volume} \tag{8}$$

3. Turbulence models

The numerical simulations will be performed with a Reynolds Stress-ω model, the baseline (BSL-RSM) Reynolds Stress turbulence model. This selection of models is considered representative enough of the state of the art in turbulence engineering modeling to allow for a good assessment of the numerical computations of the flow over a rough surface. The advantage of ω-equation based models is that they have a more accurate near wall treatment.

The equations of motion are the Reynolds averaged equations of continuity and momentum for an incompressible flow. Denoting the mean and fluctuating velocities in x_i-direction by U_i and u_i respectively, the density and kinematic viscosity by ρ and ν and mean pressure by P, the equations can be written as

$$\partial_i U_i = 0, \qquad \partial_t U_i + U_j\, \partial_j U_i = -\partial_i P + \partial_j[\nu(\partial_j U_i + \partial_i U_j) - \overline{u_i u_j}] \tag{9}$$

where Einstein's notation of repeated indexes has been used for conciseness.

The pressure term has been divided by density.

A general way to model a turbulent flow is to compute every component of the Reynolds stress tensor from transport equations derived directly by algebraic manipulations of the Navier-Stokes equations. The resulting loss of information implied by the averaging process must then be recovered by an adequate modeling of each of the terms present in the equations. Most models consider the same basic set of rules to close the equations. All turbulent quantities are considered to be a function of Reynolds stress, κ, ϵ (or alternatively ω), mean flow quantities and related thermodynamics variables. The diffusion of turbulent quantities, in particular, is taken

to be proportional to the local gradient of the quantity. The dissipation of turbulent kinetic energy is supposed to occur at very small scales where turbulence is isotropic.

Constants appearing in the models are *ad hoc* so that they must be fixed through experimental calibration. The models also need to be consistent with the common requirements of symmetry, invariance and permutation.

Models that use the ϵ-equation frequently have to resort to complex non-linear damping functions in the near wall region. An alternative two-equation model that is claimed to circumvent this difficulty is the κ-ω model (Wilcox (1988)). In fact, the great advantage of the κ-ω formulation is supposed to be exactly the near-wall treatment, which can accept higher values of y^+=(yu_τ/ν), the non-dimensional distance from the wall. The κ-ω model has the additional advantage of providing near wall analytical solutions for both the viscous and the fully turbulent regions.

Despite the superior handling of the wall conditions, the κ-ω formulation struggles with its strong sensitivity to free stream conditions. Thus, given the different zonal strengths and, for that matter, weaknesses of the κ-ϵ and the κ-ω formulations, a good balance can be achieved between both models if a blending is introduced between the κ-ω formulation near the surface and the κ-ϵ model in the outer flow. This solution was proposed by Menter (1994), who introduced the so-called baseline κ-ω model (BSL).

The Reynolds stress model, formulated in terms of the ω-equation, can be written as

$$\partial_t(\overline{u_i u_j}) + \partial_k(U_k \overline{u_i u_j}) = \partial_k\Big(\Big((\nu_t/\sigma^*) + \nu\Big)\partial_k \overline{u_i u_j}\Big) - P_{ij} - \Pi_{ij} + (2/3)\beta'\omega\kappa\delta_{ij} \tag{10}$$

The ω-equation, can be written as

$$\partial_t\omega + \partial_k U_k\omega = \partial_k\Big(\Big(\nu + \nu_t/\sigma_{\omega 3}\Big)\partial_k\omega\Big) - \alpha_3\frac{\omega}{\kappa}P - \beta_3\omega^2 + 2(1-F_1)(\sigma_2\omega)^{-1}\partial_k\kappa\partial_k\omega. \tag{11}$$

The coefficients in the ω-equation (with subscripts 3) are blended between two sets of constants, one to be used near the wall corresponding to ω-based models (with subscripts 1, given below, Eqs. 19) and another used in the free stream corresponding to ϵ-based models (with subscripts 2, given below, Eqs. 20).

The definition of the several terms in the above equations is

$$\nu_t = \kappa/\omega, \tag{12}$$

$$P_{ij} = \tau_{ik}\partial_k U_j + \tau_{jk}\partial_k U_j,\ \tau_{ik} = -\overline{u_i u_k}; \qquad P = (1/2)P_{kk} \tag{13}$$

$$D_{ij} = \tau_{ik}\partial_j U_k + \tau_{jk}\partial_i U_k, \tag{14}$$

$$\Pi_{ij} = \beta' C_1\omega\,(\tau_{ij} + (2/3)\kappa\delta_{ij}) - \hat{\alpha}\,(P_{ij} - (2/3)P\delta_{ij}) - \hat{\beta}\,(D_{ij} - (2/3)P\delta_{ij}) - \hat{\gamma}\kappa\,(S_{ij} - (1/3)S_{kk}\delta_{ij}) \tag{15}$$

The blending of coefficients is made through the following linear interpolation function

$$\phi_3 = F\phi_1 + (1-F)\phi_2, \qquad \phi = \text{dummy variable} \tag{16}$$

where $F = \tanh(\arg^4)$ with

$$\arg = \min\Big[\max\Big(\frac{\sqrt{\kappa}}{\beta'\omega\,y}, \frac{500\nu}{y^2\omega}\Big), \frac{4\rho\kappa}{CD_{\kappa\omega}\ \sigma' y^2}\Big] \tag{17}$$

and

Figure 1: General view of wind tunnel.

$$CD_{\kappa\omega} = \max\Big(2\rho(\sigma'/\omega)\nabla\kappa\nabla\omega, 10^{-10}\Big), \qquad \sigma' = 1/0.856 \tag{18}$$

where the following model constants apply

$$\omega - \text{region},\ \sigma_1^* = 2,\ \sigma_1 = 2,\ \beta_1 = 0.075,\ \alpha_1 = 0.553 \tag{19}$$

$$\epsilon - \text{region},\ \sigma_2^* = 1,\ \sigma_1 = 0.856,\ \beta_2 = 0.0828,\ \alpha_2 = 0.44 \tag{20}$$

and

$$\sigma^* = 2,\ \sigma' = 1.168,\ \beta' = 0.09,\ \hat{\alpha} = 0.775,\ \hat{\beta} = 0.196,\ \hat{\gamma} = 0.495. \tag{21}$$

4. Experimental procedure

The experiments were carried out in the low-turbulence wind tunnel located in the Laboratory of Turbulence Mechanics of PEM/COPPE/UFRJ. The tunnel is an open circuit tunnel with a test section of dimensions 300 mm x 300 mm x 4,000 mm. The test section is divided into two sections of equal length which can be fitted with surfaces having different types of roughness. In the present experiment however, just one type of rough surface was tested. A general view of the wind tunnel is shown in Fig. 1.

The rough surface was a rib-type roughness constructed with rectangular aluminum bars of 6.35 by 4.76 mm rectangular cross section (see Fig. 2). The flow before reaching the rough surface traveled through a short smooth surface section whose leading edge was faired into the wind-tunnel floor by a 200-mm long ramp.

Every roughness element was made removable so that another element constructed with pressure taps could be fitted anywhere in the roughness pattern. The pressure taps, seven in all, were drilled directly onto an aluminum bar. The pressure tubes were connected directly to an inclined manometer that was operated at an angle of 2^o and was filled with alcohol. Pressures were therefore measured to an accuracy of 0.028 mm of water.

Instrumentation consisted of hot-wire anemometry. The x-probes, Dantec model P61, were operated by two Kauri constant temperature bridges. Probes were calibrated against a Pitot-static tube at the beginning of each run. The data was acquired at with a sampling frequency of 10.000 Hz and sampling time of 50 s. An uncertainty analysis of the data was performed according to the procedure described in Kline (1985). The uncertainty associated with the velocity measurements was: $U = 0.064$ m/s precision, 0 bias (P=0.95).

To obtain accurate measurements (Bruun (1985)), the mean and fluctuating components of the output signal of the anemometer were treated separately. Two output channels of the anemometer were used. The mean velocity profiles were calculated directly from the untreated signal of channel one. The signal given by channel two was 1 Hz high-pass filtered leaving, therefore, only the fluctuating velocity. The later signal was then amplified with a gain controlled between 1 and 500 and shifted by an offset so as to adjust the amplitude of the signal to the range of the A/N converter.

The measurements were performed for values of the free-stream velocity of 8 m/s; the free stream-level of turbulence was about 0.2%. .

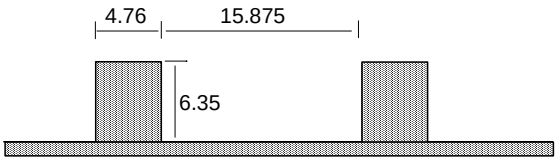

Figure 2: Geometry of roughness elements. Dimensions are in mm.

Figure 3: Detail of ramp and of pressure taps.

5. Computational details

The equations governing the problem were solved using the well known code ANSYS CFX, release 10. The model solves the Reynolds averaged Navier-Stokes equations (RANS) through a finite-volume approach. The solution strategy consists in solving the momentum equations using a guessed pressure. Next, a pressure correction is obtained which typically needs a large number of iterations to reach a converged solution. The code uses a coupled solver that solves the equations for the flow parameters as a single system. This procedure uses a fully implicit discretization of the equations at any given time. In the present steady state case, the time step behaves like an acceleration parameter to find the approximate solutions in a physically meaningful framework to a time independent solution.

The dimensions of the computational domain were defined in accordance to the experimental model. However, due to the high computer-storage and runtime efforts that are necessary to carry out computations over the full length of the experimental model, the extension of the computational domain was defined so as to include just two consecutive measurement stations. That meant performing the computations over five roughness elements. This strategy permitted the specification a very refined grid, particularly around the roughness elements where high velocity gradients occur. The height of the computational grid was taken to be twice the local boundary layer thickness to keep to a minimum any boundary condition influence on computations for the surface layer. A two-dimensional model was achieved by considering just one grid element in w-direction.

The above solution strategy depends for its success on a very fine representation of the near wall region. The present version of ANSYS CFX 10.0, controls near wall computations by an automatic method. Depending on the mesh refinement in the near-wall region, the method automatically switches the solution approach from wall-functions to a low-Re near wall formulation. The controlling parameter is the viscous region scale y^+ ($=y\ u_\tau/\nu$). Provided $y^+ < 2$, the low-Re model will be employed. With the present mesh, y^+ varies between 1.96 and 0.62.

Computations were carried out on a series of structured meshes that were generated consisting of hexahedrons. An extensive grid-dependence test was performed resulting in a final non-uniform, body-fitted mesh with 486.102 elements. The mesh was particularly refined in the near wall region so as to completely resolve the inner turbulent and viscous sub-layers. The refined mesh region extended up to 1.0 k (k = roughness height) above the top of the roughness elements.

Inlet conditions were prescribed directly from the experimental data. At the outlet, the turbulent intensity was automatically calculated by the model. At the side walls a symmetry condition was imposed. At ground level, the no-slip boundary condition was used.

The computations were performed on two Pentium 4, 3.0 GHz, with 2 Gb DDR400 RAM operating in a cluster configuration.

6. Results

Comparison will be made for the second measuring station. The general flow pattern that is formed in the cavity defined by two consecutive roughness elements is shown in Fig. 4 as yielded by the BSL-RSM model. A large recirculating flow region is observed which, however, does not span the whole length of the cavity. In fact, two large regions of recirculating flow are identified. In a 'd' type rough wall, stable vortices are formed in the cavities and shedding from the protuberances into the flow is negligible. In this case, the external flow passes relatively undisturbed over the top of the protuberances. In a 'k' type rough wall, on the other hand, large eddies with a length scale proportional to the height of the roughness elements are shed into the external flow blending smoothly with the surroundings. According to the present computations, our present roughness appears to be of the 'd' type. In fact, it must be pointed out that the present flow pattern is somewhat different from the flow visualization studies that were presented in Perry et al. (1969). In this work, for both 'd' and 'k' type roughness, just one large eddy was observed to develop in the cavities. Here, however, two large eddies are apparent. A distinct feature of a 'd' type roughness, however, is the presence of a stagnation streamline on the leading face of the roughness element. Notice the pressure distribution on both sides of the roughness elements (Fig. 5). A stagnation streamline is located very close, but below, to the top of the protuberances.

Figure 5) presents data for the numerical pressure distribution prediction, as well as data obtained directly from the pressure readings. With the help of Eq. 2, the skin-friction velocity can be evaluated from a direct numerical integration of the pressure profiles given by both procedures.

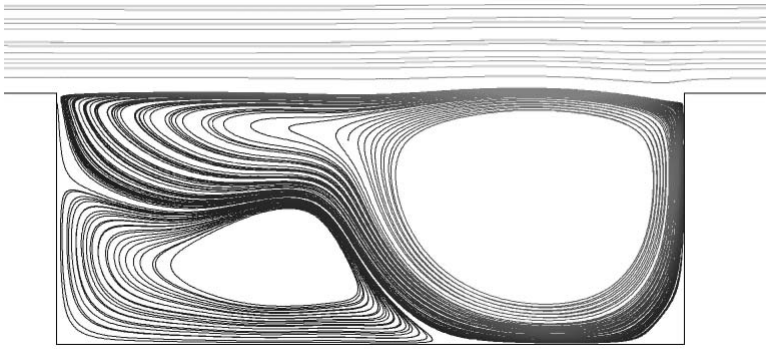

Figure 4: Flow streamlines between roughness elements.

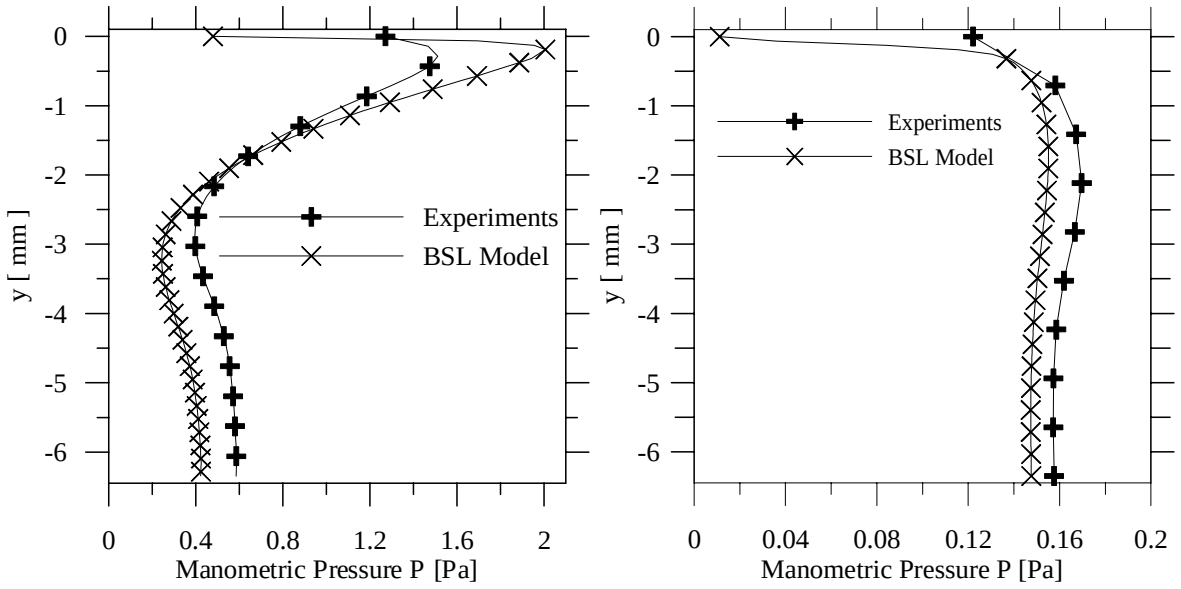

Figure 5: Pressure distribution around roughness elements.

Over a rough surface, the flow structure has to contain at least two characteristic regions. Adjacent to the rough wall the flow is strongly influenced by each roughness element and is not spatially homogeneous. This region, the roughness sublayer (RS), has a thickness of about 2-5k. Above the RS there is an inertial sublayer (IS) within which similarity theory is applicable. Therefore, in the IS the flow properties are homogeneous on the scale of the roughness spacing, the mean velocity profile is logarithmic and the turbulent statistics are nearly constant.

The velocity distribution in different flow stations is shown in Fig. 6a in linear coordinates. The extent of the inertial sublayer can be seen in Fig. 6b where the profiles are plotted in semi-log co-ordinates. Predicted turbulence properties are seen in Fig. 7. The longitudinal Reynolds stresses are underestimated by the BSL-RSM model by almost one third of its experimental value in the near wall region. The shear stresses are also much underestimated, now by a margin of 50% of the experimental values.

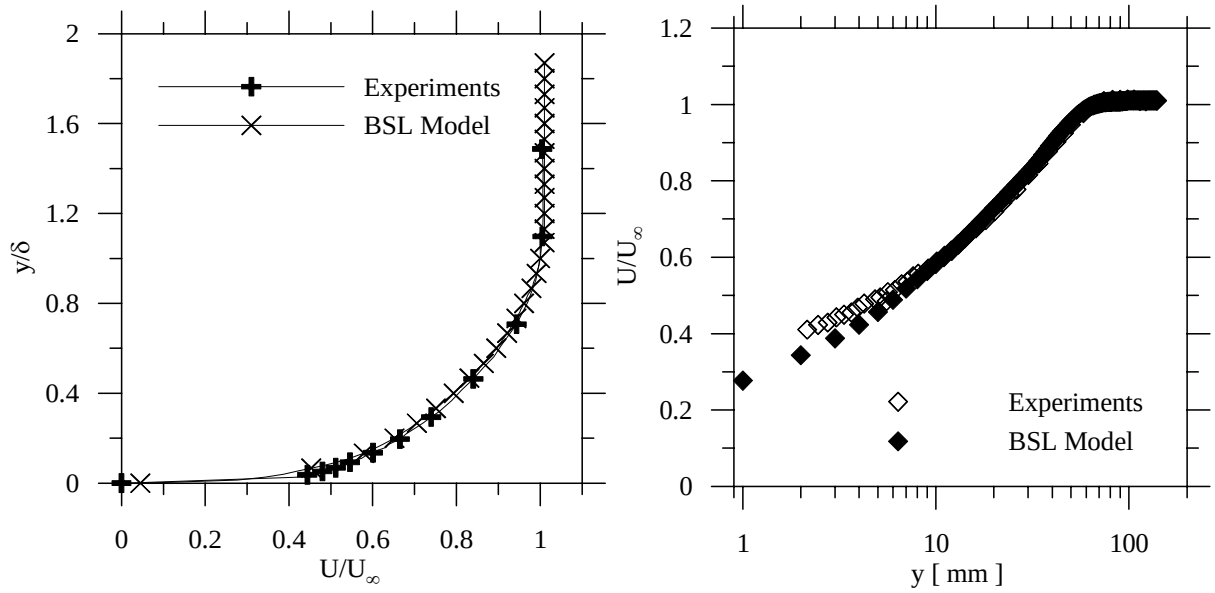

Figure 6: Velocity distribution on top of roughness elements.

The shear stress in the inertial region is often used by authors to evaluate the surface shear stress. By averaging $u'v'$ in the inertial region one may consider $\sqrt{-\overline{u'v'}} = u_\tau$. However, within the RS, $u'v'$ varies significantly with both y and x (Cheng and Castro, 2002). The implication is that the height where the averaging of $u'v'$ is to be taken must be chosen judiciously. Figure 8 shows the predicted values of $\overline{-u'v'}$ according to the BSL-RSM for various distances above the roughness element. For very short distances from the wall, the shear stress is observed to oscillate strongly. For the highest distance, $y/k = 1.0$, the shear stress is observed to drop to some very low values, much below the significant values near the wall.

The prediction of u_τ according to the several techniques introduced in this work is presented in Fig. 9. The overall agreement is very good.

7. Final Remarks

The present word has shown how sophisticated computational techniques can be combined with classical procedures to furnish reliable data on the wall shear stress for flows over rough surfaces. The proposal here was to use CFD to find local results that upon a further processing through integral methods resulted in reliable wall shear stress predictions.

Overall, the mean results were very good. However, prediction of turbulent quantities was very poor. In fact, due to the complexity of the problem this was the expected trend. The proposed method to find u_τ was then conceived to be robust and dependent on mean flow properties. The feature makes this method a very attractive method to be used in the determination of the displacement in origin and of the effective roughness.

Acknowledgements. APSF is grateful to the Brazilian National Research Council (CNPq) for the award of a Research Fellowship (Grant No 304919/2003-9). The work was financially supported by CNPq through Grant No 472215/2003-5 and by the Rio de Janeiro Research Foundation (FAPERJ) through Grants E-26/171.198/2003 and E-26/152.368/2002.

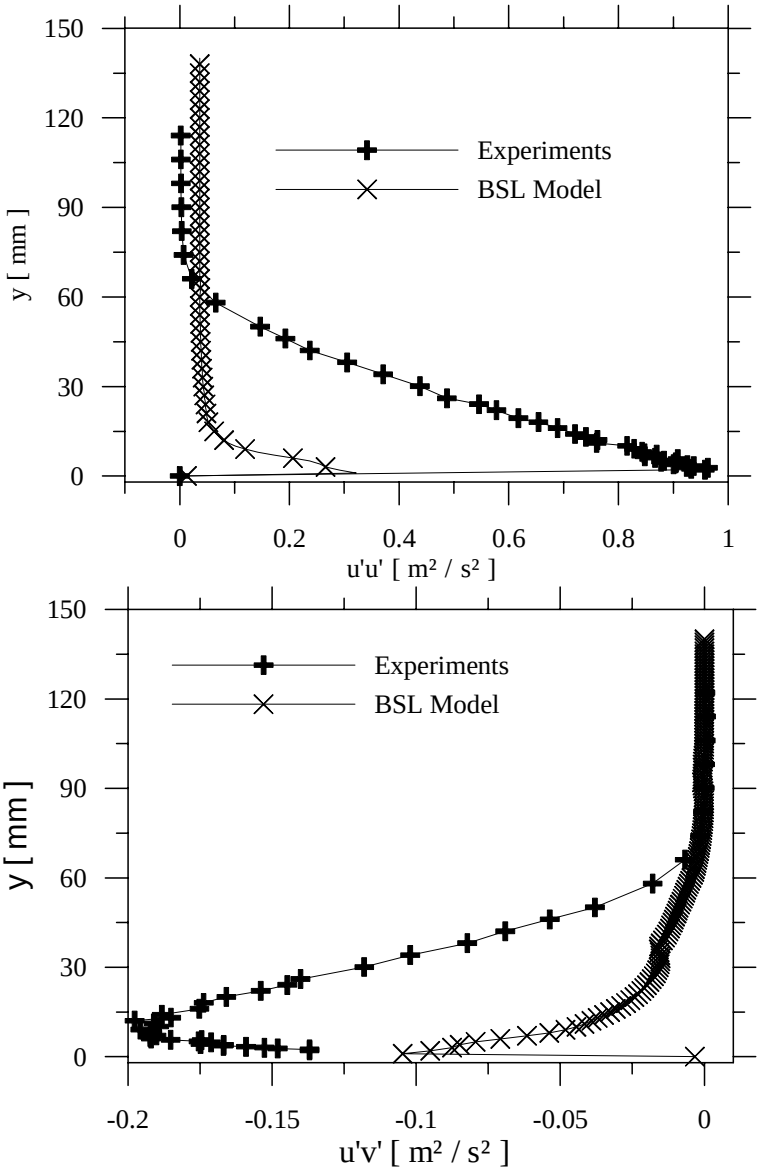

Figure 7: Turbulent longitudinal and shear stresses on top of roughness elements.

8. References list

Bruun, H. H., 1995, Hot-wire Anemometry - Principles and Signal Analysis, Oxford University Press.

Cheng, H. and Castro, I. P., 2002, Near-Wall Flow Development After a Step Change in Surface Roughness, BLM, 105, 411-432.

Einstein, H.A., El-Samni, E.-S. A., 1949, Hydrodynamic forces on a rough wall, Review of Modern Physics, 21, 520–524.

Hopf, L. 1923, Die Messung der Hydraulischen Rauhigkeit, ZAMM, 3, 329-339.

Kline, S.J., 1985, The Purpose of Uncertainty Analysis, J. Fluids Engineering, 107, 153-160.

Nikuradse, J., 1933, Stromungsgesetze in Rauhen Rohren, Forschg. Arb. Ing.-Wes. No 361.

Perry, A.E., and Joubert, P.N., 1963, Rough Wall Boundary Layers in Adverse Pressure Gradients, J. Fluid Mechanics, 17, 193–211.

Perry, A.E., Schofield, W.H. and Joubert, P.N., 1969, Rough Wall Turbulent Boundary Layers, J. Fluid Mechanics, 37, 383–413.

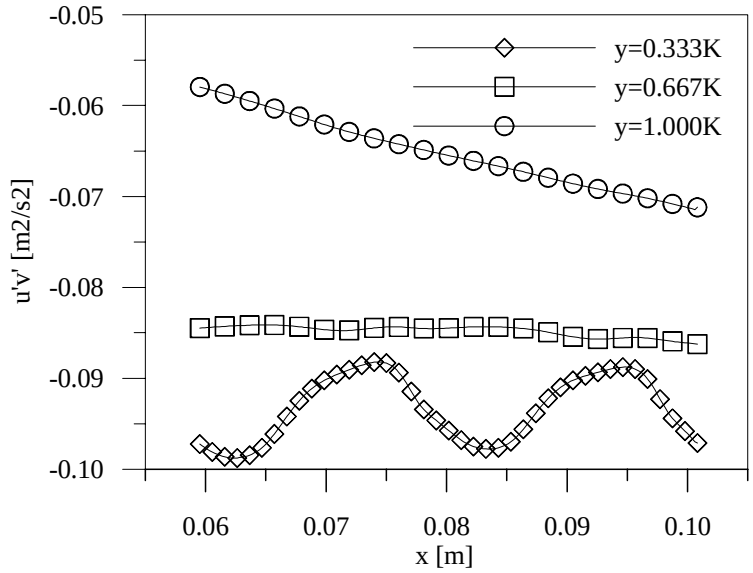

Figure 8: Predictions of $\overline{-u'v'}$ according to the BSL-RSM.

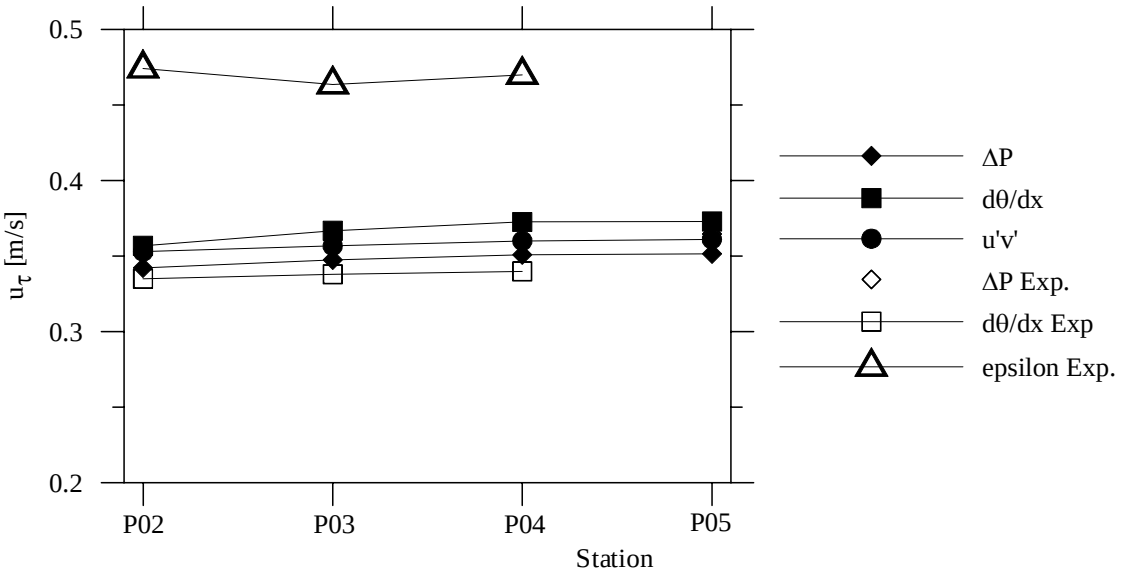

Figure 9: Predictions of u_τ according to the several techniques compared with the experimental data.

Proceedings of the 11th Brazilian Congress of Thermal Sciences and Engineering – ENCIT 2006
Braz. Soc. of Mechanical Sciences and Engineering – ABCM, Curitiba, Brazil, Dec. 5-8, 2006

Paper CIT06-0725

FLOW OVER A STEEP ROUGH HILL

André Sampaio Monteiro
PEM/COPPE/UFRJ
zpandrezp@yahoo.com.br

Juliana B. R. Loureiro
PEM/COPPE/UFRJ
jbrloureiro@mecanica.coppe.ufrj.br

Fernando T. Pinho
CEFT, Faculdade de Engenharia da Universidade do Porto,
Rua Dr. Roberto Frias s/n, 4200-465, Porto,
Universidade do Minho, Largo do Paço, 4704-553, Braga, Portugal
fpinho@dem.uminho.pt

Atila P. Silva Freire
PEM/COPPE/UFRJ
Federal University of Rio de Janeiro
C. P. 68503, Cep. 21.945-970, RJ.
atila@mecanica.coppe.ufrj.br

Abstract. *This paper presents the study of the effects that a steep topographical elevation exerts on the properties of a neutrally stratified, fully rough turbulent boundary layer. The main concern of the present work is to experimentally investigate the influence of surface roughness on the behaviour of the mean and turbulent velocity fields along the topography. Laser-Doppler anemometry was used to measure the longitudinal and vertical mean velocities and its fluctuation components, in a water-channel environment. Original and detailed measurements of the recirculation region downstream of the crest are presented.*

keywords: *Flow over hills, Roughness, Separation, Laser-Doppler anemometry, Turbulence.*

1. Introduction

In micrometeorology, the mathematical description of the flow field over an arbitrary terrain is always a difficult exercise. In fact, the natural non-uniformities resulting from changes in the land surface pose many problems that are of difficult modelling and solution.

In the past, owing to its simplicity, most of the systematic investigations on the surface layer and on its overlying boundary layer were confined to the simplest topography, the boundary layer over a flat, open land. Studies involving more complex situations such as flows over flat but heterogeneous surfaces or over hills were then just a few. The causes for the scarcity in analyses were clear. From the mathematical standpoint, atmospheric fluid motion is governed by a set of non-linear, second order, partial differential equations, and that renders the development of practical useful solutions a very difficult affair. On the other hand, on the experimental front, the difficulties in conducting field measurements frequently result on logistical requirements of an unsurpassable nature.

For low hills, with a gentle slope and an idealised shape, the equations of motion can be linearized to furnish simple analytical solutions that can be used to find mean wind velocity changes near the surface and rudimentary predictions of the flow turbulence structure. However, for large, steep hills the occurrence of flow separation and the formation of a large scale recirculating flow region adds much complexity to the problem. In fact, when hills become steep enough to form large downstream separation regions, many of the classical theories based on perturbation techniques break down. The pressure field cannot be simply approximated by the potential flow around the hill, but must be calculated considering the hill shape and the separation region. Thus, when separation occurs, not only the flow in the separation region changes, but significant changes occur in the whole flow field over the hill.

Moreover, the characteristics of the recirculation region, as well as the position of the separation and reattachment points are deeply dependent on the properties of the surface roughness. As a consequence, quantifying

the separated flow and the surface roughness parameter is a necessary and fundamental step for a faithful characterization of the velocity field.

The purpose of this work is to study the flow over hills which are steep enough so that large separation regions are formed on its downstream side. Our main concern is to experimentally investigate the influence of the surface roughness on the behaviour of the mean and turbulent velocity fields over the elevation. In particular, our interest is to study the characteristics of the flow inside and in the neighbourhood of the recirculation region that is formed on the lee side of the hill. A neutrally stratified, fully rough boundary layer flowing over a steep model hill has been simulated in a water channel environment. The rough surface used in the present work was essentially two-dimensional. It was comprised by a sequence of square bars equally distributed over the smooth wall of the water channel. The two-dimensional hill was constructed with a Witch of Agnesi shape with a maximum 18.6^o slope. Measurements of longitudinal and vertical components of mean velocity and its turbulent components were carried out with the aid of laser Doppler anemometry. The present results allow a thorough description of the near-wall flow, extending from the upstream region, along into the separated zone to the downstream lee side.

As a consequence of the presence of the recirculation region, the prediction of turbulent flow over a steep hill naturally lends itself to the use of non-linear models. That has, indeed, been the general trend over the last 10 years. The natural increase in computer power, together with the development of a host of turbulence models, has witnessed a large increase on the number of non-linear numerical simulations of atmospheric flows. Typical numerical simulations included two-equation eddy-viscosity turbulence models, algebraic Reynolds stress models, second-order closure models and large eddy simulation. All simulations, however, irrespective of the type of closure scheme chosen, suffer with the specification of the boundary conditions at the wall.

From this perspective, the main contribution of the present manuscript is to provide detailed and refined experimental data on neutrally stratified flows over a steep rough hill, in particular inside the recirculation region. These data are representative of a typical problem which commonly occurs in nature and technology. In fact, this work constitutes a further step in extending the problem to more complex situations. A previous and more fundamental step, which considered solely the effects of a smooth steep hill on the properties of a turbulent boundary layer has been made by Loureiro et al. (2006). Indeed, it is crucial to have a well-established knowledge of the main mechanisms involved on the separation behind smooth hill crests before proceeding to study additional features such as the roughness effects. Our aim is now to consider only the effects of hill roughness, shape and slope. Other contributions such as stratification effects are not in the scope of this work.

2. A brief literature review

Many theoretical and experimental studies have been carried out to analyse the effects that two and three-dimensional hills cause on the mean velocity and turbulence fields of the atmospheric boundary layer. In the following, we present some representative work of previous contributions. This short review, we expect, will provide the reader with a good idea on the state of the art for the experimental representation of the flow over hills.

Without any doubt, the works that have had a most profound influence on the way one thinks about the problem are the works of Hunt and his co-workers. These works have resorted to asymptotic methods to describe the flow over low hills, where the equations of motion can be linearized. Hunt has suggested the existence of a flow structure equivalent to the classical two-layered model developed for the aerodynamic boundary layer. In the inner layer, the flow is expected to be in equilibrium with the current boundary conditions so that its structure can be predicted on the basis of the wall laws. In the outer layer, turbulence is expected to be modified according to the rapid distortion theory of Townsend (1972).

In a seminal work, Jackson and Hunt (1975) showed that, for a low hill of rough surface, the eddy viscosity distribution for equilibrium flow near a wall can still be used to determine the changes in Reynolds stress. The theory also showed that for a log-profile upwind the increase in wind speed near the surface of the hill is $O((H/L)U_o(L))$ where H and L are respectively the characteristic height and length of the hill and $U_o(L)$ is the velocity of incidence wind at L. The conclusion was that the increase in surface winds can be considerably greater than that furnished by potential flow theory. Another conclusion was that at the point above the top of the hill where velocity reaches its maximum value, the velocity is approximately equal to the velocity at the same elevation above ground level upwind of the hill. The surface stress was found to be very sensitive to changes in elevation, being doubled by a hill with slope as small as one in five.

Britter et al. (1981) studied an air flow over a two-dimensional hill. The emphasis was on characterizing the velocity speed up, the surface roughness effects and the properties of turbulence. The hill was two-dimensional, bell shaped, with a maximum slope 0.26. Mean and fluctuating longitudinal velocities were measured with a constant temperature anemometer and a pulsed wire anemometer. The mean velocity profiles were compared with predictions given by the two-layered model of Jackson and Hunt(1975) furnishing close agreement for locations upwind of the hill top but not in the separated flow region. In a second experiment, flow over a

smooth hill with a rough surface was studied. The authors showed that, for this geometry, flow speed up can be evaluated by a linear superposition of effects provoked by the changes in elevation and in roughness. In the lee of the hill, however, the roughness completely changed the flow configuration suppressing separation and the linear superposition effect.

The structure of strongly stratified flow over three-dimensional hills was discussed by Snyder et al. (1985) both from a theoretical and experimental point of view. The paper discusses extensively the dividing streamline concept, taking as a basis for the analysis Sheppard's energy arguments for an estimation of the height of this dividing streamline. The authors analyse an extensive range of laboratory observations and measurements of stratified flows over a range of hills with different geometries subjected to different oncoming flows.

Concerned with the effects that hills provoke on turbulence, Zeman and Jensen (1987) developed a new model where the von Mises transformation was applied to the mean momentum equations and the second-order closure type turbulence equations were solved. All predictions were compared with data from the Askervien Hill project.

At around the same time, Snyder and Britter (1987) carried out an experimental research very similar to Arya and Gadiyaram(1986), triangular and bell shaped hills with varying crosswind aspect ratio were studied. Velocity measurements were made with a cross-film anemometer. This fact prevented the characterization of the wake region. The separation region was observed to decrease in size with increasing aspect ratio and changes in the flow parameters were explained with the notion that the effective hill shape was formed by the hill and the resulting recirculation region.

Castro and Apsley (1997) performed computations for the flow and dispersion over two-dimensional hills of various slopes in a neutrally stable boundary layer. The results were compared with laboratory data. The authors showed that a suitably modified κ-ϵ model generally produced good agreement for the mean behaviour, but lower values for the turbulent kinetic energy and the lateral plume spread. Corrections in the standard κ-ϵ model allowed the authors to account for streamline curvature effects. For a hill with a sufficiently large slope the levels of concentration were found to be well predicted. For hills with lower slopes that provoked intermittent separation, less satisfactory results were observed.

The prospects for the application of large eddy modeling to the description of flows over hills were analyzed by Wood (2000). After recognizing the remarkable progresses that have been achieved through linear theories, the author emphasizes the urgent need for the development of a computationally cheap method for the prediction of mean and turbulent flow in the lee of steep hills for which non-linear processes dominate. The author further reminds us that the dynamics and the structure of separation and turbulent wakes are still poorly understood. In this scenario, it is argued that large-eddy simulations seem to be a well suited technique for the numerical investigation of flow in complex terrain.

A wind tunnel study of turbulent flow over a 3-D steep hill was performed by Simpson et al. (2002). Through three -velocity component laser Doppler velocimeter measurements, the complex vortical separations that occur on the lee of the hill were characterized in a plane downstream of the hill. The authors conclude that only two large streamwise vortices are formed, one on each side of the centerline.

Two dimensional steep hills in both neutral and stably stratified flow conditions were also studied by Ross et al.(2004). Turbulence models that used one-and-a-half and second-order closure schemes were used to predict the mean and turbulent quantities of the flow. The numerical predictions were compared to new wind tunnel experiments carried out for two hills with different slopes, one of which was steep enough to cause flow separation. The data, obtained through laser Doppler anemometry included mean and turbulent properties of the flow. The wall flow region was treated accordingly to the procedure of Ying and Canuto (1997). The authors report a reasonable prediction for mean flow characteristics for all flow conditions. However, large differences are observed in the separated flow region in the lee side of the hill.

The ability of non-linear eddy-viscosity and second-moment models to describe the flow over two- and three-dimensional hills was investigated by Wang et al. (2004). Five turbulence models were analyzed: two cubic eddy-viscosity models, an explicit algebraic Reynolds-stress model, a quadratic eddy-viscosity model and a Reynolds-stress-transport model. The one major objective of the paper was to examine the flow separation patterns that occur on the lee side of 2D- and 3D-hills. The authors report that in 2D-flow the predicted separation differs greatly from one model to the other, with just one non-linear model performing well. In 3D-flow, none of the models were found to give a good representation of the complex multi-vortical separation pattern.

3. Experimental apparatus

The rapid development of the aeronautical industry during the sixties has established wind tunnels as the most appropriate and low-cost facility to simulate natural flow conditions. In the past, though, several investigators have resorted to water experimentation in order to examine the flow over hills and other obstacles.

Long (1959), Snyder (1985) and more recently by Gyüre and Jánosi (2003) are quite clear examples of the use of the towing tank method. Indeed, towing tanks are quite appropriate when considering atmospheric flows dominated by blocking, lee waves, inversions and strong stratification effects. However, as explained by Meroney (1990), the towing tank method may distort surface layer predictions because the uniform approach profile simulated is not equivalent to shear flow found near the earth's surface. Water-channel experiments, on the other hand, do not suffer from this weakness. The mean and turbulent boundary layer profile can be accurately reproduced in this facility. The ratios of longitudinal and vertical fluctuation components of the simulated inner layer are comparable to atmospheric data, as presented in the results section.

3.1. Water channel

The present experiments were conducted at the Hydraulics Laboratory (FEUP). The problem under study has been simulated in a 17 m long water channel, with cross sectional area of 0.60 m high per 0.40 m wide. The side walls of the channel were made of glass, so as to make it convenient to perform any visual inspection of the flow, as well as to permit an appropriate use of the laser-Doppler anemometer.

The water recirculation system consists of two underground tanks, four pumps with a maximum capacity of 150 l/s and one upper stabilizing tank. The working section was 3 m long, and was situated 10.3 m downstream of the channel entrance. The model of the hill was located 12 m from the channel entrance.

During a typical run, two pumps sufficed to be used to keep the system running in a steady state, with a maximum flow rate variation of $\pm$ 0.8 %. At the entrance of the channel, the water was made to pass through a series of screens and filters so as to stabilize, make uniform and suppress any excessive level of turbulence. The screens and filters were also used to control the grain-size of the particles in suspension in the water. To guarantee a flow rate control of 0.001 l/s, a magnetic flowmeter was installed in the supply line. The water depth along the channel was controlled by a vertical steel gate. For the present measurements a flow rate of 26.7 l/s and water height of 267.5 mm were employed during the whole experimental campaign. An illustration of the water channel is shown in Figure (1.a), and the hill is shown in Figure (1.b).

Figure 1: Illustration of the water channel and model hill.

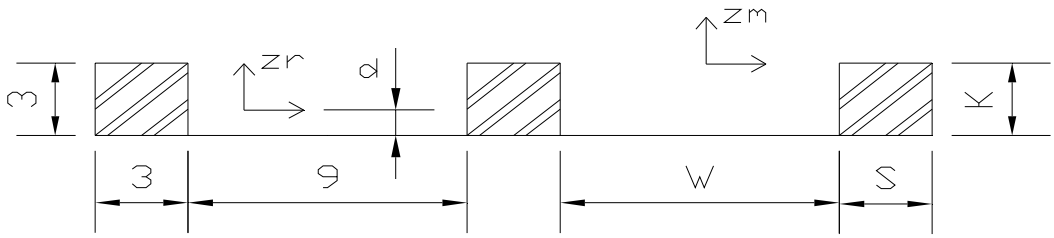

Figure 2: Geometrical details of the simulated rough surface. Dimensions in mm.

3.2. Characteristics of the hill and rough surface

For the present work, the same model used in the work of Loureiro et al. (2005) has been used. Following the geometrical characteristics used by Loureiro et al. (2000, 2001), the shape of the hill was given by a modified "Witch of Agnesi" profile, according to the equation

$$z_H = H_1[1 + (x/L_H)^2]^{-1} - H_2. \tag{1}$$

Thus, it follows that H $(=H_1 - H_2)(= 60$ mm) is the hill height and L_H $(= 150$ mm) is the characteristic length of the hill representing the distance from the crest to the half-height point. Co-ordinates x and z represent the longitudinal and the vertical axes, respectively. This curve has been extensively used in literature, e. g. Britter and Hunt (1981) and Arya et al. (1987).

The rough surface was simulated through the use of rubber strips of 3 mm per 3 mm cross section spaced by 9 mm gaps. These bars have been regularly distributed along the test section. The rough surface extended from 1.5 m upstream of the hill top until 1.5 m downstream. The geometrical details of the simulated surface are given in Figure (2). Please note that measurements have been carried out considering the top of the roughness elements as the origin of the vertical profiles, as illustrated in Fig. (2). However, the actual origin of the velocity profile is located somewhere between the flat floor and the height of the roughnesses elements. This shift in origin is usually called the displacement height d, which be explained further in the manuscript.

3.3. Instrumentation

A two-component Dantec laser-Doppler anemometry system was used in the forward scatter mode to conduct the measurements of the mean and fluctuating velocity field. A Bragg cell unit was used to introduce a total optical-electronic shift of 0.6 MHz, allowing the resolution of the direction of the flow field and the correct measurement of near-zero mean velocities. The beams were made to pass through a series of conditioning optical elements, in order to achieve a small measurement volume and to improve the optical alignment. Front lenses of 500 mm focus length were mounted on the probe in order to accurately position the measurement volume on the centerline of the water channel. Before being collected by the photomultiplier, the scattered light was made to pass through an interference filter of 514.5 nm, so that only the green light is acquired. The same procedure was carried out to acquire the blue light, with a filter of 488nm. The signal from the photomultiplier was band-pass filtered and processed by a Burst Spectrum Analyzer, operating in the single measurement per burst mode. A series of LDA biases were avoided by adjusting the strictest parameters on the data processor. For this set of experiments, a level validation of 8 and a signal to noise ratio of 5 was chosen. For the simultaneous measurements of longitudinal and the vertical velocities, a coincidence window of 5000 μs was used. For each point measured, a sample size of 20,000 values has been considered. Table (1) lists the main characteristics of the laser-Doppler system used.

Table 1: Main characteristics of the laser-Doppler system.

Wavelength	514.5 nm (green) 488nm (blue)
Half-angle between beams	1.604^o
Fringe spacing	9.191 μm (green) 8.718 μm (blue)
Beam spacing	28 mm
Beam diameter	2.2 mm
Dimensions of the measurement volume	
Major axis	5.31 mm (green) 5.04 mm (blue)
Minor axis	149.0 μm (green) 141.0 μm (blue)

This whole system was used to measure both the longitudinal and the vertical velocity components. Typical uncertainties associated to the mean velocity data, U, W, are lower than 0.2% of the free stream velocity, u_δ. Further downstream of the hilltop, in high level turbulence regions, these maximum uncertainties increase to about 0.3% of the free stream velocity. As for the Reynolds stress components $u'u'$, $w'w'$, $u'w'$, uncertainties were estimated in 2.3%, 1.8%, 4.2% of the friction velocity in the undisturbed flow (for the Reynolds shear stress the uncertainty is given in percentage of the square of the friction velocity of the undisturbed flow), respectively, increasing to 3.8%, 3.5% and 6.9% in regions of high turbulence.

4. Results

Firstly, the properties of the undisturbed boundary layer are shown and discussed. Then, the results for the perturbed flow field over the hill are presented. For clarity, and to identify which mechanisms are dominant in each region, the results will be particularly split into three blocks: data for the flow field upstream of the top of the hill, data for the recirculation region and data for the returning to equilibrium region . Hereafter, all the data are shown in reference to a Cartesian coordinate system located at the symmetrical axis of the hill. All the profiles were measured at the centerline of the water-channel. Measurements were taken at 11 stations along the test section, and Figure (3) illustrates its spatial distribution.

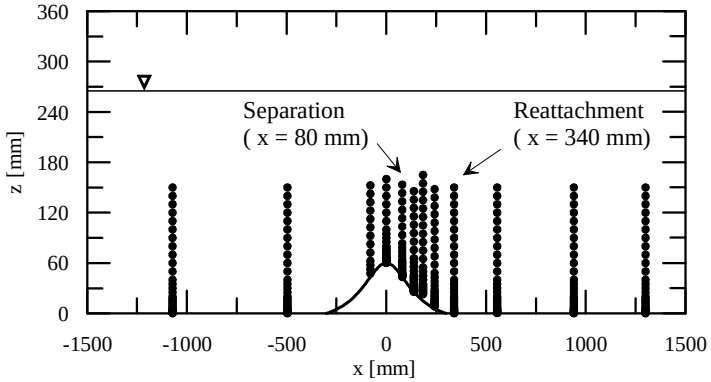

Figure 3: Spatial distribution of the measured profiles and illustration of the coordinate system.

4.1. Undisturbed Boundary Layer

The characterisation of the undisturbed flow will provide reference data for the evaluation of the perturbed flow field over the hill. For the present experiment, the reference mean and turbulent velocity profiles were measured at station x = -1072 mm. Figure (4.a) shows the longitudinal mean profile in normalised physical coordinates, where δ denotes the boundary layer thickness and U_δ the free stream velocity. The streamwise fluctuation profile measured in the undisturbed station is shown in Figure (4.b). Measurements assure that the oncoming boundary layer was fully developed and followed approximately the $(z/\delta)^{1/7}$ power law behaviour.

For a rough surface, the law of wall can be written as:

$$U = \frac{u_\tau}{\varkappa} ln\left(\frac{z-d}{z_0}\right), \tag{2}$$

where $\varkappa$ is the von Karman constant, d is the displacement height and z_0 is the roughness length. Eq. (2) is, in engineering and meteorological literature, a customary way to write the logarithmic law for the velocity profile over rough surfaces, e. g. Perry and Joubert (1963), Jackson (1981), Malhi (1996).

In order to evaluate the friction velocity for the undisturbed boundary layer over rough surface, the Reynolds shear stress profile was used. Assuming that at some distance from the wall the turbulent stresses are the dominant part of the total shear stresses, a region of constant distribution can be identified in the $-\overline{u'w'}$ profile. The mean value of $-\overline{u'w'}$ in this region can then be used to calculate u_τ. The value of the friction velocity was calculated as $u_\tau = 0.072\ U_\delta$. This value is in 5% agreement with the data of Britter et al. (1981), $u_\tau = 0.0685\ U_\delta$, and Athanassiadou and Castro (2001), $u_\tau = 0.06\ U_\delta$.

Once the friction velocity is known, the roughness related parameters d and z_0 can be found through Eq. (2). According to Malhi (1996), the displacement height d is mainly a dynamic quantity, and is related to the behaviour of the transport mechanisms. On the other hand, the roughness length z_0 is considered as uniquely related to the geometry of the underlying surface and is independent of meteorological variables. Using the graphical method of Perry and Joubert(1963), the velocity profile was plotted in a log-linear graph in dimensional coordinates, Fig. (4.c). Then, the normal distance from the flat surface (bottom of the roughness elements) was decremented in steps of 0.1 mm and a straight fit was applied to the logarithmic region. The angular coefficient of this fit was kept constant through the specification of u_τ previously calculated from $-\overline{u'w'}$ profile. The most appropriate curve was chosen by searching for the maximum coefficient of determination, R-squared, thus providing us with the best value for d. Others statistical parameters were also considered in

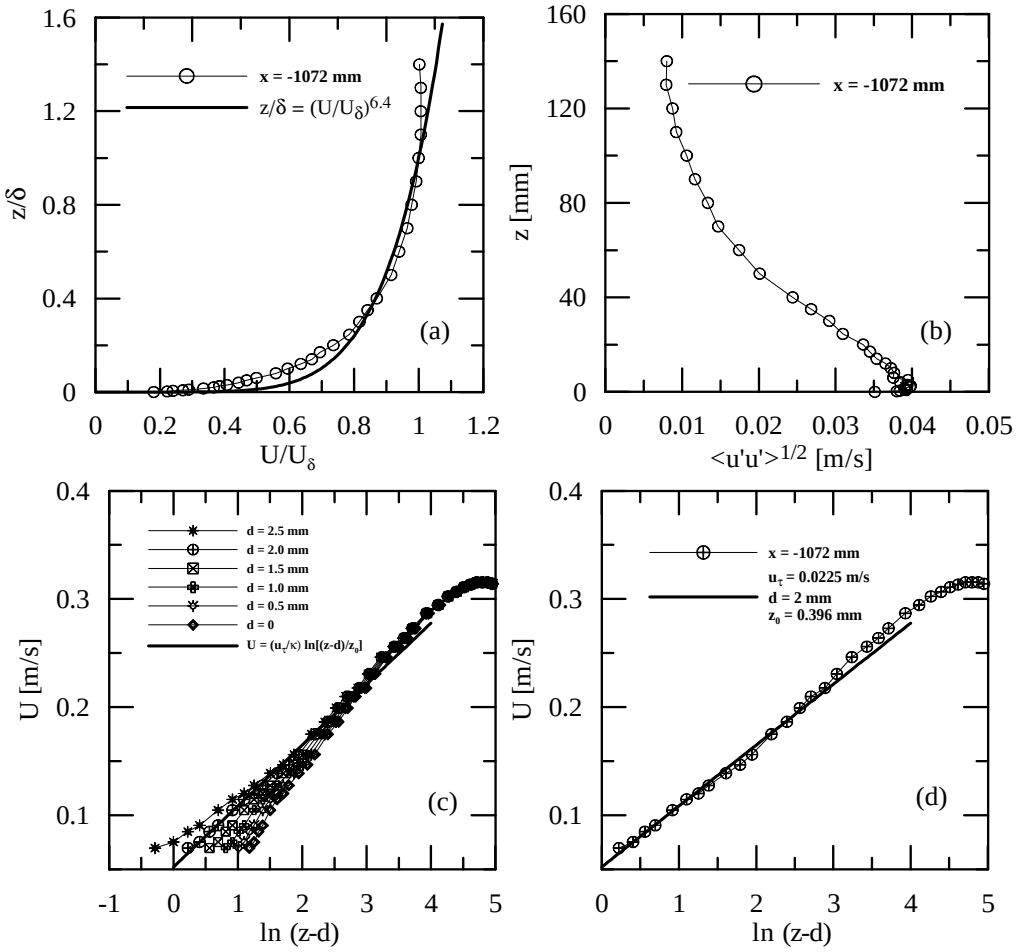

Figure 4: Undisturbed streamwise flow. (a) Mean velocity profile, (b) Turbulent velocity profile, (c) Estimation of d and z_0 (d) Logarithmic velocity profile.

this evaluation process. The determination of the error in origin for the velocity boundary layer is illustrated in Figure (4.c). Consequently, according to Eq. (2), the value of z_0 is calculated from the linear coefficient of the most appropriate curve fit.

The selected curve fit is illustrated in Fig. (4.d). The global and local properties of the undisturbed boundary layer are presented in Table (2).

Table 2: Properties of undisturbed profile.

Boundary layer thickness	δ	100 mm
External velocity	U_δ	0.3133 m/s
Friction velocity	u_*	0.022537 m/s
Roughness length	z_0	0.396 mm
Reynolds roughness length	$U_\delta z_0/\nu$	123

Longitudinal mean velocity profiles are presented in Figure (5). Please note the argument $(z - z_H)$ shifts the origin of the coordinate system from the flat surface to the hill surface, see Eq. (1) and Fig (3). Measurements performed upstream of the hill top are shown in Fig. (5.a). The region of accelerated flow upwind to the crest can be clearly noted.

The profiles along the separation region are introduced in Fig (5.b), where the reversed near-wall flow region is fairly well characterised. The separation point was observed to occur approximately at x = 80 mm, and reattachment was observed at around x = 400 mm. Fig (5.c) presents the velocity profiles downstream of the

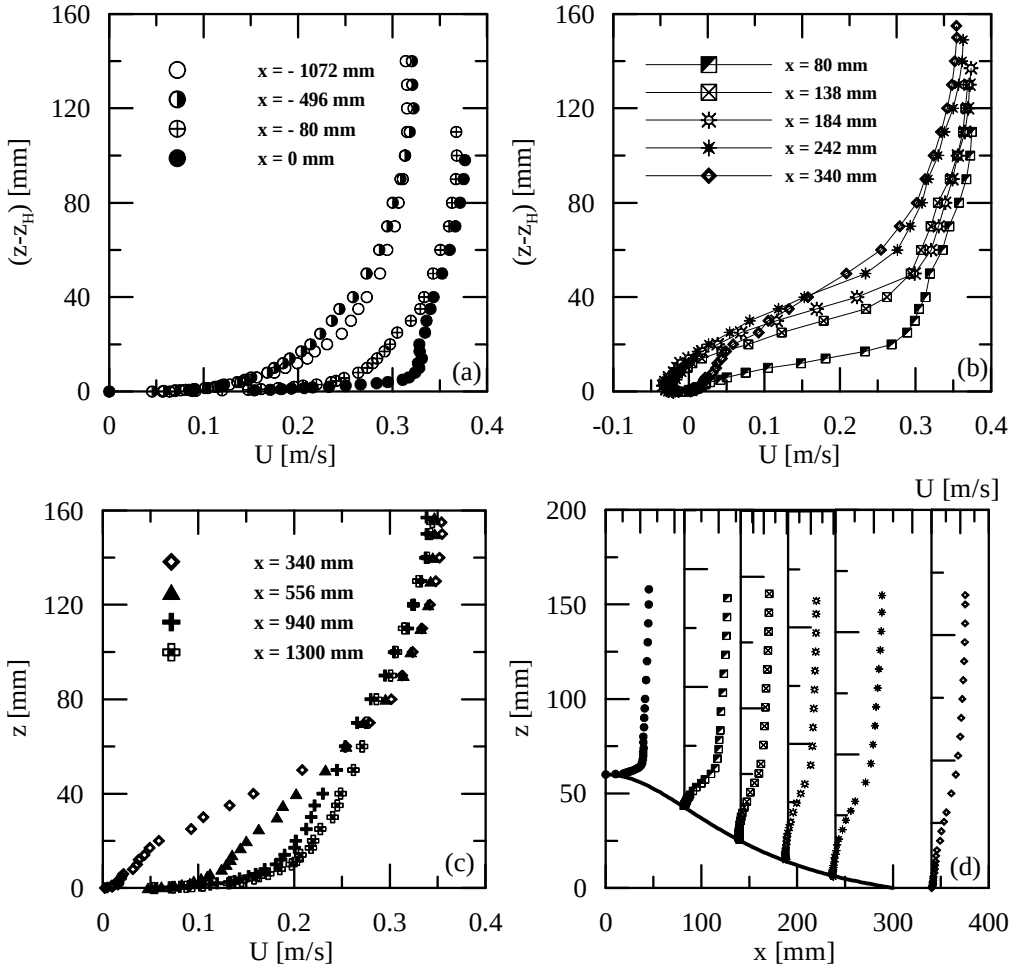

Figure 5: Mean longitudinal velocity at the 11 measured stations.

wake, where the boundary layer is returning to its equilibrium conditions. An overview of the recirculation is shown in the Fig (5.d).

The changes in the longitudinal fluctuating velocity profiles are shown in Fig. (6). In the accelerated flow region upstream of the hill (Fig. 6.a), $\overline{u'u'}$ is observed to increase slightly along the upwind slope (x/H = -2.5), until the crest is reached. At the hill top, $\overline{u'u'}$ is about 2.5% its undisturbed value in the near-wall region.

In the separated flow region (Fig. 6.b), the peak value for $\overline{u'u'}$ increases by 75% as compared with its undisturbed profile. In addition, the large increase in peak values for $\overline{u'u'}$, as well as its increasing distancing from the wall toward the shear layer results from the turbulence production term $P_{uu} = -2\overline{u'w'}(\partial U/\partial z)$. The maximum peak value for $\overline{u'u'}$ is located at x = 340 mm, approximately the reattachment point, z = 30 mm. Downstream of the hill (Fig. 6.c), at stations x = 940 mm and 130 mm, the $\overline{u'u'}$ profiles can still be distinguished from each other and from the undisturbed profile.

In general, in this region, turbulence profiles are characterized by an elevated maximum whose distance to the wall increases with increasing distance from the hill.

The behaviour of $-\overline{u'w'}$ is presented in Fig. (7). On the upwind side of the hill the changes in the Reynolds shear stress profiles are relatively small and vary slowly with height (Fig. 7.a). Notable changes in $-\overline{u'w'}$ are observed just as the flow passes the hill top. Then, a large increase in $-\overline{u'w'}$ is observed, of the order of five times. This behavior can be explained by the enhanced shear effects through the production term $P_{u'w'} = 2\overline{w'^2}(\partial U/\partial z)$. Similar to the peak locations for $\overline{u'u'}$, the highest value of $-\overline{u'w'}$ is found at position x = 380, z = 40 mm. No inner region of constant $-\overline{u'w'}$ was noted in the separated flow region. Downstream of the hill, at stations x = 556 and 940, $-\overline{u'w'}$ shows a nearly constant near wall region, but the difference in $-\overline{u'w'}$ between these stations is around a factor of two.

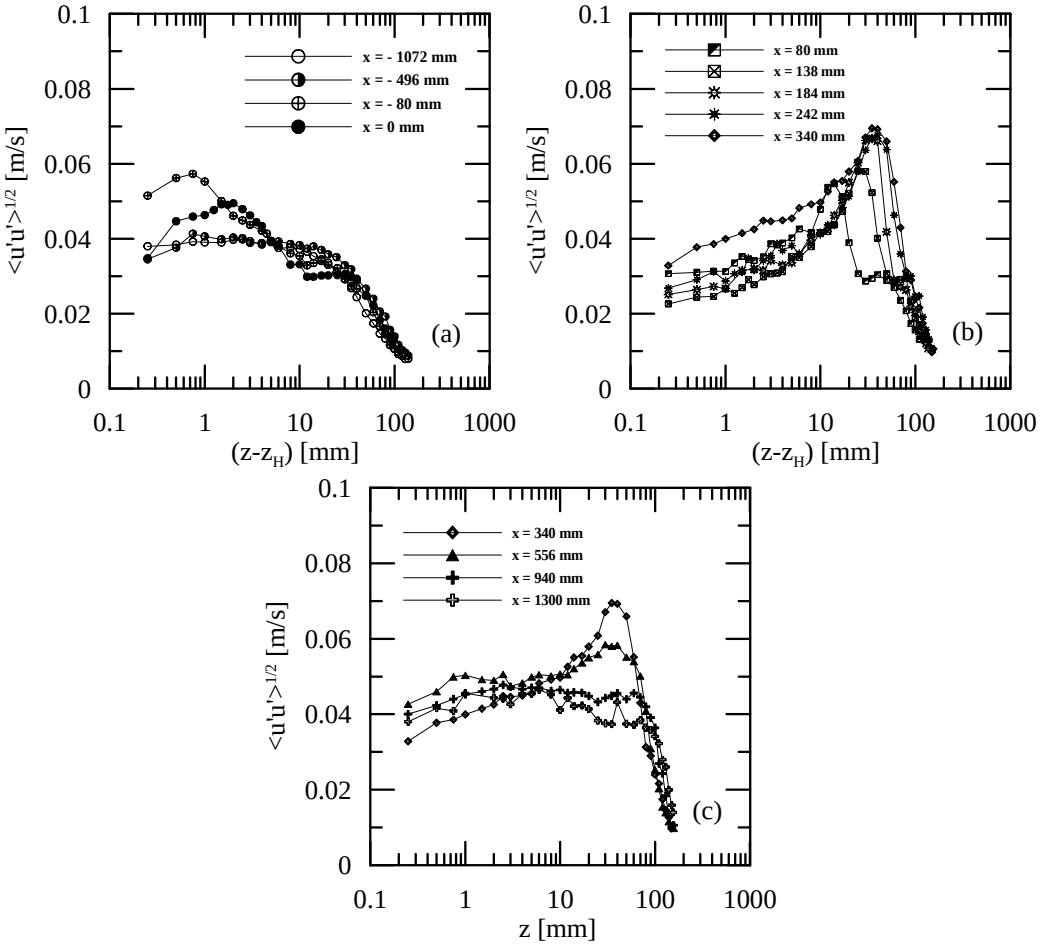

Figure 6: Streamwise turbulent velocity profiles measured along the hill.

5. Final remarks

This work has experimentally investigated the influence of the surface roughness on the behaviour of the mean and turbulent velocity fields along a steep hill. Particular attention was dedicated to the study of the characteristics of the recirculation region. A neutrally stratified flow over a steep rough elevation has been simulated in a water channel environment. Measurements of longitudinal and vertical components of mean velocity and its fluctuation components were conducted with the aid of a two-component laser Doppler anemometry.

At the present stage, the research has striven in characterising the flow in four distinct regions: in the undisturbed region upstream of the hill, on the top of the hill, inside the and in the undisturbed region downstream of the hill. The present results allow a thorough description of the inner region of the boundary layer, providing good quality near-wall data to serve as a test case for numerical simulations.

6. Acknowledgements

ASM benefited from a Research Scholarship from CNPq. ASM is also thankful to CNPq (Grant No 472215/2003-5) and to the Rio de Janeiro Research Foundation (FAPERJ) (Grants E-26/171.198/2003) for the concession of further financial help regarding his stay at Oporto University. JBRL benefited from a Research Scholarship from the Brazilian National Research Council (CNPq). JBRL is also grateful to the Programme Alban, European Union Programme of High Level Scholarships for Latin America, identification number E03M23761BR. APSF is grateful to the Brazilian National Research Council (CNPq) for the award of a Research Fellowship (Grant No 304919/2003-9). The work was financially supported by CNPq through Grant No 472215/2003-5 and by the Rio de Janeiro Research Foundation (FAPERJ) through Grants E-26/171.198/2003 and E-26/152.368/2002. ASM, JBRL and FTP are grateful to Prof. Maria Fernanda Proença and the Hydraulics Laboratory at Oporto University for all their help in setting up the flow rig and technical discussions.

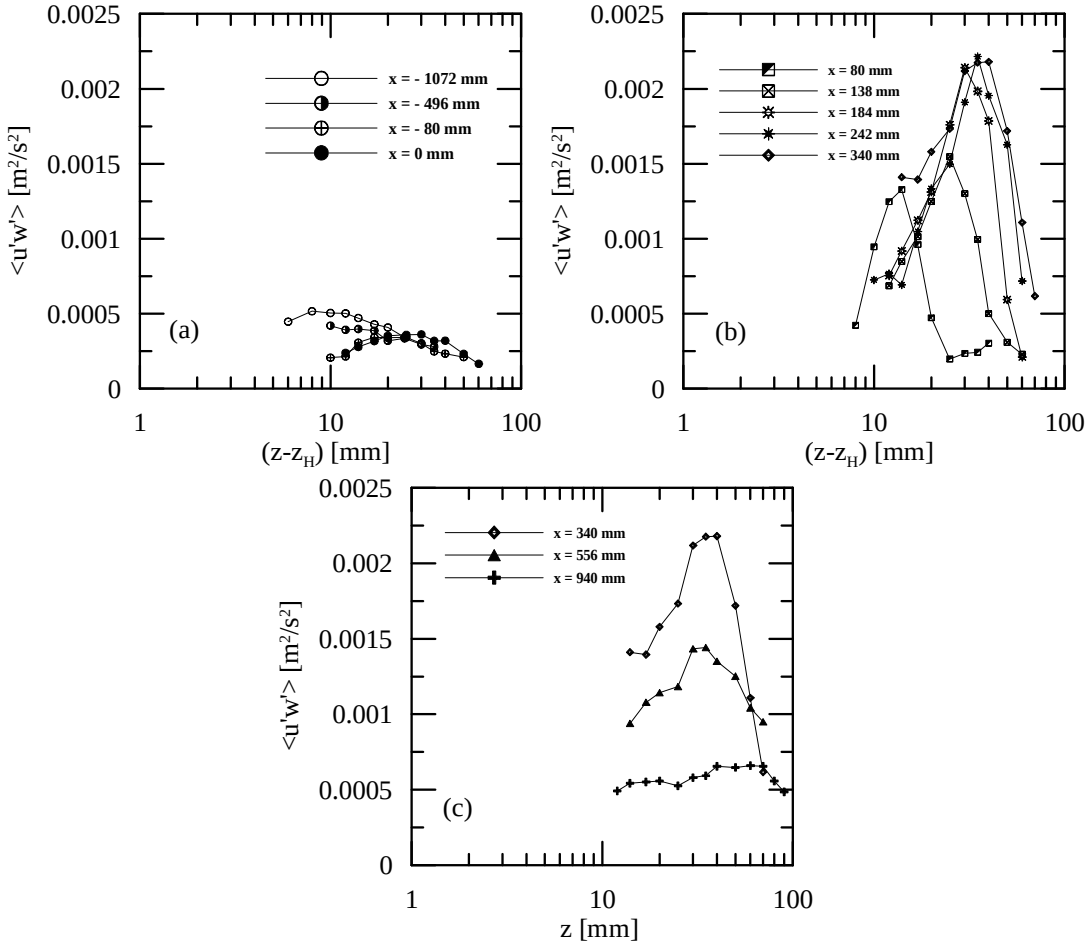

Figure 7: Reynolds stress profiles measured along the hill.

7. References

Arya, S. P. S. and Shipman, M. S.; "An Experimental Investigation of Flow and Diffusion in The Disturbed Boundary-layer Over a Ridge, Part I: Mean Flow and Turbulence Structure", Atmospheric Environment, vol. 15, 1173-1184, 1986.

Arya, S. P. S., Capuano, M. E. and Fagen, L. C.; "Some Fluid Modelling Studies of Flow and Dispersion Over Two-Dimensional Low Hills", Atmospheric Environment, vol. 21, 753-764, 1987.

Athanassiadou, M. E Castro, I. P., "Neutral Flow Over a Series of Rough Hills: A Laboratory Experiment", Boundary-Layer Meteorology, vol. 101, 1-30, 2001.

Britter, R. E., Hunt, J. C. R. and Richards, K. J.; "Airflow Over a Two-dimensional Hill: Studies of Velocity Speedup, Roughness Effects and Turbulence", Q. J. R. Meteorological Society, vol. 107, 91-10, 1981.

Castro, I. P. and Apsley, D. D.: 'Flow and dispersion over topography: a comparison between numerical and laboratory data for two-dimensional flows', Atmospheric Environment, 31, 839–850, 1997.

Jackson, P. S. and Hunt, J. C. R.; "Turbulent Wind Flow Over a Low Hill", Q. J. R. Meteorological Society, vol. 101, 929-955, 1975.

Jackson, P. S., "On the displacement height in the logarithmic velocity profile", J. Fluid Mech., 111, pp. 15-25, 1981.

Gyure, B. and Janosi, I. M.; "Stratified Flow Over Asymmetric and Double Bell–shaped Obstacles", Dynamics of Atmospheres and Oceans, vol. 37, 155-170, 2003.

Long, R. R.; "The Motion of Fluids with Density Stratification", J. Geophysical Research, vol. 64, 2151–2163, 1959.

Loureiro, J. B. R., Vasques, F. S., Rodrigues, D. A., Terra, R. J. and Silva Freire, A. P.; "A wind tunnel study of turbulent flow over hills. Part II: Large changes in surface elevation", VII National Congress of Thermal Sciences (ENCIT) , Porto Alegre, October, 2000b.

Loureiro, J. B. R., Cataldi, M. and Silva Freire, A. P.; "An experimental study of turbulent stratified flows over

hills with large changes in surface elevation", XVI Brazilian Congress of Mechanical Engineering (COBEM), Uberlândia, December, 2001.

Loureiro, J. B. R., Soares, D. V., Fontoura Rodrigues, J. L. A., Pinho, F. T. and Silva Freire, A. P.; "Investigation of turbulent flow over a steep hill using laser Doppler anemometry.", XVI Brazilian Congress of Mechanical Engineering (COBEM), Ouro Preto, December, 2005.

Loureiro, J. B. R., Soares, D. V., Fontoura Rodrigues, J. L. A., Pinho, F. T. and Silva Freire, A. P.; "Water tank and numerical model studies of flow over steep smooth two-dimensional hills.", Boundary-layer Meteorology, in press, 2006.

Malhi, Y.; "The Behaviour of The Roughness Length for Temperature Over Heterogeneous Surfaces", Q. J. R. Meteorological Society, vol. 122, 1095–1125, 1996.

Meroney, R. N.; "Fluid Dynamics of Flow Over Hills/Mountains - Insights Obtained Through Physical Modeling", In: Atmospheric Processes Over Complex Terrain, Chapter 7, 145-171, American Meteorological Society, 1990.

Perry, A.E. and Joubert, P.N., "Rough-wall boundary layers in adverse pressure gradients", J. Fluid Mech, 17, 193-211, 1963.

Ross, A. N., Arnold, S., Vosper, S. B., Mobbs, S. D., Nixon, N. and Robins, A. G.: A comparison of wind-tunnel experiments and numerical simulations of neutral and stratified flow over a hill, Boundary Layer Meteorology, vol. 113, 427-459, 2004.

Simpson, R. L., Long, C. H. and Byun, G.: 'Study of vortical separation from an axisymmetric hill', Int. J. Heat and Fluid Flow, 23, 582–591, 2002.

Snyder, W. H. and Britter, R. E., 'A wind tunnel study of the flow structure and dispersion from sources upwind of three-dimensional hills', Atmospheric Environment, 21, 735–751, 1987.

Snyder, W. H., Thompson, R. S., Eskridge, R. E., Lawson, R. E., Castro, I. P., Lee, J. T., Hunt, J. C. R. and Ogawa, Y.; The structure of strongly stratified flow over hills: dividing streamline concept", J. Fluid Mechanics, 152, 249-288, 1985.

Townsend, A. A.; "Structures of Turbulent Shear Flow", Cambridge University Press, 1972.

Ying, R. and Canuto, V. M.: "Numerical simulation of the flow over two-dimensional hills using a second-order turbulence closure model", Boundary Layer Meteorology, 85, 447–474, 1997.

Wang, C., Jang, Y. J. and Leschziner, M. A.: 'Modelling two- and three-dimensional separation from curved surfaces with anisotropy-resolving turbulence closures', Int. J. Heat and Fluid Flows, 25, 499–512, 2004.

Wood, N.: 'Wind flow over complex terrain: a historical perspective and the prospect for large-eddy modelling', Boundary Layer Meteorology, 96, 11–32, 2000.

Zeman, O. and Jensen, N. O.: 'Modification of turbulence characteristics in flow over hills', Q. J. R. Meteorological Society, 113, 55–80, 1987.

Proceedings of the 11th Brazilian Congress of Thermal Sciences and Engineering -- ENCIT 2006
Braz. Soc. of Mechanical Sciences and Engineering -- ABCM, Curitiba, Brazil,- Dec. 5-8, 2006

Paper CIT06-0733

ON THE SOLUTION OF DIFUSION-CONVECTION PROBLEMS BY MEANS OF RBF APPROXIMATIONS

Marcelo J. Colaço
Military Institute of Engineering
Department of Mechanical Engineering
Pç Gen. Tibúcio, 80, Rio de Janeiro, RJ, 22290-270, Brazil
colaco@ime.eb.br

Helcio R. B. Orlande
Federal University of Rio de Janeiro
Department of Mechanical Engineering
Cx. Postal 68503, Rio de Janeiro, RJ, 21945-970, Brazil
helcio@mecanica.coppe.ufrj.br

Nilson C. Roberty
Federal University of Rio de Janeiro
Department of Nuclear Engineering
Cx. Postal 68503, Rio de Janeiro, RJ, 21945-970, Brazil
nilson@con.ufrj.br

Carlos Alves
Instituto Superior Técnico
Department of Mathematics
Av. Rovisco Pais, 1049-001, Lisboa Codex, Portugal
calves@math.ist.utl.pt

Vitor Leitão
Instituto Superior Técnico
Department of Civil Engineering
Av. Rovisco Pais, 1049-001, Lisboa Codex, Portugal
vitor@civil.ist.utl.pt

Abstract. *In this work we use the Kansa's Method, also known as Radial Basis Functions Collocation Method to solve diffusive problems, like steady-state heat transfer and also convective-diffusive problems, like the incompressible steady-state Navier-Stokes equations. No pressure-velocity schemes neither the so called artificial compressibility scheme are used. Also, no interpolation function is needed for the convective terms. In fact, the solution of the original problem is reduced to the solution of a simple system of algebraic equations. Test-cases of practical interest are examined in the paper.*

Keywords. *Meshless Methods, RBF, Linear Heat Conduction, Forced Convection*

1.Introduction

The recent advances in computer technology have provided powerful tools for the simulation of natural phenomenon. Numerical schemes such as finite volume method, finite difference method and the finite element method becomes very popular among them, as they have been studied from its numerical aspects and widely used in various areas. Their success mainly relies on the mesh of good quality. Thus, mesh generation often challenge the numerical simulations associated with industrial and environmental applications, especially for those problems with complex geometry.

Recent development in the automatic mesh generation techniques for mesh-based methods relieves the difficulties. However, to maintain detailed structural information about the computational mesh is still expensive. These make mesh generation, modification, and re-meshing a very complicated task for programmers, mathematicians and engineering.

To overcome the above mentioned difficulties, mesh-free and meshless methods are been developed. Seeking to avoid the drawbacks or weakness of the standard numerical methods, and yet preserving the ability to accommodate geometric complexity. From the viewpoint of kernel interpolation/approximation techniques, many mesh-free methods are based on the moving least square technique. This group of mesh-free methods has been successfully applied to many practical but difficult problems in engineering that are to be solved by the traditional mesh-based methods.

One of the most popular mesh-free kernel approximation technique is radial basis functions (RBFs). Initially, RBFs were developed for multivariate data and function interpolation. It was found that RBFs were able to construct an

interpolation scheme with favorable properties such as high efficiency, good quality and capability of dealing with scattered data, especially for higher dimension problems. It is well-known that a good interpolation scheme also has great potential for solving partial differential equations. It was Kansa who made the first step forward in employing RBFs to deal with PDEs. He proposed a simple collocation method using RBFs.

In the present study, the same RBF are used to interpolated velocity and pressure in a two-dimensional Pouiseulle flow without heat transfer numerical experiment. In the second part of the paper, a RBF approximated solution is tested against an analytical solution for a laminar thermally developing flow inside a parallel plate channel.

2. RBF Background

Radial basis functions are essential ingredients of the techniques generally known as "meshless methods". In a way or another all meshless techniques require some sort of radial function to measure the influence of a given location on another part of the domain.

The use of radial basis functions (RBF) followed by collocation, a technique first proposed by Kansa (Kansa, 1990), after the work of Hardy (Hardy, 1971) on multivariate approximation, is now becoming an established approach and various applications to problems of structures and fluids have been made in recent years – see, for example Leitão (Leitão, 2001; Leitão, 2004).

Kansa's method (or asymmetric collocation) starts by building an approximation to the field of interest (normally displacement components) from the superposition of radial basis functions (globally or compactly supported) conveniently placed at points in the domain (and, or, at the boundary).

The unknowns (which are the coefficients of each RBF) are obtained from the (approximate) enforcement of the boundary conditions as well as the governing equations by means of collocation. Usually, this approximation only considers regular radial basis functions, such as the globally supported multiquadrics or the compactly supported Wendland (Wendland, 1998) functions.

Radial basis functions (RBFs) may be classified into two main groups:

1. the globally supported ones namelly the multiquadric (MQ, $\sqrt{\left(x-x_j\right)^2+c_j^2}$, where c_j is a shape parameter), the inverse multiquadric, thin plate splines, guassians, etc;
2. the compactly supported ones such as the Wendland (1998) family (for example, $(1-r)_+^n + p\left(r\right)$ where $p(r)$ is a polynomial and $(1-r)_+^n$ is 0 for r greater than the support).

In a very brief manner, interpolation with RBFs may take the form:

$$s\left(x_i\right) = f\left(x_i\right) = \sum_{j=1}^{N} \alpha_j \phi\left(\left|x_i - x_j\right|\right) + \sum_{k=1}^{\hat{N}} \beta_k p_k\left(x_i\right) \tag{1}$$

where $f(x_i)$ is known for a series of points x_i and $p_k(x_i)$ is one of the $\hat{N}$ terms of a given basis of polynomials, see Buhmann (Buhmann, 2003). This approximation is solved for the α_j unknowns from the system of N linear equations, subject to the conditions (for the sake of uniqueness) $\sum_{j=1}^{N} \alpha_j p_k\left(x_j\right) = 0$.

By using the same reasoning it is possible to extend the interpolation problem to that of finding the approximate solution of partial differential equations. This is made by applying the corresponding differential operators to the radial basis functions and then to use collocation at an appropriate set of boundary and domain points.

In short, the non-symmetrical collocation is the application of the domain and boundary differential operators *LI* and *LB*, respectively, to a set of *N-M* domain collocation points and *M* boundary collocation points.

From this, a system of linear equations of the following type may be obtained

$$\begin{aligned} LIu_h\left(x_i\right) &= \sum_{j=1}^{N} \alpha_j LI\phi\left(\left|x_i - \varepsilon_j\right|\right) + \sum_{k=1}^{\hat{N}} \beta_k LIp_k\left(x_i\right) \\ LBu_h\left(x_i\right) &= \sum_{j=1}^{N} \alpha_j LB\phi\left(\left|x_i - \varepsilon_j\right|\right) + \sum_{k=1}^{\hat{N}} \beta_k LBp_k\left(x_i\right) \end{aligned} \tag{2.a,b}$$

subject to the conditions $\sum_{j=1}^{N} \alpha_j p_k\left(x_j\right) = 0$ where the α_j and β_k unknowns are determined from the satisfaction of the domain and boundary constraints at the collocation points.

3. Numerical Examples

In this paper, we used the Kansa's Method to solve two different sample problems dealing with convection-diffusion equations. The main purpose of this section is to compare the results obtained through the RBF approximations with the benchmark solutions of these problems found in the literature.

3.1. Pouiseulle Flow

In this section, we will present the approximate results obtained by the RBF expansion for the hydrodynamically developing flow, without heat transfer, within a parallel plate channel with length L and weight h. The mathematical formulation for this problem is given by the mass, x-momentum and y-momentum conservation equations

$$\frac{\partial u}{\partial x}+\frac{\partial v}{\partial y}=0 \quad \text{in } 0<x<L;\ 0<y<h \tag{3.a}$$

$$u\frac{\partial u}{\partial x}+v\frac{\partial u}{\partial y}=\frac{\mu}{\rho}\left(\frac{\partial^2 u}{\partial x^2}+\frac{\partial^2 u}{\partial y^2}\right)-\frac{1}{\rho}\frac{\partial P}{\partial x} \quad \text{in } 0<x<L;\ 0<y<h \tag{3.b}$$

$$u\frac{\partial v}{\partial x}+v\frac{\partial v}{\partial y}=\frac{\mu}{\rho}\left(\frac{\partial^2 v}{\partial x^2}+\frac{\partial^2 v}{\partial y^2}\right)-\frac{1}{\rho}\frac{\partial P}{\partial y} \quad \text{in } 0<x<L;\ 0<y<h \tag{3.c}$$

subjected to the following boundary conditions

$$u=u_0 \qquad \text{at } x=0;\ 0<y<\text{h} \tag{4.a}$$

$$v=0 \qquad \text{at } x=0;\ 0<y<h \tag{4.b}$$

$$u=v=0 \qquad \text{at } y=0 \text{ and } y=h;\ 0<x<L \tag{4.c}$$

where no boundary condition is assumed to $x=L$; $0<y<h$. Classical numerical methods, like the Finite Volume Method and the Finite Difference Method need to use some kind of pressure-velocity coupling scheme, like the SIMPLEC (Van Doormaal and Raithby, 1984), in order to obtain velocity fields in the x and y-momentum equations that satisfies the mass conservation equation. Also, the convective terms are usually treated by some sort of hybrid or upwind method, like the WUDS (Raithby and Torrance, 1974) and the UTOPIA (Leonard et al, 1995). In this section, instead, we will expand the variables u, v and P by using the following expressions

$$u(x,y)=\sum_{i=1}^{N}\phi_i\psi(\mathbf{r}_i) \tag{5.a}$$

$$v(x,y)=\sum_{j=1}^{N}\phi_j\psi(\mathbf{r}_j) \tag{5.b}$$

$$P(x,y)=\sum_{k=1}^{N/\partial\Omega}\phi_k\psi(\mathbf{r}_k) \tag{5.c}$$

where the functions ψ are the same for the three expansions, but the parameters ϕ are different for each one. Also, the number N and the locations $\mathbf{r}$ of the centers are the same for the u and v expansions. The expansion for the pressure doesn't include the boundary of the domain, since this would imply in an over-specified condition. In other words, if one specify the velocity at the entrance, there is no need to specify also the pressure.

Using Eqs. (5) into Eqs. (3) and (4) we obtain

$$\sum_{i=1}^{N}\phi_i\frac{\partial\psi_i}{\partial x}+\sum_{j=1}^{N}\phi_j\frac{\partial\psi_j}{\partial x}=0 \quad \text{in } 0<x<L;\ 0<y<h \tag{6.a}$$

$$\left(\sum_{i=1}^{N}\phi_i\psi_i\right)\left(\sum_{i=1}^{N}\phi_i\frac{\partial\psi_i}{\partial x}\right)+\left(\sum_{j=1}^{N}\phi_j\psi_j\right)\left(\sum_{i=1}^{N}\phi_i\frac{\partial\psi_i}{\partial y}\right)=\frac{\mu}{\rho}\left(\sum_{i=1}^{N}\phi_i\frac{\partial^2\psi_i}{\partial x^2}+\sum_{i=1}^{N}\phi_i\frac{\partial^2\psi_i}{\partial y^2}\right)-\frac{1}{\rho}\sum_{k=1}^{N/\partial\Omega}\phi_k\frac{\partial\psi_k}{\partial x} \quad \text{in } 0<x<L;\ 0<y<h \tag{6.a}$$

$$\left(\sum_{i=1}^{N}\phi_i\psi_i\right)\left(\sum_{j=1}^{N}\phi_j\frac{\partial\psi_j}{\partial x}\right)+\left(\sum_{j=1}^{N}\phi_j\psi_j\right)\left(\sum_{j=1}^{N}\phi_j\frac{\partial\psi_j}{\partial y}\right)=\frac{\mu}{\rho}\left(\sum_{j=1}^{N}\phi_j\frac{\partial^2\psi_j}{\partial x^2}+\sum_{j=1}^{N}\phi_j\frac{\partial^2\psi_j}{\partial y^2}\right)-\frac{1}{\rho}\sum_{k=1}^{N/\partial\Omega}\phi_k\frac{\partial\psi_k}{\partial x} \quad \text{in } 0<x<L;\ 0<y<h \tag{6.a}$$

$$\sum_{i=1}^{N}\phi_i\psi_i=u_0 \qquad \text{at } x=0;\ 0<y<h \tag{7.b}$$

$$\sum_{i=1}^{N} \phi_j \psi_j = 0 \qquad \text{at } x=0;\ 0<y<h \tag{7.b}$$

$$\sum_{i=1}^{N} \phi_i \psi_i = \sum_{i=1}^{N} \phi_j \psi_j = 0 \qquad \text{at } y=0 \text{ and } y=h;\ 0<x<L \tag{7.c}$$

which results in a non-linear system for ϕ_i, ϕ_j and ϕ_k that can be solved by a quasi-Newton method. Note that no pressure-velocity coupling neither an upwind method was used.

For this comparison, we considered water at 20 ^{o}C, with the following physical properties: ρ=1000.52 kg/m^3, μ=0.001 kg/m.s. The height of the channel was taken as 0.05 m and the mean velocity was taken as 0.001 m/s, which gives a Reynolds number equal to 100. In order to validate the results with an analytical solution, the length of the channel was taken in order to have a fully developed flow. According to Bodoia and Osterle (1961), such length is given as

$$\frac{L}{2h\,\mathrm{Re}} = 0.0110 \tag{8.a}$$

which results in L=0.11 m. For the fully developed flow, the velocity profile is given as

$$u(y) = -\frac{6u_{av}}{h^2}\left(y^2 - hy\right) \tag{8.b}$$

where u_{av} is the average velocity along the y-direction and v is zero everywhere.

Figure (1) shows the results obtained by using a multiquadrics function given by

$$\phi_i(x,y) = \left[(x-x_i)^2 + (y-y_i)^2 + c_i^2\right]^{\beta} \tag{9}$$

where the exponent β was varied and the parameter c was automatically obtained by the minimization of the mean square root of the residual of Eqs. (6) and (7). Note the large discrepancy of the results, when comparing the percentual errors appearing in Fig. (1.b).

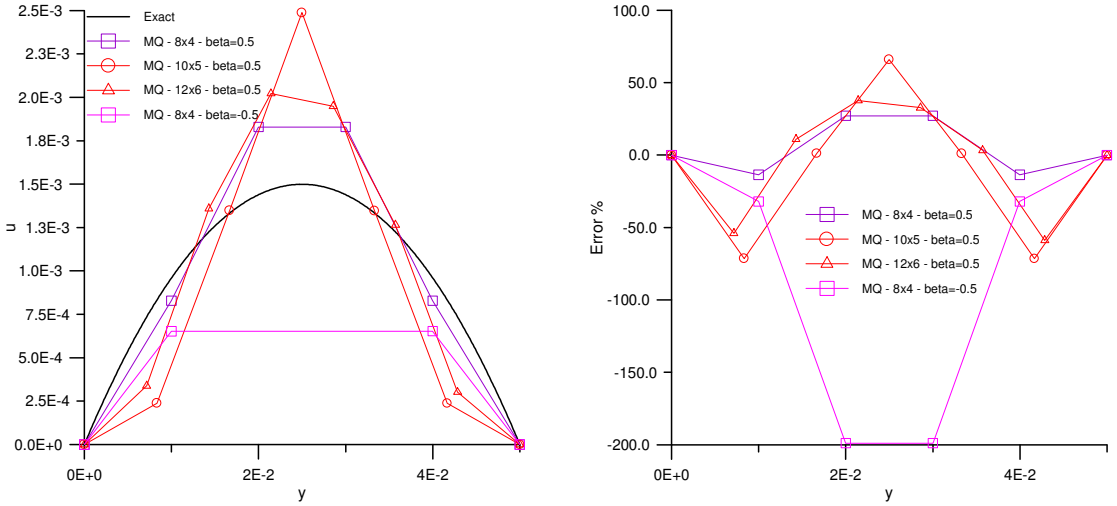

(a) (b)

Figure 1. Results using the multiquadrics approximation

Figure (2) shows the results obtained by using Wendland functions given by

$$\text{W41:}\quad \phi_i(x,y) = \left(\sqrt{(x-x_i)^2 + (y-y_i)^2} - 1\right)_+^4 \left(1 + 4\sqrt{(x-x_i)^2 + (y-y_i)^2}\right) \tag{10.a}$$

$$\text{W42:}\quad \phi_i(x,y) = \left(\sqrt{(x-x_i)^2 + (y-y_i)^2} - 1\right)_+^6 \left\{3 + 18\sqrt{(x-x_i)^2 + (y-y_i)^2} + 35\left[(x-x_i)^2 + (y-y_i)^2\right]\right\} \tag{10.b}$$

$$\text{W43:}\quad \phi_i(x,y)=\left(\sqrt{(x-x_i)^2+(y-y_i)^2}-1\right)_+^8 \left\{1+8\sqrt{(x-x_i)^2+(y-y_i)^2}+25\left[(x-x_i)^2+(y-y_i)^2\right]+32\left[(x-x_i)^2+(y-y_i)^2\right]^{3/2}\right\} \tag{10.c}$$

Note that the solutions are better than those presented in Fig. (1). Also the percentual errors are lower as shown in Fig. (1.b). In all these solutions, the number of expansion points is limited by the ill-conditioness of the problem. Large centers imply in a more ill-conditioned problem. Note, also in Fig. (1.b) that the Wendland function W41 is better than the W42 and W43, for this problem.

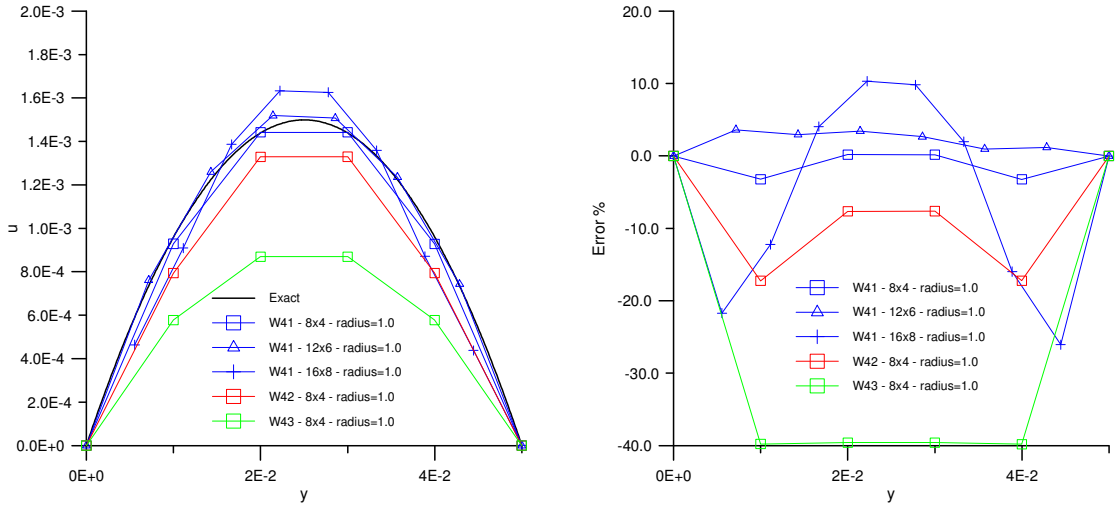

(a) (b)

Figure 2. Results using the Wendland approximation

It is quite interesting that the W41 function with only 8x4 centers presented a relative error less than 3 %. Just for comparison, the same problem solved by the Finite Volume Method, using the SIMPLEC pressure velocity scheme and the WUDS interpolation scheme with 50x60 grid cells (Colaço, 2001), gives an relative error equal to 1.43 % at y=0.4 mm. This is quite remarkable when one check that this result was obtained only in 0.84 seconds, as showed in Table (1).

Table 1 – Computational time

Type of function	Points in the expansion	Expoent - β	Shape factor - c	Residual - ε	CPU time (seconds)
MQ	8x4	0.5	0.001	8.35 E-5	1.40
		-0.5	0.001	1.76 E-5	1.45
	10x5	0.5	0.0002	1.68 E-5	4.32
	12x6	0.5	0.0005	5.31 E-5	11.11
W41	8x4	N/A			0.84
	10x5				7.38
	12x6				6.06
	16x8				61.93
W42	8x4				1.78
W43					2.91

Finally, Fig. (3) shows the plot of the velocity component u along the entire channel obtained by the W41 approximation with 16x8 points and by the FVM with a 50x60 grid cells (Colaço, 2001). One can see that the W41 expansion gives a reasonable approximation, considering its very low computational cost and the low number of centers.

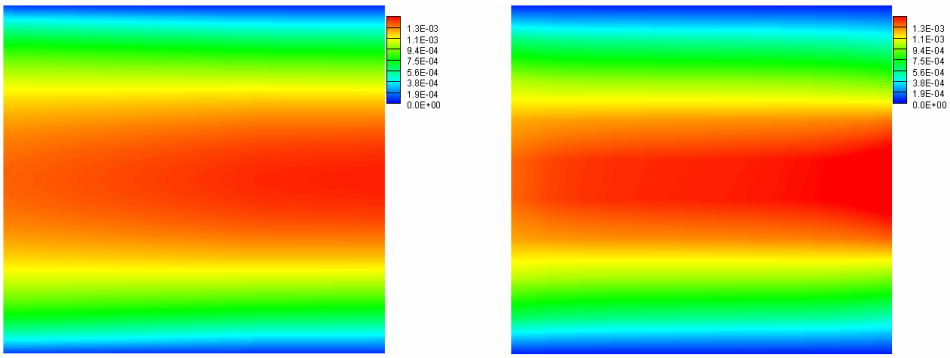

(a) (b)

Figure 3. Component *u* of velocity field obtained from the (a) FVM and (b) RBF solutions

3.2. Thermally Developing Flow

In this section, the RBF approximation solution was tested against an analytical solution (Cotta and Özisik, 1986) for a laminar thermally developing flow inside a parallel plate channel with length L and weight h, subjected to a constant heat flux q at the walls. The density ρ, the conductivity k and the specific heat at constant pressure c_p were considered constants, and the mathematical formulation for this steady-state problem is given by the following energy equation

$$u\frac{\partial T}{\partial x}+v\frac{\partial T}{\partial y}=\frac{k}{\rho\, c_p}\left(\frac{\partial^2 T}{\partial x^2}+\frac{\partial^2 T}{\partial y^2}\right) \quad \text{in } 0<x<L;\ 0<y<h \tag{11.a}$$

subjected to the following boundary conditions

$$T=T_0 \qquad \text{at } x=0;\ 0<y<h \tag{11.b}$$

$$k\frac{\partial T}{\partial y}=q \qquad \text{at } y=0;\ 0<x<L \tag{11.c}$$

$$-k\frac{\partial T}{\partial y}=q \qquad \text{at } y=h;\ 0<x<L \tag{11.d}$$

where the velocity field was considered fully developed. Thus, u has a parabolic distribution given by Eq. (8.b)

The temperature T can be written as an RBF expansion over N centers distributed over the entire domain, including the boundaries. Note that in this approach there is no need to use an upwind scheme, since the derivatives of T are obtained directly from the following equation.

$$T(x,y)=\sum_{i=1}^{N}\phi_i\psi(\mathbf{r}_i) \tag{12}$$

where $\mathbf{r}_i$ is the distance between the point (x,y) and the center (x_i,y_i).

Thus, applying Eq. (12) to Eqs. (11.a)-(11.d) we obtain

$$u\sum_{i=1}^{N}\phi_i\frac{\partial\psi(\mathbf{r}_i)}{\partial x}+v\sum_{i=1}^{N}\phi_i\frac{\partial\psi(\mathbf{r}_i)}{\partial y}=\frac{k}{\rho\, c_p}\left[\sum_{i=1}^{N}\phi_i\frac{\partial^2\psi(\mathbf{r}_i)}{\partial x^2}+\sum_{i=1}^{N}\phi_i\frac{\partial^2\psi(\mathbf{r}_i)}{\partial y^2}\right] \quad \text{in } 0<x<L;\ 0<y<h \tag{13.a}$$

$$\sum_{i=1}^{N}\phi_i\psi(\mathbf{r}_i)=T_0 \qquad \text{at } x=0;\ 0<y<h \tag{13.b}$$

$$k\sum_{i=1}^{N}\phi_i\frac{\partial\psi(\mathbf{r}_i)}{\partial y}=q \qquad \text{at } y=0;\ 0<x<L \tag{13.c}$$

$$-k\sum_{i=1}^{N}\phi_i\frac{\partial\psi(\mathbf{r}_i)}{\partial y}=q \quad \text{at } y=h;\ 0<x<L \tag{13.d}$$

or, in matricial form

$$\mathbf{\Psi\Phi}=\boldsymbol{\beta} \tag{14}$$

where $\mathbf{\Psi}$ is the matrix of the RBF functions and their derivatives, $\mathbf{\Phi}$ is the vector of the unknown parameters and $\boldsymbol{\beta}$ is the RHS of the equations. Since the velocity field is known, the problem is linear.

The analytical solution of this problem was obtained by Cotta and Özisik (1986) and it was given in terms of the Nusselt number at the top surface of the channel as a function of the non-dimensional axial length, which are given as

$$Nu(Z)=\frac{2hq}{k[T(x,y=h)-T_{av}(x)]};\quad Z=\frac{(k/\rho c_p)x}{4u_{av}h^2} \tag{15.a,b}$$

where u_{av} is the mean velocity in the x direction and T_{av} is the average temperature, defined as

$$T_{av}=\frac{\int_0^h u(x,y)T(x,y)dy}{u_{av}h} \tag{16}$$

For this comparison, we considered water at 20 ^{o}C, with the following physical properties: ρ=1000.52 kg/m^3, k=0.597 W/m.K, c_p=4.1818 KJ/kg.^{o}C. The height of the channel was taken as 0.05 m and the length as 1 m. The mean velocity was taken as 0.001 m/s, which gives a Reynolds number equal to 100. Notice that the total length is not large enough to have the flow fully thermally developed. According to the results of Cotta and Özisik (1986), the total length should be approximately equal to 7 m. However, we are interested only in the portion close to the entrance, where the variation of the Nusselt number is very large.

Figure (4.a) shows the results obtained by Colaço (2001) using the Finite Volume Method, with a WUDS scheme for the convective terms, for a length equal to 7 m and Figure (4.b) shows the same graphic for 0<x<1.

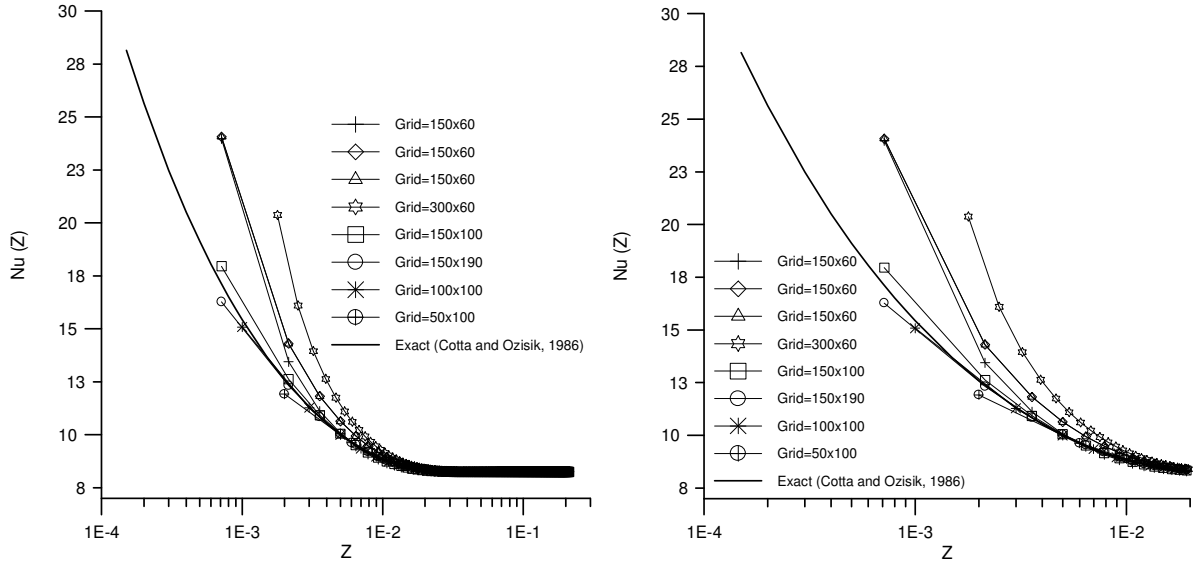

Figure 4. Results using the Finite Volume Method (Colaço and Orlande, 2001)

Note, from Fig. (4), that all grids are capable of estimate the Nusselt number at the fully developed region, but there are large discrepancies close to the entrance. In fact, the better results are obtained by using 100x100 and 150x190 grid cells.

In Fig. (5) the MQ results were obtained by using the multiquadrics expression given by Eq. (9). The W4x expansions were defined by using the Wendland compact form as showed in Eqs. (10.a)-(10.c)

Figure (5.a) shows very poor results when using β=0.5 for 80x4, 100x5 and 120x6 grid points. Although the solution by RBF's doesn't require a uniform distribution of points, we choose a uniform distribution in order to

compare with the results presented in Fig. (4). We also tried the Wendland's function for this test case, but the results were very poor, as one can see from Fig. (5.a).

Note, in Fig. (5.b), the great improvement in the solution when we used β = -0.5 for the 120x6 expansion, when compared with β = 0.5 from Fig. (5.a). Also, other values of β show better results than those from Fig. (5.a). Figure (5.c) shows the results for a 140x7 expansion, when the results are even better, although still far away from the analytical solution from Cotta and Özisik. It is interesting to note the small number of points in the *y*-direction for all test cases.

Also, Fig. (5.d) shows the results obtained through the RBF, when compared with those obtained by the Finite Volume Method. It is very interesting to note the dependency of the FVM solution with the number of points in the *y* direction as one can see by comparing the results obtained by using 150x60 with 60x100 grid cells. This fact doesn't occur with the RBF solutions.

It is worth to mention that the better RBF solution is still very poor when compared with the better FVM solution. In fact, when one tries to increase the number of centers in the RBF approximation beyond the ones presented in the Fig. (5), the system becomes too ill-conditioned to solve and no physical solution is obtained. Also, all the RBF solutions presented here were obtained after a proper choice of the shape parameter *c*, appearing in Eq. (9). Such choice was made in order to minimize the residual of the Eq. (14), defined as:

$$\varepsilon = \left\| \boldsymbol{\Psi\Phi} - \boldsymbol{\beta} \right\| \tag{17}$$

where ||.|| denotes the Euclidian norm of the vector.

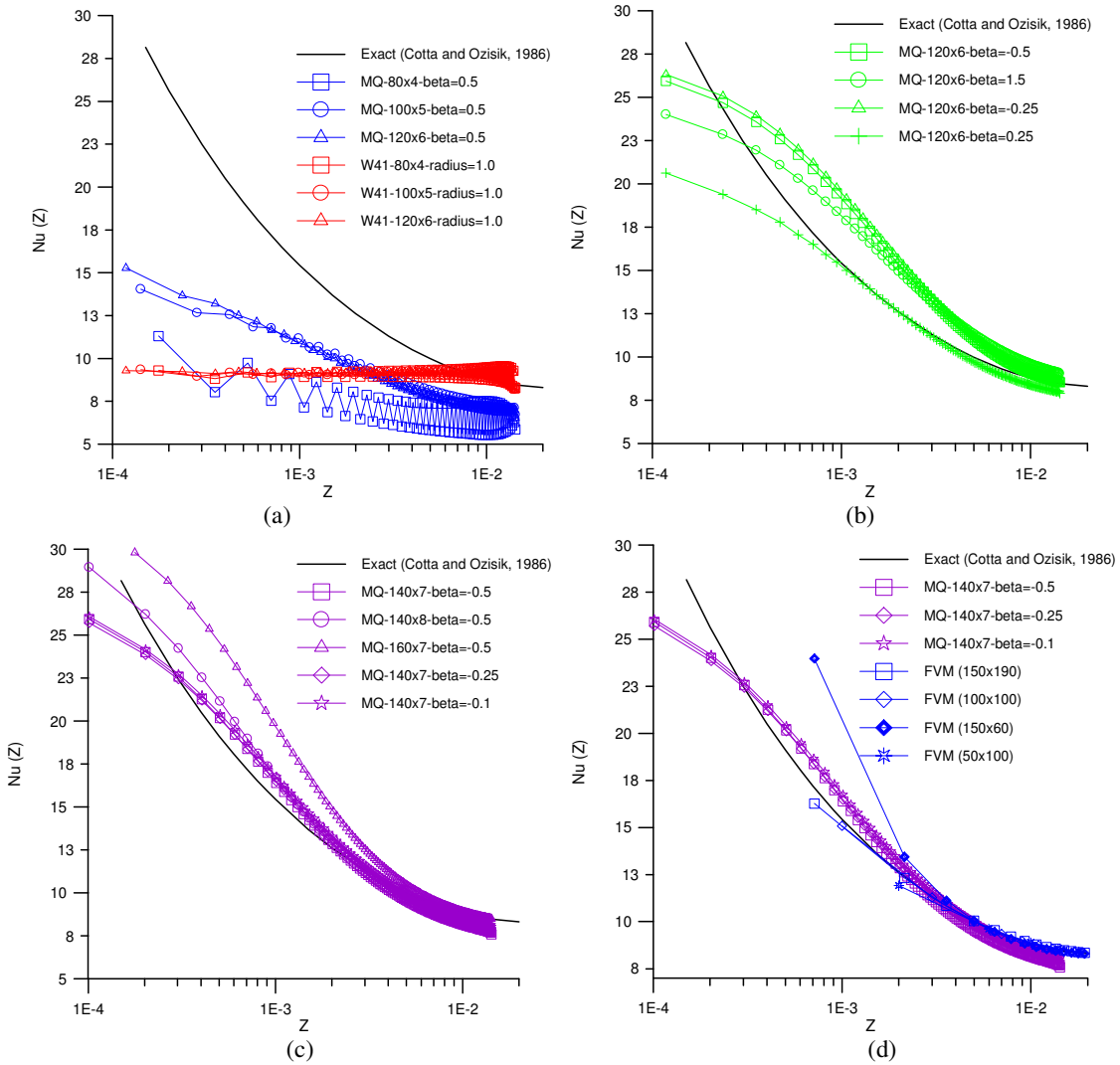

Figure 5. Results using the RBF expansion

Finally, Table (2) presents the shape parameter used in each one of the expansion, as well as the CPU time in seconds (in an Intel Centrino 1.5 GHz with 1.5 Gb RAM) and the value of the residual ε. While the RBF results presented in Fig. (5) don't present a very good accuracy, when compared with the analytical solution, the execution time obtained in their solution is very small (less than 2 seconds) and they can used as an estimative of the correct answer. Also, if better solvers for the linear system were used and a better choice of the shaper parameter c or the exponent β was employed, better results could be obtained. Note also that the general temperature field is similar for the two methods, as one can see in Fig. (6) for the FVM with 100x100 grid cells (Colaço, 2001) and for the RBF with 140x7 points. The sharpness of the RBF solution is due to the lack of points in the y-direction (only 7 against 100 in the FVM).

Table 2 – Results from the RBF expansion

Points in the expansion	Shape parameter - c	Expoent - β	Residual - ε	CPU time (seconds)
80x4	0.003	0.5	7495	0.08
120x6	0.043	-0.5	1295	0.81
	0.011	1.5	41049381	0.79
	0.043	-0.25	1185	0.88
	0.015	0.25	8564	0.78
	0.004	0.5	2311	0.83
100x5	0.006		9790	0.33
140x7	0.024	-0.5	9614	1.96
	0.021	-0.25	2504	1.98
	0.001	0.5	44736	1.96
	0.020	-0.1	3084	1.98
140x8	0.023	-0.5	5158	2.6
160x7	0.038		6575	2.9

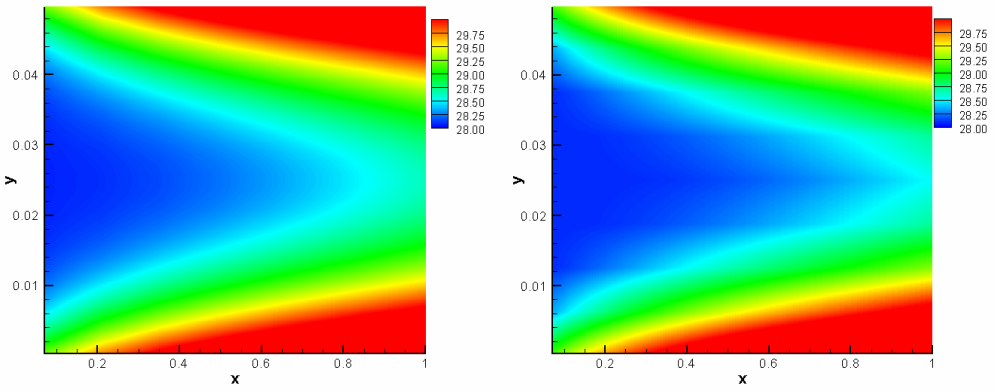

(a) (b)

Figure 6. Temperature field obtained from the (a) FVM and (b) RBF solutions

4. Acknowledgements

This work was partially funded by CNPq, CAPES (agencies for the fostering of science from the Brazilian Ministry of Science and Education, respectively) and GRICES (agency for the fostering of science from the Portugal Ministry of Science and Education).

5. References

Bodoia, J.R. and Osterle, J.F., 1961, "Finite Difference Analysis of Plane Poiseuilee an d Couette Flow Developments", Appl. Sci. Res., A10, pp. 265-276.

Buhmann, M.D., 2003, "Radial Basis Functions on Grids and Beyond", International Workshop on Meshfree Methods, Lisbon.

Colaço, M.J., 2001, "Inverse Convection Problems in Irregular Geometries", D.Sc. Thesis, COPPE/UFRJ.

Cotta, R.M. and Özisik, M.N., 1986, "Laminar Forced Convection to Non-Newtonian Fluids in Ducts with Prescribed Wall Heat Flux", Int. Comm. Heat & Mass Transver, Vol. 13, Iss. 3, May-June.

Hardy, R.L., 1971, "Multiquadric Equations of Topography and Other Irregular Surfaces", Journal of Geophysics Res., Vol. 176, pp. 1905-1915.

Kansa, E.J., 1990, "Multiquadrics – A Scattered Data Approximation Scheme with Applications to Computational Fluid Dynamics – II: Solutions to Parabolic, Hyperbolic and Elliptic Partial Differential Equations", Comput. Math. Applic., Vol. 19, pp. 149-161.

Leitão, V.M.A., 2001, "A Mesheless Method for Kirchhoff Plate Bending Problems", International Journal of Numerical Methods in Engineering, Vol. 52, pp. 1107-1130.

Leitão, V.M.A., 2004, "RBF-Based Meshless Methods for 2D Elastostatic Problems", Engineering Analysis with Boundary Elements, Vol. 28, pp. 1271-1281.

Leonard, B.P., MacVean, M.K. and Lock, A.P., 1995, "The Flux Integral Method for Multidimensional Convection and Diffusion", Appl. Math. Modelling, Vol. 19, pp. 333-342.

Raithby, G.D. and Torrance, K.E., 1974, "Upstream-Weighted Differencing Scheme and their Application to Elliptic Problems Involving Fluid Flow", Computers & Fluids, Vol. 2, pp. 191-206.

Van Doormaal, J.P. and Raithby, G.D., 1984, "Enhancements of the SIMPLE Method for Predicting Incompressible Fluid Flow", Numerical Heat Transfer, Vol. 7, pp. 147-163.

Wendland, H., 1998, "Error Estimates for Interpolation by Compactly Supported Radial Basis Functions of Minimal Degree", Journal of Approximation Theory, Vol. 93, pp. 258-272.

6. Copyright Notice

Proceedings of the 11th Brazilian Congress of Thermal Sciences and Engineering -- ENCIT 2006
Braz. Soc. of Mechanical Sciences and Engineering -- ABCM, Curitiba, Brazil, Dec. 5-8, 2006

Paper CIT06-0734

ESCOAMENTO TURBULENTO MACROSCÓPICO EM UM CANAL COM UM LEITO POROSO FORMADO POR HASTES SÓLIDAS

Renato A. Silva
Marcelo J.S. de Lemos[1]
Departamento de Energia – IEME
Divisão de Engenharia Aeronáutica e Mecânica
Instituto Tecnológico de Aeronáutica – ITA
12228-900 – São José dos Campos, SP - Brasil
[1]Autor para correspondência, delemos@ita.br

Resumo. Neste trabalho é utilizado o conceito da média volumétrica para transportar os resultados numéricos, obtidos em um canal parcialmente preenchido com diversas hastes sólidas, do domínio "microscópico" para o domínio macroscópico. Através desta metodologia são obtidos os valores de permeabilidade e de porosidade da camada porosa, além disso, são analisados os efeitos do número de Darcy e da porosidade no comportamento do escoamento. Os resultados numéricos obtidos mostraram a necessidade de se contabilizar o efeito do regime do escoamento no cálculo da permeabilidade do meio poroso. Além disso, o comportamento dos resultados distribuídos encontrados na literatura corrobora o comportamento dos resultados aqui apresentados, indicando, em última análise, que a metodologia de integração utilizada preserva a maioria das informações do escoamento distribuído.

Palavras chave: escoamento turbulento, média volumétrica, meio poroso, meio limpo, método numérico.

1. Introdução

Os fenômenos de transporte em um canal com leito poroso são de interesse de várias áreas da ciência e engenharias tais como: hidrologia, sismologia, engenharia de petróleo, onde se faz necessário o entendimento da influência que esta região exerce sobre o comportamento do escoamento. Kuwahara et al. (1998) resolveram o escoamento interno a um meio poroso infinito formado por hastes quadradas com um arranjo espacialmente periódico, utilizando um modelo de turbulência de baixo Reynolds. Os autores constataram a presença de turbulência em $Re_H>10^4$ e que nessas condições o modelo estendido Darcy-Forchheimer apresenta bons resultados. Pedras e de Lemos (2001*a*-*b*) desenvolveram um modelo macroscópico de turbulência onde uma constante foi introduzida na equação da energia cinética de turbulência. O valor desta constante foi obtido através da simulação numérica do escoamento em um meio poroso formado por hastes cilíndricas, com um arranjo espacialmente periódico. Esta constante foi posteriormente ajustada para hastes elípticas longitudinal e transversal em Pedras e de Lemos (2001*c* e 2003). Silva e de Lemos (2003*a*-*b*) estenderam o modelo macroscópico de Pedras e de Lemos (2001*a*-*b*) para levar em conta a condição de salto de tensão cisalhante na interface proposto em Ochoa-Tapia e Whitaker (1995*a*. Prinos et al. (2003) investigaram numérica e experimentalmente as características do escoamento turbulento em um canal aberto com uma camada porosa formada de hastes cilíndricas. Neste trabalho, as equações de Navier-Stokes média, juntamente com modelo k-ε de baixo Reynolds são numericamente resolvidas na fase líquida ao redor das hastes sólidas. Na abordagem experimental foi utilizado um anemômetro de fio quente para medir os valores das velocidades médias e das tensões turbulentas. Os autores mostraram que os valores de velocidade na região limpa, tanto numericamente quanto experimentalmente diminuem com o aumento do número de Darcy, devido à intensa troca de quantidade de movimento próximo a interface entre o meio limpo e o meio poroso, e a correspondente penetração da turbulência na camada porosa para meios altamente permeáveis. Além disso, os autores constataram através de simulação numérica uma redução significativa da capacidade de descarga do canal, quando comparada com um canal com uma parede impermeável localizada na interface. Para escoamento laminar, Prinos et al. (2003), mostraram efeitos opostos do meio poroso sobre o escoamento no meio limpo. Kuznetsov e Xiong (2003) investigaram o escoamento em um duto parcialmente preenchido com material poroso, considerando que o escoamento é laminar devido à baixa penetração da turbulência na região porosa e na região limpa, turbulenta. No entanto este tipo de consideração é válido apenas para meios porosos com baixa permeabilidade. Kuznetsov e Becker (2004) propuseram um modelo matemático que levou em conta o efeito da rugosidade da interface entre um meio poroso e um meio limpo no comportamento termo-hidrodinâmico do escoamento turbulento, e constataram que esta abordagem leva a valores de Nusselt ligeiramente superiores aos encontrados para uma interface lisa. Breugem et al. (2004-2005) e Breugem e Boersma (2005) utilizaram a Simulação Numérica Direta (SND) para avaliar o fechamento do termo de arrasto na equações macroscópicas de Navier-Stokes e de dois modelos de transferência de quantidade de movimento para escoamento laminar sobre uma parede porosa. Os autores mostraram que a solução analítica de Ochoa-Tapia e Whitaker (1995b), para o perfil de velocidade, baseado no modelo de transferência de quantidade de movimento para a região de interface, apresentou uma boa concordância com a Simulação Numérica Direta. Além disso, os resultados mostraram que a permeabilidade depende não somente da porosidade, mas também do gradiente da velocidade de Darcy, implicando numa mudança para desenvolver novos

modelos para a variação da permeabilidade na região de interface. Silva e de Lemos (2005*a*-*b*) investigaram a interação entre as camadas de fluido acima e abaixo da interface entre um meio limpo e um meio contendo hastes sólidas. Os autores constataram, para escoamento laminar em um canal parcialmente preenchido com hastes sólidas, que a intensidade de mistura entre as camadas de fluido é inversamente proporcional ao número de Darcy. Por outro lado, para o escoamento turbulento, a intensidade de mistura entre as camadas de fluido e a penetração da turbulência na camada de hastes são diretamente proporcionais ao número de Darcy, isto é, o aumento do número de Darcy leva a um aumento da mistura entre as camadas de fluido e, conseqüentemente, da penetração da turbulência na camada com hastes.

Neste trabalho será apresentado a metodologia de integração utilizada para "passar" os resultados distribuídos ou "microscópicos" obtidos para o escoamento turbulento em Silva e de Lemos (2005b), para o domínio macroscópico. Para isto, serão utilizados os conceitos de média volumétrica e de célula de cálculo. Além disso, o efeito da porosidade e do número de Darcy no comportamento dos resultados macroscópicos serão analisados.

2. Metodologia de Integração

Os resultados numéricos obtidos em Silva e de Lemos (2005a) foram integrados na célula de cálculo apresentada na Figura 1, a qual percorre todo o domínio com deslocamento transversal (passo de integração), δ, (vide Figura 1), usando o conceito da média volumétrica, h_c é a distância entre a parede e o centro da terceira haste.

Para a escolha desta célula de cálculo foram levas em conta as seguintes considerações, propostas em Breugem (2004):

i) A célula de cálculo deve-se ajustar à topologia do meio poroso;

ii) Garantir que o campo de escoamento mediado no volume da célula seja contínuo, isto é, que o tamanho da célula deve ser suficientemente grande tal que nenhuma condição de contorno seja necessário no interior do meio poroso. Por outro lado, o tamanho da célula de cálculo deve ser suficientemente pequena para preservar a maioria das informações do escoamento distribuído no campo do escoamento mediado no volume (integrado);

iii) Que a variação entre a propriedade mediada no volume de uma célula e da célula subseqüente seja pequena.

Com o uso da célula de cálculo surge a relação entre o volume de fluido, V_l, e o volume total, V_t, da célula, que é definido como porosidade, $\phi_c=V_l/V_t$, uma das propriedades que definem o meio poroso. Note, na Figura 1, que a camada porosa é divida em duas regiões, uma região onde a porosidade é constante (meio poroso homogêneo) e uma região onde a porosidade varia (região de interface), ou seja, onde o volume de fluido aumenta. A região onde o volume de fluido é igual ao volume total é denominado meio limpo, ou seja, $\phi_c=1$. Esta célula de cálculo foi construída para a integração dos resultados distribuídos num canal com hastes cilíndricas, posteriormente, foi aplicado aos casos com hastes elíptica transversal, quadrada e elíptica longitudinal.

As propriedades do escoamento foram integradas no volume da célula de cálculo, mostrada na Figura 1, utilizando o conceito da média volumétrica, onde a propriedade do escoamento associada ao volume de fluido, ΔV_f, é ponderada pelo volume total da célula de cálculo, ΔV_t, da seguinte forma:

$$\langle \varphi \rangle^v = \frac{1}{\Delta V_t} \int_{\Delta V_f} \varphi dV \tag{1}$$

onde φ pode ser a velocidade axial, u, ou transversal, v. Note que o sobrescrito v indica média volumétrica.

Além da porosidade, para caracterizar o meio poroso é necessária a definição de outra propriedade denominada permeabilidade, K_c, que indica a facilidade com que fluido permeia a estrutura porosa. Para estimar a permeabilidade foi utilizado a lei de Darcy (1856), que é expressa por

$$\mu \mathbf{u}_D = -K_c \nabla \langle P \rangle^i \tag{2}$$

onde μ é a viscosidade dinâmica do fluido, $\mathbf{u}_D$ é a velocidade de Darcy e $\langle P \rangle^i$ é a média intrínseca da pressão no fluido. No entanto, esta relação é restrita a escoamentos onde as forças viscosas sobrepujam as forças de inércia. Para simular esta condição foi realizado um experimento numérico numa célula, vide área hachurada na Figura 1, com condição inicial de fluxo mássico prescrito, onde $Re_H<0,1$, e condições de contorno de periodicidade espacial nas faces oeste e leste, e de simetria nas faces norte e sul.

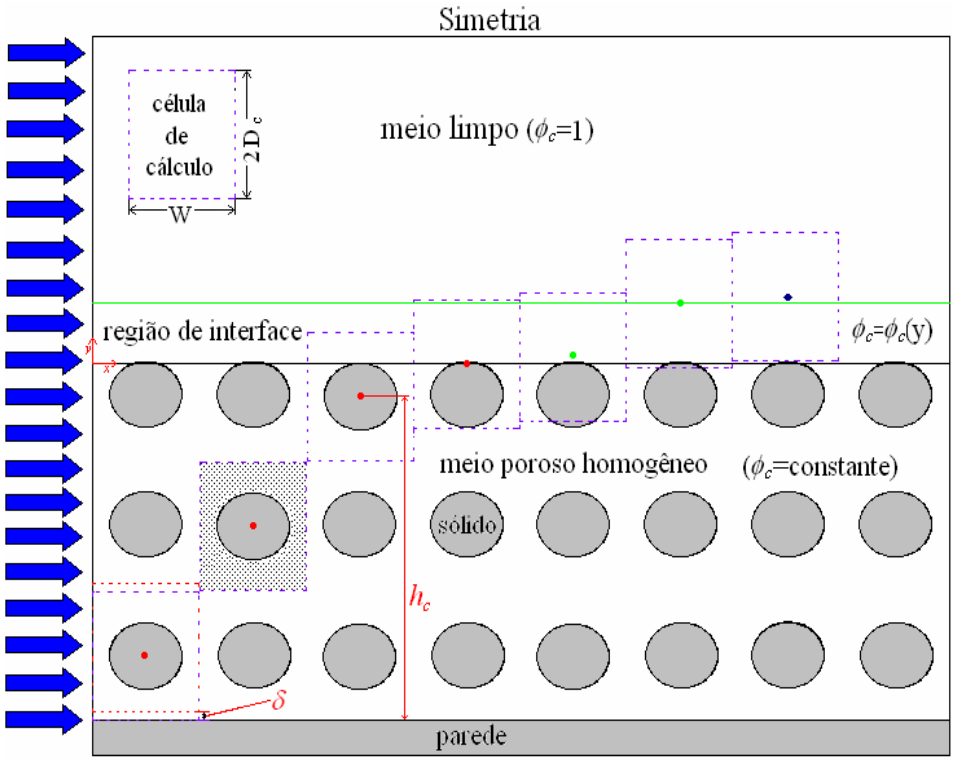

Figura 1: Exemplo do esquema de integração dos resultados "*microscópicos*" em um canal parcialmente preenchido com haste cilíndrica.

3. Resultados

Na Tabela 1 foi mostrado o valor da porosidade, ϕ_c, calculado na região homogênea, da permeabilidade, K_c, estimada através da célula hachurada apresentada na Figura 1 e do número de Darcy ($Da_c = K_c / H_d^2$). Note a altura da camada porosa, H_d, apresenta uma defasagem de 0,01 em relação a altura do canal, H, inicialmente definida (vide Silva e de Lemos (2005a)), isto se deve a localização das propriedades integradas no centro da célula de cálculo. Como esperado, o valor da porosidade aumenta com o aumento do volume de fluido na célula de cálculo, ou seja, o aumento do comprimento da célula, W. Além disso, observa-se um aumento do valor da permeabilidade, K_c, com a diminuição da resistência imposta ao escoamento pela forma da haste e com o aumento do valor da porosidade, ϕ_c, indicando uma dependência da permeabilidade com a porosidade.

A Tabela 2 apresenta o valor da espessura da camada porosa homogênea, h_{pm}, a espessura da região de interface, e_i, e a altura da haste, h^*. Note que a espessura da camada porosa homogênea, h_{mp}, diminui com o aumento da altura da haste, h^*. Por outro lado, a espessura da região de interface, e_i, aumenta com o aumento da altura da haste, h^*. Este comportamento, indica a dependência da espessura da camada porosa homogênea, h_{mp}, e da espessura da região de interface, e_i, da altura da haste, h^*.

Tabela 3 apresenta os valores de porosidade, ϕ_c, Darcy, $Da_c = K_c / H_d^2$, e Reynolds, $Re_{H_d} = \rho U_D H_d / \mu$, baseado na altura do canal, H_d. Observe que o aumento da vazão no canal, indicado pelo número de Reynolds, se deve ao aumento do número de Darcy. No entanto, para os casos com meio poroso formado de hastes quadradas e ou com ϕ_c=0,7382 (vide Tabela 1) ocorre uma substancial canalização do escoamento entre as hastes (vide Silva e de Lemos (2005b)), fazendo com que a vazão para estes casos seja superior ao esperado, ou seja, a vazão encontrada para haste quadrada com ϕ_c=0,7382 ou ϕ_c=0,8429 é superior a vazão encontrada para outras morfologias, além disso, a vazão observada na tabela 3 para ϕ_c=0,7382 é superior a vazão constatada para ϕ_c=0,8429. Este comportamento indica que há canalização do escoamento para ϕ_c=0,7382.

Nas Figuras 2*a* e 2*b* são mostrados os perfis de porosidade ao longo da seção transversal do canal parcialmente preenchido com material poroso, para W=0,015m e W=0,025m, respectivamente. Observe que existe uma região onde o valor da porosidade permanece constante, uma região onde o valor da porosidade aumenta progressivamente (região de interface, indicada na Figura), até atingir o valor de meio limpo, ou seja, ϕ_c=1. Note que a espessura da região de interface não depende do comprimento do canal, W, apenas da forma da haste (vide Tabela 2). Além disso, observa-se uma variação linear da porosidade com a forma da haste e a posição, na região de interface.

Na Figura 3*a* (note que a linha tracejada delimita a região de interface de maior espessura da região de interface) foi evidenciado o efeito do número de Darcy no perfil de velocidade axial, para ϕ_c=0,7382 e H_d=0,075m. Note que há uma diminuição da vazão no canal e da penetração do escoamento na camada porosa, com a diminuição do número de Darcy. No entanto, para Da_c=1,1360×10^{-3}, ocorre o inverso, isto é, há um aumento da vazão no canal e na penetração do escoamento na camada porosa, este comportamento se deve a canalização do escoamento ocasionado pela forma da haste que compõe o meio poroso, vide Silva e de Lemos (2005b).

A Figura 3*b* mostra a influência do número de Darcy no perfil de velocidade axial, para ϕ_c=0,7382 e H_d=0,095m. Observe que a utilização do conceito da média volumétrica para a obtenção do perfil de velocidade integrado reproduz o mesmo comportamento do perfis de velocidade evidenciados no trabalho de Silva e de Lemos (2005b), que investiga o escoamento turbulento em um canal com hastes sólidas. Além disso, para Da_c=7,0806×10^{-4} há uma maior penetração do escoamento na camada porosa homogênea, próxima a região de interface.

Na Figura 3*c* foi apresentado o efeito de Darcy no escoamento em um canal parcialmente preenchido com material poroso, para ϕ_c=0,7382 e H_d=0,115m. Note que o aumento do número de Darcy implica no aumento da vazão, por outro lado, a maior vazão no canal é encontrada para Da_c=4,8319×10^{-4}, isto ocorre devido a canalização do escoamento, ocasionado pela forma da haste que forma a camada porosa. Observe ainda, que existe uma região porosa dentro da camada porosa homogênea, onde a permeabilidade determina a vazão.

A Figura 4*a* apresenta a influência do número de Darcy no comportamento do escoamento, para ϕ_c=0,8429 e H_d=0,075m. Observe que, quanto maior o valor do número de Darcy, maior a penetração do escoamento na camada porosa. Além disso, os maiores valores de Darcy implicam nas maiores vazões. No entanto, a maior vazão no canal é encontrada para meio poroso formado de hastes quadradas (Da_c =1,5543×10^{-3}), este comportamento se deve a canalização do escoamento devido a forma da haste.

Na Figura 4*b* foi mostrado o efeito do número de Darcy no comportamento do escoamento em um canal parcialmente preenchido com material poroso, para ϕ_c=0,8429 e H_d=0,095m. Note que o aumento do número de Darcy implica numa maior vazão no canal e numa maior penetração do escoamento na camada porosa, respectivamente. Observe ainda, que no caso com Da_c=9,6876×10^{-4}, ocorre a canalização do escoamento no meio poroso, ocasionando uma vazão no canal maior que a esperada.

A Figura 4*c* evidencia a influência do número de Darcy no perfil de velocidade axial, para ϕ_c=0,8429 e H_d=0,115m. Observe que nos casos com meio poroso formado de hastes elíptica transversal, cilíndrica e elíptica longitudinal, respectivamente, quanto maior o número de Darcy (vide Tabela 3) maior a vazão no canal, porém, a maior vazão no canal é encontrada para o meio poroso formado de haste quadrada, este comportamento se deve a canalização do escoamento. Por outro lado, o aumento do número de Darcy implica num aumento da penetração do escoamento na camada porosa.

Na Figura 5*a* foi investigado o efeito do número de Darcy no perfil de energia cinética de turbulência, para ϕ_c=0,7382 e H_d=0,075m. Note que existe um aumento na penetração da turbulência na camada porosa com o aumento do número de Darcy. Além disso, os picos de energia cinética de turbulência estão localizados na interface entre o meio limpo e a região de interface.

A Figura 5*b* mostra a influência do número de Darcy no perfil de energia cinética de turbulência, para ϕ_c=0,7382 e H_d=0,095m. Observe que a penetração da turbulência na camada porosa para Da_c=7,0806×10^{-4} e Da_c=7,2585×10^{-4}, são praticamente iguais, no entanto, para Da_c=1,1080×10^{-3} ocorre uma maior penetração da turbulência no meio poroso. Note ainda, que os picos de energia cinética de turbulência ocorrem na interface entre o meio limpo e o meio poroso.

Na Figura 5*c* apresenta o efeito do número de Darcy no perfil de energia cinética de turbulência, para ϕ_c=0,7382 e H_d=0,115m. Os picos de energia cinética de turbulência ocorrem na interface entre o meio limpo e o meio poroso, como mostrado na Figura. Observe ainda, que o aumento do número de Darcy implica num aumento da penetração da turbulência no meio poroso.

Na Figura 6*a* é analisado a influência do número de Darcy no perfil de energia cinética de turbulência, para ϕ_c=0,8429 e H_d=0,075m. Observe que há um aumento da penetração da turbulência na camada porosa com o aumento do número de Darcy. Além disso, os picos de energia cinética de turbulência estão localizados na interface entre o meio limpo e a camada porosa.

A Figura 6*b* evidencia o efeito do número de Darcy no perfil de energia cinética de turbulência, para ϕ_c=0,8429 e H_d=0,095m. Note que a penetração da turbulência para Da_c=9,6876×10^{-4} e Da_c=1,0648×10^{-3}, são praticamente iguais, no entanto, pode-se constatar um aumento da penetração da turbulência no meio poroso com o aumento do número de Darcy.

Na Figura 6*c* foi mostrado o efeito do número de Darcy no perfil de energia cinética de turbulência, para ϕ_c=0,8429 e H_d=0,115m. Observe que o aumento do número de Darcy implica num aumento da penetração da turbulência na região porosa, além disso, os picos de energia cinética turbulenta ocorrem na interface entre o meio limpo e o meio poroso.

Tabela 1: Propriedades do meio poroso homogêneo.

Caso	W [m]	H_d [m]	ϕ_c	$K_c \times 10^{-6}$ [m^2]	$Da_c \times 10^{-4}$	$K_c \times 10^{-6}$ [m^2]	$Da_c \times 10^{-4}$	$K_c \times 10^{-6}$ [m^2]	$Da_c \times 10^{-4}$	$K_c \times 10^{-6}$ [m^2]	$Da_c \times 10^{-4}$
				Haste Elíptica Transversal		Haste Quadrada		Haste Cilíndrica		Haste Elíptica Longitudinal	
150-30		0,075			5,6165		11,360		11,646		17,778
150-50	0,015	0,095	0,7382	3,1593	3,5006	6,3902	7,0806	6,5508	7,2585	10,000	11,080
150-70		0,115			2,3889		4,8319		4,9533		7,5614
250-30		0,075			8,7632		15,543		17,084		24,220
250-50	0,025	0,095	0,8429	4,9293	5,4618	8,7431	9,6876	9,6097	10,648	13,624	15,096
250-70		0,115			3,7273		6,6110		7,2663		10,302

Tabela 2: Características da região de interface.

Morfologia da haste	$\times 10^{-2}$ [m]		
	h_{mp}	e_i	h^*
Elíptica Transversal	4,35	1,25	1,2910
Quadrada	4,55	0,90	0,8862
Cilíndrica	4,50	1,00	1,0000
Elíptica Longitudinal	4,60	0,75	0,7746

Tabela 3: Características hidrodinâmicas do escoamento.

ϕ_c	H_d [m]	$Da_c \times 10^{-4}$	$Re_{H_d} \times 10^4$
0,7382	0,075	11,360	1,2013
		11,646	0,78387
		17,778	0,95979
	0,095	7,0806	2,6400
		7,2585	1,6340
		11,080	1,9341
	0,115	4,8319	4,5675
		4,9533	2,6940
		7,5614	3,2223
0,8429	0,075	8,7632	0,49425
		15,543	0,77509
		17,084	0,60463
		24,220	0,77438
	0,095	5,4618	1,1609
		9,6876	1,7812
		10,648	1,3298
		15,096	1,5980
	0,115	3,7273	2,0816
		6,6110	3,1759
		7,2663	2,3145
		10,302	2,7030

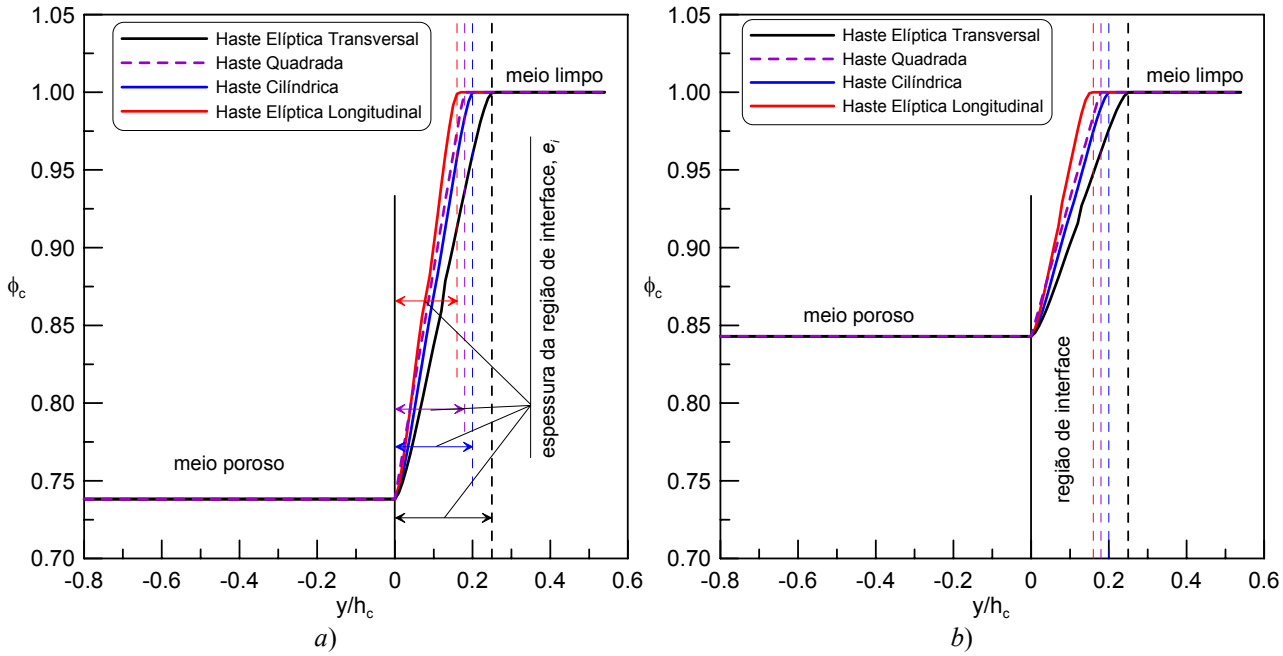

a) *b*)

Figura 2: Perfil da porosidade ao longo da seção transversal do canal, para: *a*) W=0,015m, *b*) W=0,025m

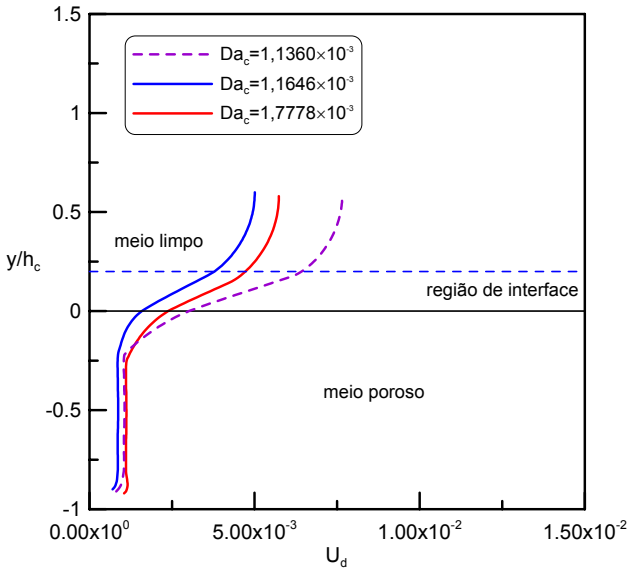

a)

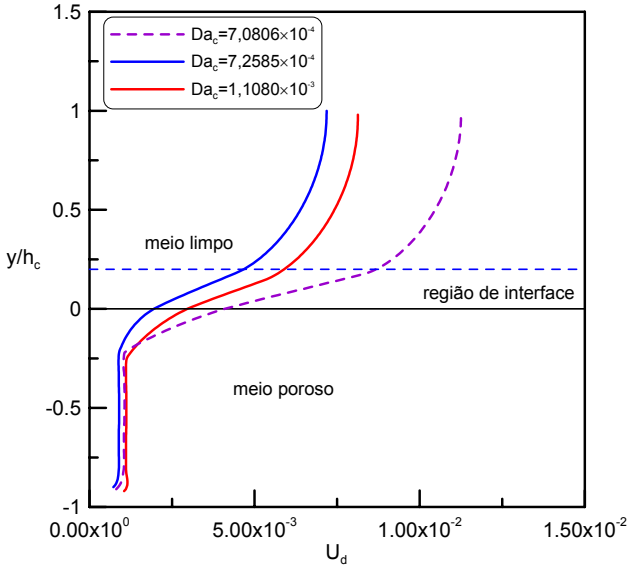

b)

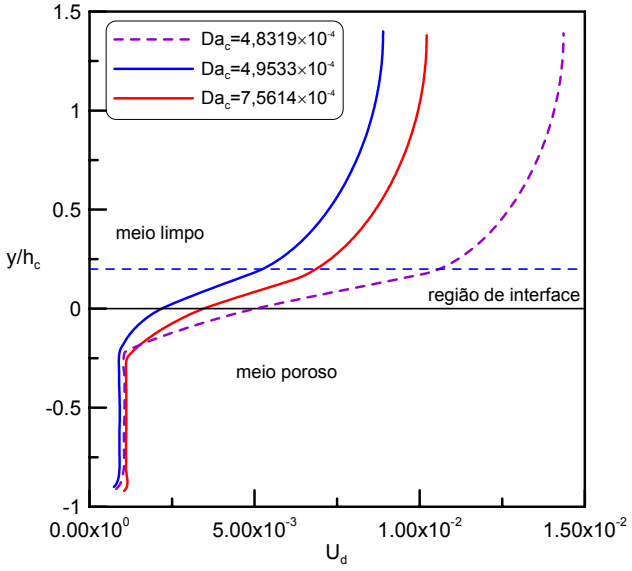

c)

Figura 3: Efeito do número de Darcy no perfil de velocidade adimensional, $U_d = \mu u_D \Big/ h_c^2 \left(-\nabla \langle p \rangle^i\right)$, com ϕ_c=0,7382, para: *a*) H_d=0,075m, *b*) H_d=0,095m, *c*) H_d=0,115m.

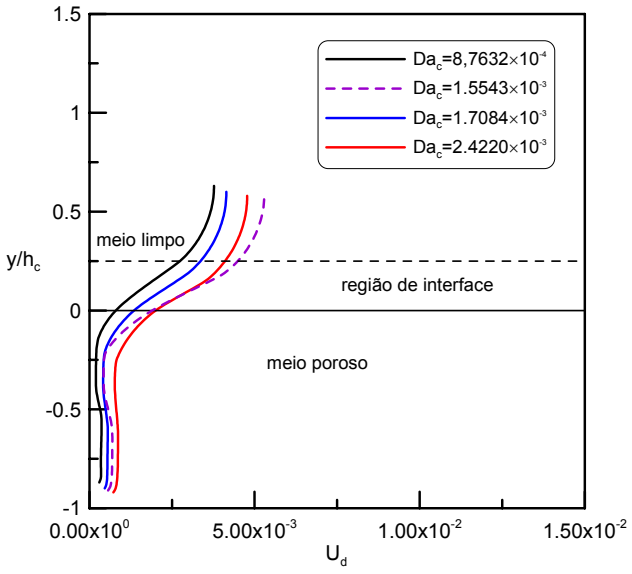

a)

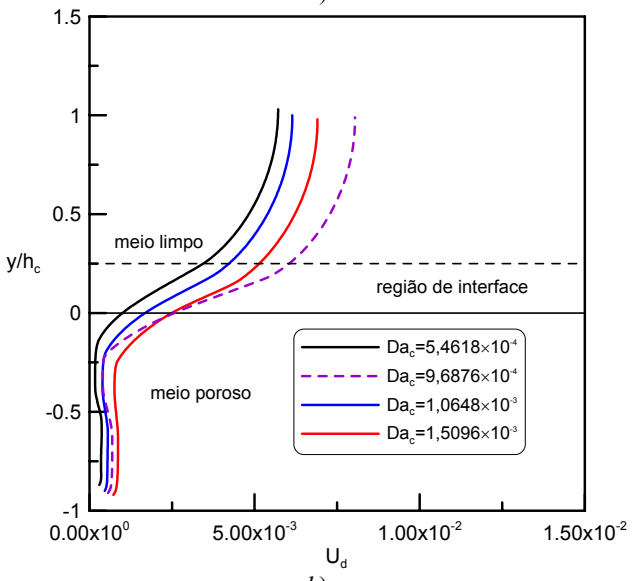

b)

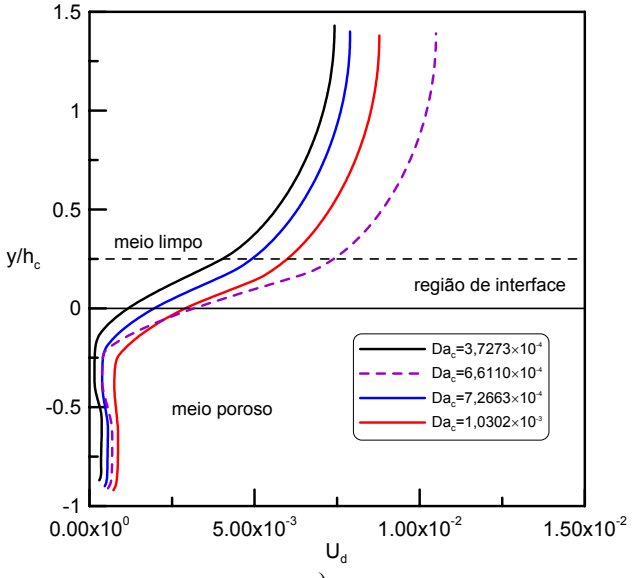

c)

Figura 4: Efeito do número de Darcy no perfil de velocidade adimensional, $U_d = \mu u_D \Big/ h_c^2 \left(-\nabla \langle p \rangle^i\right)$, com ϕ_c=0,8429, para: *a*) H_d=0,075m, *b*) H_d=0,095m, *c*) H_d=0,115m.

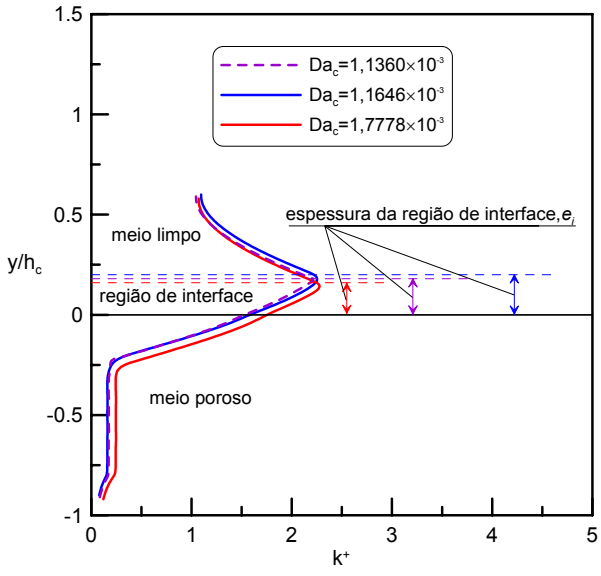

a)

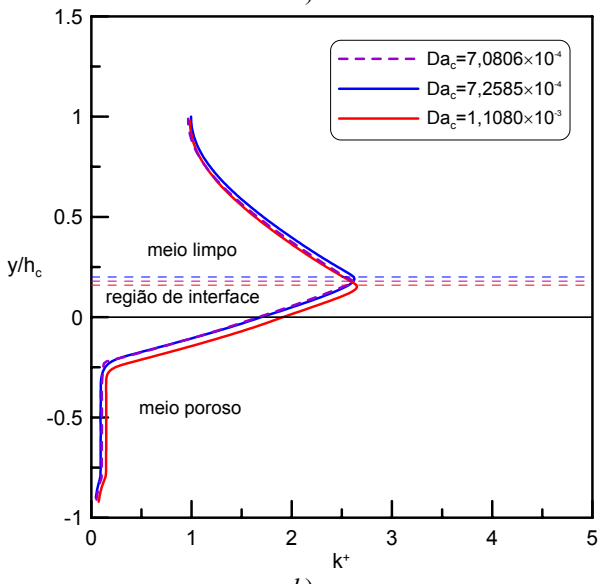

b)

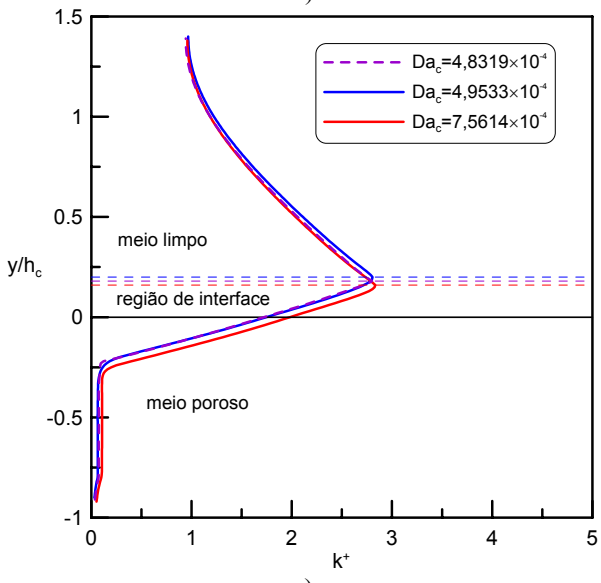

c)

Figura 5: Efeito do número de Darcy no perfil de energia cinética de turbulência adimensional, $k^+ = k/\left[u^*\right]^2$, com ϕ_c=0,7382, para: *a*) H_d=0,075m, *b*) H_d=0,095m, *c*) H_d=0,115m.

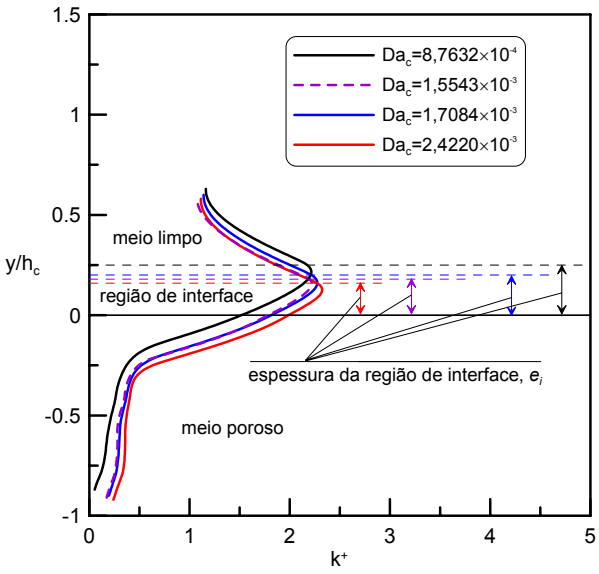

a)

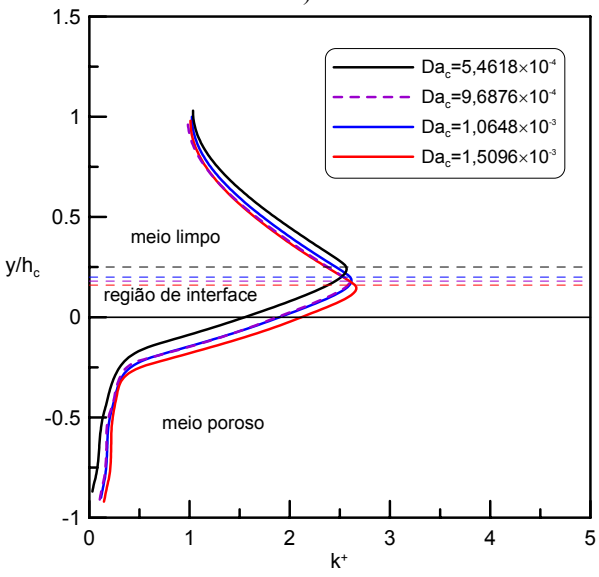

b)

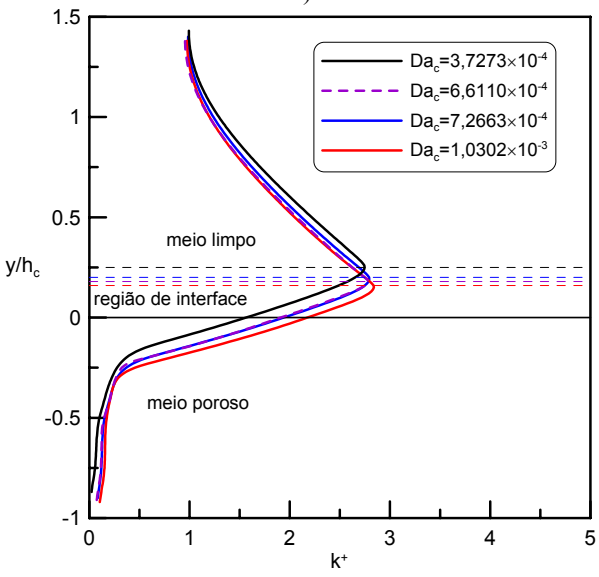

c)

Figura 6: Efeito do número de Darcy no perfil de energia cinética de turbulência adimensional, $k^+ = k/\left[u^*\right]^2$, com ϕ_c=0,8429, para: *a*) H_d=0,075m, *b*) H_d=0,095m, *c*) H_d=0,115m.

4. Conclusões

Os resultados mostram que no caso com ϕ_c=0,7382, há uma vazão no canal maior do que a encontrada no caso com ϕ_c=0,8429, para os mesmos valores de Darcy. Além disso, observa-se que o meio poroso formado de hastes quadradas exerce uma influência na vazão do canal que não é captada pela permeabilidade calculada segundo a lei de Darcy. Estes resultados são contrários aos resultados macroscópicos obtidos para escoamento laminar (vide Silva e de Lemos (2006)), sugerindo que o regime do escoamento deve ser contabilizado no cálculo da permeabilidade do meio poroso. Por outro lado, os perfis de energia cinética de turbulência apresentados mostram ser função das propriedades do meio poroso, uma vez que, quanto maior a porosidade, para valores de Darcy constante, ou quanto maior o valor de Darcy, para valores de porosidade constante, maior a penetração da turbulência na camada porosa. Além disso, o comportamento dos resultados distribuídos para escoamento turbulento encontrado em Silva e de Lemos (2005b) corrobora o comportamento dos resultados aqui apresentados, indicando que a metodologia de integração utilizada preserva a maioria das informações do escoamento distribuído.

5. Agradecimentos

Os autores são gratos ao CNPq e à FAPESP pelo apoio financeiro durante o curso desta pesquisa.

6. Referências

Breugem, W.P., 2004. "The influence of wall permeability on laminar and turbulent flow*"*. 190f. Doctoral Thesis - Delft University of Technology, Nederland.

Breugem, W.P., Boersma, B.J. and Uittenbogaard, R.E., 2004, "Direct Numerical Simulations of Plane Channel Flow Over a 3D Cartesian Grid of Cubes". Proceedings of the International Conference on Porous Media and Applications, (on CD-ROM), Évora, Portugal.

Breugem, W.P., Boersma, B.J. and Uittenbogaard, R.E., 2005, "The Laminar Boundary Layer Over a Permeable Wall", Transport in Porous Media, Vol. 59, pp. 267-300.

Breugem, W.P. and Boersma, B.J., 2005, "Direct Numerical Simulations of Turbulent Flow Over a Permeable Wall Using a Direct and a Continuum Approach", Physics Fluids, Vol. 17, N. 2.

Darcy, H., 1856. "Les fountaines publiques de la ville de Dijon*"*, Paris: Victor Dalmond.

Kuwahara, F., Kameyama, Y., Yamashita, S., and Nakayama, A., 1998, "Numerical Modeling of Turbulent Flow in Porous Media Using a Spatially Periodic Array", Journal of Porous Media, Vol. 1, pp. 47-55.

Kuznetsov, A.V. and Xiong, M., 2003, "Development of an Engineering Approach to Computations of Turbulent Flows in Composite Porous/Fluid Domains", International Journal of Thermal Science*s*, Vol. 42, pp. 913-919.

Kuznetsov, A.V. and Becker, S.M., 2004, "Effect of the Interface Roughness on Turbulent Convective Heat Transfer in a Composite Porous/Fluid Duct", International Communication of Heat and Mass Transfer, Vol. 31, N. 1, pp. 11-20.

Launder, B.E. and Sharma, B.I., 1974, "Application of the Energy-Dissipation Model of Turbulence to the Calculation of Flow Near a Spinning Disc", Letters in Heat and Mass Transfer, Vol. 1, pp. 131-138.

Ochoa-Tapia, J.A. and Whitaker, S., 1995*a,* "Momentum Transfer at the Boundary between a Porous Medium and a Homogeneous Fluid – I", International Journal of Heat and Mass Transfer*,* Vol. 38*,* pp. 2635-2646.

Ochoa-Tapia, J.A. and Whitaker, S., 1995*b*, "Momentum Transfer at the Boundary between a Porous Medium and a Homogeneous Fluid – II", International Journal of Heat and Mass Transfer, Vol. 38*,* pp. 2647-2655.

Pedras, M.H.J. and de Lemos, M.J.S., 2001*a*, "Macroscopic Turbulence Modelling for Incompressible Flow Through Undeformable Porous Media", International Journal of Heat and Mass Transfer, Vol. 44, N. 6, pp. 1081-1093.

Pedras, M.H.J. and de Lemos, M.J.S., 2001*b*, "Simulation of Turbulent Flow in Porous Media Using a Spatially Periodic Array and a Low-Re Two-Equation Closure", Numerical Heat Transfer - Part A – Applications, Vol. 39, N. 1, pp. 35-59.

Pedras, M.H.J. and de Lemos, M.J.S., 2001*c*, "On the Mathematical Description and Simulation of Turbulent Flow in a Porous Medium Formed by an Array of Elliptic Rods" Journal of Fluids Engineering, Vol. 123, N. 4, pp. 941-947.

Pedras, M.H.J. and de Lemos, M.J.S., 2003, "Computation of Turbulent Flow in Porous Media Using a Low-Reynolds k-ε Model an Infinite Array of Spatially Periodic Elliptic Rods", Numerical Heat Transfer – Part A – Applications, Vol. 43, N. 6, pp. 585-602.

Prinos, P., Sofialidis, D. and Keramaris, E., 2003, "Turbulent Flow Over and Within a Porous Bed", Journal of Hydraulic Engineering, Vol. 129, N. 9, pp. 720-733.

Silva, R.A. and de Lemos, M.J.S., 2003*a*, "Turbulent Flow in a Channel Occupied by a Porous Layer Considering the Stress Jump at the Interface", International Journal of Heat and Mass Transfer, Vol. 46, pp. 5113-5121.

Silva, R.A. and de Lemos, M.J.S., 2003*b*, "Numerical Analysis of the Stress Jump Interface Condition for Laminar Flow over a Porous Layer", Numerical Heat Transfer - Part A – Applications, Vol. 43, pp. 603-617.

Silva, R.A. and de Lemos, M.J.S., 2005*a*, "Effect of Medium Morphology on Laminar Flow in a Channel Partially Filled With a Porous Bed", Proceedings of the 18th International Congress of Mechanical Engineering, (on CD-ROM), Ouro Preto, MG, Brazil.

Silva, R.A. e de Lemos, M.J.S., 2005*b*, "Efeito da Morfologia do Meio no Escoamento Turbulento em um Canal Parcialmente Preenchido com um Leito Poroso Formado por Hastes Cilíndricas e Elípticas", Proceedings of 26th Iberian Latin-American Congress on Computational Methods in Engineering, (on CD-ROM), Guarapari, ES, Brazil.

Silva, R.A. e de Lemos, M.J.S., 2006, "Escoamento Macroscópico Sobre um Leito Poroso Formado de Hastes Sólidas", Proceedings of 27th Iberian Latin-American Congress on Computational Methods in Engineering, Belém, PA, Brazil.

MACROSCOPIC TURBULENT FLOW IN A CHANNEL WITH A POROUS BED COMPOSED BY SOLID RODS

Renato A. Silva
Marcelo J.S. De-Lemos[1]
Departamento de Energia – IEME
Divisão de Engenharia Aeronáutica e Mecânica
Instituto Tecnológico de Aeronáutica – ITA
12228-900 – São José dos Campos, SP - Brazil
[1] Corresponding author, delemos@ita.br.

Abstract: In this work the volume average concept is used to transport numerical results, which were obtained for a channel partially filled with solid rods, from the *microscopic* domain to a *macroscopic* domain. Through that methodology, values of permeability and porosity are calculated for the porous layer. Also, the effects of the Darcy number and porosity on the flow behavior are analyzed. Numerical results have shown the need of accounting the flow regime in the permeability evaluation. Moreover, the behavior of the results found in the available literature corroborates the behavior of the present results indicating, ultimately, that the integration methodology employed preserves most of the information of the flow.

Keywords: turbulent flow, volume averaged, porous medium, clear fluid, numerical method.

Proceedings of the 11th Brazilian Congress of Thermal Sciences and Engineering -- ENCIT 2006
Braz. Soc. of Mechanical Sciences and Engineering -- ABCM, Curitiba, Brazil,- Dec. 5-8, 2006

Paper CIT06- 0741

SIMULATION OF FLOW PAST AN ABRUPT CONTRACTION WITH A POROUS INSERT USING LINEAR AND NONLINEAR k-ε MODELS

Reinaldo M. Orselli
Cleges Fischer
Marcelo J.S. De-Lemos[1]
Departamento de Energia - IEME
Instituto Tecnológico de Aeronáutica - ITA
12228-900 - São José dos Campos - SP – Brasil
[1] Corresponding author, delemos@ita.br.

Abstract. *This work presents a numerical investigation for the turbulent flow in an abrupt contraction pipe (section area ratio of 0.285) with a porous insert placed past the contraction. The Reynolds number considered is 50,000 based on the pipe inlet diameter. The flow equations are discretized by using the control volume method and the SIMPLE algorithm is applied for the velocity-pressure coupling. Results for the hybrid medium are obtained using linear and nonlinear k-ε macroscopic models. Parameters such as permeability and thickness of the porous insert are varied in order to analyze their effects on the flow pattern. Pressure losses and streamlines results obtained by the two turbulence models are compared for the cases without and with a porous insert. For the cases without porous insert, whereas the minor loss obtained by the linear model over-predicts the experimental data, good agreement was found for the minor loss obtained by the nonlinear model indicating an advantage of the nonlinear closure in predicting more realistic results. For the cases with porous insert, the results show that despite the attenuation or the suppression of the recirculating bubble, the flow losses are always higher in comparison with the cases without porous insert and the losses are significantly more affected by the porous insert permeabity than its thickness.*

Keywords*. Porous Media, Sudden Contraction, Numerical Simulation, Turbulent flow*

1. Introduction

Flow studies in pipes with sudden contraction have been the subject of numerous publications. Streeter (1961) and Rouse (1950) showed experimental values of minor losses as a function of S_{ex}/S_{in}, the ratio between the pipe outlet cross section area (S_{ex}) and its inlet section area (S_{in}), for turbulent flows. Benedict *et al*. (1966) compared experimentally losses considering incompressible and compressible turbulent flows through pipes with abrupt enlargements and contractions, reviewed the basis of the theory concerning the loss coefficients for abrupt enlargements and contractions and discussed some references about the subject. Durst & Loy (1985) investigated laminar flows for S_{ex}/S_{in} = 0.285. In that work, experimental and numerical results for velocity profiles, recirculating bubble dimensions and pressures losses were compared. Ajayi *et al.* (1998) investigated experimentally the effect on the flow losses of a perturbation upstream a pipe sudden contraction (S_{ex}/S_{in} = 0.25) from laminar to moderately high Reynolds numbers. Also, numerical simulations were performed for the cases without upstream perturbation and good agreement between numerical and experimental results was found for the contraction loss coefficient.

Many articles have been recently published in the literature concerning numerical simulations of flows past planar channels with porous insert. In the works of Assato & de Lemos (2002, 2003) and Assato *et. al.* (2005) it was simulated numerically a turbulent flow through a backward-facing step and in Assato & de Lemos (2004a-b) it was simulated the case of a flow past a forward-facing step. In general, these articles showed a comparison of numerical results applying both linear and non-linear turbulence models and in order to analyze the effects of the porous insert on the flow pattern some parameters such as porosity, permeability and thickness were varied. In addition, with regard to this subject, other recent works can be mentioned such as the work of Chan & Lien (2005) where it was examined the influence of permeability, forchheimer's constant and thickness on the flow (turbulent) in a planar channel which suffers a sudden expansion (back-step). And the work of de Lemos & Tofaneli (2003) where it was analyzed the influence of porosity, permeability and Reynolds number on the flow pressure drop in a parallel-plate channel containing porous fins.

Concerning numerical simulations of turbulent flow through an axisymmetric sudden contraction with porous insert, some articles have been recently published such as the works of Orselli & de Lemos (2004, 2005a-c), where, essentially, it was investigated the effect of permeability and thickness on the flow pattern past a sudden contraction pipe with section area ratio of 0.10 and 0.285. And, also, the work of Orselli & de Lemos (2006) where numerical results applying linear and nonlinear turbulence models were shown with a section area ratio of 0.10.

In the present work, numerical results for turbulent flow through a sudden contraction pipe (section area ratio of 0.285) with a porous insert (located past the sudden contraction section) are presented in which both linear and nonlinear eddy viscosity macroscopic models are employed.

Developments of nonlinear eddy viscosity models (NLEVM) have recently been the subject of many publications such as in Speziale (1987), Nisizima & Yoshizawa (1987), Rubinstein & Barton (1990), Shih *et al.* (1993) and Park & Sung (1995). The NLEVM which corresponds to an extension of the linear eddy viscosity models (LEVM) have presented some advantage over the LEVM mainly for flows in which anisotropy of the normal Reynolds stresses is important (Assato & de Lemos, 2000, Wilcox, 1998).

Therefore, in this work, comparisons of results simulated with both linear and nonlinear macroscopic k-ε turbulence models for turbulent flow past a sudden contraction pipe without and with a porous insertion are presented. In addition, parameters such as permeability and thickness of the porous insert are varied in order to analyze particularly its influence on the flow losses and on the damping of the recirculating bubble.

2. Geometry Under Consideration

Figure (1a) shows the geometry under consideration where due to the sudden contraction the flow direction changes abruptly resulting in a recirculating bubble past the contraction section. The recirculating bubble causes a reduction of the effective flow area, phenomenon known as *vena contracta*, whose minimum area is denoted S_c. Figure (1b) presents a sketch of the porous insert in the pipe, the subscripts in and ex represent the pipe inlet and outlet, respectively. In Figs. (1a) and (1b), U_{in} and U_{ex} are the mean velocities at a pipe cross section in the stream-wise direction, l_{in} and l_{ex} are the pipe lengths, d_{in} and d_{ex} or $2\,r_{in}$ and $2\,r_{ex}$ correspond to the diameters and a is the porous insert thickness. In this work, two porous insert thickness are considered which are $a/r_{ex} = 0.083$ and $a/r_{ex} = 0.166$. The adopted section pipe ratio is $S_{ex}/S_{in} = 0.285$ which corresponds to $r_{ex}/r_{in} = 0.534$.

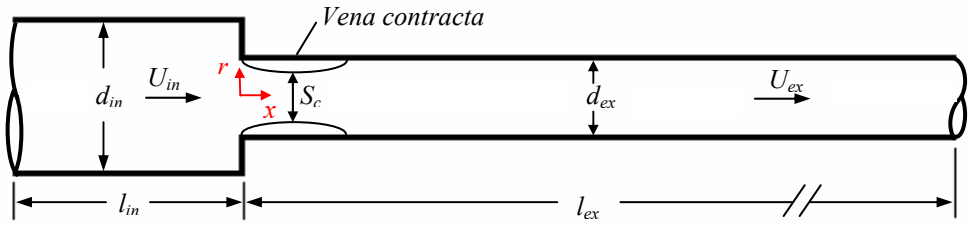

a)

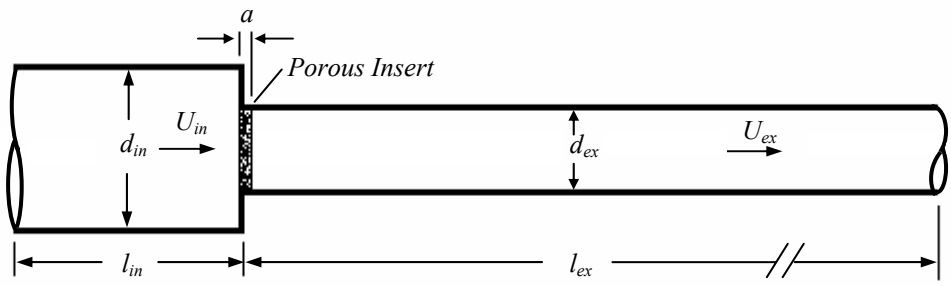

b)

Figure 1. Simple sketch of the pipe geometry: a) *vena contracta*; b) Porous insert.

3. Mathematical Model

The governing equations applied here have already been derived in details, Pedras & de Lemos (2001a-c), and for this reason their derivation need not to be repeated here. Considering the porous medium homogeneous, rigid and saturated in an incompressible single-phase fluid, the macroscopic form of the governing equations is obtained by employing the volumetric average to the time-averaged equations, where this development is based on the concept of double decomposition, de Lemos & Pedras (2001), Pedras & de Lemos (2000).

In the following governing equations, the transient and the gravitational terms are neglected.

The macroscopic continuity equation can be written as,

$$\nabla \cdot \overline{\mathbf{u}}_D = 0 \tag{1}$$

where $\overline{\mathbf{u}}_D$ is the average surface velocity ("seepage" or Darcy velocity). Equation (1) was found by applying the Dupuit-Forchheimer relationship, $\overline{\mathbf{u}}_D = \phi\langle\overline{\mathbf{u}}\rangle^i$, where ϕ is the porous medium porosity and $\langle\overline{\mathbf{u}}\rangle^i$ is the intrinsic (liquid) average of the local velocity vector $\overline{\mathbf{u}}$ (Gray & Lee, 1977).

The macroscopic momentum equation is given by,

$$\rho\nabla\cdot\left(\frac{\overline{\mathbf{u}}_D\,\overline{\mathbf{u}}_D}{\phi}\right) = -\nabla(\phi\langle\overline{p}\rangle^i) + \mu\nabla^2\overline{\mathbf{u}}_D + \nabla\cdot(-\rho\phi\langle\overline{\mathbf{u}'\mathbf{u}'}\rangle^i) - \left[\frac{\mu\phi}{K}\overline{\mathbf{u}}_D + \frac{c_F\phi\rho|\overline{\mathbf{u}}_D|\,\overline{\mathbf{u}}_D}{\sqrt{K}}\right] \tag{2}$$

where the correlation $-\rho\overline{\mathbf{u}'\mathbf{u}'}$ is obtained by employing the time-average operator to the local instantaneous momentum equation. Then, applying the volume-average procedure to the entire momentum equation (see Pedras & de Lemos, 2001a for details), results in the term $-\rho\phi\langle\overline{\mathbf{u}'\mathbf{u}'}\rangle^i$ of Eq. (2). This term is here recalled the Macroscopic Reynolds Stress Tensor (MRST). Then, making use the relationship $\overline{\mathbf{u}}_D = \phi\langle\overline{\mathbf{u}}\rangle^i$, Eq. (2) is finally obtained. The last two terms in the right hand side of Eq. (2) represent the Darcy-Forchheimer contributions where the constant c_F is the Forchheimer coefficient. In addition, the term $\langle\overline{p}\rangle^i$ is the intrinsic average pressure of the fluid, ρ is the fluid density, μ represents the dynamic fluid viscosity and the symbol K corresponds to the porous medium permeability. Also, the equations given are valid for the clear medium as well, setting $\phi = 1$ ($K \to \infty$) and discarding the last two terms.

As proposed by Pedras & de Lemos (2001a), the term MRST is modeled considering a linear stress-strain relationship in analogy with the Boussinesq concept for clear flow case as,

$$-\rho\phi\langle\overline{\mathbf{u}'\mathbf{u}'}\rangle^i = \mu_{t_\phi}\langle\overline{\mathbf{D}}\rangle^v - \frac{2}{3}\phi\rho\langle k\rangle^i\mathbf{I} \tag{3}$$

where $\langle k\rangle^i$ represents the intrinsic average of the turbulent kinetic energy (k) and the term

$$\langle\overline{\mathbf{D}}\rangle^v = \left[\nabla\overline{\mathbf{u}}_D + [\nabla\overline{\mathbf{u}}_D]^T\right] \tag{4}$$

corresponds to the mean macroscopic deformation tensor and $\mathbf{I}$ is the unity tensor. In Eq. (3), the term μ_{t_ϕ} is the macroscopic eddy viscosity which is modeled similarly to case of clear fluid and a proposal for it was presented in Pedras & de Lemos (2001a) as follows,

$$\mu_{t_\phi} = \rho c_\mu \frac{\langle k\rangle^{i2}}{\langle\varepsilon\rangle^i} \tag{5}$$

where $c_\mu = 0.09$ and $\langle\varepsilon\rangle^i$ is the intrinsic average of the dissipation rate of k.

The macroscopic transport equations for $\langle k\rangle^i = \langle\overline{\mathbf{u}'\mathbf{u}'}\rangle^i/2$ and $\langle\varepsilon\rangle^i = \mu\langle\overline{\nabla\mathbf{u}':\left(\nabla\mathbf{u}'\right)^T}\rangle^i/\rho$ in the k-ε High-Reynolds form were proposed in Pedras & de Lemos (2001a) as,

$$\rho\nabla\cdot(\overline{\mathbf{u}}_D\langle k\rangle^i) = \nabla\cdot\left[(\mu + \frac{\mu_{t_\phi}}{\sigma_k})\nabla(\phi\langle k\rangle^i)\right] - \rho\langle\overline{\mathbf{u}'\mathbf{u}'}\rangle^i:\nabla\overline{\mathbf{u}}_D + c_k\rho\frac{\phi\langle k\rangle^i|\overline{\mathbf{u}}_D|}{\sqrt{K}} - \rho\phi\langle\varepsilon\rangle^i \tag{6}$$

$$\rho\nabla.\left(\overline{\mathbf{u}}_D\langle\varepsilon\rangle^i\right) = \nabla.\left[\left(\mu + \frac{\mu_{t_\phi}}{\sigma_\varepsilon}\right)\nabla\left(\phi\langle\varepsilon\rangle^i\right)\right] + c_1\left(-\rho\left\langle\overline{\mathbf{u}'\mathbf{u}'}\right\rangle^i:\nabla\overline{\mathbf{u}}_D\right)\frac{\langle\varepsilon\rangle^i}{\langle k\rangle^i} + c_2c_\kappa\rho\frac{\phi\langle\varepsilon\rangle^i|\overline{\mathbf{u}}_D|}{\sqrt{K}} - c_2\rho\phi\frac{\langle\varepsilon\rangle^{i2}}{\langle k\rangle^i} \tag{7}$$

where $\sigma_k = 1.0$, $\sigma_\varepsilon = 1.33$, $c_1 = 1.44$, $c_2 = 1.92$ are non-dimensional empirical constants and, specially for the porous medium, c_k was found to be equal to 0.28 through numerical calculations by Pedras & de Lemos (2001a-c, 2003).

In this work, numerical results involving nonlinear eddy viscosity models (NLEVMs) are analyzed. Differently from the linear stress-strain rate relationship, Eq. (3), a more general nonlinear constitutive equation is employed. The NLEVMs here adopted is based on the developments of Speziale (1987), Nisizima & Yoshizawa (1987), Rubinstein & Barton (1990), Shih *et al.* (1993) among others. In these works, quadratic products were introduced involving the strain rate and vorticity tensors with different derivations and calibrations for each model. These nonlinear constitutive

relations offer some advantages over the Boussinesq approximation, most notably for flows in which anisotropy of the normal Reynolds stresses plays an important role, for example, in capturing secondary motion in noncircular ducts or in predicting reattachment length for the back-facing step (Wilcox, 1998, Assato & de Lemos, 2000).

The nonlinear macroscopic k-ε turbulence model here analyzed is composed of the same system of equations (1)-(7). The sole difference between both macroscopic models (linear and nonlinear) lies on the macroscopic Reynolds stress expression, brought to the second order. The macroscopic nonlinear stress-strain expression, in the indexed form, is given as follows:

$$
\begin{aligned}
-\rho\phi\langle\overline{u_j' u_j'}\rangle^i = \left(\mu_{t_\phi}\langle\overline{D}_{ij}\rangle^v\right)^L &- \left(c_{1NL}\mu_{t_\phi}\frac{\langle k\rangle^i}{\langle\varepsilon\rangle^i}\left[\langle\overline{D}_{ik}\rangle^v\langle\overline{D}_{kj}\rangle^v - \frac{1}{3}\langle\overline{D}_{kl}\rangle^v\langle\overline{D}_{kl}\rangle^v\delta_{ij}\right]\right)^{NL1} \\
&- \left(c_{2NL}\mu_{t_\phi}\frac{\langle k\rangle^i}{\langle\varepsilon\rangle^i}\left[\langle\overline{\Omega}_{ik}\rangle^v\langle\overline{D}_{kj}\rangle^v + \langle\overline{\Omega}_{jk}\rangle^v\langle\overline{D}_{ki}\rangle^v\right]\right)^{NL2} \\
&- \left(c_{3NL}\mu_{t_\phi}\frac{\langle k\rangle^i}{\langle\varepsilon\rangle^i}\left[\langle\overline{\Omega}_{ik}\rangle^v\langle\overline{\Omega}_{jk}\rangle^v - \frac{1}{3}\langle\overline{\Omega}_{lk}\rangle^v\langle\overline{\Omega}_{lk}\rangle^v\delta_{ij}\right]\right)^{NL1} - \left(\frac{2}{3}\phi\delta_{ij}\rho\langle k\rangle^i\right)^L
\end{aligned}
\tag{8}
$$

where δ_{ij} is Kronecker delta; the superscripts L and NL indicate, respectively, the liner and nonlinear contributions, $\langle\overline{D}_{ij}\rangle^v$ and $\langle\overline{\Omega}_{ik}\rangle^v$ are, respectively, the macroscopic deformation and vorticity tensors which can be written in the indexed form as:

$$
D_{ij} = \left(\frac{\partial u_i}{\partial x_j} + \frac{\partial u_j}{\partial x_i}\right),\ \Omega_{ij} = \left(\frac{\partial u_i}{\partial x_j} - \frac{\partial u_j}{\partial x_i}\right) \tag{9}
$$

The nonlinear model proposed by Shih *et al.* (1993) is here adopted whose non-dimensional constants are given by:

$$
c_\mu = \frac{2/3}{1{,}25 + s + 0{,}9\Omega},\ c_{1NL} = \frac{0{,}75}{c_\mu(1000 + s^3)},\ c_{2NL} = \frac{3{,}8}{c_\mu(1000 + s^3)},\ c_{2NL} = \frac{4{,}8}{c_\mu(1000 + s^3)} \tag{10}
$$

where $s = \langle k\rangle^i/\langle\varepsilon\rangle^i\sqrt{0.5\ \langle\overline{D}_{ij}\rangle^v\langle\overline{D}_{ij}\rangle^v}$ and $\Omega = \langle k\rangle^i/\langle\varepsilon\rangle^i\sqrt{0.5\ \langle\overline{\Omega}_{ij}\rangle^v\langle\overline{\Omega}_{ij}\rangle^v}$.

4. Boundary Conditions and Numerical Details

A developed profile of velocity, k and ε (obtained numerically) was imposed at the pipe inlet cross section, and, at its outlet, it was applied a zero diffusion flux condition. In addition, the classical logarithmic wall function was employed for describing the flow near the wall.

In order to solve numerically the flow equations, it was employed the finite volume method applied to a boundary-fitted coordinate system. Equations were discretized in a bi-dimensional axisymmetric domain involving both the clear and the porous medium. Moreover, the SIMPLE algorithm was used for handling the velocity-pressure coupling, (Patankar, 1980) and residues for all transport equations were brought down to 10^{-6}. For more details about the numerical method implemented, see Pedras & de Lemos (2001b).

In order to verify grid independence on the numerical results, besides the axisymmetric mesh of size 202 x 82 (upstream the pipe contraction) and 924 x 46 (downstream the pipe contraction), two additional grids were generated: a coarser mesh with size of 135 x 52 and 616 x 28 and a refined mesh with size of 267 x 115 and 1233 x 64. The differences between the results given by the two more refined meshes were less than 1% for the contraction minor loss coefficient, k_c, whose definition is presented in the following section. Therefore, the grid of size 202 x 82 and 924 x 46 was considered to be sufficiently refined and Fig. (2) presents a partial view of the grid points distribution at the contraction region where it can be observed a concentration of grid points towards the wall and the contraction corner.

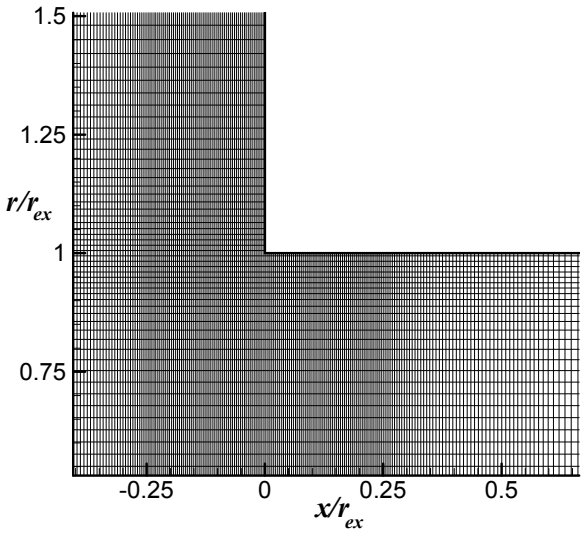

Figure 2. Partial view of the axysimmetric grid at the contraction region: grid size of 202 x 82 (upstream the contraction) and 924 x 46 (downstream the contraction).

5. Results and Discussion

5.1. Clear flow

As presented in Fig. (1), the geometry considered is of a pipe which suffers a sudden contraction whose section area ratio (S_{ex}/S_{in}) is 0.285. In order to have a negligible influence of the inlet and outlet pipe sections on the results, the inlet and outlet pipe length were found to be, respectively, l_{in}/r_{in} = 2.965 and l_{ex}/r_{ex} = 80. Moreover, it was verified that the outlet pipe length was long enough to assume the flow fully developed in its outlet cross section, condition necessary to use Eq. (14) (shown below) and to assure the validity of a zero diffusion flux as a boundary condition at the pipe outlet.

In all results presented in this work, it was adopted an inlet Reynolds number (Re_{in}) of 50,000 based on the pipe inlet diameter (d_{in}) which corresponds to an outlet Reynolds number (Re_{ex}) of 93,627 based on the pipe outlet diameter (d_{ex}). The inlet and the outlet Reynolds number are, respectively, defined as,

$$Re_{in} = \frac{U_{in} d_{in}}{\nu} \tag{11}$$

$$Re_{ex} = \frac{U_{ex} d_{ex}}{\nu} \tag{12}$$

where U_{in} and U_{ex} are the stream-wise bulk velocities, respectively, upstream and downstream the pipe contraction and ν is the kinematic viscosity.

According to the definition given in Fox & McDonald (1998), the minor loss due to the contraction (h_c) can be written as,

$$h_c = k_c \frac{U_{ex}^2}{2} \tag{13}$$

where k_c is the contraction minor loss coefficient which is a non-dimensional parameter. In Streeter (1961) and Rouse (1950), experimental values of k_c without porous insert are presented for several geometries for turbulent flows. It was observed that the experimental values of Streeter (1961) and Rouse (1950) are presented independently of the Reynolds number which indicates that the k_c values are not significantly affected by the Reynolds number for fully turbulent flows. Thus, according to Streeter (1961) and Rouse (1950), the k_c value was found to be, respectively, 0.367 and 0.408 for S_{ex}/S_{in} = 0.285.

According to Fox & McDonald (1998), considering the energy conservation between two cross sections of steady incompressible flow, under the assumption of no external work and uniform pressure and internal energy across the two sections results,

$$h_T = \left(\frac{p_{in}}{\rho} + \alpha_{in} \frac{U_{in}^2}{2} + g z_{in} \right) - \left(\frac{p_{ex}}{\rho} + \alpha_{ex} \frac{U_{ex}^2}{2} + g z_{ex} \right) \tag{14}$$

where h_T is the total head loss between the two sections, p is the pressure in each section, g is the acceleration of gravity, α is the kinetic energy coefficient and z is the coordinate which corresponds to the height level of the pipe section. Subscriptions in and ex represent the inlet and outlet cross section area, respectively. The kinetic energy coefficient, α , is defined as,

$$\alpha = \frac{\frac{1}{S}\int_S \rho \bar{u}^3 dS}{\rho U^3} \tag{15}$$

where $\bar{u}$ is the time average of the local instantaneous velocity in the axial direction.

The major losses, h_l , can be written as a function of the friction factor, f ,

$$h_l = f \frac{l}{d} \frac{U^2}{2} \tag{16}$$

The total head loss is the sum of all major and minor losses and considering the case of a pipe with a sudden contraction, h_T is given by,

$$h_T = h_l + h_c = f_{in} \frac{l_{in}}{d_{in}} \frac{U_{in}^2}{2} + f_{ex} \frac{l_{ex}}{d_{ex}} \frac{U_{ex}^2}{2} + k_c \frac{U_{ex}^2}{2} \tag{17}$$

where, respectively, f_{in} and f_{ex} are the friction factor due to the major losses upstream and downstream the pipe contraction.

We can define the pressure coefficient, Cp , as,

$$Cp = \frac{p - p_{ref}}{\rho U_{ex}^2 / 2} \tag{18}$$

where, p_{ref} is a reference pressure which is, here, assumed to be null, and, p is a local pressure.

Substituting Eq. (17), (18) in Eq. (14), considering fully developed flow at the inlet and outlet pipe cross section and assuming the pipe sections at same height level, the minor loss coefficient can be obtained as,

$$k_c = (Cp_{in} - Cp_{ex}) + \left[\alpha_{in} \left(\frac{U_{in}}{U_{ex}} \right)^2 - \frac{f_{in}}{2} \frac{l_{in}}{r_{in}} \left(\frac{U_{in}}{U_{ex}} \right)^2 - \frac{f_{ex}}{2} \frac{l_{ex}}{r_{ex}} - \alpha_{ex} \right] \tag{19}$$

where the last four terms (between square brackets) depend only on the pipe geometry, the Reynolds number and the friction factor of the corresponding developed flow. Therefore, they do not vary in the cases, here, analyzed. Thus, the k_c value depends only on the pressure coefficient difference ($Cp_{in} - Cp_{ex}$) between the pipe inlet and outlet cross sections.

In Eq. (19), the values of α_{in} and f_{in} were obtained through a numerical simulation, for Re = 50,000, in a pipe with only the pipe inlet diameter (d_{in}), where a periodic condition between its inlet and outlet was employed. The values of f_{ex} were obtained applying the same periodic conditions but with the outlet pipe diameter (d_{ex}) and Re = 93,627. In addition, the values of α_{ex} were calculated by employing its definition given by Eq. (15) at the pipe outlet section. Table (1) presents the values of $Cp_{in} - Cp_{ex}$, α_{in} , α_{ex} , f_{in} and f_{ex} which were obtained through the

numerical simulations using both the linear and nonlinear macroscopic k - ε turbulence models. Then, making use of Eq. (19), the k_c values can be calculated which are presented in Table (2).

Table 1 - Values of Eq. (19) obtained from the numerical simulations.

Macroscopic k - ε turbulence model	$Cp_{in} - Cp_{ex}$	α_{in}	α_{ex}	f_{in}	f_{ex}
Linear	2.180	1.062	1.057	0.02097	0.01836
Nonlinear	2.063	1.063	1.056	0.02054	0.01796

Table 2 - Values of k_c obtained from the numerical calculations for the case without porous insert.

Macroscopic k - ε turbulence model	k_c	Deviation from experimental value of k_c = 0.367 (Streeter, 1961)	Deviation from experimental value of k_c = 0.408 (Rouse, 1950)
Linear	0.473	28.8 %	15.8 %
Nonlinear	0.373	1.5 %	-8.7 %

According to the results presented in Table (2), it is noted that the nonlinear macroscopic k - ε turbulence model predicts well the experimental values of k_c while the linear one over-predicts their values. These results confirm (as demonstrated in the literature – Wilcox, 1998 and Assato & de Lemos, 2000) the better performance of the nonlinear eddy viscosity model (NLEVM) over the linear one for flows characterized by high streamlines curvatures and separation which is the case here analyzed.

In Fig. (3), it is shown the streamlines numerical results of the flow in the pipe for the case without porous insert which were obtained by applying both the linear (Fig. 3a) and nonlinear (Fig. 3b) k - ε turbulence models. Comparing the streamlines results given by the two turbulence models, it is clearly observed that the recirculating bubble size of the nonlinear model is considerably greater than the one obtained by the linear model indicating that, in this case, the anisotropy of the normal Reynolds stresses (predicted by the nonlinear model) affects significantly the streamlines results. In Figs. (3a) and (3b), it is observed an area surrounded by dashed lines which corresponds to the region used to present the streamlines results of Figs. (4) and (5) in the following subsection.

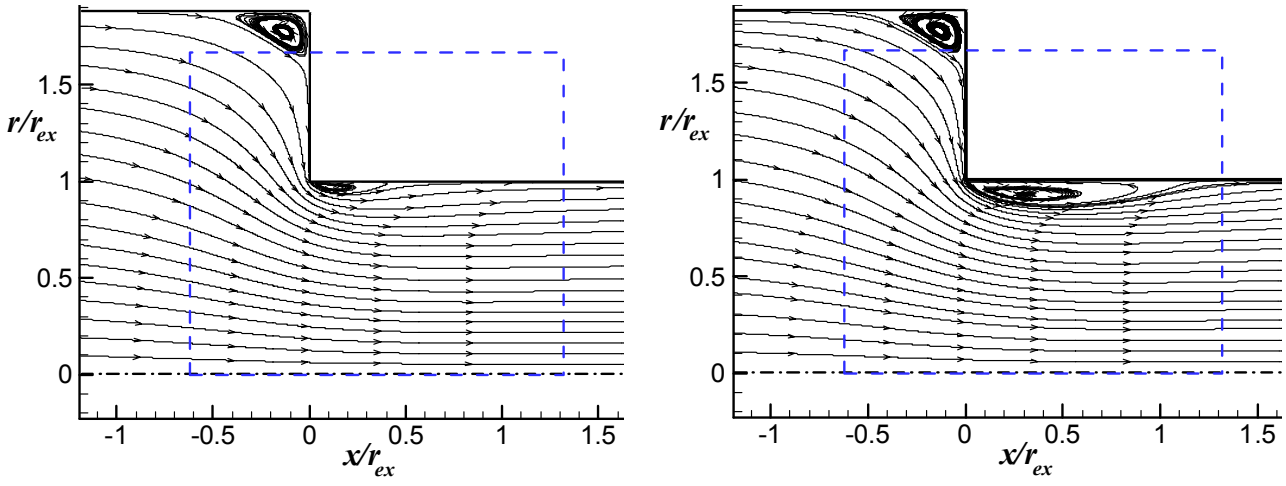

(a) (b)

Figure 3. Streamlines numerical results of the flow in the pipe without porous insert showing an area surrounded by dashed lines to be used in the results of Figs. (4) and (5): a) linear k - ε turbulence model; b) nonlinear k - ε turbulence model.

5.2. Porous insert

Concerning the flow in a pipe with a sudden contraction for the case without porous insert, the recirculating bubble which reduces the effective flow area (*vena contracta*) is the main cause of the minor loss due to the contraction. Therefore, one of the objectives of the porous insert is to suppress or reduce the recirculating bubble, although the porous insert itself increases the losses. This way, there is a compromise between the losses caused by the porous insert and the gain in eliminating or damping the recirculating bubble. Moreover, the numerical results given by both

nonlinear and linear macroscopic eddy viscosity models are compared in order to asses their influence on the flow behavior.

In this subsection, it is presented the numerical results of the flow past a sudden contraction pipe with a porous insert. Concerning the porous insert properties, it was considered two different thicknesses ($a/r_{ex}=0.083$ and $a/r_{ex}=0.166$), a porosity of $\phi=0.85$ and three values of permeability represented by the Darcy Number ($Da=8.56x10^{-3}$, $Da=8.56x10^{-5}$, $Da=8.56x10^{-7}$) which makes 6 different porous insertions. The Darcy number is a non-dimensional parameter related to the permeability (K) whose definition is given by,

$$Da=\frac{K}{(d_{ex})^2} \tag{20}$$

From the numerical simulations, the values of k_c were calculated for each porous insert considered, using both linear and nonlinear macroscopic turbulence models, whose results are presented in Tab. (3).

Table 3 - k_c numerical values for each porous insert, $\phi=0.85$

Macroscopic k - ε turbulence model	a/r_{ex}	Da	k_c
Linear	0	-	0.473
	0.083	8.56 x 10^{-3}	1.05
		8.56 x 10^{-5}	5.46
		8.56 x 10^{-7}	50.07
	0.166	8.56 x 10^{-3}	1.54
		8.56 x 10^{-5}	10.41
		8.56 x 10^{-7}	100.45
Nonlinear	0	-	0.373
	0.083	8.56 x 10^{-3}	1.02
		8.56 x 10^{-5}	5.39
		8.56 x 10^{-7}	50.02
	0.166	8.56 x 10^{-3}	1.53
		8.56 x 10^{-5}	10.34
		8.56 x 10^{-7}	100.41

According to the results of k_c presented in Table (3), it is noted an increase of the minor flow losses in the pipe for lower Darcy values and, also, for higher porous insert thicknesses, being the losses significantly more affected by the Darcy number than the porous insert thickness. Moreover, as the minor losses increase, the differences between the k_c values obtained by the linear and the nonlinear turbulence models become less pronounced. Therefore, the addition of nonlinear terms on the stress-strain expression (resulting in more computing cost) makes little difference on the minor losses results for the cases where the porous insert effect on the flow is more significant (cases with lower Darcy values and higher porous insert thicknesses).

Figures (4) and (5) presents the streamlines numerical results obtained through the linear and the nonlinear k - ε macroscopic turbulence models for the cases without porous insert and with each of the 6 porous inserts considered. In addition, the two vertical lines observed in Figs. (4) and (5) correspond to the upstream and downstream porous insert interfaces. According to the streamlines results of Figs. (4) and (5), it is noticed that the recirculating bubble is significantly damped for $Da=8.56x10^{-3}$ and it is completely suppressed for $Da=8.56x10^{-5}$ and $Da=8.56x10^{-7}$. Moreover, for the cases with $Da=8.56x10^{-5}$ and $Da=8.56x10^{-7}$, it is observed nearly no difference on the streamlines results given by the linear and the nonlinear turbulence models. A possible explanation for this behavior is that the porous insert effect on the flow, which tends to flatten the Darcy velocities profiles, is more dominant than the influence of both the linear and nonlinear approaches given to the macroscopic Reynolds stress tensor. Nevertheless, when $Da=8.56x10^{-3}$, it can be observed that the recirculating bubble predicted by the nonlinear turbulence model is significantly greater than the one obtained by the linear turbulence model which indicates, in this case, that the added nonlinear terms of the turbulence model still have a prominent influence, despite the porous insert effects, on the flow behavior.

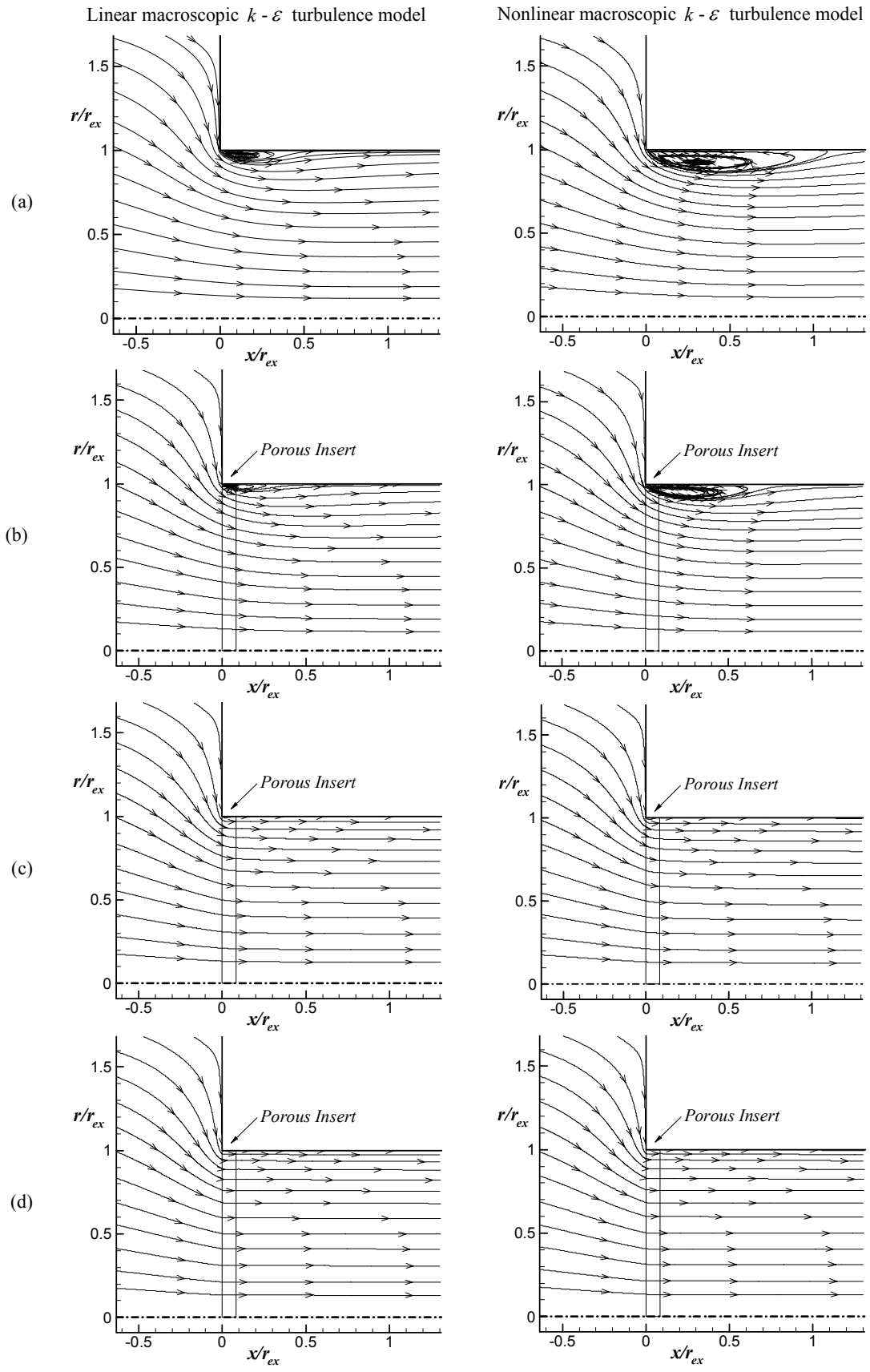

Figure 4. Comparison of streamlines between the linear and nonlinear macroscopic $k-\varepsilon$ turbulence models for $a/r_{ex} = 0.083$ ($\phi = 0.85$): (a) Without porous insert; (b) $Da = 8.56x10^{-3}$; (c) $Da = 8.56x10^{-5}$; (d) $Da = 8.56x10^{-7}$.

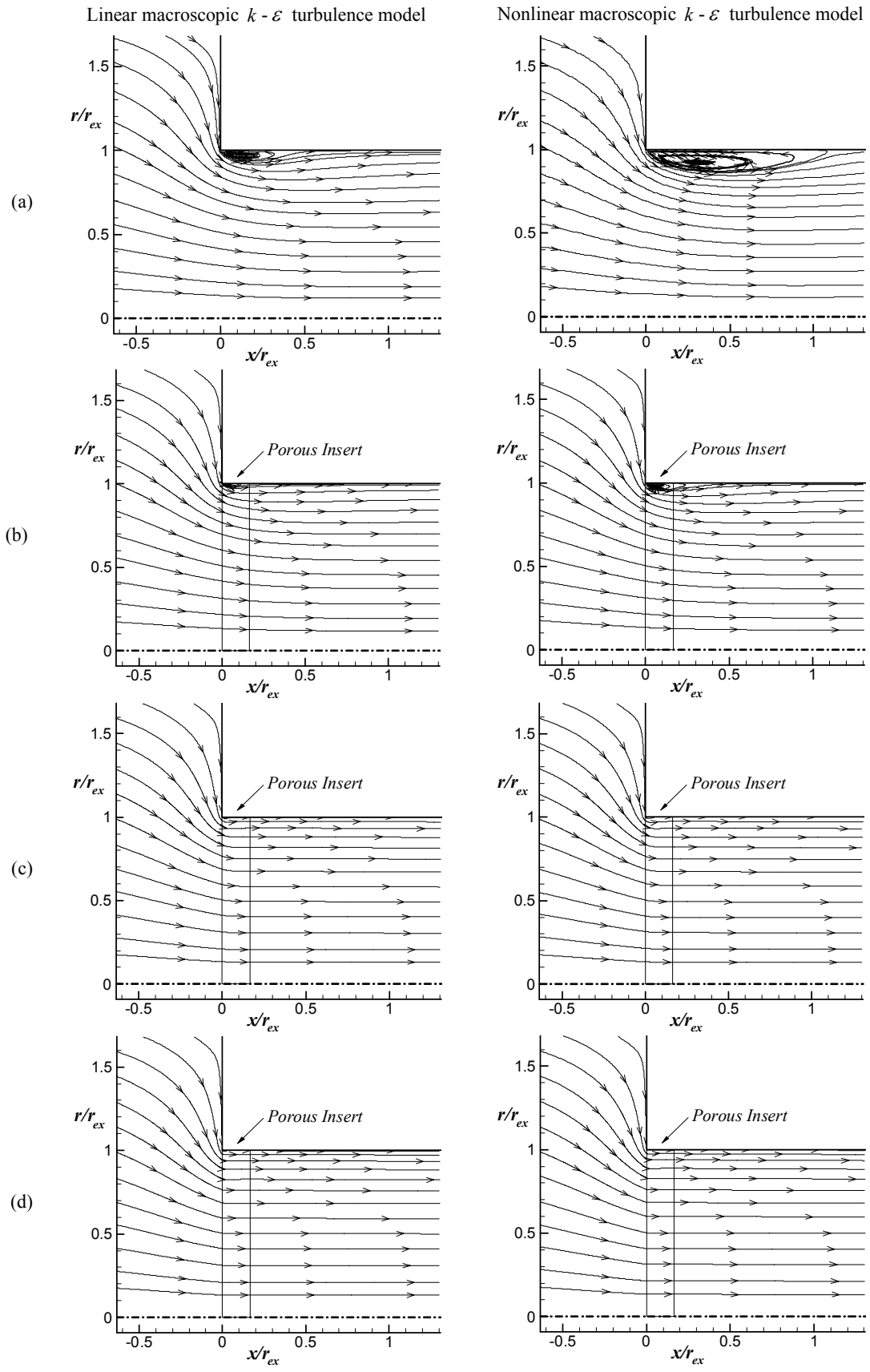

Figure 5. Comparison of streamlines between the linear and nonlinear macroscopic $k-\varepsilon$ turbulence models for $a/r_{ex} = 0.166$ ($\phi = 0.85$): (a) Without porous insert; (b) $Da = 8.56x10^{-3}$; (c) $Da = 8.56x10^{-5}$; (d) $Da = 8.56x10^{-7}$.

6. Conclusion

In this article, both linear and nonlinear turbulence models were applied for simulating the flow past a sudden contraction pipe with a porous insert. In order to asses the effects of the porous insert properties on the flow pattern, parameters such as Darcy number and thickness were varied.

In order to validate the numerical results, the obtained k_c values for the case without porous insert were compared with the experimental ones of Streeter (1961) and Rouse (1950). Whereas the k_c numerical value given by the linear turbulence model over-predicts the experimental data, good agreement was found for the k_c value given by the nonlinear model indicating an advantage of nonlinear closure in predicting more realistic results.

Figures (3)-(5) showed that the recirculating bubble predicted by the linear model was always shorter than the one obtained by the nonlinear model. In addition, it was noted that as the Darcy values decreased and as the porous insert thicknesses increased, the differences between the results obtained by the two turbulence models became less pronounced indicating that the greater the effect of the porous insert on the flow, the lower the influence of the turbulence model on the results.

Moreover, it was observed that the damping of the recirculating bubble and the increase of the flow losses were more affected by the Da values than by the porous insert thicknesses. In addition, no recirculating bubble was observed for $Da = 8.56x10^{-5}$ and $Da = 8.56x10^{-7}$, regardless of the turbulence model used.

Finally, results showed that the minor losses for the cases with porous insert were always higher than the case without porous insert despite the reduction of the recirculating bubble size which indicates that the losses caused by the porous insert itself are more significant than the gain due to the damping of the recirculating bubble. In spite of it, the effect of the permeability and thickness of the porous insert on the flow behavior was analyzed whose findings may be useful in the design of thermo-mechanical equipments, for instance, in the optimization of the heat exchange downstream the pipe contraction section as showed for a forward-facing step geometry in Assato & de Lemos (2004a-b).

7. Acknowledgement

The authors are thankful to CNPq and FAPESP, Brazil, for their financial support during the course of this research.

8. References

Ajayi, K. T., Papadopoulos, G. & Durst, F., 1998, " Influence of upstream development on the losses incurred by flow past an axysymmetric sudden contraction", Proc. 36th Aerospace Sciences Meeting and Exhibit, AIAA-98-0794, Reno, USA.

Assato, M. & de Lemos, M.J.S., 2000, "Tratamento numérico e aplicações de um modelo de viscosidade turbulenta não linear para alto e baixo Reynolds" (in portuguese), Escola Brasileira de Primavera Transição e Turbulência, Uberlândia, Brazil, pp. 459-483.

Assato, A., M. & de Lemos, M.J.S, 2002, "Heat transfer in a suddenly expanded turbulent flow past a porous insert using linear and non-linear eddy-viscosity models", Proc. ASME Int. Mechanical Eng. Congress and Exposition, IMECE2002-39402, New Orleans, USA.

Assato, M. & de Lemos, M.J.S., 2003, "Heat transfer in a back-step flow past a porous insert using a Non-Linear Turbulence model and a Low Reynolds wall treatment", Proc. 3rd Int. Conf. on Computational Heat and Mass Transfer, on CD-ROM, Univ. of Calgary, Banff, Canada.

Assato, M. & de Lemos, M.J.S., 2004a, "Estudo da transferência de calor turbulenta em uma contração abrupta com inserto poroso usando modelos de turbulência linear e não linear" (in Portuguese), Proc. 10th Brazilian Cong. of Thermal Sciences and Engineering, on CD-ROM, Rio de Janeiro, Brazil.

Assato, M. & de Lemos, M.J.S., 2004b, "Flow and heat transfer past a sudden contraction with a porous insert using linear and non-linear turbulence models", Proc. ASME Int. Mechanical Eng. Congress and Exposition, IMECE2004-62407, Anaheim, USA.

Assato, M., Pedras, M.H.J. & de Lemos, M.J.S., 2005, "Numerical solution of turbulent flow past a backward-facing-step with a porous insert using linear and non-linear k-ε models", J.Porous Media, Vol. 8, No.1, pp.13-29.

Benedict R.P., Carlucci, N.A. & Swetz, S.D., 1966, "Flow Losses in abrupt enlargements and contractions", Journal of Engineering for Power, Transactions of ASME, Vol. 88, pp. 73-81.

Chan, C.C. & Lien, F-S, 2005, "Permeability effects of turbulent flow through a porous insert in a backward-facing-step channel, Transport in Porous Media", Vol. 59, No. 1, pp. 47-71.

Durst, F. & Loy, T., 1985, "Investigations of laminar flow in a pipe with sudden contraction of cross section area", Comp. & Fluids, Vol. 13, no. 1, pp. 15-36.

de Lemos, M.J.S. & Pedras, M.H.J., 2001, "Recent mathematical models for turbulent flow in saturated rigid porous media", J. Fluids Eng., Vol. 123, pp. 935-940.

de Lemos, M.J.S & Tofaneli, L.A., 2003, "Pressure drop characteristics of parallel-plate channel flow with porous obstructions at both walls", Proc. ASME Int. Mechanical Eng. Congress and Exposition, IMECE2003-41453, Washington, USA.

Fox, R. W. & McDonald, A. T., 1998, "Introduction to Fluid Mechanics", 5th ed., John Wiley & Sons, New York.

Gray, W.G., Lee, P.C.Y., 1977, "On the theorems for local volume averaging of multiphase system", Int. J. Multiphase Flow, Vol.12, pp.401-410.

Nisizima, S. & Yoshizawa, A., 1987, "Turbulent channel and Couette flows using an anisotropic k - ε model, AIAA J., Vol. 25, No. 3, pp. 414-420.

Orselli, R.M. & de Lemos, M.J.S, 2004, "Escoamento turbulento em contração súbita com inserto poroso" (in portuguese), Proc. 10th Braz. Cong. Thermal Sciences Eng., on CD-ROM, Rio de Janeiro, Brazil.

Orselli, R.M. & de Lemos, M.J.S, 2005a, "Sudden contraction in a turbulent flow with a porous insert, Latin American Journal of Solids and Structures", Vol. 2, No. 3, pp. 269-290.

Orselli, R.M. & de Lemos, M.J.S, 2005b, "Sudden contraction in a turbulent flow with a porous insert using the macroscopic Low Reynolds model", Proc. XXVI Iberian Latin-American Cong. Comp. Meth. Eng., on CD-ROM, Guarapari, Brazil".

Orselli, R.M. & de Lemos, M.J.S., 2005c, "Simulation of turbulent in a sudden contraction with a porous insert", Proc. 18th Int. Cong. Mechanical Engineering, on CD-ROM, Ouro Preto, Brazil.

Orselli, R.M. & de Lemos, M.J.S., 2006, "Simulation of flow past a sudden contraction with a porous insert using linear and nonlinear k - ε models", Proc. XXVII Iberian Latin-American Cong. Comp. Meth. Eng., Belém, Brazil.

Park, T. S. & Sung, H. J., 1995, "A nonlinear low-Reynolds-number k-epsilon model for turbulent separated and reattaching flows", Int. J. Heat and Mass Transfer, Vol. 8, pp. 2657-2666.

Patankar, S.V., 1980, "Numerical heat transfer and fluid flow", Mc-Graw Hill, Hemisphere.

Pedras, M.H.J. & de Lemos, M.J.S., 2000, "On the definition of turbulent kinetic energy for flow in porous media", Int. Commun. Heat and Mass Transfer, Vol. 27, No. 2, pp. 211-220.

Pedras, M.H.J. & de Lemos, M.J.S., 2001a, "Macroscopic turbulence modeling for incompressible flow through undeformable porous media", Int. J. Heat Mass Transfer, Vol. 44, No. 6, pp. 1081-1093.

Pedras, M.H.J. & de Lemos, M.J.S., 2001b, "Simulation of turbulent flow in porous media using a spatially periodic array and a Low Re Two-Equation closure", Numerical Heat Transfer - Part A Appl., Vol. 39, No. 1, pp. 35-59.

Pedras, M.H.J. & de Lemos, M.J.S., 2001c, "On the mathematical description and simulation of turbulent flow in a porous media formed by an array of elleptic rods", J. Fluids Eng., Vol. 123, No.4, pp.941-947.

Pedras, M. H. J. & de Lemos, M.J.S., 2003, "Computational of turbulent flow in porous media using a Low-Reynolds k - ε model and an infinite array of transversally displaced elliptic rods", Numerical Heat Transfer – Part A Appl., Vol. 43, No.1, pp. 585-602.

Rouse, H., 1950, "Enginnering Hydraulics", John Wiley & Sons, New York.

Rubinstein, R. & Barton, J. M., 1990, "Renormalization group analysis of the stress transport equation", Phys. Fluids A, Vol. 2, No. 8, pp. 1472-1476.

Shih, T. H., Zhu, J & Lumley, J. L., 1993, "A Realizable Reynolds Stress Algebraic equation model", NASA TM-105993.

Speziale, C.G., 1987, "On non-linear k - and - models of turbulence", J. Fluid Mech., Vol. 176, pp. 459-475.

Streeter, V.L., 1961, ed., "Handbook of Fluid Dynamics", McGraw-Hill, New York.

Wilcox, D. C., 1998, "Turbulence modeling for CFD", 2nd ed. La Canada: DCW Ind.

9. Copyright Notice

Proceedings of the 11th Brazilian Congress of Thermal Sciences and Engineering -- ENCIT 2006
Braz. Soc. of Mechanical Sciences and Engineering -- ABCM, Curitiba, Brazil, Dec. 5-8, 2006

Paper CIT06-0752

DETERMINAÇÃO EXPERIMENTAL DO CAMPO DE VELOCIDADE EM DIFUSORES RADIAIS

Maurício P. Giovanela
POLO – Laboratórios de Pesquisa em Refrigeração e Termofísica
Departamento de Engenharia Mecãnica
Universidade Federal de santa Catarina
mauricio@polo.ufsc.br

César J. Deschamps
Departamento de Engenharia Mecãnica
Universidade Federal de santa Catarina
deschamps@polo.ufsc.br

Resumo. *O trabalho apresenta uma caracterização experimental do escoamento em difusores radiais, complementada por resultados numéricos. Esta classe de escoamento tem atraído a atenção de diversos pesquisadores devido à presença de um número de fenômenos fundamentais, associados a regiões de estagnação, separação, recirculação e reatamento. Medições do campo de velocidade mostraram que o escoamento é marcado pela presença de uma grande região de separação na entrada do difusor, a qual permite explicar a assimetria do perfil de velocidade na saída do difusor e também discutir um processo de instabilidade originado pela presença de vórtices junto às paredes. Além de permitir uma análise do escoamento em difusores radiais, os dados experimentais fornecidos são também úteis para a validação de metodologias numéricas desenvolvidas para a solução de escoamentos turbulentos.*

Palavras chave: *difusor radial, turbulência, laminarização, válvulas.*

1. Introdução

Além de sua relevância tecnológica, o escoamento em difusores radiais apresenta uma série de fenômenos fundamentais da mecânica dos fluidos, incluindo regiões de estagnação, gradientes adversos de pressão, separação, linhas de corrente curvas e laminarização. O difusor radial é formado por dois discos paralelos e o escoamento é suprido através de um orifício central de diâmetro d localizado no disco anterior. Após ser defletido pelo disco frontal de diâmetro D, o fluido escoa entre as superfícies dos dois discos. A Fig. 1 apresenta diferentes padrões de escoamento possíveis de serem encontrados em difusores radiais, e a correspondente distribuição de pressão sobre o disco frontal, de acordo com o afastamento s/d entre os discos, mas mantendo a vazão e a relação de diâmetros D/d (= 3.0) constante. Para pequenos valores de afastamentos, s/d, e números de Reynolds, Re (= $U_{in}d/\nu$), o escoamento é laminar e variação de pressão ao longo do difusor decorre essencialmente da ação viscosa. Aumentando a vazão, o número de Reynolds na entrada pode exceder um certo valor crítico e o regime turbulento ocorrerá na região entre os discos. Nessa condição pode haver uma transição reversa do regime turbulento para o laminar, uma vez que a velocidade decai no difusor com a posição radial. Se os níveis de velocidade forem suficientemente elevados, o escoamento será completamente turbulento e os termos de inércia tornam-se dominantes sobre os termos viscosos na determinação da distribuição de pressão sobre, e a pressão aumentará com a posição radial. À medida que o afastamento entre os discos é aumentado, o escoamento eventualmente separará na entrada do difusor e reatará a jusante, formando uma região de recirculação anular. Finalmente, se o afastamento é aumentado ainda mais, a região de recirculação aumentará até que, a partir de um certo ponto, deixará de reatar e o escoamento ocorrerá na forma de um jato sobre o disco frontal

Moller (1963) foi o primeiro pesquisador a realizar extensivas medições de perfis de velocidade média para o escoamento turbulento em difusores radiais, utilizando tubos de Pitot, e sugeriu um processo de laminarização evidenciado pelo aumento de espessura da subcamada limite viscosa. Experimentos de Bakke & Kreith (1969) mostraram que a laminarização não chega efetivamente a acontecer em sua totalidade, com a produção de energia cinética turbulenta de fato aumentando na direção radial. Apesar disto, ponderaram que não se pode atribuir a este termo a manutenção do regime turbulento, uma vez que em muitos casos o mesmo é pequeno quando comparado ao mecanismo de dissipação.

Linhas de corrente do escoamento em difusores radiais foram obtidas pela primeira vez por Marple et al. (1974) através de uma técnica eletrolítica de visualização, para efeito de validação da solução numérica sob duas condições de vazão (Re = 700 e 2.300). Por outro lado, Böswirth (1982) forneceu uma descrição básica dos principais fenômenos físicos em difusores radiais, empregando um modelo ampliado em um túnel de fumaça, incluindo detalhes sobre o padrão de separação do escoamento, a formação de esteiras e a estagnação do escoamento junto ao disco frontal. Posteriormente, Böswirth (1986) complementou sua investigação com medições de velocidade junto às paredes do orifício de passagem e do disco frontal, bem como em duas seções transversais do jato formado na saída do difusor.

Ferreira e Driessen (1986) realizaram medições da distribuição de pressão sobre o disco frontal e, com o auxílio dos resultados de Böswirth (1982), apresentaram uma caracterização do escoamento em função do afastamento, conforme ilustrado na Fig. 1 para uma relação de diâmetros D/d = 3,0. Conforme indicado pelos autores, o afastamento entre os discos tem um papel extremamente importante na configuração do escoamento.

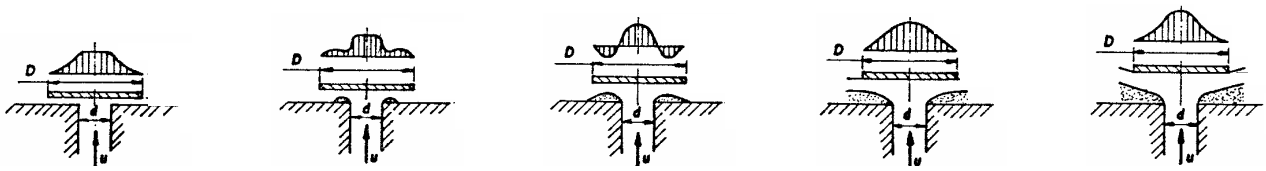

(a) s/d < 0,02 (b) 0,02 < s/d < 0,05 (c) 0,05 < s/d < 0,50 (d) 0,50 < s/d < 1,0 (e) s/d > 1,0

Figura 1. Distribuição de pressão sobre o disco frontal de acordo com o afastamento entre os discos; adaptado de (Ferreira e Driessen, 1986).

Tabatabai e Pollard (1987) analisaram experimentalmente o escoamento turbulento em um difusor radial, com ênfase no mecanismo do decaimento da turbulência, considerando uma relação de diâmetros (D/d ≅ 10) e um afastamento (s/d ≅ 0,08). Observaram que para números de Reynolds elevados (Re > 100.000) o comportamento do escoamento é similar ao escoamento turbulento plenamente desenvolvido em canais. Para números de Reynolds menores (Re < 30.000), constataram que a turbulência decai à medida que o escoamento progride ao longo do difusor, tornando o perfil de velocidade semelhante àquele do regime laminar. Concluíram que o decaimento da turbulência é lento em função do mecanismo de geração da turbulência se manter mesmo para números de Reynolds reduzidos. Os resultados mostraram a condição de equilíbrio local para números de Reynolds elevados. Por outro lado, mostraram também que a condição de equilíbrio era destruída à medida que a espessura da subcamada limite viscosa aumentava em direção ao plano médio do afastamento entre os discos. Finalmente, verificaram que estruturas turbulentas de grandes escalas persistem no escoamento mesmo sob um processo de laminarização.

Ervin *et al.* (1989) empregaram a anemometria de fio quente para realizar medições de componentes axial e radial da velocidade instantânea do escoamento, para uma relação de diâmetros (D/d ≅ 9) e um afastamento (s/d = 0,122). A partir dos dados foram então obtidos diversos parâmetros do escoamento (perfis de velocidade média, tensões de Reynolds, intensidade da turbulência, entre outros). Observaram que a hipótese de perfil universal de velocidade não é adequada para a região de entrada do escoamento, mas que é satisfatória em regiões mais afastadas ao longo do difusor. Além disto, verificaram que a intensidade da turbulência é bem elevada na saída do difusor, mesmo nas situações onde as tensões cisalhantes de Reynolds são de magnitudes praticamente desprezíveis.

Tramschek e Nasr (1992) realizaram medições de perfis de velocidade entre os discos de um difusor radial, empregando Anemometria Laser Doppler. Dados para a componente radial de velocidade, obtidos para afastamentos s/d < 0.2 e D/d = 2,8, demonstraram a extensão da região de separação formada na entrada do difusor (r/d =0,5).

Myung e Lee (2002) empregaram a velocimetria por imagem de partículas (PIV) para visualizar o escoamento em um difusor radial, com D/d = 1,25, para dois afastamentos s/d (= 0,15 e 0,25). Embora de forma qualitativa, os resultados mostram o aumento do tamanho da região de recirculação com o afastamento entre os discos.

Souto e Deschamps (2002) investigaram experimentalmente o escoamento em difusores radiais, apresentando dados de perfis de velocidade média e de tensões normais turbulentas na saída do difusor. Os autores apresentaram resultados numéricos, obtidos com a metodologia desenvolvida por Salinas et al. (1999), e mostraram uma boa concordância dos mesmos com dados experimentais de velocidade média e tensões turbulentas.

Da revisão de investigações realizadas em difusores radiais, fica evidente que a maioria utilizou técnicas de medições locais, tais como anemometria de fio quente e velocimetria laser Doppler, para fornecer dados de velocidade em pontos de interesse do escoamento. Dados foram fornecidos em função do tempo e permitiram a determinação de diversas correlações baseadas em uma média temporal. O objetivo deste trabalho é a caracterização do campo de velocidade em difusores radiais, através da velocimetria por imagem de partículas (PIV). Uma outra finalidade é o fornecimento de dados para a validação de metodologias numéricas, especialmente aquelas destinadas à modelação de escoamentos turbulentos.

2. Bancada experimental

Conforme ilustrado na Fig. 2a, a bancada experimental é formada por três reservatórios de ar comprimido, com elementos de controle de pressão, umidade e impurezas. Um medidor de vazão, construído de acordo com a norma British Standard 1042 (1989), é posicionado entre dois tubos de alumínio com diâmetro interno de 34,9 mm e comprimento de 2 m. A seção de testes é composta por um difusor radial e um sistema de alta precisão para o posicionamento do disco frontal, conforme ilustrado na Fig. 2b. O diâmetro dos discos anterior e frontal é igual a 104,7 mm, enquanto o diâmetro do orifício de passagem, d, é igual a 39 mm. Desta forma a relação entre os diâmetros do disco frontal e do orifício de passagem, D/d, é igual 3.

No experimento são necessárias medições de temperatura, pressão e velocidade. A temperatura foi medida com o emprego de um termopar tipo T, enquanto que os valores de pressão manométrica referentes à placa de orifício foram obtidos com transdutores indutivos da HBM, modelo PD1, calibrados através de um manômetro de coluna de água em "U". Um barômetro de mercúrio foi utilizado para determinar a pressão atmosférica.

Para a aquisição de dados e controle da bancada foi desenvolvido um programa computacional com auxílio da plataforma LabView v. 6i (National Instruments, 2000).

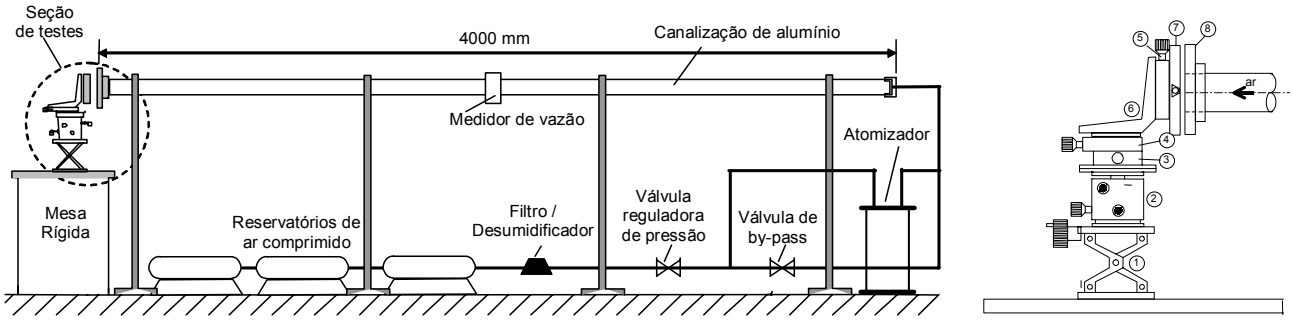

(a) (b)

Figura 2. Bancada experimental (a) e seção de teste (b).

O sistema PIV é composto de dois lasers Nd:Yag independentes, uma câmera digital de 8 bit com uma resolução de 1008 x 1018 pixels, um sincronizador e uma unidade para controlar todo o sistema e processar os sinais. Uma vez que a velocidade do escoamento é medida indiretamente através da medição da velocidade de partículas adicionadas ao escoamento, um gerador de partículas também é necessário. As partículas devem seguir perfeitamente o escoamento e isto requer que seus diâmetros sejam extremamente pequenos; neste trabalho da ordem de 1 μm. As partículas espalham muito pouco a luz e, portanto, lasers pulsados de potência elevada são essenciais para a iluminação das pequenas partículas imersas no escoamento.

O procedimento de medição consiste em formar imagens das partículas suspensas no escoamento sob investigação, iluminando-as com uma lâmina de laser pulsado orientada na direção normal ao eixo de uma câmera fotográfica, como pode ser observado na Fig. 3(a). A câmera registra as posições das partículas no escoamento, as quais são iluminadas com dois pulsos de luz separadas por um intervalo muito pequeno. Através da medição do deslocamento das partículas neste intervalo de tempo, representadas pelas imagens A e B na Fig. 4, o vetor velocidade local pode ser estimado. No sistema empregado neste trabalho, cada laser possui um pulso de energia máximo de 100 mJ, comprimento de onda de 532 nm (espectro verde), e são capazes de operar com uma freqüência de 15 Hz. Para permitir o registro de duas imagens em uma sucessão rápida, a câmera deve estar perfeitamente sincronizada com o laser.

A quantidade de partículas de óleo no escoamento, a potência do laser e a defasagem entre os disparos dos dois lasers foram ajustadas de acordo com a condição de escoamento. Este é um aspecto do procedimento experimental pois afeta a precisão dos resultados. Para as medições realizadas, a defasagem foi ajustada entre 5 e 30 μs, de acordo com a magnitude da velocidade, de tal forma a garantir que o deslocamento das partículas não fossem maior do que 4 pixels na imagem, onde a relação entre deslocamento e pixel é dada por M = 45,87 μm/pixel.

O processamento das imagens é baseado em uma análise de correlação cruzada aplicada em subáreas de 16^2 pixel, sobrepostas em 50% (8 pixels). Assume-se que se essas áreas forem suficientemente pequenas, o deslocamento relativo entre as partículas de uma área entre a imagens A e B é muito pequeno. Baseando-se nesse princípio, utilizam-se softwares de correlação cruzada para procurar na segunda imagem (B) um padrão de partículas existente em uma subárea da primeira imagem (A), conforme ilustrado na Fig. 4. Para que a correlação cruzada forneça resultados precisos é recomendável que existam pelo menos 10 partículas em cada uma dessas subáreas. Além disto, é importante que o deslocamento das partículas entre a imagem A e a imagem B, defasadas de um intervalo de tempo dT, não supere 25% do comprimento referente a aresta da subárea, no presente caso sendo equivalente a 4 pixels. Como M = 45,87 μm/pixel, o deslocamento das partículas não deve ser, portanto, superior a 183,48 μm. Maiores detalhes da velocimetria por imagem de partículas podem ser encontrados em Azevedo e Almeida (2002).

3. Procedimento experimental

O ajuste do posicionamento do disco frontal é de fundamental importância na realização dos experimentos, devendo ser posicionado de maneira que fique o mais paralelo e concêntrico possível em relação ao disco anterior. Para o ajuste do paralelismo foi utilizada uma esfera de rolamento de 5,0029 ± 0,0008 mm de diâmetro colada a uma linha fina. Através de mesas de deslocamento micrométrico, a posição do disco é ajustada até que a esfera deslize suavemente entre os discos e com a mesma interferência ao longo de todo o difusor, determinando assim um afastamento conhecido.

A concentricidade do disco frontal em relação ao difusor é feita logo após o ajuste do paralelismo, levando-se em conta que os diâmetros dos discos anterior e frontal são iguais. Após essa etapa tem-se o disco frontal posicionado concêntrica e paralelamente com um afastamento conhecido, podendo movê-lo para qualquer outra posição através das mesas de deslocamento.

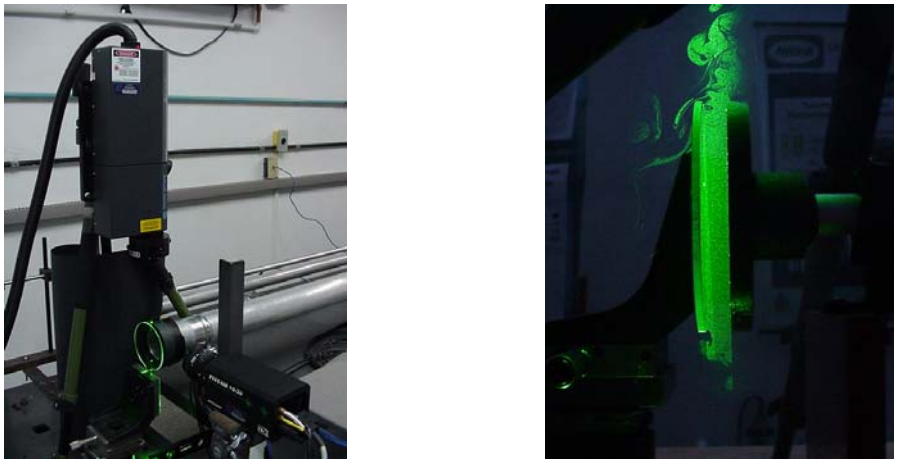

(a) (b)

Figura 3. Sistema PIV (a) e seção de teste iluminada pelo laser (b).

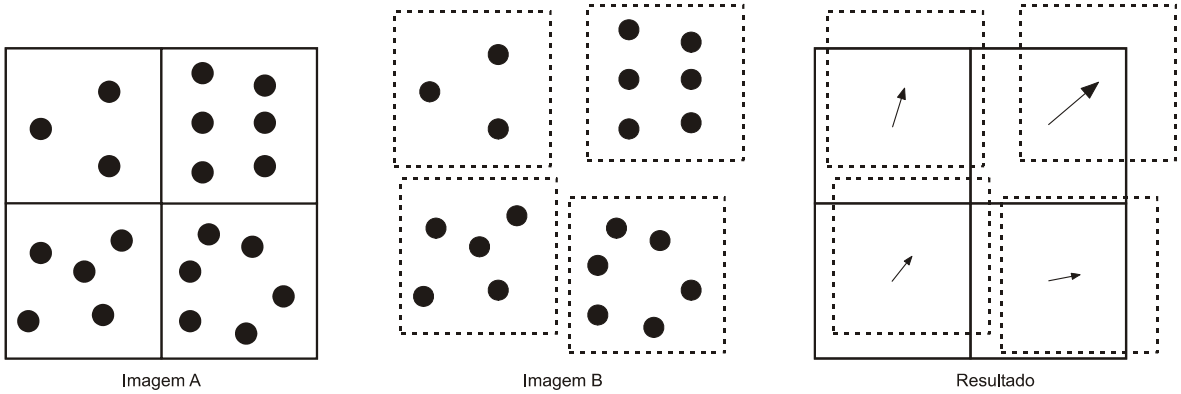

Figura 4. Processamento do campo de velocidade via PIV.

O PIV é posicionado visualmente com o auxílio de um medidor de nível, para garantir que o cabeçote do laser e a câmera não estejam inclinados. O foco da câmera é ajustado de forma a se obter a melhor nitidez da imagem no plano de medição e, então, obtém-se o fator de ampliação M. A quantidade de partículas, a intensidade do laser e o intervalo entre os disparos do laser são ajustados de forma iterativa. Assim, algumas medições são realizadas previamente de forma a obter a melhor regulagem do sistema. A quantidade de partículas é modificada utilizando-se uma válvula *by-pass*, que altera a vazão de ar comprimido no atomizador. A defasagem de tempo entre os disparos dos lasers, dT, é selecionado em função da velocidade máxima atingida pelas partículas no difusor. Somente quando todos esses parâmetros foram ajustados é que o teste é realizado.

O sistema registrou imagens do escoamento saindo do orifício de passagem em dois afastamentos s/d (= 0,10 e 0,20) uma condição número de Reynolds igual a 15.000 (6,45 m/s). As partículas traçadoras de 1 μm de diâmetro foram geradas através de atomizador de óleo de oliva pressurizado com ar comprimido. As imagens foram obtidas para a região do difusor radial, correspondente à região entre as superfícies dos discos anterior e frontal, usando uma lente 60mm/f2.8. Na presente investigação, a câmera registrou pares de imagens com uma freqüência de 15 Hz durante um período de 4s, as quais foram então selecionadas, transferidas e armazenadas em um computador para processamento posterior. Os resultados a serem apresentados são, desta forma, a média das 60 medições.

4. Resultados

O escoamento foi investigado para um número de Reynolds (Re = 15000) e dois afastamentos adimensionais (s/d = 0,10 e 0,20). Uma vez que o suprimento de ar para a seção de teste acorre através de uma tubulação com uma relação comprimento/diâmetro de aproximadamente 60, o escoamento na entrada na região do orifício de passagem do difusor

pode ser assumido completamente desenvolvido. A Fig.5 apresenta os campos de vetores velocidade, obtidos na região do difusor entre os discos para os dois afastamentos investigados. Em cada uma das figuras indica-se a escala empregada para representar a magnitude do vetor velocidade. Devido à razão de aspecto entre o comprimento e a largura do difusor, o resultado para cada afastamento foi subdividido em duas regiões: a primeira compreendida entre a entrada do difusor até a posição radial r = 35 mm e, a segunda, de r = 35 mm até a saída do difusor.

Como pode ser observado, a separação do escoamento na entrada do difusor (r ≈ 17,5 mm) ocorre em ambas as situações, sendo que a região de recirculação é bem maior no caso do maior afastamento. Esta diferença decorre do fato de que para s/d = 0,20 a transferência de quantidade de movimento na direção transversal do escoamento é menos efetiva. Desta forma, o déficit de quantidade de movimento junto à superfície do disco anterior é maior e a região de separação se estende até praticamente a saída do difusor. É interessante notar também os níveis levados de velocidade junto à superfície do disco frontal em r ≈ 17,5 mm, decorrente da mudança brusca da direção do escoamento. Por outro lado, percebe-se claramente a ação viscosa na redução da velocidade junto à superfície do disco frontal a partir da entrada do difusor.

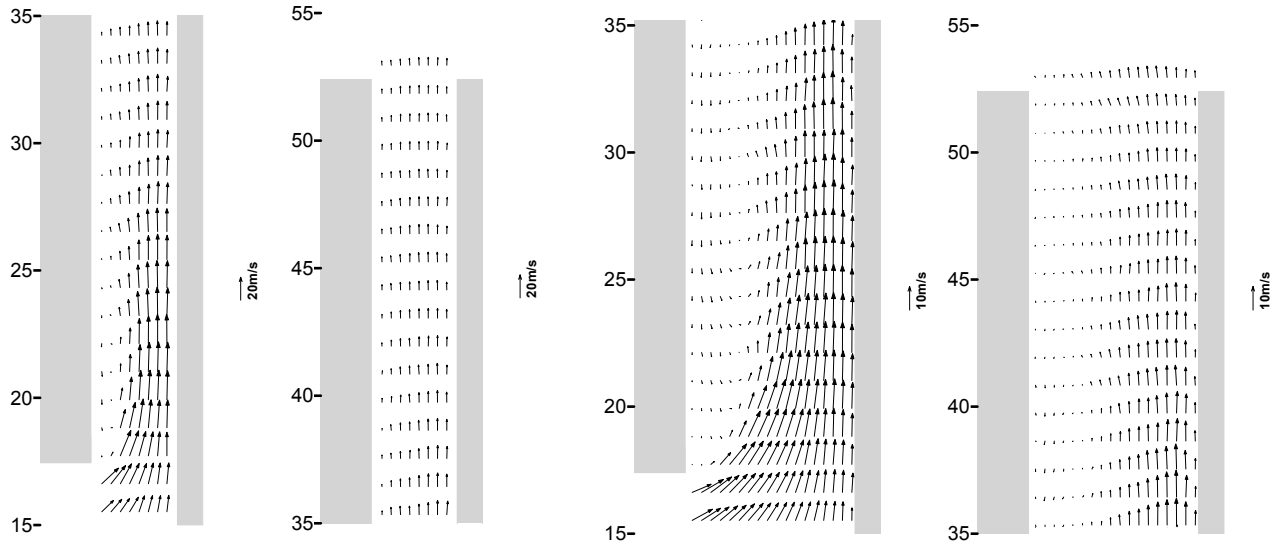

(a) s/d = 0,10. (b) s/d = 0,20.

Figura 5. Vetores velocidade no difusor radial para Re = 15.000.

Perfis para a componente radial de velocidade V* (= V/U_{in}) são apresentados a seguir para quatro posições radiais do difusor: (a) r = 20 mm; (b) r = 25 mm; (c) r = 30 mm; (d) r = 52,35 mm; esta última representando a saída do difusor. Para o afastamento s/d = 0,10, é incluído o perfil de velocidade na saída do difusor obtido experimentalmente por Souto e Deschamps (2004) através da anemometria de fio quente.

Para efeito de complementação da análise, além dos dados experimentais são apresentados também resultados numéricos do escoamento obtidos com o modelo de turbulência RNG k-ε. Este modelo tem sido usado na análise do escoamento em difusores radiais, com uma boa concordância entre resultados numéricos e experimentais para a distribuição de pressão sobre o disco frontal. Para informações detalhadas a respeito dos diversos parâmetros do procedimento de solução, bem como uma discussão sobre as condições de contorno das equações governantes, sugere-se o trabalho de Salinas-Casanova *et al*. (1999).

As regiões de recirculação evidenciadas na Fig. 5 aparecem também nas Figs. 6 e 7, com a região de fluxo reverso bem definida. Outro aspecto interessante é característica praticamente invíscida do escoamento na região central da entrada do difusor, a qual vai desaparecendo à medida que o escoamento progride ao longo do difusor, conforme pode ser observado nas posições subseqüentes, r = 25 mm e 30 mm. A assimetria do perfil de velocidade na saída do difusor verificada para o menor afastamento (s/d = 0,10) é confirmada pelos dados de anemometria de fio quente e também pela previsão numérica.

O nível de concordância entre os resultados numérico e experimental é satisfatório, principalmente na entrada do difusor onde o efeito da separação do escoamento é mais intenso. No entanto, o desenvolvimento do escoamento ao longo do difusor previsto numericamente não corresponde perfeitamente aos dados experimentais. Isto pode visto através do exame das posições r =25 mm e 30 mm para s/d = 0,10 e das posições r = 30 mm e 52,35 mm para s/d = 0,20.

Visualizações do escoamento turbulento junto a superfícies sólidas (Kline *et al.*, 1967; Kim *et al.*, 1971) identificaram a presença de um processo de desprendimento repentino de vórtices na região próxima à parede. Tal processo é composto de três fases principais: i) ejeção de fluido com baixa quantidade de movimento da proximidade da parede; ii) rompimento da porção do escoamento ejetado em uma posição afastada da parede; iii) transporte de fluido

com alta quantidade de movimento para a região da parede. Em um número de Reynolds elevados, o transporte de fluido com baixa quantidade de movimento para regiões de velocidades elevadas afastadas da parede representa uma contribuição importante para a geração da turbulência. Tabatai e Pollard (1987) verificaram a persistência de estruturas de grande escala no escoamento em difusores radiais e argumentaram que elas são as responsáveis por manter a turbulência, mesmo em situações onde o perfil de velocidade se aproxima do formato laminar, sugerindo um processo de laminarização. Outros autores também observaram um fenômeno semelhante ao detectado por Tabatai e Pollard (1987). Por exemplo, Ervin *et al*. (1989) encontrou um padrão de instabilidade no escoamento, o qual foi associado principalmente à região de entrada do difusor, e também apontaram que o fenômeno se deve ao desprendimento de vórtices. A Fig. 8 apresenta resultados experimentais para campos instantâneos de velocidade, obtidos de quatro imagens consecutivas do sistema PIV. Fica evidente a presença de vórtices no escoamento e também a instabilidade da região de separação, marcada pela grande variação do campo de velocidade. Além disto, percebe-se também movimentos de porções de fluido com alta quantidade de movimento em direção à parede, conforme descrito por Kline *et al.* (1967) e Kim *et al.* (1971).

Um aspecto a ser investigado em trabalhos futuros é o efeito da relação entre os diâmetros do disco frontal e do orifício de passagem, D/d, sobre o escoamento. Com base nos resultados apresentados aqui, pode-se antecipar que, para valores menores de D/d, a região de recirculação se estenderá até fora do difusor. Por outro lado, para relações D/d elevadas, a desaceleração do escoamento devido ao aumento da área com o raio pode fazer surgir o processo de laminarização mencionado por Tabatai e Pollard (1987) e Ervin *et al*. (1989).

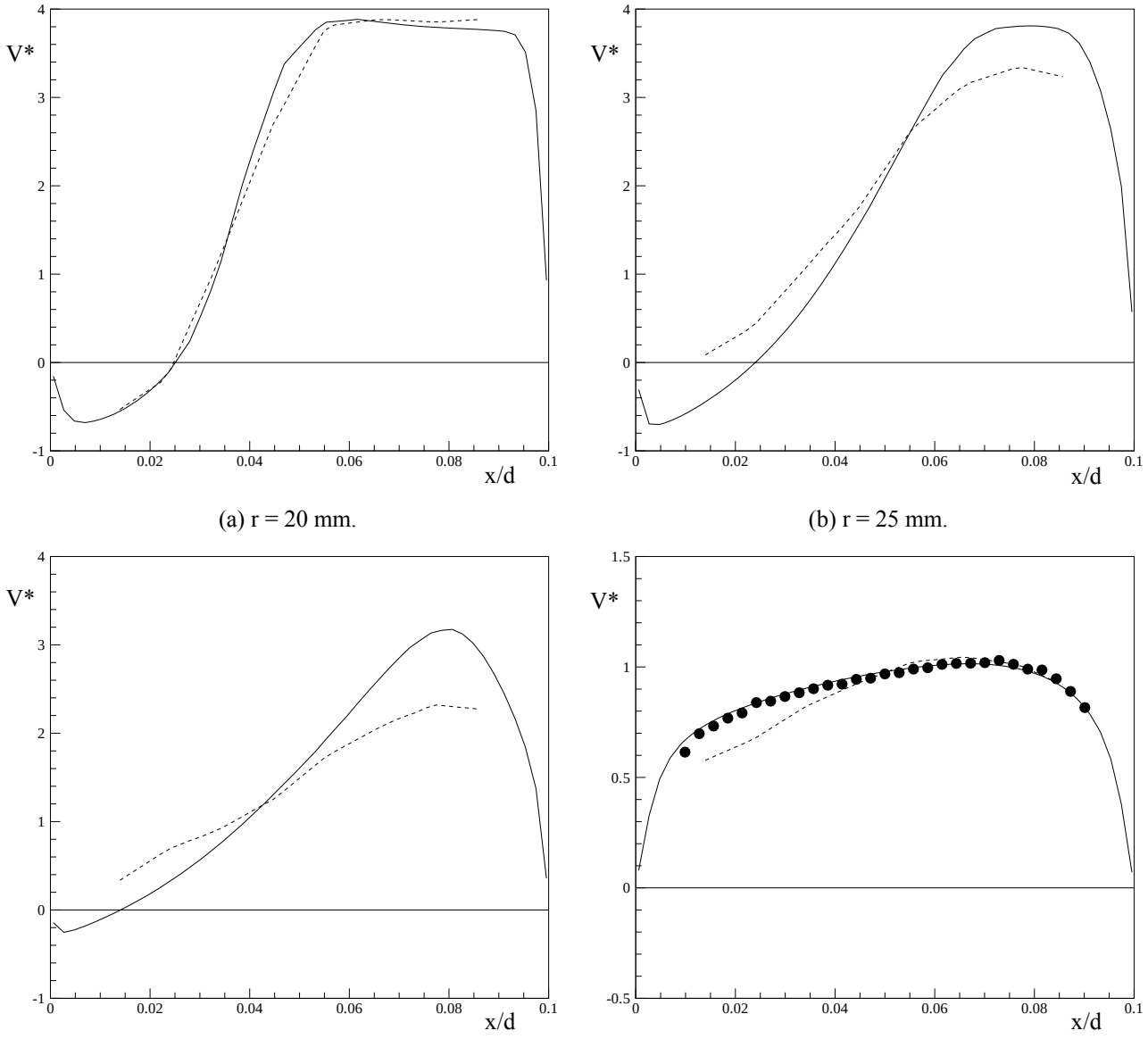

Figura 6. Perfis para a componente radial de velocidade V* (= V/U_{in}); s/d 0,10.
—— Resultado numérico; - - - - Dado exp. PIV; ● Dado exp. (HWA).

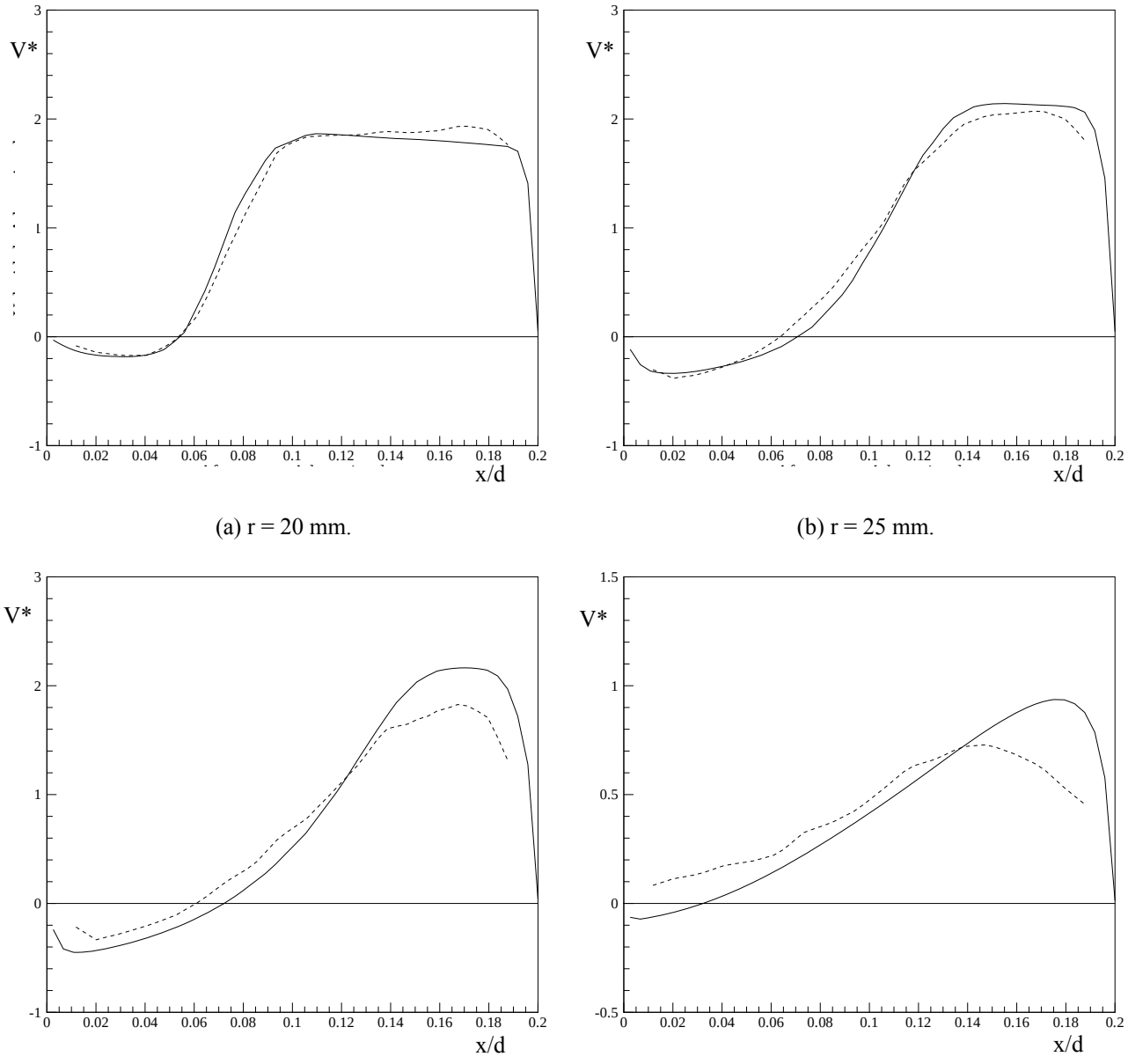

Figura 7. Perfis para a componente radial de velocidade V* (= V/U_{in}); s/d 0,20.
—— Resultado numérico; - - - - Dado exp. PIV.

5. Conclusões

O presente trabalho apresentou uma investigação experimental do escoamento em difusores radiais através da velocimetria por imagem de partículas. A análise dos resultados é complementada com perfis de velocidade obtidos via anemometria de fio quente e previsões numéricas. Esta classe de escoamento tem atraído a atenção de diversos pesquisadores devido à presença de alguns fenômenos fundamentais da mecânica dos fluidos, tais como regiões de estagnação, separação, recirculação e reatamento. Medições do campo de velocidade do escoamento revelaram a presença de uma região de separação significativa sobre a superfície do disco anterior, a qual geral uma assimetria no perfil de velocidade na saída do difusor. Além de sua importância no entendimento do escoamento, os dados experimentais obtidos na presente investigação são úteis também para a validação de metodologias numéricas desenvolvidas para a modelação de escoamentos turbulentos. Uma etapa futura considerará o efeito da relação entre os diâmetros do disco frontal e do orifício de passagem, bem como a possibilidade da ocorrência de um processo de laminarização do escoamento em vazões mais baixas, originada pela redução da velocidade local com o aumento da área de passagem no difusor.

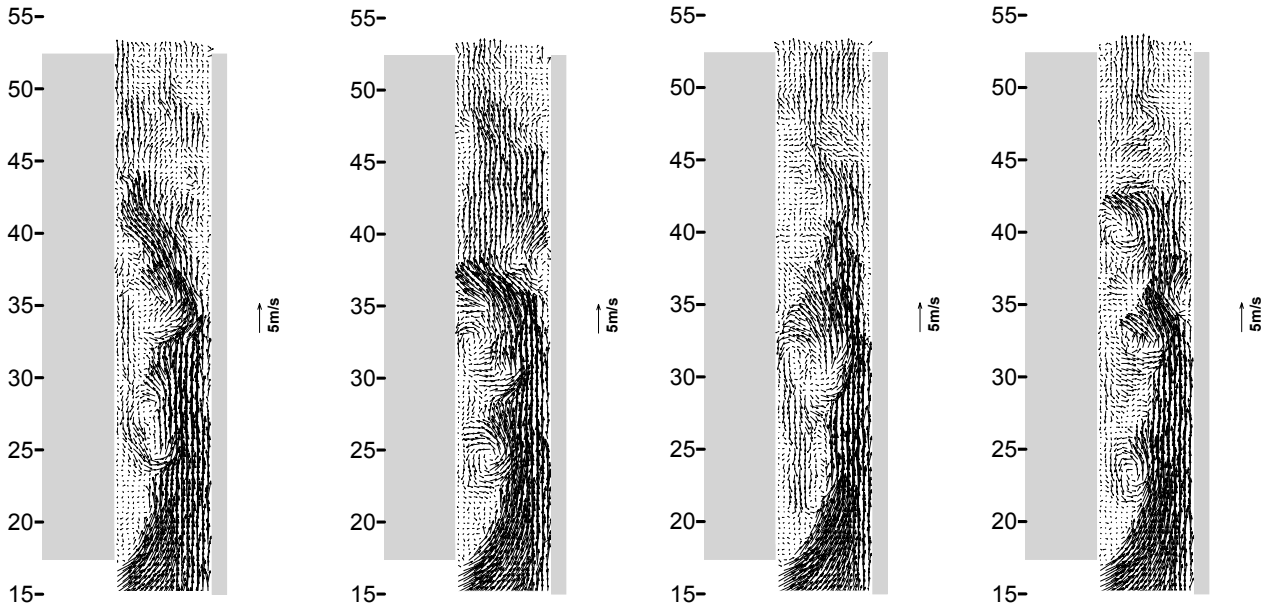

Figura 8. Imagens consecutivas do campo instantâneo de velocidade: s/d = 0,10.

6. Agradecimentos

Este trabalho teve o apoio da Empresa Brasileira de Compressores S.A. (EMBRACO). Os autores agradecem também o auxílio do eng. Evandro L.L. Pereira na realização de simulações numéricas do escoamento e também na preparação do manuscrito.

7. Referências

Bakke, E. e Kreith, F., 1969, "Inverse Transition in Radial Diffusers", ASME-AIChE Heat Transfer Conference, Minneapolis, USA, Paper 69-HT-33.

Böswirth, L., 1982, "Theoretical and Experimental Study on Flow in Valve Channels – Part I", Proc. 5th Purdue Int. Compressors Technology Conference, West Lafayette, USA, pp. 38-45.

Böswirth, L., 1986, "Valve Flow Experiments with Enlarged Models – Part I", Proc. 8th Purdue Int. Compressors Technology Conference, West Lafayette, USA, pp. 28-44.

British Standard Institution, 1989, "Measurement of Fluid Flow in Closed Conduits", BS 1042, Section 1.2.

Ervin, J.S., Suryanarayana, N.V., Chai Ng, H., 1989, "Radial Turbulent Flow of a Fluid Between Two Coaxial Disks", Journal of Fluids Engineering, vol. 111, pp. 378-383.

Ferreira, R.T.S., Driessen, J.L., 1986, "Analysis of the Influence of Valve Geometric Parameters on the Effective Flow and Force Areas", 9th Purdue Int. Compressors Technology Conference, West Lafayette, USA, pp. 632-646.

Kim, H.T., Kline, S.J., Reynolds, W.C., 1971, "The Production of Turbulence Near a Smooth Wall in a Turbulent Boundary Layer", J. Fluid Mechanics, v. 50, pp. 133-160.

Kline, S.J., Reynolds, W.C., Schraub, F.A., Runstadler, P.W., 1967, "The Structure of Turbulent Boundary Layers", J. Fluid Mechanics, v. 30, pp. 741-774.

Moller, P. S., 1963, "Radial Flow Without Swirl Between Parallel Discs", The Aeronautical Quarterly, pp. 163-186.

Myung, H.J., Lee, I.S., 2000, "Investigation of the Discharge Flow of a Reciprocating Compressor using PIV, Proc. 11th Purdue Int. Compressors Technology Conference, West Lafayette, USA, pp. 391-396.

National Instruments Inc., 2000, "LabView – User Manual", Part Number 320999C-01.

Salinas-Casanova, D.A., Deschamps, C.J., Prata, A.T. 1999. Turbulent flow through a valve with inclined reeds. Proc. International Conference on Compressor and Their Systems, London, UK, pp. 443-452.

Souto, L.M., Deschamps, C.J., 2002, "Investigação Experimental do Escoamento em Turbulento em Difusores Radiais", Proc. 9th Brazilian Congress of Thermal Engineering and Sciences, Caxambu - MG, 10 p.

Tabatabai, M., Pollard, A., 1987, "Turbulence in Radial Flow Between Parallel Disks at Medium and Low Reynolds Numbers", J. Fluid Mech., vol. 185, pp. 483-502.

Tramschek, A.B., Nasr, A., 1992, " CFD and LDA Studies of Flow Through a Plate Valve", Proc. 11th Purdue Int. Compressors Technology Conference, West Lafayette, USA, pp. 1227-1239.

EXPERIMENTAL CHARACTERIZATION OF VELOCITY FIELD IN RADIAL DIFFUSERS

Maurício P. Giovanela
POLO – Research Laboratories for Emerging Technologies in Cooling and Thermophysics
Department of Mechanical Engineering
Federal University of Santa Catarina
mauricio@polo.ufsc.br

Cesar J. Deschamps
Department of Mechanical Engineering
Federal University of Santa Catarina
deschamps@polo.ufsc.br

Abstract

The paper presented an experimental characterization of the flow through radial diffusers, complemented by numerical results. This class of flow has attracted the attention of several researchers because it contains a number of fundamental phenomena, associated to regions of stagnation, separation, recirculating and reattachment. Measurements of the velocity field showed the flow is mainly distinguished by the presence of a large separated flow region at the diffuser entrance, which affects the velocity profile at the diffuser exit. In addition to allowing the analysis of the radial diffuser flow, the experimental data made available herein are also useful to validate numerical methodologies developed to solve turbulent flows. A further step in the investigation will consider the different diameter ratios between the front disk and the feeding orifice, and the phenomenon of laminarization that occurs at lower mass flow rate.

Keywords: radial diffuser, particle image velocimetry, adverse pressure gradient, turbulence modeling.

Proceedings of the 11th Brazilian Congress of Thermal Sciences and Engineering -- ENCIT 2006
Braz. Soc. of Mechanical Sciences and Engineering -- ABCM, Curitiba, Brazil, Dec. 5-8, 2006

Paper CIT06-0768

ANÁLISE DO ESCOAMENTO EM CONDUTOS DE ADMISSÃO NA PRESENÇA DE JUNÇÕES

Sérgio de Morais Hanriot
Programa de Pós-Graduação em Engenharia Mecânica - Pontifícia Universidade Católica de Minas Gerais
hanriot@pucminas.br

Rudolf Huebner
Programa de Pós-Graduação em Engenharia Mecânica - Pontifícia Universidade Católica de Minas Gerais
rudolf@pucminas.br

Ismael Alves Coutinho
Pontifícia Universidade Católica de Minas Gerais
ismael_coutinho@yahoo.com

Resumo. *Os condutos de admissão em motores de combustão interna têm como tarefa conduzir o ar da atmosfera até os cilindros, distribuindo de modo uniforme a massa de ar admitida com a menor perda de pressão possível. Devido ao movimento alternativo dos pistões e das válvulas, o campo de escoamento do gás presente no conduto de admissão apresenta oscilações de pressão. Tais oscilações podem ser utilizadas para aumentar a quantidade de massa de ar admitida. Este fato está relacionado basicamente à geometria do conduto de admissão envolvendo variáveis tais como o diâmetro do conduto, junções, comprimento e acessórios. No presente trabalho foi realizada uma análise numérica e experimental das ondas de pressão no interior do conduto de admissão na presença de junções e os efeitos da posição da junção na quantidade de massa de ar admitida através das válvulas de admissão. Os resultados mostraram que a localização da junção afeta a eficiência volumétrica do motor.*

Palavras chave: Escoamento transiente, Motores, Junções.

1. Introdução

Nos projetos de condutos de admissão de motores de combustão interna observa-se que a geometria afeta consideravelmente a quantidade de massa de ar admitida. Isso ocorre porque a massa de ar que entra nos cilindros é função da freqüência dos pulsos de pressão produzidos pelo movimento alternativo dos pistões e das válvulas de admissão. Os condutos de admissão devem ser projetados de modo a aumentar a massa de ar admitida pelos cilindros para um determinado intervalo de rotação do motor. Basicamente, o processo consiste em considerar o conduto de maneira que um pulso de pressão positivo alcance a porta da válvula de admissão no instante em que o pistão encontra-se no ponto morto inferior (Winterbone, 1999, 2000). Winterbone (1990) mostrou que o conduto de admissão ressonando no modo de um ressonador de Helmholtz tem uma grande influência nos efeitos de pressão no cilindro no momento de fechamento da válvula de admissão.

Benajes (1997) apresentou um modelo com base na teoria de ondas para o projeto de condutos de admissão. O modelo foi capaz de calcular as dimensões para um conduto de admissão com valores ótimos de rendimento volumétrico. As curvas, caixas ressonantes e as junções são exemplos de acessórios em que pode existir uma reflexão dos pulsos de pressão. Além disso, as ondas de pressão também são influenciadas pelos pulsos de pressão produzidos por outros cilindros que não estão no curso de admissão, causando ainda um fluxo reverso e uma diminuição considerável da quantidade de massa de ar admitida.

A presença de junções no conduto implica em uma perda de pressão adicional. Algumas vezes tais perdas são desprezíveis, enquanto em outras podem afetar o rendimento volumétrico. Os projetistas se deparam com uma série de situações envolvendo junções e acessórios, mas em linhas gerais é necessária a realização de testes experimentais para o entendimento dos fenômenos que ocorrem no interior do conduto.

De fato, são três as possibilidades para a obtenção dos dados:

- Execução de testes para análise do escamento envolvendo as junções;
- Resultados experimentais da literatura;
- Expressões empíricas e analíticas para a estimativa da perda de carga nas junções.

Os coeficientes de perda de pressão apresentados na literatura são obtidos experimentalmente considerando-se escoamento permanente. Este é um processo complexo e caro pois que requer a confecção de junções previamente projetadas. Ocorre que há certos desenhos de junções que não são apresentadas pela literatura.

É conveniente classificar as junções em dois tipos distintos: Junções ‘T’ e ‘Y’. As junções T consistem em um duto reto com área constante de seção reta, com uma interseção lateral inclinada em relação ao duto principal. Uma junção ‘T’ de 90º é um caso da junção T geral. Junções Y são formadas pelo duto principal que se bifurca em dois dutos de

mesmo ângulo em relação ao duto principal. Winterbone e Pearson (2000) descreveram como se realizar as medições de perdas de pressão em tais junções.

Neste trabalho, os efeitos produzidos por uma junção 'Y' de 20^o presente no conduto de admissão foram estudados. A junção foi inserida alternadamente em três posições do conduto de admissão visando estabelecer qual posição apresentou a maior quantidade de ar admitida. O objetivo do trabalho foi realizar uma comparação entre os resultados numéricos obtidos a partir de um código numérico que utiliza o Método das Características com os experimentais e avaliar os efeitos da diferença de pressão entre a porta da válvula e o interior do cilindro.

1.2 Revisão da Literatura

Morse et al (1938) foram um dos primeiros a mencionar o fenômeno de pulsos de pressão nos condutos de admissão. Eles estudaram as vibrações em um conduto de admissão de quatro tempos e mono cilindro. No trabalho foi mostrado que o movimento transiente do ar produz ondas estacionárias no conduto. Nessa condição, se durante a revolução a onda de pressão atinge um valor em amplitude menor que a média do ciclo nas imediações do fechamento da válvula de admissão, ocorrerá uma diminuição do rendimento volumétrico.

Os projetistas têm conhecimento que a geometria dos condutos de admissão afeta substancialmente o desempenho de motores de combustão interna. Isso ocorre porque o ar admitido pelos cilindros é função da freqüência das ondas de pressão produzidas pelo movimento alternativo das válvulas e do pistão. Os condutos de admissão podem ser projetados de modo a permitir uma melhoria do rendimento volumétrico em motores de combustão interna (Hanriot et al, 2000). Os condutos de admissão de comprimento variável são exemplos dessa aplicação. Considerando a natureza do processo de admissão de ar, o mecanismo básico de aumento da quantidade de ar admitida segue o conceito de um pico de pressão atingir a porta da válvula de admissão próximo ao fechamento da mesma (Winterbone, 1999, 2000).

Winterbone (1990) mostrou que podem ser considerados dois diferentes modos de vibração no projeto dos condutos. Tais modos visam estabelecer uma relação entre a geometria do conduto e as conseqüências no rendimento volumétrico: um em que o ar no interior do conduto vibra como um tubo de freqüência de um quarto de onda e outro que vibra como um ressonador de Helmholtz. Nessa condição, foi mostrado que maiores rendimentos ocorrem quando o pico da onda de pressão atinge a porta da válvula nas imediações de seu fechamento e abertura. Ambos os modos são importantes, porém o do ressonador de Helmholtz parece ter uma maior influência na eficiência volumétrica devido aos efeitos da pressão no cilindro quando a válvula de admissão se fecha.

O estudo do sistema completo de admissão pode ser realizado considerando-se dois sub-sistemas: Os pistões e as válvulas, que se movem periodicamente e atuam como fonte excitante; e o conduto de admissão, como um sistema que responde à excitação de acordo com sua geometria. A interação mútua afeta consideravelmente a condição de escoamento transiente, e consequentemente o processo global de admissão de ar.

O caso simples de um tubo, com uma extremidade aberta e a outra fechada, que vibra com uma freqüência natural de um quarto de onda é relevante para motores mono ou multi-cilindros com condutos de admissão independentes, ou mesmo em motores cujos condutos de admissão primário estão conectados em uma câmara intermediária. Nesta condição, a Eq.(1) mostra a relação.

$$f = \frac{a}{4L} \tag{1}$$

Onde f=$w/2\pi$ e L é o comprimento efetivo do conduto e a representa a velocidade da onda no tubo.

Benajes (1997) apresentou um modelo baseado na teoria acústica de ondas, capaz de calcular as dimensões principais de um conduto de admissão. Nesse trabalho foi mostrado que o local onde ocorrem as reflexões das ondas de pressão é importante no projeto dos condutos. Alguns parâmetros que consideram a relação dinâmica existente entre o conduto e o motor foram definidos. No emprego desses parâmetros, o modelo pôde ser aplicado para dois modos complementares: análise acústica no conduto e o estabelecimento de uma geometria ótima para as condições de projeto. A Eq. (2) mostra a resposta acústica do conduto de admissão na presença de junções e câmaras intermediárias.

$$Z_1 \tan\frac{wL_1}{a} = Z_2 \frac{A_2}{A_1}\cot\frac{wL_2}{a} - \frac{wV}{aA_1} \tag{2}$$

Z representa o número de condutos primários e secundários, w a freqüência natural do conjunto do conduto de admissão, L os comprimentos dos condutos, a velocidade do som, A a área da seção reta e V o volume da câmara intermediária, se existir.

À parte da resposta dinâmica do conjunto completo do conduto de admissão, o fenômeno de reflexão das ondas de pressão nas junções e eventualmente câmaras intermediárias é similar àquele descrito para um motor mono-cilindro. Isso significa que em tais motores duas freqüências naturais podem ser ajustadas: a freqüência natural do conjunto completo (Eq. 2), e freqüências de alta ordem ligadas ao conduto primário, dada pela Eq. (1).

O parâmetro que relaciona a freqüência do sistema e a do motor é chamado parâmetro de freqüência Q, definido pela Eq. (3):

$$Q = \frac{f_{sistema}}{f_{motor}} \tag{3}$$

Estudos teóricos e experimentais mostraram (Morse, 1938) que condutos de admissão ótimos seriam aqueles cujo parâmetro de freqüência situa-se entre 3 e 5. Alguns resultados publicados por Ohata a Ishida (1982) permitiram derivar uma expressão (Eq. 4) de um valor ótimo de *Q* em função da rotação do motor para um motor com características específicas:

$$Q_{ótimo} = 2{,}7 + \frac{N}{3333} \tag{4}$$

Sendo que a rotação do motor (em rpm) variava de 1204 a 6004 rpm.

2. Metodologia Analítica e Simulação Numérica

No presente trabalho os fenômenos de onda no interior dos condutos de admissão são analisados através de um modelo analítico unidimensional utilizando o "*método das características*". Este método utiliza uma técnica de solução de equações diferenciais parciais hiperbólicas transformando-as em equações diferenciais ordinárias (Benson, 1973, 1982, Onorati, 1998; Winterbone e Pearson, 2000).

As equações governantes unidimensionais que descrevem um escoamento compressível e não homeontrópico para um gás ideal são (Winterbone e Pearson, 1999, 2000):

$$\frac{\partial V}{\partial t} + A\frac{\partial V}{\partial x} + C = 0 \tag{5}$$

onde:

$$V = \begin{bmatrix} \rho \\ u \\ p \end{bmatrix},\ A = \begin{bmatrix} u & \rho & 0 \\ 0 & u & \frac{1}{\rho} \\ 0 & a^2\rho & u \end{bmatrix} \qquad C = \begin{bmatrix} \rho u \\ 0 \\ a^2\rho u \end{bmatrix}\frac{1}{F}\frac{dF}{dx} + \begin{bmatrix} 0 \\ G \\ (\kappa - 1)\rho(q + uG) \end{bmatrix} \tag{6}$$

sendo *x* a distância, *t* o tempo, *p* a pressão, *u* a velocidade do escoamento, ρ a massa específica e *a* a velocidade do som. *F* é a área da seção transversal e *d* o diâmetro do conduto. $G = 4f_w u|u|/2d$, onde f_w é o fator de atrito na parede do conduto, *q* é a transferência de calor por unidade de massa e *k* é a razão entre os calores específicos. Esta série de equações diferenciais parciais é um sistema hiperbólico não-linear, e a integração pode ser obtida através de esquemas numéricos aptos para utilizar as informações contidas ao longo das linhas características no campo do escoamento (Roe, [12]). Três linhas características são usadas em um método não homeontrópico (Winterbone, 2000): características se movendo para a direita e esquerda $dx/dt = u \pm a$ (representa as inclinações (distúrbios) que são relatados para as velocidades das ondas em relação ao escoamento médio) e a trajetória da linha $dx/dt = u$, que segue (acompanha) o movimento do escoamento no conduto.

2.1 – Simulação Numérica

Inicialmente foram realizadas simulações numéricas em um programa computacional disponível para verificar as características do escoamento do ar no conduto de admissão considerando a presença da junção. O programa, escrito em linguagem Fortran, foi implementado no Centro de Pesquisas da FIAT (CRF), Itália, para validar experimentos no banco de fluxo. A metodologia utilizada foi considerar as válvulas defasadas de 180º.

Os parâmetros fornecidos ao programa como dados de entrada para a obtenção da vazão mássica e da pressão com a defasagem das válvulas eram os seguintes: número de cilindros e número de válvulas por cilindro, rotação do eixo de manivelas, diferença de pressão entre o ambiente e o tanque de equalização no banco de fluxo, temperatura ambiente e do tanque de equalização de pressão, dimensões, conexões e fator de atrito nos dutos, valor das quedas de pressão localizadas, coeficiente de exaustão na entrada das válvulas, relação entre o deslocamento angular e a respectiva área isentrópica para a primeira e a segunda válvula, quantidade e localização dos transdutores de pressão e pontos da malha para o cálculo e saída dos parâmetros.

O programa fornecia como resultado as seguintes variáveis nos pontos da malha definida: variação da pressão absoluta em função do ângulo do eixo de manivelas, variação do número de Mach em função do ângulo do eixo de manivelas e variação da vazão mássica em função do ângulo do eixo de manivelas.

O modelo computacional simulou situações em que o banco de fluxo utilizava o cabeçote de um motor de oito válvulas. A análise da variação da vazão mássica e da pressão no escoamento transiente ocasionado pelo movimento das válvulas de admissão foi feita com apenas dois cilindros em operação. As simulações numéricas foram realizadas na faixa de rotação realizadas nos experimentos. Na análise numérica foram consideradas tomadas de pressão nas portas das válvulas de admissão e em pontos distribuídos ao longo do conduto.

3. Aparato Experimental e Procedimentos

O banco de fluxo (Fig.1) é um aparato experimental usado para o estudo do escoamento permanente e transiente do ar em condutos de admissão e descarga de motores de combustão interna alternativos em condições de diferencial de pressão constante. O aparato permite a medição da vazão do escoamento por meio de medidores de fluxo laminar (Hanriot, 2001).

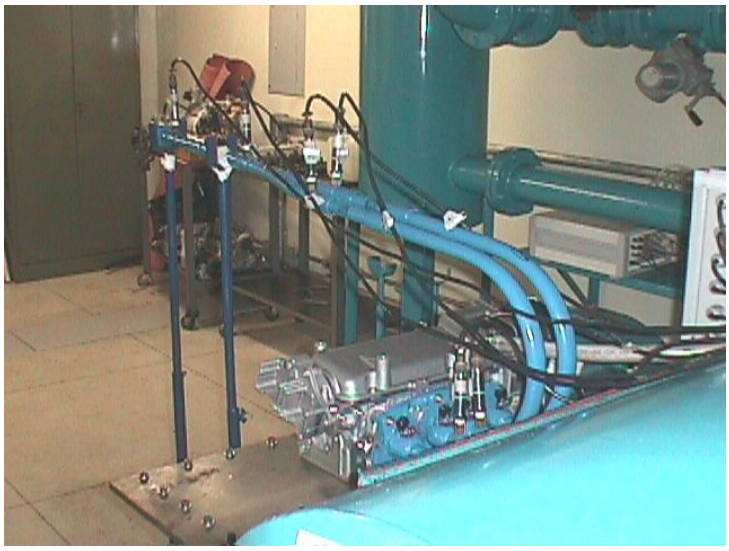

Figura 1 – Vista do aparato experimental – Banco de Fluxo

A diferença de pressão constante é obtida através de um reservatório de grande volume ao qual o sistema de admissão é conectado em conjunto com o cabeçote do motor. Na outra extremidade, o reservatório é conectado a um ventilador centrífugo que produz a diferença de pressão. O reservatório é utilizado para atenuar os pulsos de pressão gerados pelo soprador e assim somente as variações de pressão que ocorrem no interior do conduto de admissão são analisadas. A queda de pressão é obtida através de um conjunto de válvulas entre o soprador e o reservatório de equalização (também chamado de plenum), com capacidade de 350 litros. O presente trabalho, somente o cabeçote foi conectado ao reservatório. As válvulas do cabeçote do motor foram acionadas através de um motor elétrico conectado ao cabeçote através de uma correia dentada. O motor elétrico usado possui potência de 30 kW e rotação máxima de 3500 rpm.

As pressões dinâmicas no conduto de admissão foram obtidas através de transdutores piezoresistivos com intervalos de medição de ± 2 bar. Os termopares de temperatura são do tipo resistência de platina, com utilização entre 0 a 60º C. Um cabeçote de um motor de 1000 cm³, quatro cilindros foi conectado ao reservatório de equalização. Somente as válvulas de admissão do segundo e terceiro cilindros foram colocadas em operação, enquanto as outras válvulas foram desconectadas. Um tubo de aço de 2,155 m de comprimento e diâmetro de 22,3 mm contendo uma junção foi conectado à porta das duas válvulas.

Seis transdutores de pressão foram utilizados e distribuídos ao longo do conduto de admissão conforme o desenho esquemático da Fig. 2. Os transdutores foram nomeados como P1, P2, ..., P6, sendo que os de nome P1 e P2 foram conectados o mais próximo possível da porta da válvula. Três configurações do posicionamento da junção foram testadas e os respectivos comprimentos (em milímetros) são mostrados na Tab. 1.

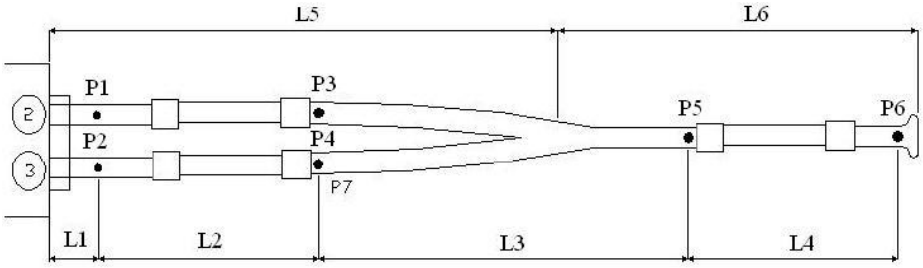

Figura 2 – Desenho esquemático da junção e dos transdutores de pressão no conduto de admissão.

Tabela 1 – Posicionamento das configurações da junção testada

	L1	L2	L3	L4	L5	L6
Configuração 1	200	268	260	1216	598	1517
Configuração 2	200	810	260	714	1140	1015
Configuração 3	200	1309	260	215	1639	516

Basicamente a Configuração 1 era aquela cuja junção se posicionava mais próxima da porta da válvula e a Configuração 3 mais distante.

Os experimentos foram realizados para a faixa de rotação de 602 a 3002 rpm do eixo comando de válvulas, com intervalos entre rotação de 200 rpm. A Fig. 3 mostra um desenho esquemático do conjunto de teste do banco de fluxo.

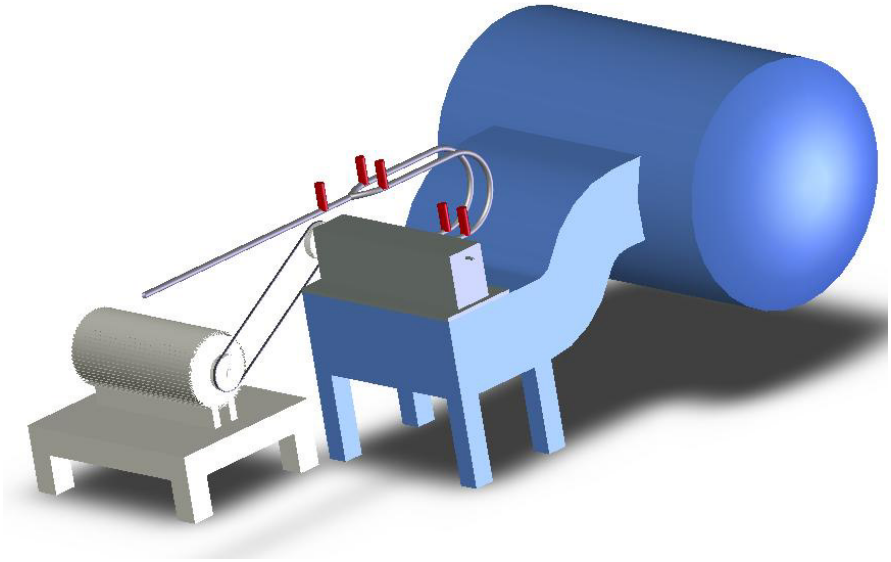

Figura 3 – Desenho experimental do conjunto de teste - Banco de Fluxo.

4. Resultados

A vazão mássica obtida numericamente e a experimental são mostradas nas Fig. 4 a 6 para as três posições estudadas da junção. Inicialmente observa-se que o modelo é capaz de reproduzir a variação da vazão mássica em função da rotação do eixo comando de válvulas. Os pontos de rotação em que a vazão é máxima e mínima são captados pelo programa computacional com elevada eficiência. Quanto aos valores de vazão mássica, há ligeira divergência, indicando que os dados de entrada do modelo necessitam de um refinamento maior. Entretanto, em modelos unidimensionais como o código mencionado, a relevância maior encontra-se na variação da curva de vazão mássica ao longo da faixa de rotação e o acompanhamento dos pontos de máximo e mínimo da curva. Assim, o modelo foi capaz de reproduzir o fenômeno de forma coerente.

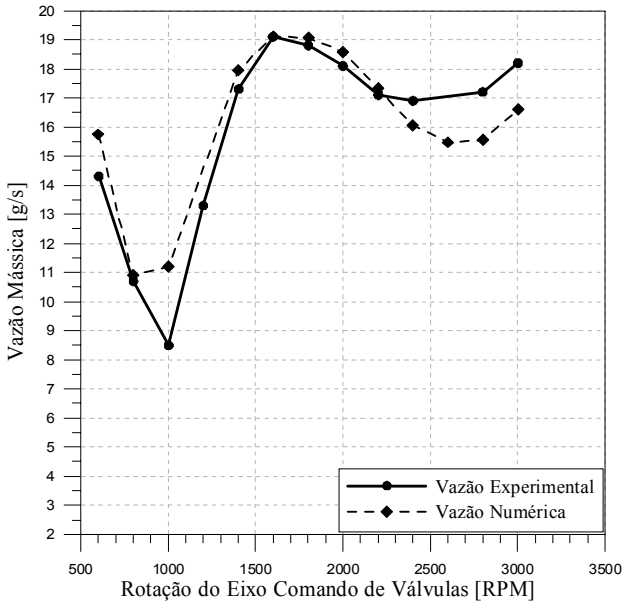

Figura 4 – Vazão numérica e experimental para a Configuração 1

Quanto aos pontos de máximos e mínimos das curvas apresentadas, observa-se que o primeiro mínimo ocorre entre 800 e 1000 rpm para as três configurações. Entretanto, a Configuração 1 apresenta uma vazão mássica experimental menor, em torno de 8 g/s. Quanto ao primeiro máximo de vazão, nas Configurações 1 e 3 ocorrem em torno de 1600 rpm e na Configuração 2 em 2000 rpm. Um ponto importante é que a partir do máximo, as Configurações 2 e 3 apresentam curvas descendentes, enquanto a Configuração 1 apresenta um aumento da vazão a partir de 2000 rpm. Todas essas alterações da vazão estão ligadas às ondas de pressão que atingem a porta da válvula e a interação entre a freqüência de excitação e do conduto de admissão. Quando se calcula a vazão mássica média em toda a faixa de trabalho, a Configuração 1é aquela que apresenta o maior valor, igual a 16,3 g/s, seguida pela Configuração 2, de vazão igual a 15,0 g/s e pela Configuração 3, com vazão igual a 12,1 g/s. Na faixa de rotação até 1600 rpm, a Configuração 1 ainda apresenta valores de vazão maiores se considerarmos a faixa de rotação até 1600 rpm e também para o intervalo de rotação de 1600 a 3000 rpm, seguida pelas Configurações 2 e 3, respectivamente.

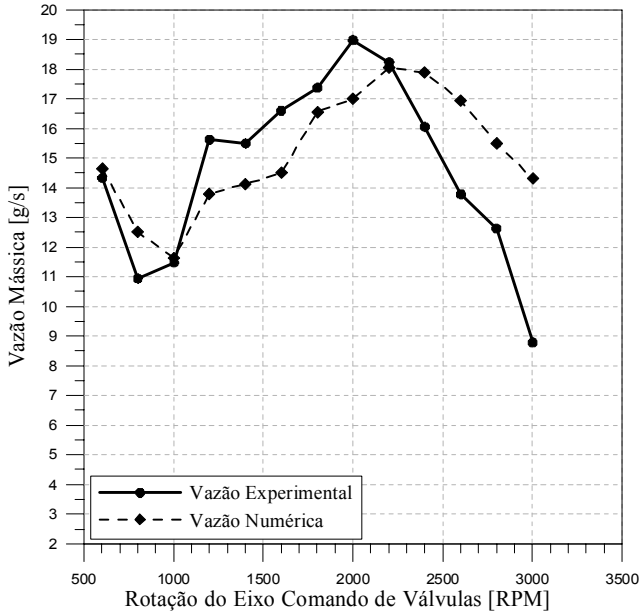

Figura 5 – Vazão numérica e experimental para a Configuração 2

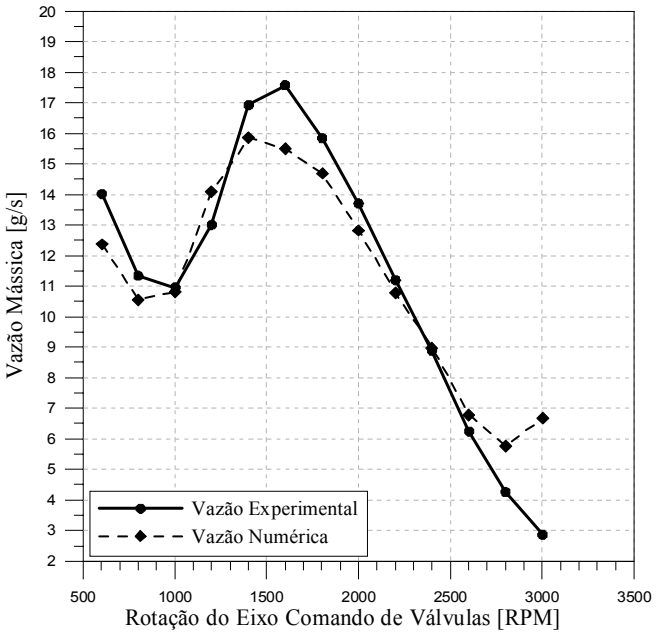

Figura 6 – Vazão numérica e experimental para a Configuração 3

As Fig. 7 a 9 apresentam a variação da pressão manométrica no cilindro 2 em função da rotação do eixo comando de válvulas para os primeiros mínimos de vazão nas três configurações.

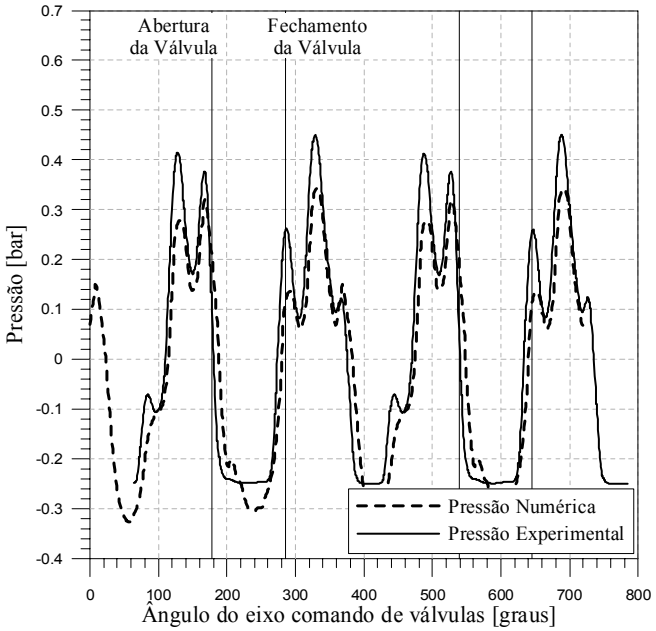

Figura 7 – Pressão em função do ângulo do eixo comando de válvulas no cilindro 2 (Configuração 1) – Rotação de 1002 rpm

Observa-se pela Fig. 7 que o código computacional é capaz de reproduzir as ondas de pressão ao longo do eixo comando. Os picos e vales são captados de forma adequada.

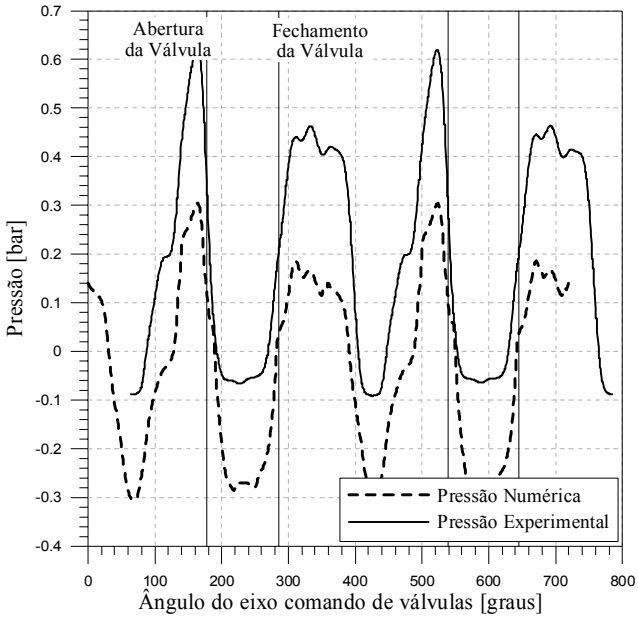

Figura 8 – Pressão em função do ângulo do eixo comando de válvulas no cilindro 2 (Configuração 2) – Rotação de 1002 rpm

Observa-se pela Fig.8 que apesar do código reproduzir as ondas de pressão e de não existir defasagem nos mínimos e máximos em relação ao ângulo do eixo comando de válvulas, há um deslocamento da onda em amplitude, indicando a possível necessidade de um maior refinamento das condições de entrada do código numérico.

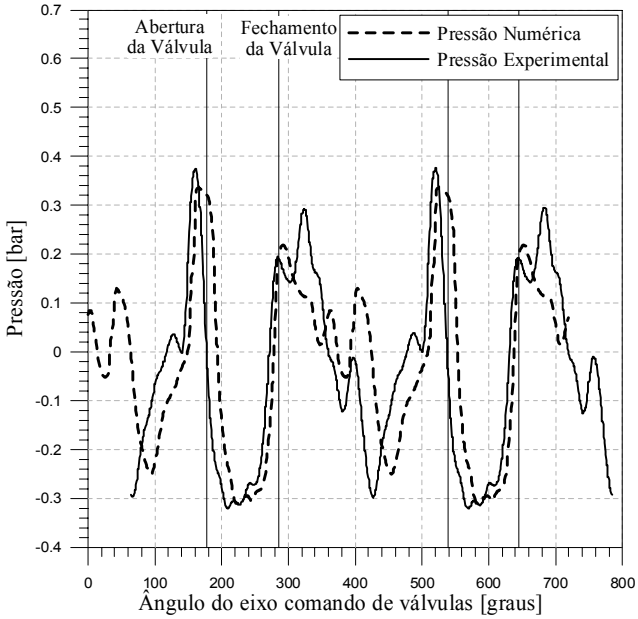

Figura 9 – Pressão em função do ângulo do eixo comando de válvulas no cilindro 2 (Configuração 3) – Rotação de 1002 rpm

A Fig. 10 apresenta a variação da pressão manométrica no cilindro 2 em função da rotação do eixo comando de válvulas para o primeiro máximo de vazão na Configuração 1. Os máximos das outras configurações são semelhantes e não serão apresentados.

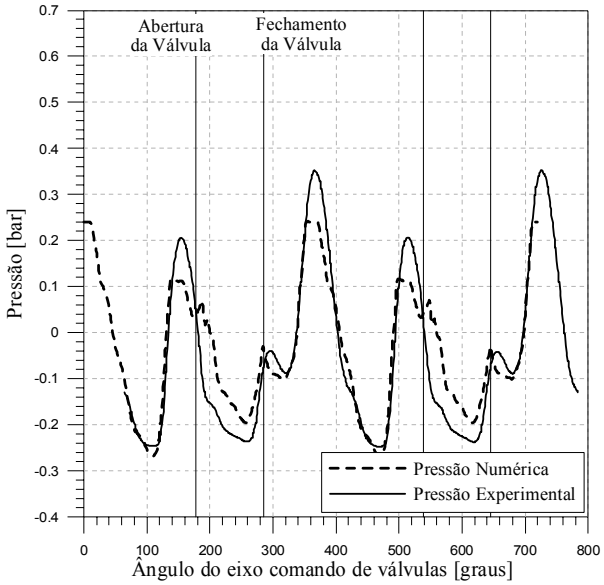

Figura 10 – Pressão em função do ângulo do eixo comando de válvulas no cilindro 2 (Configuração 1) – Rotação de 1600 rpm

Uma informação importante surge das análises espectrais realizadas das ondas de pressão para os mínimos e máximos das configurações. A Fig. 11 apresenta a análise para o sensor P1 mostrado na Fig.7, próximo à porta da válvula para a Configuração 1. As curvas da análise numérica e da experimental se sobrepõem. A freqüência fundamental é igual a 16,7 Hz e não é a de maior amplitude, sendo esta aquela do primeiro harmônico, na freqüência de 33, 4 Hz. Esta amplificação está ligada à freqüência natural do conduto de admissão com a junção, que conforme o cálculo efetuado através da Eq. 2 foi de 32,5 Hz.

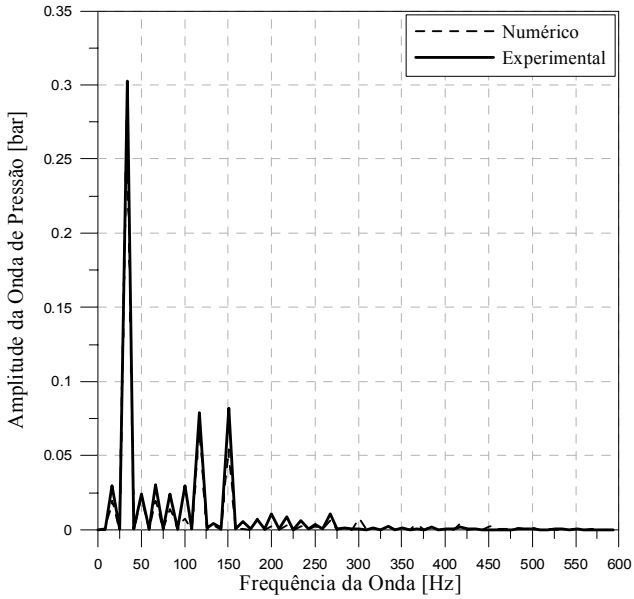

Figura 11 – Análise espectral para o sensor P1 da Configuração 1 – Rotação de 1002 rpm

A amplificação dos 6º e 8º harmônicos na Fig. 11 parece estar ligada ao comprimento primário do conduto, aquele entre a porta da válvula e a junção. Este comprimento, conforme apresentado na Tab. 1 é igual a L5= 0,598 m, representando uma freqüência natural de um tubo de um quarto de onda igual a 142, Hz, calculado a partir da Eq. 1. As freqüências dos 6º e 8º harmônicos são 133,6 e 150 Hz, respectivamente. Entretanto deve-se levar em consideração que a Eq. 1 considera a freqüência natural de um tubo fechado-aberto, enquanto que no caso apresentado a válvula de admissão permanece cerca de três quartos fechada e um quarto do período aberta. Sendo assim, é razoável admitir que tais amplificações estejam relacionadas ao comprimento do ramo primário do conduto. A razão da não amplificação do 7º harmônico ainda não está suficientemente explicada.

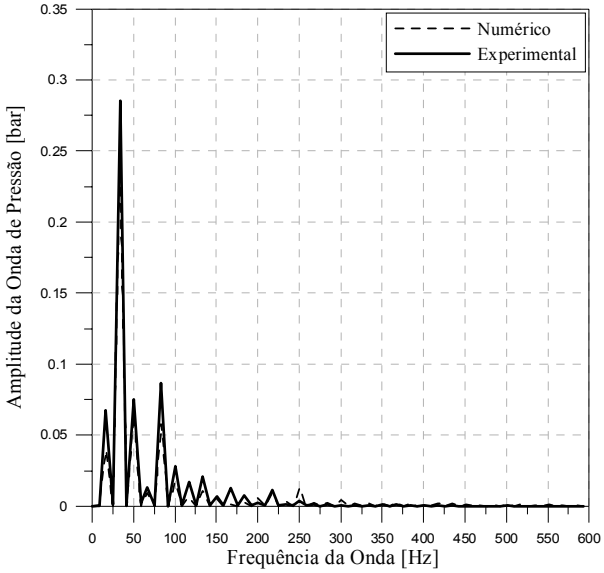

Figura 12 – Análise espectral para o sensor P1 da Configuração 2 – Rotação de 1002 rpm

A análise espectral da Configuração 2 (Fig. 12) para a rotação de um mínimo de vazão mássica mostra uma amplificação do primeiro harmônico. De acordo com a Eq. 2, a freqüência natural do conjunto do conduto de admissão é igual a 32,9 Hz. Como a freqüência do primeiro harmônico é igual a 33,4 Hz, sua amplificação se deve a ressonância da freqüência da fonte excitante (no caso a freqüência da válvula) com a freqüência do conjunto do conduto de admissão.

A análise espectral da Configuração 3 não será apresentada, uma vez que é semelhante a da Configuração 2.

Uma análise interessante pode ser realizada quando se obtém a vazão mássica numérica instantânea nos cilindros 2 e 3 das configurações estudadas. Os valores apresentados nas Fig. 13 e 14 consideram as curvas de vazão para as rotações que apresentam mínimos e máximos da vazão. Os resultados da Configuração 3 não serão apresentados, pelo fato de apresentar resultado semelhante ao da Configuração 2.

Pode-se observar que há semelhança entre as curvas dos cilindros 2 e 3 , indicando que o escoamento de ar é semelhante nos dois cilindros. Na Configuração 1 (Fig. 13) há ainda uma diminuição da vazão a partir do ponto em que ocorre o início do fechamento da válvula de admissão para a rotação de 1002 rpm. Na rotação de 1600 rpm, quando ocorre um ponto de máximo, a curva da vazão mássica não apresenta alterações significativas entre a parte de abertura da válvula e de seu fechamento.

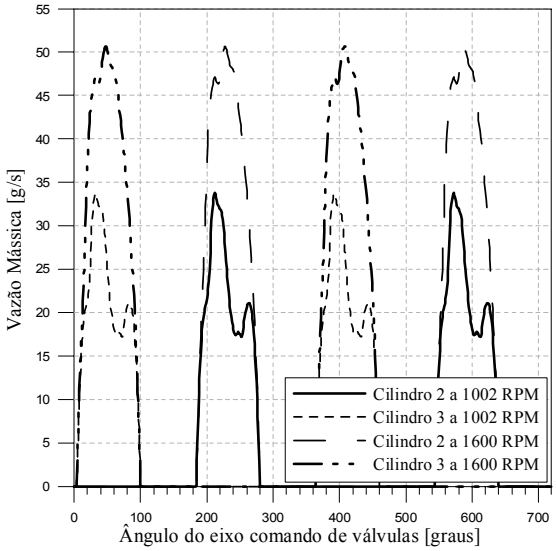

Figura 13 – Vazão mássica instantânea ao longo da abertura da válvula de admissão (Configuração 1) – Simulações para rotações de 1002 rpm e 1600 rpm

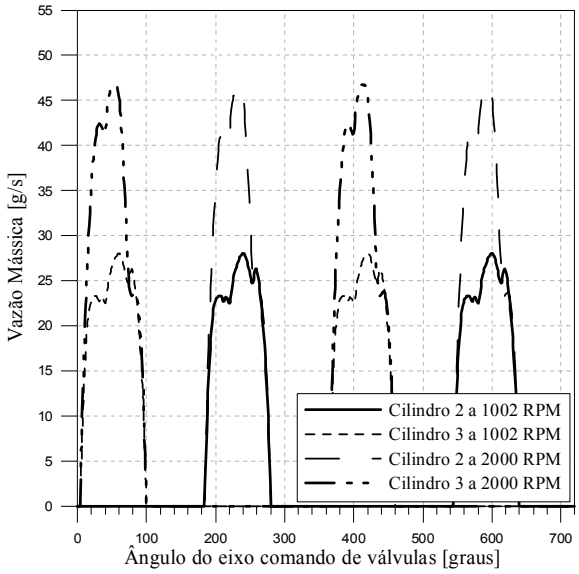

Figura 14 – Vazão mássica instantânea ao longo da abertura da válvula de admissão (Configuração 2) – Simulações para rotações de 1002 rpm e 1600 rpm

A Fig. 15 apresenta a curva do número de Mach em função do ângulo do eixo comando de válvulas para a Configuração 1 nas rotações de 1002 rpm (mínimo de vazão) e de 1600 rpm (máximo de vazão), para os dois cilindros. O escoamento é incompressível para a maior faixa de abertura da válvula de admissão, sendo, entretanto compressível nas imediações da região onde a válvula possui máxima abertura para a condição de máximo de vazão (1600 rpm).

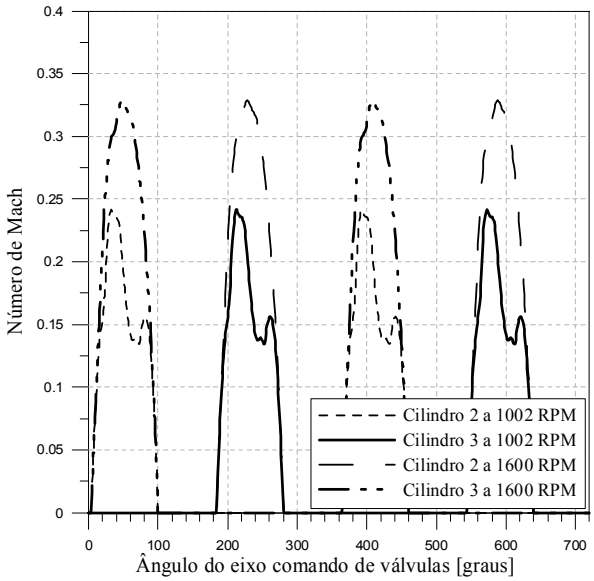

Figura 15 – Número de Mach em função do ângulo do eixo comando de válvulas (Configuração 1) – Simulações para rotações de 1002 e 1600 rpm

As Configurações 2 e 3 também apresentam curvas de número de Mach semelhantes à aquela mostrada na Fig. 15 e não serão apresentadas.

5. Conclusões

Através dos estudos conduzidos no trabalho, pode-se chegar a algumas conclusões acerca dos fenômenos transientes que ocorrem em um conduto de admissão na presença de junções. A posição em que a junção é inserida no

conduto afeta a curva de vazão mássica. A configuração que apresenta a junção localizada mais próxima da válvula de admissão foi aquela de maior vazão mássica média O modelo numérico foi capaz de reproduzir as curvas de vazão mássica e pressão ao longo da faixa de rotação estudada, indicando que informações adicionais poderão ser obtidas e analisadas, como aquelas que mostram a vazão mássica numérica instantânea e a curva do número de Mach. O escoamento é compressível nas proximidades de abertura máxima da válvula de admissão para as situações de faixas de rotação de vazões mássicas máximas. A freqüência natural do sistema foi determinada analítica e experimentalmente.

6. Referências

Benajes, J. et al, 1997, "Pre-Design Model for Intake Manifolds in Internal Combustion Engines", SAE Paper n. 970055.

Benson, R. S., 1973, "A Comprehensive Digital Computer Program to Simulate a Compression Ignition Engine Including Intake and Exhaust Systems", SAE Paper n. 710173.

Benson, R. S., 1982, "The Thermodynamics and Gas Dynamics of Internal Combustion Engines", SAE Paper n. 970055.

Hanriot, S. M., Valle, R. M., Medeiros, M. A F., 2000, "An Experimental and Numerical Study from Pulsating Flow in Intake Manifold", SAE Paper n. 2000-01-3162 E.

Hanriot, S. M., 2001, "*Estudo dos Fenômenos Pulsantes do Escoamento de ar nos Condutos de Admissão em Motores de Combustão Interna"*, Tese de Doutorado, Departamento de Engenharia Mecânica, UFMG, Belo Horizonte, MG, Brasil.

Morse, P. H., Boden, R. H., Schecter, H., 1938, "Acoustic Vibrations an Internal Combustion Engine Performance", Journal of Applied Physics, v. 9, jan.

Ohata, A., Ishida, Y., 1991, "Dynamic Inlet Pressure and Volumetric Efficiency of Four-Cycle Cylinder Engine", SAE Paper n. 911042.

Onorati, A., Ferrari, G., 1998, "Modeling of 1-D Unsteady Flows in I.C. Engine Pipe Systems: Numerical Methods and Transport of Chemical Species", SAE Paper n. 980782.

Winterbone, D. E., Yoshitomi, M., 1990. *The Accuracy of Calculating Wave Action in Engine Intake Manifolds.* SAE Paper n. 900677.

Winterbone, D. E.; Pearson, R. J., 1999. *Design Techniques For Engine Manifolds: Wave Action Methods for IC Engines*. USA, Warrendale: SAE International.

Winterbone, D. E., Pearson, R. J., 2000. *Theory of Engine Manifolds Design: Wave Action Methods for IC Engines*. USA, Warrendale: SAE International.

ANALYSIS OF THE INTAKE FLOW IN THE PRESENCE OF JUNCTIONS

Sérgio de Morais Hanriot
Pontifícia Universidade Católica de Minas Gerais
Programa de Pós-Graduação em Engenharia Mecânica
hanriot@pucminas.br

Rudolf Huebner
Pontifícia Universidade Católica de Minas Gerais
Programa de Pós-Graduação em Engenharia Mecânica
rudolf@pucminas.br

Ismael Alves Coutinho
Pontifícia Universidade Católica de Minas Gerais
ismael_Coutinho@yahoo.com

Abstract
The main task of the intake manifold in internal alternative combustion engines is to drive the air of the atmosphere to the cylinders, distributing the mass of air in a uniform way with the smallest loss of pressure possible. Due to the alternative movement of the pistons and of the valves, the gas in the intake manifold presents pressure oscillations. Such oscillations can be used to increase the amount of mass of air admitted. This task is linked basically to the geometry of the intake manifold and involves variables such as the diameter of the manifold, junctions, length and present accessories. In the present work a numeric and experimental analysis of the pressure waves was performed inside the intake manifold considering the presence of a junction. The junction position effect over the mass flow rate through the admission valves was evaluated. Results shown the junction position affects the engine volumetric efficiency.

Keywords: Transient Flow, Engines, Junction

Proceedings of the 11th Brazilian Congress of Thermal Sciences and Engineering -- ENCIT 2006
Braz. Soc. of Mechanical Sciences and Engineering -- ABCM, Curitiba, Brazil, Dec. 5-8, 2006

Paper CIT06-0770

Avaliação experimental do desempenho de um Banco de Bocais Sônicos

Maria Luiza Moraes dos Santos
CETEC – Fundação Centro Tecnológico de Minas Gerais
31170.000 Av. José Cândido da Silveira, 2000 - Cidade Nova
Belo Horizonte - Minas Gerais
maria.luiza.moraes@cetec.br

Ramon Zeferino
CETEC – Fundação Centro Tecnológico de Minas Gerais
31170.000Av. José Cândido da Silveira, 2000 - Cidade Nova
Belo Horizonte - Minas Gerais
ramon.zeferino@cetec.br

Geraldo Augusto Campolina França
Departamento de Engenharia Mecânica da UFMG
31270.000 Av. Antônio Carlos, 6627 - Pampulha
Belo Horizonte - Minas Gerais
gacf@ufmg.br

Resumo. *A vazão é uma grandeza derivada que depende da medição de outros parâmetros para a sua dedução. Os métodos para estabelecimento do valor da vazão de gases, que proporcionam as mais altas exatidões, fundamentam-se na medição de grandezas de base do Sistema Internacional de Unidades. Dentre estes métodos destacam-se, o volumétrico, que utiliza as unidades comprimento, temperatura termodinâmica e tempo, e o gravimétrico, que emprega as unidades massa e tempo. Entretanto, estes métodos, que constituem padrões primários da grandeza vazão, requerem, por natureza, complexos e trabalhosos procedimentos operacionais, não sendo, portanto, indicados para medições rotineiras. A transferência deste valor mais exato para outros sistemas de medição de vazão de gás é realizada por meio da estruturação de uma cadeia de rastreabilidade, onde, por exemplo, o padrão primário calibra um medidor padrão secundário, que por sua vez calibra um medidor padrão de trabalho, o qual finalmente calibra um medidor de vazão operacional. O Laboratório de Vazão de Gás do CETEC com o intuito de estabelecer uma cadeia interna de rastreabilidade já estruturou o primeiro elo desta cadeia, constituído por um conjunto de medidores do tipo bocal sônico, calibrados na faixa de 1 kg/h a 109 kg/h, contra um padrão primário do laboratório do tipo volumétrico. Estes bocais sônicos são montados em um arranjo de tubulações paralelas, compondo um sistema de calibração secundário denominado "banco de bocais sônicos", com capacidade para medir vazões de gás na faixa de 1 kg/h a 545 kg/h. O objetivo deste trabalho é apresentar os resultados experimentais obtidos na avaliação do desempenho deste banco, cujo projeto mecânico possui uma concepção para medições em laboratório com flexibilidade para uma fácil e rápida troca dos medidores bocais sônicos que o compõem.*

Palavras chave: bocal sônico, banco de bocais sônicos, fluxo crítico, medição de vazão de gás.

1. Introdução

Na composição de uma cadeia de rastreabilidade, o ideal é que os medidores padrão que sucedem o padrão primário aliem flexibilidade, ou seja, portabilidade, robustez e facilidade operacional, a um mínimo de perda na transferência da exatidão do padrão contra o qual foi calibrado. Vários tipos de medidores se enquadram nesta categoria, tais como, a turbina, o rotativo de lóbulos e o bocal sônico. Entretanto, o bocal sônico possui, ainda, a vantagem de não exigir re-calibrações freqüentes. A sua concepção tecnológica desprovida de componentes móveis ou eletrônicos lhe garante uma excelente estabilidade metrológica. Esta aptidão do bocal sônico foi verificada pelo National Institute of Standards and Technology, NIST, onde para 23 bocais sônicos calibrados contra seus padrões primários, no período de 1970 a 1998, foi encontrada uma variação média no valor dos seus coeficientes de descarga de apenas +0,003 %, por ano de utilização do medidor, [Wright, 1998].

O presente artigo apresenta os resultados da avaliação do desempenho de um banco de bocais sônicos, BBS, desenvolvido no Laboratório de Vazão de Gás da Fundação Centro Tecnológico de Minas Gerais, CETEC, para se constituir em um de seus padrões de calibração. A concepção construtiva foi estabelecida com características para a sua utilização em laboratório e operação na faixa de vazão de 1 kg/h a 545 kg/h. O desempenho deste novo padrão foi avaliado experimentalmente num processo compreendido por duas etapas. Numa 1ª etapa, bocais sônicos instalados no BBS foram individualmente calibrados contra um padrão primário, em vazões de até 110 kg/h. Numa 2ª etapa um medidor do tipo rotativo de lóbulos recém adquirido pelo laboratório foi calibrado contra o novo padrão BBS na faixa de 24 kg/h a 545 kg/h. Os resultados obtidos foram comparados com os resultados da calibração do medidor rotativo de lóbulos realizada no instituto nacional de metrologia da Holanda, NMi, os quais foram tomados como valores de referência. O grau de concordância entre as calibrações foi avaliado com o emprego do método do erro normalizado *En*, cujo valor calculado para cada ponto de vazão calibrado, variou dentro do intervalo de -1 a +1, permitindo decidir pela

validação das medições realizadas com o BBS e de sua inclusão como um dos padrões de calibração de medidores de vazão de gás do CETEC.

2. O medidor de vazão de gás bocal sônico

Se um disco perfurado for introduzido em uma tubulação gerando uma restrição, conforme mostrado na Fig. (1), o fluido é acelerado ao longo da região de estreitamento do escoamento, até atingir um valor máximo na seção mais estreita gerada na corrente fluida, conhecida como veia contraída. Mantendo-se a pressão de montante P_1 constante, quanto menor for a pressão de jusante P_2, maior será a vazão do escoamento. Entretanto, há um limite, para os escoamentos compressíveis. Quando a razão de contrapressão P_2/P_1 atinge um valor de aproximadamente 0,5 (entre ≈0,4867 e ≈0,6065, dependendo do gás), a vazão em massa do fluxo torna-se invariável e correspondente à vazão máxima fisicamente possível de atravessar a restrição para a pressão P_1, mesmo com a diminuição de P_2. Neste momento o gás atingiu sua velocidade sônica na veia contraída e o escoamento adquire um comportamento conhecido como estado crítico, sônico, bloqueado, "engasgado" ou "choked", em inglês.

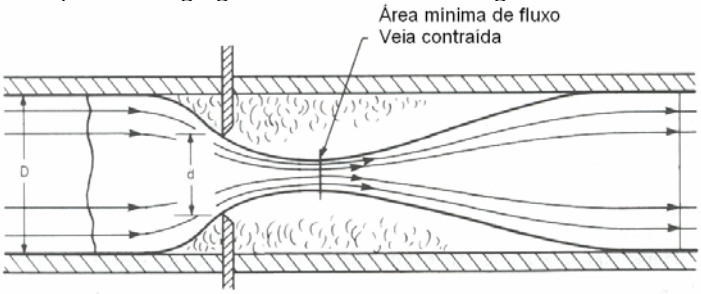

Figura 1. Disco perfurado introduzido na seção de uma tubulação onde existe um fluido em escoamento.
Fonte: Miller, 1989, p. 9.9.

O medidor de vazão bocal sônico foi idealizado em função desta característica física de um escoamento gasoso adquirir o estado crítico. Conforme ilustrado na Fig. (2), este medidor consiste basicamente de um segmento de tubo constituído por uma seção convergente, em forma de sino, na sua entrada, imediatamente seguida por uma seção divergente cônica, gerando uma restrição ou garganta. Em razão desta geometria convergente divergente, o estado de escoamento sônico pode ser atingido para razões P_2/P_1 bem maiores do que aquela obtida com um disco perfurado, o que facilita a sua aplicação nos processos práticos.

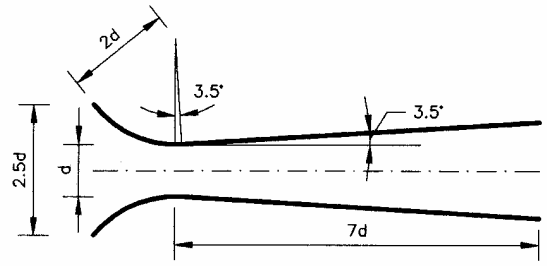

Figura 2. Geometria típica de um bocal sônico

2.1. Equação idealizada da vazão em massa crítica que atravessa o bocal sônico

A equação teórica da vazão em massa medida na condição crítica pode ser deduzida considerando um volume de controle que compreenda desde um grande reservatório imaginário a montante do bocal até a sua garganta, conforme ilustrado na Fig. (3).

Figura 3. Volume de controle para dedução da equação do bocal sônico.

No reservatório a temperatura e a pressão não variam e a energia cinética do fluido é desprezível. O gás é considerado perfeito e sua expansão até a garganta é idealizada como um processo unidimensional e isentrópico. As propriedades T_0 P_0 do fluido no reservatório hipotético passam então a representar as propriedades locais de estagnação, assim definidas: "As propriedades locais isentrópicas de estagnação são aquelas que seriam obtidas em qualquer ponto de um campo de escoamento se o fluido naquele ponto fosse desacelerado das condições locais para a velocidade zero, seguindo um processo sem atrito, adiabático (isentrópico)" [Fox & McDonald, 1998].

A Equação (1) é deduzida para o cálculo da vazão em massa idealizada de um fluxo crítico de um gás perfeito, como uma função das condições de estagnação de montante, onde A_d é a área da seção transversal da garganta, R é a constante do gás e C_{*i} é a "função do escoamento crítico para um escoamento unidimensional e isentrópico de um gás perfeito".

$$\dot{m}_i = A_d C_{*i} \frac{P_0}{\sqrt{RT_0}} \tag{1}$$

2.2. Equação da vazão em massa crítica que atravessa o bocal sônico em condições reais

Para corrigir a presença da camada limite e os efeitos multidimensionais resultantes do perfil curvo, um fator multiplicador de correção, denominado coeficiente de descarga, *Cd*, é acrescentado na Eq. (1). Como estes efeitos interferem no escoamento reduzindo a velocidade, este coeficiente é menor do que a unidade. As proporções geométricas do medidor bocal sônico são projetadas combinando um contorno suave e polido com um pequeno ângulo divergente de forma a reduzir os efeitos das forças radiais inerentes a um escoamento através de um trecho convergente e os efeitos da separação da camada limite no trecho divergente. Deste modo, quanto maior a vazão mais próximo da unidade fica o *Cd*.

A função C_{*i} da Eq. (1) foi deduzida para um escoamento isentrópico de um gás perfeito. Para as condições reais esta função é obtida baseada em equações de estado empíricas e passa a ser denominada "função do escoamento crítico para um escoamento unidimensional de um gás real" e simbolizada por C_*. A determinação de C_* demanda um procedimento de cálculo relativamente complexo e requer uma equação de estado do gás de alta exatidão. Um dos trabalhos mais recentes foi publicado por Stewart, Watson e Vaidya (2000), no qual eles apresentam expressões polinomiais para o cálculo de C_*, do tipo da Eq. (2), com uma incerteza expandida considerando um fator de abrangência de 95%, $U_{95\%}$, estimada em 0,5%. Os coeficientes n_i, p_i e t_i são tabelados para i variando de 1 a 14 e p_c e T_c, são, respectivamente, a pressão e a temperatura críticas do fluido (para o ar, p_c = 3,786 MPa e T_c = 132,5306 K).

$$C_* = \sum_i n_i (p_0 / p_c)^{p_i} (T_0 / T_c)^{t_i}, \tag{2}$$

A equação resultante para o cálculo da vazão em massa baseada nas condições reais do escoamento que atravessa o bocal sônico é:

$$\dot{m} = Cd\ A_d C_* \frac{P_0}{\sqrt{RT_0}} \tag{3}$$

O principal fator da equação do bocal sônico é o seu *Cd*. Estudos analíticos demonstram que os efeitos multidimensionais contribuem com apenas 0,1% no seu valor, o qual é, portanto, praticamente dependente da camada limite gerada [Ishibashi & Takamoto, 2000]. O *Cd* é usualmente determinado experimentalmente em sistemas de calibração, nos quais são utilizados medidores padrão para determinação da vazão em massa. A expressão para o cálculo do coeficiente de descarga do bocal sônico, Eq. (4) é derivada da Eq. (3), onde $\dot{m}_{padrão}$ é a vazão em massa do fluxo medida pelo padrão.

$$Cd = \frac{\dot{m}_{padrão} \sqrt{RT_0}}{A_d P_0 C^*} \tag{4}$$

O resultado da calibração é fornecido na forma de tabela ou gráfico, onde o *Cd* é apresentado como uma função do número de Reynolds na garganta, Re_d, o qual é tradicionalmente definido pela Eq. (5), onde μ_0 é a viscosidade dinâmica do gás nas condições de estagnação.

$$Re_d = \frac{4\dot{m}}{\pi d \mu_0} \tag{5}$$

Conhecidas as propriedades C_* e R do fluido, o diâmetro da garganta d e o coeficiente de descarga Cd do bocal sônico, a vazão em massa do escoamento pode ser determinada, apenas com a medição da pressão P_1 e da temperatura T_1 do fluxo na região a montante do medidor. Se o número de Mach, Ma, na região a montante do bocal for menor que 0,01, os valores medidos para P_1 e T_1 podem ser diretamente considerados, respectivamente, como P_0 e T_0, (Nakao et al., 1996), caso contrário estas propriedades são obtidas pelas Eq. (6) e (7).

$$T_0 = T_1\left[1+\frac{(\gamma-1)}{2}Ma_1^{\,2}\right] \tag{6}$$

$$P_0 = P_1\left[1+\frac{(\gamma-1)}{2}Ma_1^{\,2}\right]^{\gamma/(\gamma-1)} \tag{7}$$

4. O banco de bocais sônicos desenvolvido no CETEC

Uma tendência que vem se consolidando nos últimos anos é o emprego de um medidor formado por um conjunto de bocais sônicos ou banco de bocais sônicos. Nesta técnica, os bocais são instalados em tubulações paralelas conectadas a uma câmara comum, por meio da qual o fluxo de ar é alimentado e distribuído para os bocais. Cada uma das tubulações em paralelo é provida de uma ou mais válvulas de bloqueio instaladas a jusante do bocal, o que permite que o fluxo seja dirigido para um ou mais bocais componentes do banco. Este tipo de arranjo permite a obtenção de um sistema de medição de fácil operação e com uma larga faixa de trabalho, em função do número e do tamanho dos bocais que o compõem. Um desenho esquemático do BBS desenvolvido no CETEC é mostrado na Fig. 4 e uma foto na Fig. 5

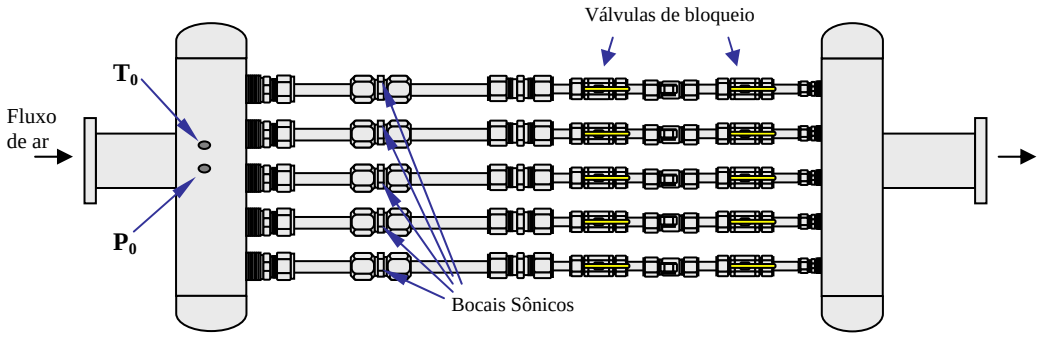

Figura 4. Desenho esquemático do BBS

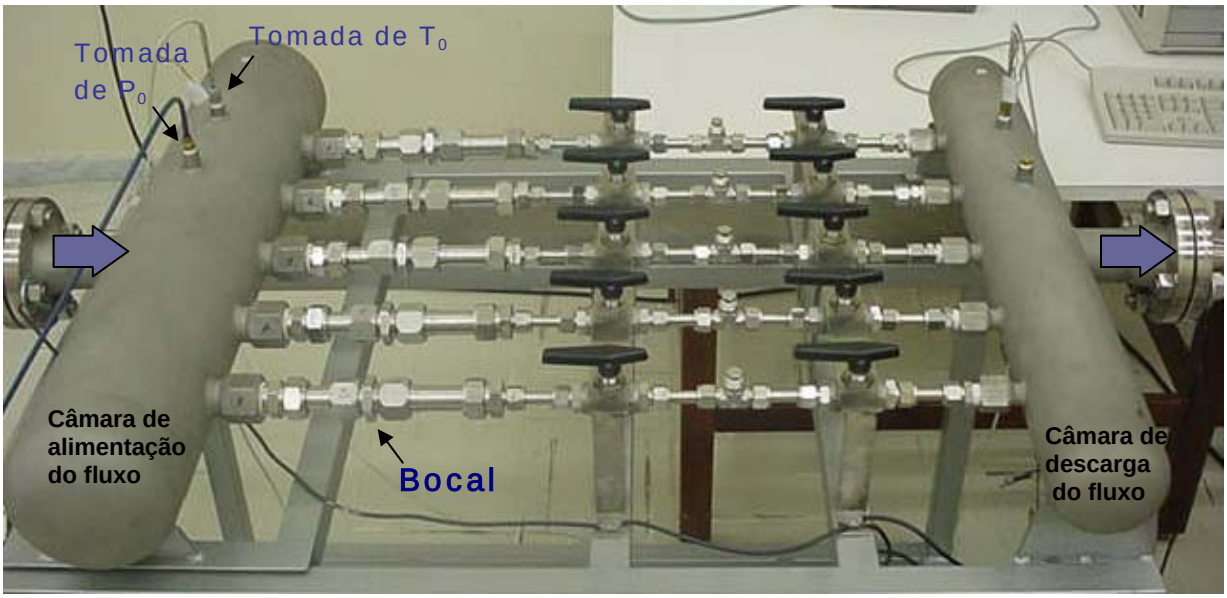

Figura 5. Foto do BBS

O projeto mecânico deste BBS possui uma concepção própria que foi inicialmente testada em um protótipo de pequena capacidade (vazão máxima de 32 kg/h ou ≈27 m^3/h), tema da dissertação de mestrado "Montagem e calibração de um banco de bocais sônicos"(Santos, 2002). A experiência obtida neste protótipo forneceu subsídios confiáveis para aplicação de seu projeto conceitual em um modelo de maior capacidade.

Como pode ser observado na Fig (5), o BBS consiste em uma montagem mecânica do tipo manifold, com cinco ramais independentes para a passagem do fluxo de ar, que é admitido em uma câmara comum de entrada e descarregado através de uma segunda câmara comum de saída. O fluxo de ar é admitido sob pressão e distribuído para um dos bocais ou simultaneamente para dois ou mais. Para isto os bocais sônicos são instalados em cada um dos ramais seguidos de duas válvulas de bloqueio. O BBS pode operar com até cinco bocais sônicos, de diferentes tamanhos, os quais podem ser facilmente instalados e intercambiados. A vazão máxima de projeto deste banco é de 545 kg/h ou, aproximadamente, 450 m^3/h nas condições padrão de 20°C e 1 atm.

5. Características dos bocais sônicos utilizados no BBS

Cinco tamanhos de bocais sônicos foram selecionados para realizar a faixa de vazão projetada para o BBS, com diâmetros nominais DN na garganta de 0,79 mm, 1,1 mm, 2,2 mm, 4,50 mm e 6,35 mm, os quais passarão a ser referenciado, respectivamente, por Bs1, Bs2, Bs3, Bs4 e Bs5. Nove bocais sônicos se revezam no BBS, em função do valor da vazão a ser medida, sendo um Bs1, um Bs2, um Bs3, um Bs4 e cinco Bs5. A Fig. (6) mostra uma foto do Bs1 e de um dos Bs5. Externamente, todos os bocais são geometricamente iguais, com um aspecto semelhante a um niple, com aproximadamente 56 mm de comprimento e 33 mm de largura. Os bocais sônicos propriamente ditos são usinados no interior dessas peças em aço inoxidável. Eles possuem em comum o ângulo do tronco de cone, α, da região divergente, que é igual a 5°, e o diâmetro da entrada do bocal que equivale a 3*d*. Entretanto, o comprimento da região divergente, ou difusor, é proporcionalmente diferente nos cinco tamanhos de medidores. Quanto menor o diâmetro do bocal maior é o comprimento relativo do seu difusor. A Figura 7 mostra a geometria do menor e do maior bocal sônico.

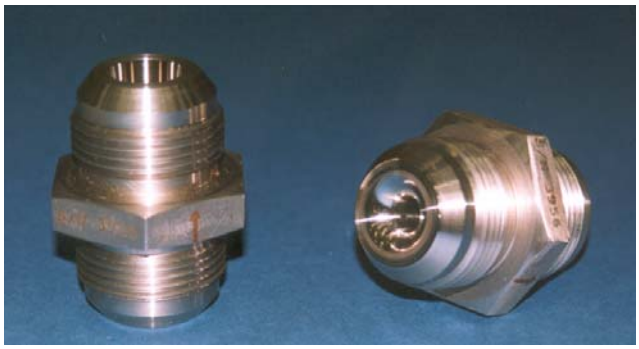

Figura 6. Foto do bocal Bs4 e de um dos bocais Bs6

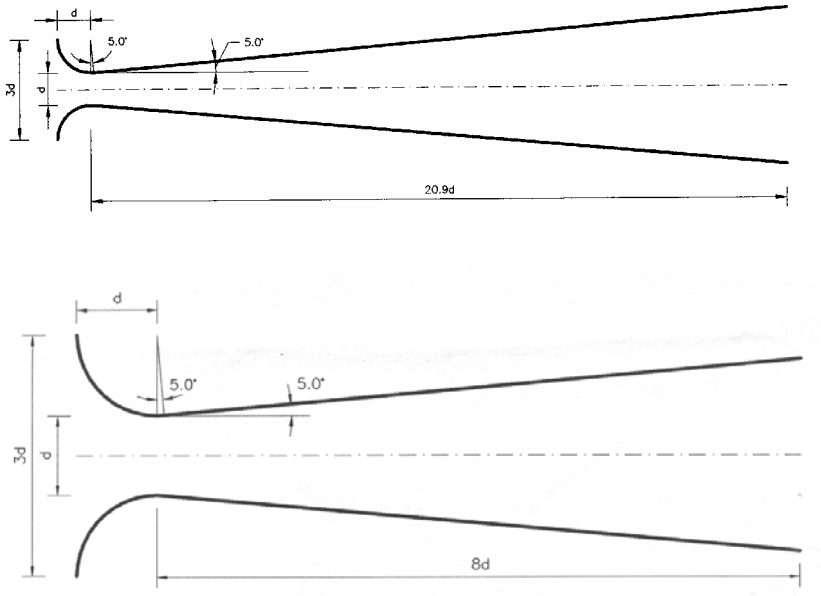

Figura 7. Geometria do menor bocal Bs1 e do maior bocal Bs5

6. Calibração dos bocais sônicos

Os bocais sônicos foram calibrados no sistema de calibração primário do LVG que utiliza um medidor do tipo "Bell Prover" como padrão. A Figura (8) apresenta um desenho esquemático da instalação experimental utilizada nesta 1ª etapa do trabalho.

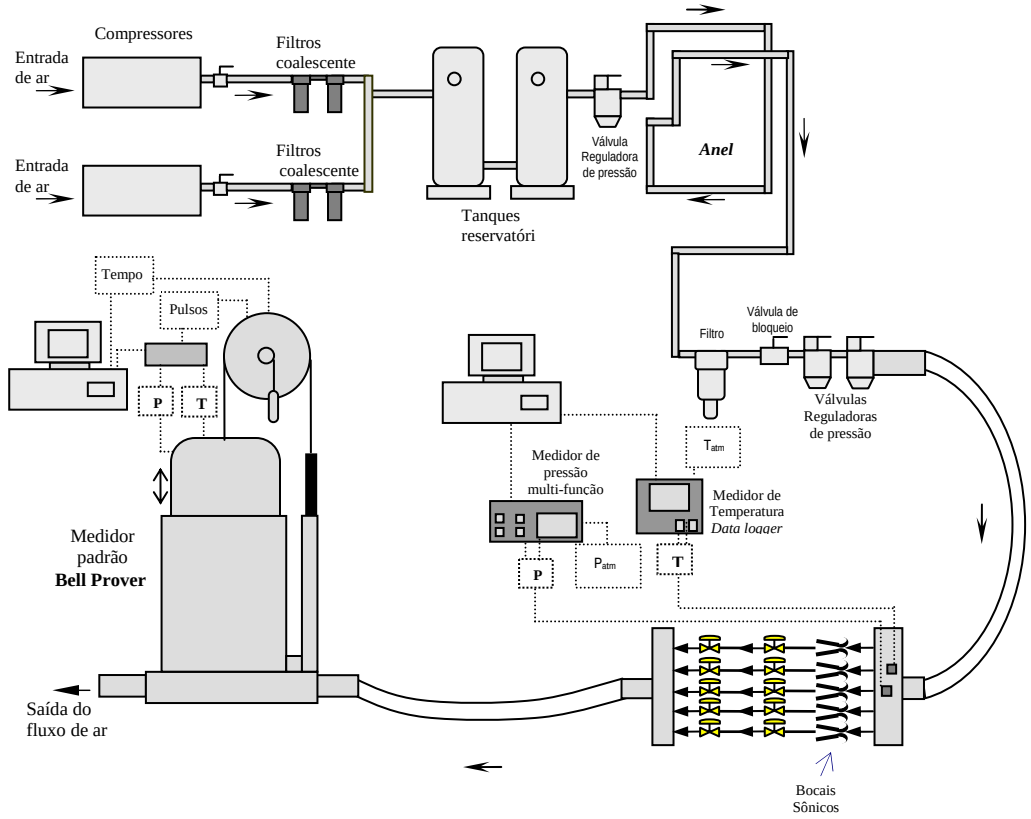

Figura 8 – Desenho esquemático da instalação utilizada na calibração dos bocais sônicos

O fluxo de ar que alimenta o BBS é gerado a uma pressão de 900 kPa em dois compressores providos de secadores. Filtros e tanques reservatórios garantem a ausência de particulados e oscilações no escoamento. Para se obter uma maior estabilidade de P_0, o fluxo passa por três válvulas reguladoras de pressão antes de ser admitido na câmara de entrada do BBS. Por outro lado, para que T_0 mantenha-se estável, a tubulação de escoamento do ar é prolongada formando um anel, para que o fluxo troque calor com o ambiente durante o seu percurso e alcance o BBS com uma temperatura em equilíbrio com a temperatura ambiente.

Nas calibrações dos bocais, o BBS foi instalado a montante do padrão "Bell Prover". O fluxo de ar ao deixar o BBS é admitido pela base do padrão, preenchendo a sua câmara de coleta ou campânula, promovendo o seu deslocamento linear ascendente. A campânula consiste em um cilindro com dimensões rastreáveis ao NIST. Uma vez que a sua área é conhecida, o volume de ar coletado durante uma medição é determinado pela distância deslocada pela campânula durante sua ascensão. A medição desta distância é realizada por meio de um codificador rotativo (encoder), acoplado ao eixo de uma polia sobre a qual corre o cabo que sustenta a campânula e um contrapeso. O codificador produz pulsos proporcionais ao movimento vertical da campânula, os quais são eletronicamente contados e sincronizados a um cronômetro de alta exatidão. O cronômetro é gatilhado pelos pulsos do encoder, de modo que o intervalo de tempo de coleta corresponde exatamente ao intervalo de contagem de pulsos. O volume de ar preenchido na campânula e o tempo de sua coleta determinam a vazão volumétrica do fluxo de ar. Os parâmetros temperatura e pressão no interior da campânula são medidos, para obtenção do valor da vazão em massa correspondente.

6.1 Método de cálculo

O balanço de massa do processo de calibração de um bocal sônico no sistema de calibração "Bell Prover", operando em regime permanente, é estabelecido pela Eq. (8), onde o subscrito *Bs* refere-se ao bocal sônico e o subscrito *Bell* refere-se ao padrão primário,.

$$\dot{m}_{Bs} = \dot{m}_{Bell} \tag{8}$$

A vazão em massa estabelecida pelo padrão é obtida a partir da Eq. (9), onde V_{Bell} e ρ_{Bell} são, respectivamente, o volume coletado e a massa específica da ar no interior da campânula e τ_{bell} o intervalo de tempo de coleta.

$$\dot{m}_{Bell} = \rho_{Bell} \frac{V_{Bell}}{\tau_{Bell}} \tag{9}$$

O volume de coleta correspondente ao deslocamento da campânula é correlacionado ao número de pulsos emitidos pelo encoder N_e por meio da constante k_e do encoder. Esta constante k_e fornece o número de pulsos emitidos pelo encoder por unidade de volume coletado na campânula. Desta forma, V_{Bell} é expresso por:

$$V_{Bell} = \frac{N_e}{k_e} \tag{10}$$

Substituindo a Eq. (10) na Eq. (9), obtém-se:

$$\dot{m}_{Bell} = \rho_{Bell} \frac{N_e}{k_e \tau_{Bell}} \tag{11}$$

6.1.1 Determinação do coeficiente de descarga do bocal sônico

Substituindo a Eq. (3) e a Eq. (11) na Eq. (8) e rearranjando obtém-se a Eq. (12) para o cálculo do *Cd* do bocal em função da massa específica do ar no interior da campânula do padrão primário.

$$Cd = \rho_{Bell} \frac{N_e}{k_e \tau_{Bell}} \frac{\sqrt{RT_0}}{A_d P_0 C^*} \tag{12}$$

A massa específica do fluido é obtida pela equação de estado do gás real:

$$\rho_{Bell} = \frac{P_{Bell}}{Z\, R\, T_{Bell}} \tag{13}$$

Substituindo a Eq. (13) na Eq. (12), obtém-se a equação final para o cálculo do *Cd* do bocal sônico calibrado:

$$Cd = \frac{P_{Bell}}{Z\, R\, T_{Bell}} \frac{N_e}{k_e \tau_{Bell}} \frac{\sqrt{RT_0}}{A_d P_0 C^*} \tag{14}$$

7. Validação do banco de bocais sônicos

Para garantir a exatidão e a confiabilidade das medições de vazão realizadas pelo BBS desenvolvido no CETEC, as mesmas foram verificadas por meio de um processo de comparação com um medidor padrão do laboratório, do tipo rotativo de lóbulos, com apenas algumas dezenas de horas de uso, calibrado no NMi. O BBS calibrou o medidor rotativo e os resultados foram comparados com aqueles obtidos no NMi. A Figura (9) apresenta um desenho esquemático da instalação utilizada nesta 2ª etapa do trabalho. O medidor rotativo é instalado em série e a jusante do padrão. O fluxo de ar proveniente da rede de ar comprimido do laboratório é introduzido sob pressão na câmara de entrada do BBS após fazer o mesmo percurso descrito no item 6. Com o ajuste das válvulas de bloqueio instaladas a jusante dos bocais sônicos, o fluxo de ar é dirigido para um ou mais bocais em função da vazão a ser medida.

A faixa de medição de um medidor rotativo de lóbulos está relacionada aos vazamentos que ocorrem em estreitas folgas existentes entre suas peças internas que formam o volume preenchido pelo gás em cada ciclo de rotação. Estes vazamentos podem se tornar significativos em baixas vazões. A norma BS 7405:1991 da British Standard recomenda uma relação de vazão de 20:1. Como a vazão máxima estipulada pelo fabricante do medidor rotativo de lóbulos utilizado no trabalho é de 650 m^3/h (780 kg/h para o ar), nas condições padrão, o seu limite mínimo de medição recomendado seria de 33 m^3/h (40 kg/h para o ar). Entretanto, como o medidor é de alta qualidade uma relação de 30:1 foi avaliada como segura. Assim sendo, o BBS calibrou o medidor rotativo a partir da vazão de 22 m^3/h. Considerando o limite máximo de medição do BBS, a faixa de calibração estabelecida foi de 22 m^3/h a 450 m^3/h ou de 24 kg/h a 545 kg/h. Para que os mesmos efeitos paramétricos, relativos à condição em que o medidor rotativo foi calibrado na Holanda, fossem reproduzidos na calibração realizada no CETEC, foi empregado como parâmetro de comparação, o número de Reynolds do fluxo passando no medidor Re_{Rot}, calculado pela Eq. (15), onde D_{Rot} é o DN do medidor.

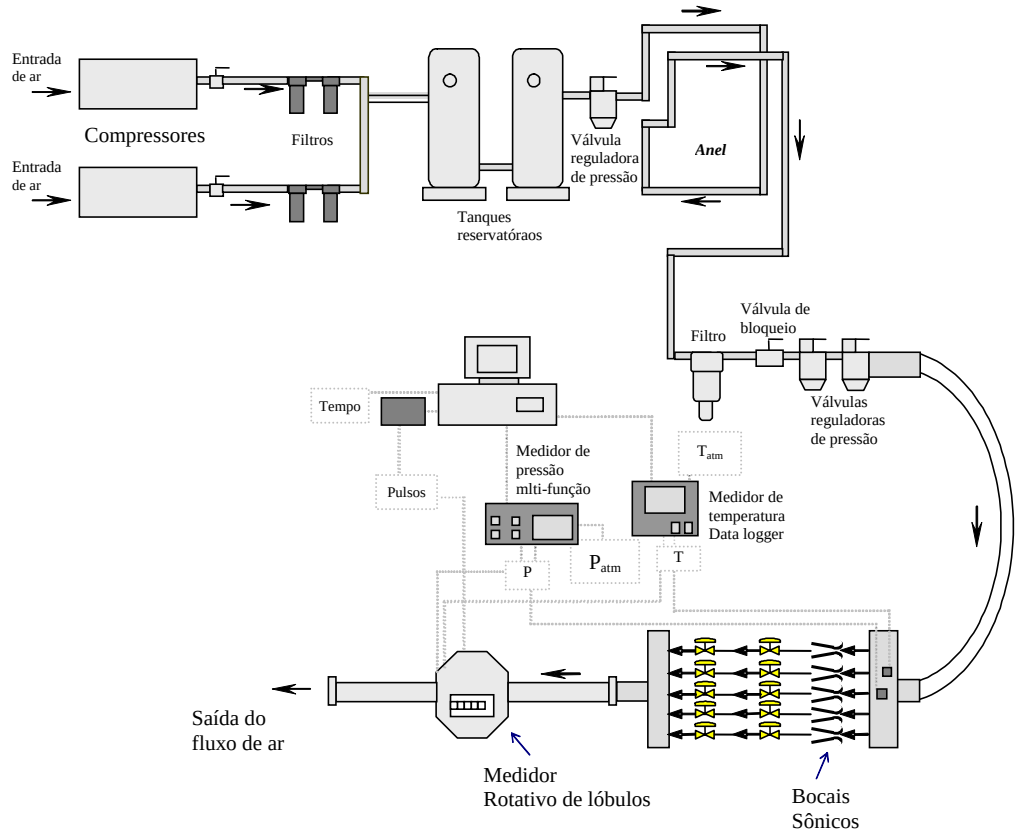

Figura 9 – Desenho esquemático da instalação utilizada na validação do BBS

$$\mathrm{Re}_{Rot} = \frac{4\dot{m}}{\pi D_{Rot} \mu_{Rot}} \tag{15}$$

7.1 Método de cálculo

O balanço de massa no processo de calibração do medidor rotativo de lóbulos contra o BBS, operando em regime permanente, onde o subscrito *Rot* refere-se ao medidor rotativo e o subscrito *Bs* refere-se ao bocal sônico ou bocais sônicos utilizados como padrões, é estabelecido pela Eq. (16).

$$\dot{m}_{Rot} = \dot{m}_{BBS} \tag{16}$$

A vazão em massa estabelecida no BBS é medida por apenas um bocal ou simultaneamente por até 5 bocais, em função da vazão a ser medida. Considerado a condição limite em que o escoamento é subdividido para medição por 5 bocais, a vazão em massa do padrão é dada por:

$$\dot{m}_{BBS} = \dot{m}_{Bs1} + \dot{m}_{Bs2} + \dot{m}_{Bs3} + \dot{m}_{Bs4} + \dot{m}_{Bs5}$$

A vazão em massa crítica do bocal sônico é calculada pela Eq. (3). O valor de R é uma função do fluido em escoamento, sendo igual para todos os bocais sônicos. A pressão de estagnação P_0 e a temperatura de estagnação T_0 são medidas na câmara a montante do banco, sendo, portanto, os seus valores os mesmos para todos os bocais sônicos em operação. Por outro lado, C_* também é um parâmetro igual para todos os bocais, uma vez que ele é uma função de P_0 , de T_0 e do fluido. A vazão em massa crítica do banco de bocais sônicos é calculada pela Eq. (17).

$$\dot{m}_{BBS} = \frac{C_* P_0}{\sqrt{RT_0}} [(Cd.A_d)_{Bs1} + (Cd.A_d)_{Bs2} + (Cd.A_d)_{Bs3} + (Cd.A_d)_{Bs4} + (Cd.A_d)_{Bs5}] \tag{17}$$

O medidor rotativo fornece, em sua placa de identificação, um valor aproximado do número de pulsos que o seu sensor de alta freqüência emite para a vazão de 1 m^3 do fluxo que o atravessa. Este valor é de 720,262 pulsos/m^3 e será

aqui denominado de fator indicado do medidor K_{ind}. Portanto, uma estimativa da vazão volumétrica do fluxo que atravessa o medidor rotativo pode ser obtida utilizando-se este fator, a partir da contagem do número de pulsos N_{Rot} gerados pelo medidor durante o intervalo de tempo τ_{Rot} de uma medição. Esta vazão volumétrica é denominada vazão indicada, Q_{ind}, sendo obtida por meio da Eq. (18).

$$Q_{ind} = \frac{N_{Rot}}{K_{ind}\,\tau_{Rot}} \tag{18}$$

A diferença relativa entre a vazão volumétrica que realmente atravessou o medidor rotativo Q_{Rot}, e a vazão volumétrica indicada Q_{ind} é denominada erro relativo "*e*", o qual é definido pela Eq. (19) e geralmente expresso em porcentagem.

$$e = \frac{Q_{ind} - Q_{Rot}}{Q_{Rot}} = \frac{Q_{ind}}{Q_{Rot}} - 1 \qquad \text{(valor adimensional)} \tag{19}$$

O objetivo da calibração do medidor rotativo é encontrar o seu erro relativo *e* como uma função da vazão medida ou do número de Reynolds no medidor. O valor da vazão do fluxo de ar que realmente o atravessou é admitido como sendo o valor da vazão volumétrica estabelecido pelo padrão e corrigido para as condições de pressão e temperatura do medidor rotativo. Rearranjando a Eq. (19) a vazão do fluxo no medidor rotativo sob calibração é obtida pela Eq. (20).

$$Q_{ind} = Q_{Rot}(1 + e) \tag{20}$$

Substituindo a Eq. (20) na Eq. (18), obtém-se:

$$Q_{Rot} = \frac{N_{Rot}}{K_{ind}\,\tau_{Rot}(1 + e_m)} \tag{21}$$

7.1.1 Determinação de erro relativo do medidor rotativo de lóbulos

A Eq. (16) em termos da vazão volumétrica Q_{Rot}, fica:

$$\rho_{Rot} Q_{Rot} = m_{BBS} \qquad \Rightarrow \qquad Q_{Rot} = \frac{m_{BBS}}{\rho_{Rot}} \tag{22}$$

A massa específica do fluido é obtida pela equação de estado do gás real:

$$\rho_{Rot} = \frac{P_{Rot}}{Z\,R\,T_{Rot}} \tag{23}$$

Substituindo as Eq. (17), (21) e (23) na Eq. (22) obtém-se:

$$\frac{P_{Rot}}{ZRT_{Rot}} \frac{N_{Rot}}{K_{ind}\,\tau_{Rot}(1 + e_m)} = \frac{C_* P_0}{\sqrt{RT_0}} [(Cd\ A_d)_{Bs1} + ...] \tag{24}$$

Uma vez que o parâmetro que se quer determinar na operação de calibração é o erro do medidor rotativo de lóbulos e_{Rot}, a equação para seu cálculo é obtida rearranjando a Eq. (24).

$$e_{Rot} = \frac{P_{Rot}}{ZT_{Rot}} \frac{N_{Rot}}{K_{ind}\,\tau_{Rot}} \frac{\sqrt{RT_0}}{C_* P_0 [(CdA_d)_{Bs1} + ...]} - 1 \tag{25}$$

7.2. Incerteza

A incerteza dos resultados das medições realizadas foi estimada de acordo com as orientações do Guia para expressão da incerteza de medição [INMETRO, 1998]. A incerteza expandida $U_{95\%}$ declarada é a incerteza padrão combinada de medição, multiplicada por um fator de abrangência igual a 2, correspondente a um nível da confiança de aproximadamente 95%. A incerteza padrão ou é o desvio padrão experimental da média, quando obtida por meio de observações repetidas, ou é obtida por meio de julgamento científico, quando a análise estatística não se aplica.

7.3 Erro normalizado

Para interpretar o significado das diferenças entre os erros encontrados nas calibrações realizadas no CETEC e no NMi para os diferentes valores de Re_{Rot} foi empregado o método do erro normalizado *En* estabelecido pela Eq. (26) Este método está entre aqueles utilizados em comparações interlaboratoriais, onde as calibrações entre dois laboratórios são consideradas compatíveis se o valor de *En* for maior que –1 e menor que 1.

$$En = \frac{e_{CETEC} - e_{NMi}}{\sqrt{u^2(e_{CETEC} - e_{NMi})}} \tag{26}$$

8. Resultados

A Tabela 1 apresenta as faixas de vazão e de pressão de estagnação em que foram calibrados os nove bocais sônicos. As faixas de vazão em que cada bocal sônico foi calibrado foram determinadas de modo a proporcionar uma superposição de valores entre eles e que, ao mesmo tempo, garantisse que a condição crítica estivesse estabelecida. A superposição de valores de vazão ficou mais estreita entre os menores bocais, onde ocorre o menor valor para a pressão absoluta de estagnação, de 150 kPa, para os bocais Bs3 e Bs4. Para este valor de P_0, a razão de contrapressão nos bocais é de aproximadamente 0,62, o que representa um valor seguro, uma vez que, em avaliações experimentais realizadas nestes bocais, a condição crítica é garantida até uma razão de contrapressão de 0,8.

Tabela 1. Faixas de vazão em que os bocais sônicos foram calibrados

Designação	Diâmetro da garganta – *d*		Faixa da Pressão de estagnação – P_0	Faixa da vazão em massa	Faixa da vazão em volume (20°C; 1 atm)
Bs	(in)	(mm)	(kPa)	(kg/h)	(m^3/h)
Bs1	0,031	0,79	260 – 520	1 – 2	0,9 – 1,5
Bs2	0,044	1,1	260 – 610	2 – 5	1,5 – 4
Bs3	0,088	2,2	150 – 600	5 – 20	4 – 16,5
Bs4	0,177	4,50	150 – 610	20 – 80	16,5 – 66,5
Bs5-1	0,250	6,35	170 – 410	45 – 109	37,5 – 90
Bs5-2	0,250	6,35	170 – 410	45 – 109	37,5 – 90
Bs5-3	0,250	6,35	170 – 410	45 – 109	37,5 – 90
Bs5-4	0,250	6,35	170 – 410	45 – 109	37,5 – 90
Bs5-5	0,250	6,35	170 – 410	45 – 109	37,5 – 90

A curva de calibração *Cd* x Re_d de cada um dos bocais foi construída tomando-se no mínimo 12 pontos de vazão. A Figura (10) mostra as curvas de calibração dos bocais sônicos superpostas. Para o mesmo valor de Re_d a maior diferença entre os *Cd* dos bocais sônicos foi de 0,0005, menor do que a incerteza de 0,002 ($U_{95\%}$ = 0,23%). O valor do *Cd* variou de 0,976 a 0,989, os quais correspondem a valores de Re_d que variaram de 2,6 x 10^4 a 3,7 x 10^5.

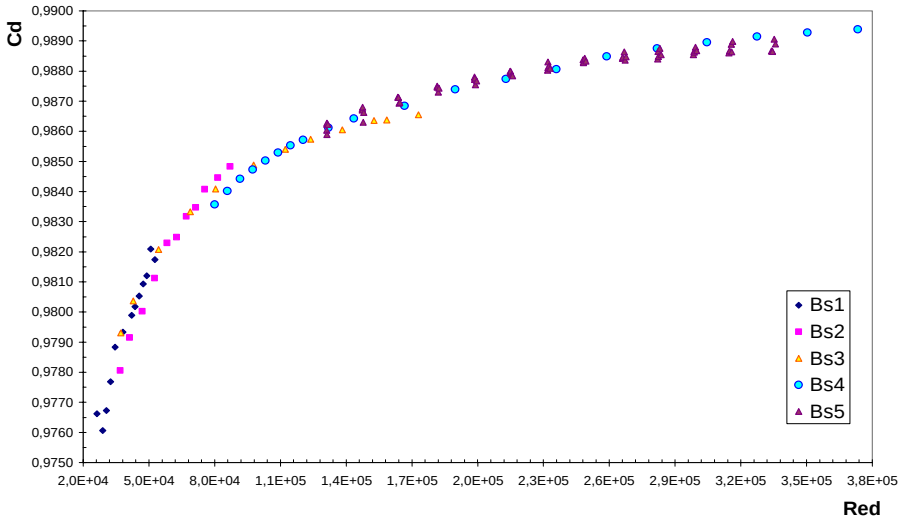

Figura 10 – Resultados das calibrações dos 9 bocais sônicos - *Cd x* Re_d

A Figura (11) apresenta os resultados encontrados para o erro relativo do medidor rotativo de lóbulos e_{Rot}, nas calibrações realizadas no CETEC e no NMi, para valores de Re_{Rot} de 4,6 x 10^3 a 1,1 x 10^5, os quais correspondem a vazões de 24 kg/h a 545 kg/h. Como pode ser observado as maiores diferenças entre os resultados ocorreram nas vazões mais baixas, de 24 kg/h a 70 kg/h, correspondentes, respectivamente, a Re_{Rot} de 4,6 x 10^3 a 1,4 x 10^4. Entretanto, a diferença "$e_{CETEC} - e_{NMi}$" não ultrapassou 0,3 %, o que fez com que o erro normalizado *En* não extrapolasse a faixa de -1 a +1 como mostrado na Fig (12). Por outro lado, para os pontos de vazão acima de 70 kg/h, ou seja, para Re_{Rot} acima de 1,4 x 10^4, houve um elevado grau de concordância entre os resultados, com os valores de *En* compreendidos dentro da faixa de -0,5 a +0,5. As calibrações foram realizadas com combinações de bocais sônicos no BBS que garantissem a utilização de todos os 9 bocais sônicos. A Tabela 2 mostra dez dos resultados obtidos.

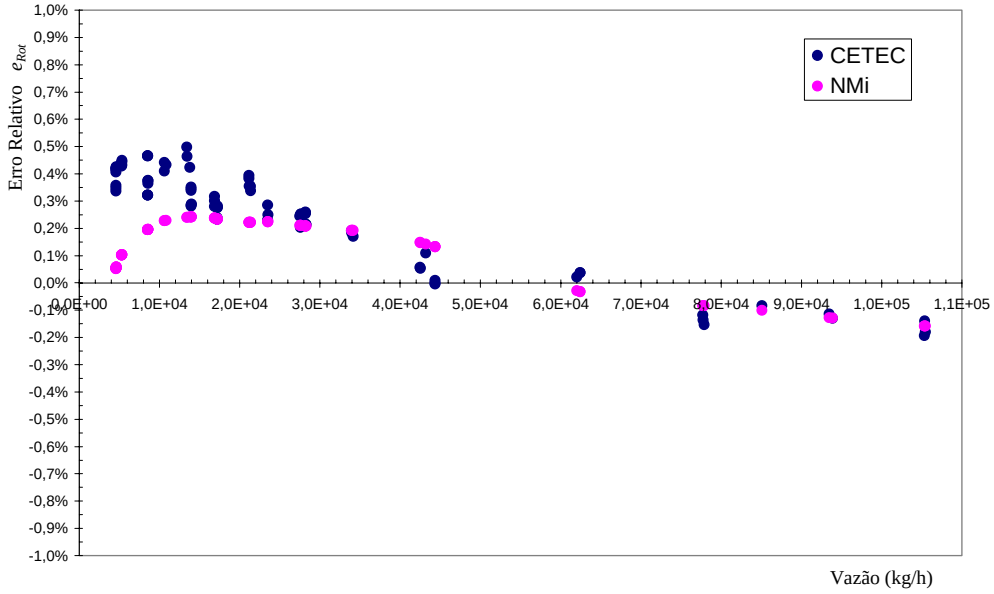

Figura 11 – Resultados das calibrações do medidor rotativo de lóbulos - e_{Rot} x Re_{Rot}

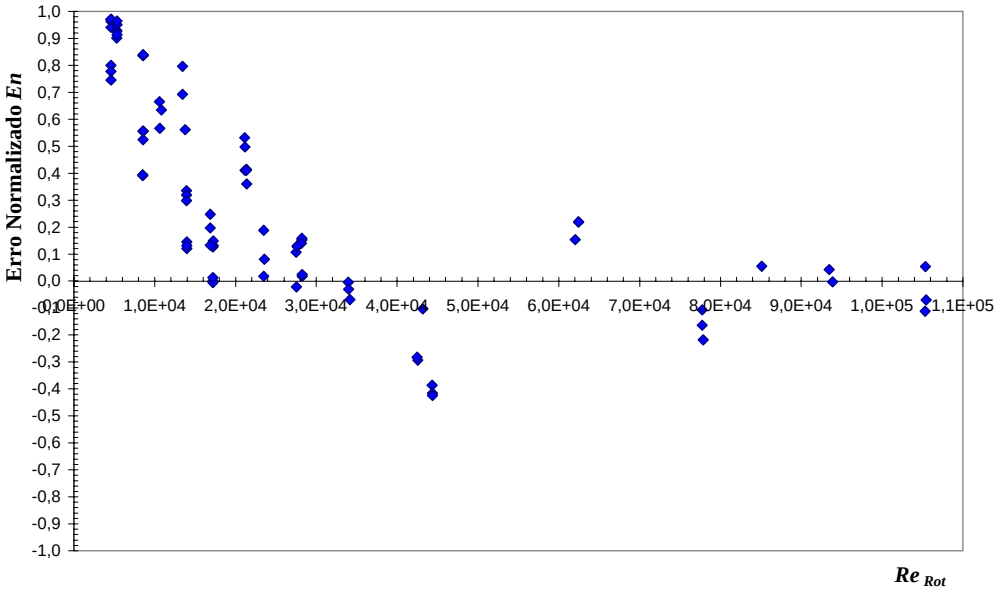

Figura 12 – Erro Normalizado *En* encontrado para os diferentes pontos de vazão calibrados

Tabela 2. Resultados de 10 pontos de vazão do medidor rotativo de lóbulos calibrados pelo BBS e comparados com os resultados de sua calibração no laboratório do NMi para o mesmo número de Reynolds no medidor

PARÂMETROS		Ponto 1	Ponto 2	Ponto 3	Ponto 4	Ponto 5	Ponto 6	Ponto 7	Ponto 8	Ponto 9	Ponto 10
BOCAIS SÔNICOS UTILIZADOS NA MEDIÇÃO		Bs1 Bs2 Bs3	Bs1 Bs4	Bs1 Bs5-1	Bs3 Bs4 Bs5-1	Bs5-1 Bs5-2	Bs5-1 Bs5-2 Bs5-3	Bs5-1 Bs5-2 Bs5-3 Bs5-4	Bs5-1 Bs5-2 Bs5-3 Bs5-4 Bs5-5	Bs5-1 Bs5-2 Bs5-3 Bs5-4 Bs5-5	Bs5-1 Bs5-2 Bs5-3 Bs5-4 Bs5-5
Parâmetros medidos no BBS											
Vazão em massa total	m (kg/h)	24	44	88	145	175	222	319	400	484	545
Pressão de estagnação	P_0 (kPa)	512	319	326	333	328	279	299	301	364	410
Temp. de estagnação	T_0 (ºC)	20	19	19	19	21	21	20	22	23	23
Pressão atmosférica	P_{atm} (kPa)	93	92	92	92	92	92	92	92	92	92
Parâmetros medidos no medidor rotativo de lóbulos											
Vazão real	Q_{Rot} (m³/h)	22	40	80	130	160	200	279	341	402	499
Número de Reynolds	Re_{Rot}	4,6E+3	8,6E+3	1,7E+4	2,8E+4	3,4E+4	4,3E+4	6,2E+4	7,8E+4	9,4E+4	1,1E+5
Temperatura	***TRot (ºC)***	20	20	20	19	21	22	21	22	22	22
Pressão absoluta	P_{Rot} (kPa)	93	92	93	94	92	94	96	99	102	93
Erro relativo e Incerteza											
Erro relativo CETEC	e_{CETEC} (%)	0,34	0,36	0,23	0,22	0,19	0,11	0,02	-0,12	-0,13	-0,14
Erro relativo NMi	e_{NMi} (%)	0,05	0,20	0,23	0,21	0,19	0,14	-0,03	-0,08	-0,13	-0,16
Incerteza CETEC	$U_{95\%CETEC}$ (%)	0,33	0,26	0,26	0,26	0,26	0,26	0,26	0,26	0,26	0,26
Incerteza NMi	$U_{95\%NMi}$ (%)	0,19	0,19	0,19	0,19	0,19	0,19	0,19	0,19	0,19	0,19
Erro Normalizado	***En***	0,75	0,53	0,00	0,02	0,00	-0,10	0,15	-0,11	0,00	0,05

8. Conclusões

O procedimento utilizado na validação das medições realizadas pelo banco de bocais sônicos BBS desenvolvido no CETEC mostrou-se bastante eficaz. Um medidor rotativo do laboratório foi calibrado contra o BBS e em seguida, os resultados obtidos foram comparados com aqueles da calibração deste mesmo medidor realizada no instituto nacional de metrologia da Holanda NMi, aplicando-se o método do erro normalizado, no qual os resultados obtidos no NMi foram tomados como valores de referência. Em toda a faixa de medição da calibração os valores obtidos para o erro normalizado situaram-se entre -1 e +1. O elevado grau de concordância entre as medições realizadas com o BBS desenvolvido no CETEC e aquelas realizadas no NMi, especialmente para as vazões acima de 10 % da vazão máxima do medidor rotativo, permite concluir pela sua validação. O desempenho do BBS mostrou-se adequado para o propósito de utilizá-lo como padrão do laboratório em calibrações de medidores de vazão de gás. Os resultados obtidos nos testes de validação do BBS demonstraram, também, que o coeficiente de descarga do medidor bocal sônico *Cd* é uma função do número de Reynolds na sua garganta Re_d. Os valores para o *Cd* obtidos em calibrações individuais dos bocais sônicos, contra um padrão primário do laboratório, podem ser empregados no uso concomitante dos mesmos no BBS. O sistema banco de bocais sônicos permitiu medições de vazões de até 545 kg/h utilizando, em operação conjunta, bocais sônicos calibrados em vazões de até 109 kg/h.

9. Referências

British Standard “BS 7405:1991 Guide to selection and application of flowmeters for the measurement of fluid flow in closed conduits”. 230 p.

Fox, R. W.; McDonald, A. T., 1998, “Introdução à Mecânica dos Fluidos”. Ed. LCT Livros Técnicos e Científicos Editora S. A., Rio de Janeiro. 662 p.

INMETRO, ABNT, SBM, 1998, “Guia para a expressão da incerteza de medição”. Segunda Edição Brasileira do “Guide to the Expression of Uncertainty in Measurement”, Rio de Janeiro, 121 p.

Johnson, A.; Kegel, T., 2004, “Uncertainty and traceability for the CEESI Iowa natural gas facility”. J. Res. Natl. Inst. Stand. Technol. Vol. 109, No. 3, pp. 345-369.

Santos, M. L. M., 2002, “Montagem e calibração de um banco de bocais sônicos”. Dissertação (Mestrado em Engenharia Mecânica) – Escola de Engenharia da UFMG, Belo Horizonte.175 p.

Stewart, D. G.; Watson, J. T.; Vaidya, A. M., 2000, “A new correlation for the critical mass flux of natural gas mixtures”. Flow Measurement and Instrumentation. Vol. 11, dez., pp. 265-272.

Wright, J. D., 1998, “The long term calibration stability of critical flow nozzles and laminar flowmeters”. NCSL Workshop & Symposium. pp. 443-462.

TITLE

Experimental evaluation of the performance of a sonic nozzles bank

Maria Luiza Moraes dos Santos
CETEC - Technological Center Foundation of the State of Minas Gerais
Gas Flow Laboratory
Av. José Cândido da Silveira, 2000 - Cidade Nova
Belo Horizonte - Minas Gerais
maria.luiza.moraes@cetec.br

Ramon Zeferino
CETEC - Technological Center Foundation of the State of Minas Gerais
Gas Flow Laboratory
Av. José Cândido da Silveira, 2000 - Cidade Nova
Belo Horizonte - Minas Gerais
ramon.zeferino@cetec.br

Geraldo Campolina França
Federal University of the State of Minas Gerais
Departament of Mechanical Engineering
Av. Antônio Carlos, 6627 - Pampulha
Belo Horizonte - Minas Gerais
gacf@ufmg.br

Abstract
The flowrate is a derived quantity that depends on the measurement of other parameters for its deduction. The methods for establishment the value of the gas flowrate that provide the highest accuracies are based on the measurement of the SI base quantity. Amongst these methods it can be distinguished, the volumetric one, that uses the units' length, thermodynamic temperature and time, and the gravimetric one, that uses the units mass and time. However, these methods, that constitute primary standards of the flowrate quantity, they require, by nature, complexes and laborious operational procedures, not being, therefore, indicated for routine measurements. The transference of this more accurate value for others systems of flowrate measurement is accomplished by means of the structuring of a traceability chain, where, for example, the primary standard calibrates a secondary standard meter, that in turn calibrates a working standard meter, which finally calibrates a operational flowmeter. The CETEC Gas Flowrate Laboratory with the intention to establish an internal traceability chain already structuralized the first link of this chain, constituted by a set of sonic nozzles meters type, calibrated in the range from 1 kg/h to 110 kg/h, against a volumetric primary standard of the laboratory. These sonic nozzles are mounted in an array of parallel tubes, composing a calibration secondary system called "sonic nozzles bank", with capacity to measure gas flowrates in the range from 1.5 kg/h to 545 kg/h. The objective of this work is to present the experimental results obtained in the evaluation of the performance of this bank, whose mechanic project possesses a conception for use in laboratory with flexibility for an easy and fast change of the sonic nozzles flow meters that compose it

Keywords: sonic nozzle, chocked flow, gas flow measurement

Proceedings of the 11th Brazilian Congress of Thermal Sciences and Engineering – ENCIT 2006
Braz. Soc. of Mechanical Sciences and Engineering – ABCM, Curitiba, Brazil, Dec. 5-8, 2006

Paper CIT06-0792

TEORIA DE TRÁFEGO DE FLUIDO PARA UM SISTEMA MACROSCÓPICO

Adriana Luiza do Prado
Departamento de Matemática, Universidade Federal do Paraná, Caixa Postal 019081, CEP81531-990, Curitiba, Paraná
alprado@mat.ufpr.br

Eloy Kaviski
Departamento de Hidraúlica e Saneamento, Universidade Federal do Paraná
eloy.dhs@ufpr.br

Liliana M Gramani Cumin
Departamento de Matemática, Universidade Federal do Paraná, Caixa Postal 019081, CEP81531-990, Curitiba, Paraná
gramani@mat.ufpr.br

Resumo. *As teorias de tráfego de fluido buscam descrever de uma maneira matemática as interações entre veículos, motoristas e a infra-estrutura. A infra-estrutura consiste no sistema da estrada e em todos os seus elementos operacionais, incluindo dispositivos de controle, semáforos e sinais de trânsito. Estas teorias são indispensáveis em todos os modelos de tráfego e ferramentas para à análise de operações nas ruas e estradas. O estudo científico do fluxo de tráfego teve seu início na década de 30, com o aumento significativo do uso dos automóveis e da expansão do sistema da estrada, surgiu um estudo de características do tráfego, através de modelos microscópicos e macroscópicos. Os modelos macroscópicos do fluxo, descartam as componentes individuais do sistema, adotando uma vista macroscópica do tráfego em uma rede. As variáveis consideradas são a densidade veicular e a velocidade média do tráfego. O objetivo deste trabalho é resolver as equações macroscópicas do fluxo de tráfego derivadas das equações reduzidas de Paveri-Fontana para modelos com valores especificados de velocidade prevista para a estrada através do método das características. A análise destes modelos fornece aos controladores do tráfego meios para avaliarem o sistema e determinar estratégias de controle em áreas urbanas*

Palavras chave: *Teoria de tráfego de fluido, Modelos macroscópicos, Equação de Paveri-Fontana, Método das Características.*

1. Introdução

Existe na literatura um grande número de modelos macroscópicos de tráfego que descrevem o movimento de veículos ao longo de uma rodovia ou nas redes urbanas como um fluido unidimensional compressível (Helbing, 2001). Nos problemas de trânsito modelados por um problema de mecânica dos fluidos faz-se variar a velocidade, a compressibilidade, a viscosidade e outras propriedades do fluido consoante a situação concreta que se pretende estudar.

O estudo científico do fluxo de tráfego teve seu início na década de 30 com a aplicação da teoria de probabilidade à descrição do tráfego de estrada e com os estudos de modelos que relacionavam o volume, a velocidade e a investigação do desempenho do tráfego nos cruzamentos. Com o aumento significativo do uso dos automóveis e da expansão do sistema da estrada, surgiu um estudo de características do tráfego, através de modelos microscópicos e macroscópicos. Os modelos macroscópicos do fluxo, descartam à vista microscópica do tráfego em termos das velocidades individuais dos veículos ou as componentes individuais do sistema (tais como as ligações ou os cruzamentos), adotando uma vista macroscópica do tráfego em uma rede.

As teorias de tráfego de fluido buscam descrever de uma maneira matemática as interações entre veículos, motoristas e a infra-estrutura. A infra-estrutura consiste no sistema da estrada e em todos os seus elementos operacionais, incluindo dispositivos de controle, semáforos e sinais de trânsito. Estas teorias são indispensáveis em todos os modelos de tráfego e ferramentas para à análise de operações nas ruas e estradas.

A análise de modelos fornece aos controladores do tráfego meios para avaliarem o sistema e determinar estratégias de controle em áreas urbanas.

Na teoria cinética dos gases, o sistema formado pela equação de Boltzmann e com condições de contorno, para alguns casos particulares pode ser solucionada analiticamente pelos métodos clássicos de Chapman-Enskog e pelo método de Grad, os quais diferem fundamentalmente pelo número de campos básicos empregados (Fernandes, 1996). Muitas vezes estas soluções dependem do uso de procedimentos numéricos para a produção de resultados finais. Os métodos de solução de maior interesse são numéricos.

Neste trabalho o objetivo é resolver as equações macroscópicas do fluxo de tráfego derivadas das equações reduzidas de Paveri-Fontana, tipo-Boltzmann para o fluxo de tráfego levando-se em conta o comportamento individual do veículo,

para modelos específicos da velocidade desejada através do método das características. As variáveis consideradas são a densidade veicular e a velocidade média do tráfego.

2. Equação de Paveri-Fontana para Velocidades Previstas Especificadas

Com o objetivo de se corrigir algumas deficiências do modelo de tráfego obtido através da teoria cinética dos gases proposta por (Prigogine e Herman, 1971), ou seja, equação cinética de tráfego, Paveri-Fontana desenvolveu um tratamento do tipo-Boltzmann para o fluxo de tráfego levando-se em conta o comportamento individual do carro, ou seja, sua aceleração. No modelo de Paveri-Fontana o estado do tráfego é caracterizado pela função de distribuição de um veículo $g(x, c, w, t)$ tal que $g(x, c, w, t)dx\,dc\,dw$ dado um tempo t fornece o número de veículos numa estrada entre as posições x e $x + dx$ e velocidade atual entre c e $c + dc$, com velocidade desejada entre w e $w + dw$. Para uma estrada de mão única, após ocorrer uma ultrapassagem, a função de distribuição satisfaz a seguinte equação cinética de tráfego

$$\frac{\partial g}{\partial t} + c\frac{\partial g}{\partial x} + \frac{\partial}{\partial c}\left(g\frac{\partial c}{\partial t}\right) + \frac{\partial}{\partial w}\left(g\frac{\partial w}{\partial t}\right)$$

$$= f(x,c,t)\int_c^\infty (1-p)(c'-c)g(x,c',w,t)dc' - g(x,c,w,t)$$

$$\times \int_0^c (1-p)(c-c')f(x,c',t)dc', \tag{1}$$

na qual

$$f(x,c,t) = \int_0^\infty g(x,c,w,t)dw \tag{2}$$

é a função de distribuição da velocidade de um veículo.

O lado direito da Eq. (1) é denominado de termo de interação (ou colisão) e descreve o processo de desaceleração do fluxo que é causado por veículos mais lentos que não podem ser imediatamente ultrapassados. O lado esquerdo corresponde à situação na qual o veículo com velocidade c' deve desacelerar para a velocidade c causando um decrescimento na função de distribuição. Basicamente considera-se que os veículos mais lentos podem ser imediatamente ultrapassados com uma probabilidade p.

Assumindo-se que os motoristas aproximam-se exponencialmente da velocidade desejada num tempo com uma constante de relaxação de tempo τ, pode-se escrever

$$\frac{dc}{dt} = \frac{w-c}{\tau} \qquad \text{e} \qquad \frac{dw}{dt} = 0. \tag{3}$$

A lei da aceleração dada pela Eq. (3) representa uma boa aproximação, desde que os motoristas reduzam gradualmente a aceleração após alcançar a velocidade desejada.

A equação cinética do tráfego de Paveri-Fontana, Eq. (1), uma equação íntegro-diferencial, apresenta uma grande dificuldade quanto à obtenção de uma solução analítica para todos os casos nos quais os processos de interação não podem ser abandonados. Para superar esta dificuldade, a Eq. (1) é integrada com respeito a velocidade desejada, obtendo-se uma equação reduzida de Paveri-Fontana

$$\frac{\partial f}{\partial t} + c\frac{\partial f}{\partial x} + \frac{\partial}{\partial c}\left(f\frac{V_0 - c}{\tau}\right) = f(x,c,t)\int_0^\infty (1-p)(c'-c)f(x,c',t)dc' \tag{4}$$

na qual

$$V_0(x,c,t) = \int_0^\infty w\frac{g(x,c,w,t)}{f(x,c,t)}dw, \tag{5}$$

representa a velocidade média desejada.

Ao se considerar o tráfego homogêneo e estacionário, a velocidade média desejada para os veículos é diretamente proporcional a velocidade atual c. Sendo esta relação dada por:

$$V_0(x,c,t) = V_0(c) = kc, \tag{6}$$

ou seja, esta velocidade será independente do tempo e da posição na qual o veículo se encontra na estrada. Este é um caso particular que simplifica a Eq. (4) para a velocidade média desejada.

Sabe-se que a função de distribuição deve satisfazer as seguintes condições de contorno

$$\lim_{w\to 0} g(x,c,w,t) = 0 \qquad \text{e} \qquad \lim_{w\to\infty} g(x,c,w,t) = 0. \tag{7}$$

Então, a Eq. (4) torna-se

$$\frac{\partial f}{\partial t} + c\frac{\partial f}{\partial x} + \frac{\partial}{\partial c}\left(f\frac{kc-c}{\tau}\right) = \mathcal{C}(c,c'), \tag{8}$$

sendo que $C(c,c')$ representa o termo de colisão. Denominando-se por $\beta = \frac{k-1}{\tau}$, na qual k e τ são constantes, então a Eq. (8) transforma-se em

$$\frac{\partial f}{\partial t} + c\frac{\partial f}{\partial x} + \beta\frac{\partial (cf)}{\partial c} = \mathcal{C}(c,c'). \tag{9}$$

3. Equações Macroscópicas do Tráfego

As equações macroscópicas para as variáveis relevantes podem ser derivadas do cálculo da média entre a equação cinética sobre a velocidade instântanea. Este procedimento é bem-conhecido na teoria cinética (Chapman e Cowling, 1970) assim como suas aplicações em problemas de fluxo de tráfego.

O método utilizado na dedução das equações macroscópicas é semelhante ao desenvolvido em (Velasco e Marques, 2005), isto é, para as equações de Euler e Navier-Stokes. Por se tratar de um problema não fechado, existem vários modos de se obter os resultados.

Usa-se, neste trabalho, os valores encontrados para a Pressão do Tráfego $\mathcal{P}$ e uma condição para a velocidade média desejada $\mathcal{W}$. Os cálculos numéricos são realizados com base no método das características (Streeter, 1997).

Nas equações reduzidas de Paveri-Fontana do tráfego, as quantidades macroscópicas ρ e V são funções da função de distribuição da velocidade de um veículo. Para qualquer função de distribuição $f(x,c,t)$, a densidade veicular ρ e a velocidade média V são definidas através de:

$$\rho(x,t) = \int_0^\infty f(x,c,t)dc \tag{10}$$

e,

$$V(x,t) = \int_0^\infty \frac{f(x,c,t)}{\rho(x,t)}dc. \tag{11}$$

respectivamente.

A integração da equação reduzida do tráfego de Paveri-Fontana (4) sobre todos os atuais valores da velocidade c, produz a equação da continuidade

$$\frac{\partial \rho}{\partial t} + \frac{\partial \rho V}{\partial x} = 0 \tag{12}$$

e a equação da velocidade como sendo

$$\rho\left(\frac{\partial V}{\partial t} + V\frac{\partial V}{\partial x}\right) + \frac{\partial \mathcal{P}}{\partial x} = \rho\frac{\mathcal{W}-V}{\tau} - \rho(1-p)\mathcal{P} \tag{13}$$

obtida pela multiplicação da Eq. (4) por c e efetuando a integral sobre todos os valores da velocidade atual. Nas equações (12) e (13) foram introduzidas a velocidade média prevista

$$\mathcal{W} = \int_0^\infty V_0(x,c,t)\frac{f(x,c,t)}{\rho(x,t)}dc \tag{14}$$

e a pressão do tráfego

$$\mathcal{P} = \int_0^\infty (c-V)^2 f(x,c,t)dc, \tag{15}$$

que esta relacionada com a variância, $\Theta(x,t)$, da velocidade através da equação

$$\mathcal{P} = \rho(x,t)\Theta(x,t). \tag{16}$$

As equações (10)-(16) são válidas desde que a função de distribuição f satisfaça a condição

$$\lim_{c\to 0} f(x,c,t) = 0 \qquad \text{e} \qquad \lim_{c\to\infty} f(x,c,t) = 0. \tag{17}$$

Neste trabalho soluciona-se as equações (12) e (13) considerando-se a hipótese de que $\mathcal{W}$ é constante $(= V_0)$ aproximando (Velasco e Marques, 2005)

$$p = 1 - \frac{\rho}{\hat{\rho}}, \tag{18}$$

e

$$\mathcal{P} = \frac{\rho V^2}{\alpha} \tag{19}$$

sendo $\hat{\rho}$ representando a densidade veicular máxima da estrada e α é uma constante adimensional.

4. Método das Características

Considera-se o problema de valor inicial para a equação de primeira ordem quase linear, dadas as funções $a(x,t,u), b(x,t,u)$ e $d(x,t,u)$. O objetivo é encontrar $u(x,t)$, tal que

$$\begin{cases} a(x,t)u_x + b(x,t)u_t + d(x,t) = 0, \quad t > 0, -\infty < x < \infty, \\ u(x,0) = u_0(x). \end{cases} \tag{20}$$

A equação diferencial de primeira ordem (20), definida inicialmente no sistema de coordenadas (x,t) será reescrita em um outro sistema de coordenadas (s,t) definido convenientemente. Sejam as curvas $x(s)$ e $t(s)$ definidas por:

$$\begin{aligned} \frac{dx}{ds} &= a(x(s),t(s),u), \qquad & x(0) &= x_i, \\ \frac{dt}{ds} &= b(x(s),t(s),u), \qquad & t(0) &= t_i, \end{aligned} \tag{21}$$

estas são denominadas curvas características no espaço (x,t,u). Aplicando a regra da cadeia para se derivar $u(x(s),t(s))$, ao longo das características, tem-se

$$\frac{du}{ds} = u_x\frac{dx}{ds} + u_t\frac{dt}{ds} = a(x,t,u)u_x + b(x,t,u)u_t. \tag{22}$$

Comparando a Eq. (22) com a Eq. (20) obtem-se

$$\begin{cases} \dfrac{du}{ds} = -d(x(s),t(s),u), \\ u(0) = u_0(x_i). \end{cases} \tag{23}$$

isto é, define-se uma equação diferencial ordinária no novo sistema de coordenadas (s,t).

Comparando as equações (20) e (23), observa-se que a equação diferencial parcial transformou-se em um sistema de equações diferenciais ordinárias.

Assim a solução será encontrada em pontos que estão sobre as características. Um processo de interpolação pode ser utilizado se estas características se afastam em algumas regiões. Este método é considerado um método para solução analítica de equações diferenciais parciais de primeira ordem.

O método das características pode ser aplicado para solucionar sistemas de duas equações diferenciais parciais de primeira ordem quase lineares e hiperbólicas.

Sejam L_1 e L_2 equações contendo as variáveis dependentes, ρ, a densidade veicular, e V, a velocidade média. Essas equações serão combinadas por meio de um multiplicador desconhecido λ, como $L = L_1 + \lambda L_2$. Quaisquer valores reais distintos de λ fornecem duas equações em ρ e V que representam o mesmo fenômeno físico que as duas equações originais, L_1 e L_2, e que podem substituí-las diante de qualquer solução. Substituindo L_1 e L_2 na expressão de L, obtem-se, após um rearranjo, as equações que representam as derivadas totais, $\dfrac{d\rho}{dt}$ e de $\dfrac{dV}{dt}$, respectivamente.

Atribui-se L_2 a equação da continuidade (12) e L_1 a equação da velocidade (13),

$$L_2 = \frac{\partial\rho}{\partial t} + \rho\frac{\partial V}{\partial x} + V\frac{\partial\rho}{\partial x} = 0. \tag{24}$$

e

$$L_1 = \rho\left(\frac{\partial V}{\partial t} + V\frac{\partial V}{\partial x}\right) + \frac{\partial \mathcal{P}}{\partial x} = \rho\frac{\mathcal{W} - V}{\tau} - \rho(1-p)\mathcal{P}. \tag{25}$$

Substituindo-se na equação da velocidade (13), $\mathcal{W} = V_0$ e a pressão do tráfego dada pela Eq. (19), encontra-se

$$\rho\left(\frac{\partial V}{\partial t} + V\frac{\partial V}{\partial x}\right) + \frac{\partial}{\partial x}\left(\frac{\rho V^2}{\alpha}\right) = \rho\frac{V_0 - V}{\tau} - \rho(1-p)\frac{\rho V^2}{\alpha}. \tag{26}$$

Na Eq. (26), ρ e V são funções de x e α é uma constante adimensional dada por

$$\alpha = \frac{\rho_e\,(1-p)\,V_e}{\beta}, \tag{27}$$

na qual ρ_e e V_e referem-se ao estado estacionário.

Desenvolvendo a parcial com relação a x na Eq. (24) e agrupando as derivadas parciais da mesma função e aplicando o método das características, ou seja, $L = L_1 + \lambda L_2$, encontra-se

$$L_1 = \frac{\partial V}{\partial t} + \frac{\partial V}{\partial x}v_{c(L_1)} \tag{28}$$

e

$$L_2 = \frac{\partial \rho}{\partial t} + \frac{\partial \rho}{\partial x}v_{c(L_2)} \tag{29}$$

sendo genericamente $v_c = \frac{dx}{dt}$.

Com a condição de que $v_{c(L_1)} = v_{c(L_2)}$, a equação abaixo terá que ser satisfeita

$$\rho\lambda^2 + \frac{2V}{\alpha}\lambda - \frac{V^2}{\rho\alpha} = 0, \tag{30}$$

que representa uma equação do segundo grau em λ. Para o caso deste trabalho, tem-se duas raízes reais e distintas para λ,

$$\lambda = \frac{V}{\alpha\rho}(-1 \pm \sqrt{1+\alpha}), \tag{31}$$

ou seja, solução do tipo hiperbólico.

Substituindo a Eq. (31) em $L = L_1 + \lambda L_2$, encontra-se quatro equações diferenciais ordinárias

$$C^+\begin{cases} \dfrac{dV}{dt} + \dfrac{V}{\alpha\rho}(-1+\sqrt{1+\alpha})\dfrac{d\rho}{dt} + (1-p)\dfrac{\rho V^2}{\alpha} - \dfrac{(V_0 - V)}{\tau} = 0, \\ \dfrac{dx}{dt} = V - \dfrac{V}{\alpha}(-1+\sqrt{1+\alpha}), \end{cases} \tag{32}$$

e também

$$C^-\begin{cases} \dfrac{dV}{dt} + \dfrac{V}{\alpha\rho}(-1-\sqrt{1+\alpha})\dfrac{d\rho}{dt} + (1-p)\dfrac{\rho V^2}{\alpha} - \dfrac{(V_0 - V)}{\tau} = 0, \\ \dfrac{dx}{dt} = V - \dfrac{V}{\alpha}(-1-\sqrt{1+\alpha}). \end{cases} \tag{33}$$

As equações (32) e (33) são as equações do método das características, nas quais C^+ e C^- representam as curvas características positivas e negativas, respectivamente. Ambas possuem inclinações positivas pois o fluxo de tráfego é maior do que a velocidade das ondas sonoras (Sivaloganathan, 1974 e Sivaloganathan, 1978). Conhecidas as condições iniciais e de contorno pode-se traçar a malha das curvas características.

4.1. O Processo Geral do Método das Características

Devido à inclinação das características começa-se o processo de discretização da malha da condição de contorno para a posição do trecho $0 \leq x \leq L_t$.

O esquema deste processo, denominado esquema das distâncias especificadas do método das caracteristicas (Sivaloganathan, 1974), diferenciado do esquema da malha retangular (Sivaloganathan, 1978), está representado na Fig. 1 na qual:

- Divide-se o comprimento da estrada em n partes iguais de comprimento Δx.
- Inicia-se pela condição de contorno em $A,\ x = L_t$, com $P_{1C_1} = (L_t, 0)$, traçando-se uma curva característica positiva C_1.
- Em $B,\ x = L_t - \Delta x$, com $P_{1C_2} = (L_t - \Delta x, 0)$, traça-se uma curva característica positiva C_2 e em AB, ponto médio de A e B, traça-se uma curva de característica negativa. A intersecção destas curvas ocorre no ponto M.
- Em A traça-se uma curva característica negativa, encontrando-se o ponto N sobre a curva C_2. Interpola-se os pontos M e N encontrando o ponto P_{2C_2}.
- Em $C,\ x = L_t - 2\Delta x$, com $P_{1C_3} = (L_t - 2\Delta x, 0)$, traça-se uma curva característica positiva C_3 e em BC, ponto médio de B e C, traça-se uma curva característica negativa. A intersecção destas curvas ocorre no ponto M^*.
- Em B traça-se uma curva característica negativa, encontrando-se o ponto P_{2C_3}.
- Em N traça-se uma curva característica negativa encontrando-se N^* sobre a curva C_3. Interpola-se os pontos P_{2C_3} e N^* encontrando o ponto P_{3C_3}.
- Em $D,\ x = L_t - 3\Delta x$, com $P_{1C_4} = (L_t - 3\Delta x, 0)$, e em CD, ponto médio de C e D, traça-se uma curva característica positiva e negativa, respectivamente. Encontra-se o ponto M^{**}.
- De C traça-se uma curva característica negativa encontrando-se P_{2C_4}. De P_{2C_3} e N^* traçam-se curvas características negativas obtendo-se P_{3C_4} e N^{**}, respectivamente. Interpolando-se os pontos P_{3C_4} e N^{**} encontra-se P_{4C_4}.
- e assim sucessivamente vai-se discretizando a malha.

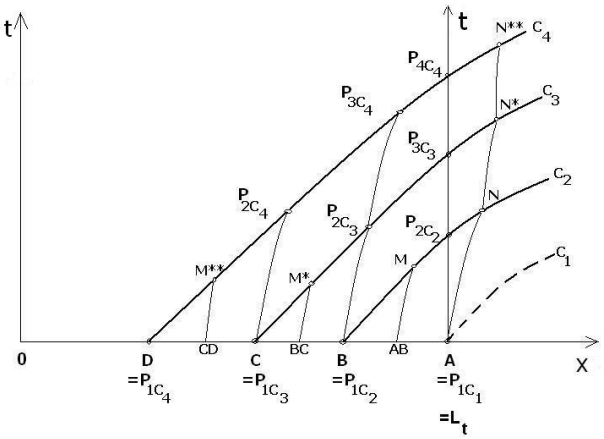

Figura 1: Discretização da malha.

De um modo geral, associa-se L a curva característica positiva C^+ e R a curva característica negativa C^-, conforme a Fig. 2. A determinação do ponto M, ou seja, t_M, x_M, ρ_M e V_M, sendo conhecidos os dados dos pontos L e R é obtido através do seguinte procedimento computacional:

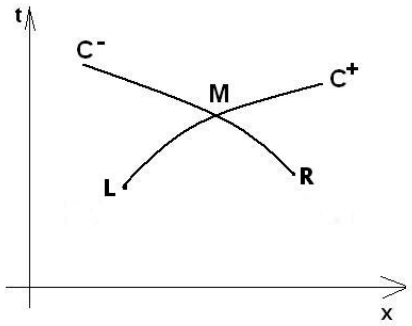

Figura 2: Gráfico no plano xt das características, sobre as quais encontra-se a solução.

- (Passo1) Atribuindo-se $b_\pm = \dfrac{-1 \pm \sqrt{\alpha+1}}{\alpha}$ e $q_\pm = \dfrac{(\alpha+1) \pm \sqrt{\alpha+1}}{\alpha}$ e substituindo a Eq. (18), as equações (32) e (33) serão escritas na forma:

$$\frac{1}{V}\frac{dV}{dt} + \frac{b_\pm}{\rho}\frac{d\rho}{dt} = \underbrace{\frac{V_0 - V}{\tau V} - \frac{\rho V}{\alpha}\left(1 - \frac{\rho}{\hat{\rho}}\right)}_{f(V,\rho)}, \tag{34}$$

e

$$\frac{dx}{dt} = V q_\pm, \tag{35}$$

respectivamente.

- (Passo 2) Calcula-se $f_L(V_L, \rho_L)$ e $f_R(V_R, \rho_R)$ sendo conhecidos a velocidade e a densidade em L e R através das equações:

$$f_L(V_L, \rho_L) = \frac{V_0 - V_L}{\tau V_L} - \frac{\rho_L V_L}{\alpha}\left(1 - \frac{\rho_L}{\hat{\rho}}\right) \tag{36}$$

e

$$f_R(V_R, \rho_R) = \frac{V_0 - V_L}{\tau V_R} - \frac{\rho_R V_R}{\alpha}\left(1 - \frac{\rho_R}{\hat{\rho}}\right) \tag{37}$$

- (Passo 3) Inicia-se, como primeira aproximação, fazendo-se a determinação M como

$$t_M = \frac{t_L + t_R}{2},\ x_M = \frac{x_L + x_R}{2},\quad \rho_M = \frac{\rho_L + \rho_R}{2} \text{ e } V_M = \frac{V_L + V_R}{2}. \tag{38}$$

- (Passo 4) Calculam-se novas aproximações das variáveis no ponto M do item anterior, denotadas por $t_M^*,\ x_M^*,\ \rho_M^*,\ V_M^*$.
  - Cálculo de t_M^* e x_M^*.

    Integrando a Eq. (35), obtém-se um sistema para x_M e t_M formado pelas equações

$$x_M - x_L = \frac{q_+}{2}(V_M + V_L)(t_M - t_L) \tag{39}$$

e

$$x_M - x_R = \frac{q_-}{2}(V_M + V_R)(t_M - t_R); \tag{40}$$

Denominando

$$a_L = \frac{q_+}{2}(V_M + V_L) = \frac{(\alpha+1) + \sqrt{\alpha+1}}{\alpha}(V_M + V_L) \tag{41}$$

e

$$a_R = \frac{q_-}{2}(V_M + V_R) = \frac{(\alpha+1) - \sqrt{\alpha+1}}{\alpha}(V_M + V_R), \tag{42}$$

reescreve-se o sistema (39) e (40):

$$x_M^* - x_L = a_L(t_M^* - t_L) \tag{43}$$

e

$$x_M^* - x_R = a_R(t_M^* - t_R), \tag{44}$$

no qual chamou-se x_M por x_M^* e t_M por t_M^* para denotar que se está calculando uma nova aproximação para estas variáveis. Resolvendo o sistema descrito pelas equações (43) e (44) encontra-se

$$t_M^* = \frac{x_R - x_L + a_L t_L - a_R t_R}{a_L - a_R} \tag{45}$$

e

$$x_M^* = x_L + a_L(t_M^* - t_L). \tag{46}$$

– Cálculo de ρ_M^* e V_M^*.

Integrando a Eq. (34) obtém-se um sistema para ρ_M e V_M dados pelas equações:

$$b_+(ln\ \rho_M - ln\ \rho_L) + ln\ V_M - ln\ V_L = \left[\frac{f_M(V_M, \rho_M) + f_L(V_L, \rho_L)}{2}\right](t_M^* - t_L) \tag{47}$$

e

$$b_-(ln\ \rho_M - ln\ \rho_R) + ln\ V_M - ln\ V_R = \left[\frac{f_M(V_M, \rho_M) + f_R(V_R, \rho_R)}{2}\right](t_M^* - t_R), \tag{48}$$

na qual utilizou-se para f_M a definição dada na Eq. (36), substituindo M por L.
Denominando

$$b_L = \left[\frac{f_M(V_M, \rho_M) + f_L(V_L, \rho_L)}{2}\right](t_M^* - t_L) \tag{49}$$

e

$$b_R = \left[\frac{f_M(V_M, \rho_M) + f_R(V_R, \rho_R)}{2}\right](t_M^* - t_R), \tag{50}$$

as equações (47) e (48), para $\rho_M^* = \rho_M$ e $V_M^* = V_M$, formam o sistema

$$b_+(ln\ \rho_M^* - ln\ \rho_L) + ln\ V_M^* - ln\ V_L = b_L \tag{51}$$

e

$$b_-(ln\ \rho_M^* - ln\ \rho_R) + ln\ V_M^* - ln\ V_R = b_R, \tag{52}$$

cuja solução é dada por

$$\rho_M^* = exp\{[b_L - b_R + \ln(V_L) - \ln(V_R) + \frac{\sqrt{\alpha+1}-1}{\alpha}\ln(\rho_L) + \frac{\sqrt{\alpha+1}+1}{\alpha}\ln(\rho_L)]\frac{\alpha}{2\sqrt{\alpha+1}}\} \tag{53}$$

e

$$V_M^* = exp\{b_L + \ln(V_L) + \frac{\sqrt{\alpha+1}-1}{\alpha}[\ln(\rho_L) - \ln(\rho_M^*)]\}. \tag{54}$$

- (Passo 5) Com os valores da aproximação anterior e com os valores da aproximação do passo 4, verifica-se a convergência através das condições:

$$|x_M - x_M^*| < \varepsilon\, x_M, \quad |t_M - t_M^*| < \varepsilon\, t_M, \quad |V_M - V_M^*| < \varepsilon\, V_M, \quad \text{e } |\rho_M - \rho_M^*| < \varepsilon\, \rho_M, \tag{55}$$

nas quais ε representa a precisão da convergência. No programa numérico adotou-se $\varepsilon = 10^{-7}$. Se as condições dadas em (55) forem satisfeitas, a determinação do ponto M foi encontrada. Caso contrário, atribui-se

$$x_M = x_M^*,\ t_M = t_M^*,\ V_M = V_M^* \ \text{ e } \ \rho_M = \rho_M^* \tag{56}$$

e volta-se ao passo 4, repetindo este processo, até se obter a precisão desejada.

5. Simulação Numérica e Resultados

O sistema de equações diferenciais ordinárias (32) e (33) requerem a especificação das condições iniciais e de contorno. Com o objetivo de simplificar a análise, serão consideradas condições de contorno periódicas para a densidade veicular $\rho(0,t) = \rho(L_t,t)$ e a velocidade média $V(0,t) = V(L_t,t)$, no qual L_t representa a extensão da estrada estudada.

Neste trabalho, considera-se um tráfego homogêneo e estacionário,

$\rho_e = 28$ veículos/km

e

$$V_e(\rho_e) = 84 \text{ km/h} \tag{57}$$

que sofre uma pequena perturbação periódica na velocidade média (Helbing, 1996) representando alguns veículos movendo-se mais rapidamente e outros mais lentamente. Assim, as condições iniciais consideradas são:

$\rho(x,0) = \rho_e = 28$ veículos/km

e

$$V(x,0) = 84 + 0,84 \sin\left(\frac{2\pi x}{L_t}\right), \tag{58}$$

com $0 \leq x \leq L_t$ dados em km. Implementa-se para o método numérico a extensão da estrada igual a $L_t = 12$ km e a constante de relaxação de tempo como $\tau = \frac{1}{120}h$. Adota-se $\hat{\rho} = 140$ veiculos/km e $\alpha = 75$, obtido a partir de resultados experimentais (Velasco e Marques, 2005).

Utililizando-se a Eq. (27), calcula-se β, a qual fornecerá a constante k e consequentemente V_0. Para tempos posteriores, na Eq. (27) se utiliza a Eq. (58) para a expressão da velocidade e repete-se o processo para se obter V_0.

Na Tab. 1 apresenta-se a evolução da densidade veicular ρ em função do trecho da estrada x e do tempo t para as sete primeiras características positivas, ver Fig. 1, que emanam do eixo x, considerando-se a divisão do trecho da estrada em 200 partes iguais, $n = 200$.

Os dados numéricos obtidos estão de acordo com a análise considerada, ou seja, como o estado é estacionário a densidade veicular permanece praticamente constante, sendo a variação numérica máxima de $\pm 0,003$.

Tabela 1: Valores de x, t e ρ para sete primeiras curvas características positivas.

Curva Característica	Pontos	x (km)	t (h)	$\rho(x,t)$ (veículos/km)
C_1	P_{1C_1}	12,0000000000	0,00000000000	28,0000000000
C_2	P_{1C_2}	11,9400000000	0,00000000000	28,0000000000
	P_{2C_2}	12,0000000000	0,00057933167	27,9937050000
C_3	P_{1C_3}	11,8800000000	0,00000000000	28,0000000000
	P_{2C_3}	11,9637510000	0,00080890147	27,9912210000
	P_{3C_3}	12,0000000000	0,00118491460	28,0161420000
C_4	P_{1C_4}	11,8200000000	0,00000000000	28,0000000000
	P_{2C_4}	11,9037510000	0,00080914379	27,9912380000
	P_{3C_4}	11,9888370000	0,00169197860	28,0497530000
	P_{4C_4}	12,0000000000	0,00181541310	28,0488290000
C_5	P_{1C_5}	11,7600000000	0,00000000000	28,0000000000
	P_{2C_5}	11,8437510000	0,00080938542	27,9912640000
	P_{3C_5}	11,9288360000	0,00169245210	28,0498060000
	P_{4C_5}	12,0000000000	0,00247950630	28,0439160000
C_6	P_{1C_6}	11,7000000000	0,00000000000	28,0000000000
	P_{2C_6}	11,7837510000	0,00080962614	27,9912980000
	P_{3C_6}	11,8688350000	0,00169292360	28,0498740000
	P_{4C_6}	11,9525720000	0,00261924750	28,0429550000
	P_{5C_6}	12,0000000000	0,00317363900	28,0789390000
C_7	P_{1C_7}	11,6400000000	0,00000000000	28,0000000000
	P_{2C_7}	11,7237510000	0,00080986570	27,9913410000
	P_{3C_7}	11,8088350000	0,00169339260	28,0499570000
	P_{4C_7}	11,8925710000	0,00261993040	28,0430560000
	P_{5C_7}	11,9774830000	0,03612677800	28,1074930000
	P_{6C_7}	12,0000000000	0,03888570200	28,1050790000

Na Tab. 2 tem-se a evolução da velocidade média V em função do trecho da estrada x e do tempo t para as sete primeiras curvas características positivas com $n = 200$.

Observa-se, em cada das sete curvas características positivas apresentadas, que a velocidade média é uma função decrescente em relação a variação do tempo e do trecho da estrada, atingindo para estas, o seu valor mínimo de aproximadamente $64,42$ km/h após $0,038$h do início da análise do tráfego.

Os resultados apresentados nas tabelas (1) e (2) ilustram uma pequena amostra dos 266.112 pontos calculados, considerando-se $n = 200$, para simular uma hora do movimento.

6. Conclusões

Neste trabalho apresentam-se resultados obtidos da simulação do fluxo de tráfego para condições de contorno periódicas tanto para a densidade veicular, ρ, como para a velocidade média V, como exemplo, uma pista circular. Os cálculos numéricos foram realizados usando-se o denominado esquema das distâncias especificadas do método das características. Por meio deste esquema são determinados os resultados das variáveis dependentes, V e ρ, para as curvas características positivas que emanam em pontos fixados no eixo x. Como o fluxo de tráfego é maior do que a velocidade das ondas sonoras (fluxo super-crítico), as curvas características positivas e negativas têm inclinações positivas, que se propagam na pista simulada, a primeira característica examinada emana do ponto $x = L_t$, a segunda de $x = L_t - \Delta x$, e assim sucessivamente.

Em geral o esquema do método das características das distâncias especificadas, quando comparado com o esquema da malha retangular, utiliza menor tempo de processamento embora ocupe maior espaço de memória do computador. Com os resultados obtidos pelo esquema adotado neste trabalho, ou seja, obtenção da densidade veicular e velocidade média nos pontos $(P_{1C_1}, P_{1C_2}, P_{2C_2}, \ldots)$ da malha discretizada, facilmente consegue-se determinar os resultados para uma malha retangular através de interpolação.

A equação reduzida de Paveri-Fontana foi resolvida através do método das características das distâncias especificadas para o caso particular, no qual o tráfego é homogêneo e estacionário, sendo a velocidade média desejada diretamente proporcional a velocidade atual.

Observa-se que a densidade veicular permanece praticamente constante e que a velocidade média é uma função decrescente para as sete primeiras curvas características positivas. Estes comportamentos se extendem ao longo de todas as

Tabela 2: Valores de x, t e $V(x,t)$ para sete primeiras curvas características positivas.

Curva Característica	Pontos	x (km)	t (h)	$V(x,t)$ (km/h)
C_1	P_{1C_1}	12,0000000000	0,00000000000	84.0000000000
C_2	P_{1C_2}	11,9400000000	0,00000000000	83.9736150000
	P_{2C_2}	12,0000000000	0,00057933167	79.6660920000
C_3	P_{1C_3}	11,8800000000	0,00000000000	83.9472560000
	P_{2C_3}	11,9637510000	0,00080890147	77.9387100000
	P_{3C_3}	12,0000000000	0,00118491460	75.7474480000
C_4	P_{1C_4}	11,8200000000	0,00000000000	83.9209490000
	P_{2C_4}	11,9037510000	0,00080914379	77.9164920000
	P_{3C_4}	11,9888370000	0,00169197860	72.7768340000
	P_{4C_4}	12,0000000000	0,00181541310	72.2241640000
C_5	P_{1C_5}	11,7600000000	0,00000000000	83.8947200000
	P_{2C_5}	11,8437510000	0,00080938542	77.8943370000
	P_{3C_5}	11,9288360000	0,00169245210	72.7584790000
	P_{4C_5}	12,0000000000	0,00247950630	69.2381310000
C_6	P_{1C_6}	11,7000000000	0,00000000000	83.8685950000
	P_{2C_6}	11,7837510000	0,00080962614	77.8722670000
	P_{3C_6}	11,8688350000	0,00169292360	72.7401920000
	P_{4C_6}	11,9525720000	0,00261924750	68.6011810000
	P_{5C_6}	12,0000000000	0,00317363900	66.6796080000
C_7	P_{1C_7}	11,6400000000	0,00000000000	83.8426000000
	P_{2C_7}	11,7237510000	0,00080986570	77.8503040000
	P_{3C_7}	11,8088350000	0,00169339260	72.7219920000
	P_{4C_7}	11,8925710000	0,00261993040	68.5862640000
	P_{5C_7}	11,9774830000	0,03612677800	65,1488970000
	P_{6C_7}	12,0000000000	0,03888570200	64,4258810000

outras curvas características positivas que compõe a malha discretizada.

O esquema do método das características utilizado mostrou-se adequado para solucionar o sistema de equações quase-lineares (12) e (13) que governam o fluxo de tráfego simulado. Em geral o esquema do método das características das distâncias especificadas não apresenta grandes dificuldades para ser implementado computacionalmente quando usado para solucinar problemas de fluxo unidimensional, como o caso do problema investigado.

7. Agradecimentos

Os autores agradecem ao Dr. Wilson Marques Junior por suas discussões sobre este artigo. Os autores também agradecem à Fundação Araucária pelo suporte a essa pesquisa.

8. Referências

Chapman, S. and Cowling, T., 1970, "The Mathematical Theory of Non-Uniform Gases", Cambridge University Press, Cambridge, 428 p.

Fernandes, A. S., 1996, "Teoria Cinética dos Gases Poliatômicos", PhD thesis, Universidade de São Paulo, Brasil.

Helbing, D., 1996, Gas-Kinetc derivation of Navier-Stokes-like traffic equations, "Physical Review", Vol. 53, No. 4, pp. 1067–1141.

Helbing, D., 2001, Traffic and Related Self-Driven Many-Particle, "Rev. of Mod. Phys.", Vol. 73, No. 4, pp. 1067–1141.

Prigogine, I. and Herman, R., 1971, "Kinetic Theory of Vehicular Traffic", American Elsevier, New York.

Sivaloganathan, K., 1974, Free Surface Flow Computations by Characteristics, "Journal Of The Hydraulics Division", Vol. 4, No. 13707, pp. 543–556.

Sivaloganathan, K., 1978, Flood Routing By Characteristic Methods, "Journal Of The Hydr. Div.", Vol. 7, No. 5, pp. 1076–1091.

Streeter, V. L., 1997, "Mecânica dos Fluidos", McGraw-Hill do Brasil, Brasil.

Velasco, R. M. and Marques, W., 2005, Navier-Stokes Equations for Traffic Flow, "Phys. Rev.", Vol. 4, No. 72, pp. 046102(1–9).

TRAFFIC FLOW THEORY FOR A MACROSCOPIC SYSTEM

Adriana Luiza do Prado
Departamento de Matemática, Universidade Federal do Paraná, Caixa Postal 019081, CEP81531-990,Curitiba, Paraná
alprado@mat.ufpr.br

Eloy Kaviski
Departamento de Hidraúlica e Saneamento, Universidade Federal do Paraná eloy.dhs@ufpr.br

Liliana M Gramani Cumin Departamento de Matemática, Universidade Federal do Paraná, Caixa Postal 019081, CEP81531-990,Curitiba, Paraná gramani@mat.ufpr.br

Abstract. *The theory of traffic flow search to describe in a mathematic way interactions between vehicles and the infrastructure. The infrastructure consists of the systems of roads and in all its operational elements, including devices of control, semafaros and signals. These indispensable theories are in all the models of traffic and tools for analyses of operations in the streets and roads. With the significant increase of the use of automobiles and expansion of the system of road, a study of characteristics of the traffic appeared, through microscopic and macroscopisc models. The macroscopic models of the traffic flow, discard the microscopic sight of the traffic in terms of individual speeds of vehicles or the individual components of system(such as the linkings or the crossings), adopting a macroscopic sight of the traffic in a net. The considered variables are intensity of the traffic, density of the road and the average speed. The objetive of this work is to decide the macroscopic equations of the traffic flow for specific models of the speed desired through the characterist method. The new model is compared with currently known models for traffic flow networks under several situations. Finally, the model is used for network simulation.*

Keywords *. Traffic Flow Theory, Macroscopic model, Paveri-Fontana Equation, Characteristic Method*

Proceedings of the 11th Brazilian Congress of Thermal Sciences and Engineering -- ENCIT 2006
Braz. Soc. of Mechanical Sciences and Engineering -- ABCM, Curitiba, Brazil, Dec. 5-8, 2006

Paper CIT06-0795

ANÁLISE DE TRANSIENTES EM LINHAS PARA ALTO-FORNO

Angela Ourivio Nieckele
Departamento de Engenharia Mecânica – Pontifícia Universidade Católica de Rio de Janeiro
R. Marques de São Vicente 225 – Gávea, Rio de Janeiro, RJ, Brasil
nieckele@mec.puc-rio.br

Luis Fernando Gonçalves Pires
Núcleo de Simulação Termohidráulica de Dutos – Dept. de Eng. Mecânica – Pontifícia Universidade Católica de Rio de Janeiro
R. Marques de São Vicente 225 – Gávea, Rio de Janeiro, RJ, Brasil
lpires@mec.puc-rio.br

Arturo Jesús Ortega
Núcleo de Simulação Termohidráulica de Dutos – Dept. de Eng. Mecânica – Pontifícia Universidade Católica de Rio de Janeiro
R. Marques de São Vicente 225 – Gávea, Rio de Janeiro, RJ, Brasil
arturo@mec.puc-rio.br

Sergio Luis Mosckem
Especialista de Engenharia Mecânica, Divisão de Engenharia Mecânica – IUN, Arcelor , Brasil - CST
sergio.mosckem@arcelor.com.br

Resumo. Processos de sopro em linhas para alto-fornos são caracterizados por escoamento de ar, com altas vazões e temperaturas, em dutos de grandes diâmetros e comprimento relativamente pequeno. O fechamento indevido de válvulas ao longo da tubulação, bloqueando o escoamento, pode trazer conseqüências indesejadas, como o surgimento da situação de "surge", colocando em risco os componentes do sistema de alto-forno. O objetivo do presente trabalho consiste em analisar numericamente o escoamento com transferência de calor, num processo de sopro para um alto-forno numa indústria siderúrgica. Os campos de velocidade, pressão e temperatura são obtidos através da solução das equações de conservação de massa, quantidade de movimento linear e energia, utilizando o método das diferenças finitas. Considera-se a presença dos diversos componentes típicos num sistema de alto-forno, como compressores axiais, sistemas anti-surge, válvulas de bloqueio e regeneradores. São avaliados os efeitos sobre o turbo-soprador e o desempenho dos sistemas de proteção, decorrentes de transientes nas operações provocadas pelo fechamento de válvulas no duto, da manobra de troca de alimentação dos regeneradores e da queda do alto-forno.

Palavras chave: Sopro alto-forno, análise transiente, sistema "anti-surge", golpe de aríete.

1. Introdução

Na indústria siderúrgica, o alto forno é alimentado com ar, através de turbo-sopradores. Tipicamente as vazões são altas e as tubulações apresentam grande diâmetro, porém possuem comprimento relativamente pequeno. Ao longo da linha, diversas válvulas podem ser encontradas, como válvulas de bloqueio e válvulas de alívio (ABIME, 1987). Uma operação indevida das válvulas pode causar picos de pressão no interior do duto, danificando equipamentos e interrompendo a operação do alto forno, podendo levar a grandes prejuízos.

Vários aspectos envolvendo problemas com fechamento de válvulas vêm sendo estudados por muitos pesquisadores (Sharp, 1974, Azoury et al , 1986, Liou, 1991). Muitos desses assumiram escoamentos sem atrito, porém Sharp (1974) discutiu o efeito do escoamento com atrito na máxima pressão atingida, ressaltando a importância da correta determinação do mesmo. Recentemente, uma série de trabalhos foi desenvolvida visando avaliar correlações não permanente para a avaliação do fator de atrito durante operações transientes (Bouazza, 2004 e Vitkovsky et al, 2004).

Uma pesquisa na literatura mostra alguns trabalhos relacionados com operação de alto forno. A análise de sistema de operação de altos fornos devido à injeção de gás foi realizada por Burgler et al. (2004), enquanto que Valle (1999) investigou o uso de compressores axiais como sopradores para o alto forno. O problema de *surge* no compressor na linha de alimentação de altos fornos foi estudado por Strut e Suter (1965). Recentemente, Ziebik e Stanek (2006) avaliaram a influência nos parâmetros térmicos na perda de calor na operação de altos fornos.

A motivação do presente trabalho consiste em evitar pressões altas no interior da tubulação de maneira de evitar a situação de *surge* no turbo-soprador, durante as operações habituais numa linha para alto-forno. Portanto, o objetivo do presente trabalho consiste em analisar numericamente o escoamento de ar uma linha de sopro para alto-forno, simulando condições de operações que podem ocorrer numa indústria siderúrgica. São analisadas condições de escoamento decorrentes de operações indevidas dos componentes, visando avaliar o sistema de proteção dos turbo-sopradores. A presença de elevados picos de pressão se torna um problema maior em tubulações de pequeno comprimento, pois a distância percorrida pela onda de pressão é menor, não dando tempo para a mesma se dissipar.

O algoritmo computacional foi desenvolvido utilizando o método das diferenças finitas (Anderson et al., 1984, Press, 1992) o qual resolve as equações de conservação de massa, quantidade de movimento linear e energia, incorporando a capacidade de simulação de escoamento de ar num duto alimentado por um turbo-soprador. Além do modelo para este componente, foram também desenvolvidos modelos para o sistema *anti-surge*, válvulas e demais equipamentos presentes no sistema do alto-forno.

2. Modelo do sistema de sopro simulado

Num sistema de sopro os turbo-sopradores alimentam os dutos que levam o ar ao alto forno. Ao longo das linhas tanto válvulas de bloqueio como válvulas de alívio podem ser encontradas. Um sistema típico de sopro de um alto forno encontra-se representado isometricamente na Fig. (1).

Na linha de sucção do turbo-soprador (*blast blower*) existe um sistema de filtragem para eliminação de particulado. A descarga do turbo-soprador está conectada a um duto de 1,4m de diâmetro onde estão localizadas duas válvulas *anti-surge*. Após a derivação para as válvulas *anti-surge*, estão localizadas duas válvulas, uma de bloqueio e outra de retenção. Uma expansão, localizada cerca de 24m após o turbo-soprador, transforma o diâmetro do duto para 1,6m. Cinqüenta e um metros após a expansão está localizada uma válvula de bloqueio de manobra de linhas, que isola a linha de sopro atual de outra linha. Uma nova expansão para 1,7m está localizada após esta válvula. O duto prossegue até os regeneradores, distante cerca de 650m. Neste ponto existe uma outra válvula de bloqueio e logo após a derivação para os quatro regeneradores. Na entrada de cada regenerador está instalada uma válvula de bloqueio para isolar o regenerador específico. Após os regeneradores, o duto segue para o alto-forno.

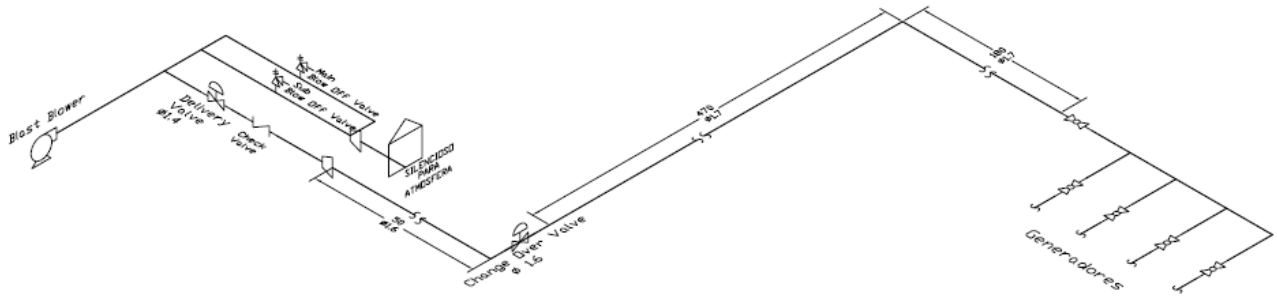

Figura 1. Isométrico da linha de sopro 1.

2.1. Turbo-soprador

As curvas características do turbo-soprador podem ser representadas por um diagrama das curvas características típicas de um compressor axial, sendo a vazão controlada pelo ângulo das palhetas do estator. Num compressor axial observa-se que as linhas, representando um determinado ângulo de palheta, são quase verticais o que caracteriza uma vazão praticamente constante para uma grande faixa de pressão. Pontos de controle de *surge* são definidos através de pontos de ajuste de alarme, proteção (abertura da válvula *sub blow off*) e crítico (abertura da válvula *main blow off*).

2.2. Válvulas *anti-surge*

As válvulas *anti-surge*, também chamadas de *main blow off* e *sub blow off* , estão localizadas a cerca de 20m da descarga do turbo-soprador. A válvula *sub blow off* tem um diâmetro de 730mm e a válvula *main blow off* tem um diâmetro de 1,050m.

A válvula *sub blow off* e a válvula *main blow off* podem ter sua atuação comandada manualmente ou através de uma malha de controle, ajustada para valores de pressão obtidos na descarga do turbo-soprador. O tempo de abertura total destas válvulas é ajustado e pode variar de 6 a 30s.

Utilizando a modelagem matemática de válvulas indicada nas normas ISA S75.01-S75.02 para fluidos compressíveis, pode-se determinar a vazão através das válvulas de acordo com:

$$Q = N\, F_p C_v\, P_u\, Y \left[\left(\frac{x}{SG\, T_u\, Z_u} \right) \right]^{0,5} \tag{1}$$

onde Q é a vazão volumétrica nas condições padrões (m^3/s); N é uma onstante numérica ($8,8 \times 10^{-10}$); F_p é o fator que considera as mudanças geométricas dos dutos conectados na válvula (1); C_v ‘o coeficiente da válvula [$(m^3/s)/Pa^{0,5}$]; P_u é a pressão absoluta a montante da válvula (kPa); T_u é a temperatura absoluta a montante da válvula (K); Z_u é o fator de

compressibilidade a montante da válvula, *SG* é a gravidade específica do gás; *x* é a taxa relativa de queda de pressão, e *Y* é o fator de expansão.

A taxa relativa de queda de pressão e o fator de expansão são fornecidos pelas Eqs. (2) e (3).

$$x = \frac{P_u - P_d}{P_u} \quad ; \quad Y = 1 - \frac{x}{3 F_K x_T} \tag{2}$$

onde x_T é o máximo valor de *x*, dependente da característica física da válvula selecionada, F_k é a relação de expoentes isentrópicos do gás com respeito ao ar $F_k = k/1{,}4$; onde $k = cp/cv$ é a razão entre o calor específico a pressão constante *cp* e a volume constante *cv*.

As relações anteriores são usadas quando *x* não excede a $F_k x_T$, caso contrário o valor de $F_k x_T$ é usado no lugar de *x* e *Y* fica igual a 0,667. Os valores de C_v utilizados para as válvulas *main* e *sub blow off* são de 8,86 $\times 10^{-3}$ $(m^3/s)/Pa^{0,5}$ e de 2,01 $\times 10^{-3}$ $(m^3/s)/Pa^{0,5}$ respectivamente.

2.3. Válvulas de bloqueio intermediárias

Ao longo do duto existem três válvulas com capacidade para bloquear totalmente a linha. A válvula próxima à descarga do turbo-soprador (*delivery valve*) é uma válvula tipo gaveta, com tempo de fechamento em torno de 120 e 50 s. Visando permitir a manobra das linhas de sopro para substituição dos turbo-sopradores, encontra-se uma válvula do tipo guilhotina (*change over valve*), de passagem plena, com o mesmo tempo de atuação. A terceira válvula encontra-se próxima aos regeneradores, sendo do tipo gaveta. Na entrada de cada um dos quatro regeneradores existe uma válvula, com um tempo de atuação entre 15 a 20 s. Elas possuem inter-travamento duplo/redundante de forma a evitar o fechamento simultâneo das quatro válvulas. Os diâmetros destas válvulas e os C_V utilizados estão apresentados na Tab. (1).

Tabela 1 – Características das válvulas de bloqueio intermediárias

Válvula	D_N **(m)**	C_V **$(m^3/s)/Pa^{0,5}$**
Válvula próxima à descarga do turbo-soprador (*delivery valve*)	1,5	0,106
Válvula de manobra de linhas (*change over valve*)	1,6	0,106
Válvula próxima dos regeneradores	1,7	0,106
Válvula de manobra dos regeneradores	1,5	0,106

3. Resultados

Tendo em vista que o objetivo do trabalho é avaliar situações de operação normal ou acidental que possam comprometer a operação do turbo-soprador, foi imposta uma vazão típica de operação na entrada da linha, correspondente a Q = 103,3 Nm^3/s = 372000 Nm^3/hr e os seguintes eventos foram selecionados para serem investigados:

i) Fechamento indevido de válvulas de bloqueio no duto.
ii) Manobra de troca de regeneradores.
iii) Troca dos sopradores em operação.

Uma vez ajustados os parâmetros dos diversos equipamentos da linha de alimentação do alto forno com dados de campos, diferentes cenários de operação que poderiam comprometer os sopradores foram investigados. Inicialmente considerou-se o fechamento das válvulas de bloqueio, tanto de manobra de linhas quanto de chegada aos regenerados. Nestes casos, investigou-se o comportamento do escoamento sem e com a utilização das válvulas *anti-surge*. A influência no escoamento do tempo de abertura das válvulas *anti-surge* também foi investigada.

A seguir, analisou-se a influência no escoamento da operação indevida de válvulas na de troca de regeneradores e finalmente a influência da troca dos sopradores em operação levando a atuação simultânea dos dois sopradores.

3.1. Fechamento das válvulas de bloqueio intermediária sem sistema *anti-surge*

O primeiro teste realizado consistiu em investigar o efeito no campo de velocidade e pressão do fechamento da válvula de bloqueio de manobra de linhas (*change over valve*), sem utilizar o sistema *anti-surge*.

O transiente foi obtido ao fechar a válvula de bloqueio de manobra de linhas usando um tempo de fechamento de 120s. As variações da pressão e da vazão com o tempo na válvula de bloqueio encontram-se ilustradas na Fig. (2). O fechamento se inicia no instante 360s e no momento do fechamento total da válvula de bloqueio (480s) a pressão atinge o valor de 931,6 kPag (9,50 kgf/cm²g), já tendo ultrapassado a pressão crítica de 686,5 kPag (7 kgf/cm²g), 2s antes do fechamento total. Com o duto bloqueado, a pressão se eleva praticamente de forma linear, atingindo valores elevados muito rapidamente.

Vale ressaltar que como a queda de pressão ao longo do duto é muito pequena, o comportamento da pressão na válvula de bloqueio é análogo ao comportamento da pressão no compressor. Este resultado ilustra que o comportamento da válvula de bloqueio de manobra de linhas apresenta uma influência grande no escoamento.

A segunda análise realizada consistiu em verificar a influência da válvula de bloqueio próxima os regeneradores, também sem utilizar o sistema *anti-surge*. O transiente foi gerado pelo fechamento desta válvula, utilizando um tempo de 120s.

A variação com o tempo da pressão e vazão, nesta válvula, é apresentada na Fig. (3). Pode-se observar que o fechamento da válvula se inicia no instante igual a 360s. No momento do fechamento total da válvula de bloqueio (480s) a pressão atinge o valor de 476,6 kPag (4,86 kgf/cm²g). Com o duto bloqueado, a pressão se eleva praticamente de forma linear, atingindo o valor de 686,5 kPag (7 kgf/cm²g) (valor de *surge*) no instante 497s, isto é, 17s após o fechamento total da válvula de bloqueio. Pode-se observar que o aumento da pressão nesta válvula, próxima aos regeneradores, foi muito mais lento do que o aumento na válvula de bloqueio de manobra de linha. Novamente, devido à pequena queda de pressão na linha, o comportamento da pressão nos sopradores é análogo.

A partir destas duas análises realizadas, verifica-se que quanto mais próximo do soprador for o bloqueio do duto, mais severo e rápido é o transiente.

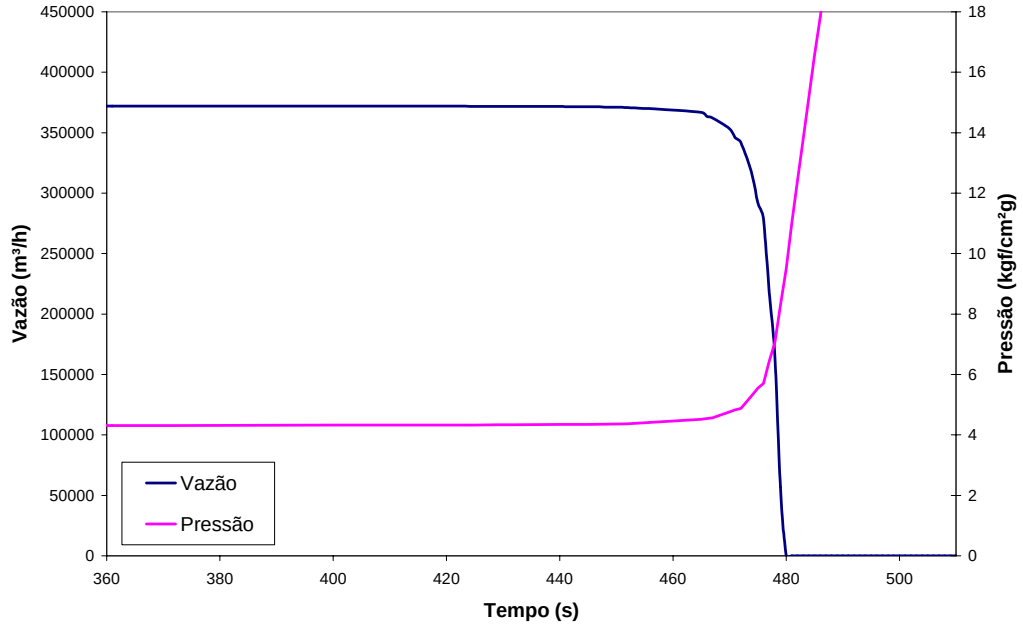

Figura 2. Variação da pressão e vazão na válvula de bloqueio de manobra de linhas.

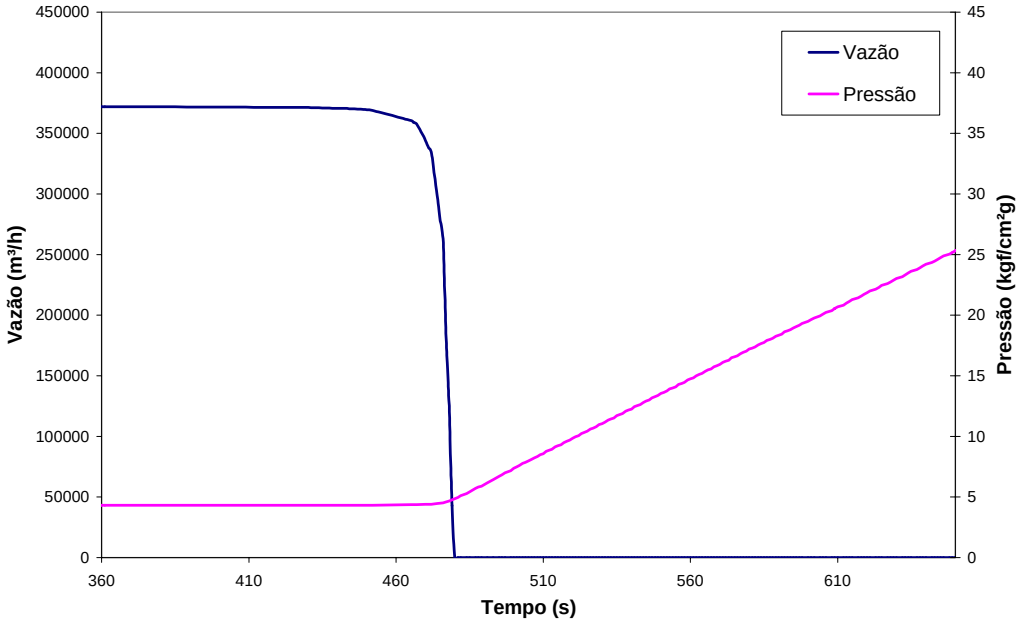

Figura 3. Variação da pressão e vazão na válvula de bloqueio da linha de chegada aos regeneradores.

3.2. Fechamento das válvulas de bloqueio intermediárias com sistema *anti-surge*

Dando continuidade às analises, como no caso anterior, a válvula de bloqueio da linha de chegada aos regeneradores foi fechada no instante de 360s, utilizando um tempo de fechamento de 120s. Neste caso, os parâmetros operacionais utilizados para as válvulas *anti-surge* encontram-se na Tab. (2).

Tabela 2 – Parâmetros operacionais utilizados para as válvulas *anti-surge*

	Tempo de abertura (s)	***Setpoint* (kPag)**
sub blow off	6	520
main blow off	6	559

As variações da pressão e da vazão com o tempo encontram-se ilustradas nas Figs. (4) e (5), para a válvula de bloqueio da linha de chegada aos regeneradores e as válvulas *anti-surge*, respectivamente. Observa-se na Fig. (4), o aumento da pressão na válvula de bloqueio, no instante de fechamento total da válvula. Praticamente no mesmo instante, a válvula *anti-surge sub-blow off* é aberta, pode-se observar o aumento da vazão na mesma na Fig. (5). Porém, como a pressão continua a subir, poucos segundos após a válvula *anti-surge main-blow off* também é aberta. Obteve-se a máxima pressão, na posição das válvulas *anti-surge*, igual a 571,7 kPag (5,83 kgf/cm²g). Devido à aberta das duas válvulas *anti-surge*, a pressão começa a cair, e conseqüentemente também a vazão em cada uma das válvulas *anti-surge*. Note que, como já mencionado, devido à baixa perda de carga na linha o comportamento da pressão nas duas válvulas (de bloqueio e *anti-surge*) é análogo.

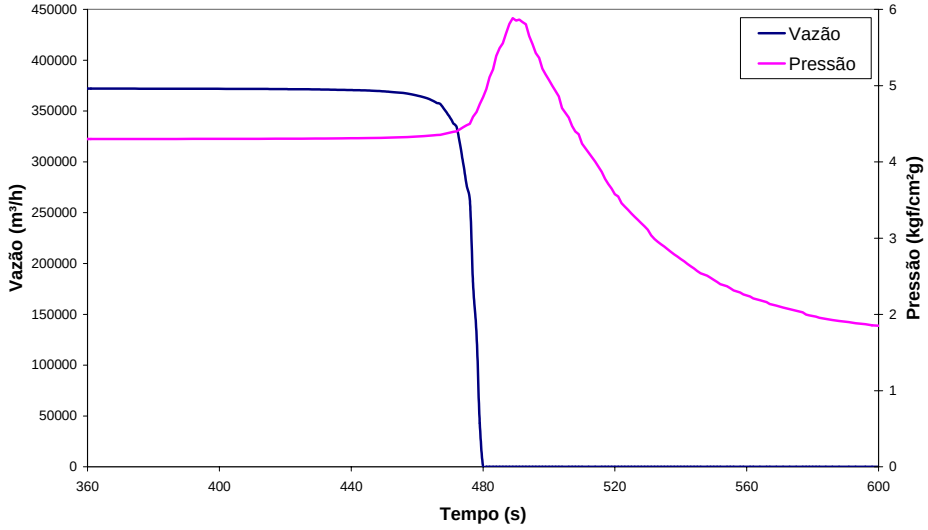

Figura 4. Variação da pressão e vazão na válvula de bloqueio da linha de chegada aos regeneradores.

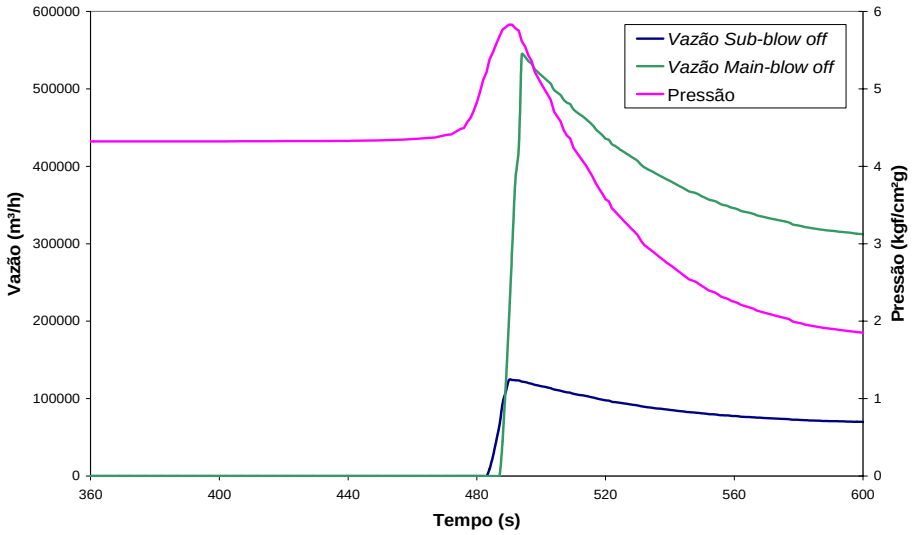

Figura 5. Variação da pressão e vazão nas válvulas *anti-surge*.

Num segundo teste, o comportamento da pressão na válvula de bloqueio de manobra de linhas, utilizando o sistema *anti-surge* é analisado. Novamente, manteve os mesmos parâmetros de operação da válvula de bloqueio (fechamento no instante de 360s, com duração de 120s). Neste caso, os parâmetros operacionais utilizados para as válvulas *anti-surge* são os mesmos do caso anterior os quais se encontram na Tab. (2).

As variações da pressão e da vazão com o tempo na válvula de bloqueio de manobra de linhas encontram-se ilustradas na Fig. (6), enquanto que a Fig. (7) apresenta a pressão e vazão nas válvulas *anti-surge*. Pode-se observar que o comportamento do escoamento é qualitativamente semelhante ao descrito no item anterior. Porém, como a resposta da pressão para a válvula de bloqueio de manobra de linhas é mais rápida, observa-se um aumento acentuado da pressão e uma pequena perturbação no instante de abertura das válvulas *anti-surge*. Nota-se que a abertura consecutiva das duas válvulas *anti-surge* consegue controlar o aumento da pressão, a qual atinge o valor máximo de 574,7 kPag (5,86 kgf/cm²g).

A presente análise mostra que o correto funcionamento do sistema *anti-surge* é fundamental para evitar pressões que possam danificar o soprador.

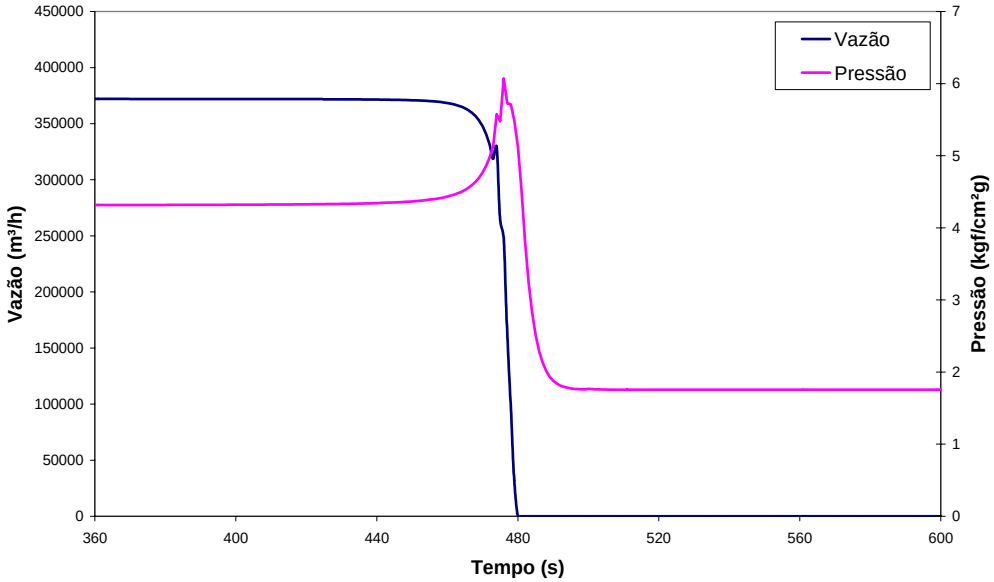

Figura 6. Variação da pressão e vazão na válvula de bloqueio de manobra de linhas.

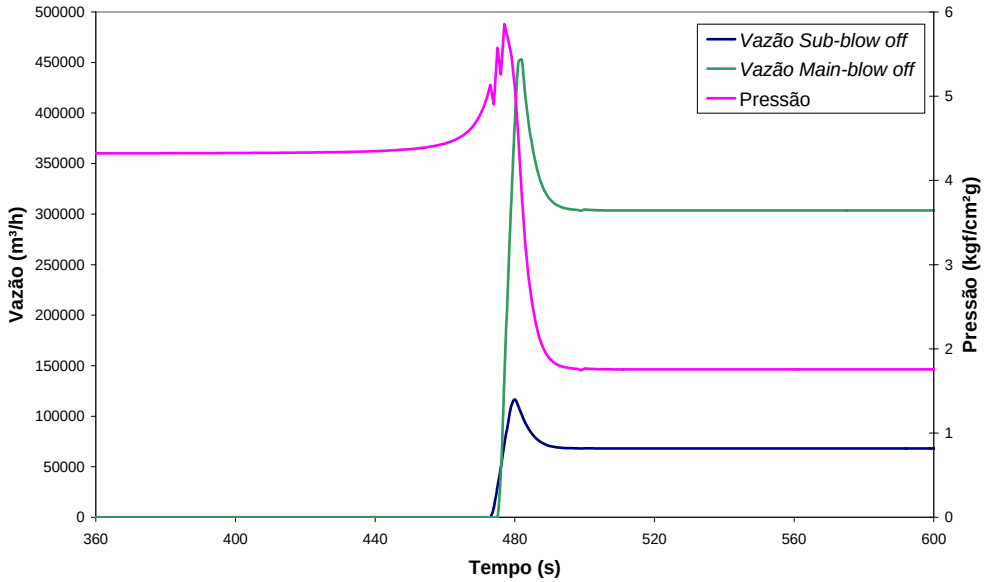

Figura 7. Variação da pressão e vazão nas válvulas *anti-surge*.

3.3. Avaliação do tempo de abertura das válvulas *anti-surge* para o bloqueio do duto

Para avaliar a influência do tempo de abertura das válvulas *anti-surge* na atuação das mesmas na válvula de bloqueio de manobra de linhas e na válvula próxima aos regeneradores, repetiu-se os testes anteriores, utilizando-se

dois tempos diferentes para abertura das válvulas *anti-surge*.

Como nos testes anteriores, duas simulações foram realizadas. Na primeira a válvula de manobra de linhas foi fechada no instante igual a 360s e utilizou-se um tempo de fechamento da mesma igual a 120s, manteve-se a válvula de bloqueio próxima aos regeneradores completamente aberta. Na segunda simulação, inverteu-se a situação, i.e., fechou-se a válvula próxima aos regeneradores mantendo a válvula de manobra de linhas aberta. Nas válvulas *anti-surge* os mesmos *setpoint* de pressão que os utilizados nos testes anteriores foram especificados, Tab.(2). Para investigar a influência do tempo de abertura, consideraram-se tempos de abertura de 6s e de 30s.

A distribuição de pressão nas válvulas *blow off* durante o fechamento da válvula de manobra de linhas é ilustrada na Fig. (8) para os dois tempos de abertura da válvula *anti-surge*. Enquanto que a Fig. (9) apresenta os resultados devido ao fechamento da válvula próxima aos regeneradores.

Observa-se que para o bloqueio do duto provocado pelo fechamento da válvula de bloqueio próxima aos regeneradores, mesmo para um tempo de abertura das válvulas de *blow off* igual a 30s, a pressão máxima não ultrapassa o valor crítico de 686,5 kPag. Isto já não se verifica para o caso da válvula de bloqueio de manobra de linhas. Neste caso a abertura das válvulas de *blow off* num tempo de 30s provoca uma elevação de pressão superior à pressão critica, chegando a 1118 kPag (11,4 kgf/cm²g). Este valor de pressão poderia levar o compressor para uma situação de *surge*.

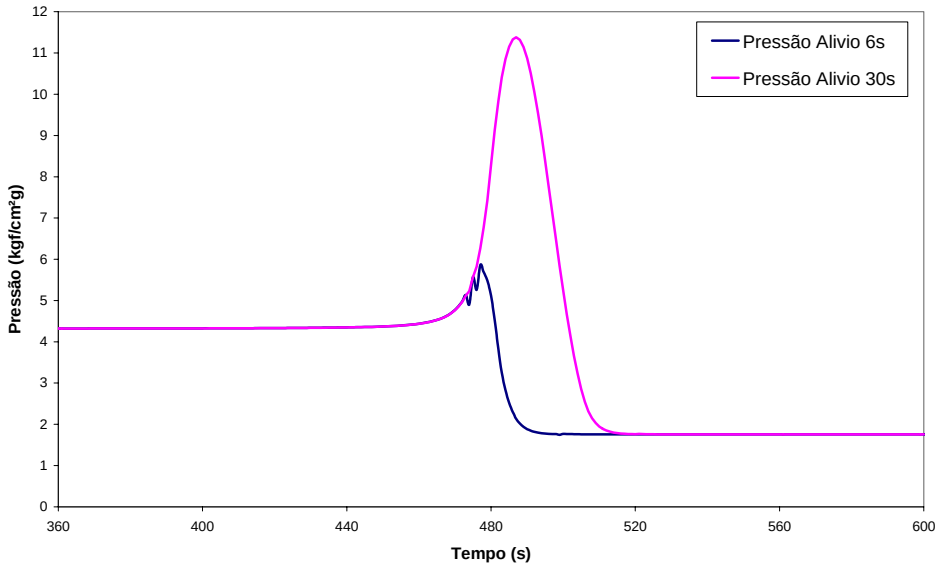

Figura 8. Comparação entre as variações de pressão para atuação das válvulas *anti-surge* com 6s e 30s, fechamento da válvula de bloqueio de manobra de linhas.

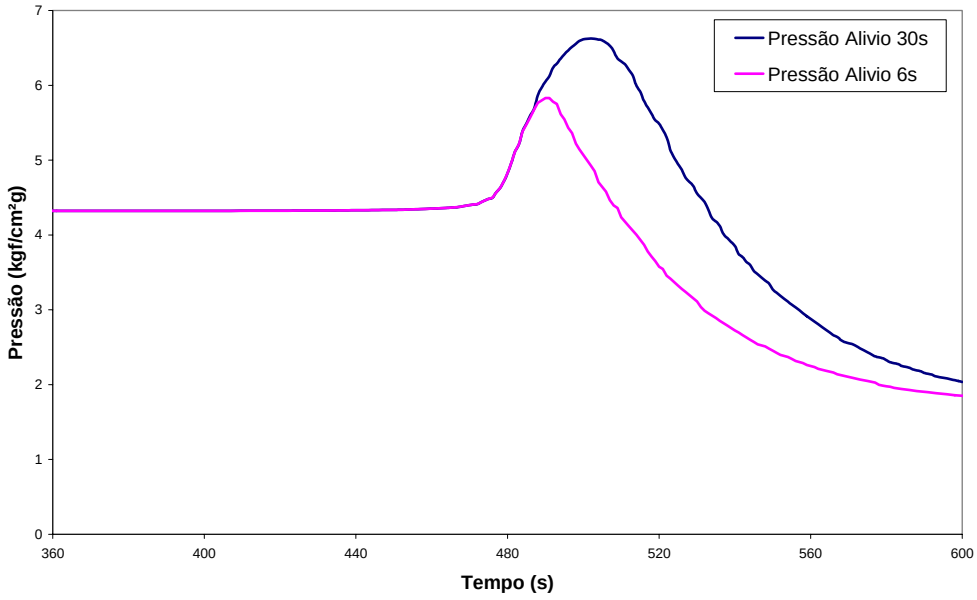

Figura 9. Comparação entre as variações de pressão para atuação das válvulas *anti-surge* com 6s e 30s, fechamento da válvula de bloqueio próxima aos regeneradores.

3.4. Operação indevida das válvulas durante a troca dos regeneradores

O processo de troca dos regeneradores é caracterizado pela elevação momentânea da vazão de sopro enquanto a válvula de um regenerador é fechada, e a válvula do regenerador que estava aquecendo é aberta. Desta forma, uma operação equivocada destas válvulas poderia levar ao fechamento do regenerador que sairia de linha, sem a abertura do outro. Este fato produziria uma restrição para o escoamento, mas não o completo bloqueio do duto. Este evento foi simulado considerando que a elevação da vazão de 103,3 Nm³/s (372000 Nm³/h) para 120 Nm³/s (432000 Nm³/h) ocorre em 60s, e logo após a válvula de um regenerador é fechada em 20s, fazendo com que o escoamento ocorra somente por dois regeneradores.

A Figura (10) apresenta a variação da pressão na descarga do turbo-soprador, durante a troca dos regeneradores como descrito acima. Observa-se que a queda de pressão no regenerador para a vazão mais elevada, quando somente dois regeneradores encontram-se abertos, é de 25,5 kPag (0.26 kgf/cm²g), cerca do triplo da existente em condição normal. Porém, a pressão no soprador atinge um valor máximo de 530,5 kPag (5,41 kgf/cm²g), não comprometendo o equipamento, mesmo sem a atuação do sistema *anti-surge*.

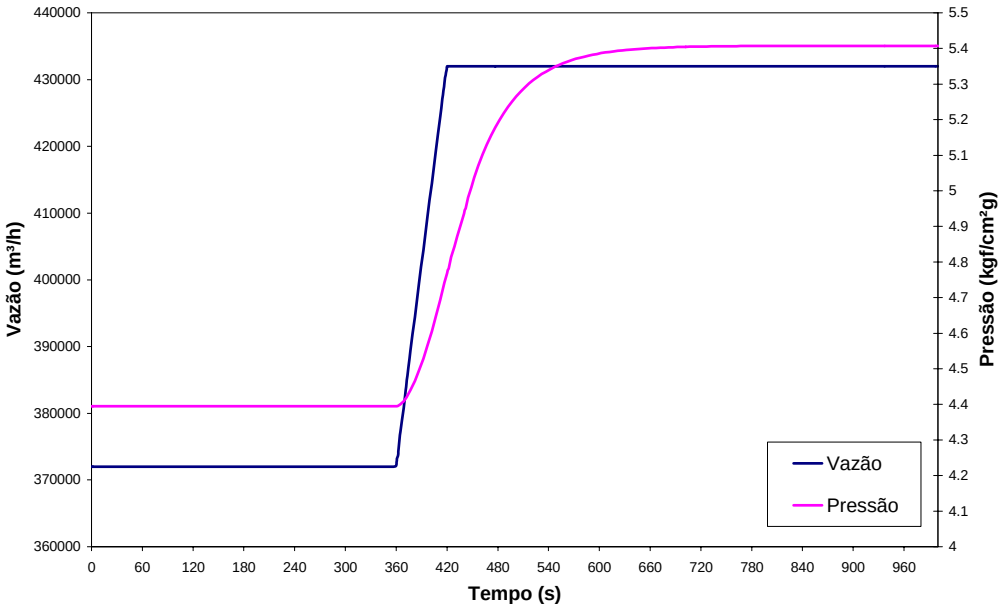

Figura 10. Variação da pressão e vazão na descarga do turbo-soprador durante a troca indevida dos regeneradores.

3.5. Atuação simultânea dos dois sopradores

A troca dos sopradores sem interrupção do processo pode caracterizar uma situação na qual a manobra indevida das válvulas pode colocar os sopradores em situação de *surge*. O caso analisado parte da situação da linha de sopro sendo alimentada por um soprador 1 e com outro soprador 2 descarregando para a atmosfera através de suas válvulas de *blow off*. Nesta condição, o retorno do sopro da linha pelas válvulas de *blow off* do soprador 2 é impedido pela válvula de retenção na descarga do soprador 2.

O transiente é gerado pelo comando manual de fechamento das válvulas de *blow off* do soprador 2 provocando uma rápida elevação de pressão no pequeno trecho de duto entre o soprador 2 e sua válvula de retenção. Quando a pressão atinge o valor existente do outro lado desta válvula, esta se abre permitindo o escoamento do ar para a linha principal. Dois cenários foram investigados. No primeiro não se considerou a atuação das válvulas *anti-surge* do soprador 1, as quais foram acionadas no segundo cenário.

A Figura (11) ilustra a variação da vazão e pressão na válvula de *blow off* do soprador 2, juntamente com a vazão nos regeneradores, correspondente a operação descrita acima, sem acionar as válvulas *anti-surge* de proteção dos equipamentos.

Pode-se observar que a medida que a válvula de *blow off* são fechadas, a pressão começa a subir. Após o fechamento completo da válvula de *blow off*, devido ao aumento da pressão na válvula de retenção, esta é aberta e a vazão em ambos sopradores passa a ser adicionada à linha, levando a um aumento da vazão nos regeneradores. Devido as grandes dimensões do duto, a elevação de pressão torna-se mais suave e a vazão na entrada dos regeneradores acompanha esta elevação, até atingir um valor constante igual ao valor da soma da descarga dos dois sopradores. Observa-se que devido à ausência da atuação das válvulas *anti-surge* o valor crítico de pressão é ultrapassado.

A seguir, o mesmo teste foi realizado, porém com a atuação das válvulas *anti-surge* do soprador 1. A variação temporal da pressão e vazão nas válvulas de *blow off* dos dois sopradores encontra-se ilustrada na Fig. (12).

Observa-se que a partir de 15s (início do fechamento das válvulas de *blow off* do soprador 2) a pressão se eleva gradativamente, como descrito no teste anterior. Quando a pressão atinge 520 kPag (5,3 kgf/cm²g) a válvula *sub blow off* do soprador 1 abre. A pressão continua se elevando, porém com uma taxa de crescimento bem menor. Quando a pressão atinge a 559 kPag (5,7 kgf/cm²g), a válvula *main blow off* do soprador 1 abre. Após este instante, a pressão do soprador 1 cai bruscamente e a pressão do soprador 2 começa gradativamente a descer, não atingindo valores que provoquem problemas para os sopradores.

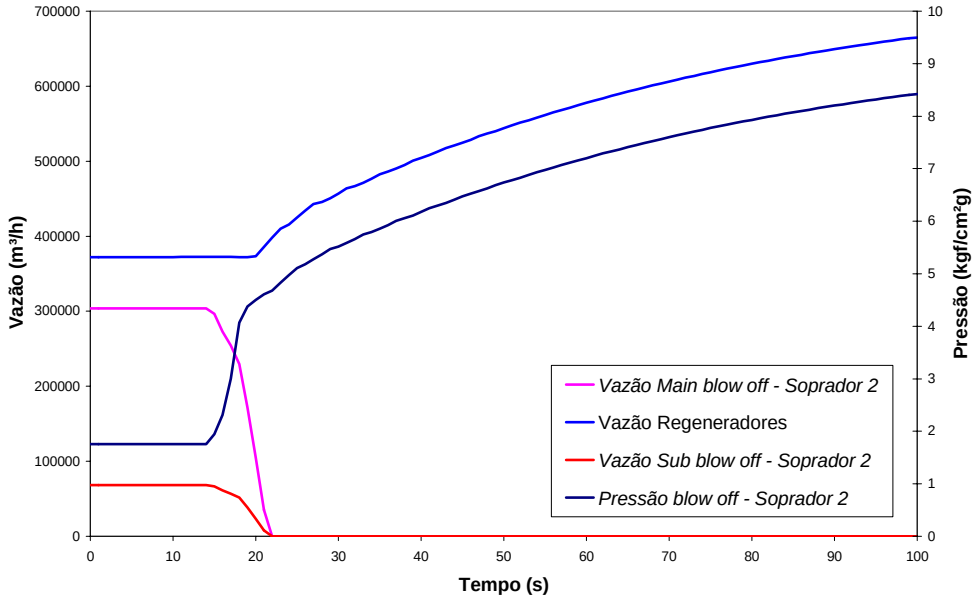

Figura 11. Variação da pressão e vazão nas válvulas *anti-surge* do soprador 2 e da vazão na entrada dos regeneradores.

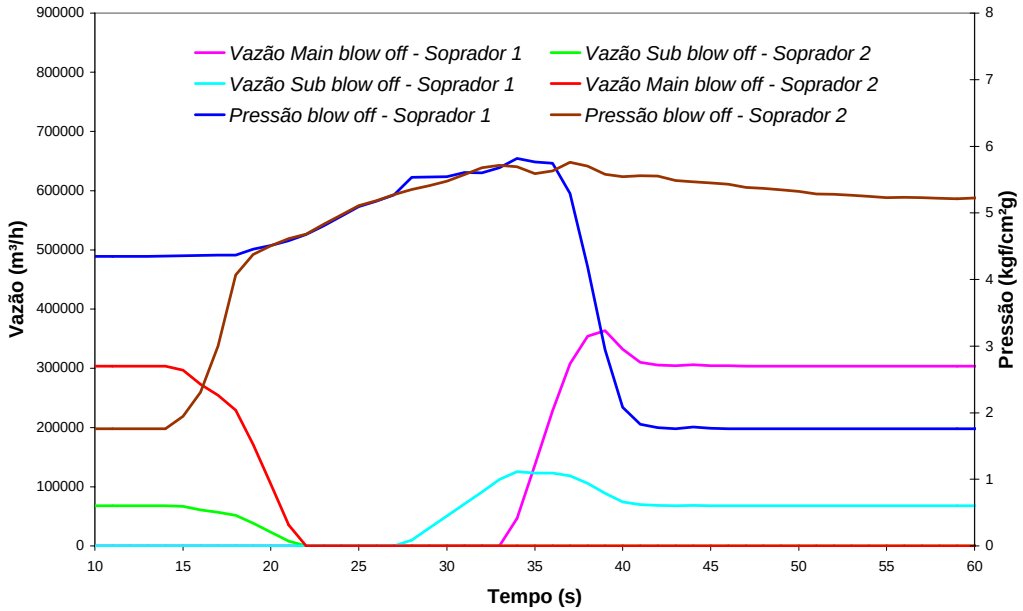

Figura 12. Variação da pressão e vazão nas válvulas *anti-surge* dos sopradores 1 e 2.

4. Conclusões

O fechamento indevido da válvula de bloqueio de manobra de linhas gera um transiente muito mais severo que o ocasionado pelo fechamento da válvula de bloqueio próximo aos regeneradores.

A operação de troca dos regeneradores, mesmo com a operação indevida das válvulas de forma a manter somente dois regeneradores abertos, não leva ao soprador para uma condição de risco.

A operação imprópria da troca dos sopradores sem interromper o processo provoca elevações de pressão que podem ser controladas com a atuação das válvulas *anti-surge* de um dos sopradores. Recomenda-se que as válvulas do sistema *anti-surge* tenham um tempo de abertura o menor possível, visando a segurança dos sopradores.

Nas análises apresentadas, considerou-se que as válvulas do sistema *anti-surge* iniciavam a abertura no mesmo instante no qual a pressão atingia os valores de *setpoint*. Eventuais retardos provocados pela mecânica de atuação das válvulas e pelo tempo morto da instrumentação não foram considerados. Recomenda-se que o sistema tenha manutenções e ajustes periódicos de forma a manter estes tempos o mais baixo possível.

O tempo de abertura das válvulas *anti-surge* influencia nos resultados de máxima pressão para os transientes avaliados. No caso do bloqueio do duto pela válvula de manobra de linha, o tempo de abertura de 30s leva ao soprador para uma condição que ultrapassa a linha de *surge*. De todos os transientes avaliados esta configuração se mostrou como a única na qual o soprador seria colocado nesta situação.

5. Agradecimentos

Os autores desejam agradecer à Companhia Siderúrgica de Tubarão CST-Arcelor Brasil pela colaboração para a execução deste trabalho.

6. Referências

Anderson, D. A., Tannehil, J.C., Pletcher, R.H., 1984, "Computational Fluid Mechanics and Heat Transfer", McGrawHill.

ABIME, Associação Brasileira Da Indústria De Máquinas E Equipamentos, 1987, Válvulas Industriais Brasileiras.

Bouazza, Z., 2004, "A new friction model for transient pipe flows", 9th International Conference on Pressure Surges, Vol. II, pp. 391-404

ISA S75.01, 1989, "Flow Equations for Sizing Control Valves, standards and recommended practices for instrumentation and control", 10th ed., Vol. 2.

ISA S75.02, 1989, "Control Valve Capacity Test Procedure, standards and recommended practices for instrumentation and control", 10th ed., Vol. 2.

Hutchison, J. W,.1976, "ISA Handbook of Control Valves", Instrument Society of America, 2da.

Liou, C. P., 1991, Maximum Pressure Head Due to Linear Valve Closure, Journal of Fluids Engineering, vol. 113/643.

Press, W.H. et al., 1992. Numerical recipes in Fortran. The art of scientific computing. Cambridge University Press. Second edition.

Sharp, B. B.,1974, Discussion of Water Hammer Charts for Various Types of Valves, Journal of Hydraulic Engineering, ASCE, 100, 323-326.

Streeter, V. L., Wylie, B. E., 1967, "Hydraulic Transients", McGraw-Hill Book Company.

Sturb, R. A., Suter, P., 1965, "Compressor Surge In Gas Turbines And Blast Furnace Compressor Installations", Journal Of Engineering For Power 87 (2): pp. 193.

Valle A, 1999, "Axial compressors as blast furnace blowers" Stahl Und Eisen 119 (6-7): pp. 149.

Vitkovsky, J., Stephens, M., Lambert, M,m Simpson, A., 2004, "Efficiente and accurate calculation of Ziele and Vardy Brown unsteady friction in pipe transients", 9th International Conference on Pressure Surges, Vol. II, pp. 404-420.

Ziebik A, Stanek W , 2006,"Influence of blast-furnace process thermal parameters on energy and exergy characteristics and exergy losses ", International Journal Of Energy RESEARCH 30 (4): 203-219 Mar 25 2006.

7. Direitos autorais

Proceedings of the 11th Brazilian Congress of Thermal Sciences and Engineering -- ENCIT 2006
Braz. Soc. of Mechanical Sciences and Engineering -- ABCM, Curitiba, Brazil, Dec. 5-8, 2006

Paper CIT06-0795

ANALYSIS OF TRANSIENT IN LINES FOR BLAST-FURNACE

Angela Ourivio Nieckele
Departamento de Engenharia Mecânica – Pontifícia Universidade Católica de Rio de Janeiro
R. Marques de São Vicente 225 – Gávea, Rio de Janeiro, RJ, Brasil
nieckele@mec.puc-rio.br

Luis Fernando Gonçalves Pires
Núcleo de Simulação Termohidráulica de Dutos – Dept. de Eng. Mecânica – Pontifícia Universidade Católica de Rio de Janeiro
R. Marques de São Vicente 225 – Gávea, Rio de Janeiro, RJ, Brasil
lpires@mec.puc-rio.br

Arturo Jesús Ortega
Núcleo de Simulação Termohidráulica de Dutos – Dept. de Eng. Mecânica – Pontifícia Universidade Católica de Rio de Janeiro
R. Marques de São Vicente 225 – Gávea, Rio de Janeiro, RJ, Brasil
arturo@mec.puc-rio.br

Sergio Luis Mosckem
Especialista de Engenharia Mecânica, Divisão de Engenharia Mecânica – IUN, Arcelor , Brasil - CST
sergio.mosckem@arcelor.com.br

Abstract. *Blow processes for blast-furnaces lines are characterized by air flowing at high rates and temperatures, in ducts of large diameter and relatively small length. The improper closing of valves along of the line, blocking the flow, can lead to undesired phenomena, such as the appearance of a surge situation, which can damage the components of the blast-furnace system. The objective of the present work consists of analyzing numerically the flow and temperature field of a blow process for a blast-furnace in an iron and steel industry. The velocity, pressure and temperature fields are obtained through the solution of the conservation equations of mass, linear momentum and energy, using the finite difference method. The presence of several typical components in a blast-furnace system, such as axial compressors, anti-surge systems, block valves and regenerators, are considered. The effect on the turbo-blower and the performance of the protection systems are evaluated due to the transient operations provoked by the closing of valves in the pipeline, the coupling of different regenerators to the flow line and the interruption of the blast-furnace operation.*

Keywords: Blow blast-furnace, transient analysis, anti-surge systems, water hammer.

Proceedings of the 11th Brazilian Congress of Thermal Sciences and Engineering -- ENCIT 2006
Braz. Soc. of Mechanical Sciences and Engineering -- ABCM, Curitiba, Brazil, - Dec. 5-8, 2006

Paper CIT06-0798

A Numerical Study of the Flow past an Normally Oscillating Circular Cylinder

Danilo Gonçalves Carneiro
University of Brasilia, Brasilia, DF, 70910-900, Brazil
danilocarneiro@gmail.com

Roberto Francisco Bobenrieth Miserda
University of Brasilia, Brasilia, DF, 70910-900, Brazil
rfbm@unb.br

Abstract. *The objective of this work is the numerical simulation of the two-dimensional laminar flow over a circular cylinder with a forced normal oscillation in order to asset the effect of different combinations of the cylinder's maximum linear velocity and angular frequency on the dynamic response of the system in terms of the resultant aerodynamic coefficients. The system of equations is written using a non-inertial frame of reference that is fixed to the oscillating circular cylinder. The effect of this motion is accounted by the introduction of pseudo-force and pseudo-work terms in the right-hand side of the compressible Navier-Stokes equations. These equations are numerically solved using a finite volume discretization, and the fluxes of mass, momentum and total energy are evaluated using the anti-symmetric form of Ducros' fourth-order numerical method. The time marching is achieved using the third-order Runge-Kutta method proposed by Shu. The linear amplitude of vertical motion is defined as sinusoidal in time with an angular frequency tied to the simulated vortex-emission frequency of the static circular cylinder. The system response to different combinations of velocities and frequencies showed different kinds of vortex systems topologies and different behaviors of the unsteady aerodynamic coefficients. These responses were periodic and symmetric, periodic and anti-symmetric, pre-chaotic and even chaotic.*

Keywords: *Numerical Simulation, Circular Cylinder, Normal Oscillation, Laminar Flow, Non-Inertial Frame*

1. Introduction

The main purpose of the present work is the numerical simulation of the laminar flow over a circular cylinder submitted to a forced normal oscillation. Flows over circular cylinders are present in several areas of engineering, as structural design, especially high towers and transmission cables of electrical energy, that are usually submitted to strong winds, offshore structures, thermo-fluids, aerospace sciences, where the landing gear, for example, is commonly submitted to strong winds and aerodynamic forces, among others. These kinds of flows, as they generate vortex-streets, induce unsteady aerodynamic forces over the structure capable of developing oscillation motions that can even destruct the structure by fracture. Being so, a good understanding of the vortex- street topology and the behavior of the unsteady aerodynamics coefficients, is essential.

Previous work, Jared *et al* (1997), showed the behavior of the flow over a static circular cylinder in a considerable range of Reynolds number using numerical simulations that had laminar model and also turbulent models. Blackburn and Henderson (1999), showed in their work an analysis of the laminar flow over an oscillating circular cylinder in cross flow, fixing the Reynolds number to 500 and varying the ratio between the oscillation frequency of the cylinder and the natural vortex-emission frequency. The main objective of their work was to determine how this variation changes the aerodynamic forces utilizing an incompressible formulation and analyzing only the near-wake region.

In order to simulate the normal oscillation of the circular cylinder using a compressible formulation and analyzing the effect of different combinations of the cylinder's maximum linear velocity and angular frequency on the dynamic response of the system in terms of the resultant aerodynamic coefficients, the compressible Navier-Stokes equations are modified in this work using the concept of pseudo-forces and pseudo-work in order to represent the oscillation of the cylinder from a non-inertial frame of reference. They are solved using Ducros' fourth-order skew-symmetric scheme for calculating the fluxes in a finite-volume discretization in conjunction with a third-order Runge-Kutta time-marching method, as proposed by Bobenrieth Miserda and Mendonça (2005).

2. Mathemetical Model

The system of equation utilized in the present work is written using a non inertial frame of reference fixed to the oscillating circular cylinder. The effect of this motion is accounted by a pseudo-force term in the right-hand side of the momentum equation that acts as a body force, Batchelor (1983). In similar manner, the work done by this pseudo-force is accounted by a pseudo-work term in the right-hand side of the energy equation. With these considerations, the nondimensional form of the Navier-Stokes equations can be written as:

$$\frac{\partial \rho}{\partial t} + \frac{\partial}{\partial x_i}(\rho u_i) = 0 \tag{1}$$

$$\frac{\partial}{\partial t}(\rho u_i)+\frac{\partial}{\partial x_j}(\rho u_i u_j)=-\frac{\partial p}{\partial x_i}+\frac{\partial \tau_{ij}}{\partial x_j}+f_i \tag{2}$$

$$\frac{\partial}{\partial t}(\rho e_T)+\frac{\partial}{\partial x_i}(\rho e_T u_i)=-\frac{\partial}{\partial x_i}(p u_i)+\frac{\partial}{\partial x_i}(\tau_{ij}u_j)-\frac{\partial q_{x_i}}{\partial x_i}+f_i u_i \tag{3}$$

In the equations above all the variables are in a nondimensional form: ρ is the density, t is the temporal coordinate, u_i is the *i*-direction component of the velocity vector, x_i is the *i*-direction spatial coordinate, p is the pressure, τ_{ij} is the stress tensor, f_i is the pseudo-force due to the oscillating motion, e_T is the total energy per unit of mass and q_{x_i} is the heat-flow density in the *i*-direction

The nondimensional form of the flow variables and properties are obtained using the following relations:

$$\begin{gathered} x_i=\frac{x_i^*}{d^*},\quad u_i=\frac{u_i^*}{U_\infty^*},\qquad t=\frac{t^*}{d^*/U_\infty^*},\quad p=\frac{p^*}{\rho_\infty^*\left(U_\infty^*\right)^2},\qquad \rho=\frac{\rho^*}{\rho_\infty^*},\quad e_T=\frac{e_T^*}{\left(U_\infty^*\right)^2}, \\ \mu=\frac{\mu^*}{\mu_\infty^*},\qquad e=\frac{e^*}{\left(U_\infty^*\right)^2},\qquad e_k=\frac{e_k^*}{\left(U_\infty^*\right)^2},\qquad c_v=\left[\frac{T_\infty^*}{\left(U_\infty^*\right)^2}\right]c_v^*,\quad T=\frac{T^*}{T_\infty^*}, \end{gathered} \tag{4}$$

where the asterisk denotes dimensional quantities and x_i^* is the i-direction spatial coordinate, d^* is the cylinder's diameter, U_∞^* is the undisturbed velocity magnitude, t^* is the temporal coordinate, p^* is the pressure, ρ^* is the density, ρ_∞^* is the density of the undisturbed flow, $e_T{}^*$ is the total energy per unit of mass, μ is the nondimensional dynamic viscosity μ^* is the dynamic viscosity μ_∞^* is the dynamic viscosity of the undisturbed flow, e is the nondimensional internal energy per unit mass, e^* is the internal energy per unit mass, e_k is the nondimensional kinetic energy per unit mass, $e_k{}^*$ is the kinetic energy per unit mass, c_v is the nondimensional specific heat at constant volume c_v^* is the specific heat at constant volume, T is the nondimensional temperature T^* is the temperature and T_∞^* is the temperature of the undisturbed flow. The nondimensional viscous stress tensor is given by

$$\tau_{ij}=\frac{1}{\mathrm{Re}}\left(\mu S_{ij}\right)=\frac{1}{\mathrm{Re}}\left\{\mu\left[\left(\frac{\partial u_i}{\partial x_j}+\frac{\partial u_j}{\partial x_i}\right)-\frac{2}{3}\delta_{ij}\frac{\partial u_k}{\partial x_k}\right]\right\} \tag{5}$$

where S_{ij} is the nondimensional rate-of-strain tensor, δ_{ij} is the Kronecker delta and the Reynolds number is defined as

$$\mathrm{Re}=\frac{\rho_\infty^* U_\infty^* d^*}{\mu_\infty^*} \tag{6}$$

The total energy is given by the sum of the internal and kinetic specific energy as

$$e_T=e+e_k=c_v T+\frac{u_i u_i}{2} \tag{7}$$

and the nondimensional heat flux density, where γ is the specific heat ratio, is given by

$$q_{x_i}=-\frac{\mu}{(\gamma-1)M^2\,\mathrm{Re}\,\mathrm{Pr}}\left(\frac{\partial T}{\partial x_i}\right) \tag{8}$$

In Eq. (8), M is the Mach number and Pr is the Prandtl number, being defined as

$$M = \frac{U_\infty^*}{\sqrt{\gamma R^* T_\infty^*}}, \qquad \Pr = \frac{c_p^*}{k_\infty^*}\mu_\infty^* \tag{9}$$

where R is the specific gas constant, c_p^* is the specific heat at constant pressure and k_∞^* is the thermal conductivity of the undisturbed flow.

In the present work, the Prandtl number is assumed to be a constant with the value $\Pr = 0.72$. Being so, for a thermally and calorically perfect gas, the nondimensional equation of state assume the following form

$$p = (\gamma - 1)\rho e \tag{10}$$

and

$$T = \frac{\gamma M^2 p}{\rho} \tag{11}$$

The nondimensional molecular viscosity is obtained using Sutherland's formula

$$\mu = C_1 \frac{T^{3/2}}{T + C_2}, \qquad C_1 = \left[\frac{\left(T_\infty^*\right)^{1/2}}{\mu_\infty^*}\right] C_1^*, \qquad C_2 = \frac{C_2^*}{T_\infty^*}. \tag{12}$$

where C_1 is the nondimensional first gas constant in Sutherland's formula, C_1^* is the first gas constant in Sutherland's formula, C_2 is the nondimensional second gas constant in Sutherland's formula and C_2^* is the second gas constant in Sutherland's formula.

As the primary objective of this work is to analyze the effect of the oscillating motion over the resulting aerodynamic forces, the pseudo-force, f_i that appears in Equations (2) and (3), accounts for this motion when the Navier-Stokes equations are written for a non-inertial frame or reference. The imposed motion has a sinusoidal linear amplitude in time and the components of the pseudo-force, f_i are given by

$$f_i = \frac{1}{2}\rho A_i \omega_i^2 \sin(\omega_i t) \tag{13}$$

where the nondimensional maximum amplitude, A_i, and angular frequency, ω_i, are defined as

$$A_i = \frac{A_i^*}{d^*}, \qquad \omega_i = \frac{\omega_i^*}{U_\infty^* / d^*}. \tag{14}$$

with A^* and ω^* being the maximum amplitude of motion and angular frequency of the sinusoidal motion respectively.

The boundary conditions at the wall of the circular cylinder are a no-slip condition for the velocity field, an adiabatic wall for the temperature field and a null gradient in the normal direction at the wall for the pressure field.

3. Numerical Method

Since the geometry of interest is a circular cylinder and the flow is laminar, the two-dimensional form of the Navier-Stokes equations is used. In order to numerically solve these equations using a finite volume approach, Equations (1), (2) and (3) are written in the following vector form, Anderson *et al.* (1983):

$$\frac{\partial \mathbf{U}}{\partial t} + \frac{\partial \mathbf{E}}{\partial x} + \frac{\partial \mathbf{F}}{\partial y} = \mathbf{R} \tag{15}$$

where **U** is the nondimensional conservative-variables vector, **E** and **F** are nondimensional flux vectors and **R** is the nondimensional vector associated with the oscillating motion. The first three vectors are given by

$$\mathbf{U}=\begin{bmatrix}\rho\\ \rho u\\ \rho v\\ \rho e_T\end{bmatrix},\quad \mathbf{E}=\begin{bmatrix}\rho u\\ \rho u^2+p-\tau_{xx}\\ \rho uv-\tau_{xy}\\ (\rho e_T+p)u-u\tau_{xx}-v\tau_{xy}+q_x\end{bmatrix},\quad \mathbf{F}=\begin{bmatrix}\rho v\\ \rho vu-\tau_{xy}\\ \rho v^2+p-\tau_{yy}\\ (\rho e_T+p)v-u\tau_{xy}-v\tau_{yy}+q_y\end{bmatrix}. \tag{16}$$

where u is the nondimensional *x*-direction component of the velocity vector and v is the nondimensional *y*-direction component of the velocity vector.

The oscillating motion of the cylinder in this work is imposed in the *y*-direction, and consequently, the **R** vector is defined as:

$$\mathbf{R}=\begin{bmatrix}0\\ 0\\ \frac{1}{2}\rho A_y\omega_y^{\,2}\sin(\omega_y t)\\ \frac{1}{2}\rho A_y\omega_y^{\,2}\sin(\omega_y t)v\end{bmatrix}. \tag{17}$$

Defining the flux tensor Π as

$$\Pi=\mathbf{E}\otimes\mathbf{i}+\mathbf{F}\otimes\mathbf{j} \tag{18}$$

Equation (15) can now be written as

$$\frac{\partial\mathbf{U}}{\partial t}+\nabla\cdot\Pi=\mathbf{R} \tag{19}$$

Integrating Eq. (19) over the control volume *V*, and applying the divergence theorem to the first term of right-hand side results

$$\frac{\partial}{\partial t}\int_V\mathbf{U}\,dV=-\int_V(\nabla\cdot\Pi)dV+\int_V\mathbf{R}\,dV=-\int_S(\Pi\cdot\mathbf{n})dS+\int_V\mathbf{R}\,dV \tag{20}$$

where *S* is the surface of control an **n** is the normal unit vector. Defining the volumetric mean of vectors **U** and **R** in the control volume *V* as

$$\overline{\mathbf{U}}\equiv\frac{1}{V}\int_V\mathbf{U}\,dV,\qquad \overline{\mathbf{R}}\equiv\frac{1}{V}\int_V\mathbf{R}\,dV, \tag{21}$$

Equation (20) can be written as

$$\frac{\partial\overline{\mathbf{U}}}{\partial t}=-\frac{1}{V}\int_S(\Pi\cdot\mathbf{n})dS+\overline{\mathbf{R}} \tag{22}$$

For the volume (i, j), the first-order approximation of the temporal derivative is given by

$$\left(\frac{\partial\overline{\mathbf{U}}}{\partial t}\right)_{i,j}=\frac{\Delta\overline{\mathbf{U}}_{i,j}}{\Delta t}+O(\Delta t) \tag{23}$$

where $\Delta\overline{\mathbf{U}}_{i,j}$ is the variation of the nondimensional conservative-variables vector and Δt is the nondimensional time step. The temporal approximation of Eq. (22) for a quadrilateral and two-dimensional control volume is

$$\Delta\overline{\mathbf{U}}_{i,j} = -\frac{\Delta t}{V_{i,j}}\left[\int_{S_{i+1/2}}(\Pi\cdot\mathbf{n})dS + \int_{S_{i-1/2}}(\Pi\cdot\mathbf{n})dS + \int_{S_{j+1/2}}(\Pi\cdot\mathbf{n})dS + \int_{S_{j-1/2}}(\Pi\cdot\mathbf{n})dS\right] + \Delta t\,\overline{\mathbf{R}} \tag{24}$$

where $S_{i+1/2}$ is the common surface between volume (i, j) and volume $(i+1, j)$. Defining the flux of tensor Π over the control surface $\mathcal{F}\left(\overline{\mathbf{U}}\right)$ as

$$\mathcal{F}\left(\overline{\mathbf{U}}\right)_{i,j} = (\Pi\cdot\mathbf{S})_{i+1/2} + (\Pi\cdot\mathbf{S})_{i-1/2} + (\Pi\cdot\mathbf{S})_{j+1/2} + (\Pi\cdot\mathbf{S})_{j-1/2} \tag{25}$$

where **S** is the surface vector, the spatial approximation of Eq. (24) is

$$\Delta\overline{\mathbf{U}}_{i,j} = -\frac{\Delta t}{V_{i,j}}\left[\mathcal{F}\left(\overline{\mathbf{U}}\right)_{i,j} - \mathcal{D}\left(\overline{\mathbf{U}}\right)_{i,j}\right] + \Delta t\,\overline{\mathbf{R}} \tag{26}$$

where $\mathcal{D}\left(\overline{\mathbf{U}}\right)_{i,j}$ is an artificial dissipation. It is important to note that Eq. (26) is a spatial approximation of Eq. (24) because tensor Π is considered constant over each of the four control surfaces that define the control volume.

In order to calculate $\mathcal{F}\left(\overline{\mathbf{U}}\right)_{i,j}$, the flux of tensor Π trough the control surfaces must be calculated. The explicit form of this calculation as well as the implementation of the artificial dissipation, $\mathcal{D}\left(\overline{\mathbf{U}}\right)_{i,j}$, is given by Bobenrieth Miserda and Mendonça (2005). For the time marching of Eq. (26), a third-order Runge-Kutta is used as proposed by Shu, Yee (1997). This yield to

$$\overline{\mathbf{U}}^1 = \overline{\mathbf{U}}^n - \frac{\Delta t}{V_{i,j}}\left[\mathcal{F}\left(\overline{\mathbf{U}}^n\right) - \mathcal{D}\left(\overline{\mathbf{U}}^n\right)\right] + \Delta t\,\overline{\mathbf{R}}^n \tag{27}$$

$$\overline{\mathbf{U}}^2 = \frac{3}{4}\overline{\mathbf{U}}^n + \frac{1}{4}\overline{\mathbf{U}}^1 - \frac{1}{4}\left\{\frac{\Delta t}{V_{i,j}}\left[\mathcal{F}\left(\overline{\mathbf{U}}^1\right) - \mathcal{D}\left(\overline{\mathbf{U}}^1\right)\right] + \Delta t\,\overline{\mathbf{R}}^1\right\} \tag{28}$$

$$\overline{\mathbf{U}}^{n+1} = \frac{1}{3}\overline{\mathbf{U}}^n + \frac{2}{3}\overline{\mathbf{U}}^2 - \frac{2}{3}\left\{\frac{\Delta t}{V_{i,j}}\left[\mathcal{F}\left(\overline{\mathbf{U}}^2\right) - \mathcal{D}\left(\overline{\mathbf{U}}^2\right)\right] + \Delta t\,\overline{\mathbf{R}}^2\right\} \tag{29}$$

As used in this work, the resulting numerical method is fourth-order accurate in space and third-order accurate in time.

4. Results

In order to analyze the effects of the oscillating motion, is realized a study of several cases and for each one of these the Mach number is set to 0.2 and the Reynolds number to 100. For the definition of each one of the cases is generated a combination of two created key parameters, the vertical velocity of reference and the angular frequency of reference, respectively defined as

$$V_{ref} = \frac{v_{\max}}{U_\infty} \quad , \quad \omega_{ref} = \frac{\omega_y}{\omega_s} = \frac{\omega_y}{2\pi St} \tag{30}$$

where ω_s is the angular frequency related to the simulated vortex-emission frequency of the static circular cylinder at the same Mach and Reynolds numbers, represented by the Strouhal number, St, in Eq. (30). From previous research, the value of this Strouhal number is known to be 0.15. Being so, when the angular frequency of reference is set to one, it results in an oscillating motion with a frequency equal to the vortex-emission frequency of the static case.

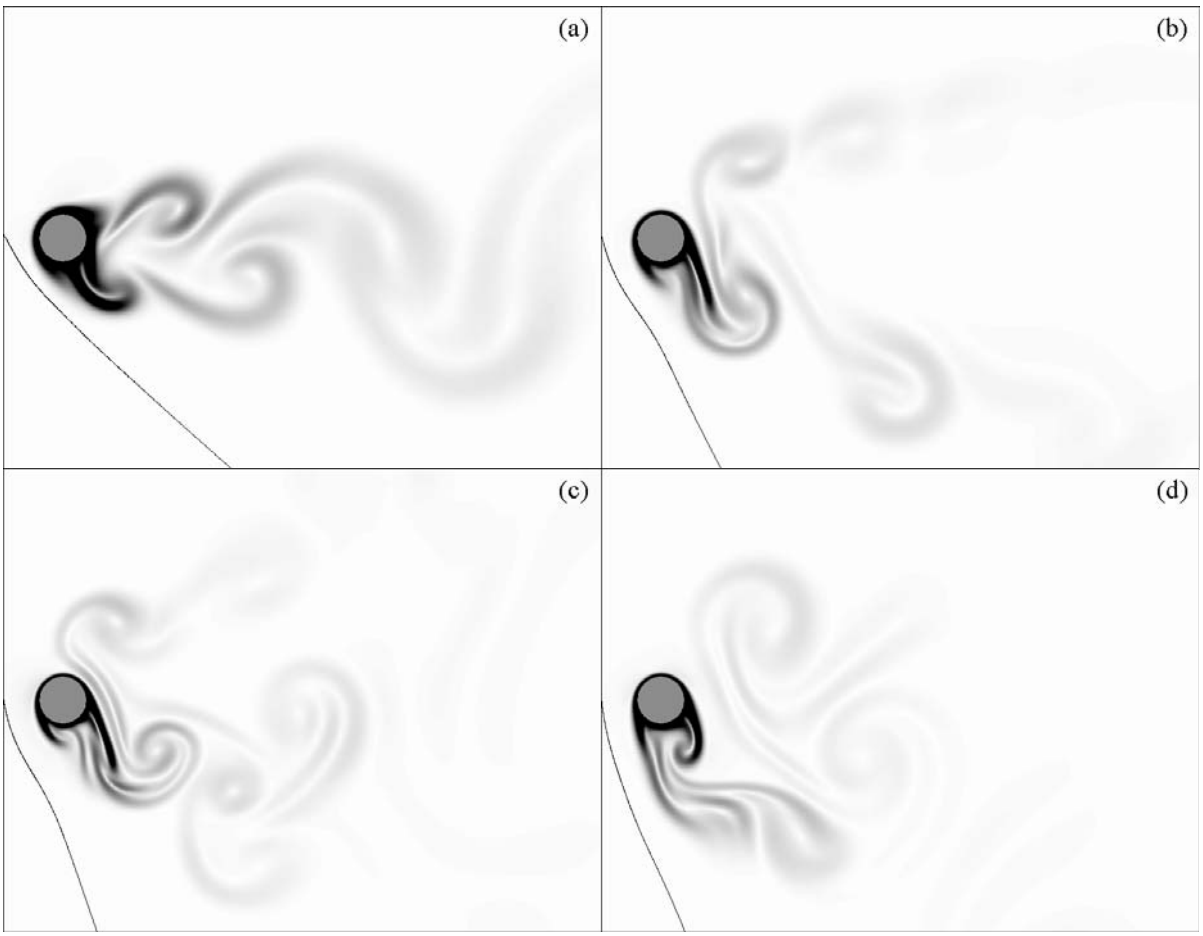

Figure 1. Visualizations of the oscillation motion for four different cases: (a) - V_{ref} set to 1.0 and ω_{ref} set to 2.0, (b) - V_{ref} and ω_{ref} set to 2.0, (c) - V_{ref} and ω_{ref} set to 3.0, (d) - V_{ref} set to 3.0 and ω_{ref} set to 1.0.

Figure (1) shows visualizations of the oscillation motion for four different cases, Fig. (1a) to (1d), at the maximum upward velocity instant, the inserted streamline helps at this determination. The plotted variable is the nondimensional magnitude of the temperature gradient. In the visualizations, white corresponds to 0 and black corresponds to 0.6. Each one of the above visualizations corresponds to one of the four distinct kind of cases studied. Figure (1a) displays a very regular and defined Von-Kármán vortex street, showing a periodic and symmetric vortex system topology. In a similar way, Fig. (1b) shows a well defined vortex street that looks like the Von-Kármán one, but in this case there is an oblique asymmetry between the vortices emitted in the upper and lower position of the cylinder that reveals a periodic although anti-symmetric vortex system topology. Different from the first two visualizations, Fig. (1c) and (1d) no longer show a well defined vortex street. However, in the visualization displayed in Fig. (1c) is still possible to see some periodicity of the vortex-street, revealing a pre-chaotic state of the system. In Fig. (1d) no periodicity is noticeable and a much disorganized vortex-street is present, characterizing a chaotic state of the vortex street topology.

These characteristics can also be appreciated in Fig. (2) that shows the unsteady lift force coefficient as a function of time. In Fig. (2) the black signal corresponds to instantaneous values and the gray corresponds to mean values of the lift coefficient. Figure (2a) and (2b) shows a very periodic behavior of the instantaneous signal that is directly associated with the well defined vortex street of these two particular cases. However, different from Fig. (2a), Figure (2b) no longer shows a mean signal floating around zero. This unique characteristic shows that the oblique asymmetry of the vortex street, Fig. (1b), generates a non-null resulting lift coefficient over the cylinder's surface. The instantaneous signal of Fig. (2c) shows a non-linear response of the lift coefficient, but still has a slightly periodic behavior, showing the transition from a periodic to chaotic state of the system. In Fig. (2d) is displayed the chaotic response of the lift coefficient that is associated with a very disorderly vortex-street.

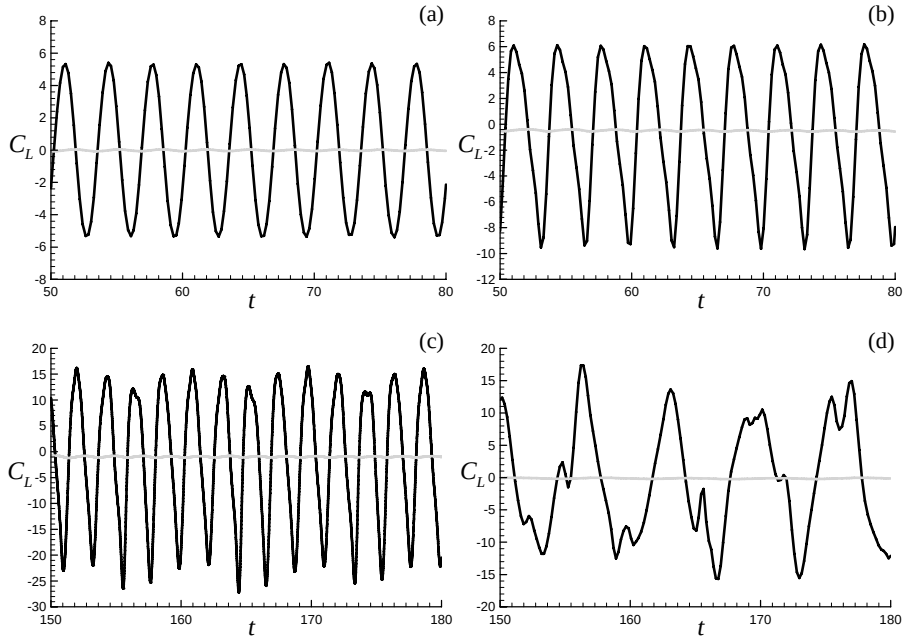

Figure 2. Unsteady lift force coefficient as a function of time: (a) - V_{ref} set to 1.0 and ω_{ref} set to 2.0, (b) - V_{ref} and ω_{ref} set to 2.0, (c) - V_{ref} and ω_{ref} set to 3.0, (d) - V_{ref} set to 3.0 and ω_{ref} set to 1.0.

Figure (3) shows the phase diagram for the unsteady lift coefficient. The phase path in the diagram of Fig. (3a) and in the one of Fig (3b) are very well defined as a consequence of a very well behavior of the system. In Fig. (3b) is also noticeable the presence of a non-null lift coefficient as the phase diagram is not centered at 0, in the horizontal axis. In Fig. (3c) is observed a intense deviation of the phase paths occasioned by the temporal variation of the maximum and minimum values of the lift coefficient, but is not entirely disorganized, emphasizing the transition from a periodic state to a chaotic one. Figure (3d) shows a phase diagram, in which the phase path follows no pattern and reveals the completely disorderly state of the system.

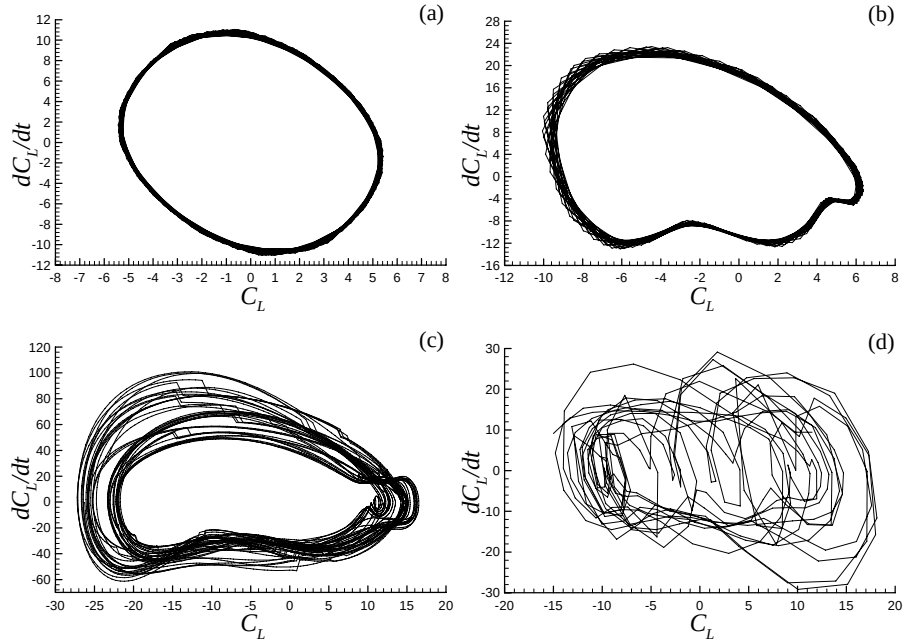

Figure 3. Phase diagram for the unsteady lift coefficient: (a) - V_{ref} set to 1.0 and ω_{ref} set to 2.0, (b) - V_{ref} and ω_{ref} set to 2.0, (c) - V_{ref} and ω_{ref} set to 3.0, (d) - V_{ref} set to 3.0 and ω_{ref} set to 1.0

The power spectrums for the unsteady lift coefficient of the four cases focused in the present work are showed in Fig. (4). The power spectrum of the first two cases, Fig. (4a) and (4b), shows only the fundamental frequency associated with low energy sub-harmonics. On the other hand, for the last two, Fig. (4c) and (4d), the spectrum is broader close to the fundamental frequency, becoming impossible to make a precise definition of sub-harmonics. This particular characteristic is caused by the non-linearity of the system in the two cases corresponding to Fig. (4c) and (4d).

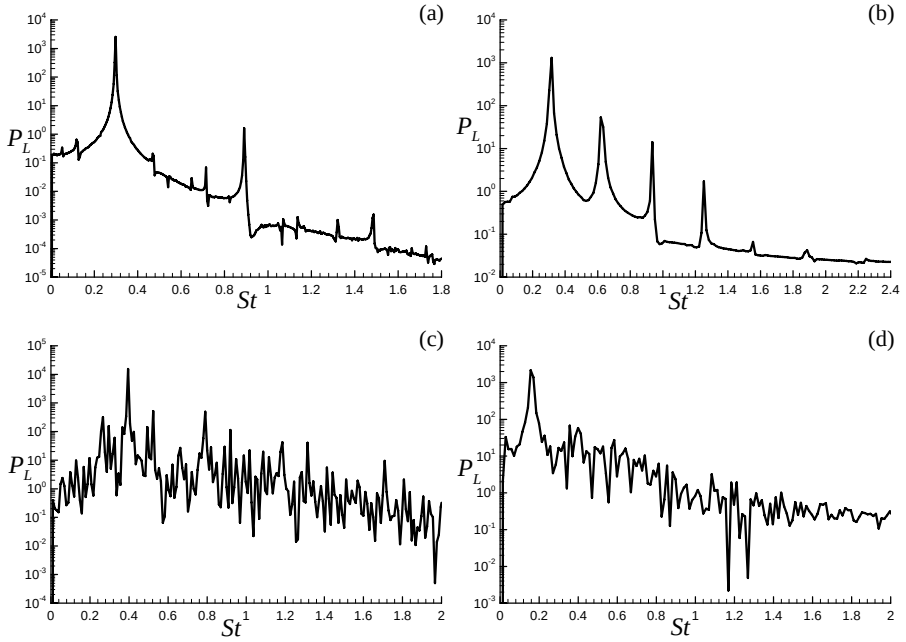

Figure 4. Power spectrum for the unsteady lift coefficient: (a) - V_{ref} set to 1.0 and ω_{ref} set to 2.0, (b) - V_{ref} and ω_{ref} set to 2.0, (c) - V_{ref} and ω_{ref} set to 3.0, (d) - V_{ref} set to 3.0 and ω_{ref} set to 1.0

Figure (5) shows a classification of all the studied cases, based on each one's vortex system topology (symmetric and anti-symmetric) and phase behavior of the unsteady lift coefficient (periodic, pre-chaotic and chaotic). These criteria results in four groups, namely the periodic and symmetric, periodic and anti-symmetric, pre-chaotic and chaotic cases. In this figure four linking lines are also shown. The first (horizontal) line links the cases where $V_{ref} = 1.0$. The second (vertical) line links the cases where $\omega_{ref} = 1.0$, and the third (oblique, with a 45º inclination) line, links the cases where the amplitude of motion is held constant. The fourth (oblique, with a 135º inclination) line links the cases that are orthogonal to the previous line. These cases were studied in order to define the local limit of the periodic and anti-symmetric behavior.

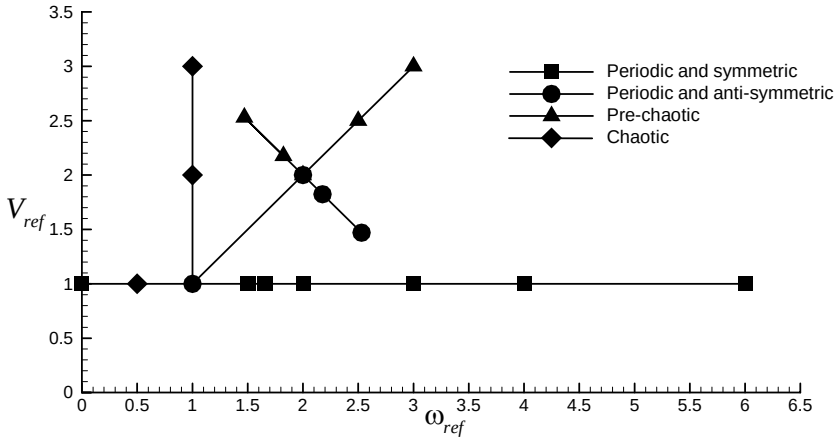

Figure 5. Classification of the cases studied, based on the topology of the vortex wake (symmetric and anti-symmetric) and the phase behavior of the unsteady lift coefficient (periodic, pre-chaotic and chaotic).

As we advance from the first case ($\omega_{ref} = 0.0$) to the last one over the first (horizontal) line ($\omega_{ref} = 6.0$), the system becomes more periodic and symmetric, except the case $\omega_{ref} = 1.0$, where the system shows itself to be periodic and anti-symmetric, and the case $\omega_{ref} = 0.5$, where the system has a chaotic behavior. This growing periodicity of the system is due to the fact that the system approaches a quasi-static situation, as the oscillation frequencies become higher than the static vortex-emission frequency. These high frequencies are also associated to very small amplitudes of motion.

Figure (5) also shows the higher sensibility to changes into the maximum linear velocity of oscillation when compared to changes into the angular frequency of oscillation. This higher sensibility is due to the fact that a small increment of 1.0 in V_{ref}, when ω_{ref} remains constant, results in the completely disorganization of the system, the system moves from a periodic state to a chaotic one. In contrast, an increment of 6.0 in ω_{ref}, when V_{ref} remains constant, not only keeps the system stable and periodic, but also makes the system even more stable as it moves forward a quasi-static situation.

5.Conclusions

In the present work is proposed a methodology, used to simulate the laminar flow over a normally oscillating circular cylinder, created by the insertion of pseudo-force and pseudo-work terms to the momentum and energy equations, respectively, to solve the system of governing equations from a non-inertial frame of reference fixed at the cylinder., as proposed by Bobenrieth Miserda e Mendonça (2005). In order to analyze the effects of the oscillating motion, two key parameters, V_{ref} and ω_{ref}, were created, and different combination of these two parameters resulted into four groups of cases: Periodic and symmetric, Periodic and anti-symmetric, Pre-chaotic and Chaotic.

The cases with a periodic and symmetric behavior, concentrated over the line in which ω_{ref} is constant and equal to 1.0, showed a very well define vortex-street associated with a signal of the unsteady lift coefficient that has a periodic and quasi-linear behavior resulting in a phase diagram with a well define phase path and a power spectrum, that shows, with definition, the fundamental frequency of the related case and sub-harmonics of low energy. Similar to these cases, the ones with a Periodic and anti-symmetric behavior, also showed a well defined vortex-street associated with a periodic and quasi-linear signal of the unsteady lift coefficient. However, the vortex-street topology revealed an oblique asymmetry that resulted into a non-null lift coefficient over the cylinder's surface.

On the other hand, the cases with a pre-chaotic behavior, although showed a slightly periodicity, were in a transition state between periodic and chaotic, showing a complex vortex-street, as theirs phase diagram displayed phase paths with great deviation, but they still seemed to follow a certain pattern, and their power spectrum no longer showed, with clear definition, the fundamental frequency and sub-harmonics. The chaotic cases no longer showed any periodic behavior of the unsteady lift coefficient signal associated with a complex and disorderly vortex street that resulted in a phase diagram without any pattern and a power spectrum that also makes impossible to clearly define the fundamental frequency and sub-harmonics.

The system also showed a higher sensibility to changes into the maximum linear velocity of oscillation when compared to changes into the angular frequency of oscillation. This emphasizes the importance of the maximum velocity of oscillation and the maximum amplitude of oscillation as they showed to be critical parameters. Any small increment of these parameters, at a fixed frequency of oscillation, can bring serious structure damage as they rapidly remove the system stability.

6. References

Anderson, D. A., Tannehill, J. C. and Pletcher, R. H., Computational Fluid Mechanics and Heat Transfer, 1st ed., Hemisphe Publishing Corporation, New York, 1983, Chap. 5.

Batchelor, C. K., 1983, An Introduction to Fluid Dynamics, 1st ed., University Press, Cambridge, 1983, Chap. 3.

Blackburn H. M., Henderson R.D., "A Study of Two-Dimensional Flow Past an Oscillating Cylinder", 1999, Journal of Fluid Mechanics, Vol. 385, pp. 255 - 286.

Bobenrieth Miserda, R.F., Mendonça, A.F. de, "Numerical Simulation of the Vortex-Shock Interactions in a Near-Base Laminar Flow", AIAA 43rd Aerospace Sciences Meeting and Exhibit, AIAA 2005-0316, Reno, Nevada, 2005.

Jared S. C. et al, "Computation of Vortex Shedding and Radiated Sound for a Circular Cylinder', 4th International Symposium of Fluid-Structure Interactions , Aeroelasticity, Flow-Induced Vibration and Noise, Dallas, Texas, November 16 - 21, 1997.

Yee, H. C., "Explicit and Implicit Multidimensional Compact High-Resolution Shock-Capturing Methods: Formulation," Journal of Computational Physics, Vol. 131, No. 1, 1997, pp. 216, 232.

Proceedings of the 11th Brazilian Congress of Thermal Sciences and Engineering – ENCIT 2006
Braz. Soc. of Mechanical Sciences and Engineering – ABCM, Curitiba, Brazil, Dec. 5-8, 2006

Paper CIT06-0851

STABILITY OF THE CHEMICAL AND HYDRODYNAMIC FIELDS CLOSE TO A ROTATING DISK ELECTRODE: NON-SYNCHRONOUS PERTURBATIONS

J. Pontes
Metallurgy and Materials Engineering Department/EP-COPPE – Federal University of Rio de Janeiro
PO Box 68505 21941-972 Rio de Janeiro RJ, Brazil
jopontes@metalmat.ufrj.br

N. Mangiavacchi
Mechanical Engineering Department, State University of Rio de Janeiro
R. São Francisco Xavier 524 20550-013 Rio de Janeiro, RJ, Brazil
norberto.mangiavacchi@gmail.com

O. E. Barcia
Institute of Chemistry/IQ – Federal University of Rio de Janeiro
PO Box 68505 21941-972 Rio de Janeiro RJ, Brazil
barcia@metalmat.ufrj.br

O. R. Mattos
Metallurgy and Materials Engineering Department/EP-COPPE – Federal University of Rio de Janeiro
PO Box 68505 21941-972 Rio de Janeiro RJ, Brazil
omattos@metalmat.ufrj.br

B. Tribollet
UPR15 – CNRS, Physique des Liquides et Electrochimie
4 place Jussieu, 75252 Paris Cedex 05, France
bt@ccr.jussieu.fr

Abstract. *Polarization curves experimentally obtained in the electro-dissolution of iron in a 1* $\mathbf{M\ H_2SO_4}$ *solution using a rotating disk as the working electrode present a current instability region within the range of applied voltage in which the current is controlled by mass transport in the electrolyte. According to the literature (Barcia, 1992) the electro-dissolution process leads to the existence of an axial viscosity gradient in the interface metal-solution, which leads to a deviation from von Kármán's classical solution for rotating disk flow. On two previous papers, Pontes et al (J. of the Braz. Soc. Mechanical Sciences, Vol. XXIV, pp. 139, 2002, and Phys. of Fluids, Vol. 16, No. 3, pp. 707, 2004) showed that stability of the steady flow, affected by a time-independent viscosity gradient pointing in the axial directions, is strongly affected by the stratified viscosity profile. In this work, we go one step beyond, by considering the stability of the hydrodynamic field, coupled through the viscosity, to the chemical field originated by the transport of one species. A phenomenological law is assumed, relating the viscosity to the concentration of chemical species. The viscosity at the interface with the electrode is estimated by relating the experimental value of the current density, to the concentration gradient of the relevant chemical specie at that point. The steady state of the problem is obtained and a linear stability analysis of the coupled fields is made. The resulting eigenvalue-eigenfuction problem is presented, as well as the neutral stability curves for disturbances turning with the same angular velocity of the disk (stationary) and for disturbances turning with angular velocity different from the disk one(non-stationary).*

keywords: *Rotating Disk, Hydrodynamic Stability, Electrochemistry*

1. Introduction

Electrochemical cells using a rotating disk electrode are a widely used experimental tool in electrochemistry, due the simplicity of the setup and the fact that the mass flux is independent of the radial position along the disk, at steady state conditions (Levich, 1962). Furthermore, the rate of transfer of ions close of the electrode is

conveniently controlled by imposing an adequate angular velocity to the electrode. This rate of transfer defines the maximum steady state current attained in an experiment.

Two current instabilities are observed in the region where the current is controlled by mass transport (Ferreira *et al.*, 1994). The first instability is intrinsic to the system, while the current instability close to the active-passive transition is affected by the output impedance of the control equipment. This instability can be suppressed by using a negative feedback resistance (Epelboin *et al.*, 1979), that gives rise to a continuous transition.

Most explanations presented in the literature for the current instabilities are based on mechanisms proposing a $\mathbf{FeSO_4}$ film precipitated at the electrode surface (Russel and Newman, 1986). In fact, changes in the ohmic voltage drop due to precipitation and dissolution of a $\mathbf{FeSO_4}$ film provide an acceptable explanation for the instability observed in the active/passive transition region, coupled with the output impedance of the control equipment. However, this model can not be generalized to explain oscillations observed at the beginning of the current plateau. Indeed, using electro-hydrodynamic (EHD) impedance measurements (Tribollet and Newman, 1983), Barcia *et al.* (1992) studied the electro-dissolution of iron electrodes in 1 $\mathbf{M\ H_2SO_4}$ at the current plateau, before and after the first instability region. They propose that the electro-dissolution process leads to the existence of a viscosity gradient in the diffusion boundary layer, which could affect the stability of the hydrodynamic field and explain the observed current instability.

To investigate the importance of the hydrodynamics in the electro-dissolution of iron, Ferreira *et al.* (1994) and Geraldo *et al.* (1998) studied the influence of the viscosity on the current oscillations observed at the beginning of the current plateau region of the above described experiment. These authors found that increasing the bulk electrolyte viscosity – and therefore decreasing the Reynolds number of the experiment – by adding glycerol to the solution, the current signals evolve from chaotic to periodic, and to a stationary regime, where the instability is suppressed. They also found that the current oscillations are enhanced by an increase in the angular velocity of the electrode.

The existence of a hydrodynamic instability in rotating disk flow has been the object of a number of investigations, both experimental and theoretical in the case of fluids with uniform viscosity. The main result shows that the steady flow becomes unstable beyond a certain non-dimensional distance from the axis of rotation.

The flow develops corotating vortices which spiral outward with their axes along logarithmic spirals of angle $90° + \varepsilon$ ($\varepsilon \approx 13°$) with respect to radius of the disk. Malik (1986) determined the neutral stability curve for stationary vortex disturbances, which turn with the angular velocity of the disk. Neutral curves were presented in the $\alpha \times R$, $\beta \times R$ and $\varepsilon \times R$ planes for zero-frequency disturbances, where α and β are the components of the real perturbation wave-vector along the radial and azimuthal directions and ε is the angle between the perturbation and the radial direction, given by $\varepsilon = \tan^{-1} \beta/\alpha$. The critical Reynolds number was found to be in good agreement with experimental results, at a value of $R = 285.36$.

A comprehensive review of the literature on the subject, concerning research made until 1989 can be found in the paper by Reed and Saric (1989).

Faller (1991) determined the neutral stability curves for setup configurations consisting of rotating or stationary disks and flows approaching the disk with (rotating flow) or without (stationary flow) bulk angular velocity. Critical Reynolds number for the case of rotating disk and stationary fluid was found as 69.4.

Lingwood (1995) presented the neutral curve for vortices turning with several angular velocities and theoretical results concerning the asymptotic response of the flow to an impulsive excitation exerted in the flow at a certain radius at $t = 0$. Additionally, Lingwood's work addresses the case where the wavenumber component along the radial direction, α, is complex, leading to an exponential growth along that direction. The curve for this case defines the region of absolute instability, with a critical Reynolds number of $R = 510.625$.

It is well known that boundary layers can be destabilized by increasing the viscosity close to the wall and stabilized by decreasing, through heating or cooling the wall (Schlichting and Gersten, 1999). Schäfer *et al.* (Schäfer *et al.*, 1995) deduced an asymptotic expression for the critical Reynolds number for moderate temperature differences in boundary layers developed over flat plates, taking into account the temperature dependency of the viscosity. Turkyilmazoglu Cole and Gajjar (1998)) studied the influence of heat transfer on the convective and absolute instability of compressible boundary layers in rotating disk flow.

On two previous papers, Pontes *et al.* (2002, 2004) , showed that stability of the steady flow, affected by a time-independent viscosity gradient pointing in the axial directions, is strongly affected by the stratified viscosity profile. In this work, we go one step beyond, by considering the stability of the hydrodynamic field, coupled through the viscosity, to the chemical field resulting from the transport of the relevant chemical specie. A phenomenological law is assumed, relating the viscosity to the concentration of chemical specie. The viscosity at the interface with the electrode is estimated by relating the experimental value of the current density, to the concentration gradient of the chemical specie at that point. The steady state of the problem is obtained and a linear stability analysis of the coupled fields is made. The resulting eigenvalue-eigenfuction problem is presented, as well as the neutral stability curves for stationary disturbances, turning with the same angular velocity of the disk and for disturbances turning with angular velocity different from the disk one.

2. Governing Equations

The problem is governed by the continuity and the Navier-Stokes equations, coupled through the viscosity, to the transport equation of the relevant chemical specie. These equations, written in the frame attached to the surface of the rotating disk read:

$$\operatorname{div}\mathbf{v} = 0 \tag{1}$$

$$\frac{D\mathbf{v}}{Dt} = -2\boldsymbol{\Omega}\times\mathbf{v} - \boldsymbol{\Omega}\times(\boldsymbol{\Omega}\times\mathbf{r}) - \frac{1}{\rho}\,\mathbf{grad}\,p + \frac{1}{\rho}\operatorname{div}\tau \tag{2}$$

$$\frac{DC_T}{Dt} = \operatorname{div}(D\mathbf{grad}\,C_T) \tag{3}$$

where τ is the viscous stress tensor for a newtonian fluid with variable viscosity, C_T is the total concentration of the chemical specie and the factor D, multiplying the concentration gradient in Eq. (3) is the variable diffusion coefficient of the specie.

The evolution equations are written in non-dimensional form. Variables having units of length or its reciprocal (radial and axial coordinates, perturbation wavenumber along the radial direction) are made non-dimensional with the length used to measure the thikness of the boundary layer, $(\nu_\infty/\Omega)^{1/2}$, where ν_∞ is the bulk viscosity of the fluid. Velocity components are divided by the local imposed azimuthal velocity $r_e\Omega$, pressure is divided by the reference pressure $\rho(r_e\Omega)^2$, viscosity is divided by the bulk value, time and the eigenvalue of the linearized problem are made non-dimensional with the time required by a particle, turning with the azimuthal velocity $r_e\Omega$, to move a distance equal to the reference length, $(\nu_\infty/\Omega)^{1/2}$. Here, r_e is the dimensional coordinate along the radial direction where the stability analysis is carried. The non-dimensional concentration of the chemical specie is defined by:

$$C = \frac{C_T - C_\infty}{C_S - C_\infty} \tag{4}$$

We define also the Reynolds and the Schmidt numbers by the relations:

$$R = r_e^*\left(\frac{\Omega}{\nu_\infty}\right)^{1/2} \qquad \text{and} \qquad Sc = \frac{D_\infty}{\nu_\infty} \tag{5}$$

At this point, we assume that the viscosity depends on the concentration of the chemical specie, and, consequently, on the axial coordinate z. We also assume the Stokes-Einstein law, which postulates that the product of the diffusion coefficient by the viscosity is constant:

$$D\nu = D_\infty\,\nu_\infty \tag{6}$$

where D_∞ and ν_∞ are the bulk diffusion coefficient and the bulk viscosity, respectively. In adition, we assume that the viscosity varies with the concentration, according to:

$$\nu = \nu_\infty \exp(mC) \tag{7}$$

Using the bulk viscosity and diffusion coefficientes, ν_∞ and D_∞, to adimensionalize Eqs. (6) and (7) we obtain:

$$D\nu = 1 \qquad \text{and} \qquad \nu = \exp(mC) \tag{8}$$

Equations (1 – 3) take the following form, after introducing the adimensionalizing factors

$$\operatorname{div}\mathbf{v} = 0 \tag{9}$$

$$\frac{D\mathbf{v}}{Dt} = -2\,\mathbf{e}_z\times\mathbf{v} - \mathbf{e}_z\times\mathbf{grad}\,p + \frac{1}{R}\operatorname{div}\tau \tag{10}$$

$$\frac{DC_T}{Dt} = \frac{1}{R\,Sc}\operatorname{div}(D\,\mathbf{grad}\,C_T) \tag{11}$$

3. The Base State

3.1. Base state equations

The base state is the Von Kármán similarity solution for a fluid with the viscosity depending on the concentration field, which is assumed to vary along the axial coordinate only. In dimensional variables:

$$\begin{pmatrix} \bar{v}_r \\ \bar{v}_\theta \\ \bar{v}_z \\ p \\ \bar{C} \end{pmatrix} = \begin{pmatrix} r\,\Omega\,F(z) \\ r\,\Omega\,G(z) \\ (\nu_\infty\,\Omega)^{1/2}\,H(z) \\ \rho\nu_\infty\Omega P(z) \\ C_\infty + (C_S - C_\infty)C(z) \end{pmatrix} \tag{12}$$

Here, C_S and C_∞ are, respectively, the concentration of the chemical specie at the electrode surface and in the bulk. Boundary conditions for F, G, H and P are $F = G = H = P = 0$ at the disk surface ($z = 0$), $F = H' = P' = 0$ and $G' = -1$ in $z \longrightarrow \infty$. The non-dimensional concentration profile, C, varies from 1, $z = 0$, to 0, in $z \longrightarrow \infty$.

Eq. (12) is rewritten in nondimensional form:

$$\begin{pmatrix} \bar{v}_r \\ \bar{v}_\theta \\ \bar{v}_z \\ p \\ \bar{C} \end{pmatrix} = \begin{pmatrix} rF/R \\ rG/R \\ H/R \\ p/R^2 \\ C \end{pmatrix} \tag{13}$$

Introducing Eq. (13) in Eqs. (9 – 11), together with Eqs. (8), we obtain the ordinary nonlinear system for the axial profiles F, G, H, P and C:

$$2F + H' = 0 \tag{14}$$

$$F^2 - (G+1)^2 + HF' - \nu F'' - \nu' F' = 0 \tag{15}$$

$$2F(G+1) + HG' - \nu G'' - \nu' G' = 0 \tag{16}$$

$$P' + HH' - \nu H'' - 2\nu' H' = 0 \tag{17}$$

$$Sc\, HC' - \frac{C''}{\nu} + \frac{\nu'}{\nu^2} C' = 0 \tag{18}$$

where ν is given by Eq. (8) and

$$\nu' = m \exp(mC)\, C' \tag{19}$$

3.2. Evaluation of the Viscosity at the Electrode/Electrolyte Interface

Eqs. (14 – 18) are solved using the Newton method, in a uniform grid of points, with space derivatives represented by second order approximations. Solving these equations require specification of two parameters: the bulk Schmidt number ($Sc = 2000$) and the parameter m appearing in Eq. (7), which ultimately define de electrolyte viscosity at the interface with the electrode, where the non-dimensional concentration of the relevant chemical specie is equal to 1. Though both questions were adressed in a separate paper by the authors (Barcia 2005, submitted) we briefly review the key points of the subject for the sake of completness.

The bulk Schmidt number is easily estimated by noting that the viscosity of the 1 **M** $\mathbf{H_2SO_4}$ solution is $\nu_\infty = 1.0 \times 10^{-2} cm^2/s$ and the diffusion coefficient of the $\mathbf{Fe^{+2}}$ ion in the electrolyte is $D_\infty =$.

The limit current density at the interface is given by the relation:

$$i = nF \frac{1}{Sc} \frac{1}{\nu_0/\nu_\infty} (C^*_\infty - C^*_s) \sqrt{\nu_\infty \Omega}\, \left.\frac{dC}{dz}\right|_{z=0} \tag{20}$$

where i is expressed in A/cm^2, n is the valency number of the chemical specie ($n = 2$), $F = 96500\, C/mol$, is the Faraday constant, $C^*_s = 2.0 \times 10^{-3} mol/cm^3$ is the dimensional concentration of the specie at saturation conditions and $C^*_\infty = 0\, mol/cm^3$. The limit current density is obtained experimentaly as $i = 0.8810\, A/cm^2$ at $900\, rpm$. The remainning variables in Eq. (20), ν_0/ν_∞ and the nondimensional derivative of the concentration profile at the interface, $dC/dz|_{z=0}$, depend on the concentration profile, which is obtained by solving Eqs. (14 – 18). The profile is iteratively solved until the RHS of Eq. (20) converges to the experimental value of the limit current density. Convergence is attained for $\nu_0/\nu_\infty = 2.255$.

3.3. Base State Profiles

The high Schmidt number of the problem leads to a rather thin concentration boundary layer. The ratio between the thiknesses of the hydrodynamic (δ_h) and the concentration (δ_h) bondary layers is given, for the rotating disk flow problem, by (Levich, 1962):

$$\frac{\delta_h}{\delta_c} \approx 2\, Sc^{1/3} \tag{21}$$

The thin concentration boundary layer results in velocity profiles very close to the ones obtained for the constant viscosity case, outside the concentration boundary layer, which extends to $z \approx 0.25$. In particular, we obtain $H = -0.88559$ far from the disk for the variable viscosity flow considered, whereas $H = -0.88447$ for the constant viscosity case. The non-dimensional velocity, viscosity and concentration profiles, F, G, H, ν, the variable diffusion coefficient D and C, obtained for $\nu_0/\nu_\infty = 2.255$ and $Sc = 2000$ are shown in Fig. (1).

However, the derivatives of the velocity profiles are strongly affected by the concentration boundary layer, as shown in Fig. (2). Upon assuming a thickness of $\delta_h = 6$ for the hydrodynamic boundary layer we estimate a thickness of $\delta_c = 0.24$ for the concentration one, using Eq. (21). The profiles numerically obtained agree with this estimation.

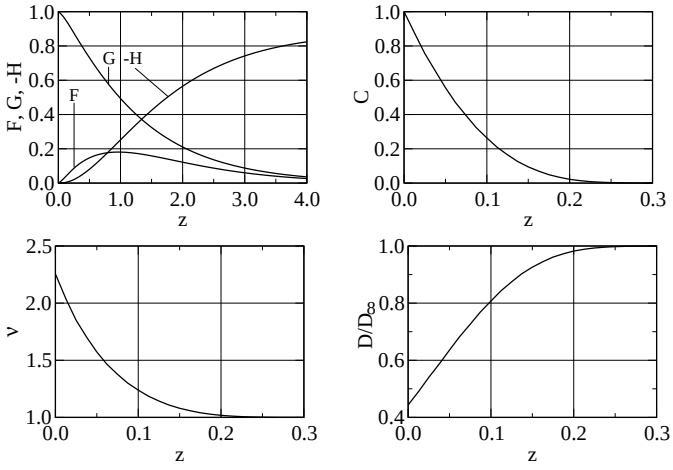

Figure 1: Dimensionless velocity, concentration and viscosity profiles for $\nu_0/\nu_\infty = 2.255$ and $Sc = 2000$.

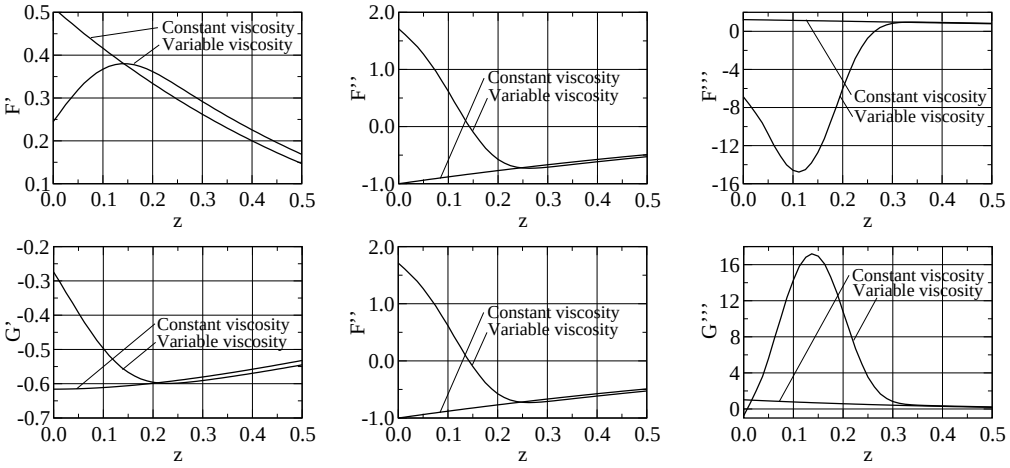

Figure 2: The first three derivatives of the non-dimensional velocity profiles, F and G, for the constant and variable viscosity cases.

4. Stability of the Base State

4.1. Stability equations

We turn now to the question of the stability of the base state with respect to small disturbances. The hydrodynamic and chemical fields are written as a summ of the base state plus a perturbation:

$$\left.\begin{array}{llllll} v_r &=& \bar{v}_r + \tilde{v}_r & v_\theta &=& \bar{v}_\theta + \tilde{v}_\theta \\ v_z &=& \bar{v}_r + \tilde{v}_z & p &=& \bar{p} + \tilde{p} \qquad C_T = \bar{C} + \tilde{C} \end{array}\right\} \tag{22}$$

where the perturbation is given by, in dimensional form:

$$\begin{pmatrix} \tilde{v}_r \\ \tilde{v}_\theta \\ \tilde{v}_z \\ \tilde{p} \\ \tilde{C} \end{pmatrix} = \begin{pmatrix} r_e \Omega\, f \\ r_e \Omega\, g \\ r_e \Omega\, h \\ \rho \nu_\infty \Omega\, \pi \\ C_\infty + (C_s - C_\infty)\, c \end{pmatrix} \exp\left[i(\alpha r + \beta R\theta - \omega t)\right] + cc \tag{23}$$

where ω is a complex number, with $\Re(\omega)$ and $\Im(\omega)$ being, respectively, the frequency and the rate of growth of the perturbation. The parameters α and β are the components of the perturbation wave-vector along the

radial and azimuthal directions. For a given time, the phase of the perturbation is constant along branches of a logarithmic spiral, with the branches curved in the clockwise direction if β/α is positive and counter-clockwise, if negative. The structure turns counter-clockwise if ω/β is positive and clockwise, if negative. In non-dimensional form:

$$\begin{pmatrix} \tilde{v}_r \\ \tilde{v}_\theta \\ \tilde{v}_z \\ \tilde{p} \\ \tilde{c} \end{pmatrix} = \begin{pmatrix} f \\ g \\ h \\ \pi \\ c \end{pmatrix} \exp\left[i(\alpha r + \beta R\theta - \omega t)\right] + cc \tag{24}$$

The perturbation variables are introduced in Eqs. (9 – 11) and nonlinear terms are dropped. The parallel flow hypothesis is assumed, in order to confirm the assumption that perturbation variables are separable. To conclude, terms of order R^{-2} are dropped, leading to the following complex, non-symmetric, generalized eigenvalue-eigenfuction problem:

$$\begin{pmatrix} A_{11} & A_{12} & A_{13} \\ A_{21} & A_{22} & A_{23} \\ A_{31} & & A_{33} \end{pmatrix} \begin{pmatrix} h \\ \eta \\ c \end{pmatrix} = \omega R \begin{pmatrix} B_{11} & & \\ & B_{22} & \\ & & B_{33} \end{pmatrix} \begin{pmatrix} h \\ \eta \\ c \end{pmatrix} \tag{25}$$

where $\eta = \alpha g - \beta f$, missing elements in the matrices are zero and the operators A_{ij} and B_{ij} are given by:

$$\left.\begin{array}{llllllll} A_{11} &=& a_{114}D^4 + a_{113}D^3 + a_{112}D^2 + a_{111}D + a_{110} & & A_{12} &=& a_{121}D + a_{120} \\ A_{13} &=& a_{132}D^2 + a_{131}D + a_{130} & & A_{21} &=& a_{211}D + a_{210} \\ A_{22} &=& a_{222}D^2 + a_{221}D + a_{220} & & A_{23} &=& a_{231}D + a_{230} \\ A_{31} &=& a_{310} & & A_{33} &=& a_{332}D^2 + a_{331}D + a_{330} \\ & & & & & & \\ B_{11} &=& D^2 - \bar{\lambda}^2 \qquad B_{22} = 1 & & B_{33} &=& iSc \end{array}\right\}$$

where $D^n = d^n/dz^n$ and the coefficients a_{ijk} are given by:

$$a_{114} = i\nu \qquad a_{113} = i(2\nu' - H) \qquad a_{112} = i\nu'' - i\nu\left(\lambda^2 + \bar{\lambda}^2\right) + R\left(\alpha F + \beta G\right) - i\left(H' + F\right)$$

$$a_{111} = -i\nu'\left(\lambda^2 + \bar{\lambda}^2\right) + iH\bar{\lambda}^2 \qquad a_{110} = i\bar{\lambda}^2\left(\nu'' + \nu\lambda^2\right) - R\left(\alpha F + \beta G\right)\bar{\lambda}^2 - R\left(\bar{\alpha}F'' + \beta G''\right) + iH'\bar{\lambda}^2$$

$$a_{121} = 2\left(G + 1\right) \qquad a_{120} = 2G'$$

$$a_{132} = R\left(\bar{\alpha}F' + \beta G'\right)\gamma \qquad a_{131} = \left[2R\left(\bar{\alpha}F'' + \beta G''\right) + 6i\bar{\lambda}^2 F\right]\gamma + 2R\left(\bar{\alpha}F' + \beta G'\right)\gamma'$$

$$a_{130} = \left(R\bar{\lambda}^2\left(\alpha F' + \beta G'\right) + R\left(\bar{\alpha}F''' + \beta G'''\right) + 4i\bar{\lambda}^2 F'\right)\gamma + \left(2R\left(\bar{\alpha}F'' + \beta G''\right) + 6i\bar{\lambda}^2 F\right)\gamma' + R\left(\bar{\alpha}F' + \beta G'\right)\gamma''$$

$$a_{211} = 2\left(G + 1\right) \qquad a_{210} = -iR\left(\alpha G' - \beta F'\right) \qquad a_{222} = i\nu \qquad a_{221} = i\left(\nu' - H\right)$$

$$a_{220} = -i\nu\lambda^2 + R\left(\alpha F + \beta G\right) - iF$$

$$a_{231} = iR\left(\alpha G' - \beta F'\right)\gamma \qquad a_{230} = iR\left(\left(\alpha G'' - \beta F''\right)\gamma + \left(\alpha G' - \beta F'\right)\gamma'\right)$$

$$a_{310} = RScC' \qquad a_{332} = -\frac{1}{\bar{\nu}} \qquad a_{331} = \frac{1}{\bar{\nu}}\left(\frac{\bar{\nu}'}{\bar{\nu}} + \frac{1}{\bar{\nu}}C'\gamma + Sc\,\bar{\nu}H\right)$$

$$a_{330} = iRSc\left(\alpha F + \beta G\right) - \frac{1}{\bar{\nu}}\left(-\bar{\lambda}^2 + \frac{1}{\bar{\nu}}\left(\left(2\frac{\bar{\nu}'}{\bar{\nu}}\gamma - \gamma'\right)C' - \gamma C''\right)\right)$$

where $\gamma = d\nu/dC$. Boundary conditions of the problem require non-slip flow and vanishing axial component of the velocity at the electrode surface. These conditions are already fulfilled by the base-state, so the hydrodynamic field cannot be modified by the perturbation at the electrode surface. In consequence we must require $h = \eta = c = 0$ in $z = 0$. Moreover, we conclude from the continuity equation, that $h' = 0$ at the electrode surface. In $z \longrightarrow \infty$ we require that the perturbation vanishes ($h = \eta = c = 0$) and that $h' = 0$.

The eigenvalue-eigenfuction problem defined by Eq. (25) is solved numerically. Space derivatives are replaced by discrete second-order representations, transforming the original problem in an eigenvalue-eigenvector problem, which is solved through the inverse power method.

4.2. Results

The neutral stability curves for stationary disturbances and for disturbances turning with $\omega = 0.025$, obtained by solving the eigenvalue-eigenfunction problem are presented in Fig. 3. Figs. 3(a) and 3(b) show the neutral curves associated to the constant and the variable viscosity cases, in the $\alpha \times R$ and $\beta \times R$ plane, respectively. Fig. 3(c) shows the curves of the variable viscosity case, in the $\alpha \times \beta$ plane. This figure shows that the coupling of the mass concentration field to the hydrodynamic field through the variable viscosity affects the

stability properties of the coupled fields, by strongly perturbing the neutral curve of the hydrodynamic modes and by introducing a new family of much more unstable modes, associated to the mass trasnport equation.

The critical Reynolds number of the hydrodynamic modes is reduced to approximately 50% of value for constant viscosity fluids. In addition, the unstable region is strongly enlarged and extends to modes with higher wavenumbers, than in the constant viscosity case. The neutral curve for constant viscosity fluids presents two minima, the second one occuring at $R \approx 440$ and being associated two a second unstable mode, which holds a profile along the axial direction which is different from the profile associated to the most unstable mode. This second mode is more affected by the variable viscosity field and becomes the most unstable hydrodynamic mode, in the variable viscosity case.

However, the new critical Reynolds number is now associated to the new unstable modes, which emerge from the modified flow dynamics, resulting from the coupling with the transport of the relevant chemical specie, through the concentration dependent viscosity. The new critical Reynolds number for stationary disturbances is $R = 52.3$, a number significantly smaller than 285.36, the critical value for constant viscosity fluids (Malik, 1986).

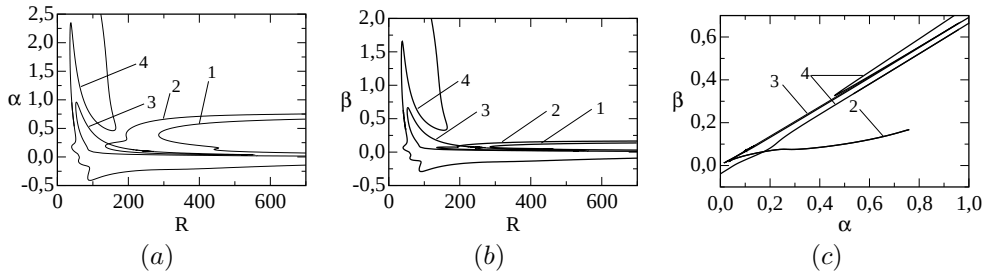

Figure 3: The neutral satbility curves of stationary perturbations ($\omega_r = 0.000$), in the $\alpha \times R$ (a), $\beta \times R$ (b) and $\alpha \times \beta$ (c) planes. Curves No. 1 refer to constant viscosity fluids; Curves No. 2 refer to the stability limit of the hydrodynamic mode associated to the variable viscosity case; Curves No. 3 refer to the stability limit of the chemical mode associated to the variable viscosity case. Curves No. 4 refer to perturbations turning with angular velocity $\omega = 0.025$. These last curves are preliminary.

5. Conclusions

In conclusion, we studied the effect of the coupling, of a mass concentration field, on the stability of the hydrodynamic field close to an iron rotating disk electrode. The mass concentration field is generated by the electro-dissolution of the electrode in a 1 **M** $\mathbf{H_2SO_4}$ solution and the coupling of the two fields occurs through the dependence of the viscosity, on the concentration of the chemical specie. The fluid viscosity at the electrode surface was evaluated using the experimental value of the current density. The critical Reynolds number of the hydrodynamic modes are reduced to approximately 50% of the value associated to constant viscosity flows and the unstable region is enlarged to much higher wavenumbers. In addition, a new class of unstable modes, associated to the transport dynamics of the relevant chemical specie emerges and the absolute minimum Reynolds number of the coupled fields locates in the new curve. The absolute minimum is $R = 52.3$, a number more than five times smaller than the critical Reynolds number for constant viscosity fluids, $R = 285.36$. The stability analysis was performed for stationary disturbances, turning with the angular viscosity of the electrode.

6. Acknowledgments

N. M. acknowledges financial support from CNPq (Brazil). The authors acknowledge the Center of Parallel Computing (NACAD/COPPE) of the Federal University of Rio de Janeiro, where the numerical calculations were performed.

7. References

Barcia, O. E., Mattos, O. R., and Tribollet, B., 1992, Anodic dissolution of iron in acid sulfate under mass transport control, "J. Eletrochem. Soc.", Vol. 139, pp. 446–453.

Epelboin, I., Gabrielli, G., Keddam, M., Lestrach, J. C., and Takenouti, H., 1979, Passivation of Iron in Sulfuric acid Medium, "J. Eletrochem. Soc.", Vol. 126, pp. 1632–1637.

Faller, A. J., 1991, Instability and Transition of the Disturbed Flow Over a Rotating Disk, "J. Fluid Mech.", Vol. 230, pp. 245–269.

Ferreira, J. R. R. M., Barcia, O. E., and Tribollet, B., 1994, Iron dissolution under mass transport control: the effect of viscosity on the current oscillation, "Eletrochim. Acta", Vol. 39, pp. 933–938.

Geraldo, A. B., Barcia, O. E., Mattos, O. R., Huet, F., and Tribollet, B., 1998, New results concerning the oscillations observed for the system iron-sulphuric acid, "Electrochim. Acta", Vol. 44, pp. 455–465.

Levich, V. G., 1962, "Physicochemical Hydrodynamics", Prentice Hall, Englewood Cliffs, NJ.

Lingwood, R. J., 1995, Absolute instability of the boundary layer on a rotating disk, "J. Fluid Mech.", Vol. 299, pp. 17–33.

Malik, M. R., 1986, The Neutral Curve for Stationary Disturbances in Rotating-disk Flow, "J. Fluid Mech.", Vol. 164, pp. 275–287.

Pontes, J., Mangiavacchi, N., Barcia, O. E., Mattos, O. R., and Tribollet, B., 2005, Rotating Disk Flow Stability in electrochemical Cells: Effect of the Transport of a Chemical Specie, "Proceedings of the 18th International Congress of Mechanical Engineering", Ouro Preto, MG, Brasil. ABCM.

Pontes, J., Mangiavacchi, N., Conceição, A. R., Barcia, O. E., Mattos, O. E., and Tribollet, B., 2002, Instabilities in Electrochemical Systems with a Rotatinng Disk electrode, "J. of the Braz. Soc. of Mechanical Sciences", Vol. XXIV-3, pp. 139–148.

Pontes, J., Mangiavacchi, N., Conceição, A. R., Barcia, O. E., Mattos, O. E., and Tribollet, B., 2004, Rotating Disk Flow Stability in Electrochemical Cells: Effect of Viscosity Stratification, "Phys. Fluids", Vol. 16, No. 3, pp. 707–716.

Reed, H. L. and Saric, W. S., 1989, Stability of Three-Dimensional Boundary Layers, "Ann. Rev. Fluid Mech.", Vol. 21, pp. 235–84.

Russel, P. and Newman, J., 1986, Current oscillations observed within the limiting current plateau for iron in sulfuric acid, "J. Eletrochem. Soc.", Vol. 133, pp. 2093–2097.

Schäfer, P., Severin, J., and Herwin, H., 1995, The effect of heat transfer on the stability of laminar boundary layers, "Int. J. Heat Mass Transfer", Vol. 38-10, pp. 1855–1863.

Schlichting, H. and Gersten, K., 1999, "Boundary Layer Theory", Springer, Berlin.

Tribollet, B. and Newman, J., 1983, The modulated flow at a rotating disk electrode, "J. Eletrochem. Soc.", Vol. 130, pp. 2016–2026.

Turkyilmazoglu, M., Cole, J. W., and Gajjar, J. S. B., 1998, Absolute and Convective Instabilities in the Compressible Boundary Layer on a Rotating Disk, CLSCM Report CLSCM-1998-001, University of Manchester, Manchester.

Proceedings of the 11th Brazilian Congress of Thermal Sciences and Engineering – ENCIT 2006
Braz. Soc. of Mechanical Sciences and Engineering – ABCM, Curitiba, Brazil, Dec. 5-8, 2006

Paper CIT06-0867

Filtering the Infinite Eigenvalues Originated from Linear Stability Analysis of Incompressible Flows

J. V. Valério
Department of Mechanical Engineering, Pontificia Universidade Catolica do Rio de Janeiro, Rua Marques de Sao Vicente 225, Gavea, Rio de Janeiro, RJ, 22453-900, Brazil
juvianna@mec.puc-rio.br

C. Tomei
Department of Mathematics, Pontificia Universidade Catolica do Rio de Janeiro, Rua Marques de Sao Vicente 225, Gavea, Rio de Janeiro, RJ, 22453-900, Brazil
carlos@mat.puc-rio.br

M.S. Carvalho
Department of Mechanical Engineering, Pontificia Universidade Catolica do Rio de Janeiro, Rua Marques de Sao Vicente 225, Gavea, Rio de Janeiro, RJ, 22453-900, Brazil
msc@mec.puc-rio.br

Abstract. *Steady state, two-dimensional flows can become unstable to two and three-dimensional disturbances if the flow parameters exceed some critical values. In many practical examples, determining the parameters at which the flow becomes unstable is an essential ingredient of the full understanding of the situation. Linear hydrodynamic stability of a laminar flow may be determined by slightly disturbing the flow and tracking the fate of that disturbance. It may die away, persist as a disturbance of similar magnitude, or grow indefinitely leading to a different laminar flow state, to a transient flow, or even to a turbulent flow. Linear stability formulation leads to a generalize eigenvalue problem (GEVP) where the eigenvalues correspond to the rate of growth of the disturbances and the eigenfunction to the amplitude of the perturbation. Solving the GEVP has been highly challenging, because the incompressibility of the liquid creates singularities that lead to aphysical infinite eigenvalues that require intricate reformulation and heavy computation to get around. The complexity and high computational cost of solving the GEVP have probably discouraged the use of linear stability analysis of incompressible flows as a general engineering tool for design and optimization. In this work, a new procedure to eliminate the "infinite eigenvalues" from the GEVP that comes from linear stability analysis of incompressible flow is proposed. The procedure takes advantage of the structure of the matrices involved and avoids the computational effort of common mapping techniques used to compute the spectrum of incompressible flows. As an example, the proposed method is applied in the solution of linear stability analysis of plane Couette flow.*

keywords: *eigenvalues, stability analysis, matrix transformation, incompressible flows.*

1. Introduction

Thorough understanding of viscous flows in many situations requires not only the two-dimensional, steady state solution of the governing equations, but also the sensitivity of those flows to small upsets and to episodic perturbations, i.e. stability analysis. For example, when studying the flow that occurs in many manufacturing processes, where a steady state flow is crucial for uniform product quality, the stability limits of the flow determine bounds for the operability limits of the process.

In many situations, an asymptotic analysis with respect to infinitesimal disturbances is sufficient to predict the critical flow parameters at which a two-dimensional steady flow becomes unstable. There are many examples of such analysis in the literature. Ruschak, 1983, Christodoulou and Scriven, 1988, Coyle *et al.*, 1990 and Carvalho and Scriven, 1999 studied stability analysis of different coating flows. Ramanan and Homsy, 1994 studied the linear stability of the flow inside a lid-driven cavity, and Severtson and Aidun, 1995 analyzed the stability of stratified liquid layers in inclined channels. Linear stability analysis involves the linearization of the governing equations about the steady state flow. The perturbation variables are described by a linear system of coupled differential equations. The discretization of the system of linear differential equations that describe the amplitude of the perturbations and its rate of growth leads to a non-hermitian, generalized eigenvalue problem (GEVP) of the form

$$\mathbf{Jc} = \sigma \mathbf{Mc}.$$

where the eigenvalue σ is the growth rate of disturbances. $\mathbf{J}$ and $\mathbf{M}$ are usually referred to as the Jacobian and Mass matrices.

Finding the solution of the GEVP is extremely challenging. The level of discretization needed to describe the perturbed fields is usually high, leading to large sparse matrices. The large dimension of the problem rules out the calculation of the full spectrum. Only the leading eigenvalues, those with the largest real part, are calculated. Iterative methods have to be used to compute the relevant part of the spectrum. Moreover, the mass matrix $\mathbf{M}$, which is associated with the transient terms of the governing equations, is singular because the continuity equation for incompressible flows does not have a time dependent term. This singularity gives rise to "infinite eigenvalues". The presence of these very large eigenvalues represents an important difficulty in solving this class of problem, because most iterative methods favor the eigenvalues with the largest modulus, not those with the largest real part. Therefore, the aphysical "infinite eigenvalues" should be eliminated before the solution of the eigenproblem, otherwise they would be the first ones to be computed.

The most effective techniques to solve GEVP are the methods based on some form of preconditioning and Krylov subspace projection methods, such as Arnoldi's and Lanczos methods (see Saad, 1996). A simple way to eliminate the infinite eigenvalues is to use the shift-and-invert transformation, that maps the infinite eigenvalues to zero. However, iterative methods used to solve the transformed problem will favor the eigenvalues closest to the shift parameter, not the leading ones. Christodoulou and Scriven, 1988 used approximately exponential preconditioning by rational transformation to overcome these difficulties. The eigenvalues of the transformed problem are the exponentials of the original eigenvalues, and consequently this transformation maps leading eigenvalues of the original problem to ones of largest modulus, which are favored by the iterative procedures, like Arnoldi's algorithm. All the proposed preconditioning are computationally expensive and do not really eliminate the infinite eigenvalues from the problem. The dimension of the transformed eigenproblem is the same as the original one. The eigenvalues are only mapped to a part of the spectrum of the transformed eigenproblem that will not be favored by the iterative methods.

In this work, realization on how incompressibility leads to infinite eigenvalues and analysis of the structure of the mass and jacobian matrices that arise from linear stability analysis of incompressible flows enabled us to eliminate the infinite eigenvalues. The procedure proposed transforms the generalized eigenproblem (GEVP) into a simple eigenproblem (EVP) whose dimension is smaller than the original one. Unlike the condensation procedure used by Ruschak, 1983 and Coyle *et al.*, 1990 for viscous free surface flows, and by Arora and Sureshkumar, 2002 for viscoelastic flows, the method proposed in this work is not limited to vanishing Reynolds number. Unlike the compressible flow formulation proposed by Sureshkumar, 2004, the proposed method does not include a penalty term in the mass conservation equation. The complete set of eigenvalues of the transformed problem is formed by all the finite eigenvalues of the original generalized eigenproblem. Therefore, the method presented really eliminates the infinite eigenvalue from the problem and also reduces the size of the matrices involved in the calculation. The proposed algorithm reduces not only the memory requirement but also the CPU time needed to compute the leading eigenvalues of incompressible viscous flows.

As an example, the proposed method is applied in the solution of linear stability analysis of plane Couette flow.

2. Linear Stability Analysis of Viscous Flow

2.1. Formulation

The velocity $\mathbf{v}$ and pressure p fields of two-dimensional, steady state, incompressible flow are governed by the continuity and momentum equations:

$$\nabla \cdot \mathbf{v} = 0, \tag{1}$$

$$Re\ \mathbf{v} \cdot \nabla \mathbf{v} = -\nabla p + \nabla \cdot \boldsymbol{\tau}. \tag{2}$$

The Reynolds Number $Re \equiv \rho V L/\mu$ characterizes the ratio of inertial to viscous forces; V and L are suitable characteristic values of velocity and length, ρ is the liquid density and μ, the liquid viscosity. $\boldsymbol{\tau} \equiv \nabla \mathbf{v} + (\nabla \mathbf{v})^{\mathrm{T}}$ is the viscous stress tensor for Newtonian fluid.

The goal of linear stability analysis is to determine if a two-dimensional, steady flow is stable with respect to infinitesimal disturbances. The stability of the flow can be judged by solving the time-dependent Navier-Stokes system for the long time behavior of infinitesimal perturbations to the base flow. Accordingly, the disturbed fields, i.e. velocity and pressure, are written as the sum of the base state and an infinitesimal perturbation

$$\mathbf{v}(\mathbf{x}, t) = \mathbf{v_0}(\mathbf{x}) + \epsilon\ \mathbf{v}'(\mathbf{x}) e^{\sigma t}, \tag{3}$$

$$p(\mathbf{x},t) = p_0(\mathbf{x}) + \epsilon\ p'(\mathbf{x})e^{\sigma t}. \tag{4}$$

$\mathbf{v_0}$ and p_0 are the velocity and pressure fields of the base flow, i.e. the two-dimensional, steady-state solution, which is known *a priori*. $\mathbf{v}'$ and p' are the fields that describe the amplitude of the perturbation and σ is the growth factor. If $\Re(\sigma) < 0$ ($\Re$ denotes the real part), the perturbation dies and the flow is said to be stable. If $\Re(\sigma) > 0$, the disturbance grows with time and the flow is said to be unstable .

The velocity $\mathbf{v}$ and pressure p of the disturbed flow are governed by the time-dependent Navier-Stokes system with the appropriate boundary conditions.

A system of linear differential equations that describe the perturbed fields is obtained after substituting the perturbed fields, e.g. eqs.(3,4), onto the transient Navier-Stokes system and neglecting terms of order $\mathcal{O}(\epsilon^2)$:

$$\nabla \cdot \mathbf{v}' = 0, \tag{5}$$

$$Re[\sigma\mathbf{v}' + \mathbf{v_0}\cdot\nabla\mathbf{v}' + \mathbf{v}'\cdot\nabla\mathbf{v_0}] = -\nabla p' + \nabla\cdot[\nabla\mathbf{v}' + \nabla\mathbf{v}'^T] = 0, \tag{6}$$

The unknowns of the problem are the perturbed fields $\mathbf{v}'$ and p' and the growth factor of the perturbation σ.

2.2. Discretization by Galerkin's Method and Finite Element Basis Functions

The perturbation fields $\mathbf{v}', p'$ and its rate of growth σ can be found by applying Galerkin's weighted residual method to eqs. (5, 6). The weighting functions used for the momentum equation ϕ_j and continuity equations χ_j are piecewise Lagrangean biquadratic and linear discontinuous polynomial basis functions, respectively. The weighted residual equations of continuity and x component of the momentum conservation are

$$R_c^j = \int_\Omega (\frac{\partial u_h'}{\partial x} + \frac{\partial v_h'}{\partial y})\ \chi_j\ d\Omega, \tag{7}$$

$$R_{mx}^j = \sigma\int_\Omega Re\ u_h'\ \phi_j\ d\Omega\ + \int_\Omega Re\left[u_0\frac{\partial u_h'}{\partial x} + v_0\frac{\partial u_h'}{\partial y} + u_h'\frac{\partial u_0}{\partial x} + v_h'\frac{\partial u_0}{\partial y}\right]\ \phi_j + \tag{8}$$

$$\left[-p_h' + 2\frac{\partial u_h'}{\partial x}\right]\frac{\partial\phi_j}{\partial x} + \left[\frac{\partial u_h'}{\partial y} + \frac{\partial v_h'}{\partial x}\right]\frac{\partial\phi_j}{\partial y}\ d\Omega - \int_\Gamma [\mathbf{n}\cdot(-p' + \boldsymbol{\tau}')]_x\phi_j\ d\Gamma,$$

the y component is similar to x one, Γ is the boundary of the two-dimensional domain Ω. Each perturbed field is approximated with a linear combination of the same basis functions.

$$\mathbf{u}_h' = \begin{bmatrix} u_h' \\ v_h' \end{bmatrix} = \begin{bmatrix} \sum_{k=1}^n U_k\phi_k \\ \sum_{k=1}^n V_k\phi_k \end{bmatrix}, \quad p_h' = \sum_{k=1}^m P_k\ \chi_k.$$

Once all the variables are represented in terms of the basis functions, the system of partial differential equations reduces to simultaneous algebraic equations for the coefficient of the basis functions of all fields and the growth rate σ. The number of algebraic equations is $N = 2n + m$, where n is the number of basis functions used to expand each component of the velocity perturbation and m is the number of basis functions used to expand the pressure disturbance. In vector form, the set of algebraic equations leads to a generalized eigenvalue problem:

$$\mathbf{Jc} = \sigma\mathbf{Mc}. \tag{9}$$

where $\mathbf{c}$ is the column vector of coefficients of the finite element basis function with which the perturbation of velocity and pressure are represented. $\mathbf{M}$, which multiplies the growth rate σ, is called the mass matrix and $\mathbf{J}$ is the jacobian matrix. It follows that the discretization of the differential equations that describe the perturbation fields give rise to a generalized, non-Hermitian eigenproblem.

3. Elimination of the "infinite eigenvalues"

As shown in the previous section, the linear stability analysis led to a generalized eigenproblem (9). The mass matrix $\mathbf{M}$ is diagonal by blocks and singular, because the continuity equation for incompressible liquids does not have a time derivative term. Consequently, the number of eigenvalues of (9) is smaller than the dimension of the problem $N = 2n+m$. The missing eigenvalues are commonly referred to as "infinite eigenvalues", because if the mass matrix is slightly perturbed to remove the singularity, e.g. $\mathbf{M}^* = \mathbf{M} + \epsilon\mathbf{I}$, large eigenvalues appear in the spectrum, and they grow unbounded as $\epsilon \to 0$. Truncation errors in the numerical methods used to

calculate the spectrum of (9) are equivalent to perturbations on the mass matrix and lead to the appearance of very large eigenvalues (the infinite eigenvalues). Christodoulou and Scriven, 1988 discusses that the number of infinite eigenvalues is equal the number of algebraic constrains (equations with no time derivative) in the discrete eigenproblem, i.e. the number of rows identically equal to zero in the mass matrix. In viscous flows of incompressible liquids, they represent the number of continuity residuals (number of degrees of freedom associated with the pressure field) plus the number of essential boundary conditions on the velocity field.

The presence of these very large eigenvalues represent an important difficulty in solving this class of problem, because most numerical methods to calculate the eigenvalues of a large eigenproblem favors the eigenvalues with the largest modulus. Therefore, these eigenvalues have to be eliminated before the solution of the eigenproblem. A common simple approach is to use transformations that map these infinite eigenvalues to zero, as the shift-and-invert transformation. In this case, the eigenproblem (9) is rewritten as

$$[(\mathbf{J}-\lambda\mathbf{M})-(\sigma-\lambda)\mathbf{M}]\,\mathbf{c}'=0.$$

$$\mathbf{A}\mathbf{c}'=\mu\mathbf{c}' \quad ; \qquad \mathbf{A}\equiv(\mathbf{J}-\lambda\mathbf{M})^{-1}\,\mathbf{M} \quad ; \qquad \mu\equiv 1/(\sigma-\lambda). \tag{10}$$

The shift-and-invert procedure transforms the generalized eigenproblem (9) to a simple eigenproblem (10). The eigenvalues σ of the GEVP can be calculated in terms of the eigenvalues μ of the simple EVP and of the shift parameter λ. The infinite eigenvalues are mapped to zero. However, the numerical methods to solve the simple eigenproblem will favors the largest eigenvalues μ, that correspond to the eigenvalues of the original problem σ closest to the shift λ.

Other more appropriate transformations can be use, such as bilinear and exponential transformations. Christodoulou and Scriven, 1988 and Ramanan and Homsy, 1994 used exponential transformation to map the leading eigenvalues to ones of largest modulus. They both found the method to be very robust, however the computational cost was extremely large, since the methods involves inverting a linear combination of the jacobian and mass matrices several times.

In the next section, a new method to filter the infinite eigenvalues of the GEVP (9) is proposed, taking advantage of the structure of the mass and jacobian matrices that come from linear stability analysis of flows of incompressible liquids. The analysis also shows that the number of infinite eigenvalues is actually larger than that proposed by Christodoulou and Scriven, 1988, it is equal to twice the number of residual equations associated with the mass conservation equations (twice the number of degrees of freedom associated with the pressure field) plus the number of residuals associated with essential boundary conditions on velocity.

3.1. Proposed Transformation

Following the ordering scheme explained before, both the mass and jacobian matrices are divided into blocks according to the equivalent residual equations and corresponding degrees of freedom.

$$\mathbf{M}=\left(\begin{array}{c|c|c} \mathbf{M_{11}} & \mathbf{0} & \mathbf{0} \\ \hline \mathbf{0} & \mathbf{M_{22}} & \mathbf{0} \\ \hline \mathbf{0} & \mathbf{0} & \mathbf{0} \end{array}\right)\begin{array}{c} n \\ n \\ m \end{array} \qquad \mathbf{J}=\left(\begin{array}{c|c|c} \mathbf{J_{11}} & \mathbf{J_{12}} & \mathbf{J_{13}} \\ \hline \mathbf{J_{21}} & \mathbf{J_{22}} & \mathbf{J_{23}} \\ \hline \mathbf{J_{31}} & \mathbf{J_{32}} & \mathbf{0} \end{array}\right)\begin{array}{c} n \\ n \\ m \end{array} \tag{11}$$

$n \quad n \quad m \qquad\qquad n \quad n \quad m$

m and n indicate the dimension of each block, for example $[\mathbf{M_{11}}]=n\times n$.

The eigenvalues σ of the GEVP (9) are the roots of the characteristic polynomial

$$p(\sigma)\equiv det(\mathcal{A})\equiv det(-\sigma\mathbf{M}+\mathbf{J}). \tag{12}$$

As mentioned before, the algebraic equations associated with the Dirichlet's boundary conditions do not have a time derivative, and the perturbed velocity field at these boundaries are identically zero. Therefore, eliminating the rows and columns related to these equations and unknowns will not change the roots of the characteristic polynomial $p(\sigma)$. This is the first step in the procedure of eliminating the "infinite eigenvalues". The size of the new matrix $\mathbf{A}$ is $2n+m-b$, where b is the number of rows/columns related to the Dirichlet's boundary conditions that were eliminated from the eigenproblem. After eliminating the rows and columns associated with essential boundary conditions, it is also convenient to divide the new matrix $\mathbf{A}\equiv-\sigma\mathbf{M}+\mathbf{J}$ into a different structure of blocks, as shown below.

$$\mathbf{A}=\left(\begin{array}{c|c|c} \mathbf{A_{11}}(\sigma) & \mathbf{A_{12}}(\sigma) & \mathbf{A_{13}} \\ \hline \mathbf{A_{21}}(\sigma) & \mathbf{A_{22}}(\sigma) & \mathbf{A_{23}} \\ \hline \mathbf{A_{31}} & \mathbf{A_{32}} & \mathbf{0} \end{array}\right)\begin{array}{c} m \\ 2n-m-b \\ m \end{array}$$

$m \qquad 2n-m-b \qquad m$

The blocks $\mathbf{A_{13}}$, $\mathbf{A_{23}}$, $\mathbf{A_{31}}$ and $\mathbf{A_{32}}$ do not have any contribution from the mass matrix and consequently do not depend on the growth factor σ.

The blocks $\mathbf{A_{23}}$ and $\mathbf{A_{32}}$ can be eliminated using the following transformation:

$$\widetilde{\mathbf{A}} = \left(\begin{array}{c|c|c} \mathbf{A_{11}}(\sigma) & \widetilde{\mathbf{A}}_{\mathbf{12}}(\sigma) & \mathbf{A_{13}} \\ \hline \widetilde{\mathbf{A}}_{\mathbf{21}}(\sigma) & \widetilde{\mathbf{A}}_{\mathbf{22}}(\sigma) & \mathbf{0} \\ \hline \mathbf{A_{31}} & \mathbf{0} & \mathbf{0} \end{array}\right) = \mathbf{T_l}\ \mathbf{A}\ \mathbf{T_r}, \tag{13}$$

where

$$\mathbf{T_l} = \left(\begin{array}{c|c|c} \mathbf{I}_{[m]} & \mathbf{0} & \mathbf{0} \\ \hline -\mathbf{A_{23}}\mathbf{A_{13}^{-1}} & \mathbf{I}_{[2n-m-b]} & \mathbf{0} \\ \hline \mathbf{0} & \mathbf{0} & \mathbf{I}_{[m]} \end{array}\right) \quad , \qquad \mathbf{T_r} = \left(\begin{array}{c|c|c} \mathbf{I}_{[m]} & -\mathbf{A_{31}^{-1}}\mathbf{A_{32}} & \mathbf{0} \\ \hline \mathbf{0} & \mathbf{I}_{[2n-m-b]} & \mathbf{0} \\ \hline \mathbf{0} & \mathbf{0} & \mathbf{I}_{[m]} \end{array}\right). \tag{14}$$

The characteristic polynomial $p_1(\sigma)$ of the transformed matrix $\widetilde{\mathbf{A}}$ is

$$p_1(\sigma) = det(\widetilde{\mathbf{A}}) = det(\mathbf{T_l}) \cdot det(\mathbf{A}) \cdot det(\mathbf{T_r}) = det(\mathbf{A}) = p(\sigma). \tag{15}$$

Because the blocks used in the definition of $\mathbf{T_l}$ and $\mathbf{T_r}$ do not contain the eigenvalue σ, the determinants of these matrices are independent of the eigenvalue. Moreover, because each transformation matrix is a triangular matrix with diagonal entries equal to one, their determinants are equal to one. Therefore, the characteristic polynomial of the transformed matrix $\widetilde{\mathbf{A}}$, $p_1(\sigma)$ is exactly the characteristic polynomial of the original matrix $\mathbf{A}$, $p(\sigma)$; both polynomials have the same roots. The multiplication of $\mathbf{A}$ by $\mathbf{T_l}$ and $\mathbf{T_r}$ does not change the spectrum of the original problem.

The determinant of the transformed matrix may be calculated using the cofactor expansion of the matrix:

$$p_1(\sigma) = det(\widetilde{\mathbf{A}}) = det(\left(\begin{array}{c|c|c} \widetilde{\mathbf{A}}_{\mathbf{11}}(\sigma) & \widetilde{\mathbf{A}}_{\mathbf{12}}(\sigma) & \mathbf{A_{13}} \\ \hline \widetilde{\mathbf{A}}_{\mathbf{21}}(\sigma) & \widetilde{\mathbf{A}}_{\mathbf{22}}(\sigma) & \mathbf{0} \\ \hline \mathbf{A_{31}} & \mathbf{0} & \mathbf{0} \end{array}\right)) = det(\mathbf{A_{13}}) \cdot det(\left(\begin{array}{c|c} \widetilde{\mathbf{A}}_{\mathbf{21}}(\sigma) & \widetilde{\mathbf{A}}_{\mathbf{22}}(\sigma) \\ \hline \mathbf{A_{31}} & \mathbf{0} \end{array}\right)) =$$

$$-det(\mathbf{A_{13}}) \cdot det(\mathbf{A_{31}}) \cdot det(\widetilde{\mathbf{A}}_{\mathbf{22}}(\sigma)) = \kappa \cdot det(\widetilde{\mathbf{A}}_{\mathbf{22}}(\sigma)) = \kappa \cdot p_2(\sigma).$$

Consequently, the characteristic polynomial of the original matrix, $p(\sigma)$, is proportional to the characteristic polynomial of the $(2n-m-b) \times (2n-m-b)$ matrix $\widetilde{\mathbf{A}}_{\mathbf{22}}$; both polynomial have the same roots. Because the matrix $\widetilde{\mathbf{A}}_{\mathbf{22}}$ is non-singular, the number of roots of its characteristic polynomial is $2n-m-b$, the number of finite eigenvalues of the original problem. The number of infinite eigenvalues is twice the number of degrees of freedom associated with the mass conservation equation plus the infinite eigenvalues that come from essential boundary conditions, i.e. $2m+b$.

Because the infinite eigenvalues were eliminated by the transformations, the generalized eigenvalue problem (GEVP) can be transformed into a simple eigenvalue problem (EVP) ($\widetilde{\mathbf{M}}_{\mathbf{22}}$ is not singular):

$$\left(-\sigma\ \widetilde{\mathbf{M}}_{22} + \widetilde{\mathbf{J}}_{22}\right)\mathbf{c} = 0 \quad \Rightarrow \quad \underbrace{\widetilde{\mathbf{M}}_{22}^{-1}\widetilde{\mathbf{J}}_{22}}_{\mathbf{D}}\,\mathbf{c} = \sigma\mathbf{c} \tag{16}$$

The computational cost of the proposed matrix transformations corresponds to the cost of inverting two $m \times m$ matrices and one $(2n-m-b) \times (2n-m-b)$ matrix. The benefits is that the complete physically relevant spectrum of the original problem can be evaluated by solving a simple EVP that is approximately $1/3$ of the size of the original GEVP.

4. Example: Stability of Plane Couette Flow

4.1. Perturbed Equations and Solution Method

The method described in the previous section to eliminate the infinite eigenvalues of the spectrum is applied to study the stability of plane Couette flow.

The flow geometry and boundary conditions are shown in Fig.1: liquid flows between two parallel plates located at $y = \pm 1$ that are moving with velocity $U = \pm 1$.

The steady state solution is $\mathbf{v_0} = (y, 0, 0)$ and $p_0 = 0$. The base flow is perturbed as

$$\mathbf{v}(x,y,t) = \mathbf{v_0}(y) + \epsilon\ \mathbf{v}'(y)e^{i\alpha x+\sigma t} \text{ and } p(x,y,t) = p_0(y) + \epsilon\ p'(y)e^{i\alpha x+\sigma t}. \tag{17}$$

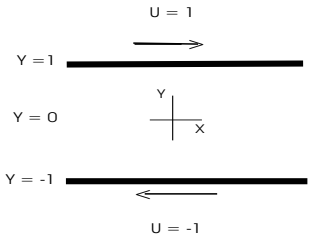

Figure 1: Configuration of plane Couette flow.

For simplicity, only two-dimensional perturbation was considered. α is the wavelength of the periodic perturbation along the flow direction. Substituting the perturbed fields into the transient conservations equations and neglecting the higher order terms ($\mathcal{O}(\epsilon^2)$), a system of differential equations on the perturbed variables, e.g. $\mathbf{v}' = (u', v')$ and p', is obtained:

$$
\begin{aligned}
& i\alpha u' + \frac{dv'}{dy} = 0, \\
& Re[(\sigma + i\alpha y)u' + v'] = -i\alpha p' + \frac{d^2u'}{dy^2} - \alpha^2 u', \\
& Re[(\sigma + i\alpha y)v'] = -\frac{dp'}{dy} + \frac{d^2v'}{dy^2} - \alpha^2 v'.
\end{aligned}
\tag{18}
$$

This system of equation can be manipulated to eliminate the pressure field, and by using the definition of stream function, a fourth order operator on the amplitude of the perturbed stream function can be obtained (the Orr-Sommerfeld operator).

It is common practice to analyze the stability of Couette flow by working with the Orr-Sommerfeld operator. The fourth-order operator is usually discretized by spectral methods. An example of such procedure is presented by Dongarra *et al.*, 1996, that used Chebyshev-τ method to discretize the Orr-Sommerfeld equation and QZ method to solve the generalized eigenvalue problem. They reported that the singularity of the mass matrix $\mathbf{M}$ might account for the appearance of the spurious eigenvalues.

In this work, instead of using stream function formulation (Orr-Sommerfeld equation), the stability analysis is formulated in terms of primitive variables, i.e. velocity and pressure eqs.(18). At a fixed wave number α, the amplitude of the perturbation u', v' and p', and its growth rate σ are found by applying Galerkin's weighted residual method to eqs.(18), as explained in the previous section. In this example, the velocity perturbations are expanded using piecewise Lagrangian quadratic polynomials ϕ_j and the pressure perturbation are approximated using piecewise linear discontinuous polynomials χ_j.

At each row corresponding to the Dirichlet boundary condition applied at both walls, e.g. $u' = 0$ and $v' = 0$, all the entries of the mass and jacobian matrices are equal to zero, except the diagonal entry of the jacobian matrix, which is equal to one.

4.2. Filtering the infinite eigenvalues

In order to illustrate the structure of the matrices at each step of the process of filtering the infinite eigenvalues for the plane Couette flow, a case with only three finite elements is discussed first. For this discretization level, the total number of degrees of freedom of the problem is $N = 2n + m = 20$, as $n = 7$ and $m = 6$. The scheme used to number the elements, nodes and degrees of freedom of the problem is illustrated in Fig.2.

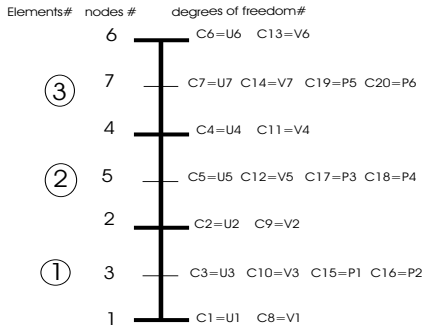

Figure 2: Numbering scheme for elements, nodes and degrees of freedom for a mesh with three finite elements.

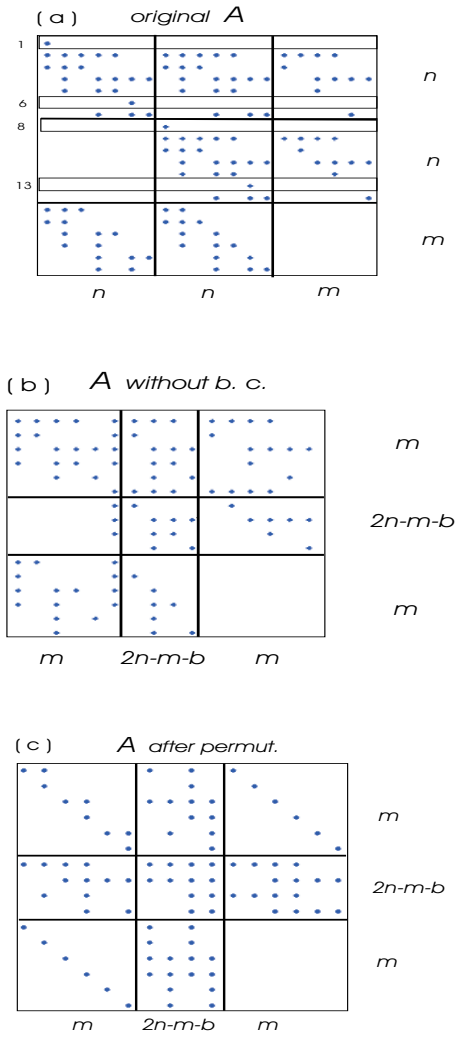

Figure 3: Example of the structure of the matrix $-\sigma\mathbf{M}+\mathbf{J}$ during the different steps of the proposed procedure. (a) Structure of the original matrix $\mathcal{A}$; (b) structure of the matrix after eliminating rows and columns associated with the Dirichlet boundary conditions $\mathbf{A}$; (c) Structure of the matrix after permutation of rows and columns to create diagonal sub-matrices that are easy to invert.

The structure of the non-zero entries of the matrix $\mathcal{A} = -\sigma\mathbf{M} + \mathbf{J}$ is shown in Fig.3(a). The only entries in rows $1, 6, 8$ and 13 (the ones associated with the Dirichlet boundary conditions) different than zero are the diagonal elements, that are equal to one. As explained before, the first step is to remove the rows and columns associated with the essential boundary conditions. The structure of the resulting matrix is shown in Fig.3(b). The next step is to eliminate the blocks $\mathbf{A_{32}}$ and $\mathbf{A_{23}}$ using the transformation defined in eq.(14). In order to

construct the transformation matrices $\mathbf{T_l}$ and $\mathbf{T_r}$, the inverse of the blocks $\mathbf{A_{13}}$ and $\mathbf{A_{31}}$ need to be evaluated. In the particular case of a one-dimensional problem, like this one, it is possible use the structure of the matrix to minimize the time to compute the inverse of these sub-matrices. A permutation of the first $2n-b$ columns and the first $2n-b$ rows will lead to the matrix structure shown in Fig.3(c). The blocks $\mathbf{A_{13}}$ and $\mathbf{A_{31}}$ became diagonal matrices, and the evaluation of the inverse is extremely fast. The structure of the resulting transformed matrix $\widetilde{\mathbf{A}} = \mathbf{T_l}\ \mathbf{A}\ \mathbf{T_r}$ is shown in Fig.4. All the information on the spectrum of the original problem is contained in the $(2n-m-b)\times(2n-m-b)$ central block in the transformed matrix (4×4 in this particular case), indicated in Fig.4.

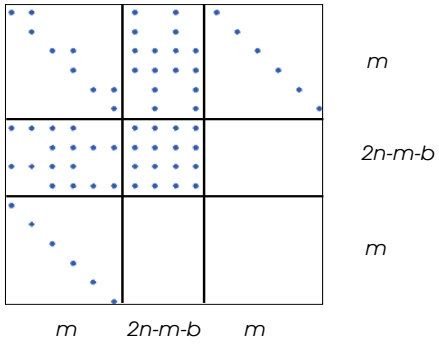

Figure 4: Structure of final transformed matrix $\widetilde{\mathbf{A}}$. The complete finite portion of the eigenspectrum of the original problem is contained in the center $(2n-m-b)\times(2n-m-b)$ block.

4.3. Results

To compare the spectrum of the plane Couette flow predicted with the method described in this work with the one presented by Bottaro *et al.*, 2003, the analysis was performed at $Re = 500$ and $\alpha = 1.5$.

In order to verify the independence of the predicted eigenvalues to the level of the discretization (number of elements), the spectrum of the original generalized eigenproblem — eq.(9) — was solved using QZ method. The leading (largest real part, not considering the infinite numbers) eigenvalues predicted with three different meshes are shown in Fig. 5, together with the results presented by Bottaro *et al.*, 2003. In the range of $-3.5 < \Re(\sigma) < 0$, doubling the number of elements from 100 to 200 did not affect the predicted spectrum. A mesh of 100 elements was considered to be fine enough to predict the leading eigenvalues of the problem. The results obtained with the formulation based on the primitive variables (velocity and pressure) and discretization by Galerkin's / Finite Element method agree well with the one obtained by solving the Orr-Sommerfeld operator using Chebyshev-τ method.

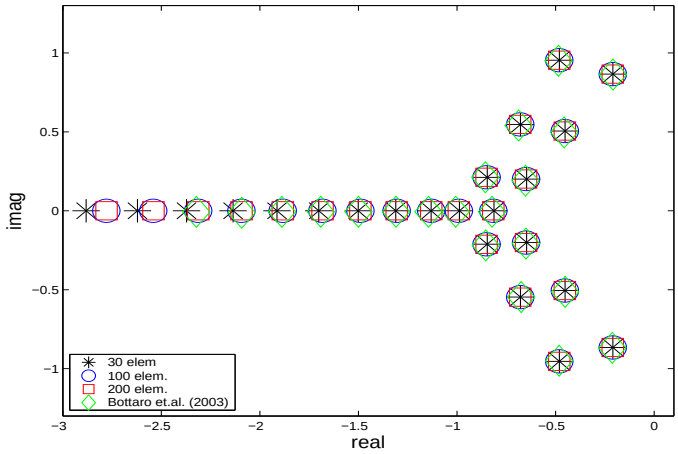

Figure 5: Leading part of the spectrum of plane Couette flow at $Re = 500$ and $\alpha = 1.5$ reported by Botaro and computed using the QZ method to solve the original GEVP with 30, 100 and 200 elements.

With 100 elements, the number of degrees of freedom of the problem (dimension of the original generalized eigenproblem) is $N = 602$, with $n = 201$, $m = 200$ and $b = 4$. After using the transformations presented here

to eliminate the infinite eigenvalues of the problem, the reduced matrix, that contains all the information of the spectrum of the problem, has a dimension of $2n - m - b = 198$. Considering that typically $\mathcal{O}(n) \simeq \mathcal{O}(m)$, the dimension of the original GEVP is $N = 2n + m \simeq \mathcal{O}(3n)$. Because the number of essential boundary conditions is usually much smaller than the number of degrees of freedom associated with each velocity component, i.e. $b << n$, the dimension of the reduced EVP is $2n - m - b \simeq \mathcal{O}(n)$, approximately 1/3 of the size of the original problem.

The reduced simple EVP (16) was solved by the LAPACK routine ZGEEV (for non-Hermitian matrix). As expected, the eigenvalues of the simple EVP corresponded to the finite portion of the spectrum of the GEVP. The leading eigenvalues computed with both formulations are shown in Fig.6; they are exactly the same.

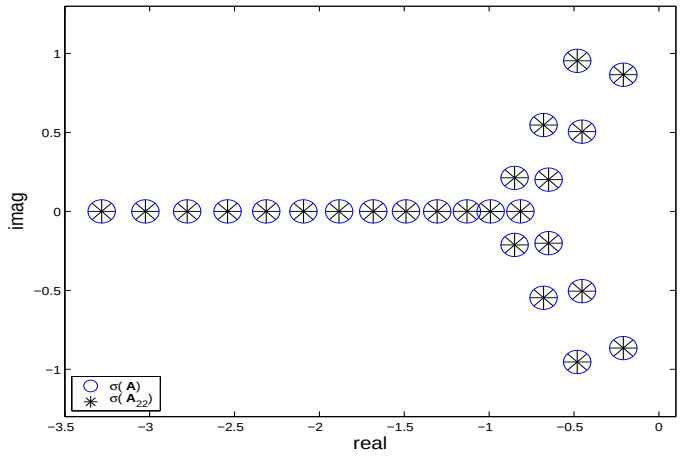

Figure 6: Comparison of the spectrum computed by solving the GEVP using the QZ method and by solving the reduced EVP.

The method presented in this work reduces significantly the time of computation. Table 1 presents the CPU time, in seconds, required to solve the original GEVP by the QZ method t_{GEVP} and to solve the reduced EVP by the LAPACK ZGEEV routine t_{EVP} for different meshes. The later includes the time to compute all the operations necessary to obtain the reduced EVP, which, as mentioned before, consists of inverting two $m \times m$ matrices, one $(2n-m-b) \times (2n-m-b)$ matrix, and some matrix-matrix products. In the particular case of the one-dimensional problem used as an example here, a simple row and column permutations transforms the sub-blocks into diagonal matrices, making the method even more efficient. The CPU time using the permutations, t^P_{EVP},is also presented in Table 1. All calculations were performed on a machine with 1.00 GB of RAM and 1.83 GHz Intel T-2400 processor using MatLab, version 6.5.

Table 1: CPU time, in seconds, required to compute the eigenvalues by the different methods: (a) solving the original GEVP by QZ method; (b) solving the reduced EVP using LAPACK routine; (c) solving the reduced EVP taking advantage of the matrix structure to invert the sub-blocks.

# ele	Size of original matrix	Size of transformed matrix	GEVP time	EVP time	EVP-Perm time	$\frac{t_{GEVP}}{t_{EVP}}$	$\frac{t_{GEVP}}{t^P_{EVP}}$
100	602	198	16.250	1.031	0.625	15.761	26.000
150	902	298	55.547	3.281	1.921	16.934	28.915
200	1202	398	131.438	7.031	4.219	18.694	31.1538
300	1802	598	474.750	27.422	14.547	17.312	32.635
350	2102	698	791.657	46.906	21.578	16.883	36.688

The proposed method is faster by a factor of approximately 17 for $N > 600$. The speed up is even greater (factor of approximately 35) if the matrix structure of the one-dimensional problem is taken into account to optimize the inversion of the two sub-matrices during the process of obtaining the reduced EVP.

5. Final Remarks

A new method to eliminate the "infinite eigenvalues" of the generalized eigenvalue problem that arises from linear stability analysis of incompressible flows is presented. The algorithm transforms the original generalized eigenproblem (GEVP) into an equivalent simple eigenvalue problem (EVP), whose dimension is approximately 1/3 of the original problem. The eigenvalues of the transformed EVP correspond exactly to the finite eigenvalues of the original GEVP.

The main advantages of the proposed methods are:

- Eliminates the "infinite eigenvalues" without the need of mapping or preconditioning techniques, which are computationally expensive;
- Reduces the size of the eingenproblem without loss of accuracy. Previous methods that reduced the size of the eigenproblem were restricted to creeping flow analysis (zero Reynolds number) or penalty methods;
- The transformed and smaller mass matrix is non-singular and consequently, the original GEVP can be easily re-written as a simple EVP.

All the above features bring significant reduction on the computational cost required to evaluate the eigenspectrum of an incompressible flow. In the example presented here, the proposed method was faster by an order of magnitude (factor of approximately 17) when compared to the solution of the original GEVP.

The analysis also shows that the number of infinite eigenvalues of a incompressible viscous flow is actually larger than that proposed by Christodoulou and Scriven, 1988; it is equal to twice the number of residual equations associated with the mass conservation equations (twice the number of degrees of freedom associated with the pressure field) plus the number of residuals associated with essential boundary conditions on velocity.

Although the formulation and the example used in this work was of a linear stability analysis of incompressible flow, this procedure may be also used to any generalized eigenproblem that comes from linear stability analysis with algebraic restriction (like incompressibility, for example).

6. Acknowledgements

Juliana Vianna Valério was supported by a fellowship from the Science Foundation of State of Rio de Janeiro (FAPERJ). This work was funded by grants from the Brazilian Research Council (CNPq).

7. References

Arora, K. and Sureshkumar, R., 2002, Efficient computation of the eigenspectrum of viscoelastic flows using submatrix-based transformation of the linearized equations., "Journal of non-Newtonian Fluid Mechanics.", Vol. 104, pp. 75–85.

Bottaro, A., Corbett, P., and Luchini, P., 2003, The effect of base flow variation on flow stability, "Journal of Fluid Mechanics.", Vol. 476, pp. 293–302.

Carvalho, M. S. and Scriven, L. E., 1999, Three-dimensional stability analysis of free surface flows: Application to foward deformable roll coating, "Journal of Computational Physics.", Vol. 151, pp. 534–562.

Christodoulou, K. N. and Scriven, L. E., 1988, Finding leading modes of a viscous free surface flow: an asymmetric generalized eigenproblem., "Journal of Scientific Computation", Vol. 03, pp. 355–406.

Coyle, D. J., Macosko, C. W., and Scriven, L. E., 1990, Stability of symmetric film-splitting between counter-rotating cylinders, "Journal of Fluid Mechanics.", Vol. 216, pp. 437–458.

Dongarra, J. J., Straugham, B., and Walker, D. W., 1996, Chebyshev tau-QZ methods for calculating spectra of hydrodynamic stability problems, "App. Numer. Math.", Vol. 22, pp. 399–434.

Ramanan, N. and Homsy, G. M., 1994, Linear stability of lid-driven cavity flow, "Physics and Fluids.", Vol. 06, No. 08, pp. 2690–2701.

Ruschak, K. J., 1983, A three-dimentional linear stability analysis for two-dimentional free boudary flows by the finite-element method, "Computers and Fluids.", Vol. 11, No. 04, pp. 391–401.

Saad, Y., 1996, "Iterative methods for saprse linear systems", PWS publishing N.Y.

Severtson, Y. C. and Aidun, C. K., 1995, Stability of two-layer stratified flow in inclined channels: application to air entrainment in coating systems, "Journal of Fluid Mechanics.", Vol. 312, pp. 173–200.

Sureshkumar, R., 2004, Stability analysis using compressible viscoelastic formulations., "Journal of non-Newtonian Fluid Mechanics.", Vol. 116, pp. 471–477.

Paper CIT06-0871

SIMULAÇÃO NUMÉRICA DE ESCOAMENTOS SOBRE AEROFÓLIOS MÓVEIS USANDO O MÉTODO DE FRONTEIRA IMERSA

José Eduardo Santos Oliveira
Universidade Federal de Uberlândia - FEMEC - LTCM
Campus Santa Mônica - Av. João Naves de Ávila, 2.121 CEP 38.400-902 Uberlândia - MG
email: jesoliveira@gmail.com

Ana Lúcia Fernandes de Lima e Silva
Universidade Federal de Itajubá - IEM
Campus Prof. José Rodrigues Seabra - Av. BPS, 1.303 CEP 37.500-903 - Itajubá - MG
email: alfsilva@unifei.edu.br

Aristeu da Silveira Neto
Universidade Federal de Uberlândia - FEMEC - LTCM
Campus Santa Mônica - Av. João Naves de Ávila, 2.121 CEP 38.400-902 Uberlândia - MG
email: aristeus@mecanica.ufu.br

Resumo. *No presente trabalho são apresentados resultados da simulação numérica de escoamentos sobre um aerofólio em movimento oscilatório de arfagem. O escoamento obtido através da solução das equações de Navier-Stokes em uma malha cartesiana a geometria do corpo imerso é representado através do método da fronteira imersa com o modelo físico virtual (IB/VPM). A metodologia dispensa o procedimento de remalhagem, necessário nos métodos clássicos e por isso é uma ferramenta promissora. No presente trabalho é estudado o efeito da freqüência reduzida nos coeficientes de forças aerodinâmicas e na formação das estruturas típicas do escoamento a Reynolds* 10^4 *sobre um aerofólio NACA 0012 oscilando em movimento harmônico. Os resultados foram comparados a trabalhos experimentais e numéricos, comprovando a potencialidade da metodologia.*

Palavras chave: *fronteira imersa, modelo físico virtual, fronteiras móveis, aerofólio, arfagem*

1. Introdução

Escoamentos sobre corpos imersos em movimento sempre foram objeto de estudos de cientistas e engenheiros, principalmente em aerodinâmica, onde o cálculo das forças que o escoamento exerce sobre uma determinada estrutura é de crucial importância. Um dos mais clássicos exemplos de problemas envolvendo fronteiras móveis é certamente o chamado fenômeno de estol dinâmico (*dynamic stall*) que é estudado desde a década de 70. Sua importância advém por estar presente em muitas aplicações práticas, podendo citar, escoamentos sobre rotores de helicópteros, turbomáquinas, manobras de aeronaves e mais recentemente estudos em bio-fluidodinâmica e micro-aviões, como tem sido relatado na literatura (McCroskey, 1981; Carr, 1988; Carr e Chandrasekhara, 1996; Ekaterinaris e Platzer, 1997 e Mittal, 2004). O termo estol dinâmico é utilizado para descrever o processo transiente no qual a força de sustentação cai repentinamente enquanto o ângulo de ataque de um aerofólio aumenta. O fenômeno se diferencia da situação de estol comum que ocorre em aerofólios estáticos. Pelo fato do aerofólio estar em movimento o estol pode ser postergado para ângulos de ataque superiores ao da situação estática. Nesta situação as cargas devidas às forças aerodinâmicas tendem a ser mais severas. Os eventos do estol dinâmico possuem uma forte dependência temporal com relação à movimentação do aerofólio, de forma que se torna quase impossível obter resultados realísticos quando se despreza a movimentação do corpo e sua interação com o escoamento.

No presente trabalho, pretende-se estudar numericamente, a influência da velocidade de movimentação dos aerofólios no comportamento transiente dos coeficientes de força aerodinâmica e na formação das estruturas características do escoamento. Foi escolhido um escoamento a número de Reynolds 10^4 , sobre um aerofólio NACA 0012 em movimento oscilatório de arfagem. O escoamento é resolvido através da solução numérica das equações de Navier-Stokes considerando uma aproximação bi-dimensional, com modelagem da turbulência. Utilizou-se o modelo de turbulência Spalart-Allmaras que foi escolhido segundo resultados de um estudo previo mostrado por Oliveira *et al.*, 2006.

Foram realizadas simulações em três diferentes velocidades de movimentação. Para modelar o cormo imerso no escoamento, é utilizado um método baseado no conceito de fronteira imersa proposto por Peskin, 1972. O método é denominado Modelo Físico Virtual (MFV) e foi proposto no Laboratório de Transferência de Calor e Massa e Dinâmica

dos Fluidos (LTCM/UFU) por Lima e Silva *et al.*, 2003. Esta metodologia se apresenta como uma alternativa eficiente aos métodos clássicos de 'body-fitted' no tratamento de problemas com interfaces móveis, uma vez que dispensa o procedimento de reconstrução da malha.

2. Modelo Matemático

A principal idéia associada aos métodos de fronteira imersa é o uso de duas malhas geometricamente independentes para a modelagem de corpos imersos em um escoamento. Com isso, busca-se evitar a necessidade de utilizar no domínio ocupado pelo fluido malhas complexas que se ajustam à geometria do corpo. Uma malha fixa, denominada euleriana, é usada para na discretização das equações governantes do fluido. A outra malha, denominada lagrangiana, representa a interface sólido-fluido. As formulações matemáticas para o fluido e para a interface são apresentadas a seguir.

2.1. Equações de Navier-Stokes Filtradas

O domínio de cálculo é tratado como se estivesse ocupado somente pelo fluido sendo o corpo imerso modelado através do termo fonte de força adicionado às equações do movimento. O escoamento foi modelado pelas equações filtradas de Navier-Stokes, Eq. (1), onde foi utilizada a hipótese de Boussinesq para modelar o tensor sub-malha de Reynolds, que advém do processo de filtragem e pela equação da continuidade, Eq. (2). Para um escoamento incompressível de um fluido newtoniano com propriedades constantes, tem-se:

$$\frac{\partial\left(u_i\right)}{\partial t}+\frac{\partial}{\partial x_j}\left(u_i u_j\right)=-\frac{1}{\rho}\frac{\partial p}{\partial x_i}+\frac{\partial}{\partial x_j}\left[\nu\left(\frac{\partial u_i}{\partial x_j}+\frac{\partial u_j}{\partial x_i}\right)\right]+f_i, \tag{1}$$

$$\frac{\partial u_i}{\partial x_i}=0, \tag{2}$$

As equações acima são resolvidas na malha euleriana e o acoplamento com a malha lagrangiana é feito pelo termo fonte de força (f_i), que é diferente de zero somente sobre a interface imersa. Este processo de troca de informações entre as duas malhas é representado matematicamente pela Eq. (3), onde a força lagrangiana (F_i) é distribuída para os pontos da malha euleriana ($\vec{x}$) mais próximos da interface ($\vec{x}_k$):

$$\vec{f}\left(\vec{x},t\right)=\int_{\Gamma}\vec{F}\left(\vec{x}_k,t\right)\delta\left(\vec{x}-\vec{x}_k\right)d\vec{x}_k \tag{3}$$

onde Γ representa a interface do corpo imerso e δ a função núcleo de Dirac.

2.2. Modelo Físico Virtual

O MFV avalia de maneira dinâmica a força exercida pelo fluido sobre o corpo imerso. A força $\vec{F}(\vec{x}_k,t)$ é calculada sobre os pontos lagrangianos usando a equação de conservação da quantidade de movimento. Assim a força lagrangiana é expressa por:

$$\vec{F}_i\left(\vec{x}_k,t\right)=\rho\frac{\partial\left(u_{k\,i}\right)}{\partial t}+\frac{\partial\left(p_{k\,j}\right)}{\partial x_{k\,j}}+\rho\frac{\partial}{\partial x_{k\,j}}\left(u_{k\,i}u_{k\,j}\right)-\frac{\partial}{\partial x_j}\left[\nu_{ef}\left(\frac{\partial u_{k\,i}}{\partial x_{k\,j}}+\frac{\partial u_{k\,j}}{\partial x_{k\,i}}\right)\right]. \tag{4}$$

Para o cálculo dos diferentes termos do lado direito da Eq. (4) é preciso conhecer a priori os campos de velocidade e pressão. Estes campos são dados pela solução numérica das equações de Navier-Stokes, e portanto, são conhecidos apenas na malha euleriana. Entretanto, o termo de força deve ser calculado sobre a interface lagrangiana. Para contornar este problema os campos eulerianos são interpolados sobre pontos lagrangianos auxiliares como mostrado por Lima e Silva *et al.*, 2003.

3. Modelagem da Turbulência

As equações de Navier-Stokes são capazes de simular com boa precisão uma extensa gama de problemas em engenharia, incluindo escoamentos turbulentos. Entretanto é necessário resolver todos os graus de liberdade do escoamento, o que é bastante caro computacionalmente. Uma maneira alternativa de tratar este tipo de problema é o uso de simplificações como o processo de filtragem proposto por Germano, 1986. Neste processo as equações governantes são apropriadamente filtradas, dando origem ao problema de fechamento da turbulência, que é atualmente resolvido com os modelos de turbulência. No presente trabalho é empregado o modelo de turbulência de Spalart-Allmaras descrito a seguir.

3.1. Modelo de Spalart-Allmaras

Spalart e Allmaras, 1994, propuseram um novo modelo a uma equação de transporte para o cálculo da viscosidade turbulenta. Este modelo tem sido usado com bastante sucesso na simulação de escoamentos aerodinâmicos. O modelo de Spalart-Allmaras usa uma variável de trabalho $\tilde{\nu}$ dada pela seguinte equação de transporte:

$$\frac{\partial \tilde{\nu}}{\partial t} + \frac{\partial}{\partial x_j}(u_j \tilde{\nu}) = c_{b1}\tilde{S}\tilde{\nu} - c_w f_w \left[\frac{\tilde{\nu}}{d_w}\right]^2 + \frac{1}{\sigma}\left[\frac{\partial}{\partial x_j}\left((\nu+\tilde{\nu})\frac{\partial \tilde{\nu}}{\partial x_j}\right) + c_{b2}\frac{\partial \tilde{\nu}}{\partial x_j}\frac{\partial \tilde{\nu}}{\partial x_j}\right] \tag{5}$$

onde os termos do lado direito representam, respectivamente: a produção de viscosidade turbulenta, o termo de destruição, o termo de difusão da viscosidade turbulenta e molecular, sendo o último termo a dissipação da viscosidade turbulenta.

A viscosidade turbulenta é definida em termos da variável de trabalho $\tilde{\nu}$ e de uma função de parede f_{v1}, dada por:

$$\nu_t = \tilde{\nu}\, f_{v1}. \tag{6}$$

4. Método Numérico

As equações governantes, Eq. (1) e (2), foram discetizadas no espaço usando o método de diferenças finitas, esquema CDS, e no tempo pelo método de Runge-Kutta de segunda ordem. O acoplamento pressão-velocidade feito pelo método de passo fracionado como proposto por Armfield e Street, 1999. O cálculo do campo de força sobre a interface e a solução das equações de momento foram feitos de maneira explícita.

O domínio de cálculo utilizado nas simulações tem um comprimento de $10c$ por uma altura de $8c$, onde c é a corda do aerofólio. Essas dimensões foram escolhidas de modo a minimizar os efeitos do contorno no desenvolvimento do escoamento. Testes para verificar a independência do resultado em relação a malha computacional foram executados. Utilizou-se uma malha não-uniforme com 278×198 pontos distribuídos em três regiões para cada direção, como ilustrado na Fig. (1). Na direção x a primeira seção tem 50 pontos e se estende até a posição $2,7c$. A última seção tem $5,8c$ de comprimento com 120 pontos. Na direção y as duas regiões de malha não-uniforme são idênticas e de comprimento $3,83c$, discretizadas com 84 pontos em cada região. O aerofólio foi posicionado dentro de uma caixa retangular de malha uniforme, de dimensões $1,5c$ de comprimento por $0,36c$ de altura.

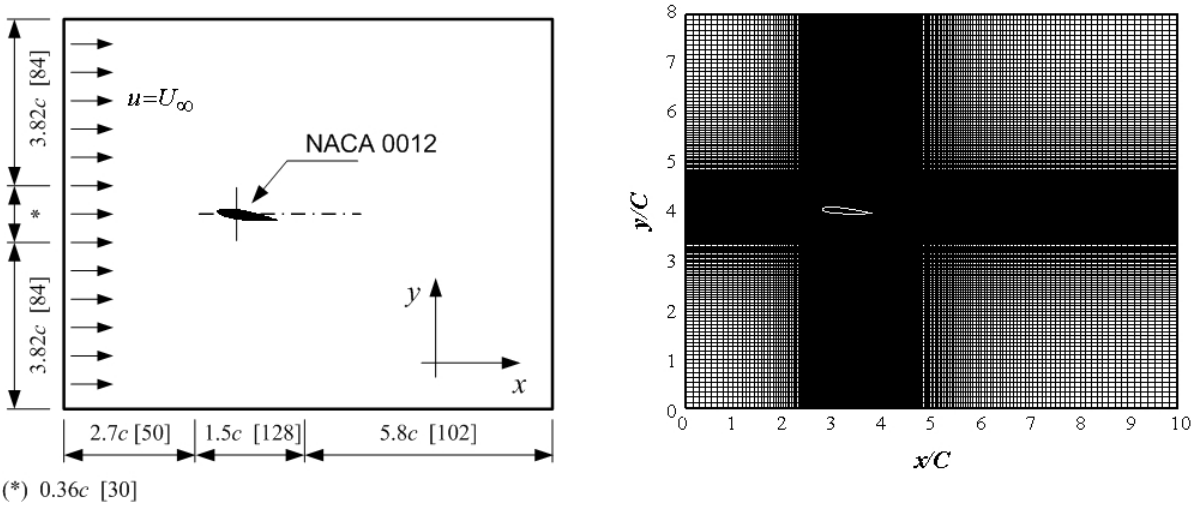

Figura 1: Esquema do domínio de cálculo e malha computacional utilizada.

Um perfil de velocidade uniforme $u = U_\infty$ foi imposto na entrada do domínio, de maneira que o escoamento ocorresse da esquerda para a direita (Fig. 1). Condições de contorno de Neumann foram impostas para a velocidade em todas as outras faces do domínio. Para a correção de pressão, foi imposta derivada nula na entrada do domínio e zero nas demais faces. Deve se destacar que malha euleriana permanece fixa e inalterada. Somente a malha lagrangiana se movimenta, através da variação do ângulo de ataque. Foi imposta uma movimentação oscilatória harmônica, em torno de um eixo posicionado no quarto de corda do aerofólio, dada por:

$$\alpha\,(t) = \bar{\alpha} + \Delta\alpha\ \sin\left(\Omega\, t\right), \tag{7}$$

onde $\bar{\alpha}$ é o ângulo de ataque médio e $\Delta\alpha$ é a amplitude de oscilação do movimento de arfagem. A velocidade angular do movimento é dada por $\Omega = 2\pi\ f$ e a freqüência de oscilação é representada pela variável f. Usualmente f é escrita em termos da freqüência reduzida κ, definida como:

$$\kappa = \frac{\pi\ f\ c}{U_\infty}. \tag{8}$$

5. Resultados e Dicussão

Um resumo dos casos simulados para aerofólios oscilantes é apresentado na Tab. (1). Os experimentos foram planejados de maneira a avaliar os efeitos do número de Reynolds e da freqüência reduzida no escoamento.

Tabela 1: Casos simulados para aerofólios em movimento oscilatório de arfagem.

	κ	$\bar{\alpha}$	$\Delta\alpha$	Re_c
Caso 1	0.15	15^o	10^o	1×10^4
Caso 2	0.25	15^o	10^o	1×10^4
Caso 3	0.50	15^o	10^o	1×10^4

Na Fig. (2) são mostrados os coeficientes de sustentação e arrasto para simulações a $Re_c = 10^4$, um ângulo médio de incidência igual a $\bar{\alpha} = 15^o$, uma amplitude de oscilação de $\Delta\alpha = 10^o$ e com o movimento oscilatório sendo executado no quarto de corda do aerofólio ($x/c = 0,25$). Foram simuladas três diferentes freqüências reduzidas: Fig. 2(a) $\kappa = 0,15$, Fig. 2(b) $\kappa = 0,25$ e Fig. 2(c) $\kappa = 0,50$. Observe que o movimento oscilatório imposto provoca histerese nos coeficientes de força. Este comportamento é atribuído às diferenças existentes entre os escoamentos que ocorrem sobre o aerofólio, já que a sua movimentação afeta significativamente a dinâmica de formação e desprendimento dos vórtices, principalmente, o descolamento e recolamento da camada limite.

Note que o efeito de histerese é observado em todas as simulações da Fig. (2), independente da freqüência reduzida. Entretanto, o comportamento é fortemente dependente da magnitude de κ. Nas Fig. 2(a) e Fig. 2(b) observando o coeficiente de sustentação, verifica-se que a histerese ocorre porque a força de sustentação durante o movimento ascendente do aerofólio é maior do que durante o movimento descendente, provocando um ciclo de histerese no sentido horário. Já para freqüência reduzida $k = 0,50$, Fig. 2(c), o ciclo de histerese ocorre no sentido anti-horário com a força de sustentação maior durante o decréscimo do ângulo de ataque. Sendo assim, os eventos que levam ao surgimento da histerese na força são essencialmente diferentes e dependem da freqüência reduzida, como será mostrado mais adiante.

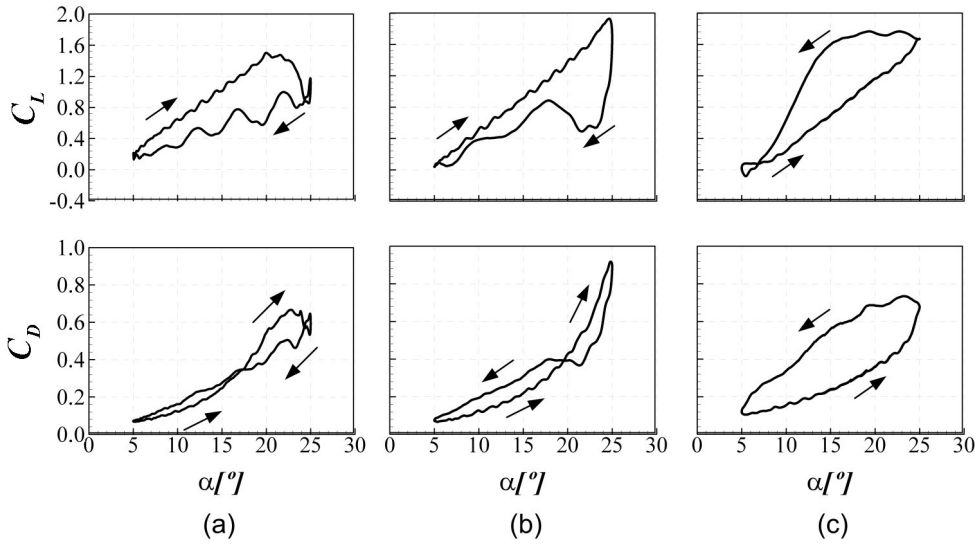

Figura 2: Histerese nos coeficientes de sustentação e arrasto para aerofólios em movimento oscilatório; freqüências reduzidas: (a) $\kappa = 0,15$ (b) $\kappa = 0,25$ e (c) $\kappa = 0,50$.

Outro efeito fortemente relacionado à freqüência reduzida é o atraso ou total supressão do estol durante o movimento de subida, como se pode observar na Fig. (3). O estol foi atrasado, em relação à situação estática que ocorre, segundo

simulações estaticas de Akbari e Prince, 2003, para $\alpha \approx 15^o$, para $\alpha \approx 21^o$, isso para a menor das freqüências reduzidas simuladas que foi $\kappa = 0,15$. Já para o caso $\kappa = 0,50$, não ocorre descolamento durante o movimento de subida e, em conseqüência, o estol é totalmente inibido. Pode-se então concluir que com aumento da freqüência reduzida o estol é postergado para maiores valores do ângulo de ataque α ou completamente inibido durante a subida.

Como pode-se verificar, um aerofólio oscilando em grandes amplitudes, acima do seu ângulo de ataque estático, apresenta grande histerese nos coeficientes aerodinâmicos. Conseqüência do aumento da complexidade dos eventos transientes na camada limite, o principal e mais influente dos eventos é, sem duvida, o crescimento e desprendimento de um vórtice de bordo de ataque (comumente conhecido na literatura como LEV do inglês *Leading-Edge Vortex*). Uma análise detalhada dos principais eventos do escoamento para cada caso simulado é apresentada nas Fig. (4), (5) e (6). Foram escolhidos pontos representativos dos principais eventos do escoamento. Nas figuras é também apresentada a visualização do campo instantâneo de vorticidade ($-50 \leq \omega_z \leq 50$) do respectivo ponto, para o último ciclo oscilatório. Pode-se assim, identificar e associar o efeito da estrutura característica do escoamento sobre o comportamento da força de sustentação.

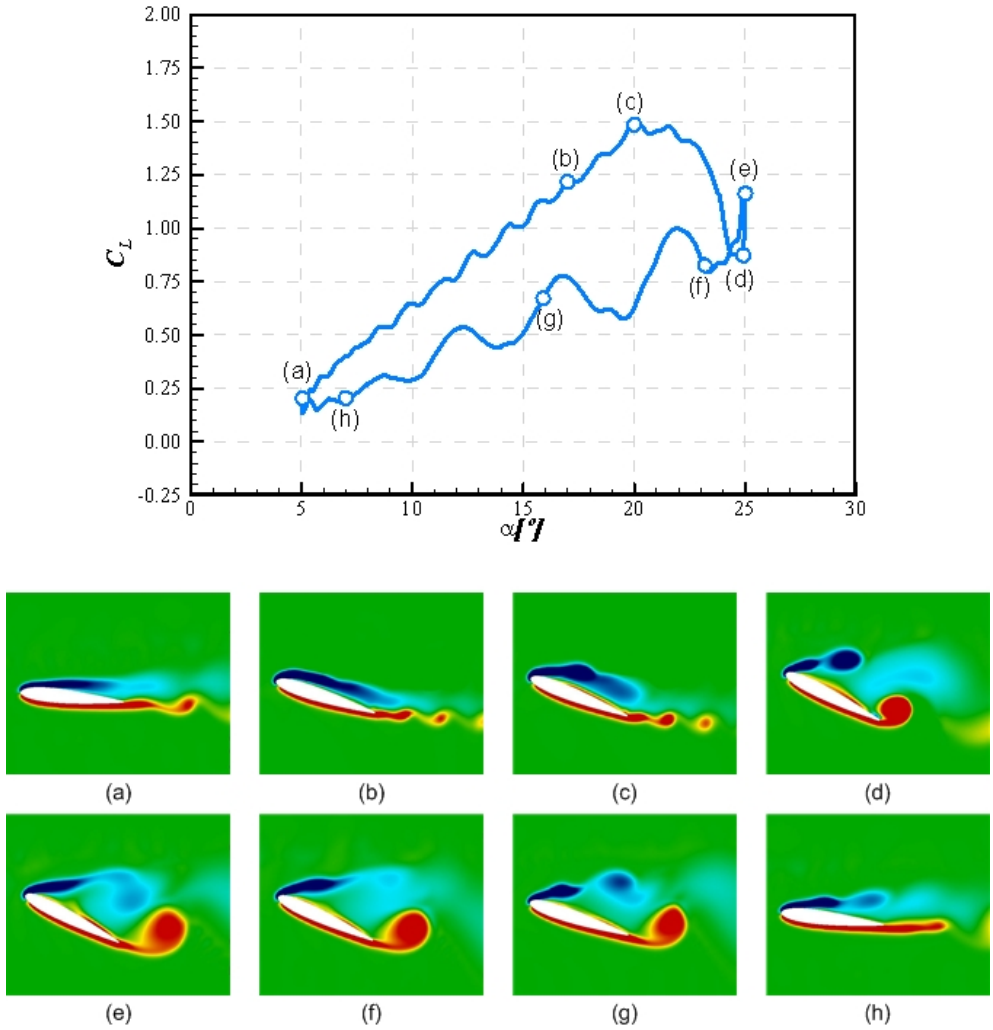

Figura 3: Eventos característicos do estol dinâmico no coeficiente de sustentação para o caso $\kappa = 0,15$.

Na Fig. (4) estão representados os principais eventos durante o ciclo de histerese para a força de sustentação relativos a freqüência reduzida $\kappa = 0,15$. Inicia-se um novo ciclo a partir da posição de $\alpha_{\min} = 5^o$, ponto (a), neste instante o escoamento está ainda junto ao aerofólio. O coeficiente de sustentação aumenta com o aumento do ângulo de incidência, alcançando o ponto (b), superando o ponto de estolagem estática. Já é possível visualizar a formação de uma bolha junto ao bordo de fuga do aerofólio, indicando o aparecimento de escoamento reverso no extradorso do aerofólio. No ponto (c), o coeficiente de sustentação alcança o valor máximo e o escoamento reverso já está sobre quase toda a superfície do aerofólio. Em seguida ocorre o estol em $\alpha \approx 21^o$. No ponto (d) o coeficiente de sustentação alcança o menor valor

durante o movimento de subida. O escoamento já está totalmente descolado quanto se inicia o crescimento de um novo LEV que provoca um aumento súbito da sustentação no final do movimento de subida, ponto (e). O LEV é transportado em direção ao bordo de fuga, causando redução do coeficiente de sustentação, trecho (e-f). Como durante o movimento de descida o escoamento já está descolado o coeficiente de sustentação é menor do que durante a subida, apresentando o efeito de histerese. As oscilações de grande amplitude, durante o movimento de descida, são devidos a formaçã o e desprendimento dos LEV. Finalmente ao final do ciclo, ponto H, o escoamento volta a recolar junto a parte superior do aerofólio.

Os eventos para a simulação na freqüência reduzida $\kappa = 0,25$ estão representados no diagrama da Fig. (5). Observa-se que existem diferenças relevantes entre o ciclo de histerese com respeito a freqüência $\kappa = 0,15$, as quais estão associadas às diferenças entre o tempo de formação das estruturas e seu deslocamento sobre o aerofólio. O estol ocorre agora próximo ao ângulo de incidência máximo $\alpha \approx 25^o$, ponto (d), onde o coeficiente de sustentação alcança também o máximo valor. O completo descolamento do escoamento é postergado para o ponto (e), já durante o movimento de descida, cabe aqui resaltar que o crescimento do primeiro LEV começou ainda durante o movimento de subida (d). As oscilações no coeficiente de sustentação indicam a formação e desprendimento de pelo menos 3 LEV durante decréscimo do ângulo de ataque e pelo menos 5 LEV verificados durante o movimento descentende para a simulação anterior (Fig. 4). O segundo LEV é bem visualizado pelas linhas de corrente, ponto (g). O recolamento ocorre no ponto (h) para ângulo de ataque $\alpha \approx 7^o$.

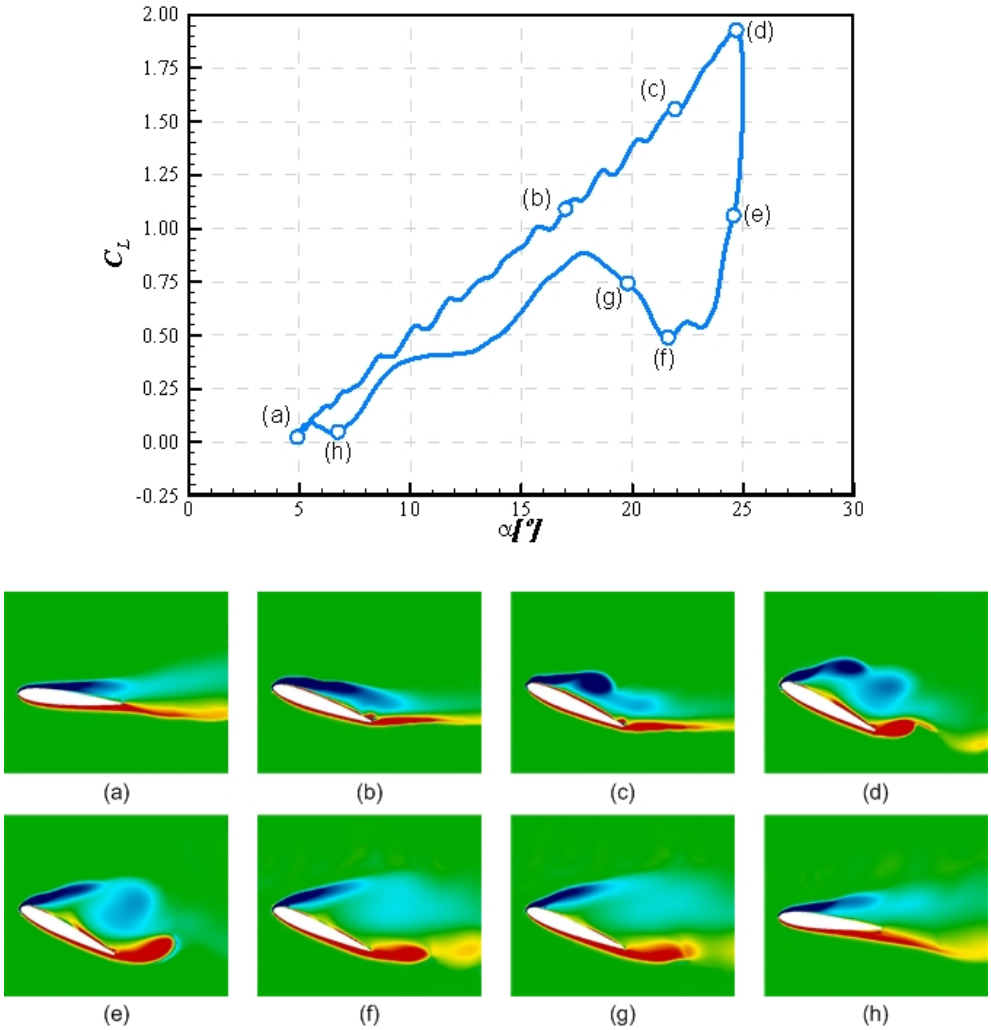

Figura 4: Eventos característicos do estol dinâmico no coeficiente de sustentação para o caso $\kappa = 0,25$.

O ciclo de histerese obtido na simulação para o último caso simulado apresenta diferenças consideráveis com relação às outras simulações. Como já foi observado anteriormente os ciclos de histerese ocorreram no sentido anti-horário. Como se sabe a formação do vórtice no bordo de ataque é o principal responsável pelo aumento no coeficiente de sustentação,

devido à sucção que ele induz na superfície superior do aerofólio. Note que esta freqüência de oscilação do aerofólio é bastante elevada e acaba por inibir a formação de vórtices durante o movimento de subida do aerofólio e a formação do primeiro vórtice ocorre somente no final da subida (d) de forma bem incipiente.

No ponto (e), o LEV já se encontra desenvolvido quando então começa a ser advectado ao longo do aerofólio, provocando aumento na força de sustentação durante a movimentação de descida. O descolamento total do escoamento ocorre no ponto (g), já com o ângulo de ataque em $\alpha \approx 15^o$. Como a movimentação do aerofólio é bastante rápida, não ocorre o desenvolvimento de nenhum outro LEV e todo ciclo de oscilação é completado com o desprendimento de apenas um vórtice. Observe que não há tempo para o escoamento se recuperar do descolamento. Como se pode ver, as linhas de corrente próximas ao bordo de ataque, ponto (h), não estão alinhadas com a superfície do aerofólio, apresentando instabilidades que caracterizam a presença de estruturas no escoamento. O coeficiente de sustentação alcança valores negativos para valores bem próximos do ângulo de ataque mínimo $\alpha_{\min} = 5^o$, ainda durante o movimento de descida. Como não ocorre o recolamento, o aumento do coeficiente de sustentação, do ponto (h) para (a), se deve ao início do movimento de subida do próximo ciclo.

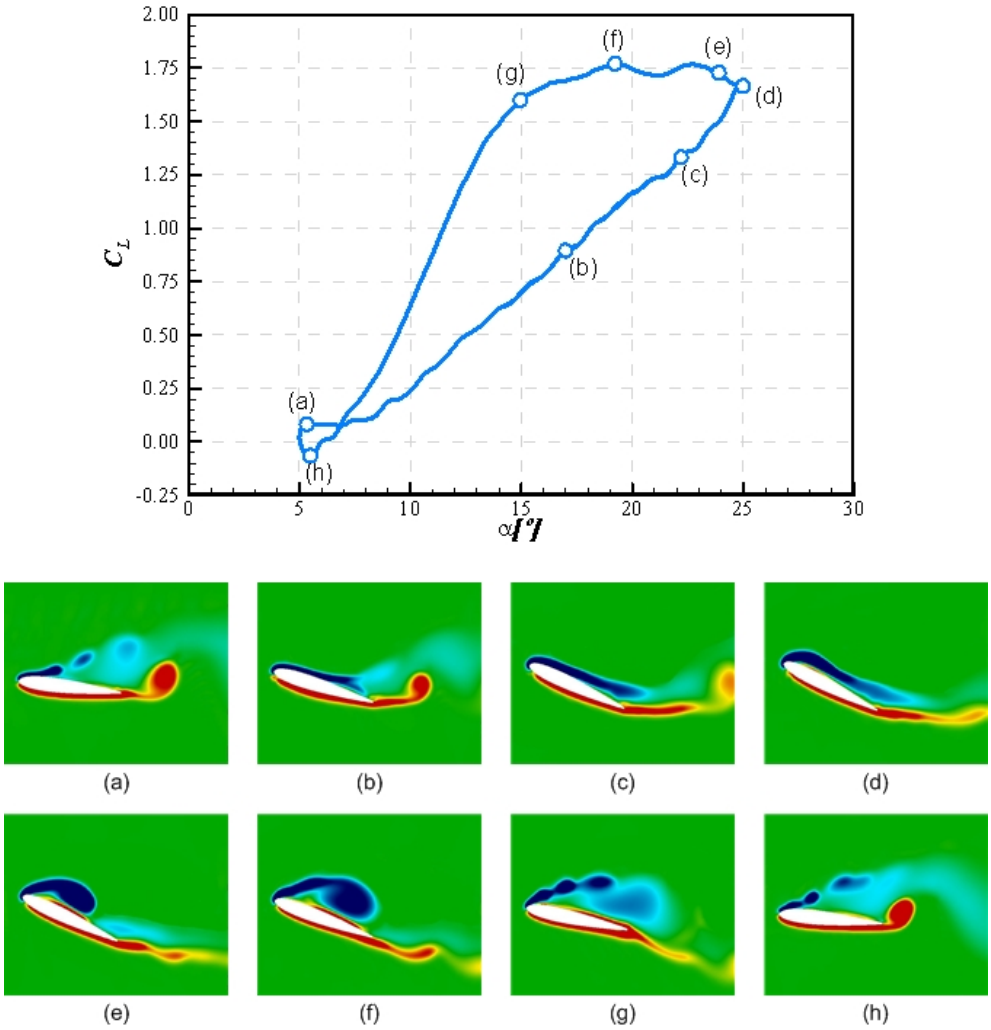

Figura 5: Eventos característicos do estol dinâmico no coeficiente de sustentação para o caso $\kappa = 0, 50$.

Comparações com resultados numéricos (Fig. 7) são mostradas a seguir. Os resultados numéricos foram obtidos por Akbari e Prince, 2003, que utilizaram formulação vorticidade-função corrente para resolver as equações de Navier-Stokes para um escoamento incompressível. A malha computacional é fixa ao corpo imerso e se move juntamente com o aerofólio à medida em que ele oscila no tempo. Para efeito de comparação com os resultados dos autores são apresentados o coeficientes normal (C_N) e o de arrasto (C_D).

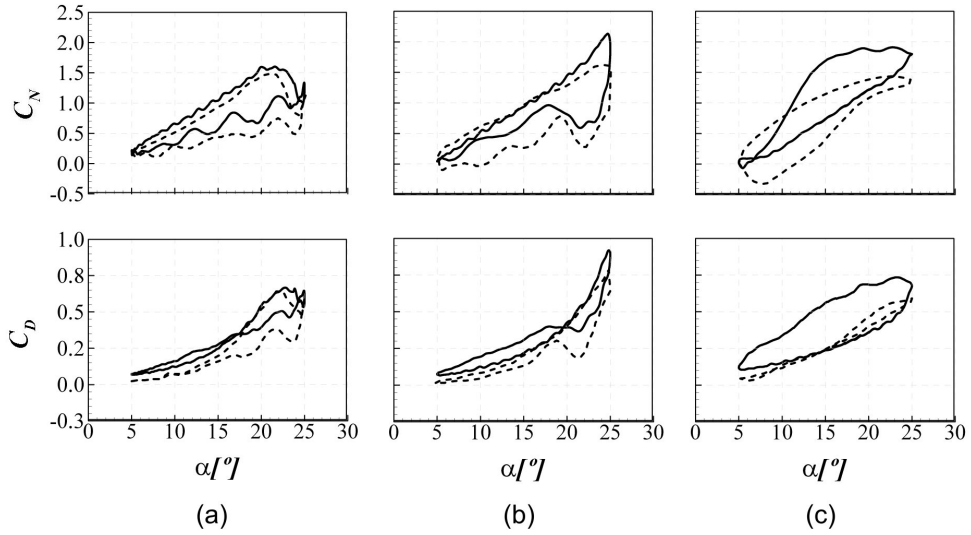

Figura 6: Comparação do ciclo de histerese nos coeficientes normal e de arrasto: —— presente trabalho e - - - resultados numéricos de Akbari e Prince (2003); (a) $\kappa = 0,15$ (b) $\kappa = 0,25$ e (c) $\kappa = 0,50$.

O caso simulado para a freqüência reduzida $\kappa = 0,15$, é apresentado na Fig. 7(a). Nesta simulação os resultados obtidos foram bastante similares em comportamento e magnitude. Durante o movimento ascendente do aerofólio é observado um desvio sistemático da ordem de 5% com relação aos resultados da referência (Akbari e Prince, 2003). Observe que o estol é previsto na mesma posição para ambas as simulações. De forma geral os eventos são bastante similares, inclusive o *overshot* do coeficiente normal que ocorre próximo ao ângulo máximo de incidência. O número de oscilações de grande amplitude, devido ao desprendimento de grandes LEV, ao longo do ciclo de histerese, é o mesmo. Somente ao final do movimento de descida que se observa diferença na posição onde os dois últimos vórtices se desprendem. No presente trabalho os vórtices se desprendem próximo a $\alpha = 15^o$ e a $\alpha = 10^o$ contra $\alpha = 12^o$ e $\alpha = 7,5^o$ nos resultados obtidos pelos autores. A histerese verificada por Akbari e Prince, 2003, é bem maior do que a observada em nossas simulações. Durante todo o movimento de descida o coeficiente normal calculado no presente trabalho apresentou valores aproximadamente 20% maiores. Também para o coeficiente de arrasto as diferenças são bastante significativas, sendo o valor calculado sempre superior aos resultados da referência. Próximo ao ângulo de ataque $\alpha \approx 16^o$ ocorre uma inversão no ciclo, ou seja, nesta posição a força de arrasto calculada durante o movimento descendente passa a superar os valores calculados durante o movimento ascendente. Evento semelhante foi observado no resultado usado como referência, porém com menor intensidade de modo que os resultados do arrasto durante a subida passaram a coincidir com os valores calculados durante a descida.

Na Fig. 7(b), para freqüência reduzida $\kappa = 0,25$, observou-se também um comportamento bastante semelhante. As maiores diferenças também ocorrem ao final do movimento descendente. Os resultados se assemelham em magnitude durante grande parte da subida, mas a diferença se acentua a partir do ângulo de ataque $\alpha \approx 20^o$. O aumento do coeficiente normal induzido pelo LEV é maior em nossa simulação, chegando a um valor de $C_N = 2,1$ contra um $C_N = 1,6$ da referência. Comparações para o último caso são mostradas na Fig. 7(c). De todas as simulações realizadas, as maiores diferenças foram observadas para esta freqüência. A característica mais marcante para esta freqüência reduzida é sem dúvida a inversão do ciclo de histerese, que passa a ocorrer no sentido anti-horário. Segundo as simulações de Akbari e Prince, 2003, a evolução do coeficiente normal com o aumento do ângulo de ataque segue no sentido horário, não tendo sido observada nenhuma inversão com relação as simulações para a freqüências reduzidas mais baixas. Comparando os resultados para esta freqüência reduzida, $\kappa = 0,50$, observa-se que as simulações não guardam nenhum tipo de semelhança no comportamento, tanto para a força normal quanto para o arrasto. Além disso, os valores também apresentam grande diferença em magnitude. Porém a inversão do ciclo de histerese é relatada experimentalmente já para $\kappa > 0,4$ em casos a Reynolds mais elevados, como mostrado por Panda e Zaman, 1994.

6. Conclusões

Simulações de escoamentos a Reynolds moderados sobre aerofólios em movimento foram realizadas com o modelo de turbulência de Spalart-Allmaras. Foi investigada as características e os mecanismo que dão origem ao estol dinâmico, fenômeno típico que ocorre neste tipo de escoamento. Com isto pôde-se também avaliar o uso do método IB/VPM em aplicações práticas de aeronáutica. Os resultados mostraram-se consistentes e com indicativos de uma razoável precisão. Foi simulado o escoamento sobre um aerofólio NACA 0012 em movimentos oscilatórios de arfagem em grandes am-

plitudes de movimentação A fenomenologia do estol dinâmico foi estudada e associada a eventos do escoamento, as observações estão em relativa concordância com trabalhos numéricos da literatura. A metodologia mostrou-se apropriada na investigação deste tipo de problema, que envolve corpos em movimento.

7. Agradecimentos

Os autores agradecem ao Conselho Nacional de Desenvolvimento Científico e Tecnológico e a Faculdade de Engenharia Mecânica da Universidade Federal de Uberlândia pelo auxílio financeiro.

8. Referências

Akbari, M. and Prince, S., 2003, Simulation of dynamic stall for a NACA 0012 airfoil using a vortex method, "Journal of Fluids and Structures", Vol. 17, pp. 855–874.

Armfield, S. and Street, R., 1999, The fractional-step method for the Navier-Stokes equations on staggered grids: the accuracy of three variations, "Journal of Computational Physics", Vol. 153, No. 2, pp. 660–665.

Carr, L., 1988, Progress in analysis and prediction of dynamic stall, "Journal of Aircraft", Vol. 25, No. 1, pp. 6–17.

Carr, L. and Chandrasekhara, M., 1996, Compressibility effects on Dynamic Stall, "Progress in Aerospace Sci", Vol. 32, pp. 523–573.

Ekaterinaris, J. and Platzer, M., 1997, Computational prediction of airfoil dynamic stall, "Progress in Aerospace Science", Vol. 33, pp. 759–846.

Germano, M., 1986, A proposal for a redefinition of the turbulent stresses in filtred Navier-Stokes equations, "Phys. Fluids", Vol. 29, No. 7, pp. 2323–2324.

Lima e Silva, A., Silveira-Neto, A., and Damasceno, J., 2003, Numerical Simulation of Two Dimensional Flows over a Circular Cylinder using the Immersed Boundary Method, "Journal of Computational Physics", Vol. 189, pp. 351–370.

McCroskey, W., 1981, The phenomenon of dynamic stall, "*NASA TM 81264*".

Mittal, R., 2004, Computational modeling in bio-hydrodynamics: Trends, challenges, and recent advances, "IEEE Journal of Oceanic Engineering", Vol. 29, pp. 595–604.

Oliveira, J. E. S., Lima e Silva, A. F. L., and Silveira-Neto, A., 2006, Influência de Modelos de Turbulência na Simulação de Escoamentos sobre Aerofólios Móveis usando o Método de Fronteira Imersa, "IV Congresso Nacional de Engenharia Mecânica".

Panda, J. and Zaman, K., 1994, Experimental investigation of the flow field of an oscilating airfoil and estimation of lift from wake surveys, "Journal of Fluid Mechanics", Vol. 265, pp. 65–95.

Peskin, C., 1972, Flow patterns around heart valves: A numerical method, "Journal of Computational Physics", Vol. 10, pp. 252–271.

Spalart, P. and Allmaras, S., 1994, A One-Equation Turbulence Model for Aerodynamic Flows, "La Recherche Aérospatiale", Vol. 1, pp. 5–21.

NUMERICAL SIMULATION OF FLOWS OVER A PITCHING AIRFOIL USING IMMERSED BOUNDARY METHOD

José Eduardo Santos Oliveira
Universidade Federal de Uberlândia - FEMEC - LTCM
Campus Santa Mônica - Av. João Naves de Ávila, 2.121 CEP 38.400-902 Uberlândia - MG
e-mail jesoliveira@gmail.com

Ana Lúcia Fernandes de Lima e Silva
Universidade Federal de Itajubá - IEM
Campus Prof. José Rodrigues Seabra - Av. BPS, 1.303 CEP 37.500-903 - Itajubá - MG
e-mail alfsilva@unifei.edu.br

Aristeu da Silveira-Neto
Universidade Federal de Uberlândia - FEMEC - LTCM
Campus Santa Mônica - Av. João Naves de Ávila, 2.121 CEP 38.400-902 Uberlândia - MG
e-mail aristeus@mecanica.ufu.br

Abstract. *In the present work a study of fluid flow behavior over airfoils in transient pitching moving is presented. The flow is simulated through the numeric solution of the Navier-Stokes equations in a Cartesian mesh the body was model using the Immersed Boundary Method with Virtual Physical Model. This methodology avoids the re-meshing procedure needed by the classical methods to handle moving boundary problems. In the present work the effect of reduced frequency in the aerodynamic force coefficients for a NACA 0012*

pitching airfoil at Reynolds 10^4 *was presented. The simulation was compared with numerical and experimental results available in the literature, the IB/VPM methodology show good results..*

Keywords *immersed boundary, virtual physical model, moving boundaries, pitching airfoil*

Paper CIT06-950

A Numerical Study of Turbulent Wake Flow Behind a Finite Cylinder

Luciano G. Noleto
Universidade de Brasília. Departamento de Engenharia Mecânica, LEA - Laboratório de Energia e Ambiente. 70910-900 Brasília. DF. Brazil.
lucianonoleto@unb.br

Antonio C. P. Brasil Junior
Universidade de Brasília. Departamento de Engenharia Mecânica, LEA - Laboratório de Energia e Ambiente. 70910-900 Brasília. DF. Brazil.
brasiljr@unb.br

Abstract. *In this work a numerical study concerning the turbulent flow over a finite cylinder attached on a flat plate is presented. The flow is simulated using three different methodologies: Unsteady Reynolds Averaged Navier Stokes equations (URANS), Detached Eddy Simulation (DES) and Large Eddy Simulation (LES). The results of the simulation have been used to study the turbulence characteristics in the wake flow behind the cylinder, and the interactions between the great structures of the unsteady flow, with the fine turbulence. Numerical simulations were performed with a finite volume method with unstructured tetrahedral meshes, which can promote a most adequate discretization for this kind of flow. The URANS and DES simulations were performed using SST model. This model is used for closuring of the averaged equation, and also as a subgrid model for the DES approach. The results show the average flow for the three methodologies, as well as velocity profiles compared with experimental results.*

keywords: *Large Eddy Simulation, Detached Eddy Simulation, URANS, Finite Cylinder, Vortex formation*

1. Introduction

The flow around a circular cylinder has several applications. One of them is at canopy flows, where the cylinder can represent an obstacle, being this obstacle one or several trees in a forest or buildings in a major city. The immediate engineering application is at fluid structure interaction. This happens at flows under bridges, oil platforms and buildings. The circular cylinder can be represented by a bluff body that shows 3-Dimensional altered flow characteristics in the axial direction. It is caused by the non-uniformity of free stream flow, longitudinal vortices and low aspect ratio of the cylinder. The flow pattern is a horseshoe vortex close to the wall that the cylinder is mounted, and depending of the flow characteristics, a vortex shedding is developed downstream, with a 3-Dimensional separated flow at the free end surface. The shedding is linked to the aspect ratio of the cylinder. The fact of the cylinder being finite influences the topology of the flow. The use of modern tools for numerical simulation of this kind of flow allows the capture of several turbulent phenomena inherent to the flow. Between those tools, there are large eddy simulation and, more recently, detached eddy simulation (Noleto and Brasil-Junior, 2005).

DES was tested in several cases of Large Eddy Simulation (LES), to check the reliability of the model for engineering cases. Constantinescu and Squires, 2003, investigated the flow over a sphere in super critical regime with LES and DES. The authors had concluded that the DES model accurately predict massively separated flows and it was able to predict also the large scale shedding of hairpin-like structures and the formation of Kelvin-Helmholtz instabilities. Squires *et al.*, 2002, made a analysis of massive separated flows in aircrafts using DES, concluding that the prediction of lift and drag are accurate in comparison with flight data, and also predicts with accuracy the pressure in the supersonic flow over the aircraft. The work of Forsythe *et al.*, 2001, is the use of detached eddy simulation to predict the flow over a forebody cross section, concluding that the predictions of the model are robust, with little differences between experimental data and the simulation. Frohlich and Rudi, 2004, made a numerical study of the flow past a finite cylinder using LES. The authors chose a cylinder aspect ratio of 2.5 in order to capture some vortex shedding. First, the results were analyzed in the light of subgrid modeling. With coarse grids, the dynamic model show deficient results when compared with the Smagorinsky model. Then the results were analysed in the light of physics, showing the existence of tip and arch vorticity in the average flow. Kanda *et al.*, 2004, performed LES at a simple cube array in order to study urban canopy flow. A comparison with experimental results is showed. Their results are analyzed using spatial and time averaging. It shows the presence of canyon-type flows between the cubes. The recirculation within the canopy had influenced the turbulent statistics.

Concerning to finite cylinder flows, there is the confirmation of the presence of a pair of vortices around the free end surface from iso-velocity lines in the wake near the tip region and this work identified this pair of vortices as trailing side tip vortices (Kawamura *et al.*, 1984). There is also a work (Baban *et al.*, 1989) who observed an increase in drag force fluctuations due to highly turbulent recirculation flow in the wake region, especially in the shear layer separated from the end of the cylinder. A visualization of the flow over the free end surface of a finite cylinder mounted on a flat plate using oil-streak line methods and smoke-laser. Roh and Park, 2003, showed that the flow at the free end surface is topologically characterized by two spiral nodes and a separation saddle point in the front portion and two attachment nodes and a separation saddle point in the rear part. A study of the free end effects in finite cylinder flows (Park and Lee, 2000) observed that the vortex shedding frequency decreases and the the vortex formation region increases as the aspect ratio decreases. The vortex formation region and periodic vortex shedding disappear very close to the free end. A experimental study of a small forest model based on a single cylinder and a cylinder matrix (Cala, 1996) in wind tunnel obtained profiles who holds great resemblance with similar work.

This paper will show results of the numerical simulation of a circular cylinder mounted in a flat plate with ANSYS-CFX commercial software. The used formulations were large eddy simulation, detached eddy simulation and URANS. The chosen case is the single cylinder studied by Cala, 1996.

2. Mathematical Modeling

2.1. Large Eddy Simulation

The large eddy simulation modeling uses a spatial averaging. The aim is to separate the small eddy from the large eddy. The large eddy is solved directly, and the small eddy is modeled using a subgrid model (Silveira-Neto, 2002, Lesieur and Métais, 1996, Silvestrini, 2003). The Navier-Stokes equations are given as follows:

$$\frac{\partial u_i}{\partial x_i} = 0 \tag{1}$$

$$\frac{\partial u_i}{\partial t} + \frac{\partial (u_i u_j)}{\partial x_j} = -\frac{1}{\rho}\frac{\partial p}{\partial x_i} + \nu \left[\frac{\partial}{\partial x_j} \left(\frac{\partial u_i}{\partial x_j} + \frac{\partial u_j}{\partial x_i} \right) \right] \tag{2}$$

u is the velocity, p is the pressure and ν is the kinematic viscosity. The separation of the eddies is performed as follows, for any given variable of the flow f:

$$f = \overline{f} + f' \tag{3}$$

The large eddy part $\overline{f}$ can be written as:

$$\overline{f}(x_i, t) = \int_V G(x_i - x_i') f(x_i, t) dx_i' \tag{4}$$

$G(x_i - x_i')$ is the tophat filter, written as follows:

$$G(x_i) = \begin{cases} \frac{1}{\Delta^3}; & \text{se } |x_i| \leq \frac{\Delta}{2} \\ 0; & \text{se } |x_i| > \frac{\Delta}{2} \end{cases} \tag{5}$$

Δ is the characteristic size of the filter. The filtered Navier-Stokes equations are given as follows:

$$\frac{\partial \overline{u}_i}{\partial x_i} = 0 \tag{6}$$

$$\frac{\partial \overline{u_i}}{\partial t} + \frac{\partial \overline{u_i u_j}}{\partial x_j} = -\frac{1}{\rho}\frac{\partial \overline{p}}{\partial x_i} + \nu \left[\frac{\partial}{\partial x_j} \left(\frac{\partial \overline{u}_i}{\partial x_j} + \frac{\partial \overline{u}_j}{\partial x_i} \right) \right] \tag{7}$$

Developing the convective part of equation 7 with equation 3 yields to:

$$\overline{u_i u_j} = \overline{u}_i \overline{u}_j + \overline{\overline{u_i} u_j'} + \overline{\overline{u_j} u_i'} + \overline{u_i' u_j'} + L_{ij} \tag{8}$$

Using 8 yields the filtered Navier-Stokes equations to:

$$\frac{\partial \overline{u}_i}{\partial t} + \frac{\partial \overline{u_i u_j}}{\partial x_j} = -\frac{1}{\rho}\frac{\partial p}{\partial x_i} + \frac{\partial}{\partial x_j} \left[\nu \frac{\partial \overline{u}_i}{\partial x_j} - (\tau_{ij} + C_{ij} + L_{ij}) \right] \tag{9}$$

$$\frac{\partial \overline{u}_i}{\partial x_i} = 0 \tag{10}$$

Where:

- $L_{ij} = \overline{\overline{u}_i \overline{u}_j} + \overline{\overline{u}_i u_j'}$ - Leonard tensor
- $C_{ij} = \overline{\overline{u}_j u_i'} + \overline{u_i' u_j'}$ - Crossed terms
- $\tau_{ij} = \overline{u_i' u_j'}$ - Subgrid Reynolds tensor

2.1.1. Smagorinsky Subgrid Model

The subgrid Reynolds tensor is modeled using the Boussinesq eddy viscosity (ν_t) assumption:

$$\tau_{ij} = \nu_t \left(\frac{\partial \overline{u_i}}{\partial x_j} + \frac{\partial \overline{u_j}}{\partial x_i} \right) - \frac{2}{3} k \delta_{ij} \tag{11}$$

The production ($\wp$) is denoted as a function of the shear rate and the dissipation (ε) is denoted as a function of the velocity and of the subgrid characteristic length:

$$\wp = 2\nu_t S_{ij} S_{ij} \tag{12}$$

$$\varepsilon = \frac{-c_1 (\overline{u_i' u_j'})^{1,5}}{\ell} \tag{13}$$

The velocity scale is related with the filtered velocity gradients by an analogy of the Prandtl mixing length. So, with scaling and the production and dissipation equations, the eddy viscosity can be written as follows:

$$\nu_t = (C_s \ell)^2 \sqrt{2 S_{ij} S_{ij}} \tag{14}$$

Here, C_s is the Smagorinsky constant and S_{ij} is the rate-of-strain tensor. The value of the Smagorinsky constant for the present work is equal to 0,2.

2.1.2. Wall Damping

To avoid high values of the eddy viscosity, a wall damping function is used. The damping is made using a combination of the mixing length and a damping function for the eddy viscosity:

$$\nu_t = min(l_{mix}, f_\nu C_s \Delta)^2 \sqrt{2 S_{ij} S_{ij}} \tag{15}$$

Here, f_ν is the damping function, C_s is the Smagorinsky constant and S_{ij} is the rate-of-strain tensor. The mixing length is given as follows:

$$l_{mix} = K y_{wall} \tag{16}$$

The default value of the Smagorinsky constant and the K constant is 0,1 e 0,4 respectively. The damping function used at the present work is the Piomelli function (Rudman and Blackburn, 1999), given by:

$$f_\nu = \sqrt{1 - exp\left[\left(\frac{-\widetilde{y}}{A} \right)^3 \right]} \tag{17}$$

A is the damping factor, equal to 25. The normalized wall distance is given by:

$$\widetilde{y} = \frac{y \widetilde{u}}{\nu} \tag{18}$$

2.2. Reynolds Averaging - The SST Model

In a frame work for turbulence modeling, for incompressible turbulent flows, the conservation of mass, and momentum (equations 1 and 2) can be expressed by the classical Reynolds averaged equations given by:

$$\frac{\partial u_i}{\partial x_i} = 0 \tag{19}$$

$$\rho \left(\frac{\partial u_i}{\partial t} + u_j \frac{\partial u_i}{\partial x_j} \right) = -\frac{\partial p}{\partial x_i} + \frac{\partial}{\partial x_i} \left[(\mu + \mu_t) \frac{\partial u_i}{\partial x_j} \right] \tag{20}$$

In those equations u_i and p are the mean velocity and pressure fields. Menter (Menter and Kuntz, 2003) created the SST model, and its principle lies on blending the $k - \epsilon$ and the $k - \omega$ model. Far from the wall, the model uses the $k - \epsilon$ formulation, and near the wall, the model uses the $k - \omega$ model. The turbulent eddy viscosity is defined by:

$$\nu_t = \frac{a_1 k}{\max(a_1 \omega, S F_2)} \tag{21}$$

The transport equations are:

$$\rho\left(\frac{\partial k}{\partial t}+u_i\frac{\partial k}{\partial x_i}\right)=P_k-\beta' k\omega\rho+\frac{\partial}{\partial x_i}\left[(\mu+\frac{\mu_t}{\sigma_k})\frac{\partial k}{\partial x_i}\right] \tag{22}$$

$$\rho\left(\frac{\partial \omega}{\partial t}+u_i\frac{\partial \omega}{\partial x_i}\right)=\alpha\rho S^2+\beta\rho\omega+\frac{\partial}{\partial x_i}\left[(\mu+\frac{\mu_t}{\sigma_\omega})\frac{\partial \omega}{\partial x_i}\right]+2(1-F_1)\rho\sigma_{\omega 2}+\frac{1}{\omega}\frac{\partial k}{\partial x_i}\frac{\partial \omega}{\partial x_i} \tag{23}$$

S is an invariant measure of the rate-of-strain tensor S_{ij} and F_2 is one of two blending functions of the model. The formulation of the blending functions F_1 and F_2 are based on the distance of proximity of the surface and on the flow's variables. The blending functions F_1 and F_2 are given as follows:

$$F_1=\tanh(\arg_1^4) \tag{24}$$

$$\arg_1=\min\left[\max\left(\frac{\sqrt{k}}{\beta'\omega},\frac{500\nu}{y^2\omega}\right),\frac{4\rho\sigma_{\omega 2}k}{CD_{k\omega}y^2}\right] \tag{25}$$

$$CD_{k\omega}=\max(2\rho\sigma_{\omega 2}\frac{1}{\omega}\nabla k\nabla\omega,1,0.10^{-10}) \tag{26}$$

Here, y is the distance to the wall. F_1 is equal to zero away from the surface ($k-\epsilon$ model), and switches over to 1 inside the boundary layer ($k-\omega$ model). F_2 is given by:

$$F_2=\tanh(\arg_2^2) \tag{27}$$

$$arg_2=\max\left(\frac{2\sqrt{k}}{\beta'\omega y},\frac{500\nu}{y^2\omega}\right) \tag{28}$$

F_2 restrains the limitator for the boundary layer wall. A production limiter is used to avoid the growth of turbulence in stagnation regions:

$$P_k=\mu_t\frac{\partial U_i}{\partial x_j}\left(\frac{\partial U_i}{\partial x_j}+\frac{\partial U_j}{\partial x_i}\right) \tag{29}$$

$$\widetilde{P_k}=max(P_k,10\cdot\rho\beta^*k\omega) \tag{30}$$

The model's constants are accounted by a blend of the corresponding constants of the $k-\epsilon$ and $k-\omega$ models with the following function:

$$\alpha=\alpha_1F+\alpha_2(1-F)+... \tag{31}$$

The constants are β'=0.09, α_1=5/9, β_1=3/40, σ_{k1}=0.5, $\sigma_{\omega 1}$=0.5, α_2=0.44, β_2=0.0828, σ_{k2}=1, $\sigma_{\omega 2}$=0.856. The analytical expression for ω provided by ω-equation turbulence models allows a near-wall formulation, which gradually switches from wall-functions to low-Re near wall formulations. At the same time, the mesh is refined in wall normal direction.

2.3. Detached Eddy Simulation

The DES model is a hybridization of a LES approach (Spalart, 2000). DES takes advantage of the RANS method where the mean flow remains attached and steady while offering, like LES, the sensitivity to capture, for instance, wakes or recirculation zones. There are two issues in this approach:

- How fast the turbulent structures will develop after the formulation change to RANS from LES?
- How the changing formulation mechanism must be modeled, in order to avoid a grid induced separation?

The answer lies in the blending functions of the SST model. These functions will "shield" the boundary layer and minimize the grid-induced separation. The formulation change will happen when the turbulent length scale obtained in the RANS section of the model surpasses the local grid spacing. The modeling of the DES SST model uses the SST model and the switching modeling, given as follows:

$$\varepsilon=k\beta'\omega=\frac{k^{\frac{3}{2}}}{L_t}\Rightarrow\frac{k^{\frac{3}{2}}}{C_{DES}\Delta} \tag{32}$$

For $C_{DES}\Delta < L_t$:

$$\Delta = max(\Delta_i); L_t = \frac{\sqrt{k}}{\beta'\omega} \tag{33}$$

Here, the switch from the SST model to an LES formulation is made only in regions where the turbulent length, L_t, predicted by the RANS model is larger than the local grid spacing. Strelets, 2001 propose the following modification to the model, formulated as a multiplier of the destruction term in the turbulent kinetic energy:

$$\varepsilon = k\beta'\omega \Rightarrow k\beta'\omega F_{DES}; F_{DES} = max(\frac{L_t}{C_{DES}\Delta}, 1) \tag{34}$$

Here, $C_{DES} = 0,61$ is the limiter who should be active in the RANS region, specifically in the $k-\epsilon$ region. The numerical formulation is also switched from an upwind biased in the RANS region and a central difference scheme in the DES region. The third blending function is modeled in CFX as follows:

$$F_{DES-SST} = max(\frac{L_t}{C_{DES}\Delta}(1 - F_{SST}), 1) \tag{35}$$

Putting $F_{SST} = 0$ recovers the Strelets formulation. F_2, showed before, shields more of the boundary layer and is therefore the desired default. However, even F_2 does eliminate the problem, but reduces it by an order of magnitude. The set-up of the DES SST model was set according with the work of Menter and Kuntz, 2003.

3. Computational Details and Boundary Conditions

For inflow surfaces the values of velocity, kinetic energy of turbulence and dissipation fields are prescribed. For outflow boundaries, the homogeneous Neumann conditions are prescribed for the same variables and the homogeneous Dirichlet boundary condition is used for the pressure field.

The single cylinder case studied by Cala *et al.*, 1996 is a cylinder without pendulum movement, attached to the lower wall. For this case, experimental results of transversal and vertical velocity and respective fluctuations are available. Here, the cylinder has 75 mm of height and diameter of 19 mm. The inlet boundary condition is the velocity profile measured by Cala *et al.*, 1996. This profile was approximated by a $1/6$ exponencial function, given by:

$$\frac{u}{u_0} = 1,089\left(\frac{z}{H}\right)^{\frac{1}{6}} \tag{36}$$

u_0 is the non-disturbed flow and H is the cylinder height. Figure 1 shows the unstructured mesh used. There is a refinement at the surroundings of the cylinder and immediate downstream of the domain. The mesh has this topology in order to capture all the phenomena that occur at the wake behind the cylinder, and filter any numerical inconsistency downstream. Here, the mesh has 97813 nodes, 538989 elements and 3960 prismatic elements. All the simulations of the present work are transient with time step of 10^{-4} seconds with a total time of 100 seconds. The initial conditions are zero value of all the variables. The convergence criterion is set as 10^{-4} in RMS value of all fields norm.

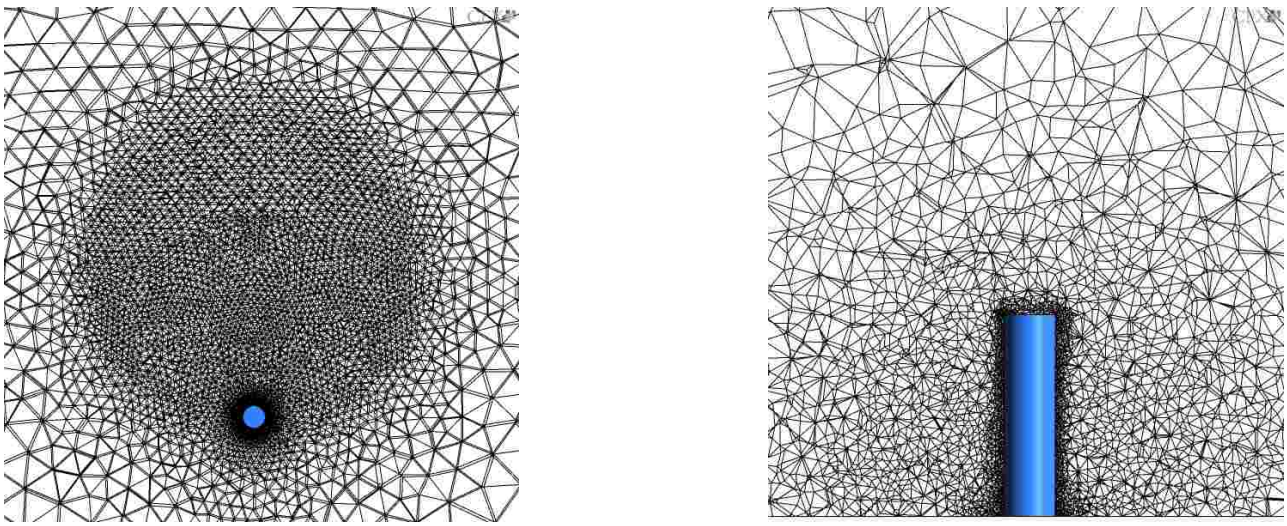

Figure 1: Cylinder mesh

4. Results and Discussion

Figures 2, 3, 4, 5, shows the obtained averaged results. The flow around a circular cylinder holds great engineering interest due to the combined effect of vortex shedding, Kelvin-Helmholtz instabilities and free end flow. Due to that a lot of open issues are shown at the literature. The streamlines show the inherent complexity of that flow. The boundary layer over the finite cylinder is far more complex than the infinite cylinder case. At the 2-Dimensional case, there is a vortex shedding which happens in a characteristic frequency. The length scale varies proportionally with $l^{1/2}$. For the finite cylinder case, the wake topology stands in the way of vortex shedding for cylinders who have low aspect ratio (Kawamura *et al.*, 1984). This occurs due to the strength of tip and necklace vortices who overcome the Kàrman vortices generated between the tip and the junction. The averaged results present at the figures do not show any kind of vortex shedding. The downward motion of the streamlines behind the cylinder junction is followed by the strong upward motion and further downstream (Figure 2). The streamlines located near the bottom wall has a tendency of downward velocity near the stagnation points toward the junction of the cylinder and the bottom wall. This trend results in the downdraft near the cylinder junction (Figure 3). Those visualizations also show the separation of the flow at the top of the cylinder, which agrees with the work of Roh and Park, 2003. The experimental result of Cala, 1996 show, near the plate, a peak of the velocity fluctuation spectra. This can indicate a vortex shedding at that specific point, with a characteristic frequency. At the top of the cylinder, the flow presents itself as unorganized. The appearance of vortex shedding and Von Kárman wakes is governed by the aspect ratio of the cylinder. Eventually, this kind of vorticity appears at the bottom of the cylinder. The flow moves upward and accelerates near the free end, to separate from the cylinder circumference at the free end. At the central wake, the separated shear layer is declined, showing the same effect observed by Park and Lee, 2000. The URANS result show a small recirculation zone, when the LES result show a bigger recirculation zone when compared with the other results. The DES result show small ribbon structures, where the URANS result show a ribbon structure close to the halfway of the cylinder. The LES result has its ribbon structure more attached to the free end. According to Frohlich and Rudi, 2004, this ribbon structure comes as a consequence of the free end vorticity. It can leave the main vortex and stretch downstream in spiralled movement. This effect is observed for the three results, where the LES result show a more spiralled movement.

Figures 3, 4 shows surface streamlines place at the surface of the cylinder. The main objective of this visualizations is to show evidence of tip vortices that separate from the free end and reach down to the wake. It can be seen for the three cases the stagnation lines at the rear of the cylinder and at the oblique left. Close to the bottom of the cylinder, at the oblique stagnation line there is the occurring of a saddle point, which indicates the oncoming of the boundary layer. Close to the free end, there is a point which is a starting point for several streamlines. The LES and DES results shows this points at the same place, and the URANS result shows this place close to the half of the cylinder. Along the stagnation line it can be seen a upward motion, more evident at the URANS result. The LES and DES results shows more homogeneous upward movement. The vertical and horizontal profiles taken at distances of 2D, 4D and 6D are presented at figures 6, 7, 8, 9, 10 and 11. The graphical analysis show that the similar behavior of the profiles downstream of the flow is not observed to regions close to the cylinder in the transversal and vertical profiles. At 2D, for both transversal and vertical profiles, the profile has a different pattern if compared with the other profiles. The tridimensional structure of the flow induces a growth of the velocity close to its symmetry line. This behavior was observed by Cala, 1996, and the author interpreted the mentioned result as a recuperation of the velocity behind the recirculation zone. The numerical results of transversal profiles at 4D and 6D denotes inflexions at points far from the cylinder, disagreeing with the experimental results. Only at 6D, the LES result did not show the inflexion. Those inflexions are an indication of the underestimation of the transversal phenomena from the numerical results. At 2D, all the numerical results had predicted the peak at the fluctuation profile, observed at 1,5R, differently than the experimental results. According to Cala, 1996, this is the limit where the vortex structure produces an important generation rate of turbulent kinetic energy. But the shape of the profile were predicted differently by each numerical result. The LES and DES results were more accurate previewing the shape of the profile, where the URANS results predict a narrower profile. The vertical profiles show the wake form, which shows the recuperation of the kinetic energy downstream where slowly, the level of turbulent intensity diminishes downstream. All the numerical results had shown limited results in predicting those profiles. The worst case happens at 4D, where only the DES result is close to experimental result. This can be as a effects of necklace vortex at the free end and horseshoe vortex at the ground. Numerically, that kind of structure holds great difficulty in prediction due to its small length scale, which requires a even more refined grid to capture those phenomena.

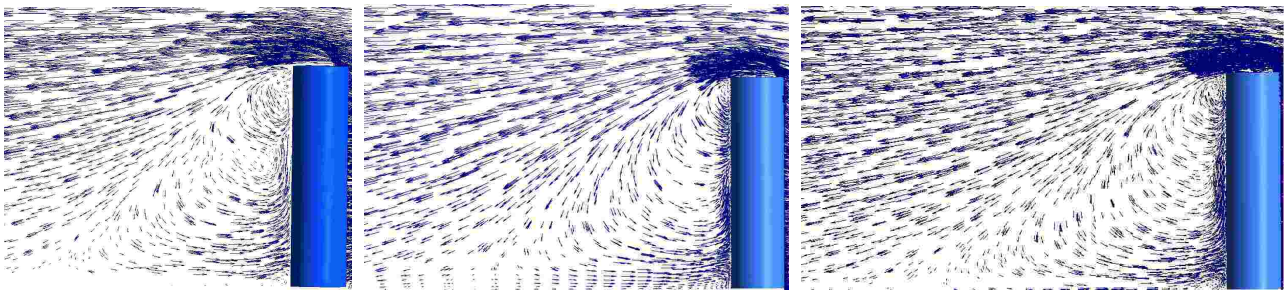

Figure 2: Velocity vectors - From left to right - URANS, DES and LES

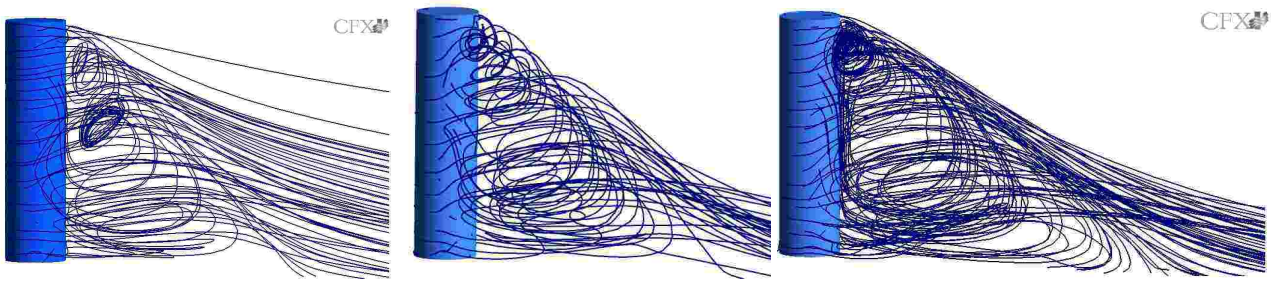

Figure 3: Streamlines - From left to right - URANS, DES and LES

Figure 4: Surface streamlines at rear view of the cylinder - From left to right - URANS, DES and LES

Figure 5: Surface streamlines at a left oblique view of the cylinder - From left to right - URANS, DES and LES

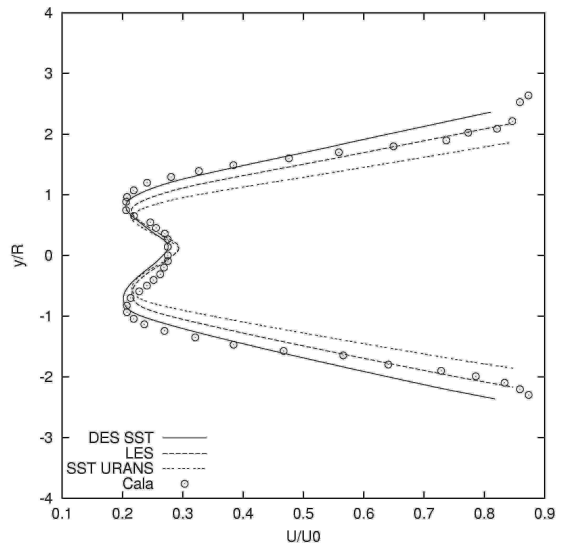

Figure 6: X=2D - Transversal Profile

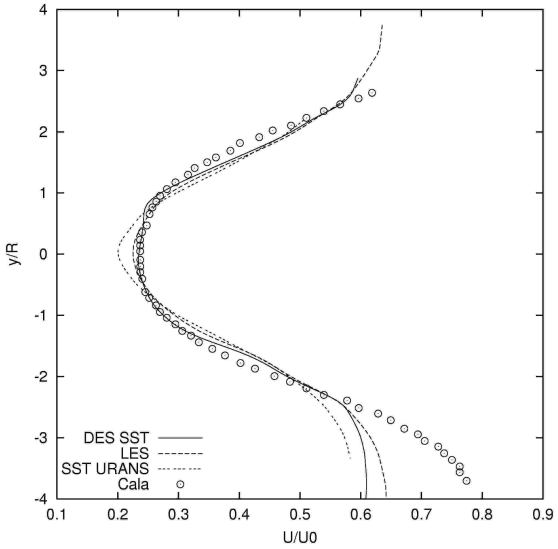

Figure 7: X=4D - Transversal Profile

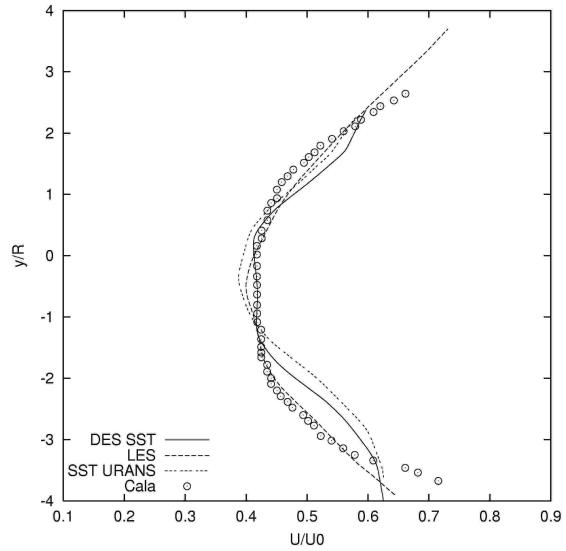

Figure 8: X=6D - Transversal Profile

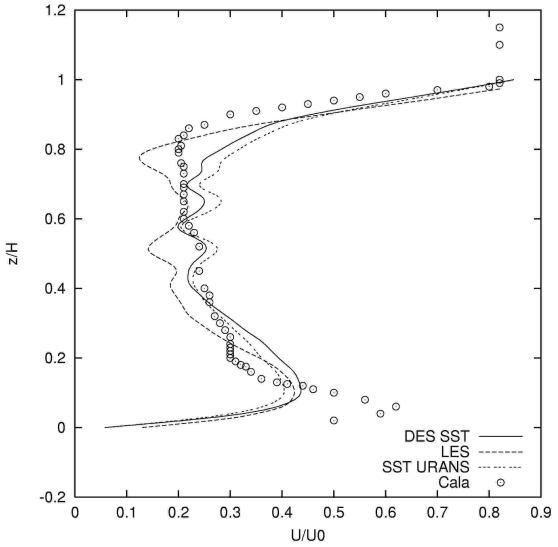

Figure 9: X=2D - Vertical Profile

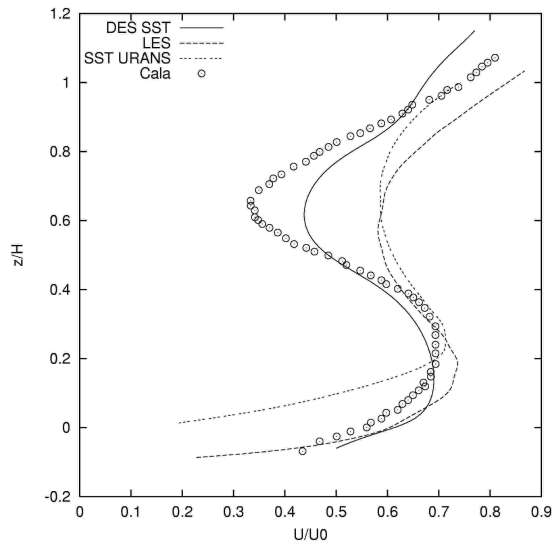

Figure 10: X=4D - Vertical Profile

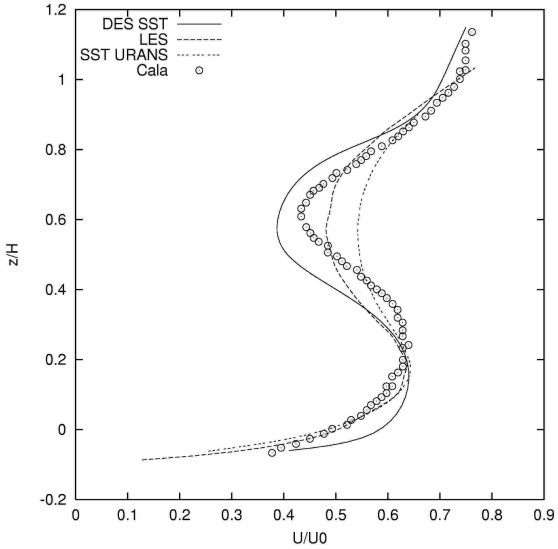

Figure 11: X=6D - Vertical Profile

5. Conclusion

Results of a numerical simulation over a finite cylinder mounted at a flat plate were made. The results are presented at velocity vectors, streamlines at its wake, surface streamlines and graphical validation, where the numerical data obtained by large eddy simulation, detached eddy simulation and URANS is compared to experimental data.

The velocity vectors and streamline display show the behavior of the wake of this kind of flow, where a von Kàrman vortex shedding is expected in theory. The effects that suppress the shedding were visualized. There is also flow separation at the free end of the cylinder, which agrees with experimentation. The surface streamlines at the cylinder shows stagnation line at its rear and close to end at a left oblique view. There are also saddle points which denote the oncoming of boundary layer. The graphical analysis shows that the numerical results have resemblance with experimental result, but the vertical profiles denoted differences when compared with experimentation.

Based on the results, the three models were able to predict fairly the flow. For a more profound analysis, other URANS models should be used. Besides that, for LES analysis, a comparing with different values of the Smagorinsky constant can be done in order to see how the Smagorinsky subgrid model is accurate for this flow. The DES model can also has a similar comparing, with different turbulence models. As a future work, turbulent intensity profiles, spectrum analysis and a analysis of the instantaneous flow will be made in order to make a thorough analysis of the transient result.

6. References

Baban, F., So, R., and Otugen, M., 1989, Unsteady Forces on circular cylinders in a cross-flow, “Experiments in Fluids”, Vol. 7, pp. 293–302.

Cala, C., Brasil-Junior, A. C. P., and Sousa, A. J., 1996, Escoamento Turbulento em Torno de um Cilindro Pendular, “Proceedings of VI ENCIT - Brazilian Congress of Thermal Sciences and Engineering”, Florianópolis, Brazil.

Cala, C. E. C., 1996, Estudo do Escoamento Turbulento Dentro e Sobre uma Matriz de Cilindros Pendulares, Master’s thesis, Universidade de Brasília, DM-018.

Constantinescu, G. S. and Squires, K. D., 2003, LES and DES Investigations of Turbulent Flow over a Sphere at Re=10,000, “Flow, Turbulence and Combustion”, Vol. Vol. 70, pp. pp. 267–298.

Forsythe, J. R., Squires, K. D., and Spalart, P. R., 2001, Detached Eddy Simulation of the Separated Flow over a Forebody Cross Section, B. J. Geurtz, R. F. and Metais, O., editors, “Direct and Large Eddy Simulation IV”, Vol. 8 of “ERCOFTAC Series”, pp. 481–500.

Frohlich, J. and Rudi, W., 2004, LES of the flow around a circular cylinder of finite height, “International Journal of Heat and Fluid Flow”, Vol. 25, pp. 537–548.

Kanda, M., Moriwaki, R., and Kasamatsu, F., 2004, Large Eddy Simulation of Turbulent Organized Structures Within and Above Explicitly Resolved Cube Arrays, “Boundary-Layer Meteorology”, Vol. 112, pp. 343–368.

Kawamura, T., Hiwada, M., Hibino, T., Mabuchi, I., and Kumada, M., 1984, Flow around a finite circular cylinder on a flat plate, “Bull JSME 27:2142-2151”.

Lesieur, M. and Métais, O., 1996, New Trends in Large Eddy Simulation of Turbulence, "Annual Reviews of Fluid Mechanics", Vol. 28, pp. 45–82.

Menter, F. R. and Kuntz, M., 2003, Development and application of a zonal DES turbulence model for CFX 5, Ansys cfx validation report.

Noleto, L. G. and Brasil-Junior, A. C. P., 2005, DES Simulation of a Finite Cylinder Mounted on a Flat Plate, "Proceedings of 18th COBEM - 18th International Congress of Mechanical Engineering", Ouro Preto, Brazil.

Park, C. and Lee, S., 2000, Free end effects on the near wake flow structure behind a finite circular cylinder, "Journal of Wind Engineering and Industrial Aerodynamics", Vol. 88, pp. 231–246.

Roh, S. and Park, S., 2003, Vortical flow over the free end surface of a finite circular cylinder mounted on a flat plate, "Experiments in Fluids", Vol. 34, pp. 63–67.

Rudman, M. and Blackburn, H. M., 1999, Large Eddy Simulation of Turbulent Pipe Flow, "Second International Conference on CFD in Minerals and Process Industries".

Silveira-Neto, A., 2002, Simulação de Grandes Escalas de Escoamentos Turbulentos, Freire, A. P. S., Menut, P., and Su, J., editors, "Turbulência", Vol. 1, pp. 157–188. ABCM.

Silvestrini, J. H., 2003, Simulação Numérica Direta e de Grandes Escalas de Escoamentos Transicionais e Turbulentos, Silveira-Neto, A. and Mansur, S. S., editors, "Turbulência", Vol. 2, pp. 1–72. ABCM.

Spalart, P. R., 2000, Strategies for Turbulence Modelling and Simulation, "International Journal of Heat and Fluid Flow", Vol. 21, pp. 252–263.

Squires, K. D., Forsythe, J. R., Morton, S. A., Strang, W. Z., Wurtzler, K. E., Tomaro, R. F., Grismer, M. J., and Spalart, P. R., January 2002, Progress of Detached Eddy Simulation of Massively Separated Flows, "AIAA 2002-1021".

Strelets, M., 2001, Detached Eddy Simulation of massively Separated Flows, "AIAA 2001-0879".

Proceedings of the 11th Brazilian Congress of Thermal Sciences and Engineering -- ENCIT 2006
Braz. Soc. of Mechanical Sciences and Engineering -- ABCM, Curitiba, Brazil, Dec. 5-8, 2006

Paper CIT06-0957

SIMULAÇÃO HÍBRIDA RANS/LES DE ESCOAMENTOS TURBULENTOS

Cleber Spode
Universidade Federal de Uberlândia - 38400-902 Uberlândia – MG, Brasil.
cleber.spode@ufrgs.br

Rubens Campregher
Dalhousie University – Mechanical Engineering Department, Canada.
rubenscamp@dal.ca

Aristeu da Silveira Neto
Universidade Federal de Uberlândia - 38400-902 Uberlândia – MG, Brasil.
aristeus@mecanica.ufu.br

Resumo. *A Simulação Numérica Híbrida RANS/LES juntamente com o método dos Volumes Finitos é aqui utilizada para simular o escoamento turbulento sobre o degrau em uma aproximação adiabática, tridimensional e transiente. Este caso clássico constitui um excelente teste para a avaliação de novas metodologias de modelagem da turbulência por apresentar, apesar da geometria simples, uma complexa formação de estruturas tridimensionais, influenciando enormemente o fenômeno da transição à turbulência e propriedades como freqüências características de emissão de vórtices e comprimento de recolamento. Um modelo híbrido RANS/LES, baseado no modelo de Spalart-Allmaras, chamado DES (Detached-Eddy Simulation) é testado com o intuito de avaliar esse tipo de metodologia na descrição de escoamento com descolamentos e gradiente adverso de pressão. Os resultados para o comprimento de recolamento, perfis de velocidade, tensor de Reynolds e coeficiente de pressão, demonstram que métodos híbridos RANS/LES são eficazes na descrição de escoamentos turbulentos.*

Palavras chave: Turbulência, Modelagem Híbrida RANS/LES.

1. Introdução

A turbulência nos fluidos tem sido pesquisada por mais de um século, mas nenhuma teoria completamente fechada sobre ela foi escrita (Tennekes & Lumley, 1994). A diversidade de escalas e freqüências envolvidas em um escoamento turbulento aumenta de forma estrondosa à medida que cresce o número de Reynolds.

Calcular todas as escalas da turbulência definitivamente não é uma tarefa fácil. Metodologias como a Simulação Numérica Direta (DNS – Direct Numerical Simulation), que consiste em resolver as equações de Navier-Stokes diretamente, sem a imposição de um modelo, procuram resolvê-las. Isso implica na utilização de uma malha capaz de descrever todo o espectro de freqüências, desde as menores (grandes estruturas) até a as maiores (Escala de Kolmogorov – pequenas estruturas de altas freqüência). Além do refino de malha, são exigidos esquemas de discretização espacial e temporal de alta ordem, que não imponham difusão numérica ao cálculo. Soma-se a isso o cuidadoso uso de condições de contorno adequadas com níveis de perturbação específicos para cada caso. O emprego da DNS tem aumentado consideravelmente nos últimos anos devido ao avanço dos computadores, que, mais potentes, já são capazes de processar cálculos para números de Reynolds mais elevados. Estudos referentes à camada limite e escoamentos de base têm utilizado DNS, obtendo resultados muito interessantes, que auxiliam no estudo da topologia de estruturas turbilhonares e da transição à turbulência.

Não podendo resolver todas as escalas da turbulência, surge o conceito de decomposição das escalas da turbulência, podendo ser realizada via filtragem temporal ou espacial. Quando se aplicada a filtragem temporal, decompondo a velocidade em uma parte média e outra flutuante, obtêm-se as Equações Médias de Reynolds (RANS – Reynolds Average Navier-Stokes). Para os casos onde é aplicada a filtragem espacial das equações de Navier-Stokes surgem as equações utilizadas na metodologia de Simulação de Grandes Escalas (LES – Large-Eddy Simulation). Diferente dos métodos RANS onde todo o espectro de energia é modelado, na metodologia LES as grandes escalas são resolvidas e apenas as menores escalas são modeladas, dependendo obviamente da discretização espacial e temporal empregadas.

Independente da metodologia, o problema em fazer uma filtragem temporal ou espacial é o surgimento de novos termos nas equações de Navier-Stokes, ficando assim com um sistema que possui mais incógnitas do que equações: é o chamado problema de fechamento da turbulência. Modelos são desenvolvidos para suprir essa necessidade, os chamados modelos de turbulência, que tem por objetivo modelar o tensor de Reynolds, o mais importante termo derivado do processo de filtragem.

Boussinesq, em 1877, através do conceito de viscosidade turbulenta introduz o fechamento das equações de Navier-Stokes modelando o tensor de Reynolds em uma analogia ao modelo de viscosidade molecular adotado por Stokes, existindo duas grandes correntes filosóficas de modelagem da turbulência baseado nessa hipótese:

- As equações médias de Reynolds (RANS – Reynolds-Average Navier-Stokes), através das quais as escalas da turbulência são divididas em uma parte média e outra flutuante;

- Equações de Navier-Stokes filtradas, através das quais as grandes escalas são resolvidas e apenas as pequenas são modeladas, é a chamada Simulação de Grandes Escalas (LES – Large Eddy Simulation).

Procurando tirar proveito das duas metodologias acima, um terceiro campo de pesquisa na modelagem da turbulência surge recentemente:

- A modelagem híbrida da turbulência, que vem a utilizar a boa descrição parietal de escoamentos turbulentos das metodologias RANS juntamente com a boa descrição dos escoamentos livres das metodologias LES, são os chamados modelos híbridos RANS/LES.

O foco do presente trabalho é apresentar essa nova linha de modelos híbridos RANS/LES, demonstrando sua potencialidade na descrição de escoamentos turbulentos através do modelo DES (Detached-Eddy Simulation) aplicado à simulação do escoamento sobre o degrau. O modelo DES é uma modificação do modelo RANS proposto por Spalart-Allmaras (1994) onde a distância à parede recebe um tratamento especial, fazendo com que o modelo opere como RANS em regiões parietais e como LES em zonas de escoamento cisalhante livre. Outros modelos na linhagem híbrida são encontrados em publicações recentes, destacando-se:

- O modelo de Nichols e Nelson (2001), desenvolvido em conjunto com o modelo SST a duas equações de Menter e Rumsey (1994) e recebeu o nome de Multi-Scale. Esse método apresenta uma suave transição entre as partes modelada por URANS e LES, Nichols e Nelson (2003);

- O modelo Híbrido LES-RANS de Davidson e Peng (2001), que combina o modelo de Yoshizawa (1993) juntamente com um modelo k-ω. Nesse modelo há uma linha bem definida que divide a parte modelada por LES e por RANS, sendo essa distância imposta explicitamente pelo usuário do modelo;

- O modelo LNS – Limited Numerical Scales proposto por Baten et al. (2002) faz uma mescla de um modelo k-ε com o modelo de Smagorinsky e através de um fator α decide automaticamente o uso de URANS ou LES;

- O modelo BLS – Baldwin-Lomax-Smagorinsky proposto por Camelli e Löhner (2002) utiliza o clássico modelo de Baldwin-Lomax para as regiões parietais e o modelo de Smagorinsky para as demais localidades do escoamento. Os resultados obtidos são animadores, porém a necessidade de um ponto de divisão entre as duas modelagens deixa o modelo suscetível ao erro do usuário ao definir uma distância incorreta;

- O modelo SAS – Scale-Adaptive Simulation de Menter et al. (2003) que tem sua formulação baseada em uma equação de transporte adicional para a viscosidade cinemática com um termo de destruição que dinamicamente decide pela utilização de URANS ou LES;

As seguir são apresentadas as equações de Navier-Stokes filtradas juntamente com as três metodologias de modelagem da turbulência LES, RANS e Híbrida RANS/LES avaliadas no presente trabalho.

2. Modelagem Matemática e Método Numérico

O processo de filtragem espacial ou temporal das Equações de Navier-Stokes, apesar de diferentes em essência, convergem para as equações filtradas:

$$\frac{\partial \overline{u_i}}{\partial t} + \frac{\partial}{\partial x_j}\left(\overline{u_i u_j}\right) = -\frac{1}{\rho}\frac{\partial \overline{p}}{\partial x_i} + \frac{\partial}{\partial x_j}\left[\nu\left(\frac{\partial \overline{u_i}}{\partial x_j} + \frac{\partial \overline{u_j}}{\partial x_i}\right)\right], \tag{1}$$

$$\frac{\partial \overline{u_i}}{\partial x_i} = 0. \tag{2}$$

Ambas as metodologias (RANS ou LES) partem da decomposição:

$$f\left(\vec{x},t\right)=\overline{f}\left(\vec{x}\right)+f'\left(\vec{x},t\right), \tag{3}$$

onde $\overline{f}\left(\vec{x}\right)$ representa o comportamento médio e $f'\left(\vec{x},t\right)$ o comportamento flutuante do sinal de pressão ou velocidade para metodologias RANS, e $\overline{f}\left(\vec{x}\right)$ representa as escalas filtradas e $f'\left(\vec{x},t\right)$ as escalas flutuantes ou sub-malha para metodologias LES.

A grande diferença entre as metodologias se dá no tratamento do produto filtrado $\left(\overline{u_i u_j}\right)$, que não apresenta uma solução direta, sendo interessante reescrevê-lo como:

$$\overline{u_i u_j}=\overline{u}_i\overline{u}_j+\tau_{ij}, \tag{4}$$

obtendo a Eq. (1) na forma:

$$\frac{\partial\overline{u}_i}{\partial t}+\frac{\partial}{\partial x_j}\left(\overline{u}_i\overline{u}_j\right)=-\frac{1}{\rho}\frac{\partial\overline{p}}{\partial x_i}+\frac{\partial}{\partial x_j}\left[\nu\left(\frac{\partial\overline{u}_i}{\partial x_j}+\frac{\partial\overline{u}_j}{\partial x_i}\right)-\tau_{ij}\right]. \tag{5}$$

Através da modelagem do tensor τ_{ij}, via hipótese de Boussinesq, que o correlaciona com a viscosidade turbulenta, numa alusão ao modelo de viscosidade de Stokes, se dá o processo de fechamento das Equações Filtradas de Navier-Stokes. A proposta de Boussinesq consiste em expressar esse tensor extra em função da taxa de deformação gerada pelo campo de velocidades filtrado e da energia cinética turbulenta:

$$\tau_{ij}=-\nu_t\left(\frac{\partial\overline{u}_i}{\partial x_j}+\frac{\partial\overline{u}_j}{\partial x_i}\right)+\frac{2}{3}k\delta_{ij}, \tag{6}$$

onde a viscosidade turbulenta ν_t pode ser calculada via um modelo de turbulência e a energia cinética turbulenta é incorporada à pressão, sendo gerada um pressão modificada p^*.

Considerando as hipóteses acima, podemos reescrever a Eq. (5) na forma:

$$\frac{\partial\overline{u}_i}{\partial t}+\frac{\partial}{\partial x_j}\left(\overline{u}_i\overline{u}_j\right)=-\frac{1}{\rho}\frac{\partial\overline{p^*}}{\partial x_i}+\frac{\partial}{\partial x_j}\left[\left(\nu+\nu_t\right)\left(\frac{\partial\overline{u}_i}{\partial x_j}+\frac{\partial\overline{u}_j}{\partial x_i}\right)\right], \tag{7}$$

restando definir o modelo para calcular a viscosidade turbulenta ν_t. Os modelos aqui utilizados são: Smagorinsky e Smagorinsky com função de amortecimento para a metodologia LES, Spalart-Allmaras (SA) para a metodologia RANS e o modelo híbrido RANS/LES *Detached-Eddy Simulation* (DES).

2.1 O Modelo de Smagorinky

A avaliação da viscosidade turbulenta proposta por Smagorinsky (1963) é dada por:

$$\nu_t=\left(C_S\ell\right)^2\sqrt{2\overline{S}_{ij}\overline{S}_{ij}}, \tag{8}$$

onde C_S é o coeficiente de Smagorinsky, ℓ é o comprimento característico e S_{ij} o tensor taxa de deformação:

$$\ell=\sqrt[3]{\prod_{i=1}^{3}\Delta x_i}, \tag{9}$$

$$\overline{S}_{ij}=\frac{1}{2}\left(\frac{\partial\overline{u}_j}{\partial x_i}+\frac{\partial\overline{u}_i}{\partial x_j}\right). \tag{10}$$

A dependência do tensor taxa de deformação e do filtro utilizado garantem um caráter totalmente tridimensional ao modelo. Fisicamente, a hipótese de que os turbilhões se comportam como moléculas é bastante razoável para escoamentos turbulentos totalmente desenvolvidos, sendo possível calibrar o modelo para essa classe de escoamentos através da cosntatante C_s. Lilly (1966) determinou C_s =0,18 para turbulência homogênea isotrópica, entretanto, seu valor em aplicações práticas é na faixa de $0,05 \le C_S \le 0,30$.

Essa dependência da constante de proporcionalidade de Smagorinsky tem fortes efeitos colaterais quando tratamos com escoamentos parietais, devido aos altos gradientes de velocidade que acarretam produção excessiva de viscosidade turbulenta devida a dependência do tensor taxa de deformação. Diferentemente dos chamados modelos dinâmicos, onde a constante é função do tempo e espaço, o modelo de Smagorinsky não faz nenhuma consideração com relação à proximidade de paredes, sendo necessário adicionar uma função externa de amortecimento que compute esse efeito e leve a zero o seu valor próximo às paredes.

Uma solução bem sucedida para zerar a constante próximo a paredes de forma consistente é o amortecimento de Van Driest, que modifica a constante C_s conforme:

$$C_S = C_{S0}\left(1 - e^{-d^+/A^+}\right)^2 \tag{11}$$

onde $d^+ = du_\tau/\nu$ é a distância à parede, $u_\tau = \sqrt{\tau_w/\rho}$ a velocidade de cisalhamento, τ_w a tensão de cisalhamento junto a parede, A^+ uma constante de valor 25 (Ferziger e Peric, 1999) e $C_{S0} = 0,05 - 0,3$ é a constante de Smagorinsky.

2.2 O Modelo de Spalart-Allmaras

O modelo de Spalart-Allmaras foi desenvolvido e calibrado com base em relações empíricas de diferentes tipos de escoamentos e análise dimensional. O modelo é baseado em uma equação de transporte para a variável auxiliar $\tilde{\nu}$:

$$\frac{\partial \tilde{\nu}}{\partial t} + \frac{\partial}{\partial x_j}\left(u_j \tilde{\nu}\right) = c_{b1}\tilde{S}\tilde{\nu} - c_w f_w \left[\frac{\tilde{\nu}}{d_w}\right]^2 + \frac{1}{\sigma}\left[\frac{\partial}{\partial x_j}\left(\left(\nu + \tilde{\nu}\right)\frac{\partial \tilde{\nu}}{\partial x_j}\right) + c_{b2}\frac{\partial \tilde{\nu}}{\partial x_j}\frac{\partial \tilde{\nu}}{\partial x_j}\right]. \tag{12}$$

A Eq. (12) constitui o modelo de Spalart-Allmaras em uma versão simplificada, desconsiderando os termos de transição, que são inexpressivos em escoamentos turbulentos completamente desenvolvidos como o caso do degrau aqui analisado.

Os termos do lado direito da Eq. (12) representam a produção, destruição, difusão molecular e turbulenta, dissipassão de viscosidade respectivamente.

A viscosidade turbulenta ν_t é definida através da viscosidade modificada $\tilde{\nu}$ e amortecida pela função f_{v1} junto a paredes:

$$\nu_t = \tilde{\nu} f_{v1}\,, \qquad f_{v1} = \frac{\chi^3}{\chi^3 + c_{v1}^3} \qquad \text{e} \qquad \chi = \frac{\tilde{\nu}}{\nu}. \tag{13}$$

Para regiões distantes da parede a função de amortecimento f_{v1} tende à unidade, obtendo-se: $\nu_t = \tilde{\nu}$.

O termo de produção também apresenta dependência com relação à distância parietal, sendo amortecido pela função f_{v2}:

$$\tilde{S} = S + \frac{\tilde{\nu}}{\left(kd_w\right)^2} f_{v2} \qquad \text{e} \qquad f_{v2} = 1 - \frac{\chi}{1 + \chi f_{v1}}, \tag{14}$$

onde d_w é a distância à parede mais próxima e S o módulo do tensor taxa de deformação:

$$S = \sqrt{2S_{ij}S_{ij}}. \tag{15}$$

A função f_w é definida como unitária para a região logarítmica da camada limite, intensificando o termo de produção à medida que se aproxima da parede e tendendo a zero para as regiões mais distantes, sendo definida como:

$$f_w = g\left(\frac{1+c_{w3}^6}{g^6+c_{w3}^6}\right)^{1/6}, \qquad g = r + c_{w2}\left(r^6 - r\right) \qquad \text{e} \qquad \text{r} \equiv \frac{\tilde{\nu}}{\tilde{S}k^2 d_w^2}. \tag{16}$$

As demais constantes de modelo são:

$$c_{w1} = \frac{c_{b1}}{k^2} + \frac{(1+c_{b2})}{\sigma}, \qquad c_{w2} = 0,3, \qquad c_{w3} = 2, \qquad k = 0,41$$

$$c_{v1} = 7,1, \qquad \sigma = 2/3, \qquad c_{b1} = 0,1355, \qquad c_{b2} = 0,622, \tag{17}$$

$$c_{t1} = 1, \qquad c_{t2} = 2, \qquad c_{t3} = 1,2, \qquad \text{e} \qquad c_{t4} = 0,5.$$

A quantidade de variáveis do modelo deixa claro que ele foi projetado com base em escoamentos conhecidos, principalmente camada limite turbulenta.

2.3 Modelagem Híbrida RANS/LES

Peculiaridades à parte, a formulação final das equações de Navier-Stokes filtradas no espaço ou no tempo converge para uma só idéia através do conceito da viscosidade turbulenta de Boussinesq, proporcionando intercambiabilidade entre as formulações LES e RANS.

Spalart *at al*. (1997) propuseram uma nova abordagem de modelagem da turbulência, procurando tirar proveito de características positivas das metodologias de Grandes Escalas (LES) e Equações Médias de Reynolds (RANS) através do modelo *Detached-Eddy Simulation* (DES). O modelo é em essência o modelo de Spalart-Allmaras (SA) com a substituição da distância à parede d_w por uma distância modificada $\tilde{d}$, que automaticamente seleciona as regiões onde o modelo atuará como LES ou RANS.

$$\tilde{d} = \min\left(d_w, C_{DES}\Delta\right) \qquad \text{onde} \qquad \Delta = \max(\Delta x, \Delta y, \Delta z). \tag{18}$$

Essa nova distância $\tilde{d}$ age como um filtro, um novo comprimento de escala para o modelo de Spalart-Allmaras. Em regiões de camada limite $\left(\tilde{d} < \Delta C_{DES}\right)$ o modelo atua como RANS, recuperando a formulação original do modelo SA. Já para regiões afastadas de paredes $\left(\tilde{d} > \Delta C_{DES}\right)$ o comprimento de escala torna-se dependente do tamanho da malha $\left(\tilde{d} = \Delta C_{DES}\right)$, fazendo com que os termos de produção e destruição sejam balanceados e o modelo opere de forma muito semelhante a um modelo sub-malha algébrico, onde $\tilde{\nu} \propto S\Delta^2$. Além disso, o modelo DES apresenta uma constante de proporcionalidade, assim como no modelo de Smagorinsky, calibrada para turbulência homogênea e isotrópica $\left(C_{DES} = 0,65\right)$.

2.4 Método Numérico

As equações são resolvidas utilizando o método dos Volumes Finitos em um domínio cartesiano, com acoplamento pressão velocidade SIMPLEC e arranjo co-localizado com interpolação de Rhie-Chow. A discretização espacial é de segunda ordem centrada e o avanço temporal feito pelo esquema implícito *three-time-level*. O *solver* SIP é utilizado para a equação de correção da pressão e o *solver* SOR para as componentes de velocidade *u*, *v*, e *w* bem como para a viscosidade modificada, $\tilde{\nu}$, no modelo de Spalart-Allmaras.

3. Domínio computacional, condições de contorno e avanço temporal

A configuração básica do domínio computacional utilizado no presente estudo é apresentada na Figura 1 e parâmetros de malha dados pela Tabela 1. Suas dimensões são: $L = 23h$, $H = 6h$, $W = 4h$ e $X_i = 3h$.

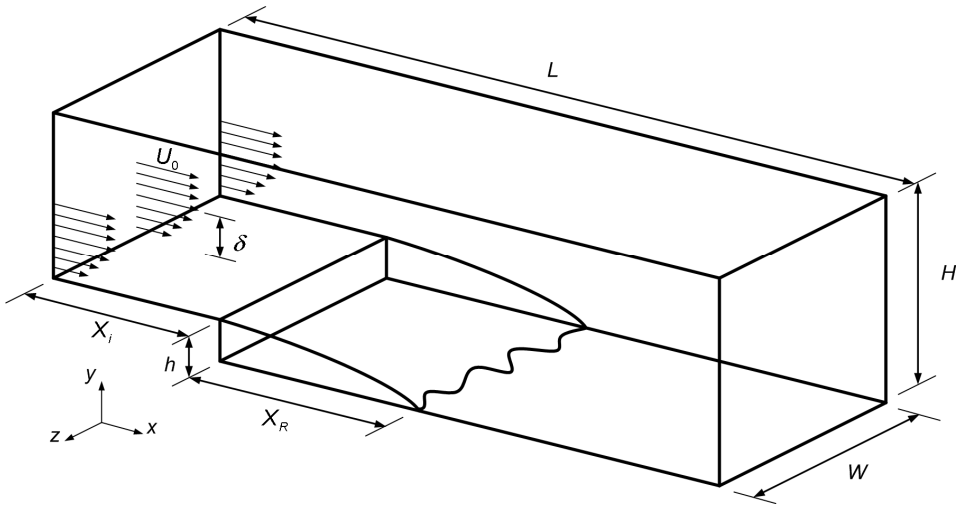

Figura 1. Domínio computacional utilizado.

O número de Reynolds baseado na altura do degrau é definido como:

$$\mathrm{Re} = \frac{U_0 h}{\nu} = 5000, \tag{19}$$

sendo U_0 a velocidade média na corrente livre, ν a viscosidade cinemática e $\delta = 1{,}15h$ espessura da camada limite.

Tabela 1. Dados da malha.

Dimensão	**N° de volumes**	
x ---> $L = 23h$	230	$\Delta x^+ \approx 24$
y ---> $H = 6h$	81	$\Delta y^+_{\max} \approx 83$, $\Delta y^+_{\min} \approx 3{,}7$
z ---> $W = 4h$	40	$\Delta z^+ \approx 24$

A malha é uniforme na direção *x* e *z* e não uniforme na direção *y*, com refinamento próximo às paredes. Dos 81 volumes utilizados na direção *y*, 36 deles foram utilizados na região abaixo do degrau e o restante acima. Um elevado número de volumes acima do degrau se fez necessário para uma boa descrição da camada limite de entrada.

As condições de contorno aplicadas ao domínio são de fluxo nulo na face superior,

$$v = 0, \quad \frac{\partial u}{\partial y} = \frac{\partial w}{\partial y} = 0. \tag{20}$$

Na direção *z* o escoamento é assumido como homogêneo e a periodicidade é aplicada e na face inferior e sobre o degrau é assumida condição de não deslizamento. Na face leste do domínio, à saída, aplica-se a condição de derivada nula da componente *u* da velocidade e anulam-se as componentes *v* e *w*:

$$\frac{\partial u}{\partial x} = 0, \qquad v = w = 0. \tag{21}$$

Um perfil de velocidade é aplicado na entrada do domínio, obtido dos dados de Jovic e Driver (1994) e interpolados através de uma *spline* para os nós da malha.

O avanço temporal é constante e o $\Delta t = 0{,}01 h/U_0$, com um tempo total de simulação $T_{total} = 2500\, h/U_0$, dos quais, os primeiros $500\, h/U_0$ são descartados das estatísticas, eliminando resquícios das condições iniciais impostas.

4. Resultados

A comparação entre os modelos de turbulência aqui analisados se dá através de dados qualitativos de campos de velocidade e viscosidade; e de forma quantitativa através do comprimento de recolamento, coeficiente de pressão, perfis de velocidade média, flutuações de velocidade e tensor de Reynolds.

Os casos computados são nomeados e classificados de acordo com as diferentes metodologias utilizadas e nomeadas de acordo com a Tabela 2.

Tabela 2. Nomenclatura dos casos analisados.

CASO	Descrição
LES	Metodologia de Grandes Escalas (LES) aplicando o modelo de Smagorinsky ($C_s = 0{,}1$).
LESVD	Metodologia de Grandes Escalas (LES) , modelo de Smagorinsky ($C_s = 0{,}1$) com adição da função de amortecimento de Van Driest.
SA	Metodologia de Equações Médias de Reynolds (URANS ou RANS), utilizando o modelo de Spalart-Allmaras.
DES	Metodologia híbrida, utilizando o modelo de Spalart-Allmaras modificado para atuar como URANS junto às paredes e LES no restante do domínio.

4.1 Resultados Topológicos

A presença de estruturas coerentes no escoamento sobre o degrau foi objeto de amplo estudo de Silveira Neto *et al* (1993). O comportamento semelhante a uma camada de mistura foi evidenciado, com a existência de instabilidade de Kelvin-Helmholtz e vórtices longitudinais contrarotativos. Delcayre e Lesieur (1997) também conseguiram através de simulação de grandes escalas e modelo de função estrutura de velocidade evidenciar estruturas coerentes no escoamento sobre o degrau a Reynolds 5.000. Entretanto, a existência de estruturas coerentes em escoamentos altamente turbulentos sobre o degrau é objeto de discussão, sendo defendido por muitos autores que em um escoamento em que a camada limite de entrada é turbulenta, estruturas coerentes não são facilmente identificáveis, ou ocorrem apenas em um breve período de transição.

Campos de velocidade instantânea *u* são apresentados na Figura 2 para as metodologias de modelagem aplicadas em um plano *x-y* central na coordenada *z=W/2*. Percebe-se a descrição transiente obtida com as metodologias LES, LESVD e DES, com a formação de estruturas características de uma camada cisalhante turbulenta que incide sobre a parede inferior do domínio. Para o modelo SA, há ausência de estruturas, apresentado um campo totalmente médio.

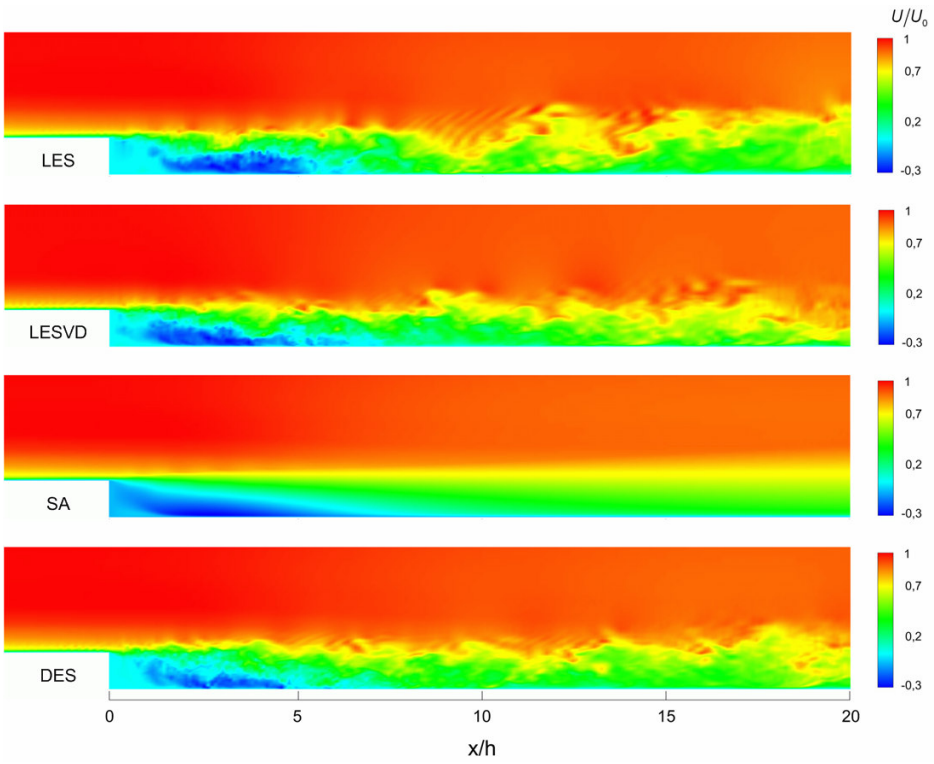

Figura 2. Campos de velocidade instantânea *u*, $z = W/2$ e $t = 2000\,h/U_0$.

A formação e transporte de estruturas turbilhonares são observados nas metodologias LES, LESVD e DES. Algumas diferenças são observadas quanto ao comprimento de recolamento, que, apesar de instantâneo, é maior para o caso LES em relação aos casos LESVD e DES.

O comportamento difusivo do modelo de Spalart-Allmaras fica mais claro quando observamos o campo de viscosidade efetiva (viscosidade molecular + viscosidade turbulenta) em um plano *x-y*, Figura 3.

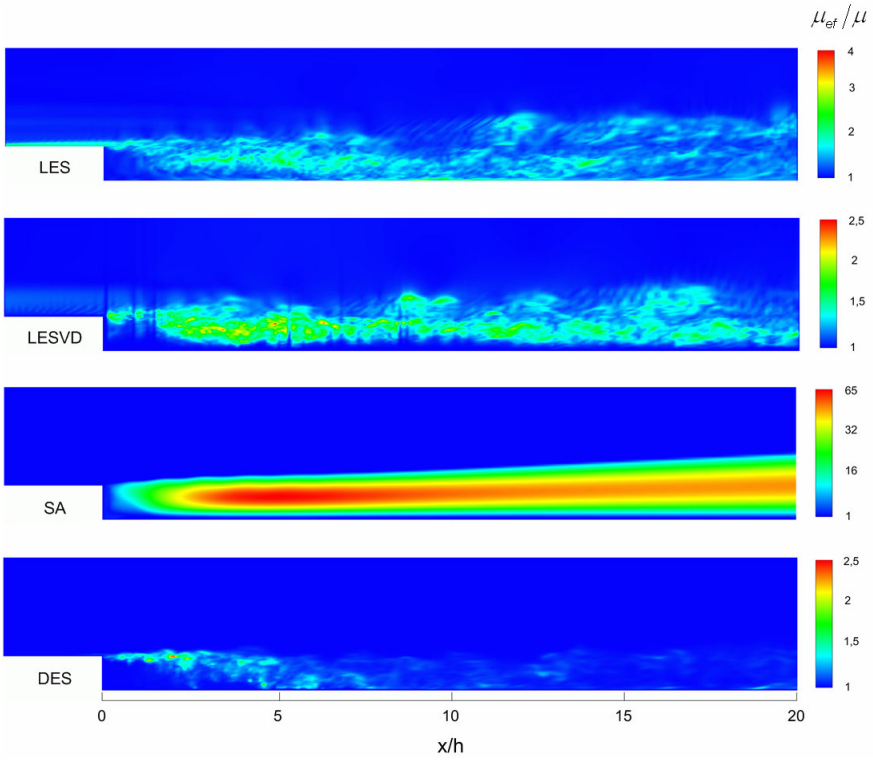

Figura 3. Campos de viscosidade efetiva. Plano *x-y*, $z = W/2$ e $t = 2000\,h/U_0$.

Os níveis de viscosidade efetiva gerados pelo modelo SA são bastante elevados quando comparado aos outros modelos, sendo o pico cerca de 25 vezes maior que a viscosidade gerada pelos modelos LESVD e DES. Esse comportamento revela uma característica problemática dos modelos URANS, que é o excesso de produção de viscosidade. Agravando esse fato, o refinamento da malha não auxilia na diminuição substancial desses altos níveis. Diferentemente dos modelos LES e híbridos RANS/LES, onde com o refinando da malha, o modelo diminui a sua contribuição através da viscosidade gerada. Os modelos RANS e URANS se mostram menos sensíveis ao refinamento, não apresentando grande dependência desse parâmetro depois de certo ponto.

Um fato interessante é observado no caso LESVD na Figura 3, onde descontinuidades são observadas devido a forma de cálculo de amortecimento da constate de Smagorinsky no modelo de Van Driest. Apesar dessas descontinuidades, os demais resultados topológicos e quantitativos se mostram satisfatórios para o caso LESVD.

4.2 Comprimento de recolamento, coeficiente de pressão e perfis de velocidade

O comprimento de recolamento reúne em uma só quantidade todas as propriedades do escoamento sobre o degrau. Os resultados para os diferentes modelos são apresentados na Tabela 3.

Tabela 3. Comprimento de recolamento.

	Comprimento de recolamento X_R			
CASO	Velocidade Média (x/h)	p.d.f. (x/h)	Média (x/h)	Erro (%)
Jovic e Driver (1994) - Experimental	-	-	6,0±0,15	-
LES	6,94	7,23	7,09	18,2%
LESVD	6,31	6,43	6,37	6,1%
SA	7,26	7,26	7,26	21%
DES	6,36	6,56	6,46	7,6%

Duas metodologias foram utilizadas para a determinação do comprimento de recolamento, uma baseada na velocidade média nula na célula imediatamente superior à face inferior do domínio e outra na função densidade de probabilidade de velocidade (p.d.f.). Confirmando as expectativas e observações dos campos de velocidade instantânea apresentados anteriormente, os casos LESVD e DES foram os que apresentaram o melhor comprimento de recolamento quando comparados aos resultados experimentais de Jovic e Driver (1994).

O caso SA foi o que apresentou o pior resultado, seguido pelo caso LES, que também apresenta um comprimento de recolamento bastante superior ao experimental. No caso SA, já é esperado um comprimento de recolamento ruim, visto que a ausência de estruturas tridimensionais denuncia sua má descrição do comportamento turbulento do escoamento. Já no caso LES, apesar da descrição topológica seguir o mesmo padrão dos casos LESVD e DES, um comprimento de recolamento bastante superior ao experimental é verificado.

O coeficiente de pressão médio para os casos computados é exibido na Figura 4 e definido como:

$$C_p = \frac{P - P_{REF}}{\frac{1}{2}\rho U_0^2}, \tag{22}$$

onde P_{REF} representa a pressão de referência tomada sobre o degrau na estação x/h=-3.

Os resultados apresentam-se próximos aos dados experimentais de Jovic e Driver (1994), com exceção do caso LES onde há certa defasagem, com sua curva adiantada em relação ao experimento e aos demais modelos. Essa defasagem esta associada ao comprimento de recolamento estimado, que sendo maior, provoca esse resultado. Além da defasagem, o patamar atingido na região de desenvolvimento da nova camada limite, x/h >20, é inferior ao experimento e a curva apresenta uma inclinação positiva, enquanto os dados experimentais seguem uma linha próxima da horizontal.

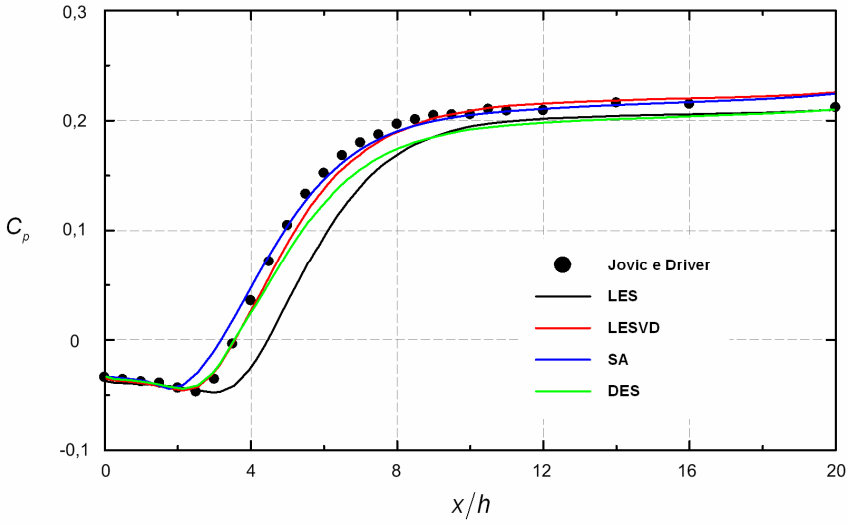

Figura 4. Coeficiente de pressão.

Os perfis de velocidade média U são apresentados na Figura 5 em quatro estações: antes do recolamento (x/h =4), próximo ao recolamento (x/h =6), depois do recolamento (x/h =10) e afastado do recolamento (x/h =19).

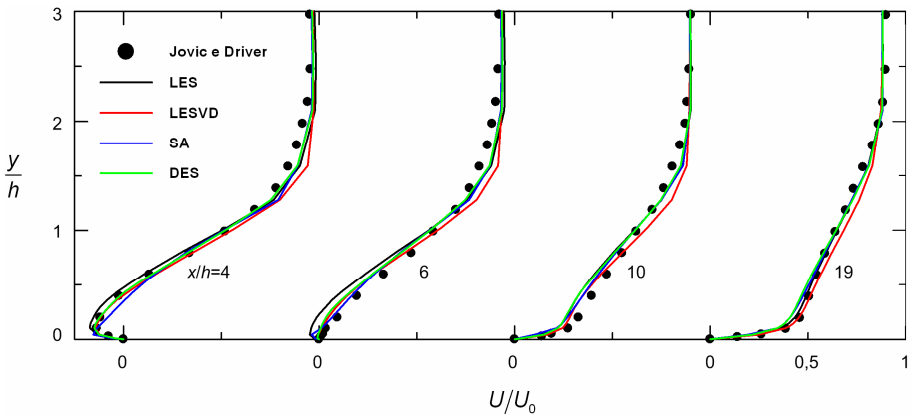

Figura 5. Perfis de velocidade média U.

Aparentemente todos os modelos apresentam bons resultados, sendo as discrepâncias mais visíveis a subpredição do modelo LES e a superpredição do modelo SA nas proximidades da parede inferior para a estação x/h =4. O grande comprimento de recolamento previsto pelo caso LES tende a atrasar tanto o perfil de velocidade em x/h =4 e x/h =6, causando o seu afastamento dos dados de Jovic e Driver (1994).

Apesar de muito próximo dos outros resultados, o caso SA apresenta uma forma diferente para o perfil de velocidade na estação x/h =4 próximo à parede inferior, com uma mudança brusca de velocidade, o que não acontece para os casos LES, LESVD e DES, onde os perfis têm uma mudança suave de velocidade, acompanhando a tendência dos dados experimentais.

O caso LESVD apresenta fidelidade para as regiões parietais assim como o caso DES, porém já possui uma certa defasagem na estação x/h =4 para y/h >1, onde sua velocidade é superestimada. Essa defasagem tende a se dissipar originando um perfil adiantado na estação x/h =19. O caso DES é o que apresenta os melhores resultados, praticamente reproduzindo os dados experimentais na estação x/h =4, com uma pequena subpredição na estação x/h =6 para y/h <0,5 e seguindo muito bem os dados experimentais para x/h =10 e x/h =19.

Perfis de valores RMS para as componentes u e v e para o tensor de Reynolds $\overline{u'v'}$ são apresentados na Figura 6 para as quatro estações juntamente com os dados de Jovic e Driver (1994).

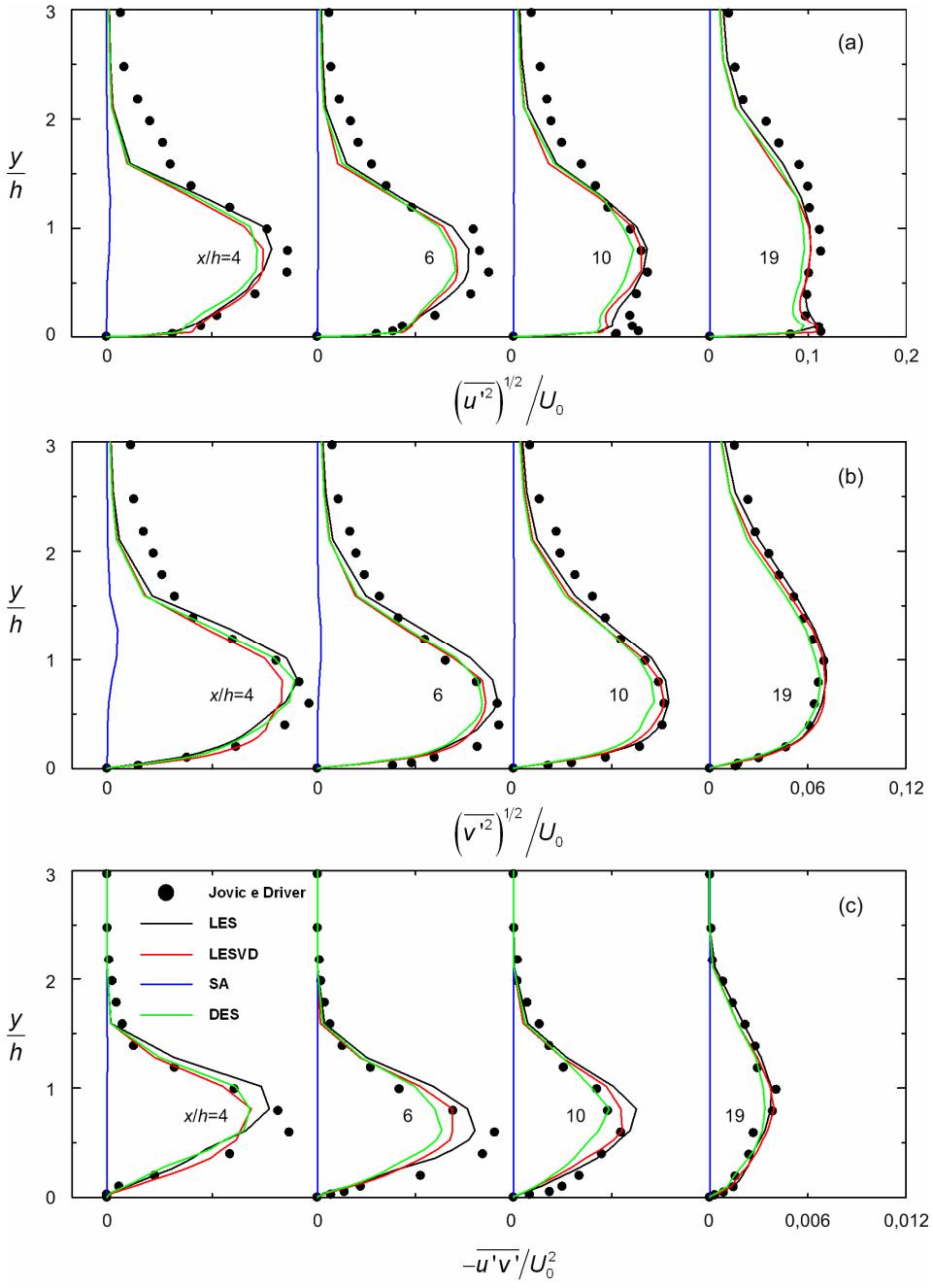

Figura 6. Perfis RMS de velocidade e Tensor de Reynolds.

Os resultados são satisfatórios para os casos LES, LESVD e DES, com boa reprodução dos dados experimentais, mas algumas diferenças também são visíveis. Já o caso SA simplesmente não apresenta qualquer nível de flutuação significativo. Na Figura 6(a), percebe-se que na estação x/h =4 todos os modelos apresentam um nível de flutuação $u´$ mais baixo que o experimental, causado pela falta de informação turbulenta na camada limite de entrada. Esse déficit é amenizado ao longo do escoamento, com a produção de turbulência na zona de recolamento e iteração com a camada cisalhante, mas mesmo na estação x/h =10 ela se mostra influente. Além disso, para todos os casos, os níveis máximos de flutuação $u´$ média máxima são inferiores aos dados experimentais, podendo ser esse fato decorrente da modelagem ou das condições de contorno constantes impostas.

Para a estação x/h =10 os dados de Jovic e Driver (1994) têm o pico de flutuação mais desenvolvido junto à parede, fato esse ocorrido também na simulação numérica direta de Le, Moin e Kim (1997). Já na estação x/h =19, esse pico é alcançado pelos casos LES e LESVD mas ainda é tímido no caso DES. Apesar de elevado, o pico no caso LES ocorre a uma altura y/h superior aos casos DES, LESVD e aos dados experimentais, possivelmente pelas dificuldades apresentadas pelo modelo em escoamentos parietais.

Na Figura 6 (b) nota-se também a falta de informação turbulenta da camada limite de entrada, sendo as flutuações $v´$ captadas por todos os modelos abaixo dos níveis experimentais para y/h >1,5. Com exceção dessa subpredição na região cisalhante, os níveis previstos pelos modelos LES, LESVD e DES são muito bons. Ainda que ínfimo, o caso SA apresenta um pequeno nível de flutuação nas proximidades de y/h =1.

Diferenças maiores em relação aos dados experimentais e entre os diversos modelos testados são constadas quando analisamos o tensor de Reynolds, Figura 6 (c). Para a estação x/h =4 o pico experimental não é alcançado por nenhum modelo, sendo o LES o que chega mais próximo. Os casos LESVD e DES apresentam resultados iguais, prevendo um pico máximo inferior ao experimental. Para a estação x/h =6 mantém-se essa subpredição, mas com um distanciamento entre os resultados dos casos LESVD e DES, com o LESVD prevendo um máximo mais próximo de experimental. Na estação x/h =10 os resultados já são melhores, acontecendo até uma superpredição do pico máximo pelo caso LES. Já o modelo LESVD prevê com acerácea a curva experimental, seguida pela curva do caso DES, levemente atrasada na faixa y/h <1 onde todos os modelos subestimam o tensor de Reynolds. Na estação x/h =19 os resultados são muito próximos aos experimentais, destacando-se o leve atraso da curva do caso DES.

Assim como para as componentes de flutuação $u´$ e $v´$ o tensor de Reynolds mostra-se nulo em todas as estações para o caso SA na Figura 6 (c). Diferente de muitos modelos RANS, onde a energia cinética turbulenta é uma das variáveis de transporte, o modelo de Spalart-Allmaras tem por sua variável uma viscosidade modificada. Isso faz com que não se possa pós-processar quantidades como flutuações, o que poderia ser feito em casos onde a energia cinética é uma variável do modelo, mesmo que não se manifestando fisicamente através do escoamento instantâneo.

5. Conclusões

Com base nos dados apresentados no presente trabalho é possível avaliar as qualidades de cada um dos modelos de turbulência testados. Seus méritos e deficiências são realçados no escoamento sobre o degrau, que apesar de simples geometricamente, consegue simular regiões parietais, cisalhantes livres, descolamento, recolamento e interação entre essas zonas. Os casos LES, LESVD e DES apresentam resultados topológicos muito semelhantes, formando os mesmos tipos de estrutura e diferindo mais drasticamente no comprimento de recolamento. O caso SA é muito diferente, não gerando nenhum tipo de instabilidade ou flutuação, apresentando uma solução média no tempo e perdendo bastante informação da física do escoamento.

O uso do método híbrido RANS/LES através do modelo DES se mostrou bastante interessante, fazendo uma descrição bastante realista do escoamento do ponto de vista topológico e sendo eficiente do ponto de vista estatístico, sendo o seu uso recomendado na simulação numérica de escoamentos turbulentos.

A influência das condições de contorno de entrada afetam os resultados aqui obtidos, sendo as mesmas objeto de estudo de Spode *et al*. (2006) e Spode (2006), onde demonstra-se a sua influência na simulação do escoamento turbulento sobre o degrau.

6. Agradecimentos

Os autores Cleber Spode e Aristeu da Silveira Neto agradecem o financiamento do CNPq e Rubens Campregher à Dalhousie University pelo suporte.

7. Referências

Baten, P. Goldberg, U., Chakravarthy, S., 2002. "LNS – An approach towards embedded LES", AIAA paper AIAA-2002-0427.

Camelli, F. E., Löhner, R., 2002, "Combining the Baldwin Lomax and Samgorinsky Turbulence Models to Calculate Flows with Separation Regions". 40th AIAA Aerospace Sciences Meeting & Exhibit, AIAA-2002-0426.

Davidson, L., Peng, S-H., 2001. "A Hybrid LES-RANS Model based on a one-equation SGS Model and Two-Equation k-ω model". The Second Int. Symp. On Turbulence and Shear Flow Phenomena, Vol. 2, pp. 175-180. Stockholm, 2001.

Delcayre, F., Lesieur, M., 1997. "Topological feature in the reattachment region of a backward facing step". Firtst AFOSR International Conference on DNS and LES.

Ferziger, J. e Peric, M, 2002, Computational Methods for Fluid Dynamics 3rd Ed.Springer Verlag, New York, USA.

Jovic, S., Driver, D., 1994, "Backward-Facing Step Measurements at Low Reynolds Number, Re_h=5000", NASA Technical Memorandum 108807.

Le, H., Moin, P., Kim, J., 1997. "Direct numerical simulation of turbulent flow over a backward-facing step". Journal of Fluid Mechanics, Vol. 330, pp. 349-374.

Lilly, D. K., 1966, "On the Application of the Eddy Viscosity Concept in the Inertial Subrange of Turbulence". NCAR Manuscript 123.

Menter, F., Roland, B., Kuntz, M. 2003. "A scale-adaptive simulation model for turbulent flow predictions" In 41st AIAA Aerospace Sciences Meeting & Exhibit, Reno, NV; USA; 6-9 Jan. 2003.

Menter, F. R., Rumsey, C. L., 1994. "Assessment of Two-Equation Turbulent Models for Transonic Flows", AIAA-94-2343, June 1994.

Nichols, R. H., Nelson, C. C., 2001. "Weapons Bay Acoustic Predictions Using a Multi-Scale Turbulence Model" Proceedings of the ITEA 2001 Aircraft-Stores Compatibility Symposium, March 2001.

Nichols, R. H., Nelson, C. C., 2003. " Applications of Hybrid RANS/LES Turbulence Models". AIAA-2003-0083.

Silveira Neto, A., Grand, D., Metais, O., Lesieur, Marcel., 1993. "A numerical investigation of the coherent vortices in turbulence behind a backward-facing step". Journal of Fluid Mechanics, Vol. 256, pp. 1-25.

Smagorinsky, J., 1963, "General Circulation Experiments with Primitive Equations", Mon. Weather Rev., vol. 91, pp. 99-164.

Spalart, P.R. and Allmaras, S.R. "A One-Equation Turbulence Model for Aerodynamic Flows", La Recherche Aérospatiale, 1994, 1, p.5.

Spalart, P. R., Jou, W-H., Strelets, M., Allmaras, S. R., 1997. "Comments on the feasibility of LES for wings, and on a hybrid RANS/LES approach". First AFSOR International Conference on DNS/LES, 4-8 August 1997, Rouston, LA. Advances in DNS/LES.

Spode, C., 2006 "Simulação de Grandes Escalas e Simulação Híbrida RANS/LES do escoamento sobre o degrau com condições de contorno turbulentas". Dissertação de Mestrado, Universidade Federal de Uberlândia.

Spode, C., Campregher, R., Silveira Neto, A., 2006, "Influência das condições de contorno na Simulação de Grandes Escalas de Escoamentos Turbulentos". Submetido à EPTT2006, Rio de Janeiro – Brasil.

Tennekes, H. Lumley, J. L., 1994. " A First Course in Turbulence". 15ª ed. The MIT Press, Massachusetts.

Yoshizawa, A., 1993. "Bridging between eddy-viscosity-type and second-order models using a two-scale DIA". In 9th Int. Symp. On Turbulent Shear Flow, Volume 3, pp. 23.1.1-23.1.6. Kyoto, Japan.

HIBRID RANS/LES SIMULATION OF TURBULENT FLOWS

Cleber Spode
Federal University of Uberlândia - 38400-902 Uberlândia – MG, Brazil.
cleber.spode@ufrgs.br

Rubens Campregher
Dalhousie University – Mechanical Engineering Department, Canada.
rubenscamp@dal.ca

Aristeu da Silveira Neto
Federal University of Uberlândia - 38400-902 Uberlândia – MG, Brazil.
aristeus@mecanica.ufu.br

Abstract. *Hybrid RANS/LES approach is used to predict the adiabatic three-dimensional turbulent flow over a backward-facing step by the Finite Volume Method applied to the incompressible Navier-Stokes equations. This classical flow is a benchmark for new fluid dynamics codes due to the fact that, despite its simple geometry, it presents a complex generation of three-dimensional structures, influencing transition phenomenon and the properties such as characteristic frequencies of vortex emission and re-attachment length. A hybrid RANS/LES technique based on the Spalart-Allmaras one equation model, also called DES (Detached-Eddy Simulation) was performed. The objective of this work is to evaluate the feasibility of hybrid methods to describe turbulent flows with massively separation by performing this test case. The results for re-attachment length around 6h, for the velocity profiles, and for Reynolds stress tensor present good agreement against experimental data.*

Key-words: Turbulence, Hybrid RANS/LES Modeling.

Paper CIT06-1006

SIMULAÇÃO NUMÉRICA DA INFLUÊNCIA DO *SWIRL* NO ESCOAMENTO EM DIFUSORES

José Gustavo Coelho
University of Brasilia. Departament of Mechanical Engineering.
70910-900 Brasilia. DF. Brazil
josegustavo@unb.br

Antonio C.P. Brasil Junior
University of Brasilia. Departament of Mechanical Engineering.
70910-900 Brasilia. DF. Brazil
brasiljr@unb.br

Resumo. *Nesse artigo é apresentado um estudo numérico sobre a influência do swirl no escoamento em um difusor. As simulações numéricas foram obtidas em ferramentas comerciais de cálculo de escoamentos (CFX-10), utilizando o modelo de turbulência SST, que permite uma descrição do campo fluidodinâmico em regiões bem próximas à parede. A estratégia de simulação tem em vista identificar precisamente o descolamento da camada limite próximo à parede do difusor. Resultados foram obtidos para diferentes intensidades de swirl. No primeiro caso um estudo de validação das metodologias de simulação foram desenvolvidas, de maneira à reproduzir resultados confiáveis, compatíveis com dados experimentais disponíveis na literatura. Por fim, resultados qualitativos e quantitativos foram conseguidos considerando diferentes intensidades de swirl.*

Palavras chave: difusor, swirl, SST.

1. Introdução

Os difusores são largamente usados para converter energia cinética em energia de pressão em escoamento e assim, possuem inúmeras utilidades industriais, como as turbo-máquinas, combustores de turbinas a gás, exaustores, tubeiras de foguetes, etc. Como a sua utilização é bastante ampla, existe a procura de um método que modele o escoamento no seu interior de forma precisa, com o intuito de melhorar a sua eficiência.

Juntamente com os difusores, outro tema que também tem se mostrado de grande interesse para a engenharia é a análise do efeito do giro do escoamento (*swirl*). A literatura possui inúmeros estudos, tanto experimentais como numéricos, sobre esses temas e alguns merecem destaque, como a análise realizada por Hach (1983), que calcula para diferentes difusores a influência da inserção do *swirl* e de eventuais distorções na entrada do difusor; Azad *et al* (1989) que faz uma análise do escoamento em difusores, objetivando o escoamento turbulento; Armfield *et al* (1990) determina as quantidades turbulentas do *swirl* no escoamento em difusores cônicos; Ishizaka (1993), que faz um estudo utilizando *CFD (Computational Fluid Dynamics*) em difusores de turbinas a gás; Clausen *et al* (1993), mede o desenvolvimento do *swirl* na camada limite turbulenta de um difusor cônico; e Edwards *et al* (1993) que compara duas técnicas experimentais para quantificar o *swirl* na entrada de um difusor anular.

Alguns trabalhos mais atuais também merecem destaque, como o realizado por Japikse (2000) que determina a correlação da geometria, do *swirl* e do bloqueio aerodinâmico (*blockage*) para a eficiência de um difusor anular; e Iaccarino (2000), que compara os resultados obtidos por diferentes códigos comerciais no estudo da turbulência em escoamentos em difusores.

Em muitas aplicações, principalmente na área de combustão, a pressão recuperada pelo difusor tem pouca importância, assim se introduz o *swirl* deliberadamente para induzir a aceleração da reação. Porém, na maioria dos empregos do difusor, a eficiência está diretamente relacionada com a quantidade de pressão que esse consegue recuperar. Para que o difusor apresente um bom rendimento, uma das mais importantes preocupações é o descolamento, que é a separação do escoamento da parede do difusor. O surgimento desse descolamento pode ser explicitado como sendo função das:

- Condições de entrada do difusor;
- Condições de saída;
- Número de Reynolds (Re);
- Número de Mach;
- Geometria do difusor.

Essa última é considerada de maior importância. Quando o número de Reynolds é acima de $5x10^4$, tem-se que a separação do escoamento se torna função basicamente da geometria do difusor, conforme Blevins (1894).

O presente trabalho visa o estudo de difusores em duas fases distintas. Primeiramente faz-se uma análise do trabalho experimental realizado por Clausen *et al* (1993), com o intuito de validar o modelo de turbulência escolhido. Posteriormente, faz-se a variação do *swirl* e se analisa as influências dessa variação para o desenvolvimento do escoamento e assim, para a eficiência do difusor.

A estratégia adotada para modelar a turbulência será RANS (*Reynolds Averaged Navier-Stokes*), visto que essa metodologia tem apresentado excelentes resultados, mesmo sem a utilização de computadores de grande porte. O modelo de turbulência escolhido foi o *SST* (*Shear Stress Transport*), pois esse modelo traz em sua formulação uma junção das melhores qualidades de outros dois modelos de fechamento de primeira ordem, o κ-ε e o κ-ω.

Os *softwares* utilizados nesse estudo são todos eles comerciais. Para a geração da geometria, utiliza-se o SOLIDWORKS e para a obtenção e pos processamento dos dados, usa-se o CFX-10 da ANSYS.

2. Equações Governantes e Modelagem da Turbulência

As equações governantes do escoamento analisado são as equações da continuidade (Eq. 1) e a da conservação do movimento (Eq. 2). Essas equações podem ser expressas em sua forma média como:

$$\frac{\partial}{\partial x_j}\left(\overline{u_j}\right) = 0; \tag{1}$$

$$\frac{\partial}{\partial t}\rho\left(\overline{u_j}\right) + \frac{\partial}{\partial x_k}\rho\left(\overline{u_j}\,\overline{u_k}\right) = -\frac{\partial \overline{p}}{\partial x_i} + \frac{\partial \overline{\tau_{ij}}}{\partial x_i} + \frac{\partial}{\partial x_k}\rho\left(\nu_\tau\left(\frac{\partial \overline{u_j}}{\partial u_k} + \frac{\overline{\partial u_k}}{\partial u_j}\right)\right), \tag{2}$$

onde u_i são as componentes de velocidade, ρ é a massa específica, p é a pressão, τ_{ij} é o tensor de tensões viscosas e ν_t é a viscosidade turbulenta, que será modelada dentro de um contexto de fechamento em primeira ordem utilizando o modelo *SST*.

Esse modelo de turbulência foi criado por Menter *et al* (2003) e sua lógica de funcionamento se dá de maneira bem simples. Para descrever o interior da camada limite, utiliza-se do modelo de turbulência k-ω e na parte central do escoamento usa-se o modelo k-ε. Essa mistura de modelos é realizada com o intuito de unir as melhores características de cada modelo. O modelo k-ω por exemplo, dispensa leis de parede ou funções de amortecimento, é numericamente estável e quando utilizado na região logarítmica da camada limite, responde bem a gradientes adversos de pressão e em escoamentos compressíveis. Porém, quando se passa a analisar a região da esteira turbulenta, esse modelo não apresenta bons resultados. Esse modelo não é muito indicado para analisar escoamentos cisalhantes livres, como jatos e camadas de mistura. Para que essa troca de modelos funcione, o *SST* utiliza-se de duas funções de combinação que estão relacionadas com a distância até a parede. As equações de transporte adicionais do modelo são dadas por:

$$\rho\frac{\partial k}{\partial t} + \rho\overline{u_j}\frac{\partial k}{\partial x_j} = \frac{\partial}{\partial x_j}\left(\left(\mu + \frac{\mu_t}{\sigma_k}\right)\frac{\partial k}{\partial x_j}\right) + \widetilde{P}_k - \beta^*\rho\kappa\omega, \tag{3}$$

onde:

$$P_k = \mu_t\frac{\partial u_i}{\partial x_j}\left(\frac{\partial u_i}{\partial x_j} + \frac{\partial u_j}{\partial x_i}\right) \Rightarrow P_k = \min(P_k, 10\cdot\beta^*\rho\kappa\omega); \tag{4}$$

$$\rho\frac{\partial \omega}{\partial t} + \rho\overline{u_j}\frac{\partial \omega}{\partial x_j} = \frac{\partial}{\partial x_j}\left(\left(\mu + \sigma_\omega\mu_t\right)\frac{\partial \omega}{\partial x_j}\right) + \alpha\rho S^2 - \beta\rho\omega^2 + 2(1-F_1)\rho\sigma_{w2}\frac{1}{\omega}\frac{\partial \kappa}{\partial x_i}\frac{\partial \omega}{\partial x_i}, \tag{5}$$

onde F_1 é definida como:

$$F_1 = \tanh\left\{\left\{\min\left[\max\left(\frac{\sqrt{\kappa}}{B^* \omega y}, \frac{500\nu}{y^2\omega}\right), \frac{4\rho\sigma_{\omega 2}\kappa}{CD_{\kappa\omega} y^2}\right]\right\}^4\right\}, \tag{6}$$

com

$$CD_{\kappa\omega} = \max\left(2\rho\sigma_{\omega 2}\frac{1}{\omega}\frac{\partial\kappa}{\partial x_i}\frac{\partial\omega}{\partial x_i}, 10^{-10}\right), \tag{7}$$

e y é a distância da superfície de não deslizamento.

As outras constantes são todas oriundas dos modelos $\kappa - \varepsilon$ e $\kappa - \omega$ com alguns ajustes e são determinadas como: β^*=0,09, α_1=5/9, β_1=3/40, σ_{k1}=0,85, $\sigma_{\omega 1}$=0,5, α_2=0,44, β_2=0,0828, σ_{k2}=1 e $\sigma_{\omega 2}$=0,856. (Menter, 2003).

Nota-se que a viscosidade de turbulência é calculada neste modelo como:

$$\nu_t = \frac{a_1 k}{\max(a_1\omega, \left(S_{ij}S_{ij}\right)^{\frac{1}{2}} F_2)}, \tag{8}$$

onde $\left(S_{ij}S_{ij}\right)^{\frac{1}{2}}$ é uma medida invariante do tensor taxa de deformação e F_2 é uma das funções de combinação e é determinada por:

$$F_2 = \tanh\left\{\left[\max\left(\frac{2\sqrt{\kappa}}{B^* \omega y}, \frac{500\nu}{y^2\omega}\right)^2\right]\right\}. \tag{9}$$

As formulações das funções de mistura F_1 e F_2 são baseadas na distância até a parede e nas variáveis. As funções de mistura têm como característica a delimitação de zonas aonde cada modelo irá atuar. Através do valor encontrado para as funções, o modelo irá mudar a formulação nas equações de transporte, onde a primeira função de mistura (F_2) é responsável pela troca de modelos na formulação da viscosidade turbulenta e a outra função de mistura, F_1 (Eq. 6) é responsável pela determinação das constantes do modelo, e pela troca de modelos na equação de transporte de ω. F_1 é igual a 1, considerando afastado da parede (utiliza a função $\kappa - \varepsilon$) e é igual a zero quando considera a função próxima à parede (nesse caso, faz uso da função $\kappa - \omega$).

3. Metodologia Numérica

Nesse trabalho, o método utilizado é o de volume finitos onde as equações aproximadas são obtidas através do balanço de conservação da propriedade evolutiva (massa, quantidade de movimento, etc.) no volume elementar. Para a obtenção das equações aproximadas, parte-se da equação diferencial na sua forma conservativa, integrando-a sobre o volume finito.

A discretização do domínio em volume de controle finito se realiza através de uma malha, Fig. 1, onde nessa os nós são cercados pelas superfícies que compreendem o volume. Esses nós são os responsáveis pela armazenagem de todas as propriedades dos fluidos e as soluções das variáveis. Nesse estudo, a malha se compreende de um conjunto de tetraedros não sobrepostos.

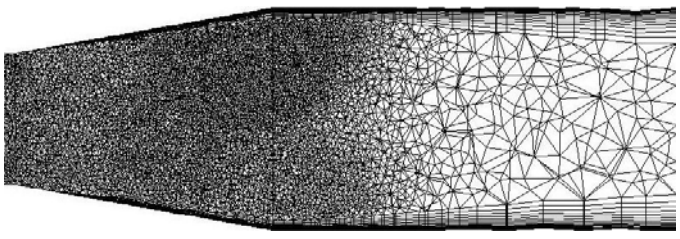

Figura 1: Discretização do domínio.

A malha de discretização não estruturada descrita acima, foi obtida a partir do uso de um sólido 3D. A criação desse sólido se efetua no programa SOLIDWORKS e a implementação de pós-processamento se realiza no CFX-10 (POST e CAD2MESH). A malha utilizada nesse trabalho se compõe de 1815960 elementos (345273 nós). Quando se trabalha com simulação numérica, costumeiramente se faz um estudo de malha para saber se a discretização realizada está obtendo resultados reais. Porém, nesse trabalho, esse estudo não será ilustrado, uma vez que os resultados numéricos são validados através da comparação com os resultados experimentais aqui mostrados.

Uma observação que merece destaque é o refinamento da malha nas regiões próximas da parede. Esse adensamento se faz necessário pelos fortes gradientes dos campos hidrodinâmicos localizados nessas regiões e por imposição do modelo de turbulência escolhido (*SST*). Para a realização desse refinamento, utiliza-se do recurso de inflação (*inflated mesh*) que consiste em posicionar camadas de elementos prismáticos, gerados paralelamente à superfície sólida próxima da qual se deseja o adensamento, Fig. 2.

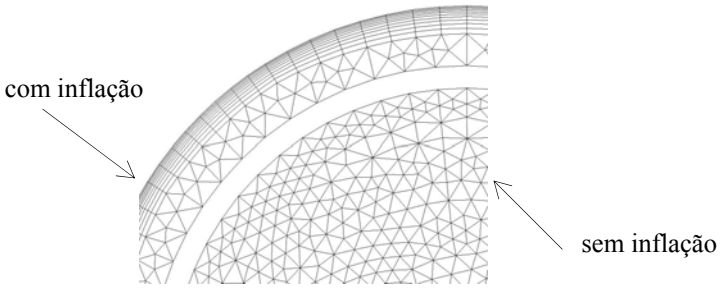

Figura 2: Exemplificação da função *inflated.*

A constituição do domínio se dá apenas pelo difusor e por um prolongamento da parte final. Realiza-se esse prolongamento para que eventuais influências das condições de contorno não sejam notadas, o que poderia produzir instabilidades numéricas.

Para as condições de contorno de entrada, utilizam-se perfis de velocidade. Esses perfis são oriundos do trabalho experimental realizado por Clausen *et al* (1993), onde os perfis de velocidade axial e tangencial são fornecidos.

A condição de contorno de saída foi imposta através da pressão, onde se fixa a pressão relativa como sendo nula, assim, a pressão de saída do difusor será a pressão atmosférica. Para a parede, utiliza-se a condição de contorno de não deslizamento.

4. Resultados e Discussões

Quando se analisa o comportamento do escoamento em difusores, uma grande preocupação se refere ao descolamento da camada limite. Essa análise tem grande relevância devida sua direta relação com a quantidade de energia de pressão que o difusor consegue recuperar, e assim, sua eficiência. Essa separação do escoamento se deve ao alto gradiente de pressão localizado nessa região, desacelerando e provendo um rápido alargamento da camada limite, causando recirculação próxima à parede.

Nesse estudo e escoamento apresenta *swirl* na entrada, o que acarreta num direcionamento do escoamento para a parede devido à força centrifuga, fazendo com que a camada limite tenha uma tendência menor a descolar, mesmo utilizando-se de uma angulação total acentuada. Isso acaba acarretando num aumento da pressão recuperada pelo difusor. Por outro lado, um aumento exagerado da intensidade do *swirl* reduz drasticamente a velocidade axial do escoamento na parte central, induzindo recirculações nessa região, o que acaba diminuindo consideravelmente a eficiência do difusor.

Em seu trabalho experimental, Clausen *et al* (1993), determina a intensidade do *swirl*, para uma geometria com angulação total, 2θ, igual a 20º (Fig. 3). Nesse estudo, faz-se a reprodução numérica desse experimento, com o intuito de inicialmente recuperar os dados obtidos para uma comparação/validação do modelo de turbulência e posteriormente, analisar as influências da variação do *swirl* para o desenvolvimento do escoamento e para o rendimento do difusor.

Os perfis de velocidade axial e tangencial usados são mostrados nas Fig. 4 e 5. Esses dados estão adimensionalizados, onde r* é o raio de entrada, igual a 0,13m e u* é a velocidade axial média na entrada do difusor, igual a 11,6 m/s.

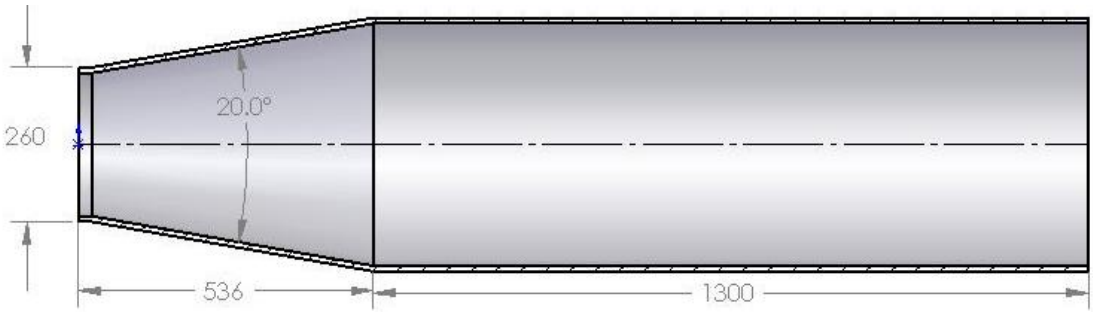

Figura 3: Dimensões da geometria utilizada por Clausen *et a l*(1993).
As dimensões estão em mm.

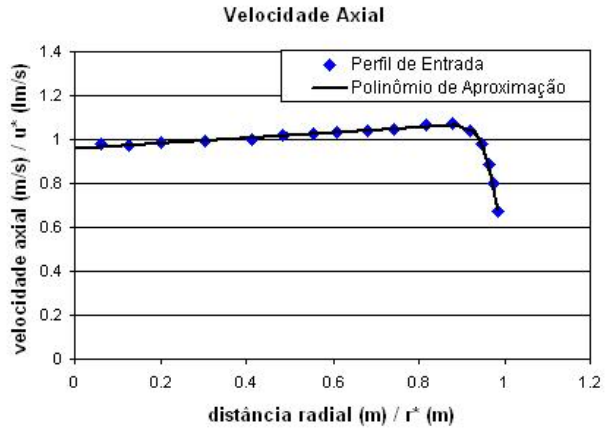

Figura 4: Aproximação numérica utilizada para o perfil de velocidade axial
na entrada do difusor, onde os pontos em azul são os dados experimentais.

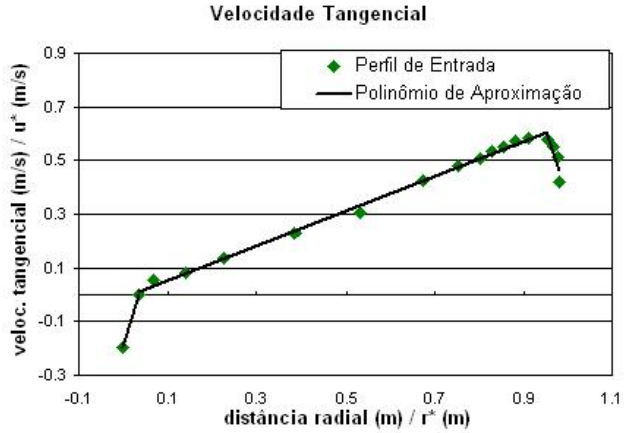

Figura 5: Aproximação numérica utilizada para o perfil de velocidade tangencial
na entrada do difusor, onde os pontos em verde são os dados experimentais.

Como citado anteriormente, a variação de pressão encontrada no difusor está diretamente relacionada com a sua eficiência. Nesse trabalho, opta-se por determinar a eficiência de um difusor através do coeficiente de pressão recuperada, *Cp,* equacionado na Eq. 10. Esse coeficiente pode ser definido como a razão entre a pressão recuperada pela pressão dinâmica disponível.

$$Cp = \frac{p - p_1}{\frac{1}{2}\rho U^2}. \tag{10}$$

onde, p é a pressão média em posições ao longo do difusor, p_1 é a pressão estática na entrada do difusor, ρ é a densidade da água e U a velocidade média na entrada do difusor.

A validação do modelo de turbulência se realiza através do Cp encontrado numericamente e experimentalmente, Fig. 6. Analisando essa variação de pressão na parede do difusor, pode-se perceber que inicialmente a pressão recuperada é muito grande, decaindo rapidamente. Esse rápido decréscimo é resultado da grande angulação usada nessa geometria.

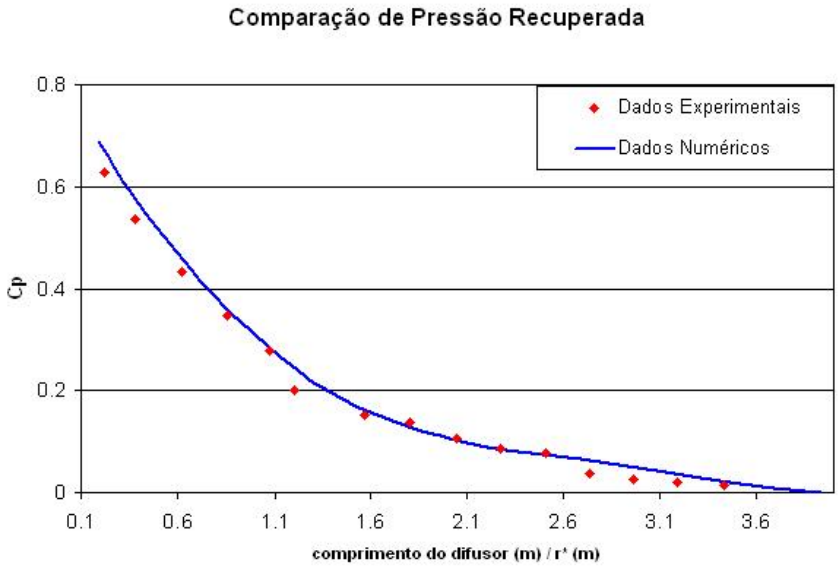

Figura 6: Comparação entre o Cp experimental e numérico.

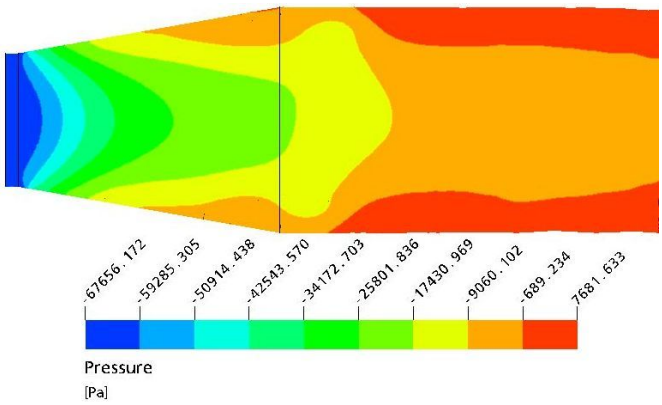

Figura 7: Contorno de pressão.

O aparecimento de gradiente de pressão adverso pode ser notado através dos contornos de pressão, Fig. 7. Essa visualização tem um importante caráter para a análise do difusor, pois mostra o aumento da pressão ao longo do seu comprimento longitudinal.

A redução da velocidade ao longo do difusor pode ser visualizada na Fig. 8 que mostra os contornos de velocidade. Essa redução de velocidade se dá devido à mudança de área e pode ser explicada pela equação da continuidade.

As linhas de corrente desse escoamento também foram analisadas, onde na Fig. 9 têm-se as linhas de corrente e na Fig. 10 as linhas de cisalhamento na parede do difusor. Através dessas figuras, pode-se perceber que essa geometria realmente possui uma angulação total muito grande. Recirculações na parte central do escoamento não são percebidas, porém, essa angulação total acrescida acarreta separação na região próxima da parede. Esse descolamento torna-se perceptível após a metade do difusor.

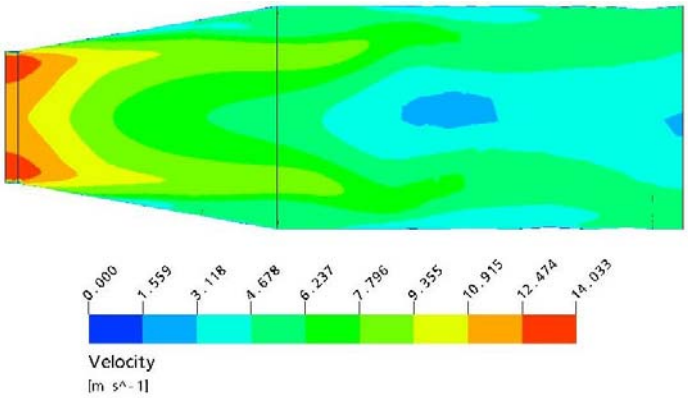

Figura 8: Contornos de velocidade.

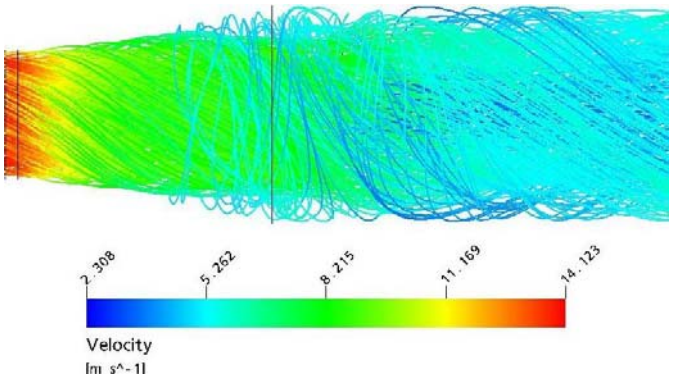

Figura 9: Visualização das linhas de corrente.

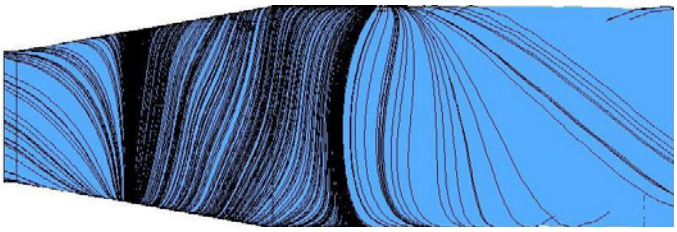

Figura 10: Visualização das linhas de cisalhamento na parede do difusor.

A manifestação mais intensa do *swirl* se dá a montando do difusor, se suavizando nas regiões mais a jusante (Fig. 10). Na parte prolongada do difusor, percebe-se que o desenvolvimento se assemelha ao encontrado à jusante, mostrando que esse artifício de prolongar a parte final da geometria realmente torna o escoamento no interior do difusor menos suscetível às condições de contorno.

O número de *swirl* utilizado até o presente momento é de 0,59 e sua determinação se realiza pela razão entre a velocidade máxima tangencial e a média da velocidade axial na entrada do difusor, u^*. Fazendo-se a variação da velocidade tangencial, se tem uma variação do *swirl*. Os outros números de *swirl* analisados nesse trabalho são 0,29; 0,46; 0,73; e 0,87.

O desenvolvimento do escoamento para os diferentes números de swirl se dá de forma diferenciada, conforma Fig. 11 a 15, onde se mostra a visualização num plano longitudinal. Com o intuito de ilustrar mais claramente o desenvolvimento do fluido, a quantidade de linhas de corrente foi reduzida no momento da geração da figura.

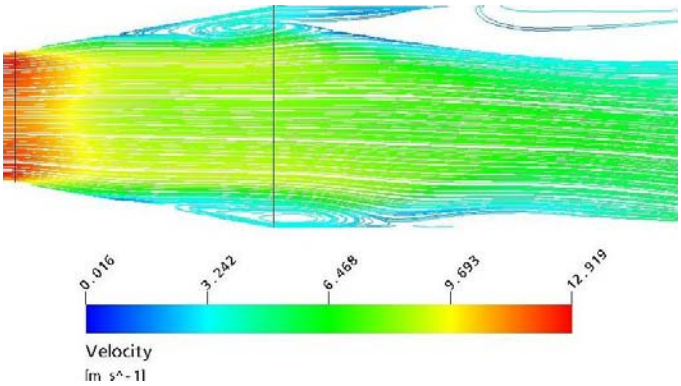

Figura 11: Visualização do escoamento no plano longitudinal, para um número de *swirl* de 0,29.

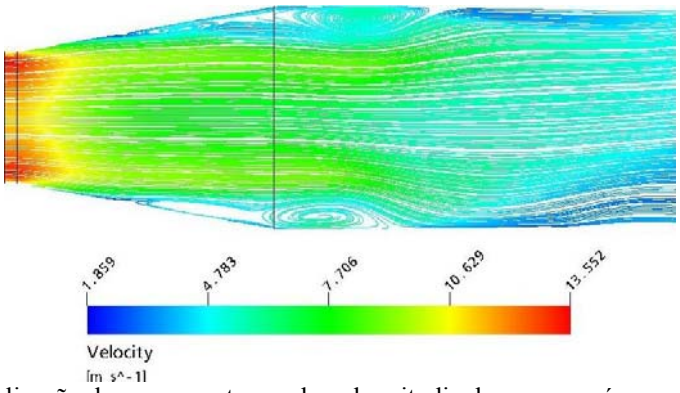

Figura 12: Visualização do escoamento no plano longitudinal, para um número de *swirl* de 0,46.

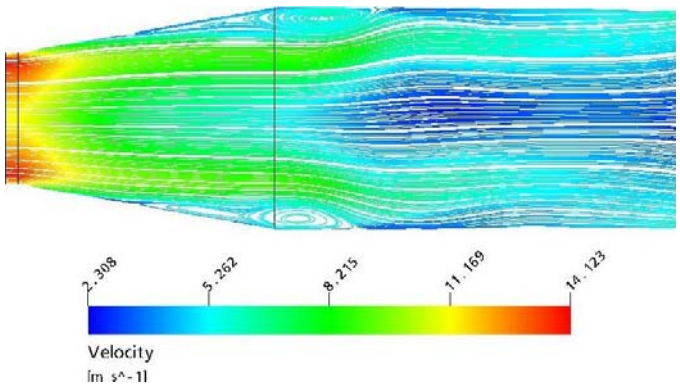

Figura 13: Visualização do escoamento no plano longitudinal, para um número de *swirl* de 0,59.

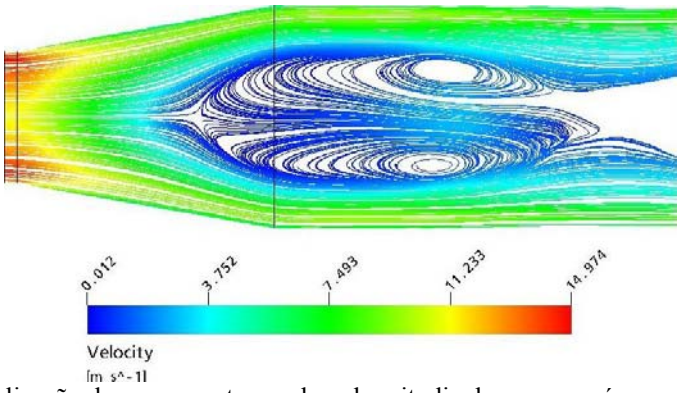

Figura 14: Visualização do escoamento no plano longitudinal, para um número de *swirl* de 0,73.

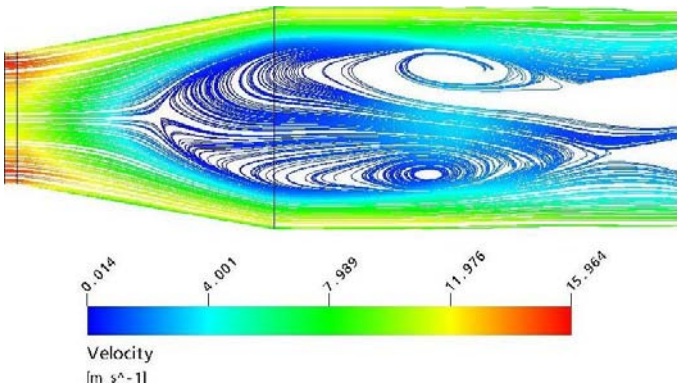

Figura 15: Visualização do escoamento no plano longitudinal, para um número de swirl de 0,87.

Conforme condição imposta na entrada, o aumento da velocidade tangencial resulta no aumento da intensidade do *swirl* e vice-versa.

Nas Fig. 11 e 12, a intensidade do giro do escoamento se apresenta de forma bem suave. Assim, o escoamento tem a tendência de se descolar da parede do difusor, diminuindo assim a sua capacidade de recuperar energia de pressão. A separação se torna perceptível após a metade da geometria. Esse descolamento já era esperado, uma vez que quando se trabalha com escoamentos sem *swirl*, a angulação total sugerida como sendo a "ótima" é de 7º. Blevins (1984) e Dixon (1998). Analisando a parte central do difusor, percebe-se que nessa região o escoamento não apresenta recirculações.

Nas Fig. 14 e 15, o alto número de *swirl* faz com que o escoamento literalmente "cole" na parede, fazendo com que nenhuma separação seja percebida, mesmo se tratando de uma angulação bem expressiva. Porém, essa alta intensidade do giro do escoamento, faz com que recirculações na parte central do escoamento sejam percebidas. Essa recirculação do escoamento na parte central acaba acarretando um decréscimo no seu rendimento.

O número de *swirl* que apresenta um melhor rendimento é o analisado experimentalmente por Clausen *et al* (1993). Descolamento na parte final do difusor é percebido, mas em uma intensidade menor que nos outros exemplos analisados, enquanto que na parte central, recirculações não são percebidas.

Uma comparação mais completa da eficiência dessas geometrias se dá na Fig. 16, onde o *Cp* para cada geometria é disposto.

Como já era esperado, o escoamento sem recirculações apresenta um rendimento melhor. Essa maior capacidade de recuperar energia se deve à diminuída separação do escoamento e à recirculação inexistente na parte central do escoamento.

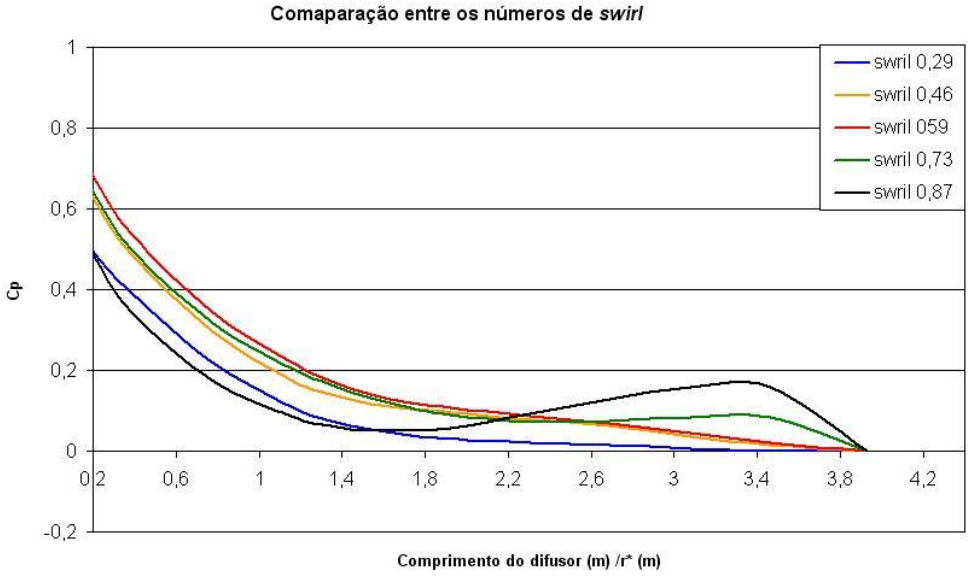

Figura 16: Comparação entre os Cp's para os números de *swirl* analisados.

Uma importante conclusão que pode ser tirada se refere à comparação da importância do descolamento e da recirculação do escoamento. Analisando os dois extremos (número de *swirl* igual a 0,29 e 0,73) percebe-se que ambos possuem rendimentos parecidos mesmo possuindo diferentes causas para a baixa quantidade de pressão recuperada.

Para os números de *swirl* mais elevados, percebe-se um aumento de rendimento na parte final. Esse "salto" do *Cp* se deve ao aumento de velocidade próxima da parede. Essa velocidade acentuada afeta o *Cp* porque a medida da pressão recuperada se realiza na parede do difusor.

Analisando a Fig. 16, pode-se fazer uma curva relacionando a intensidade do swirl com o coeficiente de pressão recuperada, conformo mostrado na Fig. 17.

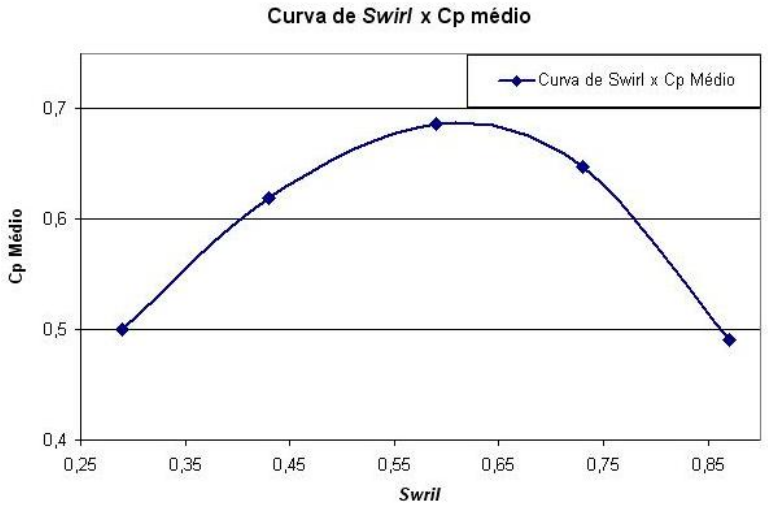

Figura 17: Curva da intensidade do número de *swirl* versus o coeficiente de pressão recuperada.

5. Conclusões

Um estudo numérico sobre as influências da variação do *swirl* no desenvolvimento do escoamento e no rendimento do difusor foi realizado. Inicialmente se faz a validação do modelo de turbulência, para posteriormente analisar as influências da variação do *swirl*.

O modelo de turbulência escolhido para esse trabalho, *SST*, mostra-se mais uma vez ser capaz de obter resultados satisfatórios, mesmo num caso extremo como é o estudo de difusores com angulação total elevada.

O prolongamento da geometria cumpre sua missão, não permitindo que condições de contorno influenciem o escoamento na parte interna do difusor.

A análise o *swirl* se mostra de grande valia, pois pôde comprovar a existência de uma intensidade de *swirl* ótima, ou seja, diminuindo ou aumentando o giro do escoamento o difusor começa a perder rendimento gradativamente. Esse decréscimo da pressão recuperada pode ser resultado de diferentes fenômenos hidrodinâmicos: o descolamento da parede do difusor (com número de *swirl* baixo) ou a recirculação na parte central do escoamento (número de *swirl* elevado).

6. Referências

Armfield S. W., Cho N. and Fletcher A. J., 1990, " Prediction of Turbulence Quantities for Swirling flow in Conical Diffusers", American Institute of Aeronatucis and Astronautics, Vol. 23, No 3 , pp. 453 - 460.

Azad R. S. and Kassab, S. Z, 1989, " Turbulent flow in a conical diffuser: Overview and implications", american Institute of Phisics, A 1 (3), pp.564 – 573.

Blevins R. D., 1984, "Applied Fluid Dynamics Handbook", Van Nostrand Reinhold Company, England, 145 p.

Clausen, P. D., Koh, S. G. and Wood D. H., 1993, " Measurement of a Swirling Turbulent Boundary Layer Developing in a Conical Diffuser", Experimental Thermal and Fluid Science, Vol. 6, pp. 39-48.

Dixon S. L., 1998, "Fluid Mechanics and Thermodynamics of Turbomachinery", Butterworth-Heinemann, England.

Edwards, R. J., Jambunathan K., Button B. L. and Rhine J. M., 1993, A Comparison of Two Swirl Measurement Techniques, Experimental Thermal and Fluid Science, Vol. 6, pp. 5-14.

Fontoura Rodrigues, J. L. A. F., 2003, "Escoamentos Turbulentos Parietais". In A. Silveira Neto and S. S. Mansur (Eds.),Turbulência,Volume 2, ABCM,Rio de Janeiro, Brasil, pp. 151–199.

Gotjans H., 2001, "Simulation of Draft Tube Flow with CFX", Second ERCOFTAC Worshop on Draft Tube Flow, Vattenfall Utvercling AB, Älvkarleby, Sweden.

Hach, C, 1983, "Calculation of Various Diffuser Flows with Inlet Swirl and Inlet Distortion Effects", American Institute of Aeronatucis and Astronautics, Vol. 21, No 8 , pp. 1127 – 1133.

Iaccarino G., 2000, Prediction of the Turbulent Flow in a Diffuser with Commercial CFD Codes, Annual Research Briefs 2000, pp. 271-279.

Ishizaka, K., Wakazono S., Yuri M. and Takahashi R., 2003, "CFD Studies of Industrial Gas Turbine Exhaust Diffusers", Proceeding of International gas Turbine Congress, Tokyo.

Japikse D,2000, "Correlation of Annular Diffuser Performance with Geometry, Swirl, and Blockage", 11Th Thermal ans Fluid Analysis Worshop, Cleveland, Ohio.

Maliska, C. R., 2002, "Transferência de Calor e Mecânica dos Fluidos Computacional", Livros Técnicos e Científicos Editora S. A.. Rio de Janeiro, Brasil, 424p.

Menter F. R., Kuntz M. and Langtry R., 2003, "Tem Years of Industrial Experience with the SST Turbulent Model", Turbulence, Heat and Mass Transfer, Vol 4.

Noleto, L. G.,2005, Comunicação Interna, Universidade de Brasilia, Brasil .

Silvestrini, J. H., 2003, "Simulação Numérica Direta e de Grandes Escalas de Escoamentos Transicionais e Turbulentos". In A. Silveira-Neto and S. S. Mansur (Eds.), Turbulência, Volume 2, ABCM, Rio de Janeiro, Brasil. pp. 1 – 72

Silveira Neto, A., 2002a, "Fundamentos da Turbulência nos Fluidos". In A. P. S. Freire, P. Menut, and J. Su (Eds.), Turbulência, Volume 1, ABCM, Rio de Janeiro. pp. 1 - 46.

Silveira Neto, A., 2002b, "Simulação de Grandes Escalas de Escoamentos Turbulentos".,In A. P. S. Freire, P. Menut, and J. Su (Eds.), Turbulência, Volume 1, ABCM, Rio de Janeiro, Brasil., pp. 157–188.

Silva Freire, A. P. ,2002, "Equações do Movimento e Resultados Assintóticos Aplicados à Teoria de Camada Limite". In A. P. S. Freire, P. Menut, and J. Su (Eds.), Turbulência, Volume 1, ABCM, Rio de Janeiro, Brasil, pp. 49–99.

Shuja S. Z. and Habib M. A., 1996, "Fluid flow and heat transfer characteristic in axisymmetric annular diffusers", Vol. 25 No. pp 133 – 150.

NUMERICAL SIMULATION OF THE INFLUENCE OF THE SWIRL IN THE FLOW IN DIFFUSERS

José Gustavo Coelho
University of Brasilia. Departament of Mechanical Engineering.
70910-900 Brasilia. DF. Brazil
josegustavo@unb.br

Antonio C.P. Brasil Junior
University of Brasilia. Departament of Mechanical Engineering.
70910-900 Brasilia. DF. Brazil
brasiljr@unb.br

Abstract

This article presents a numerical study about the influence of the swirling flow inside a conical diffuser. The simulations were performed with the ANSYS CFX commercial code using the SST turbulence model. This model allows an accurate description of the wall bounded flow. This simulation aim to identify the boundary layer separation near to the wall of the diffuser. The results were obtained for different swirling intensities. First, a validation study of simulation methodologies was made. The aim is to compare the numerical results with experimentation, in order to determine the reliability of the simulation. Finally, quantitative and qualitative results were obtained for different swirling intensities.

Keywords: diffuser, swirl, SST

Proceedings of the 11th Brazilian Congress of Thermal Sciences and Engineering – ENCIT 2006
Braz. Soc. of Mechanical Sciences and Engineering – ABCM, Curitiba, Brazil, Dec. 5-8, 2006

Paper CIT06-1018

COMPUTATIONAL RESULTS FOR WALBURN-SCHNECK AND CASSON MODELS FOR BLOOD IN SMALL VESSELS

Márcio A. A. Bortoloti
LNCC - Laboratório Nacional de Computação Científica, Av. Getúlio Vargas, 333, Quitandinha, 25651-070, Petrópolis-RJ, Brasil
marciob@lncc.br

José Karam F.
LNCC - Laboratório Nacional de Computação Científica, Av. Getúlio Vargas, 333, Quitandinha, 25651-070, Petrópolis-RJ, Brasil
jkfi@lncc.br

Abstract. *From the several constitutive models that have been proposed for blood, in this work we focus attention in the classical Casson model, considering an yield stress term, that have been adapted to allow hematocrit variation effects by Wang and Stoltz and the Walburn-Schneck four-parameters model that was developed based on an apparent viscosity consisting of two exponential functions of the hematocrit and of the protein content. In this work, blood flow behaviour is computationally investigated for the Walburn-Schneck and the Casson rheological models, in case of small vessels with non-uniform diameter. Computational results have been obtained here by a stabilized mixed finite element method in velocity and discontinuous pressure interpolations.*

keywords: *Blood Flow, Pseudoplastic Flow, Finite Element Method, Wlburn-Schneck Relation, Casson Relation*

1. Introduction

It is very well known that blood is a very complex fluid that alter its structure depending on the place it is passing along the circulatory loop. These differences come out depending on several factors, being very evident if blood is flowing in large or in small vessels. From the fluid mechanics point of view blood behaves in non-newtonian manner when going from large (in general Newtonian) to small vessels.

As a suspension of cells, in a nearly newtonian fluid called plasma with major part of the suspension in number being the red blood cell, it is commonly accepted that the aggregative phenomenon that happens at low shear rate combined with the rate of cells to whole blood (hematocrit) are two important factors to produce blood non-Newtonian behaviours.

Several constitutive equations have been proposed in order to describe the non-Newtonian behaviour of blood, none of them being the general one and experiments supply the constitutive parameters from viscometric flows only.

In order to investigate the flow characterization of two of those constitutive equations that were built from experimental viscometric data results, when they are applied to non viscometric flows, in this work computational experiments are performed for stenosed vessels in "meso-micro" circulation to the classical Casson relation compared with the Walburn-Schneck model considering the dependence of hematocrit and shear rate (through the complete deformation rate tensor) on the viscosity. Viscometric data have been used from the measurements of Wang and Stoltz, 1994 for the Casson model.

From the mathematical point of view, the nonlinearity and the divergence free internal restriction impose some care to be taken when approaching numerically these models. Computational results are obtained here by a mixed stabilized finite element method in continuous velocity and discontinuous pressure interpolations which generalizes the formulation of Karam and Loula, 1992 for non linear problems, allowing equal interpolation orders that are prohibited when classical methods are used.

2. Rheology of Blood in Brief

Blood is a concentrated suspension of several big and small components in an approximate newtonian fluid, the plasma. It can be divided as 55% vol. being plasma and 45% being cells or formed elements. Hematocrit is an important quantity defined as the volume rate of cells relative to the whole blood volume. Cells consist of approximately 95% of red blood cells - RBC - (without cell structure), 0.13% of white cells - WBC- and 4.5%

of platelets by number. Plasma is a dilute electrolytic solution with 8% of proteins in weight. These ingredients are sufficient to make blood a very complex structure that is able to adapt itself in a great extent depending on several circumstances to which it is submitted combined with the function it has to perform. This capability of adaptability reflects in altering the viscosity along the circulatory loop.

A general behaviour of blood in terms of its resistance to flow is characterized by a pseudoplastic effect when the shear rate is low, as is the case in small vessels, and a constant viscosity (Newtonian behaviour) when the shear rate increases, as is the general case in large vessels (macrocirculation). Blood rheology concentrates in the lower shear rate region where complexities, difficulties in measuring and modelling are challenging.

Some of the more important effects that can alter blood viscosity are briefly commented in the following.

2.1. Effect of temperature on the viscosity

There are many open questions in this item. But as the shear rate decreases more sensitive is the viscosity with the temperature. Viscosity decreasing inversely with temperature. This is important for filtration processes.

2.2. Effect of particle shape on the viscosity

Although the behaviour of the eritrocytes relative to the variability of the shape (as is the case inside the blood vessels) be very difficult to measure, it is known that in a suspension with rigid particles non-Newtonian behaviour increases when the particle shape is more different than the spherical one. For low shear rate, in experiments with red cells in Dextran 40 aqueous solution Whitmore, 1979 observed several non-Newtonian behaviours.

2.3. Effect of protein composition on the viscosity

Three of the numerous proteins are very important for the alteration of the viscosity. Fibrinogen, globulin and albumin. Globulin is responsible to augment blood viscosity and albumin tends to lower it. It is coherent with the known fact that albumin does not participate in the aggregation process rather than fibrinogen, globulin. If the only protein present is the globulin, viscosity increases relative to whole blood (only without fibrinogen) and it has a non-Newtonian behaviour by decreasing with increased shear rate and reaching a constant value when shear rate is high. If only fibrinogen is present it lowers the viscosity but it is constant even for low shear rate (newtonian behaviour). Fibrinogen and globulin participate in the clotting net process. Then fibrinogen is took out when making measurements. It is impossible to measure viscosity directly without breaking the clotting process. Then it is impossible to make direct experiments with whole blood.

2.4. Effect of hematocrit on the viscosity

Effect of hematocrit on the viscosity can be estimated through viscometric flows at constant shear rates. Viscosity increases linearly for high shear rate and high hematocrit. It is pseudoplastic when shear rate decreases and more pseudoplastic when hematocrit increases, in this case.

2.5. Effect of shear rate on the viscosity

Every effect is related to the shear rate. For low shear rate region, blood apparent viscosity increases when shear rate decreases. This is associated with two effects: (a) red cells of blood tend to aggregate forming *rouleaux* when shear rate decreases and aggregation is broken when shear rate increases, lowering again the viscosity; (b) for high shear rate, the flexible RBCs deform and tend to align with the flow direction, without aggregation, lowering the viscosity.

These are some of the effects that alter viscosity, and by them one can feel the difficulties in measuring apparent viscosity and mathematical modelling to characterize blood behaviour. Pathologies can alter the viscosity, as well.

To generate constitutive equations for fluids, one can measure the apparent viscosity in a rheometer (for blood, capillary or Couette type viscometers are most used) and then a curve fitting is performed. However, to measure the apparent viscosity, the shear rate has to be fixed with the fluid assumed to be Newtonian in each experiment. Moreover, it is difficult, or impossible, to make measurements and control all the variables that play a complex game. Then, taking some constitutive equation models, it is of interest to know how they behave and what are the differences among their results when they are applied to non-viscometric flows. This is important specially when in case of micro or non-macrocirculation, where shear rate is low and non-Newtonian behaviours are expected. For macrocirculation, Newtonian, linear and constant viscosity, is a suitable model since high shear rates are the case. Two of the above effects are focused here: hematocrit and shear rate.

3. Mathematical Model

For the purposes of these work, and considering small vessels where pulsating flow is negligible, we assume stationary creeping flow that can be characterized by solving the following system:

$$-\operatorname{div}\sigma = \mathbf{f} \tag{1}$$

$$\operatorname{div}\mathbf{u} = 0 \tag{2}$$

with the stress tensor

$$\sigma = -p\mathbf{I} + \tau, \tag{3}$$

where p is the hydrostatic pressure, $\mathbf{I}$ is the identity tensor, $\mathbf{f}$ denotes the body forces, $\mathbf{u}$ is the velocity field and τ is the nonlinear shear rate tensor coming from each of the following constitutive equations.

3.1. Casson Model

One of the first non linear constitutive equations to model blood is the classical Casson's equation, (Casson, 1959), originally conceived for paint suspension and firstly used by Scott-Blair, 1959 for blood

$$\tau^{1/2} = \tau_y^{1/2} + \eta|\gamma|^{1/2} \tag{4}$$

that predict an "yield stress", τ_y, and η being an asymptotic "Newtonian" value for high shear rate. It can be rewritten to allow hematocrit dependence as:

$$\tau(H)^{1/2} = \tau_y(H)^{1/2} + \eta(H)|\gamma|^{1/2} \tag{5}$$

And using the data measured by Wang and Stoltz, 1994 these functions become

$$\tau_y = (0.625H)^3 \tag{6}$$

$$\eta = \eta_P(1-H)^{-2.5}, \tag{7}$$

$$\eta_P = 1.22mPa\,s \qquad 0 < H < 1. \tag{8}$$

Without entering the discussion on the existence of an yield stress, for blood, we are considering this equation only as a two function parameters constitutive relation.

3.2. Walburn-Schneck Model

Starting from the power-law relation, given in a general form by

$$\tau = \mu_{app}\gamma^{n-1} \tag{9}$$

$$\mu_{app} = K|\gamma|^{n-1} \tag{10}$$

where μ_{app} is the apparent viscosity, K is the consistence parameter and n is the power index, that comes from the Cross model, (Cross, 1965), Walburn and Schneck, 1976 proposed an empirical equation, with four parameters, for the shear stress×shear rate relation, depending on the hematocrit, and, additionally, including a fixed amount of proteins:

$$\mu_{app} = C_1 \exp(100HC_2)\exp\left(\frac{C_4 TPMA}{(100H)^2}\right)\gamma^{-100HC_3} \tag{11}$$

with
$C_1 = 0.797mPa\,s$,
$C_2 = 0.608$,
$C_3 = 0.00499$,
$C_4 = 14.585lg^{-1}$,
$TPMA = 25.9gl^{-1}$.

and $TPMA$ being the amount of proteins except albumin. Basically it is composed of fibrinogen and globulin.

4. Finite element method used

By introducing each of the above models in the Eqs. (1) framework, the system has been solved here by applying the mixed stabilized finite element method in velocity-discontinuous pressure interpolations introduced in Bortoloti and Karam, 2004 which generalizes the formulation of Karam and Loula, 1992, for non linear problems, allowing equal interpolation orders and a Uzawa algorithm to solve for the nonlinearities.

5. Computational results

Numerical experiments have been performed for an axisymmetric 50% stenosed vessel whose mesh is illustrated in Fig. 1, with dimensions $d_1 = 500\mu m$, $d_2 = 50\mu m$. Meshes have been constructed with 2000 biquadratic elements. Hematocrits of 30% to 55% have been tested, and the range from 30% to 40% is considered as pathological. It was prescribed an inlet velocity of $250\mu m/s$. Results may be observed from Figs. 2(a)-4(f) in terms of pressure along the center axis ($d_1/2$), Fig. 2, velocity profiles, Fig. 3, and apparent viscosities, Fig. 4, at the center section of the stenose ($d_2/2$).

From the pressure results, in Fig 2, it can be seen that Casson's model gives lower pressure values along all the vessel, also giving a lower global pressure gradient. For very low hematocrit, 30%, it can be observed that Casson's model gives lower values than the Newtonian pressure profile, while Walburn-Schneck's gives higher values even in this case. By observing the stenosed area, the two models give almost the same pressure gradient for low hematocrits, but Walburn-Schneck's gives a higher gradient when the concentration increases Figs 2(e,f).

From the velocity profiles, it is very difficult to distinguish Casson results from the Newtonian behaviour, while the Walburn-Schneck's model varies from nearly Newtonian for low hematocrit to more non-Newtonian when the hematocrit increases.

From the apparent viscosity results, Fig. 4, it can be observed that for very low hematocrit, 30% and 35%, Casson's model is very close to the Newtonian behaviour while Walburn-Schneck's exhibit more differences, with higher values than those of the Casson's model along all the stenosed section. For medium hematocrit, 40% and 45%, the two models almost equal apparent viscosity magnitudes near the wall, but maintain the differences in the core of the section. Increasing the hematocrit, the two models invert places at the region near the wall, with Walburn-Schneck's giving lower apparent viscosity values than the Casson's, butwith even higher values in the core.

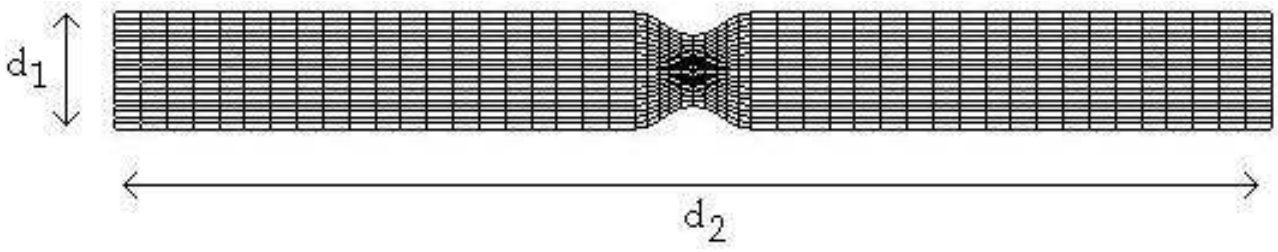

Figure 1: Stenotic mesh

.

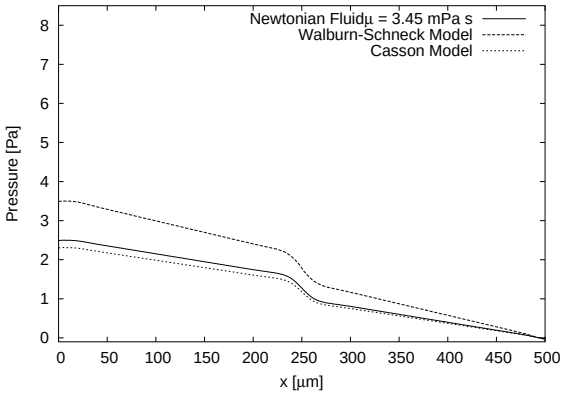

(a) H=0.3

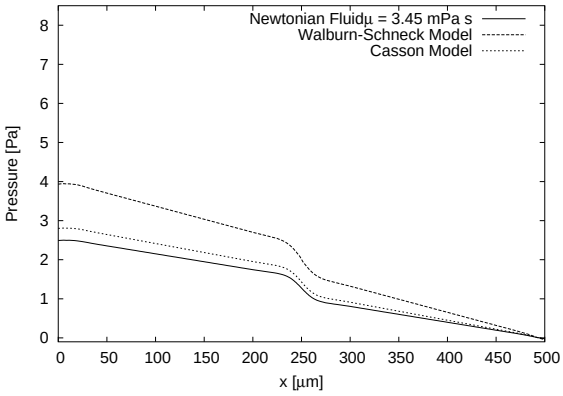

(b) H=0.35

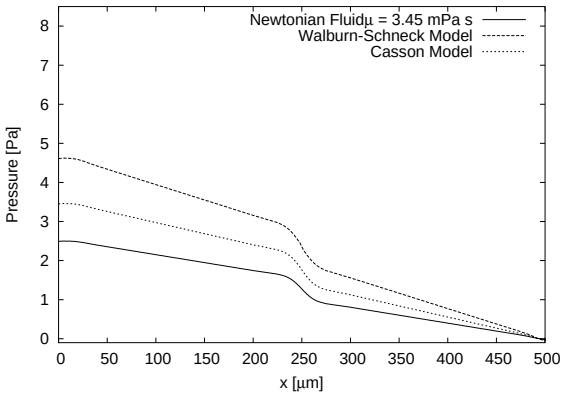

(c) H=0.4

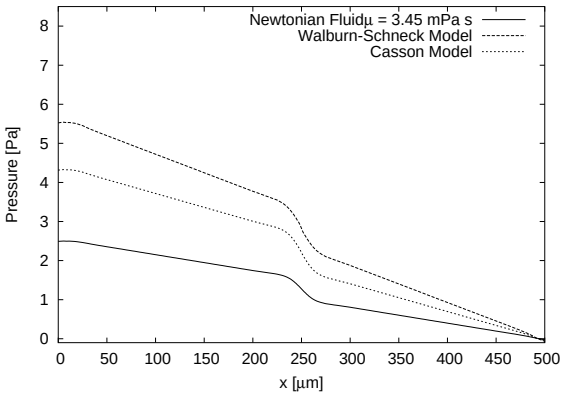

(d) H=0.45

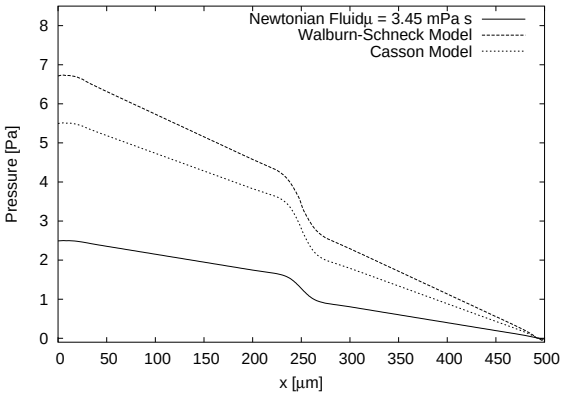

(e) H=0.5

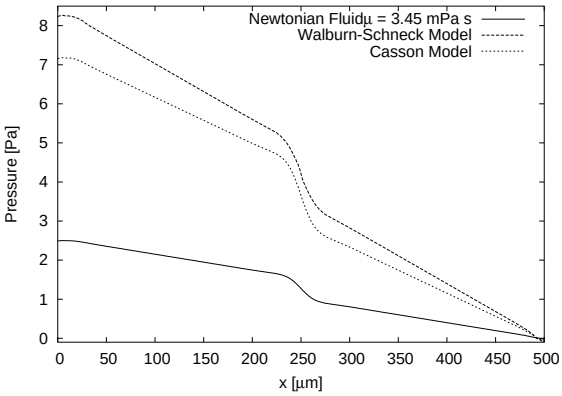

(f) H=0.55

Figure 2: Pressures

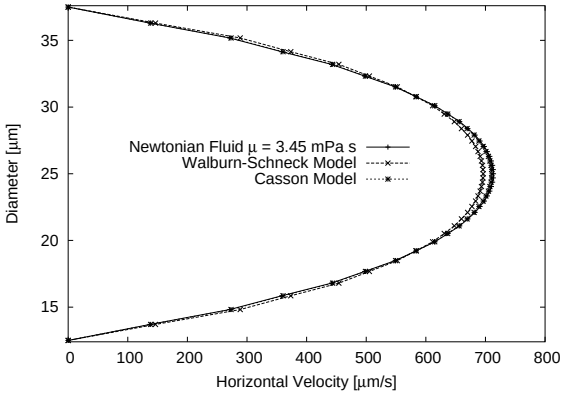

(a) H=0.3

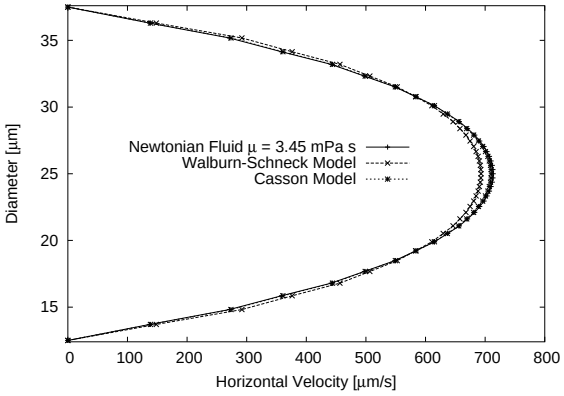

(b) H=0.35

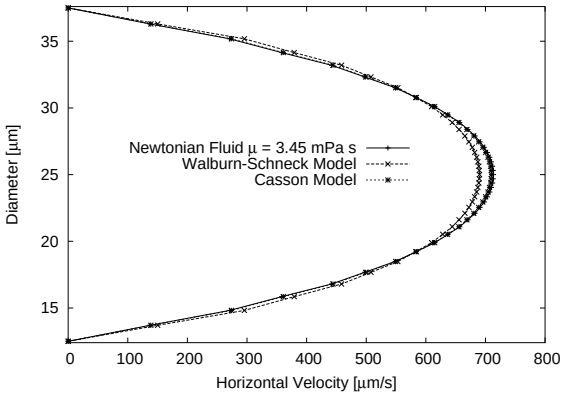

(c) H=0.4

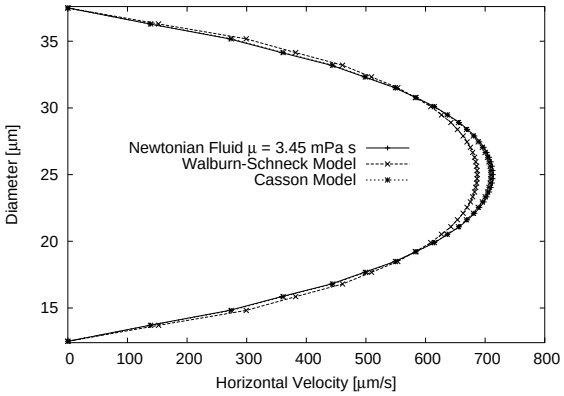

(d) H=0.45

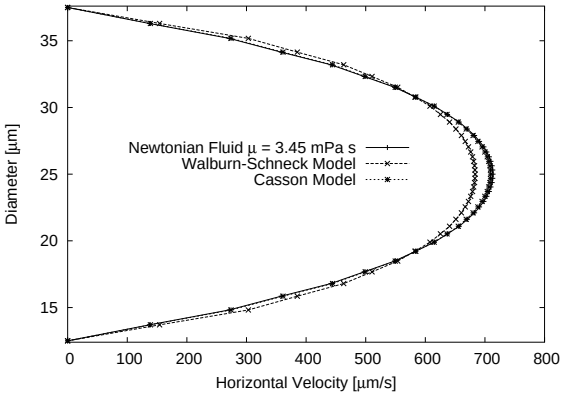

(e) H=0.5

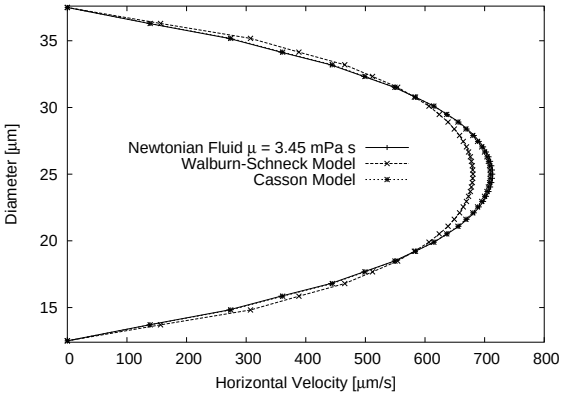

(f) H=0.55

Figure 3: Velocities

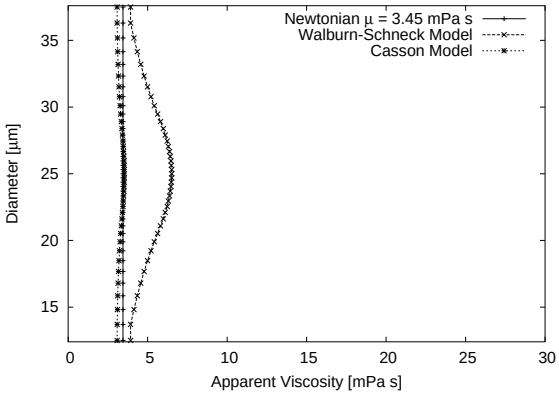

(a) H=0.3

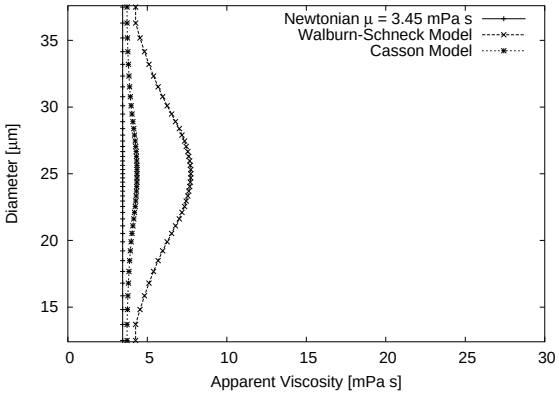

(b) H=0.35

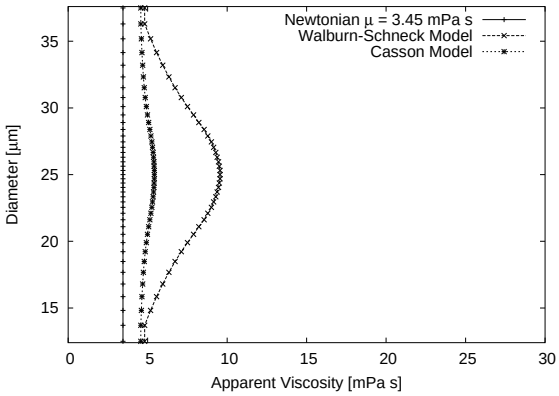

(c) H=0.4

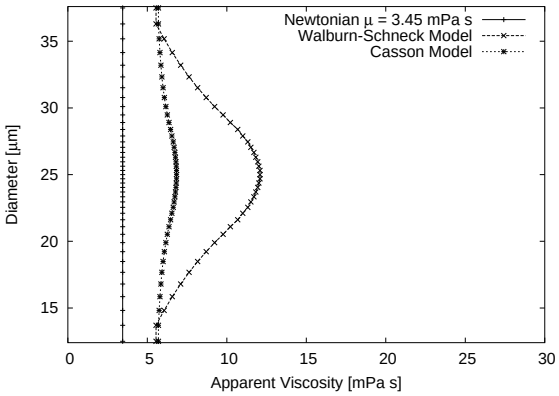

(d) H=0.45

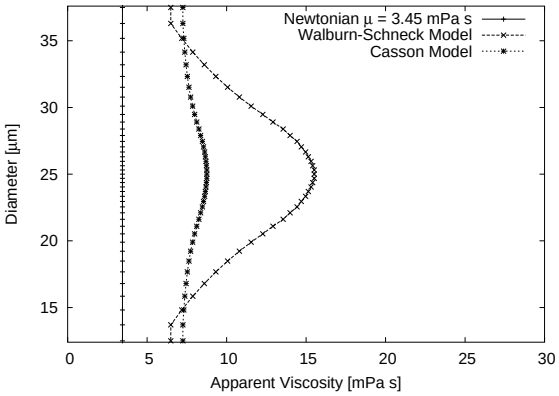

(e) H=0.5

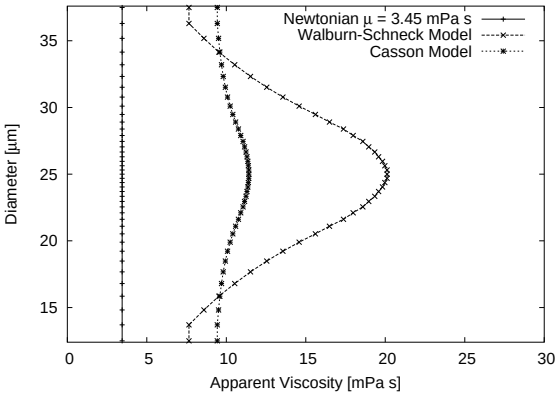

(f) H=0.55

Figure 4: Apparent viscosities

6. Conclusions and Remarks

In this work, some differences between Casson and Walburn-Schneck models models have been studied, considering the dependence of the apparent viscosity with hematocrit besides the shear rate for blood flow in small stenosed vessels for a simple non-viscometric case, for hematocrit ranging from 30% to 55%.

A mixed stabilized finite element method in velocity-discontinuous pressure has been used, allowing equal order interpolations and ensuring more accuracy once the constraint is locally satisfied.

The numerical results reveal different behaviours when Casson and Walburn-Schneck models are considered, with hematocrit and shear playing important roles. The Walburn-Schneck model shown to be more able to capture the non-Newtonian behaviour when increasing the hematocrit, even suggesting, indirectly from the apparent viscosity results, that a kind of sigma-effect is being captured in this case.

7. Acknowledgements

M. A. A. Bortoloti would like to acknowledge CAPES/BR for his graduate grant.

J. Karam F. would like to acknowledge PRONEX/FAPERJ project no. E-26/171.199/2003.

8. References

Bortoloti, M. A. A. and Karam, J., 2004, Equal-order v-p stabilized finite element methods for pseudoplasticity, "Proceedings of the II - Brazilian Conference on Rheology", Vol. 1, pp. 73–74, Rio de Janeiro.

Casson, N., 1959, "A flow equation for pigment-oil suspensions of the printing-ink type, In Rheology of Disperse System", Pergamon Press (Oxford-NY), S.Paulo, Brazil, C. C. Mill Ed.

Cross, M. M., 1965, Rheology of non-Newtonian fluids: a new flow equation for pseudoplastic system, "Journal of Colloidal Science", Vol. 20, pp. 417–437.

Karam, J. and Loula, A. F. D., 1992, On stable equal-order finite element formulations for incompressible flow problems, "International Journal for Numerical Methods in Engineering", Vol. 34, No. 2, pp. 655–665.

Scott-Blair, G., 1959, An Equation for the Flow of Blood, Plasma and Serum Through Glass Capillaries, "Nature", Vol. 183, pp. 613–614.

Walburn, F. and Schneck, D., 1976, A constitutive equation for whole human blood, "Biorheology", Vol. 13, pp. 201–218.

Wang, X. and Stoltz, J., 1994, Characterization of pathological bloods with a new rheological relationship, "Clinical Hemorheology", Vol. 14, No. 2, pp. 237–244.

Whitmore, R., 1979, a, "Proceedings of the I-National Conference on Rheology", Vol. a, pp. 43–45, Melbourne.

Proceedings of the 11th Brazilian Congress of Thermal Sciences and Engineering -- ENCIT 2006
Braz. Soc. of Mechanical Sciences and Engineering -- ABCM, Curitiba, Brazil,- Dec. 5-8, 2006

Paper CIT06-1026

AN ALTERNATIVE PROCEDURE FOR SIMULATING A CLASS OF HYPERBOLIC SYSTEMS

Maria Laura Martins-Costa
Laboratory of Theoretical and Applied Mechanics (LMTA), Mechanical Engineering Department (TEM-PGMEC)
Universidade Federal Fluminense, Rua Passo da Pátria, 156, 24210-240 Niterói/RJ, Brazil; laura@gar.uff.br

Eliane Maracajá Porto
Laboratory of Theoretical and Applied Mechanics (LMTA-PGMEC), Universidade Federal Fluminense, Niterói/RJ, Brazil
National Laboratory of Scientific Computation (LNCC), Petrópolis/RJ, Brazil; eliane@lncc.br

Rogério M. Saldanha da Gama
Mechanical Engineering Department, Universidade do Estado do Rio de Janeiro
Rua São Francisco Xavier, 524, 20550-013, Rio de Janeiro, RJ, Brazil; rsgama@domain.com.br

Abstract. *This work presents an alternative numerical procedure for simulating nonlinear hyperbolic systems, using Glimm's method for advancing in time. The standard procedure to implement this methodology suffers from the disadvantage of requiring a complete solution of the associated Riemann problem – a task, in general, not easily reached. The alternative procedure introduced in this article consists in approximating the solution of the associated Riemann problem by piecewise constant functions always satisfying the jump condition – thus circumventing the difficulty of solving the Riemann problem and giving rise to an approximation easier to implement with lower computational cost. In order to illustrate the good performance of the alternative methodology proposed, the transport of a pollutant an environment representing an atmosphere is simulated. Comparison with the standard procedure, employing the complete solution of the associated Riemann problem for implementing Glimm's scheme, has shown good agreement.*

Keywords*. Glimm's scheme, Riemann solver, shock waves, pollutant transport.*

1. Introduction

Most transport phenomena description involve parabolic or elliptic partial differential equations which always admit regular solutions whose simulation may employ well known numerical tools like finite elements, finite differences or finite volumes. Hyperbolic systems, on the other hand, allow very realistic descriptions, since the propagation of any quantity – or information – in real natural phenomena is characterized by a finite speed. Glimm's scheme – a reliable method for simulating hyperbolic systems whose accuracy is mathematically ensured (Glimm, 1965; Chorin, 1976) is based on a theory presenting a solid thermodynamic basis (Smoller, 1983). Two important features of this numerical scheme, actually the scheme that better preserves the shock identity among the numerical procedures adequate to cope with discontinuous problems, deserve a special remark. First, if the width of the steps tends to zero, the approximation obtained by Glimm's method tends to the exact solution of the problem – considering its weak formulation. Another characteristic of this scheme is that it does not dissipate shocks, preserving their magnitude (no diffusion being observed) and position. Nevertheless, the standard procedure for its implementation – when simulating problems with any initial data and/or boundary condition – suffers from the disadvantage of requiring previous knowledge of the complete solution of the Riemann problem associated with the hyperbolic system, since Glimm's method approximates hyperbolic nonlinear problems by appropriately gathering the solution of a certain number of associated Riemann problems. The determination of the complete solution of the associated Riemann problem, besides its inherent difficulty, renders the computational implementation more expensive.

This article is focused on the proposition of a Riemann solver allowing to build a simple and efficient procedure for simulating hyperbolic systems circumventing the requirement of a complete solution for the associated Riemann problem. This solution is approximated by piecewise constant functions satisfying the jump conditions, but not necessarily the entropy condition. The above-mentioned procedure, associated with Glimm's scheme, provides a convenient way for simulating hyperbolic systems. Simulations of the transport of a pollutant in the atmosphere exemplify the methodology.

The simplified mathematical modeling for the transport of a pollutant in the air employed in this work combines the mass and linear momentum balances for the air-pollutant mixture – the classical equations of gas dynamics – with the pollutant mass balance, giving rise to a nonlinear system of hyperbolic partial differential equations presenting discontinuities – which will be shock waves in case they satisfy the entropy condition – in addition to classical solutions. Besides, this genuinely nonlinear hyperbolic resulting problem presents a very interesting feature – a contact shock characterized by presenting the same speed of the second eigenvalue. Along this shock there is a jump in the

pollutant concentration but, on the other hand, the mass density and the velocity remain constant, i.e. they do not jump (Martins-Costa and Saldanha da Gama, 2003).

2. Mechanical model

The transport of a pollutant in the air is described by considering a simplified model based on the mass and linear momentum conservation for the air-pollutant mixture and the mass balance for the pollutant along with some hypotheses. First the mass transfer is supposed to be caused by an advection process of the pollutant – from now on denoted as *A* constituent – in the air, which is assumed as an ideal gas (all viscosity effects being neglected). Diffusion will be neglected, when compared to advection. Also, supposing the presence of a sufficiently small quantity of the constituent *A* in the air – at any time instant, along with mass densities with the same order of magnitude for both air and the *A* constituent, the mass and linear momentum balance equations for the mixture can be approximated by mass and linear momentum balances for the air. Additional simplifying assumptions are absence of chemical reactions which could alter the quantity of the constituent *A* and the pressure acting on the air being *p* considered as a function of the air mass density ρ only, its derivative satisfying $\hat{p}'(\rho) > 0$. Finally, a plane horizontal flow is considered so that the air velocity field $\mathbf{v}$ may be reduced to a single component on the flow direction $\mathbf{v} = v\mathbf{i}$ and gravitational effects may be omitted. Considering all the above stated hypotheses, the transport of a pollutant in the air is mathematically described by the following nonlinear homogeneous hyperbolic system

$$\begin{aligned}
&\frac{\partial \rho}{\partial t} + \frac{\partial}{\partial x}(\rho v) = 0 \\
&\frac{\partial}{\partial t}(\rho v) + \frac{\partial}{\partial x}(\rho v^2 + p) = 0 \\
&\frac{\partial}{\partial t}(\rho \omega_A) + \frac{\partial}{\partial x}(\rho \omega_A v) = 0
\end{aligned} \tag{1}$$

in which ω_A represents the pollutant concentration in the mixture, expressed by the ratio between the pollutant mass density and the mixture (or air) mass density. Defining the following dimensionless quantities

$$\eta = \frac{x}{L} \quad \tau = \frac{t\breve{v}}{L} \quad \tilde{\rho} = \frac{\rho}{\breve{\rho}} \quad \tilde{v} = \frac{v}{\breve{v}} \quad \tilde{p} = \frac{p}{\breve{\rho}\breve{v}^2} \tag{2}$$

in which L is a reference length, $\breve{v}$ a reference velocity and $\breve{\rho}$ a reference mass density. Now, the following redefinition of variables is considered: $F \equiv \tilde{\rho}$, $G \equiv \tilde{\rho}\tilde{v}$, $H \equiv \tilde{\rho}\omega_A$. So problem (1), which is subjected to a given data at $t = t_n$ ($F = \hat{F}_n(x)$, $G = \hat{G}_n(x)$ and $H = \hat{H}_n(x)$ at $t = t_n$) is rewritten as

$$\begin{aligned}
&\frac{\partial F}{\partial \tau} + \frac{\partial G}{\partial \eta} = 0 \\
&\frac{\partial G}{\partial \tau} + \frac{\partial}{\partial \eta}\left(\frac{G^2}{F} + \tilde{p}(F)\right) = 0 \\
&\frac{\partial H}{\partial \tau} + \frac{\partial}{\partial \eta}\left(\frac{GH}{F}\right) = 0
\end{aligned} \tag{3}$$

3. Numerical approximation

Considering the Riemann problem associated with the hyperbolic system (3), its generalized solution is reached by connecting the left (*L*) and right (*R*) states by means of two intermediate constant states (*1 and *2) as follows: $(F_L, G_L, H_L) \rightarrow (F_{*1}, G_{*1}, H_{*1}) \rightarrow (F_{*2}, G_{*2}, H_{*2}) \rightarrow (F_R, G_R, H_R)$. The connection between the states $L \rightarrow *1$, $*1 \rightarrow *2$ and $*2 \rightarrow R$ may be performed either by rarefactions or shocks. A particular type of link is verified in the Riemann problem associated to (1) – the connection between intermediate states *1 and *2 is always a contact shock, where there is no jump for both variables F and G – in such a way that $F_{*1} = F_{*2}$ and $G_{*1} = G_{*2}$. The jump is verified solely for H, with a propagation speed G/F. A contact shock may be viewed as the limiting case of a rarefaction in which the rarefaction fan is reduced to a single line; namely a discontinuity with associated eigenvalue corresponding exactly to the shock speed (Martins-Costa and Saldanha da Gama, 2003).

System (3) is approximated by employing Glimm's scheme, described in details in Martins-Costa and Saldanha da Gama (2003), to advance from time τ_n to time τ_{n+1}. Glimm's method for building a solution for an initial value

problem consists in appropriately gathering the solution of a certain previously chosen number of Riemann problems to successively march from time $\tau = \tau_n$ to time $\tau_{n+1} = \tau_n + \Delta\tau$. The arbitrary initial condition given by a function of the position η ($F(\eta,0) = F_0(\eta)$, $G(\eta,0) = G_0(\eta)$, $H(\eta,0) = H_0(\eta)$) is approximated by piecewise constant functions, by convenience, with equal width steps:

$$\begin{aligned} F &= \hat{F}_n(\eta) \approx F_{n_i} = \hat{F}_n(\eta_i + \theta_n \Delta\eta) \\ G &= \hat{G}_n(\eta) \approx G_{n_i} = \hat{G}_n(\eta_i + \theta_n \Delta\eta) \qquad \text{for} \quad \eta_i - \frac{\Delta\eta}{2} < \eta < \eta_i + \frac{\Delta\eta}{2} \\ H &= \hat{H}_n(\eta) \approx H_{n_i} = \hat{H}_n(\eta_i + \theta_n \Delta\eta) \end{aligned} \tag{4}$$

in which θ_n is a number randomly chosen in the open interval $(-1/2,\ +1/2)$ and $\Delta\eta$ is the width of each step ($\Delta\eta = \eta_{i+1} - \eta_i$). In the sequence, a Riemann problem – an initial value problem whose initial condition must be a step function – is to be solved for each two consecutive steps.

The above approximations for the initial data give rise, for each two consecutive steps, to the following Riemann problem – associated with equations (3)-(4):

$$\begin{aligned} &\frac{\partial F}{\partial \tau} + \frac{\partial G}{\partial \eta} = 0 \\ &\frac{\partial G}{\partial \tau} + \frac{\partial}{\partial \eta}\left(\frac{G^2}{F} + \tilde{p}(F) \right) = 0 \\ &\frac{\partial H}{\partial \tau} + \frac{\partial}{\partial \eta}\left(\frac{GH}{F} \right) = 0 \end{aligned} \tag{5}$$

with

$$\begin{aligned} &(F,G,H) = (F_{n_i}, G_{n_i}, H_{n_i}) \qquad \text{for} \quad \tau = \tau_n\ ,\ -\infty < \eta < \eta_i + \frac{\Delta\eta}{2} \\ &(F,G,H) = (F_{n_{i+1}}, G_{n_{i+1}}, H_{n_{i+1}}) \qquad \text{for} \quad \tau = \tau_n\ ,\ \eta_i + \frac{\Delta\eta}{2} < \eta < \infty. \end{aligned} \tag{6}$$

Denoting by $\bar{F}_{n_i}, \bar{G}_{n_i}$ and $\bar{H}_{n_i}$ the generalized solution of equations (5)-(6), the approximation for the solution of equations (3)-(4) at time τ_{n+1} is given as follows:

$$\begin{aligned} F &= \hat{F}_{n+1}(\eta) \approx \bar{F}_{n_i}(\eta,\ \tau_{n+1}) \\ G &= \hat{G}_{n+1}(\eta) \approx \bar{G}_{n_i}(\eta,\ \tau_{n+1}) \qquad \text{for} \quad \eta_i < \eta < \eta_{i+1} \\ H &= \hat{H}_{n+1}(\eta) \approx \bar{H}_{n_i}(\eta,\ \tau_{n+1}) \end{aligned} \tag{7}$$

Remark: In order to prevent interactions among nearby shocks of adjacent Riemann problems, the time step $\Delta\tau$ and, consequently, τ_{n+1} for problem (5)-(6), must be chosen in such a way that the Courant-Friedrichs-Lewy condition (Smoller, 1983) be satisfied, thus assuring the solution uniqueness:

$$\tau_{n+1} - \tau_n \le \frac{\Delta\eta}{2|\lambda|_{\max}} \tag{8}$$

where $|\lambda|_{\max}$ is the maximum (in absolute value) propagation speed of shocks, considering all the Riemann problems at time τ_n.

4. The alternative procedure

The procedure proposed in this work consists in replacing the exact solution of the Riemann problem (5)-(6) by an approximation – built in by assuming any two given states always connected by a discontinuity which may not satisfy the entropy conditions – in order to advance in time through Glimm's scheme. Essentially the approximation consists in searching for a weak solution for the associated Riemann problem within a space of functions with a maximum of two jumps.

A generalized solution for the Riemann problem described in equations problems (5)-(6), depending on (η,τ), may be expressed as a function of a similarity variable $\xi=\eta/\tau$ (Smoller, 1983; Saldanha da Gama, 1990) being constructed by connecting the left (*L*) and right (*R*) states to an intermediate state $(*)$ by rarefactions or shocks as follows: $(F_L,G_L,H_L) \rightarrow (F_*,G_*,H_*) \rightarrow (F_R,G_R,H_R)$ or $(F_L,G_L) \rightarrow (F_*,G_*) \rightarrow (F_R,G_R)$.

A particular type of link is verified in problem (5)-(6) – the connection between intermediate states *1 and *2 is a contact shock (Lax, 1971; Smoller, 1983). In other words, the connection that would be called a 2-rarefaction – and would give rise to a continuous solution – cannot be found in problem (5)-(6), in which the second eigenvalue is coincident with the velocity that must be constant (Martins-Costa and Saldanha da Gama, 2003). This contact shock is characterized by absence of jump for both variables ρ and ρv – in such a way that $(\rho)_{*1}=(\rho)_{*2}$ and $(\rho v)_{*1}=(\rho v)_{*2}$. The jump is verified solely for $\rho\omega_A$, with a propagation speed v ($s_2=\lambda_2=v$) – the speed assuming the same value of the corresponding eigenvalue. A contact shock may be viewed as the limiting case of a rarefaction in which the rarefaction fan is reduced to a single line; namely a discontinuity with associated eigenvalue corresponding exactly to the shock speed (there is no entropy generation). Unlike ordinary shocks, the contact shock is reversible, without any associated entropy generation (Saldanha da Gama, 1990). So, the connections in the Riemann problem referred in equations (5)-(6) to be summarized as (Martins-Costa and Saldanha da Gama, 2003):

$$\begin{array}{ccccc} L & \underset{R1\text{ or }S1}{\Longrightarrow} & *1 & \underset{\text{Contact Shock}}{\Longrightarrow} & *2 \quad \underset{R3\text{ or }S3}{\Longrightarrow} \quad R \\ & & \omega_{A_1}=\omega_{A_L} & & \omega_{A_2}=\omega_{A_R} \\ & & \rho_{*1}=\rho_{*2}=\rho_* & & \\ & & v_{*1}=v_{*2}=v_* & & \end{array} \tag{9}$$

in which *R1* and *R3* denote possible rarefaction in connections 1 and 3 while *S1* and *S3* refer to possible shock in these connections. The result stated in equation (9) gives rise to an important simplification, allowing the former three-variables problem (5)-(6) to be reduced to a two variables (v and ρ) one with only two connections to be determined, namely, $L \underset{R1\text{ or }S1}{\Longrightarrow} * \underset{R3\text{ or }S3}{\Longrightarrow} R$. So, the referred states may be connected either by an *i*-rarefaction or an *i*-shock.

4.1. On the Riemann solver

The considerations above allow expressing the associated Riemann problem to system (5)-(6) as:

$$\left.\begin{array}{r} \dfrac{\partial F}{\partial\tau}+\dfrac{\partial G}{\partial\eta}=0 \\ \dfrac{\partial G}{\partial\tau}+\dfrac{\partial}{\partial\eta}\left(\dfrac{G^2}{F}+p(F)\right)=0 \end{array}\right\} \quad \tau>\overline{\tau}\,, \qquad -\infty<\eta<\infty \tag{10}$$

$$\begin{array}{ll} (F,G)=(F_L,G_R) & \text{for} \quad \tau=\overline{\tau}\,, \quad \eta<\overline{\eta} \\ (F,G)=(F_R,G_R) & \text{for} \quad \tau=\overline{\tau}\,, \quad \eta>\overline{\eta} \end{array} \tag{11}$$

The eigenvalues of (10) are given (in increasing order) by

$$\lambda_i=\frac{G}{F}+(-1)^i(p^{\backslash})^{1/2}=v+(-1)^i(p^{\backslash})^{1/2} \qquad i=1,2 \tag{12}$$

Since $p^{\backslash}>0$ for all η and τ, (10)-(11) is a hyperbolic system (genuinely nonlinear provided $p^{\backslash\backslash}$ is positive (or negative) everywhere). Problem (10)-(11) is called a Riemann problem whose generalized solution depends on the ratio $(\eta-\overline{\eta})/(\tau-\overline{\tau})$, being reached by connecting the left state (F_L,G_L) and the right state (F_R,G_R) to an intermediate state (F_*,G_*), as stated before $L \underset{Raref\text{ or }Shock}{\Longrightarrow} * \underset{Raref\text{ or }Shock}{\Longrightarrow} R$.

Two states are connected by an *i*-rarefaction (Lax, 1971; John, 1974) – a continuous solution of the associated Riemann problem – when the corresponding eigenvalues λ_i are increasing functions of $(\eta-\overline{\eta})/(\tau-\overline{\tau})$ between these states. In this case the solution (F,G) depends continuously on $(\eta-\overline{\eta})/(\tau-\overline{\tau})$ between these two states and associated to an an *i*-rarefaction there exists a Riemann invariant given by:

$$R_i = v - (-1)^i \int \frac{\sqrt{p'}}{\rho} d\rho = \text{constant} \qquad i = 1, 2 \tag{13}$$

This invariant is a constant between two states connected by an *i*-rarefaction.

If the eigenvalues λ_i are decreasing functions of $(\eta - \overline{\eta})/(\tau - \overline{\tau})$, the states are connected by an *i*-shock (a discontinuous solution) with speed s_i and the entropy conditions are automatically satisfied. Since weak solutions cannot assure uniqueness of solution (Keyfitz and Kranzer, 1978), the so-called entropy condition must be verified in order that uniqueness is preserved. Considering two given states connected by an *i*-Shock with speed s_i, the following jump conditions – denoted as Rankine-Hugoniot conditions – associated with equation (10), must be satisfied:

$$s_i = \frac{[\![G]\!]}{[\![F]\!]} = \frac{[\![G^2/F + p]\!]}{[\![G]\!]} \tag{14}$$

in which s_i represents the speed of discontinuity propagation and $[\![f]\!]$, the jump of a quantity f.

The main purpose of the present work is the proposition of a Riemann solver, which consists of assuming the solution within a space of piecewise constant functions. So that any two given states will be connected by a shock. In other words

$$(F_L, G_L) \rightarrow \text{1-shock} \rightarrow (F_*, G_*) \rightarrow \text{2-shock} \rightarrow (F_R, G_R) \tag{15}$$

This approximation no longer requires considering the original four possible solutions: $(F_L, G_L) \underset{\text{Raref or Shock}}{\Longrightarrow} (F_*, G_*) \underset{\text{Raref or Shock}}{\Longrightarrow} (F_R, G_R)$. On the other hand, the entropy conditions are not ensured. It is to be noticed that the conservation laws are satisfied in a weak sense.

The (generalized) solution of (10)-(11), within a space of piecewise constant functions, is reached as follows ($z = (\eta - \overline{\eta})/(\tau - \overline{\tau})$)

$$(F, G) = \begin{cases} (F_L, G_L) & \text{if} \quad -\infty < z < s_1 \\ (F_*, G_*) & \text{if} \quad s_1 < z < s_2 \\ (F_R, G_R) & \text{if} \quad s_2 < z < \infty \end{cases} \tag{16}$$

For instance, when $p = \rho^2$, we have

$$\begin{aligned} v_* - v_L &= -(\rho_* - \rho_L)\left[\left(\frac{p_* - p_L}{\rho_* - \rho_L}\right)\frac{1}{\rho_* \rho_L}\right]^{1/2} \\ v_R - v_* &= (\rho_R - \rho_*)\left[\left(\frac{p_R - p_*}{\rho_R - \rho_*}\right)\frac{1}{\rho_R \rho_*}\right]^{1/2} \end{aligned} \tag{17}$$

being ρ_* the unique positive root (always exists) of

$$v_R - v_L = (\rho_R - \rho_*)\left[\left(\frac{p_R - p_*}{\rho_R - \rho_*}\right)\frac{1}{\rho_R \rho_*}\right]^{1/2} - (\rho_* - \rho_L)\left[\left(\frac{p_* - p_L}{\rho_* - \rho_L}\right)\frac{1}{\rho_* \rho_L}\right]^{1/2} \tag{18}$$

while the shock speeds are given by

$$s_1 = \frac{G_* - G_L}{F_* - F_L} = \frac{\rho_* v_* - \rho_L v_L}{\rho_* - \rho_L} \quad \text{and} \quad s_2 = \frac{G_R - G_*}{F_R - F_*} = \frac{\rho_R v_R - \rho_* v_*}{\rho_R - \rho_*} \tag{19}$$

It is convenient to evaluate v_* from

$$v_* - v_L = \frac{1}{2}\left\{-(\rho_* - \rho_L)\left[\left(\frac{p_* - p_L}{\rho_* - \rho_L}\right)\frac{1}{\rho_* \rho_L}\right]^{1/2} - (\rho_R - \rho_*)\left[\left(\frac{p_R - p_*}{\rho_R - \rho_*}\right)\frac{1}{\rho_R \rho_*}\right]^{1/2}\right\} + \frac{v_L + v_R}{2} \tag{20}$$

In all the above stated solutions the quantities λ and s are such that

$$\begin{aligned}
&\lambda_{1_L} = (G/F)_L - \sqrt{(\tilde{p}')_L} \qquad \text{with} \quad (\tilde{p}')_L = \left.\frac{d\tilde{p}}{dF}\right|_{F=F_L} \\
&\lambda_{1_*} = (G/F)_* - \sqrt{(\tilde{p}')_*} \qquad \text{with} \quad (\tilde{p}')_* = \left.\frac{d\tilde{p}}{dF}\right|_{F=F_*} \\
&\lambda_{3_*} = (G/F)_* + \sqrt{(\tilde{p}')_*} \qquad \text{with} \quad (\tilde{p}')_* = \left.\frac{d\tilde{p}}{dF}\right|_{F=F_*} \\
&\lambda_{3_R} = (G/F)_R + \sqrt{(\tilde{p}')_R} \qquad \text{with} \quad (\tilde{p}')_R = \left.\frac{d\tilde{p}}{dF}\right|_{F=F_R}
\end{aligned} \tag{21}$$

and

$$s_1 = \frac{G_L - G_*}{F_L - F_*} \qquad s_2 = (G/F)_* \qquad s_3 = \frac{G_* - G_R}{F_* - F_R}. \tag{22}$$

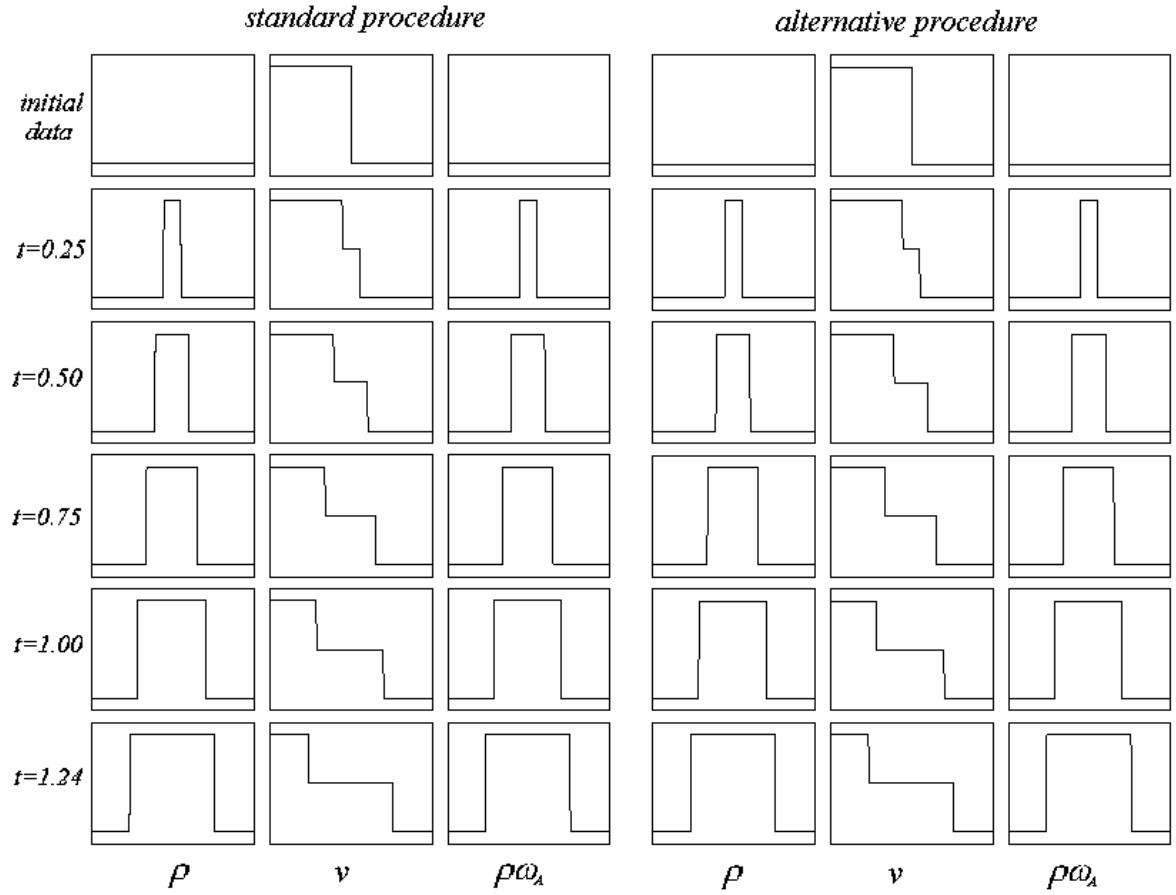

Figure 1. Gas density, velocity and pollutant concentration per unit volume variation with position - Left: Riemann exact solution; Right: Riemann solver. Initial data: constant ρ and ω_A and step function for v.

5. Some results

Figures 1 to 4 show results for gas density, velocity and pollutant concentration per unit volume for five selected time instants, allowing to observe the good performance of the Riemann solver presented in this work. In all the depicted results the vertical axis corresponds to the numerical value assumed by one of these three considered variables, the horizontal one being the spatial coordinate *x*. Besides, all the qualitative results exhibited were obtained by employing a convenient normalization, in such a way that zero and unit displayed values for the variables associated with ρ, v and $\rho\omega_A$ correspond to the minimum and maximum actual values in which ρ, v and $\rho\omega_A$ are redefined as:

$$\frac{\rho-(\rho)_{\min}}{(\rho)_{\max}-(\rho)_{\min}}\rightarrow\rho \qquad \frac{v-(v)_{\min}}{(v)_{\max}-(v)_{\min}}\rightarrow v \qquad \frac{\rho\omega_A-(\rho\omega_A)_{\min}}{(\rho\omega_A)_{\max}-(\rho\omega_A)_{\min}}\rightarrow \rho\omega_A.. \tag{23}$$

It is important to notice that neither ρ nor ω_A assume negative values. In all the results an unbounded domain $(-\infty < x < \infty)$ is considered with distinct initial data to show the evolution of gas density, velocity and pollutant concentration per unit volume.

The three columns at the left hand side – namely a set composed by three columns and six lines, each line representing a distinct time instant, the first one being the imposed initial condition – depict ρ, v and $\rho\omega_A$ obtained by employing Glimm's scheme with 300 steps for each time advance built from the exact solution of the associated Riemann problem. The three columns at the right hand side show equivalent results for ρ, v and $\rho\omega_A$ also obtained by using Glimm's scheme with 300 steps for each advance in time but constructed by using the Riemann solver proposed in this work.

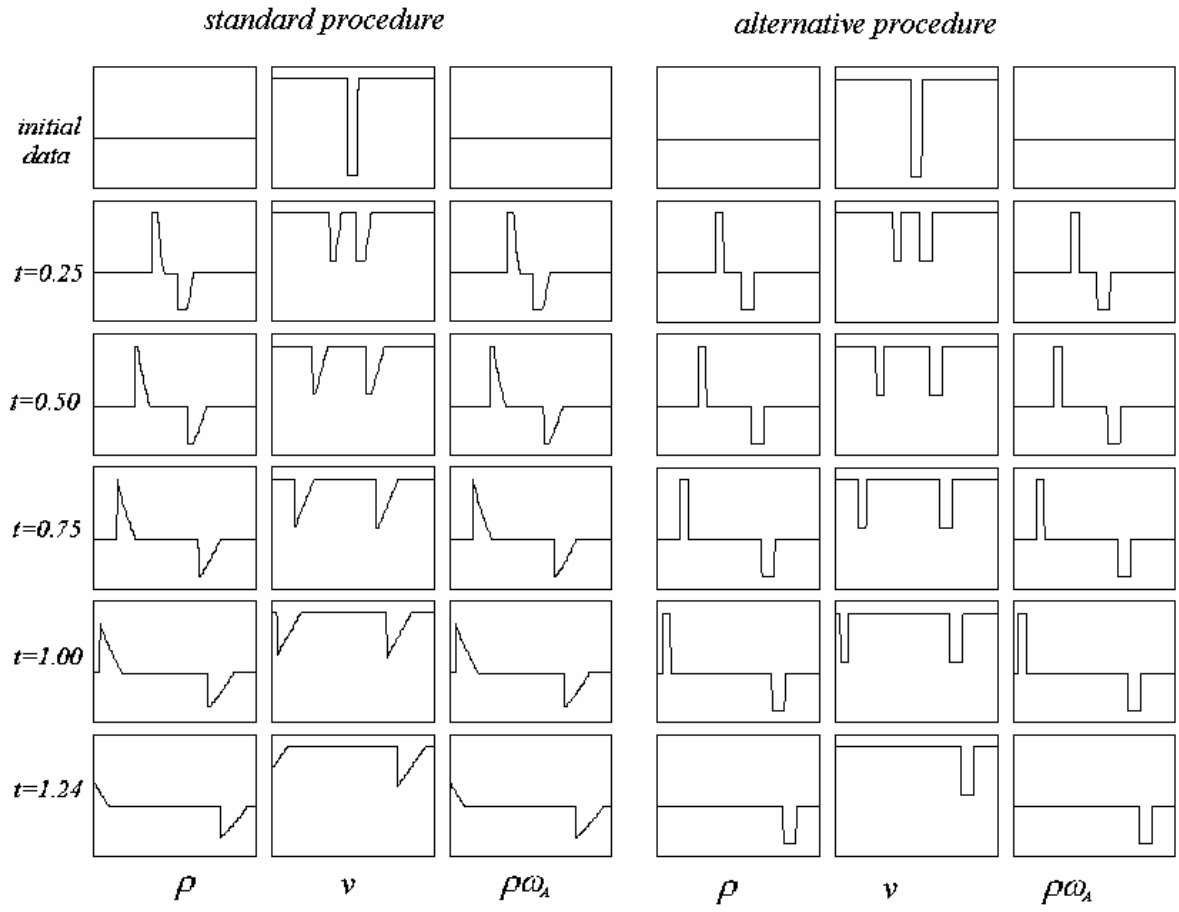

Figure 2. Gas density, velocity and pollutant concentration per unit volume variation with position - Left: Riemann exact solution; Right: Riemann solver. Initial data: constant ρ and ω_A and a small low velocity region for v.

In Fig. 1 the initial data consist of a shock prescribed for the velocity while constant values are prescribed for both the mass density and the concentration of the constituent *A* (pollutant) in the mixture. Since the results obtained through the exact solution of Riemann problem – depicted at the first three columns –give rise essentially to connections by shocks, the Riemann solver presented in this work (depicted at the three last columns) shows a very good agreement with those obtained by employing the exact solution. It is important to mention that a relatively small number of time steps (namely 300) was employed for all the considered cases, resulting in a very rapid convergence in both cases.

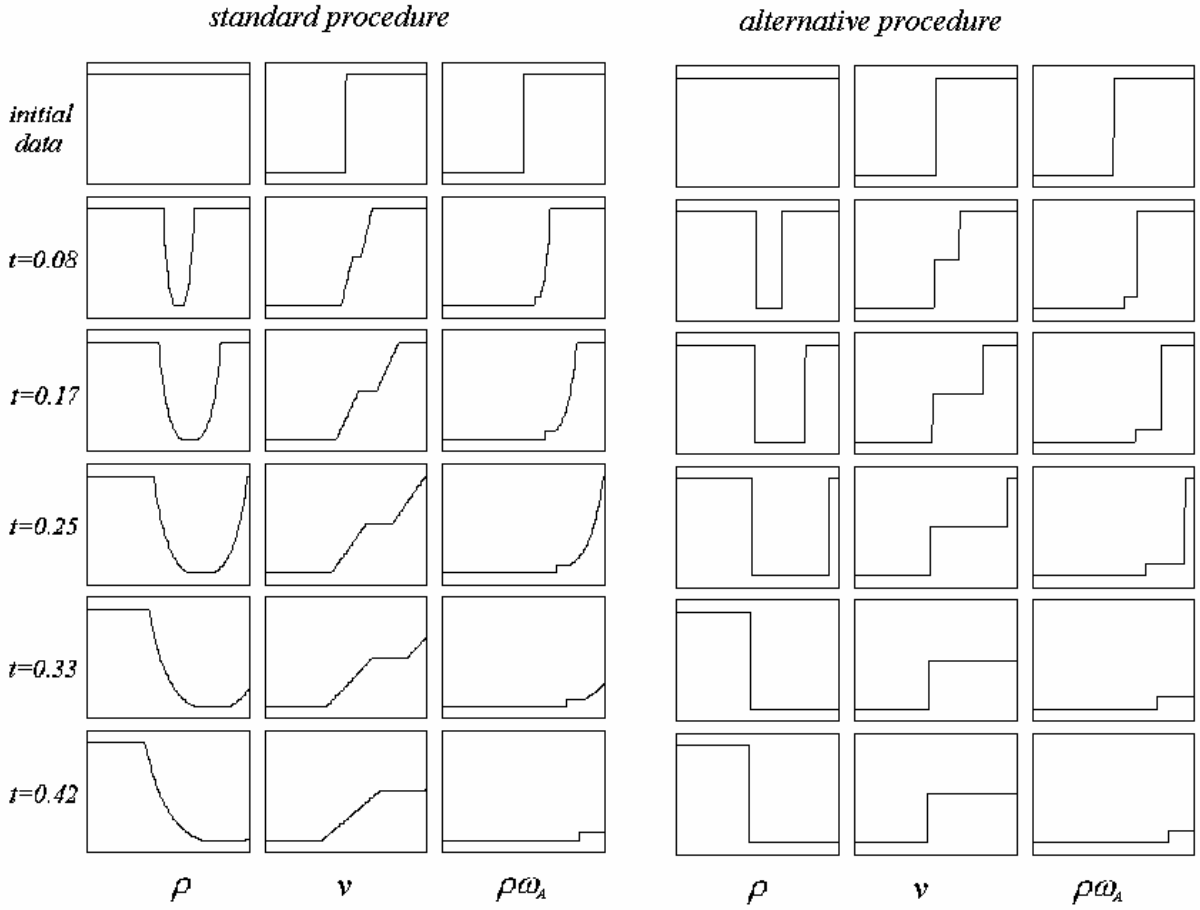

Figure 3. Gas density, velocity and pollutant concentration per unit volume variation with position - Left: Riemann exact solution; Right: Riemann solver. Initial data: constant ρ and distinct step functions for v and ω_A, being $v_L > v_R$ and $\omega_{AL} < \omega_{AR}$

Figure 2 has been obtained by considering as initial data a constant (unit) value for the mass density ρ and a constant value for the pollutant concentration ($\omega_A = 0.5$). A very small low velocity region (with $v = -1.0$) was imposed near the center of the depicted domain, while outside this region a higher value ($v = 0$) has been considered. Comparing the results obtained through Riemann problem exact solution to those using the alternative procedure proposed in this work, a good agreement may be noticed, the shocks being at the same spatial position in both cases, although the proposed Riemann solver is – as expected – unable to capture exactly the connections by rarefactions obtained in the exact solution.

Figure 3 has been obtained by considering as initial data a constant (unit) value for the mass density ρ, step functions for the velocity – placed near the center of the depicted domain, being $v_L > v_R$ and another step function for ω_A, with $\omega_{AL} < \omega_{AR}$, its jump absolute value being ten times smaller than the velocity one. A tendency to present a very low density region – which size increases with time – may be detected by observing Figure 3. Comparing the results obtained by the standard (exact) procedure with those obtained through the proposed Riemann solver, although

the shocks are at the same spatial position in both cases, the alternative procedure was unable to capture the smooth connections presented when the exact solution is used, due to this Riemann solver philosophy which consists in substituting both continuous and discontinuous solutions by shocks.

It is worth mentioning that the three columns at the left hand side of figures 2 and 3 have already been presented in Martins-Costa and Saldanha da Gama (2003), in which they are compared aiming at analyzing the influence of discontinuities imposed on the velocity field in an infinite domain.

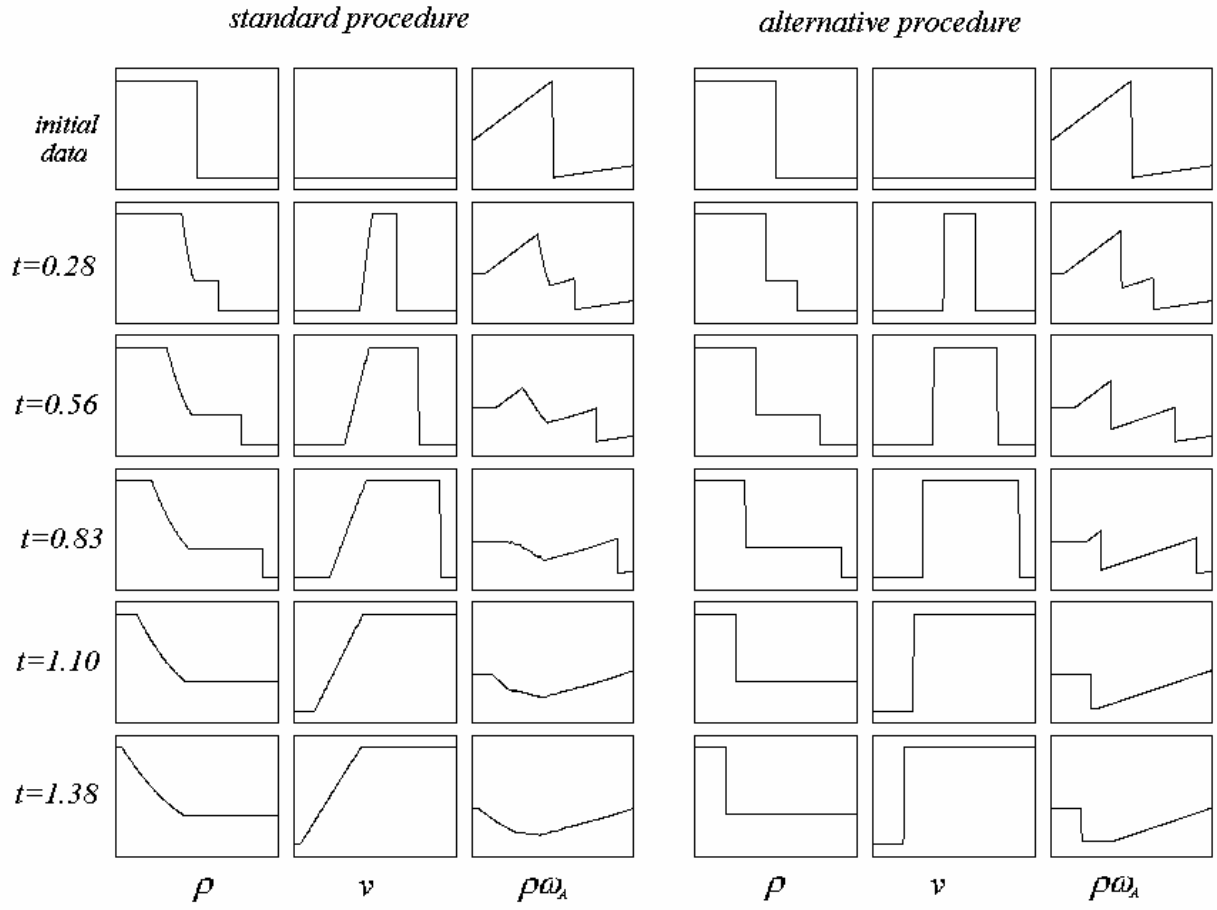

Figure 4. Gas density, velocity and pollutant concentration per unit volume variation with position - Left: Riemann exact solution; Right: Riemann solver. Initial data: zero v and step function for ρ and a discontinuous ω_A with two distinct linear functions.

Figure 4 shows results for gas density, velocity and pollutant concentration per unit volume variation with position considering both the exact and the approximate solution for the associated Riemann problem and initial conditions given by zero v and step function for ρ and a discontinuous ω_A with two decreasing linear functions with distinct inclination. As expected, all the connections by shocks obtained through the exact solution are preserved at their exact position by employing the Riemann solver.

6. Final remarks

Glimm's method is a convenient tool for solving nonlinear hyperbolic problems, exhibiting features such as low storage costs (no matrix storage is required – only 10 vectors with 300 positions have been used) and low computational effort (circa 2 minutes CPU time in a Pentium IV, 2.4 GHz, 128 Mb RAM), when compared to other numerical procedures to approximate nonlinear problems.

Regarding its accuracy, the method is free from numerical dissipation – preserving shock waves magnitude and presenting a deviation from the correct position smaller than the width of each step – preserving shock waves position. Besides, if the width of the steps tends to zero, Glimm's approximation tends to the exact solution of the problem. However, two important shortcomings of this methodology must be mentioned: the former its applicability being restricted to one-dimensional problems and the latter its implementation requiring previous knowledge of a solution of the associated Riemann problem – usually not an easy task.

The numerical methodology presented in this work allowed the good approximation of a nonlinear system of three partial differential equations representing mathematically the transport of a pollutant in the atmosphere. Additional effects not considered in this work such as diffusion of the pollutant in the atmosphere, generation of the pollutant (by chemical reactions, for instance) as well as gravitational effects could be accounted for by employing an operator splitting technique (see Martins-Costa and Saldanha da Gama, 2001 and references therein).

7. Acknowledgement

The authors M.L. Martins-Costa and R.M. Saldanha da Gama gratefully acknowledge the financial support provided by the agency CNPq.

8. References

Chorin AJ, 1976, Random choice solution of hyperbolic systems. J. Comput. Physics. Vol. 22, pp. 517-533.

Glimm J., 1965, Solutions in the large for nonlinear hyperbolic systems of equations. Comm. Pure Appl. Math. Vol. 18 pp. 697-715.

John F., 1974, Formation of singularities in onedimensional nonlinear wave propagation. Comm. Pure Appl. Math. Vol. 27, pp. 337-405.

John F., 1982, Partial Differential Equations. Berlin, Springer-Verlag.

Keyfitz, B., Kranzer, H., 1978, Existence and uniqueness of entropy solutions to the Riemann problem for hyperbolic systems of two nonlinear conservation laws. J. Diff. Eqns. Vol. 27, pp. 444-476.

Lax, P., 1971, Shock Waves and Entropy, in Contributions to Nonlinear Functional Analysis. New York: Academic Press.

Martins-Costa, M.L. and Saldanha da Gama, R.M., 2003, "Glimm's Method Simulation for the Pollutant Transport in an Isothermal Atmosphere", Comput. Mech., Vol. 32, No. 3, pp. 214-223.

Saldanha da Gama, R.M., 1990, An Alternative Procedure for Simulating the Dynamical Response of Non-Linear Elastic Rods, Int. J. Num. Meth. Engng., Vol. 29, pp. 123-139.

Smoller J., 1983, Shock-Waves and Reaction-Diffusion Equations. Berlin, Springer-Verlag.

9. Copyright Notice

Paper CIT06-1037

ESTUDO EXPERIMENTAL E NUMÉRICO DE ESCOAMENTO COM BAIXOS NÚMEROS DE REYNOLDS EM PLACA DE ORIFÍCIO DE ENTRADA CÔNICA

Mara Nilza Estanislau Reis
Centro Federal de Educação Tecnológica de Minas Gerais – Av. Amazonas, 5253 – Nova Suiça – Belo Horizonte – MG – Brasil – CEP 30480-000.
Departamento de Engenharia Mecânica da Pontifícia Universidade Católica de Minas Gerais - Av.Dom José Gaspar, 500 – Coração Eucarístico – Belo Horizonte – MG – Brasil –
CEP 30535-610.
mara@pucminas.br

Cleide Barbosa Soares
Centro Federal de Educação Tecnológica de Minas Gerais – Av. Amazonas, 5253 – Nova Suiça – Belo Horizonte – MG – Brasil – CEP 30480-000.
cleide.barbosa@ig.com.br

Leonardo Roberto da Silva
Centro Federal de Educação Tecnológica de Minas Gerais – Av. Amazonas, 5253 – Nova Suiça – Belo Horizonte – MG – Brasil – CEP 30480-000.
lrsilva@feb.unesp.br

Geraldo Augusto Campolina França
Departamento de Engenharia Mecânica da Universidade Federal de Minas Gerais - Av. Antônio Carlos 6627 – Pampulha – Belo Horizonte – MG – Brasil – 31270-901
franca@demec.ufmg.br

J. A. Soares
Estudante de Engenharia de Controle e Automação da Pontifícia Universidade Católica de Minas Gerais – Av. Dom José Gaspar, 500 – Coração Eucarístico – Belo Horizonte – MG – Brasil –
CEP 30535-610
joaosoares@yahoo.com.br

C. H. L. Fossa
Estudante de Engenharia de Controle e Automação da Pontifícia Universidade Católica de Minas Gerais – Av. Dom José Gaspar, 500 – Coração Eucarístico – Belo Horizonte – MG – Brasil –
CEP 30535-610
cal_bhz@yahoo.com.br

Resumo. Apesar dos avanços tecnológicos que permitem disponibilizar medidores de vazão cada vez mais sofisticados, destacam-se os medidores do tipo pressão diferencial, dentre os quais os mais difundidos são placa de orifício, venturi e bocal.Para escoamentos com baixos números de Reynolds, não devem ser utilizadas placas de orifício de canto vivo, devido uma grande variação do coeficiente de vazão em função do número de Reynolds (BS 1042). Nesta situação, utilizam-se placas de orifício de entrada cônica. As placas de orifício de entrada cônica mantêm constante o valor do coeficiente de vazão mesmo para baixos números de Reynolds, tornando-as adequadas para medição de vazões de fluidos viscosos. Neste trabalho é feito um estudo experimental e numérico do escoamento com baixos números de Reynolds em placa de orifício de entrada cônica com relação de diâmetros, $\beta = 0{,}53$. Alguns modelos de turbulência foram usados nas simulações através do software CFX. Os coeficientes de vazão foram comparados com os dados experimentais disponíveis e com os valores recomendados pela norma BS 1042. Os resultados numéricos estão em boa concordância com os experimentais para o número de Reynolds abaixo de 3150 na tubulação.

Palavras chave*: placas de orifício de entrada cônica, coeficiente de vazão, modelamento numérico, metodologia experimental.*

1. Introdução

A placa de orifício mantém-se ainda como um dos elementos primários mais usados na medição de vazão na indústria e, apesar do avanço tecnológico que tem disponibilizado medidores de vazão cada vez mais sofisticados, não se espera que a participação desse dispositivo no mercado seja inferior a 40% num futuro próximo. Devido à simplicidade de instalação e manutenção, boa exatidão e custo relativamente baixo, os medidores do tipo orifício representam ainda cerca de 80% dos sistemas de medição de vazão nos diversos segmentos industriais. Dentre esses

medidores, as placas de orifício são as mais utilizadas, pois, além das vantagens já citadas, têm uma ampla aplicabilidade, inclusive para fluidos corrosivos (Martins, 1998).

A placa de orifício concêntrico de cantos vivos foi extensivamente estudada. Para altos números de Reynolds o coeficiente de vazão é bem definido chegando a ser quase constante. Para escoamentos com baixos números de Reynolds, como normalmente acontece para fluidos viscosos, as placas de orifício concêntrico de cantos vivos não podem ser utilizadas, pois neste caso apresentam uma grande variação do coeficiente de vazão em função do número de Reynolds. Tendo em vista a importância industrial da medição de tais fluidos, existe um grande interesse entre usuários dos medidores de vazão do tipo pressão diferencial em todo o dispositivo que possua um coeficiente de vazão constante para baixos números de Reynolds. Vários perfis de placas foram experimentados para casos de medição de vazão onde o número de Reynolds é relativamente baixo. Das várias formas experimentadas, algumas são mais difundidas e comentadas em normas como a AFNOR NF 10-101 ou a BS 1042 [1989]. A placa de orifício de entrada cônica é a forma que se revelou mais adequada para medição de vazão de fluidos viscosos com baixos números de Reynolds, conforme ilustra a Fig.1.

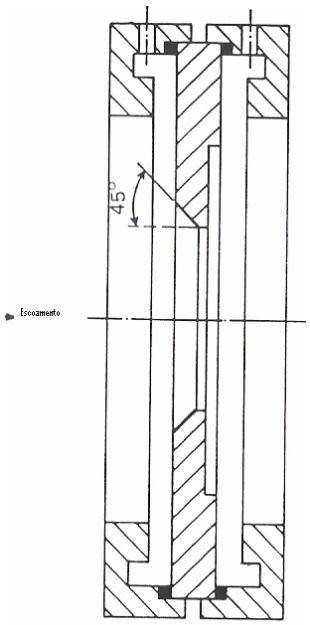

Figura 1. Representação Esquemática da Placa de Orifício de Entrada Cônica.

A placa de orifício de entrada cônica foi inicialmente desenvolvida em 1930 por H.E. Dall da George Kent Ltd assim como Kent PL. Alguns dados sobre Kent PL estão disponíveis nas especificações de patentes dos Estados Unidos (US Patent, 1938), e Linford (1961) referenciados no trabalho de Dall, que resultaram nas curvas características apresentando as variações do coeficiente de vazão em função do número de Reynolds. Os dados da placa de orifício de entrada cônica são mencionados na BS 1042: Parte 1: 1964 e são baseados na informação obtida pela George Kent Ltd. A placa com orifício de entrada cônica é usada em aplicações onde o número de Reynolds inferior varia de 25 a 75, de acordo com o valor da relação β.

Desde a publicação da BS 1042: Parte 1: 1964 foram exploradas as características da placa de orifício de entrada cônica por vários pesquisadores (Kastner e McVeigh, 1965; Stoll e Zientara, 1974; McVeigh, 1974; Turton, 1975; Ho e Leung, 1985). Entretanto, muitos dos resultados obtidos nestes estudos foram em placas de orifício de entrada cônica que não atendem as especificações de dimensionamento recomendadas pela norma. Deste modo, poucos resultados experimentais sobre as placas de orifício de entrada cônica que satisfazem às especificações da norma estão relativamente disponíveis, fazendo-se necessário um estudo mais aprofundado sobre suas características.

As características dos medidores de vazão são afetadas por vários parâmetros, dentre as quais, existe uma grande variação da escala em relação aos valores encontrados na prática. Devido ao grande avanço tecnológico na área computacional, simulações numéricas podem ser feitas com descrição espacial detalhada das grandezas de interesse e sua evolução ao longo do tempo, rapidez e baixo custo, qualidades difíceis de serem obtidas nas simulações experimentais. O esforço experimental pode ser então extremamente reduzido. Assim, o uso do modelo apropriado da simulação de turbulência no computador pode ser de extremamente útil no estudo da performance dos medidores de vazão.

Neste trabalho é feito um estudo experimental e numérico do escoamento com baixos números de Reynolds em placa de orifício de entrada cônica com relação de diâmetros, $\beta = 0{,}53$. Alguns modelos de turbulência foram usados nas simulações através do software CFX.

Os coeficientes de vazão foram comparados com os dados experimentais disponíveis e com os valores recomendados pela norma BS 1042 [1989].

Os resultados numéricos estão em boa concordância com os experimentais para o número de Reynolds abaixo de 3150 na tubulação.

2. Descrição geral e funcionamento do banco de fluxo

O banco de fluxo consiste em uma bancada experimental para estudo do escoamento transiente em um sistema de medição de vazão do tipo placa de orifício. Para tal estudo, a propagação de uma flutuação de vazão conhecida é relacionada a uma flutuação de pressão, permitindo a calibração dinâmica do sistema de medição. A flutuação de vazão em torno de um escoamento médio, também conhecido, é produzida pelo movimento harmônico de um êmbolo. A variação de pressão através do orifício é determinada experimentalmente através de transdutores de pressão acoplados a um sistema de aquisição dinâmica de dados.

O esquema geral do sistema é mostrado na Fig. 2.

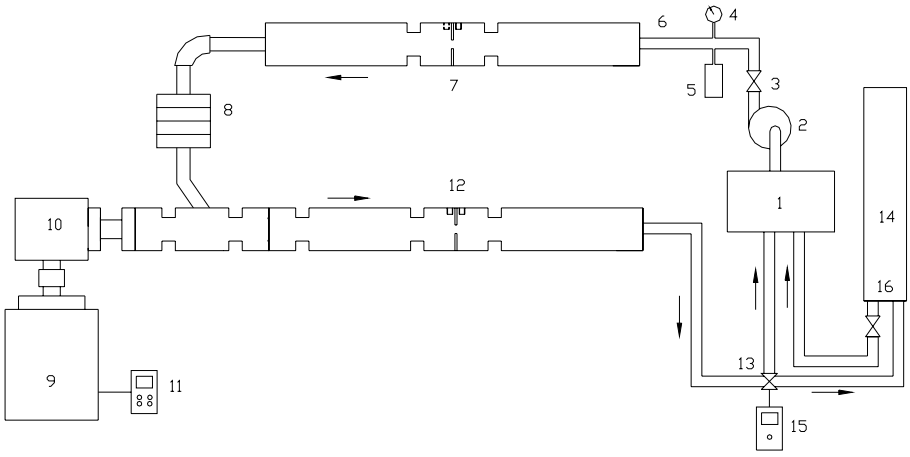

Figura 2. Esquema Geral do Banco de Fluxo.

Utilizando a Fig. 2 é apresentada a seguir uma descrição completa do banco de fluxo utilizado para o estudo do escoamento transiente (pulsante) de líquidos.

O óleo contido no tanque de armazenamento (l) é bombeado pela bomba de palhetas (2) a uma vazão constante Q_b. A vazão da bomba é controlada por uma válvula reguladora de vazão com compensação de temperatura (3). Um acumulador (5) utilizando gás nitrogênio a 4 bar de pressão é responsável pela minimização da pulsação provocada pela bomba na linha. O óleo segue pela tubulação de acrílico (6) até o primeiro sistema de medição de vazão (7). Este sistema é constituído pela mesma placa de orifício utilizada no sistema dinâmico e dois transdutores de pressão do tipo capacitivos. Sua finalidade é comprovar que o comprimento de tubo reto utilizado no sistema de medição de vazão dinâmica é grande o bastante para não interferir nos valores de vazão encontrados em regime permanente. Depois de passar pelo amortecedor tipo ressonador em série (8), o óleo entra em contato com o gerador de flutuação de vazão (10) através de uma ramificação presente na tubulação. Este dispositivo é acionado por um motor de corrente alternada (9), sendo sua rotação alterada pelo uso de um inversor de freqüência (11). Em seguida, o óleo segue para o segundo sistema de medição de vazão (12), constituído por uma placa de orifício e um par de transdutores de pressão capacitivos. Quando o gerador de pulsos é acionado, o sistema (12) indica uma diferença de pressão que equivale a uma vazão média acrescida de uma flutuação de vazão amortecida e defasada. O amortecedor (8), associado à inclinação do tubo que leva o óleo ao sistema de medição de vazão dinâmica, tem como finalidade impedir a propagação desta flutuação para o sistema de medição (7). Depois de passar pelo sistema de medição dinâmica (12), o óleo passa por uma válvula direcional (13), que alterna o caminho percorrido pelo óleo entre a cuba de medição (14) e o tanque (1). Para a calibração do sistema e determinação da vazão estática Q_o, utiliza-se um temporizador (15), que atua sobre a abertura da válvula direcional, permitindo a entrada do óleo circulante para a cuba graduada durante um determinado intervalo de tempo.

2.1. A Placa de orifício

A placa possui orifício de entrada cônica, de diâmetro (d = 11,6 mm), com relação de diâmetros β = 0,53 foi construída segundo a norma BS 1042. O orifício de entrada cônica, mostrado na Fig.3, é usado em aplicações onde o número de Reynolds inferior varia entre 80 e $2x10^5\beta$.

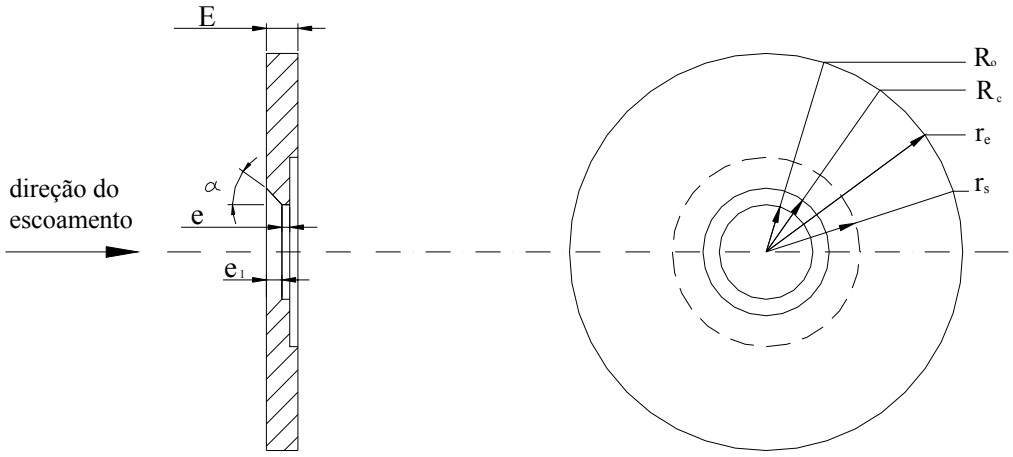

Figura 3. Placa de Orifício Cônica.

A Tabela 1 contém as dimensões da placa utilizada no experimento.

Tabela 1 - Dimensões (em mm) da placa de orifício de entrada cônica.

Placa de entrada cônica								
d/D = β	R_o	r_e	E	e	e_1	α	R_c	r_s
0,53	5,8	28,5	3,0	0,2	0,5	45,0	6,15	23,2

3. O modelo numérico

3.1. O código computacional

O pacote CFX apresenta um código *CFD* com aplicação geral, que utiliza o método dos volumes finitos. O pacote combina um processo avançado de resolução de equações discretizadas com ferramentas de pré e pós-processamento. Nos métodos tradicionais de modelamento com códigos *CFD*, geometrias complexas apresentam grandes limitações e requerem grandes investimentos e tempo para definir o problema. O pacote CFX supera estas dificuldades ao incorporar um pré-processamento baseado em *CAD* (desenho assistido por computador) para a geometria e malha o *ANSYS WORKBENCH*, que apresenta ferramentas para a criação de geometrias e um gerador automático de malhas não estruturadas. O pacote apresenta ainda um pré-processador físico, CFX-Pre, que permite definir todas as características físicas do problema, material, modelo de turbulência, etc., com grande detalhe e ampla gama de opções, e ainda um pós-processador, CFX-Post, que oferece inúmeras ferramentas para tratamento quantitativo e qualitativo dos resultados.

O conjunto de equações resolvidas são as equações transientes de Navier-Stokes na sua forma conservativa.

3.2. Modelo de turbulência

A placa de orifício de entrada cônica é essencialmente usada nas condições de baixo número de Reynolds. Portanto, um modelo turbulento de baixo número de Reynolds seria necessário para o estudo de suas características. Uma das vantagens da formulação *k-ω* é o tratamento próximo da parede para computações com baixo número de Reynolds, modelo desenvolvido por Wilcox (1986). O modelo não envolve as funções complexas não lineares requeridas para o modelo do *k-ε* e é consequentemente mais exato e mais robusto. Um modelo *k-ε* de baixo Reynolds exigiria tipicamente uma definição próxima da malha muito refinada, enquanto um modelo *k-ω* requer um refinamento dez vezes menor. Em escoamentos industriais, mesmo refinamentos dez vezes menores não podem ser garantidos na maioria das aplicações e para esta razão, um novo tratamento próximo da parede foi desenvolvido para os modelos *k-ω*. Ele permite o deslocamento suave de uma formulação de baixo Reynolds para uma formulação de função de parede. (Neto, 2004)

O problema principal com o modelo *k-ω* é sua sensibilidade forte às condições de escoamento livre. Dependendo do valor especificado para *ω* na entrada, uma variação significativa nos resultados do modelo pode ser obtida. O modelo *S.S.T.,* desenvolvido por Menter (1993), consiste em uma transformação do modelo do *k-ε* a uma formulação *k-ω* e uma adição subseqüente das equações correspondentes. O modelo *k-ω* é multiplicado desse modo por uma função acopladora *F1* e o modelo transformado *k-ε* por uma função *1-F1*. *F1* se torna igual a um perto da superfície e a zero na camada limite. Na borda e na parte externa da camada limite, o modelo padrão do *k-ε* é recuperado. O modelo leva em consideração o transporte das tensões turbulentas e dá predições altamente exatas do início e da quantidade de separação do escoamento sob gradientes adversos de pressão. As equações finais do modelo são as seguintes:

A equação k:

$$\frac{\partial(\rho k)}{\partial t} + \nabla \bullet (\rho U k) = \nabla \bullet \left[\left(\mu + \frac{\mu_t}{\sigma_{k3}} \right) \nabla k \right] + \left(P_k - \beta' \rho k \omega \right) \tag{1}$$

Onde: *k* é a energia cinética turbulenta e *Pk* é o produto turbulento devido a viscosidade e forças de empuxo.

A equação *ω*:

$$\frac{\partial(\rho \omega)}{\partial t} + \nabla \bullet (\rho U \omega) = \nabla \bullet \left[\left(\mu + \frac{\mu_t}{\sigma_{\omega 3}} \right) \nabla \omega \right] + (1 - F1) 2\rho \frac{1}{\sigma_{\omega 2} \omega} \nabla k \nabla \omega + \alpha_3 \frac{\omega}{k} P_k - \beta_3 \rho \omega^2 \tag{2}$$

Onde: ω é a freqüência turbulenta.

Além às variáveis independentes, a densidade, ρ, e o vetor da velocidade, *U*, são tratados como as quantidades sabidas do método de Navier Stokes.

Os coeficientes do modelo novo são uma combinação linear dos coeficientes correspondentes dos modelos subjacentes:

$$\Phi_3 = F1 \Phi_1 + (1 - F1) \Phi_2 \tag{3}$$

Sendo Φ_1 os coeficientes do modelo *k-ω* e Φ_2 os coeficientes do modelo *k-ε*.

O comportamento apropriado do transporte pode ser obtido por um limitador a formulação da viscosidade turbulenta:

$$v_t = \frac{a_1 k}{\max(a_1 \omega, SF2)} \tag{4}$$

Onde: $v_t = \mu_t / \rho$ (5)

F2 é uma função de acoplamento, que restringe o limitador à camada limite da parede, porque as suposições subjacentes não estão corretas para escoamentos livres. *S* é uma medida invariante da taxa da tensão.

As funções de acoplamento são criticas ao sucesso do método. Sua formulação é baseada na distância à superfície mais próxima e nas variáveis do escoamento.

$$F1 = \tanh\left(\arg_1^4\right)$$
$$\arg_1 = \min\left[\max\left(\frac{\sqrt{k}}{\beta' \omega y}, \frac{500v}{y^2 \omega} \right), \frac{4\rho k}{CD_{kw} \sigma_{\omega 2} y^2} \right] \tag{6}$$

Onde *y* é a distância à parede mais próxima e *v* é a viscosidade cinemática e:

$$CD_{k\omega} = \max\left(2\rho \frac{1}{\sigma_{\omega 2} \omega} \nabla k \nabla \omega, 1x10^{-10} \right) \tag{7}$$

$$F2 = \tanh\left(\arg_2^2\right)$$
$$\arg_2 = \max\left(\frac{2\sqrt{k}}{\beta' \omega y}, \frac{500v}{y^2 \omega} \right) \tag{8}$$

Essas equações, juntamente com as da conservação de massa e a de momento, foram aplicadas para o escoamento através da placa de orifício de entrada cônica; considerando que o escoamento é constante e laminar. As coordenadas cilíndricas e polares foram utilizadas no modelamento matemático.

3.3. Geometria da placa

A seção da placa de orifício utilizada no modelamento numérico encontra-se representada na Fig.4.

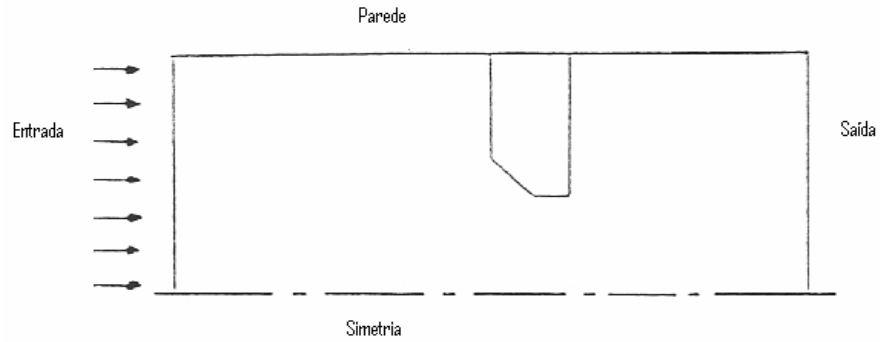

Figura 4. Representação da Seção Utilizada no Modelamento Numérico.

O parâmetro utilizado para criar a malha é o comprimento de escala, que é o tamanho máximo do elemento triangular a ser criado nas faces do sólido.

Nas regiões onde o escoamento apresenta grandes gradientes de velocidade, vórtices ou alguma característica que seja importante é necessário densificar a malha criando o que se chama de refino de malha.

A geometria utilizada inicialmente foi uma simetria de 1/8 que equivale a um ângulo de 45º.

O comprimento de escala utilizado foi de 0,9mm, ou seja, o maior elemento tem 0,9mm.

Na região refinada, mostrada na Fig. 5, que fica nas proximidades da placa de orifício, o comprimento de escala utilizado foi de 0,3mm.

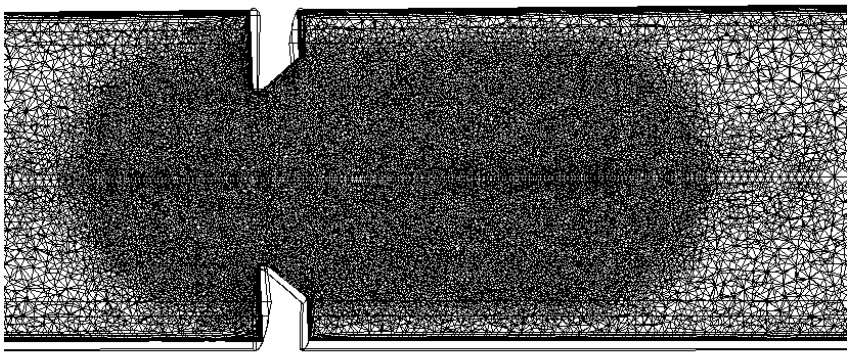

Figura 5. Refino da Malha Próximo a Placa de Orifício.

Além disso, foi criado um tipo de refino próximo à parede do tubo, chamado *Inflation*, que é a região estruturada na vizinhança da parede. Para o *inflation*, foram criadas 7 camadas, com o comprimento total máximo das 7 camadas de 2 mm, Fig. 6.

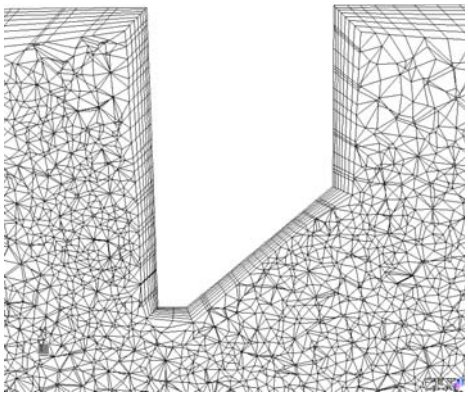

Figura 6. Detalhe do Refino e do *Inflation.*

O coeficiente de vazão é o parâmetro de maior importância para um medidor do tipo pressão diferencial. Conseqüentemente, pode se dizer que modelo correto foi obtido quando a escolha dos trechos retos de 55 D a montante e 16 D a jusante da placa de orifício foram suficientemente grandes, de modo que quaisquer acréscimos nestes trechos não afetaram no resultado do coeficiente de vazão. Um maior refinamento de malha foi feito para que o coeficiente de vazão continuasse inalterado.

Os limites de aplicação para placas de orifício de entrada cônica estão especificados na BS 1042: Seção1.2: 1989 para relações de diâmetros, β, $0{,}1 \leq \beta \leq 0{,}316$, e para o número de Reynolds na tubulação $Re_D\, 80 \leq Re_D \leq 2x10^5 \beta$. Os testes foram realizados com a relação de diâmetros, $\beta = 0{,}53$ e com o valor de Reynolds Re_D de 3150.

3.4. Condições de contorno

As condições de contorno do problema são:
- fronteira oeste em (z = 0): velocidade prescrita na entrada (vazão conhecida);
- fronteira leste em (z = L): escoamento localmente parabólico;
- fronteira norte em (r = R): parede impermeável;
- fronteira sul em (r = 0): simetria.

A Fronteira Norte é constituída pela parede do tubo, onde as velocidades são iguais a zero.

$$v_z = 0 \qquad v_r = 0 \tag{9}$$

A Fronteira Sul é constituída pelo centro do tubo, onde é imposta a condição de simetria.

$$\frac{\partial v_z}{\partial r} = 0 \qquad \frac{\partial v_r}{\partial r} = 0 \qquad \text{ou} \quad (v_r(t) = 0) \tag{10}$$

A Fronteira Oeste corresponde a extremidade da tubulação, a montante da placa de orifício, onde inicia-se a análise. O comprimento da tubulação até a face de entrada da placa de orifício é 15 D. Este comprimento de entrada é sugerido pela ISO 5167 [1991] como sendo suficiente para que o perfil de velocidade desenvolva-se totalmente.

$$v_z = 2\overline{U}\left[1 - \left(\frac{r}{R}\right)^2\right] \tag{11}$$

$$v_r = 0$$

Onde $\overline{U}$ é obtida a partir da vazão total $Q_t(t)$ ou Q_o.

A Fronteira Leste corresponde à última seção da tubulação, a jusante da placa de orifício, analisada durante a simulação. A distância desta tubulação à face de saída da placa de orifício é de 55 D. Considerou-se que esta distância da placa de orifício foi suficiente para que o perfil de velocidade novamente se desenvolvesse.

4. Resultados

O modelo numérico S.S.T. foi usado para simular a vazão através de uma placa de orifício de entrada cônica. Resultados numéricos foram obtidos usando tubulação de 21,89 mm de diâmetro, sendo o fluido utilizado óleo hidráulico Móbil DTE 24 (ISO VG 32) com densidade de 864 kg/m^3 e viscosidade absoluta de 26,78 x 10^{-3} Pa.s.

As dimensões reais para a placa de orifício de entrada cônica foram utilizadas na simulação.

Os coeficientes de vazão obtidos a partir dos resultados da simulação estão apresentados na Tab.2. Para a placa de orifício de entrada cônica, o valor do coeficiente de vazão é dado na BS 1042: Seção 1.2: 1989 foi de 0.734 (com incerteza de 2%) para valores de Reynolds entre 80 e 2 x $10^5\beta$. Assim, pode-se observar que o modelo desenvolvido pode nos predizer o valor do coeficiente de vazão entre ±3% do valor determinado pela norma.

Com a necessidade de verificar a validação do modelo, os coeficientes de vazão obtidos numericamente devem ser comparados com os resultados experimentais disponíveis. Apenas um número limitado de resultados experimentais havia sido publicado sobre a placa de orifício de entrada cônica (Kastner e McVeigh, 1965; Stoll e Zientara, 1974; McVeigh, 1974; Turton, 1975; Ho e Leung, 1985). Das informações disponíveis, aquelas apresentadas por Stoll e Zientara, cobriram uma grande margem de valores de Reynolds e relações de diâmetros, β. Os outros trabalharam com uma margem limitada.

Tabela 2 - Coeficientes de vazão obtidos numericamente.

β	Re	Cd
0,53	80	0,7239 (-1,38%)
	1000	0,7476 (1,85%)
	2000	0,7520 (2,45%)
	4000	0,7545 (2,79 %)
	6000	0,7556 (2,94%)
	10000	0,7492 (2,07 %)

A Figura 7 mostra o coeficiente de vazão obtido numericamente com os resultados experimentais obtidos e de Stoll e Zientara. O coeficiente de vazão calculado numericamente é relativamente menor que os dados experimentais para os valores de baixos Reynolds e maiores que os dados experimentais para os valores de altos Reynolds. Enquanto os dados experimentais mostram um decréscimo do coeficiente de vazão em um valor crítico de Reynolds de 2000, o modelo numérico tende a predizê-lo com um valor maior de Reynolds. A comparação do coeficiente de vazão obtido numericamente com os resultados experimentais pode ser considerada razoável.

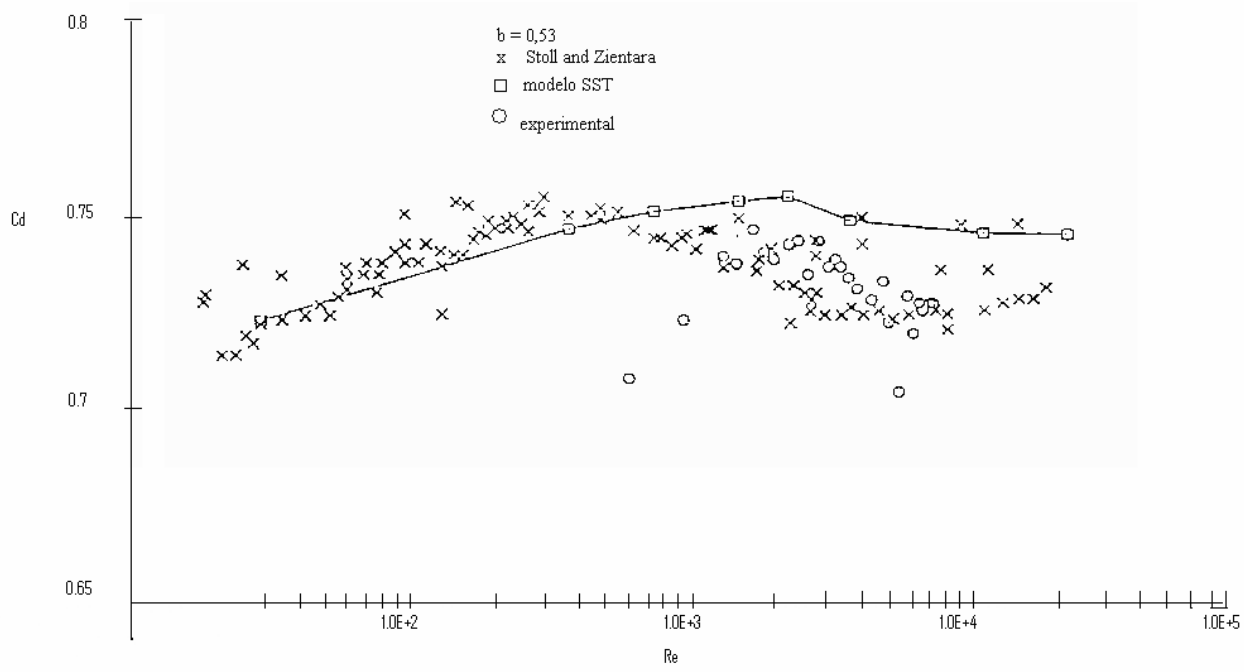

Figura 7. Comparação Entre os Valores Obtidos Numericamente e Experimentalmente.

5. Conclusões

O trabalho apresentado neste documento mostra a aplicação do modelo *S.S.T.,* para a simulação de vazão através da placa de orifício de entrada cônica. O modelo numérico desenvolvido mostra que é capaz de predizer o valor do coeficiente de vazão da placa de orifício de entrada cônica com um erro de até ±3% do valor estabelecido na norma e encontrado experimentalmente. Como existe um número limitado de resultados experimentais disponíveis sobre as características da placa de orifício de entrada cônica, o modelamento numérico pode ser bastante útil para fornecer maiores dados sobre estas características.

Assim, o uso do modelo apropriado de turbulência na simulação pode ser extremamente útil no estudo da performance da placa de orifício de entrada cônica, isso, somado com os experimentos realizados, ajudará a direcionar para uma melhor compreensão dos dados obtidos, acarretando em uma melhor utilização da placa de orifício de entrada cônica como um medidor de vazão para baixos números de Reynolds.

6. Referências

AEA Technology plc. CFX-5.7 Documentation, 2003, AEA Technology Engineering Software Ltd, United Kingdom.

BS 1042, 1989, "Measurement of Fluid Flow in Closed Conduits" (Section 1.2) – British Standard Institution.

Ho, Y. S., and Leung, T. P., 1985, "Performance of conical entrance orifice plates at low Reynolds numbers". Int J Heat & Fluid Flow, 6(2), June, pp.122-125.

ISO 5167-1, 1991, "Measurements of Fluid Flow by Means of Pressure Diferential Devices" – part 1: Orifice Plates, Nozzles and Venturi Tubes Inserted in Circular Cross- section Conduits Running Full – International Organization for Standardization.

ISO/TR 3313, 1994, "Measurements of Pulsating Flow in a Pipe by Means Orifice Plates, Nozzles or Venturi Tubes Inserted, in Particular in the case of sinusoidal or Square Wave Intermitent Periodic Type Fluctuations" – International Organization for Standardization.

Kastner, L. J., and McVeigh, J. C., 1965, "A reassessment of metering orifices for low Reynolds numbers". Proc Instn Mech Engrs, 180(Part 1) (13), pp.331-345.

Launder, B. E., and Spalding D. B., 1974, "The numerical computation of turbulence flows". Computer Methods in Applied Mechanics and Engineering, 3, pp. 269-289.

Martins, N., 1998, "Manual de medição de vazão: através de placas de orifício, bocais e venturis". Rio de Janeiro: Interciência: Petrobrás, 297p.

McVeigh, J. C., 1974, "The effect of installation conditions on the discharge coefficient of the conical entrance orifice plate at low Reynolds numbers". Flow, Its Measurement and Control in Science and Industry. 1(2), pp.533-537 Intrument Society of América.

Menter, F. R., 1993, "Multiscale model for turbulent flows". Na 24th Fluid Dynamics Conference. American Institute of Aeronautics and Astronautics.

Menter, F. R., 1994, "Two-equation eddy-viscosity turbulence models for engineering applications". AIAA-Journal., 32(8).

Neto, A. S., 2004, "Turbulência nos Fluidos Aplicada" – Universidade Federal de Uberlândia, Faculdade de Engenharia Mecânica.

Patel, V. C., Rodi, W., and Scheuerer, G., 1985, "Turbulence models for near-wall and low Reynolds number flows: A review". AIAA Journal, 23, Sep, pp.1308-1319.

Stoll, H. W., and Zientara, D., 1974, "The conic entrance orifice plate, An investigation of its performance characteristics". Flow, Its Measurement and Control in Science and Industry, 1(2), pp.517-522. Instrument Society of América.

Turton, R. K., 1975, "A note on flow through conical entrance orifice plates". Conf on Fluid Flow Mearurement in the Mid-1970's, Glasgow, Paper A-3.

Valle, R. M., 1994, "Escoamento Laminar em Placas de Orifício – Análise Teórica e Experimental em Regime Permanente e Transiente", Tese de Doutorado, Universidade Federal de Santa Catarina.

Wilcox, D.C., 1986, "Multiscale model for turbulent flows". Na 24^{o} AIAA (Aerospace Sciences Meeting. American Institute of Aeronautics and Astronautics).

EXPERIMENTAL AND NUMERICAL STUDY OF FLOW WITH LOW REYNOLDS NUMBERS IN CONICAL ENTRANCE ORIFICE PLATE.

Mara Nilza Estanislau Reis
Centro Federal de Educação Tecnológica de Minas Gerais – Av. Amazonas, 5253 – Nova Suiça – Belo Horizonte – MG – Brasil – CEP 30480-000.
Departamento de Engenharia Mecânica da Pontifícia Universidade Católica de Minas Gerais - Av.Dom José Gaspar, 500 – Coração Eucarístico – Belo Horizonte – MG – Brasil – 30535-610.
mara@pucminas.br

Cleide Barbosa Soares
Centro Federal de Educação Tecnológica de Minas Gerais – Av. Amazonas, 5253 – Nova Suiça – Belo Horizonte – MG – Brasil – CEP 30480-000.
cleide.barbosa@ig.com.br

Leonardo Roberto da Silva
Centro Federal de Educação Tecnológica de Minas Gerais – Av. Amazonas, 5253 – Nova Suiça – Belo Horizonte – MG – Brasil – CEP 30480-000.
lrsilva@feb.unesp.br

Geraldo Augusto Campolina França
Departamento de Engenharia Mecânica da Universidade Federal de Minas Gerais - Av. Antônio Carlos 6627 – Pampulha – Belo Horizonte – MG – Brasil – 31270-901
franca@demec.ufmg.br

J. A. Soares
Estudante de Engenharia de Controle e Automação da Pontifícia Universidade Católica de Minas Gerais – Av. Dom José Gaspar, 500 – Coração Eucarístico – Belo Horizonte – MG – Brasil –
CEP 30535-610
joaosoares@yahoo.com.br

C. H. L. Fossa
Estudante de Engenharia de Controle e Automação da Pontifícia Universidade Católica de Minas Gerais – Av. Dom José Gaspar, 500 – Coração Eucarístico – Belo Horizonte – MG – Brasil –
CEP 30535-610
cal_bhz@yahoo.com.br

Abstract

Despite the technological advances that make available ever more sophisticated flow meters, the differential pressure meters stand out. Among the most widely used of them all are orifice plate, venturi and nozzles. For flow with low Reynolds numbers, concentric orifice plates should not be used due to a great variation in the coefficient of discharge resulting from the Reynolds number (BS 1042). In this situation, conical entrance orifice plates are used. The conical entrance plates keep the value of the same coefficient of discharge constant for low Reynolds numbers, therefore lending itself to the measurement of viscous fluid. This paper presents an experimental and numerical study of the flow with low Reynolds numbers in conical entrance plate with diameter ratio,$\beta = 0{,}53$. Some models of turbulence had been used in the simulations through software CFX. The coefficients of discharge were compared with the experimental data available and the values recommended in BS 1042. The numerical results are in good agreement with the experimental results for the Reynolds number below 3150 in the tube.

Keywords: conical entrance orifice plate, coefficient of discharge, numerical modelling, experimental methodology.